SF2A 2012
S. Boissier, P. de Laverny, N. Nardetto, R. Samadi, D. Valls-Gabaud and H. Wozniak (eds)

Proceedings of the annual meeting of the French Society of Astronomy & Astrophysics Nice, June 5-8, 2012

Credit: Christine Julienne

Contents

Foreword

The 2012 annual meeting of the French Society of Astronomy and Astrophysics (Société Française d'Astronomie et d'Astrophysique – SF2A) was hosted by the University of Nice Sophia-Antipolis and the Observatoire de la Côte d'Azur from June 4 to 7. These "Journées" gathered about 420 professional astronomers and astrophysicists, who participated to plenary sessions organized by the SF2A and to workshops organized by the scientific committees of the "National Programs" and "Actions Spécifiques" of INSU-CNRS, several of them in collaboration with our special guest, the Sociedade Astronomica Brasileira.

During the plenary sessions excellent scientific reviews were presented on outstanding scientific results obtained recently by our community. Also, general interest talks led to topical discussions on scientific projects (e.g. at CFHT and at CNES as presented respectively by D.Simons and J.L.Counil) as well as on the organization and the future of french astronomical research in the international environment; in particular, the reform of the International Astronomical Union was introduced by the new General Secretary T.Montmerle, the activities of the European Astronomical Society and of the Sociedade Astronomica Brasileira were presented by their respective presidents T.Courvoisier and E.Janot Pacheco, and J.F.Stephan and J.M.Hameury brought us the latest news from the Institut National des Sciences de l'Univers (INSU-CNRS).

This year, not less than seventeen scientific workshops were organized on topical subjects, and three additional sessions were devoted to outreach and communication in astronomy and in sciences of the universe at large, to the organization of astronomy teaching at the Master level, and to the preservation of the french astronomical patrimony. This "record" number of sessions obviously reflects the great wealth and breadth of exchanges across thematic boundaries as well as the growing role played by the "Journées" and SF2A in animating our community and in initiating fruitful discussions and collaborations in a friendly and stimulating atmosphere.

A large number of SF2A members attended the General Assembly where the annual activity and financial reports of our Society were presented by the president and treasurer of the SF2A Council, C.Charbonnel and S.Boissier. The 2012 SF2A "Thesis Prize" was presented to M.Godard, and the 2012 SF2A prizes "Jeune Chercheur" and "Jeune Enseignant Chercheur" were presented respectively to V.Wakelam and A.Crida by J.F.Stephan, director of INSU/CNRS. We warmly thank the sponsors of these prizes, respectively EdP Sciences and the HP and AMD companies, for their continuing interest in our science and support to our Society. This year, a special prize "Astronomie en Societé" was awarded by the SF2A Council to A.Riazuelo. Following the award ceremony an excellent cocktail sponsored by AMD and OCA was served in the beautiful settings of Mont Gros where a memorable visit of the historical buildings was kindly organized by our colleagues of the Observatoire de la Côte d'Azur.

Along the Journées a number of social, outreach, and cultural events were organized. The SF2A Prize "Découvrir l'Univers" sponsored by EdP Sciences and by the company Optique et Vision was presented to the laureate pupils of the Collège Roger Carlès and of the Centre International de Valbonne by O.Suarez and D.Rouan during the reception offered by the Mairie de Nice at the Villa Masséna where we received the warmest of welcomes by the deputy mayor A. Rampal. J.Guy and F.Mignard gave excellent public conferences, and we had the pleasure to welcome the artists and scientists of the Compagnie Ithérée who presented their poetic musical tale "Les gens ont des étoiles qui ne sont pas les mêmes". Last but not least, the transit of Venus was one of the highlights of the week.

We wish to thank the INSU-CNRS, the Observatoire de la Côte d'Azur and the laboratories J.L.Lagrange, Artémis, GéoAzur and Galilée, as well as the CNES, the CEA, the National Programs and Actions Spécifiques

of INSU-CNRS, the Mairie de Nice, and the Région Provence Alpes Côte d'Azur for their financial and organisational support. We are extremely grateful to the University of Nice Sophia-Antipolis and its Président F.Vidal for hosting the Journées.

We warmly thank F.Vakili, director of the Observatoire de la Côte d'Azur, and the members of the Local Organizing Committee: the chairs, P.De Laverny and P.Stee, and the team C.Baudouin, P. Bendjoya, S.Boissier, O.Chesneau, O.Crida, S. Goletto, C.Julienne, I.Lapassat, N.Nardetto, G.Niccolini, G.Métris, A.Recio-Blanco, S.Rousset, O.Suarez, as well as the cook Kalhed. Their outstanding work and their generous contributions were absolutely crucial for making the "Journées" such a great and "Nice" success. We also thank V. Sessa, responsible for events on the St Jean d'Angely campus, and the "Ensemble instrumental Amadeus" for the musical ambiance during the cocktail on Mont Gros. Thanks also to SF2A board and council for its active contribution, and to the editors of these proceedings.

Corinne Charbonnel Présidente de la SF2A

List of participants

ADAMI Christophe (christophe.adami@oamp.fr)
AGABI Karim (agabi@unice.fr)
AIME Claude (claude.aime@unice.fr)
ALECIAN Evelyne (evelyne.alecian@obspm.fr)
ALEXANDROVA Olga (olga.alexandrova@obspm.fr)
ALMENARA Jose Manuel (josemanuel.almenara@oamp.fr)
ALVAN Lucie (lucie.alvan@cea.fr)
ALVES Sânzia (sanzia@dfte.ufrn.br)
ANDREI Alexandre Humberto (oat1@on.br)
ANSORGE Wolfgang (w.ansorge@rams-con.de)
ARISTIDI Eric (aristidi@unice.fr)
ARNOLD Luc (luc.arnold@oamp.fr)
AUBOURG Eric (eric@aubourg.net)
AUMONT Jonathan (jonathan.aumont@ias.u-psud.fr)
AUSSEL Hervé (herve.aussel@cea.fr)
BABUSIAUX Carine (carine.babusiaux@obspm.fr)
BAGLIN Annie (annie.baglin@obspm.fr)
BALLET Jean (jballet@cea.fr)
BANCELIN David (bancelin@imcce.fr)
BARBAN Caroline (caroline.barban@obspm.fr)
BARRET Didier (didier.barret@irap.omp.eu)
BARTHELEMY Mathieu (mathieu.barthelemy@obs.ujf-grenoble.fr)
BAUDOUIN Cyrille (cyrille.baudouin@oca.eu)
BEAULIEU Jean-Philippe (beaulieu@iap.fr)
BEAUVALET Laurène (chewie_lina@yahoo.fr)
BELKACEM Kevin (kevin.belkacem@obspm.fr)
BENCHEIKH Jordan (jordan.bencheikh@polytechnique.org)
BENDJOYA Philippe (bendjoya@unice.fr)
BENHIDA Abdelmjid (abdelmjidbenhida@yahoo.fr)
BERNÉ Olivier (olivier.berne@gmail.com)
BIGOT Lionel (lbigot@oca.eu)
BITEAU Jonathan (biteau@in2p3.fr)
BOCH Thomas (thomas.boch@astro.unistra.fr)
BOGAERT Gilles (bogaertgb@gmail.com)
BOISSE Isabelle (isabelle.boisse@astro.up.pt)
BOISSIER Samuel (samuel.boissier@oamp.fr)
BOMMERSBACH Loïc (loic.bommersbach@univ-lyon1.fr)
BONNEAU Daniel (daniel.bonneau@oca.eu)
BOQUIEN Médéric (mederic.boquien@oamp.fr)
BORGES FERNANDES Marcelo (borges@on.br)
BOSELLI Alessandro (Alessandro.Boselli@oamp.fr)
BOSMA Albert (bosma@oamp.fr)
BOT Caroline (caroline.bot@astro.unistra.fr)
BOTTI Thierry (Thierry.botti@oamp.fr)
BOUCHEZ GIRET Aurelia (aurelia.bouchez@irap.omp.eu)

BOUCHY Francois (bouchy@iap.fr)
BOURDA Géraldine (bourda@obs.u-bordeaux1.fr)
BOURRIER Vincent (bourrier@iap.fr)
BRAGA BEZERRA Lupercio (lupercio@elogica.com.br)
BRITTO Richard (richard.britto@saha.ac.in)
BROCHIER-ARMANET Celine (celine.brochier-armanet@univ-lyon1.fr)
BRUN Allan Sacha (sacha.brun@cea.fr)
BRUNO Giovanni (giovanni.bruno@oamp.fr)
BUCHLIN Eric (eric.buchlin@ias.u-psud.fr)
BURGEY Edith (edith.burgey@utinam.cnrs.fr)
BUSSCHAERT Clotilde (clotilde.busschaert@obspm.fr)
CABANAC Rémi (rcabanac@irap.omp.eu)
CAFFAU Elisabetta (ecaffau@lsw.uni-heidelberg.de)
CAMBRESY Laurent (cambresy@astro.unistra.fr)
CANTO MARTINS Bruno (brunocanto@dfte.ufrn.br)
CAPLAN James (james.caplan@oamp.fr)
CARBILLET Marcel (marcel.carbillet@unice.fr)
CARRASCO Nathalie (nathalie.carrasco@latmos.ipsl.fr)
CAUCHIES Natacha (natacha.cauchies@obs.ujf-grenoble.fr)
CHADID Merieme (chadid@unice.fr)
CHALLOUF Mounir (mounir.challouf@oca.eu)
CHANIAL Pierre (pierre.chanial@cea.fr)
CHARBONNEL Corinne (Corinne.Charbonnel@unige.ch)
CHARDIN Jonathan (jonathan.chardin@astro.unistra.fr)
CHARDONNET Pascal (chardonnet@lapp.in2p3.fr)
CHARLOT Patrick (charlot@obs.u-bordeaux1.fr)
CHARPINET Stephane (stephane.charpinet@irap.omp.eu)
CHAULAGAIN Uddhab Prasad (uddhab.chaulagain@obspm.fr)
CHAUVINEAU Bertrand (chauvineau@oca.eu)
CHEMIN Laurent (chemin@obs.u-bordeaux1.fr)
CHESNEAU Olivier (Olivier.Chesneau@oca.eu)
CHIAVASSA Andrea (achiavas@ulb.ac.be)
CHIEZE Jean-Pierre (chieze@cea.fr)
CLAVEL Maïca (maica.clavel@obspm.fr)
COLAS François (colas@imcce.fr)
COLLIN-ZAHN Suzy (suzy.collin@obspm.fr)
COMBES Francoise (francoise.combes@obspm.fr)
COMBET Celine (celine.combet@lpsc.in2p3.fr)
COMPARAT Johan (johan.comparat@oamp.fr)
CORBEL Stéphane (stephane.corbel@cea.fr)
COTTALORDA Eric (cottalorda.eric@voila.fr)
COUGRAND Catherine (catherine.cougrand@ias.u-psud.fr)
COULAIS Alain (alain.coulais@obspm.fr)
COURVOISIER Thierry (thierry.courvoisier@unige.ch)
COUTURIER Camille (ccouturi@lpnhe.in2p3.fr)
CREEVEY Orlagh (ocreevey@oca.eu)
CRIDA Aurélien (crida@oca.eu)
CRIFO Francoise (francoise.crifo@obspm.fr)
CRUZALEBES Pierre (pierre.cruzalebes@oca.eu)
CURIR Anna (curir@oato.inaf.it)
DAIGNE Frédéric (daigne@iap.fr)
DAMIANI Cilia (cilia.damiani@oamp.fr)
DE LA NOE Jérôme (delanoe@obs.u-bordeaux1.fr)
DE LAVERNY Patrick (laverny@oca.eu)
DE PASCALE Marco (depascale@oca.eu)

DE SÁ Lionel (lionel.desa@obspm.fr)
DECERPRIT Guillaume (gdecerprit@hep.anl.gov)
DELAYE Lauriane (lauriane.delaye@obspm.fr)
DELFOSSE Xavier (Xavier.Delfosse@obs.ujf-grenoble.fr)
DELUBAC Timothée (timothee.delubac@cea.fr)
DENNEFELD Michel (dennefel@iap.fr)
DESCHAMPS Romain (rdescham@ulb.ac.be)
DÍAZ Rodrigo (rodrigo.diaz@oamp.fr)
DINTRANS Boris (boris.dintrans@irap.omp.eu)
DO CAO Olivier (olivier.do-cao@cea.fr)
DO NASCIMENTO José-Dias (dias@dfte.ufrn.br)
DOISY Anabelle (anabelle.doisy@uvsq.fr)
DOMICIANO Armando (armando.domiciano@unice.fr)
DORNIC Damien (dornic@cppm.in2p3.fr)
DOUCHIN Dimitri (dimitri.douchin@mq.edu.au)
DOUGADOS Catherine (catherine.dougados@obs.ujf-grenoble.fr)
DUBOIS Yohan (dubois@iap.fr)
DUC Pierre-Alain (paduc@cea.fr)
DUCOURANT Christine (ducourant@obs.u-bordeaux1.fr)
DUMAS Gaelle (dumas@iram.fr)
DURRET Florence (durret@iap.fr)
EGRET Daniel (Daniel.Egret@obspm.fr)
EL MOUTAMID Maryame (maryame.elmoutamid@obspm.fr)
EL OURABI El Haj (elourabi2012@yahoo.fr)
EPCHTEIN Nicolas (epchtein@unice.fr)
EPINAT Benoît (benoit.epinat@oamp.fr)
ESCOFFIER Stephanie (escoffier@cppm.in2p3.fr)
ETCHEVERRY Sylvie (sylvie.etcheverry@obs-mip.fr)
ETIENNE Christine (christine.etienne@oca.eu)
EXERTIER Pierre (Pierre.Exertier@obs-azur.fr)
FAMAEY Benoit (benoit.famaey@astro.unistra.fr)
FAURE Carole (carole.faure@etu.unistra.fr)
FAUROBERT Marianne (marianne.faurobert@unice.fr)
FÉLIX Sophie (sophie.felix@cea.fr)
FERRARI Chiara (chiara.ferrari@oca.eu)
FIENGA Agnes (agnes@obs-besancon.fr)
FIGON Patrick (patrick.figon@oamp.fr)
FOUCHET Thierry (Thierry.Fouchet@obspm.fr)
FOURNIER Jean-Daniel (fournier@oca.eu)
FRAIX-BURNET Didier (fraix@obs.ujf-grenoble.fr)
FRISCH Helene (frisch@oca.eu)
GALATÀ Salvatore (galata@cppm.in2p3.fr)
GALLAIS Pascal (pascal.gallais@cea.fr)
GALLET Florian (florian.gallet@obs.ujf-grenoble.fr)
GALTIER Sébastien (sebastien.galtier@ias.u-psud.fr)
GARGAUD Muriel (gargaud@obs.u-bordeaux1.fr)
GARSDEN Hugh (hugh.garsden@cea.fr)
GAY Jean (jean_gay_astro@yahoo.fr)
GERARD Eric (eric.gerard@obspm.fr)
GIEBELS Berrie (berrie@in2p3.fr)
GIRARD Julien (julien.girard@obspm.fr)
GODARD Marie (marie.godard@nasa.gov)
GOLDWURM Andrea (andrea.goldwurm@cea.fr)
GOLETTO Sylvie (sylvie.goletto@oca.eu)
GONZALEZ Jean-François (Jean-Francois.Gonzalez@ens-lyon.fr)

GRATIER Pierre (gratier@iram.fr)
GUÉDÉ Céline (celine.guede@obspm.fr)
GUENNOU Loïc (loic.guennou@oamp.fr)
GUIGLION Guillaume (gg702390@etu.unice.fr)
GUILET Jérôme (jg613@cam.ac.uk)
GUIRIEC Sylvain (sylvain.guiriec@gmail.com)
GUITTET Mélanie (melanie.guittet@obspm.fr)
GUY Julien (guy@lpnhe.in2p3.fr)
GUYOT Sylviane (sylviane.guyot@oamp.fr)
HADJARA Massinissa (massinissa.hadjara@oca.eu)
HALBWACHS Jean-Louis (jean-louis.halbwachs@astro.unsitra.fr)
HAMDANI Slim (slim.hamdani@cosmostory.fr)
HAMEURY Jean-Marie (samuel.boissier@gmail.com)
HARDY Emilie (emilie.hardy@onera.fr)
HAVEL Mathieu (mathieu.havel@gmail.com)
HAYWOOD Misha (Misha.Haywood@obspm.fr)
HÉBRARD Guillaume (hebrard@iap.fr)
HÉBRARD Eric (hebrard@obs.u-bordeaux1.fr)
HENNEBELLE Patrick (patrick.hennebelle@ens.fr)
HENRI Gilles (Gilles.Henri@obs.ujf-grenoble.fr)
HESTROFFER Daniel (hestro@imcce.fr)
HILL Vanessa (vanessa.hill@oca.eu)
IBGUI Laurent (laurent.ibgui@obspm.fr)
JABLONKA Pascale (pascale.jablonka@epfl.ch)
JACHOLKOWSKA Agnieszka (Agnieszka.Jacholkowska@cern.ch)
JANOT-PACHECO Eduardo (janot@astro.iag.usp.br)
JOSSELIN Eric (eric.josselin@univ-montp2.fr)
JOUVE Laurene (ljouve@irap.omp.eu)
JULIENNE Marie-Christine (Christine.Julienne@oca.eu)
JULLO Eric (eric.jullo@oamp.fr)
KILIÇOĞLU Tolgahan (tkilicoglu@ankara.edu.tr)
KLUSKA Jacques (jacques.kluska@obs.ujf-grenoble.fr)
KLUTSCH Alexis (klutsch@astrax.fis.ucm.es)
KNÖDLSEDER Jürgen (jurgen.knodlseder@irap.omp.eu)
KOECHLIN Laurent (laurent.koechlin@ast.obs-mip.fr)
KORDOPATIS Georges (gkordo@ast.cam.ac.uk)
KOTERA Kumiko (kotera@iap.fr)
KOUTCHMY Serge (koutchmy@iap.fr)
KRAL Quentin (quentin.kral@obspm.fr)
LAGADEC Eric (elagadec@eso.org)
LAGAGE Pierre-Olivier (pierre-olivier.lagage@cea.fr)
LAGE Claudia (lage@biof.ufrj.br)
LAIBE Guillaume (guillaume.laibe@monash.edu)
LAMBERT Julien (julien.lambert@univ-montp2.fr)
LANZ Thierry (thierry.lanz@oca.eu)
LAPASSAT Isabelle (isabelle.lapassat@oca.eu)
LE BERTRE Thibaut (thibaut.lebertre@obspm.fr)
LE BORGNE Damien (leborgne@iap.fr)
LE GUET TULLY Françoise (leguet@oca.eu)
LE PONCIN-LAFITTE Christophe (christophe.leponcin@obspm.fr)
LE SERGEANT D'HENDECOURT Louis (ldh@ias.u-psud.fr)
LEBRE Agnès (Agnes.Lebre@univ-montp2.fr)
LEBRETON Yveline (yveline.lebreton@obspm.fr)
LECONTE Jeremy (jeremy.leconte@lmd.jussieu.fr)
LELLOUCH Emmanuel (emmanuel.lellouch@obspm.fr)

LENOIR Benjamin (benjamin.lenoir@onera.fr)
LIGI Roxanne (roxanne.ligi@oca.eu)
LINTZ Michel (michel.lintz@oca.eu)
LION Guillaume (Guillaume.Lion@oca.eu)
LOPEZ ARISTE Arturo (arturo@themis.iac.es)
MACIAS-PEREZ Juan Francisco (macias@lpsc.in2p3.fr)
MARCELIN Michel (michel.marcelin@oamp.fr)
MARCELL Tessenyi (m.tessenyi@ucl.ac.uk)
MARIN Frédéric (frederic.marin@astro.unistra.fr)
MARSHALL Douglas (douglas.marshall@irap.omp.eu)
MARTIN Jean-Michel (jean-michel.martin@obspm.fr)
MARTINS Fabrice (fabrice.martins@univ-montp2.fr)
MATHIS Stéphane (stephane.mathis@cea.fr)
MATT Sean (sean.matt@cea.fr)
MAUROGORDATO Sophie (Sophie.Maurogordato@oca.eu)
MECHERI Redouane (r.mecheri@craag.dz)
MEHEUT Heloise (heloise.meheut@space.unibe.ch)
MEKARNIA Djamel (mekarnia@oca.eu)
MERLE Thibault (thibault.merle@oca.eu)
METRIS Gilles (Gilles.Metris@oca.eu)
MICHEL Eric (eric.michel@obspm.fr)
MIGNARD Francois (francois.mignard@oca.eu)
MILLOUR Florentin (fmillour@oca.eu)
MIRABEL Felix (felix.mirabel@cea.fr)
MONIER Richard (Richard.Monier@unice.fr)
MONNIER RAGAIGNE Delphine (monnier@lal.in2p3.fr)
MONTMERLE Thierry (montmerle@iap.fr)
MONTMESSIN Franck (franck.montmessin@latmos.ipsl.fr)
MORBIDELLI Alessandro (morbydelli@gmail.com)
MORIN Julien (jmorin@gwdg.de)
MOTTE Frédérique (motte@cea.fr)
MOTTEZ Fabrice (fabrice.mottez@obspm.fr)
MOULAI-ROUS Monique (monique.moulai-rous@oamp.fr)
MOURARD Denis (denis.mourard@oca.eu)
MOUSIS Olivier (olivier.mousis@obs-besancon.fr)
MOUTOU Claire (claire.moutou@oamp.fr)
NAMOUNI Fathi (namouni@obs-nice.fr)
NARDETTO Nicolas (Nicolas.Nardetto@oca.eu)
NATAF Henri-Claude (Henri-Claude.Nataf@ujf-grenoble.fr)
NEINER Coralie (Coralie.Neiner@obspm.fr)
NICCOLINI Gilles (nicolin@oca.eu)
NOULLEZ Alain (anz@obs-nice.fr)
NOVAK Jerome (jerome.novak@obspm.fr)
PANTIN Eric (eric.pantin@cea.fr)
PARIS Silvia (silvia.paris@unice.fr)
PARIZOT Etienne (parizot@apc.univ-paris7.fr)
PASCAL Robert (rpascal@univ-montp2.fr)
PEIRANI Sébastien (peirani@iap.fr)
PELASSA Véronique (Veronique.Pelassa@uah.edu)
PELLETIER Guy (Guy.Pelletier@obs.ujf-grenoble.fr)
PENIN Aurelie (aurelie.penin@oamp.fr)
PERROT Clément (perrot@iap.fr)
PETIT Pascal (ppetit@irap.omp.eu)
PETITDEMANGE Ludovic (lpetitdemange@hotmail.com)
PETY Jérôme (pety@iram.fr)

PICHON Bernard (Bernard.Pichon@oca.eu)
PIERRE Marguerite (mpierre@cea.fr)
PIETER Neyskens (pieter.neyskens@ulb.ac.be)
PILLING Sergio (sergiopilling@yahoo.com.br)
PINTO Rui (rui.pinto@cea.fr)
PONTY Yannick (Yannick.Ponty@oca.eu)
POSBIC Hélène (helene.posbic@obspm.fr)
PRADIER Thierry (pradier@in2p3.fr)
PRAT Vincent (vincent.prat@irap.omp.eu)
RABBIA Yves (rabbia@oca.eu)
RAJPUROHIT Arvind Singh (arvind@obs-besancon.fr)
RAULIN Francois (francois.raulin@lisa.u-pec.fr)
RECIO-BLANCO Alejandra (arecio@oca.eu)
REESE Daniel (daniel.reese@ulg.ac.be)
REMUS Françoise (francoise.remus@obspm.fr)
REMUSAT Laurent (remusat@mnhn.fr)
REVAZ Yves (yves.revaz@epfl.ch)
REYLÉ Céline (celine@obs-besancon.fr)
RIAZUELO Alain (riazuelo@iap.fr)
RICHARD Andy (arichard@imcce.fr)
RICHARD Johan (johan.richard@univ-lyon1.fr)
RIVET Jean-Pierre (jean-pierre.rivet@oca.eu)
ROQUES Françoise (francoise.roques@obspm.fr)
ROSTAGNI Florent (rostagni@oca.eu)
ROUAN Daniel (daniel.rouan@obspm.fr)
ROUILLARD Alexis (arouillard@irap.omp.eu)
ROUSSEL Hélène (roussel@iap.fr)
ROUSSET Sophie (sophie.rousset@oca.eu)
ROYER Frédéric (frederic.royer@obspm.fr)
SACUTO Stéphane (stephane.sacuto@physics.uu.se)
SALABERT David (salabert@oca.eu)
SALOMÉ Philippe (philippe.salome@obspm.fr)
SALOMON Jean-Baptiste (jbcarnac1@hotmail.com)
SAMADI Réza (reza.samadi@obspm.fr)
SAMUEL Benjamin (benjamin.samuel@obspm.fr)
SANTERNE Alexandre (alexandre.santerne@oamp.fr)
SAUNDERS Will (will@aao.gov.au)
SCHMIDER François-Xavier (schmider@oca.eu)
SCHMIDT Wolfram (schmidt@astro.physik.uni-goettingen.de)
SCHULTHEIS Mathias (mathias@obs-besancon.fr)
SEFYANI LAKRIZI Fouad (sefyani2002@yahoo.fr)
SELSIS Franck (selsis@obs.u-bordeaux1.fr)
SEMELIN Benoit (benoit.semelin@obspm.fr)
SERVILLAT Mathieu (mathieu.servillat@cea.fr)
SHANKAR Francesco (francesco.shankar@obspm.fr)
SIEBERT Arnaud (arnaud.siebert@astro.unistra.fr)
SIELLEZ Karelle (karelle.siellez@obspm.fr)
SIMONS Doug (simons@cfht.hawaii.edu)
SIQUEIRA MELLO JUNIOR Cesar Henrique (cesar.siqueira@obspm.fr)
SLEZAK Eric (eric.slezak@oca.eu)
SOBECK Jennifer (jsobeck@oca.eu)
SODRÉ Laerte (laerte@astro.iag.usp.br)
SOUBIRAN Caroline (soubiran@obs.u-bordeaux1.fr)
SOUCAIL Geneviève (genevieve.soucail@irap.omp.eu)
SOULAT Laurence (laurence.soulat@unice.fr)

SPALLICCI Alessandro (spallicci@cnrs-orleans.fr)
SPANG Alain (alain.spang@oca.eu)
STEE Philippe (Philippe.Stee@oca.eu)
STEFANELLI Letizia (letizia.stefanelli@oca.eu)
STEHLE Chantal (chantal.stehle@obspm.fr)
STEPHAN Jean-François
STRUGAREK Antoine (antoine.strugarek@cea.fr)
SUAREZ Olga (olga.suarez@oca.eu)
SYLVAIN Fouquet (fouquet.sylvain@gmail.com)
TAGGER Michel (michel.tagger@cnrs-orleans.fr)
TAJEDDINE Radwan (tajeddine@imcce.fr)
TALLON Michel (mtallon@obs.univ-lyon1.fr)
TASSE Cyril (cyril.tasse@obspm.fr)
THEUREAU Gilles (gilles.theureau@obs-nancay.fr)
THIÉBAUT Éric (eric.thiebaut@univ-lyon1.fr)
THIERY Sabrina (sabrina.thiery@obspm.fr)
TORCHINSKY Steve (torchinsky@obs-nancay.fr)
TORRES MACHADO Diego (torres@subatech.in2p3.fr)
TRIC Emmanuel (tric@unice.fr)
TROVA Audrey (Audrey.Trova@obs.u-bordeaux1.fr)
TURON Catherine (catherine.turon@obspm.fr)
VAKILI Farrokh (vakili@oca.eu)
VALIO Adriana (adrivalio@gmail.com)
VAN DER SWAELMEN Mathieu (swaelmen@oca.eu)
VAN DRIEL Wim (wim.vandriel@obspm.fr)
VARNIERE Peggy (varniere@apc.univ-paris7.fr)
VAUGLIN Isabelle (vauglin@obs.univ-lyon1.fr)
VECCHI Manuela (vecchi@cppm.in2p3.fr)
VERNOTTE Francois (francois.vernotte@obs-besancon.fr)
VIALLET Maxime (mviallet@astro.ex.ac.uk)
VIEIRA-MARTINS Roberto (rvm@on.br)
VINCENT Frédéric E. (fvincent@iap.fr)
VINCENT Frédéric (frederic.vincent@obspm.fr)
VINET Jean-Yves (vinet@oca.eu)
WAKELAM Valentine (wakelam@obs.u-bordeaux1.fr)
WEBB Natalie (Natalie.Webb@irap.omp.eu)
WILLIGER Gerard (gerard.williger@unice.fr)
WORLEY Clare (cworley@oca.eu)
WOUTERS Denis (denis.wouters@cea.fr)
WOZNIAK Hervé (herve.wozniak@astro.unistra.fr)
ZAHN Jean-Paul (Jean-Paul.Zahn@obspm.fr)
ZARKA Philippe (philippe.zarka@obspm.fr)
ZEGOUMOU Mohammed (zagoumou1@hotmail.com)
ZOUBIAN Julien (zoubian@cppm.in2p3.fr)
ZURLO Alice (alice.zurlo@oamp.fr)

Session SF2A

Joint session

SF2A 2012
S. Boissier, P. de Laverny, N. Nardetto, R. Samadi, D. Valls-Gabaud and H. Wozniak (eds)

USING VIRTUAL OBSERVATORY TOOLS FOR SCIENCE

C. Bot[1, 2] and T. Boch[1,2]

Abstract. In a dozen years, the astronomical Virtual Observatory has evolved from a prototype to an infrastructure in production, servicing science. Through a few examples, we demonstrate how the VO tools can be used to locate data of interest, manipulate and visualize them.

Keywords: Virtual observatory tools, data discovery, data access

1 Introduction

The idea of the Virtual Observatory (VO) project began around the years 2000, when a data avalanche in astronomy was already forecasted and it became clear that tools to deal with it were needed. The idea was to have all the data existing anywhere in the world be accessible to all and be able to analyze large data quantities outside the researcher's computer.

While we often mention the Virtual Obervatory, one could talk about Virtual Observatories since many independent projects exist around the world. For France, one can mention the VO-France project as well as the EuroVO project for Europe. All VO projects belong to the IVOA (International Virtual Observatory Alliance) to enable coordination among them.

Since the beginning of the VO, an enormous effort of standardization has been achieved. Standards on protocols, data models, meta-data and more have emerged. The VO gives access to a number of databases that are compatible with these standards, as well as tools that were developed in this context.

While all dream-ideas of the beginning of the VO have not been achieved, many things can be done with the Virtual Observatory tools/data. We feel that there is an under-usage of the VO tools due to a lack of knowledge of them in the scientific community. This talk/paper aims at spreading the word of what exists in term of very generic tools/functionalities for scientists.

In the following, we will present excerpts of science cases to show what can be done with a few key tools: `Aladin` (for images), `TOPCAT` (for tables), and `VOSpec` (for spectra). The full tutorials as well as the list of all VO tools are available on the EuroVO webpage (`http://www.euro-vo.org/`). The examples were chosen to answer the following question:

1. How do I deal with large catalogs?
2. How do I find all the available data for one object?
3. How to explore the sky at different wavelengths?
4. How do I visualize spectra?

We will then demonstrate how these tools are able to interact with each other, which is at the core of the VO idea.

[1] Université de Strasbourg, Observatoire Astronomique de Strasbourg, F-67000 Strasbourg, France.
[2] CNRS, Observatoire Astronomique de Strasbourg, UMR7550, F-67000 Strasbourg, France.

2 How to deal with large catalogs?

TOPCAT is a great tool to deal with numerical tables and catalogues in general. It can be downloaded from the website `http://www.star.bris.ac.uk/~mbt/topcat/` and installed easily. We presented a mini-demonstration of its usage by showing step by step part of the "*Discovery of Brown Dwarfs mining the 2MASS and SDSS databases*" science case (this science case is available entirely at `http://www.euro-vo.org/pub/fc/workflows/BDs.html`). The idea is to search for brown dwarf candidates using color and magnitude criteria. To do so, the 2MASS and SDSS catalogs around the position 08^h30^m $+01°30'$were loaded in TOPCAT and cross-matched together with a $4''$error, keeping only the best matches. A selection on the cross-matched sources was done using criteria based on color and magnitude (i.e. u>22.0 and g>22.2, $(J-H)$<0.3 and $(H-K)$<0.3). The full catalogs and the subset can be easily visualized in TOPCAT and this was shown by plotting both on a color-color plot. A single brown-dwarf candidate was found at the end of the process.

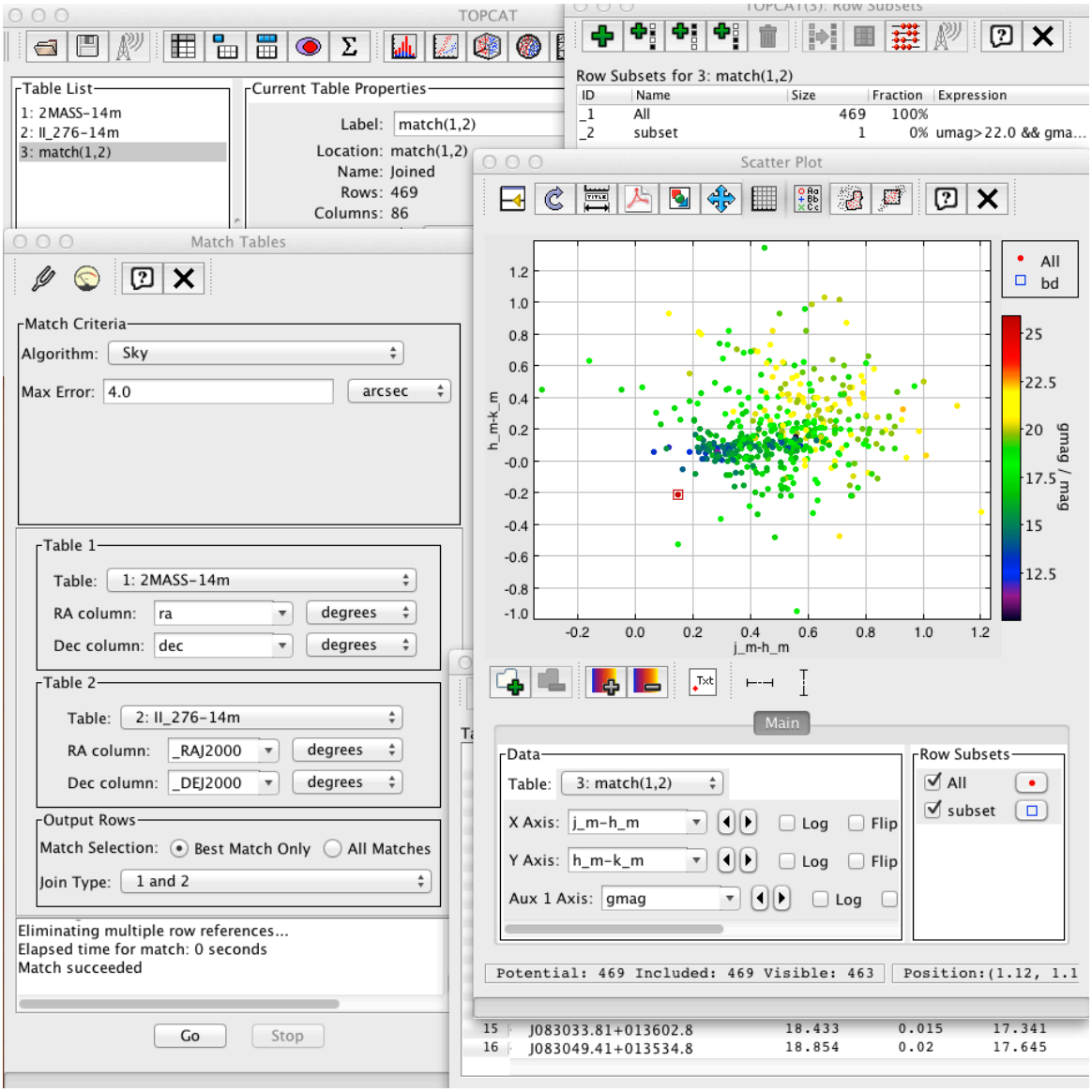

Fig. 1. Using TOPCAT to cross-match, visualize, and do selection of tabular data

3 How to find all the available data for one object?

Aladin is great tool to deal with images, but it is also a portal to the Virtual Observatory in general, which means that one can know about existing data for a region of the sky with `Aladin`, whether this data is a spectrum, a table or an image. We demonstrated how to query all available data for the region of the sky around M51 and how to explore the sky at different wavelengths by loading data from the X-ray (XMM), UV (GALEX), optical (Sloan Digital Sky Survey), infrared (IRAS), radio (NVSS, HI and CO data). We made heavy use of the all sky capabilities of `Aladin` and of the all sky surveys at different wavelengths available through `Aladin` itself. We also loaded catalogues and images specific to the region of M51, made a three color image to visualize the multi-wavelength information, showed the multi-view options and made use of the transparency between the different layers (images, catalogs). This demonstration was based on the Euro-VO science case "*Searching for Data available for the bright galaxy M51*" which is available on the website `http://www.euro-vo.org/pub/fc/workflows/M51.html`.

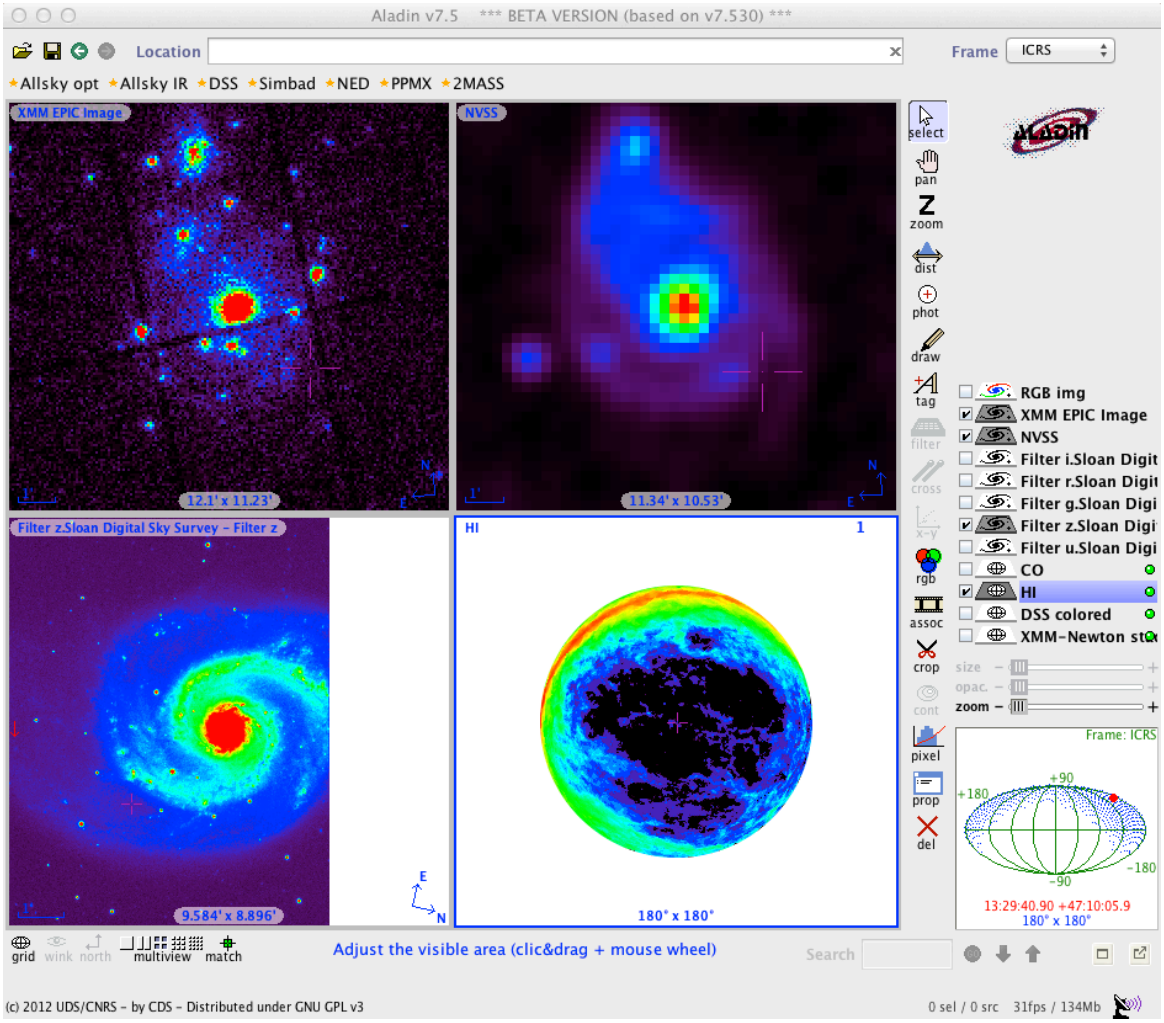

Fig. 2. Using `Aladin` to explore data at different wavelengths in the region of M51

4 Dealing with spectral data with VOSpec

`VOSpec` was chosen as the tool to display spectra. We searched for available spectral data for the star HD 141569. Different spectra from the ISO, IUE, INES, ESO and FUSE data bases were loaded and displayed. Capabilities to zoom in and out, and select a region where shown, as well as the link with theoretical data bases. Indeed, we accessed the NIST atomic spectra database and searched for the line data available for a

wavelength subset of one spectrum where a line was visible. The different possible lines corresponding to it appeared overlaid on the spectrum when browsing over it with the mouse. This mini-demo was extracted from the tutorial "*Classifying the SEDs of Herbig Ae/Be stars*" available on the website `http://www.euro-vo.org/pub/fc/workflows/Herbig.html`.

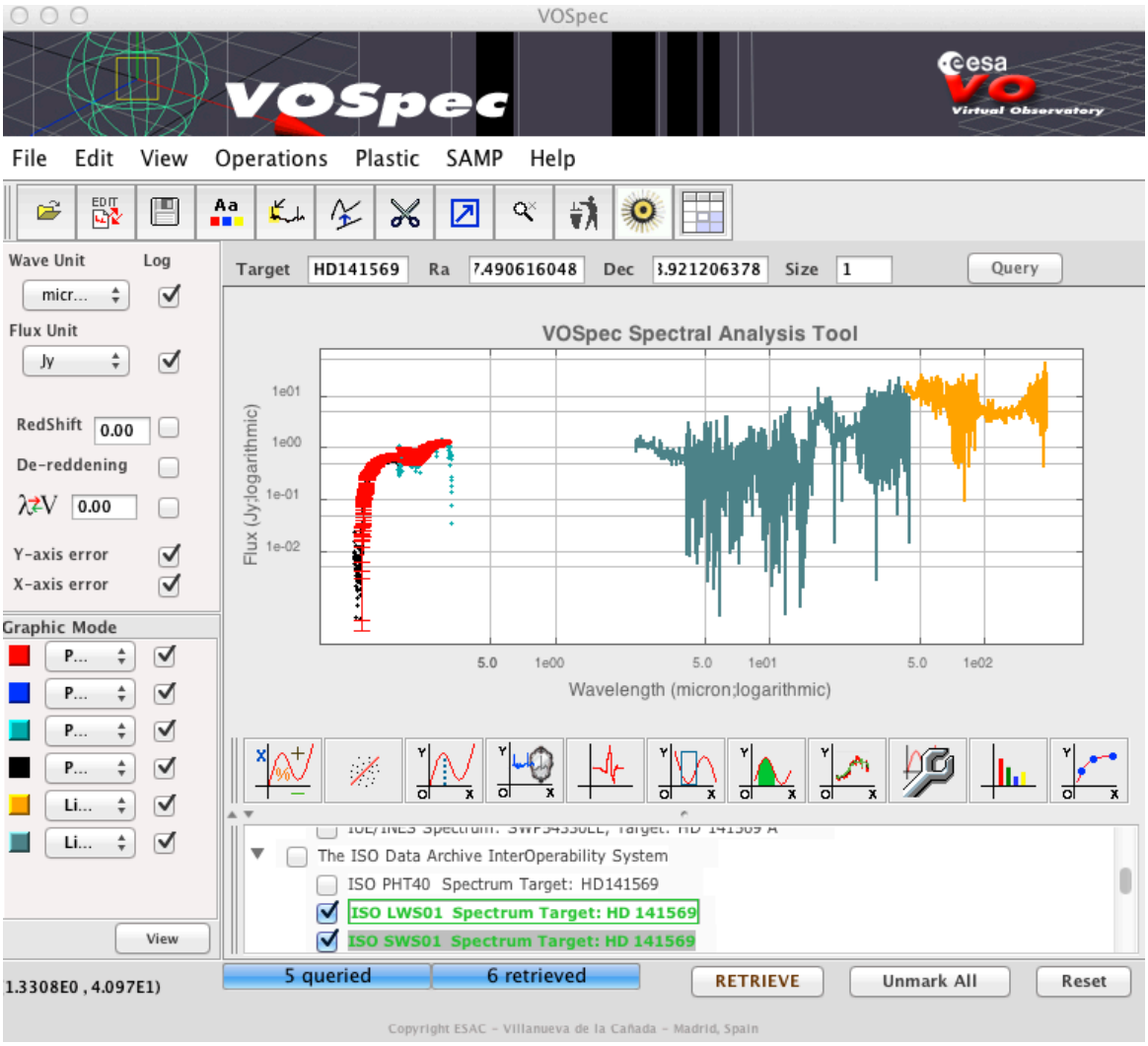

Fig. 3. A typical `VOSpec` session with multi-wavelength, multi-origins spectra loaded for the target HD 141569

5 Conclusion: Interoperability of the tools

After showing independently the `TOPCAT` tool for catalogs, the `Aladin` tool for images and the `VOSpec` tool for spectra, we showed what makes the core interest of the Virtual Observatory project and is based on all the standards developed in this context: all VO tools can interact with each other and function as a single one. We demonstrated this capability by taking the brown dwarf candidate found in the `TOPCAT` mini-demo and sending it to the `Aladin` tool to visualize its location on top of an all sky view. We also showed that selections done in `TOPCAT` can be viewed simultaneously in `Aladin`. We then searched for the star HD 141569 in `Aladin` and looked for available spectra thanks to the `allvo` tab, select some spectral data and load it from `Aladin` to `VOSpec`.

6 Perspectives

Following the recommendations of the Science Commitee, standardization work in on-going at the IVOA level. Current high-priority topics include SEDs (Spectral Energy Distribution) building, cross-match, and complex queries to tabular data.

In order to stay tuned about latest development of VO tools and services, you might consult the IVOA newsletter available at `http://www.ivoa.net/newsletter` . It provides, twice a year, with highlights about new features in VO tools, as well as a summary of VO enabled science papers.

We thank the organizers for giving us this opportunity to present VO tools to the French community at large.

SF2A 2012
S. Boissier, P. de Laverny, N. Nardetto, R. Samadi, D. Valls-Gabaud and H. Wozniak (eds)

CHARACTERIZING THE BIBLIOGRAPHIC PRODUCTION OF FRENCH ASTROPHYSICS IN 2011

D. Egret[1]

Abstract. We have used the SAO/NASA ADS information system to collect a complete database of refereed publications from French Astronomy (i.e. with at least one of the authors with affiliation in a French institution). We find about 2150 publications for the year 2011 and we present some statistics to characterize the scientific production of this community. We also find a rapid increase in the number of authors per paper in the recent years.

Keywords: bibliometry

1 Introduction

In this paper we use the SAO/NASA ADS information system in order to extract and characterize a complete data collection of refereed publications issued from French Astrophysics for the year 2011.

2 Selection criteria

We have used the following selection criteria:

- Refereed articles: We have used the filter for "refereed articles" as available from the SAO/NASA ADS interface, with minor adjustments.
- Astrophysics domain: We have restricted the data collection to articles from the ADS Astrophysics database, which roughly corresponds to the Astronomy-Astrophysics (hereafter AA) domain of the French Institut National des Sciences de l'Univers (INSU).
- Affiliation in a French institution: an article is retained in the list if and only if one of the authors provides an affiliation with a French institution (i.e. with an address in France). Publications from French astronomers in international organizations such as ESO have not been retained, while productions of foreign colleagues temporarily associated to a French institution are included.

3 Query modes

In order to be very complete we have used two complementary approaches, and merged their results.

One is the *Affiliation search* mode of ADS —which is presented in the ADS system as having a "limited usefulness" due to inconsistency of this specific field in the databases. In the present context, it proved to be quite efficient, as least for recent years.

The other query mode is the classical *search by author names*: for that, lists of permanent staff have been extracted from the CNRS directory of laboratories and research units. About thirty research units or "UMR" are relevant to the AA domain. These units are generally located in Observatories (with the notable exception of AIM-SAp —a department of the French nuclear research center CEA) and they actually constitute the core of French professional astrophysics.

By using this double query approach we are rather confident that we are more than 95% complete, missing only a few papers not known to ADS, and some articles which are not signed by a permanent staff and for which the affiliation is absent or incomplete.

[1] LUTH, Observatoire de Paris, PSL, Univ. Paris Diderot, Sorbonne Paris Cité, CNRS UMR 8102, Place Jules Janssen, 92190 Meudon, France

4 Result: a bibliographic list of 2150 articles for the year 2011

We have compiled through the method described above a data collection of 2150 refereed articles constituting the bibliography of French Astrophysics for the year 2011. This database is a managed as a *private library* within the ADS system, and is available from the author on request.

This collection is about 14% of the overall production of astrophysics that we estimate to be about 15,000 papers per year.

Of course, because of very frequent wide international co-authorship, this does not mean that French contribution counts for 14% of the total world production in the Astrophysics domain (a more correct estimation is 6%, see below).

If we restrict ourselves to the twelve principal astronomy and astrophysics journals, French production concerns 1550 articles out of a total of 10,000 papers.

4.1 In which journals do French authors publish ?

Figure 1 provides the distribution of published articles by journals: 32% are published in the European journal *Astronomy & Astrophysics* (A&A) —this is 33% of the articles published in 2011 in this journal— and 18% in the *Astrophysical Journal*.

75% of the 2150 articles are published in a journal or review focused on the astrophysics domain, while 25% appear in physics, geophysics or astroparticle journals or reviews (although we have retained from these journals only articles dealing with astrophysical topics).

5 Characterizing the production of French research units

As a reference, we first give in Fig. 1 the list of French research units sorted according to their number of permanent research staff. Only research units for which the main scientific domain is AA are listed in this Figure.

5.1 From which research units are issued the scientific publications ?

The research mode we have used for this study allowed us to precisely locate the research units in which the French authors of astrophysical publications are affiliated, among the main thirty research units of current professional French astrophysics. Note that a paper may be attributed to several research units, according to the affiliations of the different authors.

Figure 2 provides the histogram of the distribution of refereed articles issued from the main astrophysics research labs for the year 2011. Note that the total number of entries is larger than the number of articles because of the multiple authorship.

For research units dealing with several domains (e.g. astrophysics and geophysics, or astrophysics and astroparticles), this does not reflect the total number of publications of the unit, because only astrophysics publications are counted here.

About 250 articles (i.e. 12%) from our data collection are not assigned to any of the French astrophysics labs : this is mainly due to co-authorships from French colleagues from other disciplines (geophysics, chemistry, instrumentation, etc.) contributing to an astrophysical study, together with astrophysicists from other countries.

5.2 Histograms related to the first (or main) author of the paper

We have looked for those articles whose first author is affiliated in a French institution. In the following, an article is therefore attributed to a single institution. In the specific case of "Collaborations" (e.g. Planck Collaboration, HESS collaboration, etc.) we have used, whenever possible, the *corresponding author* as the main author.

Among the 2150 articles of our data collection, 42% (900 articles) have a first author in a French institution, among which 80% in one of the thirty astrophysics laboratory.

This implies that 6% of the world publication in astrophysics (900 over 15000 articles) has a first author in a French institution.

The changes in ranking from Fig. 2 to Fig. 3 tend to favor those scientific teams that carry a leadership role in collaborative projects.

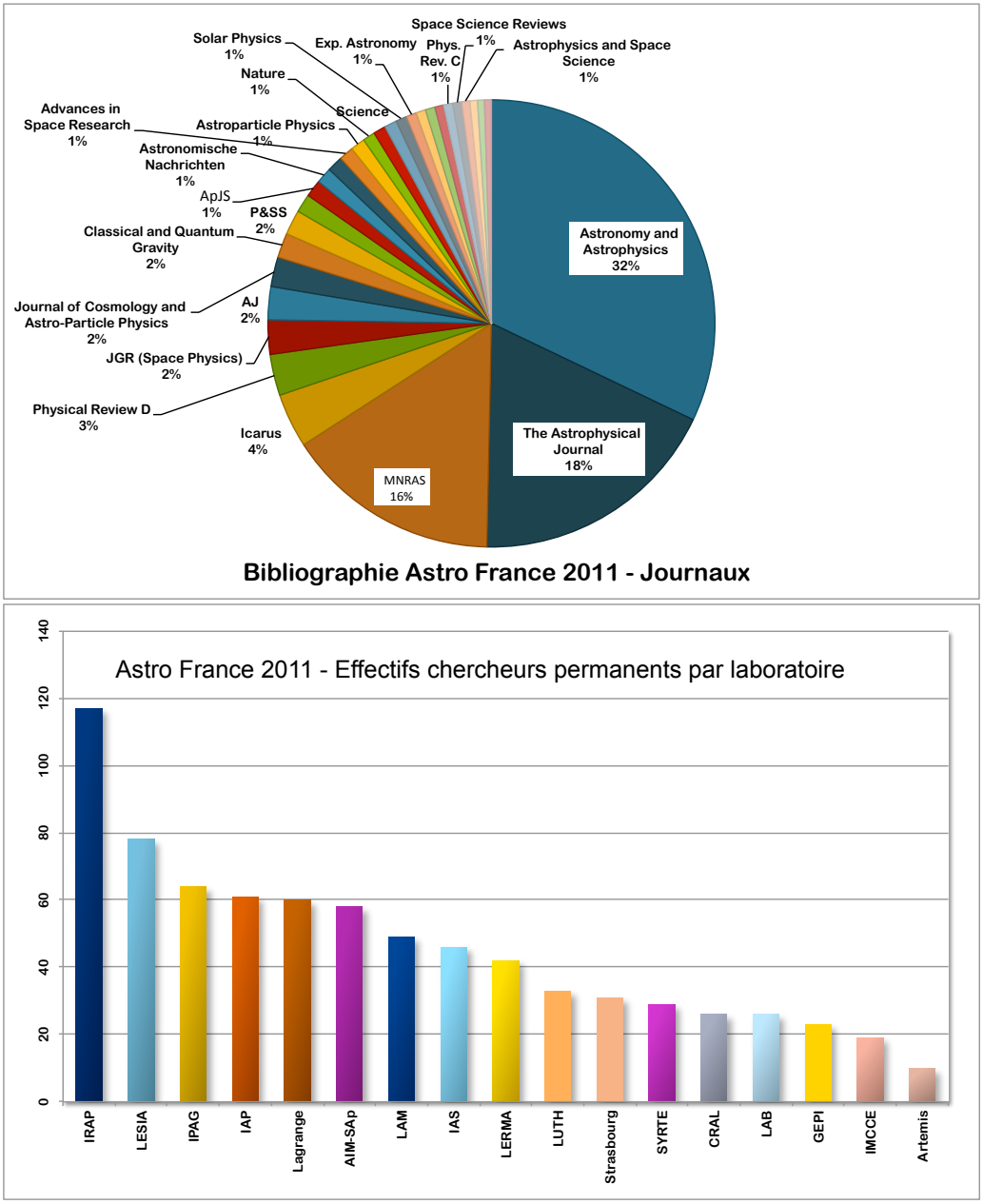

Fig. 1. Top : Bibliography Astro France 2011 : Distribution of Journals and reviews in which the articles are published. **Bottom**: French Astrophysics: number of permanent scientific staff in selected research units.

6 A striking characteristic: the number of co-authors per paper is increasing rapidly

Figure 4 illustrates the number of authors per paper. In 2011 (histogram on the right) 50% of the papers have more than 6 authors, 12% have more than 30 authors. Average is 21.

This is a recent trend, consistent with the international evolution of our science (Trimble 2009). The histograms in Fig. 4 illustrate the evolution in 5 years (2006-2011) —a period in which the number of publications of French astrophysics increased by 20%.

The fraction of single-author papers has declined from about 6% to less than 3% in five years, while the fraction of papers with more than 30 authors increased from 7% to 12%.

The median number of authors increased from 5 to 7 and the average number of authors from 11 to 21. This constitutes an important factor for explaining the yearly progression of bibliographic production of our

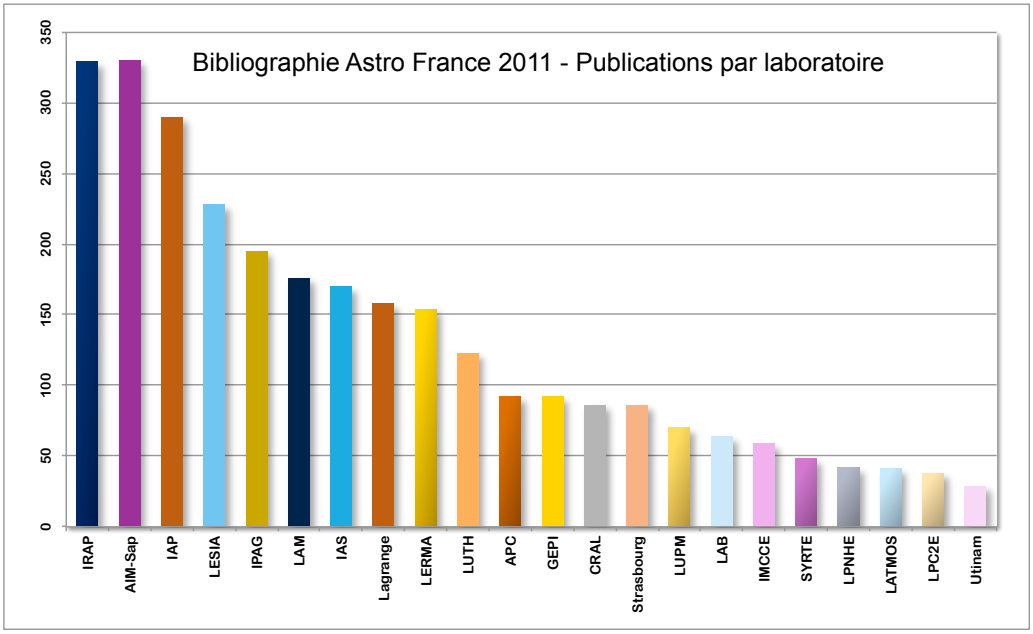

Fig. 2. Astro France 2011: research units sorted by their number of refereed publications.

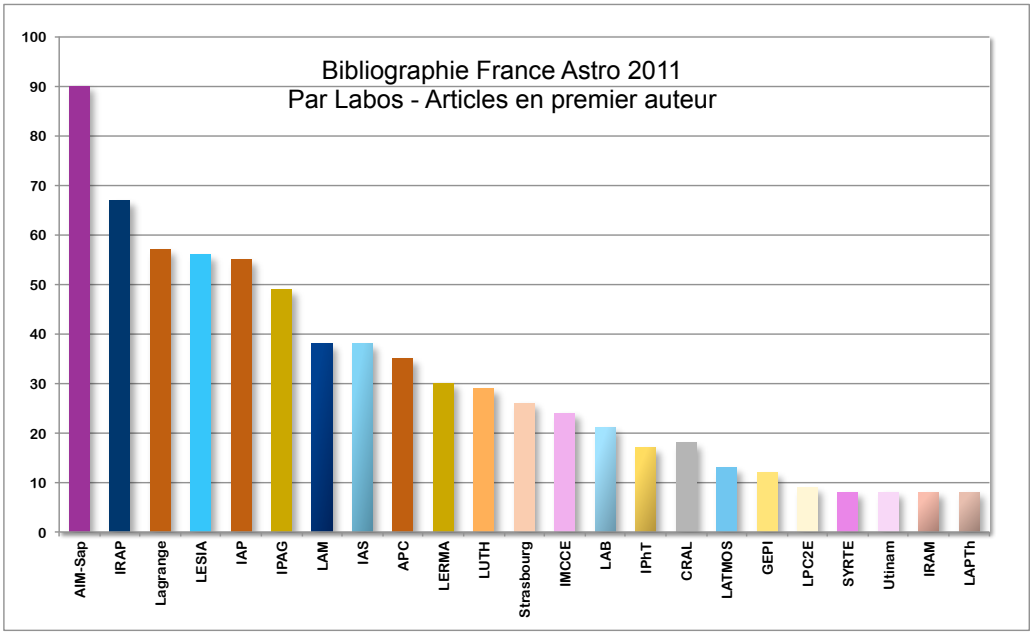

Fig. 3. Astro France 2011: research units sorted by their number of refereed publications in first author.

institutions: this reflects an increased weight of large international collaborative projects.

7 Conclusion

This paper is a first of a series to characterize the current production of French Astrophysics, and analyze the trends. The first trend shown here is a rapid increase of the number of co-authors, reflecting the growing implication in large international collaborative projects.

I thank Piercarlo Bonifacio, Stéphane Mazevet and Claude Bertout for useful discussions.

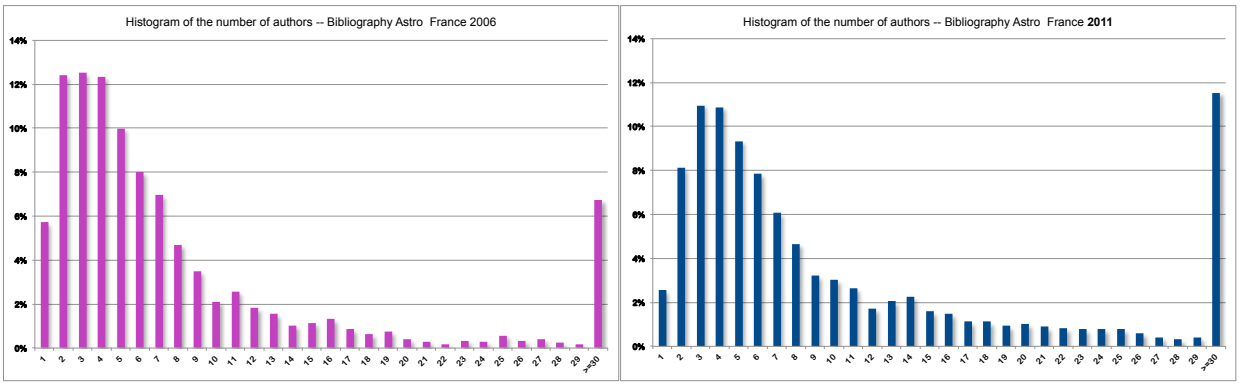

Fig. 4. Astro France 2006 (**left**) and 2011 (**right**): histograms of the number of authors per article.

This research has made use of SAO/NASA's *Astrophysics Data System*.

References

Trimble, V. 2009, Experimental Astronomy, 26, 133

SF2A 2012
S. Boissier, P. de Laverny, N. Nardetto, R. Samadi, D. Valls-Gabaud and H. Wozniak (eds)

GAIA AND THE DYNAMICS OF THE GALAXY

B. Famaey[1]

Abstract. Gaia is an ambitious ESA space mission which will provide photometric and astrometric measurements with the accuracies needed to produce a kinematic census of almost one billion stars in our Galaxy. These data will revolutionize our understanding of the dynamics of the Milky Way, and our knowledge of its detailed gravitational potential and mass distribution, including the putative dark matter component and the non-axisymmetric features such as spiral arms. The Gaia mission will help to answer various currently unsettled questions by using kinematic information on both disk and halo stellar populations. Among many others: what does the rotation curve of the outer Galaxy look like? How far from axisymmetry and equilibrium is the Galaxy? What are the respective roles of hierarchical formation and secular evolution in shaping the Galaxy and its various components? Are the properties of the Galaxy in accordance with expectations from the standard model of cosmology?

Keywords: Galaxy: kinematics and dynamics, Galaxy: evolution

1 Introduction

The Milky Way is a unique laboratory in which to test our models of galaxy formation, structure, and evolution. The story of the efforts to obtain stellar kinematic data in the solar neighbourhood during the 20th century has culminated with ESA's Hipparcos astrometric catalogue (Perryman et al. 1997), and with the complementary ground-based spectroscopic surveys that have provided the missing information on the line-of-sight velocities (e.g., Nordström et al. 2004, Famaey et al. 2005). In recent years, drastic improvements in acquisition of stellar kinematic data outside of the close solar vicinity have been made through various large spectroscopic surveys, including the RAVE survey (Siebert et al. 2011a), as well as, for instance, SEGUE, SEGUE-2 and APOGEE, as part of SDSS (Eisenstein et al. 2011). Some of these newest data might actually slightly complicate our picture of the Galaxy, through possible signatures of significant deviations from axisymmetry and equilibrium. However, their interpretation is yet made difficult by sometimes complicated selection functions, and some of these data could also still be plagued by systematic errors, currently preventing us from drawing really secure conclusions. One of the most important sources of error could come from the distances of stars. In view of this, having an astrometric mission dedicated to parallax and proper motion measurements covering the whole sky will be of prime importance in order to refine our detailed understanding of the dynamics of the Galaxy. This is mainly what the Gaia mission will be about.

Scheduled to be launched from Kourou at the end of 2013, ESA's Gaia satellite (see, e.g., Prusti 2012) will perform astrometry and photometry of more than 1 billion objects up to a magnitude $V \sim 20$, as well as spectrosocopy for some 150 million objects up to $V \sim 16$. In order to get six-dimensional phase-space information for the whole Galaxy, the mission will have to be completed with ground-based spectrosocpic surveys, such as 4MOST and WEAVE, for stars with $16 < V < 20$. Although there will be a plethora of science topics addressed by the mission, its primary objective will be to provide a detailed mapping of the Galaxy, and to develop, through dynamical means, a precise mass model including all of its components (interstellar gas, various stellar populations, as well as the yet hypothetical dark matter component needed in Newtonian gravity), giving us insight into its formation and evolutionary history.

[1] Observatoire Astronomique, Université de Strasbourg, CNRS UMR 7550, F-67000 Strasbourg, France

This main objective will be achieved through dynamical models of the Galaxy. Such models have to rely on assumptions, such as axisymmetry and equilibrium. These very legitimate first order assumptions allow us to make use of Jeans' theorem constraining the phase-space distribution function to depend only on three isolating integrals of motion. There are various ways in which to compute these integrals (e.g., Binney 2012, Bienaymé & Traven 2012). In this context, the action integrals are the best suited, since they are adiabatically invariant and are, with their conjugate angle variables, the natural coordinates of perturbation theory. By constructing distribution functions depending on these action integrals (e.g., Binney 2010), one can, e.g., disentangle the various stellar populations such as the thin and thick disk in a much more reliable way than with naive kinematic decomposition. In principle, one can iterate the fits with different gravitational potentials until the best-fitting potential is found, giving access to the underlying mass distribution, and hints into the missing mass question. It is also possible to take into account the main non-axisymmetric component (e.g., the bar) by modelling the system in its rotating frame. The other non-axisymmetric components should then be treated through perturbations. In the presence of multiple perturbers with significant amplitude, it is however not clear that this approach would work. In general, the consequences of assuming dynamical equilibrium when it is not the case might bias the results from the 0th order approach, assuming axisymmetry and equilibrium. In this respect, it will be extremely useful to test the Jeans approach on non-equilibrium models from simulations. The answer to such theoretical questions will have an important impact on the interpretation of future kinematical data.

Here, we list a series of questions that are still unsettled and sometimes overlooked when dealing with stellar kinematic data in our Galaxy. These questions will only be answered through a joint theoretical and observational effort, and using datasets with well-understood errors and selection functions, such as those that Gaia will provide. Answering these questions will certainly help refine our understanding of the structure, formation, and evolution of our Milky Way galaxy, and of galaxies in general.

2 What does the rotation curve of the outer Galaxy look like?

Rotation curves are the primary observational constraint on the gravitational field and the missing mass problem in external late-type galaxies (e.g., Gentile et al. 2004, Chemin et al. 2011). Paradoxically, even though one can obtain data with incomparable precision on the kinematics of individual stars in the Milky Way, our position inside the Galactic disk makes it difficult to measure the outer rotation curve with a similar precision as in external galaxies. This indeed requires to know our distance from the Galactic center R_0, the local circular velocity at the Sun's position V_{c0} and the peculiar velocity of the Sun with respect to this circular velocity, as well as the precise distance to tracers used to measure the rotation curve in the outer Galaxy. Combining Gaia astrometric data with spectroscopic ones for the brightest stars, and with ground-based radial velocities for the faintest stars, should allow us to pin down the relevant quantities with the necessary precision. Note that the modelling should include an asymmetric drift correction for the tracer population. A possible caveat would however be that the non-axisymmetry of the Galaxy biases the estimation of the relevant parameters in an axisymmetric model (see Sect. 4). If the non-axisymmetry was too severe, the whole concept of a rotation curve would not even make sense anymore.

Nowadays, estimates of R_0 can vary, at the extremes, from $\sim$6.5 kpc to $\sim$9.5 kpc, while associated measurements of the local circular velocity vary from $\sim$180 km/s to $\sim$300 km/s, all these values being heavily model-dependent (McMillan & Binney 2010, Schönrich 2012, Bovy et al. 2012a). Note that the currently often preferred value of $V_{c0} \sim 240$ km/s (see McMillan & Binney 2010, Schönrich 2012) would curiously make the Milky Way a significant fast-rotating outlier from the Tully-Fisher relation (see e.g. Flynn et al. 2006, Hammer et al. 2012 for a discussion). These values are however slightly degenerate with the peculiar motion of the Sun, and in particular with its azimuthal component, which is currently poorly constrained within a factor of five, lying in the interval between 5 km/s (Dehnen & Binney 1998) and 25 km/s (Bovy et al. 2012a).

Independently of the absolute value of the circular velocity, another important question is the *shape* of the rotation curve in the outer Galaxy, which is crucial in determining the gravitational field and its associated putative dark matter distribution. It has long been argued that a dip at 9 kpc followed by a bump at 11 kpc is observed in the outer rotation curve of the Galaxy, which has notably been interpreted as the signature of the presence of ring-like dark matter structure (e.g., de Boer & Weber 2011). Notwithstanding the fact that such a behavior could also be created by a dark matter halo with very large constant density core or by spiral arms,

the interpretation of such a feature has also been attributed to a bias in the distribution of tracers (Binney & Dehnen 1997), and the feature is not required in the recent dynamical modelling of APOGEE data (Bovy et al. 2012a). The case for the presence or absence of such a feature in the outer Galaxy rotation curve will certainly be settled with Gaia data, and will be of prime importance for ascertaining the presence or absence of dark matter substructures inside the Milky Way disk, in parallel with a better understanding of the precise density distribution of stars in the outer Galaxy, including features such as the Monoceros overdensity.

3 Is the Galactic disk in vertical equilibrium?

One of the great achievements of the Hipparcos mission in terms of Galactic dynamics (Crézé et al. 1998, Siebert et al. 2003, Holmberg & Flynn 2004) has been to deduce the local dynamical mass in the Solar neighbourhood – the Oort limit and the column density – from the positions and velocities of tracer stars in the direction perpendicular to the Galactic plane, and relying on the Boltzmann and Poisson equations. Recently, using the kinematics of stars at heights of 1 to 4 kpc above the plane, the surface density as a function of height has been computed in the solar vicinity (Bovy & Tremaine 2012), which allows to constrain the vertical structure of the dark matter halo. With parallax distances from Gaia, the precision on such measures will become watertight, and it should also be possible to directly measure the dynamical density in the disk as a function of position in the Galactic plane, allowing us to measure the dynamical scale-length and to compare it with the baryonic scale-length in order to test for the presence of a (real or effective) "dark disk" component (Read et al. 2008, Bienaymé et al. 2009).

However, this relies on the *a priori* reasonable assumption that the disk is in vertical equilibrium. This assumption might be challenged by recent observations from SDSS (Widrow et al. 2012) measuring a 10% North-South asymmetry in a 1 kpc-wide cylinder around the Sun comprising about 300000 stars: the asymmetry follows a wave-like behavior, with a South overdensity at heights of 500 pc and a North overdensity at 1 kpc. Complementary measurements of radial velocities for 11000 stars with SEGUE also reveal that the *mean* vertical motion can reach up to 10 km/s at heights of 1.5 kpc (to be compared with the assumed null mean vertical velocity in the plane yielding a solar reflex motion of $\sim$7 km/s), echoing previous similar results by Smith et al. (2012). If real, these nonzero mean vertical velocities of stars outside of the Galactic plane are very intriguing, and could be a signature of the Galactic warp, or of vertical perturbations excited by the recent passage of a satellite galaxy in the plane (Widrow et al. 2012). Alternatively, they could be due to self-excited vertical instabilities due to spiral arms, despite the presence of such bulk motions at relatively large heights above the plane.

4 How far from axisymmetric is the Galaxy?

Galactic disk instabilities, and their associated non-axisymmetric perturbations, including the bar and spiral arms, are known to be among the main drivers of the secular evolution of disks. Questions about their nature – transient, quasi-stationary, or both types co-existing – , about their detailed structure and dynamics – e.g., amplitude and pattern speed – , as well as questions about their influence on secular processes such as stellar migration (see Sect. 5), are all essential elements for a better understanding of Galactic evolution.

4.1 Moving groups

Six-dimensional phase-space information for stars in an increasingly large volume around the Sun will allow us to set new dynamical constraints on the non-axisymmetric perturbations of the Galactic potential. The resonances of the non-axisymmetric modes of the galactic potential are important agents locally disturbing the stellar velocity field. They create velocity substructures known as "moving groups" in the Solar neighbourhood. These local velocity-space substructures have been reliably shown to be made of stars of very different ages and chemical compositions, so that the clumping cannot be due to irregular star formation (e.g., Dehnen 1998, Famaey et al. 2005, 2007, 2008, Pompéia et al. 2011): they are nowadays the main stellar kinematical constraints on the non-axisymmetric components of the Galaxy. However, various models have argued to be able to represent these structures equally well, using transient or quasi-static spirals, with or without the help of the outer Lindblad resonance from the bar. However, all these models are making drastically different predictions on the velocity substructures when moving away from the Solar neighbourhood. Locating moving groups in velocity space outside of the solar neighbourhood is thus mandatory to discriminate between these models, and

to obtain definitive constraints on the characteristics of the spiral arms and bar. The RAVE survey has for instance allowed (Antoja et al. 2012) to demonstrate that the Hercules moving group has a larger azimuthal velocity for regions inside the solar circle and a lower value outside, in accordance with what is expected from models where the Sun is located just outside the outer Lindblad resonance of the bar (e.g., Quillen et al. 2011).

4.2 Oort constants

The local effects of non-axisymmetric perturbations can also be analyzed by Taylor expanding to first order the planar velocity field in the cartesian frame of the Local Standard of Rest (LSR), an approximation roughly valid up to a distance of less than 2 kpc. This is done by generalizing the classical Oort constants to the case of a non-axisymmetric disk, yielding the constants A, measuring the azimuthal shear, B, measuring the vorticity, C, measuring the radial shear, and K, measuring the local divergence. Axisymmetry implies $C = K = 0$ (but not the reverse, they can, e.g., be zero if the main non-axisymmetric perturbation is symmetric w.r.t. the Sun-Galactic center axis). Proper motions of a large sample of stars allow for a measurement of A, B, and C, while line-of-sight velocities projected onto the Galactic plane give access to A, C and K. While old, rather imprecise, data were actually compatible with the axisymmetric values $C = K = 0$ (Kuijken & Tremaine 1994), a modern analysis of ACT/Tycho-2 proper motions, after corrections for the mode-mixing and asymmetric drift, yielded (Olling & Dehnen 2003) $C = -10\,\mathrm{km/s/kpc}$ for the red giants population, with a typical $\sigma_R \sim 40\,\mathrm{km/s}$. The measurement of the Oort constant K was, on the other hand, recently performed with the RAVE survey (Siebert et al. 2011b) in the longitude interval $-140° < l < 10°$, thanks to the line-of-sight velocities (projected onto the Galactic plane) of 213713 stars (dominated by red giants) with spectro-photometric distances $d < 2\,\mathrm{kpc}$ from the Sun. This analysis confirmed the above proper-motion value of $C = -10$, and found a value $K = +6$, also different from zero. This value would actually imply a Galactocentric radial velocity gradient of $C + K = \partial V_R/\partial R \simeq -4\,\mathrm{km/s/kpc}$ in the extended solar neighbourhood.

4.3 Radial velocity gradient and LSR motion

To check the actual existence of this radial velocity gradient implied by the above-measured value of $C+K$, the projection onto the plane of the mean line-of-sight velocity as a function of $d\,\mathrm{cos}l\,\mathrm{cos}b$ for $|l| < 5°$, was examined both for the full RAVE sample and for red clump candidates (with an independent method of distance estimation). The observed mean velocities were then compared to the expected velocities for a thin disk in circular rotation with an additional radial gradient. This clearly confirmed that the RAVE data are not compatible with a disk in circular rotation. They are, on the other hand, roughly compatible with a linear gradient of $\partial V_R/\partial R \simeq -4\,\mathrm{km/s/kpc}$ (Siebert et al. 2011b). This gradient in $\langle V_R \rangle$ is however not really linear. It is almost absent at small distances, and becomes steep at large distances from the Sun in the inner Galaxy. This means that it affects stars substantially above the plane, keeping in mind that RAVE lines of sight are typically at $b >\sim 20°$: the zone where the gradient is steep concerns stars with $|z| \sim 500\,\mathrm{pc}$, located in the inner Galaxy and moving towards the anticenter. However, if the LSR itself is moving radially towards the inner Galaxy with ~ 5 km/s, then it would mean that the Galactic disk is locally affected by a motion towards the inner Galaxy, which slows down when one moves away from the Sun towards the Galactic center (see Fig. 4 in Famaey et al. 2012). Said in another way, one could have $\langle V_R \rangle \sim -5$ km/s in the Solar neighbourhood at $R \sim 8\,\mathrm{kpc}$, and $\langle V_R \rangle \sim 0$ km/s at $R \sim 6.5\,\mathrm{kpc}$ along the GC-Sun axis and at $|z| \sim 500\,\mathrm{pc}$. This could explain the offset of 5 km/s between the local and non-local estimates of the radial motion of the Sun (Schönrich 2012).

As a first step in understanding this gradient, one could assume that, to first order, what is seen slightly above the plane is a reflection of what would happen in a razor-thin disk, and that the spiral arms are tightly wound and long-lived (although this is heavily debated and most probably wrong to some extent), and described by the analytic Lin-Shu density wave model. This then allows us to constrain the shape, amplitude and dynamics of spiral arms, leaving the radial motion of the Sun as a free parameter. In Siebert et al. (2012) we showed that the best-fit model is obtained for a two-armed perturbation with the Sun close to the inner ultra-harmonic $4:1$ resonance, with a pattern speed $\Omega_s = 18.6^{+0.3}_{-0.2}\,\mathrm{km/s/kpc}$, and an amplitude of 14% of the background density. In this fit the radial motion of the Sun stays within 1 km/s of its locally determined value. While very promising in giving a satisfactory fit, the model limitations nevertheless obviously prevent from drawing definitive conclusions about the cause of the gradient as well as the fitted parameters. It is for instance very likely that the bar also plays a role in this observed behavior.

4.4 Implications

Constraining the non-axisymmetries of the Galactic potential is very important for several reasons. First of all, interpreting the kinematic data in an axisymmetric model (see Sect. 2) could potentially lead to erroneous results, and thereby bias the estimate of the mass distribution in the outer Galaxy. Secondly, such non-axisymmetries are among the main drivers of the secular evolution of the Galactic disk (see Sect. 5), and can play an important role in driving stellar migrations, having dramatic consequences for the chemical evolution of the Galaxy. Thirdly, non-axisymmetric baryonic features, such as spiral arms, can be essential in breaking the disk-halo degeneracy: a large amplitude of the spiral structure cannot simply be traded for mass in the dark matter halo when fitting non-axisymmetric motions (see, e.g., Famaey & Binney 2005 for a discussion). Finally, it is by disentangling the effects of the various non-axisymmetric components that the possible triaxiality of the dark matter halo could be spotted (or excluded) in the outer Galaxy. Such a triaxiality is predicted at large radii from the ΛCDM cosmological model. For this final point, the most promising approach is to use, as dynamical probes, the tidal streams of disrupting satellite galaxies in the potential of the Milky Way, keeping in mind that these do not precisely delineate orbits. Kinematical information from Gaia should allow us to detect many such new streams in the stellar halo, and studying their shape and respective orbit is a very promising tool in constraining the shape of the Galactic potential at large radii. Many streams are indeed required for this method to be reliable, since the orbit of a single stream such as the Sagittarius stream (Ibata et al. 1994) could not break the degeneracy between the possible triaxiality of the halo and the shape of the rotation curve in the outer Galaxy. In this respect, combining dynamical constraints on streams with a reliable measure of the outer rotation curve (see Sect. 2) would be immensely useful for constraining the shape of the potential at large radii.

5 What are the respective roles of hierarchical formation and secular evolution in shaping the Galaxy?

One of the major goals of the dynamical modelling of stellar kinematical data obtained from Gaia will be to disentangle the various components of the Galaxy (bulge, stellar halo, thin disk, thick disk), and unravel their history and origin. Information on the chemical composition of the various stellar populations, obtained with ground-based spectroscopic surveys, will also be of prime importance in order to refine this understanding.

5.1 The bulge and the stellar halo

Two major processes are at play in the evolution of galaxies: hierarchical formation and secular evolution (see, e.g., Debattista et al. 2006 for an overview). The question of whether the Milky Way bulge is the result of an early major merger, of monolithic collapse, or simply of secular evolution through buckling of the central bar, or a combination of these processes, is still unsettled (Babusiaux et al. 2010). Similarly, we still do not know whether the stellar halo (see Helmi 2008 for a review) partially formed *in situ* through dissipational mergers of the first gaseous proto-galactic clumps, potentially resulting in a substantial fraction of its current inner regions, or through the dissipationless accretion of a vast number of small galaxies (creating the aforementioned tidal streams in the outer halo, see Sect. 4). The existence of two such separate halo components and whether they could bear distinct kinematical signatures is still under heavy debate (Schönrich et al. 2011, Beers et al. 2012). Obviously, the number of stellar streams newly detected with Gaia in the outer halo, as well as their phase-space characteristics and chemical composition (e.g., Prantzos 2011), will also allow us to quantify the role of hierarchical formation and merger rate in a cosmological context, testing the predictions of the ΛCDM model (see also Sect. 6).

5.2 The thick disk

On the other hand, the origin of the thick disk component is still a deep mystery: one possibility is that it was born *in situ*, e.g. from the internal gravitational instabilities in a gas-rich, turbulent, clumpy disk (Bournaud et al. 2009), or in the turbulent phase associated with numerous gas-rich mergers (Brook et al. 2004). It could also have been created through direct in-plane accretion of galaxy satellites, although modern data seem to rule out this extragalactic possibility (Ruchti et al. 2010, Wilson et al. 2011). The formation of the thick disk can either happen fast, on a Gyr timescale, in an early violent epoch, or as a secular process throughout the Galaxy lifetime. In the first case, the thick disk would appear as a clear distinct component in chemistry and phase-space, while in the latter case it would rather be seen as a gradual, continuous transition: modern data seem to favour this second option (Bovy et al. 2012b). On the other hand, studying the orbits of stars within

the thick disk, notably their eccentricities at different galactocentric radii with Gaia data, will be a powerful tool for determining its origin (Sales et al. 2009, Di Matteo et al. 2011).

5.3 Radial migration

Driven by the absence of age-metallicity relation in the solar neighbourhood, chemical similarities between metal-poor bulge stars and the local thick disk (e.g., Meléndez et al. 2008), and the fact that stars labelled as local members of the thick disk can have orbital properties suggesting an origin at different galactocentric radii (Haywood 2008), there has recently been a growing convinction that stellar radial migration can result in the thick disk formation by bringing out stars with high velocity dispersion from the inner disk and the bulge (Schönrich & Binney 2009). Sellwood & Binney (2002) indeed showed that transient spirals can efficiently redistribute angular momentum across their corotation radius without heating: if the amplitude of the perturber grows and decays on a timescale comparable to half the libration period of a horseshoe orbit around corotation, the spiral will deposit stars on the other side of corotation and vanish before pulling it back. In the presence of multiple patterns, horseshoe orbits are however necessarily destroyed at corotation when it overlaps with the Lindblad resonances of other patterns, unavoidably resulting in a very moderate degree of chaotic behaviour, even though this is disputed by some studies (Roskar et al. 2012). While differing from the previous process in contributing somewhat to the heating of the Galactic disk with time, this effect has been shown to also significantly enhance the efficiency of migration at corotation (Minchev & Famaey 2010): in particular, in the presence of a strong central bar, transient spirals with corotation close to its outer Lindblad resonance are more efficient at mixing the disk, resulting in a peak of the redistribution of angular momentum at this radius (Minchev et al. 2011), revealing the important role of the bar for chemo-dynamical models taking into account stellar migration (see also Brunetti et al. 2011). For instance, the observed non-linearity of the metallicity gradient in the Milky Way, exhibiting at R_0 a step-like feature with overlapping metallicties characteristic of the inner and outer disk (Lépine et al. 2011), might be directly linked to the coupling between the outer Lindblad resonance of the bar and the corotation of one of the Milky Way spiral patterns. Note also that the multiplicity of spiral patterns lead to the appearance of short-lived density peaks growing and decaying much faster than the spiral waves themselves, also greatly enhancing the efficiency of migration (Comparetta & Quillen 2012). Generally speaking, stellar migration has, in any case, dramatic consequences on the chemo-dynamical evolution of the Milky Way disk, and of galaxy disks in general (e.g., Roskar et al. 2008). For instance, it flattens abundance gradients (probably more so in barred disks, Martin & Roy 1994), and it creates extended stellar disks (up to 10 scale-lengths) with continuous (Type I) or downturning (Type II) density profiles (Minchev et al. 2012a), with steeper slopes for younger populations (Radburn-Smith et al. 2012). Additional smooth gas accretion could create additional spiral instabilities and more migration in the outer parts, thereby generating extended disks with upturning (Type III) profiles. In the Milky Way, it will be extremely interesting to check, with Gaia and complementary surveys such as WEAVE, whether an extended disk does exist, and whether it exhibits such signatures of radial migration, allowing us to quantify the roles of the non-axisymmetric components in the past chemo-dynamical evolution of the disk.

Schönrich & Binney (2009) have shown, with a simple chemical evolution model parametrizing radial migrations, that this mixing could explain most of the chemical properties of the thick disk. It was subsequently shown in Tree-SPH and cosmological simulations that stellar migrators tend to create a flared disk component rather than a thick disk of constant scale-height (Minchev et al. 2012b), meaning that radial migration does *not* thicken the disk in the inner parts. Given the hierarchical formation of the Galaxy, it is however also possible that the thick disk might have been formed without too much flaring through a combination of heating and radial migration caused by instabilities linked to mergers at high-redshift (Minchev et al. 2012c), i.e. quite rapidly in comparison with the Schönrich & Binney (2009) scenario but still in accordance with the Bovy et al. (2012b) results. Testing whether the thick disk has a constant scale-height as a function of radius, as in external galaxies, or whether it is rather strongly flared, would be very important to check whether secular evolution from radial migration alone can explain the creation of such a component. In that case, the scale-height should not be constant, and vertical chemical gradients should also vary with radius, while estimates of the average vertical action (see Sect. 1) for different populations of stars should reveal different variation with radius (flattening for older groups of stars).

6 Is the global structure of the Galaxy in accordance with cosmological expectations?

6.1 The Milky Way in a cosmological context

Quantifying the hierarchical formation history of the Galaxy from understanding its various components as outlined above (notably the respective role of minor and major mergers in the formation of the bulge, thick disk and stellar halo) is of fundamental importance in order to test the predictions of the current standard ΛCDM cosmological model at low redshift. It should however be remembered that, on galaxy scales, predictions of this model are plagued by the enormous complications of baryonic astrophysics (e.g., Silk & Mamon 2012). With this in mind, Milky Way observations nevertheless provide a unique, extremely useful tool in order to set constraints, and to present observational challenges that must be addressed by any scenario of galaxy formation. For instance, the existence of a large number of extended thin disk galaxies without classical bulges is in itself a challenge to the expectations from the number of major mergers in the cosmological model. Thus, tracing back the origin of the Milky Way bulge (Babusiaux et al. 2010 and Sect. 5 hereabove) would be extremely useful to set a benchmark allowing to compare it to the bulges of other galaxies, in order to determine their merger, bar-induced, or mixed origins. Similarly, a slow secular origin for the thick disk might be challenging to the number of expected mergers at high redshift in the standard cosmological scenario, and determining the exact origin of the thick disk and its relation with other components of the Galaxy is thus extremely important in this context (see Sect. 5).

6.2 Dark matter distribution in ΛCDM

A long-standing problem of ΛCDM is the fact that the numerical simulations of the collapse of dark matter halos lead to a density distribution as a function of radius, ρ, which is well fit by a smooth function asymptoting to a central cusp with slope $\mathrm{dln}\rho/\mathrm{dln}r \propto -r^{(1/n)}$ in the central parts (with $n \sim 6$ for a Milky Way-sized halo, meaning that the slope is still -1 at 200 pc from the center), while rotation curves of external galaxies lead to values of n that are much closer to a constant density core (Chemin et al. 2011). In the Milky Way, non-axisymmetric motions (see Sect. 4) and microlensing events in the disk leave no room to trade mass from the stellar disk to the dark matter halo, and rule out a cuspy distribution (see, e.g., Famaey & Binney 2005). Confirmation of this current state of affairs is expected from Gaia. The state-of-the-art solution to this problem is to enforce strong supernovae outflows that move large amounts of low-angular-momentum gas from the central parts and that pull on the central dark matter concentration to create a core (Governato et al. 2012), but this is still a relatively fine-tuned process, which fails to account for cored profiles in the smallest galaxies, and fails to produce their observed baryon fractions ([stars+gas]/total).

6.3 Satellite galaxies: paucity and geometry

Satellite galaxies of the Milky Way are also extremely useful tools to test the ΛCDM predictions. For instance, a lot of low-mass satellites are still missing (e.g., Bovill & Ricotti 2011), which could be due to incomplete sky coverage from current surveys such as the SDSS. Discovering more dwarf galaxies around the Milky Way, especially ultra-faint ones is thus of immense importance for future surveys including Gaia. Sooner, the Pan-STARRS survey should already give us interesting results in this respect[i]. In addition to this challenge from the actual quantity of observed satellites, the distribution of dark subhalos around Milky Way-sized halos is also predicted by ΛCDM to be isotropic, or moderately flattened (Wang et al. 2012). However, the Milky Way satellites are currently observed to be highly correlated in phase-space: they lie within a seemingly rotationally supported thin disk (see, e.g., Kroupa et al. 2010). Young halo globular clusters define the same disk, and streams of stars and gas, roughly tracing the orbits of the objects from which they are stripped, seem to preferentially lie in this disk, too. While this might perhaps be explained by the infall of one or two groups of galaxies that would have retained correlated orbits, this solution is challenged by the fact that no nearby groups are observed to be anywhere near as spatially small as the Milky Way's disk of satellites (e.g., Kroupa et al. 2010). But since the SDSS survey covered only one fifth of the sky, it will of course be most interesting to see whether future surveys such as Pan-STARRS and Gaia will confirm this state of affairs. Precise proper motions observed with Gaia for the faintest galaxies and stellar streams will also be extremely important: this

[i]Independently of future surveys, note that the most massive subhaloes currently predicted by ΛCDM are incompatible with hosting any of the MW satellites: the "too big to fail" challenge (Bovill & Ricotti 2011, Boylan-Kolchin et al. 2012)

will allow us to trace back the orbits in a ΛCDM context (see, e.g., Angus et al. 2011), and will allow us to check whether the whole polar structure is indeed rotationally supported. Whether or not such a satellite phase-space correlation would be unique to the Milky Way should also be carefully checked: the Milky Way can be a statistical outlier, but if the ΛCDM model is a realistic description of nature, then the average satellite configurations in external galaxies should be only moderately flattened (Wang et al. 2012). If this is not the case, i.e. if flattened configurations are the norm, one possibility to investigate in detail would be a heavily heterogeneous and asymmetric reionization coming from internal sources, in the spirit of Ocvirk & Aubert (2011), preserving only small regions of the proto-galaxy corresponding to the current disk of satellites.

6.4 Modified gravity?

Another more radical solution to this disk-of-satellites problem[ii] might be that most satellite galaxies are actually not primordial galaxies but rather tidal dwarf galaxies created in a major merger event, having occured in the Milky Way (e.g., Pawlowski et al. 2012) or even in M31 (Fouquet et al. 2012): this could possibly account for their presently correlated phase-space distribution, but would be in severe conflict with the fact that tidal dwarf galaxies are not supposed to harbour large dark matter fractions, while observations point to these objects being the most dark matter dominated objects in the Universe. This could however be reminiscent of young tidal dwarf galaxies observed in the tidal tails of external galaxies to also harbour substantial amounts of missing mass (Bournaud et al. 2007). One obvious solution might be to seriously reconsider the possibility that a large fraction of missing mass in disk galaxies is in the form of cold molecular gas distributed fractally in the disk (e.g., Pfenniger & Combes 1994, Davies 2012). This would need us to rethink most of our understanding of galaxy formation. Another, even more baffling possibility, would be that there is actually no missing mass on galaxy scales (which would *not* mean that dark matter does not exist on cosmological scales), but that gravity is non-Newtonian. This would help explaining why many observed scaling relations in external galaxies (Famaey & McGaugh 2012) involve the ubiquitous appearance of an acceleration constant $a_0 \sim \Lambda^{1/2} \sim 10^{-10}\mathrm{m\,s^{-2}}$, whose origin is mysterious in the standard context. Most of these scaling relations can indeed be summarized by the empirical formula of Milgrom (1983), the success of which means that the gravitational field in galaxies mimicks, for whatever reason, an effectively modified force law on galaxy scales, known as Modified Newtonian Dynamics (MOND). This theory would for instance naturally explain why young tidal dwarf galaxies exhibit a mass discrepancy (Gentile et al. 2007) where dark matter is not expected to show up. The advent of Gaia will yield precise measurements allowing us to test the possibility that the success of Milgrom's formula is linked to modified gravity. These include the measurement of the outer rotation curve and its possible deviation from the baryonic Tully-Fisher relation (see Sect. 2), as well as the various effect of the "phantom dark disk" of MOND (Bienaymé et al. 2009) on vertical velocity dispersions (see Sect. 3) and on the tilt of the stellar velocity ellipsoid, the precise shape of tidal streams around the Galaxy (see Sect. 4), or the effects of the external gravitational field in which the Milky Way is embedded on fundamental parameters such as the local escape speed. All these predictions can however slightly vary depending on the exact formulation of MOND, and will heavily depend on our precise knowledge of the underlying baryonic mass distribution. Should these tests be compatible with the predictions of MOND, the biggest challenge for such a theory would however remain to design a cosmological framework that could compete with the successes of ΛCDM on cosmological scales.

7 Conclusion

Today, there are still a lot of largely unknown answers to many old questions regarding the dynamics of the Milky Way, such as the local circular speed at the Sun's radius, the peculiar motion of the Sun, the degree of non-axisymmetry of the gravitational potential, the degree of North-South symmetry around the Galactic plane, or the geometry of the satellite system of the Galaxy. Recent data coming from large surveys are questioning many of the old assumptions that were made regarding these issues. Since it is still possible that some of these new results may turn out to be caused by systematic errors, notably in the stellar spectrophotometric distances, or from improper correction for complicated selection biases, it will be of prime importance to re-investigate all these questions with the distances and proper motions from Gaia at hand. Whatever the final answers to all these questions are, they will surely help us refine our understanding of the evolution of galaxies, and will give

[ii] Note that to maintain such a coherent rotating structure, the predicted triaxiality (see Sect. 4) of dark matter halos at large radii would also be severely challenged.

us new insights into modern questions about the gravitational field of the Milky Way and its connection to the dark matter mystery and cosmology.

References

Angus G., et al., 2011, MNRAS, 416, 1401
Antoja T., et al., 2012, MNRAS, arXiv:1205.0546
Babusiaux C., et al., 2010, A&A, 519, A77
Bienaymé O., et al., 2009, A&A, 500, 801
Bienaymé O., Traven G., 2012, A&A
Binney J., Dehnen W., 1997, MNRAS, 287, L5
Binney J., 2010, MNRAS, 401, 2318
Binney J., 2012, MNRAS, arXiv:1207.4910
Beers T., et al., 2012, ApJ, 746, 34
Bournaud F., et al., 2007, Science, 316, 1166
Bournaud F., et al., 2009, ApJ, 707, L1
Bovill M., Ricotti, M., 2011, ApJ, 741, 18
Bovy J., et al., 2012a, ApJ, arXiv:1209.0759
Bovy J., et al., 2012b, ApJ, 751, 131
Bovy J., Tremaine S., 2012, ApJ, 756, 89
Boylan-Kolchin M., et al., 2012, MNRAS, 422, 1203
Brook C., et al., 2004, ApJ, 612, 894
Brunetti M., et al., 2011, A&A, 534, A75
Chemin L., et al., 2011, AJ, 142, 109
Comparetta J., Quillen A., 2012, MNRAS, arXiv:1207.5753
Crézé M., et al., 1998, A&A, 329, 920
Davies J., 2012, arXiv:1204.4649
Debattista V., et al., 2006, ApJ, 645, 209
De Boer W., Weber M., 2011, JCAP, 04, 002
Dehnen W., 1998, AJ, 115, 2384
Dehnen W., Binney J., 1998, MNRAS, 298, 387
Di Matteo P., et al., 2011, A&A, 525, L3
Eisenstein D., et al., 2011, AJ, 142, 72
Famaey B., et al., 2005, A&A, 430, 165
Famaey B., Binney J., 2005, MNRAS, 363, 603
Famaey B., et al., 2007, A&A, 461, 957
Famaey B., et al., 2008, A&A, 483, 453
Famaey B., et al., 2012, EPJWC, 19, 07001
Famaey B., McGaugh S., Living Reviews in Relativity, 15, 10
Flynn C., et al., 2006, MNRAS, 372, 1149
Fouquet S., et al., 2012, MNRAS, arXiv:1209.4077
Gentile G., et al., 2004, MNRAS, 351, 903
Gentile G., et al., 2007, A&A, 472, L25
Governato F., et al., 2012, MNRAS, 422, 1231
Hammer F., et al., 2012, EPJWC, 19, 01004
Haywood M., 2008, MNRAS, 388, 1175
Helmi A., 2008, A&ARv, 15, 145
Holmberg J., Flynn C., 2004, MNRAS, 352, 440
Ibata R., et al., 1994, Nature, 370, 194
Kroupa P., et al., 2010, A&A, 523, A32

Kuijken K., Tremaine S., 1994, ApJ, 421, 178
Lépine J., et al., 2011, MNRAS, 417, 698
Martin P., Roy J.-R., 1994, ApJ, 424, 599
McMillan P., Binney J., 2010, MNRAS, 402, 934
Meléndez J., et al., 2008, A&A, 484, L21
Milgrom M., 1983, ApJ, 270, 365
Minchev I., Famaey B., 2010, ApJ, 722, 112
Minchev I., et al., 2011, A&A 527, A147
Minchev I., et al. 2012a, A&A, arXiv1203.2621
Minchev I., et al., 2012b, A&A, arXiv1205.6475
Minchev I., et al., 2012c, arXiv1208.1506
Nordström B., et al., 2004, A&A, 418, 989
Ocvirk P., Aubert D., 2011, MNRAS, 417, L93
Olling R., Dehnen W., 2003, ApJ, 599, 275
Pawlowski M., et al., 2012, MNRAS, 424, 80
Perryman M., et al., 1997, A&A, 323, L49
Pfenniger D., Combes F., 1994, A&A, 285, 94
Pompéia L., et al., 2011, MNRAS, 415, 1138
Prantzos N., 2011, arXiv:1101.2108
Prusti T., 2012, AN, 333, 453
Quillen A., et al., 2011, MNRAS, 417, 762
Radburn-Smith D., et al., 2012, ApJ, 753, 138
Read J., et al., 2008, MNRAS, 389, 1041
Roskar R., et al., 2008, ApJ, 684, L79
Roskar R., et al., 2012, MNRAS, arXiv:1110.4413
Ruchti G., et al., 2010, ApJ, 721, L92
Sales L., et al., 2009, MNRAS, 400, L61
Schönrich R., Binney J., 2009, MNRAS, 399, 1145
Schönrich R., et al., 2011, MNRAS, 415, 3807
Schönrich R., 2012, MNRAS, arXiv:1207.3079
Sellwood J., Binney J., 2002, MNRAS, 336, 785
Siebert A., et al., 2003, A&A, 399, 531
Siebert A., et al., 2011a, AJ, 141, 187
Siebert A., et al., 2011b, MNRAS, 412, 2026
Siebert A., et al., 2012, MNRAS, 425, 2335
Silk J. Mamon G., 2012, Res. in Astron. and Astrophys., 12, 917
Smith M., et al., 2012, ApJ, 746, 181
Wang J., et al., 2012, MNRAS, arXiv:1206.1340
Widrow L., et al., 2012, ApJ, 750, L41
Wilson M., et al., 2011, MNRAS, 413, 2235

SF2A 2012
S. Boissier, P. de Laverny, N. Nardetto, R. Samadi, D. Valls-Gabaud and H. Wozniak (eds)

INPOP: EVOLUTION, APPLICATIONS, AND PERSPECTIVE

A. Fienga[1], J. Laskar[2], A. Verma[1], H. Manche[2] and M. Gastineau[2]

Abstract. The INPOP ephemerides have known several improvements and evolutions since the first INPOP06 release in 2008 (Fienga et al. 2008). In 2010, anticipating the IAU 2012 resolutions, adjustement of the gravitational solar mass with a fixed astronomical unit (AU) has been for the first time implemented in INPOP10a (Fienga et al. 2011) together with improvements in the asteroid mass determinations. With the latest INPOP10e version (Fienga et al. 2012), such advancements have been enhanced and studies about solar corona have also been investigated (Verma et al. 2012). The use of planetary ephemerides for several physical applications are presented here from electronic densities of solar slow and fast winds to asteroid mass determinations and tests of general relativity operated with INPOP10a. Perspectives will also be drawn especially related to the analysis of the Messenger spacecraft data for the planetary orbits and future computation of the time variations of the gravitational mass of the sun.

Keywords: Planetary ephemerides, numerical integration, space missions, tests of general relativity, asteroid masses

1 Introduction

Since 2006, INPOP (Integration Numerique Planetaire de l'Observatoire de Paris) has become an international reference for space navigation (to be used for the GAIA mission navigation and the analysis of the GAIA observations) and for scientific research in dynamics of the solar system objects and in fundamental physics. A first version of INPOP, INPOP06, was published in 2008 ((Fienga et al. 2008)). This version is very close to the reference ephemerides of JPL in its dynamic model and in its fit procedure. With MEX and VEX tracking data provided by ESA, lunar laser ranging observations and the development of new planetary and moon ephemeris models and new adjustment methods, INPOP08 (Fienga et al. 2009) and INPOP10a (Fienga et al. 2011b) were constructed. These versions of INPOP have established INPOP at the forefront of global planetary ephemerides because its precision in terms of extrapolation to the position of planets is equivalent to the JPL ephemerides. Its dynamic model follows the recommendations of the International Astronomical Union (IAU) in terms of i) compatibility between time scales (TT, TDB), ii) metric in the relativistic equations of motion (consistency in the computation of the position of the barycenter of the solar system) and iii) in the fit of the sun gravitational mass with a fixed AU.

INPOP provides to the user, positions and velocities of the planets, the moon, the rotation angles of the earth and the moon as well as TT-TDB chebychev polynomials at `http://www.imcce.fr/inpop`. INPOP10a was the first planetary ephemerides in the world built up with a direct estimation of the gravitational mass of the sun with a fixed astronomical unit instead of the traditional adjustment of the AU scale factor. With INPOP10a, we have demonstrated the feasibility of such determination helping the IAU of taking the decision of fixing the astronomical unit (see resolution B2 of the 35th IAU general assembly, 2012).

The INPOP01e (Fienga et al. 2012) is the latest INPOP version developed for the Gaia mission final release and available for users. Compared to INPOP10a, new sophisticated procedures related to the asteroid mass determinations have been implemented: bounded value least squares have been associated with a-priori sigma estimators (Kuchynka 2010; Fienga et al. 2011a) and solar plasma corrections (Verma et al. 2012). Very recent Uranus observations provided by Viera Martins & Camargo (2012) have been added as well as positions of Pluto deduced from HST (Tholen et al. 2008).

[1] Institut UTINAM-CNRS 6213, Université de Franche-Comté, Besançon, France
[2] Astronomie et Systèmes Dynamiques, IMCCE-CNRS UMR8028, Paris, France

Table 1. Values of parameters obtained in the fit of INPOP10e and INPOP10a to observations.

	INPOP10e $\pm 1\sigma$	INPOP06 $\pm 1\sigma$	DE423 $\pm 1\sigma$
(EMRAT-81.3000)$\times 10^{-4}$	(5.700 $\pm$ 0.020)	5.6	(5.694 $\pm$ 0.015)
$J_2^{\odot} \times 10^{-7}$	(1.80 $\pm$ 0.25)	(1.95 $\pm$ 0.5)	1.80
$GM_{\odot}$ - 132712440000 [km^3. s^{-2}]	(50.16 $\pm$ 1.3)	17.987	40.944
AU - 1.49597870700 $\times 10^{11}$ [m]	9.0	9.0	(-0.3738 $\pm$ 3)
[$M_{\odot}$ / M_{EMB}] - 328900 $\times 10^{11}$	5.5253 $\pm$ 0.0027	5.6140	5.5915 $\pm$ NC

Adjustment of the gravitational mass of the sun is performed as recommended by the IAU resolution B2 as well as the sun oblateness (J_2), the ratio between the mass of the earth and the mass of the moon (EMRAT) and the mass of the Earth-Moon barycenter. Estimated values are presented on Table 1.

Masses of the planets have been as well updated to the IAU best estimated values (Luzum et al. 2012).

Thanks to the added solar corrections and to the improvement in the fit procedure, 152 asteroid masses have been estimated (see section 3). Comparisons to other planetary ephemerides, postfit and extrapolated residuals are discussed in section 2.

2 Estimation of uncertainties

2.1 Comparisons to other planetary ephemerides

In order to better estimate the INPOP10e uncertainties, comparisons are made between INPOP10e, INPOP10a and the JPL DE423 (Folkner 2010) in spherical coordinates (table 2) for the planets relative to the earth and in cartesian coordinates (table 3) for the earth relative to the solar system barycenter in the ICRF (also called BCRS) over a period of 20 years before and after J2000. With these figures, differences in the dynamic model, fitting procedures and data sample can be impacted on planetary positions and velocities for an interval of time corresponding to the most accurate data sets.

The DE423 ephemerides have been fitted on a data set similar to the INPOP10e one. Fitting procedures differ with less asteroid masses adjusted in DE423 (63) and smoother behavior in the Mars residuals during the fitted period (see table 1). INPOP10e differs from INPOP10a by new corrections in the Messenger data, new implementation in the fit of the asteroid masses and in the correction of the solar plasma, and the use of very recent observations of Uranus (Viera Martins & Camargo 2012) inducing modifications in the weighting schema of the adjustment. Differences between INPOP10e, DE423 and INPOP10a can be seen as good estimations of the state-of-art uncertainties of planetary ephemerides.

As expected, the uncertainties of the positions of inner planets are quite smaller than those obtained for the outer planets. This can easily be explained by the use in the ephemeris construction of high accurate data deduced from the tracking of inner planet orbiters during the past 40 years.

For Jupiter, the uncertainty in geocentric distance is about 1 km but the angular differences are not quite similar from one ephemeris to another: from 10 mas with INPOP10a to less than 1 mas with DE423.

Due to these important variations and to the expected lack of accurate Jupiter observations in the near future, the accuracy of the Jupiter orbit is very likely to degrade in the coming years. For Saturn, the ephemerides give more consistent results reflecting the important role of the Cassini observations in the Saturn orbit determination. For Uranus, Neptune and Pluto, the important differences illustrate the lack of accurate estimations of distances and angular positions for these objects.

Differences in the earth BCRS positions and velocities obtained for several planetary ephemerides (see table 3) are about 1 kilometer in positions and smaller than 0.1 $mm.s^{-1}$ in velocities. Comparisons between DE423 and DE421 (Folkner et al. 2008) which differ mainly by the data sample are equivalent to those obtained with the two consecutive INPOP versions (INPOP10e and INPOP10d (Verma et al. 2012)). In the case of INPOP10e and INPOP10a, these figures can be explained up to 85 % by differences in the estimation of the gravitational mass of the sun.

2.2 Comparisons to observations, extrapolation and link to the ICRF

The INPOP10e observational sample has 3 times more data than the INPOP06 one (the first INPOP release) which ended in 2005.45. The statistical distribution of the supplementary data sets is not uniform and is mostly constituted with MEX and VEX observations (60 %). However, the two flyby points of Uranus and Neptune and the five flybys of Jupiter are of crucial importance for the accuracy of these orbits. The three positions of Mercury deduced from the Messenger flybys play also an important role for the Mercury orbit determination even if their distribution in time was very limited (less than 2 years).

On table 1 are given some examples of postfit and extrapolated residuals obtained with INPOP10e and other ephemerides. For Mars, INPOP10e faces an improvement of the extrapolated residuals compared to INPOP10a and obtains the same level of accuracy as the JPL DE423. The Saturn residuals presented in table 1 are good examples of the improvement of the outer planet orbits obtained with INPOP10e compared to the previous INPOP versions. In particular, a reduction of a factor more than 10 is obtained in Cassini range residuals. This improvement is also confirmed with the Uranus and Neptune flyby residuals. By providing measured distances between the earth and the outer planets, the flyby data brought new informations to the fit when only optical observations were used in the INPOP06 and INPOP08 adjustments. As a result, one can notice the satisfactory INPOP06 residuals obtained for the outer planet accurate spacecraft tracking data (Cassini in table 1) in right ascension and declination (at the level of the accuracy of the optical data used in the INPOP06 fit) but the very poor estimations in distances.

For Jupiter, the expected accuracy of the ephemerides will not be better than the postfit residuals obtained by comparison to flyby positions which reach up about 2 kilometers (see Fig. 1). Unfortunately, no direct accurate observation of Jupiter (such as radio or VLBI tracking of a spacecraft in its vicinity) are planned in the near future in order to maintain the constraints over the Jupiter orbit. Calibration of possible Jupiter orbit degradation would only be partially possible through indirect constraints from Cassini Solstice mission, Dawn, Messenger, present and future Mars orbiters. However, contrary to Jupiter, new Saturn positions would be obtained during the Cassini Solstice mission through 2017 and would then be helpful for constraining the Saturn orbit in the coming years.

For the inner planets, the orbits are very well constrainted thanks to spacecraft tracking data of Mars orbiters, VEX and Messenger missions. However, we note a rapid degradation of the Mars orbit accuracy as estimated by comparison between planetary ephemerides and observed MEX distances not included in the fit of the ephemerides. Such comparisons are called extrapolation in the top charts of the Fig. 1. The differences between estimated distances and the observed one reach up to 30 meters after 32 months and are mainly due to un-modeled perturbations of main-belt asteroids.

Even if not seen as a major planet anymore, Pluto orbit is also included in the INPOP planetary ephemerides. For our latest version, we work on the improvement of the Pluto orbit in including stellar occultations (as in INPOP10a) but also positions of the Pluto-Charon barycentric system obtained in 2008 with HST by Tholen et al. (2008). In the opposite of DE423, INPOP10e shows un-biased residuals in right ascension and declination as one can see on Fig. 1.

The tie between INPOP ephemerides and the ICRF (McCarthy & Petit 2003) is maintained by the use of VLBI differential observations of spacecraft relative to ICRF sources. Such methods give milliarcsecond (mas) positions of a spacecraft orbiting a planet directly in the ICRF. Combining such VLBI observations with spacecraft navigation, positions of planets can be deduced relatively to the ICRF sources. The link between modern planetary ephemerides and the ICRF is then obtained at the accuracy of the VLBI localization of the space missions. Based on the most recent Mars, VEX and Cassini VLBI observations, the link between the INPOP10e reference frame and the ICRF is maintained with an accuracy of about 1 mas for the last 10 years.

3 Applications

3.1 Solar physics

As one can see on the left-hand side chart of the Fig. 2, range observations of MGS, MEX and VEX spacecraft were highly affected by solar plasma perturbations during solar conjunctions, but also before and after these critical periods. In the opposite side of the spectrum, solar physicists are interested in characterizing electronic densities of two specific area on the sun surface: the regions in which dominates a slow wind (mainly following the magnetic neutral line) and the regions (higher in solar latitudes) corresponding to fast winds (Schwenn & Marsch 1990, 1991). By analyzing the path of the radiometric signal from the spacecraft to the earth, it is

Table 2. Maximum differences between INPOP10e, INPOP10a and DE423 from 1980 to 2020 in spherical geocentric coordinates and distances.

Geocentric Differences	INPOP10e - INPOP10a 1980-2020			INPOP10e - DE423 1980-2020		
	α	δ	ρ	α	δ	ρ
	mas	mas	km	mas	mas	km
Mercury	1.4	3.1	0.6	1.58	1.7	0.65
Venus	0.27	0.43	0.021	0.85	0.42	0.045
Mars	1.26	0.37	0.185	2.1	0.62	0.47
Jupiter	4.13	9.94	0.88	0.81	0.74	1.11
Saturn	0.54	0.52	0.51	0.82	0.53	1.82
Uranus	226.9	120.2	1370	98.1	38.9	359.73
Neptune	12.6	6.5	1081	51.0	91.3	2054.8
Pluton	25.53	154.8	3447.1	703.2	152.7	37578.6

Table 3. Maximum differences between INPOP10e and other planetary ephemerides from 1980 to 2020 in cartesian coordinates of the earth in the BCRS.

Earth Barycentric Differences	XYZ	VxVyVz
	km	$mm.s^{-1}$
INPOP10e - INPOP10a	-1.0	0.050
INPOP10e - DE423	0.84	0.113
DE423-DE421	0.37	0.070
INPOP10e-INPOP10d	0.34	0.050

possible to estimate such electronic densities for the two regions during the ingress and the egress parts of the signal and for different phases of the solar activity (Verma et al. 2012). On the right-hand chart of the Fig. 2, the distributions of MGS, MEX and VEX analyzed data in slow and fast wind regions are plotted and the obtained electronic densities for the two regions are also given. After the estimation of the electronic densities, solar plasma corrections were applied to the radiometric signal from the Mars and Venus orbiters, as one can see on the left-hand side chart of the Fig. 2. Such corrections allow to re-introduce in the INPOP fit 8% of supplementary data, previously rejected, and then to improve the extrapolation capabilities of INPOP10e and the asteroid mass determinations (Verma et al. 2012).

3.2 Asteroid masses

Due to the perturbations of the main belt asteroids over the Mars and the earth orbits, asteroid mass determinations deduced from the construction of planetary ephemerides and the analysis of the high accurate Mars orbiter tracking distances are done regularly (Konopliv et al. 2011; Fienga et al. 2011a; Somenzi et al. 2010; Konopliv et al. 2006). However, the inversion problem is here very complex as only less than 50 asteroid masses (to be compared with the 300 asteroids included in the dynamic model of the ephemeris) are known and as all the perturbations cumulate over the Mars geocentric distances. Sophisticated procedures have been tested for years (Standish & Fienga 2002; Kuchynka 2010; Kuchynka et al. 2010). Thanks to the implementation of bounded value least squares associated with a-priori sigma estimators and to the corrections of solar plasma perturbations, we have been able to estimate 152 asteroid masses presented in Fienga et al. (2012). This release is quite satisfactory: comparisons between INPOP10e values and values obtained by other authors either by planetary ephemeris construction (Konopliv et al. 2011; Kuchynka 2012) or by close-encounter methods (Zielenbach 2011; Baer et al. 2011) are indeed in good agreement. As one can see on Fig. 3, asteroids inducing more than 7 meter perturbations over the Mars-earth distances have very consistent densities. This limit is consistent with the dispersion of the postfit residuals presented on Fig. 1 which is about 9 meters for all the data sample and 4 meters out of the conjunction periods. Furthermore, for small perturbers, and contrarily to the previous

INPOP versions, INPOP10e does not provide unrealistic densities, smaller than 0.5 g.cm^{-3} or greater than 6 g.cm^{-3}.

3.3 Tests of fundamental physics

Thanks to the high precision obtained by INPOP08 and INPOP10a, computations have also included determinations of the PPN parameter β with considerable precision and estimates of the perihelion advances of the 8 planets of the solar system. No new advance and no β-deviation of the unit could be clearly demonstrated, confirming the validity of general relativity to the level of 10^{-5} (Fienga et al. 2010, 2011b). Combined estimations of PPN parameters β and γ were also obtained with great accuracy using INPOP10a as well as sharp constraints on supplementary advances of nodes and perihelia of the planets. These latest estimations give stringent constraints on cosmological models of gravity such as MOND (Blanchet & Novak 2011). Tests of acceptable supplementary Pioneer-like accelerations were also done and confronted to the most accurate observations of outer planets. As one can see on the Fig. 3, only an acceleration with an amplitude smaller 5.10^{-13} m.s^{-2} is compatible with the observed geocentric Saturn distances deduced from the Cassini tracking data.

4 Conclusions

Planetary ephemerides are not a only crucial tool for celestial mechanics or the preparation of space missions. They can also play an important role in testing gravity, studying the asteroid physics by estimating their masses or in solar physics with the analysis of the solar corona signatures over radiometric tracking observations of planet orbiters. We present here the latest INPOP version. It appears to be as accurate as the JPL DE ephemerides and allows several applications in solar physics, planetology and gravity testing. At the end of 2012, the analysis of the Messenger tracking data should be completed and implemented in INPOP. These new observations would be crucial especially for gravity tests. We will also implement the estimation of possible variation of the gravitational mass of the sun. This parameter would give stringent limits to theoretical developments predicting variations with time of the gravitational constant. More observations of Saturn deduced from the Solstice extended Cassini mission should also be available. These data would be very helpful to maintain the accuracy of the outer planet orbits.

References

Baer, J., Chesley, S. R., & Matson, R. 2011, AJ, 212

Blanchet, L. & Novak, J. 2011, MNRAS, 412, 2530

Fienga, A., Kuchynka, P., Laskar, J., Manche, H., & Gastineau, M. 2011a, in EPSC-DPS Joint Meeting 2011, 1879

Fienga, A., Laskar, J., Kuchynka, P., et al. 2010, American Astronomical Society, IAU Symposium #261. Relativity in Fundamental Astronomy: Dynamics, Reference Frames, and Data Analysis 27 April - 1 May 2009 Virginia Beach, VA, USA, #6.02; Bulletin of the American Astronomical Society, Vol. 41, p.881, 261, 602

Fienga, A., Laskar, J., Manche, H., Gastineau, M., & Verma, A. 2012, DPAC INPOP final release: INPOP10e, ArXiv e-prints

Fienga, A., Laskar, J., Manche, H., et al. 2011b, Celestial Mechanics and Dynamical Astronomy, 111, 363

Fienga, A., Laskar, J., Morley, T., et al. 2009, A&A, 507, 1675

Fienga, A., Manche, H., a. L. J., & Gastineau, M. 2008, A&A, 477, 315

Folkner, W. 2010, JPL Interoffice Memorandum IOM 343.R-10-001: Planetary Ephemeris DE423 fit to Messenger encounters with Mercury, Tech. rep., JPL Interoffice Memorandum IOM 343.R-10-001

Folkner, W. M., Williams, J. G., & Boggs, D. H. 2008, jPL Interoffice Memorandum IOM 343R-08-003

Konopliv, A. S., Asmar, S. W., Folkner, W. M., et al. 2011, Icarus, 211, 401

Konopliv, A. S., Yoder, C. F., Standish, E. M., Yuan, D.-N., & Sjogren, W. L. 2006, Icarus, 182, 23

Kuchynka, P. 2010, PhD in astronomy, Observatoire de Paris

Kuchynka, P. 2012, private communication

Kuchynka, P., Laskar, J., Fienga, A., & Manche, H. 2010, A&A, 514, A96+

Luzum, B., Capitaine, N., Fienga, A., et al. 2012, Transactions of the International Astronomical Union, Series A, 28, 50

McCarthy, D. D. & Petit, G. 2003, IERS Technical Note No 32, Tech. rep., IERS Convention Centre, http://www.iers.org/iers/publications/tn/tn32/

Schwenn, R. & Marsch, E. 1990, Physics of the Inner Heliosphere I.: Large-Scale Phenomena. (Springer)

Schwenn, R. & Marsch, E. 1991, Physics of the Inner Heliosphere II.: Particles, Waves and Turbulence. (Springer)
Somenzi, L., Fienga, A., Laskar, J., & Kuchynka, P. 2010, Planetary and Space Science, 58, 858
Standish, E. M. & Fienga, A. 2002, A&A, 384, 322
Tholen, D. J., Buie, M. W., Grundy, W. M., & Elliott, G. T. 2008, AJ, 135, 777
Verma, A. K., Fienga, A., Laskar, J., et al. 2012, ArXiv e-prints
Viera Martins, R. & Camargo, J. I. B. 2012, private communication
Zielenbach, W. 2011, AJ, 142, 120

MGS/Odyssey/MEX
INPOP10e : σ_{postfit} =9 m, σ_{extrap} = 30 m

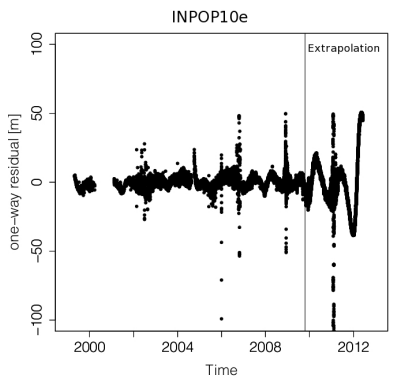

MGS/Odyssey/MEX
INPOP10a : σ_{postfit} =13 m, σ_{extrap} = 65 m

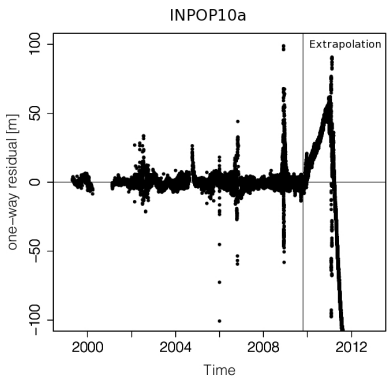

MGS/Odyssey/MEX
DE423 : σ_{postfit} =10 m, σ_{extrap} = 31 m

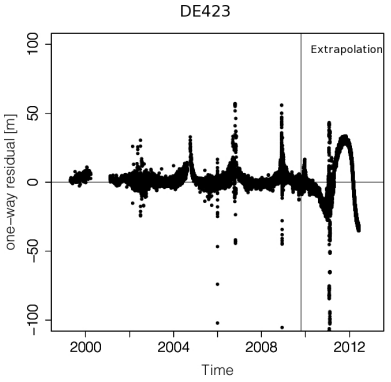

Cassini α
INPOP10e: σ = 4 mas
INPOP06: σ = 5 mas, offset = 33 mas

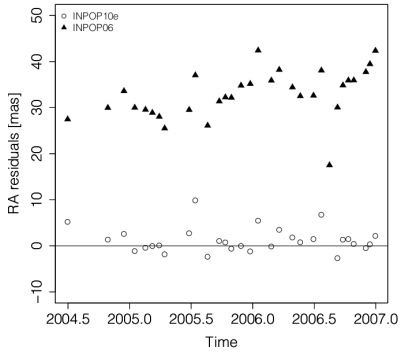

Cassini δ
INPOP10e: σ = 7 mas
INPOP06: σ = 7 mas, offset = 28 mas

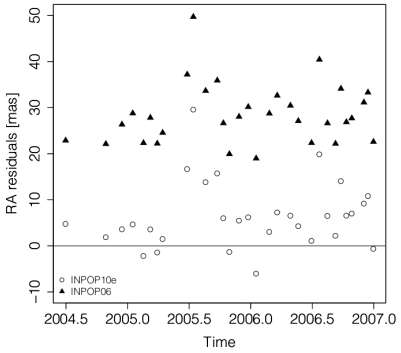

Cassini range
INPOP10e: σ = 17 m
INPOP06: σ = 27 km, offset = -72 km

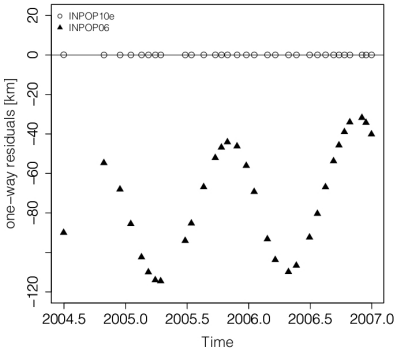

Jupiter flyby range
INPOP10e: σ = 1.6 km
INPOP06: σ = 3.3 km

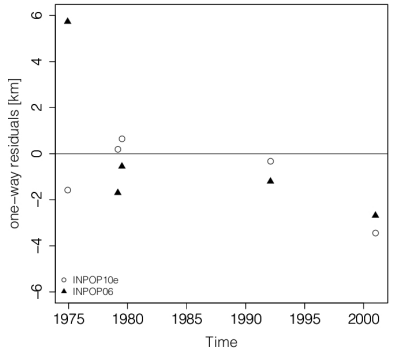

Pluto Occultation + HST α
INPOP10e: σ = 48 mas
DE423: σ = 44 mas, offset = -47 mas

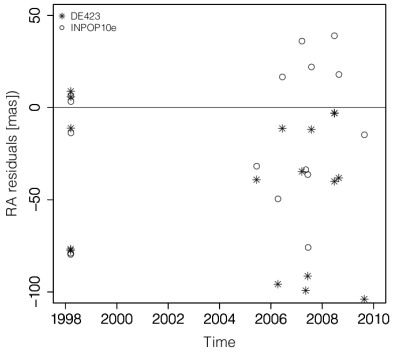

Pluto Occultation + HST δ
INPOP10e: σ = 32 mas
DE423: σ = 36 mas

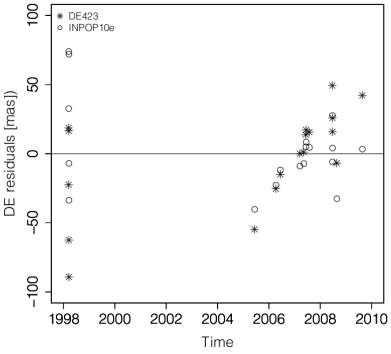

Fig. 1. Some examples of postfit and extrapolated residuals obtained with INPOP10e, INPOP10a, INPOP06 and DE423. The given σ (resp. offset) are the 1-σ dispersion (resp. mean) of the residual distributions. Only statistically meaningful offsets are given.

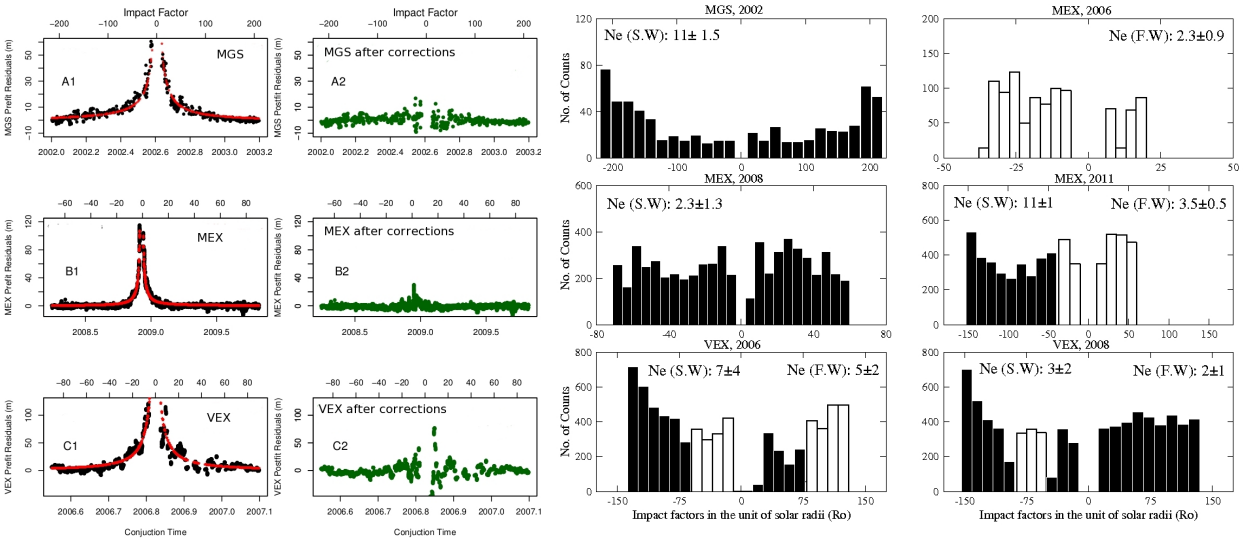

Fig. 2. Solar physics applications: a) Corrections of solar plasma applied to MGS, MEX and VEX range measurments. b) Histograms of the distributions of MGS, MEX and VEX data during solar conjunctions in slow (black) and fast (white) wind regions. Are also given the values of the obtained electronic density (N_e) at 1 AU in electrons.cm^{-3}.

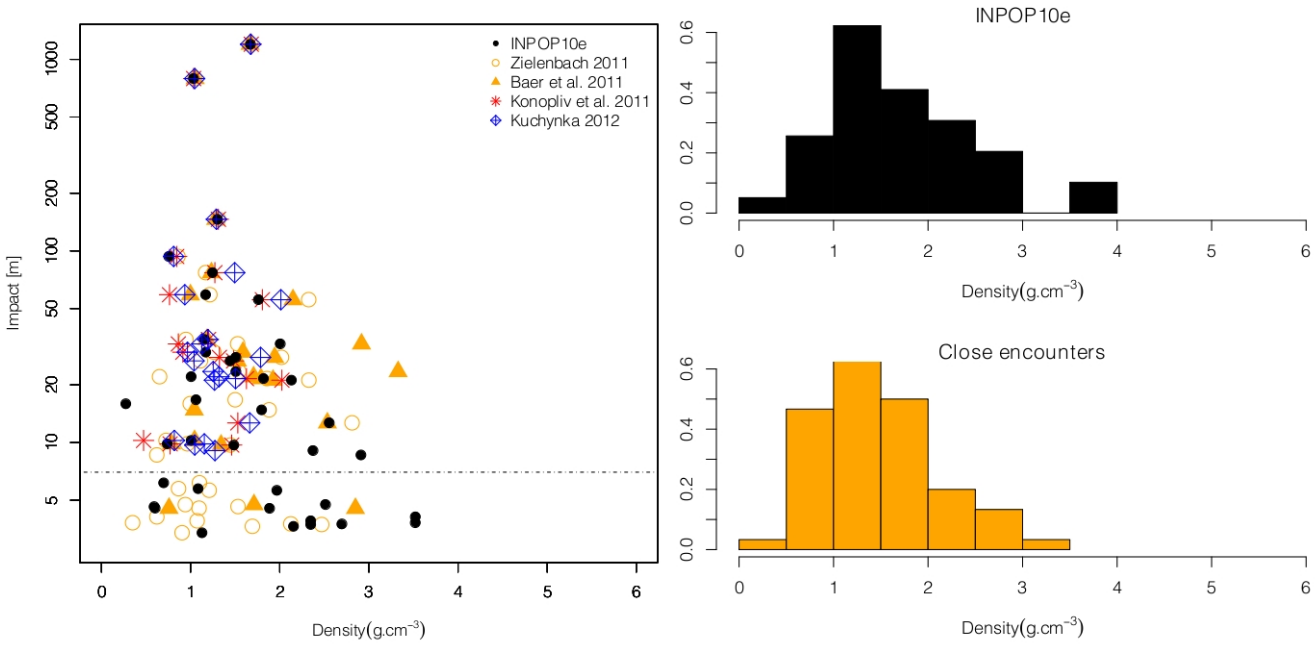

Fig. 3. INPOP10e Asteroid mass determination: a) INPOP10e asteroid densities compared to other published values versus the impact of the asteroids over the Mars-earth distances during a 1970 to 2012 period. b) Histograms of distribution of the asteroid densities obtained with INPOP10e and with close-encounter methods (right-hand side chart).

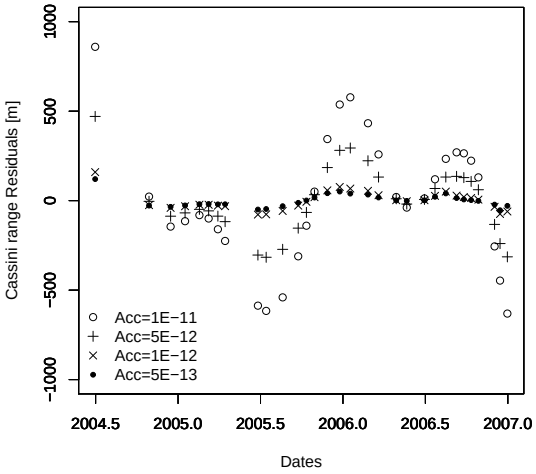

Fig. 4. Differences between Cassini range data and earth-Saturn distances obtained with supplementary Pioneer-like acceleration on the Saturn orbit.

SF2A 2012
S. Boissier, P. de Laverny, N. Nardetto, R. Samadi, D. Valls-Gabaud and H. Wozniak (eds)

IMPROVED ANGULAR MOMENTUM EVOLUTION MODELS FOR SOLAR-LIKE STARS

F. Gallet[1] and J. Bouvier[1]

Abstract. We present improved models for the angular momentum evolution of solar-like stars between 1 Myrs and 10 Gyrs. The models include a new braking law based on numerical simulations of magnetized stellar winds from Matt et al. (2012). Specific dynamo and mass-loss prescriptions are adopted to tight them to angular velocity. We assume constant angular velocity during the disk accretion lifetime and the models allow for core-envelope decoupling with a coupling timescale that varies between slow and fast rotators (Bouvier 2008). Stellar structure models of solar-mass stars are taken from Baraffe et al. (1998). We developed rotational evolution models for slow, median and fast rotators from the pre-main sequence (PMS) to the age of the Sun. The models are compared to the distributions of rotational periods observed for solar-type stars between 1 Myr and 5 Gyr in a number of star forming regions and young open clusters. We find that the model parameters accounting for the slow and median rotators are very similar to each other but differ significantly for fast rotators. We speculate that these differences may be related to different magnetic topologies in slow/median and fast rotators.

Keywords: Stars: solar-type, evolution, rotation, mass-loss, magnetic field

1 Introduction

Studying the angular velocity evolution is fundamental to understand how the stars lose and gain angular momentum during their life. For example, at its formation the angular momentum of the Sun was about thousand times greater than the current one which means that a large fraction of the initial angular momentum is lost by the stars between 1 Myr and the age of the Sun. The aim here is to understand how this huge quantity of angular momentum is extracted from the star, i.e., to highlight the involved physical processes. Stars lose angular momentum through two main ways 1) thanks to interactions with their surrounding disk which is expected to extract a large amount of angular momentum from them and 2) thanks to stellar winds which produce a braking torque on the stellar surface. Many theoretical advances about both the star/disk interaction (Ferreira et al. 2000; Matt & Pudritz 2005a,b; Zanni & Ferreira 2009; Matt et al. 2010; Zanni & Ferreira 2011) and the stellar wind (Matt & Pudritz 2008a,b; Matt et al. 2011) have been made since the first works of Ghosh & Lamb (1978) and Kawaler (1988), which provide us with a better comprehension of the angular momentum gain/loss processes. Stars evolve through three main stages namely the pre-main sequence (PMS), the zero age main-sequence (ZAMS) and the main-sequence (MS). On the PMS, during the first 10 Myr of their life, the stars are believe to be magnetically linked to their disk that results in a transfer of angular momentum $J \approx \Omega_* I$ (where I is the moment of inertia and Ω_* the angular velocity of the star) between the two. In response to this interaction the angular velocity of the convective envelope seems to remain more or less constant during all the disk lifetime (Bouvier 2008; Irwin & Bouvier 2009). Nowadays, this star/disk interaction still not has an accepted explanation but it is clear that it is needed in order to explain the small rotation periods observed for CTTs which are on average below ≈ 8 days, corresponding to angular velocity ≤ 10 % of their break-up speed. After the disk dissipation ($\approx$ 1-10 Myr), the stars are free to spin-up, because of the stellar contraction, until they reach the ZAMS at about 30 Myr where the contraction stops. Then, the stars reach the MS where the braking by stellar wind becomes dominant so that they will slowly spin-down. In the model we used the Matt et al. (2012) breaking law which gives the angular momentum loss rate as a function of the stellar parameters (B_*, Ω_*, R_*, $\dot{M}_{wind}$). We also used the magnetic dynamo relationship and the mass loss rate prescription of Cranmer & Saar (2011).

[1] UJF-Grenoble 1/CNRS-INSU, Institut de Planétologie et d'Astrophysique de Grenoble (IPAG) UMR 5274, F-38041 Grenoble, France

2 Model assumption

2.1 Internal structure

Low mass stars are composed of two regions : an inner radiative core and an outer convective envelope. We follow MacGregor & Brenner (1991) by assuming that both the core and the envelope rotate as solid bodies but with different angular velocity. The amount of angular momentum ΔJ to be transferred from the core to the envelope in order to balance their angular velocities is given by $\Delta J = (I_{env} J_{core} - I_{core} J_{env})/(I_{core} + I_{env})$ where I and J refer to the moment of inertia and angular momentum, respectively, of the radiative core and the convective envelope. As in Allain (1998), we assume that ΔJ is transferred over a time-scale τ_{c-e}, which we refer to as the core-envelope coupling timescale.

2.2 Stellar winds

The angular momentum loss rate due to stellar winds can be expressed as $dJ/dt \approx \Omega_* \cdot \dot{M}_{wind} \cdot r_A^2$ where r_A is the averaged value of the Alfvén radius that accounts for the magnetic lever arm, Ω_* is the angular velocity at the stellar surface and $\dot{M}_{wind}$ is the mass outflow rate. Most angular momentum evolution models so far have used Kawaler (1988) prescription to estimate the amount of angular momentum losses due to stellar winds, with some modifications such as magnetic saturation (Krishnamurthi et al. 1997; Bouvier et al. 1997) or a different dynamo prescription (Reiners & Mohanty 2012). The main difference between previous models and the ones we present here is that we base our estimates of angular momentum loss on the recent stellar wind simulations performed by Matt et al. (2012) who derived the following expression for r_A:

$$r_A = K_1 \left[\frac{B_p^2 R_*^2}{\dot{M}_{wind} \sqrt{K_2^2 v_{esc}^2 + \Omega_*^2 R_*^2}} \right]^m R_* \tag{2.1}$$

where $K_1 = 1.30$, $K_2 = 0.0506$ and $m = 0.2177$ are obtained from numerical simulations of a stellar wind flowing along the opened field lines of a dipolar magnetosphere.

We know that the magnetic strength does not follow a single power law with the velocity (Mestel & Spruit 1987; Saar 1996, 2001; Reiners et al. 2009) but instead it seems to saturated at a certain angular velocity threshold, which means that the magnetic activity becomes constant regardless of the angular speed of the star. We assume the stellar magnetic field to be dynamo generated, i.e., that the mean surface magnetic field strength scales to some power of the angular velocity. We thus have: $f_* B_* \propto \Omega_*^b$ where b is the dynamo exponent (cf. Cranmer & Saar 2011), B_* is the strength of the magnetic field and f_* is the filling factor, i.e., the fraction of the stellar surface that is magnetized (cf. Reiners & Mohanty 2012). Magnetic field measurements suggests that the magnetic field strength B_* is proportional to the equipartition magnetic field strength B_{eq} : $B_* \approx 1.13\ B_{eq}$ where B_{eq} is define as

$$B_{eq} = \sqrt{\frac{8\pi \rho_* k_B T_{eff}}{\mu m_H}} \tag{2.2}$$

with ρ_* the photospheric density, k_B the Boltzmann's constant, T_{eff} the effective temperature, μ the mean atomic weight and m_H the mass of a hydrogen atom. While the magnetic field strength appears to be more or less constant regardless of the angular velocity (Saar 1996; Cranmer & Saar 2011), the magnetic filling factor f_*, in contrast, strongly depends on the Rossby number $Ro = P_{rot}/\tau_{conv}$ where τ_{conv} is the convective turnover time. According to Saar (1996) $f_* \propto P_{rot}^{-1.8}$ while Cranmer & Saar (2011) provides two different fits for f_* that are respectively the lower and upper shape of the f_*-Ro plot : f_{min} that is the magnetic filling factor linked to the open flux tubes in non active magnetic region and f_{max} that is linked to the closed flux tubes in active regions. Their empirical fits give $f_{min} \propto Ro^{-3.4}$ and $f_{max} \propto Ro^{-2.5}$. In the framework of our model the most relevant filling factor is obviously f_{min} that is related to the open flux tube which can carry matter through stellar outflow, thus $f_* B_* \propto Ro^{-3.4} \propto \Omega_*^{3.4}$ and $b \approx 3.4$. The mean magnetic field strength saturation strongly depends on f_* and in the case where $f_* = f_{min}$ the saturation occurs for $\Omega_* \geq 10\ \Omega_\odot$. Observation of solar-type stars magnetic field suggests that saturation is reached when $Ro < 0.1 - 0.13$ (see Reiners et al. 2009, Figure 6). For solar-like stars (i.e. spectral type G0-K5), Reiners et al. (2009) adopted $\tau_{conv} \approx 20$ d, which is slightly larger than the empirical value of $\tau_{conv} \approx 15$ d derived by Wright et al. (2011). With these estimates of τ_{conv}, dynamo saturation is found to occurs at $\Omega_{sat} \sim 10 - 16\ \Omega_\odot$ which is coherent with the value of the saturation threshold found by Cranmer & Saar (2011). In Equation 2.1, B_p is the strength of the dipole magnetic field at

the stellar equator. Even though, the real stellar magnetic field is certainly not a perfect dipole we identify B_p to the strength of the mean magnetic field $B_* f_*$.

The mass-loss rates of solar-type stars at various stages of evolution are unfortunately difficult to estimate directly from observation. We therefore have to rely mainly on the results of numerical simulations of stellar winds, calibrated onto a few, mostly indirect, mass-loss measurements (e.g. Wood et al. (2002, 2005)). We used here the results from the numerical simulations of Cranmer & Saar (2011). Assuming that the wind is driven by gas pressure in a hot corona, as is likely the case for G-K stars, they found that $\dot{M}_{wind} \propto \Omega_*^{2.4}$. In our model we used directly the output of the subroutine BOREAS[i], developed by Cranmer & Saar (2011), to get the mass loss rate $\dot{M}_{wind}$ as a function of several stellar parameters like the angular velocity, the luminosity and the radius. Mass loss rate also appears to saturate at a certain velocity threshold (Holzwarth & Jardine 2007) and just like the magnetic field, the mass loss rate strongly depends on f_*. With $f_* = f_{min}$, the saturation of $\dot{M}_{wind}$ appears at about 10 $\Omega_\odot$ corresponding exactly to the saturation threshold of the magnetic field. By combining Equations 2.1, the dynamo and the mass loss rate prescription with the expression of dJ/dt, we finally express the angular momentum loss-rate as a function of angular velocity.

3 Results

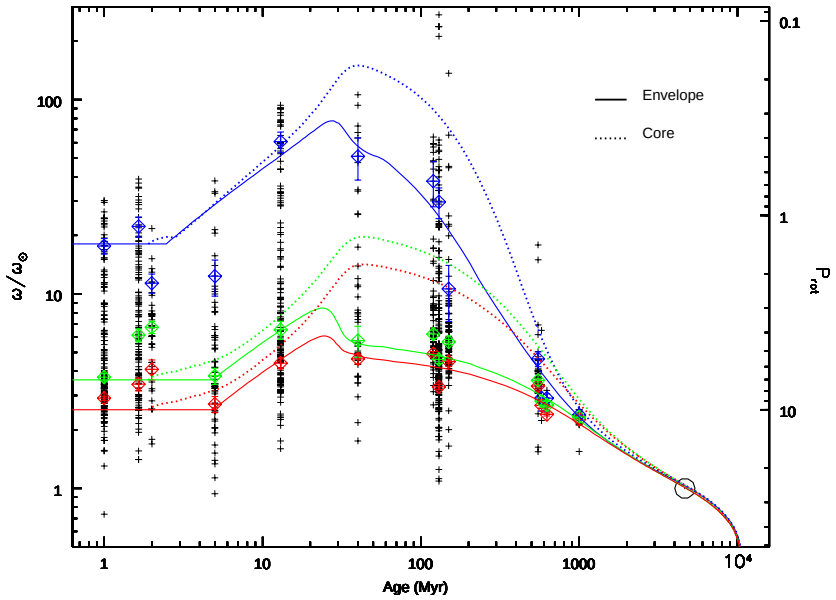

Fig. 1. Angular velocity evolution of the core and the envelope in the case of fast (blue), median (green) and slow (red) rotator models. The blue,red and green tilted square represents respectively the 90^{th} quartile, the 25^{th} quartile and the median of each rotation distributions. The open circle is the angular velocity of the present Sun.

Table 1 contains the parameters used for each rotator model presented in Figure 1. In this figure we plotted the angular velocity evolution for three rotator models and we confront them to the angular velocity distribution of 13 star forming regions and open clusters covering the age range from 1 Myr to 625 Myr plus the Sun (represented as an open circle in the figure).

4 Discussion

We present angular momentum evolution models of solar-like stars for slow, median and fast rotators from the pre-main sequence to the age of the present Sun and compare them to the distribution of rotational periods observed for solar-type stars between 1 Myr and 5 Gyr. By using the most recent physical advances about

[i] https://www.cfa.harvard.edu/~scranmer/Data/Mdot2011/

Table 1. Model parameters

Parameter	Fast	Median	Slow
P_{init} (days)	1.4	7	10
τ_{ce} (Myr)	12	28	30
τ_{disk} (Myr)	2.5	5	5
K_1	1.55	1.7	1.7
m	0.20	0.20	0.20

the stellar mass loss rate, wind braking and magnetic dynamo process we have developed rotational evolution models that reproduce reasonably well the observations. We do not include a fitting method yet so that the fitting is simply done by eye. We find that the slow and median rotator models have almost the same parametrization which is significantly different from that of the fast rotator model. This is particularly the case for the values of the K_1 parameter used for the three rotator models which is somehow related to the braking efficiency : $dJ/dt \propto K_1^2$. Given the Table 1, it seems that the slow/median rotators need a more efficient braking ($K_1 = 1.7$) compare to the fast rotators ($K_1 = 1.55$). This suggests that a change appears between the slow/median rotator models and the fast ones which may be due to a change of the magnetic field topology.

We thank the SF2A organisational committee for this very nice and fruitful week in Nice. We also thank Sean Matt from Laboratoire AIM Paris-Saclay, CEA/Irfu for all the help he has provided us.

References

Allain, S. 1998, A&A, 333, 629
Baraffe, I., Chabrier, G., Allard, F., & Hauschildt, P. H. 1998, A&A, 337, 403
Bouvier, J. 2008, A&A, 489, L53
Bouvier, J., Forestini, M., & Allain, S. 1997, A&A, 326, 1023
Cranmer, S. R. & Saar, S. H. 2011, ApJ, 741, 54
Ferreira, J., Pelletier, G., & Appl, S. 2000, MNRAS, 312, 387
Ghosh, P. & Lamb, F. K. 1978, ApJ, 223, L83
Holzwarth, V. & Jardine, M. 2007, A&A, 463, 11
Irwin, J. & Bouvier, J. 2009, in IAU Symposium, Vol. 258, IAU Symposium, ed. E. E. Mamajek, D. R. Soderblom, & R. F. G. Wyse, 363–374
Kawaler, S. D. 1988, ApJ, 333, 236
Krishnamurthi, A., Pinsonneault, M. H., Barnes, S., & Sofia, S. 1997, ApJ, 480, 303
MacGregor, K. B. & Brenner, M. 1991, ApJ, 376, 204
Matt, S. & Pudritz, R. E. 2005a, ApJ, 632, L135
Matt, S. & Pudritz, R. E. 2005b, MNRAS, 356, 167
Matt, S. & Pudritz, R. E. 2008a, ApJ, 678, 1109
Matt, S. & Pudritz, R. E. 2008b, ApJ, 681, 391
Matt, S. P., MacGregor, K. B., Pinsonneault, M. H., & Greene, T. P. 2012, ApJ, 754, L26
Matt, S. P., Pinzón, G., de la Reza, R., & Greene, T. P. 2010, ApJ, 714, 989
Matt, S. P., Pinzon, G., Greene, T. P., & Pudritz, R. E. 2011, ArXiv e-prints
Mestel, L. & Spruit, H. C. 1987, MNRAS, 226, 57
Reiners, A., Basri, G., & Browning, M. 2009, ApJ, 692, 538
Reiners, A. & Mohanty, S. 2012, ApJ, 746, 43
Saar, S. H. 1996, in IAU Symposium, Vol. 176, Stellar Surface Structure, ed. K. G. Strassmeier & J. L. Linsky, 237
Saar, S. H. 2001, in Astronomical Society of the Pacific Conference Series, Vol. 223, 11th Cambridge Workshop on Cool Stars, Stellar Systems and the Sun, ed. R. J. Garcia Lopez, R. Rebolo, & M. R. Zapaterio Osorio, 292
Wood, B. E., Müller, H.-R., Zank, G. P., & Linsky, J. L. 2002, ApJ, 574, 412
Wood, B. E., Müller, H.-R., Zank, G. P., Linsky, J. L., & Redfield, S. 2005, ApJ, 628, L143
Wright, N. J., Drake, J. J., Mamajek, E. E., & Henry, G. W. 2011, ApJ, 743, 48
Zanni, C. & Ferreira, J. 2009, A&A, 508, 1117
Zanni, C. & Ferreira, J. 2011, ApJ, 727, L22

SF2A 2012
S. Boissier, P. de Laverny, N. Nardetto, R. Samadi, D. Valls-Gabaud and H. Wozniak (eds)

EARLY EARTH'S ENVIRONMENT: AN EXOBIOLOGICAL PERSPECTIVE

E. Hébrard[1, 2]

Abstract. The purpose of this review is to assess the current state of our knowledge of the physico-chemical conditions that prevailed on the early Earth when Life originated. The early Earth environment was subjected to a very peculiar flux of primordial matter and solar energy. It may have therefore displayed physico-chemical conditions very different from today. The terrestrial geological record can potentially provide a lot of information about these ancient times. Their direct study is strongly influenced by the preservation of the oldest terrains and in particular the survival of volcano-sedimentary supracrustal rocks (ie remnants of the outer part of the Earth's surface), formed by a direct interaction with the hydrosphere, atmosphere and, possibly, primitive biosphere. Their study in recent years helped to clarify the existence of a primitive ocean, to study its physico-chemical conditions, but also to use the elemental and isotopic composition of sediments as a tracer of some key atmospheric chemical processes of biotic or abiotic origin. Studying and understanding the primitive terrestrial environment at the most ancient times the geological record allows us to access, possibly as far back as 4.28 billion years, allow us already to glimpse these unique conditions, certainly limited in time, which constituted nevertheless a prelude to, or even fostered, Life and its evolution on our home planet.

Keywords: early Earth, Life, exobiology

1 Introduction

Throughout Earth's history there have been major reorganisations of the whole Earth system. The driving forces behind these changes, and the controls on the intervening periods of relative stability, involve long term feedbacks between our home planet and Life that science is still struggling to comprehend. We know that dynamic interactions between the non-living and the living world have together regulated Earth's surface conditions over geological time. Since the atmosphere is so closely linked to the lithosphere, hydrosphere and, once arisen, biosphere, it is of prime interest to study how these interactions might have impacted the Earth's atmosphere and what clues these interactions may have left in the geologic record. Indeed, information about the atmosphere is elusive owing to the lack of direct records whereas much of the history of the lithosphere and hydrosphere is contained within the geological inventory. For years, sedimentary minerals, fossils and geochemical proxies have been used to constrain the concentrations of atmospheric and oceanic constituents over Earth's history. There have been remarkable advances in recent years and it has now become possible to investigate the long term controls on the physico-chemical composition of the terrestrial surface layers to understand how these relate to Earth's - and Life's - evolution.

2 Conditions during the Precambrian

First evidence for microbial life in the Archean has been derived from microfossils or stromatolites/microbial mats in rocks of ages between 2.5 and 3.5 billion years (Schopf 2006). Besides the fact that all Life on Earth is based on the existence of liquid water, there are multiple lines of independent evidence suggesting its existence on the surface well before this period. Only tentative evidence for liquid water on the early Earth can be found in the Hadean. Almost no rocks are known from these ancient times due to the exponential decrease of preservation with age. O'Neill et al. (2008) produced ^{142}Nd data for rocks from the Nuvvuagittuq greenstone

[1] Centre de Recherches Pétrographiques et Géochimiques, 15 rue Notre Dame des Pauvres 54500 Vandœuvre-lès-Nancy, France
[2] on behalf of the Société Française d'Exobiologie `http://www.exobiologie.fr`

belt in northern Quebec which seem to indicate a very old model age for extraction from the mantle (from 3.8 up to 4.28 billion years old). The fact that these samples may represent the oldest preserved rocks on Earth is however still under debate. Surprisingly, some information on the surface conditions during earlier times can be derived from the mineral zircon $ZrSiO_4$ preserved in younger rocks (Harrison 2009). Zircon grains enclosed in metamorphosed sandstone conglomerate in the Jack Hills, Western Australia, may provide evidence for liquid water as early as 4.404 billion years (Mojzsis et al. 2001; **?**). Geologic evidence for liquid surface water during the Archean is mostly based on sedimentary rock laid down in a variety of aqueous conditions up to 3.5 billion years ago and possibly as early as 3.8 billion years ago, and there is no evidence for widespread glaciations during the entire Archean (Walker 1982). Telltale signs of liquid water include pillow lavas that are formed when lava extrudes under water, ripple marks resulting from sediment deposition under the influence of waves, and mud cracks.

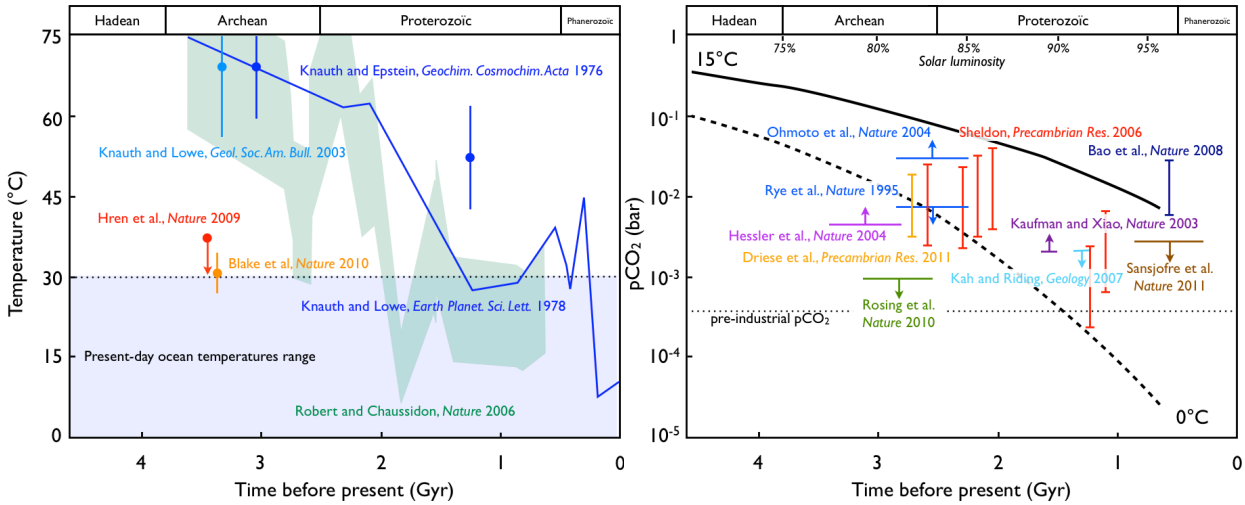

Fig. 1. Geological constraints on oceans temperature (left) and carbon dioxide CO_2 partial pressure (right) during the Precambrian, along with calculations based on a radiative-convective climate model representing the pressures needed to maintain average global surface temperatures of 288 K (solid black line) and 273 K (dashed black line). Modified and updated after Walker (1982) and Kasting (2010).

Since water remains liquid over a rather wide range of temperatures, it is quite legitimous to wonder how warm the Precambrian environment actually was. The constraints on and estimates of Archean ocean temperatures discussed below are summarized in Figure 1. Upper limits to Archean climate temperatures were first derived from the presence of evaporite minerals in the geological record dating back to 3.5 billion years. Since many of these were originally precipitated in the form of gypsum ($CaSO_4$,$2H_2O$), which is converted to anhydrite $CaSO_4$ at temperatures above 58 ℃ in pure water (and at lower temperatures in seawater), temperatures should not have been higher than this value (Holland 1978; Walker 1982). Conflicting with these upper limits from evaporites, low values of the $\delta^{18}O$ isotope ratio in 3.0 to 3.05 billion years old cherts were interpreted by some researchers as evidence of a hot climate with oceanic temperature of 55-85 ℃ (Knauth & Epstein 1976; Knauth & Lowe 1978, 2003). The long-term cooling of the oceans inferred from those data has been questioned because the $\delta^{18}O$ isotope signature could have been reset through the exchange with hydrothermal fluids after deposition of the sediments (van den Boorn et al. 2007) or could be representative of very localized ancient seawater rather than global ocean temperatures (Kasting & Howard 2006; Jaffrés et al. 2007). Moreover, recent analysis combining $\delta^{18}O$ and δD isotope ratios in 3.4 billion years old cherts (Hren et al. 2009) or investigating the compositions of phosphates in sediments from the 3.2-3.5 billion years old Barberton Greenstone Belt in South Africa (Blake et al. 2010) indicate much more moderate ocean temperatures in the range 26-40 ℃. Yet, the $\delta^{30}Si$ isotopic composition of cherts more than 550 million years old seems to show systematic variations with age that support the earlier conclusion of long-term ocean cooling and exclude post-depositional exchange as the main source of the isotopic variations (Robert & Chaussidon 2006). There appears to be no strong argument in favor of or against high archean temperatures. Even if the question of how warm the early Earth's atmosphere appears to be not quite settled yet, it was almost certainly warm enough to keep the ocean surface from freezing completely despite the low solar luminosity.

3 Some answers to the Faint Young Sun paradox

Models of stellar evolution predict a solar energy input to the early Earth climate system that is about 25% lower than today (Bahcall et al. 2001). If all other parameters controlling Earth's climate had been the same, this would have resulted in a completely frozen world over the first 2 billion years in the history of our planet. Yet, as we discussed above, there is ample evidence for the presence of liquid surface water and even Life in the Precambrian. This issue to explain the existence of liquid water in a climate powered by a feeble Sun has been termed the "faint young Sun paradox" (see Feulner (2012) for a complete review). It is only a paradox, of course, if the parameters controlling the climate in the Archean were indeed similar to today's values, an assumption that appears naive considering the profound changes Earth has experienced in its long history. Indeed, changes in atmospheric concentrations of greenhouse gases are one of the possibilities to resolve the apparent inconsistency between the faint young Sun and the climate on early Earth.

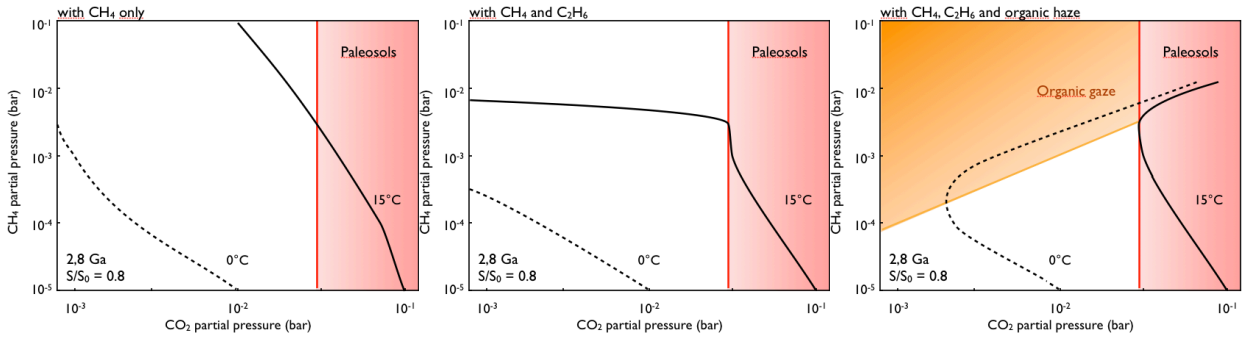

Fig. 2. Parameter space for a Late Archean methane greenhouse. (a) The solid black line shows the methane CH_4 and carbon dioxide CO_2 partial pressures required to sustain a global average surface temperature T = 288 K based on the model calculations for a CH_4-CO_2-H_2O greenhouse at 1 bar total pressure and a 0.8 solar luminosity corresponding to a 2.8 billion years ago (Haqq-Misra et al. 2008); the dashed line indicates the partial pressures for T = 273 K. The haze formation zone is indicated in orange, and the paleosol upper limit on the CO_2 partial pressure is indicated in red. (b) Same as Fig. 2a but for model calculations explicitly taking into account additional warming by ethane C_2H_6 (Haqq-Misra et al. 2008). (c) Same as Fig. 2a but for model calculations explicitly taking into account additional warming by ethane C_2H_6 and cooling by organic haze (Haqq-Misra et al. 2008) (adapted from Feulner (2012).

Carbon dioxide CO_2 seemed first a perfect candidate in the sense that the long-term evolution of its atmospheric concentration is controlled by the inorganic carbon cycle, part of an important negative feedback loop that stabilizes Earth's climate on geological timescales (Walker et al. 1981). Geochemical analysis of paleosols and banded iron formations seem to provide constraints on the atmospheric CO_2 concentration during the Late Archean to values much lower than required to solve the faint young Sun paradox; see Figure 1. The absence of siderite $FeCO_3$ from all of the paleosols older than 2.2 billion years was used to establish upper limits during the Late Archean and early Proterozoic (Rye et al. 1995; Sheldon 2006; Driese et al. 2011). An even lower upper limit for the CO_2 partial pressure, down to only about 3 times the present-day level, was derived from the coexistence of siderite and magnetite Fe_3O_4 in Archean banded iron formations (Rosing et al. 2010). These latest results conflict however with the lower limits derived from weathering rinds on 3.2 billion years old river gravels (Hessler et al. 2004), for which the presence of iron-rich carbonates requires CO_2 partial pressures of about 10 times preindustrial levels for the same environmental temperature. There is conflicting evidence for a CO_2-richer atmosphere at these times based on the actual occurrence of siderite in banded iron formations (Ohmoto et al. 2004). Despite these debates, geochemical data suggest that CO_2 partial pressures were likely smaller than a few hundred times preindustrial levels in the Late Archean and early Proterozoic. Carbon dioxide CO_2 alone would have been therefore most likely unable to provide enough warming during Precambrian times and a contribution from another greenhouse gas to CO_2 warming seems to be required.

Methane CH_4 requires ultraviolet light of much shorter wavelengths (< 145 nm) than ammonia NH_3 to photodissociate. Photochemical models showed that even under the more intense ultraviolet radiation emitted by the young Sun, the lifetime of methane CH_4 in a terrestrial atmosphere low in carbon dioxide CO_2 is of the order of 10^3 to 10^4 years in contrast to less than 10 years for ammonia NH_3 (Zahnle 1986). Three

sources of methane may have contributed to the atmospheric budget during Precambrian times: impacts from space, geological sources, and anaerobic ecosystems. Such processes may have sustained low concentrations of methane CH_4 in the atmosphere: from an order of 10 ppmv in the early Archean and up to 1000 ppmv after the origin of Life and before the first major rise in atmospheric oxygen (Kasting 2005; Kharecha et al. 2005). However, laboratory experiments showed that higher-order hydrocarbons were expected to form in an atmosphere containing methane and exposed to ultraviolet radiation. An organic haze even start to form at CH_4/CO_2 mixing ratios close to 0.1 (Trainer et al. 2004, 2006). While higher-order hydrocarbons, such as ethane C_2H_6 could therefore have contributed to the Precambrian greenhouse by an additional warming effect, a (non-fractal) organic haze layer may on the contrary have exhibited an antigreenhouse effect (McKay et al. 1991, 1999). This haze would have thus cooled the planet by effectively limiting the greenhouse warming achievable by methane and higher-order hydrocarbons in the early atmosphere. Figure 2 compares some calculations of the potential of methane CH_4 to contribute to an Archean CO_2 greenhouse with the constraints existing from haze formation and geochemistry of paleosols. However, one should point out that a fractal nature of organic haze particles seems to limit drastically the antigreenhouse effect of the organic haze layer (Wolf & Toon 2010).

It has therefore been hypothesized that, before widespread oxygenation about 2.45 billion years ago, the Earth's atmosphere contained an organic haze similar to that on Titan. Zerkle et al. (2012) recently used multiproxy geochemical analyses of sediments from the 2.65-2.5 billion years old Ghaap Group, in South Africa, to reconstruct ocean and atmospheric chemistry during this time. Carbon and sulphur isotopes indicate that localized oxygenation from microbial mats and surface waters occurred at the time under a reduced atmosphere that was periodically rich in methane, consistent with the prediction of a hydrocarbon haze. Through the use of a photochemical model to corroborate their geochemical data., Zerkle et al. (2012) predicted transitions between two stable atmospheric states, one with organic haze and the other haze-free. The transitions are presumably governed by variations in the amount of biological methane production during the Archean eon.

4 Mass-independent fractionation (MIF) in the early Earth atmosphere

Earth's history and biogeochemical processes are usually characterized by the distribution of stable isotopes in geological materials. The sedimentary record holds pervasive evidence for materials with mass-independent fractionation (MIF), an uncommon isotope fractionation that differs significantly from those expected from typical equilibrium and kinetic fractionations, where the amount of separation scales in proportion with the difference in the masses of the isotopes. At present, the most viable explanation for MIF signatures in the geologic record involve atmospheric chemistry. MIF signatures have become a powerful research tool in Earth system sciences because it is a sensitive marker of particular chemical reactions that are not affected by most biogeochemical processes. Multiple isotope research has blossomed over the last decade and is now focused on critically addressing the mechanisms responsible for the production of these MIF anomalies in the atmosphere and their preservation in the geologic record. Despite significant advances, there are certain issues that have not yet been fully addressed and records that have not been fully investigated, from the most ancient times to the present.

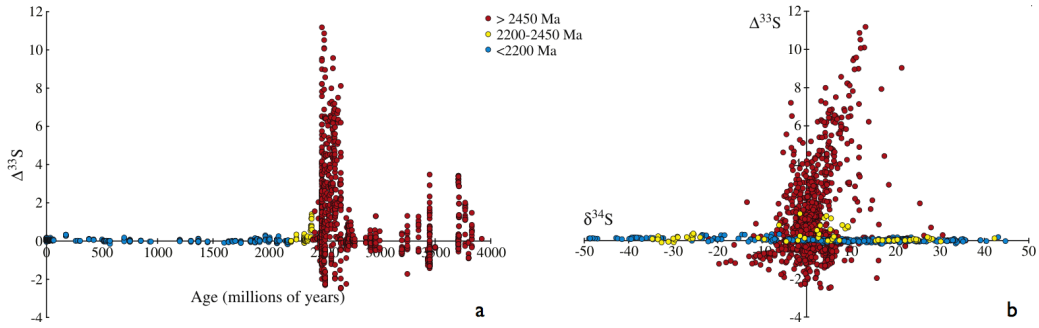

Fig. 3. Two presentations of published ^{33}S data. a) Classic plot of $\Delta^{33}S$ versus geological age highlighting the existence of a prominent MIF signal prior to 2450 Myr, with the remainder of the record appearing to be dominated by mass-dependent fractionations MDF. b) A more diagnostic means of assessing the relative influence of MIF material is through the relationship between $\delta^{34}S$ and $\Delta^{33}S$. Generally, Archean MIF data plot with $\delta^{34}S$ near zero, whereas larger MDF characterize Proterozoic and Phanerozoic records (adapted from Johnston (2011).

The enigmatic signals known as sulfur mass-independent isotopes fractionation (S-MIF) are seen in aerosol particles in the stratosphere, within ice core sulfates, as well as among the most ancient sedimentary rocks on the planet, with ages of up to 3.8 billion years (Figure 3). The presence of S-MIF in the Archean and the earliest Proterozoic records is thought to be a defining signature of sedimentary rocks laid down prior to the Great Oxidation Event, the global rise of atmospheric oxygen O_2 that geological evidence place between 2.45 and 2.32 billion years. Subtle variations in the magnitude of S-MIF are even thought to reflect changes in the concentrations of carbon dioxide CO_2, biogenic sulfur compounds, and the presence of a Titan-like organic haze during the early periods of Earth's history (Ueno et al. 2009; Halevy et al. 2010; Zerkle et al. 2012). The occurrence of a $\delta^{34}S$-$\Delta^{34}S$ correlations is thought to reflect widespread, UV-triggered photodissociation of sulphur dioxide SO_2 that was released into the atmosphere by short-lived but intense bursts of subaerial volcanic activity (Philippot et al. 2012). Neoproterozoic and Phanerozoic multiple sulfur isotope records may also carry the potential to shed light on many issues (such as episode of anoxic water during mass extinctions, early diagenesis and the deep sub-surface biosphere) which remain largely unstudied from an atmospheric chemistry point of view and constitute therefore prime targets.

The "snowball Earth" hypothesis postulates that our planet was entirely covered by ice for millions of years in the Proterozoic era and attributes the subsequent rapid thaw to a buildup of greenhouse gases during the glaciation. The oxygen isotope composition of sulphates deposited on Earth surfaces from ancient evaporites and barites shows variable mass-independent isotopes fractionation (O-MIF) anomalies over the past 750 million years. It has been proposed that these O-MIF anomalies trace those of atmospheric molecular oxygen O_2 and may in turn reflect the partial pressure of carbon dioxide pCO_2 in the past (Bao et al. 2008). Evidence for elevated CO_2 levels in the aftermath of the Marinoan glaciation $\sim$ 635 million years ago have been consequently inferred from O-MIF data, consistently with the "snowball Earth" hypothesis. However, a recent re-interpretation of the same O-MIF data has provided however a completely different picture of the late Neoproterozoic environment, with low atmospheric concentrations of carbon dioxide CO_2 that are inconsistent with a snowball Earth (Sansjofre et al. 2011). This latest work not only challenges part of the "snowball Earth" hypothesis, but also implies that these glacial episodes were not as intense as previously suggested. Before examining alternative deglaciation mechanisms, improved constraints on the underlying atmospheric processes would obviously be extremely important, although certainly challenging to obtain. Even the exact magnitude of the mass-independent ^{17}O anomaly for current atmospheric molecular oxygen O_2, ozone O_3 and carbon dioxide CO_2 still debated. Details of the transfer mechanism of the isotope anomaly are not yet understood because of large uncertainties attached to the fractionation kinetics in the O_2-CO_2-O_2 photochemical system (Miller 2002).

5 Conclusions

We still have a limited knowledge of the conditions on early Earth, although the last decades have seen considerable progress, and some parameters are now better constrained than they used to be in the past. Nevertheless, improved constraints on atmospheric composition during the Archean eon would obviously be extremely important, although certainly challenging to obtain. Despite the difficulties involved, there have certainly been remarkable advances in recent years and it has now become possible to investigate the long term controls on the chemical composition of the atmosphere and oceans and to understand how these relate to Life evolution and biodiversity. Note, for example, that most of the geochemical constraints on Archean and Proterozoic oceans temperature and carbon dioxide partial pressure shown in Figure 1 were derived within the last decade, no matter how inconsistent they appear. In addition to better field data, however, improvements in the efforts on modeling the Earth's atmospheric chemistry during the Precambrian are urgently needed. Much has been executed this past decade to address the mechanisms underpinning the production and preservation of the mass-independent isotope fractionation (MIF) anomalies discussed briefly above. However, a robust and quantitative answer to further quantify any possible connection to the evolution of Earth's atmospheric chemistry remains elusive. It is of prime importance to tackle the most relevant issues described above by taking advantages from the most recent advances in the fieds of geochemistry, atmospheric (photo)chemistry and numerical modelling.

The author personally acknowledges support from the European Research Council (ERC Starting Grant 209622: E3ARTHs and ERC Advanced Grant 267255: NOGAT). A description of the Société Française d'Exobiologie and a list of its members, indicating which outreach, technical or scientific activities they are involved in, can be found at `http://www.exobiologie.fr`

References

Bahcall, J. N. et al. 2010, ApJ, 555, 990
Bao H. M. et al. 2008, Nature, 453, 504
Blake, R. E. et al. 2010, Nature, 464, 1029
Driese, S. G. et al. 2011, Precambrian Res., 189, 1
Feulner, G. 2012, Rev. Geophys., 50, RG2006
Halevy I. et al. 2010, Science, 329, 204
Haqq-Misra, J. D. et al. 2008, Astrobiology, 8, 1127
Harrison, T. M. 2009, Annu. Rev. Earth Planet. Sci., 37, 479
Hessler, A. M. et al. 2004, Nature, 428, 736
Hren, M. T. 2009, Nature, 462, 205
Holland, H. D. 1978, The Chemistry of the Atmosphere and Oceans, Wiley (New York)
Jaffrés, J. B. D. et al. 2007, Earth Sci. Rev., 83, 83
Johnston, D.T. 2011, Earth-Sci. Rev., 106, 161
Kasting, J. F. 2005, Precambrian Res., 137, 119
Kasting, J. F. 2010, Nature, 464, 687
Kasting, J. F. & Howard, M. T. 2006, Philos. Trans. R. Soc. B, 361, 1733
Kharecha, P. et al. 2005, Geobiology, 3, 53
Knauth, L. P., & Epstein, S. 1976, Geochim. Cosmochim. Acta, 40, 1095
Knauth, L. P., & Lowe, D. R. 1978, Earth Planet. Sci. Lett. 41, 209
Knauth, L. P., & Lowe, D. R. 2003, Geol. Soc. Am. Bull., 115, 566
McKay, C. P. et al. 1991, Science, 253, 1118
McKay, C. P. et al. 1999, Icarus, 137, 56
Miller, M. F. 2002, Geochim. Cosmochim. Acta, 66, 1881
Mojzsis, S. J. et al. 2001, Nature, 409, 178
O'Neill, J. et al. 2008, Science, 321, 1828
Ohmoto, H. et al. 2004, Nature, 429, 395
Philippot, P. et al 2012, Nat. Geosci. 5, 668
Robert, F. & Chaussidon, M. 2008, Nature, 443, 969
Rosing, M. T. et al. 2010, Nature, 464, 744
Rye, R. et al. 1995, Nature, 378, 603
Sansjofre P. et al. 2011, Nature, 478, 93
Schopf, J. W. 2006, Philos. Trans. R. Soc. B, 361, 869
Sheldon, N. D. (2006), Precambrian Res., 147, 148
Trainer, M. G. et al. 2004, Astrobiology, 4, 409
Trainer, M. G. et al. 2006, Proc. Natl. Acad. Sci. U. S. A.
Ueno, Y. et al. 2009, P. Natl. A. Sci., 106, 14784
van den Boorn, S. H. J. M. et al. 2007, Geology, 35, 939
Walker, J. C. G. et al. 1981, J. Geophys. Res., 86, 9776
Walker, J. C. G. 1982, Palaeogeogr. Palaeoclimatol. Palaeoecol., 40, 1
Walker, J. C. G. et al. 1983, in Earth's Earliest Biosphere: Its Origin and Evolution, ed. J. W. Schopf, Princeton Univ. Press, (Princeton, New Jersey), pp. 260
Wilde, S. A. et al. 2001, Nature, 409, 175
Wolf, E. T., & Toon, O. B. 2010, Science, 328, 1266
Zahnle, K. J. 1986, J. Geophys. Res., 91, 2819
Zerkle A. et al. 2012, Nat. Geosci., 5, 359

SF2A 2012
S. Boissier, P. de Laverny, N. Nardetto, R. Samadi, D. Valls-Gabaud and H. Wozniak (eds)

THE HOBYS KEY PROGRAM: WHEN HERSCHEL LINKS HIGH-MASS STAR FORMATION TO CLOUD STRUCTURE

F. Motte[1], S. Bontemps[2], M. Hennemann[1], T. Hill[1], Q. Nguyen Luong[3], N. Schneider[2], P. Didelon[1], F. Louvet[1], A. Zavagno[4] and the HOBYS consortium

Abstract. With its unprecedented spatial resolution and high sensitivity in the far-infrared to submillimetre regime, Herschel is revolutionizing our understanding of star formation. The HOBYS key program is an Herschel mapping survey dedicated to the formation of OB-type stars (Motte, Zavagno, Bontemps et al. 2010; see http://hobys-herschel.cea.fr. HOBYS aims at 1) discovering and characterizing the progenitors of high-mass stars, 2) making the link between the latters and their filamentary background, and 3) assessing the importance of triggering. Among the HOBYS highlights is the discovery of "mini-starburst ridges" defined as high-density dominating filaments supersonically contracting and efficiently forming clusters of high-mass stars. Their existence is predicted by dynamical models of cloud formation such as converging flows and is favoring a (high-mass) star formation scenario involving gas flows and global infall. The present star formation rate measured within these ridges is high enough for these 1–10 pc^2 regions to be considered as miniature and instantaneous models of extragalactic starbursts.

Keywords: dust, ISM: clouds, ISM: structure, stars: formation, submillimeter, IR: Herschel, H II regions

1 Introduction: From cloud to high-mass star formation

High-mass stars (OB-type, $M_\star > 8\ M_\odot$) play a major role in the energy budget and enrichment of galaxies but their formation remains poorly understood. The picture which is starting to emerge states that *OB stars form through very dynamical processes* such as (1) a powerful accretion driven by a high degree of turbulence (e.g. McKee & Tan 2002; Hosokawa & Omukai 2009) or (2) colliding flows initiated by competitive accretion or cloud formation (e.g. Bonnell & Bate 2006; Hartmann et al. 2012). From a purely observational point of view, gravitational streamers and shearing motions have been reported from the cloud to the protostellar scales in a few high-mass star-forming regions (on $10 - 0.1$ pc scales; Schneider et al. 2010a; Csengeri et al. 2011). These pioneering studies suggest that the formation of OB stars is tightly linked to the density and kinematics of their parental cloud.

At the dawn of *Herschel*[i], our knowledge of high-mass star formation and the evolutionary sequence of their earliest phases was still rather schematic. Bright *IRAS* sources embedded within massive envelopes have been recognized as high-mass protostellar objects (HMPOs) containing evolved high-mass protostars (e.g. Beuther et al. 2002). Cold massive dense cores (MDCs) associated with weak mid-infrared emission, but with clear signposts of OB-type protostars, have been qualified as IR-quiet and observed to harbor high-mass class 0 protostars (Motte et al. 2007; Bontemps et al. 2010b). Controversy was remaining about the existence and the lifetime of high-mass analogs of prestellar cores, since infrared dark clouds (IRDCs) are numerous (e.g. Peretto & Fuller 2010) but only a few harbor starless, massive, and dense enough cores (Motte et al. 2007; Russeil et al. 2010). Large surveys covering the far-infrared to millimeter continuum regime were thus required to improve the statistics of these studies and constrain models proposed for the formation of high-mass stars. Ground-based submillimeter surveys such as ATLASGAL (Schuller et al. 2009) started to help but they need to be completed by *Herschel* imagings.

[1] Laboratoire AIM, CEA/IRFU – CNRS/INSU – Université Paris Diderot, CEA-Saclay, F-91191 Gif-sur-Yvette Cedex, France
[2] Laboratoire d'Astrophysique de Bordeaux, 33271 Floirac cedex, France
[3] The Canadian Institute for Theoretical Astrophysics, Toronto, M5S 3H8, Canada
[4] Laboratoire d'Astrophysique de Marseille, F-13388 Marseille cedex 13, France
[i] *Herschel* is an ESA space observatory with science instruments provided by European-led Principal Investigator consortia and with important participation from NASA.

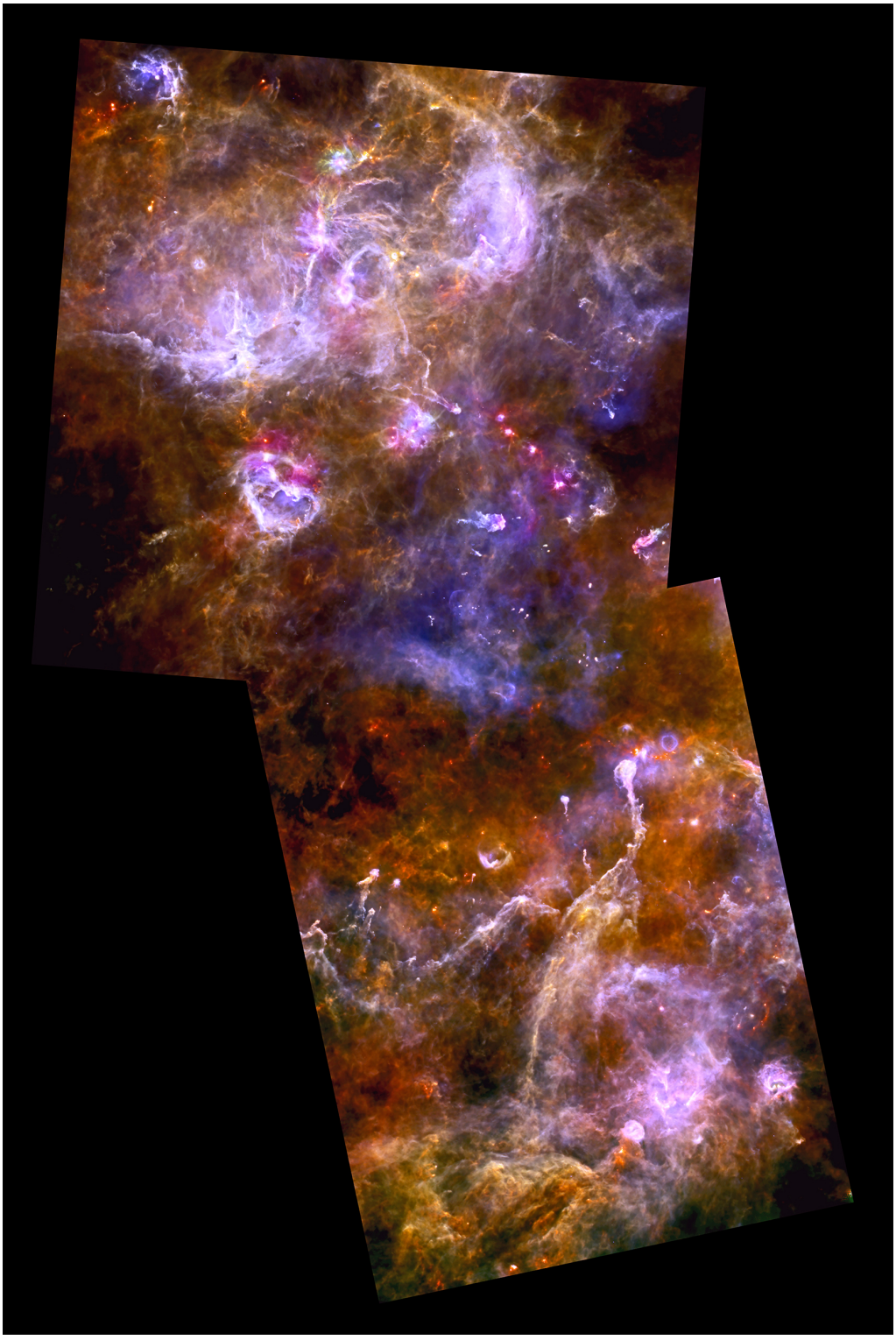

Fig. 1. Composite 3-color *Herschel* image of the Cygnus X molecular complex with red=250 μm, green=160 μm, and blue=70 μm (taken from Hennemann et al. 2012, and Hennemann et al. in prep.). The mosaic performed by the HOBYS key program approximately covers a $5^\circ \times 2.5^\circ$ or $120\,\mathrm{pc} \times 60\,\mathrm{pc}$ area. The angular resolutions are $HBPW \sim 6''$ at 70 μm, $\sim 12''$ at 160 μm, and $\sim 18''$ at 250 μm. The diffuse blue emission in the center is an H II region powered by the Cyg OB2 cluster while earlier stage star-forming sites are seen as red filaments.

The "*Herschel* imaging survey of OB Young Stellar objects" (HOBYS, Motte et al. 2010, see `http://hobys-herschel.cea.fr`) is a guaranteed time key program jointly proposed by the SPIRE and PACS consortia, and the Herschel Science Centre. Since October 2009, it used the SPIRE and PACS cameras (Griffin et al. 2010; Poglitsch et al. 2010) of the *Herschel* satellite (Pilbratt et al. 2010) to image essentially all of the regions forming OB-type stars at distances less than 3 kpc from the Sun ($d = 0.7 - 3.2$ kpc) and target a few prototypical regions of triggered star formation at the periphery of H II bubbles. Two other key programs have mapped massive young stellar objects (YSOs): EPoS targeting well-known HMPOs and IRDCs (Ragan et al. 2012) and HiGAL surveying most of the Galactic plane (Molinari et al. 2010). *HOBYS allows both a more statistically meaningful and more comprehensive study of cloud structure and YSOs at a fixed ∼0.1 pc resolution.* HOBYS images revealed networks of filaments and clusters of burgeoning YSOs (see Fig. 1) similar to those observed for the more nearby Gould Belt clouds (see André et al. 2010, $d = 100 - 500$ pc). The most obvious differences arise from the heating and structural impact of stellar clusters and H II regions associated/embedded within the HOBYS molecular cloud complexes (see e.g. Fig. 1). While triggered star formation is obvious around isolated H II regions Zavagno et al. (2010); Anderson et al. (2012); Deharveng et al. (2012), it is not yet unambiguously proven in cloud complexes (see however Schneider et al. 2010b; Hill et al. 2012, Minier et al. submitted).

2 HOBYS cloud structures: Ridges, the necessary conditions for clusters of high-mass stars to form

The cloud structure of HOBYS molecular complexes is investigated through column density images built from the far-infrared and submillimeter *Herschel* images. Indeed, the 160 μm PACS and 250/350/500 μm SPIRE images mostly trace optically thin emission of cold dust/big grains that follow the general density structure of the cloud. In contrast, the 70 μm emission originates from hot dust/small grains close to protostars or within H II regions/photo-dissociation regions. Dust temperature and column density maps (see e.g. Figs. 2b-c) were therefore drawn by fitting pixel-by-pixel spectral energy distributions (SEDs) for $\lambda > 160$ μm and using a modified blackbody model (see Hill et al. 2012, for a detailed description). Prior to fitting, the *Herschel* data were convolved to a common 37″ resolution and the zero offsets were applied to the individual maps (see details in Bernard et al. 2010). A dust opacity per unit mass given by $\kappa_\nu = 0.1$ cm^2 g^{-1} $\times$ (ν/1000 GHz)$^\beta$ and a dust spectral index of $\beta = 2$ (Motte et al. 2010) was used. HOBYS column density images generally display networks of filaments among which *a few well-ordered, dominating ridges which are privileged sites to form massive stars* (Hill et al. 2011; Nguyen Luong et al. 2011a; Hennemann et al. 2012). The DisPerSE algorithm (Sousbie 2011), based on Morse theory and the concept of persistence to identify topological structures, was used to take a census of the filaments/ridges (see dotted points in Fig. 2b).

Hill et al. (2011) studied the Vela C molecular cloud complex ($d = 700$ pc) and defined the two ∼3 pc-long filaments with column density above 10^{23} cm^{-2} as "ridges". They showed that these high-density, elongated cloud structures are dominating and shaping their surroundings in marked contrast to other less-organized sub-regions of Vela C. Indeed, the density profile of ridges perpendicular to their crest suggests a (five times) larger radius of influence (∼0.5 pc) than averaged filaments. The multi-resolution distribution of the cloud shows a high concentration of the gas (∼40%, twice larger than in averaged regions) at scales smaller than 3 pc. Moreover, the column density probability distribution (PDF) has a high column density tail above 0.5×10^{23} cm^{-2}, consistent with formation of the cloud through large-scale gas flows (e.g. Federrath et al. 2010). Hill et al. (2011) proposed that *ridges are both shaping and shaped by their surroundings as they represent a gravitational well and could have been formed by dynamical scenarios such as converging flows* (e.g. Heitsch et al. 2006). Minier et al. (submitted) showed that additional pressure arising from the ionization of the RCW36 OB cluster has helped shaping and could even be the main process responsible for making the Vela C center ridge denser. They compared the column density structure, mid-infrared and Hα emission to numerical simulations (Tremblin et al. 2012) and located the RCW36 cluster at ∼1 pc from the center ridge of Vela C.

Hennemann et al. (2012) studied the DR21 ridge, the densest and most massive cloud structure of the Cygnus X molecular complex ($d = 1.4$ kpc, see Figs. 1-2): $M_{\rm total} = 15\,000$ $M_\odot$ within a 4 pc $\times$ 1 pc elongated clump. This prototypical ridge contains 9 MDCs and is forming a cluster of ∼20 high-mass stars (Motte et al. 2007; Bontemps et al. 2010b). Schneider et al. (2010a) showed that the DR21 ridge is undergoing a global collapse and proposed it is fed by three sub-filaments called F1–F3. Hennemann et al. (2012) used the *Herschel* column density image to define the extent of the DR21 ridge by the $N_{\rm H_2} = 10^{23}$ cm^{-2} contour and trace connected sub-filaments with DisPerSE (see Fig. 2b). The perpendicular column density profile of the DR21 ridge displays two peaks and the northern and possibly southern parts of the ridge show two extensions (see Fig. 2). These branchings and complex structure suggest the DR21 ridge could have been formed by dynamical scenarios such

as the merging of several filaments (Hennemann et al. 2012). Schneider et al. (2012) similarly proposed that intermediate-mass star clusters in Rosette would preferentially form at the junction of filaments as predicted by Dale & Bonnell (2011). The DR21 sub-filaments display decreasing dust temperature towards the ridge, indicating the pile-up of material which cools down (see Fig. 2c). These sub-filaments are also gravitationally supercritical and indeed already form cores and protostars (see Figs. 2a-b). Given their mass, they merely represent remnant flows but *the accretion of both the cool gas and cores/protostars is probably helping building up a future cluster of high-mass stars within the DR21 ridge*. Such a dynamical scenario for cloud and then cluster formation is consistent with the kinematics measured in a few ridges and shocks observed with e.g. SiO (Schneider et al. 2010a, Motte et al. in prep., Nguyen Luong et al. in prep.).

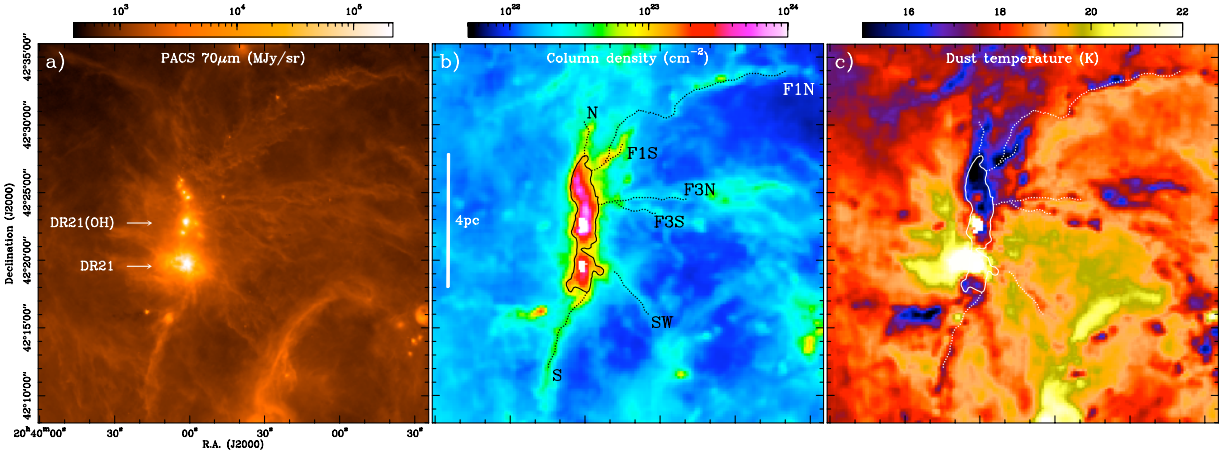

Fig. 2. *Herschel* maps of the DR21 environment showing a) 70 μm emission, b) column density, and c) dust temperature. The DR21 ridge is delineated by the $N_{H_2} = 10^{23}$ cm^{-2} contour plotted in panels b) and c) and covering a 2.3 pc^2. The sub-filaments connected to the ridge are named and marked with dots along their crests in b) and c).

3 HOBYS YSO population: Short lifetimes for high-mass star precursors and burst of star formation

HOBYS identified thousands of YSOs in 8 molecular complexes of 50-100 pc sizes such as Cygnus X (see Fig. 1). *Herschel* compact sources were extracted using the multi-scale, multi-wavelength *getsources* algorithm (see Men'shchikov et al. 2012). At the detection step, the five *Herschel* images were decomposed into multi-resolution cubes as in the MRE-GCL method (see Motte et al. 2007). The five wavelength cubes were then combined, with greater weight being given to the higher resolution images, and the compact sources were detected within the resulting cube. At the measurement step, the initial *Herschel* and other complementary images, were used to compute the sources properties at their detected location, after the background had been subtracted and overlapping sources had been deblended. The strength of this approach is to allow the simultaneous detection, at all wavelengths, of compact but still resolved sources. In the final *getsources* catalogue, each *Herschel* compact source has a single position and one FWHM size (and integrated flux) at each of the wavelength considered. To limit the influence of different *Herschel* resolutions and restrict the study to the dense cores size ($\sim$0.1 pc), the fluxes at $\lambda > 160\,\mu$m were linearly scaled to the source size measured at 160 μm (procedure introduced by Motte et al. 2010; Nguyen Luong et al. 2011a). The spectral energy distributions of the extracted dense cores were compared to grey-body models to characterize their cold gas component. The bolometric luminosity, envelope mass, and submillimeter-to-bolometric luminosity ratio were estimated for each *Herschel* compact source.

HOBYS is therefore providing an unbiased census of intermediate- to high-mass dense cores, with $\sim$0.1 pc sizes, which can be used to start constraining the evolutionary sequence of OB-type YSOs. Mass-luminosity ($M_{\rm env}$ vs. $L_{\rm bol}$) diagrams were built to determine the low- or high-mass star potential and the evolutionary status (IR-quiet/class 0 versus IR-bright/class I) of protostellar dense cores (Hennemann et al. 2010, see also Bontemps et al. 2010a, Hennemann et al. in prep.). Among the preliminar but homogeneous and complete samples of massive YSOs, *no good candidate for being a high-mass prestellar core was yet found*. The few intermediate-mass starless dense cores discovered in Rosette suggest a statistical lifetime ($\sim 8 \times 10^4$ yr, Motte et al. 2010) intermediate between those found in nearby low-mass star-forming regions ($\sim 2 \times 10^5$ yr, Kirk et al.

2005) and high-mass star-forming complexes ($\sim 5 \times 10^4$ yr, Motte et al. 2007; Russeil et al. 2010). If confirmed, this result could suggest either that the prestellar lifetime depends on the final mass of the star that they will form or that statistical lifetimes cannot be used since star formation often proceeds in bursts.

As said above, ridges are the privileged sites for the formation of high-mass star clusters and YSO populations can be used to compute their star formation rate (SFR, see Fig. 3). Nguyen Luong et al. (2011a) counted YSOs in the G035.39–0.33 ridge (cf. Fig. 3a) and assumed a mass transfer efficiency from dense core to star depending on their mean density, typically 25% for MDCs. The clustering of IR-quiet MDCs and class 0 dense cores within the G035.39–0.33 ridge suggests they are simultaneously forming, probably just after the formation of the ridge itself (Vázquez-Semadeni et al. 2008). Nguyen Luong et al. (2011a) estimated a YSO lifetime close to the dense core free-fall time, typically 10^5 yr, and assumed that the initial mass function of Kroupa (2001) applies. The resulting SFR estimates are very uncertain but remain *direct measurements* like those done from *Spitzer* YSOs counting (Heiderman et al. 2010) and in contrast to those made from the impact of OB-type stars/H II regions on the interstellar medium (e.g. Nguyen Luong et al. 2011b). They also correspond to *present SFRs* in opposition to the past SFRs measured within nearby galaxies or Gould Belt cloud from the infrared or centimeter emission of already formed stars. The star formation rate densities measured within the G035.39–0.33, W43-Main, and DR21 ridges are high: $\Sigma_{\rm SFR}$ $10-100$ $M_\odot$ /yr /kpc^2 on $1-10$ pc^2 areas (see Motte et al. 2003; Nguyen Luong et al. 2011a, Hennemann et al. in prep.). They are worthy of starburst galaxies usually defined by $\Sigma_{\rm SFR} > 1$ (Kennicutt 1998) and *ridges qualify as mini-starburst regions* (see Fig. 3b).

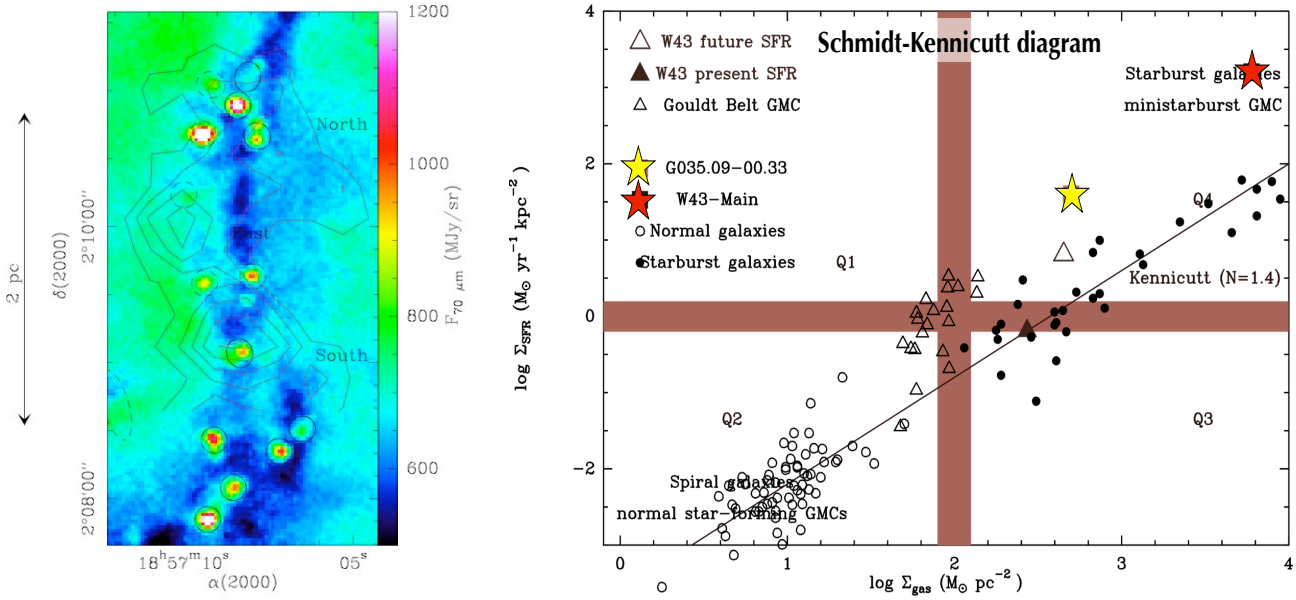

Fig. 3. Left: The G035.39–00.33 ridge seen at 70 μm (color) and in SiO (contours from Jiménez-Serra et al. 2010). The dense cores with mass >20 $M_\odot$ are indicated by continuous ellipses, those with mass <20 $M_\odot$ by dashed ellipses. **Right:** The G035.39–0.33 and W43-Main starburst ridges placed in the Schmidt-Kennicutt diagram, a plot of the star formation density as a function of mass density originally built to separate starburst and spiral galaxies.

4 Conclusions

HOBYS studies defined "ridges" as high-column density ($A_V > 100$ mag), elongated (several pc) cloud structures concentrating the mass of their surroundings and forming high-mass stars. With their filamentary structure, high density, and low temperature, ridges are extreme infrared-dark clouds. While turbulence could have formed most cloud filaments, more dynamic scenarios such as converging flows and/or filaments merging are advocated to form ridges. The HOBYS survey statistically showed that ridges are privileged sites for the formation of high-mass star clusters and are currently developing local bursts of star formation. In such a scenario, high-mass prestellar cores that will collapse independently from their surrounding cannot exist, in agreement with

the lack of their discovery. The HOBYS survey is a necessary step towards Galaxy-wide studies of high-mass star formation since it will soon make the global study of cloud structure and star formation activity in the closest Galactic arm with the unmatched resolution of ∼0.1 pc.

The HOBYS Key Program is developed by the SPIRE consortium Specialist Astronomy Group "Star formation" (SAG3) and the PACS consortium. Part of this work was supported by the ANR (french *Agence Nationale pour la Recherche*) project "PROBeS", number ANR-08-BLAN-0241.

References

Anderson, L. D., Zavagno, A., Deharveng, L., et al. 2012, A&A, 542, A10
André, P., Men'shchikov, A., Bontemps, S., et al. 2010, A&A, 518, L102
Bernard, J.-P., Paradis, D., Marshall, D. J., et al. 2010, A&A, 518, L88
Beuther, H., Schilke, P., Menten, K. M., et al. 2002, ApJ, 566, 945
Bonnell, I. A. & Bate, M. R. 2006, MNRAS, 370, 488
Bontemps, S., André, P., Könyves, V., et al. 2010a, A&A, 518, L85
Bontemps, S., Motte, F., Csengeri, T., & Schneider, N. 2010b, A&A, 524, A18
Csengeri, T., Bontemps, S., Schneider, N., Motte, F., & Dib, S. 2011, A&A, 527, A135
Dale, J. E. & Bonnell, I. 2011, MNRAS, 414, 321
Deharveng, L., Zavagno, A., Anderson, L. D., et al. 2012, ArXiv e-prints
Federrath, C., Roman-Duval, J., Klessen, R. S., Schmidt, W., & Mac Low, M.-M. 2010, A&A, 512, A81
Griffin, M. J., Abergel, A., Abreu, A., et al. 2010, A&A, 518, L3
Hartmann, L., Ballesteros-Paredes, J., & Heitsch, F. 2012, MNRAS, 420, 1457
Heiderman, A., Evans, II, N. J., Allen, L. E., Huard, T., & Heyer, M. 2010, ApJ, 723, 1019
Heitsch, F., Slyz, A. D., Devriendt, J. E. G., Hartmann, L. W., & Burkert, A. 2006, ApJ, 648, 1052
Hennemann, M., Motte, F., Bontemps, S., et al. 2010, A&A, 518, L84
Hennemann, M., Motte, F., Schneider, N., et al. 2012, A&A, 543, L3
Hill, T., Motte, F., Didelon, P., et al. 2011, A&A, 533, A94
Hill, T., Motte, F., Didelon, P., et al. 2012, A&A, 542, A114
Hosokawa, T. & Omukai, K. 2009, ApJ, 691, 823
Jiménez-Serra, I., Caselli, P., Tan, J. C., et al. 2010, MNRAS, 406, 187
Kennicutt, Jr., R. C. 1998, ApJ, 498, 541
Kirk, J. M., Ward-Thompson, D., & André, P. 2005, MNRAS, 360, 1506
Kroupa, P. 2001, MNRAS, 322, 231
McKee, C. F. & Tan, J. C. 2002, Nature, 416, 59
Men'shchikov, A., André, P., Didelon, P., et al. 2012, A&A, 542, A81
Molinari, S., Swinyard, B., Bally, J., et al. 2010, A&A, 518, L100
Motte, F., Bontemps, S., Schilke, P., et al. 2007, A&A, 476, 1243
Motte, F., Schilke, P., & Lis, D. C. 2003, ApJ, 582, 277
Motte, F., Zavagno, A., Bontemps, S., et al. 2010, A&A, 518, L77
Nguyen Luong, Q., Motte, F., Hennemann, M., et al. 2011a, A&A, 535, A76
Nguyen Luong, Q., Motte, F., Schuller, F., et al. 2011b, A&A, 529, A41
Peretto, N. & Fuller, G. A. 2010, ApJ, 723, 555
Pilbratt, G. L., Riedinger, J. R., Passvogel, T., et al. 2010, A&A, 518, L1
Poglitsch, A., Waelkens, C., Geis, N., et al. 2010, A&A, 518, L2
Ragan, S., Henning, T., Krause, O., et al. 2012, ArXiv e-prints
Russeil, D., Zavagno, A., Motte, F., et al. 2010, A&A, 515, A55
Schneider, N., Csengeri, T., Bontemps, S., et al. 2010a, A&A, 520, A49
Schneider, N., Csengeri, T., Hennemann, M., et al. 2012, A&A, 540, L11
Schneider, N., Motte, F., Bontemps, S., et al. 2010b, A&A, 518, L83
Schuller, F., Menten, K. M., Contreras, Y., et al. 2009, A&A, 504, 415
Sousbie, T. 2011, MNRAS, 414, 350
Tremblin, P., Audit, E., Minier, V., Schmidt, W., & Schneider, N. 2012, A&A, 546, A33
Vázquez-Semadeni, E., González, R. F., Ballesteros-Paredes, J., Gazol, A., & Kim, J. 2008, MNRAS, 390, 769
Zavagno, A., Russeil, D., Motte, F., et al. 2010, A&A, 518, L81

SF2A 2012
S. Boissier, P. de Laverny, N. Nardetto, R. Samadi, D. Valls-Gabaud and H. Wozniak (eds)

ABOUT THE SOCIEDADE ASTRONÔMICA BRASILEIRA AND ITS 36TH ANNUAL MEETING (2011)

E. Janot-Pacheco[1]

Abstract. We present an overview of the Brazilian Astronomical community and of its available observational facilities. We explain how is organized the Brazilian Astronomical Society (S.A.B.) and present some information on our last annual meeting, held in 2011.

Keywords: Sociedade Astronômica Brasileira

1 Introduction

The Sociedade Astronômica Brasileira is the association that gathers people working profissionally with astronomy and/or related areas.

Fig. 1. Logo of SAB and official website: `http://www.sab-astro.org.br/`

2 The Brazilian community

The Brazilian community comprises about 700 people ($\sim$ 350 with permanent positions and $\sim$ 350 with fellowships). There are about 40 centers in Brazil were research in astronomy is performed. In most cases, research centers are hosted in federal and state universities. Research funding is provided by agencies dependent on Ministry of Science, Technology and Innovation, but almost each state has also its own funding agency. Salaries and day-to-day expenses are mainly provided by Universities.

[1] Instituto de Astronomia, Geofísica e Ciências Atmosféricas, Universidade de São Paulo, 05508-090 São Paulo, Brazil

3 Observational facilities

Brazilian participation in the CoRoT satellite is three fold: ground software, data-reception station and science teams including pre-launch ground-based observations. Our national optical observatory in Brazil (Laboratório Nacional de Astrofísica) has a 1.6 m Boller and Chivens telescope equipped with cassegrain and Coudé spectrographs, optical and IR cameras, photometers and polarimeters. The observatory is installed at a mountain 1,680 m high in a region not too dry of the southern part of the country. Brazil shares the 4.2 m SOAR telescope (Cerro Pachón, Chile) with NOAO, North Caroline State University and Michigan State University. We have one third of telescope time. SOAR is equipped with an optical imager (SOI, 310-1050 nm), an IR imager (SPARTAN) and a medium-dispersion visible spectrograph (Goodman). Brazil rents about 5% of Gemini telescopes time and about 50 hours per year of CFHT. Ministry of Science, Techonology and Innnovation has approved in 2011 an agreement to join ESO. It will be submitted to Parliament approval in the current of 2012. We have a 13.7 m radiotelescope antenna working in 22 - 44 GHz equipped also with a polarimeter (7 GHz) and VLF receiver. We share with Argentina the SST-Solar submillimetric telescope (Casleo, Argentina) and participate on the Pierre Auger UHE observatory (also in Argentina).

4 The Sociedade Astronômica Brasileira

S.A.B board is composed by a President, Vice-President, Secretary General, Secretary and Treasurer plus specialized commissions. The directory meets presentially at least once per semester and organizes an annual meeting. We have commissions for admissions, editing, elections, education and outreach, for the Brazilian Astronomy Olympiad and the Braziliam Astronomy Commission that represents the country before IAU. The Brazilian Astronomy Olympiad is worth mention: those annual competitions exist since 1995 and for 2011 more than 800,000 students between 13 and 17 years old applied. Winners are selected to compete into the international olympiads.

5 The S.A.B. 2011 Annual Meeting

S.A.B meeting have a 3.5 day format with invited conferences, short communications, poster sessions and a General Assembly. In 2011 we had about 330 attendants from 30 institutions that presented 327 contributions: 14 invited conferences, 61 oral presentations and 252 posters. Subjects covering many astronomical themes were presented, *viz.*, astrobiology, astrometry, celestial mechanics, cosmology, extragalactic astronomy, exoplanets, the Galaxy and the Magellanic Clouds, astronomical instrumentation, the ISM, plasmas and high energy astrophysics, Relativity and gravitation, solar physics, the Solar System, stars, teaching and history of astronomy. For the invited conferences colleagues from France, Holland, Spain and USA were received. In 2011 a special ESO session was organized, and the Director General and six other colleagues from Garching and Chile presented various scientific and technical aspects of the ESO organization.

We thank SF2A for inviting S.A.B to participate of this meeting as the invited society for 2012 and for inviting me to present S.A.B to the french astronomical community

SF2A 2012
S. Boissier, P. de Laverny, N. Nardetto, R. Samadi, D. Valls-Gabaud and H. Wozniak (eds)

WHAT DOES THE INTERPLANETARY HYDROGEN TELL US ABOUT THE HELIOSPHERIC INTERFACE ?

F. E. Vincent[1], L. Ben-Jaffel[1] and W. M. Harris[2]

Abstract. The heliospheric interface results from the interaction between the solar wind and the local interstellar medium (LISM). The interplanetary hydrogen (IPH), a population of neutrals that fill the space between planets inside the heliosphere, carries the signature of the LISM and the heliospheric interface: as the incoming ISM ionized component deflects at the heliopause, charge exchange reactions decelerate the bulk motion of the neutrals that penetrate the heliosphere. Inside the heliosphere, the IPH is further affected by the Sun and resonantly scatters the solar Lyman-alpha photons. Solar cycle 23 provided the first partial temporal map of the IPH velocity. We present an updated analysis of IPH velocity measurements from *Hubble Space Telescope* spectrometers (Goddard High Resolution (GHRS) and Space Telescope Imaging Spectrograph (STIS)) and compare these results with those of the *Solar and Heliospheric Observatory* (SOHO)/Solar Wind ANisotropies (SWAN) instrument and two different time-dependent models. With updates to the HST data points, we now find that all data can be fit by the existing models to within 1σ, with the exception of SWAN observations taken at solar minimum (1997/98). We interpret this discrepancy as a possible effect due to the obliquity of the local interstellar magnetic field. New observations are required to determine the detailed characteristics of the solar cycle dependence and to monitor the possible changes in the LISM parameters as recently reported by the *Interstellar Boundary Explorer* (*IBEX*) spacecraft.

Keywords: Ultraviolet: stars, interplanetary medium, Sun: heliosphere, ISM: general

1 Introduction

The Solar system is moving through the Local Interstellar Cloud, a diffuse warm and partially ionized medium, mainly composed of atomic hydrogen (Frisch 2009). The fundamental aspect of the interaction between the solar wind (SW) and the local interstellar medium (LISM) is the dynamic equilibrium between two counter-flowing magnetized plasmas that meet and are separated along a tangential discontinuity, the heliopause (Parker 1961; Baranov et al. 1971; Axford 1972). The overall shape and location of the heliopause is determined by the relative velocity of the solar wind and LISM and the plasma densities on either side of the barrier. In the generalized model of the interaction, the SW and the ionized LISM are decelerated to subsonic speeds through shocks that are respectively located inside (the termination shock) and outside (the bow shock) the heliopause, as shown in figure 1. However recent observations from the *Interstellar Boundary Explorer* (*IBEX*) spaceraft show that the relative motion of the Sun with respect to the LISM is currently slower (23.2 ± 0.3 km/s, McComas et al. (2012)) than previously measured (~ 26 km/s) by Doppler triangulation (Bertin et al. 1993) and the *Ulysses* spacecraft (Witte et al. 1993), so almost certainly slower than the fast magnetosonic speed, which would prevent the formation and the existence of the bow shock ahead of the heliosphere.

Because of a large mean free path, a fraction of interstellar hydrogen atoms penetrates inside the heliosphere without any interaction with the interface (Blum & Fahr 1970), forming the primary population of the interplanetary hydrogen (IPH). Early space based studies of the sky background confirmed the presence of the incoming hydrogen flow (Bertaux & Blamont 1971; Thomas & Krassa 1971). Subsequent UV spectroscopic and imaging experiments provided limited access to the IPH velocity distribution (Bertaux et al. 1976, 1985; Adams & Frisch 1977; Clarke et al. 1984, 1995) and revealed a deceleration of the hydrogen flow relative to the LISM (Bertin et al. 1993).

[1] Institut d'Astrophysique de Paris, CNRS-UPMC, 98 bis, Boulevard Arago, 75014 Paris, France
[2] Department of Mechanical and Aerospace Engineering, University of California, One Shields Avenue, Davis, CA 95616, USA

The observed neutral LISM deceleration is believed to be traceable to the fraction of interstellar hydrogen atoms that interact with the slowing LISM protons through resonance charge exchange reactions (Wallis 1975; Ripken & Fahr 1983). These reactions result in the formation of a secondary population with a slower bulk motion, leading to the formation of a "Hydrogen Wall" between the bow shock and the heliopause, as predicted by Baranov & Malama (1993) and then observed by Linsky & Wood (1996) with observations of absorption lines in the direction of α Centauri. By contrast, interstellar helium atoms are barely affected by the heliospheric interface because of a smaller cross-section for charge-exchange reactions, and carry the signature of the LISM inside the heliosphere (Moebius et al. 2004). Observations with the Solar Wind ANisotropies (SWAN) instrument on the *Solar Wind Heliospheric Observatory* (*SOHO*) showed that the hydrogen flow is slightly deflected by respect to the helium flow (Lallement et al. 2005, 2010).

During the last two decades, *SOHO*/SWAN and the echelle modes of the Goddard High Resolution Spectrograph (GHRS) and Space Telescope Imaging Spectrograph (STIS) on the *Hubble Space Telescope* (*HST*) have been used to measure the Ly-α Doppler shift with respect to the heliospheric referential and line profile with greater precision than previous observations (Clarke et al. 1998; Scherer et al. 1999; Ben-Jaffel et al. 2000; Quémerais et al. 2006).

Within the heliosphere, the IPH velocity is affected by several temporally dependent processes related to the solar wind and solar Ly-α intensity. The Warsaw group (Rucinski & Bzowski 1995; Bzowski et al. 1997) developed a time-dependent hot model of the inner heliosphere that predicts a $\sim$ 5 km/s modulation in IPH bulk velocity due to solar cycle changes in radiation pressure and ionization rates. More recently, fluid-kinetic models included the effects of non-stationary solar wind ram pressure on the heliospheric interface (Izmodenov & Malama 2004; Izmodenov et al. 2008; Pogorelov et al. 2010). The use of a radiative transfer model allows more precise predictions of the interplanetary background line-shifts (Scherer et al. 1999; Quémerais et al. 2008). These models all converge toward a general finding that the IPH velocity should vary by 3-4 km/s over the solar cycle, but they reach different conclusions about the rate of this change and its precise magnitude. Based on previously published values, none of them have been able to match the data consistently across the entire solar cycle (Quémerais et al. 2008).

This paper sums up the work done by Vincent et al. (2011), providing an updated analysis of the IPH velocity measurements obtained over the solar cycle 23, in particular *HST* archival data from GHRS and STIS, which are compared to previously reported measurements from *SOHO*/SWAN and model predictions of IPH velocity variations over a solar cycle. In addition, we discuss the impact of the *IBEX* results.

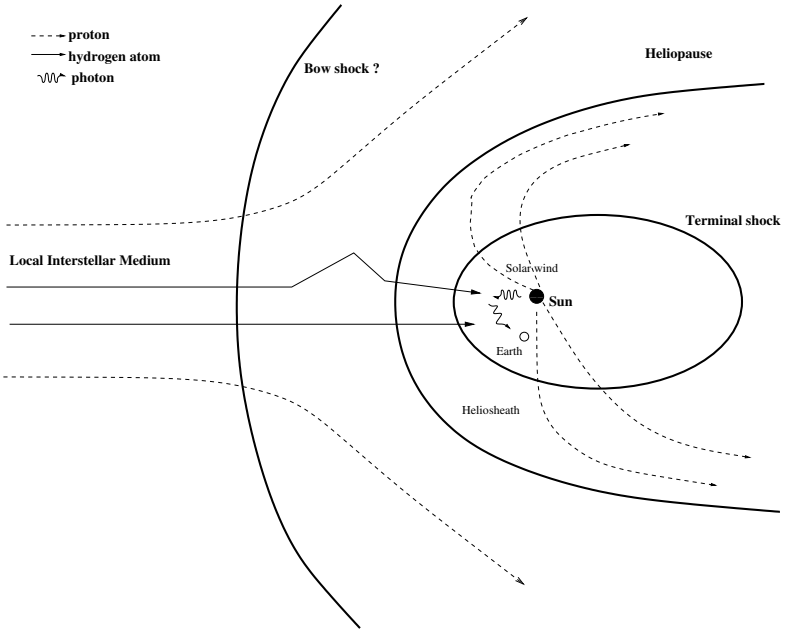

Fig. 1. Schematic of the interaction between the solar wind and the interstellar medium. The Earth's position is not to scale.

2 Data analysis

2.1 Observations

GHRS and STIS have been used to detect the backscattering of solar Lyα photons by the IPH, using the same line of sight (LOS): ($\lambda = 253.3°$, $\beta = 7.0°$) in ecliptic coordinates. The inner heliosphere (inside 40 AU) is dominated by solar EUV photoionization and charge exchange with SW protons, while the outer heliosphere is more affected by the heliospheric interface. Because of an increasing neutral hydrogen density with distance from the Sun, the medium can be considered as optically thin until 10 AU, but not beyond. Full attenuation of the line occurs over a large range of heliocentric distance beyond this point, with backscatter at all points contributing to the observed line shape and brightness distribution (Quémerais 2000).

GHRS data were obtained on 1994 April 7 and 1995 March 25, STIS data on 2001 March 29. At this period of the year (March-April), Earth's and IPH's velocity vectors are most direcly opposite to each other, which provides a maximal Doppler shift with respect to the geocorona. STIS observations used an unsupported mode (E140H grating with the large aperture 52" x 0.5"), increasing the signal from an extended source like the IPH, but resulting in blending of different orders of the echelle spectrum, as showed in Figure 2 (left).

2.2 Fitting procedure and results

GHRS and STIS spectra contain Lyα line profiles from the geocorona and the IPH, with some contamination from a geocoronal oxygen triplet line in STIS observations. Each line profile was fitted using the convolution of a Voigt profile with a measured or simulated line-spread function (LSF), and the 1σ errors were computed with $\sigma = \sqrt{\sigma_I^2 + \sigma_S^2}$, where σ_I and σ_S are respectively the instrumental and statistical uncertainties (Vincent et al. 2011). The line-shift of the IPH along the line of sight is derived from the Doppler shift between the line centers of the geocorona and the IPH, after subtraction of the velocity of the Earth along the line of sight.

Figure 2 (right) shows the fit for STIS observations. The IPH feature in the 346th order is contaminated by the 1302.168 Å O I line, so only the 347th order was used to derive the IPH line-shift. Our best fit to the STIS observations takes into account the contamination of the geocorona on the red side by the O I lines, and provides a line-shift of 22.4 ± 0.4 km/s in 2001. GHRS spectra were extracted using the existing pipeline. After fitting the lines with MPFIT and PAN, we obtained line-shifts of 24.0 ± 0.9 km/s in 1995 and 22.2 ± 1.5 km/s in 1994 (Figures 6 and 7 in Vincent et al. (2011)). The subsection 3.1. in Vincent et al. (2011) makes a comparison of this work with previous analyses of HST data.

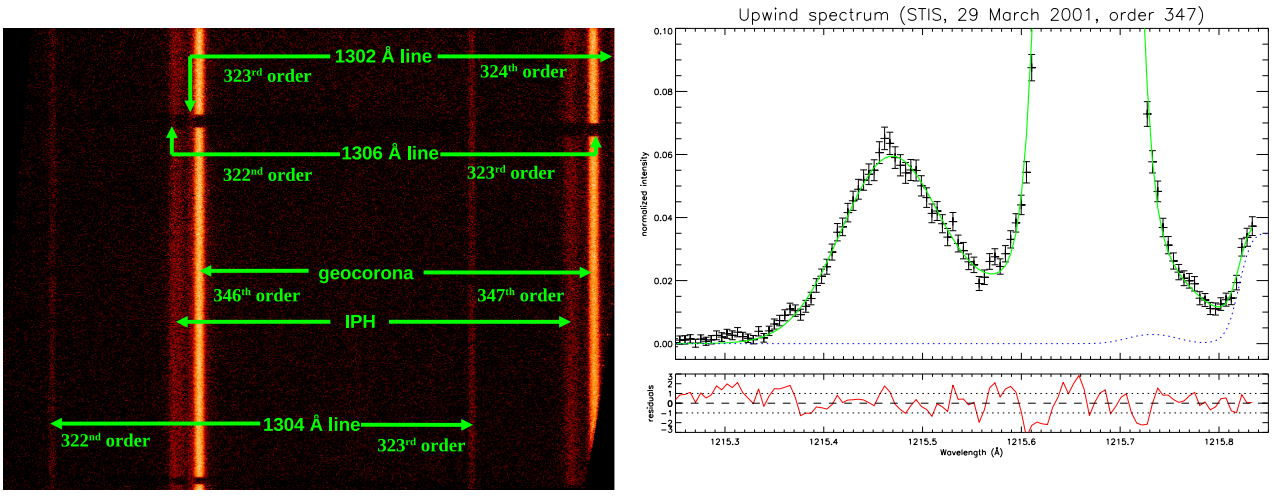

Fig. 2. Left: STIS spectro-image from observations made on 29 March 2001, after correction of the geometric distortion. The Ly-α emission from IPH and geocorona is transmitted by two orders (346 and 347) but suffers from contamination by geocoronal oxygen emission lines. The central line of the O I triplet (1304.858 Å) is isolated and clearly visible. Both other lines (1302.168 and 1306.029 Å) overlap with the Ly-α emission but appear at the location of the occulting bars where the Ly-α emission is blocked. **Right:** Fitting of STIS observations for the order 347. The blue dotted lines represent the contaminations by oxygen lines: 1306.029 Å (order 323) and 1302.168 Å (order 324), from left to right.

3 Discussion

3.1 Comparison with SWAN data and models

Quémerais et al. (2006) derived interplanetary Ly-α line profiles from annually averaged observations made by the SWAN instrument. Their findings indicate a velocity change from 25.7 ± 0.2 km/s to 21.4 ± 0.5 km/s in the solar rest frame between 1997 and 2003.

Figure 3 plots the IPH velocities found by this work for GHRS & STIS observations, and by Quémerais et al. (2006) for SWAN data and STIS observations. In order to show the possible solar cycle effect, we over-plotted the predictions of the physically realistic models developed by Quémerais et al. (2008) and Scherer et al. (1999) (noted Q2008 and S1999 respectively).

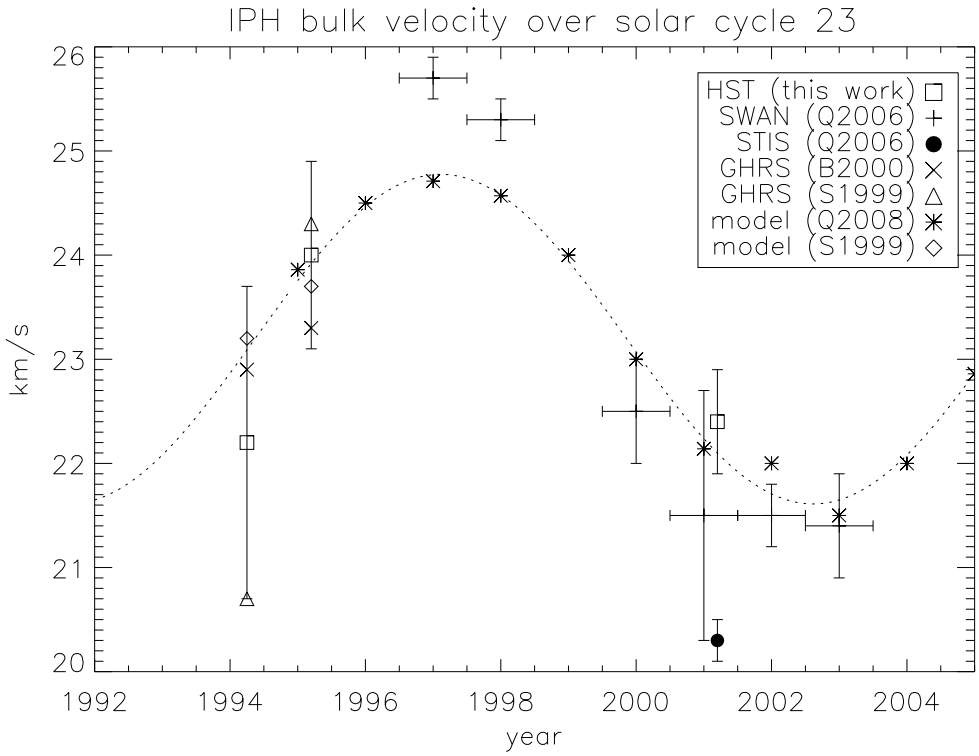

Fig. 3. IPH bulk velocity in the upwind direction over solar cycle 23, with values reported by this work (squares for GHRS and STIS), by Quémerais et al. (2006) (plus signs for SWAN data, filled circle for STIS observations), by Ben-Jaffel et al. (2000) (crosses) and Scherer et al. (1999) (triangles). The dotted curve is a Fourier interpolation of the model proposed by Quémerais et al. (2008) (asterisks). The values predicted by the model of Scherer et al. (1999) are represented with diamonds.

Compared to the value obtained by Quémerais et al. (2006), the updated STIS data reduction provides an IPH velocity that is more consistent with SWAN data and the Q2008 model for the period near solar maximum (in 2001). Similarly our revised GHRS analysis provides a much better fit to the models than that provided in Scherer et al. (1999). As a consequence, all data are within or close to 1σ from Q2008 and S1999 models, at the exception of the SWAN measurements in 1997/98.

3.2 The influence of the local interstellar magnetic field

Allowing for the statistically significant fit between the data and models near solar maximum, the primary discrepancy is found at solar minimum, where the SWAN data implies a velocity more than 2σ faster than the model. Two explanations that do not exclude one another, can be proposed to account for this difference: these include possible systematic uncertainty in the SOHO-SWAN data processing and/or an incomplete description of the IPH neutrals by the fluid-kinetic models (Scherer et al. 1999; Izmodenov et al. 2008). As explained in

the subsubsection 3.4.1. in Vincent et al. (2011), the error bars on SWAN measurements could be larger than previously estimated.

On the other hand, the discrepancy between data and models could be also an indirect effect of the interstellar influence, notably the local interstellar magnetic field that has not been taken into account by the previous authors (Scherer et al. 1999; Izmodenov et al. 2008; Quémerais et al. 2008). Models taking into account the oblique local interstellar magnetic field (LIMF) have shown severe distortion in the shape of the heliopause (Fahr et al. 1988; Ratkiewicz & Ben-Jaffel 2002; Izmodenov et al. 2005). Ben-Jaffel et al. (2000) showed that the excess of backscattered solar Ly-α photons detected by *Voyager 1* UVS can interpreted as a tilt of the heliosphere's nose by respect to the upwind direction, resulting from an oblique LIMF with a deviation $\sim 40°$ from the interstellar flow direction. Results obtained by SWAN showed that the interstellar neutral hydrogen flow is deflected relative to the helium flow, providing new evidence for the obliquity of the LIMF (Lallement et al. 2005, 2010). More recent models can account for the 10 astronomical units (AU) difference in the TS heliosheric distances observed by the *Voyager 1* and *Voyager 2* spacecraft (Ratkiewicz & Grygorczuk 2008; Pogorelov et al. 2009; Opher et al. 2009). Even more recently, *IBEX* found a ribbon of energetic neutral atoms around the heliosphere, another proxy of the influence of the LIMF (McComas et al. 2009; Heerikhuisen et al. 2010). All observations and data analyses converge on the fact that the deviation of the LIMF from the interstellar flow direction is between 30° and 60°.

Because of the tilted nose, the density maximum will be shifted from the upwind direction as shown by most magneto-hydrodynamic and kinetic hydrogen models (Izmodenov et al. 2005; Ratkiewicz et al. 2007; Pogorelov et al. 2009). Therefore the upwind line of sight may probe regions with smaller densities and less charge exchange filtration in the outer heliosphere in the upwind direction. This weaker interaction would lead to a faster velocity component in the outer heliosphere but with a smaller weight, while the inner heliosphere component would have a bigger weight, leading to a higher IPH velocity than current models predict in the upwind direction. An oblique LIMF may thus result in a larger difference of IPH velocity (compared to IPH velocity without LIMF) at solar minimum than at solar maximum.

3.3 Need for more data

The identified issues with data near solar maximum, including the consistently low velocities obtained and the larger uncertainties, along with the discrepancy between the models and the lone data points at solar minimum, all argue for the acquisition of new data.

Moreover *IBEX* data showed that the relative motion of the Sun with respect to the LISM is currently slower (23.2 ± 0.3 km/s, McComas et al. (2012)) than previously measured (~ 26 km/s, Bertin et al. (1993); Witte et al. (1993)). There are almost 20 years between measurements, so the LISM parameters may have changed, as the Sun is moving through. Fahr et al. (1993) showed that changes in LISM over such a period may give noticeable imprints on the upwind/downwind IPH velocity distribution.

New upwind IPH observations have been recently made by *HST*/STIS and are currently being analyzed (Vincent et al. 2012). However more high-resolution measurements will be necessary to reduce the current uncertainties, better characterize the trend induced by the solar cycle, and answer the questions raised by the discrepancy at solar minimum and the possible change in the LISM parameters.

4 Conclusions

Updated analyses of both *HST*/GHRS and *HST*/STIS observations provide IPH bulk velocities of 22.2 ± 1.5, 24.0 ± 0.9 and 22.4 ± 0.4 km/s in 1994, 1995 and 2001, respectively. These results are much more consistent with existing models. With the exception of the *SOHO*/SWAN data at 1997/98 near solar minimum, all of the data now trend within 1σ of the most physically realistic models.

In addition, the influence of the interstellar magnetic field on the heliosphere and its obliquity by respect to the interstellar flow have been proved by a multi-observational approach (*Voyager*, *SOHO*/SWAN and *IBEX*). We think that this obliquity may explain the discrepancy between models and data treating of the IPH velocity at solar minimum, and therefore it should be included in future time-dependent kinetic-fluid models.

The rather large uncertainty of some measurements near solar maximum, the discrepancy at solar minimum, and the possible change in the LISM parameters as suggested by the recent *IBEX* results, call for the acquisition of more high-resolution measurements with *HST*/STIS.

We thank Yan Bétrémieux (MPI) for his critical feedback, as well as John Clarke (BU) for discussions about *HST* observations. We are also very grateful to the COS/STIS help desk and to Craig Markwardt (GSFC) for their help. F.E.V. and W.M.H. acknowledge support from NASA through the grant NNX08AI98G to UCD. F.E.V. and L.B.J. acknowledge support from CNES (through the INSPIRE project), CNRS and UPMC.

References

Adams, T.F., Frisch, P. 1977, ApJ, 212, 300
Axford, W. I. 1972, in Solar Wind, ed. C. P. Sonett, P. J. Coleman, Jr., & J. M. Wilcox (NASA SP-308), 609
Baranov, V.B., Krasnobaev, K.V., Kulikovskii, A.G. 1971, Soviet Phys. Doklady, 15, 791
Baranov, V. B., Malama, Y. G. 1993, J. Geophys. Res., 98, 15157
Bertaux, J.L., Blamont, J.E. 1971, A&A, 11, 200
Bertaux, J.L., Blamont, J.E., Tabarié, N., Kurt, V.G., Bourgin, *et al.*, 1976, A&A, 46, 19
Bertaux, J.L., Lallement, R., Kurt, V.G., Mironova, E.N. 1985, A&A, 150, 1
Bertaux, J.L., et al. 1995, Sol. Phys., 162, 403
Bertin, P., Lallement, R., Ferlet, R., Vidal-Majar, A. 1993, J. Geophys. Res., 98, 15193
Ben-Jaffel, L., Puyoo, O., Ratkiewicz, R. 2000, ApJ, 533, 924
Blum, P.W., Fahr, H.J. 1970, A&A, 4, 280
Bzowski, M., Fahr, H.J., Rucinski, D. , Scherer, H. 1997, A&A, 326, 396
Clarke, J.T., Bowyer, S., Fahr, H.J., Lay, G. 1984, A&A, 139, 389
Clarke, J.T., Lallement, R., Bertaux, Quémerais, E. 1995, ApJ, 448, 893
Clarke, J.T., Lallement, R., Bertaux, J.L., Fahr, H., Quémerais, E., Scherer, H. 1998, ApJ, 499, 482
Dimeo, R. et al. 2005, http://www.ncnr.nist.gov/staff/dimeo/panweb/pan.html
Fahr H.J., Grzedzielski, S., Ratkiewicz, R. 1988, Ann. Geophys., 6(4), 337
Fahr, H.J., Rucinski, D., Judge, D.L. 1993, A&A, 268, 792
Frisch, P.C. 2009, Space Sci. Rev., 143, 191
Heerikhuisen, J., et al. 2010, ApJ, 708, 126
Izmodenov, V., Malama, Y.G. 2004, Adv. Space Res., 34, 74
Izmodenov, V., Alexashov, D., Myasnikov, A. 2005, A&A, 437, L35
Izmodenov, V., Malama, Y.G., Ruderman, M.S. 2008, Adv. Space Res., 41, 318
Lallement, R., Quémerais, E., Bertaux, J.L., Ferron, S., Koutroumpa, D., *et al.*, 2005, Science, 307, 1447
Lallement, R., Quémerais, E., Koutroumpa, D., Bertaux, J.L., Ferron, S., *et al.*, 2010, AIP Conf. Proc., 1216, 555
Linsky, J.L., Wood, B.E. 1996, ApJ, 463, 254
Markwardt, C. B. 2008, ASP Conference Series, 411, 251
McComas, D.J. et al. 2009, Science, 326, 959
McComas, D.J., Alexashov, D., Bzowski, M., Fahr, H., Heerikhuisen, J., *et al.*, 2012, Science, 336, 1291
Moebius, E. et al. 2004, A&A, 426, 897
Parker, E.N. 1961, ApJ, 134, 20
Opher, M., Richardson, J.D., Toth, G., Gombosi, T.I 2009, SSR, 143, 43
Pogorelov, N.V., et al. 2009, Adv. Space Res., 44, 1337
Pogorelov, N.V., et al. 2010, ASPC, 429, 266
Quémerais, E. 2000, A& A, 358, 353
Quémerais, E., Lallement, R., Bertaux, J.-L., Koutroumpa, D., Clarke, J., *et al.*, 2006, A&A, 455, 1135
Quémerais, E., Izmodenov, V., Koutroumpa, D., Malama, Y. 2008, A&A, 488, 351
Ratkiewicz, R., Ben-Jaffel, L. 2002, J. Geophys. Res., 107, 1007
Ratkiewicz, R., Ben-Jaffel, L., Grygorczuk, J. 2007, ASPC, 385, 189
Ratkiewicz, R., Grygorczuk, J. 2008, Geophys. Res. Lett., 35, L23105
Ripken, H.W., Fahr, H.J. 1983, A&A, 122, 181
Ruciński, D., Bzowski, M. 1995, A&A, 296, 248
Scherer, H., Bzowski, Fahr H.J., M., Ruciński, D. 1999, A&A, 342, 601
Thomas, G.E., Krassa, R.F. 1971, A&A, 11, 218
Vincent, F.E., Ben-Jaffel, L., Harris, W.M. 2011, ApJ, 738, 135
Vincent, F.E., Ben-Jaffel, L., Harris, W.M., Clarke, J.T., Quémerais, E. 2012, in progress
Wallis, M. 1975, Nature, 254, 202
Witte, M., Rosenbauer, H., Banaszkiewicz, M., Fahr, H. 1993, Adv. Space Res., 13, (6)121

Session 02

Gaia: calibrations

SF2A 2012
S. Boissier, P. de Laverny, N. Nardetto, R. Samadi, D. Valls-Gabaud and H. Wozniak (eds)

GAIA INITIAL QSO CATALOGUE: THE VARIABILITY AND COMPACTNESS INDEXES

A.H. Andrei[1], S. Anton[2], C. Barache[3], S. Bouquillon[3], G. Bourda[4], J.-F. Le Campion[4], P. Charlot[4], S. Lambert[3], J.J. Pereira Osorio[2], J. Souchay[3], F. Taris[3], M. Assafin[5], J.I.B. Camargo[6], D.N. da Silva Neto[7] and R. Vieira Martins[6]

Abstract. The manifold Gaia scientific output relies on precise astrometry accurate to submas standards. This depends on building a fundamental reference frame formed by pointlike, position stable, and allsky homogeneous grid points. In one word, quasars. The Gaia CU3 Initial Quasar Catalogue Working Package was established to beforehand produce one such list, although ultimately the satellite multiband photometry aided by astrometric monitoring has the potential to pick up a clean sample of quasars.

Keywords: Gaia, QSO, catalogues, variability, galaxy morphology

1 Introduction

The Gaia mission (Mignard 2010) ranks among the most ambitious undertakings of modern astronomy. Operating from space, free from atmospheric, thermal, and gravity constraints and with full sky visibility, it will provide completeness to more than one billion objects in survey mode, to a nearly even eighty transits of each one. The launching is planned to 2013, for a five years mission. The measurements include astrometry, multi broad band photometry, and low dispersion spectroscopy for the 20% brighter objects. The astrometric precision will attain 7μas to magnitudes up to G =12, 25μas to magnitudes from G =12 to 15, and 250μas to magnitudes beyond G =15. The astrometry primary objective is the definition and materialization of the celestial reference frame, including the stellar distance scale and standard radial velocities.

The survey mode means that will be observed solar system, galactic, and extragalactic objects. Among the latter, an expected number of about 500,000 QSOs. By QSO we express active galactic nuclei objects (AGN) at large, that is radio loud quasars, Blazars, radio quiet qsos, BL LACs, Seyfert galaxies, LINERS, or as expressed by Souchay et al. (2012), QSO in the sense of an object which can be seen as an extragalactic quasi stellar source from a certain point of view and a specific set of parameters. The satellite observations imply in proper, in the relativistic sense, reference systems to which the measurements are initially referred. These are the described in Bastian (2007) as the Center-of-Mass Reference System (CoMRS), the Scanning Reference System (SRS), the Field-of-View Reference Systems (FoVRS), and the Reference Great-Circle Systems (RGCS), but the final catalogue will comply to the IAU's sanctioned Barycentric Celestial Reference System (BCRS), resulting in the Gaia Celestial Reference Frame (GCRF) materialized by a dense mesh of fiducial QSOs. Notwithstanding, it is also worth to mention that two other quite robust extensions of the GCRF will be produced, to brighter regimes. The one formed by the unresolved galaxies (some 10 million of objects) and the QSOs that didn't make it to be in the GCRF (which would presumably contain several radio-loud quasars). And the one formed the approximately half a billion of stars with highly accurate position and proper motions.

[1] ON/MCTI, Brasil; OATo/INAF, Italy; SYRTE/OP, France; OV/UFRJ, Brasil; present address: SHAO/CAS, China
[2] CICGE/FCUP, Portugal
[3] SYRTE/Observatoire de Paris, France
[4] LAB2, France
[5] OV/UFRJ, Brasil
[6] ON/MCTI, Brasil
[7] UEZO, Brasil

2 Gaia Initial QSO Catalog

QSOs are thus crucial targets to define the GCRF, and accordingly on board means are capable of classifying them. The QSO classification contains three major orientations: getting the cleanest QSO sample to determine the GCRF; deriving the most complete QSO sample based on the full Gaia data; and determining the astrophysical parameters for each QSO. The determination itself of a Gaia source as a QSO is planned to rely primarily on comparison of the photometric output against a template of spectral energy distributions (SED), ands secondarily on astrometric observables, variability analysis and a reliable initial list of known QSOs.

The study by Claeskens et al. (2006) shows that, based on the end-of-mission colour information, supervised Artificial Neural Networks (ANNs) can virtually reject all contaminating stars (including white dwarfs), although the completeness drops to about 20% at G =20. Variability on the color and space domains is efficient to remove stellar contaminants, whereas zero proper motion and parallax constraining can single out the late type red stars and white dwarfs contaminants. An alternative method relying on the QSOs and stars different predominant spaces in the color-color spaces can also be employed providing maybe 95% efficiency to a larger sample, although the crucial u-band will not be available in Gaia, as it was for the SDSS candidates scheme (Richards et al. 2002). The template adherence method can deliver a tighter but smaller sample. Notice, however, that a sample as small as 10,0000 quasars can stabilize the GCRF to a residual rotation of less than 0.5 μas per year, provided they are well distributed over the sky.

The relatively small number of points actually required to constitute a robust GCRF brings particular relevance for an initial list of known QSOs. This is exactly the purpose of the Gaia work package Initial QSO Catalogue for Gaia (GIQC), under the CU3, Core Processing Coordination. The aim of which is to obtain a clean sample of at least 10,000 quasars, distributed all sky above $b = \|20°\|$ of galactic latitude, with magnitude brighter than V=20 and point-like PSF. This bona fide initial clean sample is useful both for the actual orientation of the GCRF and to enlarge the templates of the recognition scheme. For that, catalogue and published QSO determinations are inspected. The starting number of publications handled amounted to a few thousands, from which the main contributors were the Véron-Cetty and Véron catalogue (12th edition), the 2dF catalogue, and the SDSS (DR5) catalogue. The collection kept expanding, and a recent status of the compilation can be found in Souchay et al. (2009); Andrei et al. (2009a,b). Several criteria were enforced to acknowledge a given source, the most importants of which were at least two independent determinations and the existence of spectroscopic redshift. In the most recent versions also the aspects of morphology and variability are addressed, which is reviewed below.

Presently the GIQC contains 187,505 objects. 187, divided in thre categories - defining, candidates, and other. The defining objects are 136,643 well documented QSOs, being 103,422 from the SDSS/DR8 (Schneider et al. 2010). The candidate sources are 24,227 objects, 1.075 from the ICRF2 for which there is no reliable optical counterpart 15,373 optically point like AGNs, and 7.779 QSOs of poor record. Finally, as other there 26.635 objects, being 385 radio-quasars, 23.178 objects fainter than the 20th magnitude, 2.985 unreliable detections, and 87 empty fields. Figure 1 brings an excerpt of the catalogue (without including the still provisional morphology and variability indexes).

RA (deg)	DEC (deg)	MAG	z	Rshr	Rsrn	Rgrn	Bshr	Bsrn	Bgrn	Ishr	Isrn	Igrn	Class
0.000000	-0.032778	19.40	1.560										C P
0.002083	-0.450833	20.09	0.250										O F
0.005291	-2.033269	19.29	1.356	0.75	0.10	0.13							D
0.005735	-30.607458	19.18	1.143	0.20	0.01	0.91							D
0.007326	-31.373790	19.74	1.331	0.73	0.44	0.00				1.82	1.14	1.37	D
0.011279	-25.193609	21.56	1.314										O F
0.012178	-35.059062	17.09	0.508	0.59	0.20	0.27				0.39	0.80	0.07	D
0.022792	-27.419533	19.11	1.930	0.12	1.01	0.41							D
0.027500	0.515278	20.37	1.823										D S
0.033333	-63.593333	17.00	0.136										C A
0.034167	0.276389	20.03	1.837										D S
0.038604	15.298477	19.40	1.199	0.92	0.02	0.30	0.36	0.92	0.08	1.11	1.51	1.46	D S
0.039089	13.938450	18.29	2.240	0.59	0.23	0.14	0.63	0.91	0.09	2.07	0.16	1.43	D S

Fig. 1. Excerpt from the GIQC (version 3, 2010). The morphological indexes, columns `Rshr` to `Igrn` (from the DSS plates B, R, and I) are presented in section 2. The first Class column signals the Defining, Candidate or Other classification, while the second one details the classification.

The catalog compiles reliable redshift for 183,543 objects (97.87%), and there are reliable optical images for 159,701 objects (85.17%). The space density distribution is shown in Figure 2a.

The astrometric coordinates compiled for GIQC are presented in the LQAC2 (Souchay et al. 2012). They are the most precise ones available for each source, but their accuracy is not consistent as they originate from widely different catalogs. Their sky density (4.5 per sq.deg) and sky distribution (about 75% of the minimum distances from adjacent sources are between 1.5°and 5°) prompted to combine the set into an optical materialization of the ICRS. For this we followed the precepts established for building the LQRF (Andrei et al. 2009a,b), but now nearly doubling the number of grid points.

Obviously, only those QSOs for which there are available optical images were used. The distribution is homogeneous, with no empty zones, though there is a quantity decreasing onwards the inner galactic disk, whereas there is an enhancement on the SDSS zones. By comparing with the common ICRF-2 quasars, we find the systematic offsets $\Delta\alpha\cos\delta$=+1.6 mas (σ=154.9 mas) and $\Delta\delta$=+3.6 mas (σ=158.8 mas). Excluding the optical minus radio residuals deviating by more than 2σ, the adherence to the ICRF2 is obtained as 55.5mas on right ascension and 59.7 mas on declination. Figure 2b shows the zonal warps. They are mostly (67%) smaller than 50 mas, with just 6 zones showing systematics larger than 100 mas.

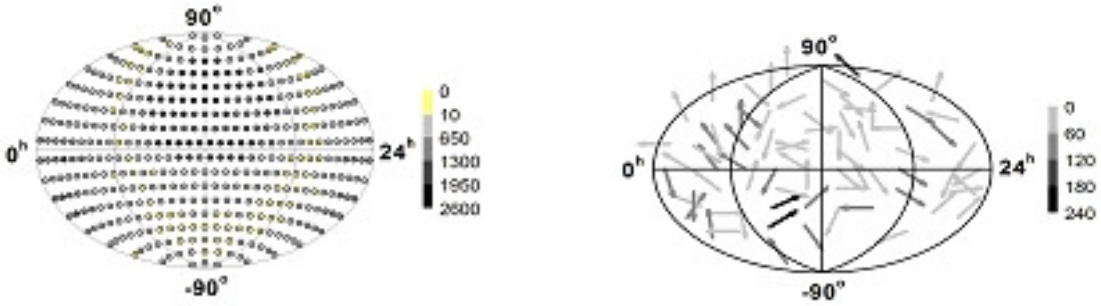

Fig. 2. Left: (a) The sky density of the GIQC based extragalactic reference frame. The counts are in bins of 10°. The zones in the inner galactic plane are less populated, while there is a density enhancement on the SDSS region. **Right:** the vectorial distribution of the systematic deviations (North up, East right) of the ICRF2 to the GIQC based extragalactic reference frame within bins of 30°. 67% of the deviations are smaller than 50 mas, while only 6 of them are larger than 100 mas.

3 Morphology

In the framework of the unified theory the classification of AGNs is largely a matter of line-of-sight perspective. Naturally a less schematic classification must consider the object interaction and merger history, dust contents, star formation waves, the rate and gyro direction of the central massive black hole spin, and the enrichment of the off accretion disk shells or regions. Nonetheless the entrusted relationship between the mass of the central black hole and the energy output from the inner regions versus the mass and luminosity of the host galaxy must generally hold. Therefore, since by optical ground observations quasars are essentially quasi stellar objects, an apparent paradox arises by which the more massive and luminous a host galaxy is, the more luminous the quasar tends to be, thus making the more invisible by contrast the host galaxy. Hubble images and active optics are now enabling the study of the host galaxy, what increases the knowledge about the quasar itself too. The presence of the host galaxy can be inferred also from color studies (Sakata et al. 2010) and from departures of the compound point spread function (PSF) of quasar and host galaxy to the purely pointlike stellar PSFs (Falomo et al. 2001). This methodology can be used to classify morphologically the quasars observed out from the atmosphere, as will be the case of the Gaia mission, hence deriving a centroid astrometrically more precise than if a stellar PSF would have been applied for the centroid determination.

We derived a PSF-based morphological classification of the GIQC objects using the available the B, R, and I DSS images. The morphological classification derives from comparing the target PSF against the local PSF. To that, neighborhoods of 5 × 5 arcmin around the QSO are obtained from the DSS plates. From the total LQAC-2 sample were obtained images of 114,606 fields from the B plates, 191,030 fields from the R plates, and 183,421 fields from the I plates. The incompleteness in most cases is due to the sky coverage, and lack

of available uncompressed digitalization for the DSS2 blue plates, but also to a residual number of faulty file transfers. In the retrieved plates there were cases where the quasar was not present or was too faint to provide a meaningful PSF (29,497 objects in the B plates, 37,790 objects in the R plates, and 29,799 objects in the I plates). Finally, there was not enough adequate comparison stars in 6 B plates, in 134 R plates, and in 86 I plates. As expected, due to the more complete sky coverage and brighter magnitude, the largest quantity of quasars corresponds to the R plates.

The IRAF task `DAOFIND` is used to detect both stars and target, as well as to derive the PSF parameters. Additionally the tasks from the `IMMATCH` IRAF's package are used to match stars and target to their catalog positions and magnitudes. Stars are collected within one magnitude from the QSO's magnitude, but in case less than five stars are picked up the magnitude limits are progressively enlarged at one magnitude steps, except to stars brighter than the tenth magnitude. Stars must be isolated from each other by an inner radius of ten pixels, and within the frame by the same threshold. If less than five comparison stars are found no morphological index is derived for that QSO on that plate. Three estimators of the PSF are used: SHARP (probing skewness), SROUND (probing roundness), and GROUND (probing normalness).

To test the power and efficiency of the above procedure applied to the DSS Schmidt plates, a comparative test was made using 1,343 objects present both on the R DSS images and on the r' SDSS images (Andrei et al. 2011). The large number of comparison objects enabled to sample regularly the SDSS quarter of sky space, as well as to collect the extreme examples on low and high redshift, bright and faint magnitudes, and the tails of the color distribution. The large number also allowed retaining only those QSOs for which at least 20 comparison stars were found. The analysis showed that there is no degeneracy of the indexes with magnitude. All nine morphological indexes, namely three parameters in three colors, behaved alike on the DSS and SDSS. Only 1% of the stars were misidentified by the morphological indexes, while for the quasars the correlation between the morphological classification and the SDSS catalogue classification was of 0.86 for the SDSS images and of 0.72 for the DSS images. Due to the better quality of the SDSS images and pixelization, the number of QSOs reckoned as extremely non-pointlike is larger from the SDSS fields (144 objects) than from the DSS fields (86 objects), but 50% of those are common. This trial thus supports using the DSS images to derive a morphological index, that describes the degree of agreement or disagreement of the quasar PSF to the local mean stellar PSF. Owing to the limited resolution, the morphological indexes are interpreted as presenting the signature of the host galaxy.

The relative distributions of the morphological indexes are shown in Figure 3. It is evident that the number of non-pointilike QSOs is small but by no means negligible. We found the least of non-pointlike quasars on the B plates and progressively more into the R and I plates, which is expected from the redder emission from the host galaxy than from the inner QSO sources of optical emission.

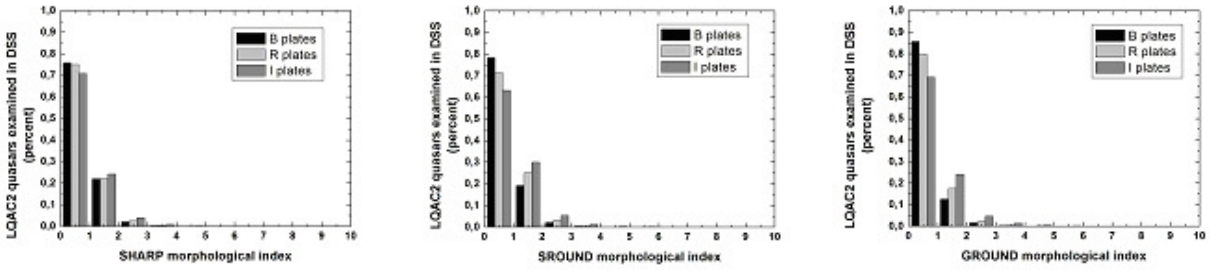

Fig. 3. From left to right the Sharp, Sround, and Ground morphological indexes, for the B, R, I plates from the DSS. Although in all cases most of the QSOs appear as pointlike sources, notice that the fraction of extended sources is non neglible, and the proportion increases from B to I, i.e., from the outshining bluer central central source to the redder host galaxy.

4 Variability

The intrinsic QSO position stability at the sub-mas level will be over important for the establishment of the GCRF. At this point, one should take into account that at the same time that QSOs are the ideal (or rather the only) choice for fiducial grid points in the establishment of a quasi-inertial celestial reference frame, as

prescribed by the ICRS/ICRF paradigm, they are the most energetic and violent, large scale structures in the Universe, active galactic nuclei powered by a super-massive black hole (SMBH). Therefore, there can be several effects that can affect precise photometric center determination of the quasars (see, e.g. Porcas 2009) for the case of chromatic AGN core positions). Additionally, the Gaia mission measurements are planned with to an unprecedent precision in photo-center position, which will allows us to investigate the astrometric stability of QSOs and the possible physical consequences. Always according to the standard model of AGNs, a QSO consists of a SMBH (10^7 to 10^{10} solar masses) surrounded by a X-ray and optical continuum emitting region, probably with an accretion disk geometry (see Sulentic et al. 2000), a broad line region (BLR) and a larger region that can be resolved in several nearby AGN, which usually is referred to as the narrow line region (NLR). These central regions are surrounded by a torodial structure of dust. The regions emit in different wavelength bands and are supposed to have different dimensions. Flux ratios observed in the different part of the QSO continuum are sensitive to substructure and geometries of the emitting regions. Due to accretion that occurs close to the SBMH, one can expect instabilities and consequently variations in brightness and spectral distribution of these objects (see, e.g., Shields et al. 2003; Popović et al. 2012a,b). There are several mechanisms which can cause variation (see Andrei et al. 2009a,b): instabilities in the accretion disc around the central black hole: supernova bursts; jet instabilities, and gravitational microlensing. On the other hand, the dusty torus is illuminated from the accretion disk and also re-emits and absorbs, and some variability can be expected in photo-center position due to different illumination of the torus. Recently, Taris et al. (2011) reported about the magnitude variations of quasars and the potentially correlated motions of their centroids, finding that in one QSO there is a correlation between the centroid motion and magnitude variation.

As discussed, one thus can expect an accretion disk emission. Its variation can be caused by an outburst from the central (compact) continuum source, but also the variation can be connected with some kind of perturbations in the accretion disk (see, e.g. Jovanović et al 2010; Popović et al. 2012a,b). In the GIQC the accretion disk and the torus dimensions are being used as variability indexes, in the sense of indicating which objects are apt to suffer a variation on their photocenter along the 5 years of Gaia mission, due to existence of an angularly extended geometry.

Popović et al. (2012a,b) elaborate this investigation of spectro-photocentric variability of quasars caused by changes in their inner structure. They consider perturbation in a relativistic accretion disk assumed to be around a SMBH in quasars; and changes in the pattern of radiation scattered by the dust particles in the surrounding torus, due to the variations in the accretion disk luminosity and dust sublimation radius. As a result it is derived how much these effects may contribute variability of photo-center, i.e. to quantify "noise" with goal to better characterize any resulting error on the position determination; as well as the estimation of the possibility to observe this effect during Gaia mission, and the group of quasars for which these effects may be dominant.

One can conclude that perturbations (or bright spots) in an accretion disk may bring offsets of the photo-center, and this effect will be resolved by Gaia observations. The best candidates are low-redshifted AGNs with massive black hole, which are in principle very bright objects. One can expect a maximal offset of the center (in the case bright spot located at disk-edge) order of a few mas. The photocenter offset can also be caused by changes in the torus structure due to different illumination of the torus, in the case when inclination of the torus is larger than 30deg. In this case, the maximal offset can be of several mas, therefore also detected by Gaia. Both types of photocenter offset can also appear connected. Causing smaller photometric variation, can also be listed variations in the BLR, in the NLR, and in the optical jet.

In principle, to avoid the possibility of the photocenter variation due to perturbations in accretion disk, or in the BLR, one may estimate the dimensions of the BLR and choose for the GCRF objects with small dimensions of the BLR. On the other hand, to avoid variations of the photocenter due to filaments in the torus, it is preferable to choose quasars where the torus is face on orientated. In short, QSOs with high variability are not good objects for construction of the GCRF. Nonetheless, if the optical variability, that is likely to be sensed by Gaia's typical sampling (about 1 month on average), can be linked to the size, if not the preferred direction, of the astrometric jitter, this can be modeled and accounted for. If this is so, the astrometric error budget is alleviated and some variable quasars can be brought back to the GCRF. Conversely, it is important to remark that Gaia astrometric measurements will be very useful for the investigation of the inner quasar structure and physical processes, especially in low redshif variable sources.

5 Conclusions

There are very few aspects of the Gaia program that are tagged as "mission critical", but for satellite, instrument, and data handling issues. This testifies of the length and breadth, and depth, of the observations along the five years of the mission. By the same token, there is no exaggeration to state that although the aspects of morphology and variability of quasars might impact on the realization of the astrometric reference frame, which is a central to the Gaia concept, the information that will be gathered on those aspects will have just as important an impact on the astrophysics of quasars.

In the case of variability is evident that a data base must be formed to keep record and to make sense of the departure from the norm, either regular or as fluctuations. But also in the case of morphology it is crucial to form a database, due to the line spread function assessment of the centroids which will be differently affected from pose to pose taken at different directions. Such data bases ought to be organized in a way to ease the evaluation object by object along the mission to account for and compensate the effects regarding a degradation of the precision of the quasar's astrometry.

Such databases might also play a role on bringing in or dispose of objects misclassified by the color loci fundamental recognition scheme. Although this will probably be an adequation percentually minor, it is a major facility for the astrophysical studies pos-mission. A natural, aggregative increment of the data base, observation by observation, with all the observational circumstances in hand, is clearly preferable than the massive task of building it from scratch afterwards the mission by mining the archives.

AHA thanks the PARSEC International Incoming Fellowship within the Marie Curie 7th European Community Framework Programme, the Visiting Professorship for Senior International Scientists of the Chinese Academy of Sciences, and the CNPq grant PQ-307126/2006-0. J.I.B.C. acknowledges CNPq financial support 477943/2007-1. D.N.S.N. thanks FAPERJ grant E-26/110.177/2009.

References

Andrei, A.H., Souchay, J., Zacharias, N., Smart, R.L., Vieira Martins, R., da Silva Neto, D.N., Camargo, J.I.B., Assafin, M., Barache, C. 2009a, A&A, 505, 385

Andrei, A.H., Bouquillon, S., Camargo, J.I.B., Penna, J.L., Taris, F., Souchay, J., Silva Neto, da D.N., Vieira Martins, R., Assafin, M. 2009b, *Proc. of the Journées 2008 Systemes de refrence spatio-temporels*, Observatoire de Paris, ed. M. Soffel and N. Capitaine, p. 199

Andrei, A.H., Gontier, A-.M., Barache, C., da Silva Neto, D.N., Taris, F., Bourda, G., LeCampion, J-.F., Souchay, J., Camargo, J.I.B., Pereira Osório, J.J., Assafin, M., Vieira Martins, R., Bouquillon, S., Anton, S. 2011, *Journées 2010 Systemes de reference spatio-temporels*, Observatoire de Paris, ed. N. Capitaine p. 125

Bastian, U. 2007, *GAIA-CA-SP-ARI-BAS-003-06*, Version 6.0.

Claeskens, J.-F., Smette, A., Vandenbulcke, L., Surdej, J. 2006, MNRAS, 367, 879

Falomo, R., Kotilainen, J., Treves, A. 2001, ApJ, 547, 124

Jovanović, P., Popović, L.Č ., Stalevski, M., Shapovalova, A.I. 2010, ApJ, 718, 168

Mignard, F. 2010, *The Gaia mission objectives, description, data processing*, ADA 6 - Sixth Conference on Astronomical Data Analysis, p. 10

Popović, L.Č., Shapovalova, A.I., Ilic, D., et al. 2012, A&A, 528, 130

Popović, L.Č., Jovanović, P., Stalevski, M., Anton, S., Andrei, A.H., Kovacevic, J., Baes, M. 2012, A&A, 538, 107

Porcas, R.W. 2009, A&A, 505, L1

Richards, G.T., Fan, X. Newberg, H.J., et al. 2002, ApJ, 123, 2945

Sakata, Y., Minezaki, T., Yoshii, Y., et al. 2010, ApJ, 711, 461

Schneider, D.P. et al. 2010, ApJ, 139, 2360

Shields, G. A., Gebhardt, K., Salviander, S., et al. 2003, ApJ, 583, 124

Souchay, J., Andrei, A.H., Barache, C., Bouquillon, S., Gontier, A.-M., Lambert, S.B., Le Poncin-Lafitte, C., Taris, F., Arias, E.F., Suchet, D., Baudin, M. 2012, A&A, 537, 995

Souchay, J., Andrei, A.H., Barache, C., Bouquillon, S., Gontier, A.-M., Lambert, S.B., Le Poncin-Lafitte, C., Taris, F., Arias, E.F., Suchet, D., Baudin, M. 2009, A&A, 494, 799

Sulentic, J. W., Marziani, P., Dultzin-Hacyan, D. 2000, ARA&A, 38, 521

Taris, F., Souchay, J., Andrei, A. H., Bernard, M., Salabert, M., Bouquillon, S., Anton, S., Lambert, S. B., Gontier, A.-M., Barache, C. 2011, A&A, 526, 25

SF2A 2012
S. Boissier, P. de Laverny, N. Nardetto, R. Samadi, D. Valls-Gabaud and H. Wozniak (eds)

CALIBRATION OF GAIA-RVS: FIRST WEEKS AROUND ECLIPTIC POLES

F. Crifo[1], L. Chemin[2], F. Mignard[3], G. Jasniewicz[4], C. Soubiran[2,], D. Katz[1,], P. Sartoretti[1,] and D. Hestroffer[5]

Abstract. At the beginning of the Gaia mission, it will be necessary to calibrate the 3 instruments, and to have data for performance check. A particular scanning mode will be used, allowing quick multiple observations over a small number of sources. This mode and the selection of corresponding sources are described.

Keywords: Stars: fundamental parameters; Techniques: radial velocities; Surveys: Gaia.

1 Introduction

During the first few weeks of the Gaia mission, a very particular mode of the scanning law will be implemented, allowing repeated scans of small areas around ecliptic poles (EPs). The aim is to observe at least four times per day a limited subset of stars in order to perform the early calibration of the three instruments on board of Gaia.

To meet this goal, it is important to have before launch a very good knowledge of these stars. For the RVS this means not only radial velocities, but also high-resolution spectra over the spectral range (847- 874 nm). As the satellite's detailed scanning parameters will not be known long in advance, all the bright stars within an area up to 2 degrees from either EP are presently under study. We present here the first selection of these objects, based on a realistic simulation of the scanning in EP-mode. The ground based procedure to collect the missing information is not identical in the NEP and SEP because of telescope availability.

2 Ecliptic Poles Scanning Law (EPSL)

The normal scanning law for Gaia allows the observation of the whole sky in 6 months, some areas being more observed than others.

At the beginning, a special mode will cause the areas around the ecliptic poles to be observed at each transit, i. e. twice every 6 hours, the density of the coverage decreasing with the distance to pole. A narrow band the width of which is the height of focal plane will be observed regularly, turning around the ecliptic poles.

Figure 1, taken from Voss & Bastian (2007), shows the progressive scanning of the sky near an ecliptic pole over 15 days. Presently about 1 to 2 months of EPSL scanning are foreseen. However the figure shows the scanning for astrometric and photometric instruments; the height of the RVS field is only 4/7 from it, in the upper half of the total field.

[1] GEPI (UMR 811 du CNRS; Université Paris 7, FRANCE), Observatoire de Paris, 92190 MEUDON, FRANCE
[2] Université Bordeaux 1, CNRS, LAB, F-33270 FLOIRAC, FRANCE
[3] OCA/Lagrange, UMR CNRS 7293, Observatory of the Côte d'Azur, Le Mont Gros, BP 4229, 06304 Nice Cedex 4, FRANCE
[4] LUPM UMR 5299 CNRS/UM2, Université Montpellier II, CC 72, 34095, Montpellier Cedex 05, FRANCE
[5] IMCCE, Observatoire de Paris, UPMC, CNRS UMR8028, 77 Av. Denfert-Rochereau, 75014, Paris, FRANCE

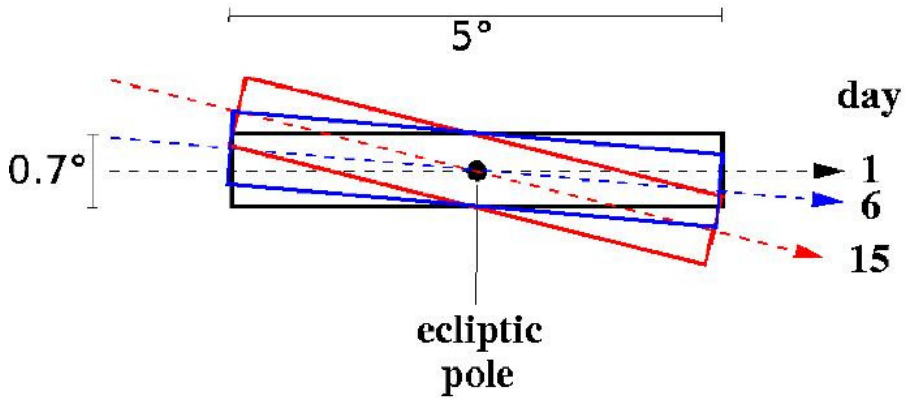

Fig. 1. Progressive coverage of the ecliptic pole area : black, blue and red zones are the sky areas scanned on days 1; 6 and 15, with a small rotation everyday. The common area with several transits is not a circle. (*from Voss & Bastian, 2007)*

3 Requirements on stars

The selection criteria were defined in several steps; and observations started before the last definition.

- These stars should be close enough to poles (1 degree at the beginning, extended later to 2 degrees), for enough transits during this rather short period; a high-resolution spectrum with good enough S/N (R∼40000 & S/N∼100) should be available for each one.

- The stars should be bright enough, but there are only very few bright stars around ecliptic poles. The limit was first set at V_t=11.5 (used for first NEP observations, together with a maximum polar distance of 1 degree); then brought down to 9 for SEP, together with the extension of the search radius to 2 degrees. The magnitude used is Vt, as the Tycho-2 catalogue is used.

- Unlike the RVS standards (see Crifo et al 2010; Soubiran et al 2012), double, multiple and variable stars are accepted, as well as early-type stars.

Figure 2 shows the final selection for each of the poles, vs Vt magnitude and polar distance. No object of the RVS standards list (see Crifo et al 2010) lays in the selection zones. The closest object of this list is indicated for each pole (heavy dark blue point).

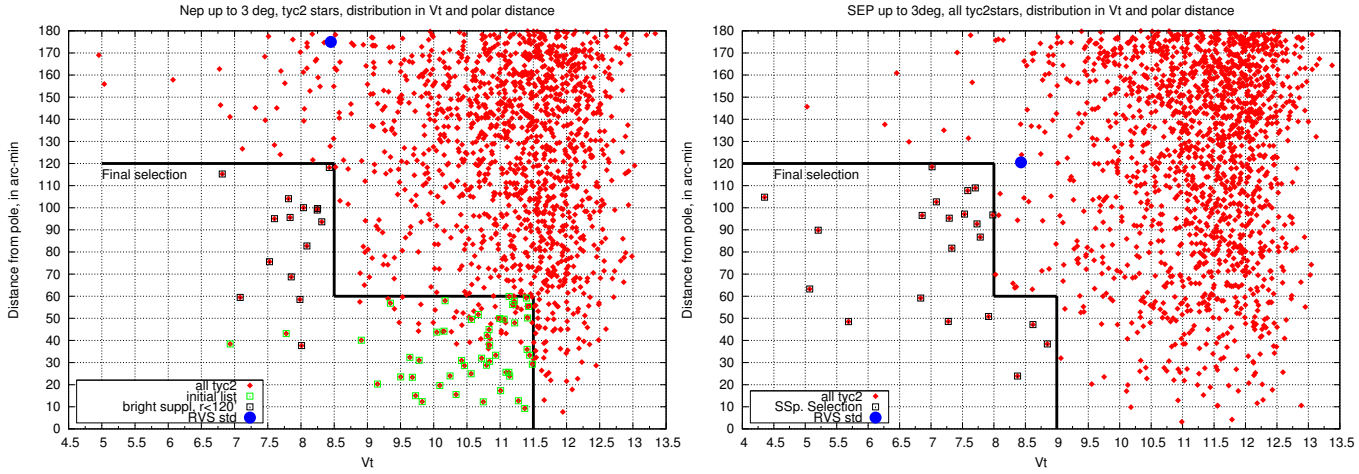

Fig. 2. Stars around each pole, magnitude/polar distance distribution. The objects kept are below the heavy dark lines. **Left:** NEP area. **Right:** SEP area.

NEP objects (63) are already observed at Pic du Midi with the Naraval spectrograph; SEP objects (21) should be observed at the end of 2012 with the RSA/ANU 2.3m echelle spectrograph at Siding Springs Observatory

(Australia).

4 Numerical simulations of scanning procedure

Unfortunately all the objects selected above will not be observed during the 1 to 2 months of EPSL, but only a fraction of them, the list of which depends on the launch date, as the sky will not be fully covered. Therefore the area covered at SEP by the RVS within these 1 to 2 months has been simulated with several possible launch dates, in order to evaluate the number of stars that might be really observed during this period.

Figure 3 show the areas scanned in 2 months by the RVS at SEP, for starts at October 1 and January 1. The selected objects are drawn in green. The non-selected objects are drawn in black. The stars within the RVS field for the considered 2 months are drawn in red.

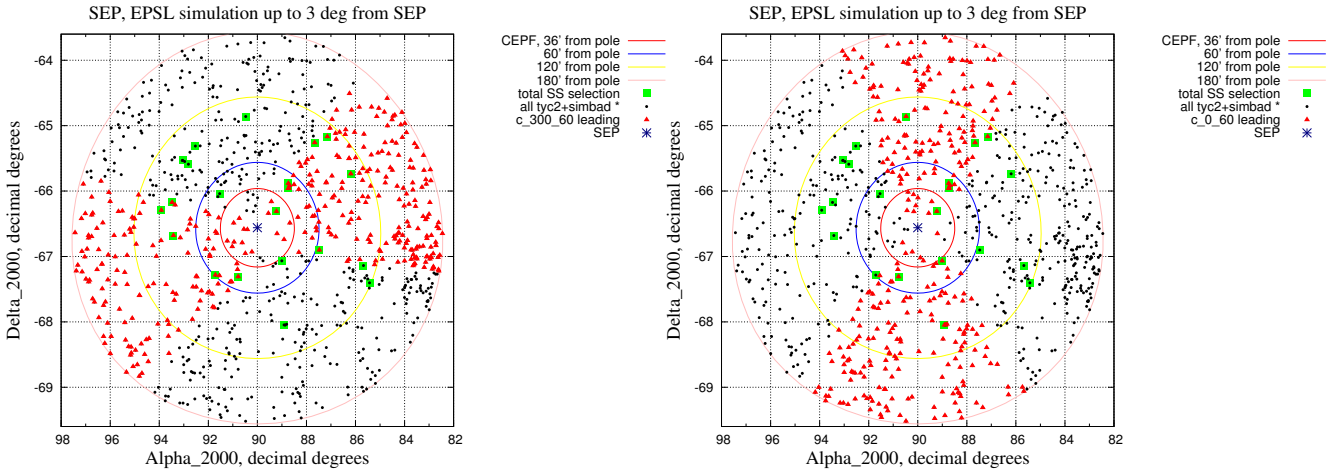

Fig. 3. Simulation of ESPL for 2 months at SEP. Green: the 21 reference objects; black: other objects (source: TYC2); red: objects in the RVS field during the 2 months. **Left:** Start on 1 october. **Right:** Start on 1 january.

At SEP, where there are only very few stars close to the pole, only 7 to 12 stars (of the 21) will be really observed: 1/3 to 1/2 of the total list.

5 Conclusion

The calibration of the RVS during the initial period will rely on a small number of stars, which must be really well-known. The requirement of high-resolution spectra available from the ground before launch over the RVS range is difficult to meet, particularly at SEP as only very few spectrographs are available.

Acknowledgements - The preparation of the GAIA-RVS is an extremely cooperative work. Many people, not listed within the already numerous above authors, have contributed to this small stone within the global building. The french PNPS and TBL staff provided the necessary financial and technical support for observations at NEP. We thank warmly Dr M. Bessell for supporting the SEP observations at Siding Springs Observatory.

References

Crifo, F.; Jasniewicz, G.; Soubiran, C.; Katz, D.; Siebert, A.; Veltz, L.; Udry, S., 2010, A&A., 524,10

Voss, B. & Bastian, U., 2007, Technical Note Gaia-C3-SP-ARI-BV-001-01, not publicly available

Soubiran, C.; Jasniewicz, G.; Chemin, L.; Crifo, F.; Udry,S.; Hestroffer, D.; Katz, D., 2012, this issue

SF2A 2012
S. Boissier, P. de Laverny, N. Nardetto, R. Samadi, D. Valls-Gabaud and H. Wozniak (eds)

THE CATALOGUE OF RADIAL VELOCITY STANDARD STARS FOR GAIA

C. Soubiran[1], G. Jasniewicz[2], L. Chemin[1], F. Crifo[3], S. Udry[4], D. Hestroffer[5] and D. Katz[3]

Abstract. The Radial Velocity Spectrograph (RVS) on board of Gaia needs to be calibrated using stable reference stars known in advance. A catalogue has being built for that purpose, including 1420 radial velocity standard star candidates selected on strict criteria in order to fulfill the Gaia-RVS requirements. We have undertaken a large programme of ground based observations in 2006 to monitor these stars and verify their stability which has to be better than 300 m s^{-1} over several years. We report 6536 radial velocity measurements for the 1420 stars. For a mean time baseline of 5.9 years, nearly 95% of the candidates (1394 stars) fulfill the stability criterion of 300 m s^{-1}. 80.4% have a stability better than 100 m s^{-1}. We compared our measurements to other sources.

Keywords: Catalogs, Radial Velocities, Stars: kinematics and dynamics

1 Introduction

The Radial Velocity Spectrograph (RVS) on board of Gaia will provide radial velocities (RV) of about 150 million stars up to 17^{th} magnitude with precisions ranging from 15 km s^{-1} at the faint end to 1 km s^{-1} or better at the bright end (Katz et al. 2004; Katz 2009). RV combined with astrometry will give access to the 6D phase space for kinematical studies. The RVS will also provide rotational velocities and atmospheric parameters for about 5 million stars up to 13^{th} magnitude and abundances for about 2 million stars up to 12^{th} magnitude. Such a large spectroscopic survey will have a tremendous impact on many science cases, such as the chemistry and dynamics of the Milky Way, the detection and characterisation of multiple systems and variable stars. The expected science yield from the RVS is described in Wilkinson et al. (2005).

The RVS has a resolution of 11500 and covers the spectral range 847-874 nm. It is an integral field spectrograph with no entrance slit and no on-board wavelength calibration source. The wavelength scale and RV zero-point will be derived from already known reference stars carefully selected for that purpose (Crifo et al. 2010). The RV standard stars used to calibrate the RVS have to be stable in radial velocity at the 300 m s^{-1} level, to be in adequation the 1 km s^{-1} precision expected from their future RVS measurements, with no drift until the end of the mission in 2019. To be qualified as a reference star, each candidate has to be observed at least twice before launch and another time during the mission in order to verify its long term stability. We describe the RV measurements available to date and the status of this new catalogue of RV standard stars in its pre-launch version.

2 RV measurements

The catalogue consists of 1420 standard star candidates whose criteria of selection are fully described in Crifo et al. (2010). The candidates have been selected in three catalogues : "Radial velocities of 889 late-type stars" (Nidever et al. 2002), "Radial velocities for 6691 K and M giants" (Famaey et al. 2005), "The Geneva-Copenhagen Survey of Solar neighbourhood" (Nordström et al. 2004), complemented by IAU standards. In the three RV

[1] LAB, CNRS UMR 5804, Univ. Bordeaux, F-33270, Floirac, France
[2] LUPM UMR 5299 CNRS/UM2, Université Montpellier II, CC 72, 34095 Montpellier Cedex 05, France
[3] GEPI, Observatoire de Paris, CNRS, Université Paris Diderot, 5 place Jules Janssen, 92190 Meudon, France
[4] Observatoire de Genève, Université de Genève, 51 Ch. des Maillettes, 1290 Sauverny, Switzerland
[5] IMCCE, Observatoire de Paris, UPMC, CNRS UMR8028, 77 Av. Denfert-Rochereau, 75014 Paris, France

catalogues, we selected the stars which have the best observational history in terms of number of consistent radial velocity measurements over several years. The observations of all these stars have been conducted on the echelle spectrographs ELODIE and SOPHIE on the 1.93 m telescope at Observatoire de Haute-Provence (OHP), NARVAL on the Télescope Bernard Lyot at Observatoire du Pic du Midi and CORALIE on the Euler-Swiss telescope at La Silla. We also used RV measurements retrieved from the public archives of SOPHIE and ELODIE at OHP (Moultaka et al. 2004), and of HARPS at the ESO Advanced Data Products database. Considering that the candidates have already a good observational history, our strategy is to have at least 2 measurements per star before launch, and then one more during Gaia operations. We have obtained nearly 100 observing nights since 2006 for this long term programme.

SOPHIE, CORALIE, ELODIE and HARPS have respectively resolving powers of R=$\lambda/\Delta\lambda$ ≈75 000, 50 000, 42 000 and 120 000. They all have similar automatic on-line data reduction softwares to derive the barycentric RV by cross-correlation of the spectra with a numerical mask (Baranne et al. 1996). The spectral type of the numerical mask is chosen to be the closest to the star observed. It can be G2, K5, M4, M5 for SOPHIE, G2, K5, M2 for HARPS and CORALIE, F0, K0 for ELODIE.

NARVAL has a resolving powers of R=$\lambda/\Delta\lambda$ ≈78 000. As this intrument has not been built for RV measurements, but for polarimetry, the on-line reduction software does not include the RV determination. We measured it by cross-correlating the observed spectra with the SOPHIE G2 mask. Our main interest in observing with NARVAL is that its spectral coverage includes the RVS range, 847-874 nm, allowing us to investigate the systematic difference occuring when measuring the RV in the full visible range and in that narrow NIR spectral range.

Table 1 gives the number of RV measurements available and the number of different stars oberved per instrument. Fig. 1 represents the distribution of the 1420 stars on the celestial sphere, with a color code indicating the number of measurements available.

To verify the stability of the stars, we need to combine their RV obtained with different instruments, having different zero-points. The zero-point is related to the instrument itself, its spectral range, resolution and calibration procedure and to the method used to measure the RV. In our case the same algorithm of cross-correlation with a numerical mask has been used which minimizes the offsets between instruments. We took care to have a sufficient number of stars observed in common with the different instruments to measure the offsets between them. We adopted the SOPHIE scale as our reference and we applied a correction to the measurements of the other instruments in order to put them in that common scale. Then for each star, we computed its mean RV, standard deviation, amplitude of the RV variation and time baseline. In this process each individual measurement is weighted according to its uncertainty.

Table 1. Number of RV measurements per instrument and number of stars

	SOPHIE	CORALIE	NARVAL	ELODIE	HARPS
number of RV meas.	2198	2421	209	1053	655
number of stars	727	775	157	292	113

Fig. 2 shows the histogram of variability of the 1420 candidates, measured by the maximum difference of individual measurements in the SOPHIE scale. We find that 94.7% of the stars have a stability better than 300 m s^{-1} which is the threshold defined for the calibration of the RVS instruments. The mean time baseline is 5.9 years. 80.4% of the stars have a stability better than 100 m s^{-1}.

3 Comparison with other catalogues

We have selected a fraction of the 1420 candidates in the catalog of Nidever et al. (2002), so we have a good intersection with it, namely 336 stars. Note that we selected only the stars from Nidever et al's table 1 which lists those with variations supposedly lower than 100 m s^{-1}. We also have a good intersection of 354 stars with the recent catalog by Chubak et al. (2012). We compare our RV in the SOPHIE scale with those of Nidever et al. and with those of Chubak et al. in Fig. 3 as a function of colour. We measure respectively offsets of 73 and 62 m s^{-1} with RMS of 40 and 98 m s^{-1} up to B−V= 1.3, after removing iteratively the 3σ outliers. The RMS of 40 m s^{-1} obtained when comparing Nidever et al. and us is an indication that the mean error of the two catalogs is lower than that value. It also confirms that the vast majority of these stars are stable. The outliers reveal the intrinsic variable stars as well as systematics due to methodology. In the range of M stars,

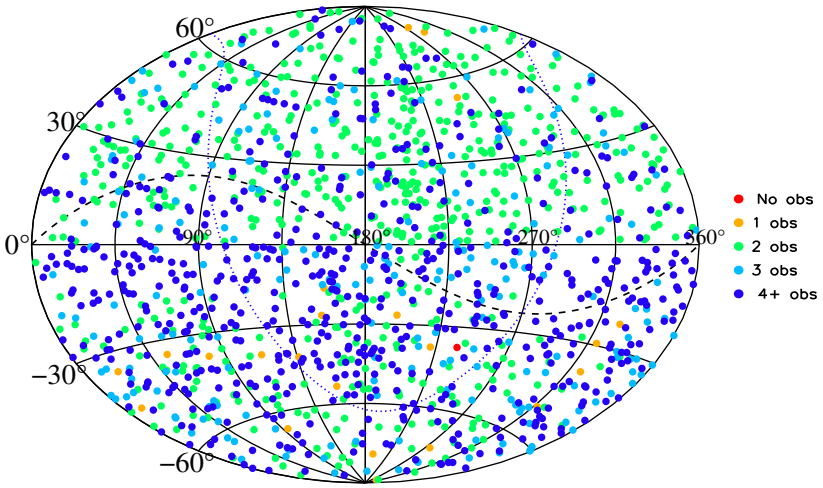

Fig. 1. Distribution of the 1420 candidate stars on the celestial sphere in equatorial coordinates, with a color code indicating the number of measurements available.

.

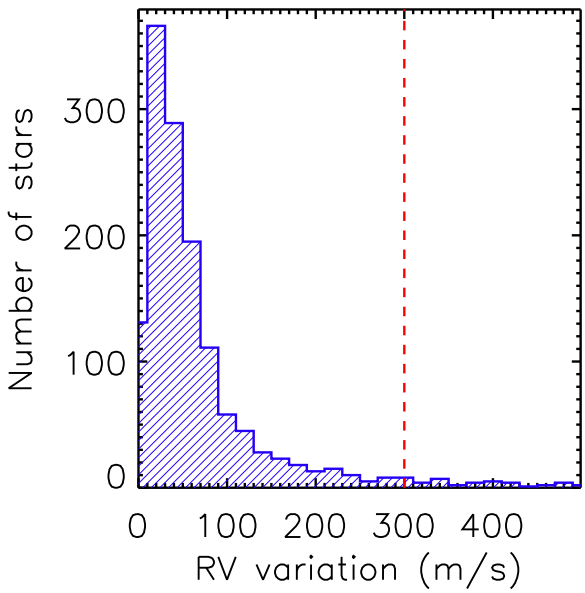

Fig. 2. Distribution of RV variations of the candidate standard stars having at least two RV measurements separated by 100 days or more. A dashed line shows the adopted 300 m s^{-1} stability threshold.

.

for B−V> 1.3, there is a clear systematic effect. We interpret this disagreement by the fact that both Nidever et al and Chubak et al use real templates for the CCF, while we use numerical masks computed from synthetic spectra.

4 Next steps

As explained in Lindegreen & Dravins (2003), there are many limitations to measuring accurate spectroscopic RV. The convective shift due to motions in the stellar atmosphere depends on stellar lines and Astrophysical

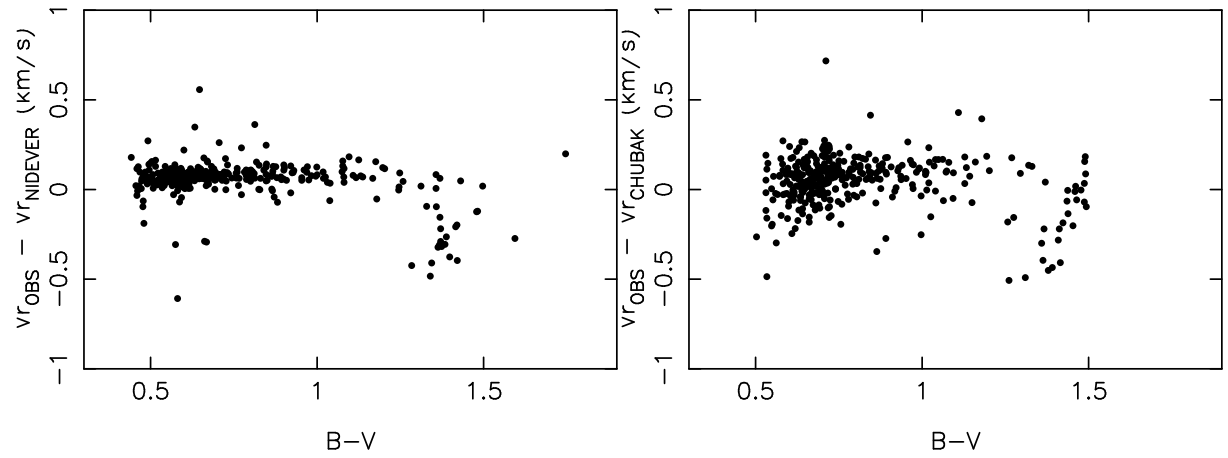

Fig. 3. RV difference between Nidever et al. (2002) and us (left panel) and between Chubak et al. (2012) and us (right panel) as a function of B-V colour.

.

Parameters (APs); it can reach +3 km s^{-1} for a CaII line in a F dwarf and −0.4 km s^{-1} for a FeI line in a K giant (Chiavassa et al. 2011). Other astrophysical effects may affect the RV of a star, such as rotation, activity, granulation as well as the presence of small-mass companions. Our on-going project is to estimate gravitational redshift (from APs) and compute convective shifts corrections in the RVS spectral interval from 3D hydrodynamical model atmospheres, in order to get the kinematic RV of each star. We will also define the RV zero-point of the catalog thanks to RV measurements and theoretical kinematic RV of asteroids. Finally our long-term plan is to re-observe the 1420 stars in 2016-2018 in order to check their long term stability.

5 Conclusion

We have presented the pre-launch version of the catalogue of RV standard stars for Gaia, assembled thanks to a long-term observing program started in 2006 on several spectrographs. Among the 1420 selected candidates, 1394 are found to be stable at the 300 m s^{-1} level, which make them suitable for the calibration of the RVS instrument. Their long-term stability will have to be confirmed with new ground-based observations during Gaia operations. We find a good agreement for FGK stars with two other catalogues, but systematic offsets for M stars.

We are indebted to AS-Gaia, PNPS and PNCG for their financial support of the observing campaigns and help in this project. We warmly thank Sergio Ilovaisky for helping us to retrieve relevant data in the OHP archive. Many thank also to Lionel Veltz who participated to the observations. We also thank the staff maintening the archives of ready-to-use spectra at OHP and ESO.

References

Baranne, A., Queloz, D., Mayor, M., et al. 1996, A&AS, 119, 373
Chiavassa, A., Bigot, L., Thévenin, F., et al. 2011, Journal of Physics Conference Series, 328, 012012
Chubak, C., Marcy, G., Fischer, D. A., et al. 2012, arXiv:1207.6212
Crifo F., Jasniewicz G., Soubiran C., et al., 2010, A&A, 524, A10
Famaey, B., Jorissen, A., Luri, X., et al., 2005, A& A, 430, 165
Katz, D. 2009, SF2A-2009: Proceedings of the Annual meeting of the French Society of Astronomy and Astrophysics, 57
Katz, D., Munari, U., Cropper, M., et al. 2004, MNRAS, 354, 1223
Lindegren, L. & Dravins, D. 2003, A&A, 401, 1185
Moultaka, J., Ilovaisky, S. A., Prugniel, P., & Soubiran, C. 2004,PASP, 116, 693
Nidever, D. L., Marcy, G. W., Butler, R. P., Fischer, D. A., & Vogt, S. S. 2002, ApJS, 141, 503
Nordström, B., Mayor, M., Andersen, J., et al., 2004, A&A, 418, 989
Wilkinson M., et al., 2005, MNRAS, 359, 1306

Session 03

Gaia: Galactic stellar populations

SF2A 2012
S. Boissier, P. de Laverny, N. Nardetto, R. Samadi, D. Valls-Gabaud and H. Wozniak (eds)

STELLAR POPULATIONS IN THE GALACTIC BULGE

C. Babusiaux[1]

Abstract. Until recently our knowledge of the Galactic Bulge stellar populations was based on the study of a few low extinction windows. Large photometric and spectroscopic surveys are now underway to map large areas of the bulge. They probe several complex structures which are still to be fully characterized as well as their links with the inner disc, the thick disc and the inner halo. I will review our current, rapidly increasing, knowledge of the bulge stellar populations and the new insight expected towards the Gaia era to disentangle the formation history of the Galactic inner regions.

Keywords: Galaxy: bulge, Galaxy: formation, Galaxy: abundances, Galaxy: kinematics and dynamics

1 Introduction

Two main scenarios, with very different signatures, have been invoked for bulge formation. The first scenario corresponds to the gravitational collapse of a primordial gas (Eggen et al. 1962; Matteucci & Brocato 1990) and/or to the hierarchical merging of subclumps (Noguchi 1999; Aguerri et al. 2001; Bournaud et al. 2009). In those cases the bulge formed before the disc and the star formation time-scale was short. The resulting stars are old and show enhancements of α elements relative to iron which are characteristic of classical bulges. The second scenario is secular evolution of the disc through a bar forming a pseudo-bulge (Combes et al. 1990; Norman et al. 1996; Kormendy & Kennicutt 2004; Athanassoula 2005). After the bar formation it heats in the vertical direction, giving rise to the typical boxy/peanut aspect.

Observations of the bulge suffer from the extinction, which varies on very small spatial scales, the crowding, and the superposition of different structures along the line of sight. However large scale surveys of the bulge are now at reach of the current instrumentation and our knowledge of this complex region is growing very fast. We will see here the different characteristics of the bulge as traced by individual stars in our Galaxy and how they relate to the different bulge formation scenarios.

2 Structure

It is now well established that the Milky Way is a barred Galaxy. Evidence for the presence of a triaxial structure in the inner Galaxy came first from gas kinematics, then from infrared luminosity distribution, star counts, red clump stars distance indicators and microlensing optical depth.

But a single structure, with a given semi-major axis and position angle, doesn't seem to reproduce all the observations at the same time. The main triaxial structure has a position angle with respect to the Sun-Galactic enter direction of about 20 ° and a semi-major axis around 2.5 kpc. But a thin long bar has been detected within $10\ ^\circ < l < 27\ ^\circ$ with an angle of about 45 ° and a semi-major axis of ~ 4 kpc (e.g. Cabrera-Lavers et al. 2008). The main bar dominates within $|l| < 10\ ^\circ$ with an angle $\sim 20\ ^\circ$ but flattens in the inner regions $|l| < 4\ ^\circ$ (Nishiyama et al. 2005; Gonzalez et al. 2011a). An inner bar is also suggested in the central molecular zone, within $|l| < 1.5\ ^\circ$ (Alard 2001; Sawada et al. 2004).

These observations have been found to be well reproduced with a single structure with N-body simulations by Martinez-Valpuesta & Gerhard (2011) and Gerhard & Martinez-Valpuesta (2012). In those simulations a stellar bar evolved from the disc, and the boxy bulge originated from it through secular evolution and buckling instability. They find that the long bar corresponds in fact to the leading ends of the bar in interaction with the

[1] GEPI, Observatoire de Paris, CNRS, Université Paris Diderot ; 5 Place Jules Janssen 92190 Meudon, France

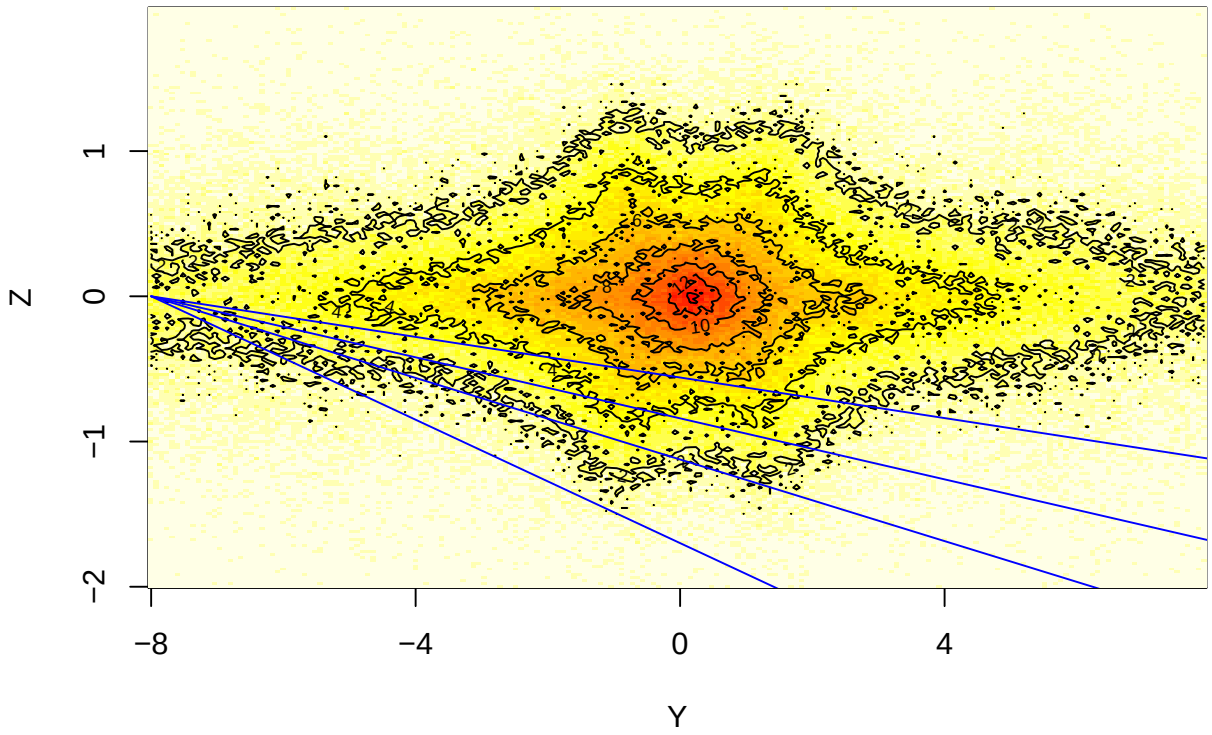

Fig. 1. Density profile of the disc particles of the Fux 1999 model projected along $|X| < 1$ kpc (square root density scale). The blue straight lines represent the lines of sight along the bulge minor axis b= −4, −6, −8, −12 °. It illustrates the dominant X-shaped structure at 5 ° $< |b| <$ 10 °.

adjacent spiral arm heads (see also Romero-Gómez et al. 2011). The change in the slope of the model longitude profiles in the inner few degrees is caused by a transition from highly elongated to more nearly axisymmetric isodensity contours in the inner boxy bulge. We also show that the nuclear star count map derived from this simulation snapshot displays a longitudinal asymmetry which could correspond to the suggested secondary nuclear bar.

Looking now at the vertical structure of the bulge, McWilliam & Zoccali (2010) and Nataf et al. (2010) found two red clump populations coexisting at latitudes $|b| > 5$ ° in the 2MASS and OGLE colour-magnitude diagrams, corresponding in fact at an X-shaped structure (Saito et al. 2011). This vertical structure is also well reproduced in N-body models such as the one of Fux (1999) (see Fig. 1) or Li & Shen (2012).

The main structures of the inner galaxy are therefore now well understood as being shaped by secular evolution. As we will see in the next sections, the other characteristics of the inner galaxy are not pointing towards this single formation scenario. Those lead Robin et al. (2012) to improve the modelling of the 2MASS star counts with the Besançon model by fitting both a triaxial boxy shape (with a slight flare to reproduce the double clump) plus a longer and thicker ellipsoid. They note that inner asymmetry is not fitted in this model, nor the long thin bar.

3 Metallicity

A metallicity gradient has been detected along the bulge minor axis (Frogel et al. 1999; Zoccali et al. 2008). In the inner regions ($|b| < 4$ °) no significant gradient in metallicity has been found (Ramírez et al. 2000; Rich et al. 2007).

Hill et al. (2011) show that the metallicity distribution in Baade's Window (l = 1 °, b = −4 °) can be decomposed in two populations of roughly equal sizes: a metal-poor component centred on [Fe/H] = −0.3 dex with a large dispersion and a narrow metal-rich component centred on [Fe/H] = +0.3 dex. The same bimodal distribution is seen in the sample of 26 microlensed bulge dwarfs of Bensby et al. (2011). Their peaks are at [Fe/H] = −0.6 and +0.3 dex. The discrepancy in the metal-poor peak metallicity should be solved by larger homogeneous spectroscopic samples.

Therefore there seems to be a mix of populations in the bulge, the metal rich population fading while moving away from the plane, while those two populations are mixed close to the plane.

The two red clumps detected in photometry at $|b| > 5$ ° has been shown recently to share the same metallicity (De Propris et al. 2011; Ness et al. 2012). Only the metal-rich population of the bulge show this split in the red clump, implying that the disc from which the boxy bulge grew had relatively few stars with [Fe/H] < −0.5 dex (Ness et al. 2012).

4 Kinematics

Babusiaux et al. (2010) show that in Baade's Window the metal rich population presents a vertex deviation typical of bar-like kinematics (confirming the results of Soto et al. (2007)), while the metal poor population shows isotropic kinematics, close to what can be expected from a classical bulge or a thick disc component. They also show that the radial velocity dispersion change with metallicity. The metal poor population shows the same velocity dispersion along the bulge minor axis, while the metal rich population goes from bar-like high velocity dispersion to disc-like low velocity dispersion while moving away from the galactic plane. This corresponds to the kinematic behaviour predicted by the N-body model of Fux (1999) which contains both a disc, which evolved to form a bar, and a spheroid component. However the spheroid component of the Fux (1999) model has a too high velocity dispersion compared to the observations. The metal poor component observed could correspond to a smaller mass spheroid or a thick disc component.

The BRAVA (Bulge Radial Velocity Assay) survey (Kunder et al. 2012), observing at $b = -4, -6, -8$ °, shows that the bulge stars follow a cylindrical rotation. Their radial velocity distribution is very well reproduced by an N-body model of a pure-disc Galaxy by Shen et al. (2010), concluding that any classical bulge contribution cannot be larger than $\sim 8\%$ of the disc mass. However Saha et al. (2012) indicate that the formation of a rapidly rotating bar can spin up a pre-existing low-mass classical bulge, leading the classical bulge to develop also cylindrical rotation.

Looking at latitudes $b > 12$ °, Ibata & Gilmore (1995) found that the outer bulge may be kinematically linked to the dissipated core of the halo.

5 Abundances

Bulge stars have been shown to be enhanced in α elements (McWilliam & Rich 1994; Zoccali et al. 2006; Fulbright et al. 2007; Lecureur et al. 2007), suggesting a short formation time-scale. Indeed, in a regime of a very fast star formation, most of the stars form with high [α/Fe] ratios, due to the predominant pollution by core-collapse supernovae. In slower star formation scenarios, Type Ia supernovae have the time to contribute, decreasing the [α/Fe] ratios.

However the metal-rich population of the bulge is not enhanced in α elements (Hill et al. 2011). Gonzalez et al. (2011b) show that those metal rich stars, showing low [α/Fe] ratios at b= −4 °, disappear at higher Galactic latitudes, in agreement with the observed metallicity gradient in the bulge. They also show that metal-poor stars ([Fe/H] < −0.2) show a remarkable homogeneity along the bulge minor axis, in agreement with the homogeneity observed in their kinematics.

Several recent studies, based on homogeneous data, also highlight the similarity in term of average metallicity and elemental trends between the metal-poor bulge sample and the thick disc (Meléndez et al. 2008; Ryde et al. 2010; Alves-Brito et al. 2010; Bensby et al. 2011). Johnson et al. (2012) also points out similarities at b = −8 ° between the most metal-poor bulge and halo abundances.

6 Ages

The study of bulge colour magnitude diagrams indicate that the bulge is mainly old (> 10 Gyr) (Zoccali et al. 2003; Clarkson et al. 2008). However with infrared photometry van Loon et al. (2003) detected, in addition

to the dominant old population, an intermediate age one plus young stars in the inner bulge. Groenewegen & Blommaert (2005) found Mira stars with ages 1−3 Gyr up to b = −6 °. The study of the density distribution of the large-amplitude and long-period variables (Mira variables or OH/IR stars) implies that they trace the bar structure of the Galactic bulge (Kouzuma & Yamaoka 2009). This association of the intermediate age population to the boxy bulge component could explain the fact that studies based on those tracers lead to larger bar angle (∼ 40 °, e.g. Sevenster et al. 1999; Groenewegen & Blommaert 2005) than studies based on older tracers such as red clump stars (∼ 20 °, e.g. Stanek et al. 1994; Babusiaux & Gilmore 2005; Nishiyama et al. 2005), the old tracers probing the mix of the metal poor component and of the boxy bulge structures. Considering the fading of the boxy bulge away from the plane shown previously, one would also expect that this intermediate age population represents only a small fraction of the colour-magnitude diagram of Zoccali et al. (2003) at b = −6 °.

However Clarkson et al. (2008) obtained a proper motion decontaminated colour magnitude diagram with a well defined old turn-off in an inner field (l = 1 ° , b = −3 °) where both the metal poor and the metal rich components would be expected to be well mixed. The analysis of the blue straggler stars in this field lead Clarkson et al. (2011) to conclude that the genuinely young (< 5 Gyr) population in the bulge must be lower than 3%.

Bensby et al. (2011) find that the metal-poor microlensed bulge dwarf stars are predominantly old with ages greater than 10 Gyr, while the metal-rich bulge dwarf stars show a wide range of ages, from 3-4 Gyr to 12 Gyr, with an average around 8 Gyr. The results of Bensby et al. (2011) and the previous discussions about the boxy bulge formation seem to be in conflict with the results of Clarkson et al. (2008). To reconcile them, Nataf & Gould (2012) suggest an elevated helium enrichment for the bulge relative to that assumed by standard isochrones. That would imply that photometric determinations are too old and spectroscopic determinations are too young.

7 Conclusions

The bulge shows a complex structure both along the major axis and the minor axis. Although the main shape of the bulge seems to be driven by secular evolution, the other characteristics of the bulge points toward a mix of stellar populations in the bulge. The X-shaped boxy bulge seem to correspond to the metal-rich component with solar abundances and bar-like kinematics. A metal-poor component enriched in alpha elements is present, corresponding to an older population with a short formation time-scale. This mixed formation scenario has been observed in external galaxies (e.g. Prugniel et al. 2001; Peletier et al. 2007; Erwin 2008), as well as predicted by several models (e.g. Samland & Gerhard 2003; Nakasato & Nomoto 2003; Athanassoula 2005; Rahimi et al. 2010; Tsujimoto & Bekki 2012). More observations are currently underway to quantify those different populations, their links both in abundances and kinematics, and the links between those populations as seen in the bulge and the other populations of the Milky Way: the inner thin disc, the thick disc and the inner halo. In the near-infrared, the photometric VISTA VVV survey has made recently its first release (Saito et al. 2011). In the optical, Skymapper (Keller et al. 2007) is underway. In spectroscopy, APOGEE in the near-infrared (Allende Prieto et al. 2008) and the Gaia-ESO Survey in the optical (Gilmore et al. 2012) are also underway. A key piece will of course be added with Gaia, observing 20 million bulge stars (Robin et al. 2005), providing parallaxes and proper motion along all the lines of sight towards the bulge and observing red clump giants in the bulge in low extinction regions with an accuracy on the parallax better than 30%, on the proper motions better than 1 km s^{-1} and on the radial velocities around 15 km s^{-1} (Babusiaux 2011).

References

Aguerri, J. A. L., Balcells, M., & Peletier, R. F. 2001, A&A, 367, 428

Alard, C. 2001, A&A, 379, L44

Allende Prieto, C., Majewski, S. R., Schiavon, R., et al. 2008, Astronomische Nachrichten, 329, 1018

Alves-Brito, A., Meléndez, J., Asplund, M., Ramírez, I., & Yong, D. 2010, A&A, 513, A35+

Athanassoula, E. 2005, MNRAS, 358, 1477

Babusiaux, C. 2011, in EAS Publications Series, Vol. 45, EAS Publications Series, 313–318

Babusiaux, C. & Gilmore, G. 2005, MNRAS, 358, 1309

Babusiaux, C., Gomez, A., Hill, V., et al. 2010, ArXiv e-prints, 1005.3919

Bensby, T., Adén, D., Meléndez, J., et al. 2011, A&A, 533, A134

Bournaud, F., Elmegreen, B. G., & Martig, M. 2009, ApJ, 707, L1
Cabrera-Lavers, A., González-Fernández, C., Garzón, F., Hammersley, P. L., & López-Corredoira, M. 2008, A&A, 491, 781
Clarkson, W., Sahu, K., Anderson, J., et al. 2008, ApJ, 684, 1110
Clarkson, W. I., Sahu, K. C., Anderson, J., et al. 2011, ApJ, 735, 37
Combes, F., Debbasch, F., Friedli, D., & Pfenniger, D. 1990, A&A, 233, 82
De Propris, R., Rich, R. M., Kunder, A., et al. 2011, ApJ, 732, L36
Eggen, O. J., Lynden-Bell, D., & Sandage, A. R. 1962, ApJ, 136, 748
Erwin, P. 2008, in IAU Symposium, Vol. 245, IAU Symposium, ed. M. Bureau, E. Athanassoula, & B. Barbuy, 113–116
Frogel, J. A., Tiede, G. P., & Kuchinski, L. E. 1999, AJ, 117, 2296
Fulbright, J. P., McWilliam, A., & Rich, R. M. 2007, ApJ, 661, 1152
Fux, R. 1999, A&A, 345, 787
Gerhard, O. & Martinez-Valpuesta, I. 2012, ApJ, 744, L8
Gilmore, G., Randich, S., Asplund, M., et al. 2012, The Messenger, 147, 25
Gonzalez, O. A., Rejkuba, M., Minniti, D., et al. 2011a, A&A, 534, L14
Gonzalez, O. A., Rejkuba, M., Zoccali, M., et al. 2011b, A&A, 530, A54
Groenewegen, M. A. T. & Blommaert, J. A. D. L. 2005, A&A, 443, 143
Hill, V., Lecureur, A., Gómez, A., et al. 2011, A&A, 534, A80
Ibata, R. A. & Gilmore, G. F. 1995, MNRAS, 275, 605
Johnson, C. I., Rich, R. M., Kobayashi, C., & Fulbright, J. P. 2012, ApJ, 749, 175
Keller, S. C., Schmidt, B. P., Bessell, M. S., et al. 2007, PASA, 24, 1
Kormendy, J. & Kennicutt, Jr., R. C. 2004, ARA&A, 42, 603
Kouzuma, S. & Yamaoka, H. 2009, AJ, 138, 1508
Kunder, A., Koch, A., Rich, R. M., et al. 2012, AJ, 143, 57
Lecureur, A., Hill, V., Zoccali, M., et al. 2007, A&A, 465, 799
Li, Z.-Y. & Shen, J. 2012, ApJ, 757, L7
Martinez-Valpuesta, I. & Gerhard, O. 2011, ApJ, 734, L20
Matteucci, F. & Brocato, E. 1990, ApJ, 365, 539
McWilliam, A. & Rich, R. M. 1994, ApJS, 91, 749
McWilliam, A. & Zoccali, M. 2010, ApJ, 724, 1491
Meléndez, J., Asplund, M., Alves-Brito, A., et al. 2008, A&A, 484, L21
Nakasato, N. & Nomoto, K. 2003, ApJ, 588, 842
Nataf, D. M. & Gould, A. P. 2012, ApJ, 751, L39
Nataf, D. M., Udalski, A., Gould, A., Fouqué, P., & Stanek, K. Z. 2010, ApJ, 721, L28
Ness, M., Freeman, K., Athanassoula, E., et al. 2012, ApJ, 756, 22
Nishiyama, S., Nagata, T., Baba, D., et al. 2005, ApJ, 621, L105
Noguchi, M. 1999, ApJ, 514, 77
Norman, C. A., Sellwood, J. A., & Hasan, H. 1996, ApJ, 462, 114
Peletier, R. F., Falcón-Barroso, J., Bacon, R., et al. 2007, MNRAS, 379, 445
Prugniel, P., Maubon, G., & Simien, F. 2001, A&A, 366, 68
Rahimi, A., Kawata, D., Brook, C. B., & Gibson, B. K. 2010, MNRAS, 401, 1826
Ramírez, S. V., Stephens, A. W., Frogel, J. A., & DePoy, D. L. 2000, AJ, 120, 833
Rich, R. M., Origlia, L., & Valenti, E. 2007, ApJ, 665, L119
Robin, A. C., Marshall, D. J., Schultheis, M., & Reylé, C. 2012, A&A, 538, A106
Robin, A. C., Reylé, C., Picaud, S., & Schultheis, M. 2005, A&A, 430, 129
Romero-Gómez, M., Athanassoula, E., Antoja, T., & Figueras, F. 2011, MNRAS, 418, 1176
Ryde, N., Gustafsson, B., Edvardsson, B., et al. 2010, A&A, 509, A20
Saha, K., Martinez-Valpuesta, I., & Gerhard, O. 2012, MNRAS, 421, 333
Saito, R. K., Zoccali, M., McWilliam, A., et al. 2011, AJ, 142, 76
Samland, M. & Gerhard, O. E. 2003, A&A, 399, 961
Sawada, T., Hasegawa, T., Handa, T., & Cohen, R. J. 2004, MNRAS, 349, 1167
Sevenster, M., Saha, P., Valls-Gabaud, D., & Fux, R. 1999, MNRAS, 307, 584

Shen, J., Rich, R. M., Kormendy, J., et al. 2010, ApJ, 720, L72
Soto, M., Rich, R. M., & Kuijken, K. 2007, ApJ, 665, L31
Stanek, K. Z., Mateo, M., Udalski, A., et al. 1994, ApJ, 429, L73
Tsujimoto, T. & Bekki, K. 2012, ApJ, 747, 125
van Loon, J. T., Gilmore, G. F., Omont, A., et al. 2003, MNRAS, 338, 857
Zoccali, M., Hill, V., Lecureur, A., et al. 2008, A&A, 486, 177
Zoccali, M., Lecureur, A., Barbuy, B., et al. 2006, A&A, 457, L1
Zoccali, M., Renzini, A., Ortolani, S., et al. 2003, A&A, 399, 931

SF2A 2012
S. Boissier, P. de Laverny, N. Nardetto, R. Samadi, D. Valls-Gabaud and H. Wozniak (eds)

AGE DATING LARGE SAMPLES OF STARS: THE GAIA CONTEXT

C. Guédé[1], Y. Lebreton[1,2], C. Babusiaux[1] and M. Haywood[1]

Abstract. The Gaia ESA mission will measure stellar parameters for 1 billion of stars in the Galaxy. We aim at dating the stars and we use a method based on their observed position in the HR diagram and the evolutionary tracks. The method is based on a Bayesian estimation. We test the precision of the program with different simulated catalogs of Gaia stars at various distances and for a different observational error on the metallicity. The goal of this study is to prepare the tools that will be used to age-date stars after the Gaia mission.

Keywords: Stars: fundamental parameters, Methods: statistical, Stars: Hertzsprung-Russell and C-M diagrams

1 Introduction

The Gaia ESA mission will observe 1 billion of stars in photometry, spectroscopy and astrometry (Perryman et al. 2001). It will be launched in 2013. The age of these stars has to be estimated to obtain information about the Galaxy such as the stellar formation history and age metallicity relation which permit to understand its formation and evolution (Freeman 1993). Also to characterize the exoplanets it is necessary to date their host stars (Havel et al. 2011).
There are several methods to determine the age of stars described by Soderblom (2010). To determine the age of stars of the Gaia ESA mission it is necessary to use a method that applies to a large sample of stars. For this purpose we use a method based on isochrones placement (Edvardsson et al. 1993). A star is plotted in the Hetzprung Russell Diagram (hereafter HRD) and the isochrone that adjusts its position is found. The most probable age corresponds to the isochrone that is closest to the star. In some regions of the HRD, the isochrones have a complex shape and stars can be adjusted by many isochrones. To select the most probable age it is useful to use a method based on the Bayesian estimation (Pont & Eyer 2004) to which we focus on the method of da Silva et al. (2006). We bring modifications on the choice of the *a priori* and on the stellar models. In the age dating we use the evolutionary tracks rather than the isochrones to reduce the number of interpolations and therefore the numerical errors.
We build a Gaia simulated catalog to evaluate the consistency between the simulated "true" age and the determined age. The catalog is constructed with the Basti evolutionary tracks and the Gaia specifications. We create several catalogs at different distances to test the precision of the determination of the ages as a function of the distance. The complementary spectroscopic observations will permit to obtain the metallicity with better observational errors. We study the effect on age determination of the observational errors on the metallicity for stars at different distances. We describe the Bayesian estimation method in Section 2 and the Gaia simulated catalogs in Section 3. We study the determination of ages as a function of the distance in Section 4 and the effect of observational error on the metallicity in the Section 5.

2 The Bayesian estimation

To date the stars we use three observables: the absolute magnitude $M_{\rm v}$, the effective temperature $T_{\rm eff}$ and the metallicity [Fe/H]. The Bayesian estimation allows to determine the most probable age with the *a posteriori*

[1] GEPI UMR 8111, Observatoire de Paris-Meudon , France
[2] IPR, Université de Rennes 1, France

probability density function $f(\tau, [\mathrm{Fe/H}], m)$ which depends on the point of the evolutionary tracks with an age τ, a metallicity [Fe/H] and a mass m. It is defined by $f(\tau, [\mathrm{Fe/H}], m) \propto f_0(\tau, [\mathrm{Fe/H}], m) L(\tau, [\mathrm{Fe/H}], m)$, where $f_0(\tau, [\mathrm{Fe/H}], m)$ is the *a priori* density function that represents the stellar and galactic properties. The likelihood $L(\tau, [\mathrm{Fe/H}], m)$ is related to the distance between the models and the star. There are several adaptations of the Bayesian estimation for the determination of the ages. Here we have chosen to use the method based on da Silva et al. (2006, hereafter DG06) who define the *a posteriori* probability density function $f(\tau_\mathrm{k})$ by:

$$f(\tau_\mathrm{k}) = \sum_\mathrm{i} p(\tau_\mathrm{k}) \frac{1}{\sigma_{[\mathrm{Fe/H}]}\sqrt{2\pi}} \exp\left[-\frac{1}{2}\left(\frac{[\mathrm{Fe/H}]_\mathrm{i} - [\mathrm{Fe/H}]^\mathrm{obs}}{\sigma_{[\mathrm{Fe/H}]}}\right)^2\right], \quad (2.1)$$

$$\text{with } p(\tau_\mathrm{k}) = \sum_\mathrm{j} \int_{m^1_\mathrm{ijk}}^{m^2_\mathrm{ijk}} \xi(m_\mathrm{ijk}) dm_\mathrm{ijk} \psi(\tau_\mathrm{k}) \exp\left[-\frac{(M_{\mathrm{v,ijk}} - M_\mathrm{v}^\mathrm{obs})^2}{\sigma^2_{M_\mathrm{v}}} - \frac{(\log T_{\mathrm{eff,ijk}} - \log T_\mathrm{eff}^\mathrm{obs})^2}{\sigma^2_{\log T_\mathrm{eff}}}\right]. \quad (2.2)$$

Where the index ijk correspond to the point of the evolutionary track with the metallicity i, the initial mass j and the age k. $\xi(m_\mathrm{ijk})$ is the initial mass function (IMF) and $\psi(\tau_\mathrm{k})$ is the stellar formation rate (SFR). σ_{M_v}, $\sigma_{\log T_\mathrm{eff}}$ and $\sigma_{[\mathrm{Fe/H}]}$ are the observational errors on the stellar parameters.
We bring several modifications to the method, in particular on the choice of the *a priori*. DG06 do not take into account any SFR. We adopt one because we have chosen not to take into account the stars that have an age greater than the Universe age. Indeed the evolutionary tracks have ages comprises between 0 and 22 Gyr for more massive stars. The SFR is defined by

$$\psi(\tau) = \begin{cases} 1 & \text{for } 0 \leq \tau \leq \ 14 \text{ Gyr} \ , \\ 0 & \text{elsewhere.} \end{cases} \quad (2.3)$$

We have chosen to use the stellar models of Basti (Pietrinferni et al. 2004). We use the evolutionary tracks rather than the isochrones to reduce the number of interpolations. Since DG06 do not specify the IMF, we have chosen to use the one of Kroupa (2002).

3 Gaia simulated catalogs

We create a simulated catalog of 10 000 stars to compare the simulated "true" age and the determined age. The simulated catalog is based on the Gaia mission specifications (Perryman et al. 2001). For each simulated star we select three parameters in the evolutionary tracks of Basti (Pietrinferni et al. 2004): metallicity, mass and age. The metallicity is selected randomly in the MDF. We defined the MDF with the 16 882 stars of the solar neighborhood of the Geneva Copenhagen Survey (GCS) of Casagrande et al. (2011). The MDF is defined by

$$\phi([\mathrm{Fe/H}]) = \frac{1}{\sigma\sqrt{2\pi}} \exp\left(-\frac{([\mathrm{Fe/H}] - \mu)^2}{2\sigma^2}\right), \quad (3.1)$$

with $\mu = -0.043$ and $\sigma = 0.19$. We take randomly the mass in the IMF of Kroupa (2002) and the age is taken randomly in the SFR (Equation 2.3). The three parameters permit to select a point of the evolutionary tracks. To fulfill the Gaia mission specifications we keep the point if the magnitude G is greater than 6, beyond this limit the star is too bright to be observable by Gaia.
To test the effect on age of the distance d of stars we create several simulated catalogs for different distances. The selection of the distance is realized thanks to the selection on the precision of the parallax. Indeed the point is kept if it has $\frac{\sigma\pi}{\pi} < 10$ %. The Gaia specification (ESA's website[i]) gives $\sigma_\pi = (9.3 + 658.1z + 4.568z^2)^{1/2} \times [0.986 + (1 - 0.986)(V - I)]$ where $z = \mathrm{MAX}[10^{0.4(12-15)}, 10^{0.4(G-15)}]$. G is determined with the transformation of Jordi et al. (2010). We create several catalogs such as 46 pc $\leq$ d $\leq$ 12 kpc. The Gaia simulated catalogs obtained for d = 46 pc, d = 1kpc and d = 10 kpc are represented in Fig. 1.
We define an observation error for each stellar parameters based on the Gaia mission (Bailer-Jones (2010) and ESA's website[i]). We assume an observational error on the effective temperature equal to 0.3% for $G \leq 15$ and increasing linearly to 4% at $G = 20$. We assume that the observational error on the metallicity is constant and equal to 0.3 dex. The error on the absolute magnitude is based on the magnitude distance relation. σ_{M_v}

[i] www.rssd.esa.int/index.php?project=GAIA&page=Science_Performance#table2

depends on the observational errors on the apparent magnitude σ_{m_v}, on the distance σ_d and on the extinction σ_{A_v}. We assume that σ_{m_V}=σ_{m_G} and the ESA's website[i] gives $\sigma_{m_G} = 10^{-3}(0.02076z^2 + 2.7224z + 0.004352)^{1/2}$. σ_{A_v} is equal to 10% of the extinction A_v (Bailer-Jones 2010).

4 Effect of the distance of the stars

We compare the simulated "true" age and the determined age for the Gaia simulated catalogs at different distances. For this purpose we define the relative difference between the two ages such as $\sigma_\tau/\tau = (\tau_{\rm simulated} - \tau_{\rm determined})/\tau_{\rm simulated}$. We get the following results as a function of the distance.

1. We find 60 % of the stars with σ_τ/τ $< 20\%$ for $1 \leq$ d ≤ 8 kpc. These stars have a well-determined age. The results of the comparison are presented in Fig. 1, Panel b for d = 1kpc. The stars in red have an ill-determined age. They are located in the same problematic regions of the HRD: close to the zero age main sequence (ZAMS), regions of massive stars in the upper main sequence (MS) and red giant branch (RGB). The degeneracy in these regions is explained by the evolutionary speed of stars. In the vicinity of the ZAMS, low mass stars evolve slowly so their ages are poorly defined. On the contrary the stars on the RGB and in the upper MS evolve quickly.

2. There are 75 % of stars with σ_τ/τ $< 20\%$ for d $<$ 1 kpc. The results for d = 46 pc are represented in Fig. 1, Panel a. The limitation on the magnitude gives a catalog with faint stars at short distances. The stars are located in the bottom of the MS which is a degeneracy region. Thus we find more stars with a poorly defined age.

3. We find 50 % of stars with σ_τ/τ $< 20\%$ for d $>$ 8 kpc. The HRD at 10 kpc is represented in Fig. 1, Panel c. When the distance is large, observational errors on the parameters become significant. It is more difficult to determine the ages.

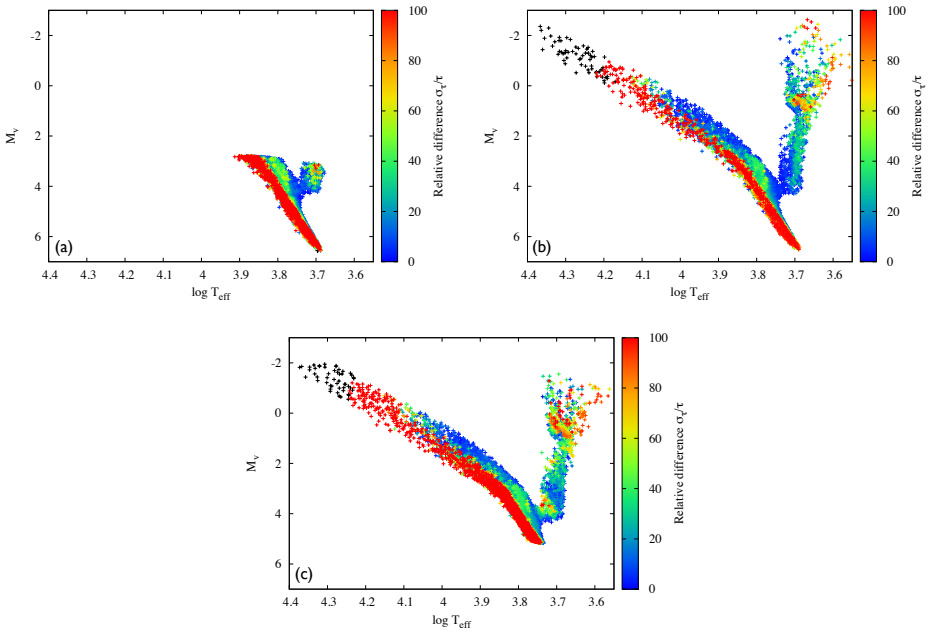

Fig. 1. Comparison of the simulated "true" age and determined age in the $\log T_{\rm eff} - M_{\rm v}$ diagram of the simulated catalogs for different distance and $\sigma_{[Fe/H]} = 0.3$ dex. **Panel a:** d = 46 pc. **Panel b:** d = 1 kpc. **Panel c:** d = 10 kpc. Colors represent the relative difference σ_τ/τ. The blue stars have a well-determined age (σ_τ/τ=0%) while the red stars have an ill-determined age (σ_τ/τ=100%). The age of black stars are undetermined.

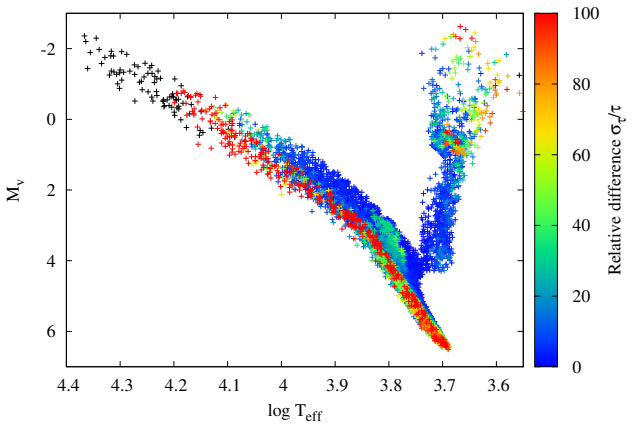

Fig. 2. Comparison of true age and estimated age in the $\log T_{\rm eff} - M_{\rm v}$ diagram of the Gaia simulated catalog with $\sigma_{[Fe/H]}$ = 0.1 dex. Colors are the same that in Fig. 1.

5 Effect of observational errors on the metallicity

The complementary spectroscopic observations of Gaia will permit to obtain the spectrum of the stars and will allow to determine the metallicity with a better observational error. We determine the ages for the same catalogs but now we take $\sigma_{[Fe/H]} = 0.1$ dex. The results of the comparison at d = 1kpc are represented in Fig. 2. We compare the determined ages and the estimated "true" ages. We find a great improvement for the stars close to the ZAMS and in the RGB. Indeed there are more than 75 % of stars with $\sigma_\tau/\tau < 20\%$ for the stars with a distance less than 10 kpc. For a distance greater than 10 kpc there are 55 % of stars with $\sigma_\tau/\tau < 20\%$. The improvement is worse for these stars because the observational errors are too important.

6 Conclusions

The Gaia ESA mission will observe 1 billion of stars. Different structures and objects will be observed depending on the distances. At less than 200 pc the Jupiter mass planets will be detected. Age of their host stars will allow to characterize these exoplanets. The open clusters, the globular clusters and the disk will also be observed by Gaia. Their dating will allow to understand the formation and evolution of the Galaxy. At these distances, there are 60 % of stars with an age well determined with our method. To promote these results we need a good accuracy on the metallicity. The complementary spectroscopic observations will allow to obtain a better accuracy, allowing a better age determination for 15 % of the stars.

References

Bailer-Jones, C. A. L. 2010, MNRAS, 403, 96

Casagrande, L., Schönrich, R., Asplund, M., et al. 2011, A&A, 530, A138

da Silva, L., Girardi, L., Pasquini, L., et al. 2006, A&A, 458, 609

Edvardsson, B., Andersen, J., Gustafsson, B., et al. 1993, A&A, 275, 101

Freeman, K. C. 1993, in Astronomical Society of the Pacific Conference Series, Vol. 49, Galaxy Evolution. The Milky Way Perspective, ed. S. R. Majewski, 125

Havel, M., Guillot, T., Valencia, D., & Crida, A. 2011, A&A, 531, A3

Jordi, C., Gebran, M., Carrasco, J. M., et al. 2010, A&A, 523, A48

Kroupa, P. 2002, Science, 295, 82

Perryman, M. A. C., de Boer, K. S., Gilmore, G., et al. 2001, A&A, 369, 339

Pietrinferni, A., Cassisi, S., Salaris, M., & Castelli, F. 2004, ApJ, 612, 168

Pont, F. & Eyer, L. 2004, MNRAS, 351, 487

Soderblom, D. R. 2010, ARA&A, 48, 581

SF2A 2012
S. Boissier, P. de Laverny, N. Nardetto, R. Samadi, D. Valls-Gabaud and H. Wozniak (eds)

NEW SB2 ORBITAL ELEMENTS FOR ACCURATE MASSES WITH GAIA: HD 9312, HD 9313 AND HD 183255*

J.-L. Halbwachs[1], F. Arenou[2], B. Famaey[1], P. Guillout[1], Y. Lebreton[2] and D. Pourbaix[3]

Abstract. We are observing a selection of about 70 double-lined binaries (SB2) with the T193/Sophie in order to improve their orbital elements. Our goal is to obtain the masses of the components with a 1 % accuracy when the astrometric observations of Gaia are available.

In the course of this program, it appeared that the orbital elements of some known SB2 were too uncertain for deriving ephemerides sufficiently reliable for planning the observations. We present new elements for a selection of three SB2 which have already received at least 4 new RV measurements per component star: HD 9312, HD 9313 and HD 183255.

Keywords: binaries: spectroscopic, stars: individual: HD 9312, HD 9313, HD 183255

1 Introduction

Gaia will provide the opportunity to derive stellar masses with errors around 1 %, by combining Gaia astrometry with accurate SB2 orbital elements. For that purpose, a large observation program is on going at the OHP observatory with the T193/Sophie, in order to improve the orbital elements of known SB (Halbwachs & Arenou 2009).

We expect to derive accurate orbital elements for about 70 SB2. The orbits published in the past are used to compute ephemerides in order to optimize the selection of the targets during the observation runs. However, some of these orbits are too obsolete for that purpose, and they were revised on the basis of our first observations.

We present hereafter three revised orbits obtained from ancient observations and from at least 4 Sophie spectra, providing at least 4 radial velocity (RV) measurements per component. This condition enable us to derive the elements of the spectroscopic orbit from the new measurements alone. This calculation is used to adjust the weights of the new and of the ancient measurements, as explained in section 3 hereafter. Each object is briefly discussed in section 4. Section 5 is the conclusion.

2 The observations and the RV measurements

The spectra of the three stars were taken between April 2010 and April 2012, using the 193 cm telescope of the Haute-Provence observatory and the Sophie spectrograph in high resolution mode. Since our stars are all rather bright (the faintest is HD 183255, a 8-mag star), an exposure shorter than 20 minutes was sufficient to reach a signal-to-noise ratio as large as 100.

The Sophie pipeline produces several reduction files, including the cross-correlation function (CCF) of the spectrum with a mask. Plots of the CCF of HD 9312 and of HD 9313 showing the peaks of the two components are presented in Halbwachs et al. (2011). The radial velocities of the SB2 components were obtained fitting the CCF with two normal distributions. The results are summarized in Table 1 hereafter. It is worth noticing that the uncertainties derived from the Gaussian fitting, σ_{V_1} and σ_{V_2}, are widely underestimated since the CCF is not exactly represented by two normal distributions subtracted from a linear background, as assumed: in reality, each correlation peak is flanked by two side lobes due to differences between the mask and the actual spectra, and the background is not perfectly linear. The uncertainties will then be revised in the next section.

* BASED ON OBSERVATIONS PERFORMED AT THE HAUTE-PROVENCE OBSERVATORY

[1] Observatoire Astronomique de Strasbourg, UMR 7550, 11, rue de l'université, F-67000 Strasbourg, France

[2] GEPI, Observatoire de Paris, F-92195 Meudon, France

[3] FNRS, Université libre de Bruxelles, CP226, boulevard du Triomphe, 1050 Bruxelles, Belgium

Table 1. The RV measurements obtained from Sophie spectra of HD 9312, HD 9313 and HD 183255. σ_V is the uncertainty derived fitting the CCF with two normal distributions, and σ'_V is the uncertainty eventually assumed in the calculation of the SB2 solution when the ancient measurements are also taken into account.

HD 9312 = HIP 7143

Epoch (BJD)	V_1 (km/s)	σ_{V_1}	σ'_{V_1}	V_2 (km/s)	σ_{V_2}	σ'_{V_2}
2455440.59494	-28.4985	0.0029	2.383	39.851	0.024	2.383
2455532.30387	30.0514	0.0015	2.383	-37.061	0.013	2.383
2455783.60406	17.5097	0.0036	2.383	-20.195	0.032	2.383
2455864.40548	30.5953	0.0032	2.383	-37.646	0.026	2.383

HD 9313 = HIP 7134

Epoch (BJD)	V_1 (km/s)	σ_{V_1}	σ'_{V_1}	V_2 (km/s)	σ_{V_2}	σ'_{V_2}
2455440.58846	10.5593	0.0017	0.348	-50.003	0.039	0.350
2455783.59352	-16.9401	0.0111	0.348	-12.129	0.213	0.408
2455864.39349	-8.2810	0.0072	0.348	-24.197	0.105	0.364
2455933.24111	-1.1507	0.0074	0.348	-33.223	0.146	0.378

HD 183255 = HIP 95575

Epoch (BJD)	V_1 (km/s)	σ_{V_1}	σ'_{V_1}	V_2 (km/s)	σ_{V_2}	σ'_{V_2}
2455306.60517	-78.7361	0.0019	0.869	-51.451	0.005	0.869
2455440.38547	-70.4586	0.0026	0.869	-58.466	0.007	0.869
2455693.56575	-60.8733	0.0059	0.869	-68.567	0.015	0.869
2455784.41810	-74.8302	0.0080	0.869	-52.909	0.021	0.869
2456034.59835	-57.7317	0.0081	0.869	-71.990	0.021	0.869

3 Calculation of the new orbital elements

The orbital elements are revised adding the Sophie RV measurements to the ancient ones. However, the relative weights of the measurements must be carefully adjusted for that calculation. This is done as follows:

- The orbital elements are derived from the ancient measurements alone, assigning to each RV measurement the weight $w_i = 1/\sigma^2_{V_i}$. The F_2 estimator of the goodness-of-fit is then derived (Stuart & Ord 1994); when it is null or very close to zero, the solution is accepted. The same noise is quadratically added to all the uncertainties, and the calculation is repeated otherwise.

- The same process is applied to the Sophie measurements. However, since the number of degrees of freedom is small, the nominal value of F_2 is not zero, but is computed by simulations. New uncertainties, usually much larger than the original ones, are thus obtained.

- All the RV measurements are considered together, with weights derived from the new uncertainties. A systematic shift between the Sophie measurements and the ancient ones, D_0, is added to the unknowns of the solution. Again, the calculation is repeated until $F_2 \approx 0$. The final uncertainties, σ'_{V_i}, are thus obtained. These uncertainties are listed in table 1 for the Sophie measurements. The uncertainties of the ancient measurements are the quadratic sum of the original values and of the supplement, $\sigma_{V\,Sup}$, which are listed in table 2 with the orbital elements. The ancient and the new orbits are shown in Fig. 1 for comparison, with the measurements folded in phase.

Table 2. The revised orbital elements of HD 9312, HD 9313 and HD 183255. $\sigma_{V\,Sup}$ is the uncertainty quadratically added to that of the ancient measurements in the calculation process. ΔT is the time span covered by all the observations; the number in parenthesis refers to the ancient observations alone.

Elements	HD 9312	HD 9313	HD 183255
N_{meas} (Ancient+Sophie)	35 + 4×2	68 + 4×2	32 + 5×2
$\sigma_{V\,Sup}$ (km/s)	3.272	0.307	0.581
ΔT (days) (ancient orbit)	27801 (1611)	16121 (2515)	9404 (1545)
Period (days)	36.51836 ± 0.00068	53.51155 ± 0.00022	166.8349 ± 0.0170
T_0 (BJD−2 400 000)	54094.16 ± 1.39	39810.78 ± 0.10	47744.60 ± 3.66
e	0.109 ± 0.042	0.39819 ± 0.00502	0.1393 ± 0.0136
ω (deg)	200.2 ± 13.5	279.60 ± 0.80	58.8 ± 8.4
V_γ (km/s)	-4.05 ± 1.06	-14.811 ± 0.116	-64.438 ± 0.145
K_1 (km/s)	31.00 ± 1.28	24.395 ± 0.162	13.810 ± 0.315
K_2 (km/s)	43.85 ± 2.50	33.75 ± 0.38	16.517 ± 0.588
D_0 (km/s)	5.51 ± 1.38	-0.023 ± 0.198	-0.522 ± 0.320
$a_1 \sin i$ (Gm)	15.47 ± 0.61	16.465 ± 0.109	31.37 ± 0.73
$a_2 \sin i$ (Gm)	21.89 ± 1.18	22.78 ± 0.27	37.53 ± 1.35
$\mathcal{M}_1 \sin^3 i$ ($\mathcal{M}_\odot$)	0.913 ± 0.120	0.4882 ± 0.0123	0.255 ± 0.022
$\mathcal{M}_2 \sin^3 i$ ($\mathcal{M}_\odot$)	0.645 ± 0.071	0.3529 ± 0.0061	0.213 ± 0.015
σ_{o-c} km/s (ancient/Sophie/all)	5.94/1.45/5.37	0.936/0.211/0.888	1.009/0.794/0.954

4 Notes to individual stars

- HD 9312 = HIP 7143. Ancient SB1 orbit of Heard (1940), who didn't provide uncertainties for individual RV measurement; the estimated "probable error" of 5.2 km/s (erroneously written as 3.2 in the publication) is assumed for each ancient measurement at the beginning of the calculation process; when $\sigma_{V\,Sup} = 3.272$ is quadratically added, one obtains $\sigma_{RV} = 6.145$ km/s for every ancient measurements. The detection of the secondary spectrum is reported in Halbwachs et al. (2011). The very large uncertainties eventually assigned to the Sophie measurements (table 1) is surprising for a G5-type star with narrow CCF–peaks, and suggest that the system could be triple in reality. This should be clarify with future observations.
- HD 9313 = HIP 7134. Ancient SB1 orbit of Griffin & Emerson (1975), who assigned the same weight to all measurements; the r.m.s. residual 0.9 km/s is used as uncertainty for each ancient measurement at the beginning of the calculation process. The detection of the secondary spectrum is reported in Halbwachs et al. (2011).
- HD 183255 = HIP 95575 = GJ 1237. Ancient SB2 orbit of Tokovinin (1991), who assigned to the primary component 10 measurements which obviously refer to blended spectra; the Julian days of these measurements are $2,400,000$ + 47007, 47012, 47022 (2 measurements), 47055, 47059, 48082, 48089, 48166 and 48175. These measurements were assumed to be linear combinations of the RV of both components, using the method described in Halbwachs, Mayor & Udry (2012); we derive the relative contribution of the primary velocity to the velocity of the blend: $C_0 = 0.797 \pm 0.032$.

5 Concluding remarks

We have presented new orbital elements for 3 SB2, including two systems which previously had only SB1 orbits. In addition to the detection of the secondary components, the orbital elements were improved thanks to the extension of the time span of the observation by a factor larger than 6, and thanks to the accuracy of the few

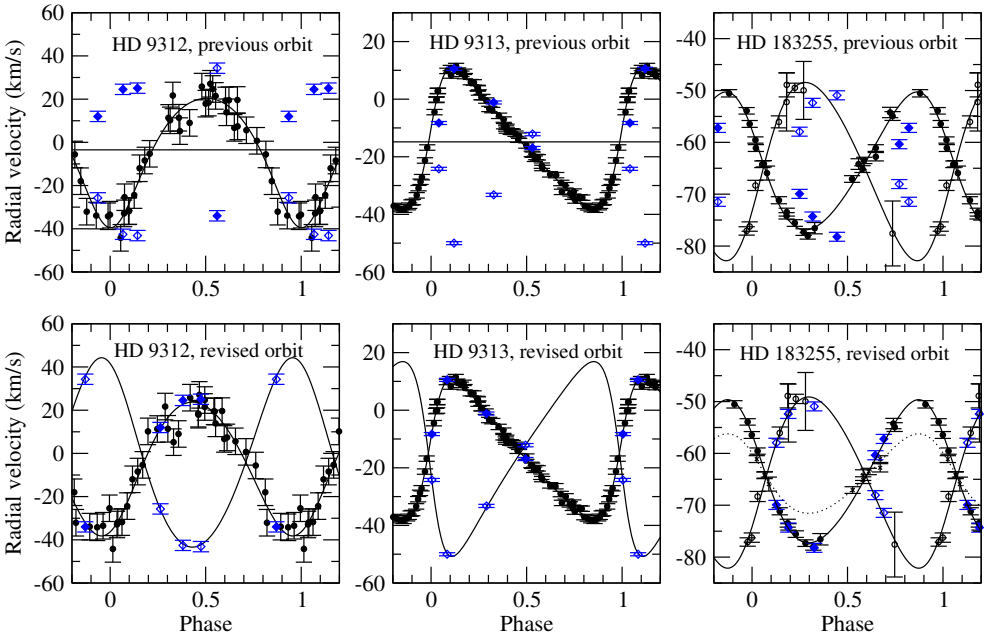

Fig. 1. The ancient (**up**) and the revised (**down**) orbits, folded in phase. The black circles refer to the ancient RV measurements, and the blue diamonds are preliminary estimations of the RV obtained from Sophie. The filled and open symbols refer to the primary and to the secondary components, respectively. The asterisks (HD 183255, revised orbit, dotted line) refer to ancient blended measurements used to derive C_0 (explanations in the notes).

additional Sophie measurements: it comes from the last line of table 2 that σ_{o-c} is respectively 4, 3, and 1.3 times smaller for the Sophie measurements than for the ancient ones.

The uncertainties of $\mathcal{M}_{1,2} \sin^3 i$ are all larger than 1 %, and are then larger than our expectation for the end of the programme. However, these orbits are preliminary, and the final ones should be better for two reasons: the calculation of the orbit will be improved by using a method more elaborated than fitting the CCF, such as TODMOR (Zucker et al. 2003; Tal-Or et al. 2011) or a method based on Markov chains (Salomon et al. 2012), and the number of Sophie spectra should be tripled. The targeted 1 % uncertainties should then be reached at the end of the programme.

This programme is supported by the PNPS and by the AS-Gaia. We are grateful to the staff of the OHP for their kind assistance. The more recent spectrum of HD 9313 was kindly taken by Lev Tal-Or. Jean-Baptiste Salomon participated to the last observation of HD 183255. The SB9 database, `http://sb9.astro.ulb.ac.be/`, (Pourbaix et al. 2004) was used to recover the ancient measurements.

References

Griffin, R.F. & Emerson, B. 1975, The Observatory, 95, 98

Halbwachs, J.-L., Arenou, F. 2009, Proceedings SF2A 2009, M. Heydary–Malayeri, C. Reylé et R. Samadi édr., p. 53

Halbwachs, J.-L., Arenou, F., Famaey, B., Guillout, P., Lebreton, Y., & Pourbaix, D. 2011, Proceedings SF2A 2011 – G. Alecian, K. Belkacem, S. Collin, R. Samadi & D. Valls-Gabaud edr., 303

Halbwachs, J.-L., Mayor, M., Udry, S. 2012, MNRAS, 422, 14

Heard, J. F. 1940, Publications of the David Dunlap Observatory, vol. 1, 194

Pourbaix, D., Tokovinin, A.A., Batten, A.H. et al. 2004, A&A, 424, 727

Salomon, J.-B., Ibata, R., Guillout, P., Halbwachs, J.-L., Arenou, F., Famaey, B., Lebreton, Y., & Pourbaix, D. 2012, Proceedings SF2A 2012

Stuart, A., & Ord, K. 1994, Kendall's Advanced Theory of Statistics, vol. 1 (Edward Arnold, London)

Tal-Or, L., Santerne, A., Mazeh, T. et al. 2011, A&A, 534, 67

Tokovinin, A. 1991, A&AS, 91, 497

Zucker, S., Mazeh, T., Santos, N. C., Udry, S., & Mayor, M. 2003, A&A, 404, 775

SF2A 2012
S. Boissier, P. de Laverny, N. Nardetto, R. Samadi, D. Valls-Gabaud and H. Wozniak (eds)

GAIA CONSTRAINTS ON THE GALACTIC THICK DISC

G. Kordopatis[1]

Abstract. The Gaia mission, with its unprecedented astrometric and photometric precision, combined with its Radial Velocity Spectrometer, will provide to the astronomical community a wealth of necessary constraints to disentangle between the different formation scenarios of the Galactic thick disc. The aim of this review is to present some of the recent results obtained spectroscopically concerning this Galactic structure, and highlight the open questions that still remain to be answered under the Gaia era. These concern mainly the measurement of the chemo-dynamical properties of the Milky Way at the inner and outer parts, which allow us to determine the total accreted mass from the mergers with satellite galaxies, and will give us an estimate of the strength of the radial migration phenomena to form such a structure.

Keywords: Surveys: Gaia, Techniques: spectroscopy, Galaxy: structure, stellar content, evolution

1 Introduction

Surveys of external galaxies seem to suggest that thick discs are inherent structures in most (if not all) disc galaxies (Yoachim & Dalcanton 2008; van der Kruit & Freeman 2011). Although the existence of such a structure for the Milky Way has been highlighted for almost thirty years now (Yoshii 1982; Gilmore & Reid 1983), its origin is still uncertain, and many scenarios have been proposed to explain it. These can be separated into those involving internal mechanisms or those requiring external accretion or trigger in order to form the thick disc (e.g.: Abadi et al. 2003; Brook et al. 2004; Villalobos & Helmi 2008; Loebman et al. 2011, and references therein).

Most of the stellar spectroscopic and photometric surveys of stars in the Milky Way have shown that the Galactic thick disc is mainly composed by old stars ($\sim$ 10 Gyr, Fuhrmann 2008), of intermediate metallicity ([M/H] ~ -0.5 dex, e.g.: Bensby et al. 2007; Kordopatis et al. 2011b) and with hotter kinematics compared to the thin disc stars (e.g.: Casetti-Dinescu et al. 2011). In addition, the thick disc stars inside the solar cylinder ($7< R <9$ kpc) have a ratio of α-element abundances over iron ([α/Fe]) which is enhanced compared to the [α/Fe] ratio of the thin disc stars (e.g.: Fuhrmann 2008; Navarro et al. 2011). This property suggests that the thick disc has been formed in relatively short timescales ($\sim$ 1 Gyr), and hence the understanding of its formation offers us the possibility to decipher the merging history of our Galaxy back to redshifts of $z \sim 1.5-2$ (Freeman & Bland-Hawthorn 2002). This exploration of the origins of the Milky Way is widely known as Galactic archaeology.

Most of the models and simulations which have been proposed in order to explain the formation of the thick disc manage to successfully reproduce the locally measured properties of this structure. Nevertheless, this success has been preventing us to really disentangle between the models, since the community was lacking large observational datasets far from the solar neighbourhood, where the models differ the most.

The advent of multi-object spectrographs (such as VLT-FLAMES), combined with the part-time dedication of large telescopes in order to make deep and statistically significant stellar surveys (e.g.: Gaia-ESO Survey, RAVE, SEGUE) has already changed our view of the Milky Way. The simplistic approach consisting to consider that the thick disc has formed only by one mechanism is most probably out of date. The true question that one would like to answer now, is what is the relative importance of each of these processes. In that sense, the Gaia mission (Perryman et al. 2001) will be a goldmine, in order to extract all the necessary information, since

[1] Institute of Astronomy, University of Cambridge, Madingley Road, Cambridge CB3 0HA, UK
email: gkordo@ast.cam.ac.uk

the satellite will map the 3D positions and kinematics, and obtain estimations of the chemical compositions of several hundreds of millions of stars.

In the following section (Sect. 2) we will briefly review the most commonly cited formation mechanisms of the thick disc. Then, in Sect. 3 we will see how these scenarios have been constrained, by enumerating the latest results that have been obtained in terms of orbits, metallicity and kinematic gradients. This section will end up with the open questions that are still remained to be answered, and show how Gaia will help to decipher the formation history of the thick disc (Sect. 4).

2 Formation of the thick disc: *in situ* versus external mechanisms

One of the first scenarios that has been proposed to explain the difference in kinematics and chemistry of the stellar population composing the thick disc is the co-planar accretion of all the necessary stellar content from dwarf satellites (Statler 1988; Abadi et al. 2003). Such a scenario is mainly defended by the hierarchical formation history of the galaxies in the ΛCDM paradigm, where the dwarf galaxies are thought to be the building blocks of larger galaxies like ours. The direct accretion scenario predicts the absence of radial or vertical chemical gradients for the thick disc, since only one population is composing this structure. In addition, the kinematics of the stars, especially at the outskirts of the Galaxy, will depend on the inclination angle of the merger as well as on the total mass of the satellite.

Nevertheless, the numerical simulations of such accretions have shown difficulties in the preservation of the existence of the thin disc after the merger. Models involving multiple minor mergers of satellites, which would heat dynamically the pre-existent thin disc in order to form the thick disc have hence been developed (Quinn et al. 1993; Villalobos & Helmi 2008). In that case, the stellar population composing the thick disc is in majority the one of the thin disc at the epoch of the bombardment ($z \sim 1.5$) and chemical or kinematical gradients could have persisted in the thick disc only if the initial thin disc had any of those.

Similarly, in order to explain the presence of the thin disc despite the massive accretion, Jones & Wyse (1983) and Brook et al. (2004, 2007) have proposed that the accretion consisted of a gas-rich merger, from the collapse of which the stars forming the existent thick disc will have formed. In that configuration, the stars are born *in situ*, but using the accreted extra-galactic gas. The orbital and chemical properties of the thick disc stars, such as radial and vertical gradients, could then be explained by the time-scale of the cloud collapse and the accretion parameters of the merger.

Finally, the last family of scenarios require no external trigger at all. Here, the stars composing the thick disc are formed entirely in the thin disc or in the bulge and are moved afterwards far from the Galactic plane due to internal mechanisms. Such a mechanism is presented for example by Bournaud et al. (2009), where it is suggested that at high redshift the turbulent primordial discs would had scattered far from the plane part of the gas and stars, forming in that way the thick discs of external galaxies as we see them today. Like for the direct accretion or the gas-rich merger, it is predicted in such a scenario that the thick disc is chemically homogeneous. More interestingly, the inside-out evolution of the thin disc will have as a consequence to form a thick disc with a shorter scale-length than the one of the thin disc.

Another evoked internal mechanism in order to create a thick disc is the radial migration of the stars due to resonances with the spiral structure or the bar of the Milky Way (e.g.: Schönrich & Binney 2009; Minchev & Famaey 2010; Loebman et al. 2011; Bird et al. 2012; Minchev et al. 2012). In such scenarios, the thick disc stars inside the solar cylinder would had come in majority from the inner radii of the Galaxy, gaining vertical velocity due to the lower Galactic potential at the outskirts, keeping a chemical signature of the interstellar medium of the regions where they have been formed. Nevertheless, the assumed dynamical evolution of the disc implies that the information concerning the origin of the stars is blurred because of the radial migration, and hence that there is no distinctive thin and thick disc components: the disc is characterised by smooth changes in its chemo-dynamical properties.

3 The observational constraints at the pre-Gaia era: The unlike scenario of a single mechanism

The advent of spectroscopic surveys either dealing with hundreds of stars (e.g. Fuhrmann 2008; Bensby et al. 2007; Kordopatis et al. 2011b), or the ones organised around big collaborations with few hundreds of thousand stars (e.g.: SEGUE, RAVE) have already brought a wealth of information in order to claim nowadays that the formation history of the Milky Way's thick disc is very likely a combination of most of the above cited scenarios.

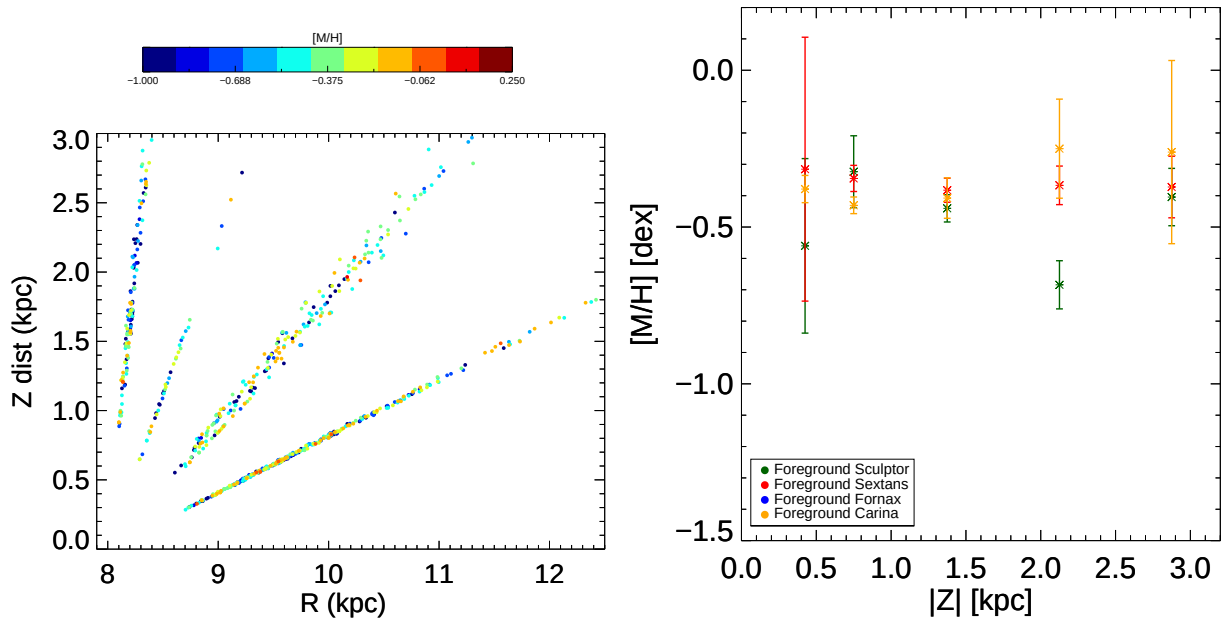

Fig. 1. Preliminary results of the study of ∼1200 foreground stars observed towards the line-of-sights of the dwarf spheroidal galaxies of Sculptor, Fornax, Sextans and Carina (Kordopatis et al. 2012, in prep.). **Left:** Metallicity of the surveyed stars at different distances above the Galactic plane and different galatocentric radii. **Right:** Measured vertical metallicity gradients towards the line-of-sights for which enough stars were available (Sculptor in green, Sextans in red, Carina in yellow). The preliminary results seem to suggest a chemically homogeneous thick disc in the studied directions.

For instance, Cheng et al. (2012b) used SEGUE data of $\sim$ 7000 stars to measure the radial metallicity gradients of the thin and thick discs, at different distances above the Galactic plane, up to $|Z| \sim 1.5$ kpc. They have shown that the farther from the plane, the flatter the gradient, suggesting that the thick disc population is chemically homogeneous, in agreement with the scenario of Bournaud et al. (2009), the one of Abadi et al. (2003) or with a radial migration mechanism (provided a strong migration rate). In a complementary approach, the analysis of ∼1200 foreground stars of several spectroscopic surveys towards the line-of-sights of the dwarf spheroidal galaxies of Sculptor, Fornax, Sextans and Carina (Kordopatis et al. 2012a, in prep) has yielded to the measurement of the vertical chemical gradient for the thick disc stars towards these four directions. The preliminary results of this study also seem to point towards a chemically homogeneous thick disc (see Fig. 1), in agreement with the result of Cheng et al. (2012b).

Nevertheless, a pure radial migration scenario as being the fundamental one in order to form the thick disc seem to be ruled out when analysing the eccentricity distribution function of the thick disc stars. The RAVE results (Wilson et al. 2011), the SEGUE ones (Dierickx et al. 2010; Lee et al. 2011) as well as the independent ones of Kordopatis et al. (2011b), obtained far from the solar neighbourhood, have shown that the thick disc stars have a peak at intermediate values ($\epsilon \sim 0.3$), with a tail going towards higher values, where merger scenarios predict that the accreted stars are found (Sales et al. 2009). In addition, Lee et al. (2011) have shown that there is a strong correlation between the metallicity and the eccentricity of the stars, a characteristic which does not seem to be existent for the thin disc stars, hence suggesting that radial migration played a less important role for the thick disc than for the thin one.

Similarly, the strong correlation between the rotational velocity and the metallicity measured by Kordopatis et al. (2011b); Lee et al. (2011); Schlesinger et al. (2011) ($\partial V_\phi / \partial$[M/H] $\sim$ 45 km s^{-1} dex^{-1}) seem to decrease again the relative importance of the radial migration in the formation of the thick disc[i]. This correlation, combined with the measurement of the vertical metallicity gradient of more than -0.1 dex kpc^{-1} (Kordopatis et al. 2011b; Ruchti et al. 2011), as well as the similarity of the [α/Fe] ratio of the metal-poor thick disc stars with the [α/Fe] ratio of the halo stars (Ruchti et al. 2010), also rules-out the pure accretion scenario.

[i]We note, however, that recently Curir et al. (2012) suceeded to simulate such a strong correlation using radial migration in a barred disk Galaxy

With such a reasoning, and using a sample of $\sim 12 \times 10^3$ G-dwarfs, Liu & van de Ven (2012) have suggested that the thick disc could be decomposed into a radial migrated population being $\alpha-$old and having circular orbits, and another one formed from extra-galactic material, composed with the most metal-poor stars ([M/H]$<$ -0.6 dex) on eccentric orbits. Worth mentioning are also the studies of Bensby et al. (2011) and Cheng et al. (2012a) who found no $\alpha-$enhanced stars at the outskirts of the galaxy, at the distances above the plane where the thick disc should be the dominant population. Whereas both studies rely on relatively poor statistics at these radii, both of them have suggested a smaller scale-length for the $\alpha-$enhanced thick disc. In particular, Cheng et al. (2012a) proposed as an explanation that the inner part of the thick disc could be consistent with a scenario in which the thick disc forms during an early gas-rich accretion phase. Furthermore, the stars far from the plane in the outer disc could have reached their current locations through heating by minor mergers. The precise measurement of the thick disc properties at these radii could hence impose important constraints on the strength of radial migration in the thin disc.

4 The Gaia legacy: determining the relative importance of each formation scenarios

The Gaia satellite is planned to be launched in September 2013. During its five year mission, the survey will aim for completeness to $V \sim 20 - 25$ mag, depending on the colour of the object, with astrometric accuracies of about 20 μas at V $\sim$15 mag. Within a radius of 10 kpc from the Sun, the 3D motions and positions of several hundreds of millions of stars will be known with accuracies better than 10%. The onboard Blue (BP) and Red (RP) spectro-photometers will deliver broadband photometry for roughly a billion stars, up to the 20th magnitude. For the brightest targets ($V \leq 17$ mag, $\sim 350 \times 10^6$ stars), these data will be complemented by the intermediate resolution spectra ($R \sim 11\,500$) gathered at the near-infrared, around the ionised Calcium triplet ($\lambda\lambda$ 847 $-$ 874 nm) from the Radial Velocity Spectrometer (RVS). The analysis of these spectra, will allow to obtain the effective temperature ($T_{\rm eff}$), surface gravity ($\log g$), overall metallicity and $\alpha-$abundances for the stars stars brighter than $V \sim 14$ mag. In particular, Kordopatis et al. (2011a) have estimated that accuracies of 100 K, 0.17 dex and 0.1 dex for the $T_{\rm eff}$, $\log g$ and [M/H], respectively, could be achieved for typical thick disc stars at a signal-to-noise ratio of 50 pixel^{-1} using their automated stellar spectra parameterisation pipeline.

The first astrometry data release is likely to be in 2016, with spectrophotometry and stellar parameters to follow later, and 2021 for the final catalogue. This wealth of data, will of course shed some light on the relative contribution of each of the previously cited mechanisms, revealing the relation between the thick disc and the other Galactic structures (thin disc, bulge and halo). In addition, the volume and the magnitudes that are going to be surveyed by Gaia, will minimise the effects of specific spatial and stellar mass sampling at the solar cylinder from which suffered previous surveys, and which according to Bovy et al. (2012), can bias the interpretation of the distinctive nature of the thick disc. More precisely, the constraints that Gaia will bring on the formation scenarios of the thick disc are the followings:

- The observation of the outskirts of the galaxy ($R > 8$ kpc) will allow to obtain estimations of the scale-length of the thick disc, both in terms of star counts, but also using a Jeans analysis. The measurement of a flaring for the thick disc will be possible, which will give valuable information about the total accreted mass of the Milky Way (Qu et al. 2011). In addition, the strength of the radial migration processes will be characterised robustly, by analysing the chemical homogeneity at the outer parts of the thick disc with a statistically significant stellar sample.

- The comparison of the star counts towards the northern and the southern Galactic cap, the search of kinematic asymmetries compared to the Galactic plane, as well as the radial gradients at different heights above the plane, will allow to detect in the thick disc the possible remnants of satellite accretions, either as stellar streams or over-densities in the phase-space. In addition, the evolution of the ellipticity of the orbits, or the variations in the correlations between the circular orbital velocity and the metallicity at different radii, will determine if there is complete mixing in the thick disc stars (Loebman et al. 2011), and perhaps constrain the influence of the Galactic bar in the radial migration of stars.

- The observation the thick disc towards the Galactic bulge will be limited by the high extinction of these regions, as well as the crowding limit of the RVS (20 000 stars deg^{-2}). Nevertheless, the chemo-dynamical characterisation of the brightest thick disc giants in that direction will reveal if there is a relation between

the bulge stars and the thick disc ones, which will be for the first time a direct proof of radial migration as one of the mechanisms forming the thick disc structure.

Finally, it should be noticed that the results of Gaia will be complemented by the already on-going Gaia-ESO public spectroscopic survey (Gilmore et al. 2012). This project employs the VLT-FLAMES instrument for high quality spectroscopy of some 100 000 Milky Way stars. Targets brighter than $V \sim 18$ mag will be observed with GIRAFFE at a resolution of $R \sim$20 000 whereas some 10 000 stars brighter than $V \sim 16$ will have UVES spectra at a resolution of $R \sim 45\,000$. At the end of this survey, it is estimated that roughly 20 000 stars belonging to the thick disc will be observed, complementing the Gaia mission with more precise stellar radial velocities and chemical abundances at the fainter magnitudes.

5 Conclusions

The understanding of the formation of the thick disc is directly linked with our understanding of the hierarchical formation of the galaxies in the Universe. This review presented the most commonly evoked scenarios to form the Galactic thick disc, and highlighted which are the most recent findings from the large spectroscopic surveys such as RAVE or SEGUE. The future Gaia mission will complement the advent of the future data releases from RAVE (Kordopatis et al. 2012b, to be submitted), SEGUE, APOGEE and Gaia-ESO survey, by mapping chemo-dynamically the regions of the thick disc in which the formation scenarios differ the most. The combination of all these projects will hence determine the relative importance of internal and external mechanisms for the origin and the evolution of the thick disc.

G.K. would like to thank the SOC for the invitation in order to give this presentation and the AS-Gaia consortium for financial support. G. Gilmore and P. de Laverny are warmly thanked for the careful reading of this proceeding.

References

Abadi, M. G., Navarro, J. F., Steinmetz, M., & Eke, V. R. 2003, ApJ, 597, 21
Bensby, T., Alves-Brito, A., Oey, M. S., Yong, D., & Meléndez, J. 2011, ApJ, 735, L46
Bensby, T., Zenn, A. R., Oey, M. S., & Feltzing, S. 2007, ApJ, 663, L13
Bird, J. C., Kazantzidis, S., & Weinberg, D. H. 2012, MNRAS, 420, 913
Bournaud, F., Elmegreen, B. G., & Martig, M. 2009, ApJ, 707, L1
Bovy, J., Rix, H.-W., & Hogg, D. W. 2012, ApJ, 751, 131
Brook, C., Richard, S., Kawata, D., Martel, H., & Gibson, B. K. 2007, ApJ, 658, 60
Brook, C. B., Kawata, D., Gibson, B. K., & Freeman, K. C. 2004, ApJ, 612, 894
Casetti-Dinescu, D. I., Girard, T. M., Korchagin, V. I., & van Altena, W. F. 2011, ApJ, 728, 7
Cheng, J. Y., Rockosi, C. M., Morrison, H. L., et al. 2012a, ApJ, 752, 51
Cheng, J. Y., Rockosi, C. M., Morrison, H. L., et al. 2012b, ApJ, 746, 149
Curir, A., Lattanzi, M. G., Spagna, A., et al. 2012, A&A, 545, A133
Dierickx, M., Klement, R., Rix, H.-W., & Liu, C. 2010, ApJ, 725, L186
Freeman, K. & Bland-Hawthorn, J. 2002, ARA&A, 40, 487
Fuhrmann, K. 2008, MNRAS, 384, 173
Gilmore, G., Randich, S., Asplund, M., et al. 2012, The Messenger, 147, 25
Gilmore, G. & Reid, N. 1983, MNRAS, 202, 1025
Jones, B. J. T. & Wyse, R. F. G. 1983, A&A, 120, 165
Kordopatis, G., Recio-Blanco, A., de Laverny, P., et al. 2011a, A&A, 535, A106
Kordopatis, G., Recio-Blanco, A., de Laverny, P., et al. 2011b, A&A, 535, A107
Lee, Y. S., Beers, T. C., An, D., et al. 2011, ApJ, 738, 187
Liu, C. & van de Ven, G. 2012, MNRAS, 425, 2144
Loebman, S. R., Roškar, R., Debattista, V. P., et al. 2011, ApJ, 737, 8
Minchev, I. & Famaey, B. 2010, ApJ, 722, 112
Minchev, I., Famaey, B., Quillen, A. C., et al. 2012, ArXiv e-prints
Navarro, J. F., Abadi, M. G., Venn, K. A., Freeman, K. C., & Anguiano, B. 2011, MNRAS, 412, 1203
Perryman, M. A. C., de Boer, K. S., Gilmore, G., et al. 2001, A&A, 369, 339

Qu, Y., Di Matteo, P., Lehnert, M. D., van Driel, W., & Jog, C. J. 2011, A&A, 535, A5
Quinn, P. J., Hernquist, L., & Fullagar, D. P. 1993, ApJ, 403, 74
Ruchti, G. R., Fulbright, J. P., Wyse, R. F. G., et al. 2010, ApJ, 721, L92
Ruchti, G. R., Fulbright, J. P., Wyse, R. F. G., et al. 2011, ApJ, 737, 9
Sales, L. V., Helmi, A., Abadi, M. G., et al. 2009, MNRAS, 400, L61
Schlesinger, K. J., Johnson, J. A., Rockosi, C. M., et al. 2011, ArXiv e-prints
Schönrich, R. & Binney, J. 2009, MNRAS, 399, 1145
Statler, T. S. 1988, ApJ, 331, 71
van der Kruit, P. C. & Freeman, K. C. 2011, ARA&A, 49, 301
Villalobos, Á. & Helmi, A. 2008, MNRAS, 391, 1806
Wilson, M. L., Helmi, A., Morrison, H. L., et al. 2011, MNRAS, 413, 2235
Yoachim, P. & Dalcanton, J. J. 2008, ApJ, 682, 1004
Yoshii, Y. 1982, PASJ, 34, 365

SF2A 2012
S. Boissier, P. de Laverny, N. Nardetto, R. Samadi, D. Valls-Gabaud and H. Wozniak (eds)

NON-LTE EFFECTS ON THE IONIZATION EQUILIBRIUM OF FE I/FE II: APPLICATION TO THE RED GIANTS OF CARINA DSPH GALAXY

T. Merle[1], M. Fabrizio[2], F. Thévenin[1], M. Nonino[3], G. Bono[2,4] and Carina Project Team

Abstract. In the context of the Carina Project, we re-analyze the iron abundances of 44 red giants of the Carina dSph galaxy to derive its metallicity distribution function. The abundance analyses were performed with the LTE spectrum synthesis fitting method using ESO/VLT high resolution spectra. Using Fe I lines, we obtained stellar metallicities of $\sim$ 0.1 dex lower than using Fe II lines. This discrepancy is classically interpreted as an error on the surface gravity (based on photometry and evolutionary tracks) which is removed by changing gravity until Fe I abundances match Fe II ones. However, the NLTE mechanism of over-ionization regarding LTE can also explain this discrepancy in giant stars. To support this idea, we performed NLTE computations with a Fe I/II model atom and show that this discrepancy is well reproduced. NLTE computations also highlight large discrepancies in individual lines of Fe I and Fe II.

Keywords: abundances, metallicity, Carina galaxy, dSph galaxies, NLTE analysis

1 Observations and data reduction

The high-resolution spectra for Carina red giants adopted in this investigation were retrieved from the ESO Scientific Archive ($R \sim 38000$ and $15 \leq S/N \leq 45$). We selected spectra from four different ESO/VLT observing programs collected with either UVES (slit mode, 9) or FLAMES/GIRAFFE-UVES (multifiber mode, 80). We ended up with a sample of 72 stars, located in the central region of Carina dSph galaxy and covering the bright portion of the red giant branch (see Fig. 1 on left). The UVES spectra (red arm, centered at 5800 Å) were reduce using IRAF. For a more detailed explanation on the observations, data reduction, and radial velocity determination see Fabrizio et al. (2011, 2012).

2 LTE spectroscopic analysis

The iron abundance analysis was performed following the classical spectrum-synthesis method for both Fe I and Fe II lines, but with one difference: we did not impose LTE ionization equilibrium between the Fe I and the Fe II lines (e.g. Kraft & Ivans 2003). We used the effective temperature $T_{\rm eff}$ and surface gravity $\log g$ (see Fig. 1 on right) determined from the optical photometry (Bono et al. 2010; Stetson et al. 2011) and BaSTI isochrones (Pietrinferni et al. 2004, 2006). Typical uncertainties are 70 K and 0.2 dex. The synthetic spectra were computed using the 1D, plane-parallel, LTE, radiative transfer code MOOG (2009 version, Sneden 1973) with VALD line list (Kupka et al. 2000) and MARCS model atmospheres (Gustafsson et al. 2008). We used a constant microturbulent velocity of 2 km s^{-1} (mean value from Shetrone et al. 2003). The resulting accuracy of the line fits ranges from 0.10 to 0.15 dex.

3 Metallicity Distribution Function corrected for NLTE effects

We obtained the iron abundances for $N_\star = 44$ red giants using Fe I lines and for $N_\star = 27$ using Fe II lines. The metallicity distribution function (MDF) is shown on left panel of Fig. 2; with a weighted mean metallicity of

[1] Laboratoire Lagrange, UMR7293, Université de Nice Sophia-Antipolis, CNRS, Observatoire de la Côte d'Azur, 06300 Nice, France
[2] Dipartimento di Fisica, Università di Roma Tor Vergata, via della Ricerca Scientifica 1, 00133 Rome, Italy
[3] INAF - Osservatorio Astronomico di Trieste, via G.B. Tiepolo 11, 40131 Trieste, Italy
[4] INAF - Osservatorio Astronomico di Roma, via Frascati 33, Monte Porzio Catone, Rome, Italy

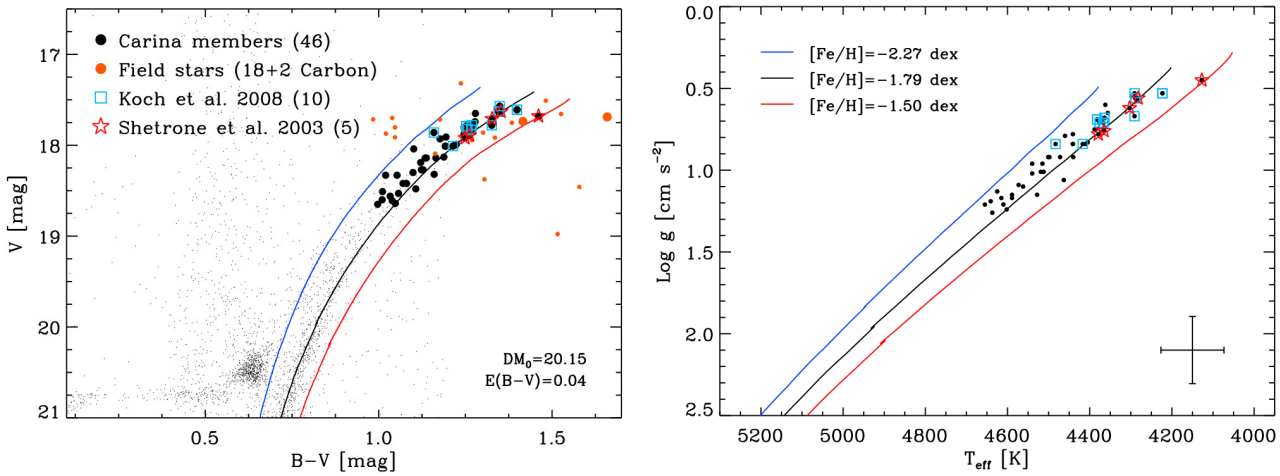

Fig. 1. Left: V, $B-V$ color-magnitude diagram of the spectroscopic targets. The black dots are the UVES targets with a radial velocity between 180 and 260 km s^{-1} (Carina candidate members), orange dots are targets with outside radial velocities. The radial velocities were measured using a dozen of heavy-element lines ranging from 6136 to 6200 Å. Two large orange dots are two carbon stars. Isochrones from BaSTI (Pietrinferni et al. 2004, 2006) at 12 Gyr are displayed for [Fe/H] = −1.50, −1.79 and −2.27 in red, black and blue, respectively. **Right:** same as the left, but the targets are in the effective temperature vs surface gravity plane.

	Fe I			Fe II		
$N_\star$	$\mu_{\rm [Fe\,I/H]}$	$\mu^{\rm weighted}_{\rm [Fe\,I/H]}$	$\sigma_{\rm [Fe\,I/H]}$	$\mu_{\rm [Fe\,II/H]}$	$\mu^{\rm weighted}_{\rm [Fe\,II/H]}$	$\sigma_{\rm [Fe\,II/H]}$
27	-1.85 ± 0.15	-1.84 ± 0.02	0.23	-1.76 ± 0.23	-1.72 ± 0.04	0.24
44	-1.93 ± 0.17	-1.90 ± 0.02	0.30	-1.84 ± 0.21	-1.80 ± 0.02	0.29

Table 1. Parameters of the MDFs as a function of number of stars and the adopted iron lines.

−1.90 and a spread of 0.30 dex. The weighted mean metallicity is computed using individual uncertainties on each star. The iron abundances deduce from Fe I lines are systematically lower than those obtained from Fe II lines (Table 3, first line). This difference is explained by assuming that Fe II is not affected by NLTE effects, at least on the ionization equilibrium, since Fe II is the dominant ionization stage in red giants. To account for NLTE effects on Fe I abundance determination, we estimated [Fe II/H] as a linear function of [Fe I/H] and corrected [Fe I/H] abundances (Table 3, second line). Then we estimated the MDF free from NLTE effects on Fe I (right panel of Fig. 2).

4 Comparison with Non-LTE models

To support the assumption that the difference in abundance is due to NLTE effect, we compute LTE (W^*) and NLTE (W) equivalent widths with MULTI (Carlsson 1986, version 2.2), for two typical model atmospheres of Carina red giants, using a model atom of Fe I/II (Collet et al. 2005). We neglected inelastic collisions with hydrogen assuming that they are less efficient than in dwarf stars. The atomic data are from: NIST for the energy levels, Nave et al. (1994); Kurucz & Bell (1995); Thévenin (1989) for oscillator strengths, Bautista (1997) for photo-ionisation cross sections, and van Regemorter (1962) for inelastic collisions with free electrons.

For iron lines between 4000 and 9000 Å, we selected weak lines ($W < 100$ mÅ) of Fe I and Fe II, and used the relation given NLTE abundance correction as a function of the ratio W/W^* (from the curve of growth theory, see e.g. Merle et al. (2011) for more details):

$$\Delta[\mathrm{Fe/H}] = [\mathrm{Fe/H}] - [\mathrm{Fe/H}]^* \approx -\log(W/W^*). \quad (4.1)$$

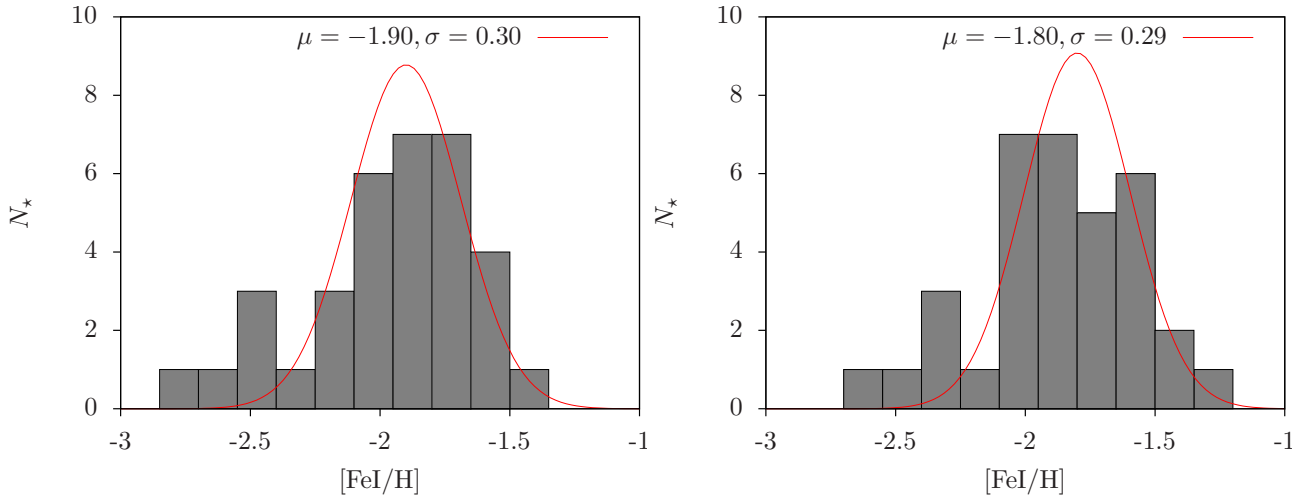

Fig. 2. MDFs of dSph Carina stars. **Left:** before NLTE correction. **Right:** after NLTE correction (using Fe II lines).

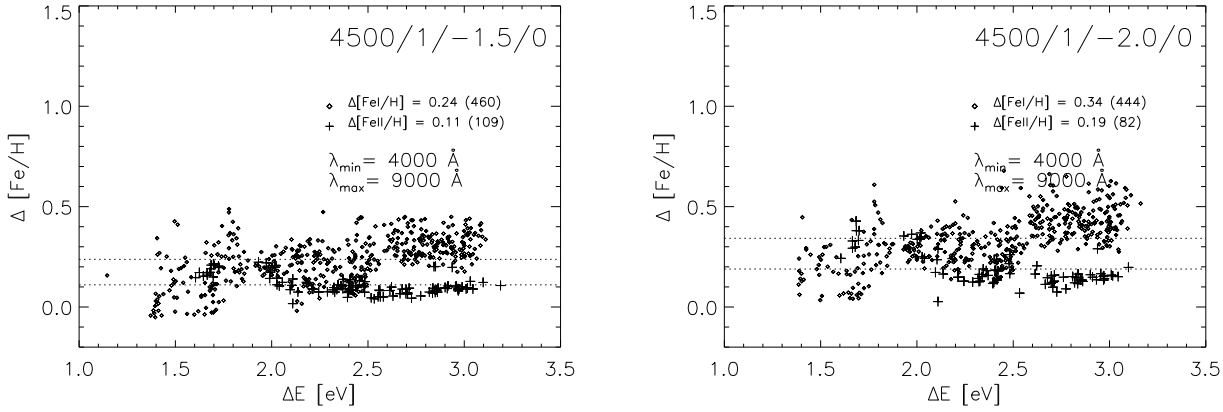

Fig. 3. Theoretical NLTE corrections Δ[Fe/H] for Fe I (diamonds) and Fe II (crosses) as a function of transition energy ΔE for two typical model atmospheres of Carina giant stars with $T_{\rm eff} = 4500$ K, $\log g = 1.0$, and [Fe/H] $= -1.50$ (**left**) or [Fe/H] $= -2.00$ (**right**). The means are given for the number of transitions written in parenthesis and plotted as dotted lines. The transitions considered have wavelengths between 4000 and 9000 Å.

The theoretical Non-LTE abundance corrections Δ[Fe/H] for the two ionization stages of iron are shown in Fig. 3 for two red giant model atmospheres: $T_{\rm eff} = 4500$ K, $\log g = 1.0$, [Fe/H] $= -1.50$ (left) and [Fe/H] $= -2.0$ (right). For Fe I lines, we noticed an increase of NLTE effects with the transition energy which is due to fact that the radiation dominate over the collisions at high transition energy. The Fe II lines are less affected by NLTE effects as expected since Fe II is the dominant ionization stage at these temperature and pressure (House 1964). Moreover, the NLTE effects are more important for the metal-poor model both for Fe I and Fe II. We found significant mean relative difference between [Fe I/H] and [Fe II/H] NLTE theoretical abundances of the order of 0.1 dex. The ensuing linear regression is in good agreement with the linear regression based on the observations analyzed in LTE (Fig. 4) without forcing ionization equilibrium between Fe I and Fe II to follow Saha's law. Furthermore, NLTE abundance corrections are also found on the excitation equilibria and they represent an upper limit for NLTE effects on iron, since inelastic collisions with hydrogen were neglected.

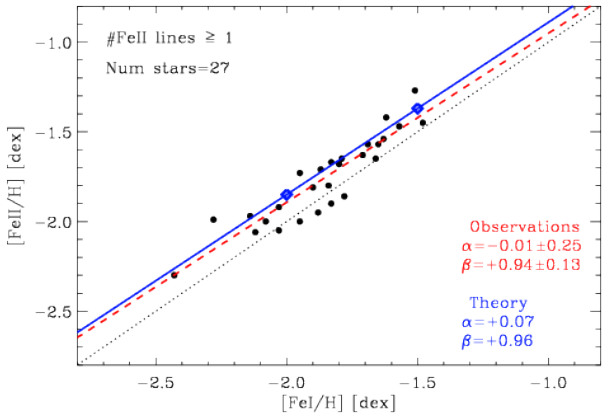

Fig. 4. NLTE effects on ionization equilibrium. [Fe II/H] as a function of [Fe I/H]. Comparison between abundances deduce from LTE analysis (black dots) and NLTE models (blue diamonds). Linear regression [Fe II/H] $= \alpha + \beta$[Fe I/H] is given for observations (dashed red line) and theory (solid blue line).

5 Conclusion

We determined the metallicity distribution function for a sample of 44 Carina RG stars. Our sample is more than a factor of four larger than any previous spectroscopic investigation based on high-resolution spectra. Detailed comparisons (Fabrizio et al. 2012) for stars in common with previous investigations (Shetrone et al. 2003; Koch et al. 2008, 2006; Lemasle et al. 2012; Venn et al. 2012) show that our iron abundance determinations are lower even when using Fe II lines only. We corrected for NLTE effects on the ionization equilibrium and we found a weighted mean metallicity of [Fe/H] = 1.80 and a dispersion of $\sigma = 0.29$ dex.

However, the current data do not allow us to determine whether the spread is either atmospheric, i.e., caused by a difference in the mean metallicity between the old and the intermediate-age population, or by measurement errors. To assess whether the different stellar populations are also characterized by different mean metallicities, new spectra with high S/N down to the red clump (intermediate-mass) and to the red horizontal branch (low-mass) stars are required.

References

Bautista, M. A. 1997, A&AS, 122, 167
Bono, G., Stetson, P. B., Walker, A. R., et al. 2010, PASP, 122, 651
Carlsson, M. 1986, Uppsala Astronomical Observatory Reports, 33
Collet, R., Asplund, M., & Thévenin, F. 2005, A&A, 442, 643
Fabrizio, M., Merle, T., Thévenin, F., et al. 2012, PASP, 124, 519
Fabrizio, M., Nonino, M., Bono, G., et al. 2011, PASP, 123, 384
Gustafsson, B., Edvardsson, B., Eriksson, K., et al. 2008, A&A, 486, 951
House, L. L. 1964, ApJS, 8, 307
Koch, A., Grebel, E. K., Gilmore, G. F., et al. 2008, AJ, 135, 1580
Koch, A., Grebel, E. K., Wyse, R. F. G., et al. 2006, AJ, 131, 895
Kraft, R. P. & Ivans, I. I. 2003, PASP, 115, 143
Kupka, F. G., Ryabchikova, T. A., Piskunov, N. E., Stempels, H. C., & Weiss, W. W. 2000, Baltic Astronomy, 9, 590
Kurucz, R. L. & Bell, B. 1995, Atomic line list CD-ROM (Cambridge, MA: Smithsonian Astrophysical Observatory)
Lemasle, B., Hill, V., Tolstoy, E., et al. 2012, A&A, 538, A100
Merle, T., Thévenin, F., Pichon, B., & Bigot, L. 2011, MNRAS, 418, 863
Nave, G., Johansson, S., Learner, R. C. M., Thorne, A. P., & Brault, J. W. 1994, ApJS, 94, 221

Pietrinferni, A., Cassisi, S., Salaris, M., & Castelli, F. 2004, ApJ, 612, 168
Pietrinferni, A., Cassisi, S., Salaris, M., & Castelli, F. 2006, ApJ, 642, 797
Shetrone, M., Venn, K. A., Tolstoy, E., et al. 2003, AJ, 125, 684
Sneden, C. 1973, ApJ, 184, 839
Stetson, P. B., Monelli, M., Fabrizio, M., et al. 2011, The Messenger, 144, 32
Thévenin, F. 1989, A&AS, 77, 137
van Regemorter, H. 1962, ApJ, 136, 906
Venn, K. A., Shetrone, M. D., Irwin, M. J., et al. 2012, ApJ, 751, 102

SF2A 2012
S. Boissier, P. de Laverny, N. Nardetto, R. Samadi, D. Valls-Gabaud and H. Wozniak (eds)

CONSTRAINING THE MILKY WAY THICK DISK FORMATION: CHEMICAL CHARACTERIZATION OF THE THICK DISK OUTSIDE OF THE SOLAR NEIGHBOURHOOD

H. Posbic[1], D. Katz[1], M. Haywood[1], P. Bonifacio[1], E. Caffau[1,2], A. Gomez[1], L. Sbordone[1,2], F. Arenou[1] and F. Royer[1]

Abstract. The formation of the Milky Way disk is still an open question. Many scenarios are proposed. Different formation scenarios predict different disk chemical trends. This work aims to chemically characterize the Milky Way disk inside and outside the solar neighbourhood, to better constrain its formation scenario. This is possible thanks to high resolution spectra of 200 disk stars observed using the Giraffe spectrograph on the Very Large Telescope (VLT). They were selected to have galactic altitudes $|Z|$ that cover both the thin and thick disk ($|Z|$ up to 2 kpc). The new automatic spectra analysis software SPADES (Stellar PArameters DEtermination Software, Posbic et al. 2012) was used to determine the stellar parameters, and most importantly, the elemental abundances of these stars. The distances of these stars were also determined. The metallicity distribution function of the disk using this sample was calculated. It showed a large contribution of the thick disk stars and a smooth transition at the metallicity of the thick disk/halo interface. The vertical behaviour of the metallicity distribution function was also studied. A vertical metallicity gradient in the disk of $\partial[Fe/H]/\partial|Z|$ = -0.19 ± 0.14 dex/kpc was marginally detected at the 1.4 sigma level. The [Ti/Fe] and [Ca/Fe] vs [Fe/H] trends for the stars are determined. The main result of the analysis is that the trends of [Ca/Fe] vs [Fe/H] and [Ti/Fe] vs [Fe/H] show no significant difference close (i.e. $|Z| \leq 1$ kpc) and farther away ($1 < |Z| < 2.5$ kpc) from the Galactic plane. This suggests that thick disk gas and stars have been enriched by the same proportion of type II and type I super-novae from the galactic plane up to at least 2.5 kpc. These results support thick disk formation scenarios like collapse or gas-rich accretion and disfavour a thick disk formed of stars captured during a merger event.

Keywords: Milky Way, thick disk, spectroscopy, spectral analysis

1 The Milky Way thick disk

The Milky Way is a spiral galaxy having 3 main components: the bulge, the disk and the halo. In the beginning of the 80s, stellar counts studies proposed the existence of 2 disk sub-components: the thin and the thick disk (Gilmore & Reid 1983). The formation of the Milky Way thick disk is still an open question. Many scenarios are suggested. A few examples are the accretion of the thick disk stars though a satellite (Abadi et al. 2003), the heating of a pre-existing thin disk by minor mergers (Qu et al. 2011), gas-rich accretion in the early Galaxy formation (Brook et al. 2004), stellar mixing and/or migration (Schönrich & Binney 2009).

Stars keep the chemical signature of the interstellar matter they were formed in. At the end of their lives massive stars return their nuclear products to the interstellar medium through stellar winds and supernovae, enriching it with heavier elements. The elemental abundance pattern of every generation of stars thus depends on the previous one. In principle, this allows for the star formation history of a galaxy to be traced using stellar elemental abundances (Freeman & Bland-Hawthorn 2002). To the stellar life cycles are added the different phenomena the Galaxy might have gone through: minor or major mergers, continuous gas accretion, etc... Each occurrence leaves chemical characteristics signatures upon the Galaxy and its components (e.g. relation between the elemental abundances, metallicity gradients etc...).

The work presented hereafter aims to bring new constraints to the scenarios of formation of the Milky Way thick disk using its chemical characteristics.

[1] GEPI, Observatoire de Paris, CNRS, Université Paris Diderot, Place Jules Janssen, 92190, Meudon, France
[2] Zentrum für Astronomie der Universität Heidelberg, Landessternwarte, Königstuhl 12, 69117, Heidelberg, Germany

2 The observations: reduction and analysis using SPADES

200 stars were selected to maximize the number of stars having $|Z| > 1$ kpc. The galactic coordinates of the centre of the observed region are $l = 357°$; $b = -39°$. The stars were observed using the multi-object VLT (Very Large Telescope) spectrograph: Giraffe. They were observed using high resolution setups: HR13 ($R = 22500$) and HR14 ($R = 28800$). No metallicity nor kinematics selections were made, and the sample is dominated by dwarfs and turn-off stars.

The esorex library of the ESO pipeline was used to reduce the data, more precisely the *gimasterbias, gimasterdark, gimasterflat, giwavecalibration,* and *giscience* functions (GIRAFFE Pipeline Team, 2010, "GIRAFFE Pipeline User Manual", VLT-MAN-ESO-19500-3883).

Potential binaries and variable stars were rejected. Because no stellar parameters are available for the stellar sample, a version (coded in Java) of the stellar parameters determination software TGMET (Katz 2001) determines a first estimation of the parameters $T_{\rm eff}$, $\log g$, and [Fe/H]. These values are used as a first value for the SPADES algorithm (Posbic et al. 2012). The stellar parameters ranges are limited by those of the reference grid used. This excludes another part of the stars leaving 123 stars which parameters were determined. Figure 1 gives the distribution of the stellar sample stellar parameters.

Once the stellar parameters determined, the abundances of the stars in Calcium and Titanium are calculated.

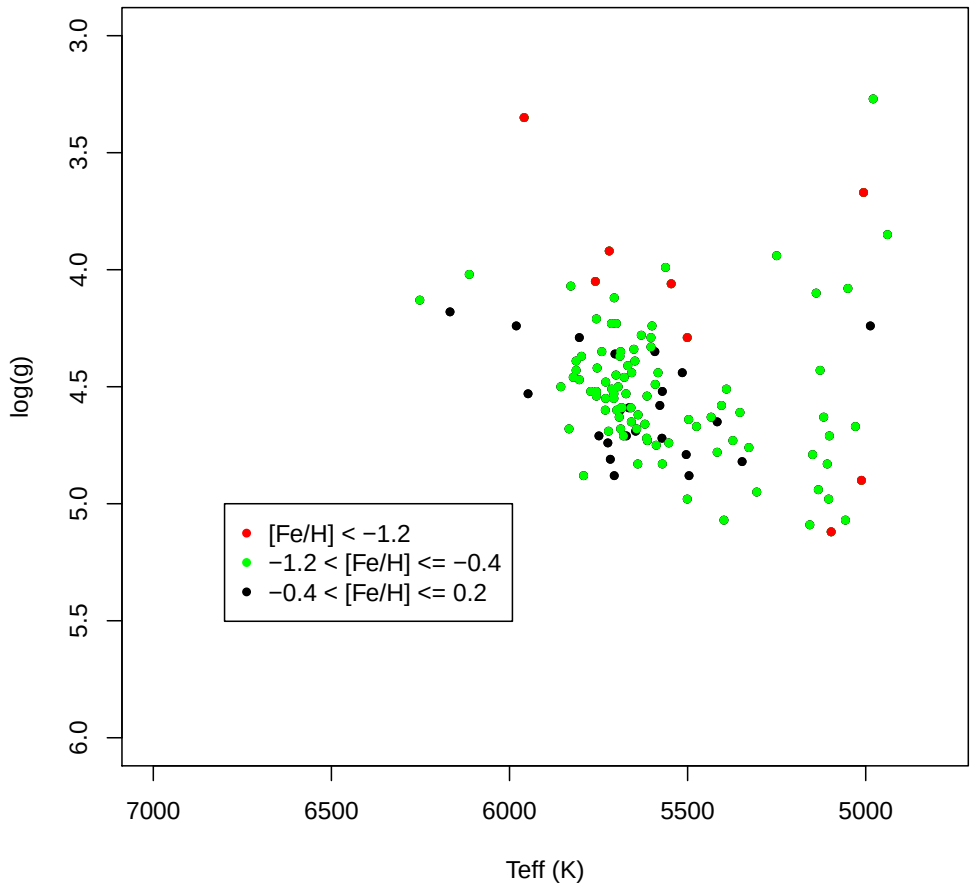

Fig. 1. The distribution of the stellar parameters of the final Giraffe stellar sample: the $T_{\rm eff}$ vs $\log g$ relation in [Fe/H] bins.

Offsets of $\Delta[Ca/Fe] = 0.073$ dex and $\Delta[Ti/Fe] = 0.08$ dex were applied to adjust our abundance scales to the scales of Takeda (2007). The offsets were derived from 5 S4N spectra (Posbic et al. 2012), analysed with SPADES and for which Takeda (2007) provide Ca, Ti and Fe abundances.

The distances (thus the galactic altitude $|Z|$) of the stars are calculated using an isochrones based method.

3 Results

The Metallicity Distribution Function was examined. The possible presence of a vertical metallicity gradient was assessed. To detect and quantify this gradient, the mean [Fe/H] by bins of $|Z|$ were calculated. The mean $|Z|$ of each bin as a function of the mean [Fe/H] of each bin are plotted in Figure 2 along with the calculated error bars. Once a linear regression is used, a mildly significant metallicity gradient with increasing $|Z|$ of a value of –0.19 ± 0.14 dex/kpc is calculated.

The relations between [Ca/Fe] (resp. [Ti/Fe]) and [Fe/H] both near ($|Z| < 1$ kpc) and at large distance ($1 \leq |Z|$ kpc) from the Galactic plane were analysed. These relations are plotted in Figure 3, in black for stars having $|Z| < 1$ kpc and in red for the stars at higher altitudes. No significant difference between the chemical trends inside ($|Z| < 1$ kpc) and outside ($1 \leq |Z|$ kpc) the solar neighbourhood can be detected.

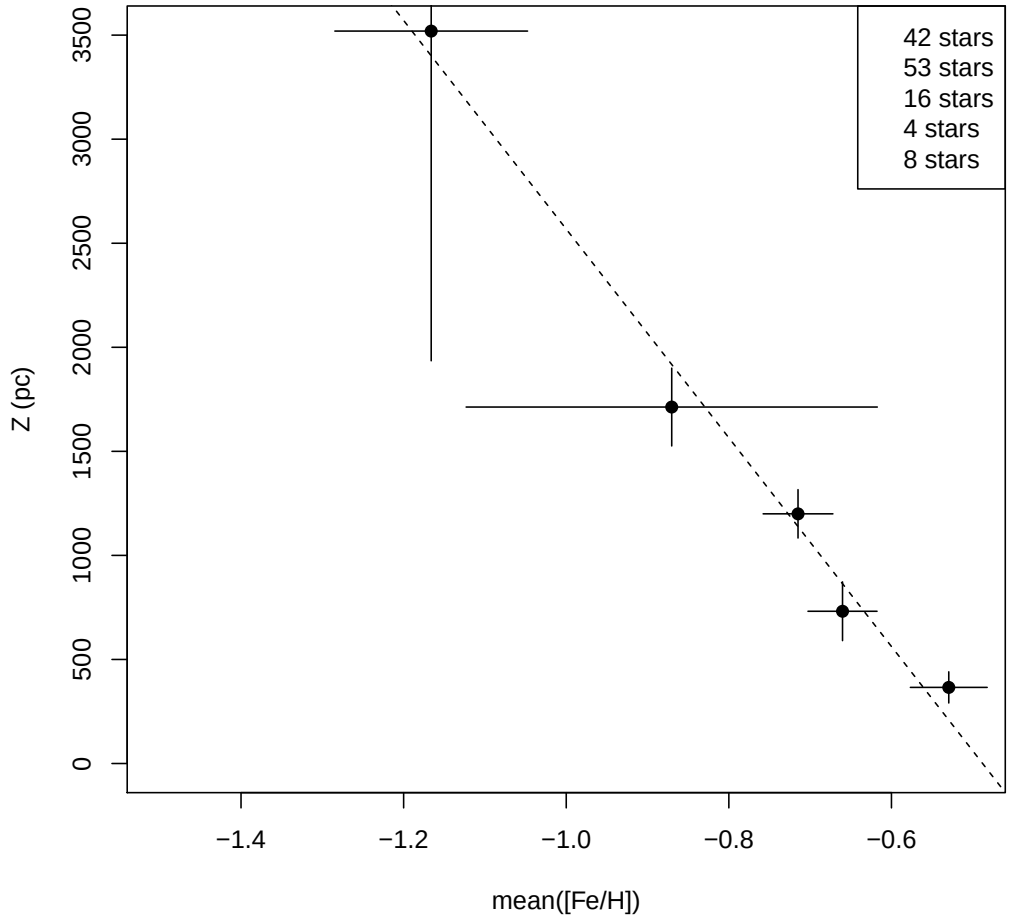

Fig. 2. The mean $|Z|$ of each bin as a function of the mean [Fe/H] of each bin.

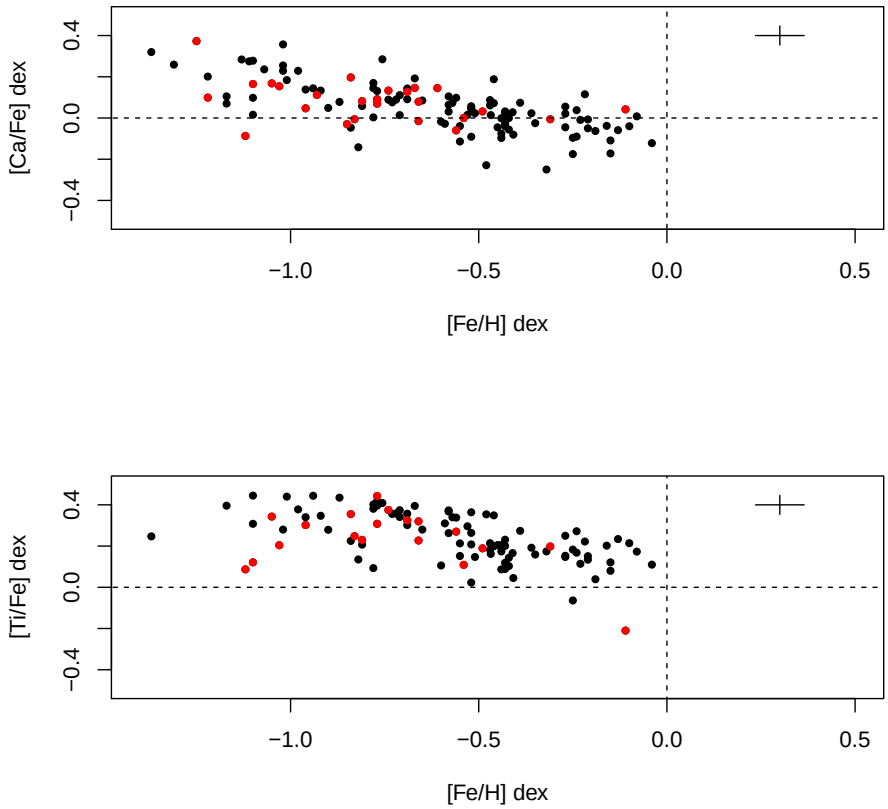

Fig. 3. $[Ca/Fe]$ versus $[Fe/H]$ (top) and $[Ti/Fe]$ versus $[Fe/H]$ (bottom), both near (|Z| < 1 kpc in black) and at large distance (|Z| ≥ 1 kpc in red) from the Galactic plane

Finally the results were confronted to different thick disk formation scenarios. The two constraints[i] considered together, favour (quasi-)monolithic collapse, gas-rich building blocs scenarios or dynamical heating by minor merger(s), while the vertical metallicity gradient would disfavour a thick disk formed of stars captured during a merger event.

The thesis during which this work was done was financed by the “Centre National de Recherches Scientifiques” (CNRS) and the “Centre National d’Etudes Spatiales” (CNES).

References

Abadi, M. G., Navarro, J. F., Steinmetz, M., & Eke, V. R. 2003, ApJ, 597, 21
Brook, C. B., Kawata, D., Gibson, B. K., & Freeman, K. C. 2004, ApJ, 612, 894
Gilmore, G. & Reid, N. 1983, MNRAS, 202, 1025
Katz, D. 2001, Journal of Astronomical Data, 7, 8
Posbic, H., Katz, D., Caffau, E., et al. 2012, A&A, 544, A154
Qu, Y., Di Matteo, P., Lehnert, M. D., & van Driel, W. 2011, A&A, 530, A10
Schönrich, R. & Binney, J. 2009, MNRAS, 396, 203
Takeda, Y. 2007, PASJ, 59, 335

[i]The suspected vertical gradient in the thick disk dominated sample, and the similarity between the abundance trends inside and outside the solar neighbourhood

SF2A 2012
S. Boissier, P. de Laverny, N. Nardetto, R. Samadi, D. Valls-Gabaud and H. Wozniak (eds)

SPECTROSCOPIC SURVEYS OF THE MILKY WAY AND THE SCIENTIFIC EXPLOITATION OF GAIA

A. Recio-Blanco[1]

Abstract. It is now one year until the launch of Gaia and spectroscopic surveys of the Milky Way are already a reality. This contribution tries to present the state of the art of ongoing and planned surveys by describing their targeted populations and spectral data properties. The importance of such Galactic Surveys for the scientific exploitation of the ESA Gaia mission is also highlighted.

Keywords: Stellar populations, Galaxy: stellar content, Gaia, Spectroscopic surveys.

1 Introduction

The advent of multiobject ground-based spectroscopy has opened new horizons in the era of Galactic Archaeology, initially driven by large photometric surveys and the preparation of the European Space Agency Gaia mission. Galaxy assembly, star formation histories, element-nucleosynthesis, cosmological initial conditions and fundamental physics have left their fingerprints in a high-dimensional parameter space constituted by spatial, kinematical and chemical distributions, plus their temporal gradients. Therefore, our understanding of the Milky Way history will always be ill-defined if only a few dimensions of that parameter space are probed.

As explained in Gilmore et al. (2012), there are four basic observational thresholds that we need to pass to have a complete view of the fossil record of our Galaxy formation and evolution. Fig. 1, taken and modified from Gilmore et al. (2012), shows the dimensionality of the data and parameter spaces, illustrating those observational challenges. The first step is source identification (or discovery) trough its position and photometric data. This is provided today by photometric surveys of the Galaxy like VISTA and VST. Secondly, the temporal domain is added, allowing us to explore a 5-dimensional space formed by parallaxes (and therefore distances) and proper motions (or transverse velocities). The Gaia mission will be revolutionary here by providing this 5-D view of the Galaxy for about one billion stars down to a magnitude of G=20. The third step is radial velocity, that allows to determine stellar orbits. Finally, if the spectral domain and resolution and the data quality are high enough, the stellar chemical abundances can be derived. Gaia, thanks to its Radial Velocity Spectrograph (RVS) will provide low resolution spectra for most stars brighter than 17th magnitude. This will allow the determination of the radial velocity, the global metallicity and whenever possible, the alpha-element abundance for several tenths of millions of stars (c.f. Fig. 3). Unfortunately, the Gaia RVS magnitude limit is three magnitudes brigther than that of astrometry and photometry. For this reason, the contribution of ground-based spectroscopic surveys is crucial in the two last observational thresholds mentioned above (radial velocity and detailed stellar chemistry). Galactic spectroscopic surveys will complement Gaia data to permit the high-dimensional view of the Milky Way, necessary to disentangle its evolution.

The general picture of on-going and planned spectroscopic surveys is presented in Fig. 2 by locating each project in a space formed by three axis: targeted galactic populations, spectral resolution and probed magnitude range. As the spectral resolution is usually fixed for a particular survey, each project appears as a plane in the above figure. The following sections will briefly descrive the characteristics of each survey, dividing them in low-resolution and high-resolution surveys. The projects for next generation halo surveys will be also mentioned in a separate section.

[1] Laboratoire Lagrange, UMR 7293, Université de Nice Sophia Antipolis, CNRS, Observatoire de la Côte d'Azur, BP 4229, 06304, Nice Cedex 4, France

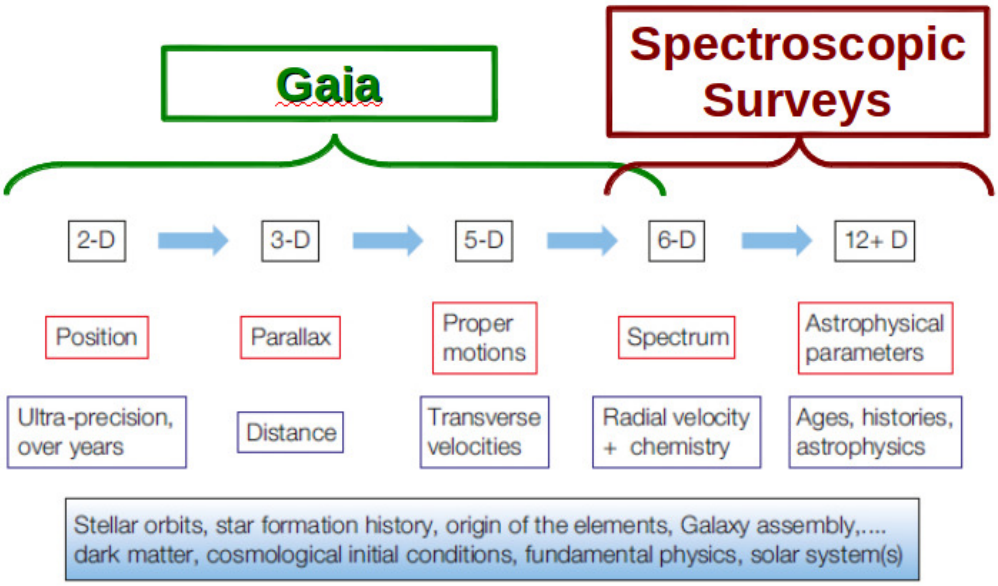

Fig. 1. Dimensionality of data and parameter spaces for Galactic Archaeology studies. The contribution of the Gaia mission and that of ground-based spectroscopic surveys is specified at the top of the picture. This figure has been taken and modified from Gilmore et al. (2012).

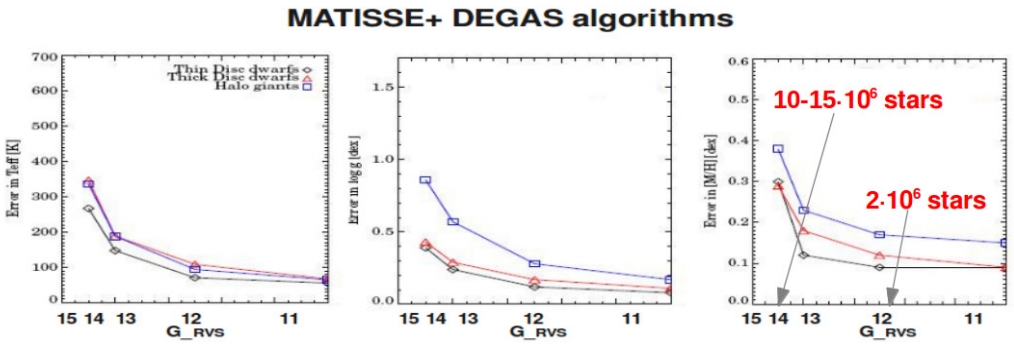

Fig. 2. Error estimations for the atmospheric parameter determinations from the Gaia/RVS spectra. The errors are taken from the results of the analysis algorithms MATISSE ((Recio-Blanco et al. 2006)) and DEGAS ((Kordopatis et al. 2011)) integrated in the analysis pipeline of the Gaia Data Processing and Analysis Consortium

2 Low-resolution surveys

The Sloan Digital Sky Survey (SDSS, (Eisenstein et al. 2011)) project, in its series of operations (SDSS I, II and III) has publised about 250K spectra from the Sloan Extension for Galactic Understanding and Exploration (SEGUE). SDSS spectra have provided only limited information on the structures revealed in the SDSS photometry, but they produced radial velocities measurements to ∼10-20 km/s and [Fe/H] abundances to 0.25 dex for stars with $14 < r < 19$ mag. SDSS3 stellar spectroscopy continues, at $\sim$ 5 stars/sq deg, as this project does not observe the Galactic thin disc and the Bulge. The spectral resolution of SEGUE data is R=1800. SEGUE has already provided several scientific results. One of the most recent ones regards the metallicity distribution of the disc ((Schlesinger et al. 2011)).

The RAdial Velocity Experiment (RAVE, (Steinmetz et al. 2009), (Steinmetz et al. 2006)) is obtaining accurate radial velocities (< 5 km/s) and global metallicities for $\sim 5{\cdot}10^5$ stars with I<13. RAVE spectra have a resolution of R=7500 and are centered in infrared CaII triplet, sharing the same spectral window of the future Gaia/RVS data. This project, due to its rather bright magnitude limit is probing essentially the galactic discs propulations. More than thirty papers have already been published up to date based to the RAVE survey and

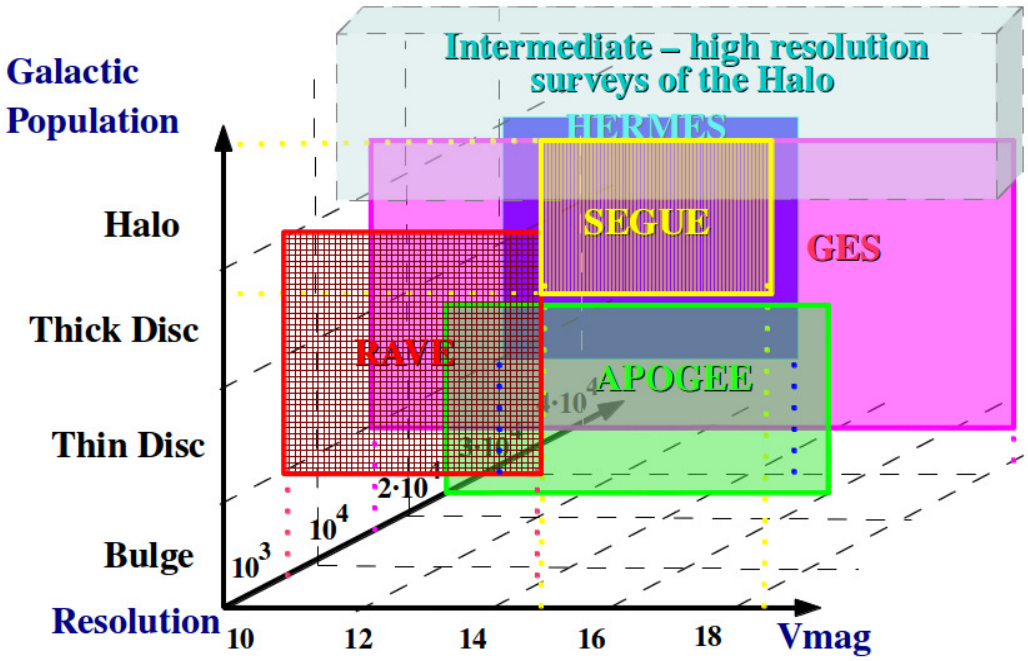

Fig. 3. General picture of on-going and planned spectroscopic surveys in a space formed by three axis: targeted galactic populations, spectral resolution and probed magnitude range.

the fourth data release is expected by the end of 2012.

Finally, the AAOmega Exploration of Galactic Structure (AEGIS) survey started end of 2011 will observe, during 45 nights accross 3 semesters, Thick Disc, Thin Disc and Halo substructures, plus extreme metal poor candidates. The spectral coverage includes a blue arm (370-570nm) at R∼3 000 and a red arm (830-885nm) at R∼11 000.

3 Intermediate and high-resolution surveys

Contrary to the low-resolution surveys started in the last decade, the recent intermediate and high resolution projects can provide the individual chemical abundances of the targeted stars. The chemical tagging approach ((Freeman & Bland-Hawthorn 2002)) can be used to associate stars to common ancient star-forming aggregates with similar abundance patterns or to to disrupting satellites.

The SDSS Apache Point Observatory Galactic Evolution Experiment (APOGEE, (Eisenstein et al. 2011)) is obtaining high-resolution (R=30 000) high signal-to-noise, H-band ($1.51\mu\text{m} < \lambda < 1.70\mu\text{m}$) spectra of 10^5 evolved, late-type stars. APOGEE will provide individual abundances for about 15 elements per star. Thanks to its infra-red observations, the APOGEE survey can probe Bulge and Thin Disc regions that are unaccesible to optical surveys. The spectrum analysis of the first APOGEE data are already producing the first scientific results ((Nidever et al. 2012)).

The Gaia-ESO Survey (GES, (Gilmore et al. 2012)) is a public spectroscopic survey began in January 2012 that will obtain high quality spectroscopy of some 100 000 Milky Way stars, in the field and open clusters, down to magnitude 19. GES employs the VLT FLAMES instrument to observe well-defined samples, based on current VISTA photometry for field stars. The survey will quantify the kinematic-multi-element abundance distribution functions of the Bulge, the Thick and the Thin Discs and the Halo stellar components, as well as a significant sample of 100 open star clusters, covering all accessible cluster ages and stellar masses. GIRAFFE spectra, with two settings (HR10 and HR21), will be obtained for statistically significant samples of stars in all major stellar populations. These will be supplemented by UVES spectra (R∼40 0000) of an unbiased sample of G-stars within 2 kpc of the Sun, providing the abundance distribution function for the local Thin Disc and Thick Disc. As shown in Fig. 4, the implication of the French comunity in the Gaia-ESO survey is very strong and it concerns several key working groups and one person of the Steering Committee. This is also reflected in the GES data-flow scheeme (Fig. 5), where the working groups with a French coordination or strong French

contribution are highlighted. More than 5 000 field stars and 7 open clusters have already been observed. The first semester data release will appear at the end of this year, including reduced 1-D spectra, associated variance spectra, radial velocities and variability information. In June 2013 is expected the firs advanced anual release with astrophysical parameters, element abundances, complementary data as appropriate, and uncertainties.

Finally, to begin observations in 2013, the Galactic Archaeology with AAO HERMES (GALAH) survey aims to obtain precision multi-element abundances for a milion stars with V<14, from high signal-to-noise, R=30 000 spectra. The HERMES-GALAH project will explore a chemical space of abundances of about 25 elements, with a dimensionality of 8 to 9. Most disc stars should inhabit a sub-region of this space.

Name			
Gerry Gilmore			
Sofia Randich			
M. Asplund			
J. Binney			
P. Bonifacio			
J. Drew			
S. Feltzing			
A. Ferguson			
R. Jeffries			
G. Micela			
I. Negueruela			
T. Prusti			
H-W. Rix			
A. Vallenari			
Target selection, Calibrators, FPOSS & OBs			
Open Clusters: membership analysis auxiliary data target selection	**WG1,2,4:** Alicante, Armagh, Torino, ETH, MSSL Vienna, MPIA, Palermo, Barcelona, Granada Bologna, Madrid (CAB), ESO, ESA, Geneva, AIP Herts, Arcetri, Uppsala, ROBelg, Leicester, Indiana, Graz, Lisbon, Grenoble Keele, IAC, Athens, Exeter, Birmingham Padova, Catania, Porto, Nice, ZAH	6	E. Alfaro (Sp) E. Paunzen (At) A. Bragaglia (I)
Galactic Plane & Field Selection	**WG3:** Camb, ZAH, ANU, MPIA, Paris, RUG, AIP, MSSL, Strasbourg, Oxford	4.5	C. Babusiaux (Fr)
Calibrators & Standards	**WG5:** AAO, AIP, Uppsala, Camb, Bordeaux Antwerp, Bologna, Madrid, Paris, MPA, ANU	1.5	E. Pancino (I)
OB/FPOSS generation: Field Survey Cluster Survey	**WG6:** Paris, ESO, Camb, Lund, AIP, ZAH Arcetri, Bologna, Catania, Padova, Palermo, IAC Exeter, Alicante, CAUP, ESO	2 2.5	T. Bensby (Se) E. Flaccomio (I)
Spectrum Extraction Pipelines			
Pipeline Raw Data: GIRAFFE Reduction UVES Reduction	**WG7:** CASU, Keele Arcetri	1 2	M. Irwin (UK) L. Morbidelli (I)
Radial Velocities	**WG8:** Camb, Keele, Arcetri, Antwerp, ZAH	2	Camb/Keele/Arcetri
Discrete Classification	**WG9:** Camb, MPIA, IAC, Madrid, MSSL, Porto, ZAH	2.5	S. Koposov (UK)
Spectrum analyses			
FGK Stars: GIRAFFE incl QC	**WG10:** Paris, MPA, Lund, Uppsala, Nice, Bordeaux Arcetri, Bologna, Liège, Geneva, Alicante Nice, ESO, Porto, ZAH, Arcetri, Naples Catania, Padova, Kaypten, IAC, ANU	17	A. Recio-Blanco (Fr) & C. Allende Prieto (Sp)
FGK Stars: UVES incl QC	**WG11:** Paris, MPA, Lund, Uppsala, Nice, Vilnius Arcetri, ANU, Bologna, AIP, Indiana, UCM, Herts Groningen, ESO, Naples, Porto, Catania, Alicante Catania, Padova, Liege, Bordeaux, ZAH, IAC, Chile	14	A. Korn (Se) & R. Smiljanic (ESO)
WG10/11 Interface	Recio-Blanco, Allende Prieto, Pasquini, Smiljanic, Korn, Hill	0.5	
Pre-Main-Sequence stars incl QC	**WG12:** Arcetri, Catania, IAA Naples, Palermo, ETH, CAUP Keele, Exeter, Madrid (UCM, CAB)	8	A. Lanzafame (I)
OBA Stars incl QC	**WG13:** Liege, RO Belg, AIP, OMA, Madrid, Paris Alicante, Uppsala, MPIA, ZAH, Leuven, Herts Calar Alto, Nice, IAA, Armagh	2	R. Blomme (Be)
Unusual Objects	**WG14:** SRON, Nijmegen, Warwick, Leuven	1	tbc
Survey Parameter Homogenisation	**WG15: & WG5:** all spectrum analysis groups	4	P. Francois (Fr)

Fig. 4. Management structure of the Gaia-ESO Survey. The French working group coordinators and the Steering Committee member are marked in pink.

4 Halo spectroscopic surveys

Probing the Galactic Halo with high enough statistics faces the obstacle of the low stellar density of the targeted fields. To tackle this problem, the used spectroscopic facilities need to have access to a wide field of view. For this reason, most of the on-going projects are not optimized for the Halo exploration, where most of the fossil substructure of Galactic formation is still hidden. Fortunately, several starting and planned surveys can change this situation.

The LAMOST survey is in transition from commissioning to full operations. It operates at a resolution of R∼1700, and will be able to observe very large numbers of Northern targets, including clusters, at intermediate magnitudes. It will provide radial velocities with a relatively low precision, but no element abundances.

In addition, several projects of multi-object spectrographs mounted in wide-field telecopes are today in a phase-A of study: the WHT Extreme Aperture Velocity Explorer (WEAVE, proposed for the William Herchel Telescope in La Palma); the 4-meter Multi-Object Spectroscopic Telescope (4-MOST, proposed for the NTT or VISTA) and the Multi-Object Optical and Near-infrared Spectrograph (MOONS, proposed for the Very Large Telescope).

5 Conclusions

Understanding how galaxies form and evolve in a ΛCDM universe needs both the observation of objects at high redshifts and the detailed examination of our Galaxy. The strenght of Galactic Archaeology relies in the possibility of analysing key physical processes that can not be accessed through the study of faint, poorly

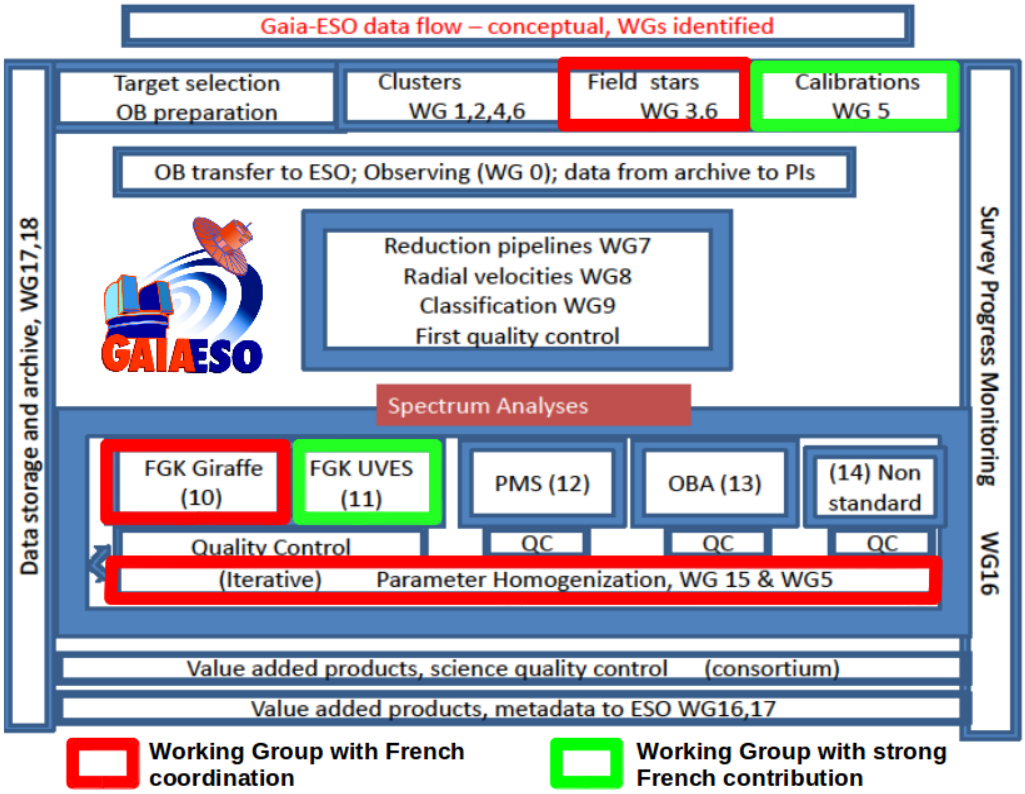

Fig. 5. Data flow of the Gaia-ESO Survey. The numbers of the corresponding working groups are indicated. The working groups with French coordination or important French contributions are highlighted.

resolved objects. In this sense, the contribution of the on going and planned spectroscopic surveys of the Milky Way is crucial for the fulfilment of the near-field cosmolgy approach.

I thank the organizers of this Sf2A meeting session for having invited me to give this contribution.

References

Eisenstein, D. J., Weinberg, D. H., Agol, E., et al. 2011, AJ, 142, 72
Freeman, K. & Bland-Hawthorn, J. 2002, ARA&A, 40, 487
Gilmore, G., Randich, S., Asplund, M., et al. 2012, The Messenger, 147, 25
Kordopatis, G., Recio-Blanco, A., de Laverny, P., et al. 2011, A&A, 535, A106
Nidever, D. L., Zasowski, G., Majewski, S. R., et al. 2012, ApJ, 755, L25
Recio-Blanco, A., Bijaoui, A., & de Laverny, P. 2006, MNRAS, 370, 141
Schlesinger, K. J., Johnson, J. A., Rockosi, C. M., et al. 2011, ArXiv e-prints (1112.2214)
Steinmetz, M., Siebert, A., Zwitter, T., & RAVE Collaboration. 2009, in IAU Symposium
Steinmetz, M., Zwitter, T., Siebert, A., et al. 2006, AJ, 132, 1645

SF2A 2012
S. Boissier, P. de Laverny, N. Nardetto, R. Samadi, D. Valls-Gabaud and H. Wozniak (eds)

ON THE NATURE OF FOSSIL STREAMS IN THE SOLAR NEIGHBOURHOOD OF THE MILKY WAY IN THE GAIA ERA

P. Re Fiorentin[1], A. Curir[1], M. G. Lattanzi[1], G. Murante[1,2] and A. Spagna[1]

Abstract. We seek signatures from the epoch of Galaxy formation, to provide insights about the chemodynamical processes that took place at the time of Milky Way formation. We produced a new kinematic survey based on spectro-photometric data from the Sloan Digital Sky Survey (SDSS) and high-quality proper motions derived from multi-epoch positions from the Guide Star Catalog II (GSC-II) data base, and used this survey to explore the solar neighbourhood of the Milky Way. We selected samples of subdwarfs within a few kpc of the Sun as tracers of the halo system. We find statistical evidence for discrete kinematic overdensities, possible accretion remnants, and compare this result to high-resolution N-body numerical simulations of the interaction between four dwarf galaxies and the Milky Way. The angular momentum distribution reveals that these imprints are possible fossil streams from low inclination retrograde and high inclination orbiting satellites. As the Gaia mission era is fast approaching, this knowledge will set the basis for future studies, and provide significant clues to constrain suggested scenarios for the formation and evolution of the Milky Way.

Keywords: Galaxy: formation, kinematics and dynamics, halo

1 Introduction

The formation and evolution of galaxies is one of the outstanding problems in astrophysics. In the context of hierachical structure formation, galaxies such as our own Milky Way grow by mergers and accretion of smaller sistems as dwarf galaxies: these satellite galaxies -torn apart by the tidal gravitational field of the parent galaxy - are progressively disrupted, giving rise to trails of stars along their orbit. After the accretion era ends, a spheroidal halo-like component may result in a more massive host galaxy.

Of all the Galactic components, the stellar halo offers the best opportunity for probing details of the merging history of the Milky Way. There is a real possibility to identify groups of halo stars that originate from common progenitor satellites (Eggen 1977; Ibata et al. 1994; Helmi et al. 1999; Harding et al. 2001; Morrison et al. 2009; Smith et al. 2009; Klement et al. 2009). However, recovering fossil structures in the solar neighborhood is considerably more difficult, as strong phase-mixing takes place.

This degeneracy can only be broken with 6-D (phase-space) or 7-D (including abundances) information achievable only by integrating astrometry, photometry, and spectroscopy. The SDSS and GSC-II Kinematic Survey is produced to serve this task (e.g., Spagna et al. 2010; Abazajian et al. 2009; Lasker et al. 2008). It provides accurate spectroscopic parameters (effective temperature, surface gravity, metallicity, and radial velocity), proper motions, and photometric distance estimates for about 27 000 FGK subdwarfs.

2 Methodology

Fossil signatures of galaxy formation can be found in the properties of high velocity stars in the inner regions of the halo, within a few kpcs from the Sun (Re Fiorentin et al. 2005). In what follows, we explore the solar neighbourhood with a stellar sample and with high resolution N-body numerical simulations of minor mergers, in order to detect and characterize such imprints.

[1] INAF - Torino Astrophysical Observatory, 10025 Pino Torinese (TO), Italy
[2] INAF - Trieste Astrophysical Observatory, 34143 Trieste, Italy

2.1 *Fossil streams in the stellar halo*

Among the sample of FGK subdwarfs from the SDSS-GSC-II Catalog, we selected samples of tracers of the Galactic halo population in the inner regions, and analyzed their full 7-D phase-space (kinematics and metallicity) distribution.

The left panel of Fig. 1 shows the kinematic distribution (velocity projections U versus W by way of illustration) of a sample of 2709 halo stars with [Fe/H] < -1.5 within 3 kpc from the Sun. Because of the strong phase-mixing that takes place in the inner halo, this distribution is relatively smooth; however, the kinematics of the highest velocity stars (highlighted as small red circles) already appears more clumped.

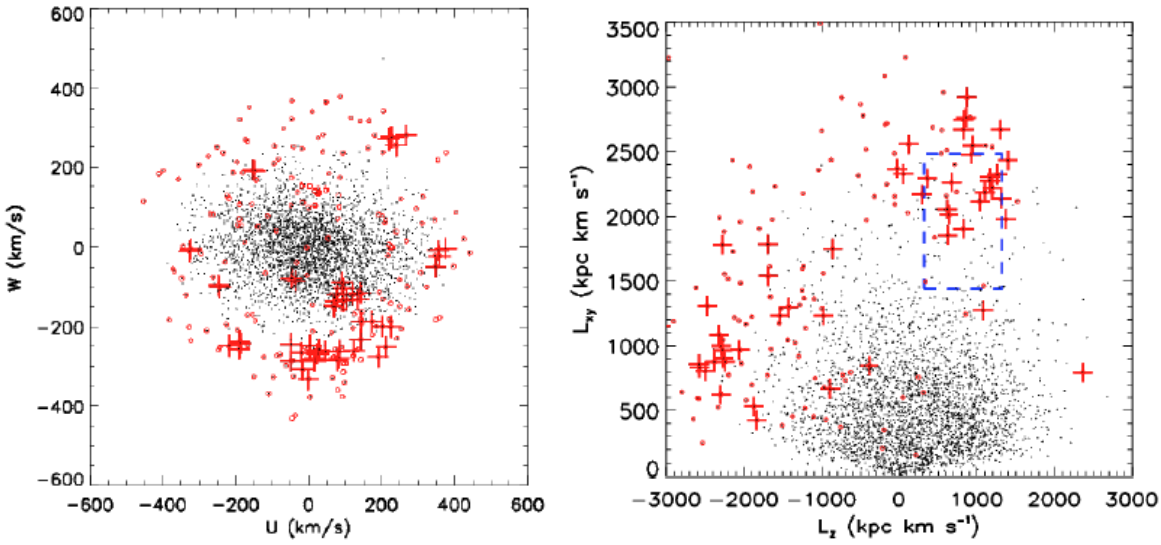

Fig. 1. Distribution of the selected halo stars (sample of 2709 elements with [Fe/H] < -1.5 and $d < 3$ kpc). The 5% fastest are highlighted (small circles). Among them, the crosses identify groups with velocity difference less than 42 km/s. **Left:** Velocity projection U vs. W. **Right:** Angular momentum components L_z vs. $L_{xy} = \sqrt{L_x^2 + L_y^2}$. As in Re Fiorentin et al. (2005), the box shows the locus of the halo stream discovered by Helmi et al. (1999).

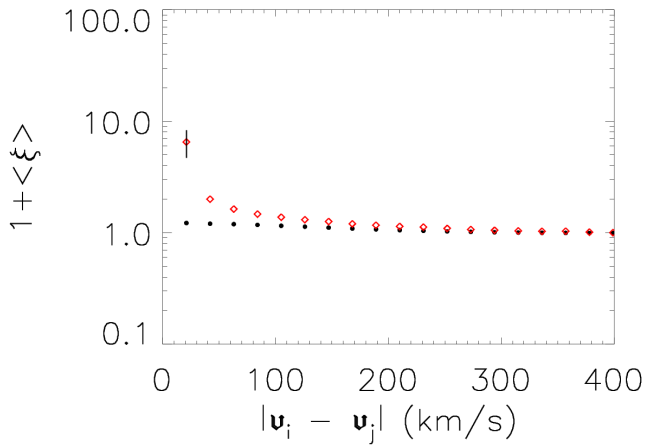

Fig. 2. Velocity correlation function for the full sample of halo stars (dots), and the 5% fastest-moving subset (diamonds) shown in Fig. 1.

The amount of kinematic substructures that remain in this volume is quantified by means of the two-point correlation function $\xi(\mathbf{v})$ on the pair velocity difference $|\mathbf{v}_i - \mathbf{v}_j|$, which measures the excess in the number of star pairs moving with a given velocity difference when compared to a representative random (smooth) sample (see Re Fiorentin et al. 2005, for more details). Stars with small velocity differences indicate the presence of

clumps/streams as objects with coherent kinematics (see Fig. 2). Among the subset of the 5% fastest stars, this signal is indeed very strong, and we find it is due to moving groups formed by those stars indicated by the crosses in Fig. 1.

This result is confirmed also in angular momentum space (see the right panel of Fig. 1), where the initial clumping of satellites should be present even after the system has phase-mixed completely.

2.2 *Fossil streams in the simulations*

In order to better understand these findings, and to study the formation of the Milky Way stellar halo system through accretion events, we use a set of high-resolution numerical N-body simulations which simulate minor mergers of prograde and retrograde orbiting satellite halos within a dark matter main halo (Murante et al. 2010).

For both the prograde mergers, in which the satellite co-rotates with the spin of the disk, and the retrograde mergers, with a counter-rotating satellite, we consider two orbits: a low-inclination orbit with a 10 degree tilt with respect to the disk plane, and a high-inclination orbit with a 60 degree tilt.

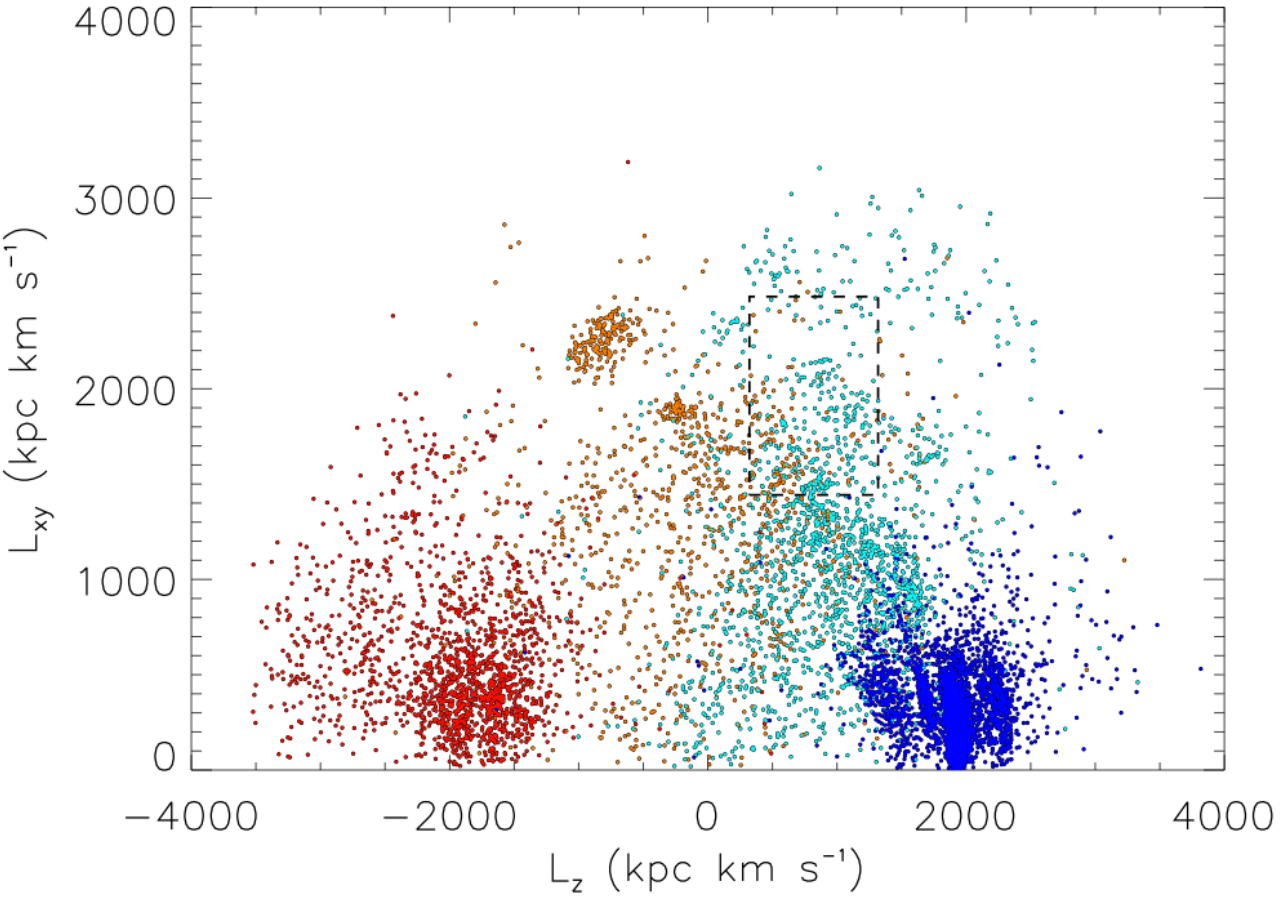

Fig. 3. Angular momentum distribution of the simulated Milky Way halo within 3 kpc of the Sun. Shown are 9471 particles accreted from four dwarf galaxies: 60 degree retrograde/prograde (orange/cyan), 10 degree retrograde/prograde (red/blue) satellites after interaction with the simulated Milky Way. The box has the same meaning as in Fig. 1.

After 4.63 Gyr (about 16 dynamical timescales of the main halo), once the four satellites have completed their merging with the primary halo, we select particles in a sphere of 3 kpc radius of the Sun, i.e. at 8 kpc from the Galaxy center, and analyze the signal left by the satellite stars.

Figure 3 shows how the debris of our four satellites are distributed in the angular momentum plane. The different colors indicate different progenitors: low-/high-inclination retrograde (red/orange), high-/low-inclination (cyan/blue) prograde satellites. Clearly, despite the chaotic build up of the parent halo, objects from accreted satellites remain strongly clumped in this space.

Any satellite is slowed down by dynamical friction exerted on it by disk and halo particles. In consideration of the drag force relation by Chandrasekar (1943), retrograde satellites are expected to suffer weaker dynamical friction with respect to prograde ones, since in the first case the velocity of the satellite is opposite to that of the disk and to the rotational velocities of the main halo particles. As a consequence, prograde orbits decay faster. This effect is even more evident for low-inclination orbits, and especially among the subsample of 5% fastest objects.

The regions of high inclination and low inclination counter-rotating mergers are well populated, consistent with observations (see again the right panel of Fig. 2), indicating that dynamical friction plays a significant role in the accretion events.

Future work will take into account how the current (e.g., SDSS-GSC-II) observations and Gaia-like observations will affect the distributions of debris of our four satellites (Re Fiorentin et al., in preparation). In the Gaia era we should indeed be able to retrieve the details of the various structures, allowing us to establish the number, as well as the characteristics, of the progenitors of the stellar halo.

3 Conclusions

We have found statistical evidence of substructure in the space motions of the fastest moving stars, due to a small number of moving groups that are strongly clustered in the angular momentum phase space. Investigation of the group members by their intrinsic properties (e.g., chemical abundance and orbits) suggest that they are possible fossil remnants of merging satellites with high inclination and low inclination retrograde orbits (cfr. Helmi et al. 1999; Klement et al. 2009, and Re Fiorentin et al. in preparation).

We have compared this result to high-resolution N-body numerical simulations of (four) minor mergers of orbiting dwarf galaxies: these satellites do appear very coherent in the local halo velocity distribution and angular momentum phase space. Among the subsample of the fastest objects, the regions of high inclination and low inclination retrograde orbits are well populated, consistent with the observations, and suggestive of the strong role played by dynamical friction in this process.

The solar neighborhood presents potentially a very large number of kinematic groups which are related to the various building blocks of the stellar halo. This implies that the merger history of the Galaxy may be unmasked in the very near future with surveys such as Gaia (e. g., Perryman et al. 2001; Turon et al. 2005; Gilmore et al. 2012, and for the latest news on the mission see `http://www.rssd.esa.int/Gaia/`), which will collect samples for millions of stars with very accurate positions and kinematics, and dramatically improve the reliability of such conclusions.

This work has been partially funded by ASI under contract to INAF I/058/10/0 (Gaia Mission - The Italian Participation to DPAC).

References

Abazajian, K. N., Adelman-McCarthy, J. K., Agüeros, M. A., et al. 2010, ApJS, 182, 543
Chandrasekar, S. 1943, ApJ, 97, 255
Eggen, O. J. 1977, ApJ, 215, 812
Gilmore, G., Randich, S., Asplund, M., et al. 2012, The Messenger, 147, 25
Harding, P., Morrison, H. L., Olszewski, E. W., et al. 2001, AJ, 122, 1397
Helmi, A., White, S. D. M., de Zeeuw, P. T., & Zhao, H. S. 1999, Nature, 402, 53
Ibata, R. A., Gilmore, G., & Irwin, M. J. 1994, Nature, 370, 194
Klement, R., Rix, H.-W., Flynn, C., et al. 2009, ApJ, 698, 865
Lasker, B. M., Lattanzi, M. G., McLean, B. J., et al. 2008, AJ, 139, 735
Morrison, H. L., Helmi, A., Sun, J., et al. 2009, ApJ, 694, 130
Murante, G., Poglio, E., Curir, A., & Villalobos, A. 2010, ApJ, 716, L115
Perryman, M. A. C., de Boer, K. S., Gilmore, G., et al. 2001, A&A, 369, 339
Re Fiorentin, P., Helmi, A., Lattanzi, M. G., & Spagna, A. 2005, A&A, 439, 551
Smith, M. C., Evans, N. W., Belokurov, V., et al. 2009, MNRAS, 399, 1223
Spagna, A., Lattanzi, M. G., Re Fiorentin, P., & Smart, R. L. 2010, A&A, 510, L4
Turon, C., O'Flaherty, K. S., & Perryman, M. A. C. eds. 2005, The Three-dimensional universe with Gaia, ESA Spec. Publ., 576

SF2A 2012
S. Boissier, P. de Laverny, N. Nardetto, R. Samadi, D. Valls-Gabaud and H. Wozniak (eds)

A NEW METHOD BASED ON MARKOV CHAINS FOR DERIVING SB2 ORBITS DIRECTLY FROM THEIR SPECTRA

J.-B. Salomon[1], R. Ibata[1], P. Guillout[1], J.-L. Halbwachs[1], F. Arenou[2], B. Famaey[1], Y. Lebreton[2], T. Mazeh[3], D. Pourbaix[4] and L. Tal-Or[3]

Abstract. We present a new method to derive orbital elements of double-lined spectroscopic binaries (SB2). The aim is to have accurate orbital parameters of a selection of SB2 in order to prepare the exploitation of astrometric Gaia observations. Combined with our results, they should allow one to measure the mass of each star with a precision of better than 1 %. The new method presented here consists of using the spectra at all epochs simultaneously to derive the orbital elements without templates. It is based on a Markov chain including a new method for disentangling the spectra.

Keywords: binaries: spectroscopic

1 Introduction

Double-lined spectroscopic binaries (SB2) form the basis of the least model–dependent methods used to derive stellar masses. Their orbital elements are employed to derive the products $\mathcal{M}_* \sin^3 i$, where $\mathcal{M}_*$ is the mass of a component and i is the inclination of the orbital plane. Therefore, when the inclination may be obtained from another technique, such as eclipse observations or astrometric measurements, the accuracy of the masses depends on that of the SB2 orbital elements.

The derivation of the elements of a spectroscopic orbit is usually based on the derivation of the radial velocities (RV) of the components from the blended spectra of the binary star. This is generally done by fitting one (Hill 1993) or two spectral templates to each spectrum (Zucker & Mazeh 1994). The approach is justifiable when the templates are similar to the actual spectra of the components, but otherwise the results are degraded by template mis-match.

Other methods do not use templates, but are based on the disentangling of the spectra (Simon & Sturm 1994; González & Levato 2006). The method presented hereafter falls into this category. It is Bayesian, since it is assumed that the radial velocities obey Keplerian motions, and the orbital elements are derived at the same time that the spectra are disentangled. It is based on Markov chains and on an new disentangling technique. The method is described in Sect. 2 hereafter. In Sect. 3, it is applied to HD 89 745.

2 A BiT MOrE with MCMC

A BiT MOrE with MCMC is an **A**lgorithm for **Bi**naries **T**o **M**atch **Or**bital **E**lements with **M**arkov **C**hain **M**onte **C**arlo. It combines a MCMC routine and a disentangling method.

[1] Observatoire Astronomique de Strasbourg, UMR 7550, 11, rue de l'Université, F-67000 Strasbourg, France
[2] GEPI, Observatoire de Paris-Meudon, F-92195 Meudon Cedex, France
[3] School of Physics and Astronomy, Raymond and Beverly Sackler Faculty of Exact Sciences, Tel Aviv University, Tel Aviv, Israel
[4] FNRS, Université libre de Bruxelles, CP226, boulevard du Triomphe, 1050 Bruxelles, Belgium

2.1 The MCMC method

Our method is based on a MCMC survey of model parameter space (see, e.g., MacKay 2003), which samples the free parameters and produces a posterior probability density function (PDF) for each dimension. To get that, the MCMC routine investigates randomly the space of parameters. Thus, it is well adapted for our case with 6 orbital elements (the systemic velocity is lost, see next section).

The MCMC algorithm requires an initial guess for the elements of the spectroscopic orbit: the amplitudes of the RV of the two components, the orbital period, the eccentricity, the epoch and the argument of the periastron. Subsequently, the MCMC routine solves the orbital equations to derive the RV for each time of observation.

2.2 The disentangling method

The goal of this step is to build a model from the orbital elements. For that, we developed a new spectral disentangling algorithm acting in Fourier space in order to extract each spectral component. It is different from iterative procedures like González & Levato (2006) or Hadrava (1995) because it does not use references line or least-square fitting.

Actually, the spectra (S) are the sum of the two components (M_A and M_B) which are shifted (δx_A and δx_B) according to their orbital RV at the time of observation j (equation 2.1).

$$S = M_A(x - \delta x_A^j) + M_B(x - \delta x_B^j) \tag{2.1}$$

The Doppler shift is used to disentangle the two components in Fourier space where the gap between each epoch is just a phase shift. The Fourier transform is calculated using Fast Fourier Transform techniques (e.g. Press et al. 1992). So, it is possible to determine, right from the initialisation step, M_A and M_B. Then, the two disentangled spectra are summed to obtain the model spectra. Note that information on the values of continua are lost in passing to Fourier space. Moreover, the systemic velocity is not derived because only RV shifts are involved.

2.3 Likelihood

Finally, the model is compared to the actual spectrum to test the likelihood of the solution. It is injected again at the beginning of the algorithm to find the next parameters. This procedure is reiterated until the Markov chain converges.

2.4 Validation

To validate our method, synthetic spectra have been built assuming a set of orbital elements. In order to be sure that the method is reliable, the computation was started assuming initial elements quite different from those used in the simulation. The algorithm was run to attempt to recover the input parameter values and their uncertainties.

3 Application

Our method was applied to a set of 11 spectra of HD 89 745, taken over 1785 days, corresponding to about 77 % of the period. These spectra arise out of a large observation program at the Haute-Provence observatory with the T193/Sophie (Halbwachs & Arenou 2009), and also from another program carried out with the same instrument (Halbwachs et al. 2012). This star was chosen for the number of spectra, although it appears somewhat atypical. In the past, it received 27 Coravel observations, and an orbit was derived after adding 7 Sophie spectra (Halbwachs et al. 2012). For this calculation, all the RV were derived from the cross-correlation function (CCF) of the spectra with a single mask or a simple template, the 1-mask technique. However, when the TODMOR algorithm was applied to a subset of 9 Sophie spectra, the two-template CCF yielded RVs quite different from those obtained with a single mask. The consequence was that the RV semi-amplitudes, K_1 and K_2, were quite different from the previous values: around 11 and 8 km s^{-1} instead of 7 and 11 km s^{-1}, respectively. The mass ratio of the binary is then changed from 0.62 to 1.30. If this discrepancy is due to a bias in the RV estimations obtained through a single template, one would expect to find it again with a disentangling technique.

A small wavelength range, just 3 orders, is taken into account between 5490.8 and 5787.9 Å to avoid telluric lines (for a the present assessment). All spectra have a good signal to noise ratio (higher than 50). The disentangling of the two components and their associated model are shown for one observation in Fig. 1. It was obtained after only 20 000 iterations in A BiT MOrE with MCMC. From the PDF (see Fig. 2), the uncertainties at one sigma around the best likelihood value can be obtained (listed in table 1).

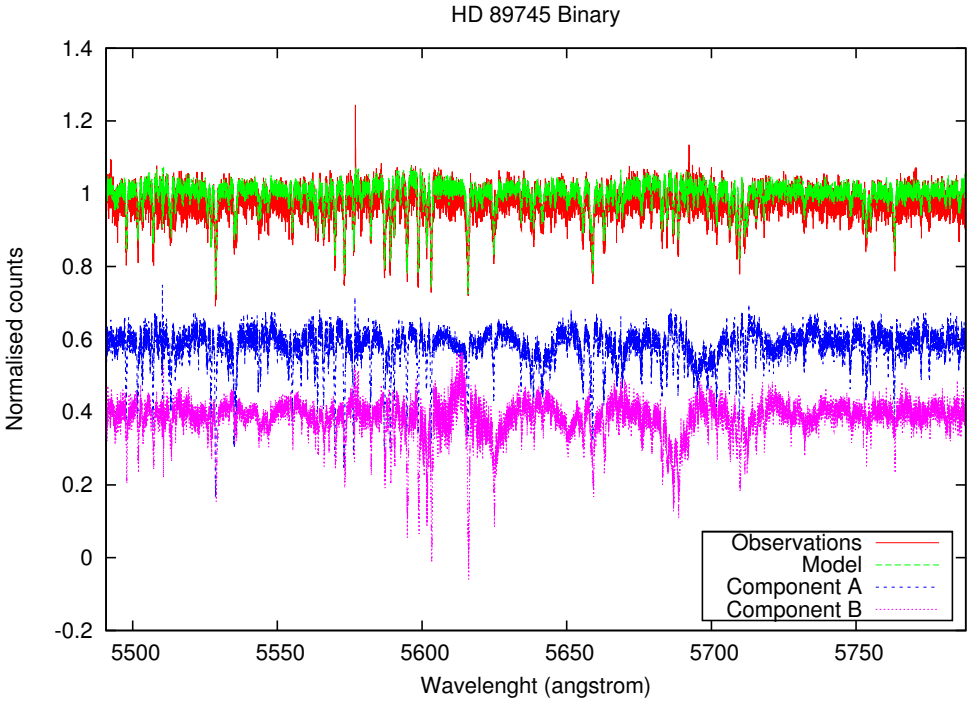

Fig. 1. Observation of HD 89 745 in red, component A in blue and B in pink, model built (sum of the two components) in green.

Table 1. Obital elements of HD 89 745 obtained by double peak cross-correlation, 1-mask technique (Halbwachs et al. 2012), column 1, by TODMOR, column 2 and by A BiT MOrE with MCMC, column 3. The elements cannot be compared since the input observations are different for each of the three techniques, see explanations in the text.

Orbital elements	Halbwachs et al. (2012)	TODMOR	A BiT MOrE with MCMC
K_1(km s^{-1})	6.983 ± 0.183	10.735 ± 0.137	$8.700^{+0.380}_{-1.641}$
K_2(km s^{-1})	11.184 ± 0.197	8.252 ± 0.146	$9.420^{+1.177}_{-0.250}$
e	0.3902 ± 0.0176	0.1197 ± 0.0120	$0.432^{+0.004}_{-0.099}$
P (jours)	2303.6 ± 10.5	$2555.684570 \pm 152.240479$	$2437.8^{+68.9}_{-87.1}$
T_0 (jours)	52093 ± 26.8	54405.2383 ± 176.9055	$52230.25^{+1.256}_{-239.426}$
ω (deg)	174.8 ± 4.8	175.03 ± 28.87	$142.5^{+12.3}_{-1.7}$
Other elements			
$M_1 \sin^3 i$ ($M_\odot$)	0.6876 ± 0.030	0.772649 ± 0.053345	$0.618^{+0.190}_{-0.018}$
$M_2 \sin^3 i$ ($M_\odot$)	0.4293 ± 0.022	1.005062 ± 0.068305	$0.640^{+0.014}_{-0.234}$

The values obtained with A BiT MOrE with MCMC are roughly in agreement with the previous values. We have large uncertainties due to the small number of spectra, the incomplete period coverage and the fact that only three orders are taken into account. However, we confirm that the mass ratio could be inversed, as found with the TODMOR reduction. It is worth noticing that this does not come from a permutation between the primary component and the secondary one, since the orbital elements T_0 and ω are in agreement with those found with the 1-mask technique. Nevertheless, these results are only preliminary and more observations are needed to draw reliable conclusions.

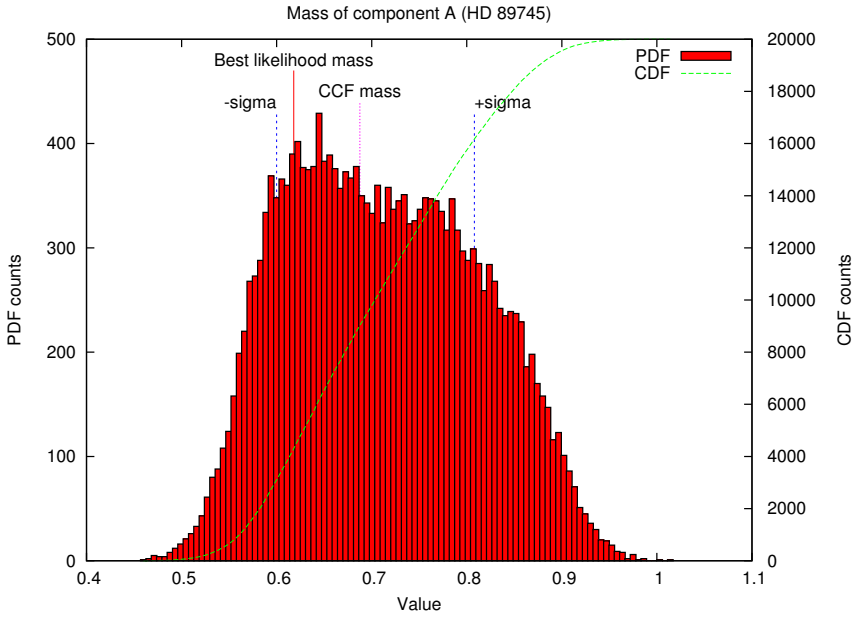

Fig. 2. Probability density function in red and cumulative density function in green of HD 89 745 component A mass ($\mathcal{M}_1 \times \sin^3 i$). The best likelihood value is indicated in red with its uncertainty in blue and the mass obtained by cross-correlation (Halbwachs et al. 2012) in pink.

4 Conclusion

The simulations have shown that A BiT MOrE with MCMC is a powerful new tool to perform orbital element calculations. This method should provide reliable orbital elements and recover the spectra of the individual stars at the same time.

We have also seen that the orbital elements obtained from a single template are only roughly consistent with those obtained when two templates are used or when the spectra are disentangled. For HD 89 745, using two templates and disentangling both leads to orbital elements rather different from those obtained from a single template, and we plan to derive a new orbit when more spectra become available.

However, more detailed investigations are required to compare the reliability of the three techniques considered here. This will be done in the future in order to obtain the most accurate masses when Gaia measurements are available.

Thanks to AS Gaia for functioning support. The observations were successful thanks to the help of the staff of the OHP. It is a pleasure to thank Eric Gosset for valuable discussions.

References

González, J. F. & Levato, H. 2006, A&A, 448, 283

Hadrava, P. 1995, A&AS, 114, 393

Halbwachs, J.-L. & Arenou, F. 2009, in SF2A-2009: Proceedings of the Annual meeting of the French Society of Astronomy and Astrophysics, ed. M. Heydari-Malayeri, C. Reylé, & R. Samadi, 53

Halbwachs, J.-L., Mayor, M., & Udry, S. 2012, MNRAS, 422, 14

Hill, G. 1993, in Astronomical Society of the Pacific Conference Series, Vol. 38, New Frontiers in Binary Star Research, ed. K.-C. Leung & I.-S. Nha, 127

MacKay, D. 2003, in Information Theory, Inference, and Learning Algorithms (Cambridge University Press)

Press, W. H., Teukolsky, S. A., Vetterling, W. T., & Flannery, B. P. 1992, Numerical recipes in FORTRAN. The art of scientific computing

Simon, K. P. & Sturm, E. 1994, A&A, 281, 286

Zucker, S. & Mazeh, T. 1994, ApJ, 420, 806

SF2A 2012
S. Boissier, P. de Laverny, N. Nardetto, R. Samadi, D. Valls-Gabaud and H. Wozniak (eds)

STATUS AND RESULTS FROM THE RAVE SURVEY

A. Siebert[1] and the RAVE collaboration

Abstract. RAVE, the RAdial Velocity Experiment, is a large spectroscopic survey which collects spectroscopic data for stars in the southern hemisphere. RAVE uses the AAO Schmidt telescope with a wavelength coverage similar to Gaia but a lower resolution of R = 7,500. Since 2003, RAVE collected over 500 000 spectra providing an unprecedented dataset to study the structure and kinematics of the Milky Way and its stellar populations. In this review, we will summarize the main results obtained using the RAVE catalogues.

Keywords: Surveys, Stars: kinematics and dynamics, Galaxy: general, Galaxy: stellar content, Galaxy: structure

1 The RAdial Velocity Experiment: overview and current status

Understanding the formation and evolution of galaxies is one of the main challenge of present day astronomy, and due to our location in its disc, the Milky Way offers a large amount of possibility to gain detailed insights on this subject. Progress on this topic more and more relies on the measurement of the six dimensions of the phase-space, positions and velocities, and the measurement of precise chemical abundances for stars in the Galaxy. The measurement of six dimensional phase-space requires the knowledge of the generally missing line-of-sight (LOS) velocity which is the primary goal of RAVE.

Taking advantage of multi-object spectroscopy which enables to acquire spectra for multiple stars simultaneously, RAVE started its observations in 2003. RAVE uses the 6dF instrument mounted on the Schmidt telescope of the AAO in Siding Spring, Australia. This instrument enables us to collect spectra for up to 150 stars in a 5.8 degrees in diameter field with a single observation. The targeted spectral region, $\lambda\lambda 8410 - 8794$, contains the infrared Calcium triplet and is similar to the wavelength domain chosen for Gaia. The effective resolution of $R \sim 7,500$ enables us to measure radial velocities with a precision better than 5 $\mathrm{km\,s^{-1}}$, the mode of the distribution being better than 2 $\mathrm{km\,s^{-1}}$. As of July 2012, RAVE collected more than 556 000 spectra for more than 468 000 individual stars. The distribution on the sky of the observed RAVE targets, as of June 2010, is shown in Fig. 1 and covers a large fraction of the sky accessible from the southern hemisphere.

So far, RAVE radial velocities and associated measurements have been released to the community in three data releases: DR1 (Steinmetz et al. 2006) provided LOS velocities for 25 000 stars covering 4 700 square degrees in the southern hemisphere, DR2 (Zwitter et al. 2008) released $\sim$ 82 000 LOS velocities and estimates of the atmospheric parameters for $\sim$ 21 000stars while DR3 (Siebert et al. 2011b) expended these numbers to 80 000 LOS velocities and atmospheric parameters for 40 000 stars. These catalogues are supplemented by catalogues providing distance estimates based on RAVE observations (Breddels et al. 2010; Zwitter et al. 2010; Burnett et al. 2011) which enable to estimate the six dimensional phase-space data of the targets and are also supplemented by a catalogue of chemical abundances by Boeche et al. (2011).

The three first data releases are based on an input catalog build using Tycho-2 and the Supercosmos Sky Survey (SSS). The next data release, DR4 (Kordopatis et al., in prep.), will release data using a new input catalogue based on DENIS I-band magnitudes and will provide improved atmospheric parameters using the DEGAS and MATISSE algorithms (Kordopatis et al. 2011; Bijaoui et al. 2012; Recio-Blanco et al. 2006).

In the next section we will review the contribution of RAVE to the study of the Milky Way and its stellar populations.

[1] Observatoire Astronomique de Strasbourg, Université de Strasbourg, CNRS, 11 rue de l'Université, 67000 Strasbourg, France

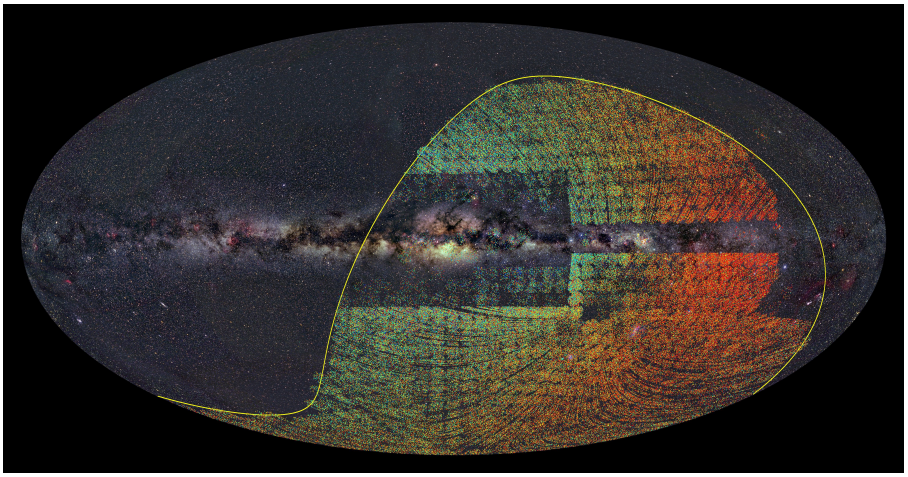

Fig. 1. Aitoff projection of the RAVE targets measured as of June 2010. The yellow line marks the location of the celestial equator. The colour follows the heliocentric line-of-sight velocity, red indicating a velocity larger than 50 km s^{-1}, blue lower than -50 km s^{-1}. The apparent dipole reflects the motion of the Sun with respect to the local standard of rest.

2 Scientific contribution of RAVE

The depth and spatial coverage of the RAVE survey makes it a well suited tool to study the structure and stellar populations of the Milky Way. Indeed, the bulk of RAVE stars samples the Galaxy at distances intermediate between Hipparcos (the solar neighbourhood) and the galactic halo which is well covered by the SDSS. Although RAVE was designed to search for the signatures of the hierarchical build-up of the Milky Way, its design and coverage proved to be useful to study many aspects of the Galaxy. Indeed, this region, between 0.5 and 2 kpc from the Sun, is dominated by the thin disc with an increased contribution of the thick disc. In the following presentation of RAVE results we will try to group the results according to some general topics: structure and kinematics of the Milky Way, origin of the thin and thick discs, moving groups, accretion events and peculiar objects.

2.1 Structure and kinematics

The first RAVE catalogue was released in 2006 and the first scientific result using the RAVE data followed shortly after with a new determination of the local escape velocity of the Milky Way by Smith et al. (2007). Their findings of $v_{esc} = 544$ km s^{-1} ($498 < v_{esc} < 608$ km s^{-1} at the 90 % confidence level), based on a sample of high-velocity stars from RAVE combined to previously published data, demonstrates the presence of a dark halo in the Milky Way. Furthermore, assuming a contracted NFW halo model, this result implied a virial mass of $1.42^{+1.14}_{-0.54} \times 10^{12}$ $M_\odot$, significantly higher than previous estimates.

Then Siebert et al. (2008), using a sub-sample of red clump giants whose distance can be estimated from the photometry alone, measured the inclination of the velocity ellipsoid at 1 kpc below the Galactic plane. This inclination, or tilt, is directly linked to the shape of the Galactic potential and of the dark halo. This measurement (7.3 degrees) was compared to predictions varying the flattening of the dark halo and using the latest mass models of the Milky Way by Binney & Tremaine (2008). Although no model could be clearly ruled out, a nearly spherical halo at the Sun's distance from the Galactic center is preferred. This also implies the scale length of the disc to be in the range 2.5-2.7 kpc.

Focusing on the disc, its vertical structure was studied by Veltz et al. (2008). In this work, the authors combined a subsample of RAVE G and K type stars towards the Galactic pole to 2MASS stars counts and UCAC2 proper motions. They were able to identify discontinuities in the kinematic and magnitude counts, discontinuities that separate the different stellar components. The clear kinematic gap between the thin and thick disc reinforced the view that the thick disc is unlikely to have formed from the thin disc in a continuous process. This work also provided new measurements of the scale heights of the thin and thick disc, the thin disc scale height being measured to be 225 ± 10 pc, and 1048 ± 36 pc for the thick disc.

Casetti-Dinescu et al. (2011) combined a sub sample of 4400 red clump giants from the RAVE DR2 catalogue with the SPM4 (Girard et al. 2011) proper motions to analyse the three-dimensional kinematics of the thick

disc population. This sample covers distances from 5 to 10 kpc from the Galactic center and reaches 3 kpc in height from the Galactic plane. They determined the global kinematic parameters of the thick disc to be $(\sigma_{V_R}, \sigma_V, \sigma_{V_z})|_{z=1} = (70.4, 48.0, 36.2) \pm (4.1, 8.3, 4.0)$ km s^{-1}, with a tilt angle of 8°. This latter value is in agreement with the determination by Siebert et al. (2008) and implies a disc scale length of 2 kpc.

Also, for a good understanding of the Milky Way, a precise knowledge of the Sun velocity vector with respect to the local standard of rest is important. This problem was studied by Veltz et al. (2008) using his model of the vertical structure of the Galactic disc and by Coşkunoğlu et al. (2011). This latter work uses a sub-sample of RAVE stars restricted to 600 pc from the Sun, based on the photometric and spectroscopic properties of the stars. Their findings are in good agreement with recent determinations (see table 1 of Coşkunoğlu et al. 2011, for a summary).

If star counts and velocity distributions are useful to decipher the global properties of the Milky Way, detailed measurements of the structure and kinematics of the stellar populations need the knowledge of the distance. Distances not only allow us to recover the full velocity vector of a star, they also allow us to sample different regions of the Galaxy (Siebert et al. 2008; Casetti-Dinescu et al. 2011, see for example). If red clump stars have proved to be a precious tool for such investigations, they represent only a small fraction of the RAVE catalogues. Thanks to the estimates of stellar atmospheric parameters, spectrophotometric distances could be computed for most of the RAVE stars by three different groups (Breddels et al. 2010; Zwitter et al. 2010; Burnett et al. 2011) with an overall very good agreement between the groups while the techniques rely on different assumptions.

The availability of distances allow a more detailed analysis of the fine structures in the disc but also allows to reduce the uncertainties on the global parameters. For example, Karataş & Klement (2012) revised the thin and thick discs velocity ellipsoid measurements using the Breddels et al. (2010) distances and found an overall good agreement with previous determinations. Siebert et al. (2011a) used the Zwitter et al. (2010) distance estimates to study the mean velocity field in the Galactic plane within 2 kpc from the Sun. They found a radial velocity gradient whose origin lies presumably in non-axisymmetric perturbations of the disc. Assuming the local disc is mostly perturbed by spiral arms, Siebert et al. (2012) used the density wave model to model the observed velocity field and constrain the parameters describing the local spiral pattern. Provided the spiral arms are long-lived, the density wave model with a 2 armed spiral perturbation succesfully reproduces the observed velocity gradients and Siebert et al. (2012) estimate the amplitude of the perturbation to be 0.55% of the background potential, having a pattern speed of 18.6 km s^{-1}. This places the Sun close to the inner 4:1 resonance, a location also suggested by the location of moving groups in the solar neighbourhood (Quillen & Minchev 2005, see for example).

2.2 Origin and evolution of the thin and thick discs

The origin and evolution of the Galactic discs are key elements in understanding the formation of the Milky Way. This information about the origin is buried both in the kinematics and in the chemical composition of the stars, such as metallicity gradients or eccentricity distributions, both being available via data provided in the RAVE catalogues.

Focusing on the thick disc chemical properties, Ruchti et al. (2010) selected a sample of 234 metal poor giants in the RAVE catalogue for a follow-up study using high-resolution spectroscopy. A detailed abundance analysis of four α elements and iron abundances revealed an enhancement of the [α/Fe] ratios as well as a lack of scatter of these ratios. This implies an enrichment that proceeded by purely core-collapse supernovae as well as a good mixing of the interstellar medium (ISM) prior to star formation. Also the ratios indicate a similar massive star initial mass function of the metal poor thick disc and of the halo. This leads the authors to conclude that direct accretion of a dwarf galaxy with similar properties than the surviving dwarf galaxies today did not play an important role in the formation of the thick disc population.

Ruchti et al. (2011a) furthered this work adding 74 main sequence stars to their sample of giant stars and confirmed their previous result. In addition they could investigate for the first time the gradient in α-enhancement in the metal poor thick disc, finding a very shallow gradient ($\partial[\alpha/\mathrm{Fe}]/\partial R, z < 0.03 \pm 0.02$ dex kpc^{-1} for [Fe/H] < -1.2 dex) while they find a $+0.01 \pm 0.04$ dex kpc^{-1} radial gradient and a -0.09 ± 0.05 dex kpc^{-1} vertical gradient in iron abundance. This further indicates a good mixing of the ISM prior to star formation for this population.

The previous work focused on the properties of the metal-poor thick disc, similar studies used thin disc stars to constrain the observed metallicity gradient using the RAVE catalogue (Karataş & Klement 2012; CoşkunoğLu et al. 2012; Bilir et al. 2012) with values for the radial gradient ranging from -0.04 to -0.07 dex kpc^{-1}. Also, a dependence with age, older populations showing a shallower radial gradient is observed. The comparison to

models of the formation of the Galactic disc suggests a contribution from stellar migration in the shaping of the disc.

Another aspect of the disc formation relies on the distribution of eccentricities. As shown by Sales et al. (2009), different scenarios of the thick disc formation leave different signatures in the distribution of eccentricities of disc stars. This signature has been investigated by different groups using the RAVE data: Casetti-Dinescu et al. (2011) used red clump stars from the DR2, Karataş & Klement (2012) did the same exercice using the DR2 sample together with Breddels et al. (2010) distances and Wilson et al. (2011) used the full RAVE sample. All studies favour an in-situ formation of the thick disc, the direct accretion scenario being in apparent contradiction with the observed distributions. The good agreement with the result based on chemical abundances and metallicity gradients further confirms the in-situ origin of the thick disc.

2.3 Moving groups

Since their discovery (Eggen 1958, 1960), moving groups have been the subject of many studies. If some of the moving groups can be associated to disrupted clusters, some of them are of resonant origin and it is now well established that the location in velocity space of these resonant structures bear useful informations on the perturbations taking place in the Galactic disc.

A first attempt to study the moving groups using the RAVE DR1 data was done by Klement et al. (2008) and continued in a later work using the DR2 catalogue (Klement et al. 2011). In these works, the authors identified four phase-space overdensities, three of which were previously known. The new stream candidate is on a radial orbit, suggesting an origin external to the Milky Way. However, their later work using DR2 data showed that only five stars belong to that overdensity, preventing clear conclusions to be drawn at this point on the origin of this overdensity.

Kiss et al. (2011) searched the RAVE database for new members of young nearby moving groups, combining the RAVE data to stellar age diagnostics and high-resolution optical spectroscopy follow-up. They were able to find one new and five likely members of the β Pictoris moving group, one likely member of the ϵ Cha group and two stars in the Tucana-Horologium association, showing the potential of RAVE to increase the census of young moving groups in the solar neighbourhood.

Hahn et al. (2011) combined data from RAVE and the Sloan Digital Sky Survey to extract a sample of stars within 200 pc of the Sun. They showed that the velocity space structures seen in the Hipparcos sample are also present in these data. They also could associate the Hyades stream to scattering process at a Lindblad resonance, indicating a resonant origin for this feature.

Thanks to the distance estimates mentionned above, it is possible to reconstruct the six-dimensional phase space information and study the evolution of the moving groups beyond the solar neighbourhood. Antoja et al. (2012) used the full RAVE sample together with distances and used a wavelet analysis to detect the moving groups. They showed that the main groups observed in the solar neighbourhood are large scale features, surviving at least 1 kpc from the Sun in the anti-rotation direction and below the Galactic plane. Furthermore, the location of these structures appears to shift in the velocity plane as one moves away from the Sun's location. These trends are consistent with dynamical models of the effects of the bar and spiral arms, again indicating a resonant origin of some of the moving groups.

2.4 Signature of accretion events

One of the main driver of the RAVE survey is the search for signatures of the hierarchical build-up of the Milky Way. Although most of the accretion events are observed in the distant halo (see for example Belokurov et al. 2006), some are believed to leave traces in the inner parts of galaxies including galactic discs. Indeed, the early simulations of the disruption of the Sagittarius dwarf galaxy predicted that the Sagittarius stream could cross the solar neighbourhood. Such an orbit would leave an asymmetry in the radial velocity distributions between the northern and southern hemisphere. Seabroke et al. (2008) analysed the RAVE data in a cylinder across the disc centered on the Sun and combined this sample to the local surveys from the Hipparcos satellite (Holmberg et al. 2007; Famaey et al. 2005). The symmetry of the velocity distributions permits to rule out the presence of the Sagittarius stream or the Virgo overdensity in the solar neighbourhood. Later simulations of the disruption of the Sagittarius dwarf galaxy showed that the stream does not cross the solar neighbourhood, intersecting the Galactic plane further out from the Sun's location, confirming this result.

More recently, Williams et al. (2011) detected an overdensity of stars, the Aquarius stream, in $30^\circ < \ell < 75^\circ$ and $-70^\circ < b < -50^\circ$, with heliocentric line-of-sight velocities $V_{los} \sim -200$ km s^{-1}. These stars are clear

outliers in the radial velocity distribution and the overdensity is statistically significant. Analysis of the RAVE stars suggest a metal poor, 10 Gyr old population. Using numerical simulations, they showed that this stream is dynamically young and therefore a debris of either a recently disrupted dwarf galaxy or globular cluster. High resolution follow-up spectroscopy of the overdensity members by Wylie-de Boer et al. (2012) showed very little dispersion in metallicity (0.1 dex) indicating a chemicaly coherent structure. The location in the nitrogen and sodium abundances plane further indicates that the Aquarius stream originates from a disrupted globular cluster.

2.5 Peculiar objetcs

The observing strategy of RAVE, a random sampling in magnitude intervals and no colour selection to mimic a magnitude limited survey, enables RAVE to be unbiased with respect to kinematic selection effects. If this strategy is well suited to the main goals of RAVE, it also preserves the discovery potential of RAVE.

Munari et al. (2009) paper is a good example of this discovery potential. Mining the database, the authors discovered stars in the multi epoch spectra of RAVE whose radial velocities and spectra appear dubious for normal Milky Way objects. These stars do not belong to the Milky Way but are Luminous Blue Variable stars (LBV) part of the Large Magellanic Cloud (LMC). Additional specific follow-up exposures were then taken one year appart for seven LBVs, including fainter known LBVs, to obtain a fairly complete sample of LBVs in the LMC. Thanks to the multi epoch spectra, the wind outflow and variability could be investigated in some cases and even cool companions could be detected.

Ruchti et al. (2011b) identified five lithium rich field giants in his metal poor sample of RAVE stars, RAVE being quite rich in metal poor stars as shown by Fulbright et al. (2010). This represents the largest sample of Li-rich giants to date, these objects being rare and important to understand the structure and physical processes taking place in stellar interior. A detailed investigation of the chemical abundances by the authors suggests that Lithium enrichement in these stars is due to cool bottom processing, a different mechanism than the one taking place at the RGB bump.

Among peculiar objects, binary stars are not uncommon and the knowledge of the fraction of stars in binary or multiple systems is an important input of Galactic models. In this respect, identifying multiple stars in the RAVE database is important. Using a method relying on the properties and shape of the cross-correlation function, Matijevič et al. (2010) were able to identify 123 double-lined binary candidates (SB2) in the second data release of RAVE, only eight of which were previously known as binary stars in Simbad. This method is sensitive to systems with orbital periods of 1 day up to 1 year. In a following paper, Matijevič et al. (2011) used repeated observations of RAVE stars to identify single-lined binary candidates (SB1). In this sample of $\sim$ 20000 stars observed more than once, about 10 to 15% of the stars are detected as binaries. Because of the time span between observations, the detection is biased towards short periods (days to weeks). Therefore the binary fraction reported is a lower limit to the true binary fraction which is the important quantity for Galactic models.

If the analysis of the cross-correlation functions and of the re-observations are efficient tools to detect binary stars, automated classification of RAVE spectra shows a remarkable ability to detect peculiar objects. Matijevič et al. (2012) used a local linear embedding technique (LLE) to automatically classify 350 000 RAVE spectra. If 90 to 95% of the spectra belong to normal single stars, there is a significant fraction of peculiar stars populated by the different types of spectroscopic binaries, chromospherically active stars (both of them containing several thousand spectra) or other peculiar objects. Among these peculiar objects one can note TiO band stars, carbon stars, Wolf-Rayet stars, Be stars etc. This shows the large potential of RAVE to increase the statistics and further the understanding of these rare objects.

Finally, if RAVE observing strategy away from the Galactic plane is meant to reproduce the characteristics of a magnitude limited sample, some fields were observed in the Galactic plane for calibration purpose or specific projects. The study of Diffuse Interstellar Bands (DIB) falls in this last category. Munari et al. (2008) investigated the behaviour of five DIBs in the RAVE spectra. They could confirm the presence of a DIB at 8648Å whose intensity appears unrelated to reddening. The two DIB at 8531 and 8572Å appear to be artifacts due to blends of underlying stellar lines while the DIB at 8439Å could not be resolved due to the strong underlying Paschen line. However the DIB at 8620Å appears strong and clean in the RAVE spectra and turns out to be a reliable estimator of reddening.

3 Conclusions

RAVE operations started in 2003 and collected over half a million spectra since its first light. So far data were released to the public in three data releases and complemented by catalogues containing distance estimates and chemical abundances. The fourth data release is scheduled in late 2012/early 2013.

If RAVE primary goal is to search for traces of the hierachical build-up of the Milky Way, the design of the survey does not restrict the scientific capabilities of the survey. Indeed, RAVE observations contributed to many topics in Galactic astronomy and provided useful measurements and results that can be grouped in five general topics:

- structure and kinematics of the Milky Way and stellar populations,
- formation and evolution of the Galactic discs,
- velocity space substructures or moving groups,
- signature of accretion events,
- search for peculiar objects.

If the data collection is close to completion, the vast amount of information buried in the RAVE catalogues and spectra still has a large potential for being used by the community. In this respect comparison to models of the Galaxy, such as the Besançon model (Robin et al. 2003) or the Galaxia model (Sharma et al. 2011), will be useful to interpret the RAVE data. This makes RAVE one of the major tools for understanding our Galaxy until the release of the Gaia catalogue.

Funding for RAVE has been provided by: the Australian Astronomical Observatory; the Leibniz-Institut fuer Astrophysik Potsdam (AIP); the Australian National University; the Australian Research Council; the French National Research Agency; the German Research Foundation (SPP 1177 and SFB 881); the European Research Council (ERC-StG 240271 Galactica); the Istituto Nazionale di Astrofisica at Padova; The Johns Hopkins University; the National Science Foundation of the USA (AST-0908326); the W. M. Keck foundation; the Macquarie University; the Netherlands Research School for Astronomy; the Natural Sciences and Engineering Research Council of Canada; the Slovenian Research Agency; the Swiss National Science Foundation; the Science & Technology Facilities Council of the UK; Opticon; Strasbourg astronomical Observatory; and the Universities of Groningen, Heidelberg and Sydney. The RAVE web site is at `http://www.rave-survey.org`

References

Antoja, T., Helmi, A., Bienayme, O., et al. 2012, MNRAS, L499
Belokurov, V., Zucker, D. B., Evans, N. W., et al. 2006, ApJ, 642, L137
Bijaoui, A., Recio-Blanco, A., de Laverny, P., & Ordenovic, C. 2012, Statistical methodology, 9, 55
Bilir, S., Karaali, S., Ak, S., et al. 2012, MNRAS, 421, 3362
Binney, J. & Tremaine, S. 2008, Galactic Dynamics: Second Edition (Princeton University Press)
Boeche, C., Siebert, A., Williams, M., et al. 2011, AJ, 142, 193
Breddels, M. A., Smith, M. C., Helmi, A., et al. 2010, A&A, 511, A90
Burnett, B., Binney, J., Sharma, S., et al. 2011, A&A, 532, A113
Casetti-Dinescu, D. I., Girard, T. M., Korchagin, V. I., & van Altena, W. F. 2011, ApJ, 728, 7
CoşkunoğLu, B., Ak, S., Bilir, S., et al. 2012, MNRAS, 419, 2844
Coşkunoğlu, B., Ak, S., Bilir, S., et al. 2011, MNRAS, 412, 1237
Eggen, O. J. 1958, MNRAS, 118, 65
Eggen, O. J. 1960, MNRAS, 120, 563
Famaey, B., Jorissen, A., Luri, X., et al. 2005, A&A, 430, 165
Fulbright, J. P., Wyse, R. F. G., Ruchti, G. R., et al. 2010, ApJ, 724, L104
Girard, T. M., van Altena, W. F., Zacharias, N., et al. 2011, AJ, 142, 15
Hahn, C. H., Sellwood, J. A., & Pryor, C. 2011, MNRAS, 418, 2459
Holmberg, J., Nordström, B., & Andersen, J. 2007, A&A, 475, 519
Karataş, Y. & Klement, R. J. 2012, New A, 17, 22
Kiss, L. L., Moór, A., Szalai, T., et al. 2011, MNRAS, 411, 117
Klement, R., Fuchs, B., & Rix, H.-W. 2008, ApJ, 685, 261

Klement, R. J., Bailer-Jones, C. A. L., Fuchs, B., Rix, H.-W., & Smith, K. W. 2011, ApJ, 726, 103
Kordopatis, G., Recio-Blanco, A., de Laverny, P., et al. 2011, A&A, 535, A106
Matijevič, G., Zwitter, T., Bienaymé, O., et al. 2012, ApJS, 200, 14
Matijevič, G., Zwitter, T., Bienaymé, O., et al. 2011, AJ, 141, 200
Matijevič, G., Zwitter, T., Munari, U., et al. 2010, AJ, 140, 184
Munari, U., Siviero, A., Bienaymé, O., et al. 2009, A&A, 503, 511
Munari, U., Tomasella, L., Fiorucci, M., et al. 2008, A&A, 488, 969
Quillen, A. C. & Minchev, I. 2005, AJ, 130, 576
Recio-Blanco, A., Bijaoui, A., & de Laverny, P. 2006, MNRAS, 370, 141
Robin, A. C., Reylé, C., Derrière, S., & Picaud, S. 2003, A&A, 409, 523
Ruchti, G. R., Fulbright, J. P., Wyse, R. F. G., et al. 2010, ApJ, 721, L92
Ruchti, G. R., Fulbright, J. P., Wyse, R. F. G., et al. 2011a, ApJ, 737, 9
Ruchti, G. R., Fulbright, J. P., Wyse, R. F. G., et al. 2011b, ApJ, 743, 107
Sales, L. V., Helmi, A., Abadi, M. G., et al. 2009, MNRAS, 400, L61
Seabroke, G. M., Gilmore, G., Siebert, A., et al. 2008, MNRAS, 384, 11
Sharma, S., Bland-Hawthorn, J., Johnston, K. V., & Binney, J. 2011, ApJ, 730, 3
Siebert, A., Bienaymé, O., Binney, J., et al. 2008, MNRAS, 391, 793
Siebert, A., Famaey, B., Binney, J., et al. 2012, MNRAS, 425, 2335
Siebert, A., Famaey, B., Minchev, I., et al. 2011a, MNRAS, 412, 2026
Siebert, A., Williams, M. E. K., Siviero, A., et al. 2011b, AJ, 141, 187
Smith, M. C., Ruchti, G. R., Helmi, A., et al. 2007, MNRAS, 379, 755
Steinmetz, M., Zwitter, T., Siebert, A., et al. 2006, AJ, 132, 1645
Veltz, L., Bienaymé, O., Freeman, K. C., et al. 2008, A&A, 480, 753
Williams, M. E. K., Steinmetz, M., Sharma, S., et al. 2011, ApJ, 728, 102
Wilson, M. L., Helmi, A., Morrison, H. L., et al. 2011, MNRAS, 413, 2235
Wylie-de Boer, E., Freeman, K., Williams, M., et al. 2012, ApJ, 755, 35
Zwitter, T., Matijevič, G., Breddels, M. A., et al. 2010, A&A, 522, A54
Zwitter, T., Siebert, A., Munari, U., et al. 2008, AJ, 136, 421

SF2A 2012
S. Boissier, P. de Laverny, N. Nardetto, R. Samadi, D. Valls-Gabaud and H. Wozniak (eds)

r-PROCESS ABUNDANCES IN THE EMP STAR CS 31082-001 USING STIS/HST

C. Siqueira-Mello Jr.[1,2], M. Spite[1], B. Barbuy[2], F. Spite[1], E. Caffau[1,3], V. Hill[4], S. Wanajo[5], F. Primas[6], B. Plez[7], R. Cayrel[1], J. Andersen[8], B. Nordström[8], C. Sneden[9], T.C. Beers[10], P. Bonifacio[1], P. François[1] and P. Molaro[11]

Abstract. We present a brief revision of the origin of heavy elements and the role of abundances in extremely metal-poor (EMP) stars, in providing improved constraints on the nature of the early nucleosynthesis mechanisms. Heavy element abundances in the EMP uranium-rich star CS 31082-001 based mainly on near-UV spectra from STIS/HST are presented. With new abundances for 9 n-elements not available in previous works (Ge, Mo, Lu, Ta, W, Re, Pt, Au, and Bi) this work makes CS 31082-001 the most completely well studied r-II object, with a total of 37 detections of n-capture elements. These results should be useful for a better characterisation of the neutron exposure(s) that produced the r-process elements in this star, as well as a guide for improving nuclear data and astrophysical site modelling.

Keywords: Galaxy: Halo, Stars: Abundances, Stars: individual: BPS CS 31082-001, Nucleosynthesis

1 Introduction

The origin of the elements is a fundamental field in modern astrophysics, and the problem of the heavy elements has been gaining attention in recent decades. In the seminal paper B^2FH (Burbidge et al. 1957) the authors propose two major mechanisms of neutron capture to explain the origin of the elements beyond iron: the s-process and the r-process. The (slow) s-process occurs with longer rates compared to the half-life of the beta decay of the newly formed nuclei, and consequently the chain of reactions must follow the valley of beta stability, while the (rapid) r-process occurs with shorter rates and it is able to produce neutron-rich nuclei far from the region of stability, which will decay after the action time of the mechanism. The n-capture elements can be composed of some isotopes built by pure r-process, other by pure s-process, and other built by the s- and r-process (Simmerer et al. 2004).

The time between the absorption of two neutrons is typically hundreds or thousands of years in the case of the s-process and 0.01 to 0.1 seconds in the case of the r-process. Completely different sites are needed to support these mechanisms.

The site of the r-process is not completely defined: the most likely sites are high-entropy neutrino-driven winds of neutron-rich matter in core-collapse supernova (Woosley et al. 1994; Wanajo 2007), but hydrodynamical simulations still encounter difficulties to reproduce the necessary neutron flux (Fischer et al. 2010; Hüdepohl et al. 2010; Martínez-Pinedo et al. 2012; Roberts 2012; Roberts & Reddy 2012), and alternative sites have been

[1] GEPI, Observatoire de Paris, CNRS, UMR 8111, F-92195 Meudon Cedex and 61 Av. de l'Observatoire, 75014 Paris,, France
[2] Universidade de São Paulo, IAG, Rua do Matão 1226, Cidade Universitária, São Paulo 05508-900, Brazil
[3] Zentrum für Astronomie der Universität Heidelberg, Landessternwarte, Königstuhl 12, 69117 Heidelberg, Germany
[4] Université de Sophia-Antipolis, Observatoire de la Côte d'Azur, CNRS UMR 6202, BP4229, 06304 Nice Cedex 4, France
[5] National Astronomical Observatory of Japan, 2-21-1 Osawa, Mitaka, Tokyo 181-8588, Japan
[6] European Southern Observatory, Karl Schwarzschild Strasse 2, 85748 Garching bei München, Germany
[7] LUPM, CNRS, UMR 5299, Université de Montpellier II, F-34095 Montpellier Cedex 05, France
[8] The Niels Bohr Institute, Juliane Maries Vej 30, DK-2100 Copenhagen, Denmark
[9] University of Texas at Austin, Department of Astronomy, Austin, TX 78712, USA
[10] Michigan State University, Department of Physics & Astronomy, and JINA: Joinst Institute for Nuclear Physics, East Lansing, MI 48824, USA
[11] INAF - Osservatorio Astronomico di Trieste, via Tiepolo 11, I-34143 Trieste, Italy

suggested, as the merging of two neutron stars or the merging of a neutron star and a black hole (Lattimer et al. 1977; Meyer 1989; Freiburghaus et al. 1999; Surman et al. 2008; Goriely et al. 2011; Wanajo & Janka 2012; Korobkin et al. 2012). The origin of the lightest trans-Fe elements gallium through cadmium adds another difficulty to this picture, since it has been attributed in varying degrees to several processes, e.g., the light element primary process (Travaglio et al. 2004); the weak r-process (Wanajo & Ishimaru 2006; Farouqi et al. 2010; Wanajo et al. 2011); and the νp-process (Fröhlich et al. 2006; Pruet et al. 2006; Wanajo 2006; Arcones & Montes 2011).

Observed abundances are the best clues to bring some light to this multiplicity of possible mechanisms, and the extremely metal-poor (EMP) Galactic halo stars have a special role in this problem. As discussed by many authors (e.g., François et al. 2007; Sneden et al. 2008; Siqueira-Mello et al. 2012a, and references therein), the neutron-capture element abundances in EMP stars should be predominantly due to the r-process, since the main s-process is significant only in later phases of the Galaxy. This assumption was first suggested by Truran (1981) based in particular in the observational studies of Spite & Spite (1978). Consequently, the analysis of these objects provides an insight into the astrophysical site(s) for the r-process.

2 The uranium-rich star CS 31082-001

CS 31082-001 was observed during the ESO large programme "First Stars" (see in particular Cayrel et al. 2004; Bonifacio et al. 2007, 2009), showing for the first time a measurable uranium abundance, using the line U II 3859.57 Å, opening up a new possibility for nucleochronology (Cayrel et al. 2001). CS 31082-001 is in the group of the 12 EMP r-II (following the classification from Beers & Christlieb 2005) giant stars known, it is one of the most extreme r-element enhanced giants, and its abundance pattern was studied in detail in the optical domain by Hill et al. (2002), showing for the first time in an EMP star the presence of an actinide boost compared with the general r-process level. The lead abundance in this star is also a puzzle, since in the purely r-process enriched photosphere of CS 31082-001, most of lead results from the decay of ^{232}Th , ^{235}U, and ^{238}U, which leaves very little space for Pb production during the r-process (Plez et al. 2004).

2.1 New abundances from STIS/HST

Observations with STIS/HST are crucial to obtain abundances of elements that have no measurable lines in the visible domain, leading us to observe CS 31082-001 with the Space Telescope Imaging Spectrograph (STIS) in the near UV. Requiring 45 orbits, the mean spectrum has good S/N $\sim$ 40 in the range 2600 - 3070 Å, with resolution of R = 30 000. We also use a new UVES spectrum centered at 3400 Å. The present abundance determinations are based on OSMARCS 1D LTE atmospheric model (Gustafsson et al. 2008) and the spectrum synthesis code Turbospectrum (Alvarez & Plez 1998). The stellar parameters are adopted from Hill et al. (2002): T_{eff} = 4825 $\pm$ 50 K, log g = 1.5 $\pm$ 0.3 [cgs], [Fe/H] = -2.9 $\pm$ 0.1 dex, and v_t = 1.8 $\pm$ 0.2 km s^{-1}. We also adopted the abundances of the elements from C to Zn determined in previous works. The calculations used the atomic line lists from the VALD2 compilation (Kupka et al. 1999), except if updated oscillator strengths were available in the literature.

The results for the heaviest r-elements were presented in Barbuy et al. (2011), the first determination of all measurable third-peak elements for an EMP r-process enhanced star, including Pt and Au. We were also able to present the first determination of Bi in a r-II star, besides confirming the deficiency in Pb obtained from the UVES/VLT spectrum. Siqueira-Mello et al. (2012b) concluded the study of the near-UV spectrum, presenting the analysis of the first and second peak of the r-elements, with new abundances for 23 n-elements, 6 of them - Ge, Mo, Lu, Ta, W, and Re - not available in previous works. Fig. 1 (left) shows the line Mo II 2660.576 Å as an example of a typical fit. When available (Andrievsky et al. 2009, 2011; Mashonkina et al. 2012), the NLTE corrections to these abundances have been applied.

Combined with theoretical calculations of the production ratios of the third-peak neutron capture elements and actinides, the result allows us to assess the consistency of the ages obtained from different radioactive chronometer pairs. The comparison of the abundance pattern observed in this star with those from different models of r-process permits to check these models. Fig. 1 (right) compares the new complete observed abundances in CS 31082-001 with the predicted abundance patterns from the hot (upper) and cold (lower) models by Wanajo (2007), as well as with the available NLTE abundances for some elements (red dots and respective error bars), and in the case of lead we also present the new NLTE+3D corrected abundance as the green symbol.

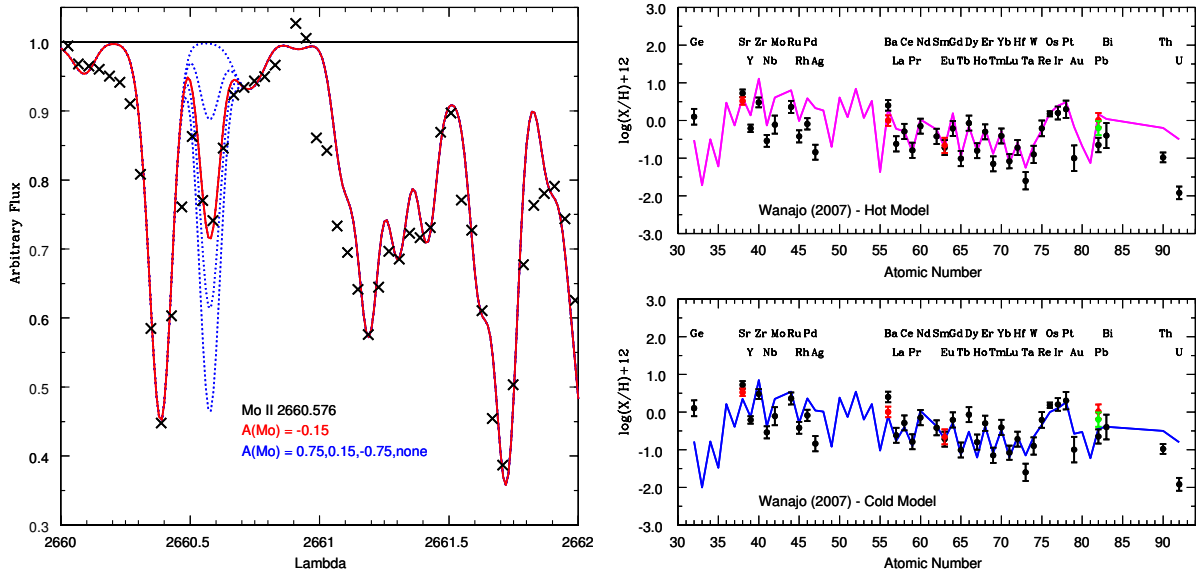

Fig. 1. Left: Fit of the observed Mo II 2660.576 Å line in CS 31082-001. Crosses: observations. Dotted lines: synthetic spectra computed for the abundances indicated in the figure. Solid line: synthetic spectrum computed with the best abundance, also indicated in the figure. **Right:** Predicted abundance patterns from the hot (upper) and cold (lower) models by Wanajo (2007) (solid lines), compared with the new complete observed abundances in CS 31082-001 (black dots and respective error bars). NLTE abundances for some elements (red dots and respective error bars) are compared with the LTE results. For Pb, the green symbol represents the NLTE+3D corrected value.

3 Conclusions

Together with the previous abundances, the new results make CS 31082-001 the most complete r-II object studied, with a total of 37 detections of n-capture elements, and a major template for studies of r-process models in this star, as well as a guide for improving nuclear data and modelling astrophysical site of elements production. The elements of the second and third peaks in this star are reasonably well represented by the abundance pattern from the cold model of Wanajo (2007), however this model overproduces the first peak elements (Sr through Ag) and is not able to explain the high abundance of Ge.

References

Alvarez, R. & Plez, B. 1998, A&A, 330, 1109

Andrievsky, S. M., Spite, F., Korotin, S. A., et al. 2011, A&A, 530, A105

Andrievsky, S. M., Spite, M., Korotin, S. A., et al. 2009, A&A, 494, 1083

Arcones, A. & Montes, F. 2011, ApJ, 731, 5

Barbuy, B., Spite, M., Hill, V., et al. 2011, A&A, 534, A60

Beers, T. C. & Christlieb, N. 2005, ARA&A, 43, 531

Bonifacio, P., Andersen, J., Andrievsky, S. M., et al. 2009, in Science with the VLT in the ELT Era, ed. A. Moorwood, 31

Bonifacio, P., Molaro, P., Sivarani, T., et al. 2007, A&A, 462, 851

Burbidge, E. M., Burbidge, G. R., Fowler, W. A., & Hoyle, F. 1957, Reviews of Modern Physics, 29, 547

Cayrel, R., Depagne, E., Spite, M., et al. 2004, A&A, 416, 1117

Cayrel, R., Hill, V., Beers, T. C., et al. 2001, Nature, 409, 691

Farouqi, K., Kratz, K.-L., Pfeiffer, B., et al. 2010, ApJ, 712, 1359

Fischer, T., Whitehouse, S. C., Mezzacappa, A., Thielemann, F.-K., & Liebendörfer, M. 2010, A&A, 517, A80

François, P., Depagne, E., Hill, V., et al. 2007, A&A, 476, 935

Freiburghaus, C., Rosswog, S., & Thielemann, F.-K. 1999, ApJ, 525, L121

Fröhlich, C., Martínez-Pinedo, G., Liebendörfer, M., et al. 2006, Physical Review Letters, 96, 142502
Goriely, S., Bauswein, A., & Janka, H.-T. 2011, ApJ, 738, L32
Gustafsson, B., Edvardsson, B., Eriksson, K., et al. 2008, A&A, 486, 951
Hill, V., Plez, B., Cayrel, R., et al. 2002, A&A, 387, 560
Hüdepohl, L., Müller, B., Janka, H.-T., Marek, A., & Raffelt, G. G. 2010, Physical Review Letters, 104, 251101
Korobkin, O., Rosswog, S., Arcones, A., & Winteler, C. 2012, ArXiv e-prints (1206.2379)
Kupka, F., Piskunov, N., Ryabchikova, T. A., Stempels, H. C., & Weiss, W. W. 1999, A&AS, 138, 119
Lattimer, J. M., Mackie, F., Ravenhall, D. G., & Schramm, D. N. 1977, ApJ, 213, 225
Martínez-Pinedo, G., Fischer, T., Lohs, A., & Huther, L. 2012, ArXiv e-prints (1205.2793)
Mashonkina, L., Ryabtsev, A., & Frebel, A. 2012, A&A, 540, A98
Meyer, B. S. 1989, ApJ, 343, 254
Plez, B., Hill, V., Cayrel, R., et al. 2004, A&A, 428, L9
Pruet, J., Hoffman, R. D., Woosley, S. E., Janka, H.-T., & Buras, R. 2006, ApJ, 644, 1028
Roberts, L. F. 2012, ApJ, 755, 126
Roberts, L. F. & Reddy, S. 2012, ArXiv e-prints
Simmerer, J., Sneden, C., Cowan, J. J., et al. 2004, ApJ, 617, 1091
Siqueira-Mello, C., Barbuy, B., Spite, M., & Spite, F. 2012a, A&A (submitted)
Siqueira-Mello, C., Spite, M., Barbuy, B., et al. 2012b, A&A (submitted)
Sneden, C., Cowan, J. J., & Gallino, R. 2008, ARA&A, 46, 241
Spite, M. & Spite, F. 1978, A&A, 67, 23
Surman, R., McLaughlin, G. C., Ruffert, M., Janka, H.-T., & Hix, W. R. 2008, ApJ, 679, L117
Travaglio, C., Gallino, R., Arnone, E., et al. 2004, ApJ, 601, 864
Truran, J. W. 1981, A&A, 97, 391
Wanajo, S. 2006, ApJ, 647, 1323
Wanajo, S. 2007, ApJ, 666, L77
Wanajo, S. & Ishimaru, Y. 2006, Nuclear Physics A, 777, 676
Wanajo, S. & Janka, H.-T. 2012, ApJ, 746, 180
Wanajo, S., Janka, H.-T., & Müller, B. 2011, ApJ, 726, L15
Woosley, S. E., Wilson, J. R., Mathews, G. J., Hoffman, R. D., & Meyer, B. S. 1994, ApJ, 433, 229

Session 04

Space missions: Reference frames and gravitation

SF2A 2012
S. Boissier, P. de Laverny, N. Nardetto, R. Samadi, D. Valls-Gabaud and H. Wozniak (eds)

COUPLING BETWEEN COROTATION AND LINDBLAD RESONANCES

M. El Moutamid[1,2], B. Sicardy[1,3] and S. Renner[2,4]

Abstract. We consider the classical Elliptic Restricted Three-Body Problem with two bodies (particle and satellite) orbiting a central planet. If we take into account the oblateness of the central body through the classical additional terms up to J_6, the secular terms causing the orbit precessions appear in the disturbing potential leading to the presence of two critical resonant arguments : $\phi = (m+1)\lambda' + m\lambda + \varpi$ and $\phi' = (m+1)\lambda' + m\lambda + \varpi'$, where m is an integer, λ and ϖ the mean longitude and the longitude of the periapsis of the particle, and the primed quantities apply to the satellite. The arguments ϕ' and ϕ respectively describe the Corotation Eccentric Resonance (CER) and the Lindblad Eccentric Resonance (LER). We developed a simple model (the CoraLin model) which encapsulate in a simple adimensional form the coupling between the two resonances. We examine the asymptotic configurations where these resonances are well separated or completely superimposed.

Keywords: Celestial mechanics

1 Introduction

We consider the classical problem of two bodies (the satellites) orbiting a central body (the planet), near a mean motion resonance. The simplest case occurs when the two satellites orbit in a common plane, and have masses μ and μ' possibly non-zero, but much smaller than the planet mass, M. From d'Alembert rules, two critical resonant angles, ϕ and ϕ', appear in the problem, see Eq. (2.1). There is a considerable amount of literature for the case $\mu = 0$ and $e' = 0$ (the planar, restricted and circular three-body problem), which has led to the so-called second fundamental model of resonance associated. For $\mu = 0$ and $e' \neq 0$, and under some simplifying hypotheses, another kind of resonances occurs, called the corotation resonances, akin to the 1:1 behavior of a particle near the L_4 and L_5 Lagrange points. In general, the two resonances associated with the angles ϕ and ϕ' are strongly coupled because they occurs at nearly the same semi-major axis, due to the usually small value of the planet oblateness. Here write the simplest system of differential equations that describes this coupling, using non-dimensional variables that permit applications in a wide variety of situations.

2 Hamiltonian formalism

We consider a system of two satellites of masses μ and μ' revolving around a planet of mass M in a common orbital plane, with $\mu, \mu' \ll M$. The masses μ, μ' and M will denotes at the same times the bodies and their mass. We assume that $\mu \to 0$, and we will call μ the "particle" and μ' the "satellite" that perturbs the particle. We use the classical notations a, e, λ, n and ϖ for the geometric semi-major axis, orbital eccentricity, mean longitude, mean motion and longitude of periapsis of μ. Similar primed notations are used for μ'. We consider a situation where μ and μ' are near a first order mean motion resonance $m+1$:m, where m is an integer such that $n/n' \approx (m+1)/m$. Near such first order resonance, d'Alembert's rules implies that the arguments of resonances are given by :

$$\begin{array}{ll} \phi = & (m+1)\lambda' - m\lambda - \varpi \\ \phi' = & (m+1)\lambda' - m\lambda - \varpi' \end{array} \tag{2.1}$$

[1] Observatoire de Paris, LESIA, UMR 8109 du CNRS, 5, Place Jules Janssen, 92195 Meudon Cedex, France
[2] Observatoire de Paris, IMCCE, UMR 8028 du CNRS, 77 avenue Denfert-Rochereau, 75014 Paris, France
[3] Université Pierre et Marie Curie, 4 Place Jussieu, 75005 Paris, France
[4] Laboratoire d'Astronomie de Lille, Université Lille 1, 1 impasse de l'observatoire, 59000 Lille, France

The situations $\dot{\phi} = 0$ and $\dot{\phi'} = 0$ correspond to the exact resonances associated with ϕ and ϕ'. where we can write the equations of motion, after approximate renormalization of the variables (El Moutamid et al *in prep*):

$$\begin{cases} \dfrac{dJ_c}{d\tau} = & -\sin(\phi') \\ \dfrac{d\phi'}{d\tau} = & J_c - J_L \\ \dfrac{dh}{d\tau} = & -(J_c - J_L + D)\cdot k \\ \dfrac{dk}{d\tau} = & +(J_c - J_L + D)\cdot h + \epsilon_L, \end{cases} \tag{2.2}$$

The corresponding Hamiltonian of the motion is

$$\mathcal{H} = \frac{(J_c - J_L)^2}{2} - \cos(\phi') - DJ_L - \epsilon_L h \tag{2.3}$$

Where J_c is the constant of Jacobi, J_L is proportional to $\frac{e^2}{2}$, $e = (h, k)$ is the the eccentricity vector, D is the distance between the Corotation and the Linblad resonances, and ϵ_L is the forcing value of the eccentricity due to the effect of Lindblad resonance. This is the simplest system that describes the combined effect of the corotation and Lindblad resonances acting on a particle. For this reason, we call it the "coraLin" model. It depends on only two dimensionless parameters, D and ϵ_L. We note that the full width of the unperturbed corotation resonance is $\Delta\chi = \Delta(J_c - J_L) = \pm 2$, and that the unperturbed Lindblad resonance occurs at $\chi = -D$, see Fig. (1)).

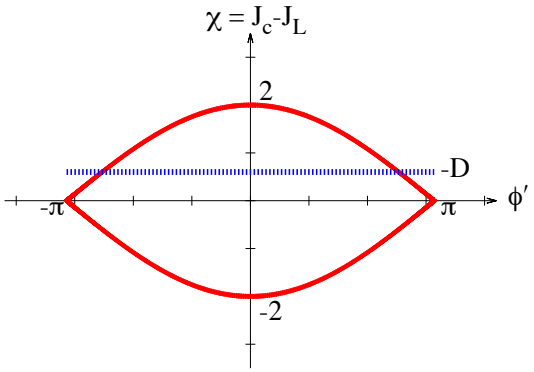

Fig. 1. System combined effect of Corotation (red) and Lindblad (blue).

3 Asymptotic behaviors

If $D = 0$ (the two resonances are superimposed), the system is integrable.
We now consider $|D| \gg 2$ i.e. when the Lindblad resonance occurs far away from the corotation region. There are two cases :

1) The particle is trapped in the corotation radius, the variations of (h, k) in the systems (2.2) are much faster than the variations of J_c and ϕ'. Consequently, the action $\oint h dk$ is adiabatically conserved. Since (h, k) essentially describe a circle centered on the forced value $(-\epsilon_L/(\chi + D), 0)$, this means that (h, k) rapidly move on a circle of constant radius, whose center slowly moves along the Ok axis. In particular, if (h, k) starts at the forced value $(-\epsilon_L/(\chi + D), 0)$, then it will stay at that value as χ slowly changes. In other words, the orbital eccentricity of the particle will permanently adjust itself so that $e = |\epsilon_L/(\chi + D|$ as χ varies.

2) The particle is trapped in the Lindblad radius, the situation is reversed, the variations of (J_c, ϕ') in the systems (2.2) are much faster than the variations of (h, k). Thus $\oint J_c d\phi'$ is adiabatically conserved.

4 Conclusions

We built a dynamic system which describes in a generic way the coupling between the Corotation and Lindblad resonances, we examined the asymptotic cases where the two resonances are almost superimposed, and the case where the two resonances are well separated, leading to a general solution based on adiabatic invariance arguments. Our 'toy model' incorporates all the ingredients of interacting CER/LER, in a non dimensional way. It can be use as a fast numerical tool to explore the probability of capture into the Corotation Resonance, in divers situations (Saturn's satellite, Neptune's arc ...).

The authors thank the organizers of the "Journées de la SF2A 2012", P. Robutel for the interesting discussions during this work and the EMERGENCE-UPMC project.

References

Ferraz-Mello, S., ed. 2007, Astrophysics and Space Science Library, Vol. 345, Canonical Perturbation Theories - Degenerate Systems and Resonance

Henrard, J. & Lemaitre, A. 1983, Celestial Mechanics, 30, 197

Laskar, J. & Robutel, P. 1995, Celestial Mechanics and Dynamical Astronomy, 62, 193

Murray, C. D. & Dermott, S. F. 2000, Solar System Dynamics, ed. Murray, C. D. & Dermott, S. F.

Sessin, W. & Ferraz-Mello, S. 1984, Celestial Mechanics, 32, 307

Sicardy, B. & Dubois, V. 2003, Celestial Mechanics and Dynamical Astronomy, 86, 321

Wisdom, J. 1986, Celestial Mechanics, 38, 175

SF2A 2012
S. Boissier, P. de Laverny, N. Nardetto, R. Samadi, D. Valls-Gabaud and H. Wozniak (eds)

INFLUENCE OF THE MEASUREMENT PROCESSING IN THE DETERMINATION OF THE EQUIVALENCE PRINCIPLE VIOLATION SIGNAL FOR THE MICROSCOPE EXPERIMENT

E. Hardy[1], A. Levy[1], G. Métris[2], A. Robert[3], M. Rodrigues[1] and P. Touboul[1]

Abstract. The MICROSCOPE space mission aims at testing the Equivalence Principle (EP) with an accuracy of 10^{-15}. The test is based on the precise measurement delivered by a differential electrostatic accelerometer onboard a drag-free satellite which includes two cylindrical test masses submitted to the same gravitational field and made of different materials. This high precision experiment is compatible with only very little perturbations. But the mathematical process applied to extract the signal at the EP violation frequency introduces numerical effects which perturb the measurement analysis. Aliasing arises from the finite time span of the measurement, and is amplified by possible small irregularities in the sampling due to telemetry losses. Numerical simulations have been run to estimate the projection rate of a perturbation at any frequency on the EP violation frequency and to test its compatibility with the mission specifications. Moreover, different procedures for the data analysis have been considered to select the one minimizing these effects taking into account the uncertainty about the frequencies of the implicated signals. After an overall presentation of the MICROSCOPE mission, this paper will focus on the numerical perturbations introduced during the data processing of the scientific measurement and describe the considered methods to minimize them.

Keywords: Techniques: miscellaneous, Cosmology: miscellaneous

1 Introduction

The Equivalence Principle (EP) is at the basis of General Relativity and states the Universality of Free Fall, that is to say that the acceleration of an object in a gravitational field is independent of its mass and its internal composition. The Universality of Free Fall has been tested throughout the centuries with an improving accuracy thanks to the Lunar Laser Ranging method or sophisticated torsion-balances. The latter have led to a record accuracy of a few 10^{-13} (Schlamminger et al. (2008)). However, the accuracy of these on-ground experiments is limited by the numerous perturbations of the terrestrial environment. In addition, some unification theories which try to merge gravitation with the three other fundamental interactions expect a violation of the EP below 10^{-14} (Damour et al. (2002)). Being performed in space, the MICROSCOPE mission will be able to test the Equivalence Principle with an accuracy of 10^{-15}.

To reach the high precision objective of the MICROSCOPE experiment, it is necessary to determine and reduce at best every perturbation. This paper focuses on the numerical effects which perturb the observation of the EP signal during the measurement processing. The time span of the measurement is necessarily finite and may not equate with a whole number of the perturbations period. That is why these perturbations are spectrally spread. A perturbation at any frequency can therefore have a component with a given projection rate at the EP frequency. Moreover, the projection rates are amplified by the accidental measurement losses. The projection values have to be estimated by taking into account the uncertainties on the considered signal frequencies in order to check their compatibility with the mission specifications.

After a general overview of the MICROSCOPE space mission, this paper will focus on the influence of the observation window which introduces the numerical effects. The influence of the measurement losses and the different methods investigated to manage them will then be presented.

[1] ONERA, 92322 Châtillon, France

[2] Université de Nice Sophia-Antipolis, Centre National de la Recherche Scientifique (UMR 6526), Observatoire de la Côte d'Azur, Géoazur, 06130 Grasse, France

[3] CNES, 31401 Toulouse, France

2 The MICROSCOPE space mission

MICROSCOPE is a 200 kg satellite developed by CNES to orbit around the Earth for a 18 months mission. The onboard payload is composed of two differential electrostatic accelerometers developed by ONERA, each one being composed of two imbricated cylindrical test masses. The masses positions are detected thanks to a capacitive method and a control loop with electrostatic actuation keeps the masses motionless at the centre of the accelerometer cage, so that they both follow the same trajectory. For one of the accelerometer, the two masses are made of different materials (titanium and platinum). A difference measured between the forces applied to maintain them on the same trajectory would therefore indicate a violation of the Universality of Free Fall (a direct consequence of the EP). The second accelerometer is composed of two test masses with the same composition and enables to assess the experiment accuracy.

There are several advantages to perform the experiment in space. The experiment is not limited by the free fall duration: it can last for several orbits. Moreover, the environment is much less disturbed than on Earth particularly because a drag-free system compensates for perturbations common to the two test masses (the so called common mode), enabling to decrease the dynamics of the individual signals. Lastly, there is no large mass close to the experiment and the Earth's gravity gradient effects are small and easy to correct.

The frequency and phase of the signal to be detected are well defined, corresponding to the Earth gravity signal. The satellite pointing can either be inertial or spinning. In the first case, the Earth gravity field is modulated by the orbital frequency and the signal frequency is: $f_{EP_i} = f_{orb}$. In the second case, the signal frequency f_{EP_s} is the sum of the spin and orbital frequencies: $f_{EP_s} = f_{orb} + f_{spin}$. In comparison, the signal frequency is increased and thus closer to the minimum of the instrumental noise.

3 Influence of the observation window

3.1 Determination of the projection rate

The Fourier transform of a sine signal of infinite duration is composed of only one spectral line: the total energy is concentrated at the sine frequency. However, the Fourier transform applied on a finite duration which does not correspond to an exact number of periods will lead to a spread spectrum.

The measurement provided by the MICROSCOPE instrument is necessarily of finite duration. That is why the perturbation signals are subjected to this spectral spread. Therefore, a perturbation at a frequency different from the EP frequency may have a component at this frequency.

Our objective is to determine the value of the projection rate of a perturbation at any frequency on the EP violation frequency to compare the result with the mission specifications. Let S_{obs} be our observation signal and S_{EP} the model, the equation to be solved in order to estimate the EP violation term δ is:

$$S_{obs} = \delta S_{EP}$$

The Least Squares estimated solution is:

$$\hat{\delta} = \frac{\langle S_{EP}, S_{obs} \rangle}{\langle S_{EP}, S_{EP} \rangle}$$

Adding a disturbing signal S_d, the parameter to be estimated will be modified by:

$$\Delta\delta = \frac{\langle S_{EP}, S_d \rangle}{\langle S_{EP}, S_{EP} \rangle}$$

The signals S_{EP} and S_d are now considered to be sine signals:

$$S_{EP} = A_{EP} sin(\omega_{EP} t + \phi_{EP})$$

$$S_d = A_d sin(\omega_d t + \phi_d)$$

The Least Squares Method leads to the same solution when applying a discrete Fourier Transform to each side of the equation. The scalar product can therefore be computed in the Fourier domain: this method is used for the numerical simulations. The scalar product can equally be computed in the temporal domain. To correspond to the discrete measurement, the scalar product is discrete and defined on a finite number of frequencies. However, it is possible to approximate it with a continuous integral for an analytical evaluation.

Table 1. Projection rate and special specifications for some of the linear combinations of f_{orb} and f_{spin} in spinning pointing.

Frequency	Projection rate	Specification
f_{orb}	9.8×10^{-6}	10^{-4}
$f_{spin} - 2f_{orb}$	3.6×10^{-5}	3.3×10^{-4}
$2f_{orb}$	2.3×10^{-5}	2.5×10^{-4}
$f_{spin} - f_{orb}$	3.2×10^{-5}	3.3×10^{-4}
$3f_{orb}$	4.8×10^{-5}	5×10^{-4}
f_{spin}	3.2×10^{-5}	3.3×10^{-4}
$f_{spin} + f_{orb}$	1	1
$f_{spin} + 2f_{orb}$	7.9×10^{-5}	10^{-3}

The resulting projection rate has been plotted as a function of the perturbation frequency f_d in figure 1, using a rectangular window. This window has been chosen because it provides worst case results in comparison with apodisation windows. The results depend on the two signals phases ϕ_{EP} and ϕ_d. The curve therefore represents a maximisation of the projection rate as a function of these two parameters, in order to reach the worst case. The projection rate oscillates as a function of the perturbation pulsation ω_d, between null and maximal values limited by an envelope which varies as the inverse of the measurement duration.

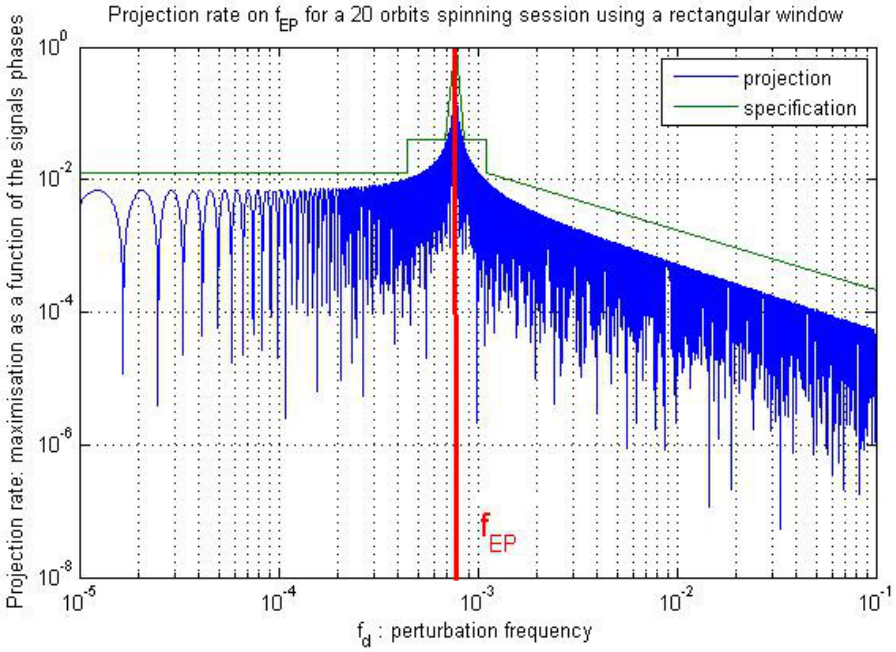

Fig. 1. Projection rate of a pertubation signal on the Equivalence Principle signal as a function of the perturbation frequency.

3.2 Choice of the measurement duration and spin frequency

The inertial and spinning motions of the satellite induce important perturbations. Most of the largest perturbations are associated to fundamental frequencies: multiples of the orbital frequency in inertial pointing and linear combinations of the orbital and the spin frequencies in spinning pointing. Very restrictive specifications, presented in the third column of table 1, have therefore been defined for the projection rate of the signals at the discrete frequencies impacted by these effects. We define the duration of the analysis window T, the orbital

period T_{orb} and the spin period T_{spin}. If the relation $T = k_1 T_{orb} = k_2 T_{spin}$, k_1 and k_2 being integers, holds, then the linear combinations of f_{spin} and f_{orb} correspond to the minima of the projection rate curve in figure 1. In case of inertial pointing, we choose $k_1 = 120$ corresponding to sessions of about 8.3 days. In case of rotating pointing, we choose $k_1 = 20$ corresponding to sessions of about 1.4 days; this sets $T_{spin} = \frac{k_1}{k_2} T_{orb}$. k_2 will be chosen between 70 and 100 in order to get a spin frequency larger than the orbital frequency and an EP frequency closer to the minimum of the instrument noise (this justifies the shorter integration time for sessions with a rotating pointing).

However, the frequencies of the implicated signals are not perfectly known. The uncertainty on the orbit determination causes an error on the orbital frequency. Moreover, the inertial and the spinning pointing cannot be exactly realised. Because of the uncertainties, the reality does not exactly match with the ideal case leading to non null projection rates. Column 2 of table 1 presents the worst projection rates computed using shifts of 2×10^{-8} rad/s on the orbital frequency with respect to the ideal case, 3×10^{-8} rad/s on the spin frequency and 1×10^{-8} rad/s on the inertial pointing realisation, and demonstrates the compatibility with the specifications.

4 Measurement losses

During the data transmission from the satellite to the ground station, a very small part of the data can be accidentally lost. The data loss may happen during the data transmission from the satellite to the ground station. Part of the data could be recollected during the next fly by, but it is impossible to guarantee a 100% recollection. The experience of the PICARD mission provides a good estimation of the losses frequency, since the MICROSCOPE satellite will follow nearly the same orbit and use the same station network. For 10 months, about 100 measurement losses happened, so the probability of such an event to happen during an orbit is about 2%; their duration ranges from a second to a few hours. An other source of data loss arises from the crackings caused by the gas contained in the six thrust tanks. The worst case is dependant on the gas pressure and the affected tanks surface and corresponds to about 40 crackings shorter than one second per orbit.

Measurement losses tend to increase the projection rate of the perturbations on the EP violation signal. For example monochromatic signals of frequencies j_1/T and j_2/T, j_1 and j_2 being integers, are orthogonal (their discrete scalar product is null) in case of regular sampling but this is no longer true in case of irregular sampling (or equivalently regular sampling with gaps). Different procedures for the data processing have been determined depending on the duration of the measurement loss.

4.1 Short measurement losses (shorter than a minute)

The projection rate in case of missing data can be computed by replacing the lost data with null values. The blue curve of figure 2 and the second column of table 2 show that the specifications are no longer satisfied when using a model of the distribution of the tank crackings. To overcome this difficulty, a simple solution consists in replacing the lost data by the mean value of the signal before and after the measurement loss. The green curve of figure 2 and the third column of table 2 show that this method is compatible with the specifications. The conclusions relating to the spinning mode are also valid for the inertial mode.

The tank crackings are numerous - about 40 per orbit - but shorter than one second. For longer measurement losses duration due to data transmission failure, the same procedure is used, but only one measurement loss whose duration is shorter than a minute is accepted per 20 orbits.

4.2 Long measurement losses (longer than a minute)

The probability that a measurement loss longer than a minute appears during a spinning mode session is weak, because the duration of the session is only 20 orbits. But for the inertial mode sessions, whose duration is 120 orbits, the probability to have at least one measurement loss longer than a minute reaches 16%. It is therefore necessary to have a method to deal with longer measurement losses.

The selected method consists in the elimination from the measurement of the entire orbit which contains the data loss, so that the duration of each data portion corresponds to a whole number of orbits. The data portions are then stick together again. The time span of the measurement for a 120 orbits inertial session is therefore reduced by a few orbits, which is still acceptable regarding the noise level. To test the compatibility of this method with the specifications, we have determined the worst case for the measurement losses duration and disposition: regular distributed losses. Analytical analysis confirmed by numerical simulations has shown that in this case the amplitude of the envelope of the projection rate as a function of the perturbation frequency

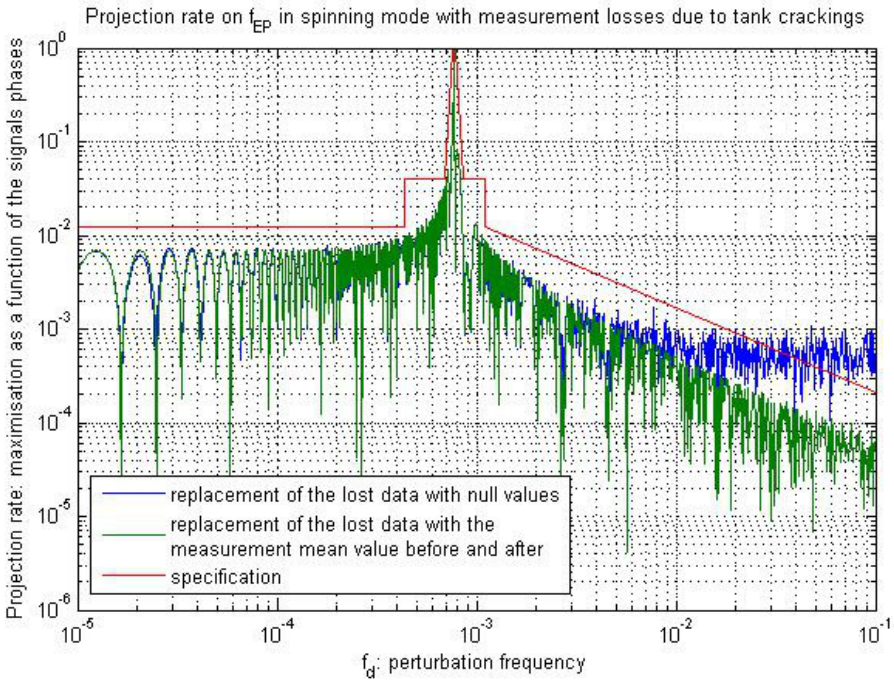

Fig. 2. Projection rate of a pertubation signal on the Equivalence Principle signal as a function of the perturbation frequency with a measurement losses scheme corresponding to the model of the tanck crackings.

Table 2. Projection rate and special specifications for some of the linear combinations of f_{orb} and f_{spin} in spinning pointing with a measurement losses scheme corresponding to the model of the tanck crackings. Method 1: replacement of the lost data with null values; method 2: replacement of the lost data by the mean value of the signal before and after the measurement loss.

Frequency	Projection rate: method 1	Projection rate: method 2	Specification
f_{orb}	7.4×10^{-4}	9.8×10^{-6}	10^{-4}
$f_{spin} - 2f_{orb}$	4.2×10^{-4}	3.6×10^{-5}	3.3×10^{-4}
$2f_{orb}$	6.0×10^{-4}	2.3×10^{-5}	2.5×10^{-4}
$f_{spin} - f_{orb}$	3.8×10^{-4}	3.2×10^{-5}	3.3×10^{-4}
$3f_{orb}$	1.8×10^{-4}	4.8×10^{-5}	5×10^{-4}
f_{spin}	6.1×10^{-4}	3.2×10^{-5}	3.3×10^{-4}
$f_{spin} + f_{orb}$	1	1	1
$f_{spin} + 2f_{orb}$	5.5×10^{-4}	8.0×10^{-5}	10^{-3}

is proportional to the inverse of the duration of one subsession and not to the inverse of the total duration of the session.

To guarantee a failure probability lower than 1%, it is necessary to be able to deal with three measurement losses longer than a minute. The worst case therefore corresponds to four subsessions of 30 orbits. The results of the numerical simulation presented in figure 3 are compatible with the specification. The efficiency of the method is therefore validated.

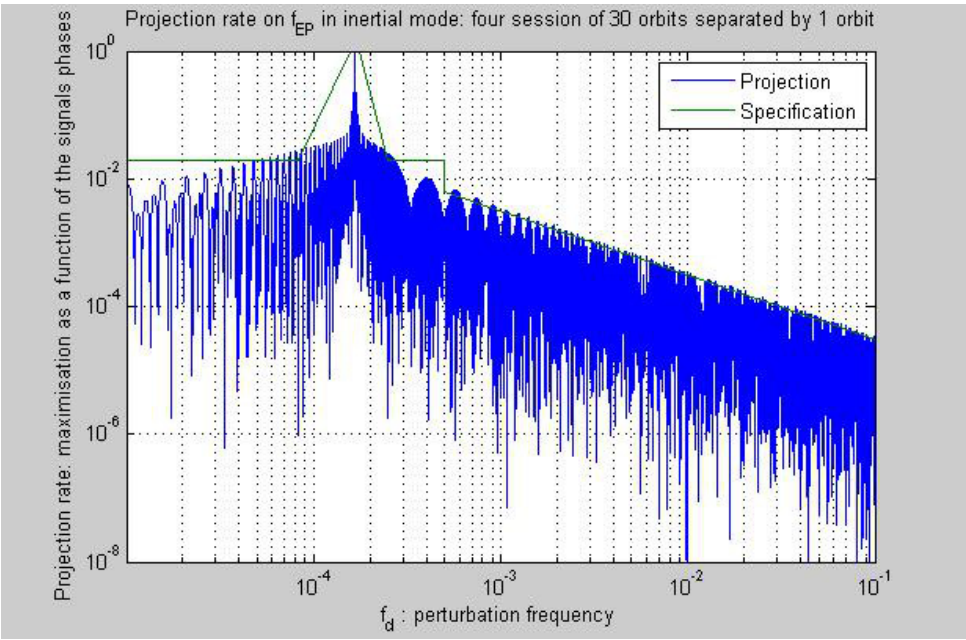

Fig. 3. Projection rate of a pertubation signal on the Equivalence Principle signal as a function of the perturbation frequency: four 30 orbits sessions separated by one orbit.

5 Conclusions

For the success of the MICROSCOPE space mission, a crucial problem is to limit the perturbations which appear during the measurement analysis. Because of the finite duration of the measurement window, a perturbation at any frequency can have a projection at the EP frequency. It is therefore necessary to adjust the frequencies corresponding to the main perturbations, mainly the orbital and the spin frequency, to get a minimal projection. However, the projection effects are amplified by the frequencies uncertainties. Numerical simulations of the projection rate taking into account these uncertainties have proved the result to be compatible with the specifications. The measurement losses increase the projection rate on the EP frequency. To deal with numerous very short losses (shorter than a second) or one loss up to a minute, the missing data are replaced by the mean value of the measurement before and after the interruption. For measurement losses longer than a minute, the inertial session is separated in several independent subsessions. Thanks to these procedures, the success probability of the mission reaches a level compatible with the specification. The rejection can still be considerably improved by using apodisation windows, like the Blackman or the Hann window, but the specifications are reached even in the worst case of a rectangular window.

The authors wish to thank the MICROSCOPE teams at CNES, OCA and ZARM for the technical exchanges. This activity has received the financial support of Onera and CNES.

References

Damour, T., Piazza, F., & Veneziano, G. 2002, Physical Review D, 66

Schlamminger, S., Choi, K., Wagner, T. A., Gundlach, J. H., & Adelberger, E. G. 2008, Physical Review Letters, 100

SF2A 2012
S. Boissier, P. de Laverny, N. Nardetto, R. Samadi, D. Valls-Gabaud and H. Wozniak (eds)

FREQUENCY SHIFT UP TO THE 2-PM APPROXIMATION

A. Hees[1,2,3], S. Bertone[2,4] and C. Le Poncin-Lafitte[2]

Abstract. A lot of fundamental tests of gravitational theories rely on highly precise measurements of the travel time and/or the frequency shift of electromagnetic signals propagating through the gravitational field of the Solar System. In practically all of the previous studies, the explicit expressions of such travel times and frequency shifts as predicted by various metric theories of gravity are derived from an integration of the null geodesic differential equations. However, the solution of the geodesic equations requires heavy calculations when one has to take into account the presence of mass multipoles in the gravitational field or the tidal effects due to the planetary motions, and the calculations become quite complicated in the post-post-Minkowskian approximation. This difficult task can be avoided using the time transfer function's formalism. We present here our last advances in the formulation of the one-way frequency shift using this formalism up to the post-post-Minkowskian approximation.

Keywords: frequency shift, relativity, fundamental physics, space navigation

1 Introduction

The treatment of light propagation in a relativistic framework is extremely important for various fields of study such as fundamental physics and astronomy, astrophysics and space navigation. Attaining very accurate measurements could allow us to observe a new range of subtle physical effects. Nowadays, a few approaches exist to model light propagation in a relativistic context. Among them, the post-Newtonian (pN) and the post-Minkowskian (pM) approximations (see for example Kopeikin & Schäfer 1999; Klioner & Zschocke 2010) are those mainly used in order to find perturbative solutions of the null geodesic equation.
In this work, an alternative formulation to compute the one way frequency shift of an electromagnetic signal is presented. Being based on the time transfer function formalism (Teyssandier & Le Poncin-Lafitte 2008), it allows us to compute this observable up to the post-post-Minkowskian approximation without integrating the null geodesic equation, allowing lighter calculations.
Section 2 contains the notations and conventions used in this document. In section 3 we give our framework and the definition of the one way frequency shift while in section 4 we provide the relations between the frequency shift and the time transfer function. These quantities will be then used in section 5 to obtain the post-Minkowskian expansion of the observable up to the 2PM approximation. Our conclusions and possible applications of this study are given in section 6.

2 Notation and conventions

In this paper c is the speed of light in a vacuum and G is the Newtonian gravitational constant. The Lorentzian metric of space-time V_4 is denoted by g. The signature adopted for g is $(+---)$. We suppose that space-time is covered by some global quasi-Galilean coordinate system $(x^\mu) = (x^0, \boldsymbol{x})$, where $x^0 = ct$, t being a time coordinate, and $\boldsymbol{x} = (x^i)$. We assume that the curves of equations $x^i = \text{const}$ are timelike, which means that $g_{00} > 0$ anywhere. We employ the vector notation $\boldsymbol{a}$ in order to denote $(a^1, a^2, a^3) = (a^i)$. For any quantity $f(x^\lambda)$, $f_{,\alpha}$ denotes the partial derivative of f with respect to x^α. The indices in parentheses characterize the order of perturbation. They are set up or down, depending on the convenience.

[1] Royal Observatory of Belgium, Avenue Circulaire 3, 1180 Uccle, Belgium
[2] SYRTE, Observatoire de Paris, CNRS, UPMC, Avenue de l'Observatoire 61, 75014 Paris, France
[3] Namur Center for Complex Systems (naXys), University of Namur (FUNDP), Belgium
[4] INAF, Astronomical Observatory of Torino / University of Torino

3 The one-way frequency shift

Consider a clock $\mathcal{O}_\mathcal{A}$ located at point $\mathcal{A}$ and a clock $\mathcal{O}_\mathcal{B}$ located at point $\mathcal{B}$ delivering, respectively, the proper frequency $\nu_\mathcal{A}$ and $\nu_\mathcal{B}$. Then, suppose that $\mathcal{O}_\mathcal{A}$ is sending an electromagnetic signal to $\mathcal{O}_\mathcal{B}$ along null geodesics of the metric (geometric optics approximation). Then, the one way frequency shift is defined by

$$\left.\frac{\Delta\nu}{\nu}\right|^{\text{one-way}}_{\text{A}\to\text{ B}} = \frac{\nu_B}{\nu_A} - 1\,. \tag{3.1}$$

It is well-known that the ratio ν_B/ν_A can be expressed as (Synge 1960)

$$\frac{\nu_B}{\nu_A} = \frac{u^\mu_B k^B_\nu}{u^\nu_A k^A_\mu} = \frac{k^B_0}{k^A_0}\frac{u^0_B + u^i_B \hat{k}^B_i}{u^0_A + u^i_A \hat{k}^A_i} = \left(\frac{d\tau}{dt}\right)_A \frac{dt_A}{dt_B}\left(\frac{dt}{d\tau}\right)_B\,, \tag{3.2}$$

where $u^\mu_{A/B} = (dx^\mu/ds)_{A/B}$ are the four-velocity of observers $\mathcal{A}$ and $\mathcal{B}$, $\hat{k}_i = \left(\frac{k_i}{k_0}\right)$ and k^A_μ and k^B_μ are the wave vectors (the null tangent vectors) at the point of emission x_A and at the point of reception x_B, respectively. Terms appearing in the right hand side of Eq. (3.2) can be expressed as

$$\left(\frac{d\tau}{dt}\right)_{A/B} = \left[g_{00} + 2g_{0i}\beta^i + g_{ij}\beta^i\beta^j\right]^{1/2}_{A/B}\,, \quad \frac{dt_A}{dt_B} = \frac{k^B_0}{k^A_0}\frac{1+\beta^i_B\hat{k}^B_i}{1+\beta^i_A\hat{k}^A_i}\,, \tag{3.3}$$

with $\beta^i_{A/B} = \frac{1}{c}\frac{dx^i_{A/B}}{dt}$ being the coordinate velocities of observers $\mathcal{A}$ and $\mathcal{B}$.

4 Relation between frequency shift and time transfer functions

We put $x_A = (ct_A, \boldsymbol{x}_A)$ the event of emission $\mathcal{A}$ and $x_B = (ct_B, \boldsymbol{x}_B)$ the event of reception $\mathcal{B}$. Moreover, we define $\mathcal{T}_e$ and $\mathcal{T}_r$ as two distinct (coordinate) time transfer functions defined as

$$t_B - t_A = \mathcal{T}_e(t_A, \boldsymbol{x}_A, \boldsymbol{x}_B) = \mathcal{T}_r(t_B, \boldsymbol{x}_A, \boldsymbol{x}_B)\,. \tag{4.1}$$

The relations between time transfer functions and the wave vectors $k^\mu = dx^\mu/d\lambda$ at emission and reception has been derived by Le Poncin-Lafitte et al. (2004) :

$$\left(\widehat{k}_i\right)_A = \left(\frac{k_i}{k_0}\right)_A = c\,\frac{\partial\mathcal{T}_e}{\partial x^i_A}\left[1 + \frac{\partial\mathcal{T}_e}{\partial t_A}\right]^{-1} = c\,\frac{\partial\mathcal{T}_r}{\partial x^i_A}\,, \tag{4.2a}$$

$$\left(\widehat{k}_i\right)_B = \left(\frac{k_i}{k_0}\right)_B = -c\,\frac{\partial\mathcal{T}_e}{\partial x^i_B} = -c\,\frac{\partial\mathcal{T}_r}{\partial x^i_B}\left[1 - \frac{\partial\mathcal{T}_r}{\partial t_B}\right]^{-1}\,, \tag{4.2b}$$

$$\frac{(k_0)_B}{(k_0)_A} = \left[1 + \frac{\partial\mathcal{T}_e}{\partial t_A}\right]^{-1} = 1 - \frac{\partial\mathcal{T}_r}{\partial t_B}\,, \tag{4.2c}$$

where $\mathcal{T}_e$ and $\mathcal{T}_r$ are evaluated at the event of emission $\mathcal{A}$ and at the event of reception $\mathcal{B}$ respectively. It's then straightforward to define the one-way frequency shift (3.1) as a function of $\mathcal{T}_{e/r}$ and their partial derivatives.

5 Post-Minkowskian expansion of the frequency shift

The expression of the time transfer functions $\mathcal{T}_{e/r}$ as a formal post-Minkowskian series has been derived by Teyssandier & Le Poncin-Lafitte (2008). In this communication, we focus on $\mathcal{T}_r$, but similar considerations hold for $\mathcal{T}_e$. $\mathcal{T}_r$ can be written in ascending power of G defined as

$$\mathcal{T}_r(\boldsymbol{x}_A, t_B, \boldsymbol{x}_B) = \frac{R_{AB}}{c} + \frac{1}{c}\sum_{n=1}^{\infty}\Delta^{(n)}_r(\boldsymbol{x}_A, t_B, \boldsymbol{x}_B)\,, \tag{5.1}$$

where $\Delta^{(n)}_r$ is of the order $\mathcal{O}(G^n)$, $R^i_{AB} = x^i_B - x^i_A$, $R_{AB} = |R^i_{AB}|$ and $N^i = \frac{R^i_{AB}}{R_{AB}}$.

Then, we can express the one-way frequency shift (3.2) as follows (in agreement with the expression found by Hees et al. (2012))

$$\frac{\nu_B}{\nu_A} = \frac{\left[g_{00} + 2g_{0i}\beta^i + g_{ij}\beta^i\beta^j\right]_A^{1/2}}{\left[g_{00} + 2g_{0i}\beta^i + g_{ij}\beta^i\beta^j\right]_B^{1/2}} \times \frac{1 - N^i\beta_B^i - \beta_B^i\frac{\partial\Delta_r}{\partial x_B^i} - \frac{\partial\Delta_r}{\partial t_B}}{1 - N^i\beta_A^i + \beta_A^i\frac{\partial\Delta_r}{\partial x_A^i}}. \tag{5.2}$$

The goal of this work is to provide a new way of computing a general form for the derivatives of the time delay function up to the post-post Minkowskian order. In order to do so, we rewrite $\Delta_r^{(1)}$ and $\Delta_r^{(2)}$ given by Teyssandier & Le Poncin-Lafitte (2008) as

$$\Delta_r^{(1)}(\boldsymbol{x}_A, t_B, \boldsymbol{x}_B) = \frac{R_{AB}}{2}\int_0^1 \left[g_{(1)}^{00} - 2N^i g_{(1)}^{0i} + N^iN^j g_{(1)}^{ij}\right]_{z^\alpha(\lambda)} d\lambda = \int_0^1 m_{(1)}(\lambda)d\lambda\,, \tag{5.3a}$$

$$\Delta_r^{(2)}(\boldsymbol{x}_A, t_B, \boldsymbol{x}_B) = \int_0^1 \left[\mathcal{I}_1(\lambda) + \mathcal{I}_2(\lambda) + \mathcal{I}_3(\lambda)\right] d\lambda\,, \tag{5.3b}$$

where

$$\mathcal{I}_1 = m_{(2)}(\lambda) - \Delta_r^{(1)}(\boldsymbol{z}(\lambda), t_B, \boldsymbol{x}_B)\; m_{(1),0}(\lambda)\,, \tag{5.4a}$$

$$\mathcal{I}_2 = \left[R_{AB}\; g_{(1)}^{0i} - R_{AB}^k\; g_{(1)}^{ik}\right]_{z^\alpha(\lambda)} \frac{\partial\Delta_r^{(1)}}{\partial x^i}(\boldsymbol{z}(\lambda))\,, \tag{5.4b}$$

$$\mathcal{I}_3 = -\frac{R_{AB}}{2}\sum_{j=1}^{3}\left[\frac{\partial\Delta_r^{(1)}}{\partial x^j}(\boldsymbol{z}(\lambda))\right]^2, \tag{5.4c}$$

$\boldsymbol{z}(\lambda) = x_B^i - \lambda R_{AB}^i$ being the spatial composantes of the Minkowskian straight line of equation $z^\alpha(\lambda) = (x_B^0 - \lambda R_{AB}, \boldsymbol{z}(\lambda))$ and

$$m_{(n),\alpha}(\lambda) = \frac{R_{AB}}{2}\left[g_{(n),\alpha}^{00} - 2N^i g_{(n),\alpha}^{0i} + N^iN^j g_{(n),\alpha}^{ij}\right]_{z^\beta(\lambda)}, \tag{5.5a}$$

$$\frac{\partial\Delta_r^{(1)}}{\partial x^i}(\boldsymbol{z}(\lambda)) = \int_0^1 \left[m_{(1),\alpha}(\lambda\mu)z_{A,i}^\alpha(\lambda\mu) + \tilde{h}_{(1)}^i(\lambda\mu)\right] d\mu\,,$$

with $z_{A/B,i}^\alpha = \partial z^\alpha/\partial x_{A/B}^i$. The derivatives of the first PM order of the delay function can be then easily calculated

$$\frac{\partial\Delta_r^{(1)}}{\partial x_{A/B}^i}(\boldsymbol{x}_A, t_B, \boldsymbol{x}_B) = \int_0^1 \left[m_{(1),\alpha}(\lambda)z_{A/B,i}^\alpha(\lambda) \pm \tilde{h}_{(1)}^i(\lambda)\right] d\lambda\,, \tag{5.6a}$$

$$\frac{\partial\Delta_r^{(1)}}{\partial t_B}(\boldsymbol{x}_A, t_B, \boldsymbol{x}_B) = \int_0^1 \left[m_{(1),0}(\lambda)\; c\right] d\lambda\,, \tag{5.6b}$$

where the function $\tilde{h}$ is defined by

$$\tilde{h}_{(n),j}^i(\lambda) = \left.\frac{\partial m_{(n),j}}{\partial x_A^i}\right|_{z^\alpha=\text{cst}} = -\left.\frac{\partial m_{(n),j}}{\partial x_B^i}\right|_{z^\alpha=\text{cst}} = \frac{1}{2}\left[-N^i g_{(n),j}^{00} + 2g_{(n),j}^{0i} - 2g_{(n),j}^{ik}N^k + N^kN^lN^i g_{(n),j}^{kl}\right]_{z^\alpha(\lambda)}. \tag{5.7}$$

These equations are equivalent to those derived by Hees et al. (2012). The same approach can be used for the 2PM order resulting in more complex formulas

$$\frac{\partial\Delta_r^{(2)}}{\partial x_{A/B}^i}(\boldsymbol{x}_A, t_B, \boldsymbol{x}_B) = \int_0^1 \left[\frac{\partial\mathcal{I}_1}{\partial x_{A/B}^i} + \frac{\partial\mathcal{I}_2}{\partial x_{A/B}^i} + \frac{\partial\mathcal{I}_3}{\partial x_{A/B}^i}\right] d\lambda \tag{5.8a}$$

$$\frac{\partial\Delta_r^{(2)}}{\partial t_B}(\boldsymbol{x}_A, t_B, \boldsymbol{x}_B) = \int_0^1 \left[\frac{\partial\mathcal{I}_1}{\partial t_B} + \frac{\partial\mathcal{I}_2}{\partial t_B} + \frac{\partial\mathcal{I}_3}{\partial t_B}\right] d\lambda \tag{5.8b}$$

where the derivatives can be expressed as follows

$$\frac{\partial \mathcal{I}_1}{\partial x^i_{A/B}} = m_{(2),\alpha} z^\alpha_{A/B,i} \pm \tilde{h}^i_{(2)} - \Delta^{(1)}_r(\boldsymbol{z}(\lambda), t_b, \boldsymbol{x}_B) \left[m_{(1),0\alpha} z^\alpha_{A/B,i} \pm \tilde{h}^i_{(1),0} \right] - m_{(1),0} \frac{\partial \Delta^{(1)}_r}{\partial x^i_{A/B}}(\boldsymbol{z}(\lambda)) \,, \tag{5.9a}$$

$$\frac{\partial \mathcal{I}_2}{\partial x^i_{A/B}} = \left[\mp N^i g^{0j}_{(1)} \pm g^{ij}_{(1)} + (R_{AB} g^{0j}_{(1),\alpha} - g^{jk}_{(1),\alpha} R^k_{AB}) z^\alpha_{A/B,i} \right] \frac{\partial \Delta^{(1)}_r}{\partial x^j}(\boldsymbol{z}(\lambda)) \tag{5.9b}$$

$$+ [R_{AB} g^{0j}_{(1)} - R^k_{AB} g^{jk}_{(1)}] \frac{\partial^2 \Delta^{(1)}_r}{\partial x^i_{A/B} \partial x^j}(\boldsymbol{z}(\lambda)) \,,$$

$$\frac{\partial \mathcal{I}_3}{\partial x^i_{A/B}} = \pm \frac{N^i_{AB}}{2} \sum_{j=1}^{3} \left(\frac{\partial \Delta^{(1)}_r}{\partial x^j}(\boldsymbol{z}(\lambda)) \right)^2 - R_{AB} \sum_{j=1}^{3} \left[\frac{\partial \Delta^{(1)}_r}{\partial x^j}(\boldsymbol{z}(\lambda)) \cdot \frac{\partial^2 \Delta^{(1)}_r}{\partial x^i_{A/B} \partial x^j}(\boldsymbol{z}(\lambda)) \right] , \tag{5.9c}$$

all quantities being taken at (λ) and where we define

$$\frac{\partial^2 \Delta^{(1)}_r}{\partial x^i_{A/B} \partial x^j}(\boldsymbol{z}(\lambda)) = \int_0^1 \left[\, m_{(1),\alpha\beta} z^\alpha_{A,j} z^\beta_{A/B,i} \pm \tilde{h}^i_{(1),\alpha} z^\alpha_{A,j} + m_{(1),\alpha} z^\alpha_{AA/AB,ji} + \tilde{h}^j_{(1),\alpha} z^\alpha_{A/B,i} \pm \bar{h}^{ji}_{(1)} \, \right]_{\lambda\mu} d\mu \,, \tag{5.10}$$

with the function $\bar{h}$ defined by

$$\bar{h}^{ik}_{(n)} = \left. \frac{\partial \tilde{h}^i_{(n)}}{\partial x^k_A} \right|_{z^\alpha = \mathrm{cst}} = - \left. \frac{\partial \tilde{h}^i_{(n)}}{\partial x^k_B} \right|_{z^\alpha = \mathrm{cst}} , \tag{5.11}$$

and $z^\alpha_{AA/AB,ji} = \frac{\partial^2 z^\alpha}{\partial x^j_A \partial x^i_{A/B}}$. Similar expressions can be written for $\partial \mathcal{I}_i / \partial t_B$.

6 Conclusions

We presented here our last advances in the formulation of the one-way frequency shift up to the post-post-Minkowskian approximation. The main result is given by Eq. (5.2) where the derivatives of Δ_r are given up to 2PM order by Eqs. (5.6-5.8). The advantage of our formulation is that it does not require the integration of the null geodesic differential equations. Instead, the frequency shift is expressed as integral of functions defined from the metric (and its derivatives) performed over a Minkowskian straight line.
Exact formulas up to 2PM order may be required for future space missions exploring the inner Solar System as shown by Tommei et al. (2010). The formulas presented here are useful to derive the frequency shift directly from the space-time metric. They can be used to derive the frequency shift up to 2PM order in a Schwarzschild space-time to validate results from Tommei et al. (2010). One can also use them to derive the frequency shift in the field of an ensemble of moving point masses in PPN formalism or in a framework improving the current IAU conventions (Minazzoli & Chauvineau 2009). The present results can also be used to derive frequency shift in alternative theories of gravity if the corresponding space-time metric is known. These applications will be presented elsewhere in a forthcoming paper.

A. Hees is research fellow from FRS-FNRS (Belgian Fund for Scientific Research) and thanks FRS-FNRS for financial support.
S. Bertone is PhD student under the UIF/UFI (French-Italian University) program and thanks UIF/UFI for the financial support.

References

Hees, A., Lamine, B., Reynaud, S., et al. 2012, ArXiv e-prints (1201.5041)
Klioner, S. A. & Zschocke, S. 2010, Classical and Quantum Gravity, 27, 075015
Kopeikin, S. M. & Schäfer, G. 1999, Phys. Rev. D, 60, 124002
Le Poncin-Lafitte, C., Linet, B., & Teyssandier, P. 2004, Classical and Quantum Gravity, 21, 4463
Minazzoli, O. & Chauvineau, B. 2009, Phys. Rev. D, 79, 084027
Synge, J. 1960, Relativity: the general theory, Series in physics (North-Holland Pub. Co.)
Teyssandier, P. & Le Poncin-Lafitte, C. 2008, Classical and Quantum Gravity, 25, 145020
Tommei, G., Milani, A., & Vokrouhlický, D. 2010, Celestial Mechanics and Dynamical Astronomy, 107, 285

SF2A 2012
S. Boissier, P. de Laverny, N. Nardetto, R. Samadi, D. Valls-Gabaud and H. Wozniak (eds)

STATUS OF DATA PROCESSING AND ANALYSIS PREPARATION FOR THE ACES MICROWAVE LINK

F. Meynadier[1], P. Delva[1], C. Le Poncin-Lafitte[1], P. Laurent[1] and P. Wolf[1]

Abstract. Our team in SYRTE-Observatoire de Paris is currently working on a software prototype for the processing and analysis of the data coming from the microwave link of the ACES (Atomic Clocks Ensemble in Space) mission. The goal of the mission is to realize, in space, a very accurate and highly stable time scale that will be compared to ground clocks. A critical part of this project is the time and frequency transfer between the ground and space stations: this will rely heavily on the microwave link, so it is critical to find a robust and accurate algorithm for this task.

Keywords: Atomic clocks, time transfer, fundamental physics experiments.

1 Introduction

The Atomic Clocks Ensemble in Spaces (ACES) mission is an international metrological space mission that will provide a highly stable and accurate time scale in space, by sending a caesium atom clock on board of the International Space Station (Salomon et al. 2007). A basic description of the time transfer mechanism as already been presented as a poster during the previous «Journées de la SF2A» (Meynadier et al. 2011). This presentation focusses on the current status of our study on the data processing and analysis.

2 Performance goals

The objective of the mission is to reach, for the clocks ensemble, a relative frequency stability (ADEV) of $\sigma_y = 10^{-13}\tau^{-\frac{1}{2}}$ (i.e. 3×10^{-16} after one day of integration, see Fig. 1), and a TDEV better than $2.1 \times 10^{-14}\tau^{-\frac{1}{2}}$ (i.e 12 ps after one day of integration, see Fig. 2), with an absolute frequency accuracy around 10^{-16}.

This translates to constraints on the microwave link stability: when comparing ground clocks to on-board clock while both ground station "see" the ISS (common view mode), the stability should be around 0.3 ps after 300 s of integration. For clock comparison through successive, non-overlapping comparison with the on-board clock (non-common view mode), it should stay within 7 ps after one day of integration. In practice, the signal will consist in pseudo-random noise which will be used to encode the date: once correlated with locally produced code it will provide a «code phase» measurement, but it will also possible to use the carrier phase for finer (albeit ambiguous) measurement.

3 Time transfer method

The desynchronisation between two clocks g and s is the proper time difference between those two clocks at a given coordinate time, $\tau^s(t) - \tau^g(t)$ (in what follows, proper times will be noted τ with a superscript denoting which clock is considered, whereas t will denote coordinate times). We can measure this by continuously encoding the proper time of clock g in a signal, send it to clock s, and then measure clock s proper time interval between the reception of the signal and the local occurrence of the same proper time. However this value will include the signal's time of flight and various internal delays, and care should be taken to convert them from proper time to coordinate time.

[1] LNE / Syrte – Observatoire de Paris, CNRS, UPMC Univ Paris 06, UMR8630, F-75005, Paris, France

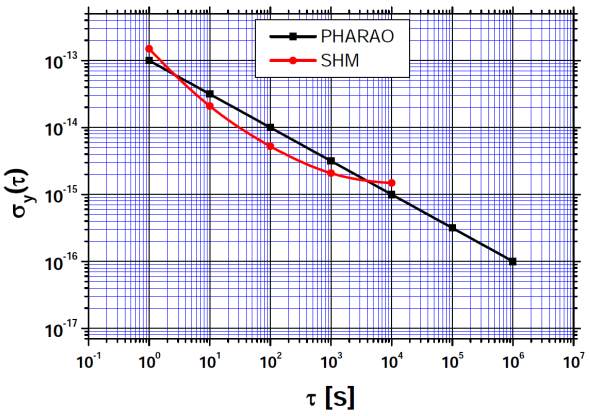

Fig. 1. PHARAO (Cesium clock) and SHM (hydrogen maser) expected performances in Allan deviation.

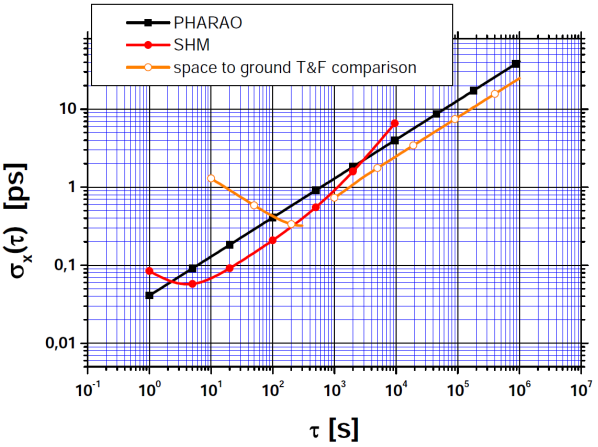

Fig. 2. Performance objective of the ACES clocks and the ACES space-ground time and frequency transfer expressed in time deviation.

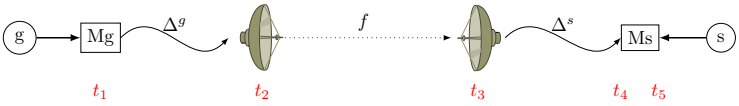

Fig. 3. Sequence of events for a one-way time transfer.

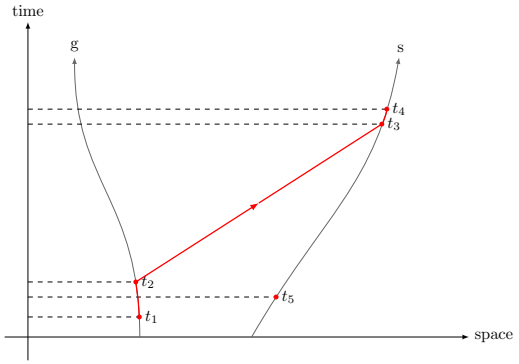

Fig. 4. Corresponding space-time diagram.

A conventional way to represent this "one-way" measurement is shown on Fig. 3 and 4. With those conventions, it is assumed that

$$\tau^g(t_1) = \tau^s(t_5) \tag{3.1}$$

i.e. the ground clock at coordinate time t_1 displays the same proper time as the space clock at coordinate time t_5. Then the signal from the ground clock travels to the emitting dish and reaches it at t_2. It will reach the receiving dish at t_3, and will finally arrive at the on-board comparator at t_4. We define

$$\Delta\tau^s(\tau^s(t_4)) = \tau^s(t_5) - \tau^s(t_4) \tag{3.2}$$

as our observable: it is the difference of proper time between the reception of a particular time code and its local production, which is susceptible of varying with the clock's proper time.

What we are looking for is the desynchronisation between the two clocks at t_4, i.e. in this case $\tau^s(t_4) - \tau^g(t_4)$. We will link this expression to the $\Delta\tau$ observable: for clarity we'll introduce the following notations: $T_{ij} = t_j - t_i$ and $[\cdot]$ for coordinate to proper time transformation (and back), a superscript indicating what transformation is performed. We also note $\Delta^g = [T_{12}]^g$ and $\Delta^s = [T_{34}]^s$, respectively, the internal delays caused by ground and space terminal.

We can then write:

$$\tau^s(t_4) - \tau^g(t_4) = -\Delta\tau^s(\tau^s(t_4)) - \left[T_{23} + [\Delta^g + \Delta^s]^t\right]^g \tag{3.3}$$

$$\tag{3.4}$$

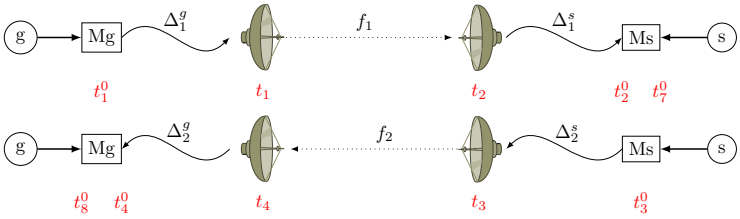

Fig. 5. Sequence of events for a two-way time transfer.

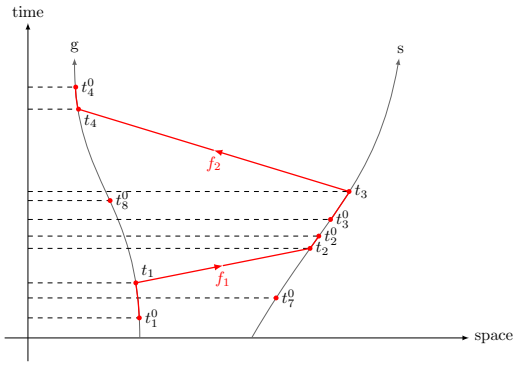

Fig. 6. Corresponding space-time diagram.

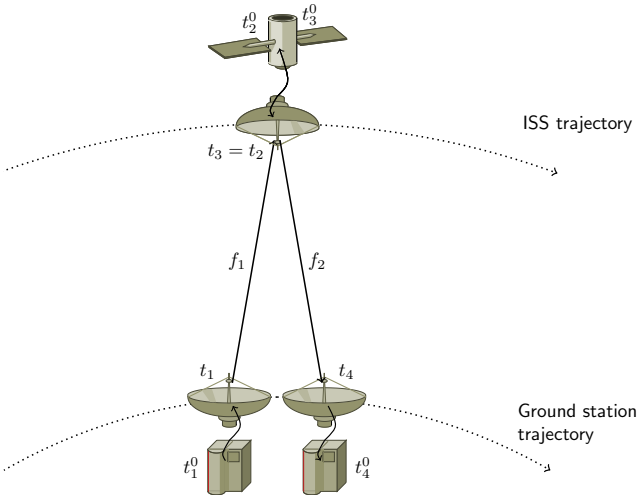

Fig. 7. Lambda configuration schema. As the ISS is supposed to be at the same point of the trajectory upon uplink signal reception and downlink signal emission, uncertainties on orbitography cancel out at the first order.

The two-way measurement is in fact a combination of two one-way measurements: such a measurement is presented on Fig. 5 and 6.

Following the same reasoning as for one-way measurements, we can get two expressions for the desynchronisation and use it to cancel most of the time-of-flight term, which is the main source of uncertainty:

$$\tau^s(t_1^0) - \tau^g(t_1^0) = \frac{1}{2}\left[\left[\Delta\tau^g_{\rm mo}(t_4^0) - \Delta\tau^s_{\rm mo}(t_2^0)\right]^t + T_{34} - T_{12}\right]^s \tag{3.5}$$

where $\Delta\tau_{\rm mo}$ stands for the "modified" observable, corrected for the internal delays (i.e. $\Delta\tau_{\rm mo} = \Delta\tau + \Delta^g + \Delta^s$).

We can even go further towards uncertainties minimization by choosing $t_2 = t_3$. This does not happen in principle, as each link's measurements are integrated over a 80 ms period which has no reason to be the synchronised on board and on ground. But we can always interpolate either downlink or uplink measurement to reach this configuration, dubbed the "Λ-configuration" (see Fig. 7).

Signal propagation is affected by the troposphere and the ionosphere, the former being modelised as a (mostly) non-dispersive medium, and the latter, which has a frequency dependant effect, being determined thanks to measurements of a secondary downlink with a much lower frequency. As it is necessary to calculate the Total Electron Content as an intermediate result for computing those delays, we'll issue the TEC as one of the scientific products of the ACES measurements.

More detailed developments of the calculations, with discussion of the various effects, can be found in Delva et al. (2012).

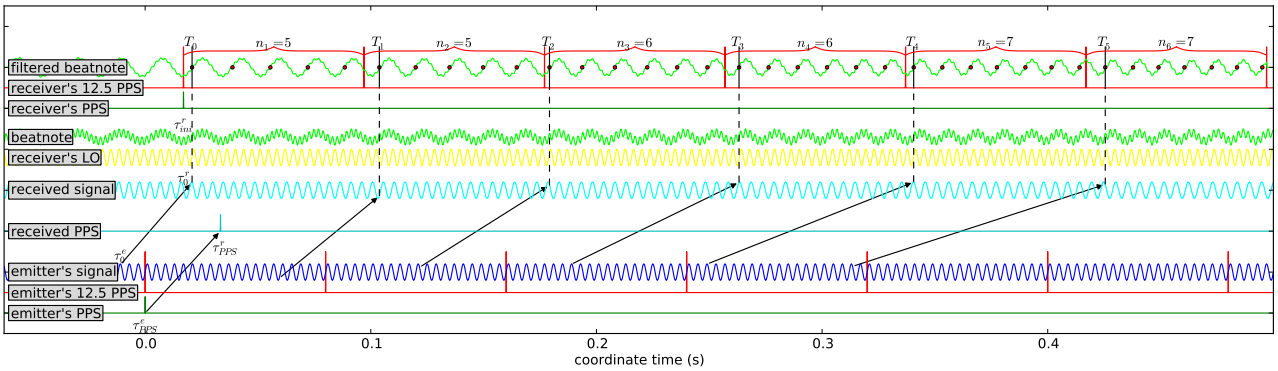

Fig. 8. From bottom to top, various steps for the generation of the data.

4 Recovering $\Delta\tau$ from hardware data

As we have seen our basic assumption is that we have access to the $\Delta\tau$ observables to get back to the desynchronisation. Unfortunately we do not have direct access to such data, and the last few months has been devoted to the recovery of $\Delta\tau$ observables (Syrte Team, or ST observables) from what the hardware gives us access to (TimeTech, or TT observables hereafter). TimeTech hardware shapes both code-phase and carrier-phase measurements the same way: they are materialized by a periodic signal which is locked on the measured phase.

Figure 8 summarizes our understanding of the measurement. It can roughly be read from bottom to top:

- The 3 bottom curves represent the emitter's time scales: 1 Pulse Per Second signal in green, a 12.5 Hz pulses that delimit the 80 ms period in red, and a blue sine wave which represents the either the code or the carrier phase that is sent through the emitter's dish.
- The "received PPS" and "received signal" represent how those signals are received with a variable delay (mostly due to the relative motion of the receiver, but it also includes all kind of delays encountered during the signal's transmission here). The propagation delay is represented by the black arrows.
- The yellow sine wave is the receiver's local oscillator: its frequency is close enough to be mixed with the incoming carrier signal and generate a beatnote (green signal above).
- The beatnote is then filtered (top green curve) and measured against the receiver's PPS and 12.5 PPS. For each 80 ms sequence, two numbers are generated: the number of ascending zero-crossing of the beatnote during the previous interval (n_m, materialized by red dots here) and the value of the local timer (T_m) at the moment when the first zero-crossing of the sequence (this timer has a roughly 10 ns resolution).

One should note that

- The number of zero-crossings is not constant throughout the measurements when the relative speed between the emitter and the receiver varies sufficiently.
- A beatnote zero-crossing does not necessarily corresponds to a carrier phase zero-crossing, which forbids direct relation between the two.

What is foreseen to be retrieved from the raw telemeasure is a list of T_m and n_m with time tags, forming what we call the «TT observables». The relation between the ST and the TT observables is iterative:

$$\Delta\tau_m(T_m) = \Delta\tau_{m-1}(T_{m-1}) + \left(\frac{\omega_{\text{L.O.}}}{\omega_e} - 1\right)(T_m - T_{m-1}) \pm \frac{2\pi n_m}{\omega_e} \tag{4.1}$$

Equation (4.1) can be interpreted as follows: from one sequence to the next, the $\Delta\tau$ changes if the proper time interval $T_m - T_{m-1}$ is different to the proper time interval corresponding to n_m cycles of the carrier, with a $\frac{\omega_{\text{L.O.}}}{\omega_e} - 1$ factor converting the (integer) number of beatnote cycles to the (possibly non-integer) number of carrier cycles. The $\pm$ in front of the last term accounts for a technical difference between code phase and carrier

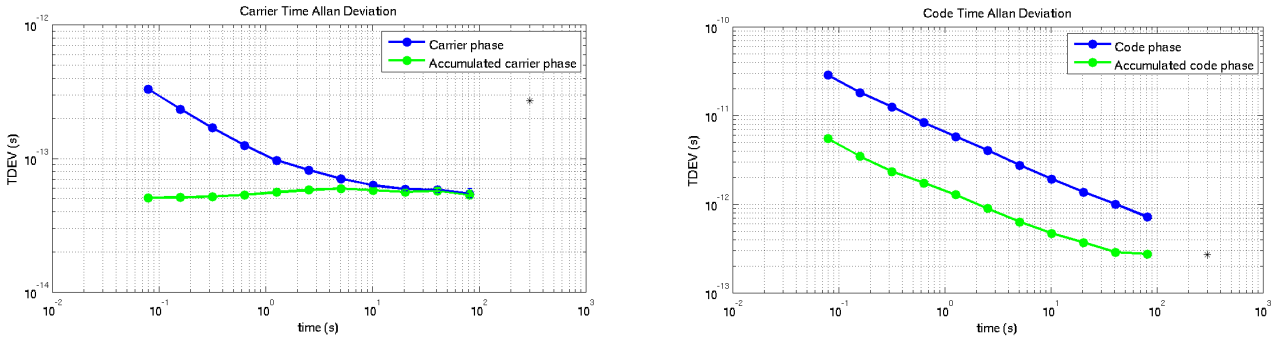

Fig. 9. Short term stability (TDEV) of ST observables, derived from carrier phase (**left**) or code phase (**right**) measurements, for both "phase" and "accumulated phase" observables.

phase measurements: in one case the local oscillator's frequency is higher than the incoming signal, and in the other case it's the opposite, thus changing the sign of $\frac{\omega_{\mathrm{L.O.}}}{\omega_e} - 1$: the $\frac{2\pi n_m}{\omega_e}$ term must have the opposite sign to compensate.

Then, we determine the initial term by using the fact that the PPS signal is unambiguous: the desynchronisation plus the propagation time will always be, in our case, of the order of a few milliseconds, so we can safely assume that the «received» PPS will always be close to the «receiver's» PPS, the interval between the two giving us a rough estimate of the $\Delta\tau_0$. By exploiting the fact that the emitted PPS is phase-coherent with the signal, we can even reach an absolute accuracy better than 100 ps on $\Delta\tau_0$ and we are currently working on a method to achieve the necessary accuracy to «bridge the gap» from one ISS transit to the next. This method relies on an additional observable, the «accumulated phase», which represents the same observable as the regular phase, but overcomes the reading uncertainty by averaging intermediate values. Figure 9 shows how much the use of «accumulated phase» observables will enhance the stability of our measurements.

5 Simulation

In parallel to the development of the data processing software, our team is developing an independent simulation software which already provides valuable data and allows to test the processing software modules. Currently implemented are:

- ISS orbitography + ground stations coordinates in ITRF, with transformation into ICRF
- Clock modelisation for ISS & ground stations, with basic noise simulation.
- Time transfer modelisation between the two terminals
- Generation of TimeTech observables, together with theoretical values against which calculated values will be compared.

A first step is to check that our pre-processing software correctly reconstructs the $\Delta\tau$ observables: an example of such a comparison is displayed on Fig. 10. This figure also illustrates the difference between carrier phase and code phase measurements: in this simulation, carrier phase data has a small dispersion (typically 0.5 ps) but a large offset with respect to the theoretical values (here, 1740 ps) whereas code phase data has around 20 ps dispersion but has a mean offset of a few ps.

Simulation software is also useful to evaluate the impact of each effect in the overall delay: figure 11 shows how several delays vary during one simulated ISS transit.

6 Conclusion

The ACES MWL data processing is still in development, but some major hurdles have been overcome this year. We have already started to implement the algorithm described by Duchayne (2008) and hope to have a working software prototype in the near future.

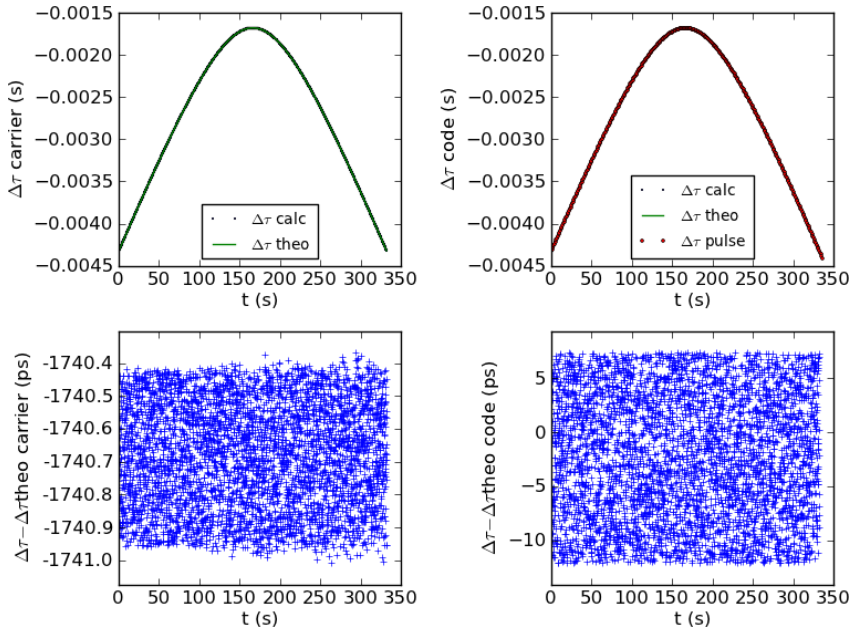

Fig. 10. Preprocessing software: comparison between ST observables calculated from simulated TT observables, and theoretical ST observables, for carrier (**left**) and code (**right**).

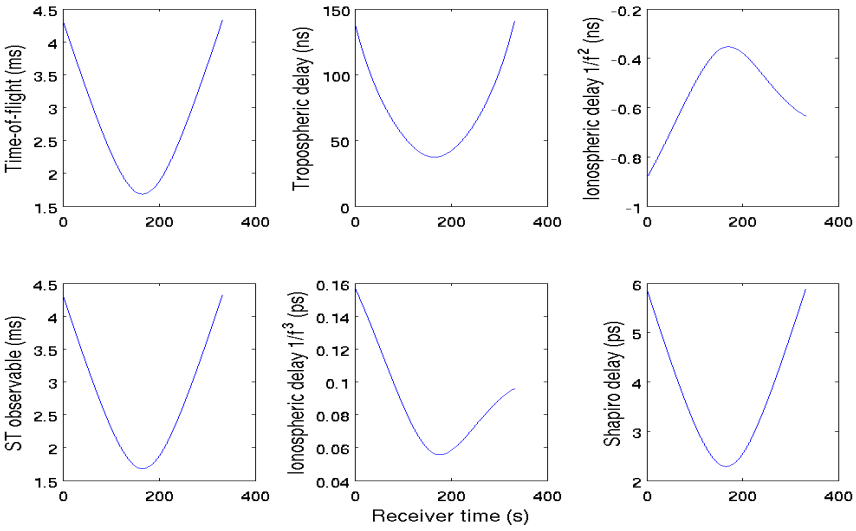

Fig. 11. Delays induced by several effects during one simulated transit, and corresponding ST observable. The main source of delay is the geometrical time of flight, followed by the tropospheric delay. The ionospheric delay is decomposed in terms of $1/f$ dependency, the second order being dominant.

References

Delva, P., Meynadier, F., Wolf, P., Le Poncin-Lafitte, C., & Laurent, P. 2012, ArXiv (1206.6239)

Duchayne, L. 2008, PhD thesis, Observatoire de Paris, France

Meynadier, F., Delva, P., Le Poncin-Lafitte, C., Laurent, P., & Wolf, P. 2011, in SF2A-2011: Proceedings of the Annual meeting of the French Society of Astronomy and Astrophysics, ed. G. Alecian, K. Belkacem, R. Samadi, & D. Valls-Gabaud, 679

Salomon, C., Cacciapuoti, L., & Dimarcq, N. 2007, International Journal of Modern Physics D, 16, 2511

SF2A 2012
S. Boissier, P. de Laverny, N. Nardetto, R. Samadi, D. Valls-Gabaud and H. Wozniak (eds)

LIBRATIONAL RESPONSE OF A THREE-LAYER TITAN

A. Richard[1] and N. Rambaux[1,2]

Abstract. The knowledge of the rotational motion is an important piece of information about the interior structure and possible process acting inside the bodies. Recently, through the observations acquired by the space mission Cassini, the rotational motion of Titan has been determined. Here, we investigate the librational motion that are the variations around the uniform rotational motion. The librations present a wide spectrum of frequencies due to the orbital variations of the satellite. In this work, we focus on the librational signature of Titan in longitude by modeling the gravitational torque of Saturn with a non-keplerian orbit and internal couplings.

Two different timescales dominate the spectrum, long periods related to the motion of the nodes of the orbit and short periods related to the orbital period of the satellite. These long period librations have amplitudes almost independent of the distribution of mass and bring no information on the geophysical interior. On contrary, the short period librations are sensitive to the interior. For example the presence of an internal ocean increases strongly the amplitude of short period librations. However, it is necessary to take into account all librations (long and short) in order to interpret the spacecraft observations.

Keywords: Libration, Titan, structure, longitude, orbital analysis, frequency

1 Introduction

Stiles et al. (2008, 2010) have investigated the motion of landmarks at the surface of Titan from flybys of Cassini spacecraft. Titan's pole location and spin rate have been obtained by this method, and the presence of an internal ocean has been suggested (Lorenz et al. 2008). They have determined an obliquity of about 0.3 deg and that the spin rate differs slightly from the synchronous spin-orbit resonance. Bills & Nimmo (2008) have shown that this obliquity is not consistent with a solid Titan in Cassini State and they suggested the existence of an internal liquid ocean to solve this problem.

The existence of the liquid ocean under Titan's surface has been studied with several methods. The Permittivity, Wave and Altimetry (PWA) instrument has measured the electric field during the *Huygens* descent through the atmosphere of Titan. These measurements revealed the possibility of an ice/ocean interface at 30-60 km depth (Béghin et al. 2010). The actual determined obliquity combined with the moment of inertia of Titan (Iess et al. 2010) and studies of Bills & Nimmo (2011) or Baland et al. (2011) suggest the existence of an internal liquid ocean as decoupling mechanism between the shell and the solid interior. A more recent determination of the variation of the quadrupole field (Iess et al. 2012) and Love number k_2 are consistent with the presence of a liquid subsurface ocean.

Here we investigate the librational motion of Titan as another method of deep structure analysis. This method has been developped and used for the Galilean satellites (Rambaux et al. 2011; Baland & Van Hoolst 2010) and for Titan for an elliptic motion (Van Hoolst et al. 2009). Librations in longitude are departures from the uniform rotational motion, caused by the variations of orbital velocity induced by the eccentricity of Titan's orbit. Here, we investigate the librational motion of Titan by including the perturbed orbital motion.

[1] IMCCE, Observatoire de Paris, CNRS UMR 8028
[2] Université Pierre et Marie Curie, UPMC - Paris 06

2 Orbital and librational motion of Titan

2.1 Longitudinal Libration equations in three layer model

We assume that Titan is composed of three principal layers: a solid ice shell, a liquid ocean and a solid inner core. The longitudinal libration equations are given by coordinate transformations of the angular momentum equation for a given layer i

$$\frac{d\boldsymbol{H}_i}{dt} = \boldsymbol{\Gamma}_i, \tag{2.1}$$

where $\boldsymbol{H}_i$ is the angular momentum expressed as $\boldsymbol{H}_i = [I]_i\boldsymbol{\omega}_i$ with $[I]_i$ the tensor of inertia, $\boldsymbol{\omega}_i$ the rotation vector and $\boldsymbol{\Gamma}_i$ the sum of the internal and external gravitational and pressure torques. Following Van Hoolst et al. (2009), Rambaux et al. (2011) derived from the third component of the angular momentum equation an expression of the equations of longitudinal libration:

$$C_s\ddot{\gamma}_s + 3n^2[(B_s - A_s) + (B'_s - A'_s)] + 2K_{int}\gamma_s - 2K_{int}\gamma_i = 3n^2[(B_s - A_s) + (B'_s - A'_s)](\nu - M - \theta_{0s}) \tag{2.2}$$

$$C_i\ddot{\gamma}_i + 3n^2[(B_i - A_i) - (B'_i - A'_i)] + 2K_{int}\gamma_i - 2K_{int}\gamma_s = 3n^2[(B_i - A_i) - (B'_i - A'_i)](\nu - M - \theta_{0i}) \tag{2.3}$$

where indices are s for the shell and i for the inner core, with A_l, B_l and C_l the principal moment of inertia of layer l ($A_l < B_l < C_l$, index $'$ denotes the moment of inertia difference caused by the pressure of the ocean), γ_l the librational angle defined as $\gamma = \theta - M - \theta_0$ with M the mean anomaly, θ the rotation angle and θ_0 the initial value of θ, n the mean motion of Titan, ν the true longitude of Titan and K_{int} the amplitude of the internal gravitational torque between the shell and the interior.

For a purely keplerian motion, the difference $\nu - M$ can be developed as a series of mean anomaly M and eccentricity e. Here we consider also the perturbations from other satellites and the Sun, so we expect frequencies corresponding to the perturbing bodies.

2.2 Frequency analysis method

To investigate the orbital motion of Titan, we perform a frequency analysis of the true longitude of Titan obtained from the JPL's Horizons ephemerides (Giorgini et al. 1996) for 400 years time span. We used the frequency analysis method developped by Laskar (1988, 2003) to identify the frequencies present in the true longitude. This method is implemented in the TRIP software developped by Gastineau & Laskar (2012). Table 1 gives the frequencies of the different components of the true longitude, where L_6 is the linear part of the mean longitude of Titan, Ω is the longitude of the node of Titan or Iapetus (Ω_6 or Ω_8), ϖ is the longitude of the pericenter of Titan or Iapetus (ϖ_6 or ϖ_8) and L_s the mean longitude of the Sun.

The most important term in the analytical decomposition of the true longitude corresponds to the orbital period of Titan with an amplitude of two times the eccentricity ($e = 0.028$). We also recognize the perturbation terms from the Sun by the saturnian annual (29.44 years) and semi-annual (14.72 years) excitation of Titan's true longitude (L_s and $2L_s$ terms respectively). We can then include these decomposition of the true longitude in the equations of libration to obtain the longitudinal libration of Titan for a chosen internal structure model.

2.3 Internal structure models

Equations (2.2) and (2.3) show that the librations are dependent on the internal structure of the satellite through the moments of inertia. Recent moments of inertia determination by Iess et al. (2010) has allowed to get information on Titan's internal structure. Fortes (2012) has explored the chemical and thermal parameters consistent with the moment of inertia of Titan, and constructed a range of possible internal structures. In our analysis, three different internal structure models have been selected from Fortes (2012). One of them includes internal liquid ocean while the other ones are solid models with different interior compositions and densities. Even if the internal liquid ocean seems to be confirmed as the analyses progress, we keep the solid models for results comparison. The different interior structures used here are described by Fortes (2012).

3 Results and discussion

For each internal structure model and each frequency of the true longitude, we compute the libration angle solution of the shell as $\gamma_s = \sum_j A_j \sin(\omega_j t + \phi_j)$, where A_j are the amplitudes of librations, ω_j the frequencies

and ϕ_j the phases. The librational motion of Titan's equator in the light internal ocean model (model 1) is plotted on Figure 1. The motion is dominated by long period terms from the annual and semi-annual components (29.44 and 14.72 years). The short period terms are visible at a lower scale in the thickness of the curve with smaller amplitudes.

Table 1. Librations in longitude of Titan due to orbital forcing (deviation in meters). The orbit comes from the Horizons ephemerides taken over 400 years (Giorgini et al. 1996). Initial date is J2000. The model 1 is the light internal ocean model (ocean density of 1000 kg m^{-3}), the model 2 is a solid model of pure water ice and a rocky core, and the model 3 is a solid model of pure water ice including a liquid iron core (developed by Fortes 2012).

		Amplitude of libration [m]			
Frequency [rad/day]	**Period [day]**	**Model 1 (ocean)**	**Model 2 (solid)**	**Model 3 (liquid core)**	**Identification**
0.39402	15.946	-319.036	-52.032	-52.034	$L_6 - \varpi_6$
0.78803	7.973	-1.422	-0.232	-0.232	$2L_6 - 2\varpi_6$
0.39408	15.944	-1.520	-0.248	-0.248	$L_6 - 2\varpi_8 + 2\Omega_6$
0.00117	5376.633	552.772	560.119	560.118	$2L_s$
0.00058	10750.365	470.287	471.838	471.838	L_s
0.39290	15.992	-0.851	-0.139	-0.139	$L_6 + \Omega_6 - 2L_s$

Table 1 gives the decomposition of the libration angle of the shell for each orbit excitation frequency in the case of a light internal ocean model (lowest density of water, model 1), and pure water ice models with and without liquid iron core (model 3 and 2 respectively). As expected, the most important terms are the annual and semi-annual components with amplitudes for model 1 of 470.287 and 552.772 meters, respectively. However, models 2 and 3 (solid) have both amplitudes of 471.8 and 560.1 meters, respectively. The differences of amplitude for these small frequencies are just a few meters, mostly due to the oceanic pressure on the solid surfaces. The low frequencies librations are almost independent of the structure models. The gravitational torque dominates the inertia of the body for low frequencies, so the amplitudes of librations are almost equal to the magnitudes of perturbations.

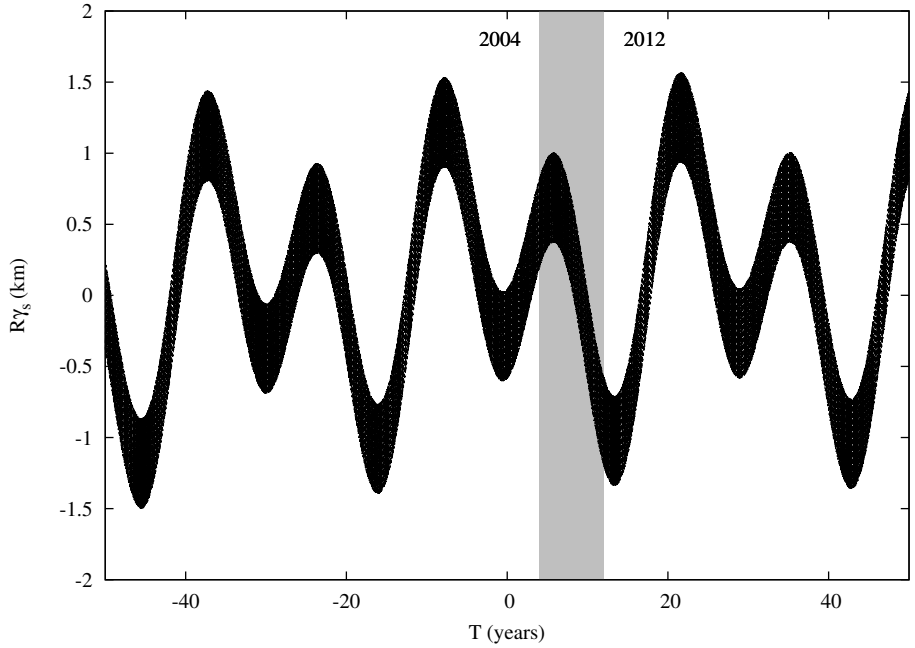

Fig. 1. Time evolution of the libration in longitude angle of Titan over 100 years. The origin of time is J2000. The grey band represents the arrival date of Cassini in Saturn system and the today value.

At high frequencies (first terms of Table 1), the amplitudes of libration are discriminating for the different models. The internal ocean model has a deviation of 319.036 meters at the orbital frequency while the solid

models have about 50 meters deviations. Indeed, for this range of frequencies, the inertia of Titan is significant on its behavior and dominates the gravitational torque.

In addition, we note that, the forcing frequencies are far from the proper frequencies of the models ($\omega_1 = 2.147\ 10^{-2}$ rad d^{-1} and $\omega_2 = 6.502\ 10^{-3}$ rad d^{-1} for model 1 and $\omega_s = 7.372\ 10^{-3}$ rad d^{-1} for model 2 and model 3) so no resonance can occur. Taking into account the atmospheric torque in the libration angle solution as in Van Hoolst et al. (2009), we had $\Gamma(t) = \Gamma_A \sin(\omega_A t + \phi_A)$ to the torques applied on Titan, with $\Gamma_A = 1.6\ 10^{17}$ Nm (Tokano & Neubauer 2005)(the amplitude of the gravitational torque is $2.63\ 10^{20}$ Nm for model 1). This forcing term has a frequency ω_A equals to the Saturn's semi-annual frequency (period of 14.72 years). At this frequency, the libration amplitude for the model 1 reaches 791.555 meters i.e. 238.783 meters of atmospheric contribution.

4 Conclusions

An accuracy of 100 meters on Titan's equator deviation would be useful to detect the presence of the internal ocean with the librations. For the moment, the SAR landmarks positions error is at best 850 meters (Stiles et al. 2008). More data are needed to obtain a better constraint on the rotation model and landmarks locations. During the actual Cassini mission lifetime, Titan must have undergo deviations of about one kilometer. This deviation should be sufficiently large to be detected by the SAR method and included in the rotation model of Titan.

We thank Jacques Laskar for fruitful discussions on the orbit frequency analysis.

References

Baland, R.-M. & Van Hoolst, T. 2010, Icarus, 209, 651

Baland, R.-M., Van Hoolst, T., Yseboodt, M., & Karatekin, Ö. 2011, A&A, 530, A141

Béghin, C., Sotin, C., & Hamelin, M. 2010, Comptes Rendus Geoscience, 342, 425

Bills, B. G. & Nimmo, F. 2008, Icarus, 196, 293

Bills, B. G. & Nimmo, F. 2011, Icarus, 214, 351

Fortes, A. D. 2012, Planet. Space Sci., 60, 10

Gastineau, M. & Laskar, J. 2012, TRIP 1.2.0, TRIP Reference manual, IMCCE, Paris Observatory, `http://www.imcce.fr/trip`

Giorgini, J. D., Yeomans, D. K., Chamberlin, A. B., et al. 1996, in Bulletin of the American Astronomical Society, Vol. 28, AAS/Division for Planetary Sciences Meeting Abstracts #28, 1158

Iess, L., Jacobson, R. A., Ducci, M., et al. 2012, Science, 337, 457

Iess, L., Rappaport, N. J., Jacobson, R. A., et al. 2010, Science, 327, 1367

Laskar, J. 1988, A&A, 198, 341

Laskar, J. 2003, arXiv:math/0305364

Lorenz, R. D., Stiles, B. W., Kirk, R. L., et al. 2008, Science, 319, 1649

Rambaux, N., Van Hoolst, T., & Karatekin, Ö. 2011, A&A, 527, A118

Stiles, B. W., Kirk, R. L., Lorenz, R. D., et al. 2008, AJ, 135, 1669

Stiles, B. W., Kirk, R. L., Lorenz, R. D., et al. 2010, AJ, 139, 311

Tokano, T. & Neubauer, F. M. 2005, Geophys. Res. Lett., 32, 24203

Van Hoolst, T., Rambaux, N., Karatekin, Ö., & Baland, R.-M. 2009, Icarus, 200, 256

SF2A 2012
S. Boissier, P. de Laverny, N. Nardetto, R. Samadi, D. Valls-Gabaud and H. Wozniak (eds)

APPROXIMATE SOLUTION FOR THE GRAVITATIONAL POTENTIAL OF THIN DISKS

A. Trova[1], J.-M. Huré[1] and F. Hersant[1]

Abstract. We are interested in the derivation of reliable formulae for the gravitational potential of disks, under the assumption of axial symmetry. As a consequence of the Newton's law, the formula contains a diverging kernel which is always difficult to manage. In the particular case of vertically homogeneous bodies, we have built an equivalent kernel which is free of singularity, and therefore, well suited to numerical computations. From this new expression, in the case of geometrically thin disks, we have derived a good approximation. This formula reproduces the potential inside the body with a relative error as low as 10^{-3} typically. We will see, through various torus shapes, that our approximation can be used for thin and relatively thick disks.

Keywords: disks, Gravitation, Methods: numerical

1 Introduction

Thin disks are found in various types of objects in the Universe: around planets, in forming stars and in galaxies. As they host a certain amount of matter, they naturally generate a gravitational potential which can influence their own structure and dynamics, especially if they are "massive enough", compared to their environment (central star, circumstellar envelope, bulge, etc.). It is therefore important to build reliable formulae enabling to analyze various aspects of disk self-gravity, and the natural starting point to this is Newton's law. This law implies that the gravitational potential of matter enclosed in a volume V writes:

$$\Psi(\vec{r}) = \int_V \frac{\rho(\vec{r'})}{\mid \vec{r} - \vec{r'} \mid} d^3\vec{r'}, \tag{1.1}$$

and this is basically the convolution product of the mass density $\rho(\vec{r'})$ with the Green function $1/\mid \vec{r} - \vec{r'} \mid$. In practice, the potential is difficult to compute due to the hyperbolic divergence of the Green function when $\vec{r} \to \vec{r'}$, and this often supports the use of multipole expansions. For an axially symmetric object, the potential takes the form (Durand 1953):

$$\begin{cases} \psi(R,Z) = -2G \int_S \rho(a,z) \sqrt{\frac{a}{R}} k \mathbf{K}(k) da dz, \\ \\ k = \frac{2\sqrt{aR}}{\sqrt{(a+R)^2 + (Z-z)^2}}, \end{cases} \tag{1.2}$$

where $\mathbf{K}$ is the complete elliptic integral of the first kind, k is the modulus, and other variables are cylindrical coordinates (a typical configuration is shown in Fig. 1). This is a double integral over the cross-section S and the function $2\sqrt{\frac{a}{R}} k \mathbf{K}(k)$ plays the role of an "axially symmetrical Green function". It is particularly well suited to toroidal systems like disks and rings. As a direct benefit of the integration over the polar angle, the divergence of this new Green function is weaker: it occurs for $k \to 1$ (i.e for $\vec{r} \to \vec{r'}$), but it is now logarithmical. This does not render the numerical computation much easier. A common method is to expand this axially symmetrical Green function into Legendre polynomials (Hachisu 1986). This effectively avoids the divergence problem but generates new difficulties such as series truncations and convergence rate (Clement 1974).

[1] Université de Bordeaux, CNRS, LAB

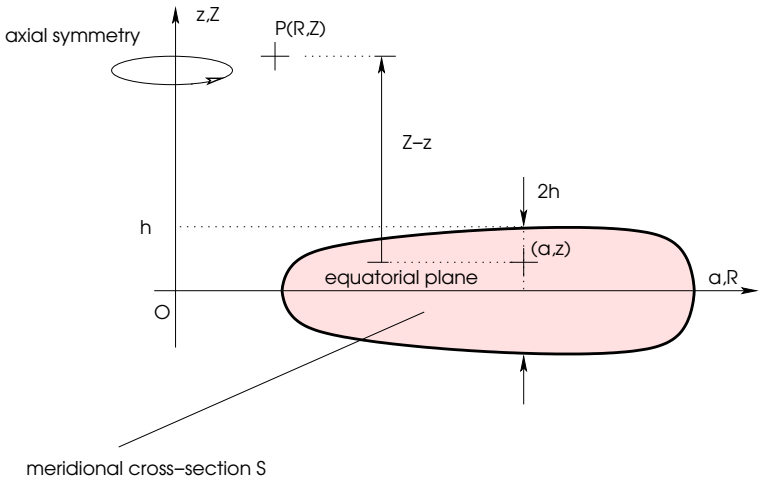

Fig. 1. Typical configuration for the gravitating, axially symmetric disk (finite size and mass, and local total thickness $2h$), and notations associated with the cylindrical coordinate system.

2 A general expression for the newtonian potential of vertically homogeneous bodies

Assuming that the mass density is, at a given radius a, independent on the altitude (i.e. there is no density stratification perpendicularly to the equatorial plane), then it is easy to rewrite the above expression as

$$\begin{cases} \psi(R,Z) = -G\int_a \mathcal{G}\Sigma da, \\ \\ \mathcal{G} \equiv \frac{1}{2h}\int_z 2\sqrt{\frac{a}{R}}k\mathbf{K}(k)dz \equiv \mathcal{G}(a,h;R,Z), \end{cases} \tag{2.1}$$

where

$$\Sigma = \int_z \rho(a)dz = 2\rho(a)h(a), \tag{2.2}$$

is the local surface density, h is the local semi-thickness (possibly a function of the radius), and $\mathcal{G}$ is the axially symmetrical Green function averaged over the disk thickness at the actual radius. This "mean Green function" is a purely geometrical function which depends on a, on the local thickness and the coordinates (R,Z) where the potential is requested. As shown in Trova et al. (2012), we can rewrite the mean Green function in the following form (see also Trova et al. 2011):

$$\begin{cases} \mathcal{G}\left(R,Z;a,h\right) = \frac{1}{h}\sqrt{\frac{a}{R}}\left[\int_{-h}^{h} k\mathbf{E}(k)dz - (Z-h)\mathbf{H}(m^2,k_+) + (Z+h)\mathbf{H}(m^2,k_-)\right], \\ \\ \mathbf{H}(m,k) = k\left[\mathbf{K}(k) - m'^2\mathbf{\Pi}(m^2,k)\right], \end{cases} \tag{2.3}$$

where $\mathbf{E}$ and $\mathbf{\Pi}$ are the complete elliptic integrals of the second and third kinds respectively, $k_\pm = k(z=\pm h)$, $m \equiv k(z=Z)$ and $m'^2 = 1-m^2$. This new form is very interesting first because each term of Eq.(2.3) is a regular function even when the modulus is unity. Actually, the divergence of the $\mathbf{H}$ function when $k_\pm = 1$ is cancelled by the presence of the multiplying factor $Z \mp h$ which is then zero. This means that the radial integral in Eq.(2.1a) using Eq.(2.3) can be performed by standard numerical techniques. Second, we have made no kind of approximation in deriving Eq.(2.3) meaning that the properties of the Newton's law are automatically saved everywhere in space. Third, the formula works for any disk shape.

3 Approximation for the potential of geometrically thin disks and rings

We see from Eqs.(2.1a) and (2.3) that the determination of the potential still requires a double integral over S. In the case of geometrically thin disks and rings (those systems where the thickness is locally small compared to the radius; see e.g. Shakura & Sunyaev 1973; Pringle 1981), we can however get a good approximation for $\mathcal{G}$,

leaving finally a single integral over a. This is achieved by considering an expansion of the term $k\mathbf{E}(k)$ around the mean modulus $\tilde{k}$ defined by:

$$\tilde{k} = \frac{k_+ + k_-}{2} \tag{3.1}$$

and which never reaches unity. From a Taylor expansion at the first order, we actually find:

$$-\int_z k\mathbf{E}(k)dz \approx \mathbf{T}_1(\tilde{k})(Z-z) + 2\sqrt{aR}\mathbf{T}_2(\tilde{k})\,\mathrm{argsh}\left(\frac{Z-z}{a+R}\right) \tag{3.2}$$

where we have set:

$$\begin{cases} \mathbf{T}_1(k) = k\left[\mathbf{K}(k) - \mathbf{E}(k)\right], \\ \\ \mathbf{T}_2(k) = 2\mathbf{E}(k) - \mathbf{K}(k). \end{cases} \tag{3.3}$$

So, if we replace Eq.(3.2) in Eq.(2.3a), we obtain an approximation of the axially symmetrical Green mean function, namely:

$$\begin{aligned} \mathcal{G} \approx 2\sqrt{\frac{a}{R}}\Bigg\{ & \mathbf{T}_1(\tilde{k}) - \mathbf{T}_2(\tilde{k})\frac{\sqrt{aR}}{h}\left[\mathrm{argsh}\left(\frac{Z-h}{a+R}\right) - \mathrm{argsh}\left(\frac{Z+h}{a+R}\right)\right] \\ & -\frac{Z-h}{2h}\mathbf{H}(m,k_+) + \frac{Z+h}{2h}\mathbf{H}(m,k_-)\Bigg\} + \mathcal{O}\left(\frac{h^4}{16a^4}\right) \equiv \mathcal{G}_{\mathrm{app.}} + \mathcal{O}\left(\frac{h^4}{16a^4}\right). \end{aligned} \tag{3.4}$$

and it is expected to work well for disk with small aspect ratios h/a. As a consequence, the gravitational potential of a thin three-dimensional disk is now given by a one-dimensional integral over the radius, namely:

$$\psi(R,Z) \approx -G\int_a \mathcal{G}_{\mathrm{app.}}(a,h;R,Z)\Sigma(a)da \equiv \psi_{\mathrm{app.}}(R,Z). \tag{3.5}$$

This approximation is in principle valid in the whole physical space. It can be used to model the internal structure of self-gravitating disks and rings. So, it is very attractive from a numerical point of view.

4 Checking the approximation

4.1 A torus with circular cross-section

To check the quality of the approximate potential, we have compared Eq.(2.1a) using Eq.(2.3) and Eq.(3.5) for circular, homogeneous torus. This case has been recently considered by Bannikova et al. (2011). Here, the center of the torus is at $(0.75, 0)$, and the radius is $L = 0.25$ (diameter $2L$). Figure 2a shows the relative deviation between the potential values when computed in the half-plane $(R, Z \geq 0)$. We see that the relative error is of the order of 10^{-3} inside the torus as well as outside, and reaches 10^{-4} locally. The error map is rather uniform. This indicates that we have a very good estimate of the quantity $\int k\mathbf{E}(k)dz$ for any R and Z, at least for vertically homogeneous systems. Interestingly enough, the error is especially low while the torus considered has a rather large aspect ratio h/a which reaches $1/3$ at the center. The approximation works well because the error is, as indicated above, depends on $(h/a)^4$. We conclude that our approximation remains satisfactory for geometrically thick disks, as long as $h/a \leq 1$.

4.2 Varying the torus cross-section

We have tested the limits of the approximation by varying independently the radial extension $2L$ and the vertical extension $2h$ of the torus considered before, while maintaining the center of the torus at $(0.75, 0)$. The exact potential and the approximate one are then compared at the center. The results are displayed in Fig. 2b. We find that the relative error for the potential at the center is not very sensitive to the radial extension of the torus, and the relative accuracy increases when h decreases. This means that the best objects this approximation is made for are thin disks and rings.

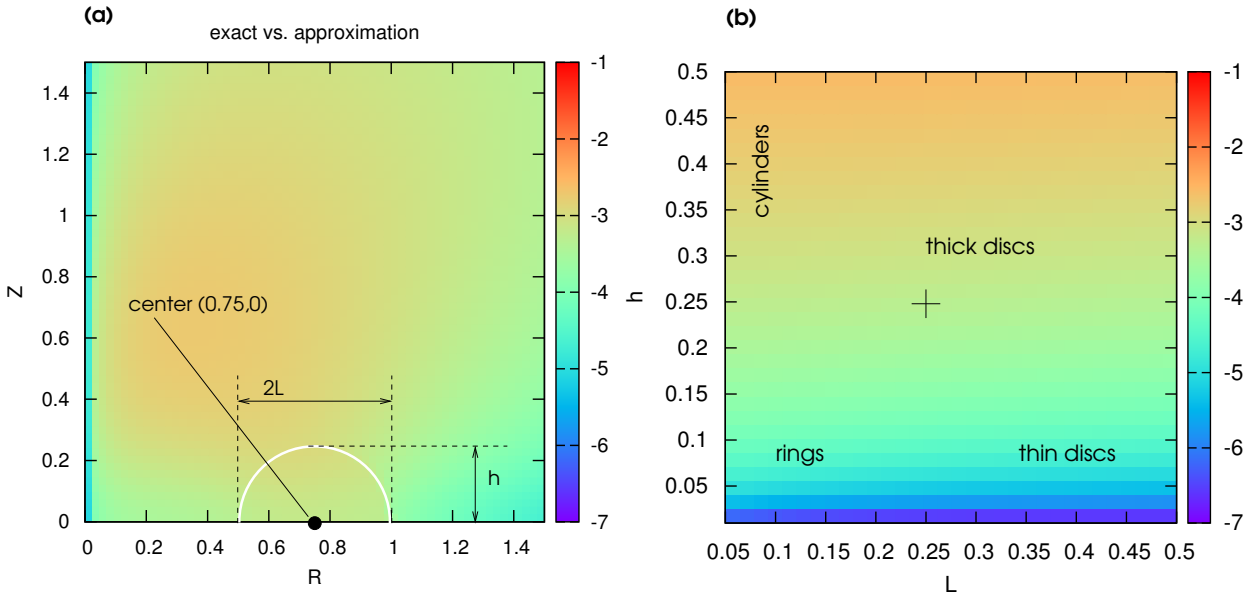

Fig. 2. Left: relative error (decimal log. scale) between the approximate potential given by Eq.(3.5) and the exact potential given by Eq.(2.1a) using Eq.(2.3) in the $(R, Z > 0)$-plane of a homogeneous torus with circular cross-section (boundary shown in white). **Right:** comparison of potential values at the center $(0.75, 0)$ of the torus when varying the diameter $2L$ and the vertical extension $2h$ of the torus (the cross corresponds to the circular torus shown left).

5 Conclusion

We have produced an equivalent expression for the gravitational potential of axially symmetrical, vertically homogeneous bodies which is free of kernel singularity. It saves the properties of Newton's law and is valid whatever the body's shape. We have also derived a reliable approximation which is especially accurate for thin disks and rings (although it works well for thick disks). This approximate formula is also numerically interesting because the potential is expressed by a radial (i.e. one dimensional) integral. Our approximation is in principle restricted to vertically homogeneous systems, and as we know, realistic systems have density gradients in three directions. We have then checked the sensitivity of the results to the $\rho(z)$ profile. As demonstrated in Trova et al. (2012), our approximate Green function gives surprisingly good results in the case of a Gaussian distribution.

References

Bannikova, E. Y., Vakulik, V. G., & Shulga, V. M. 2011, MNRAS, 411, 557

Clement, M. J. 1974, ApJ, 194, 709

Durand, E. 1953, Electrostatique. Vol. I. Les distributions. (Ed. Masson)

Hachisu, I. 1986, ApJS, 61, 479

Pringle, J. E. 1981, ARA&A, 19, 137

Shakura, N. I. & Sunyaev, R. A. 1973, A&A, 24, 337

Trova, A., Huré, J.-M., & Hersant, F. 2011, in SF2A-2011: Proceedings of the Annual meeting of the French Society of Astronomy and Astrophysics, ed. G. Alecian, K. Belkacem, R. Samadi, & D. Valls-Gabaud, 685

Trova, A., Huré, J.-M., & Hersant, F. 2012, MNRAS, 424, 2635

SF2A 2012
S. Boissier, P. de Laverny, N. Nardetto, R. Samadi, D. Valls-Gabaud and H. Wozniak (eds)

POTENTIAL GENERATED INNER AND OUTSIDE A CIRCULAR WIRE IN ITS PLANE. APPLICATION TO SATURN'S RING

N.-E. Najid[1], M. Zegoumou[1] and E.H. El Ourabi[1]

Abstract. In this article we derive the development of the potential generated by a homogeneous wire bent into a circular shape (Najid, Jammari & Zegoumou, 2005). We develop the potential as a power series of the distance from an appropriate origin to the test particle. The potential is expressed as a function of Legendre polynomials. We study both, the case where the test particle is inside or outside the circular wire. By Lagrangian formulation, we establish the differential equation of motion. The numerical resolution leads us to different orbits. Outside the wire we get a case where the test particle is confined between a maxima and minima of the radial position; while inner the wire the test particle is subjected to an escape case depending on the time of integration.

Keywords: Potential, Legendre Polynomial, Orbits.

1 Introduction

The irregular shapes of many celestial bodies (Kellog 1954)have gained a great interest during the last decades. Their physical and geometrical studies require an accurate knowledge of the potential generated by them (Danby 1992). In our study, we develop the method of calculation of the potential generated by a circular wire in a point located at the plane of the wire. The result is given directly by a series expansion in terms of R, the radius of the wire and his total mass. We are interested to the points outside and inner the circle. We established the equation of motion of a test particle and give the orbits in accordance with the initial conditions. Precession of perihelia or chaotic cases is proved (Murray & Dermott 1999).

2 Potential generated by a circular wire

We consider a circular ring of radius R and total mass M, located in the (xoy) plane (Fig.1). The gravitational potential generated by the ring at a point M (x, y) is expressed by:

$$dU = -G\frac{dm}{PM} \tag{2.1}$$

ρ The distance between the element dm centered at P, (Fig.1) and M.

- Expression of ρ :

$$PM^2 = OM^2 + OP^2 - 2OM.OP\cos(\overrightarrow{OM},\overrightarrow{OP})$$

$$\rho = PM = \sqrt{r^2 + R^2 - 2.r.R.\cos(\theta - \psi)} \tag{2.2}$$

[1] Laboratoire de Physique Théorique et Appliquée Université Hassan II Ain Chock- Faculté des Sciences Ain Chock BP 5366 Maârif Casablanca Morocco

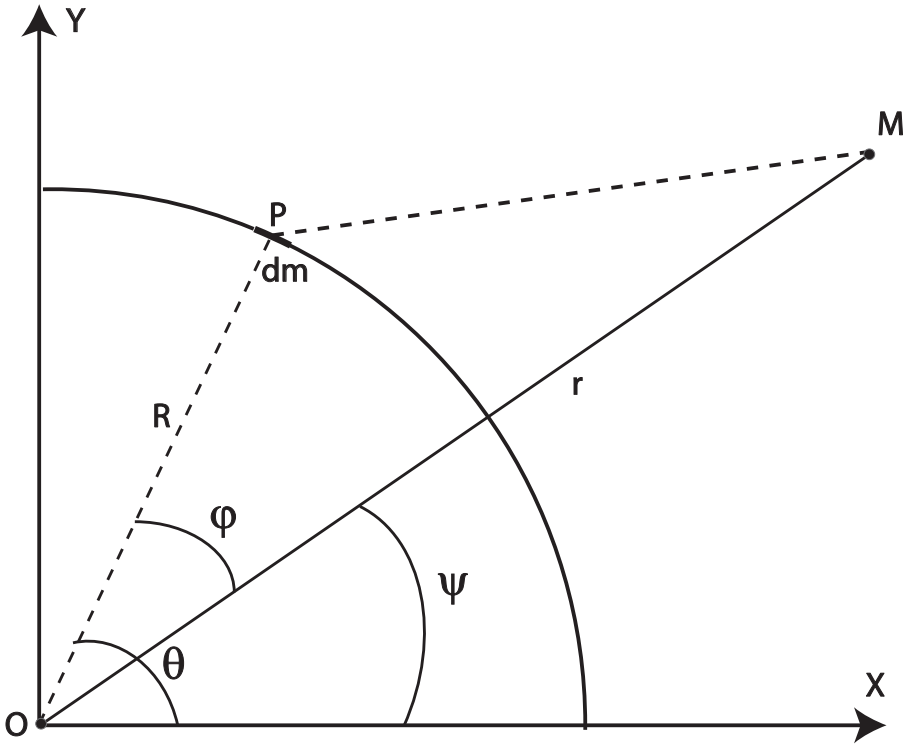

Fig. 1. Ring in the plane (xoy)

- Expression of dm:

We have:

$$dm = \lambda dl = \lambda R d\theta \tag{2.3}$$

Substituting the expressions (2.2) and (2.3) in (2.1), the potential generated by the ring is:

$$U = -G.R.\lambda \int_0^{2\pi} \frac{d\theta}{\sqrt{r^2 + R^2 - 2.r.R.\cos(\theta - \psi)}} \tag{2.4}$$

3 The potential created by a circular ring at a point outside of the ring

By means of Legendre polynomials(MacRobert 1927) in (2.4), we get:

$$\frac{1}{\sqrt{r^2 + R^2 - 2.r.R.\cos(\varphi)}} = P_0(\cos\varphi).\frac{1}{r} + P_1(\cos\varphi).\frac{R}{r^2} + P_2(\cos\varphi).\frac{R^2}{r^3} + ...$$

Limiting ourselves to order 2 we can write:

$$U = -G\lambda R\left[\int_{-\psi}^{2\pi-\psi} \frac{d\varphi}{r} + \int_{-\psi}^{2\pi-\psi} \frac{R}{r^2}\cos\varphi d\varphi + \int_{-\psi}^{2\pi-\psi} \frac{R^2\left(\cos^2\varphi - 1\right)}{2r^3} d\varphi\right]$$

After integration we find:

$$U = -\frac{G.\lambda.R}{r}.2\pi - \frac{G.\lambda.R^3}{4.r^3}.2\pi + ... \tag{3.1}$$

We add to the potential created by the ring the potential created by the planet.
This is a Keplerian potential: $U_{planet} = -\frac{G.M_{planet}}{r}$

With $M = \int dm = \int_0^{2\pi} \lambda R d\theta = 2.\pi.R.\lambda$, we arrive to :

$$U = -\frac{GM}{r} - \frac{GMR^2}{4r^3} - \frac{G.M_{planet}}{r} = -\frac{G\left(M + M_{planet}\right)}{r} - \frac{GMR^2}{4r^3}$$

$$U = \frac{A}{r} + \frac{B}{r^3} \tag{3.2}$$

The expression (3.2) represents the form of the potential, with:

$A = -G\left(M + M_{planet}\right)$ and $B = -\frac{GMR^2}{4}$.
U is viewed as two parts, one consist of the keplerian case, while the other summaries the perturbation.

3.1 The Lagrangian of the particle test

We study the dynamical behavior of a test particle, with unit mass, in the field of the homogeneous ring.
The Lagrangian of the test particle is given by:

$L = T - U$, so:

$$L = \frac{1}{2}\dot{r}^2 + \frac{1}{2}r^2\dot{\psi}^2 - \frac{A}{r} - \frac{B}{r^3} \tag{3.3}$$

3.2 Equation of motion

The equations of motion are given by: $\frac{d}{dt}\left(\frac{\partial L}{\partial \dot{r}}\right) = \frac{\partial L}{\partial r}$
with: $\frac{\partial L}{\partial r} = r\dot{\psi}^2 - \frac{G(M+M_{planet})}{r^2} - \frac{3GMR^2}{4r^4}$
and $\frac{\partial L}{\partial \dot{r}} = \dot{r}$
Therefore: $\frac{d}{dt}\left(\frac{\partial L}{\partial \dot{r}}\right) = \ddot{r}$ and subsequently we find:

$$\ddot{r} = r\dot{\psi}^2 - \frac{G\left(M + M_{planet}\right)}{r^2} - \frac{3GMR^2}{4r^4} \tag{3.4}$$

With $u = \frac{1}{r}$, we have $\ddot{r} = h^2u^2\frac{d^2u}{d\psi^2}$ and $\dot{\psi} = h.u^2$
After calculation and arrangement of expressions (3.4) we find, the differential equation of motion

$$\frac{d^2u}{d\psi^2} + \frac{3B}{h^2}u^2 + u = -\frac{A}{h^2} \tag{3.5}$$

Finally we can write this equation as:

$$\frac{d^2u}{d\psi^2} + au^2 + u = b \tag{3.6}$$

Where $a = \frac{3B}{h^2} < 0$ will be examined as a term of a small perturbation.
And $b = -\frac{A}{h^2} > 0$ corresponds to the well-known keplerian case.
The equation (3.6) represents the dynamical equation of motion of the test particle in the gravitational field generated by the homogeneous ring. This equation is nonlinear, she require then a numerical resolution.

3.3 Trajectories

Keplerian case: a=0

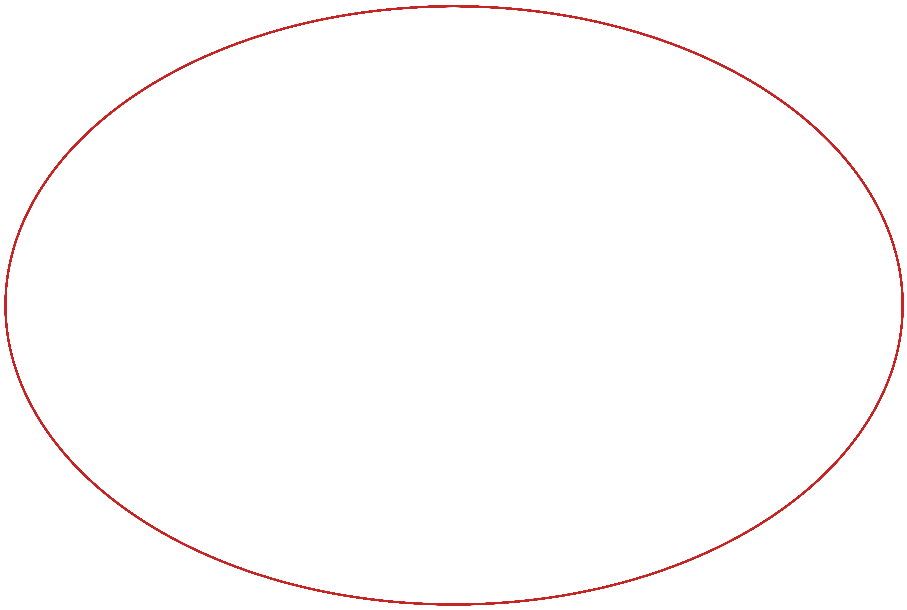

Fig. 2.

The figure 2, correspond to an elliptic orbit. This is a regular periodic orbit. The corresponding potential is $\frac{A}{r}$

General case:

From different initial conditions, we reach many different cases as in figures 3, 4, 5 and 6.
Figure 3 correspond to a precession of the perihelia.

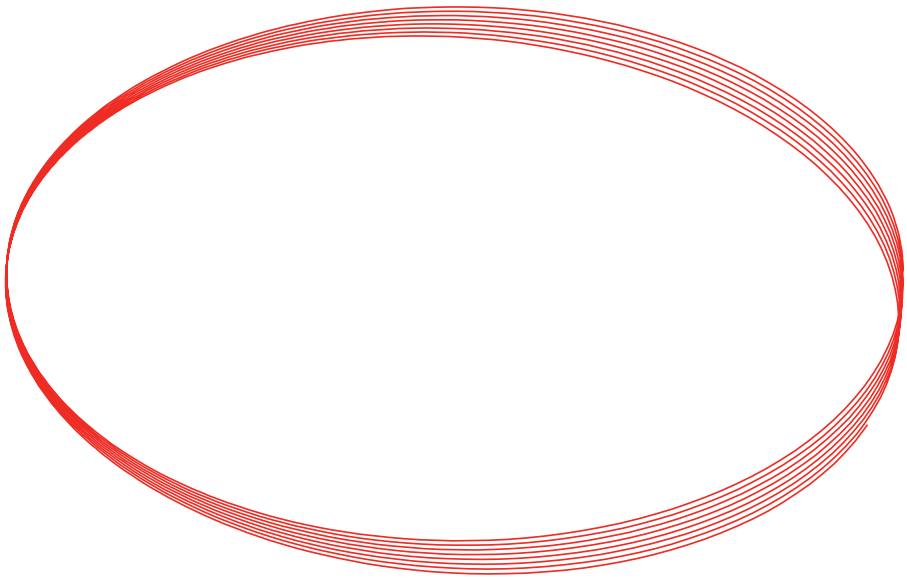

Fig. 3.

We find in fig (4, 5, 6) that when the term "a" increases the test particle is confined between two elliptic boundary trajectories. However, we approach a limit trajectories, when the disturbance term increases.

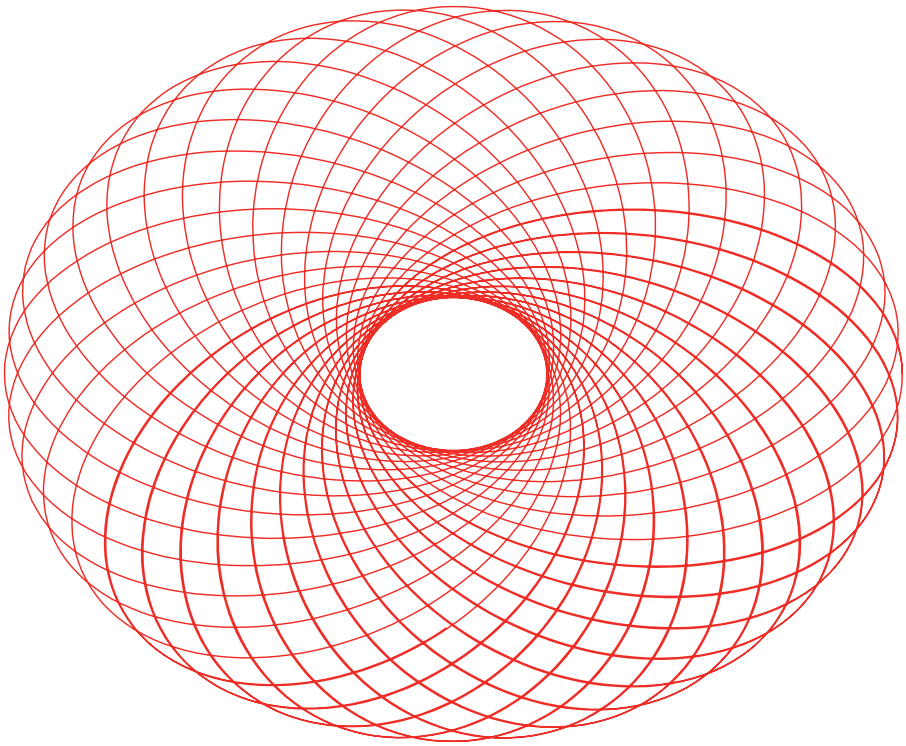

Fig. 4.

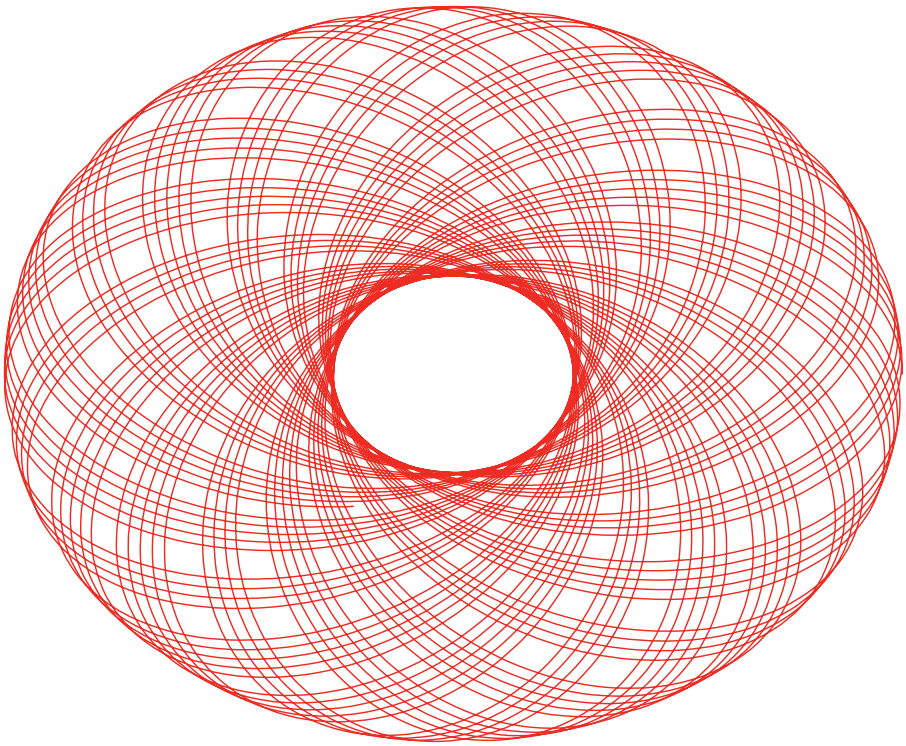

Fig. 5.

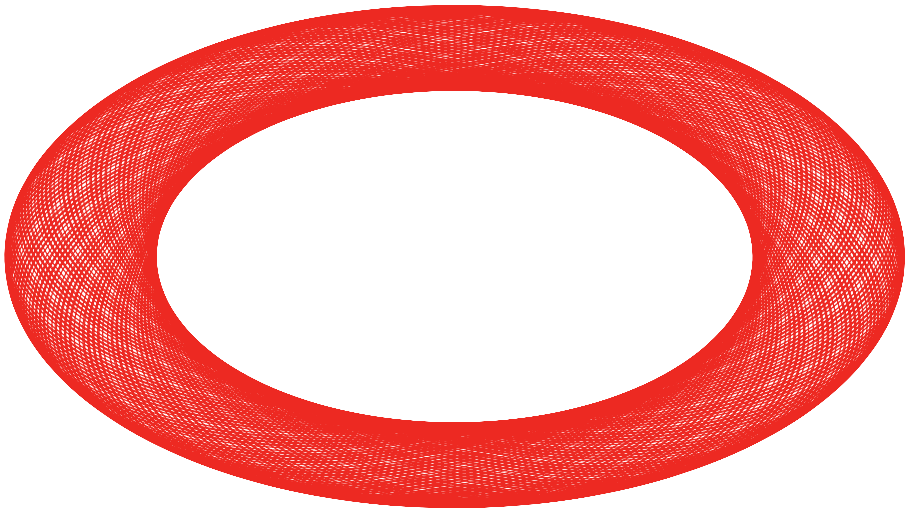

Fig. 6.

4 The potential created by a circular ring at a point inner the ring

4.1 The potential expression

The expression $\frac{1}{\sqrt{r^2+R^2-2.r.R.\cos(\varphi)}}$ is written again in this case as:

$$\frac{1}{\sqrt{r^2+R^2-2.r.R.\cos(\varphi)}} = P_0(\cos\varphi).\frac{1}{R} + P_1(\cos\varphi).\frac{r}{R^2} + P_2(\cos\varphi).\frac{r^2}{R^3} + P_3(\cos\varphi).\frac{r^3}{R^4} + ...$$

With $P_n(\cos\varphi)$ are the coefficients of LEGENDRE.
The expression of the potential becomes:

$$U = -G\lambda R \left[\begin{array}{l} \int_{-\psi}^{2\pi-\psi} \frac{d\varphi}{R} + \int_{-\psi}^{2\pi-\psi} \frac{r\cos\varphi}{R^2} d\varphi \\ + \int_{-\psi}^{2\pi-\psi} \frac{r^2\left(3\cos^2\varphi-1\right)}{R^3} d\varphi + \int_{-\psi}^{2\pi-\psi} \frac{r^3\left(5\cos^3\varphi-3\cos\varphi\right)}{R^4} d\varphi \end{array} \right]$$

After calculation we arrive at the following expression

$$U = -\frac{GM}{R} - \frac{GMr^2}{4R^3} = -\frac{GM}{R^3}\left(R^2 + \frac{r^2}{4}\right) \tag{4.1}$$

By adding the potential generated by the ring to that of the central planet, we get:

$$U = -\frac{G.M}{R^3}\left(R^2 + \frac{r^2}{4}\right) - \frac{G.M_{planet}}{r}$$

4.2 Equation of motion

As before, we arrive for a test particle of unit mass to the expression:

$$L = \frac{1}{2}\dot{r}^2 + \frac{1}{2}r^2\dot{\psi}^2 + \frac{G.M}{R^3}\left(R^2 + \frac{r^2}{4}\right) + \frac{GM_{planet}}{r}$$

The equations of motion are given by:

$$\frac{\partial L}{\partial r} = r\dot{\psi}^2 + \frac{G.Mr}{2R^3} - \frac{GM_{planet}}{r^2}$$

We have $\frac{d}{dt}\left(\frac{\partial L}{\partial \dot{r}}\right) = \frac{\partial L}{\partial r}$ with $\frac{\partial L}{\partial r} = r\dot{\psi}^2 + \frac{G.Mr}{2R^3} - \frac{GM_{planet}}{r^2}$
and $\frac{\partial L}{\partial \dot{r}} = \dot{r}$ .Therefore: $\frac{d}{dt}\left(\frac{\partial L}{\partial \dot{r}}\right) = \ddot{r}$ and subsequently we find:

$$\ddot{r} = r\,\dot{\psi}^2 - \frac{GM_{planet}}{r^2} + \frac{G.Mr}{2R^3} \tag{4.2}$$

By making the change of variable $u = \frac{1}{r}$,we can write the differential equation as follows:

$$\frac{d^2u}{d\psi^2} + u + \frac{GM}{2R^3h^2u^3} - \frac{GM_{planet}}{h^2} = 0$$

$$\frac{d^2u}{d\psi^2} + u + \frac{a}{u^3} + b = 0 \tag{4.3}$$

With : $a = \frac{G.M}{2.h^2.R^3} > 0 \quad ; \quad b = -\frac{GM_{planet}}{h^2} < 0$

5 Conclusions and perspectives

- In this work we studied the dynamical behavior of a test particle in the gravitational potential of a homogeneous circular wire. We got a few orbits depending on initial conditions.
- If r> R it was found that the test particle is confined in space between two limit trajectories, with no possibility of escape.
- Similarly for r < R we found that for specific initial conditions we obtain a closed trajectory after some laps, while for other initial conditions the test particle is located in space without a limit cycle.
- To analyze these orbits we have to use quantitative tools such as the method of Poincaré section.
- For a more realistic model, we must consider a three-dimensional wire (Pascoli 2000).
- Also, to study the behavior near the rings of Saturn, a study of a disk is in progress.

References

Danby, J.M.A. 1992, Fundamentals of Celestial Mechanics (Willmann-Bell. Inc.)

Kellog, O.D. 1954, Foundation of Potential Theory (New York : Dover Pub. Inc.)

MacRobert, T.M., Spherical Harmonics An Elementary Treatise On harmonic Functions with applications (Methuen. CO. LTD, London)

Murray, C.D., Dermott., S.F. 1999, Solar System Dynamics, Cambridge University Press.

Nadij, N.-E., Jammari, M.-K., Zegoumou, M. 2005, Condensed Matter Volume 6, number 1

Pascoli, G. 2000, Astronomie Fondamentale (Dunod Ed.)

Session 05

CoRoT/Kepler: Contribution to stars characterisation

SF2A 2012
S. Boissier, P. de Laverny, N. Nardetto, R. Samadi, D. Valls-Gabaud and H. Wozniak (eds)

DETERMINATION OF THE STARS FUNDAMENTAL PARAMETERS USING SEISMIC SCALING RELATIONS

K. Belkacem[1]

Abstract. Seismology of stars that exhibit solar-like oscillations develops a growing interest with the wealth of observational results obtained with the CoRoT and *Kepler* space-borne missions. In this framework, relations between asteroseismic quantities and stellar parameters provide a unique opportunity to derive model-independent determinations of stellar parameters (e.g., masses and radii) for a large sample of stars. I review those scaling relations with particular emphasis on the underlying physical processes governing those relations, as well as their uncertainties.

Keywords: Convection, Turbulence, Stars: oscillations, Stars: interiors

1 Introduction

The determination of accurate stellar parameters (mass, radius, effective temperature, age, and chemical composition) is a fundamental and longstanding problem in astrophysics (e.g. Soderblom 2010). When compared to many other methods, seismology is recognized to provide the most precise determination of those fundamental parameters (e.g. Lebreton 2011). Nevertheless, such a determination is only possible by means of the use of stellar models and therefore suffers from our deficient knowledge of the physical processes taking place in stars (e.g. Goupil et al. 2011b,a).

The situation recently improved with the advent of space-borne asteroseismology, more precisely with the launch of CoRoT (Baglin et al. 2006a,b; Michel et al. 2008) and *Kepler* (Borucki et al. 2010). Those two spacecrafts are providing us with high-quality photometric data. Up to now, several hundreds of main-sequence stars with solar-like oscillations have been detected and several thousands oscillating red-giant stars, allowing for statistical analysis. With such large number of stars it is not possible to performe classical seismology, *i.e.* by individual mode fitting of the power spectrum. This is very time (and man-power) consuming so that a new method emerged through the use of seismic global parameters. The latter are typical global characteristics of the oscillation spectra such that the regularities in frequency (or period), or the frequency of the maximum amplitude.

This approach gave birth to the *ensemble* asteroseismology, which cornerstones are the relations between global seismic quantities and stellar parameters. It allows ones to infer model-independent stellar parameters as well as information on stellar structure and evolution. Scaling relations between asteroseismic quantities and stellar parameters such as stellar mass, radius, effective temperature, and luminosity have initially been observationally derived by several authors (e.g. Ulrich 1986; Brown et al. 1991; Kjeldsen & Bedding 1995) using ground-based data. CoRoT and Kepler confirmed these results by providing accurate and homogeneous measurements for a large sample of stars from main-sequence to red-giant stars (e.g., Mosser et al. 2010; Baudin et al. 2011a; Mosser et al. 2011a,b, 2012b,a; Samadi et al. 2012).

Among them, the relations between the large separation ($\Delta\nu$) and the mean density ($\bar{\rho}$) as well as between the frequency of the maximum height in the power spectrum ($\nu_{\rm max}$) and the photospheric cut-off frequency ($\nu_{\rm c}$) have been known for a long time in the context of solar-like pulsators (e.g., Ulrich 1986; Brown et al. 1991; Kjeldsen & Bedding 1995; Belkacem et al. 2011). In fact, as shown below, the physical grounds of these two relations were known for an even longer time in the context of classical pulsators (stars exhibiting opacity-driven

[1] LESIA, UMR8109, Observatoire de Paris, Université Pierre et Marie Curie, Université Denis Diderot, 92195 Meudon Cedex, France. kevin.belkacem@obspm.fr

modes). This will be the subject of the first part of this review, with particular emphasize on the theoretical side. We will discuss the fundamental physical concept underlying these scaling relations and show how one can use them to infer stellar masses and radii. Section 3 will be dedicated to scaling relations that exhibit an important potential in providing information on the core properties of stars, or effective temperature. Last but not least, we will discuss the uncertainties on the seismic global parameters by showing that many biases can exist and are still to be addressed.

Finally, we note that this paper is by no means an exhaustive review. Rather it puts forth the necessity of understanding the theoretical ground of the scaling relations, unfortunately too often bypassed in the recent literature.

2 The canonical scaling relations

In this section, we will first address the problem of the relations between the large separation ($\Delta\nu$) and the mean density ($\bar{\rho}$), as well as the frequency of maximum height in the power spectrum ($\nu_{\rm max}$) and the cut-off frequency (ν_c). Those two scaling relations provide an estimate of the mass and the radius. They are now widely used and we will see that the underlying physics is known for a long time. Consequently, in this review we will denote them as *canonical* scaling relations.

2.1 Relation between the large separation ($\Delta\nu$) and the mean density ($\bar{\rho}$)

Let us first define the large separation ($\Delta\nu$). To this end, it is necessary to introduce the first-order asymptotic relation that permits us to express modal frequencies ($\nu_{n,\ell}$) as a function of the structure of the star, *i.e.*

$$\nu_{n,\ell} \approx \left(n + \frac{\ell}{2} + \frac{1}{4} + \alpha\right) \left[2\int_0^R \frac{{\rm d}r}{c_s}\right]^{-1} , \tag{2.1}$$

where n is the radial order, ℓ the angular degree, α a term that accounts for the near-surface effect (e.g. Christensen-Dalsgaard & Thompson 1997; Rosenthal et al. 1999), and c_s the sound speed. Note that such an asymptotic analysis assumes that we consider high radial-order modes (see Tassoul 1980).

Hence, from Eq. (2.1), the large separation which is defined as the frequency separation between two consecutive radial orders (for a given ℓ) is given by

$$\Delta\nu \equiv \nu_{n+1,\ell} - \nu_{n,\ell} = \left[2\int_0^R \frac{{\rm d}r}{c_s}\right]^{-1} , \tag{2.2}$$

and therefore represents the inverse of twice the time for a perturbation of pressure to cross the entire star (in other words a back and forth of a long wavelength pressure wave).

Now, we aim at deriving the scaling relation between $\Delta\nu$ and the mean density. To this end, one has to adopt the homology relations. So let us consider two stars such that for two shells verifying $r/R = r'/R'$, the corresponding mass shells equal ($m/M = m'/M'$), where M, M' are the total masses of two stars belonging of a homologous series, and R, R' their total radii. This type of approximated stellar models has been extensively discussed in the literature (e.g. Cox & Giuli 1968; Kippenhahn & Weigert 1990), and it is possible to show that pressure (p) and density (ρ) of both models are related by (see Sect. 20.1 of Kippenhahn & Weigert 1990)

$$\frac{p}{p'} = \left(\frac{M}{M'}\right)^2 \left(\frac{R}{R'}\right)^{-4} , \tag{2.3}$$

$$\frac{\rho}{\rho'} = \left(\frac{M}{M'}\right) \left(\frac{R}{R'}\right)^{-3} , \tag{2.4}$$

Then, from Eqs. (2.3) and (2.4), the relation of the sound speed immediately follows

$$\frac{c_s}{c_s'} = \left(\frac{M}{M'}\right)^{1/2} \left(\frac{R}{R'}\right)^{-1/2} . \tag{2.5}$$

Now, to demonstrate the relation between the large separation and the mean density, let us define the ratio

$$\mathcal{R} = \frac{\Delta\nu}{\Delta\nu'} . \tag{2.6}$$

Using Eq. (2.5) together with the relation $r/R = r'/R'$, it is straightforward to demonstrate the desired scaling relation, *i.e.*

$$\mathcal{R} = \left[\int_0^{R'} \frac{\mathrm{d}r'}{c'_s}\right]\left[\int_0^{R} \frac{\mathrm{d}r}{c_s}\right]^{-1} = \left(\frac{R'}{R}\right)^{3/2}\left(\frac{M}{M'}\right)^{1/2} = \left(\frac{\bar{\rho}}{\bar{\rho}'}\right)^{1/2} . \tag{2.7}$$

In other words, the large separation of a given star ($\Delta\nu$) can be related to its mean density such as

$$\Delta\nu = \left(\frac{\bar{\rho}}{\bar{\rho}_\odot}\right)^{1/2} \Delta\nu_\odot, \tag{2.8}$$

where, as classically found in the literature, the Sun has been used as the reference. Equation (2.8) demonstrates the scaling relation between $\Delta\nu$ and $\bar{\rho}$, and shows that the only underlying hypothesis is the homology, which will be discussed in Section 4.2.1.

At this stage, it is worthwhile to recall that Eq. (2.8) and its derivation is not a novelty and was known, in a hardly different framework, for many decades. Indeed, for classical pulsators, the mode frequencies are often near the fundamental mode frequency (e.g., Cepheid, δ-Scuti, β-Cephei). For fundamental radial mode (ν_0), its period (Π_0) is therefore proportional to the time for a pressure perturbation to cross the entire star, *i.e.*

$$\Pi_0 \propto \int_0^R \frac{\mathrm{d}r}{c_s} \quad \Longrightarrow \quad \Pi_0 \propto \bar{\rho}^{-1/2} \tag{2.9}$$

This relation (Eq. 2.9) is quite famous in the context of classical pulsators and one of the first authors to mention it was, to our knowledge, Eddington (1917) for explaining the periodic motion of Cepheids. Subsequently, the relation between ν_0 and the mean density had been often used as an argument to identify periodic motions of stars as pulsations. Moreover, it is the basis of the famous period-luminosity relation of Cepheids (e.g. Cox et al. 1972; Cox 1980). As a conclusion, the derivation of Eq. (2.8) is nothing but the same as for Eq. (2.9) and was proposed for a long time by several authors such as Ledoux & Walraven (1958) (see Cox 1980, for a comprehensive discussion).

2.2 Relation between the frequency of the maximum height in the power spectrum ($\nu_{\rm max}$) and the cut-off frequency ($\nu_{\rm c}$)

The derivation of the relation between $\nu_{\rm max}$ and $\nu_{\rm c}$ is more difficult. Because sometimes not fully understood (e.g., Christensen-Dalsgaard 2011a,b), we explain here how the basic physical picture is grasped and that departure from the observed relation arises from the complexity of non-adiabatic processes involving time-dependent treatment of convection and not from the failure of the physical picture. In addition, a discussion on the physics of opacity-driven pulsations in stars will bring us with the conclusion that the main physical reason for the existence of the relation between $\nu_{\rm max}$ and $\nu_{\rm c}$ is a common feature of pulsating stars.

2.2.1 Derivation of the $\nu_{\rm max} - \nu_{\rm c}$ relation

Let us first begin by recalling that solar-like oscillations are the result from a balance between mode driving and damping. Therefore, as a first approximation, each mode can be considered as a driven and damped oscillator. The driving is related to turbulent Reynolds stresses (see Samadi 2011, for a comprehensive review on stochastically excited modes) while damping is caused by a combination of physical processes not discussed here (but see Houdek (2008) for a discussion on mode damping).

Therefore, the frequency $\nu_{\rm max}$ is in principle determined by both physical mechanisms. To have a more precise view of what governs $\nu_{\rm max}$, one has first to determine which of the aforementioned process is responsible for the maximum height in the power spectrum, thus the physical mechanism controlling $\nu_{\rm max}$. We thus consider the height H of a given mode in the power spectrum, which is a natural observable. For stochastically excited modes, the height of the mode profile in the power spectrum is (e.g. Baudin et al. 2005; Chaplin et al. 2005; Belkacem et al. 2006)

$$H \;=\; \frac{P}{2\,\eta^2\,\mathcal{M}}\,, \tag{2.10}$$

where P are the excitation rates, η the damping rates, and $\mathcal{M}$ the mode masses[i]. It turns out that the depression (plateau) of the damping rates η is responsible for the presence of a maximum in the power spectrum. This is in agreement with theoretical computations (Houdek et al. 1999; Chaplin et al. 2008; Belkacem et al. 2011, 2012) and recent observations of the solar-like stars by *Kepler* (Appourchaux et al. 2012).

The subsequent issue then relies on the physical origin of the depression of the solar damping rates. This plateau originates from a destabilizing effect in the super-adiabatic layers and occurs when the modal period nearly equals the thermal time-scale (or thermal adjustment time-scale) in the superadiabatic layers. This was first mentioned by Balmforth (1992) (see his Sect. 7.2 and 7.3) and confirmed by Belkacem et al. (2011). The authors used two different non-adiabatic pulsation codes, making this conclusion quite secure. This can be expressed by the following condition

$$\mathcal{Q} = 2\pi\nu_{\rm max}\,\tau \sim 1\,, \tag{2.11}$$

with the inverse of the thermal time-scale defined as

$$\tau^{-1} = \frac{L}{4\pi r^2 \rho c_v T H_p} = \tau_{\rm conv}^{-1} + \tau_{\rm rad}^{-1}\,, \tag{2.12}$$

where L is the luminosity, r the radius, ρ the local density, $c_v = \left(\partial U/\partial T\right)_\rho$ with U the specific internal energy, H_p the pressure scale height, $\tau_{\rm rad}$ and $\tau_{\rm conv}$ the radiative and convective thermal time-scales, respectively. Note that Eq. (2.12) is a local formulation of the thermal time-scale; a non-local one can also be defined (e.g. Pesnell 1983). It is important to note that, contrary to the situation for classical pulsators, for which the envelope is dominated by the radiative transport of energy, Eq. (2.12) exhibits contributions of both the radiative and convective fluxes.

The last step is to establish the relation between the thermal time-scale (τ) and the cut-off frequency. In the mixing-length theory framework the thermal time-scale can be recast such as (Belkacem et al. 2011)

$$\frac{1}{\tau} = \frac{F_{\rm conv}}{\rho c_v T H_p}\left[1 + \frac{F_{\rm rad}}{F_{\rm conv}}\right] \propto \left(\frac{\mathcal{M}_a^3}{\alpha}\right)\left(\frac{c_s}{2H_p}\right)\left[1 + \frac{F_{\rm rad}}{F_{\rm conv}}\right]\,, \tag{2.13}$$

where $\mathcal{M}_a = \mathtt{v}_{\rm conv}/c_s$ is the Mach number, and α the mixing-length, $F_{\rm conv}, F_{\rm rad}$ the convective and radiative fluxes respectively, $c_s/(2H_p)$ the cut-off frequency. Note that the cut-off frequency appears in Eq. (2.13) as the ratio $c_s/(2H_p)$.

This relation is verified, in Fig. 1, by using a grid of stellar models. The relations between the thermal time-scale and the cut-off frequency is very tight for red giants while a dispersion is observed for main-sequence stars. Such a dispersion is explained by the dependence to the Mach number to the third power. Indeed, this can be easily understood since the Mach number predominantly depends on the effective temperature that varies much more for main-sequence and sub-giants than for red giants. Equation (2.13) is useful to explicitly show the relation between τ and $\nu_{\rm c}$, but an investigation of this relation using a set of 3D hydrodynamic numerical simulation would be desirable in the future to get more quantitative estimates.

It is nevertheless worth to emphasize that the resonance between the local thermal time-scale and the pulsation period (which is nothing but the *transition* region, see Sect. 2.2.2) explains the *tight*[ii] observed relation between $\nu_{\rm max}$ and $\nu_{\rm c}$. More interestingly, as observed in Fig. 2, the maximum dispersion predicted for main-sequence stars is in agreement with recent observations of Bedding (2011). Indeed, as depicted by Fig. 2, a departure from the scaling relation seems to occur for main-sequence stars (i.e., large $\nu_{\rm max}$) in qualitative agreement with Fig. 1.

2.2.2 The transition region: a common feature of both opacity-driven and solar-like pulsators

As explained in the preceding section, the cornerstone of the physical picture underlying the $\nu_{\rm max}$–$\nu_{\rm c}$ relation is the nearly equality between the thermal time-scale and the modal period in the super-adiabatic layers.

Let us first briefly introduce the notion of *transition* region (see Cox 1974, 1980, for a more complete discussion). Such a region is defined by the layer for which the ratio of the thermal time-scale to the modal period equals unity. Indeed, it separates the quasi-adiabatic from the non-adiabatic layers, more precisely

[i] The mode mass corresponds to the total amount of mass effectively moved by a given mode. Its definition is $\mathcal{M} = \int_0^M |\xi|^2 {\rm d}m/|\xi(r=R)|^2$.

[ii] Note that the notion of *tightness* sometimes found in the literature is very subjective and would need a more rigorous quantitative estimate.

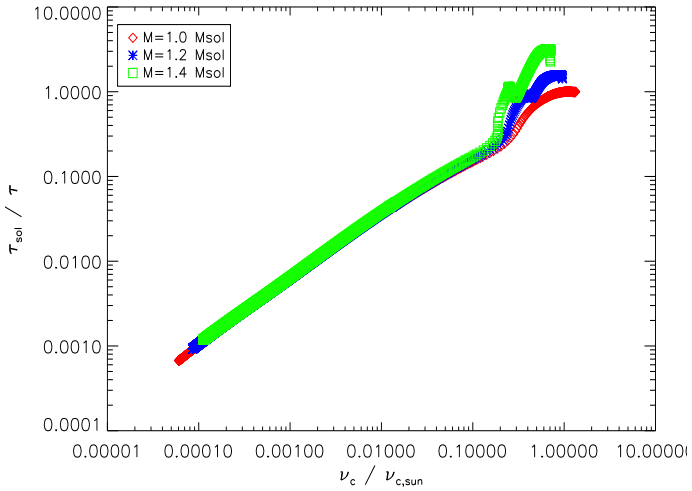

Fig. 1. Thermal frequency ($1/\tau$) computed from Eq. (2.13) versus the cut-off frequency (computed as the ratio $c_s/(2Hp)$), normalized to the solar values, for models with masses ranging from $M = 1.0\,M_\odot$, $M = 1.2\,M_\odot$ and $M = 1.4\,M_\odot$ from the ZAMS to the ascending vertical branch. The inputs physics of the models can be found in Belkacem (2011).

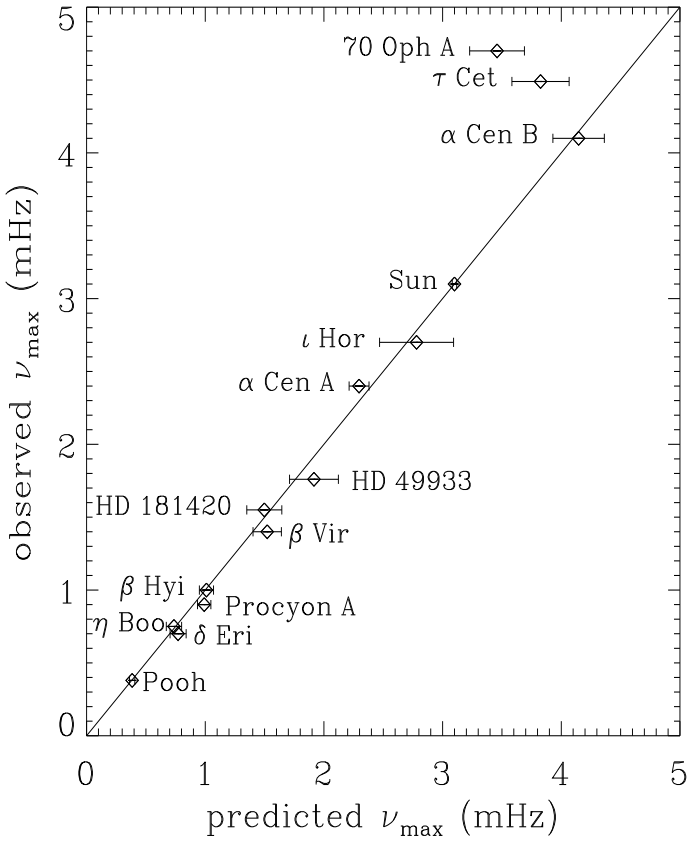

Fig. 2. Observed $\nu_{\max}$ versus predicted $\nu_{\max}$, computed using Eq. (2.17), for stars observed from the ground (see Bedding 2011, for details). Figure from Bedding (2011).

- In quasi-adiabatic regions, there is a negligible[iii] exchange of energy between the oscillations and the

[iii] By negligible we mean on the mode stability.

background. In those regions, $\mathcal{Q} \gg 1$ (see Eq. 2.11) then $\tau \gg \Pi_{osc}$, so that the background does not have time enough to react to the perturbations introduced by one cycle of the oscillation. Consequently, over a time-scale τ perturbations related to the oscillation compensate and the background experiences a nearly vanishing average over many oscillation cycles.

- In non-adiabatic regions, the energy exchange between the oscillation and the background dominates. We are in the opposite situation where $\mathcal{Q} \ll 1$ so $\tau \ll \Pi_{osc}$. Indeed, in this case the thermal structure "instantaneously" adjusts to the perturbations generated by the oscillation so that, say during compression, any accumulated energy is immediately lost and the perturbation of luminosity is nearly constant.

This transition region is an essential ingredient of the κ-mechanism in opacity-driven pulsators. In those stars, pulsations are destabilized by the perturbation of the opacity. But to be efficient, this destabilization must fulfill several conditions (e.g., Cox 1980; Cox & Giuli 1968; Pamyatnykh 1999) among which the transition region must lie in ionization region. Indeed, the destabilization occurs in the ionization region and if $\tau \ll \Pi_{osc}$ the thermal structure adapts so quickly that the flux is frozen. In the opposite situation if $\tau \gg \Pi_{osc}$ we are in the quasi-adiabatic situation as described above. Finally, one must have $\tau \approx \Pi_{osc}$ in the ionization region for the destabilization to be efficient and dominant over damping terms.

The situation is similar in solar-like pulsators, except that the destabilization by the perturbation of the opacity never dominates over damping terms and the situation is complicated by the presence of convection which modifies the thermal time-scale (see Eq. 2.11). As shown by Balmforth (1992) and Belkacem et al. (2011) the depression of the damping rates occurs when the destabilization by the perturbation of the opacity becomes efficient (and partially compensates the other damping mechanisms), i.e. when the transition region nearly coincides with the ionization region[iv]. Indeed, for low-frequency modes, $\mathcal{Q} \gg 1$ so that the destabilization is inefficient and, for high-frequency modes, $\mathcal{Q} \gg 1$ the important destabilization in the super-adiabatic layers are compensated by the damping in the atmospheric layers. Therefore destabilization have its maximum impact on the total damping rate for $\mathcal{Q} \approx 1$ in the super-adiabatic layers (near the ionization region of hydrogen), in other words when the transition region occurs in the super-adiabatic layers.

We then conclude that the observed $\nu_{\max} - \nu_{\rm c}$ relation simply results from a common feature of pulsating stars, *i.e.* the occurrence of the non-adiabatic effects in the transition region.

2.3 Inferring seismic masses and radii from global seismic quantities

Given the scaling relation described in Sections 2.1 and 2.2, it is now possible to link seismic global quantities to stellar parameters.

Let us start with the scaling relation relating the large separation to the mean density of the star (Eq. 2.8), *i.e.*

$$\Delta\nu \propto \bar{\rho}^{1/2} \propto \left(\frac{M}{R^3}\right)^{1/2} , \tag{2.14}$$

where $\Delta\nu$ is the large separation, $\bar{\rho}$ the mean density, M the total mass of the star, and R its total radius.

The second one relates the frequency of the maximum height in the power spectrum to the cut-off frequency, *i.e.*

$$\nu_{\max} \propto \nu_{\rm c} \tag{2.15}$$

The cut-off frequency can be approximatively defined for an isothermal atmosphere (see Stello et al. 2009, for a discussion) such as

$$\nu_{\rm c} = \frac{c_{\rm s}}{2H_p} , \tag{2.16}$$

where $c_{\rm s}$ is the sound speed. Through the hydrostatic equilibrium, the pressure scale height is related to the gas pressure by $P = \rho g H_p$ and using the ideal gaz equation of state $P \propto \rho T$, Eq. (2.16) becomes

$$\nu_{\rm c} \propto \frac{g}{\sqrt{T}} \propto \frac{M}{R^2\sqrt{T}} . \tag{2.17}$$

[iv] Note that in solar-like pulsators, the hydrogen ionization region is located in the uppermost atmosphere and nearly coincides with the super-adiabatic region

From Sect. 2.2, it becomes clear that the introduction of the cut-off frequency is more historical than physically justified. Indeed, Brown et al. (1991) conjectured a relation between $\nu_{\max}$ and ν_c but from a physical point of view it would be more rigorous to mention the relation between $\nu_{\max}$ and the thermal time-scale (Eq. 2.11), even if the cut-off frequency can be artificially introduced as in Eq. (2.13).

Now, using Eqs. (2.14) and (2.17), one obtains the desired relations (normalized to the solar values)

$$\frac{M}{M_\odot} \propto \left(\frac{\nu_{\max}}{{\nu_{\max}}^\odot}\right)^3 \left(\frac{\Delta\nu}{\Delta\nu_\odot}\right)^{-4} \left(\frac{T_{\rm eff}}{T_{\rm eff,\odot}}\right)^{3/2}, \tag{2.18}$$

$$\frac{R}{R_\odot} \propto \left(\frac{\nu_{\max}}{{\nu_{\max}}^\odot}\right) \left(\frac{\Delta\nu}{\Delta\nu_\odot}\right)^{-2} \left(\frac{T_{\rm eff}}{T_{\rm eff,\odot}}\right)^{1/2}. \tag{2.19}$$

where $T_{\rm eff}$ is the effective temperature. Note, however, that from Eq. (2.17) to Eqs. (2.18) and (2.19) one implicitly assumes that $T = T_{\rm eff}$. This is not obvious and would deserves further investigations.

Equations (2.18) and (2.19) constitutes the main frame of what is now commonly called the *ensemble asteroseismology* and recently gives rise to an important work that provide us the tools for a new grip on stellar physics. An all-comprehensive review of the work that make use of the above-mentioned scaling relations would be tedious but it is worth to emphasize the diversity of the applications, namely

- *Model-independent*[v] *determination of stellar parameters.* Such a type of application is now commonly used to infer masses and radii, so as to identify the observed stars (e.g., Kallinger et al. 2010; Mosser et al. 2010), but also for other applications such as the characterization of planets (e.g., Borucki et al. 2012; Jackiewicz et al. 2012).

- *Constraint on stellar evolution and population.* From the determination of stellar parameters for a large set of stars, ranging from the main-sequence to the red-giant branch, it is obvious that one of the first applications is to give constraint on stellar evolution and populations. Such work has been recently performed by many authors among which Mosser et al. (2012a) for constraining mass loss at the tip of the red giant branch, or Miglio et al. (2009, 2012a); Miglio (2012) for constraining populations in the milky way.

- *A distance indicator.* From the knowledge of stellar radius and with the effective temperature as an input, the distance is derived from a comparison with apparent magnitudes. It is claimed that such a method can provides accurate results, of the order of 10% (Miglio et al. 2012b; Silva Aguirre et al. 2012).

- *Improved determination of* $\log g$ *and* $T_{\rm eff}$. A striking example of the use of seismic scaling relations is the determination of stellar surface gravities. Classically, surface gravities are obtained by using spectroscopy and isochrone fitting. However, a look at Eq. (2.17) immediately shows that the relation between $\nu_{\max}$ and ν_c gives access to the surface gravity. It has been shown by Morel & Miglio (2012) that the seismic gravity is compatible with classical methods and that one can expect a much better accuracy from seismology than from the other methods. Last but not least, the use of this seismic gravity as an input in spectroscopic analysis provides better determination of effective temperature (e.g. Batalha et al. 2011; Creevey et al. 2012).

Those few examples offer an overview of the current multiple use of the scaling relations, but ensemble asteroseismology is not limited to these few examples and other scaling relations are promising.

3 Some promising scaling relations

In this Section, we will address three relations that from our point of view are very promising in providing us highly valuable information for stellar physics, namely the age, luminosity, and effective temperature of stars. Those relations are just beginning to be exploited, for different reasons we will discuss below.

[v] It would be more accurate to replace the term *model-independent* by *stellar-model-independent* since the derivation of the scaling relations rely on physical assumptions, therefore on a modeling.

3.1 The $\Delta\Pi$ – evolutionary status relation

Up to recently, mainly pressure modes have been detected. In contrast, gravity modes (whose restoring force is dominated by buoyancy) were very difficult to detect, especially in the solar case since they have very low amplitudes (e.g., Belkacem et al. 2009; Appourchaux et al. 2010). Nevertheless, the situation changed with the advent of space-borne missions. Indeed, since the first unambiguous detections and identification of non-radial modes in red giants by CoRoT (De Ridder et al. 2009), a great leap forward is being experienced by the stellar physics community. This has been possible because of the large amplitudes that oscillations develops in red giants compared with the main-sequence stars (Baudin et al. 2011a; Samadi et al. 2012). It then makes the detection easier, allowing for the identification and characterization of a very large number of red giants (e.g., Mosser et al. 2010).

In main-sequence stars, p-modes have high frequencies while g-modes have low frequencies. In contrast, in red-giant stars both p and g modes lie in the same frequency range. This is due to the structure of red giants, since the radiative core of red giants contracts from the end of the hydrogen burning phase while the envelope expands. Therefore, the total radius increases, the mean density decreases, then p-mode frequencies decrease during the evolution (see Eq. (2.9)). For g modes, we are in the opposite situation since their frequencies increase as the result of the contracting core and more precisely due to the increase of the buoyancy frequency (see Eq. (3.1)). Then, on the red giant branch, the p and g modes are in the same frequency range, then modes propagate in both the outer and inner cavities. Moreover, these cavities are coupled by an intermediate zone in which modes are evanescent. Consequently, red giants exhibit what we call mixed modes (e.g., Dziembowski et al. 2001; Dupret et al. 2009), *i.e.* with a g nature in the core and a p nature in the envelope. As a result, while probing the core they have enough amplitude at the surface of the stars to be detected. Those peculiar physical properties of the oscillations of red giants lead to the detection and characterization of mixed modes in a large sample of stars (e.g., Bedding et al. 2011; Mosser et al. 2011a, 2012b), giving us the opportunity of a new grip on stellar physics of advanced evolutionary stages.

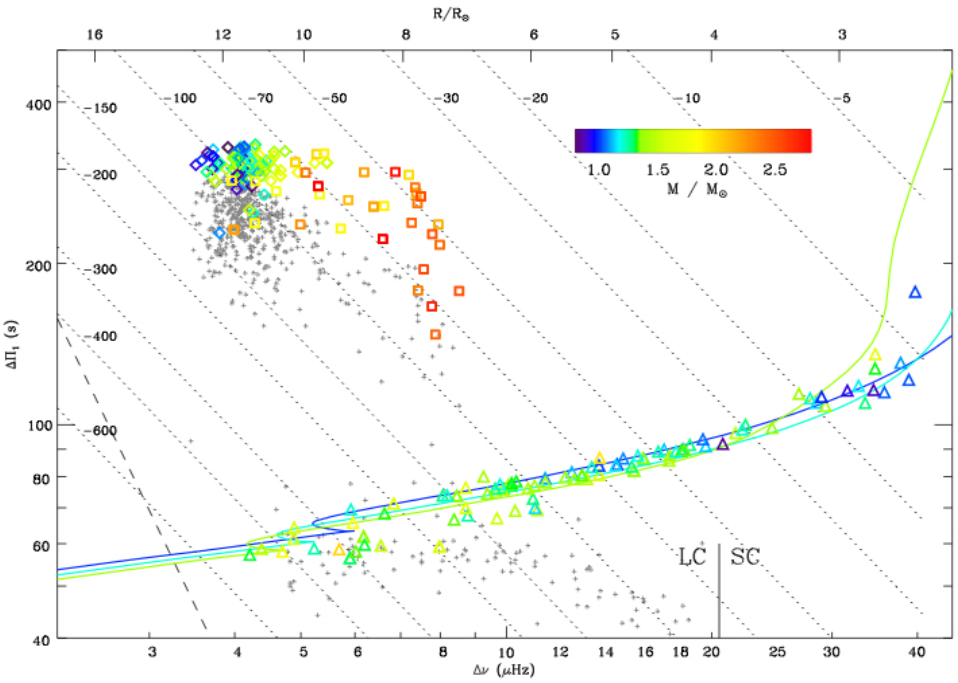

Fig. 3. Gravity-mode period spacing as a function of the pressure-mode large frequency spacing. RGB stars are indicated by triangles; clump stars by diamonds; secondary clump stars by squares. Small gray crosses indicate the bumped periods measured by Mosser et al. (2011a). The solid colored lines correspond to a grid of stellar models (see Mosser et al. 2012b, for details). Figure from Mosser et al. (2012b).

To go further, it is first essential to introduce the *period spacing*. It is the counterpart of the large separation

for gravity modes. Indeed, in the asymptotic regime, gravity mode periods follow the relation (Tassoul 1980)

$$\Pi_{n,\ell} = \Delta\Pi_\ell (n + \epsilon_g)\,, \tag{3.1}$$

where ϵ_g is a phase shift, and $\Delta\Pi_\ell$ the period spacing given by

$$\Delta\Pi_\ell = \frac{2\pi^2}{\sqrt{\ell(\ell+1)}} \left(\int_{r_1}^{r_2} N \frac{\mathrm{d}r}{r} \right)^{-1} \tag{3.2}$$

where r_1 and r_2 are the radius of the inner and outer turning points of the g-mode cavity. It is worth to note that the integral in Eq. (3.2) is related to the evolutionary state of the star. Indeed, as the star quits the main-sequence, its core contracts a nd the buoyancy frequency N increases, leading to a decrease of the period spacing. Therefore, the detection of mixed modes and the period spacing from the observation permitted to assess the evolutionary stage of red-giant stars as shown by Bedding et al. (2011) and Mosser et al. (2011a). More precisely, low-mass stars on the ascending red-giant branch (RGB) and after helium ignition (clump stars) can be found at the same location in the HR diagram. Since such stars have similar envelopes it was impossible to differentiate them from the use of p modes only. In contrast, the detection of mixed modes and the period spacing makes it possible to distinguish between those two evolutionary stages as shown by Fig. 3.

Nevertheless, there is a subtlety that cannot be avoided. In fact, the period spacing between two observed mixed modes does not follow exactly the asymptotic relation given by Eq. (3.2). This is related to the mixed nature of the mode, since the observed modes are not *pure* g-modes they are affected by their acoustic nature and a departure from Eq. (3.2) follows. To cope with this issue, Goupil (2012); Mosser et al. (2012b) proposed an asymptotic relation adapted for mixed modes (based on the formalism developed by Shibahashi (1979)), *i.e.*

$$\nu_m = \nu_{n_p,\ell=1} + \frac{\Delta\nu}{\pi} \arctan\left[q \tan\pi \left(\frac{1}{\Delta\Pi\,\nu} - \epsilon_g \right) \right]\,, \tag{3.3}$$

where ν_m is the mixed mode frequency, $\nu_{n_p,\ell=1}$ the frequency of *pure* p modes, and q a coupling factor. Therefore, using Eq. (3.3) with the measured ν_m yields a determination of the period spacing ($\Delta\Pi_\ell$). This is a crucial step for comparing the observations and the modeling as well as for determining the evolutionary stage, as illustrated by Fig. 3.

Finally, one can conclude that the scaling relation between the period spacing and the evolutionary state of stars is only in its infancy but still very promising since it provides unprecedented information of the innermost layers of stars.

3.2 Scaling relations related to mode amplitudes and linewidths

Asteroseismology is not limited to the analysis of mode frequencies but also to mode amplitudes and linewidths. The latter being related to the exchange of energy between the oscillation and the background, and not only to the star structure, they are subject to the uncertainties related to the coupling between convection and pulsation. Nevertheless, several successful attempts have been proposed to scale those seismic parameters to the stellar fundamental parameters.

3.2.1 Mode amplitude *vs* L/M

We first consider the relation between mode amplitudes and stellar parameters, both in terms of velocity and intensity fluctuations. On the basis of the theoretical calculations of Christensen-Dalsgaard & Frandsen (1983), Kjeldsen & Bedding (1995) derived the first example of a scaling relation given in terms of the maximum of the mode surface velocity (hereafter $V_{\max}$). This scaling predicts that

$$V_{\max} \propto \left(\frac{L}{M} \right)\,, \tag{3.4}$$

where L is the luminosity. Christensen-Dalsgaard & Frandsen (1983) assumed that there is an *equipartition* between the energy carried by the most energetic eddies and the modes. As mentioned by Belkacem et al. (2009) and Samadi (2011), a necessary (but not sufficient) condition for having such an equipartition is that turbulent viscosity is the dominant source of damping. However, there is currently no consensus as to what is the dominant physical processes contributing to the damping of p-modes.

Prior to the CoRoT mission, observations of mode velocity in solar-like stars were sparse (e.g. Houdek & Gough 2002) but motivated several theoretical work on the physical mechanisms underlying mode driving (Houdek et al. 1999; Houdek & Gough 2002; Samadi et al. 2007; Samadi 2011). With the launch of space-borne mission CoRoT, and its unprecedented high-quality data, such work on scaling relation of mode amplitudes became achievable (Michel et al. 2008; Baudin et al. 2011a). This has been confirmed with the *Kepler* mission, which motivated an important work on those relations (e.g. Kjeldsen & Bedding 2011; Huber et al. 2011; Mosser et al. 2012a).

The large amount of high-quality data from CoRoT and *Kepler* led to a variety of results that paradoxically complicated the picture since no clear scaling relation emerged. Samadi et al. (2012) addressed this issue for red giants, based on theoretical developments, a set of 3D numerical simulations, and the observations. They found that the maximum amplitude (in term of velocity) follows the scaling relation

$$V_{\rm max} \propto \eta_{\rm max}^{-1/2} \left(\frac{L}{M}\right)^{1.3} \left(\frac{M}{R^3}\right)^{0.525} , \tag{3.5}$$

where $\eta_{\rm max}$ is the linewidth at $\nu = \nu_{\rm max}$. In terms of intensity fluctuations, Samadi et al. (2012) showed the necessity to go beyond the adiabatic relation between velocity and intensity, especially for red giants, and proposed

$$\left(\frac{\delta L}{L}\right)_{\rm max} \propto \eta_{\rm max}^{-1/2} \left(\frac{L}{M}\right)^{1.55} \left(\frac{M}{R^3}\right)^{0.5} . \tag{3.6}$$

These scaling relations show a systematic discrepancy for red-giants, which is attributed to non-adiabatic effects. Consequently, we can state that the scaling relation of mode amplitudes is now well understood for main-sequence stars but still need to be investigated for red giants.

3.2.2 Mode linewidths *vs* $T_{\rm eff}$

For mode linewidths (or equivalently mode damping rates), scaling relations have been investigated only very recently. This is the result of the need for long-time and almost-uninterrupted monitoring to resolve individual modes and to enable their precise measurements.

Houdek et al. (1999), and later Chaplin et al. (2009), have investigated the dependence of mode-damping rates on global stellar parameters. From ground-based measurements, Chaplin et al. (2009) found that observed mode linewidths follow a power-law of the form $\eta \propto T_{\rm eff}^4$ (where $T_{\rm eff}$ is the effective temperature) and no clear tendency emerged when η is scaled with the ratio L/M. Nevertheless, these measurements were based on short-term observations and derived from an inhomogeneous set of analysis and instruments, resulting in a large dispersion. This was settled by Baudin et al. (2011a,b) (Fig. 4) using a homogeneous sample of CoRoT data. They found that a unique power-law hardly describes the entire range of effective temperature covered by main-sequence and red-giant stars and proposed that mode linewidths of main-sequence stars follow a power-law of $T_{\rm eff}^{16\pm2}$, while red-giant stars only slightly depend on effective temperature ($T_{\rm eff}^{-0.3\pm0.9}$). The latter result was later confirmed and extended by *Kepler* observations (Fig. 4) to main-sequence and sub-giant stars (Appourchaux et al. 2012). We also note that Corsaro et al. (2012) proposed that mode linewidths follow an exponential power law. In absence of a strong theoretical argument to adopt either a power law or an exponential, the statistical significance must dictate our choice and this is still to be performed. From a theoretical point of view, Chaplin et al. (2009), based on the formalism developed by Balmforth (1992); Houdek et al. (1999) and Chaplin et al. (2005), predicted a power-law of $\eta \propto T_{\rm eff}^4$ which disagrees with CoRoT and *Kepler* observations (Houdek 2012). In contrast, Belkacem et al. (2012), based on the formalism of Grigahcène et al. (2005), were able to reproduce both CoRoT and *Kepler* observations.

To get more insight into the relation between η and $T_{\rm eff}$, let us first write down the integral expression of the damping rates (e.g. Grigahcène et al. 2005)

$$\eta = \frac{1}{2\,\omega I} \int_0^M \mathcal{I}m \left[\frac{\delta\rho}{\rho_0}^* \frac{\delta P}{\rho_0}\right] {\rm d}m \,, \tag{3.7}$$

where ω is the mode frequency, $\delta\rho$ the Lagrangian perturbation of density, δP the perturbation of the total pressure (including the turbulent pressure), ρ_0 the mean density, and where the star denotes the complex conjugate. The mode inertia is given by

$$I = \int_0^M \left|\vec{\xi}\right|^2 {\rm d}m \,, \tag{3.8}$$

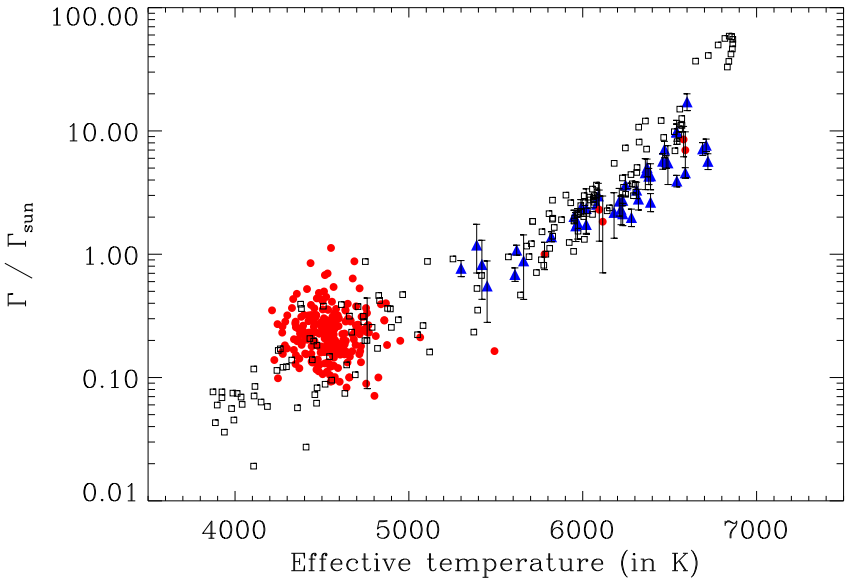

Fig. 4. Mode linewidths (normalised by the solar value, $\Gamma_{\rm sun} = 0.95\,\mu$Hz) versus effective temperature. The squared symbols represent theoretical calculations computed as explained in Belkacem et al. (2012). The triangles correspond to the observations of main-sequence stars derived by Appourchaux et al. (2012) from the *Kepler* data (with their 3-σ error-bars). The dots correspond to the observations of red giants (with $T_{\rm eff} < 5200$ K) and main-sequence (with $T_{\rm eff} > 5200$ K, with their 3-σ error-bars) stars as derived by Baudin et al. (2011a,b) from the CoRoT data.

where $\vec{\xi}$ is the eigendisplacement vector. Therefore, a look at Eqs. (3.7) and (3.8) makes it clear the need for disentangling the effects of mode inertia and the work integral (*i.e.*, the integral appearing in Eq. 3.7). The latter is related to non-adiabatic processes corresponding to a transfer of energy between pulsation and convection. Hence, it can be assumed at first glance that the work integral scales dimensionally with the ratio L/M[vi]. As verified by Belkacem et al. (2012), it follows that the relation

$$\eta\, I \propto \left(\frac{L}{M}\right)^{2.7} . \tag{3.9}$$

holds. In contrast, the mode inertia (I) does not depend on mode energy leakage but on the star's static structure[vii], and more precisely on the properties of its uppermost layers. Hence, one can expect mode inertia to scale with the surface gravity[viii]. It has been shown in Belkacem et al. (2012) that

$$I \propto g^{-2.4} . \tag{3.10}$$

Using Eq. (3.9) and Eq. (3.10), it turns out that

$$\eta \propto T_{\rm eff}^{10.8}\, g^{-0.3} . \tag{3.11}$$

This simple analysis allows us to explain qualitatively the strong dependence of mode damping rates on effective temperature. Finally, it is important to stress that Eq. (3.11) is compatible with current *Kepler* observations (T. Appourchaux, private communication).

[vi] This comes from the perturbed energy equation that shows that entropy perturbation dimensionally scales as the ratio L/M.
[vii] Except through non-adiabatic effects on mode eigendisplacement.
[viii] Note that mode inertia also scales with the dynamical timescale $\sqrt{(GM/R^3)}$ with almost the same dispersion as for the surface gravity.

4 Do seismic scaling relations give us accurate stellar global parameters?

This is a difficult and still open question issue. We explain here what are the main sources of uncertainties. The latter includes biases, all unknown and missing processes, as well as the precision of the measurements.

The typical precision of the stellar seismic indices is very good (better than 1% for $\Delta\nu$ and 5% for $\nu_{\rm max}$ in most cases). Under the assumption that the effective temperature is determined with a precision of, say, 100 K, it translates into a precision of 20% for the mass, 8% for the radius, and 0.04 dex for $\log g$. It is worth to mention that the precision on $\nu_{\rm max}$ is the limiting factor. These numbers are very encouraging and often presented as the uncertainty, but they do not include biases. Indeed, efforts are currently undertaken to assess the reliability of those numbers and more precisely to identify the biases from both the observational and the theoretical side.

4.1 Observational uncertainties

To illustrate the importance of considering the possible sources of biases with great care let us consider two examples, namely $\Delta\nu$ and $\nu_{\rm max}$.

4.1.1 Observational determination of $\Delta\nu$

As demonstrated by Verner et al. (2011) on the basis of hare-and-hound exercises and fitting of *Kepler* data by six teams, the way the large separation is determined plays an important role. Indeed, the authors conclude that the expected relative precision on $\Delta\nu$ is about 2%.

We also emphasize that the large separation is a quantity that is relevant in an asymptotic regime only. Thus, it can be extracted if the assumption underlying the asymptotic analysis is respected, here the requirement is that one must consider high radial-orders. However, in practice, solar-like oscillations are observed for low to moderate values of the radial orders, especially for red giants ($n \in [6;15]$), which make the basic assumption violated. This is a non-negligible source of biases as demonstrated by Mosser et al. (2012c), and can generate systematics as high as of 8% for the mass and 4% for the radius determination.

4.1.2 Observational determination of $\nu_{\rm max}$

The second example concerns the determination of $\nu_{\rm max}$, for which several issues arise. Since we are dealing with a stochastic process, the maximum of height in the power spectrum can vary depending on the considered time-duration of the observations. This makes the determination of $\nu_{\rm max}$ quite unsecured and requires very long observations to settle the problem (unfortunately this is not always possible) and to approach the stationary state. Therefore, except if we are able to demonstrate that stochastic effects are negligible, it is safe to consider that a possible bias of about half a large separation. The related uncertainties can be roughly estimated by considering the ratio $\Delta\nu/(2\nu_{\rm max})$. It is about 2.5% for main-sequence stars and 5% for red-giants. Note that such an effect has been considered for red giants by Mosser et al. (2011b). In addition, as for $\Delta\nu$, several methods exists for deriving $\nu_{\rm max}$ from the light-curve and Verner et al. (2011) found an average precision of about 4%.

Moreover, another issue naturally arises; *can $\nu_{\rm max}$ be observationally determined by both considering the maximum of amplitude or height in the power spectrum?* Following the work of Belkacem et al. (2011) the suitable choice (in the sense it is physically grounded) is to use the maximum height. Indeed, the relation between $\nu_{\rm max}$ and $\nu_{\rm c}$ is due to the occurrence of the transition region in the superadiabtic layers that translates, from an observational point of view, by the depression of the damping rates. Hence, the quantity one must consider must be dominated by the damping processes. It is the case for mode height, but not for mode amplitude. Indeed, mode amplitude derives from a more subtle balance between mode driving, damping, and mode inertia. Therefore, the maximum of height and amplitude is expected to be different.

4.2 Theoretical uncertainties and additional dependencies

As illustrated in Section 4.1, biases can arise from the observational determination of seismic indices. However, as shown in Sects. 2.1 and 2.2, scaling relations are based on modeling and therefore cannot be considered as perfect, so does the derived stellar parameters.

In the following, we discuss briefly the main physical reason underlying the dispersion of those relations.

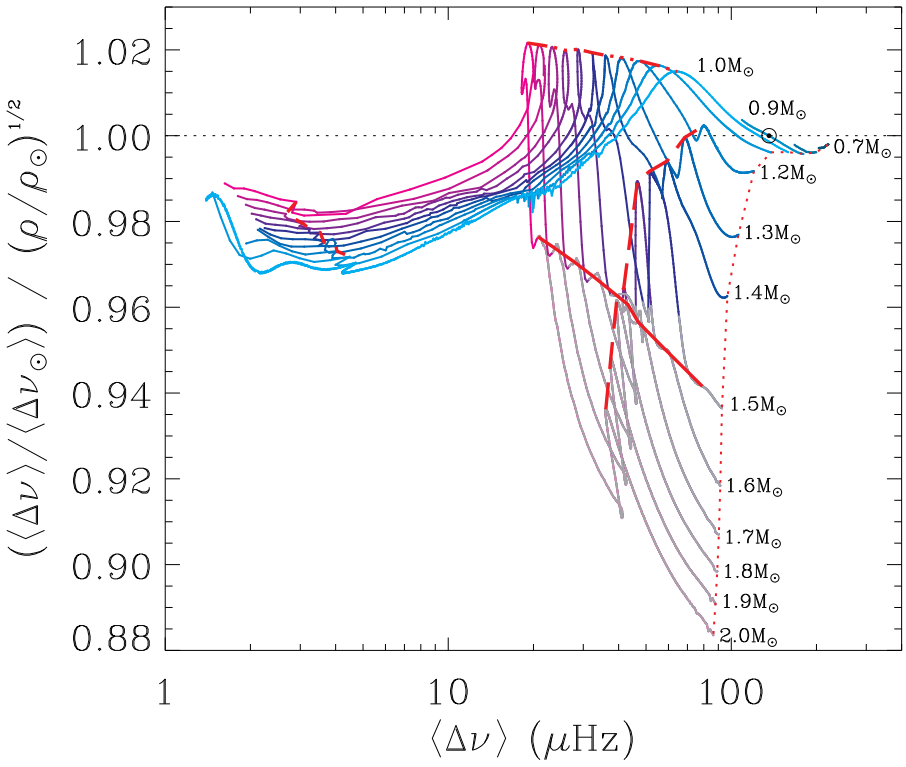

Fig. 5. Ratio between the large separation and the squared mean density of stars, normalized to the solar values, from the ZAMS to the ascending red-giant branch (see White et al. 2011, for details). Figure from White et al. (2011).

4.2.1 The limits of the homology assumption and the $\Delta\nu - \bar{\rho}$ relation

As depicted in Section 2.1, the physical assumption that permits us to relate the large separation to the mean density of a star is homology. While often considered as a crude approximation to derive the internal structure of a star, this approximation nevertheless gives ones quite a good result concerning this scaling. Figure 5 illustrates that; for typical solar-like oscillating stars, this relations holds within 3 to 4%.

To understand such a departure, it is necessary to recall the main physical hypothesis that make the homology strictly valid. The first main requirement is hydrostatic equilibrium, *i.e.* that the acceleration term in the momentum equation must vanish. The second one is thermal equilibrium, *i.e.* that the energy generated must be strictly compensated by the energy emitted (in other words, $\mathrm{d}S/\mathrm{d}t = 0$, where S is the entropy). Finally, as demonstrated by Cox & Giuli (1968), the homology requires that the constitutive equations (such as opacity, production rate of energy, etc...) must be power-laws of their arguments.

It is clear that during its evolution, a star breaks all the requirements implying a departure from the homology. This scaling relation would then need a deep investigation of the physical reason explaining precisely the origin of the departure from the homology. This requires to consider each evolutionary state (main-sequence, sub-giant, and red-giant phase) separately since the physics differs from one to another. Such a work is highly desirable in the future, to understand why this relation is so precise and to propose improvements.

4.2.2 Influence of the Mach number to the $\nu_{\max} - \nu_{\mathrm{c}}$ relation

An other example is the relation between $\nu_{\max}$ and ν_{c}, which is not exact as shown in Sect. 2.2. More precisely, the relation between the thermal frequency and the cut-off frequency is not direct and many other physical quantities appear, among which the Mach number is the more important. As already explained in Sect. 2.2, the cut-off frequency is artificially introduced for historical reasons and this subsequently leads us to introduce

the Mach number. We recall that this number is the ratio of the turbulent (or convective) velocity to the sound speed and permits us to measure the *degree* of turbulence of a flow.

In solar-like stars, this number is almost negligible in the interior ($\mathcal{M}_a \ll 1$) but increases significantly near the photosphere. In these layers, convection becomes inefficient and convective velocities increase rapidly over a relatively small radial scale to sustain the convective flux. As a result, in this region the Mach number reaches a maximum (which is of the order of 0.3 for the Sun). From one star to another, this number varies typically from 0.3 to 0.7, mainly depending on the evolutionary status and the mass of the considered stars (Houdek et al. 1999).

Therefore, from Eq. (2.13), it becomes clear that such an extra-term in the relation between $\nu_{\rm max}$ and $\nu_{\rm c}$ is to be investigated. Simple theory of convection such as mixing-length theories, aside from giving very different results for the convective velocities (Samadi et al. 2006), provides us unrealistic estimates of turbulent velocities (e.g. Samadi et al. 2003). Therefore, the only way to overcome this difficult problem is to use 3D hydrodynamical simulations to get more insight into the evolution of the Mach number across the HR diagram (work in progress).

5 Concluding remarks

In this review, we have discussed the now commonly used scaling relations ($\nu_{\rm max}$–$\nu_{\rm c}$ and $\Delta\nu$–$\bar{\rho}$) for deriving seismic masses and radii. We have shown that their physical justifications were already known, for a long time, in the context of classical pulsators. Therefore, it is striking to note that those relations derive from common features of pulsating stars and not solar-like pulsators only. We also discussed how the seismic masses and radii are derived and emphasized the numerous and important applications for improving our knowledge of stellar structure and evolution. We did not limited our discussion to these scaling relations but also addressed other scaling relations we consider as promising, namely; the relations between mode amplitudes and luminosity, between mode linewidths and effective temperature, and between period spacing and evolutionary status of stars.

We then focus our discussion on the uncertainties related to those scaling relations. It turns out that uncertainties arise from both the observational and theoretical sides. Consequently, the stellar parameters as derived from the scaling relations also suffers from those uncertainties. Therefore, one of the crucial step to obtain precise and accurate seismic stellar parameters is the calibration. Preliminary work in the direction has been achieved (e.g. Silva Aguirre et al. 2012; Huber et al. 2012), and give encouraging results.

I am grateful to M.J. Goupil, B. Mosser, and R. Samadi for reading the manuscript and for many fruitful discussions. I also thank T. Bedding and T. White for providing Figs. 2 and 5.

References

Appourchaux, T., Belkacem, K., Broomhall, A.-M., et al. 2010, A&A Rev., 18, 197

Appourchaux, T., Benomar, O., Gruberbauer, M., et al. 2012, A&A, 537, A134

Baglin, A., Auvergne, M., Barge, P., et al. 2006a, in ESA Special Publication, ed. M. Fridlund, A. Baglin, J. Lochard, & L. Conroy, Vol. 1306, 33

Baglin, A., Auvergne, M., Boisnard, L., et al. 2006b, in 36th COSPAR Scientific Assembly, Vol. 36, 3749

Balmforth, N. J. 1992, MNRAS, 255, 603

Batalha, N. M., Borucki, W. J., Bryson, S. T., et al. 2011, ApJ, 729, 27

Baudin, F., Barban, C., Belkacem, K., et al. 2011a, A&A, 529, A84

Baudin, F., Barban, C., Belkacem, K., et al. 2011b, A&A, 535, C1

Baudin, F., Samadi, R., Goupil, M.-J., et al. 2005, A&A, 433, 349

Bedding, T. R. 2011, `http://arxiv.org/abs/1107.1723`

Bedding, T. R., Mosser, B., Huber, D., et al. 2011, Nature, 471, 608

Belkacem, K., Dupret, M. A., Baudin, F., et al. 2012, A&A, 540, L7

Belkacem, K., Goupil, M. J., Dupret, M. A., et al. 2011, A&A, 530, A142

Belkacem, K., Samadi, R., Goupil, M. J., et al. 2009, A&A, 494, 191

Belkacem, K., Samadi, R., Goupil, M. J., Kupka, F., & Baudin, F. 2006, A&A, 460, 183

Borucki, W. J., Koch, D., Basri, G., et al. 2010, Science, 327, 977

Borucki, W. J., Koch, D. G., Batalha, N., et al. 2012, ApJ, 745, 120
Brown, T. M., Gilliland, R. L., Noyes, R. W., & Ramsey, L. W. 1991, ApJ, 368, 599
Chaplin, W. J., Houdek, G., Appourchaux, T., et al. 2008, A&A, 485, 813
Chaplin, W. J., Houdek, G., Elsworth, Y., et al. 2005, MNRAS, 360, 859
Chaplin, W. J., Houdek, G., Karoff, C., Elsworth, Y., & New, R. 2009, A&A, 500, L21
Christensen-Dalsgaard, J. 2011a, http://arxiv.org/abs/1106.5946
Christensen-Dalsgaard, J. 2011b, http://arxiv.org/abs/1110.5012
Christensen-Dalsgaard, J. & Frandsen, S. 1983, Sol. Phys., 82, 469
Christensen-Dalsgaard, J. & Thompson, M. J. 1997, MNRAS, 284, 527
Corsaro, E., Stello, D., Huber, D., et al. 2012, ApJ, 757, 190
Cox, J. P. 1974, Reports on Progress in Physics, 37, 563
Cox, J. P. 1980, Theory of stellar pulsation (Princeton, Princeton University Press)
Cox, J. P. & Giuli, R. T. 1968, Principles of stellar structure (New York, Gordon and Breach)
Cox, J. P., King, D. S., & Stellingwerf, R. F. 1972, ApJ, 171, 93
Creevey, O. L., Doğan, G., Frasca, A., et al. 2012, A&A, 537, A111
De Ridder, J., Barban, C., Baudin, F., et al. 2009, Nature, 459, 398
Dupret, M.-A., Belkacem, K., Samadi, R., et al. 2009, A&A, 506, 57
Dziembowski, W. A., Gough, D. O., Houdek, G., & Sienkiewicz, R. 2001, MNRAS, 328, 601
Eddington, A. S. 1917, The Observatory, 40, 290
Goupil, M. J. 2012, In preparation
Goupil, M. J., Lebreton, Y., Marques, J. P., et al. 2011a, Journal of Physics Conference Series, 271, 012032
Goupil, M. J., Lebreton, Y., Marques, J. P., Samadi, R., & Baudin, F. 2011b, Journal of Physics Conference Series, 271, 012031
Grigahcène, A., Dupret, M.-A., Gabriel, M., Garrido, R., & Scuflaire, R. 2005, A&A, 434, 1055
Houdek, G. 2008, Communications in Asteroseismology, 157, 137
Houdek, G. 2012, http://arxiv.org/abs/1201.0194
Houdek, G., Balmforth, N. J., Christensen-Dalsgaard, J., & Gough, D. O. 1999, A&A, 351, 582
Houdek, G. & Gough, D. O. 2002, MNRAS, 336, L65
Huber, D., Bedding, T. R., Stello, D., et al. 2011, ApJ, 743, 143
Huber, D., Ireland, M. J., Bedding, T. R., et al. 2012, http://arxiv.org/abs/1210.0012
Jackiewicz, J., Nettelmann, N., Marley, M., & Fortney, J. 2012, Icarus, 220, 844
Kallinger, T., Mosser, B., Hekker, S., et al. 2010, A&A, 522, A1
Kippenhahn, R. & Weigert, A. 1990, Stellar Structure and Evolution (Heidelberg: Springer-Verlag)
Kjeldsen, H. & Bedding, T. R. 1995, A&A, 293, 87
Kjeldsen, H. & Bedding, T. R. 2011, A&A, 529, L8
Lebreton, Y. 2011, ArXiv e-prints
Ledoux, P. & Walraven, T. 1958, Handbuch der Physik, 51, 353
Michel, E., Baglin, A., Auvergne, M., et al. 2008, Science, 322, 558
Miglio, A. 2012, Asteroseismology of Red Giants as a Tool for Studying Stellar Populations: First Steps, ed. A. Miglio, J. Montalbán, & A. Noels, 11
Miglio, A., Montalbán, J., Baudin, F., et al. 2009, A&A, 503, L21
Miglio, A., Montalbán, J., & Noels, A. 2012a, Red Giants as Probes of the Structure and Evolution of the Milky Way
Miglio, A., Morel, T., Barbieri, M., et al. 2012b, in European Physical Journal Web of Conferences, Vol. 19, 5012
Morel, T. & Miglio, A. 2012, MNRAS, 419, L34
Mosser, B., Barban, C., Montalbán, J., et al. 2011a, A&A, 532, A86
Mosser, B., Belkacem, K., Goupil, M. J., et al. 2011b, A&A, 525, L9
Mosser, B., Belkacem, K., Goupil, M.-J., et al. 2010, A&A, 517, A22
Mosser, B., Elsworth, Y., Hekker, S., et al. 2012a, A&A, 537, A30
Mosser, B., Goupil, M. J., Belkacem, K., et al. 2012b, A&A, 540, A143
Mosser, B., Michel, E., Belkacem, K., et al. 2012c, submitted to A&A
Pamyatnykh, A. A. 1999, Acta Astron., 49, 119
Pesnell, W. D. 1983, PhD thesis, Florida Univ., Gainesville.

Rosenthal, C. S., Christensen-Dalsgaard, J., Nordlund, Å., Stein, R. F., & Trampedach, R. 1999, A&A, 351, 689
Samadi, R. 2011, in Lecture Notes in Physics, ed. J.-P. Rozelot & C. Neiner, Vol. 832 (Berlin, Springer-Verlag), 305
Samadi, R., Belkacem, K., Dupret, M.-A., et al. 2012, A&A, 543, A120
Samadi, R., Georgobiani, D., Trampedach, R., et al. 2007, A&A, 463, 297
Samadi, R., Kupka, F., Goupil, M. J., Lebreton, Y., & van't Veer-Menneret, C. 2006, A&A, 445, 233
Samadi, R., Nordlund, Å., Stein, R. F., Goupil, M. J., & Roxburgh, I. 2003, A&A, 403, 303
Shibahashi, H. 1979, PASJ, 31, 87
Silva Aguirre, V., Casagrande, L., Basu, S., et al. 2012, ApJ, 757, 99
Soderblom, D. R. 2010, ARA&A, 48, 581
Stello, D., Chaplin, W. J., Basu, S., Elsworth, Y., & Bedding, T. R. 2009, MNRAS, 400, L80
Tassoul, M. 1980, ApJS, 43, 469
Ulrich, R. K. 1986, ApJ, 306, L37
Verner, G. A., Elsworth, Y., Chaplin, W. J., et al. 2011, MNRAS, 415, 3539
White, T. R., Bedding, T. R., Stello, D., et al. 2011, ApJ, 743, 161

SF2A 2012
S. Boissier, P. de Laverny, N. Nardetto, R. Samadi, D. Valls-Gabaud and H. Wozniak (eds)

ASTEROSEISMIC CONSTRAINTS FOR GAIA

O. L. Creevey[1] and F. Thévenin[1]

Abstract. Distances from the Gaia mission will no doubt improve our understanding of stellar physics by providing an excellent constraint on the luminosity of the star. However, it is also clear that high precision stellar properties from, for example, asteroseismology, will also provide a needed input constraint in order to calibrate the methods that Gaia will use, e.g. stellar models or `GSP_Phot`. For solar-like stars (F, G, K IV/V), asteroseismic data delivers at the least two very important quantities: (1) the average large frequency separation $\langle\Delta\nu\rangle$ and (2) the frequency corresponding to the maximum of the modulated-amplitude spectrum $\nu_{\rm max}$. Both of these quantities are related directly to stellar parameters (radius and mass) and in particular their combination (gravity and density). We show how the precision in $\langle\Delta\nu\rangle$, $\nu_{\rm max}$, and atmospheric parameters $T_{\rm eff}$ and [Fe/H] affect the determination of gravity ($\log g$) for a sample of well-known stars. We find that $\log g$ can be determined within less than 0.02 dex accuracy for our sample while considering precisions in the data expected for $V \sim 12$ stars from *Kepler* data. We also derive masses and radii which are accurate to within 1σ of the accepted values. This study validates the subsequent use of all of the available asteroseismic data on solar-like stars from the *Kepler* field (> 500 IV/V stars) in order to provide a very important constraint for Gaia calibration of `GSP_Phot` through the use of $\log g$. We note that while we concentrate on IV/V stars, both the CoRoT and *Kepler* fields contain asteroseismic data on thousands of giant stars which will also provide useful calibration measures.

Keywords: stars:fundamental parameters

1 Introduction

The ESA Gaia[i] mission is due to launch in Autumn 2013. Its primary objective is to perform a 6-D mapping of the Galaxy by observing over 1 billion stars down to a magnitude of $V = 20$. The mission will yield distances to these stars, and for about 20/100 million stars, distances with precisions of less than 1%/10% will be obtained.

Gaia will obtain its astrometry by using broad band "G" photometry (similar to a V magnitude). The spacecraft is also equipped with a spectrophotometer comprising both a blue and a red prism BP/RP, delivering *colour* information. A spectrometer will be used to determine the radial velocities of objects as far as $G = 17$ (precisions from 1–20 kms^{-1}), and for stars with $G < 11$ high resolution spectra (R$\sim$11,500) will be available.

One of the main workpackages devoted to source characterisation is `GSP_Phot` whose objectives are to obtain stellar properties for 1 billion single stars by using the G band photometry, the parallax π, and the spectrophotometric information BP/RP (Bailer-Jones 2010). The stellar properties that will be derived are effective temperature $T_{\rm eff}$, extinction $A_{\rm G}$ in the G band, surface gravity $\log g$, and metallicity [Fe/H]. Liu et al. (2012) compare different methods to determine these parameters and they estimate typical precisions in $\log g$ on the order of 0.1 - 0.2 dex for main sequence late-type stars, and mean absolute residuals (true value minus inferred value from simulations) no less than 0.1 dex for stars of all magnitudes.

A calibration plan using forty bright benchmark stars has been put in place to deliver the *best* stellar models. These will be used on $\sim$5000 calibrations stars which will be observed by Gaia. However, for most of these fainter stars $\log g$ remains quite unconstrained, and this will inherently reduce the full capacity of source characterisation with Gaia data.

In the last decade or so, much progress in the field of observational asteroseismology has been made, especially for stars exhibiting Sun-like oscillations. These stars have deep outer convective envelopes where stochastic

[1] Laboratoire Lagrange, CNRS, Université de Nice Sophia-Antipolis, Nice, 06300, France
[i] http://sci.esa.int/science-e/www/area/index.cfm?fareaid=26

turbulence gives rise to a broad spectrum of excited resonant oscillation modes e.g. Brown & Gilliland 1994. The power spectra of such stars can be characterised by two mean seismic quantities: $\langle\Delta\nu\rangle$ and $\nu_{\rm max}$. The quantity $\langle\Delta\nu\rangle$ is the mean value of the *large frequency separations* $\Delta\nu_{l,n} = \nu_{l,n} - \nu_{l,n-1}$ where $\nu_{l,n}$ is a frequency with degree l and radial order n, and $\nu_{\rm max}$ is the frequency corresponding to the maximum amplitude of the bell-shaped frequency spectrum. The following scaling relations have also been shown to hold: Eq. 1: $\langle\Delta\nu\rangle \approx M^{0.5}R^{-1.5}\langle\Delta\nu\rangle_\odot$ and Eq. 2: $\nu_{\rm max} \approx MR^{-2}(T_{\rm eff}/5777)^{-0.5}\nu_{\rm max,\odot}$ (Eq. 1) where $\langle\Delta\nu\rangle_\odot = 134.9$ μHz and $\nu_{\rm max,\odot} = 3,050$ μHz (Kjeldsen & Bedding 1995).

Of particular interest for Gaia is the *Kepler* (`http://kepler.nasa.gov`) field of view — ∼100 square-degrees, centered on galactic coordinates 76.32°, +13.5°. *Kepler* is a NASA mission dedicated to characterising planet-habitability (Borucki et al. 2010). It obtains photometric data of ∼150,000 stars with a typical cadence of 30 minutes. A subset of stars (< 1000 every month) acquire data with a point every 1 minute. This is sufficient to detect and characterise Sun-like oscillations in many stars. Verner et al. (2011) and Chaplin et al. (2011) recently showed the detections of these mean seismic quantities for a sample of >500 F, G, K IV/V stars with typical magnitudes $7 < V < 12$, while both CoRoT and *Kepler* have both shown their capabilities of detecting these same seismic quantities in 1000s of red giants (Hekker et al. 2009; Baudin et al. 2011; Mosser et al. 2012).

With the detection of mean seismic quantities in hundreds of stars, the *Kepler* field is very promising for helping to calibrate the `GSP_Phot` methods. In particular, they deliver one of the four stellar properties to be extracted by automatic analyses of Gaia data, namely $\log g$. Gai et al. (2011) studied the distribution of errors for a sample of simulated stars using seismic data and a grid-based method based on stellar evolution models. They concluded that a seismic $\log g$ is almost fully independent of the input physics in the stellar evolution models that are used. More recently Morel & Miglio (2012) compared classical determinations of $\log g$ to those derived alone from the scaling relation (Eq. [2]), and concluded that the mean differences between the various methods used is ∼0.05 dex, thus supporting the validity of a seismic determination of $\log g$. However, to date, no study has been done to validate the *accuracy* of a seismic $\log g$ (how closely it resembles the true value) by using stars with measured radii and masses. This is the objective of this work.

2 A comparison of the direct and seismic methods for determining $\log g$.

2.1 Observations and direct determination of $\log g$

We aim to compare an *asteroseismically* derived $\log g$ with the true known value for a sample of stars. We chose a sample of seven bright well-characterised stars for which the radius is known via interferometry or a binary solution and the mass is known from either the binary solution or a detailed seismic analysis. Table 1 lists the sample of stars along with the observed values of $\langle\Delta\nu\rangle$, $\nu_{\rm max}$, $T_{\rm eff}$, [Fe/H], M, and R. The final column in the table gives the *true* value of $\log g$ derived from M and R.

2.2 Seismic method to determine $\log g$

We use a grid-based method, RadEx10, to determine an asteroseismic value of $\log g$ (Creevey et al. 2012). The grid was constructed using the ASTEC stellar evolution code (Christensen-Dalsgaard 2008) without diffusion effects and the same input physics as described in Creevey et al. (2012).

The grid considers models with masses M from 0.75 – 2.0 $M_\odot$ in steps of 0.05 $M_\odot$, ages t from ZAMS to subgiant, the initial chemical composition $Z_{\rm i}$ (metallicity) spans 0.007 – 0.027 in steps of ∼ 0.003, while $X_{\rm i}$ (hydrogen) is set to 0.70: this corresponds to an initial He abundance $Y_{\rm i} = 0.263 - 0.283$. The mixing length parameter $\alpha = 2.0$ is used, which was obtained by calibrating it with solar data.

To obtain the grid-based model stellar properties ($\log g$, M, R, L, t) we perturb the set of input observations using a random Gaussian distribution, and compare the perturbed observations to the model ones. The input observations consist primarily of $\langle\Delta\nu\rangle$, $\nu_{\rm max}$, $T_{\rm eff}$, and [Fe/H], although other inputs are possible, for example, L or R. The stellar parameters and uncertainties are defined as the mean value of the fitted parameter from 10,000 realizations, with the standard deviations defining the 1σ uncertainties.

2.3 Analysis approach

We determine a seismic $\log g$ for the stars using the method explained above, and the following data sets:
(S1) $\{\langle\Delta\nu\rangle, \nu_{\rm max}, T_{\rm eff}, [{\rm Fe/H}]\}$,

Table 1. Observed properties of the reference stars

Star	$\langle\Delta\nu\rangle$ (μHz)	$\nu_{\rm max}$ (mHz)	$T_{\rm eff}$ (K)	[Fe/H] (dex)	R ($R_\odot$)	M ($M_\odot$)	$\log g$ (dex)
αCenB	161.5±0.11[1a]	4.0[1a]	5316±28[1b]	0.25±0.04[1b]	0.863±0.005[1c]	0.934±0.0061[1d]	4.538±0.008
18 Sco	134.4±0.3[2a]	3.1[2a]	5813±21[2a]	0.04±0.01[2a]	1.010±0.009[2a]	1.02±0.03[2a]	4.438±0.005
Sun	134.9±0.1[3a]	3.05[3b]	5778±20[3c]	0.00±0.01[3d]	1.000±1.010[3d]	1.000±0.010[3d]	4.438±0.002
αCenA	105.6[4a]	2.3[4a]	5847±27[1b]	0.24±0.03[1b]	1.224±0.003[1c]	1.105±0.007[1d]	4.307±0.005
HD 49933	85.66±0.18[5a]	1.8[5a]	6500±75[5b]	-0.35±0.10[5b]	1.42±0.04[5c]	1.20±0.08[5c]	4.212±0.039
Procyon	55.5±0.5[6a]	1.0[6b]	6530±90[6c]	-0.05±0.03[6d]	2.067±0.028[6e]	1.497±0.037[6f]	3.982±0.016
βHydri	57.24±0.16[7a]	1.0[7a]	5872±44[7b]	-0.10±0.07[7c]	1.814±0.017[7b]	1.07±0.03[7b]	3.950±0.015

References: [1a]Kjeldsen et al. (2005), [1b]Porto de Mello et al. (2008), [1c]Kervella et al. (2003), [1d]Pourbaix et al. (2002), [2a]Bazot et al. (2011), [3a]Taking the average of Table 3 from Toutain & Froehlich (1992), [3b]Kjeldsen & Bedding (1995), [3c]Grevesse & Sauval (1998), [3d]We adopt a typical error of 0.01 in [Fe/H], M and R, [4a]Bouchy & Carrier (2002), [5a]Using the $l = 0$ modes with Height/Noise>1 from Table 1 of Benomar et al. (2009), [5b]Kallinger et al. (2010) $Z = 0.008\pm0.002$ is referenced, [5c]Bigot et al. (2011), [6a]Eggenberger et al. (2004), [6b]Martić et al. (2004), [6c]Fuhrmann et al. (1997), [6d]Allende Prieto et al. (2002), [6e]Kervella et al. (2004), [6f]Girard et al. (2000), [7a]Bedding et al. (2007), [7b]North et al. (2007), [7c]Bruntt et al. (2010).

(S2) $\{\langle\Delta\nu\rangle, \nu_{\rm max}, T_{\rm eff}\}$, and
(S3) $\{\langle\Delta\nu\rangle, \nu_{\rm max}\}$.
For the potential sample of Gaia calibration stars, [Fe/H] is not always available, and in some cases, a photometric $T_{\rm eff}$ may have various estimations. For these reasons we include S2 and S3.

The observational errors in our sample are very small due to the brightness and proximity of the star, so we also derive an asteroseismic $\log g$ while considering observational errors that we expect for *Kepler* stars (see Verner et al. 2011). We consider three types of observational errors:
(E1) the true measurement errors from the literature,
(E2) typically "good" errors, i.e. $\sigma(\langle\Delta\nu\rangle,\nu_{\rm max},T_{\rm eff},[{\rm Fe/H}]) = 0.5$ μHz, 5%, 70 K, 0.08 dex,
(E3) "not-so-good" errors (e.g. V∼11,12), $\sigma(\langle\Delta\nu\rangle,\nu_{\rm max},T_{\rm eff},[{\rm Fe/H}]) = 1.1$ μHz, 8%, 110 K, 0.12 dex.

2.4 *Seismic versus direct* $\log g$

In Figure 1 we compare the asteroseismic $\log g$ with the true $\log g$ for the seven stars. Each star is represented by a point on the abscissa, and the y-axis shows (seismic - true) value of $\log g$. There are three panels which represent the results using the three different subsets of input data. We also show for each star in each panel three results; in the bottom left corner these are marked by 'E1', 'E2', and 'E3', and represent the results using the different errors in the observations. The black dotted lines represent (seismic - true) $\log g = 0$, and the grey dotted lines indicate ±0.01 dex.

Figure 1 shows that for all observational sets and errors $\log g$ is generally estimated to within 0.02 dex in both precision and accuracy. This result clearly shows the validity of the mean seismic quantities and atmospheric parameters for providing an extremely precise value of $\log g$. Other general trends that can be seen are that the typical *precision* in $\log g$ decreases as (1) the observational errors increase (from E1 – E3), and (2) the information content decreases (S1 – S2 – S3, for example). One noticeable result is the systematic offset in the derivation of $\log g$ for HD 49933 when we use [Fe/H] as input (S1). This could be due to an incorrect metallicity, an error in the adopted true $\log g$ or a shortcoming of the grid of models.

Figure 2 shows the *seismic* radius and mass determinations of the sample stars using S1 while considering the three sets of errors. We find that with *good* observational errors, the radii are matched to within 1% (accuracy) with typical precisions of 2–3%, while the masses are matched to within 1–4% with typical precisions of 4–7%. Here it can be seen that the offset found for HD 49933 in $\log g$ is related to the reference mass value (the radius seems to be consistent). For S2 and S3 the uncertainties begin to grow very large; 2–5% and 3–10%, respectively in radius, and 5–15% and 10-35% in mass, while the accuracies also decrease (not shown) although to within $< 1.5\sigma$ for all results. These results indicate that for the most precise determination of mass and radius, a seismic index and both $T_{\rm eff}$ and [Fe/H] are necessary, unlike $\log g$ where the seismic information alone

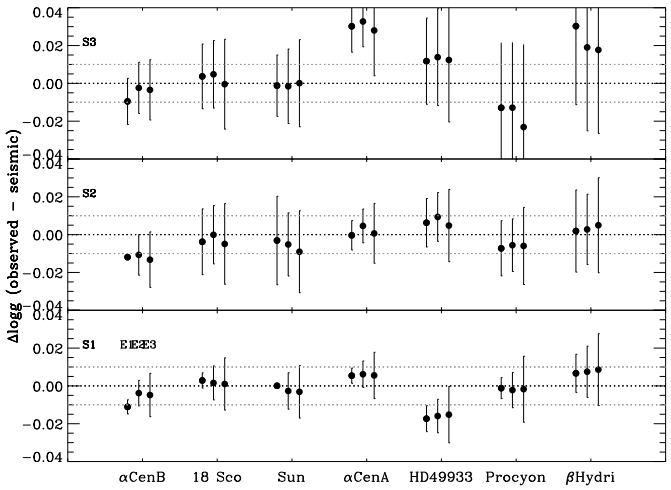

Fig. 1. *Seismic-minus-true* $\log g$ for the seven sample stars while considering different sets of input observations (different panels) and different observational errors (E1, E2, E3).

Table 2. Stellar properties for the reference stars derived by RadEx10

Star	$\log g$(dex)	R ($R_\odot$)	M ($M_\odot$)	L ($L_\odot$)	Age (Gyr)
α Cen B	4.527 ± 0.004	0.859 ± 0.007	0.905 ± 0.023	0.52 ± 0.02	9.4 ± 2.0
18 Sco	4.441 ± 0.004	1.018 ± 0.008	1.042 ± 0.019	1.07 ± 0.04	4.8 ± 0.9
Sun	4.438 ± 0.001	1.000 ± 0.002	1.000 ± 0.005	1.01 ± 0.03	6.3 ± 0.6
α Cen A	4.312 ± 0.004	1.223 ± 0.010	1.119 ± 0.024	1.56 ± 0.08	7.0 ± 0.9
HD 49933	4.195 ± 0.007	1.418 ± 0.022	1.148 ± 0.054	3.23 ± 0.22	3.5 ± 0.6
Procyon	3.981 ± 0.006	2.072 ± 0.024	1.497 ± 0.041	7.08 ± 0.54	2.1 ± 0.2
β Hydri	3.957 ± 0.010	1.840 ± 0.045	1.119 ± 0.086	3.55 ± 0.31	6.8 ± 1.0

(or including $T_{\rm eff}$) can produce an accurate result.

2.5 Systematic errors in observations

To study the effect of *systematic errors* in the atmospheric parameters, we repeated our analysis for β Hydri using three sets of input data that change only in $T_{\rm eff}$ and [Fe/H] considering the E2 errors. The first set (1) uses the North et al. (2007) values (5872, –0.10), the second set (2) uses (5964, –0.10), and the third set (3) uses da Silva et al. (2006) values (5964, –0.03). For S1 we derived $\log g$ = 3.96, 3.97, and 3.97 dex for case 1, 2, and 3, respectively (ref. value is 3.95 dex). Excluding [Fe/H] (S2) we derived $\log g$ = 3.95 and 3.96 for case 1 and 2, respectively. Here we can conclude that errors in the atmospheric parameters can change $\log g$ by up to 0.02 dex, and in the absence of an accurate [Fe/H] it is better to exclude it. To determine the mass, radius,

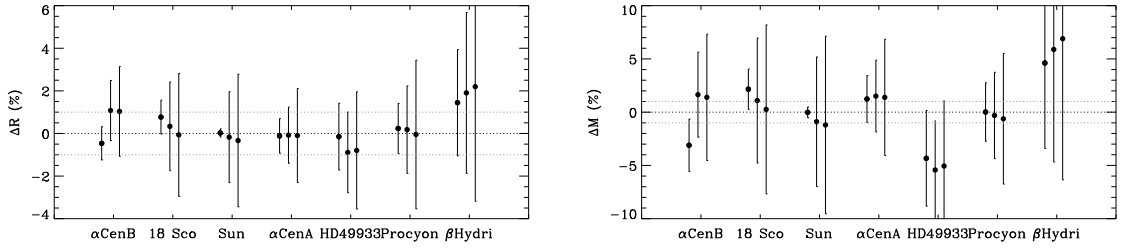

Fig. 2. *Seismic-minus-True* values of radius (left panel) and mass (right panel) using S1.

and age, however, [Fe/H] is a very imporant constraint.

3 Conclusions

We summarize the stellar properties of the sample stars in Table 2 derived by RadEx10 using $\langle\Delta\nu\rangle$, $\nu_{\rm max}$, $T_{\rm eff}$, and [Fe/H], and the true observational errors. We highlight the excellent agreement between seismically determined parameters and those obtained by direct mass and radius estimates (compare Tables 1 and 2). In only two cases (α Cen B and 18 Sco), we find that $\log g$ and mass are determined with a difference of just over 1σ for S1 and S3, while for S2 we find that $\log g$ is accurate to within its σ for all stars. This study validates the accuracy of a seismically determined $\log g$ while also highlighting the excellent precision that can be obtained using seismic data. If we relax the observational errors to those typical of what is available for the sample of ∼500 *Kepler* F, G, K IV/V *Kepler* stars, then we obtain $\log g$ with precisions of less than 0.02 dex for S1 (including [Fe/H] as a measurement) and less than 0.03 dex for S2 (excluding [Fe/H]) for even "poor" observational errors on the input seismic and atmospheric data. We also showed that we can expect to find a typical systematic error of no bigger than 0.02 dex arising from an error in the atmospheric parameters.

OLC is a Henri Poincaré Fellow at OCA, funded by the Conseil Général des Alpes-Maritimes and OCA.

References

Allende Prieto, C., Asplund, M., García López, R. J., & Lambert, D. L. 2002, ApJ, 567, 544
Bailer-Jones, C. A. L. 2010, MNRAS, 403, 96
Baudin, F., Barban, C., Belkacem, K., et al. 2011, A&A, 529, A84
Bazot, M., Ireland, M. J., Huber, D., et al. 2011, A&A, 526, L4
Bedding, T. R., Kjeldsen, H., Arentoft, T., et al. 2007, ApJ, 663, 1315
Benomar, O., Baudin, F., Campante, T. L., et al. 2009, A&A, 507, L13
Bigot, L., Mourard, D., Berio, P., et al. 2011, A&A, 534, L3
Borucki, W. J., Koch, D., Basri, G., et al. 2010, Science, 327, 977
Bouchy, F. & Carrier, F. 2002, A&A, 390, 205
Brown, T. M. & Gilliland, R. L. 1994, ARAA, 32, 37
Bruntt, H., Bedding, T. R., Quirion, P.-O., et al. 2010, MNRAS, 405, 1907
Chaplin, W. J., Kjeldsen, H., Christensen-Dalsgaard, J., et al. 2011, Science, 332, 213
Christensen-Dalsgaard, J. 2008, Ap&SS, 316, 13
Creevey, O. L., Doğan, G., Frasca, A., et al. 2012, A&A, 537, A111
da Silva, L., Girardi, L., Pasquini, L., et al. 2006, A&A, 458, 609
Eggenberger, P., Carrier, F., Bouchy, F., & Blecha, A. 2004, A&A, 422, 247
Fuhrmann, K., Pfeiffer, M., Frank, C., Reetz, J., & Gehren, T. 1997, A&A, 323, 909
Gai, N., Basu, S., Chaplin, W. J., & Elsworth, Y. 2011, ApJ, 730, 63
Girard, T. M., Wu, H., Lee, J. T., et al. 2000, AJ, 119, 2428
Grevesse, N. & Sauval, A. J. 1998, Space Sci. Rev., 85, 161
Hekker, S., Kallinger, T., Baudin, F., et al. 2009, A&A, 506, 465
Kallinger, T., Gruberbauer, M., Guenther, D. B., Fossati, L., & Weiss, W. W. 2010, A&A, 510, A106
Kervella, P., Thévenin, F., Morel, P., et al. 2004, A&A, 413, 251
Kervella, P., Thévenin, F., Ségransan, D., et al. 2003, A&A, 404, 1087
Kjeldsen, H. & Bedding, T. R. 1995, A&A, 293, 87
Kjeldsen, H., Bedding, T. R., Butler, R. P., et al. 2005, ApJ, 635, 1281
Liu, C., Bailer-Jones, C. A. L., Sordo, R., et al. 2012, ArXiv e-prints (1207.6005)
Martić, M., Lebrun, J.-C., Appourchaux, T., & Korzennik, S. G. 2004, A&A, 418, 295
Morel, T. & Miglio, A. 2012, MNRAS, 419, L34
Mosser, B., Elsworth, Y., Hekker, S., et al. 2012, A&A, 537, A30
North, J. R., Davis, J., Bedding, T. R., et al. 2007, MNRAS, 380, L80
Porto de Mello, G. F., Lyra, W., & Keller, G. R. 2008, A&A, 488, 653
Pourbaix, D., Nidever, D., McCarthy, C., et al. 2002, A&A, 386, 280
Toutain, T. & Froehlich, C. 1992, A&A, 257, 287
Verner, G. A., Elsworth, Y., Chaplin, W. J., et al. 2011, MNRAS, 415, 3539

SF2A 2012
S. Boissier, P. de Laverny, N. Nardetto, R. Samadi, D. Valls-Gabaud and H. Wozniak (eds)

AGE DATING LARGE SAMPLES OF STARS: WAYS TOWARD IMPROVED ACCURACY

C. Guédé[1], Y. Lebreton[1,2], C. Babusiaux[1] and M. Haywood[1]

Abstract. The determination of stellar ages is essential in many fields of astrophysics, for instance to understand the formation and evolution of the Galaxy or to characterize exoplanets. We focus on age-dating combining the observed position of stars in the Hertzsprung–Russell diagram and evolutionary tracks. We use a Bayesian method that provides the most probable ages. We discuss the impact of including supplementary observational constraints (seismic parameters and exoplanetary transits) in the determination of the ages.

Keywords: Stars: fundamental parameters, Methods: statistical, Stars: Hertzsprung-Russell and C-M diagrams

1 Introduction

The Gaia ESA mission (Perryman et al. 2001) will be launched in 2013 and will observe 1 billion stars in the Galaxy. Gaia will provide global stellar parameters: effective temperature, absolute magnitude and metallicity. We aim at dating large samples of stars to be observed by Gaia. Among the various methods that can be used to determine the age of stars (see Soderblom 2010), the method based on stellar isochrones placement (Edvardsson et al. 1993) is well-suited for our purpose.
The method of the isochrones placement consists in adjusting the position of a star in the Hertzsprung–Russell diagram (hereafter HDR) by model isochrones. The age of the closest isochrone then corresponds to the most probable age of the star. In this work we have chosen to use the method of da Silva et al. (2006) which is based on Bayesian estimation. We have brought several modifications to the choice of the *a priori* (initial mass function, metallicity distribution function and stellar formation rate) and we have used evolutionary tracks rather than isochrones in order to reduce the number of interpolations and the numerical errors. The method used in the present paper is described in (Guédé et al. 2012, these proceedings).
We have built a Gaia simulated catalogue to evaluate the consistency between the "true" age of the star and the age determined with the Bayesian method. The catalogue is built from Basti evolutionary tracks (Pietrinferni et al. 2004) and Gaia specifications (Perryman et al. 2001). The Gaia simulated catalogue is described in (Guédé et al. 2012, these proceedings). For this work we took an observational error on the metallicity of 0.1 dex and we simulated stars at a distance of 1 kpc.
The CoRoT (Baglin et al. 2006) and Kepler (Christensen-Dalsgaard et al. 2007) missions allow to obtain the asteroseismic parameters of observed stars and/or the parameters of the exoplanetary transits. We have added this information as constraints for the age-dating in order to study the potential improvement of the age determination. In Section 2 we present results on age determination based on three observational constraints ($M_{\rm v}, T_{\rm eff}, [{\rm Fe/H}]$). In Section 3, we describe the improvement obtained when seismic and/or planetary transit constraints are added in the age determination process.

2 Ages from HRD constraints and metallicity

We determine the ages of stars in the Gaia simulated catalogue considering three observables: the absolute magnitude $M_{\rm v}$, the effective temperature $T_{\rm eff}$ and the metallicity [Fe/H]. The comparison between the determined age and the simulated "true" age is presented in Fig. 1. We use the age relative difference defined by

[1] GEPI UMR 8111, Observatoire de Paris-Meudon , France
[2] IPR, Université de Rennes 1, France

$\sigma_\tau/\tau = (\tau_{\rm simulated} - \tau_{\rm determined})/\tau_{\rm simulated}$. We find 75 % of stars with $\sigma_\tau/\tau < 20$ %. These stars have a rather well-determined age and are mainly located in the same regions of the HRD: the turn-off, the sub-giant branch and in the main-sequence (MS) of intermediate mass stars ($1.0M_\odot < m < 2.0M_\odot$). On the other hand, the stars with an ill-determined age are located in three problematic regions of the HRD: close to the zero age main sequence (ZAMS) in particular close to the bottom of the MS (m$< 1.0M_\odot$), in the massive stars MS region (m$>2.0M_\odot$) and at the top of the red giant branch (RGB). In these regions there is a well-known degeneracy in the age-dating that can be explained by the evolutionary speed. In the vicinity of the ZAMS, low mass stars evolve very slowly and their age cannot be accurately determined from their HR diagram location. On the other hand, stars in the RGB and massive stars on the MS evolve quickly making the age determination sensitive to the uncertainty on the observed parameters.

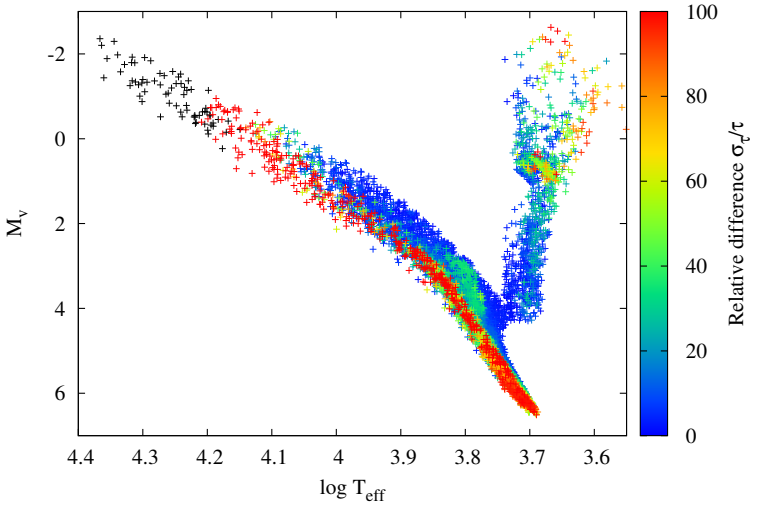

Fig. 1. Comparison of the simulated "true" age and determined age in the $\log T_{\rm eff} - M_{\rm v}$ diagram of the Gaia simulated catalog. The ages are determined with three observables ($M_{\rm v}$, $T_{\rm eff}$, [Fe/H]). Colors represent the relative difference σ_τ/τ. The blue stars have a well-determined age ($\sigma_\tau/\tau \approx 0\%$) while the red stars have an ill-determined age ($\sigma_\tau/\tau \approx 100\%$). The age of black stars cannot be determined.

3 Way toward an age improvement

To reduce the age degeneracy we now add constraints provided by the high precision photometry missions observations CoRoT (Baglin et al. 2006) and Kepler (Christensen-Dalsgaard et al. 2007). These missions detect stellar oscillations which allow to probe the interior of stars in the whole H–R diagram in particular for low mass solar-type stars and red giants. CoRoT and Kepler also detect the transit of exoplanets in front of their host-star which provides information both on the planet and on the star (Southworth 2008 and Torres et al. 2008). We add these constraints in the age-dating to evaluate the improvement on the age determination.

3.1 Adding seismic information

Seismic parameters are extracted from the oscillation power spectrum. We consider here the frequency at maximum power $\nu_{\rm max}$ and the large frequency separation Δ_ν (Brown et al. 1991, Kjeldsen et al. 2008 and Mosser et al. 2010) which corresponds to the regular spacing in the power spectrum between low degree modes ($\ell = 0, 1$) of same order. Kjeldsen & Bedding 1995 andBelkacem et al. 2011 have derived scaling relations that simply relate Δ_ν and $\nu_{\rm max}$ to the global stellar parameters (mass, radius, effective temperature):

$$\frac{\Delta\nu}{\Delta\nu_\odot} = \left(\frac{M}{M_\odot}\right)^{\frac{1}{2}} \left(\frac{R}{R_\odot}\right)^{-\frac{3}{2}} \propto \left(\frac{\rho_{\rm mean}}{\rho_{\rm mean,\odot}}\right)^{\frac{1}{2}}, \tag{3.1}$$

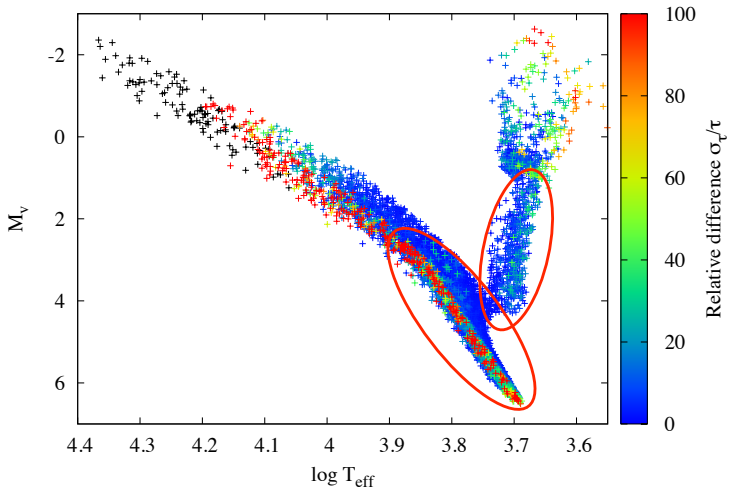

Fig. 2. Comparison of the estimated " true" age and of the determined age in the $\log T_{\rm eff} - M_{\rm v}$ diagram of the Gaia simulated catalogue. The ages are determined from three observables ($M_{\rm v}$, $T_{\rm eff}$, [Fe/H]) and two seismic constraints ($\nu_{\rm max}$, Δ_ν). Colors are the same as in Fig. 1. The red circles represent the region where solar-like oscillations are detected.

$$\frac{\nu_{\rm max}}{\nu_{\rm max,\odot}} = \left(\frac{M}{M_\odot}\right)\left(\frac{R}{R_\odot}\right)^{-2}\left(\frac{T_{\rm eff}}{T_{\rm teff,\odot}}\right)^{-\frac{1}{2}} \propto \frac{g}{g_\odot}\left(\frac{T_{\rm eff}}{T_{\rm eff},\odot}\right)^{-\frac{1}{2}}. \quad (3.2)$$

where $\Delta\nu_\odot = 134.9\ \mu Hz$ and $\nu_{\rm max,\odot} = 3050.0\ \mu Hz$ (Kjeldsen et al. 2008), g ($g_\odot$) is the (solar) gravity and $\rho_{\rm mean}$ ($\rho_{\rm mean,\odot}$) is the (solar) mean density.
The asteroseismic parameters can be calculated for stars in the Gaia simulated catalogue using the scaling relations. The observational errors on these constraints are also considered. For MS stars, we take $\sigma_{\Delta\nu} = 0.018$ $\Delta\nu$ and $\sigma_{\nu_{\rm max}} = 0.038$ $\nu_{\rm max}$ (Verner et al. 2011). For RGB stars, we adopt $\sigma_{\Delta\nu} = 0.4$ μHz, $\sigma_{\nu_{\rm max}} = 2.5$ μHz if $\nu_{\rm max} \leq 80$ μHz and $\sigma_{\nu_{\rm max}} = 1.0$ μHz if $\nu_{\rm max} > 80$ μHz (Hekker et al. 2011).
We determine the ages for all stars in the HRD but solar-like oscillations are observed in the low mass stars and on the RGB (red circles in Fig. 2). The comparison of the ages is presented in Fig. 2. We find 90 % of stars with σ_τ/τ <20 %. This is an improvement in the age-dating due to the fact that the values of Δ_ν and $\nu_{\rm max}$ vary more than $M_{\rm v}$ and $T_{\rm eff}$ in the HRD.

3.2 Adding information from planetary transits

The duration d of the exoplanetary transit is determined as a function of the period P of the orbital motion, of the projected distance b of the planet's center to the star's equator and of the mass M and radius R of the star (REF). It leads to the parameter:

$$\frac{M^{\frac{1}{3}}}{R} = \frac{1.8\sqrt{(1-b)^2}P^{\frac{1}{3}}}{d} \propto \rho_{\rm mean}^3 \quad (3.3)$$

We add $M^{1/3}/R$ and observational error $\sigma_{M^{1/3}/R}$ in the Gaia simulated catalogue. We take an observational error $\sigma_{M^{1/3}/R} = 0.022$ $\mathrm{M}^{1/3}/\mathrm{R}$, which is the mean of the observational errors found in the literature. The results of the comparison are presented in Fig. 3. We find 87 % of stars with $\sigma_\tau/\tau < 20$ % which shows that the degeneracy is reduced for RGB stars and stars close to the ZAMS.
Both $\Delta\nu$ and $\sigma_{M^{1/3}/R}$ provide similar constraints to the age-dating because the mean density $\rho_{\rm mean}$ is proportional to $\mathrm{M}^{1/3}/\mathrm{R}$ (Equation 3.3) and $\Delta\nu$ (Equation 3.2).

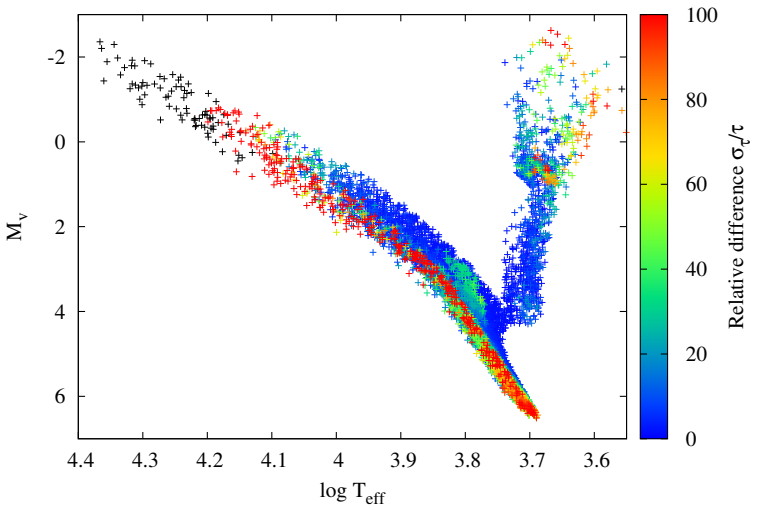

Fig. 3. Comparison of the estimated "true" age and the determined age in the $\log T_{\rm eff} - M_{\rm v}$ diagram of the simulated catalogue. The ages are determined on the basis of three observables ($M_{\rm v}$, $T_{\rm eff}$, [Fe/H]) and exoplanetary transit constraint on the stellar mean density ($M^{1/3}/R$). Colors are the same as in Fig. 1.

4 Conclusions

We used a Bayesian estimation method to date the stars that will be observed by the Gaia ESA mission. This method allows to correctly date 60 % of the stars in a simulated catalogue on the basis of three stellar observables $M_{\rm v}$, $T_{\rm eff}$ and [Fe/H]. The other stars which are mainly located in three problematic regions of the HRD (close to the ZAMS, in the upper MS and in the RGB), have badly determined ages. We added new constraints in the age-dating to improve the ages. We took the seismic parameters and the mean stellar density which can be obtained with the CoRoT and Kepler missions. We showed that it improves the determination of the ages for more of 27 % of stars. Very interestingly there is a great improvement for stars close to the ZAMS which have traditionally poorly determined ages.

References

Baglin, A., Auvergne, M., Barge, P., et al. 2006, in ESA Special Publication, Vol. 1306, ESA Special Publication, ed. M. Fridlund, A. Baglin, J. Lochard, & L. Conroy, 33

Belkacem, K., Goupil, M. J., Dupret, M. A., et al. 2011, A&A, 530, A142

Brown, T. M., Gilliland, R. L., Noyes, R. W., & Ramsey, L. W. 1991, ApJ, 368, 599

Christensen-Dalsgaard, J., Arentoft, T., Brown, T. M., et al. 2007, Communications in Asteroseismology, 150, 350

da Silva, L., Girardi, L., Pasquini, L., et al. 2006, A&A, 458, 609

Edvardsson, B., Andersen, J., Gustafsson, B., et al. 1993, A&A, 275, 101

Hekker, S., Elsworth, Y., De Ridder, J., et al. 2011, A&A, 525, A131

Kjeldsen, H. & Bedding, T. R. 1995, A&A, 293, 87

Kjeldsen, H., Bedding, T. R., & Christensen-Dalsgaard, J. 2008, in American Institute of Physics Conference Series, Vol. 1043, American Institute of Physics Conference Series, ed. V. Mioc, C. Dumitrche, & N. A. Popescu, 365–372

Mosser, B., Belkacem, K., Goupil, M.-J., et al. 2010, A&A, 517, A22

Perryman, M. A. C., de Boer, K. S., Gilmore, G., et al. 2001, A&A, 369, 339

Pietrinferni, A., Cassisi, S., Salaris, M., & Castelli, F. 2004, ApJ, 612, 168

Soderblom, D. R. 2010, ARA&A, 48, 581

Southworth, J. 2008, MNRAS, 386, 1644

Torres, G., Winn, J. N., & Holman, M. J. 2008, ApJ, 677, 1324

Verner, G. A., Elsworth, Y., Chaplin, W. J., et al. 2011, MNRAS, 415, 3539

SF2A 2012
S. Boissier, P. de Laverny, N. Nardetto, R. Samadi, D. Valls-Gabaud and H. Wozniak (eds)

INTERFEROMETRIC DETERMINATION OF EXOPLANET HOST STARS' FUNDAMENTAL PARAMETERS: θ CYGNI, 14 ANDROMEDAE, υ ANDROMEDAE AND 42 DRACONIS.

R. Ligi[1], D. Mourard[1], A.-M. Lagrange[2] and K. Perraut[2]

Abstract. We have performed observations of three exoplanet host stars using the VEGA interferometer, located on the CHARA array (Mount Wilson, CA): 14 And, υ And and 42 Dra. The data collected allow to estimate accurate fundamental parameters and exoplanets masses, which bring new reference values. Contrary to them, the fourth star we observed, θ Cygni, shows unexplained variabilities when we apply a model of limb-darkened diameter. This star is already suspected to have a quasi-periodic radial velocity of $\sim$ 150 days, detected by SOPHIE/ELODIE on the OHP, that no known stellar variations mode can explain. Kepler observations also revealed solar-like oscillations, and γ Dor pulsations have also been suspected for this star. We propose a binary model that could explain these variabilities. The best solution decreases the $\chi^2_{reduced}$ for half of VEGA data and corresponds to a companion with 15% of flux, and a distance to the primary star ρ included between 17.6 and 26.9 mas. For the CHARA/CLASSIC data, the best solution gives a flux ratio of $\sim$ 7% and a ρ of $\sim$ 25 mas that decreases the $\chi^2_{reduced}$ by a factor 2.

Keywords: Stars: fundamental parameters, Technique: high angular resolution, Instrumentation: interferometry

1 Introduction

Since the discovery of the first exoplanet (Mayor & Queloz 1995), many methods have been used to detect exoplanets host stars. The most successful one is the radial velocity (RV) method. Up to now, it has allowed to discover 535 planets. The transiting method povides the flux received from the star and the different in flux caused by the planet transiting in front of it, and allows to measure exoplanets's diameter. To enable a precise measure of exoplanets' radius and minimum masses, one can couple RV measurements with interferometric ones. Indeed, high angular resolution facilities, like the spectro-interferometer VEGA on CHARA (Mourard et al. 2009), allows to reach the first zero of visibility, and thus to access a precise measurement of the limb-darkened diameter (LDD). Diameters calculated in this way have an accuracy of more than 2%, and the exoplanets' minimum masses derived have an accuracy up to 7.6%. Waiting for Gaia first results - accurate distances of stars - one of the most important parameter still missing to study the atmospheres and structure of stars is their physical radius. By extension, the study of perturbating elements on the surface of stars, like spots or transiting exoplanets, can be improved with the arrival of this new parameter. We have performed observations of three exoplanets host stars, 14 And, υ And and 42 Dra, that host between one and four exoplanets. We have measured their LDD, calculated their radius and their exoplanets minimum masses from these measurements. They are presented in Section 3. The case of θ Cygni is different. Suspected to behave in a different way, we have performed observations of this star for two years. The squared visibilities we obtained from VEGA show discrepancies, that none of our models can fit. The RV of this star shows a quasi-period of $\sim$ 150 days that cannot be explained neither, but brings the hypothesis of eitheir a complex planetary system orbiting around it or a hidden companion. This discussion is reported in Section 4, and detailed explanations are given in Ligi et al. (2012).

[1] Laboratoire Lagrange, UMR 7293 UNS-CNRS-OCA, Boulevard de l'Observatoire, B.P. 4229 F, 06304 NICE Cedex 4, France.
[2] UJF-Grenoble1/CNRS-INSU, Institut de Planétologie et d'Astrophysique de Grenoble, UMR 5274, Grenoble, F-38041, France

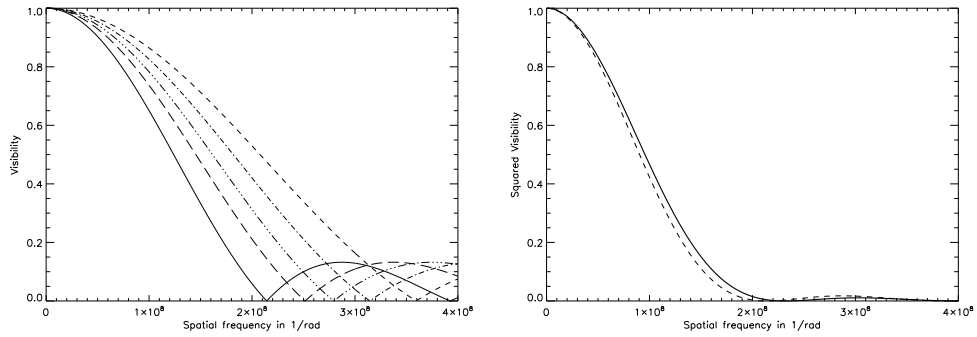

Fig. 1. Left: Theoretical visibilities for a VEGA-like instrument and different uniform disk diameters: 0.6 (solid line), 0.7, 0.8, 0.9 and 1.0 mas (long dashed line). **Right:** Squared visibility obtained for a UD diameter (solid line) and a LD diameter (dashed line). We can see the difference between both curves around the first zero of squared visibility.

2 Basics of interferometry

Interferometry is a high angular resolution technique allowing to study the spatial brightness distribution of celestial objects through measuring their spatial frequencies. By measuring the fringe contrast, also called visibility, one is able to determine the size of stars, thanks to the van Cittert-Zernike theorem (Born et al. 1980). The simplest representation of a star is a uniform disk (UD) of angular diameter $\theta_{\rm UD}$. The corresponding visibility function is given by

$$V^2 = \left| \frac{2J_1(x)}{x} \right|^2 , \tag{2.1}$$

where $J_1(x)$ is the first-order Bessel function and $x = \pi B \theta_{UD} \lambda^{-1}$. B represents the length of the projected baseline, λ the wavelength of the observation. In Figure 1 (left), we see that the zero of visibility is reached at different spatial frequencies according to the star's diameter. However, stars are not uniformly bright: a better representation of the surface brightness is the LD disk. The main differences between the two profiles arise close to the zero of visibility and in the second lobe, as shown in Figure 1 (right). Thus, the higher the spatial frequency, the smaller structures at the stellar surface we can see. The LDD is conventionally described by the function $I_\lambda[\mu]$, where μ is the cosine between the normal to the surface at that point and the line of sight from the star to the observer and u_λ the limb darkening coefficient (Hanbury Brown et al. 1974):

$$I_\lambda[\mu] = I_\lambda[1][1 - u_\lambda(1 - \mu)]. \tag{2.2}$$

A good approximation of the $\theta_{\rm LD}$ is given by (Hanbury Brown et al. 1974)

$$\theta_{LD}[\lambda] = \theta_{UD}[\lambda] \times \left[\frac{1 - u_\lambda/3}{1 - 7u_\lambda/15} \right]^{1/2} . \tag{2.3}$$

The Claret & Bloemen (2011) coefficients are listed in tables and depend on the effective temperature and the stellar surface gravity.

3 Observations of three exoplanets host stars and results

3.1 Observations with VEGA/CHARA

The CHARA array hosts six one-meter telescopes arranged in a Y shape that are oriented to the east (E1 and E2), south (S1 and S2) and west (W1 and W2). The baselines range between 34 and 331 m and permit a wide range of orientations. VEGA is a spectro-interferometer working in the visible wavelengths at different spectral resolutions: 6000 and 30000. Thus, it permits the recombination of two, three or four telescopes, and a maximum angular resolution of $\simeq$ 0.3 mas. We performed the stars observations in the 3T configuration, from October to November 2011. These observations provided measurements close to the zero or up to the second

lobe of squared visibility. Then, we used empirical laws to determine the stars' fundamental parameters. First, we used the Equation 3.1 to calculate the radius:

$$R \pm \delta R(R_\odot) = \frac{\theta_{LD} \pm \delta\theta_{LD}}{9.305 \times (\pi \pm \delta\pi)}. \tag{3.1}$$

Then, to estimate the mass, we used the modulus of the gravitational acceleration $||\overrightarrow{g}|| = GM/R^2$, where G is the gravitational constant. The error of the mass estimate is dominated by the uncertainty in parallax. Finally, the black body law $L = 4\pi R^2 \sigma T_{\rm eff}^4$ gives the effective temperature $T_{\rm eff}$ and the mass function combined to Kepler's third law gives the exoplanets masses:

$$M_{pl}\sin(i) = \frac{M_*^{2/3} P^{1/3} K (1-e^2)^{1/2}}{(2\pi G)^{1/3}}, \tag{3.2}$$

where K is the velocity semi-amplitude and e the planet eccentricity.

3.2 14 *Andromedae*

14 And (HD221345, HIP116076, HR8930) hosts one exoplanet of minimum mass $M_2 \sin i = 4.8 M_{\rm J}$ discovered in 2008. It has been shown that this star does not exhibit measurable chromospheric activity (Sato et al. 2008). This star is well-fitted by a LD diameter model that provides a $\chi^2_{\rm reduced}$ of 2.8 (see Figure 2). It is obtained with the Claret coefficient $u_\lambda = 0.700$, defined by the effective temperature and the $\log(g)$ given by Sato et al. (2008). It follows a LDD of 1.51 ± 0.02 mas. The radius, $T_{\rm eff}$ and mass found with VEGA are given in Table 1. Baines et al. (2009) found a LDD of 1.34 ± 0.01 mas for 14 And, which is smaller by $\sim 10\%$ than the one we found with VEGA. But we recorded the data in the V band, whereas their values were recorded in the K band. Sato et al. (2008) found that 14 And's exoplanet minimum mass is $M_{\rm pl}\sin(i) = 4.8 M_{\rm Jup}$, which is close to our result (see Table 2), but was derived from radial velocity data, which induces a different bias.

3.3 υ *Andromedae*

υ And (HD9826, HIP7513, HR458) is a bright F star that has undergone numerous spectroscopic investigations (Fuhrmann et al. 1998, and references therein). Four exoplanets are known to orbit around it: they were discovered between 1996 and 2010 (Schneider et al. 2011; Butler et al. 1999; Lowrance et al. 2002; Curiel et al. 2011). The data points obtained at low spatial frequency are slightly lower than the LDD model. This explains the higher $\chi^2_{\rm reduced}$ than for the other stars, which equals 6.9 (Figure 2). Then, we obtained $\theta_{\rm LD} = 1.18 \pm 0.01$ mas using $u_\lambda = 0.534$. υ And was observed by van Belle & von Braun (2009) with the Palomar Testbed Interferometer (PTI), who estimated its LDD to be 1.02 ± 0.06 mas. Baines et al. (2008) found a higher diameter with CHARA/CLASSIC (McAlister et al. 2005): 1.11 ± 0.01 mas. However, it appears that, due to the dispersion in their measurements, the value of their error bars could be underestimated. In our case, the formal uncertainty is also very small but the high value of the $\chi^2_{\rm reduced}$ indicates a poor adjustment by this simple model. No value is consistent with the respective other, ours being separated from McAlister et al. (2005)'s by more than 5σ. More observations are definitively necessary to improve the accuracy and reliability of these measurements. However, the minimum masses of υ And's exoplanets are consistent with those calculated by Curiel et al. (2011) and Wright et al. (2009), but remain lower by $\simeq 10\%$ on average, when we use the orbital periods, semi-amplitudes, and eccentricities they both give (Table 2).

3.4 42 *Draconis*

42 Dra (HD170693, HIP90344, HR6945) is an intermediate-mass giant star around which a $3.88 \pm 0.85 M_{\rm J}$ exoplanet has recently been discovered (Döllinger et al. 2009). The $\chi^2_{\rm reduced}$ obtained for 42 Dra is the lowest one: 0.2. The LDD model perfectly fits the data points. This leads to a $\theta_{\rm LD}$ of 2.12 ± 0.02 mas with a Claret coefficient of $u_\lambda = 0.725$. Baines et al. (2010) found a similar LDD to ours for 42 Dra: 2.04 ± 0.04 mas. Given the few studies of this star, this additional measurement brings a new accurate confirmation of the diameter. Concerning the planet's fundamental parameter, we found a similar $M_{\rm pl}\sin(i)$ to that calculated by Döllinger et al. (2009) (Table 2).

Table 1. Summary of the fundamental parameters of 14 And, υ And, 42 Dra and θ Cyg calculated using VEGA interferometric data. $\theta_{\rm LD}$ is the limb-darkened diameter in mas. The radius and mass are given in solar units and $T_{\rm eff}$ is given in K.

Star	Radius	Mass	$T_{\rm eff}$
14 And	12.82±0.32	2.60±0.42	4450±78
υ And	1.70±0.02	1.12±0.25	5819±78
42 Dra	22.04±0.48	0.92±0.11	4301±71
θ Cyg	1.503±0.007	1.32±0.14	6767±87

Table 2. Calculated exoplanets masses of 14 And, υ And and 42 Dra from interferometric data and comparison with previous work ([a]Sato et al. 2008 ; [b]Curiel et al. 2011 ; [c]Döllinger et al. 2009).

Planet	$P_{\rm orb}[days]$	K $[m.s^{-1}]$	e	$M_{\rm pl}\sin(i)[M_{\rm Jup}]$	
				This work	Previous work
14 And b	185.84±0.23	100.0±1.3	0	5.33±0.57	$4.8^{(a)}$
υ And b	4.62±0.23	70.51±0.45	0.022±0.007	0.62±0.09	$0.69\pm0.04^{(b)}$
υ And c	241.26±0.64	56.26±0.52	0.260±0.079	1.80±0.26	$1.98\pm0.19^{(b)}$
υ And d	1276.46±0.57	68.14±0.45	0.299±0.072	3.75±0.54	$4.13\pm0.29^{(b)}$
υ And e	3848.86±0.74	11.54±0.31	0.0055±0.0004	0.96±0.14	$1.06\pm0.28^{(b)}$
42 Dra b	479.1±6.2	112.5	0	3.79±0.29	$3.88\pm0.85^{(c)}$

4 The case of θ Cygni

4.1 Interferometric observations

θ Cyg (HD185395, $d = 18.33 \pm 0.05$ pc) is an F4V star with an M-dwarf companion of 0.35 $M_\odot$ orbiting at a projected separation of $2''$ ($\simeq$ 46 AU) and with a differential magnitude of 4.6 mag in the H band, which translates into 7.9 mag in the V band (Desort et al. 2009) using Delfosse et al. (2000) data. More recently, Roberts (2011) published adaptative optics (AO) data obtained with the AEOS telescopes in 2002, and reported a differential magnitude in the Bessel I-band of 5.89 ± 0.089 and a separation of $2.54''$, compatible with a contrast of $\simeq 7$ at the V band. A quasi-periodical RV variation with a period of approximately 150 days was detected thanks to ELODIE and SOPHIE at the Observatoire de Haute-Provence (OHP), that no known stellar variation modes can explain.

We performed nine observations of θ Cyg with VEGA/CHARA (Mourard et al. 2009) from June 2010 to October 2011. We used the three-telescope capabilities of the instrument. This allowed to reach the second lobe of visibility and to possibly identify stellar pulsations. Added to that, interferometric observations in the visible wavelengths permit to probe the same domain as the spectroscopic results.

In a first analysis, we have considered all data points. We used the LitPro software[i] (Tallon-Bosc et al. 2008) and obtained a mean UD equivalent diameter of 0.726 ± 0.003 mas. This implies a $\chi^2_{\rm reduced}$ of 8.4, which clearly indicates dispersion in the measurements or possible variations of the diameter from night to night. We also tested a linear LDD model with a coefficient $u_\lambda = 0.5$ taken from Claret & Bloemen (2011) with $T_{\rm eff} = 6745$ K and $\log(g) = 4.2$. The adjustment of the whole data set (see Figure 2) gives the value $\theta_{\rm LD} = 0.760 \pm 0.003$ mas, with a reduced $\chi^2_{\rm reduced}$ equal to 8.5.

Our final value is consistent with the diameter estimated by van Belle et al. (2008) ($\theta_{\rm LD} = 0.760 \pm 0.021$ mas) with spectral energy distribution but smaller than Boyajian et al. (2012)'s diameter obtained with CLASSIC beam combiner ($\theta_{\rm LD} = 0.845 \pm 0.015$ mas and $\theta_{\rm LD} = 0.861 \pm 0.015$ mas in 2007 and 2008 respectively). θ Cyg's fundamental parameters were estimated in the same way as for the host stars. We took $\pi = 54.54 \pm 0.15$ mas according to van Leeuwen (2007). θ Cyg 's radius is then $R = 1.503 \pm 0.007 R_\odot$. The final uncertainty is equally due to errors in the parallax and the angular diameter. This results in a mass of $1.32 \pm 0.14 M_\odot$. Finally, the $T_{\rm eff}$ was calculated using the black body law, resulting in $T_{\rm eff} = 6767 \pm 87$ K, which is also consistent with the value given by Desort et al. (2009). Boyajian et al. (2012) found a lower $T_{\rm eff}$ of 6381 ± 65 K mostly due to a

[i]Available at http://www.jmmc.fr/litpro

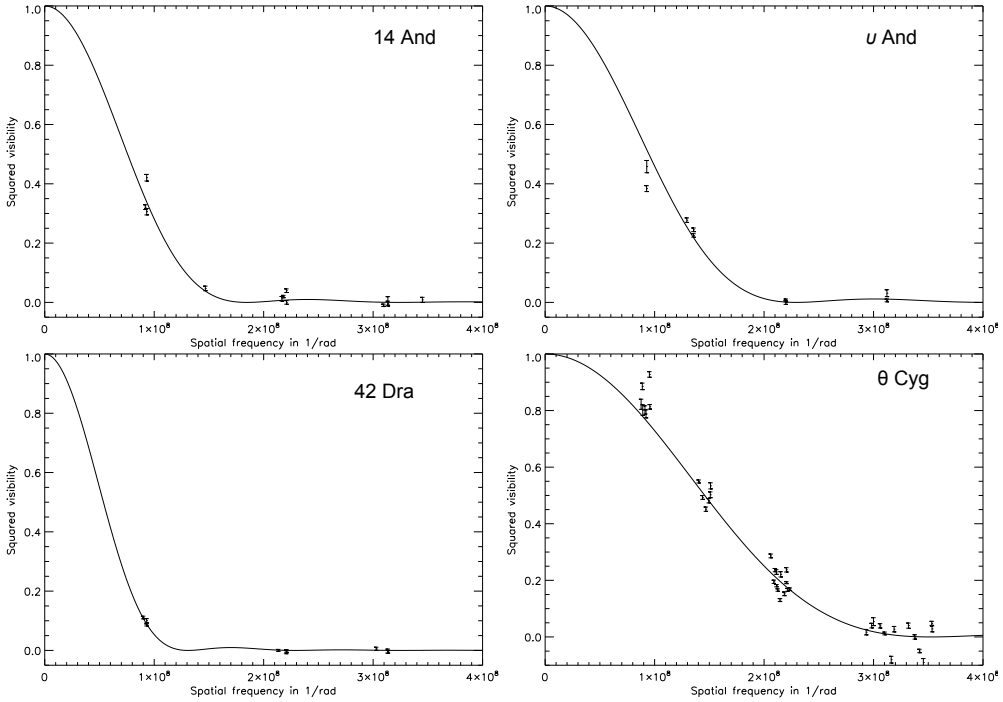

Fig. 2. Squared visibility of 14 And (top left), υ And (top right), 42 Dra (bottom left) and θ Cyg (bottom right) *versus* spatial frequency [1/rad] for VEGA data points. The solid line is the model of the limb-darkened angular diameter provided by the LITpro software.

larger LDD (see Table 1).

4.2 Discussion

As θ Cyg's visibility curve shows discrepancies, we suspect that it has unknown stellar variations or hides another companion.

Because θ Cyg's radial velocity is suspected to have a 150-day period (Desort et al. 2009), we studied a possible correlation between the variation of its diameter and the RV periodic behavior by looking its diameter night by night (see Ligi et al. 2012). It results in a variation with an amplitude of $\sim$ 13% in diameter peak to peak. Solar-like oscillations lead to lower variations in amplitude than that. Cepheid stars show similar-sized pulsations but are brighter, and their light curve presents much larger amplitude variations than θ Cyg's. Its luminosity and temperature would rather locate it near the instability branch of the HR diagram, identifying it as a δ Scuti or γ Dor star, which are also A- or F- type stars. This last possibility is also mentioned by Guzik et al. (2011), but the light curve they show does not reveal the typical γ Dor frequencies around 11 μHz, which are specific for these pulsations. Finally, we note that if the 150-day period RV variations were due to diameter variations, they would be unrealistically large, and very significant photometric variations should have been detected by Kepler. We therefore conclude that stellar variations do not explain the observed features in a satisfactory manner. We therefore consider the possibility of an unseen stellar companion for θ Cyg, and see how the present interferometric data can help to test such a scenario.

The known M-type companion to θ Cyg clearly does not affect our visibilities, because of the large separation in position (2 seconds of arc) and the large difference in magnitude (around 7). We therefore consider the presence of a second and much closer companion. Given our current accuracies in visibility measurements, this companion could be detected by interferometric instruments if its flux contribution is higher than 2%. Because θ Cyg is not classified as SB2, such a flux ratio would imply a pole-on bound system or a visual unbound binary. In this framework we performed several tests on our data set. Because the VEGA visibilities are, at first approximation, dominated by one main resolved source, that is the primary component, we adopted a diameter of the companion of 0.2 mas, corresponding to an unresolved source. The UD diameter of the primary was fixed to $\theta_{\rm UD} = 0.726$ mas, which is the diameter obtained when merging all nights. Then, by assuming

a companion's flux in the range 2% to 15%, we obtained the position angle (PA) and angular separation (ρ) corresponding to the minimum $\chi^2_{\rm reduced}$. We performed the same tests with Boyajian et al. (2012)'s CLASSIC data from 2007-2008. In half of the cases of the VEGA sets, we found a solution with a better $\chi^2_{\rm reduced}$ than with a UD model. Generally, the best solution corresponds to a companion with 15% of flux, and a ρ included between 17.6 and 26.9 mas. However, in the other VEGA cases, the data do fit the binary model and no better solution is found.
In the CLASSIC data, the $\chi^2_{\rm reduced}$ is reduced by a factor 2 when we include the binarity and the best solution gives a flux ratio of about 7% and a separation of about 25 mas.

5 Conclusion and perspectives

We have performed VEGA/CHARA interferometric observations of four stars, three of them hosting exoplanets and the last one showing discrepancies in the squared visibility we obtained. After calculating the LDD of 14 And, υ And and 42 Dra with a minimum precision of $\sim 1,3\%$, we obtained accurate values of their exoplanets masses. However, θ Cyg diameter was not so easy to confirm. We studied its variation according to the observing night, and concluded that either unknown stellar variations or a hidden close companion could explain these variations. After modeling VEGA and CLASSIC data with a companion of diameter 0.2 mas, we concluded that a companion improve the interpretation of the CLASSIC data by a factor 2 when we consider a binary component, whereas it only improves half of the VEGA data. More observations with different CHARA beams combiners allowing a larger UV coverage and the measurement of closure phases would bring additional clues to understand this complex star.

The CHARA Array is operated with support from the National Science Foundation through grant AST-0908253, the W. M. Keck Foundation, the NASA Exoplanet Science Institute, and from Georgia State University. RL warmly thanks all the VEGA observers that permitted the acquisition of this set of data. RL also acknowledges the PhD financial support from the Observatoire de la Côte d'Azur and the PACA region. We acknowledge the use of the electronic database from CDS, Strasbourg and electronic bibliography maintained by the NASA/ADS system.

References

Baines, E. K., Döllinger, M. P., Cusano, F., et al. 2010, ApJ, 710, 1365
Baines, E. K., McAlister, H. A., ten Brummelaar, T. A., et al. 2009, ApJ, 701, 154
Baines, E. K., McAlister, H. A., ten Brummelaar, T. A., et al. 2008, ApJ, 680, 728
Born, M., Wolf, E., & Haubold, H. J. 1980, Astronomische Nachrichten, 301, 257
Boyajian, T. S., McAlister, H. A., van Belle, G., et al. 2012, ApJ, 746, 101
Butler, R. P., Marcy, G. W., Fischer, D. A., et al. 1999, ApJ, 526, 916
Claret, A. & Bloemen, S. 2011, A&A, 529, A75
Curiel, S., Cantó, J., Georgiev, L., Chávez, C. E., & Poveda, A. 2011, A&A, 525, A78
Delfosse, X., Forveille, T., Ségransan, D., et al. 2000, A&A, 364, 217
Desort, M., Lagrange, A.-M., Galland, F., et al. 2009, A&A, 506, 1469
Döllinger, M. P., Hatzes, A. P., Pasquini, L., et al. 2009, A&A, 499, 935
Fuhrmann, K., Pfeiffer, M. J., & Bernkopf, J. 1998, A&A, 336, 942
Guzik, J. A., Houdek, G., Chaplin, W. J., et al. 2011, ArXiv e-prints
Hanbury Brown, R., Davis, J., Lake, R. J. W., & Thompson, R. J. 1974, MNRAS, 167, 475
Ligi, R., Mourard, D., Lagrange, A. M., et al. 2012, A&A, 545, A5
Lowrance, P. J., Kirkpatrick, J. D., & Beichman, C. A. 2002, ApJ, 572, L79
Mayor, M. & Queloz, D. 1995, Nature, 378, 355
McAlister, H. A., ten Brummelaar, T. A., Gies, D. R., et al. 2005, ApJ, 628, 439
Mourard, D., Clausse, J. M., Marcotto, A., et al. 2009, A&A, 508, 1073
Roberts, Jr., L. C. 2011, MNRAS, 413, 1200
Sato, B., Toyota, E., Omiya, M., et al. 2008, PASJ, 60, 1317
Schneider, J., Dedieu, C., Le Sidaner, P., Savalle, R., & Zolotukhin, I. 2011, A&A, 532, A79
Tallon-Bosc, I., Tallon, M., Thiébaut, E., et al. 2008, in Society of Photo-Optical Instrumentation Engineers (SPIE) Conference Series, Vol. 7013, 70131J
van Belle, G. T., van Belle, G., Creech-Eakman, M. J., et al. 2008, ApJS, 176, 276

van Belle, G. T. & von Braun, K. 2009, ApJ, 694, 1085
van Leeuwen, F. 2007, A&A, 474, 653
Wright, J. T., Upadhyay, S., Marcy, G. W., et al. 2009, ApJ, 693, 1084

SF2A 2012
S. Boissier, P. de Laverny, N. Nardetto, R. Samadi, D. Valls-Gabaud and H. Wozniak (eds)

BRAZILIAN PARTICIPATION IN THE COROT SPACE MISSION

E. Janot-Pacheco[1]

Abstract. Brazil participates in the CoRoT mission with France and other European countries. We performed software engineering, science activities and provided a ground station for data reception. A brief description of some of these contributions is presented here.

Keywords: CoRoT satellite, exoplanets, asteroseismology

1 Introduction

Brazil started participating in the CoRoT mission since 2002 by means of spectroscopic observations of seismo targets from Brazil and La Silla (Chile). A formal agreement was signed between CNES and the Brazilian space agency (AEB) in early 2003. Funding for the Brazilian participation has been secured by a wealth of federal and state public agencies and institutions as CNPq, CAPES, INPE, AEB and by universities all over the country.

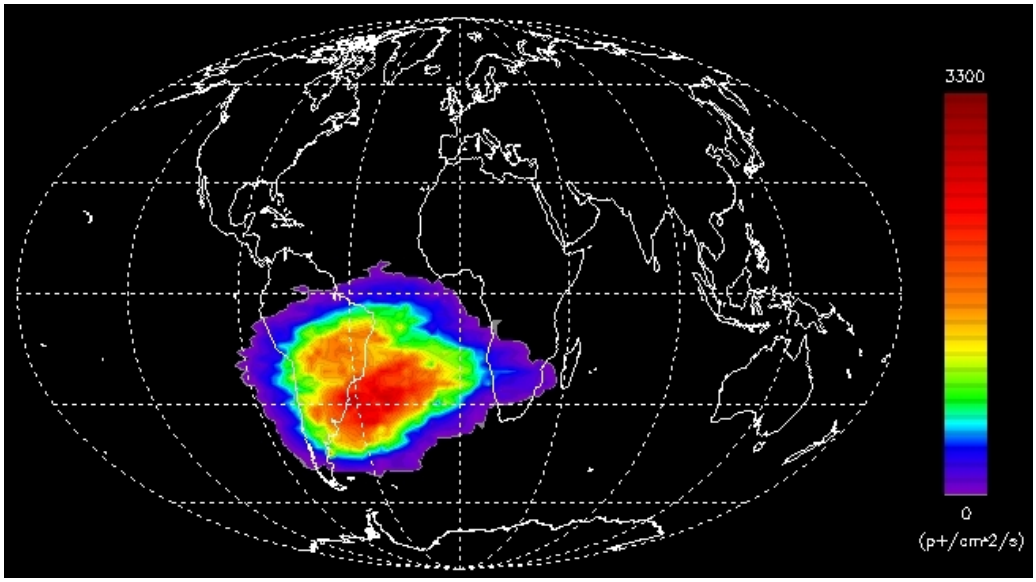

Fig. 1. Mapping the South Atlantic Anomaly with CoRoT from proton data. (Pinheiro da Silva et al. 2008)

2 Software engineering

Scientists and engineers spend from 2 to 4 years in Meudon and Toulouse observatories working in the software teams. A number of specific activities were performed by Brazilians: a) characterization of the instrument (electronic bias level, electronic gain, PSF, spontaneous generation of electrons, pixel response and proton impacts (see in Fig. 1 a determination of the South Atlantic Anomaly from proton detections by CoRoT); b) system validation and start, signal processing and instrument modeling for ground segment (PSF +Jitter, cf. Fig. 2) and noise correction (Fig. 3).

[1] Instituto de Astronomia, Geofísica e Ciências Atmosféricas, Universidade de São Paulo, 05508-090 São Paulo, Brazil

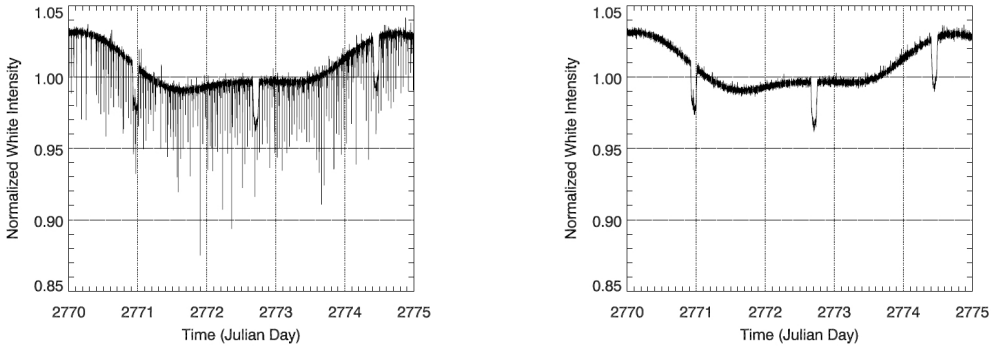

Fig. 2. Correction applied to the PSF (**left**) give spectacular results (**right**). (De Oliveira Fialho 2009)

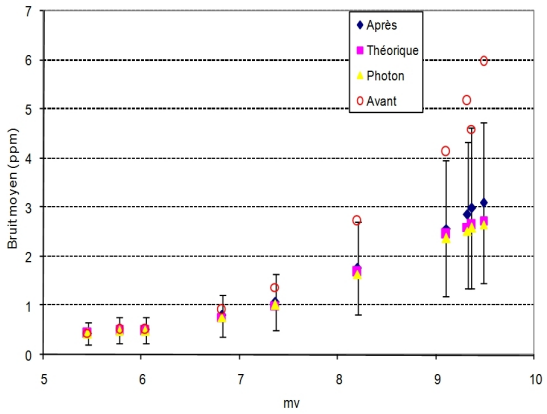

Fig. 3. Evolution of the detector noise during the corrrection procedure. Note that the average noise after the correction by means of software is quite close to the theoretical level for a large stellar magnitude range. (Auvergne et al. 2009)

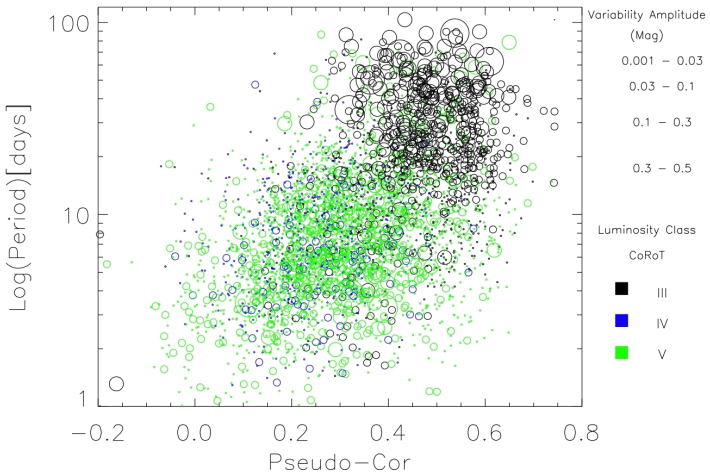

Fig. 4. Period-pseudo-color diagram for stars observed with CoRoT for which rotational periods have been estimated. The breaking effect with age is clearly seen. (De Medeiros et al. 2012)

3 Science activities

Besides the spectroscopic observations during the pre-launch phase, we leaded s series of science teams, mainly: young stars in NGC 2264 (Alencar et al. 2012), dynamics of exoplanets (Ferraz-Mello 2011), stellar seismology (Andrade et al. 2012), stellar rotation (De Medeiros et al. 2012) (see Fig. 4) and physics of stellar spots (Silva-Valio & Lanza 2011).

We thank SF2A for inviting us to present this talk.

References

Alencar, S. et al. 2012, in preparation
Andrade, L. et al. 2012, in preparation
Auvergne, M. et al. 2009, A&A 506, 411-424
De Medeiros et al. 2012, A&A, submitted
De Oliveira Fialho, F. 2009, in CoroT 36th Scientific Committee meeting
Ferraz-Mello, S. et al. 2011, A&A 531, 161-168
Pinheiro da Silva, L., et al. 2008, MNRAS, 384, 1337
Silva-Valio, A. and Lanza, A. 2011, A&A, 529, 36-40

SF2A 2012
S. Boissier, P. de Laverny, N. Nardetto, R. Samadi, D. Valls-Gabaud and H. Wozniak (eds)

SIGNATURES OF ROTATION IN OSCILLATION SPECTRA

D. R. Reese[1], V. Prat[2], C. Barban[3], C. van't Veer-Menneret[4] and K. B. MacGregor[5]

Abstract. Rotation makes oscillation spectra of rapidly rotating stars much more complicated. Hence, new strategies need to be developed in order to interpret such spectra. In what follows, we describe how multi-colour photometric mode visibilities can be generalised to rapidly rotating stars, while fully taking into account centrifugal deformation and gravity darkening. We then go on to describe some first results as well as a strategy for constraining mode identification.

Keywords: Asteroseismology, Stars: oscillations, Stars: rotation, multi-colour photometry, mode identification

1 Introduction

The space missions CoRoT (Baglin et al. 2009; Auvergne et al. 2009) and Kepler (Borucki et al. 2009) are revealing very rich pulsational spectra in rapidly rotating stars. For instance, the δ Scuti star HD 181555, a primary target of the CoRoT mission, may have up to 2000 individual pulsation modes (Michel, private communication). It is becoming increasingly clear that in order to identify modes, *i.e.* find the correspondence between observed frequencies and theoretically calculated modes, one will need more sophisticated methods than simply using equidistant patterns such as what is done in Echelle diagrams. One such approach, commonly used in non-rotating stars, is multi-colour photometry. This approach consists in observing pulsation modes in multiple photometric bands, calculating the amplitudes ratios and/or phase differences between the different bands, and comparing these with theoretical predictions. In what follows, we describe how this approach can be generalised to rapidly rotating stars.

2 Formalism

Previous efforts to calculate mode visibilities in rapidly rotating stars either approximated the effects of rotation on the pulsation modes (e.g. Daszynska-Daszkiewicz et al. 2007) or were restricted to disk-integration factors (e.g. Lignières & Georgeot 2009). Nonetheless, these studies established various important results, such as the fact that amplitude ratios depend on m, the azimuthal order, and i, the inclination, in rotating stars (Townsend 2003; Daszynska-Daszkiewicz et al. 2007) and that modes with intermediate $\ell - |m|$ values tend to become more visible as the rotation rate increases, since these become chaotic modes with irregular node spacing (Lignières & Georgeot 2009). In order to go further, we combine a complete 2D treatment of the effects of rotation with realistic calculations of mode visibilities.

Luminosity variations in a pulsating star, $\Delta E(t)$, are given by the following equation:

$$\Delta E(t) = \Re\left\{ \iint_{\text{Vis.Surf.}} \delta I(g_{\text{eff}}, T_{\text{eff}}, \mu) \vec{e}_{\text{obs.}} \cdot d\vec{S} + \iint_{\text{Vis.Surf.}} I(g_{\text{eff}}, T_{\text{eff}}, \mu) \vec{e}_{\text{obs.}} \cdot \delta(d\vec{S}) \right\}, \tag{2.1}$$

[1] Institut d'Astrophysique et Géophysique de l'Université de Liège, Allée du 6 Août 17, 4000 Liège, Belgium
[2] Université de Toulouse, UPS-OMP, IRAP, Toulouse, France
CNRS, IRAP, 14 avenue Edouard Belin, 31400 Toulouse, France
[3] LESIA, Observatoire de Paris, CNRS, UPMC Univ. Paris 06, Univ. Paris-Diderot, 5 place Jules Janssen, 92195 Meudon, France
[4] GEPI, Observatoire de Paris-Meudon, CNRS, Université Paris Diderot, 92125, Meudon Cedex, France
[5] High Altitude Observatory, National Center for Atmospheric Research, Boulder, CO 80307, USA

where δ represents a Lagrangian perturbation, $\Re\{\dots\}$ the real part of some quantity, "Vis.Surf." the visible surface, $d\vec{S}$ a surface element, $\vec{e}_{\rm obs.}$ a unit vector towards the observer, and I the specific intensity for a given orientation, $\mu = \vec{e}_{\rm obs.} \cdot d\vec{S}/\|d\vec{S}\|$, effective gravity, $g_{\rm eff}$, and temperature, $T_{\rm eff}$. In what follows, we will assume that the specific intensity has been multiplied by the transmission curve of the instrument and/or filter, and has been integrated over the wavelength spectrum. Variations of the boundary between the visible and hidden side of the star, caused by the pulsations, are neglected since these are of second order in terms of the Lagrangian displacement. In order to apply Eq. (2.1) to pulsation modes in rapidly rotating stars, we adapted each of the intervening terms to the structure of a centrifugally distorted star. In particular, a grid of Kurucz atmospheres was calculated so as to have the correct intensities (and associated derivatives) at each latitude, thereby taking gravity (and limb) darkening into account. For more details, we refer the reader to (Reese et al., submitted).

3 Results

Overall visibilities As a first step, we deal with mode visibilities in a single photometric band. The intrinsic mode amplitudes are normalised so that the maximal displacement, multiplied by the square of the co-rotating frequency, $(\omega + m\Omega)^2$, is constant. Figure 1 displays visibilities in CoRoT's photometric band at four different inclinations, for $2\,M_\odot$ models based on the Self-Consistent Field (SCF) method (Jackson et al. 2005; MacGregor et al. 2007), at two different rotation rates. The different colours indicate the values of ℓ carried over from the non-rotating case. In agreement with Lignières & Georgeot (2009), we find that modes with intermediate $\ell - |m|$ values become more visible as the rotation rate increases and at higher inclinations. However, even when the star is equator-on, some of the island modes, *i.e.* the rotating counterparts to modes with low $\ell - |m|$ values, still remain more visible, which is different from what was found previously. The pole-on configuration is particularly interesting because the non-axisymmetric modes cancel out, thereby leaving a relatively regular frequency spectrum in which island modes stand out (see also Lignières & Georgeot 2009). This suggests that rapidly rotating pole-on stars might be a good starting point for asteroseismic investigations and has motivated recent searches for pulsations in Vega (Böhm et al. 2012).

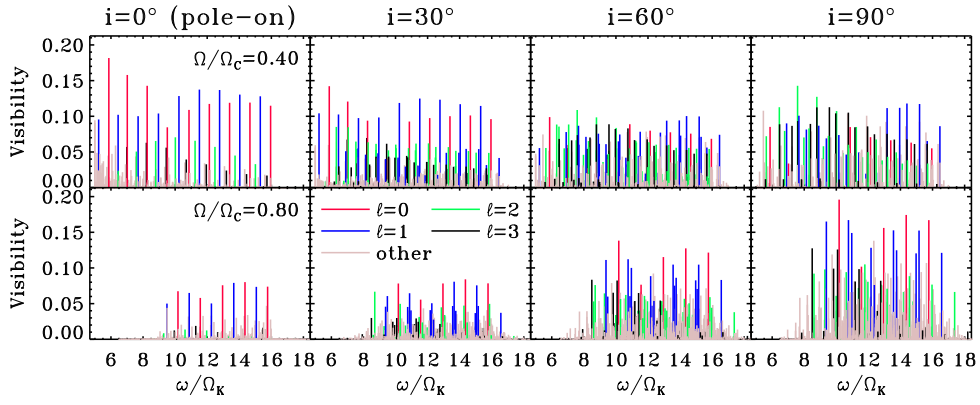

Fig. 1. Mode visibilities in CoRoT's photometric band, for two different rotation rates. Colours indicate the ℓ values.

Amplitude ratios We now turn our attention to amplitude ratios. Figure 2 displays various amplitude ratios in the Geneva photometric system for different configurations and rotation rates. As can be seen in the first column, although modes with different azimuthal orders have the same amplitude ratios in non-rotating stars, this no longer applies to rotating stars, as was previously found in Townsend (2003); Daszynska-Daszkiewicz et al. (2007). The same applies to inclination but to a lesser extent, since amplitude ratios of a given mode still remain similar even at rapid rotation rates, as shown in the second column. The third column illustrates what happens if modes with the same (ℓ, m) values and inclination are selected. The amplitude ratios can be quite similar even at rapid rotation rates. Such similarities are expected based on the asymptotic calculations by Pasek et al. (2012) which predict a similar lateral structure for these modes. Nonetheless, the middle panel at $\Omega = 0.4\Omega_{\rm C}$ shows that differences can arise between such amplitude ratios – these can be caused by avoided crossings, departures from the asymptotic regimes, or competing contributions to the mode visibilities.

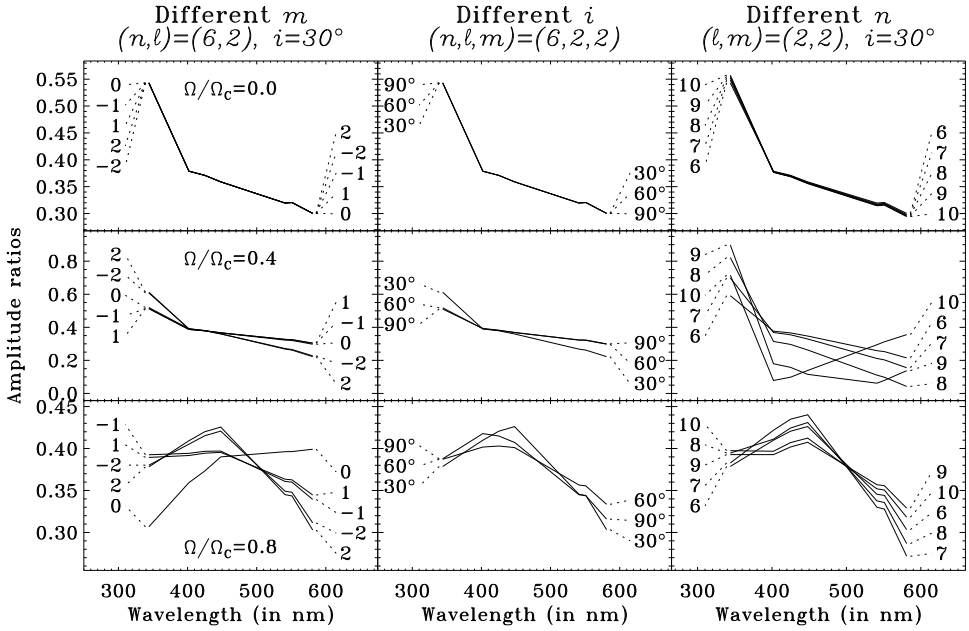

Fig. 2. Amplitude ratios. Each row corresponds to a different rotation rate, and each column to a different configuration. The values connected by dotted lines correspond to the parameter in the upper line of each title.

4 Constraining mode identification

It is then interesting to investigate whether it is possible to constrain mode identification from multi-colour photometry. In Fig. 3, we randomly choose an island mode in a model rotating at $\Omega = 0.6\Omega_{\rm C}$ with an inclination of $i = 60°$, and find 9 other modes out of a list of over 3000 modes, with the most similar amplitude ratios. The upper left plot displays the 10 sets of amplitude ratios. The upper middle panel shows the frequencies and the rank, which measures the degree of resemblance, 10 corresponding to the original mode. The upper right panel shows the most recurrent frequency differences convolved by a Gaussian. The vertical dotted and dashed lines display twice the rotation frequency, the large separation and half the large separation. Finally, the second and third rows show the meridional cross-sections of the 10 modes. The (n, ℓ, m) values, carried over from the non-rotating case, are indicated below each cross-section. As can be seen, all of the selected modes are island modes, most of which have the same ℓ and $|m|$ values. Accordingly, the frequencies follow a specific pattern as confirmed by the upper middle and right panels. If we had selected, say, an $m = 2$ island mode, another frequency pattern would have emerged with a recurrent 4Ω spacing. Hence, by studying the resultant frequency pattern, one can hope to constrain the azimuthal order and possibly the harmonic degree. Furthermore, this yields the rotation rate, as well as the large frequency separation.

5 Discussion

The next step in this work will be to include non-adiabatic effects. Indeed, this will allow us to obtain realistic effective temperature variations at the stellar surface, which is crucial for obtaining accurate mode visibilities (e.g. Dupret et al. 2002). Such calculations require thermally balanced rotating models, such as what is currently being produced in the ESTER project (Rieutord & Espinosa Lara 2009; Espinosa Lara 2010). Nonetheless, the current results may still provide a good qualitative description of the effects of rotation on multi-colour mode visibilities. In particular, rapidly rotating stars seen pole-on may be promising asteroseismic targets, given their simplified and more regular pulsation spectra. Furthermore, the above strategy for constraining mode identification does not require a full knowledge of the theoretical predictions and could already be applied to stars for which a sufficient number of modes have been observed in multi-colour photometry.

Once pulsation modes are identified in rapidly rotating stars, then it may be possible to apply inversion methods which will allow us to probe the rotation profile and stellar structure. This would provide valuable constraints on internal mixing and transport processes, and enable better predictions of the evolution and

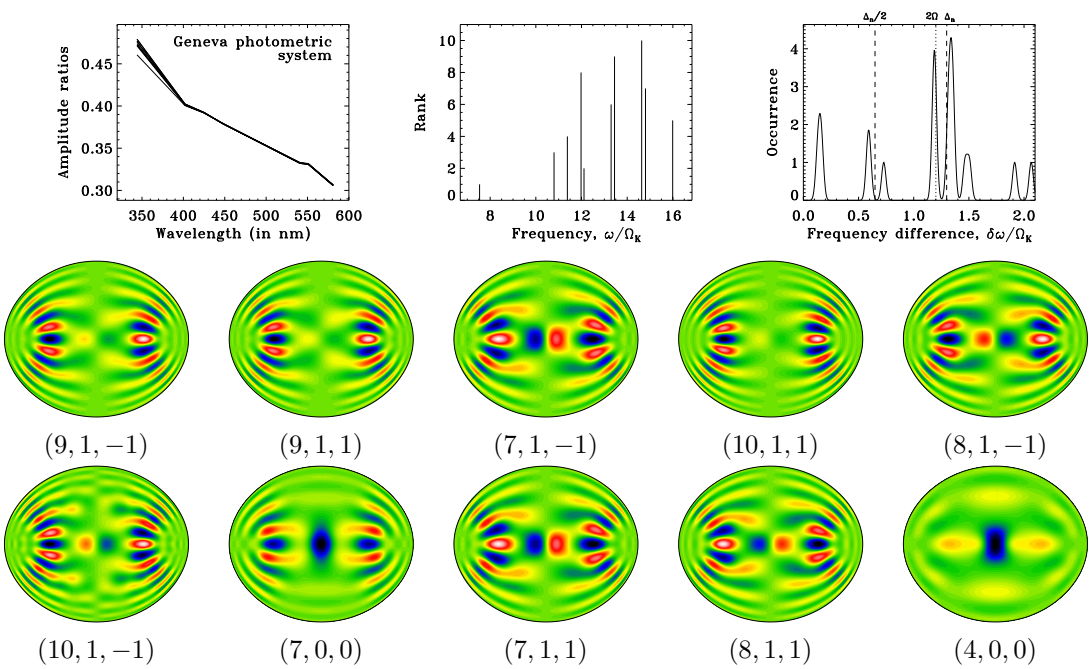

Fig. 3. In this plot, an island mode was randomly chosen, and 9 other modes with the most similar amplitude ratios were selected. See text for details.

chemical yields of rapidly rotating stars.

We thank S. Jackson, A. Skumanich and T. S. Metcalfe for their contributions to the Self-Consistent Field method, used for generating rotating stellar models. We are grateful to R. Kurucz for making his ATLAS9 code and opacity data available and open to the scientific community. DRR is financially supported through a postdoctoral fellowship from the "Subside fédéral pour la recherche 2011", University of Liège, and was previously supported by the CNES ("Centre National d'Etudes Spatiales"), both of which are gratefully acknowledged. This work was granted access to the HPC resources of IDRIS under the allocation 2011-99992 made by GENCI ("Grand Equipement National de Calcul Intensif"). The National Center for Atmospheric Research is a federally funded research and development centre sponsored by the US National Science Foundation.

References

Auvergne, M., Bodin, P., Boisnard, L., et al. 2009, A&A, 506, 411
Baglin, A., Auvergne, M., Barge, P., et al. 2009, in IAU Symposium, Vol. 253, 71
Böhm, T., Lignières, F., Wade, G., et al. 2012, A&A, 537, A90
Borucki, W., Koch, D., Batalha, N., et al. 2009, in IAU Symposium, Vol. 253, 289
Daszynska-Daszkiewicz, J., Dziembowski, W. A., & Pamyatnykh, A. A. 2007, Acta Astronomica, 57, 11
Dupret, M., De Ridder, J., Neuforge, C., Aerts, C., & Scuflaire, R. 2002, A&A, 385, 563
Espinosa Lara, F. 2010, ApSS, 328, 291
Jackson, S., MacGregor, K. B., & Skumanich, A. 2005, ApJS, 156, 245
Lignières, F. & Georgeot, B. 2009, A&A, 500, 1173
MacGregor, K. B., Jackson, S., Skumanich, A., & Metcalfe, T. S. 2007, ApJ, 663, 560
Pasek, M., Lignières, F., Georgeot, B., & Reese, D. R. 2012, A&A, 546, A11
Rieutord, M. & Espinosa Lara, F. 2009, Communications in Asteroseismology, 158, 99
Townsend, R. H. D. 2003, MNRAS, 343, 125

Session 06

CoRoT/Kepler: The new deal for exoplanets

SF2A 2012
S. Boissier, P. de Laverny, N. Nardetto, R. Samadi, D. Valls-Gabaud and H. Wozniak (eds)

PASTIS: PLANETARY ANALYSIS AND SMALL TRANSIT INVESTIGATION SOFTWARE

J.M. Almenara[1], R. F. Díaz[1], A. Santerne[1] and C. Moutou[1]

Abstract. The Transit search method to detect exoplanets is contaminated by *false positives*, produced by one of several kinds of configurations involving eclipsing binaries. Follow-up observations are used to reveal the true nature of the candidates. These observational efforts run into difficulties due, on one hand, to the faintness of the typical targets (specially for CoRoT and Kepler candidates), and on the other, due to the small-amplitude signals produced by small-mass planets. As a consequence many small planet candidates remain unsolved. We are developing a tool, called PASTIS, to solve these cases using all the available data including the light curve, photometry, radial velocity data, etc. We use bayesian methods to fit the data with different models and to compare and quantify the relative probability of different scenarios. In this way we plan to validate most of the currently unsolved cases and to increase the number of confirmed small planets.

Keywords: Planetary systems

1 Introduction

Several configurations of eclipsing binaries can produce eclipses that can mimick transits of exoplanets (see Fig. 1). There are two main kinds of *false positives*: 1) undiluted binaries, with grazing eclipses or large radius ratio, and 2) diluted binaries, eclipsing binaries whose light is diluted by a third star, physically bounded (triple system) or aligned with the line of sight of the binary, called blend. A careful inspection of the detection light curve (Alonso et al. 2004) permits identifying some *false positives*. For the ones that pass this inspection, follow-up observations are needed to confirm the planetary nature. Due to the large point-spread-function in the transit searches, eclipsing binaries contaminating the aperture are a major problem, which can be minimized using high spatial resolution observations or measurement of the photometric centroid (Batalha et al. 2010). Finally, the radial velocity observations allow obtaining the mass. However, with the current space-based transit searches, CoRoT (Baglin et al. 2009) and Kepler (Borucki et al. 2010), some candidates are too faint for spectroscopic follow-up, or the expected signals are below the current spectrographs precision, due to the small radial-velocity amplitudes produced by small-mass planets. In these cases the direct confirmation is not possible, but the candidate can still be validated as a real planet, if the probabilities greatly favor the planetary scenario over the *false positive* one. Some Kepler planets were validated using BLENDER (Torres et al. 2004, 2011; Fressin et al. 2011).

2 BLENDER

BLENDER compares models of different scenarios (star with a transiting planet, star with a background/foreground eclipsing binary, star with a background/foreground star with a transiting planet, star-eclipsing binary in a triple system or star-star-planet triple system) with Kepler light curve observations. The models assume the main star observed with fixed parameters and a blend object with 4-5 free parameters that depend on the scenario: masses for stars, radii for transiting planets, distance if its a background/foreground system, and a parameter related with the eccentricity. In the case of stars, the physical parameters are taken from an isochrone for a fixed age and metallicity. BLENDER explores the full set of parameters sampled in a regular

[1] Aix Marseille Université, CNRS, LAM (Laboratoire d'Astrophysique de Marseille) UMR 7326, 13388, Marseille, France

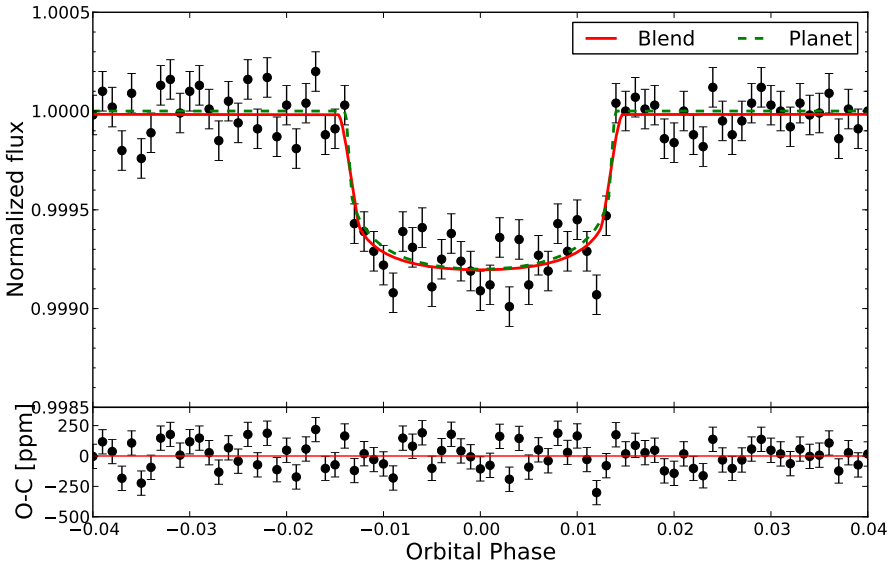

Fig. 1. A synthetic transit light curve generated from a planetary model, shown in green. The red curve is the best fit using a blend model. Both models are compatible with the data points (black dots with error bars).

grid. This process requires intensive computation resources (to compute up to 7×10^8 models), they use 1024 processors of the NASA Pleiades cluster. Then, they construct maps for two of the free parameters. The statistics in these maps is based on a χ^2 difference between the considered scenario and the best model of the star-transiting planet scenario. The confidence regions are obtained using the number of free parameters as the number of degrees of freedom, and the region outside the 3σ contour is excluded. But the general approach is not conceptually correct, as in the frequentist approach, model comparison is not possible (Gregory 2005). Moreover, this method has not been proved to be statistically consistent using, for example, simulated data. Additional observations (radial velocity, high resolution image with adaptive optics, transits observed in the infrared with Spitzer) add, a posteriori, constraints in the statistic maps produced from the χ^2 difference. These maps are used to constrain the allowed magnitude range of the blended stars (inside the 3σ contour and allowed by the additional observations). Then, they use the Besançon Galactic structure models (Robin et al. 2003) to count background/foreground stars in the allowed magnitude range. Finally, taking into account the star counts and the probability of each scenario they compute a false alarm rate for the star-transiting planet scenario. If this false alarm rate is small enough, the planet is said to be validated (Fressin et al. 2011).

Although the method is promising and has produced interesting results, no rigorous demonstration of its validity has been presented. We decided to develop our own validation code, called PASTIS, using an entirely bayesian approach that allows for statistically rigorous model comparison. Hopefully, this tool will permit confirming the Kepler validated planets and discover many more small transits in the CoRoT and Kepler candidate list.

3 PASTIS

PASTIS (Planetary Analysis and Small Transit Investigation Software) was conceived as a fully bayesian code that includes all the observations for the model comparison: light curves in different filters, radial velocity observations and photometric magnitudes in various filters, and is flexible to include new observables due to its modular structure. PASTIS models the light curve in a given filter using the JKTEBOP code (Southworth et al. 2004), based on the EBOP code (Popper & Etzel 1981; Etzel 1981; Nelson & Davis 1972), elipsoidal and reflection effect are included in the model. PASTIS analyze the radial velocity measurements (including bisector, full width at half maximum and constrast) from a simulated cross-correlation function (Díaz et al. 2012). Also, PASTIS models the spectral energy distribution to compare with the photometric magnitudes measurements. To generate these models, PASTIS use models of stellar atmospheres: ATLAS9 (Castelli & Kurucz 2004) or BT-Settl/Phoenix (Castelli & Kurucz 2004; Allard et al. 2007), stellar evolution tracks: Dartmouth (Dotter et al. 2008), *STAREVOL* (Palacios, *priv. com.*), Geneve (Mowlavi et al. 2012), COND (Baraffe et al. 2003);

limb darkening coefficients (Claret & Bloemen 2011), and galactic interstellar extinction (Amôres & Lépine 2005).

PASTIS uses a Markov Chain Monte Carlo (MCMC) algorithm to explore parameter space (Tegmark et al. 2004; Ford 2005, 2006). In this way the number of free parameters is not limited by the computational capabilities, since parameter space is explored efficiently. Principal components analysis decomposition (PCA) is used to minimize the effect of correlation between parameters (see Fig. 2), and guarantee a correct estimation of the confidence regions for all parameters.

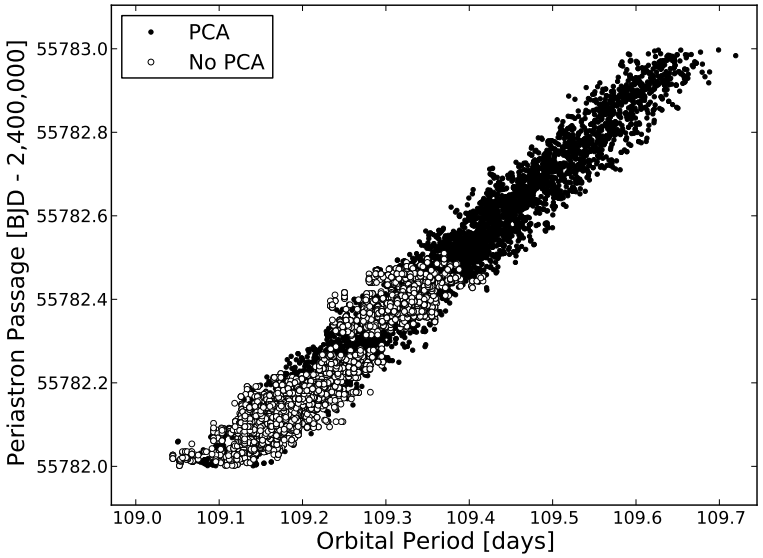

Fig. 2. The risk of correlations in MCMC. Correlated parameters (orbital period and periastron passage in this case) can effectively reduce the region parameter space explored by the chain. When PCA is used, linear correlations are not an impediment for the chain to move freely.

PASTIS is a python object-based code that provides a great flexibility in the definition of the scenarios: almost all possible conceivable false positive scenarios can be modeled using the same structure, and the odds ratio between each pair of models can be computed.

The comparison between scenarios should be made between two of them. Given two scenarios i and j, with its correspondant models M_i and M_j, the set of data D, the relative likelihood is given by:

$$O_{ij} = \frac{p\left(M_i|D,I\right)}{p\left(M_j|D,I\right)} = \frac{p\left(M_i|I\right)p\left(D|M_i,I\right)}{p\left(M_j|I\right)p\left(D|M_j,I\right)} \tag{3.1}$$

where $p\left(M_i|I\right)$ is the prior of the scenario i, and $p\left(D|M_i,I\right)$ is the global likelihood or evidence of the scenario i, and the same for j (Gregory 2005). Fig. 3 shows an example of this method. A synthetic diluted eclipsing binary light curve is fitted with a planetary model. From simple inspection of the residuals it is clear that the fit is poor: the ingress and egress times are too long to accommodate a planetary model. In this case, the ratio of global likelihoods will strongly (over 60 orders of magnitude) favor the blend scenario, and will allow to discard a planetary transit.

Additionally, PASTIS can be used just to fit a transiting planet or a binary (Santerne et al. 2012), and obtain rigorous confidence intervals for all parameters by using the MCMC algorithm.

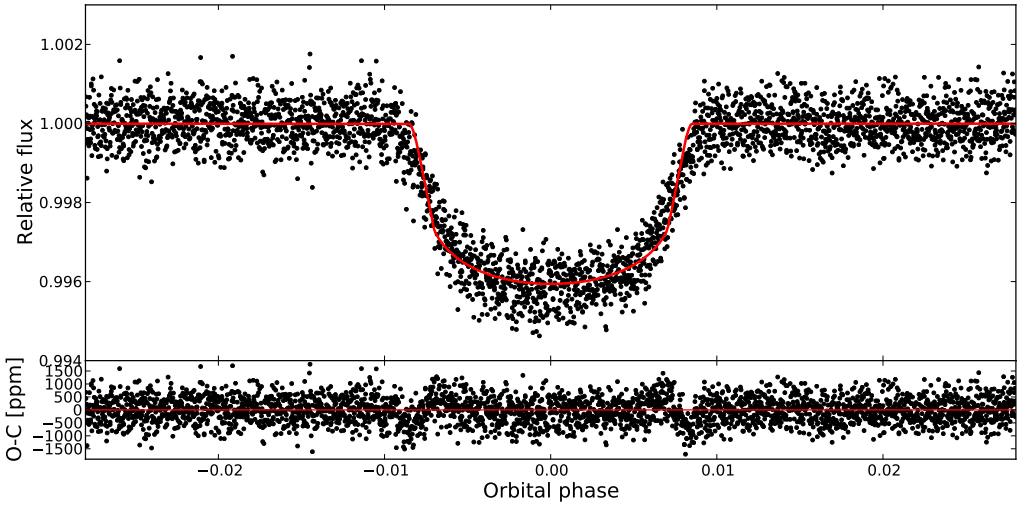

Fig. 3. Results of fitting a synthetic light curve of a diluted eclipsing binary with a planetary model. The fit is clearly poor: the ingress and egress are too long to accommodate a planetary model. In this case the ratio of global likelihoods strongly favors the *false positive* hypothesis.

References

Allard, F., Allard, N. F., Homeier, D., et al. 2007, A&A, 474, L21

Alonso, R., Deeg, H. J., Brown, T. M., & Belmonte, J. A. 2004, in ESA Special Publication, Vol. 538, Stellar Structure and Habitable Planet Finding, ed. F. Favata, S. Aigrain, & A. Wilson, 255

Amôres, E. B. & Lépine, J. R. D. 2005, AJ, 130, 659

Baglin, A., Auvergne, M., Barge, P., et al. 2009, in IAU Symposium, Vol. 253, IAU Symposium, 71

Baraffe, I., Chabrier, G., Barman, T. S., Allard, F., & Hauschildt, P. H. 2003, A&A, 402, 701

Batalha, N. M., Rowe, J. F., Gilliland, R. L., et al. 2010, ApJ, 713, L103

Borucki, W. J., Koch, D., Basri, G., et al. 2010, Science, 327, 977

Castelli, F. & Kurucz, R. L. 2004, ArXiv Astrophysics e-prints

Claret, A. & Bloemen, S. 2011, A&A, 529, A75

Díaz, R. F., Santerne, A., Sahlmann, J., et al. 2012, A&A, 538, A113

Dotter, A., Chaboyer, B., Jevremović, D., et al. 2008, ApJS, 178, 89

Etzel, P. B. 1981, in Photometric and Spectroscopic Binary Systems, ed. E. B. Carling & Z. Kopal, 111

Ford, E. B. 2005, in Protostars and Planets V, 8358

Ford, E. B. 2006, ApJ, 642, 505

Fressin, F., Torres, G., Désert, J.-M., et al. 2011, ApJS, 197, 5

Gregory, P. C. 2005, Bayesian Logical Data Analysis for the Physical Sciences: A Comparative Approach with 'Mathematica' Support

Mowlavi, N., Eggenberger, P., Meynet, G., et al. 2012, A&A, 541, A41

Nelson, B. & Davis, W. D. 1972, ApJ, 174, 617

Popper, D. M. & Etzel, P. B. 1981, AJ, 86, 102

Robin, A. C., Reylé, C., Derrière, S., & Picaud, S. 2003, A&A, 409, 523

Santerne, A., Díaz, R. F., Moutou, C., et al. 2012, A&A, 545, A76

Southworth, J., Maxted, P. F. L., & Smalley, B. 2004, MNRAS, 351, 1277

Tegmark, M., Strauss, M. A., Blanton, M. R., et al. 2004, Phys. Rev. D, 69, 103501

Torres, G., Fressin, F., Batalha, N. M., et al. 2011, ApJ, 727, 24

Torres, G., Konacki, M., Sasselov, D. D., & Jha, S. 2004, ApJ, 614, 979

SF2A 2012
S. Boissier, P. de Laverny, N. Nardetto, R. Samadi, D. Valls-Gabaud and H. Wozniak (eds)

THE ELODIE AND SOPHIE SEARCH FOR NORTHERN EXTRASOLAR PLANETS: JUPITER-ANALOGS AROUND SUN-LIKE STARS

I. Boisse[1,2], F. Pepe[3], C. Perrier[4], D. Queloz[3], F. Bouchy[2,5], N. C. Santos[1,6] and the SOPHIE team[2,3,4,5,7]

Abstract. We present radial-velocity measurements (RV) obtained in one of a number of programs underway to search for extrasolar planets with the spectrograph SOPHIE at the 1.93-m telescope of the Observatoire de Haute-Provence. Targets were selected from catalogs observed with ELODIE, which had been mounted previously at the telescope, in order to detect long-period planets with an extended database close to 15 years.

Keywords: planetary systems, techniques: radial velocimetry, stars: individual: HD 222155 HD 150706 HD 24040 HD 154345 HD 89307, magnetic cycle

1 New long-period giant planets and refined orbits

Radial velocity tables are available at the CDS via anonymous ftp to `cdsarc.u-strasbg.fr` (130.79.128.5) or via `http://vizier.u-strasbg.fr/viz-bin/VizieR?-source=J/A+A/545/A55` [i].

2 Are we observing magnetic cycle ?

The amplitudes of the RV variations are greater in the case of all stars than for all the reported active cycles in the literature (Baliunas et al. 1995; Lovis et al. 2011). We did not find any long-term correlations between the RV and the activity index in the SOPHIE measurements. We concluded that the most likely explanation of the observed RV variations is the presence of a planet.

3 A new population of long-period Jupiter-mass planets

We increase to 19 the number of planets further than 4 AU characterized from RV measurements. With planets published with partial observations (i.e. where the orbital period was not completely covered) and a small number of objects, it has been difficult to establish any significant statistical trends. Nevertheless, we discuss the main properties of this new population.

These planets are in multiplanetary systems (10 of 19 candidates). Their eccentricity distribution agrees with current observations of a significant dispersion. Most of the host stars are G-type stars (observational bias) and are significantly more metal-rich than average.

[1] Centro de Astrofísica, Universidade do Porto, Rua das Estrelas, 4150-762 Porto, Portugal
[2] Institut d'Astrophysique de Paris, UMR7095 CNRS, Université Pierre & Marie Curie, 98bis Bd Arago, 75014 Paris, France
[3] Observatoire de Genève, Université de Genève, 51 Ch. des Maillettes, 1290 Sauverny, Switzerland
[4] UJF-Grenoble1/CNRS-INSU, Institut de PlanŐtologie et d'Astrophysique de Grenoble,UMR 5274, Grenoble, F-38041, France
[5] Observatoire de Haute Provence, CNRS/OAMP, 04870 St Michel l'Observatoire, France
[6] Departamento de Física e Astronomia, Faculdade de Ciências, Universidade do Porto, 4169-007 Porto, Portugal
[7] Laboratoire d'Astrophysique de Marseille, Université de Provence & CNRS, 13388 Marseille, France

[i] Based on observations made with the ELODIE and the SOPHIE spectrographs on the 1.93-m telescope at Observatoire de Haute-Provence (OHP, CNRS/OAMP), France (program 07A.PNP.CONS) and on spectral data retrieved from the ELODIE archive at OHP.

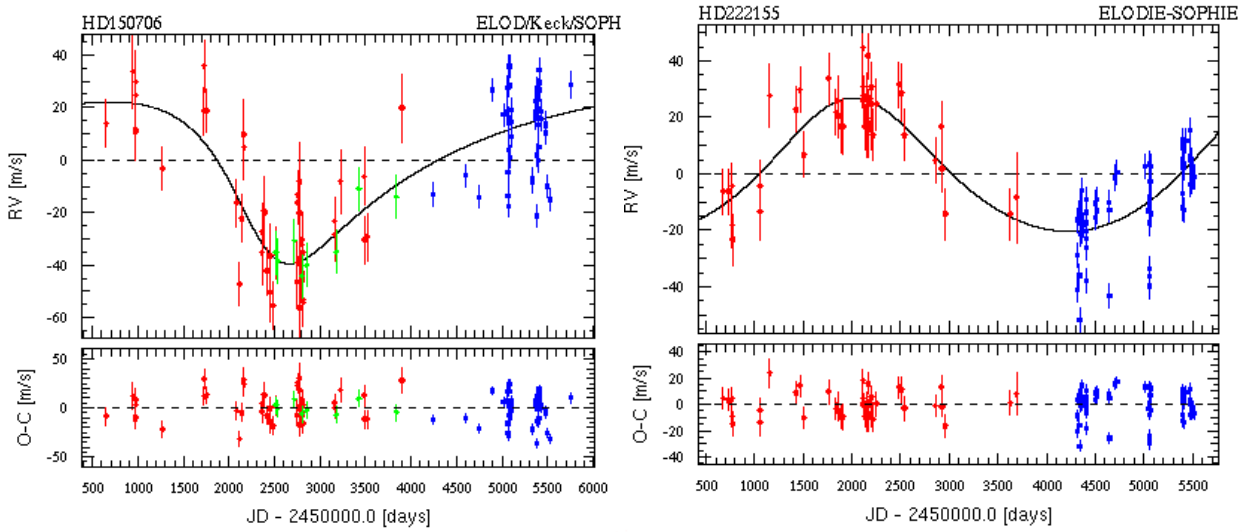

Fig. 1. Left: ELODIE (red), Keck (green), and SOPHIE (blue) RV data points and their residuals from the best-fit Keplerian model for HD 150706 as a function of barycentric Julian date. The best-fit Keplerian model is represented by the black curve with a reduced χ^2 equal to 2.6. The period is 16.1 a with a slight eccentricity e=0.38$^{+0.28}_{-0.32}$ and the planet minimum mass is 2.71 M_{Jup}. **Right:** ELODIE (red) and SOPHIE (blue) RV and residuals from the best-fit Keplerian model for HD 222155 as a function of barycentric Julian date. The best-fit Keplerian model is represented by the black curve with a reduced χ^2 equal to 2.2. The planet has a period of 10.9 a in a non-significant eccentric orbit (e=0.16$^{+0.27}_{-0.22}$), and a minimum mass of 1.90 M_{Jup}.

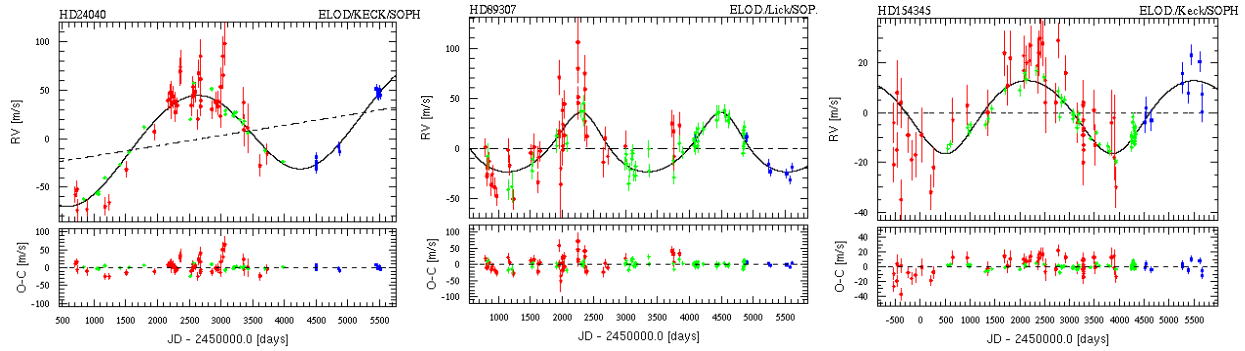

Fig. 2. Left: ELODIE (red), Keck (green) SOPHIE (blue) RV and residuals to the best-fit Keplerian model (black curve) for HD 24040 as a function of barycentric Julian date. It shows a 4.01 M_{Jup} companion with an orbital period of 10.0 a. A linear trend is fitted simultaneously pointing out the presence of a third body in the system. A massive companion was announced previously by Wright et al. (2007). **Middle:** ELODIE (blue), Lick (green), and SOPHIE (red) RV and residuals from the best-fit Keplerian model (black curve) for HD 89307 as a function of time. The fitted orbit corresponds to a planet with a minimum mass of 2.0 M_{Jup}, a period of 6.0 a, and a slightly eccentricity orbit e=0.25±0.09 in agreement with Fischer et al. (2009). **Right:** ELODIE (red), Keck (green), and SOPHIE (blue) RV and residuals of the best-fit Keplerian model (black curve) for HD154345 as a function of barycentric Julian date. The companion has a period of 9.7 a, and a minimum mass of 1.0 M_{Jup} agreeing with Wright et al. (2008).

A lack of massive planets at long period ? A solid prediction of the core-accretion formation theory

We remark that no very massive planet (>8 M_{Jup}) was found. Such a distribution agrees with population synthesis (Mordasini et al. 2012), where they showed that a decrease in frequency of massive giants planets at large distance (>4-5 AU) is a solid prediction of the core-accretion theory.

The occurrence rate of planets with minimum masses higher than 8 M_{Jup} is 1/19 for semi-major axes a>4 AU compared to 27/196 (∼1/7) for smaller orbits with 1<a<4 AU. Assuming a binomial distribution, this implies

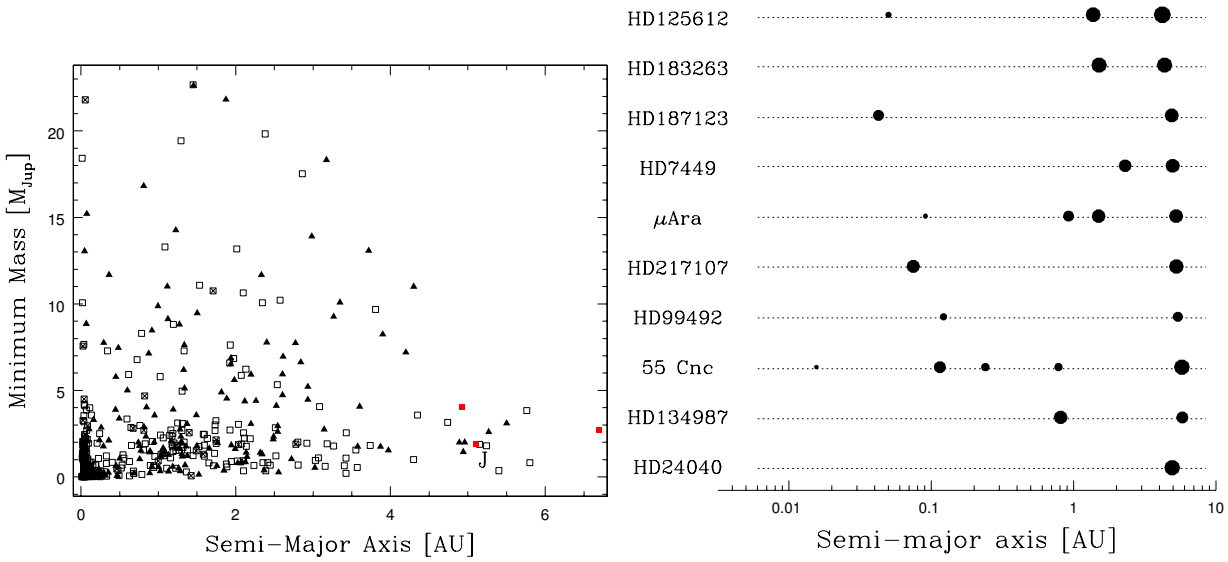

Fig. 3. Left: Minimum mass as a function of the semi-major axis for all planets detected by RV and transit surveys. Empty squared symbols (filled triangles) represent planets with eccentricities lower (higher) than 0.25. Crosses indicate fixed eccentricities at e=0. Jupiter is on the plot. Red points are the Jupiter-like planets characterized in this paper: HD 150706b, HD 222155b, and HD 24040b. **Right:** Multiple systems with semi-major axis greater than 4 AU. The size of the dots shows the minimum mass of the planet on a log scale.

that 13.8±2.5% of the planets with semi-major axes in the range 1<a<4 AU and 5.3±22.3% for those with semi-major axes a>4 AU have minimum masses higher than 8 M_{Jup}. It is unlikely that these host stars would have been discarded from planet surveys as single-lined spectroscopic binaries: for instance, a 8 M_{Jup} orbiting in 4000 days a one solar-mass star induces a RV semi-amplitude of 102 m s^{-1} for a circular orbit, which leads to a typical linear slope of ∼37 m s^{-1} yr^{-1}.

IB and NCS acknowledge the support of the European Research Council/ European Community under the FP7 through a Starting Grant, as well from Fundaccao para a Ciência e a Tecnologia (FCT), Portugal, through SFRH/BPD/81084/2011 and the project PTDC/CTE-AST/098528/2008.

References

Baliunas S. et al. 1995, ApJ, 438, 269
Fischer D. et al. 2009, ApJ, 703, 1545
Lovis C. et al. 2011, http://arxiv.org/abs/1107.5325
Meyer M.R. et al. 2004, ApJS, 154, 422
Mordasini C. et al. 2012, A&A, 541, 97
Wright J.T. et al. 2007, ApJ, 657, 533
Wright J.T. et al. 2008, ApJ, 683, 63

SF2A 2012
S. Boissier, P. de Laverny, N. Nardetto, R. Samadi, D. Valls-Gabaud and H. Wozniak (eds)

THE COROT EXOPLANET PROGRAMME: AN OVERVIEW OF RESULTS

D. Rouan[1] and The Corot Exoplanet Science Team[2]

Abstract. We present some highlights of the exoplanet programme of the CoRoT satellite, after 5.5 years of life. 27 planets have been discovered and we review here the global properties of the sample and highligth some of the most important results: the detection of Corot-7b, the first truly rocky planet, two peculiar brown dwarves, a long period planet, several blaoted planets, several hot, yet excentric, Jupiter as well as two systems of small planets.

Keywords: CoRoT satellite, brown dwarfs, exoplanets, Planets and satellites: detection

1 The CoRoT satellite and its operations

CoRoT, is a satellite dedicated to high accuracy stellar photometry. Launched end 2006 by a good old faithful Soyuz on a polar orbit, it accomplished 5.5 years of operation without any major failure but the loss of two CCDs due to cosmic hits. This review concentrates on the exoplanet program which aims at detecting the slight diming of a star when one planet of its retinue transits in front of the stellar disk.

The satellite features an afocal telescope of 27 cm pupil diameter, made with 2 parabolic mirrors, followed by a 6 lenses dioptric camera which provides a field of view of several square degrees. A very long baffle avoids light from the terrestrial horizon to enter the telescope.

The focal plane accomodates 4 CCD of 2048^2 pixels, two of them for astero-sismology and two for the exoplanets programme. The exoplanet field is of $3.45^{\circ 2}$ (half today since the lost of one CCD).

The observing strategy is based on the peculiarity of the polar orbit: CoRoT can monitor continuously a direction in the sky perpendicular to the orbit, with the sun *in the back* during 6 months and then flips on itself to start monitoring the opposite direction. This means that up to 150 days of continous observation on each field are possible. 22 fields have already been observed: 8 short and 14 long.

To detect transiting exoplanets, one monitors thousands of stars in the field and tries to locate on few of them at least 3 transit events that are periodic.

In this quest, the ennemies are the false positives which produce a signal that mimics a transiting planet, but actually are not the fact of any planet. This happens when the star is a Grazing Eclipsing Binary (GEB), or when there is an Eclipsing Binary in the Background (BEB), or when the target is an Eclipsing Binary in a dwarf/giant system. Because those false positive are much more frequent than actual planetary transits, follow-up from the ground is mandatory: the CoRoT community has mobilised its strengths around several ground-based instruments in Radial Velocity (Harps, Sophie, Keck), precise photometry (CFH, Canarias), Adaptive Optics (VLT).

2 Performances and global statistics

145 000 Light Curves were obained on the 22 fields. It resulted an amazing diversity of behaviour and clearly one great legacy of CoRoT will be a huge data set to study stellar variability. For the whole range of stellar magnitudes, the measured noise on all candidates is within the expectation, i.e. just slightly larger than the photon noise, allowing detection of small super-earth planets, at least for mR < 14. This capability of CoRoT was indeed demonstrated with Corot-7b.

[1] LESIA - CNRS - Observatoire de Paris - UPMC, Université Paris-Didierot
[2] Europe, Brazil

CoRoT team has analyzed 10^5 stars and confirmed (so far) 27 substellar objects : 25 transiting planets and 2 brown dwarves. All were detected in long runs (i.e. duration > 70 days). There has been on the average 200 to 300 detections of periodic events per run, i.e. 2 to 3 % of the monitored stars. Among them only 1 to 4 cases revealed to actually be planets, i.e. 0.5 - 2% of those periodic cases. This low figure is not a surprise. On Fig. 1, where a normalized planet detection number is presented with respect to duration and for different fields, we note a rather large scattering of detection yeld. A detailed analysis by Cabrera et al. pointed out the role of interstellar extinction to explain this effect : it limits the detection capabiliity by dimming stars which would be the most interesting statistically.

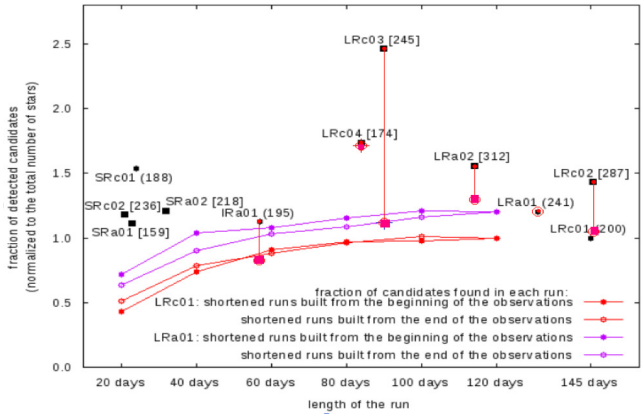

Fig. 1. Detection rate, normalized to the star number for different fields, vs time. Most of the detection are secured after 60 days. The vertical lines indicate the effect of an artificial reddening on this rate, explaining the scattering of number of detections between the fields.

CoRoT planets on the R vs M diagram

CoRoT planets cover a broad range of densities, from 0.21 to 55 g cm^{-3}. CoRoT indeed extended the mass range of transiting planets towards both extremes, with on one side Corot-15b whose mass is 65 M_{Jup} and on the other side Corot-7b, with .015 M_{Jup}. While the first one is a bona fide brown dwarf, another probable brown dwarf is Corot-3b which is right at the theoretical frontier between a planet and a brown dwarf.

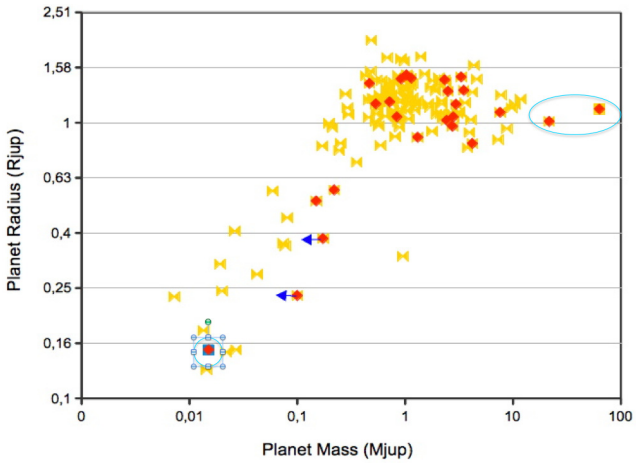

Fig. 2. The CoRoT planets (red diamonds) on the Radius / Mass diagram. The oval at right identifies the two brown dwarves and the circle at left the rock solid Super-Earth Corot-7b.

Periods of transiting systems

If we consider the distribution of orbital periods on Fig. 3, CoRoT appears to be unbiased towards both extremes: Corot-7b was for a time the shortest period ever detected, while three medium periods of 9 to 13 days and one long period of 95 days were also detected.

Massive companions for massive stars ?

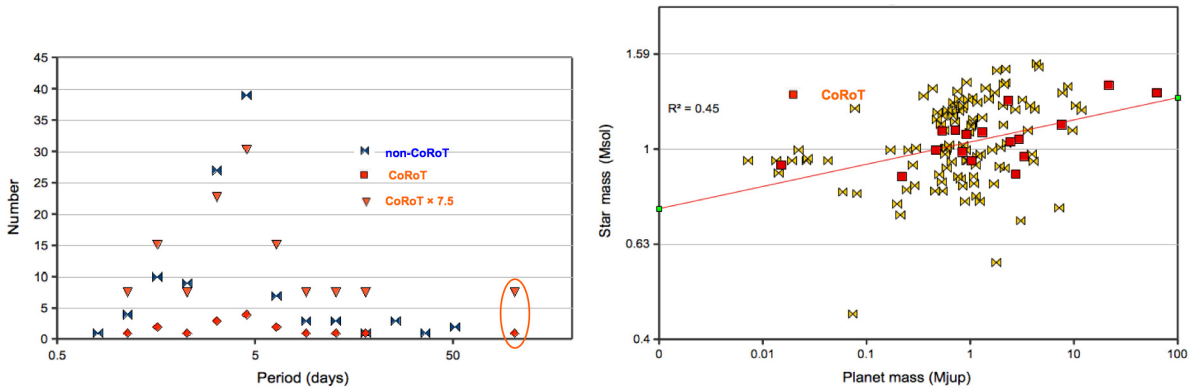

Fig. 3. Left: histogram of periods of CoRoT planets (red triangles and diamonds) and of all transiting planets (diabolo); CoRoT is on the average more efficient at rather long period. **Right:** diagram of planetary mass vs stellar mass for CoRoT (red) and other transiting planets (yellow), the line indicate a trend.

The plot of planet mass versus stellar mass (Fig. 3) indicates a significant trend for massive stars to form massive planets. This is not unexpected, considering the currently favoured core-accretion scenario for planet formation.

2.1 Highlights

Table 1 gathers the characteristics of the most peculiar planets detected by CoRoT. Among them let's distinguish more particularly:

- Corot-9b, a long period (95.3 days) planet on a Mercury-like orbit; it deserves the qualification of *temperate* planet (Deeg et al. 2010);
- Corot-3b, with a mass of 22 M_{Jup}, is it a Super-planet or a brown dwarf ? (Deleuil et al. 2008)
- Corot-15b, a bona-fide orbiting brown dwarf (Bouchy et al. 2011) ;
- Corot-8b, a Neptune-like planet of 0.22 M_{Jup} mass (Bordé et al. 2010) ;
- Corot-11b, and Corot-2b, two bloated planets of radius 1.4-1.5 R_{Jup} (Gandolfi et al. 2010; Alonso et al. 2008) ;
- Corot-10b, Corot-16b, Corot-20b, Corot-23b, four hot Jupiters which are however on eccentric orbits: a clear constraint on the quality factor Q_p of tidal dissipation (Bonomo et al. 2010; Ollivier et al. 2011; Deleuil et al. 2011; Rouan et al. 2012) ;
- Corot-24b,c the first multi-transit system of CoRoT, with two small planets of 0.10 and 0.17 M_{Jup} (Alonso & al. 2012) ;
- Corot-7b, with a radius of 1.7 R_{Earth} and a mass of 7.3 M_{Earth}, it was the first confirmed rocky planet with a density and composition that are close to the Earth's ones (Léger et al. 2009; Queloz et al. 2009). Since it must be tidally locked, its two hemispheres, the bright and the dark one, present an extremely high contrast in temperature (2200K vs 50K) and a lava ocean must occupy a large fraction of the bright side. A continent of frost H_2O, CO_2 is probably found on the dark side. Corot-7 is also the first case of a system with 2 Super-Earths, one in transit, since radial velocity measurements allowed the discovery of Corot-7c, a planet of 8.4 M_{Earth} and period 3.79 days. A third planet is even suspected.

The most recent planets discovered by CoRoT are:
- Corot-16b : an eccentric hot Jupiter around a faint solar-like star (Ollivier et al. 2011)
- Corot-19b : a low density planet orbirting an old inactive F9-V star
- Corot-24b,c : a probable multi-transit system (Alonso & al. 2012)
- Corot-21b : a doomed large Jupiter around a faint sub-giant star
- Corot-22b : a highly probable small Saturn (Moutou et al. 2011)
- Corot-23b : a dense hot Jupiter on an eccentric orbit (Rouan et al., 2011)

Table 1. Characteristics of the most peculiar planets detected by CoRoT

Name	Period (days)	Mass M_{Jup}	Radius R_{Jup}	ρ g cm^{-2}	excentricity	peculiarity
Corot-9b	**95.27**	.84	1.05	.89	.11	Long period Mercury-like orbit
Corot-3b	4.26	**21.7**	1.01	26.4	0	Super-planet or brown dwarf ?
Corot-15b	3.06	**63**	1.12	55	0	True orbiting brown dwarf
Corot-8b	6.21	**0.22**	**0.57**	1.6	0	A Neptune-like planet
Corot-11b	2.99	2.33	**1.43**	.97	0	Bloated planet
Corot-2b	1.743	3.31	**1.47**	1.29	0	Bloated planet
Corot-10b	13.24	2.75	.97	3.68	**.53**	Eccentric, despite hot Jupiter
Corot-16b	5.35	.535	1.17	.44	**.33**	Eccentric, despite hot Jupiter
Corot-20b	9.24	4.2	.84	8.65	**.56**	Dense and eccentric, despite hot Jupiter
Corot-23b	3.63	2.8	1.05	2.95	**.16**	Dense and eccentric, despite hot Jupiter
Corot-24b	5.11	.1	.24	9.3		Multi-transit system
Corot-24c	11.75	.17	.38	3.9		Multi-transit system
Corot-7b	**.854**	**.0151**	**.15**	10		The first secured rocky planet

3 Extension of the mission

Very recently approved, the extension of the mission until march 2016 will allow to exploit two peculiar niches, in the Kepler era: the capability to point different regions within two cones of radius extended from 10 to 15° and the possibility to measure bright stars. The three programmes that will be favored are : *i)* characterizing planets in the sub-Saturn regime with a focus on stars brigthter tnan mV = 15, this will free telemetry for more imagettes that give access to the centroid determination; *ii)* detection and study of planets already known by RV: this will use the asterosismology CCD and relies on the fact that 20% of Kepler candidates are multi-transit; *iii)* search for giant planets on wide orbits, with re-observation of mono or bi-transit already detected, so that period much larger than 75 days could be discovered.

References

Alonso, R. & al. 2012, A&A, in press
Alonso, R., Auvergne, M., Baglin, A., et al. 2008, A&A, 482, L21
Bonomo, A. S., Santerne, A., Alonso, R., et al. 2010, A&A, 520, A65
Bordé, P., Bouchy, F., Deleuil, M., et al. 2010, A&A, 520, A66
Bouchy, F., Deleuil, M., Guillot, T., et al. 2011, A&A, 525, A68
Deeg, H. J., Moutou, C., Erikson, A., et al. 2010, Nature, 464, 384
Deleuil, M., Bonomo, A., Ferraz-Mello, S., et al. 2011, A&A, submitted
Deleuil, M., Deeg, H. J., Alonso, R., et al. 2008, A&A, 491, 889
Gandolfi, D., Hébrard, G., Alonso, R., et al. 2010, A&A, 524, A55
Léger, A., Rouan, D., Schneider, J., et al. 2009, A&A, 506, 287
Moutou, C., Almenara, J., Alonso, M., et al. 2011, A&A, in press
Ollivier, M., Gillon, M., Santerne, A., Wuchterl, G., & Havel, M. 2011, A&A, submitted
Queloz, D., Bouchy, F., Moutou, C., et al. 2009, A&A, 506, 303
Rouan, D., Parviainen, H., Moutou, C., et al. 2012, A&A, 537, A54

Session 07

Characterisation of exoplanets

SF2A 2012
S. Boissier, P. de Laverny, N. Nardetto, R. Samadi, D. Valls-Gabaud and H. Wozniak (eds)

TEMPORAL VARIATIONS IN THE EVAPORATING ATMOSPHERE OF THE EXOPLANET HD 189733B

V. Bourrier[1,2], A. Lecavelier des Etangs[1,2], P. J. Wheatley[3], H. Dupuy[1,2], D. Ehrenreich[4], A. Vidal-Madjar[1,2], G. Hébrard[1,2], G. E. Ballester[5], J.-M. Désert[6], R. Ferlet[1,2] and D. K. Sing[7]

Abstract. Transit observations of the hydrogen Lyman-α line allowed the detection of atmospheric escape from the exoplanet HD209458b (Vidal-Madjar et al. 2003). Using spectrally resolved Lyman-α transit observations of the exoplanet HD 189733b at two different epochs, Lecavelier des Etangs et al. (2012) detected for the first time temporal variations in the physical conditions of an evaporating planetary atmosphere. Here we summarized the results obtained with the HST/STIS observations as presented in June 2012 at the SF2A 2012 meeting. While atmospheric hydrogen cannot be detected in the STIS observations of April 2010, it is clearly detected in the September 2011 observations. The atomic hydrogen cloud surrounding the transiting planet produces a transit absorption depth of 14.4±3.6% between velocities of -230 to -140 $\mathrm{km\,s^{-1}}$. These high velocities cannot arise from radiation pressure alone and, contrary to HD 209458b, this requires an additional acceleration mechanism, such as interactions with stellar wind protons. The spectral and temporal signature of the absorption is fitted by an atmospheric escape rate of neutral hydrogen atoms of about $10^9\,\mathrm{g\,s^{-1}}$, a stellar wind with a velocity of $190\,\mathrm{km\,s^{-1}}$ and a temperature of $\sim 10^5$ K.

We also illustrate the power of multi-wavelengths approach with simultaneous observations in the X-rays obtained with Swift/XRT. We detected an X-ray flare about 8 hours before the transit of September 2011. This suggests that the observed changes within the upper part of the escaping atmosphere can be caused by variations in the stellar wind properties, or/and by variations in the stellar energy input to the planet's escaping gas. This multi-wavelengths approach allowed the simultaneous detection of temporal variations both in the stellar X-ray and in the planetary upper atmosphere, providing first observational constraints on the interaction between the exoplanet's atmosphere and the star.

Keywords: Stars: planetary systems , Stars: individual: HD 189733

1 Introduction

Discovery of hot-Jupiter atmospheric escape has been carried out using observations of the transiting extrasolar planet HD 209458b in the Lyman-α line of atomic hydrogen H I (Vidal-Madjar et al. 2003). The so-called 'evaporation' is caused by energy input from the star into the upper atmosphere in the extreme ultraviolet and X-rays (Lammer et al. 2003; Lecavelier des Etangs et al. 2004; Yelle 2004). Evaporation can lead to moderate escape rates for massive planets, or to formation of planetary remnants when intense evaporation implies a dramatic change in the planet mass (Lecavelier des Etangs et al. 2004, 2007; Charpinet et al. 2011).

The escape phenomenon is of prime importance on the fate of planets at short orbital distances. Nonetheless, the details of the physics of the exospheric gas remain debated (García Munõz 2007; Schneiter et al. 2007; Holmström et al. 2008; Lecavelier des Etangs et al. 2008; Murray-Clay et al. 2009; Ben-Jaffel & Sona Hosseini 2010; Guo 2011). Moreover, we have only a limited number of observations in hand (Vidal-Madjar et al. 2004;

[1] CNRS, UMR 7095, Institut d'astrophysique de Paris, 98$^{\mathrm{bis}}$ boulevard Arago, F-75014 Paris, France
[2] UPMC Univ. Paris 6, UMR 7095, Institut d'Astrophysique de Paris, 98$^{\mathrm{bis}}$ boulevard Arago, F-75014 Paris, France
[3] Department of Physics, University of Warwick, Coventry CV4 7AL, UK
[4] Observatoire astronomique de l'Université de Genève, 51 Chemin des Maillettes, 1290 Sauverny, Switzerland
[5] Lunar and Planetary Laboratory, University of Arizona, 1541 E. University Blvd., Tucson, AZ 85721-0063, USA
[6] Harvard-Smithsonian Center for Astrophysics, 60 Garden Street, Cambridge, MA 02138, USA
[7] Astrophysics Group, School of Physics, University of Exeter, Stocker Road, Exeter EX4 4QL, UK

Ballester et al. 2007; Ehrenreich et al. 2008; Fossati et al. 2010; Linsky et al. 2010; Lecavelier des Etangs et al. 2010). Note that, because HD189733b has been discovered in 2005 after the STIS breakdown, HD189733b could be observed before May 2009 in the UV only by using the ACS spectrograph which provides non-resolved Lyman-α observations. The non-resolved Lyman-α spectra gathered in 2007-2008 provided first indications of the atmospheric escape from HD 189733b (Lecavelier des Etangs et al. 2010).

2 Observations, data analysis, and results

2.1 Observations

Lecavelier des Etangs et al. (2012) observed with HST/STIS two transits of HD 189733b in April 2010 and September 2011. The data consist of time-resolved spectra from 1195 to 1248 Å with a spectral resolution of about 20 km s^{-1}. They show stellar emission lines of H I Lyman-α, Si III (1206.5 Å), O V (1218.3 Å) and the N V doublet (1238.8 Å and 1242.8 Å). However the Si III, O V, and N V lines do not show any planetary atmosphere signatures, and here we will focus on the Lyman-α line and summarize the results obtained by Lecavelier des Etangs et al. (2012).

The Lyman-α line of HD189733b is very bright (1.8×10^{-13} erg s^{-1} cm^{-2}) and is about ten times brighter than that of HD 209458. In contrary to the STIS observations of HD209458b, there is no need to co-add several observations of HD189733b to detect the signature of the atmosphere. This provides the unprecedented opportunity to search for temporal variations in the planetary upper atmosphere.

2.2 Detection of temporal variations in the evaporating atmosphere

The resolved Lyman-α emission line from HD 189733 is composed of two peaks separated by the deep ISM absorption due to interstellar atomic hydrogen (Fig. 1). The stellar emission line is superimposed with the geo-coronal airglow from the Earth atmosphere (Vidal-Madjar et al. 2003). However, this has been shown to have a negligible effect, in particular for the September 2011 observations which benefit from a very low airglow emission level.

The Lyman-α observations of 2010 do not show any atmospheric transit signature. In 2010, the transit depth measured in the total flux of the Lyman-α line is 2.9±1.4%; this agrees with the 2.4% transit depth of the planet body alone as seen in the optical. Most importantly, there is no excess absorption during the 2010 transit in any portion of the Lyman-α spectral line profile.

This strongly contrasts with the September 2011 observations. In these observations, there is an excess absorption in the total flux of the Lyman-α line with a transit depth of 5.0±1.3%, in agreement with the results obtained with the non-resolved HST/ACS spectra of 2007-2008 (Lecavelier des Etangs et al. 2010). More importantly, deep absorptions are detected during the 2011 transit in specific wavelength domains: in the blue wing of the spectrum from -230 km s^{-1} to -140 km s^{-1}, and in the red peak of the spectrum from 60 to 110 km s^{-1}.

In the blue part of the Lyman-α spectrum of 2011, we measured an absorption depth of 14.4±3.6% (4-σ detection) from -230 to -140 km s^{-1}. This corresponds to an excess absorption of 12.3±3.6% (the 14.4% absorption is composed of 2.4% from the planetary disk, and 12.3% from atmospheric hydrogen). The false-positive probability to find this absorption during the transit anywhere in the blue wing of the spectrum is estimated to be only 3.6% (Bourrier et al., in preparation). The absorption found in the red wing of the 2011 spectrum (7.7±2.7% between 60 to 110 km s^{-1}) has a false positive probability of 24.6% and is likely not a real signature. Nonetheless it is noteworthy that a similar absorption in the red peak of the line has also been observed in HD 209458b (Vidal-Madjar et al. 2003).

The most important result is the observation of significant temporal variations of the physical conditions within the extended exosphere of this extrasolar planet between 2010 and 2011, 17 months apart (Fig. 2).

2.3 Models

The neutral hydrogen atoms detected in September 2011 present a large absorption depth (corresponding to a large extension of the absorbing cloud at high altitude in the exosphere of the planet) and a velocity range exceeding the escape velocity ($v_{esc}\sim$60 km s^{-1}). This unambiguously demonstrates that atmospheric gas is escaping from HD 189733b.

In HD 209458b, the Lyman-α excess absorption was observed between -130 to -50 $\mathrm{km\,s^{-1}}$. This can readily be explained by the stellar radiation pressure accelerating hydrogen atoms up to -130 $\mathrm{km\,s^{-1}}$ (Lecavelier des Etangs et al. 2008). The higher velocities (-230 to -140 $\mathrm{km\,s^{-1}}$) observed in HD189733b are more challenging to explain. Following the procedure described in Ehrenreich et al. (2011), we calculated the Lyman-α emission line profile as seen from the planet. We estimated that the radiation pressure accelerate hydrogen atoms up to the radial velocity of -120 $\mathrm{km\,s^{-1}}$ (below this radial velocity the stellar flux in the core of the emission line is sufficiently high for the radiation pressure to exceed the stellar gravity). We conclude that an acceleration mechanism other than radiation pressure, like the charge exchange with stellar wind protons (Holström et al. 2008; Ekenbäck et al. 2010), is required to explain the hydrogen velocities observed in 2011.

We investigate the scenario of charge exchange to interpret the observed HI light curve, using a numerical Monte-Carlo N-body simulation of the hydrogen atoms dynamics. The details of the model will be given in a forthcoming paper (Bourrier et al. in preparation). In this simulation, hydrogen atoms are released from the planet upper atmosphere. Because of the radiation pressure from the (well-known) Lyman-α stellar emission, the atoms are rapidly accelerated up to 120 $\mathrm{km\,s^{-1}}$, and then accelerated to higher velocities by charge exchange with stellar wind protons. This dynamical model allows us to reproduce the observed profile of the spectral absorption and the transit light curve (Fig. 3). The observations are well-fitted with an escape rate of neutral hydrogen of about $10^9\,\mathrm{g\,s^{-1}}$ and a stellar wind density $n{\sim}3{\times}10^3\,\mathrm{cm^{-3}}$, temperature $T{\sim}10^5$ K, and velocity ${\sim}190\,\mathrm{km\,s^{-1}}$. We also concluded that the EUV ionizing flux should be about 5 times the solar value to explain the moderate absorption after the transit of the planet (Fig. 2, Bourrier et al. in preparation).

3 Swift X-ray simultaneous observations

The energy needed for the gas to escape the planet gravitational well is brought by the X-ray/EUV irradiation from the host star. While observing the transit of September 2011 with HST/STIS, we obtained simultaneous observations with the X-ray telescope (XRT) of Swift. The star HD189733 is detected in the X-ray with a count rate of $0.0119{\pm}0.0007\,\mathrm{s^{-1}}$. By fitting the Swift XRT spectrum of HD 189733, we found an X-ray flux of $3.6{\times}10^{-13}\,\mathrm{erg\,s^{-1}\,cm^{-2}}$ in the 0.3-3 keV band. Assuming 100% evaporation efficiency, this X-ray flux corresponds to a mass loss rate of $1.0{\times}10^{11}\,\mathrm{g\,s^{-1}}$ (a lower efficiency yields a proportionally lower escape rate; see details in Lecavelier des Etangs et al. 2012). Extrapolation of the high energy flux estimates to the X-ray/EUV band yields a corresponding energy-limited evaporation rate of $4.4{\times}10^{11}\,\mathrm{g\,s^{-1}}$. Therefore, the observed X-ray irradiation is consistent with the escape rate estimated by Lecavelier des Etangs et al. (2012), which would thus require about 1% efficiency in the conversion of input energy into mass loss (Ehrenreich & Désert 2011). Note however that this is only a lower limit of the efficiency because the escape rate of neutral hydrogen atoms estimated using Lyman-α observations does not include the escape of ionized species and represent a lower limit for the net escape rate from HD189733b.

The Swift X-ray light curve shows that HD189733 exhibits significant X-ray variability (Fig. 4). Most notably, a bright flare occurred about 8 hours before the planetary transit of September 2011. This flare could explain the variations in the extended cloud of high-velocity hydrogen atoms escaping the planet. One possibility is a change of the properties of the stellar wind accelerating the atoms to the observed radial velocities, a change caused by or related to the observed X-ray flare. In another scenario, the enhanced X-ray/EUV irradiation caused by the X-ray flare can lead to a significantly enhanced escape rate which becomes detectable. A combination of these two scenarios is also possible.

4 Conclusions

Here we summarized the results obtained from HST/STIS and SWIFT/XRT simultaneous observations of HD189733b transit, as presented in Lecavelier des Etangs et al. (2012), which show the detection in Lyman-α of temporal variations in the evaporating atmosphere of HD 189733b. Further simultaneous X-ray and Lyman-α observations would be useful to improve the picture of the complex relationship between the stellar energetic input to the planet and the atmosphere's response to it, and to constrain theoretical models of a space weather event on hot-Jupiters (*e.g.* Cohen et al. 2011). The HD 189733 system appears to be the target of choice in the hot-Jupiter gallery, but future observations should also enlarge the diversity of planetary and stellar systems to better disentangle the effects of the planet-star interactions from the intrinsic (wheather-like) variability in the exoplanet atmospheres.

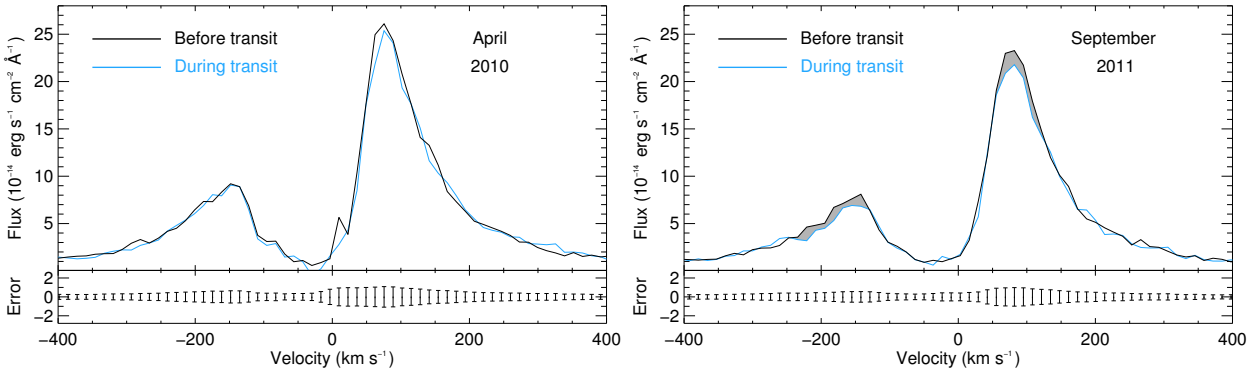

Fig. 1. Lyman-α emission line of HD 189733 measured before (black) and during the transits (blue), in 2010 and 2011. No transit signatures are detected in 2010. During the transit of September 2011 absorptions are detected at more than 3-σ at the top of the red wing and in the blue wing of the line.

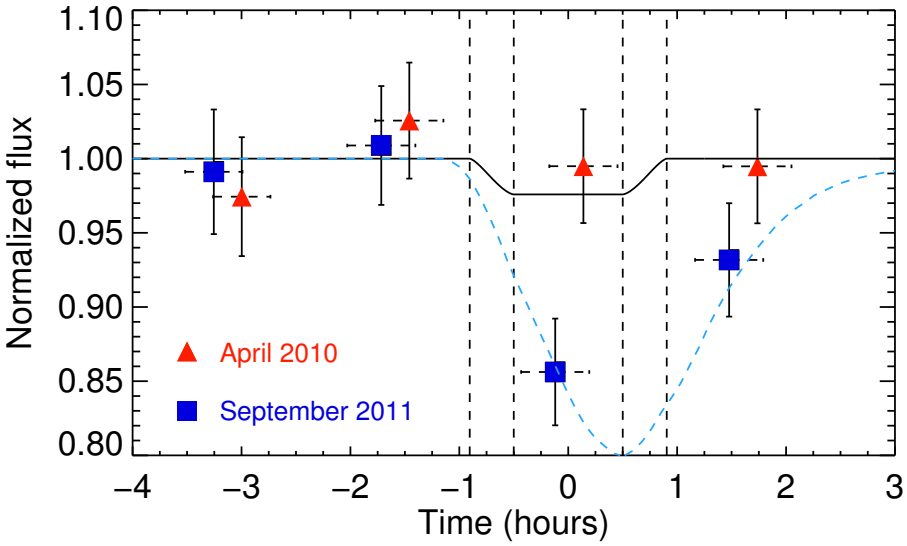

Fig. 2. Plot of the flux between -230 and -140 km s^{-1} in the blue wing of the Lyman-α line as a function of time. Dashed lines show the beginning and end (four contacts) of the transit. The red triangles are for the 2010 observations; the blue squares are for the 2011 observations. The solid black line shows the transit light curve at optical wavelengths. The blue dashed line shows the light curve calculated with the numerical simulations with an atmospheric escape rate of 10^9 g s^{-1}.

The authors are grateful to CNES for its financial support.

References

Ballester, G. E., Sing, D. K., & Herbert, F. 2007, Nature, 445, 511
Ben-Jaffel, L., & Sona Hosseini, S. 2010, ApJ, 709, 1284
Charpinet, S., Fontaine, G., Brassard, P., et al. 2011, Nature, 480, 496
Cohen, O., Kashyap, V. L., Drake, J. J., Sokolov, I. V., & Gombosi, T. I. 2011, ApJ, 738, 166
Ehrenreich, D., & Désert, J.-M. 2011, A&A, 529, A136
Ehrenreich, D., Lecavelier des Etangs, A., Hébrard, G., et al. 2008, A&A, 483, 933
Ehrenreich, D., Lecavelier Des Etangs, A., & Delfosse, X. 2011, A&A, 529, A80
Ekenbäck, A., Holmström, M., Wurz, P., et al. 2010, ApJ, 709, 670
Fossati, L., Haswell, C. A., Froning, C. S., et al. 2010, ApJ, 714, L222
García Muñoz, A. 2007, Planet. Space Sci., 55, 1426
Guo, J. H. 2011, ApJ, 733, 98
Holmström, M., Ekenbäck, A., Selsis, F., et al. 2008, Nature, 451, 970

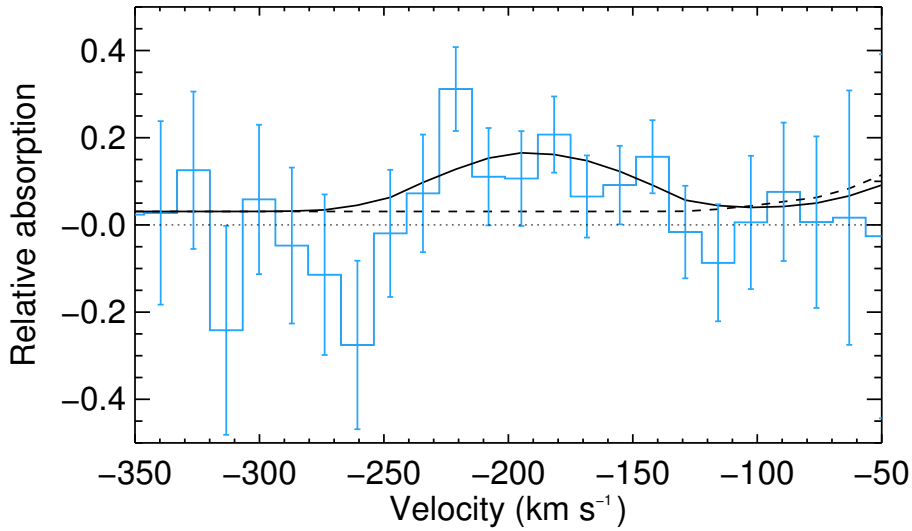

Fig. 3. Plot of the spectral profile of the transit HI absorption in the blue wing of the Lyman-α stellar line (blue histogram). The dashed line shows the model with radiation pressure only. If a stellar wind and charge exchange is considered, hydrogen atoms can be accelerated to the higher observed velocities. The model with radiation pressure, charge exchange with stellar wind protons, and an escape rate of $10^9\,\mathrm{g\,s^{-1}}$ yields a good fit to the observation with a χ^2 of 13.0 for 17 degrees of freedom (solid line).

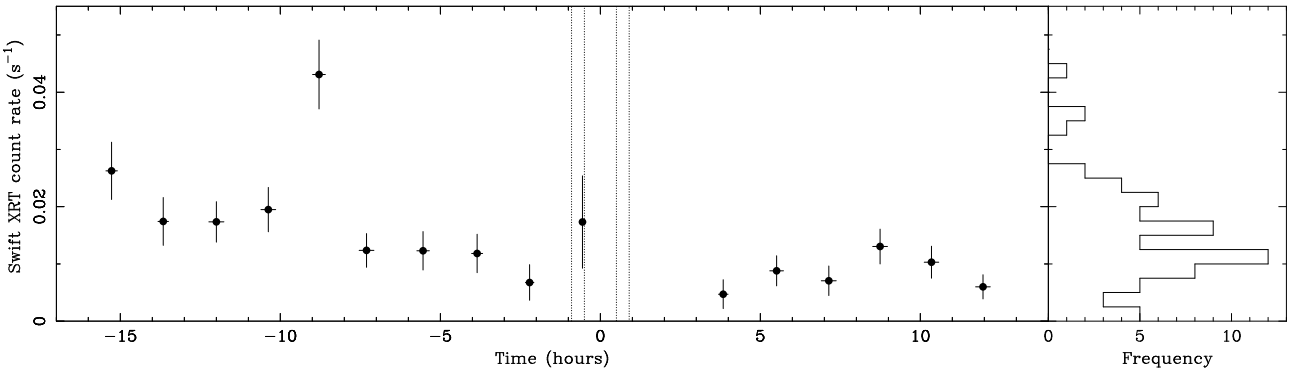

Fig. 4. Swift X-ray light curve of HD189733 in September 7, 2011. A bright X-ray flare occurred about 8 hours before the transit with an average count rate about a factor 3.6 higher than the mean value. The right panel shows the distribution for all available Swift measurements; the flare occurring before the transit is the highest X-ray flux in all of the 63 measurements.

Lammer, H., Selsis, F., Ribas, I., et al. 2003, ApJ, 598, L121
Lecavelier des Etangs, A. 2007, A&A, 461, 1185
Lecavelier des Etangs, A., Bourrier, V., Wheatley, P. J., et al. 2012, A&A, 543, L4
Lecavelier des Etangs, A., Ehrenreich, D., Vidal-Madjar, A., et al. 2010, A&A, 514, A72
Lecavelier des Etangs, A., Vidal-Madjar, A., Hébrard, G., McConnell, J. 2004, A&A, 418, L1
Lecavelier des Etangs, A., Vidal-Madjar, A., & Desert, J.-M. 2008, Nature, 456, E1
Linsky, J. L., Yang, H., France, K., et al. 2010, ApJ, 717, 1291
Murray-Clay, R. A., Chiang, E. I., & Murray, N. 2009, ApJ, 693, 23
Schneiter, E. M., Velázquez, P. F., Esquivel, A., Raga, A. C., & Blanco-Cano, X. 2007, ApJ, 671, L57
Vidal-Madjar, A., Lecavelier des Etangs, A., Désert, J.-M., et al. 2003, Nature, 422, 143
Vidal-Madjar, A., Désert, J.-M., Lecavelier des Etangs, A., et al. 2004, ApJ, 604, L69
Yelle, R. V. 2004, Icarus, 170, 167

SF2A 2012
S. Boissier, P. de Laverny, N. Nardetto, R. Samadi, D. Valls-Gabaud and H. Wozniak (eds)

LAYERED DOUBLE DIFFUSIVE CONVECTION: FROM EARTH OCEANS TO GIANT PLANET INTERIORS.

J. Leconte[1,2] and G. Chabrier[2,3]

Abstract. Many unknowns remain concerning the internal structure and composition of giant gaseous planets. The existence and the properties of an hypothetical central core, in particular, are still debated.

Contrary to conventional interior models for giant (exo)planets, we consider an inhomogeneous mixing of heavy elements in the gaseous H/He envelope of these objects. As in the oceans, such compositional gradients can give rise to layered convection which impedes large scale convection, yielding a hotter, super adiabatic interior. As a result, the metal enrichment predicted by this model is up to 30 to 60% larger than previously thought for Jupiter and Saturn. However, metals are preferentially redistributed in the gaseous envelope and coreless models can be found for Jupiter.

This inefficient, layered convection, yielding a slower cooling, can help to explain anomalously inflated Hot Jupiters, but also opens a new window on our understanding of giant planet formation and history inside our Solar System.

Keywords: Planets and satellites: interiors, Convection

1 The double diffusive instability

In hydrodynamic experiments, it is well known that the presence of a compositional gradient, causing a gradient of mean molecular weight, can change the properties of the mean flow that develops in a stratified fluid. This is due to the fact that, as temperature, the mean molecular weight influences the buoyancy of the fluid and can (de)stabilize the whole medium against the convective instability (Schwarzschild & Härm 1958; Ledoux 1947); i.e. the instability which drives a denser material to sink and a lighter one to rise until a stable stratification is reached.

However, because diffusive processes are also at play, even a "gravitationally stable" stratification of solute and temperature can be unstable. Roughly, this "double diffusive instability", first theorized by Stern (1960), can arise if the diffusivity of one of the quantities (in general heat) is significantly greater than the other. Two cases are of particular interest. The first one, known as the *fingering case*, can arise when temperature plays a stabilizing role[i] and the mean molecular weight is destabilizing. A perfect example is given by the well known "salt fingers" that form when warm salty water is put on top of cold fresh water. Then, because of the higher thermal diffusivity, a small eddy of salty water that is displaced downward will cool efficiently and the eddy will continue to sink as the positive buoyancy due to the higher temperature will not be able to counteract the negative buoyancy due to the higher mean molecular weight.

The second is the *double diffusive case*. It arises when the medium is hotter downward and has a mean molecular weight which increases with depth. Then, a hot, dense, rising eddy still has a negative buoyancy pushing it back downward, but, as it looses heat, it will have a negative buoyancy when arriving at its starting point. An oscillating motion will thus develop in the fluid, much like gravity waves, but whose amplitude will grow with time (Stern 1960; Stevenson 1979; Rosenblum et al. 2011).

[1] Laboratoire de Météorologie Dynamique, Université Pierre et Marie Curie, Institut Pierre-Simon Laplace, Paris, France, jeremy.leconte@lmd.jussieu.fr

[2] École normale supérieure de Lyon, CRAL (CNRS), Université de Lyon, 46 allée d'Italie, 69007 Lyon, France

[3] School of Physics, University of Exeter, Exeter, UK

[i] Temperature has a stabilizing effect if it increases upward or decreases less steeply than the adiabatic temperature gradient of the fluid considered. In the other case, temperature acts to destabilize the fluid and create convective motion. On the contrary, mean molecular weight plays stabilizing role by decreasing upward.

2 Transport properties of double diffusive convection

Both salt fingers and double diffusive convection are seen in experiments and in the oceans where their peculiar transport properties have a strong influence on the thermohaline circulation (Stern 1960; Turner & Stommel 1964; Schmitt 1994). And this is precisely because of these very peculiar heat transport and mixing properties that fluids developing double diffusive convection are of interest in an astrophysical context. Indeed, when modeling the evolution of stellar and substellar objects, quantifying the ability of the material to transport energy and to mix chemical elements is of prime importance. It will directly determine the rate of evolution of the body. As double diffusive convection is thought to be present in moderately massive stars (Schwarzschild & Härm 1958; Merryfield 1995), white dwarfs, and giant planets (Stevenson & Salpeter 1977; Stevenson 1979, 1985; Chabrier & Baraffe 2007; Leconte & Chabrier 2012) studying its macroscopic properties is thus mandatory to gain accuracy in the modeling of the aforementioned objects.

To model double diffusive convection[ii], the picture depicted in the previous section is incomplete as it only relies on linear stability analysis, and does not tell us what the mean flow is going to look like when the instability is fully developed. Indeed, both more sophisticated analytical models and numerical experiments show that depending on the ratio of the thermal and molecular diffusivities (κ_T and κ_μ), of the viscosity (ν), and of the sign and relative strengths of the imposed large scale gradients of buoyancy due to both temperature and mean molecular weight inhomogeneities, the mean flow can present different behaviors (Radko 2003; Rosenblum et al. 2011; Mirouh et al. 2012).

In the double diffusive case, the dimensionless parameter governing the selected behavior is the inverse density ratio,

$$R_\rho^{-1} \equiv \frac{\alpha_\mu}{\alpha_T} \frac{\left.\frac{\partial \ln \mu}{\partial \ln P}\right|_T}{\left.\frac{\partial \ln T}{\partial \ln P}\right|_\mu - \left.\frac{\partial \ln T}{\partial \ln P}\right|_{\mu,\mathrm{ad}}} \equiv \frac{\alpha_\mu}{\alpha_T} \frac{\nabla_\mu}{\nabla_T - \nabla_{\mathrm{ad}}}, \tag{2.1}$$

where $\alpha_T \equiv -\left.\frac{\partial \ln \rho}{\partial \ln T}\right|_{P,\mu}$, $\alpha_\mu \equiv \left.\frac{\partial \ln \rho}{\partial \ln \mu}\right|_{P,T}$, (Stern 1960; Rosenblum et al. 2011). At low forcing, i.e. at high R_ρ^{-1}, the medium is stable against the double diffusive instability and the fluid remains stably stratified. For $R_\rho^{-1} < (1+Pr)/(\tau+Pr)$, where $Pr = \nu/\kappa_T$ is the usual Prandlt number and $\tau = \kappa_\mu/\kappa_T$ is the inverse Lewis number, the instability grows. For $R_\rho^{-1} < 1$, which is the usual *Ledoux* criterion for convective instability, large scale convective motion develops independently of the diffusivities.

In the double diffusive regime, the finite amplitude flow depends on a critical inverse density ratio $R_{\min}$ which corresponds to the point where the solute to heat buoyancy flux ratio ($\equiv \gamma^{-1}$) stops increasing when R_ρ^{-1} decreases. $R_{\min}$ depends on the characteristics of the medium and can be estimated experimentally or numerically (Radko 2003; Rosenblum et al. 2011; Mirouh et al. 2012). For $R_\rho^{-1} > R_{\min}$, the forcing is sufficient to trigger the instability and create small scale turbulence (also called homogenous double diffusive convection) but the amplitude of the latter remains small. Transport properties in this state are more adequately represented by an eddy diffusion formalism, and the energy flux that can be transported is very limited (Rosenblum et al. 2011).

On the contrary, when $1 < R_\rho^{-1} < R_{\min}$, the fluid does not remain long in this state of homogenous double diffusive convection. As the instability grows, the system quickly develops thermo compositional layers of well mixed, convective regions separated by thin diffusive interfaces where both temperature and mean molecular weight undergo a sudden jump (Radko 2003; Rosenblum et al. 2011). In this regime, called the *layered convection* regime, the transport is much more efficient than in the case described above but is still fairly inefficient compared to large scale convection. Interestingly, Rosenblum et al. (2011) have shown that, as for large scale convection, the heat transport efficiency in the well mixed convective layers (measured by the Nusselt number which is the ratio of flux transported by convection over the flux transported by diffusion) roughly scales as a power law of the Rayleigh number which quantifies the thermal forcing (see Leconte & Chabrier (2012) for details).

3 Implications for giant planet structure

Thus to study the possible impact of layered convection on the structure of giant planets, we have developed an analytical parametrization as follows. We consider that a layered zone consists of a large number of well

[ii]The fingering case is not detailed here as it is of lower relevance in the astrophysical context. For details, the reader is referred to Stellmach et al. (2011) and reference therein.

mixed convectively unstable layers, separated by thin diffusive interfaces within which the large stabilizing compositional gradient completely inhibits convective motions. In the convective layers, the relationship between the flux to be transported and the thermal gradient is determined by the usual mixing length theory (Hansen & Kawaler 1994) but where the mixing length, $\alpha = l/H_P$, is assumed to be equal to the layer size (l; assumed small compared to the planet radius). H_P is the pressure scale height. The mixing length theory is also extended so that various power law exponents can be used. In the diffusive interfaces, the thermal gradient is equal to the one needed to transport all the flow by diffusive processes (thermal conduction by the free electrons in giant planets case).

As described in Leconte & Chabrier (2012), using this parametrization of layered convection, we were able to build internal structure models of Jupiter and Saturn with a *continuous* gradient of heavy elements in the gaseous envelope. These models fulfill all the available observational mechanical constraints, i.e. the mass, radius, rotation rate, gravitational moments (J_2 and J_4), and atmospheric heavy elements abundances derived from in situ measurements.

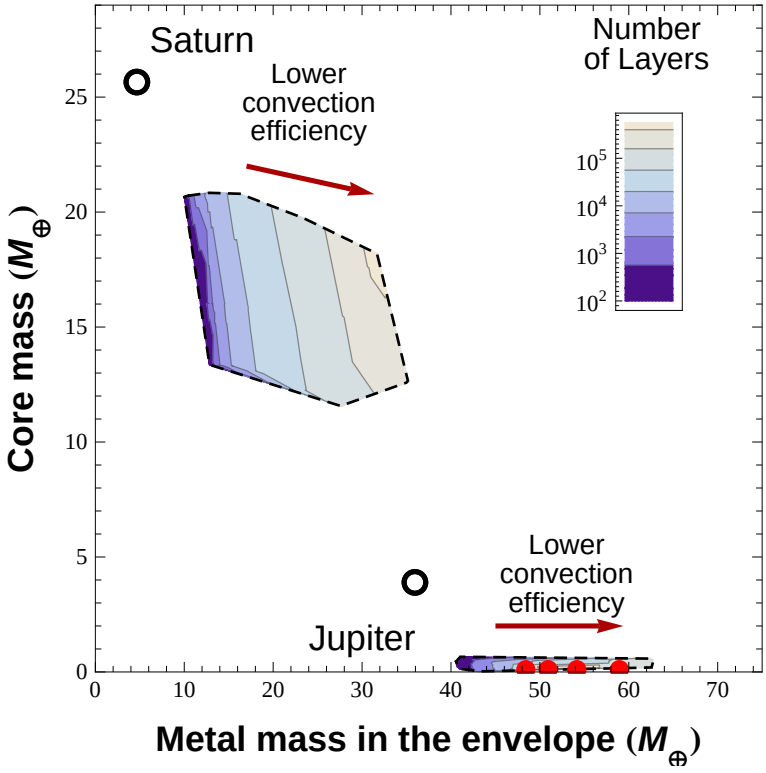

Fig. 1. Mass range of heavy elements in the core and in the envelope consistent with all observational mechanical constraints, for different numbers of layers, for Jupiter (bottom right) and Saturn (upper left). The open dots at the upper left of each region correspond to the homogeneous interior models. As the number of semiconvective layers increases, the efficiency of convection decreases, and the heavy element mass fraction increases to counteract the radius increase induced by the planet's higher internal temperature. The metals initially present in the core are then redistributed within the envelope. For Jupiter, solutions with no core at all can be found for the non adiabatic models (red dots).

As shown in Fig. 1, distribution of the heavy elements in the planet differs significantly between models with a well mixed envelope (homogeneous, adiabatic reference models) and inhomogeneous models where layered convection is present. There are two main differences:

- when a heavy element gradient is allowed in the envelope, models with a less massive core are preferred. The heavy elements are redistributed within the gaseous envelope which is more metal rich. This effect is quite independent (to zeroth order) of the change imposed to the thermal structure by the layered convection and just stems from the fact that, when the "envelope homogeneity" constraint is relaxed, measured values of J_2 and J_4 favor structures with smaller cores. This is why models with layered convection do not tend continuously towards the reference models when the number of convective/diffusive

cells is decreased.

In the case of Jupiter, because of its less massive core, this redistribution of the heavy elements has a particularly important effect as models without any core can be found to match the observational constraints.

- when the number convective/diffusive cells is increased, i.e. when the size of each individual convective layer (l) is decreased, the superadiabaticity and temperature gradient in the planet is increased. This stems from the fact that layered convection is less and less efficient and a steeper gradient is needed to transport the same heat flux. The mean internal temperature is thus higher. To keep the same observed planetary radius, a higher metal enrichment of the envelope is needed to counteract the decrease in density caused by this higher internal temperature. A decrease in the convective layer size thus entails an increase of the total heavy element mass in the object, as seen in Fig. 1 and detailed in Leconte & Chabrier (2012).

4 Concluding remarks

These points have strong implications concerning the present composition of Solar System giant planets, and their formation history. Indeed, if a significant superadiabaticity is present in Jupiter and Saturn, their total metal mass fraction could be up to 30-60% higher than previously estimated on the basis of adiabatic, homogeneous models. This higher enrichment could completely change our vision of the heavy element budget during giant planets formation. It suggests a higher density of solids in the nebula and an early and efficient capture of planetesimals for ours and, probably also, extrasolar giant planets, helping to solve the traditional formation timescale problem of giant planets (Pollack et al. 1996).

However, the possibility of less massive cores inferred here revives the question of the origin of the heavy elements in the gaseous envelope of giant planets. Indeed, the possibility that Jupiter was formed with a very small core (less massive than $5\,M_\oplus$), if any, as inferred here, is difficult to conciliate with the very efficient accretion suggested above. To address this issue, we must thus understand to what extent the enrichment of the gaseous envelope of giant planets can be primordial or caused by the erosion and dissolution of a massive initial core.

The research leading to these results has received funding from the European Research Council under the European Community's Seventh Framework Programme (FP7/2007-2013 Grant Agreement no. 247060)

References

Chabrier, G. & Baraffe, I. 2007, ApJ, 661, L81

Hansen, C. J. & Kawaler, S. D. 1994, Stellar Interiors. Physical Principles, Structure, and Evolution., (Springer, ed. Hansen, C. J. & Kawaler, S. D.)

Leconte, J. & Chabrier, G. 2012, A&A, 540, A20

Ledoux, P. 1947, ApJ, 105, 305

Merryfield, W. J. 1995, ApJ, 444, 318

Mirouh, G. M., Garaud, P., Stellmach, S., Traxler, A. L., & Wood, T. S. 2012, ApJ, 750, 61

Pollack, J. B., Hubickyj, O., Bodenheimer, P., et al. 1996, Icarus, 124, 62

Radko, T. 2003, Journal of Fluid Mechanics, 497, 365

Rosenblum, E., Garaud, P., Traxler, A., & Stellmach, S. 2011, ApJ, 731, 66

Schmitt, R. W. 1994, Annual Review of Fluid Mechanics, 26, 255

Schwarzschild, M. & Härm, R. 1958, ApJ, 128, 348

Stellmach, S., Traxler, A., Garaud, P., Brummell, N., & Radko, T. 2011, Journal of Fluid Mechanics, 677, 554

Stern, M. E. 1960, Tellus, 12, 172

Stevenson, D. J. 1979, MNRAS, 187, 129

Stevenson, D. J. 1985, Icarus, 62, 4

Stevenson, D. J. & Salpeter, E. E. 1977, ApJS, 35, 239

Turner, J. S. & Stommel, H. 1964, Proceedings of the National Academy of Science, 52, 49

SF2A 2012
S. Boissier, P. de Laverny, N. Nardetto, R. Samadi, D. Valls-Gabaud and H. Wozniak (eds)

COULD JUPITER BE A CARBON-RICH PLANET?

O. Mousis[1], J. I. Lunine[2], N. Madhusudhan[3] and T. V. Johnson[4]

Abstract. Motivated by recent spectroscopic observations suggesting that atmospheres of some extrasolar giant-planets are carbon-rich, i.e. carbon/oxygen ratio (C/O) ≥ 1, we find that the whole set of compositional data for Jupiter is consistent with the hypothesis that it be a carbon-rich giant planet. We show that the formation of Jupiter in the cold outer part of an oxygen-depleted disk (C/O $\sim$1) reproduces the measured Jovian elemental abundances at least as well as the hitherto canonical model of Jupiter formed in a disk of solar composition (C/O = 0.54). The resulting O abundance in Jupiter's envelope is then moderately enriched by a factor of $\sim$2 $\times$ solar (instead of $\sim$7 $\times$ solar) and is found to be consistent with values predicted by thermochemical models of the atmosphere.

Keywords: planets and satellites: individual (Jupiter), formation, composition, atmospheres, protoplanetary discs

1 Introduction

Observations of extrasolar planets have revealed the possible existence of a new class of giant planets, the so-called carbon-rich planets (CRPs) (Madhusudhan et al. 2011a). A CRP is defined as a planet with a carbon-to-oxygen (C/O) ratio ≥ 1. Recently, we proposed that these planets arise from beyond the snow line in circumstellar disks with oxygen abundances lower than those inferred in their parent stars (Madhusudhan et al. 2011b). In the solar system, the C/O ratio remains poorly constrained in the giant planets because obtaining a measurement of the water abundance below the meteorologically-active layer is difficult (Taylor et al. 2004). Data returned by the Galileo probe mass spectrometer in 1995 around the one-bar pressure level in Jupiter's atmosphere has provided carbon, nitrogen, sulfur, argon, krypton and xenon abundances that are relatively well matched by formation scenarios based on solar nebula models assuming solar elemental composition (Owen & Encrenaz 2006; Mousis et al. 2009) – what we refer to here as "protosolar". Below expected water condensation level, the measured oxygen abundance was unexpectedly low, an effect typically attributed to the dynamics of the region within which the probe descended (Orton et al. 1998), but which we argue here could also partly reflect a bulk abundance lower than predicted by existing formation models.

Here we find that all the observed elemental abundances of Jupiter can be explained consistently within the standard core-accretion model of Jupiter's formation beyond the snow line by only changing the C/O ratio in the formation zone. The resulting O abundance in Jupiter's envelope then becomes moderately enriched compared to solar and is found to be consistent with values predicted by thermochemical models. To do so, we derived the elemental abundances in the envelope of Jupiter by tracking the chemical condensation and accretion of planetesimals through the planet's formation and evolution. We used a numerical model that relates the formation conditions of icy planetesimals accreted by Jupiter in the primitive nebula to the volatile abundances in its present atmosphere, the latter being determined from the amount of heavy elements accreted and dissolved in the planet's envelope during its growth.

[1] Université de Franche-Comté, Institut UTINAM, CNRS/INSU, UMR 6213, Observatoire des Sciences de l'Univers de Besançon, France
[2] Center for Radiophysics and Space Research, Space Sciences Building Cornell University, Ithaca, NY 14853, USA
[3] Yale Center for Astronomy and Astrophysics, Department of Physics, Yale University, New Haven, CT 06511
[4] Jet Propulsion Laboratory, California Institute of Technology, 4800 Oak Grove Drive, Pasadena, CA, 91109, USA

2 Modeling approach

Our model is based on a predefined initial gas phase composition in which all elemental abundances, except that of oxygen, reflect the bulk abundances of the Sun (Asplund et al. 2009) and describes the process by which volatiles are trapped in icy planetesimals formed in the protoplanetary disk. Oxygen, carbon, nitrogen, sulfur and phosphorus are postulated to exist only in the form of H_2O, CO, CO_2, CH_3OH, CH_4, N_2, NH_3, H_2S and PH_3. We fix $CO/CO_2/CH_3OH/CH_4 = 70/10/2/1$ in the gas phase of the disk, a set of values consistent with the Interstellar Medium (ISM) measurements made by the Infrared Space Observatory and at millimeter wavelengths from Earth considering the contributions of both gas and solid phases in the lines of sight. The dispersion of the ISM values is large and might reflect object-to-object variation as well as uncertainties of measurements but we stress that, among the possible molecular ratios, we selected those that are close to the cometary measurements (Bockelée-Morvan et al. 2004). Once the abundances of these molecules are fixed, the remaining oxygen gives the abundance of H_2O. Sulfur is assumed to exist in the form of H_2S, with an abundance fixed to half its protosolar value, and other refractory sulfide components (Pasek et al. 2005). We also consider $N_2/NH_3 = 10/1$ in the disk gas-phase, a value predicted by thermochemical models of the solar nebula (Lewis & Prinn 1980). The process of volatile trapping in planetesimals formed in the feeding zone of proto-Jupiter is calculated using the equilibrium curves of hydrates, clathrates and pure condensates, and the thermodynamic path detailing the evolution of temperature and pressure at 5 AU (i.e. the current location of Jupiter) in the protoplanetary disk.

The top panel of Fig. 1 corresponds to the case where the gas phase abundances of various elements are solar, with the afore-mentioned gas phase molecular ratios. For each ice considered in this panel, the domain of stability is the region located below its corresponding equilibrium curve. The clathration process stops when no more crystalline water ice is available to trap the volatile species. In this case, the icy part of planetesimals is essentially made of a mix of pure condensates and clathrates. The bottom panel of Fig. 1 corresponds to the case of a disk composition similar to the one used in the top panel, except for the oxygen abundance that is set half the solar value. The subsolar O abundance adopted in the gas phase allows us to retrieve a composition of planetesimals that matches the value $C/O = 1$ in planetesimals formed in Jupiter's feeding zone. In this case, because the oxygen abundance is strongly depleted compared to previous case, this element is only distributed between carbon bearing species and the remaining water becomes zero in the initial gas phase of the protoplanetary disk. This implies that the icy part of planetesimals formed in such conditions in the protoplanetary disk is only made of pure condensates.

Finally, the intersection of the thermodynamic paths with the equilibrium curves of the different ices allows determination of the amount of volatiles that are condensed or trapped in clathrates at these locations in the disk following the approach depicted in Mousis et al. (2009) and Madhusudhan et al. (2011b). This method permits computation of the composition of the volatile phase present in the planetesimals formed in Jupiter's feeding zone. The precise adjustment of the mass of these ices accreted by Jupiter and vaporized into its envelope allows us to reproduce the observed volatile enrichments. The fitting strategy is to match the maximum number of observed volatile enrichments and to determine the uncertainty range corresponding to this matching.

3 Results

Once the composition of planetesimals has been calculated in the two cases, we adjusted the mass of heavy elements located in Jupiter's envelope to fit the maximum number of volatile abundances measured by the Galileo probe. Figure 2 represents the superimposition of the two fits with the measured volatile abundances. The figure shows that the same number of elements (carbon, nitrogen, sulfur and argon) is fitted in the two cases. However, the oxygen abundance predicted in Jupiter for an oxygen-depleted nebula is much closer to the measured abundance than the value predicted for a protosolar oxygen abundance. If the former case is correct, this supports the argument that the oxygen abundance in Jupiter derived from Galileo Probe water measurements reflects a bulk interior depletion of O relative to C, and is much less affected by atmospheric dynamical or meteorological processes than in the standard model. Neither calculation matches the observed phosphorus abundance, which is however only expected to provide lower bounds on the bulk abundance (Fletcher et al. 2009). The same remark applies for the observed krypton and xenon abundances but their relatively low values suggest the possibility of systematic error in their determination (Owen & Encrenaz 2006).

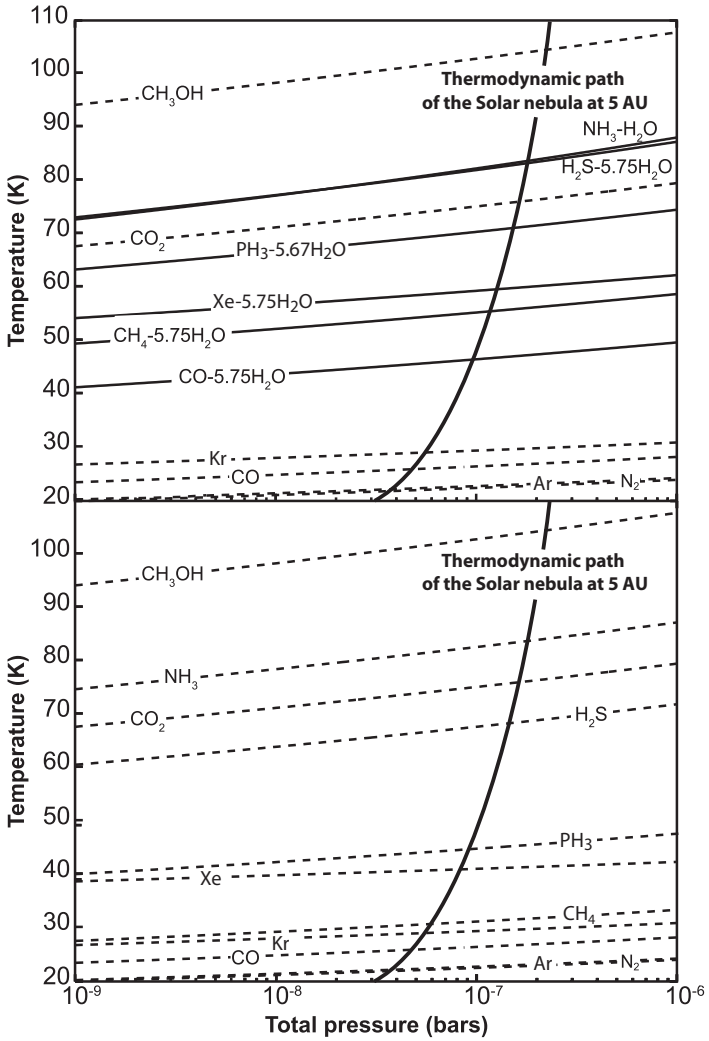

Fig. 1. Formation conditions of icy planetesimals in the solar nebula. Top panel: equilibrium curves of hydrate (NH_3-H_2O), clathrates (X-5.75H_2O or X-5.67H_2O) (solid lines), and pure condensates (dotted lines), and cooling curve of the solar nebula at 5 AU, assuming a full efficiency of clathration. Bottom panel: same as top panel but with an oxygen abundance that is half the solar value. In this case, water does not exist in the disk and only pure condensates form.

4 Discussion

Our results, as discussed above, imply that a carbon-rich Jupiter provides a better explanation for the measured elemental abundances than the canonical case based on a protosolar oxygen abundance in the nebula. Our prediction of 2 × solar enhancement of oxygen in a carbon-rich Jupiter also agrees extremely well with recent constraints on the Jovian water abundance (∼0.5–2.6 × solar) derived from tropospheric CO mixing ratios using thermochemical kinetics and diffusion models (Visscher & Moses 2011). On the other hand, our model for the protosolar case predicts 7 × solar enhancement of oxygen in Jupiter which is ruled out by the thermochemical models (Visscher & Moses 2011). The important difference between the oxygen abundances in the two cases is a consequence of the presence or not of water ice in the giant planet's feeding zone. In the case of a solar oxygen abundance, water ice is the main O-bearing volatile present in the disk and accreted by Jupiter. The oxygen enhancement in the Jovian atmosphere is also amplified by the fact that, at the formation epoch of planetesimals, water condenses at much higher disk temperature and surface density compared to the other volatiles, thus increasing its mass fraction in solids. When the oxygen abundance becomes half solar in the nebula, the water abundance tends towards zero and the main O-bearing species supplied to the protoplanet

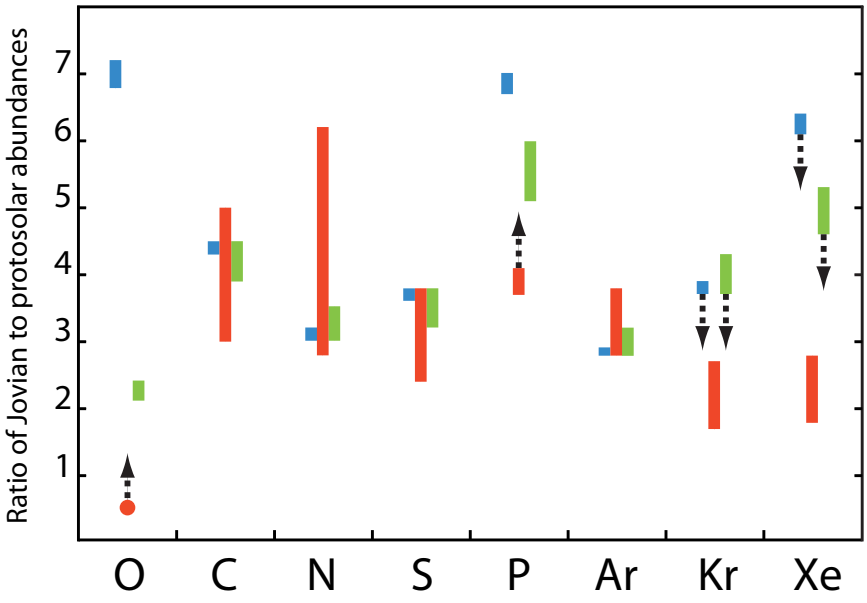

Fig. 2. Ratio of Jovian to protosolar abundances. Red bars and red dot correspond to observations. Green and blue bars correspond to calculations based on an oxygen abundance that is 0.5 and 1 times the protosolar value in the disk, giving C/O = 1 and 0.35 in Jupiter, respectively. The oxygen abundance is predicted to be 2.1–2.4 and 6.8–7.2 times protosolar in the cases of C/O = 1 and 0.35 in Jupiter, respectively. Arrows up correspond to the possibility that the measured oxygen and phosphorus abundances are lower than their bulk abundances and arrows down to the possibility that planetesimals could be impoverished in krypton and xenon.

atmosphere become CO and CO_2. These species condense at much lower disk surface density than water does and this effect increases the oxygen impoverishement in planetesimals accreted by proto-Jupiter.

A key observational test is the measurement of oxygen as water below the meteorological layer within Jupiter. A value of water about 2 × solar deep below the water clouds would confirm that Jupiter is carbon-rich. The Microwave Radiometer aboard the recently launched Juno spacecraft will probe the deep atmosphere of Jupiter at radio wavelengths ranging from 1.3 cm to 50 cm to measure the planet's thermal emissions. This instrument will obtain measurements of water at pressures down to 100 bars deep in the Jovian atmosphere (Janssen et al. 2005), thereby constraining Jupiter's O/H and C/O ratios.

References

Asplund, M., Grevesse, N., Sauval, A. J., & Scott, P. 2009, ARA&A, 47, 481
Bockelée-Morvan, D., Crovisier, J., Mumma, M. J., & Weaver, H. A. 2004, Comets II, 391
Fletcher, L. N., Orton, G. S., Teanby, N. A., & Irwin, P. G. J. 2009, Icarus, 202, 543
Janssen, M. A., Hofstadter, M. D., Gulkis, S., et al. 2005, Icarus, 173, 447
Lewis, J. S., & Prinn, R. G. 1980, ApJ, 238, 357
Madhusudhan, N., Harrington, J., Stevenson, K. B., et al. 2011a, Nature, 469, 64
Madhusudhan, N., Mousis, O., Johnson, T. V., & Lunine, J. I. 2011b, ApJ, 743, 191
Mousis, O., Marboeuf, U., Lunine, J. I., et al. 2009, ApJ, 696, 1348
Orton, G. S., Fisher, B. M., Baines, K. H., et al. 1998, J. Geophys. Res., 103, 22791
Owen, T., & Encrenaz, T. 2006, Planet. Space Sci., 54, 1188
Pasek, M. A., Milsom, J. A., Ciesla, F. J., et al. 2005, Icarus, 175, 1
Taylor, F. W., Atreya, S. K., Encrenaz, T., et al. 2004, Jupiter. The Planet, Satellites and Magnetosphere, 59
Visscher, C., & Moses, J. I. 2011, ApJ, 738, 72

SF2A 2012
S. Boissier, P. de Laverny, N. Nardetto, R. Samadi, D. Valls-Gabaud and H. Wozniak (eds)

THE ANELASTIC EQUILIBRIUM TIDE IN EXOPLANETARY SYSTEMS

F. Remus[1,2,3], S. Mathis[2], J.-P. Zahn[1] and V. Lainey[3]

Abstract. Earth-like planets have anelastic mantles, whereas giant planets may have anelastic cores. As for the fluid parts of a body, the tidal dissipation of such solid regions, gravitationally perturbed by a companion body, highly depends on its internal friction, and thus on its internal structure. Therefore, modelling this kind of interaction presents a high interest to provide constraints on planet interiors, whose properties are still quite uncertain. Here, we examine the equilibrium tide in the solid central region of a planet, taking into account the presence of a fluid envelope. We discuss how the quality factor Q depends on the rheological parameters, and the size of the core. Taking plausible values for the anelastic parameters, and examinig the frequency-dependence of the solid dissipation, we show how this mechanism may compete with the dissipation in fluid layers, when applied to Jupiter- and Saturn-like planets. We also discuss the case of the icy giants Uranus and Neptune.

Keywords: planetary systems, dynamical evolution and stability

1 Introduction

Once a planetary system is formed, its dynamical evolution is governed by gravitational interactions between its components, be it a star-planet or planet-satellite interaction. By converting kinetic energy into heat, the tides pertub their orbital and rotational properties, and the rate at which the system evolves depends on the physical properties of tidal dissipation. Therefore, to understand the past history and predict the fate of a binary system, one has to identify the dissipative processes that achieve this conversion of energy. Planetary systems display a large diversity of planets, with telluric planets having anelastic mantles and giant planets with possible anelastic cores (Santos & et al. 2007). Since the tidal dissipation is closely related with the internal structure, one has to investigate its effects on each kind of materials that may compose a planet. Studies have been carried out on tidal effects in fluid bodies such as stars and envelopes of giant planets (Ogilvie & Lin 2004, 2007; Ogilvie 2009; Remus et al. 2012). However, the planetary solid regions, such as the mantles of Earth-like planets or the rocky cores of giant planets may also contribute to tidal dissipation (see, *e.g.*, Efroimsky 2012; Remus et al. 2012). We explore here the tidal dissipation in these solid parts of planets.

2 The system

Two-layer model. – We will consider as a model a two-bodies system where the component A, rotating at the angular velocity Ω, has a viscoelastic core of complex shear modulus $\tilde{\mu}$, made of ice or rock, surrounded by a fluid envelope, such as an ocean, streching out from core's surface (of mean radius R_c) up to planet's surface (of mean radius R_p). Both core and envelope are considered homogeneous, with constant density ρ_c and ρ_o respectively. This model is represented on the left panel of Fig. 1.

Configuration. – We undertake to describe the tide exerted by B (of mass m_B) on the solid core of A, when moving in an elliptic orbit around A, with eccentricity e, at the mean motion ω. Since no assumption is made on the B's orbit, we need to define an inclination angle I to determine the position of the orbital spin of B with respect to the total angular momentum of the system (in the direction of Z_R) wich defines an inertial reference plane (X_R, Y_R), perpendicular to it. The spin axis of A then presents an obliquity ε with respect to Z_R. Refer to the right panel of Fig. 1 for a synthetic representation of the system configuration.

[1] LUTH, Observatoire de Paris, CNRS, Université Paris Diderot, 92195 Meudon, France
[2] Laboratoire AIM Paris-Saclay, CEA/DSM, CNRS, Université Paris Diderot, IRFU/SAp, 91191 Gif-sur-Yvette, France
[3] IMCCE, Observatoire de Paris, CNRS, UPMC, USTL, 75014 Paris, France

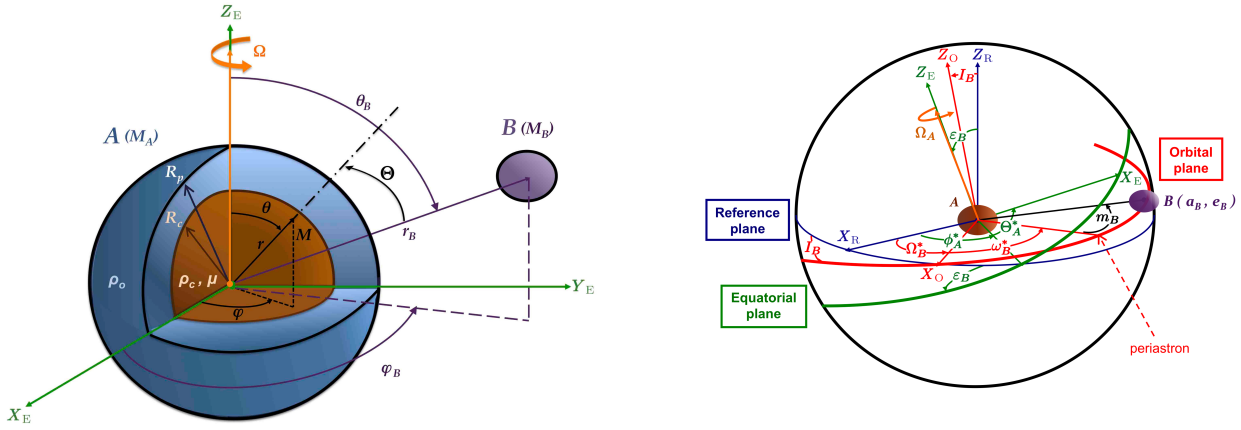

Fig. 1. Left: the system is composed by a two-layer main component A, with an homogeneous and incompressible solid core and an homogeneous static fluid envelope, and a point-mass perturber B orbiting around A. **Right:** B is supposed to move on an elliptical orbit, inclined with respect to the inertial reference plane (X_R, Y_R). The equatorial plane of A (X_E, Y_E) is also inclined with respect to this same reference plane.

To treat the complexity of the two-layer problem, we follow the methodology of Dermott (1979).

3 Tidal dissipation of the core in the case of a two-layer planet

Definition. – The tidal perturbation exerted by B on the solid core of A results on one hand in its deformation, and on the other hand in the dissipation of the tidal energy into heat leading to a lag angle δ between the line of centers and the tidal bulge. This process can be modeled by the complex second-order Love number $\tilde{k}_2$ defined as the ratio of the perturbed gravific response potential Φ' over the tidal potential U (Biot 1954, see also Tobie 2003 and Henning et al. 2009). Its real part represents then the purely elastic deformation of the potential of the core (Φ') while its imaginary part accounts for its anelastic tidal dissipation.

In practical calculations, we first have to develop U (and therefore Φ') on spherical harmonics (Y_2^m), each term having a wide range of tidal frequencies $\sigma_{2,m,p,q} = (2-2p+q)\,\omega - m\Omega$, for $(m,p,q) \in [\![-2,2]\!] \times [\![0,2]\!] \times \mathbf{Z}$, resulting from the expansion of U on the Keplerian elements using the Kaula transform (Kaula 1962, see also Mathis & Le Poncin-Lafitte 2009). Thus, the complex Love number $\tilde{k}_2$ depends on the tidal frequency and the rheology of the core, and so does the *quality factor* Q which quantifies the tidal dissipation (see, *e.g.*, Tobie 2003)

$$Q^{-1}(\bar{\mu}, \sigma_{2,m,p,q}) = -\frac{\mathcal{I}m\ \tilde{k}_2(\bar{\mu}, \sigma_{2,m,p,q})}{\left|\tilde{k}_2(\bar{\mu}, \sigma_{2,m,p,q})\right|}\ , \text{ where } \tilde{k}_2(\bar{\mu}, \sigma_{2,m,p,q}) = \frac{\Phi'(\bar{\mu}, \sigma_{2,m,p,q})}{U(\sigma_{2,m,p,q})} = \left|\tilde{k}_2\right| e^{-\boldsymbol{i}[2\delta(\bar{\mu}, \sigma_{2,m,p,q})]}\ , \quad (3.1)$$

where the quantity $\bar{\mu} \equiv \bar{\mu}_1 + \boldsymbol{i}\,\bar{\mu}_2 = \frac{19\,\tilde{\mu}}{2\,\rho_c\,g_c\,R_c}$ is the complex effective shear modulus, linked with the anelasticity (and thus the rheology) of the planet's core and its gravity g_c.

Case of a two-layer planet. – Acting as an overload on the solid core, the fluid shell, deformed by the tide, modifies both the tidal deformation and dissipation of the core. The second order Love number $\tilde{k}_2$ takes then a different form than in the fully-solid case

$$\tilde{k}_2(\bar{\mu}, \sigma_{2,m,p,q}) = \frac{1}{(B+\bar{\mu}_1)^2 + \bar{\mu}_2^2} \times \left\{ \left[(B+\bar{\mu}_1) \left(C + \frac{3}{2\alpha}\,\bar{\mu}_1 \right) + \frac{3}{2\alpha}\,\bar{\mu}_2^2 \right] - \boldsymbol{i} A\,D\,\bar{\mu}_2 \right\}\ , \quad (3.2)$$

where α, A, B, C and D account for the planet's internal structure through the ratios of radii $\frac{R_c}{R_p}$ and densities $\frac{\rho_o}{\rho_c}$.

Thus, the expression of the associated tidal dissipation rate

$$Q(\bar{\mu}, \sigma_{2,m,p,q}) = \sqrt{1 + \frac{9\,\bar{\mu}_2(\sigma_{2,m,p,q})^2}{4\alpha^2\,A^2\,D^2} \left[1 + \frac{(B + \bar{\mu}_1(\sigma_{2,m,p,q}))\ \left(\frac{2\alpha C}{3} + \bar{\mu}_1(\sigma_{2,m,p,q})\right)}{\bar{\mu}_2(\sigma_{2,m,p,q})^2} \right]^2} \quad (3.3)$$

depends on the core's parameters (its size, density and rheological parameters) and the tidal frequency. Moreover, to derive this expression of Q, no assumption has been made on the rheology of the core, except that it is linear under the small tidal perturbations (i.e. core's material obeys the Hooke's law). Hence, it is valid for any linear rheological model.

Comparison with observations. – To confront our model with observations, we need to introduce the global dissipation factor, corresponding to a *rescaling* of the previous one to the planet surface and thus involving the second-order Love number at the surface of the planet

$$Q_{\rm eff} = \left(\frac{R_p}{R_c}\right)^5 \times \left|\frac{\tilde{k}_2(R_p)}{\tilde{k}_2(R_c)}\right| \times Q\,. \tag{3.4}$$

Moreover, we need to choose a model to represent the way the core's material responds to the tidal perturbation, i.e. a *rheological model*. Thus, from now on, we assume that the core behaves like a Maxwell body of rigidity G and viscosity η (see, *e.g.*, Tobie 2003).

4 Application to giant planets

Application to gas giants. – Using astrometric data covering more than a century, Lainey et al. (2009, 2012) succeeded in determining from observations the tidal dissipation in Jupiter and Saturn: namely, $Q_{\rm Jupiter} = (3.56 \pm 0.56) \times 10^4$ (Lainey et al. 2009), and $Q_{\rm Saturn} = (1.682 \pm 0.540) \times 10^3$ determined by Lainey et al. (2012). Note that such high dissipation is required by the formation scenario of Saturn's system of Charnoz et al. (2011), in which the mid-sized satellites are formed at the edge of the rings. These values, which seem to be in agreement with other observations related to Jupiter's and Saturn's systems (see the corresponding references cited just above), are lower of up to one order of magnitude than what was expected by previous formation scenarios (see, *e.g.*, Yoder & Peale 1981; Sinclair 1983), and even lower than what the most up-to-date models of fluid tidal dissipation predict (see, *e.g.*, Ogilvie & Lin 2004; Wu 2005). Then, the question arises on the role of the possible solid central regions as sources of dissipation. Since the composition of giant planets cores is poorly constrained (Guillot 2005), we explore in Fig. 2 the tidal dissipation of Jupiter's and Saturn's core for a large range of values of the viscoelastic parameters considering the Maxwell rheological model. The other parameters (planet and core sizes and masses) are indicated in the legend.

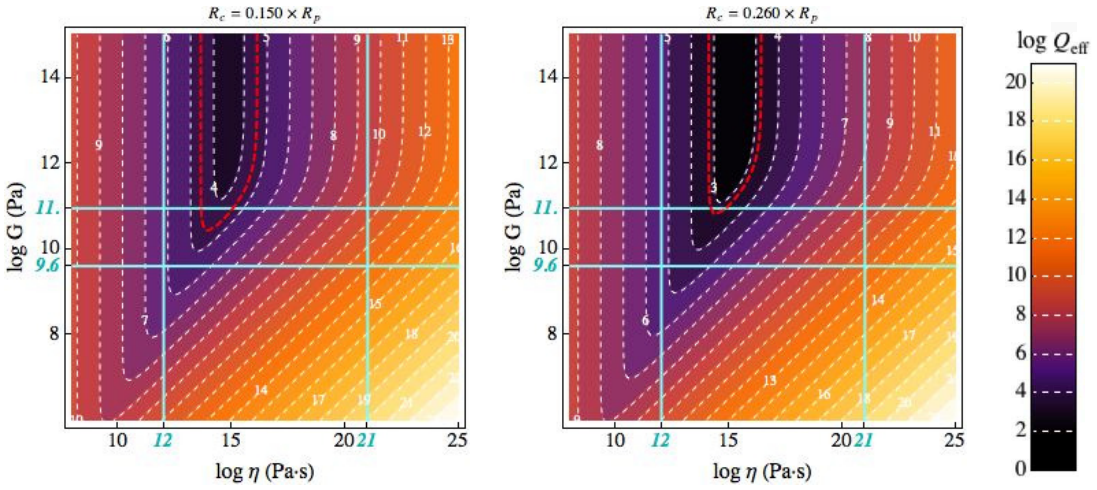

Fig. 2. Dissipation quality factor $Q_{\rm eff}$ as a function of the viscoelastic parameters G and η, of a two-layer gas giant, using the Maxwell model. **Left:** for a Jupiter-like planet at the tidal frequency of Io. **Right:** for a Saturn-like planet at the tidal frequency of Enceladus. The red dashed line indicates the value of $Q_{\rm eff} = \{(3.56 \pm 0.56) \times 10^4, (1.682 \pm 0.540) \times 10^3\}$ (for Jupiter and Saturn, respectively) determined by Lainey et al. (2009, 2012). The blue lines corresponds to the lower and upper limits of the reference values taken by the viscoelastic parameters G and η for an unknown mixture of ice and silicates. We assume the values of $R_p = \{10.97, 9.14\}$ (in units of $R_\oplus$), $M_p = \{317.8, 95.16\}$ (in units of $M_\oplus$), $R_c = \{0.15, 0.26\} \times R_p$, and $M_c = \{6.41, 18.65\}$ (in units of $M_\oplus$).

In 2004, Ogilvie & Lin studied tidal dissipation in rotating giant planets resulting from the excitation by the tidal potential of inertial waves in the convective region. Taking into account the presence of a solid core as a boundary condition for the reflexion of inertial waves, they obtained a quality factor $Q_{\rm eff} \approx 5 \times 10^5$.

The present two-layer model proposes an alternative process that may reach the values observed in Lainey et al. (2009, 2012), depending on the viscosity η and the stiffness G.

To explain the tidal dissipation observed in the gas giant planets of our Solar System, all processes have to be taken into account.

Application to ice giants. – As in gas giants, the standard three-layer models for the interior structure of ice giants predict the presence of a solid rocky core (see, *e.g.*, Hubbard et al. 1991; Podolak et al. 1995; Guillot 1999). But it still remains an incertitude on the phase state of the intermediate "icy" layer located between the rocky core and the convective atmosphere. Considering recent three-dimensional simulations of Neptune's and Uranus' dynamo that predict that this region is a stably stratified conductive fluid one (Stanley & Bloxham 2004, 2006), Redmer et al. (2011) studied the electric conductivity of warm dense water taking into account the phase diagram of water. Their results infer that part of this shell is in the superionic state, i.e. a two-component system of both a conducting proton fluid and a crystalline oxygen solid, and extends to about 0.42-0.56 of the planet radius. Thus, it seems reasonable to assume for our two-layer model that the solid central region extends from the rocky core surface up to somewhere in the superionic shell.

We explore in Fig. 3 the tidal dissipation of Uranus' and Neptune's core for a large range of values of the viscoelastic parameters, considering the Maxwell rheological model, for different core sizes.

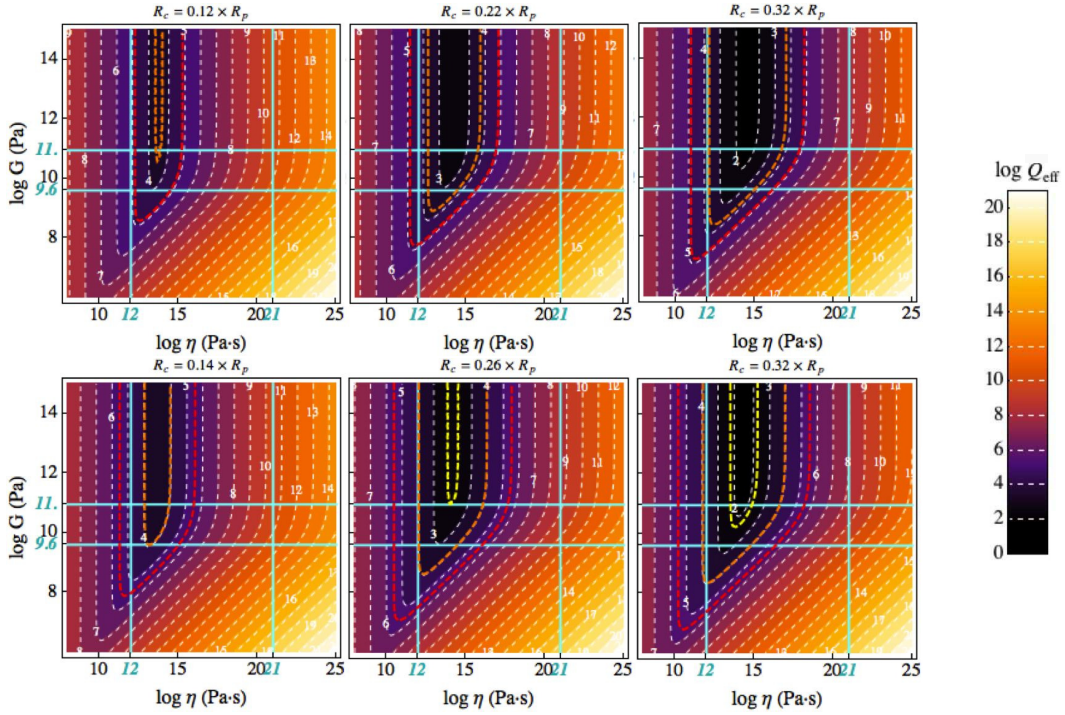

Fig. 3. Dissipation quality factor $Q_{\rm eff}$ as a function of the viscoelastic parameters G and η, of a two-layer ice giant, using the Maxwell model. **Top:** for a Uranus-like planet at the tidal frequency of Miranda, with three different core sizes $R_c = \{0.12, 0.22, 0.32\} \times R_p$. **Bottom:** for a Neptune-like planet at the tidal frequency of Triton, with three different core sizes $R_c = \{0.14, 0.26, 0.32\} \times R_p$. The red and orange dashed lines indicate, respectively, the lowest and highest values of $Q_{\rm eff}$ from formation scenarios: $Q_{\rm eff} = \{5 \times 10^3, 7.2 \times 10^4\}$ for Uranus (Gavrilov & Zharkov 1977; Goldreich & Soter 1966) and $Q_{\rm eff} = \{9 \times 10^3, 3.3 \times 10^5\}$ for Neptune (Zhang & Hamilton 2008; Banfield & Murray 1992). The yellow dashed line indicates the value of $Q_{\rm eff}$ from a study of Neptune's internal heat: $Q_{\rm eff} = 1.7 \times 10^2$ (Trafton 1974). The blue lines corresponds to the lower and upper limits of the reference values taken by the viscoelastic parameters G and η for an unknown mixture of ice and silicates. We assume the values of $R_p = \{3.98, 3.87\}$ (in units of $R_\oplus$) and $M_p = \{14.24, 16.73\}$ (in units of $M_\oplus$). The core mass is obtained by integration of the density profiles of Helled et al. (2011) up to a given core size.

5 Dynamical evolution

Due to dissipation, the tidal torque has non-zero average over the orbit, and it induces an exchange of angular momentum between each component and the orbital motion. This exchange governs the evolution of the semi-major axis a, the eccentricity e of the orbit, the inclination I of the orbital plane, the obliquity ε and the angular velocity of each component (see, *e.g.*, Mathis & Le Poncin-Lafitte 2009). Depending on the initial conditions and on the planet/star mass ratio, the system evolves either to a stable state of minimum energy (where all spins are aligned, the orbits are circular and the rotation of each body is synchronized with the orbital motion) or the planet tends to spiral into the parent star.

6 Conclusion

Our evaluations reveal a much higher dissipation in the solid cores of planets than that found by Ogilvie & Lin (2004) for the fluid envelope of a planet having a small solid core. These results seem to be in good agreement with observed properties of Jupiter's and Saturn's system (Lainey et al. 2009, 2012). In the case of the ice giants Uranus and Neptune, too much uncertainties remain on internal structure to give an order of magnitude, other than a minimum value, of solid tidal dissipation, which constitutes a first step in the study of such planets.

This work was supported in part by the Programme National de Planétologie (CNRS/INSU), the EMERGENCE-UPMC project EME0911, and the CNRS *Physique théorique et ses interfaces* program.

References

Banfield, D. & Murray, N. 1992, Icarus, 99, 390
Biot, M. A. 1954, Journal of Applied Physics, 25, 1385
Charnoz, S., Crida, A., Castillo-Rogez, J. C., et al. 2011, Icarus, 216, 535
Dermott, S. F. 1979, Icarus, 37, 310
Efroimsky, M. 2012, ApJ, 746, 150
Gavrilov, S. V. & Zharkov, V. N. 1977, Icarus, 32, 443
Goldreich, P. & Soter, S. 1966, Icarus, 5, 375
Guillot, T. 1999, Science, 286, 72
Guillot, T. 2005, Annual Review of Earth and Planetary Sciences, 33, 493
Helled, R., Anderson, J. D., Podolak, M., & Schubert, G. 2011, ApJ, 726, 15
Henning, W. G., O'Connell, R. J., & Sasselov, D. D. 2009, ApJ, 707, 1000
Hubbard, W. B., Nellis, W. J., Mitchell, A. C., et al. 1991, Science, 253, 648
Kaula, W. M. 1962, AJ, 67, 300
Lainey, V., Arlot, J.-E., Karatekin, Ö., & van Hoolst, T. 2009, Nature, 459, 957
Lainey, V., Karatekin, Ö., Desmars, J., et al. 2012, ApJ, 752, 14
Mathis, S. & Le Poncin-Lafitte, C. 2009, A&A, 497, 889
Ogilvie, G. I. 2009, MNRAS, 396, 794
Ogilvie, G. I. & Lin, D. N. C. 2004, ApJ, 610, 477
Ogilvie, G. I. & Lin, D. N. C. 2007, ApJ, 661, 1180
Podolak, M., Weizman, A., & Marley, M. 1995, Planet. Space Sci., 43, 1517
Redmer, R., Mattsson, T. R., Nettelmann, N., & French, M. 2011, Icarus, 211, 798
Remus, F., Mathis, S., Zahn, J.-P., & Lainey, V. 2012, A&A, 541, A165
Santos, N. C. & et al. 2007, in JENAM-2007, "Our Non-Stable Universe"
Sinclair, A. T. 1983, in Astrophysics and Space Science Library, Vol. 106, IAU Colloq. 74: Dynamical Trapping and Evolution in the Solar System, ed. V. V. Markellos & Y. Kozai, 19
Stanley, S. & Bloxham, J. 2004, Nature, 428, 151
Stanley, S. & Bloxham, J. 2006, Icarus, 184, 556
Tobie, G. 2003, PhD thesis, Université Paris 7 - Denis Diderot
Trafton, L. 1974, ApJ, 193, 477
Wu, Y. 2005, ApJ, 635, 688
Yoder, C. F. & Peale, S. J. 1981, Icarus, 47, 1
Zhang, K. & Hamilton, D. P. 2008, Icarus, 193, 267

SF2A 2012
S. Boissier, P. de Laverny, N. Nardetto, R. Samadi, D. Valls-Gabaud and H. Wozniak (eds)

HOW TO CONSTRAIN THE PHYSICAL PROPERTIES OF VERY HOT SUPER-EARTHS WITH THE JAMES WEB SPACE TELESCOPE?

B. Samuel[1], D. Rouan[1], A. Léger[2] and C. Cavarroc[3]

Abstract. Space missions dedicated to exoplanet transit detection led to the discovery of the first super-earths with a measured radius. Surprisingly, the two first rocky planets discovered, CoRoT-7b and Kepler 10b (Léger et al. 2009; Batalha et al. 2011) show very similar parameters: their radius is respectively 1.7 and 1.4 $R_\oplus$ and they orbitate around (resp.) a K and a G star in 0.85 days. The properties of this two objects are expected to be very exotic (Léger et al. 2011). We expect them to be phase locked, with a large lava ocean on the irradiated face (with T reaching 2500 K and 3000 K, respectively) and cold hemisphere with a temperature lower than 50-75 K. We look for observational tests to validate this model among a larger family of models. We suggest to make an observation with the instrument NIRCam on the futur JWST. We investigate the amount of information that such an observation would provide on the physical and dynamical properties of CoRoT-7b, and we focus in particular on two parameters that could influence the surface nature of the very hot super-earth: the albedo, and the phase-locking.

Keywords: super-earth, CoRoT-7b , JWST, lava ocean

1 Introduction

Rocky planets are now detected and we can estimate with a very good accurancy (down to 5%) their mass, radius and then their density. The next steps are the caracterisation of their surface properties and their atmosphere, when there is one. Present and futur space missions will allow the study of exoplanets atmosphere and ground properties in the most favorable cases, using all the available signatures, from visible to infrared (IR) wavelengths. The Hubble Space Telescope (HST), Spitzer, the James Webb Space Telescope - here after JWST - (Gardner et al. 2006), or fully dedicated projects like EChO, Exoplanet Characterisation Observatory (Tinetti et al. 2012) gives or are going to give the first physical information on exoplanets surface nature. Obviously, the case of super-earths is more tricky because the planet to star size and mass ratios are not in favor of high amplitude signals. In this short paper, we will try to show that it is be possible to get some relevent quantitative measurement in some favorable cases. We will use, as an example, the case of the very hot super-earth (SE here after) CoRoT-7b, and simulate observationq with the JWST.

2 CoRoT-7b: A super-earth at 0.017 AU from it sun like star.

The detection of super-earth with the transit method gives a signal amplitude (relatively to the star) during the primary transit (the planet hides a part of the star from the point of view of the observer)

$$\epsilon_1 \approx \left(\frac{R_p}{R_\star}\right)^2, \tag{2.1}$$

[1] LESIA, UMR 8109 CNRS, Observatoire de Paris, UVSQ, Université Paris-Diderot, 5 place J. Janssen, 92195, Meudon, France
[2] Institut d'Astrophysique Spatiale, CNRS (UMR 8617), bât. 121, Université Paris-Sud, F-91405 Orsay, France
[3] Laboratoire AIM, CEA/DSM-CNRS-Université Paris Diderot DAPNIA/Service d'Astrophysique Bât. 709, CEA-Saclay F-91191, Gif-sur-Yvette Cedex

when R_p and $R_\star$ are the radius of the planet and the star respectively. The secondary transit signal (the star hides the planet) is proportionnal to $\epsilon_2 \approx \epsilon_1 \left(\frac{T_p}{T_\star}\right)^4 \sim \epsilon_1 \left(\frac{R_\star}{a}\right)^2$ so finally

$$\epsilon_2 \sim \left(\frac{R_p}{a}\right)^2, \tag{2.2}$$

where T_p and $T_\star$ are the temperature of the planet and the stars respectively, and a the planet to star distance. We understand that, if the small size of the super-earths makes difficult the detection, CoRoT-7b, Kepler-10b and more generaly the very hot SE show a particular advantage in term of planetary emission detection thanks to the unusual proximity of their host star (< 0.02AU). Léger et al. (2011) and Rouan et al. (2011) have shown that the surface temperature of the substellar point of such objects is expected to reach 2500 to 3000K.
Furthermore, the star-planet distance and mass ratio will constrain the ability for the planet to hold an atmosphere or not, considering the surface temperature of the planet, the intensity of the stellar radiation, the stellar wind and more generaly the star activity, and the size of the roche lobe. In the special case of the very hot super-earths, a dense atmosphere is not really expected (Léger et al. 2011).
Moreover, the tidal interaction should have led to a quick circularisation of the orbit and a phase locking of the planet.
The very short distance between the planet and the star must have led, as illustrated by CoRoT-7b, to the absence of a dense atmosphere, and then to dramatically different thermal conditions between the two hemispheres of the planet: a frozen night face with a temperature that does not exceed 50 or 75 K, while the irradiated hemisphere can reach more than 2500 K, leading to the melting of a large part of the rocky surface, and giving birth to a large so called "lava-ocean" (Léger et al. 2011).

3 How to check the validity of the lava-ocean model?

These exotic predictions cannot be confirmed with the current available observations. In order to test the validity of the fundamental hypothesis of the model of Léger et al. (2011), we have tried to imagine what would be surface properties of CoRoT-7b like if, for an example, the complete phase-locking did not happen. We could imagine such a situation if a third body, such as CoRoT-7c (Queloz et al. 2009), could have excited the orbit of CoRoT-7b, and then prevented the circularization of the orbit. Other scenarios could be suggested, but our goal here is mainly to explore the discernability of a phase-locked situation from another, thanks the observations.

In this state of mind, we have modelled a rotating CoRoT-7b, with different planetary rotation periods, different albedos, and we have computed the reflected and emited thermal flux of the planet, taking into acount the particular surface temperature map that would results from the partial melting, the periodical warming and cooling drives by the violent irradiation variations undergone by the surface.

We found that a non phase-locked rocky planet, in the orbital condition of CoRoT-7b, would exhibit an ephemeral lava-ocean at its surface[i], appearing and desappearing every day as a kind of daily ice floe. The melted area would continuously follow the substellar point (Fig. 1), with a little delay from the noon stellar time, as a function of the rotationnal speed and the thermal inertia of the floor. This effect is stronger at long wavelengths, where the thermal emission of the planet dominates the reflected light from the star, than at shortest wavelengths where this is the opposite trend, as shown on Fig. 2. We have tried to see if we could take advantage of this feature to significantly detect a difference from the phase-loked case.

4 Observation with the JWST

We simulated the thermal and reflected emission from the planet surface during the orbit, thanks to the temperature map computed as explained in the previous paragraph. We choosed to simulate the observations with the instrument NIRSPEC on the JWST, wich covers a spectral range (600 nm to 5 μm) that allows to observe both reflected light from the star and thermal emisson of the planet.

[i]For this study, we did not take into account the energy dissipation due to the tidal forces applied on the rotating planet. A study including this source of energy is on progress.

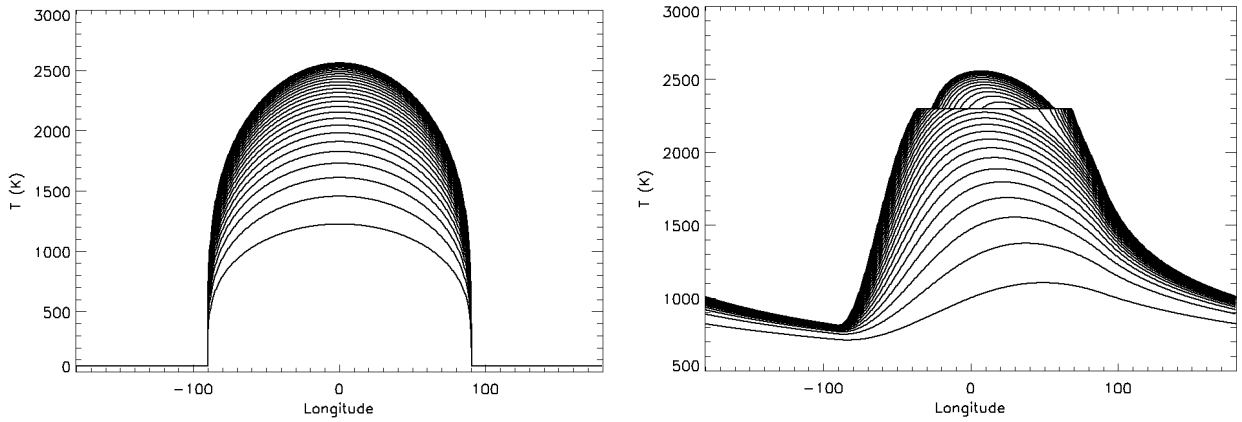

Fig. 1. Left: Temperature on the surface of a phase-locked CoRoT-7b, as a function of the longitude. From the top to the botom, each solid line represents a latitude, from the equator (lat= 0) to lat= 85. **Right:** The same situation, with a non phase-locked CoRoT-7b. The planetary rotation period is 10.5h long (more precisely, the stellar day is 10.5h long), which is one half the orbital period. The temperature threshold around latitude $-45°$and $60°$corresponds to the melting temperature, where the latent heat must be overpassed before the temperature can evolve.

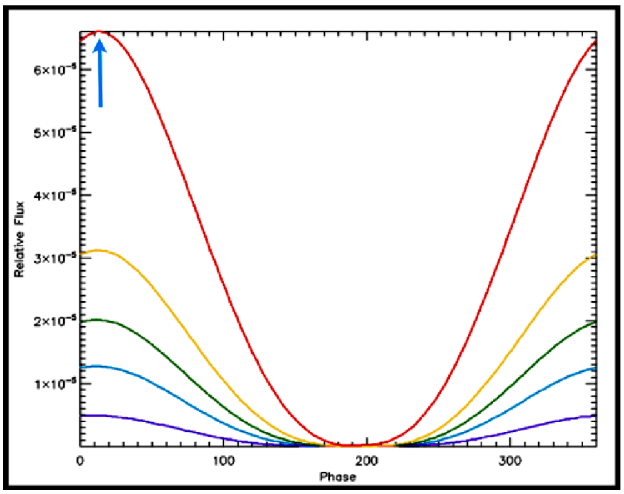

Fig. 2. We show the expected phase-curves of CoRoT-7b if it was not phase-locked. The five curves represent five different wavelengths, from 3.5 μm (red line) to 600 nm (purple line). The blue arrow points out the lag of the "hot point" alignment with the line of sight, in comparison to the phase zero (secondary transit). The shortest wavelength emission flux, dominated by the reflected light from the star, does not show this feature.

We divided the spectrum into five band centered from 800 nm to 3.5 μm and simulated the associated measurement including realistic simulated noise, using an online exposure time calculator tool `http://jwstetc.stsci.edu/etc/input/nirspec/spectroscopic/`.
We computed the phase curve of a full orbit of the planet at the different wavelengths, for the different scenarios. The near-IR channels mainly provide an information on the reflected light component from the planet (where the stellar flux dominates), while the mid-IR wavelength observation probes the thermal emission from the planet, where the planet to star flux ratio is less in favor of the star.

5 Results

In some favorable cases, the simulated observations allow to differenciate the phase-curves of a phase-locked planet from a rotating one. The confidence level is quite good when the rotation period (stellar day) of the planet is of the same order of magnitude than the orbital period ($P_{\rm orb}$ = 0.85 days in this case) as shown on Fig. 3. When we simulate the observation of a phase-locked planet, we can assess a minimum value for the

rotation period compatible with the observation. This is the way we should be able to constrain and confirm the nature of very hot SE as CoRoT-7b.

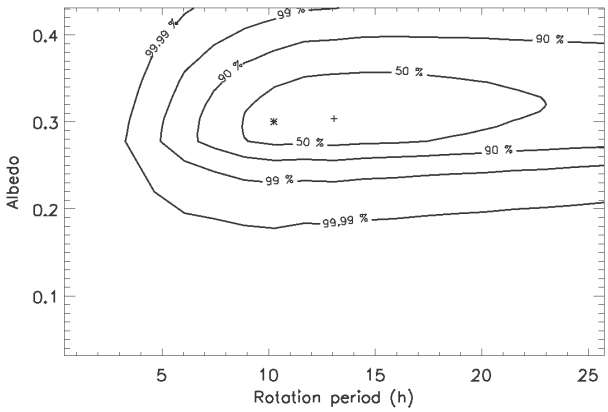

Fig. 3. On this figure, we show the result of a simulated observation of a rotating CoRoT-7b. The simulated rotation period is 10.5 hours ($P_{\rm orb}/2$) and the albedo is 0.3, as represented by the black star. This exercice shows that in this situation, we can find back the rotation period (we found $P = 13.0^{+7.7}_{-2.1}$h, and the albedo $a = 0.30^{+0.06}_{-0.02}$) as represented by the black cross. In this simulation, the phase-locked senario can be rejected with a confidence level of 13 σ.

6 Conclusion

The new generation of space telescopes with large mirrors and wide spectral range spectrographs will be a new milestone in the study of exoplanets. We already know that a lot of giant planets (and less massive planets in favorable situations) will reveal their atmosphere composition, using the differential light flux variations that occurs during the primary and the secondary transits. With this work, we show that will be able to set of information on planets, even of small radius and devoided of an atmosphere. We illustrate in this article how other interesting pieces of information will be provided by these instrument. In particular, this first study led us to the conclusion that the observation of a modulation of the emmited/reflected light from very hot super earths such as CoRoT-7b during their orbit can bring precise answers on the phase-locking, the rotation velocity, and the albedo of these objects. Studies in progress will investigate the possibility to probe the effect of an hypothetical more or less faint residual atmosphere on very-hot super earthes. Finally, we should be able to check step by step the validity of the lava-ocean planet model. Of course, we can hope that the future space telescope will lead to totaly different situations and surpring surface propertie that we did not even expected.

References

Batalha, N. M., Borucki, W. J., Bryson, S. T., et al. 2011, ApJ, 729, 27

Gardner, J. P., Mather, J. C., Clampin, M., et al. 2006, Space Sci. Rev., 123, 485

Léger, A., Grasset, O., Fegley, B., et al. 2011, Icarus, 213, 1

Léger, A., Rouan, D., Schneider, J., et al. 2009, A&A, 506, 287

Queloz, D., Bouchy, F., Moutou, C., et al. 2009, A&A, 506, 303

Rouan, D., Deeg, H. J., Demangeon, O., et al. 2011, ApJ, 741, L30

Tinetti, G., Beaulieu, J. P., Henning, T., et al. 2012, Experimental Astronomy, 35

SF2A 2012
S. Boissier, P. de Laverny, N. Nardetto, R. Samadi, D. Valls-Gabaud and H. Wozniak (eds)

CHARACTERISING EXOPLANET ATMOSPHERES WITH ECHO: UPDATED RESULTS FOR A NEW PAYLOAD DESIGN

M. Tessenyi[1], J.-P. Beaulieu[1,2], M. Ollivier[3], G. Tinetti[1], V. Coudé du Foresto[4] and J.-M. Reess [4]

Abstract. The field of exoplanets is one of the fastest growing and most novel in astrophysics, with hundreds of planetary discoveries and thousands of candidates waiting to be confirmed. Many of these planets are very different from the planets in our Solar System, yet at present we do not have an explanation nor a clear understanding of this diversity. The atmospheric composition of these remote worlds may provide a key to interpreting this diversity. Spectroscopic measurement of transiting exoplanets is the only viable technique we can use today to sound these exotic atmospheres. EChO, the Exoplanet Characterization Observatory is a Medium class ESA mission candidate, currently being assessed as part of the COSMIC VISION programme. EChO will be the first mission fully dedicated to the systematic study of the physics and chemistry of a large portfolio of exoplanet atmospheres. The targets will cover a wide range of planets: from hot planets to temperate ones, from large, gaseous Jupiter-like planets to small telluric planets. The baseline mission design is a 1.2 m off axis telescope with one instrument composed of several channels covering the spectral range 0.4-16 μm with a spectral resolution in the 300-30 range. The satellite is optimised for stability and is based on the legacy of previous successful ESA missions. EChO will observe primary transits and secondary eclipses, and also phase curves of some non-transiting planets. We present updated results for secondary eclipses, based on methods from previous studies and incorporating the evolution of the payload design.

Keywords: exoplanets, atmospheres, EChO, stars

1 The EChO Instrument

The Exoplanet Characterisation Observatory (EChO) is a proposed 1.2 m space-based telescope currently under study at the European Space Agency, as a M class mission part of the Cosmic Vision programme (Tinetti et al. 2012, `sci.esa.int/echo/`). EChO will provide simultaneous, multi-wavelength spectroscopic observations on a stable platform for a wide selection of exoplanets, from the visible to the mid-infrared. The science case of EChO is described in Tinetti et al. (2011). In Tessenyi et al. (2012) we have studied the feasibility and general performance of an EChO like mission for a broad selection of targets. In that paper, we considered a number of instrument tradeoffs, which included two telescope sizes and several possible choices for the detector technology. In this study, we focus on the performances of our most recent payload design, studied during the assessment phase by our instrument consortium (Swinyard et al. 2012, Reess et al., 2012, Adriani et al. 2012, Focardi et al. 2012, Pascale et al. 2012, Eccleston et al. 2012, Ramos Zapata et al. 2012). The updated instrument design consists of a 1.2 m telescope and detector settings which are listed in Table 1. Further studies will include results from EChOSIM, an end-to-end instrument simulator currently under development by our instrument consortium.

[1] University College of London, Gower Street, London, United Kingdom
[2] Institut d'Astrophysique de Paris, CNRS, UMPC, 98bis Boulevard Arago, 75014 Paris, France
[3] IAS - UPS - CNRS, Bat 120, 91405 Orsay, France
[4] LESIA, Observatoire de Paris, Meudon, 5 Place Jansen, 92190 Meudon, France

Table 1. Instrument settings used in our simulations, listed for each observing band used. In addition, the two following settings are the same for all four bands considered: a 30 μm pixel size and 4 illuminated pixels per spectral element are assumed.

Instrument Values	Visible	2.5 to 5 μm	5 - 11 μm	11 to 16 μm
Detector used	MCT	MCT	Si:As	Si:As
Full well capacity (electrons)	$2 \cdot 10^6$	$4 \cdot 10^6$	$2 \cdot 10^5$	$2 \cdot 10^5$
Dark current (electrons/s/pixel)	0.1	10	0.2	0.2
Quantum efficiency (electrons/photon)	0.5	0.7	0.7	0.7
Readout noise (electrons/pixel/readout)	10	400	15	15
Readout time (seconds)	0.004	0.01	3	3
Telescope temperature (K)	-	60	60	60
Instrument temperature (K)	-	45	45	45
Detector temperature (K)	170	< 45	7	7
Telescope transmission	0.86	0.86	0.86	0.86
Instrument transmission	0.7	0.32	0.35	0.35

2 Planets considered

In Tessenyi et al. (2012) a wide variety of target cases are considered, here the focus is on four key cases: a Hot Jupiter and Warm Neptune as examples of gaseous planets (HD 189733b and GJ 436b, respectively), and a Hot super-Earth and temperate super-Earth (Cnc 55 e and a possible 1.8 $R_\oplus$, 5 $M_\oplus$ super-Earth in the habitable-zone of a M dwarf). The parameters assumed for these targets are listed in Table 2. Where

Table 2. Star and planet parameters assumed for the selected targets of this study. The planet radii are given both in units of Jupiter radius and Earth radius, and the temperatures listed are an average temperature from the temperature-pressure profile.

Star	Hot Jupiter	Warm Neptune	Hot super-Earth	Temperate super-Earth
Spectral Type	K1V	M2.5V	G8V	M4.5V
Radius ($R_\odot$)	0.8	0.464	0.95	0.22
Mass ($M_\odot$)	0.8	0.452	0.91	0.22
Temperature (K)	4980	3684	5196	3300
Planet				
Radius (R_{jup} | $R_\oplus$)	1.138 | 12.77	0.365 | 4.10	0.194 | 2.18	0.16 | 1.8
Temperature (K)	1350	750	2390	250
Semi-major axis (au)	0.031	0.029	0.016	0.046
Period (days)	2.219	2.644	0.737	7.64
Transit duration (hr)	1.83	1.03	1.76	1.39

possible, the spectra of the planets presented are modelled atmospheres, and blackbody curves are used when no observational data is available. Figure 1 shows the planet/star flux ratio (contrast) of the Hot Jupiter and the Warm Neptune, which were obtained using radiative transfer codes as described in Tessenyi et al. (2012). These simulations either fit existing observations (e.g., Knutson et al. 2007, Tinetti et al., 2007b, Charbonneau et al., 2008, Grillmair et al., 2008, Swain et al., 2008, Stevenson et al. 2010, Beaulieu et al., 2011) or are an extrapolation from our knowledge of Solar System planets. Figure 2 shows the contrast values used for the Hot and Temperate super-Earths. For the Hot super-Earth case, the planet temperature is expected to be between 1980 and 2800 K, depending on the heat redistribution on the planet (Winn et al. 2011). For the integration time calculations, a mean temperature of 2390 K is used. For the Temperate super-Earth three possible atmospheres are presented: an Earth-like, Venus-like and a Small Neptune-like spectrum, reflecting the effect of atmosphere compositions on the emitted signal. An average temperature of 300 K, fitting within the temperature range of the atmosphere types, is used as planet/star flux ratio. These Temperate super-Earths will be the most challenging targets to observe, with flux ratios in the $10^{-5} - 10^{-4}$ range, and will require low resolution observations. The spectra presented for this target in Figure 2 are set at R=20.

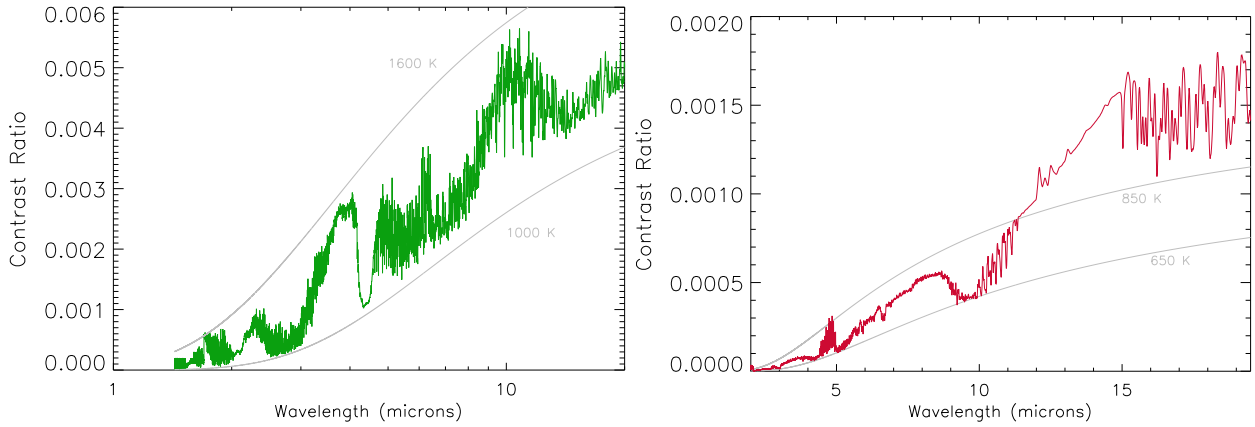

Fig. 1. Left: Modeled emission spectrum of HD 189733b (Tessenyi et al., 2012), a hot-Jupiter around a K1/2V star, mag. V=7.67, presented as planet/star flux ratio. Blackbody curves at 1000 K and 1600 K are plotted in grey for indication. **Right:** Modeled planet/star flux ratio of GJ 436b (Tessenyi et al., 2012), a warm Neptune orbiting a M2.5V star, with 650 K and 850 K blackbody curves plotted for indication.

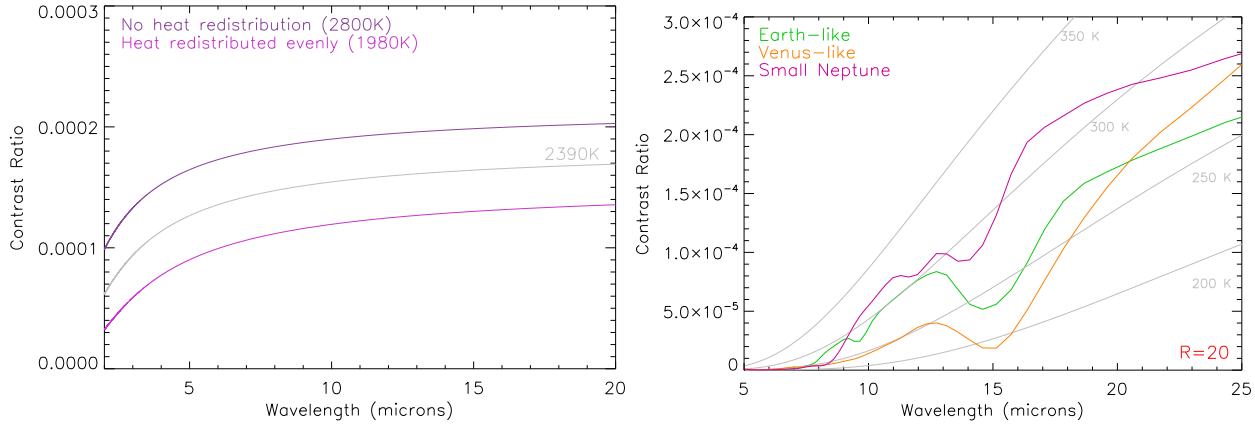

Fig. 2. Left: Blackbody planet/star flux ratio for Cnc 55 e, a 2.1 $R_\oplus$ Hot super-Earth, orbiting a G8V star. The planet temperature is estimated to be between the 2800 K and 1980 K limits, depending on the heat redistribution in the atmosphere (Winn et al. 2011). A mean temperature of 2390 is used for this study. **Right:** Low resolution (R=20) Earth-like, Venus-like and Small Neptune-like planet/star flux ratio for a possible 1.8 $R_\oplus$ Temperate super-Earth, orbiting a 3150 K M4.5V star. The three spectra show possible atmospheric types that could exist in this temperature regime. An average temperature of T=300 K is used for our calculations.

3 Updated results

The results are given as integration times in number of transits required (integration time divided by the transit duration) in Tables 3 and 4. The computed contrast value is sampled at three different wavelengths: 3, 7.5 and 13.5 μm, for a wavelength bin corresponding to a single resolution element of the channel (resolving power 300, 30 and 30 for the three channels, respectively). The integration time is computed in the bins for a range of stellar magnitudes, either in V mag of K mag, with the given contrast and a desired signal-to-noise ratio (SNR) value. A minimum SNR=5 setting is used for all targets, and where the signal permits, higher SNR integration times are presented. Table 3 shows the results for the Hot Jupiter and the Warm Neptune cases, and Table 4 presents the results for the Hot and Temperate super-Earths.

Table 3. Top: Hot Jupiter integration times (in units of "number of transits") needed to obtain the specified SNR (5 and 50) per channel for a given brightness (in Mag. V), with a 0.8 $R_\odot$, K1V star at 4980 K. For the SNR=5 requirement this planet case is easy to observe. The SNR=50 requirement requires adding up of observations, mostly due to the higher resolution required in the first channel. Within the proposed 5 year mission lifetime, this planet will complete 826 orbits. **Bottom:** Integration times (in units of "number of transits") for a Warm Neptune, orbiting a M2.5V star at 3150 K. Results are given per channel for two SNR cases (5 and 25) and a given brightness (in Mag. K). For this target, in the 1-5 μm channel, binning of the signal to a lower resolution will be required to obtain enough photons, as the contrast is low in this band. In 5 years this planet will complete 691 orbits.

Hot Jupiter – Secondary eclipse, SNR=5

Channel range	λ (μm)	Res. Power	Contrast ($*10^{-3}$)	Integration time (n. transits) V=5	V=6	V=7	V=8	V=9
1-5	3	300	0.40	0.1	0.2	0.5	1.4	3.5
5-11	7.5	30	2.77	< 0.1				
11-16	13.5	30	3.93	< 0.1				

Secondary eclipse, SNR=50

Integration time (n. transits) V=5	V=6	V=7	V=8	V=9
9	22	55	138	348
0.3	0.3	0.5	1.2	3
0.2	0.4	1	2.5	7

Warm Neptune – Secondary eclipse, SNR=5

Channel range	λ (μm)	Res. Power	Contrast ($*10^{-3}$)	Integration time (n. transits) K=5	K=6	K=7	K=8	K=9
1-5	3	300	0.02	351	*Lower Resolution*			
5-11	7.5	30	0.45	0.3	0.7	1.9	5	12
11-16	13.5	30	1.28	0.2	0.4	1.1	3.2	11

Secondary eclipse, SNR=25

Integration time (n. transits) K=5	K=6	K=7	K=8	K=9
Lower Resolution				
8	19	47	117	293
3.8	10	27	80	277

4 Conclusions

We have presented updated results of our previous work estimating the performance of EChO, building on the evolution of the instrument design. We have shown that with a 1.2 m space-based telescope and an updated payload design, key cases of transiting exoplanets can be observed spectroscopically from the visible to the mid-infrared, with a choice of SNR/resolution observation modes. These updated results confirm the strengths of EChO: a wide range of planet types can be observed within 5 years, with the flexibility of observing bright targets either at high accuracy or repeatedly at lower SNR and resolution. The repeated observation of bright targets will allow the study of atmospheric circulations, or the "slicing" of planet observations to map the planet surface during ingress and egress, maximising the science return of the mission. Challenging targets such as Temperate super-Earths can be observed with lower SNR/resolution, provided they orbit close-by and late type M dwarfs. Overall, EChO will provide full emission (and transmission) spectra from the visible to the mid-infrared for a wide variety of targets, contributing to the advancement of this new, exciting field.

References

Adriani A., Oliva E., Piccioni G., et al. 2012, Proc. SPIE 8442, 84422W

Beaulieu J.P., Tinetti G., Kipping D. et al. 2011, ApJ, 731, 16

Charbonneau D., Knutson H. A., Barman T., et al., 2008, ApJ, 686, 1341

Table 4. Top: Hot super-Earth integration times (in units of "number of transits") needed to obtain the specified SNR (5 and 25) per channel for a given brightness (in Mag. V), with a 0.95 $R_{\odot}$, G8V star at 5196 K. As the Hot Jupiter, with the SNR=5 requirement this planet case is easy to observe. The SNR=25 requirement requires adding up of observations, mostly due to the higher resolution required in the first channel. Within the proposed 5 year mission lifetime, this planet will complete 2467 orbits. **Below:** Integration times (in units of "number of transits") for a Temperate super-Earth, orbiting a M4.5V star at 3300 K. Results are given per channel with an SNR=5, resolution of 10 and a given brightness (in Mag. K). For this target the 1-5 μm channel is not used as a 300 K blackbody object will emit no radiation below $\sim$ 5 μm. Given the lower contrast values for this target, only the SNR=5 case is considered, and for the more distant stars, photometry may be required to observe a target. In 5 years this planet will complete 239 orbits.

Hot super-Earth – Secondary eclipse, SNR=5

Channel range	λ (μm)	Res. Power	Contrast ($*10^{-4}$)	Integration time (n. transits) V=5	V=6	V=7	V=8	V=9
1-5	3	300	0.94	2	4.9	13	31	78
5-11	7.5	30	1.45	1	1	2.2	6	14
11-16	13.5	30	1.62	1.1	2.8	7	19	51

Secondary eclipse, SNR=25

Integration time (n. transits) V=5	V=6	V=7	V=8	V=9
49	122	307	771	1944
26	26	54	135	339
28	69	176	460	1268

Temperate super-Earth – Secondary eclipse, SNR=5

Channel range	λ (μm)	Res. Power	Contrast ($*10^{-4}$)	Integration time (n. transits) K=5	K=6	K=7	K=8	K=9
5-11	7.5	10	0.13	159	214	*Photometry*		
11-16	13.5	10	1.06	6	14	39	115	*Ph.*

Eccleston P., Bradshaw T., Coker J., et al. 2012, Proc. SPIE 8442, 84422U-1
Focardi M., Pancrazzi M., Di Giorgio A. M., et al. 2012, Proc. SPIE 8442, 84422T
Grillmair C. J., Burrows A., Charbonneau D., et al. 2008, Nature, 456, 767
Knutson H. A., Charbonneau D., Allen L. E., et al. 2007, Nature, 447, 183
Pascale E., Forder S., Knowles P., et al. 2012, Proc. SPIE 8442, 84422Z
Ramos Zapata G., Belenguer T., Balado A., et al. 2012, Proc. SPIE 8442, 84422V
Reess J.M., Tinetti G., Baier N., et al., 2012, Proc. SPIE 8442, 84421I-1
Stevenson K. B., Harrington J., Nymeyer S., et al. 2010,
Swain M.R., Vasish G., & Tinetti G., 2008, Nature, 452, 329
Swinyard B., Tinetti G., Eccleston P., et al. 2012, Proc. SPIE 8442, 84421G
Tessenyi M., Ollivier M., Tinetti G., et al. 2012, ApJ, 746, 45
Tinetti G., Vidal-Madjar A., Liang M.C., et al., 2007b, Nature, 448, 169
Tinetti G., Cho J. Y.-K., Griffith C. A., et al. 2011, IAU Symposium, 276, 359
Tinetti G., Beaulieu J.P., Henning T. et al. 2012, Experimental Astronomy, 34, 311
Winn J., Matthews J.M., Dawson R.I., et al. 2011, ApJ, 737, L18

Session 08

Exoplanets: From Astrochemistry to Exobiology

SF2A 2012
S. Boissier, P. de Laverny, N. Nardetto, R. Samadi, D. Valls-Gabaud and H. Wozniak (eds)

FROM ASTROCHEMISTRY TO PREBIOTIC CHEMISTRY? AN HYPOTHETICAL APPROACH TOWARD ASTROBIOLOGY

L. Le Sergeant d'Hendecourt [1] and G. Danger [2]

Abstract. We present in this paper a general perspective about the evolution of molecular complexity, as observed from an astrophysicist point of view and its possible relation to the problem of the origin of life on Earth. Based on the cosmic abundances of the elements and the molecular composition of our life, we propose that life cannot really be based on other elements. We discuss where the necessary molecular complexity is built-up in astrophysical environments, actually within inter/circumstellar solid state materials known as "grains". Considerations based on *non-directed* laboratory experiments, that must be further extended in the prebiotic domain, lead to the hypothesis that if the chemistry at the origin of life may indeed be a rather universal and deterministic phenomenon, once molecular complexity is installed, the chemical evolution that generated the first prebiotic reactions that involve autoreplication must be treated in a systemic approach because of the strong contingency imposed by the complex local environment(s) and associated processes in which these chemical systems have evolved.

Keywords: Astrochemistry, Astrobiology

1 Introduction

Astrobiology encompasses all disciplinary fields, from physics to biology that are of interest to investigate the possibility for life to have emerged on the primitive Earth as well as, possibly, in other environments. However, in this rather precise wording, "astrobiology", linking biology to astrophysics suggests that life has already been observed on other locations than on Earth, which is actually not the case. Thus, this too vague definition does not establish a guideline to link each disciplinary field in order to understand life's emergence processes on Earth. In this short contribution, we propose a hypothesis that retraces organic matter formation and evolution from its appearance in astrophysical environments to its availability in specific ones for the emergence of a prebiotic chemistry. We suggest an approach, involving systemic pluridisciplinarity that may end up in the understanding of prebiotic chemistry, as strongly related to astrochemistry.
We thus propose the following hypotheses: (i) that the biological elements indeed are both present in the gas phase and in "icy" grains in space, semi-volatile molecular species. These conditions are widespread and common in molecular clouds where stellar systems and planets form; (ii) that this situation allows for very complex molecules to form on grains and be preserved for exogenous delivery of organic matter on telluric planets such as on the primitive Earth; (iii) that the solid state chemistry in space is sufficiently complex and intricate that non-directed experiments are warranted and even preferred and (iv) that the composition of the gas and the ices preordains much, if not all, of the chemical composition of life.

2 The molecular evolution of our Galaxy

2.1 The elemental constituents of life

As many stars, the Sun displays in its photosphere, an ensemble of elements, dominated by hydrogen, where the relative abundances are the result of a long suite of nucleosynthesis processes. These processes are obtained

[1] Univ. Paris-Sud, Astrochimie et Origines, Institut d'Astrophysique Spatiale, UMR-CNRS 8617, Orsay, 91405, France. ldh@ias.u-psud.fr
[2] Aix-Marseille Univ, PIIM UMR-CNRS 7345, 13397, Marseille, France. gregoire.danger@univ-amu.fr

from the evolution of our Galaxy, through many generations of preceding stars. These "cosmic abundances" are a given characteristic of our "local" interstellar medium where new stars do form even nowadays. These abundances are central to our argument. However, abundances toward a particular line of sight in our galaxy do not reflect nucleosynthesis only. Depletions, elements missing in the gas phase, are commonly observed. Whereas the cosmic abundances are the result of nucleosynthesis, the depletion pattern has nothing to do with it, but translates into the thermodynamical properties of the solids that make interstellar grains. Theories of grain formation based on thermodynamical consideration allow a correct understanding of this well known fact established from diffuse medium interstellar observations. The "average" depletion from the diffuse medium is well known in the astrophysical literature but seems not enough considered in prebiotic chemistry and certainly not in "astrobiology". A recent re-interpretation of classical data can be found in (Le Sergeant d'Hendecourt 2011). Nucleosynthesis and depletion mechanisms lead to the most abundant elements in the gas phase of the diffuse medium being (H), O, C, N, S and P, those that are available for the starting up of the (organic) chemistry, while the others (Si, Fe...), less abundant and buried in refractory grains are lost for any interesting gas chemistry and, more importantly, for solid phase chemical reactions in van der Waals solids, the interstellar ices. Phosphorus, although not much depleted in the interstellar medium is far less abundant. Its presence in outgassing ices from comets in the form of phosphine (PH_3) has been suggested by Boice and Almeida 2012 but not detected up to now (Boice & Almeida 2012). From an astrophysicist's point of view, if life is considered as merely the outcome of the evolution of the universe, the elemental composition of living systems, as in the case of life on Earth, cannot escape those selected by the physical and chemical laws that apply to these elements. Biomolecules, such as proteins, DNA or RNA, on Earth are indeed essentially based on these 6 major elements H, O, C, N, S and P. Helium although quite abundant does not possess the ability to form molecules and thus can be discarded in prebiotic chemistry. A last and important word of caution though: our hypothesis does not mean at all that life's evolution does not need all the elements from Mendeleev's table, but that is obviously a completely different story that cannot be considered in this short paper.

2.2 Cosmic molecular ices and their evolution

In the diffuse ISM, molecules are not present, and the composition of the gas phase as the one of the grains is known from the already described problem of depletion (Greenberg 1974). Entering molecular clouds where the environment becomes relatively protected from UV light because of the refractory dust concentration, molecules can form. As described by many former astronomers such as Oort and van de Hulst (Oort & van de Hulst 1946), elements like oxygen, carbon and nitrogen in a reducing H rich environment will give hydrides, that are H_2O, CH_4, NH_3 prone to form ices in the presence of the cold surfaces of grains. Besides, molecular H_2 must simultaneously form on grains (Knaap et al. 1966). The development of astrochemistry in the field of low temperature gas phase chemistry (ion-molecule chemistry driven by cosmic-ray ionization in the gas) has added to these, essentially CO and its derivatives like HCO, H_2CO (Prasad & Huntress 1980). A major part, actually the quasi totality of the observed molecules in the gas phase, is organic only because the elements H, O, C, N, and S dominate in abundances and availability. The chemistry observed in inter/circumstellar gas cannot be qualified as "complex": abundances of the detected molecules decrease very rapidly with the number of atoms in the molecule, and the number of different molecules is relatively small (150 about) up to date (ref PCMI website: http://www.pcmi.univ-montp2.fr/). Gas phase reactions in environments such as molecular clouds, are only two-body reactions. They occur in cold media rather unprotected against many destruction routes that preclude the formation of large and really complex species. By opposition, solid surfaces offer locally a huge increase in the molecular density leading to a very high molecular concentration. Van der Waals solids (ices) form the well known and observed "dirty ices" onto the refractory cores. Energetic sources and thermal processes (UV photons and cosmic rays) will allow these ices to evolve toward molecular complexity. Therefore, interstellar grains must be considered as the major chemical reactors of the ISM, which will provide the highest degree of complexity. This solid phase chemistry and its resulting complexity has been apprehended and simulated in the laboratory using non directed experiments on interstellar ice analogs.

Because of the gas species accretion on the grain surfaces, solid state molecules in a given line of sight always dominate in abundances their gas phase counterparts. Energetic processing of laboratory ice analogues from UV photons and cosmic ray particles has led to the detection of some important intermediate molecules through photochemistry processes. This photochemistry leads easily and naturally to the production of organic residues during the warm-up of these photo-processed ice analogues in the laboratory. These residues may then be used as templates for understanding the chemical evolution in the interstellar/circumstellar and cometary media. After reaching 300 K through a slow warming, an organic residue is always left on the sample holder, a semi-refractory

material that may cover the surface of most interstellar grains, especially in star forming regions. One of the interesting points about such a simulation is that it constitutes, by definition, a non-directed experiment, largely similar in its methodology to the well known Miller-Urey one. Thereafter, the composition of the produced molecular organic matter is obtained by highly sophisticated techniques issued from analytical chemistry, such as gas chromatography and mass spectrometry (GC-MS) or high resolution mass spectroscopy. In this semi-empirical approach, the evolutionary timescales of the ice can be easily accelerated since a week of experiment roughly corresponds to the lifetime of a molecular cloud. These residues are highly functionalized, and thus remain almost totally soluble in water, an important characteristic for their availability to a possible further prebiotic evolution. Finally, if one admits that the cosmic abundances of the elements are given to forming planets, we propose that the molecular complexity from these organic residues can, and must be considered as a cosmic and universal molecular complexity also given to forming planets. Furthermore, because of the previous discussed elemental depletion, these residues only contain molecules including H, C, O, N, S and P.

3 Organic residues and "prebiotic" materials

Once the planetary system has stabilized, the organic residues formed during the ISM matter cycle, may enter in the composition of various objects, such as comets and asteroids. These interplanetary reservoirs of organic matter (i.e. comets and asteroids), named exogenous reservoir, are thus a source of organic complex molecules containing mainly C, H, N, and O, like amino acids (Sephton 2002), and are considered as one of the main sources of organic matter available from meteorites falls at the surface the Primitive Earth (Pizzarello 2007). Complex organic residues formed in the laboratory have been shown to contain many amino acids when hydrolyzed as reported in (Munoz-Caro et al. 2002; Nuevo et al. 2008; Bernstein et al. 2002). In association with physical and/or chemical energy input, this organic matter can then be used on the planetary surfaces for developing a more complex chemistry, which could lead to the emergence of a prebiotic chemistry. Prebiotic chemistry characterizes the transition between the abiotic chemistry and the biochemistry. It can only occur in a specific environment, in which the development of dynamic networks far from equilibrium driven by a constant flow of matter and energy (Pascal & Boiteau 2011a,b; Pascal et al. 2005) will be favored. Furthermore, because of the complex nature of all the possible interactions involved, these chemical networks display emerging properties. The primitive Earth has been 4.5 Gyrs ago a prebiotic chemical reactor that provided the transition from an abiotic medium to extant biochemical systems. The primitive Earth environment was indeed highly specific, provided by a contingency of astrophysical, planetological, geochemical and chemical events, local conditions and constraints.. An example of experimental research in prebiotic chemistry is the formation and selection of peptides in an environment relevant with the one of the primitive Earth (Commeyras et al. 2004). If organic matter is necessary, as amino acids or derivatives like hydantoin, (de Marcellus et al. 2011) are for peptide formation, it is far from being sufficient. In order to form peptides, an energy input is also necessary through physical sources (e.g. radiation from light) (Commeyras et al. 2004) or chemical sources (e.g. cyanate or carbodiimide) (Danger et al. 2006, 2012). This association of organic matter and of energy sources will drive the evolution of chemical systems that will favor the emergence of peptides. During their elongation, the local environment will provide the selection of peptide chains, the least suited to the environment being recycled through preferential degradation. Therefore we hypothesize that organic refractory residues from ices photochemistry (see (Ciesla & Sandford 2012) for a recent reappraisal of the importance of this phenomenon in the solar nebula), so easily produced in the laboratory may become largely available in comets and asteroids and may be seriously considered as have been taking a major role in prebiotic chemistry toward the emergence of biochemical systems. They could have been delivered onto the Earth, as suggested by the heavy bombardment or the present meteorites (Chyba & Sagan 1992). This exogenous organic residue represents thus an interesting template on the primeval complex chemical input at the surface of any telluric planets.

4 Non directed experiments: a route for "astrobiology" laboratory experiments

Definitely in the laboratory, a complex organic material is produced containing hydrosoluble organic macromolecular fractions. Such experiments may be viewed as a generalization, at the cosmic scale, of Miller's experiment (Miller 1953) that pertained only to the primitive Earth's atmosphere and hydrosphere. Such as the Miller experiment, photochemistry experiments on interstellar ice analogs belong to this class of experiments that may be called non directed ones. What is indeed controlled in these experiments is the natural evolution to which some "trivial" and largely observed interstellar matter (ices) is subjected. Note that the

solid state photochemistry of ices cannot be treated in a totally reductionist (mechanistic) way. Starting from a three component ice mixture (actually H_2O, CH_3OH and NH_3), photolyzed by Lyα, it seems difficult, if not impossible to establish the precise mechanistic pathway that will result in the recently measured rather complex composition of the organic residue recently analyzed in (Meinert et al. 2012) that display 20 amino acids and 6 di-amino-acids where its prebiotic significance has been pointed out through the detection of the N-(2-Aminoethyl)glycine molecule, a possible precursor to peptide nucleic acids (PNA). The same remark can be made on the Miller's experiment. As far as the potential "prebioticity" of this material, one must then carefully relates this property to the interaction between the organic matter produced in a plausible astrophysical scenario, taking into account the astrochemistry involved in the presolar and solar nebula, with the environment that will be the one of the primitive Earth, which is the only example we know where life appearance is undeniable. Fortunately, the progressive better knowledge of this primitive Earth (early atmosphere and ocean) will allow investigating the interaction of some organics within a range of parameters (T, pH, illumination...) using the semi-empirical approach of a non-directed experiment. Placed in a prebiotic like-environment, these exogenous materials could take a part in the development of chemical networks as an open input of matter and energetic carriers in a non thermodynamical equilibrium chemical reactor in the laboratory, an experiment to be designed in a near future. This approach will not rely on synthesis chemistry but on a systemic one. Such non directed experiments may help astrochemistry to really enter the field of astrobiology by offering at least a semi-empirical but practical explanation between the molecular universe and the prebiotic one. Furthermore, since astrophysical organic refractory residues can be considered as "universal", exactly in the same astronomical meaning as the one attached to cosmic abundances for the elements in planetary systems, that type of experimentation could also be applied to future exoplanets environments in order to determine if a given exoplanet could reach a stage allowing the development of similar prebiotic chemical networks. Finally we propose a scenario that can be tested from laboratory experiments, unifying astrochemistry, as a consequence of galactic evolution, cosmochemistry in the primitive solar nebula, planetology as the proviso for environments favorable to the emergence of prebiotic chemistry prior to the emergence of life. We consider that, to understand the history of the evolution that precedes the emergence of life, it is important to start the chemical history from stars and molecular clouds where the organic matter, ultimately constituting the feed-up for prebiotic systems, may be born. The track of this evolution provides us with the understanding of the form in which the organic matter could be used for the development of a given prebiotic chemistry in which autocatalytic replication is an essential step toward obtaining a passage from the inanimate to the animate world (Pross 2012). Furthermore, this approach highlights the necessity to understand what sort of environments could be useful for the development of this very specific chemistry. Our hypothesis is not proposed as a firm rule, but as one of the scenarii to be considered, possibly bridging astrochemistry to prebiotic chemistry, and, further, as a guideline to laboratory experiments for astrobiology purpose that may consider this scenario as a systemic process which needs to be treated as such.

5 Conclusions

Astrochemistry is a well recognized discipline. Observations of numerous interstellar molecules, has allowed a better understanding of the physics and the chemistry of the interstellar and circumstellar media. Astrochemistry, especially from an experimental approach, brings us crucial information about the onset and development of molecular complexity, organic in nature, which is a pre-requisite for the starting point of prebiotic chemistry. The accepted evolution of the universe translates to a constant increase with time in complexity of the sub-structures of its components, from galaxies to living cells. Stars provide, through supernovae explosions, an increasing complexity of the interstellar medium with all the elements of the Mendeleev's table that were not synthesized in the early times. Evaporating atmospheres of red giant AGB stars allow for dust nucleation and interstellar grains formation. These grains will then drive the molecular abiotic organic complexity that is for example found on Earth today only in primitive meteorites. It is thus neither surprising nor illogic, to assume that life's emergence on Earth was the result of the natural evolution of the universe, which leads us to consider that the only example known must be the major focus of attention of the astrobiology community. Based on very general astronomical arguments, we point out the fact that the basic elements for life, H, O, C, N, S and P, the ones that are present in proteins and in DNA, with their easiness to form van der Waals hydrides (ices) that can turn into a covalent macromolecular semi refractory solid, cannot seriously be different elsewhere. Moreover, the very special chemical properties of carbon offer an extremely versatile and rich organic chemistry enhanced by liquid water for its role as a solvent and transport. For a chemist, the

number of organic molecules is virtually "infinite" a fact that is certainly determinant for prebiotic chemistry and biochemical systems. Thus organic chemistry will provide a real continuum of species which is at the heart of the Darwinian evolution and adaptability of life to ever changing environments. The focus on the studies, intimately connecting astrochemistry and prebiotic chemistry within complex organics, emerging phenomena, and the rise of the very first biomolecular reactions must be viewed as an interdisciplinary and systemic field strongly unified by cosmic evolution. Finally, our conclusions highly recommend that an experimental approach of the development of "minimal life" must be undertaken in a systemic manner that will consider an ensemble of processes in interaction with a given environment. This experimental approach, although interdisciplinary in nature, must also involve a systemic management involving a true interdisciplinary approach of this field where scientists from different disciplines must be able to interact closely and equally with each other. Such a systemic management is certainly the most important condition to successfully obtain a clear understanding of emergent phenomena but, as we must recall, at the expense of an impossible fully reductionist approach.

The authors wish to thank the CNRS EPOV program, the PCMI and the CNES for providing financial support to some of the experimental results on the evolution of ices to organics as well as the opportunity to favor a true interdisciplinary exchange between them.

References

Bernstein, M., Dworkin, J., Sandford, S., Cooper, G., & Allamandola, L. 2002, Nature, 416, 401

Boice, D. & Almeida, A. 2012, LPI, 43, 1887

Chyba, C. & Sagan, C. 1992, Nature, 355, 125

Ciesla, F. & Sandford, S. 2012, Science, 336, 452

Commeyras, A., Taillades, J., Collet, H., et al. 2004, Orig. Life Evol. Biosph., 34, 35

Danger, G., Boiteau, L., Cottet, H., & Pascal, R. 2006, J. Am. Chem. Soc., 128, 7412

Danger, G., Charlot, S., Boiteau, L., & Pascal, R. 2012, Amino Acids, 42, 2331

de Marcellus, P., Bertrand, M., Nuevo, M., Westal, F., & Le Sergeant d'Hendecourt, L. 2011, Astrobiology, 11, 847

Greenberg, J. 1974, Astrophys. J. Letters, 189, L81

Knaap, H., van den Meijdenberg, C., Beenakker, J., & van de Hulst, H. 1966, in Formation of molecular hydrogen in interstellar space, Vol. 18, 256

Le Sergeant d'Hendecourt, L. 2011, in Molecular complexity in astrophysical environments: From astrochemistry to "astrobiology"?, ed. E. Dartois & T. Pino (EPJ Web of conferences, EDP Sciences), 06001

Meinert, C., Filippi, J., de Marcellus, P., Le Sergeant d'Hendecourt, L., & UJ., M. 2012, Chem. Plus Chem., 77, 186

Miller, S. 1953, Science, 117, 528

Munoz-Caro, G., Meierhenrich, U., Schutte, W., et al. 2002, Nature, 416, 403

Nuevo, M., Auger, G., Blanot, D., & L., d. 2008, Orig. Life Evol. Biosph., 38, 37

Oort, J. & van de Hulst, H. 1946, Gas and smoke in interstellar space.

Pascal, R. & Boiteau, L. 2011a, Phil. Trans. R. Soc. B, 366, 2949

Pascal, R. & Boiteau, L. 2011b, Orig. Life Evol. Biosph., 41, 23

Pascal, R., Boiteau, L., & Commeyras, A. 2005, Top. Curr. Chem., 259, 69

Pizzarello, S. 2007, Chem. Biodiversity, 4, 680

Prasad, S. & Huntress, W. 1980, Astrophys. J. Sup., 43, 1

Pross, A. 2012, in What is Life? How chemistry becomes biology (Oxford University Press)

Sephton, M. 2002, Nat. Prod. Rep, 19, 292

SF2A 2012
S. Boissier, P. de Laverny, N. Nardetto, R. Samadi, D. Valls-Gabaud and H. Wozniak (eds)

DID METEORITES BRING THE INGREDIENTS OF LIFE ?

L. Remusat [1]

Abstract. Carbonaceous chondrites are commonly considered as the most primitive meteorites and they accreted the primordial constituents of the Solar System. They are called "carbonaceous" due their high amount in extraterrestrial organic compounds. These compounds mainly formed 4.5 billion years ago by processes involving non-biologic chemical reactions, as shown by their isotopes. Among these molecules, several are considered as of biological interest because they could participate to processes equivalent to present day metabolic pathways in living cells; they include sugars, amino acids or nucleobases. These molecules being brought continuously on Earth, they may have induced the appearance of Life on Earth and/or could have an influence on the primitive forms of life.

Keywords: carbonaceous chondrites, organic molecules, astrobiology

1 Introduction

Carbonaceous chondrites are the witnesses of the formation of our solar system. They have trapped the remnants of the parent molecular cloud and the first components formed during the different phases of the solar system evolution. Since 4.56 Ga ago, they have preserved these constituents from the intense modifications that resulted from planet formation. However, almost all carbonaceous chondrites have undergone parent body processes. Due to the rapid decay of short lived radionucleides like ^{26}Al, the temperature increased up to partial melting on some parent bodies, inducing a thermal metamorphism (or fusion) of the accreted components. On others, when ice was present, the temperature increase generated a fluid circulation leading to hydrothermal alteration. During this hydrothermal alteration, accreted organic precursors may have reacted to produce new molecules. Pre-accretion chemistry (in the molecular cloud or the protosolar nebula) associated with parent body secondary processes resulted in a large diversity of the organic content of hydrated carbonaceous chondrites (Gilmour 2003). In contrast, on chondrites showing thermal metamorphism, the organic material has been carbonized and the soluble and reactive organic material is almost entirely lost (Remusat et al. 2008). Hence, only the organic content in hydrated objects will be described here.

It must be noted that there is no molecular evidence of any biological processes in the formation of these molecules. It is commonly accepted that all the extraterrestrial organic molecules are formed by non-biologic chemical reactions, and that any molecule with a biological signature is a contaminant (Anders et al. 1964). However, the organic content of carbonaceous chondrites may have influenced the prebiotic chemistry on the early Earth.

2 Diversity of organic compounds in meteorites

Organic matter in carbonaceous chondrites can be spread in an insoluble macromolecule (Derenne & Robert 2010) and a complex suite of soluble organic molecules (Krishnamurthy et al. 1992; Kvenvolden et al. 1970). The total organic content may reach 4 wt.% in some chondrites, with the macromolecular carbon representing more than 75wt.%. As recently shown (Schmitt-Kopplin et al. 2010), the soluble organic content in carbonaceous chondrites is very diverse. The use of very high mass resolution techniques revealed the occurrence of 14,000 different molecules, containing C, H, O, N and S. These molecules can be divided in several classes (see table 1), including sugar derivatives(Cooper et al. 2001), amino acids (Kvenvolden et al. 1970) and nucleobases (Martins et al. 2008) being potential metabolic reactants and genetic information recorders.

[1] Laboratoire de Minéralogie et Cosmochimie du Muséum, UMR CNRS 7202, Muséum National d'Histoire Naturelle, CP 52, 57 rue Cuvier, 75231 Paris Cedex 05, France. remusat@mnhn.fr

Table 1. Soluble organic compounds detected in Murchison and Tagish Lake, from Pizzarello et al. (2006).

Meteorite	Murchison		Tagish Lake	
Class	Concentration (ppm)	Compounds identified	Concentration (ppm)	Compounds identified
Aliphatic hydrocarbons	> 35	140	5	12
Aromatic hydrocarbons	15-28	87	> 1	13
Polar hydrocarbons	< 120	10	n.d.	2
Carboxylic acids	> 300	48	40	7
Amino acids	60	74	<0.1	4
Hydroxy acids	15	7	n.d.	n.d.
Dicarboxylic acids	> 30	17	17.5	18
Dicarboximides	> 50	2	5.5	9
Pyridine carboxylic acids	> 7	7	7.5	7
Sulfonic acids	67	4	> 20	1
Phosphonic acids	2	4	n.d.	n.d.
N-heterocycles	7	31	n.d.	n.d.
Amines	13	20	< 0.1	3
Amides	n.d.	27	<0.1	1
Polyols	30	19	n.d.	n.d.
Imino acids	n.d	10	n.d.	n.d.

Amino acids are emblematic organic compounds in meteorites. They are often cited as possible prebiotic molecules for the origin of life and are known to be indigenous in meteorites since the 70s (Kvenvolden et al. 1970; Lawless et al. 1972). To date, about 80 amino acids have been detected in CI, CM and CR chondrites; many of them have no terrestrial counterparts (Martins & Sephton 2009). Their abundance varies between meteorites from less than 1 ppm in some CI up to 250 ppm in some CR2 (Pizzarello & Holmes 2009). Amino acids in meteorites have from 2 to 8 carbon atoms; all the possible isomers are present. The distribution of amino acids differs from one meteorite to the other. For instance, in Murchison, glycine > α-amino-isobutyric acid > alanine, whereas in Orgueil β-alanine > glycine > γ-amino-butyric acid. Branched chains are more abundant than straight ones. Moreover, α, β and γ amino acids can be detected, with an abundance order α> $\gamma > \beta$.

3 Enantiomeric excess and possible origin of homochirality on Earth

The question of chirality will only be addressed through the amino acids, however, it has been suggested to also occur in the insoluble macromolecule (Kawasaki et al. 2006) and in hydroxy acids (Pizzarello et al. 2010). Amino acids in meteorites have been found to be racemic when they were firstly reported, leading to the unambiguous interpretation of their indigenity (Kvenvolden et al. 1970). Nevertheless, progresses in GC-MS and protocols for analysis of enantiomeric excess in the 80*s* allowed the report of small excess of the L-form of some amino acids in Murchison (Engel & Nagy 1982), though doubts about contaminations raised (Bada et al. 1983). The question of contamination was solved years later with the use of compound specific isotopic measurements of ^{13}C and ^{15}N (Engel & Macko 1997). This was further confirmed by the discovery of L-excess in non-protein chiral amino acids and in other meteorites (Cronin & Pizzarello 1997).

Enantiomeric excesses are variable among meteorites (Glavin & Dworkin 2009), and also inside the same objects (Pizzarello et al. 2003) but never exceed 18%. The hydrated meteorites exhibit higher excess, pointing to a possible amplification during aqueous alteration (Glavin & Dworkin 2009). The exact process by which this amplification would occur is unknown, but some chemical reactions, like the Soai reaction (Soai et al. 1995) exhibit the property to enhance enantiomeric excess. Nevertheless, some amino acids, like 2- and 3- amino-pentanoic acids for instance, are known to undergo racemization (i.e. chemical reaction resulting in a racemic or homogeneous distribution of the two enantiomers) under hydrothermal alteration. Parent body processes hence tend to complicate the picture by amplifying, for some amino acids, the asymmetry in the distribution and, in the meantime, erasing any inherited excess (from a preaccretional process) for some others.

The primordial origin of enantiomeric excess is also an opened question. Effect of UV circularly polarized light has been suggested to explain the observed excesses (Rubenstein et al. 1983). This hypothesis is being tested by laboratory experiments (Noorduin et al. 2009; Nuevo et al. 2006; Takano et al. 2007; Meierhenrich et al. 2010) but the source of the CPL at the vicinity of the early solar system still needs to be assessed. Other processes driven by chiral mineral surfaces (Fig. 1) have also been suggested to produce the enantiomeric excesses observed in carbonaceous chondrites (Glavin & Dworkin 2009). These enantiomeric excesses found in

organic matter in chondrites may have been transferred to prebiotic molecules at the moment of the emergence of Life by various processes, including asymmetric catalysis (Blackmond 2004). This would have led to the appearance of homochirality, a strong property of terrestrial forms of life. Such hypothesis is difficult to prove, although laboratory experiments involving for instance the Soai reaction (Soai et al. 1995) have succeeded in creating homochirality during non-biologic and purely chemical reactions.

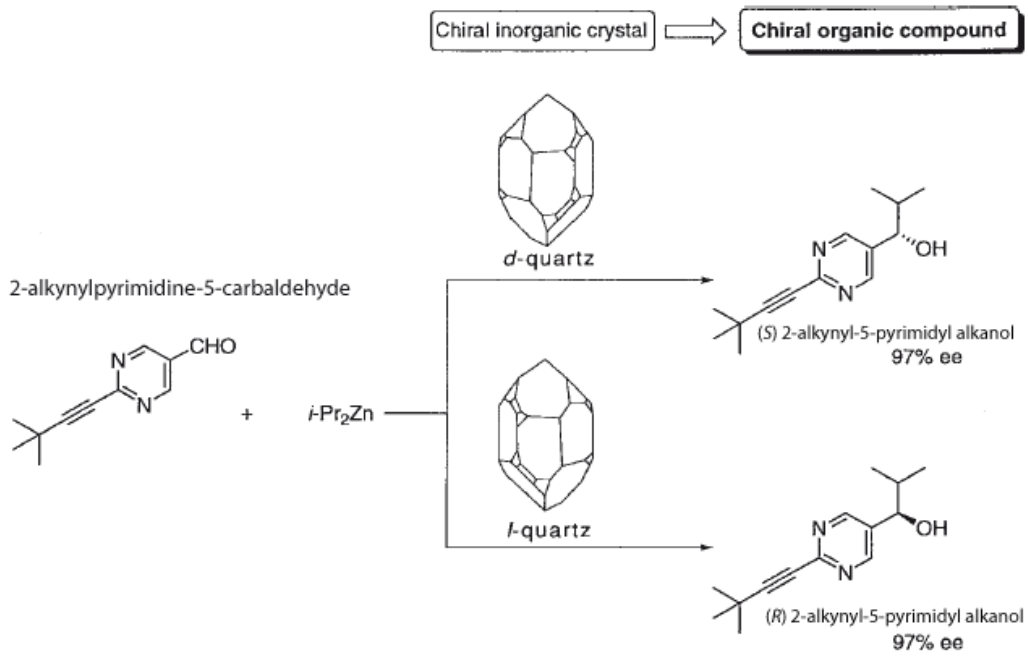

Fig. 1. Principle of the Soai reaction with the influence of a chiral inorganic mineral, from Soai et al. (2001)

4 Isotopic composition of soluble organic molecules in meteorites: understanding their origin

Organic molecules in carbonaceous chondrites are often enriched in heavy isotopes of C, N or H compared to their terrestrial counterparts. This has been used to discard contamination in many studies. Moreover, isotopic composition can be used to constrain the synthetic processes.

Amino acids constitute the best documented case for isotopic characterization in meteorites. In Murchison (Pizzarello et al. 2004), N isotopic composition seems homogeneous with $\delta^{15}N = 60$ ‰(compared to around 1‰in terrestrial proteins), whereas in the two CR2 LAP02342 and GRA95229, it is more heterogeneous and $\delta^{15}N$ ranges between 70 and 130 ‰(Pizzarello & Holmes 2009). $\delta^{13}C$ is variable (Pizzarello et al. 2004), with values ranging from -6 to +50‰(terrestrial values from -35 to -25‰). Amino acids are usually enriched in ^{13}C by 40‰compared to the other extraterrestrial soluble organic compounds except the carboxylic acids (Gilmour 2003). For C isotopes in α-amino acids, it must be noted that branched chains have higher ^{13}C content than straight ones; this may sign a secondary addition of the methyl groups. Moreover, $\delta^{13}C$ decreases with the carbon number; this has been interpreted as the result of a C addition process in the formation of the carbon chain. Amino acids have high δD, indicating low temperature chemistry during the formation of the carbon chain (Sandford et al. 2001). In Murchison Pizzarello & Huang (2005) reported δD up to 3500 ‰(i.e. $D/H=701\times10^{-6}$). Pizzarello & Holmes (2009) measured even higher values in GRA95229 (CR2 chondrite): $\delta D=$ 7245 ‰($D/H=1284\times10^{-6}$). Like for C isotopes, D distribution is heterogeneous among amino acids. There is no clear trend or correlation with any molecular parameter, indicating a complex origin for the extraterrestrial amino acids fraction. It must be noted that the 2-methyl amino acids and branched chains tend to have higher D/H than 2-H amino acids and straight chains.

The correlation between the distribution of amino acids and hydroxy acids has led to the suggestion that amino acids were synthesized by Strecker-cyanohydrin synthesis (Cronin et al. 1995). Indeed, this reaction can form, from aldehyde or ketone precursors, α-amino acids and α-hydroxy acids that will have parallel distribution. This reaction requires HCN and water as co-reactants. But this reaction can not produce the non α-amino acids

and other mechanisms like hydrolysis of lactams and Michael addition has been proposed to account for the β- and γ- amino acids (Cronin & Chang 1993). Molecular properties and isotopic ratios of both the insoluble macromolecule and the amino acids rule out an origin from the hydrolysis of the macromolecule (Remusat et al. 2005). Molecular and isotopic data on extraterrestrial amino acids thus indicate a complex origin for this fraction, with superimposition of preaccretion reactions and secondary processes. So far there is no simple mechanism adopted to explain the molecular distribution of amino acids or their isotopic compositions.

5 Conclusions

Carbonaceous chondrites contain a diverse suite of molecules that could constitute the seeds of life on Earth. However this remains debated and no laboratory experiment has proven that the organic content in chondrites could induce the emergence of life. It is nevertheless sure that the chondrites infall on the early Earth has released organic molecules in the prebiotic oceans. Interestingly, organic matter in chondrites may produce spheres (Deamer 1985) that could have helped the formation of the first cell membranes (Deamer et al. 2002). As shown in Figure 2, carbonaceous chondrites also contain hollow organic globules (Nakamura et al. 2002) that could be templates for the formation of the first chemical reactors that could have then evolved into living cells.

References

Anders, E., Dufresne, A., Fitch, F. W., et al. 1964, Science, 146, 1157

Bada, J. L., Cronin, J. R., Ho, M.-S., et al. 1983, Nature, 310, 494

Blackmond, D. G. 2004, Proc. Natl. Acad. Sci., 101, 5732

Cooper, G., Kimmich, N., Belisle, W., et al. 2001, Nature, 414, 879

Cronin, J. R. & Chang, S. 1993, in The chemistry of life's origins, ed. J. M. Greenberg & al. (Kluwer), 209

Cronin, J. R., Cooper, G. W., & Pizzarello, S. 1995, Adv. Sp. Res., 15, 91

Cronin, J. R. & Pizzarello, S. 1997, Science, 275, 951

Deamer, D., Dworkin, J. P., Sandford, S. A., Bernstein, M. P., & Allamandola, L. J. 2002, Astrobiology, 2, 371

Deamer, D. W. 1985, Nature, 317, 792

Derenne, S. & Robert, F. 2010, Met. & Planet. Sci., 45, 1461

Engel, M. H. & Macko, S. A. 1997, Nature, 389, 265

Engel, M. H. & Nagy, B. 1982, Nature, 296, 837

Garvie, L. A. J., Baumgardner, G., & Buseck, P. R. 2008, Met. & Planet. Sci., 43, 899

Gilmour, I. 2003, in Treatise on Geochemistry, ed. D. H. Heinrich & K. T. Karl (Pergamon), 269–290

Glavin, D. P. & Dworkin, J. P. 2009, Proc. Natl. Acad. Sci., 106, 5487

Kawasaki, T., Hatase, K., Fujii, Y., et al. 2006, Geochim. et Cosmochim. Acta, 70, 5395

Krishnamurthy, R. V., Epstein, S., Cronin, J. R., Pizzarello, S., & Yuen, G. U. 1992, Geochim.et Cosmochim. Acta, 56, 4045

Kvenvolden, K. A., Lawless, J., Pering, K., et al. 1970, Nature, 228, 923

Lawless, J., Kvenvolden, K. A., Peterson, E., Ponnamperuma, C., & Jarosewich, E. 1972, Nature, 236, 66

Martins, Z., Botta, O., Fogel, M. L., et al. 2008, Earth Planet. Sci. Let., 270, 130

Martins, Z. & Sephton, M. 2009, in Amino Acids, Peptides and Proteins in Organic Chemistry. Vol.1 - Origins and Synthesis of Amino Acids, ed. A. B. Hughes (Wiley), 3–42

Meierhenrich, U. J., Filippi, J. J., Meinert, C., et al. 2010, Chemistry & Biodiversity, 7, 1651

Nakamura, K., Zolensky, M. E., Tomita, S., Nakashima, S., & Tomeoka, K. 2002, Intern. J. Astrobio., 1, 179

Noorduin, W. L., Bode, A. A. C., van der Meijden, M., et al. 2009, Nature Chemistry, 1, 729

Nuevo, M., Meierhenrich, U. J., Caro, G. M. M., et al. 2006, A&A, 457, 741

Pizzarello, S., Cooper, G. W., & Flynn, G. J. 2006, in Meteorites and the Early Solar System II, ed. D. Lauretta & H. Y. McSween (Tucson, USA: University of Arizona Press), 625–651

Pizzarello, S. & Holmes, W. 2009, Geochim. et Cosmochim. Acta, 73, 2150

Pizzarello, S. & Huang, Y. 2005, Geochim. et Cosmochim. Acta, 69, 599

Pizzarello, S., Huang, Y., & Fuller, M. 2004, Geochim. et Cosmochim. Acta, 68, 4963

Pizzarello, S., Wang, Y., & Chaban, G. M. 2010, Geochim. et Cosmochim. Acta, 74, 6206

Pizzarello, S., Zolensky, M., & Turk, K. A. 2003, Geochim. et Cosmochim. Acta, 67, 1589

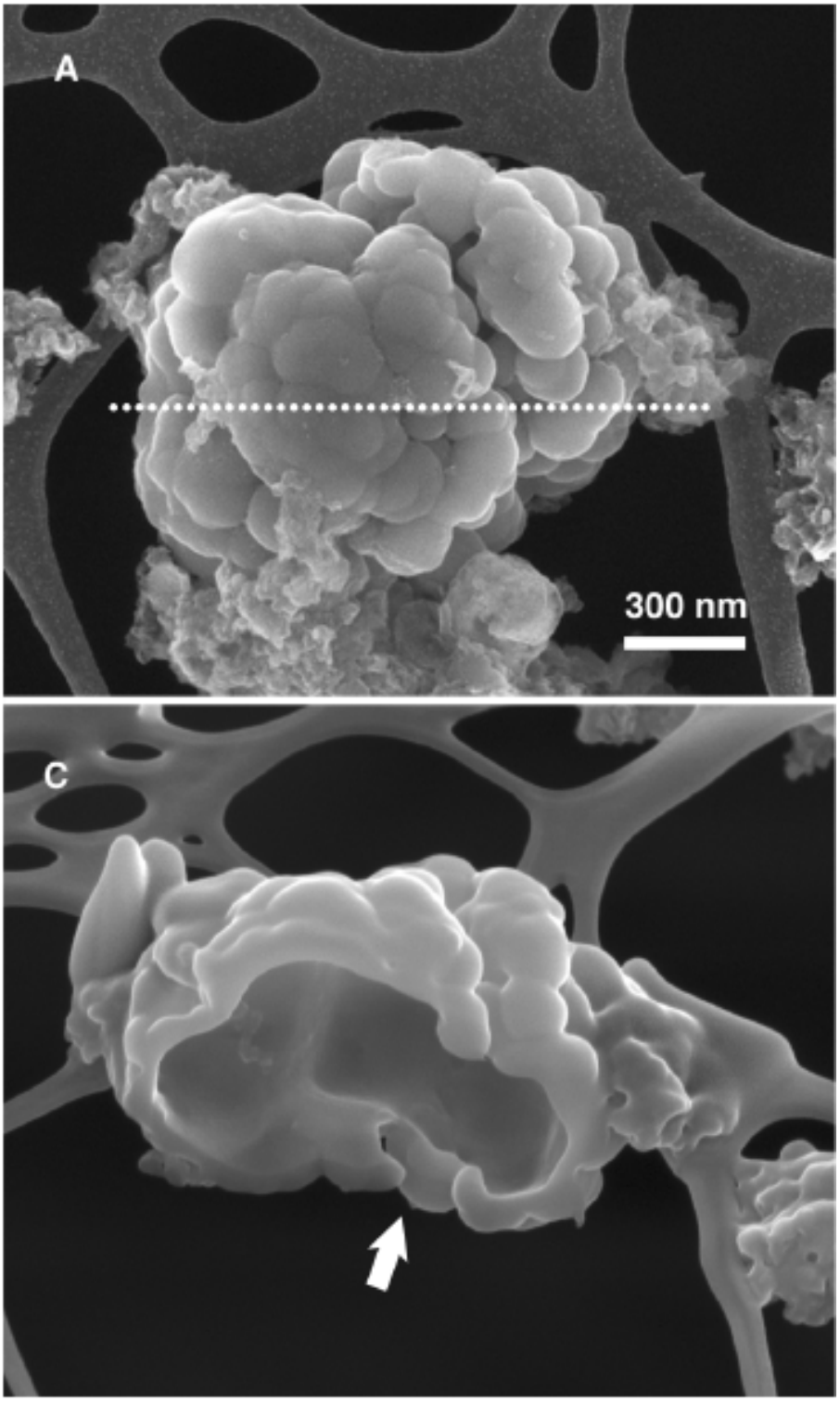

Fig. 2. Top: Image of nanoglobules found in carbonaceous chondrites, from Garvie et al. (2008). **Bottom:** cross section.

Remusat, L., Derenne, S., Robert, F., & Knicker, H. 2005, Geochim. et Cosmochim. Acta, 69, 3919
Remusat, L., Le Guillou, C., Rouzaud, J.-N., et al. 2008, Meteorit. & Planet. Sci., 43, 1099
Rubenstein, E., Bonner, W. A., Noyes, H. P., & Brown, G. S. 1983, Nature, 306, 118
Sandford, S., Bernstein, M. P., & Dworkin, J. P. 2001, Meteorit. & Planet. Sci., 36, 1117

Schmitt-Kopplin, P., Gabelica, Z., Gougeon, R., et al. 2010, Proc. Natl. Acad. Sci., 107, 2763
Soai, K., Sato, I., & Shibata, T. 2001, The Chemical Record, 1, 312
Soai, K., Shibata, T., Morioka, H., & Choji, K. 1995, Nature, 378, 767
Takano, Y., Takahashi, J., Kaneko, T., Marumo, K., & Kobayashi, K. 2007, Earth Planet. Sci. Let., 254, 106

Session 09

Plasma turbulence

SF2A 2012
S. Boissier, P. de Laverny, N. Nardetto, R. Samadi, D. Valls-Gabaud and H. Wozniak (eds)

COMPRESSIBLE TURBULENCE: A DIFFERENT PHYSICS ?

S. Banerjee[1] and S. Galtier[1]

Abstract. A possible phenomenological view is proposed for compressible hydrodynamic turbulence under isothermal closure. In the inertial zone a cascade for total energy is expected to take place due to the i) fluctuations transported by the fluid itself in subsonic case, leading to a -5/3 spectrum for density weighted turbulent velocity field ($\delta\rho^{1/3}\delta\mathbf{v}$) and ii) fluctuations transported by the sonic waves in the supersonic case, leading to a -2 spectrum for turbulent velocity field ($\delta\mathbf{v}$). A generalisation can be anticipated in polytropic case pursuing this given approach.

Keywords: Compressible, interstellar medium, phenomenology, solar wind, turbulence.

1 Introduction

Turbulence in compressible fluids (neutral or charged) is extremely complicated to be understood clearly (analtically or numerically). In astrophysics we have, however, the media like the solar plasma or the interstellar clouds which are (highly) compressible and turbulent (Elmegreen & Scalo 2004; Carbone 2012). It is therefore needed that the corresponding physics be governed by the compressible turbulence. The present article is prepared in order to give a complementary view with respect to our article of last year in this proceedings. While the article Galtier & Banerjee (2011a) presented the spectral aspects of compressible hydrodynamic turbulence (under isothermal condition) revealed from a derived exact relation (Galtier & Banerjee 2011b) and using Kolmogorov's phenomenology, here we shall try to understand those spectra by proposing a different phenomenology (of course the idea is underlying in the said exact relation) for three dimensional fully developped turbulence. For incompressible neutral fluids, turbulence is described by the phenomenology of Kolmogorov which is based on the famous concept of Richardson's energy cascade that takes place owing to the successive fragmentation of the fluid vortices (or eddies) to smaller vortices. In case of incompressible MHD fluids, the admitted phenomenology is based on the Alfvén effect where the scaling law (or the cascading of energy) is caused by the deformations of the fluctuating Alfvén modes due to sporadic interactions of two oppositely propagating fluctuating Alfvén modes. In the first case we expect a -5/3 energy (total or kinetic) spectrum (which is the famous Kolmogorov spectrum) and for the second case we predict a -3/2 energy spectrum (which is known as the Iroshnikov–Kraichnan spectrum). The situation becomes far more complicated for compressible turbulence. For neutral fluids, we can no more think of pure eddies as the compressible fluid velocity field is not solenoidal. Similarly, in case of compressible MHD turbulence, we have to abandon the idea of Alfvén effect because for compressible MHD fluids the linear wave modes consist of two compressional modes (magnetosonic waves) with Alfvén mode which is an incompressible mode. The only existing phenomenology for compressible case is using the Burger's equation which is a one-dimensional equation and predicts a -2 velocity (v^2) spectrum for supersonic turbulence (for neutral fluids) using the notion of shock formation (Frisch 1995). This phenomenology does not describe the subsonic regime. Recent numerical simulations (Kritsuk et al. 2007) predict a -5/3 spectrum for subsonic turbulence and a -2 spectrum for supersonic turbulence for three dimensional (3D) compressible isothermal turbulence. A satisfactory phenomenological description for 3D compressible fluid turbulence (and so for MHD) is yet to be developped. In the following section we shall give a possible phenomenological approach (without using directly the shock formation) for understanding the spectra of different regimes (subsonic and supersonic).

[1] Univ. Paris-Sud, Institut d'Astrophysique Spatiale, UMR 8617, bâtiment 121, F-91405 Orsay, France

2 Phenomenology for compressible hydrodynamic turbulence

We start with our derived exact relation which is written as

$$-2\varepsilon = \langle(\boldsymbol{\nabla}'\cdot\mathbf{v}')(\mathbf{R}-\mathbf{E})\rangle + \langle(\boldsymbol{\nabla}\cdot\mathbf{v})(\tilde{\mathbf{R}}-\mathbf{E}')\rangle + \boldsymbol{\nabla}_{\mathbf{r}}\cdot\left\langle\left[\frac{\delta(\rho\mathbf{v})\cdot\delta\mathbf{v}}{\mathbf{2}}+\delta\rho\delta\mathbf{e}-\mathbf{C_s^2}\bar{\delta}\rho\right]\delta\mathbf{v}+\bar{\delta}\mathbf{e}\delta(\rho\mathbf{v})\right\rangle, \quad (2.1)$$

the first two terms of right hand side present the source terms (exclusive for compressible turbulence) whereas the third one represents the flux term. We note that the source terms are having $(\nabla\cdot\mathbf{v})$ (or $\nabla'\cdot\mathbf{v}'$) as coefficient. Neglecting the dispersive effect of the flow field, we can show (by the basic equations) that $(\nabla\cdot\mathbf{v})$ propagates with a constant phase velocity C_S (sound speed in the corresponding turbulent medium). The source terms can then be written as

$$S(r)\sim\left\langle(\nabla\cdot\mathbf{v})(\frac{\mathbf{1}}{\mathbf{2}}\rho'\mathbf{v}'.\delta\mathbf{v})\right\rangle\sim\langle(\nabla\cdot\delta\mathbf{v})(\rho'\mathbf{v}'.\delta\mathbf{v})\rangle\,. \quad (2.2)$$

We can remark that in the flux terms the energy density fluctuations are transported by the fluid velocity fluctuations (represented by the $\frac{1}{2}[\delta(\rho\mathbf{v}).\delta\mathbf{v}]\delta\mathbf{v}]$ term) whereas the source terms represent the transport of the scalar $(\rho\mathbf{v}\cdot\delta\mathbf{v})$ by $(\nabla\cdot\mathbf{v})$ where the fluctuating quantity is $\delta\mathbf{v}$.

In describing a possible phenomenology for isothermal compressible hydrodynamic turbulence we use the following points:

i) For a given length scale l, there is a competition between the flux and the source terms regarding the transport of their respective fluctuating scalars (as defined above) between two points separated by l.

ii) Considering turbulence to be a phenomenon without memory, the transport which will cover the distance l later (i.e. with a greater characteristic time) will determine the characteristic non-linear energy transfer time for that length scale l.

iii) In this case, we can define two characteristic times $\tau_l(=l/v_l)$ and $\tau_C(=l/C_S)$ where $v_l\sim\mid\delta\mathbf{v}\mid$.

iv) We assume that the time rate of average total energy is a scale invariant.

2.1 *Subsonic turbulence* $(\delta v < C_S)$*:*

In this case, the transport by flux terms, being slower of the two, governs the effective energy transfer and so the characteristic time is given by $\tau_{NL}=\tau_l$. The source terms during that time cover a longer distance $l_C=\tau_l C_S$ and so is forgotten by the receiver point of our concern. This consideration leads to the following dimensional analysis

$$\text{flux}\sim\varepsilon\Rightarrow\frac{\rho_{\mathrm{l}}\mathrm{v}_{\mathrm{l}}^3}{\mathrm{l}}\sim\varepsilon\Rightarrow\mathrm{E_w(k)}\sim\varepsilon^{2/3}\mathrm{k}^{-5/3}\,, \quad (2.3)$$

where $w\equiv\rho^{1/3}v$ (Kritsuk et al. 2007; Federrath et al. 2010).

2.2 *Supersonic turbulence* $(\delta v > C_S)$*:*

In this case, the source terms being slower govern the inter-scale energy transfer of the system and the characteristic time is $\tau_{NL}=\tau_C$. Utilising the exact relation we find

$$\text{source}\sim\varepsilon\Rightarrow(\rho\mathrm{v})\frac{\mathrm{v}_{\mathrm{l}}^2}{\mathrm{l}}\sim\varepsilon\Rightarrow\mathrm{E_v(k)}\sim\varepsilon\mathrm{k}^{-2}\,, \quad (2.4)$$

as seen in some simulations (Federrath et al. 2010).

2.3 *Sonic scale* $(\delta v = C_S)$*:*

In this scale $v_l=C_S$. So the characteristic times are also equal. As it is a given scale (k given), we cannot expect a power law for that. But evaluating properly the $E_w(k)$ and $E_v(k)$ and then equalising them for $l=l_s$ we can estimate the sonic scale (l_s).

Schematically, hence we can write the compressible turbulence phenomenology as follows $(M_S\equiv v_l/C_S)$

$$\varepsilon\sim\left\{\frac{\rho_l v_l^3}{l},\frac{M_S}{\tau_C}(\rho v)v_l\right\}, \quad (2.5)$$

where the two expressions represent the average energy transfer rate respectively in the subsonic and the supersonic regime of compressible hydrodynamic turbulence.

3 Conclusions

The above phenomenology gives a possible description of compressible hydrodynamic turbulence under isothermal closure. The above approach however leaves some open questions which need to be answered for a thorough comprehension of compressible turbulence:

i) Does the total energy (kinetic energy + compressible energy) flux rate remain scale invariant in compressible case ?

ii) Are the one point quantities like (ρv) or $(\rho' v')$ come to be really inert (as we considered in our approach) in the dimension analysis for the fluctuating (or turbulent) quantities ?

iii) As reported recently by Wagner et al. (2012) that for compressible turbulence the existence and range of the inertial zone is dependent on the forcing criteria. Is the universality destroyed due to this problem ?

One can anyways attempt to give an analogical view as that of the above for polytropic closures (which is more realistic for astrophysical context) where the complexity increases considerably. In case of compressible MHD fluids, one can intuitively understand the degree of complexity depending upon the possible regimes which associates the subalfvénic and superalfvénic regimes too in addition to the subsonic and supersonic regimes. It is however expected that the recent numerical simulations (Kritsuk et al. 2009) along with a recent derived exact relation in compressible MHD turbulence (Banerjee & Galtier 2012) will help us to obtain a clearer view for the corresponding phenomenology.

References

Banerjee, S. & Galtier, S. 2012, in preparation

Carbone, V. 2012, Space Sci. Review, online first

Elmegreen, B.G. & and Scalo, J. 2004, Annu. Rev. Astron. Astrophys., 42, 211

Federrath, C. et al. 2010, Astron. Astrophys., 512, A81

Frisch, U. 1995, Turbulence: the legacy of A.N. Kolmogorov (Cambridge Univ. Press, Cambridge)

Galtier, S. & Banerjee, S. 2011a, SF2A 2011, "Scientific Highlights", Alecian et al. Eds, 379

Galtier, S. & Banerjee, S. 2011b, Phys. Rev. Lett., 107, 134501

Kritsuk, A.G., Norman, M.L., Padoan, P. & Wagner, R. 2007, Astrophys. J., 665, 416

Kritsuk, A.G., Ustyugov, S.D., Norman, M.L. & Padoan, P. 2009, ASP Conf. Series, 406, 15

Wagner, R., Falkovich, G., Kritsuk, A.G. & Norman, M.L. 2012, JFM, in press.

SF2A 2012
S. Boissier, P. de Laverny, N. Nardetto, R. Samadi, D. Valls-Gabaud and H. Wozniak (eds)

ON THE ROLE OF ALFVÉN WAVES AS PRECURSORS OF QUASI-STATIC ACCELERATION PROCESSES IN THE EARTH AURORAL ZONE

F. Mottez[1]

Abstract. In the Earth auroral zone, the electron acceleration by Alfvén waves is sometimes a precursor of the non-propagating acceleration structures. In order to investigate how Alfvén waves could generate non-propagating electric fields, a series of simulations of counter-propagating waves in a uniform plasma is presented. The waves (initially not configured to accelerate particles) propagate along the ambient magnetic field direction. It is shown that non propagating electric fields are generated at the locus of the Alfvén waves crossing. These electric fields have a component orientated along the direction of the ambient magnetic field, and they generate acceleration and a significant perturbation of the plasma density. The non-linear interaction of down and up-going Alfvén waves might be a cause of plasma density fluctuations (with gradients along the magnetic field) on a scale comparable to those of the Alfvén wavelengths.

Keywords: auroras, Alfvén waves, acceleration, inverted V, plasma cavities

1 Introduction

An auroral substorm is an abrupt increase in night-side auroral power. The largest part of the electron acceleration that triggers the auroras happens at a few thousands of kilometres above the ionosphere. Two main families of acceleration processes have been identified: those associated to quasi-static electric fields called *strong double layers*, and those associated to Alfvén wave electric fields (see Mottez 2012b, for a review on the role of the Alfvén waves). The acceleration by quasistatic, and basically non-propagating, electric fields such as double layers produces mono-energetic beams of electrons, while those by Alfvén waves are associated to broadband energy distributions. Recent observations show that these two families of processes are not independent from each other.

Evidences of acceleration structures emanating from Alfvén waves are given by the direct observation of the parallel electric field (parallel to the mean direction of the magnetic field) (Chust et al. 1998; Chaston et al. 2007) or by the estimate of the wave Poynting flux (Louarn et al. 1994; Volwerk et al. 1996; Keiling et al. 2000).

Several papers suggest that Alfvénic processes might act as the precursors of quasi-static non-propagating acceleration structures (Zou et al. 2010; Newell et al. 2010; Hull et al. 2010).

This paper summaries a series of numerical simulations that investigate the interaction of down-going incident Alfvén waves with up-going Alfvén waves reflected on the ionosphere. Their ability to create parallel stationary electric fields is questioned, as well as to prepare the auroral plasma before the setting of the acceleration processes.

In ideal MHD, Alfvén waves do not carry a parallel electric field. Therefore, they cannot accelerate auroral electrons. It has been shown in previous studies (Hasegawa & Chen 1975; Goertz 1984) that Alfvén waves with an oblique wave vector induce an electric field with a component parallel to the ambient magnetic field. In the present study, we don't suppose that the Alfvén waves are already accelerating the plasma. As the origin of their small transverse scales is not trivial, it is more careful, for the generality and the simplicity of the initial condition to neglect the presence of small transverse scale associated to the Alfvén waves.

Because of the simple setting of the simulations, the present study cannot pretend to bring any conclusion on the large scale structure of the auroral zone. For instance, we cannot involve the large scale density and magnetic field dependence with altitude, net potential drops on large scales, etc. This paper focuses on an explanation

[1] LUTH, Observatoire de Paris, CNRS, Université Paris Diderot, 91190 Meudon, France

of the physical process observed in the simulations that are in the range of "microphysics", when compared to magnetospheric scales. Nevertheless, its potential relevance to auroral physics is the main motivation of this work.

Let us notice already that we make a distinction between the X component of a vector (parallel to the ambient -and uniform- magnetic field) and its x component, that is parallel to the local value of the magnetic field. (The reason is explained in Section 4.)

2 Numerical method and simulation parameters

As in Génot et al. (2000); Génot et al. (2001); Génot et al. (2004); Mottez & Génot (2011), dedicated to the physics of auroral Alfvén waves, the numerical simulations are made with a EGC (Electron Guiding Center) electromagnetic PIC code that takes into account the motion of the electron guiding center, and the full ion motion. The boundary conditions are periodic. A complete description of this code is given in Mottez et al. (1998). The method of initalisation of the Alfvén waves is provided in Mottez (2008), and the method for the wave packets in Mottez (2012a)

The physical variables are reduced to dimensionless variables. Time and frequencies are normalized by the electron plasma frequency ω_{p0} that correspond to a reference background electron density n_0. Velocities are normalized to the speed of light c, and the magnetic field is given in terms of the dimensionless electron gyrofrequency ω_{ce}/ω_{p0}. The mass unit is the electron mass m_e. Therefore, the units (starting from the Maxwell Eq. in the MKSA system) are c/ω_{p0} for distances, ω_{p0}/c for wave vectors, e for charges, en_0 for the charge density, $c\omega_{ce}/\omega_{p0}$ for the electric field. In the following parts of this paper, all the numerical values and figures are expressed in this system of units.

3 Simulations

The left-hand side of Fig.1 shows the magnetic field B_Z of two wave packets that propagate in opposite direction. The field B_Z is a good proxy of the wave packets positions. We can see that they cross each other at $x \sim 120$ and their intersection starts at $t = 200$. The right-hand side of Fig 1 shows the parallel electric E_X field associated to the same wave packets. The alternating fine horizontal lines are associated to the plasma oscillations that are present in any plasmas (their frequency is ω_{p0}). Apart from the plasma waves, we can see that, as predicted by MHD laws, E_X is (almost) null before the intersection. But during the wave packets crossing, it is strongly enhanced. After the intersection, with a small delay, E_X becomes null again. In order to investigate this phenomenons, the problem has been simplified agin. Instead of two wave packets, the crossing of two sinusoidal waves has been studied. The resulting parallel electric field E_X is shown on Fig. 2. Here again, we can see the plasma waves, but also a time independent structure. Because it is present at the start of the simulation, it is not the consequence of an instability (it would not grow instantaneously). Actually, with the two monochromatic waves, the waves interaction starts at the beginning of the simulation since the two waves are present everywhere with the same intensity.

4 How the parallel electric field sets

An analysis of the properties of E_X was conducted in Mottez (2012a), and an explanation was provided. First, it was shown that the intensity of the field is proportional to the product of the intensity of the two sinusoidal waves. Then, it was shown that E_X is always independent of time but dependent on X, or independent of X and dependent on time. Then, it was shown that there is no critical value for this phenomenon to appear, it occurs also with low intensity waves, until it is below the noise level. We also projected the electric field along the local and instantaneous direction x of the magnetic field (that is not uniform because of the perturbation δB_1 and δB_2 of the two waves). We found that $E_x = 0$. Then, it was shown that it could be explained in the following way. The electric field is assumed to be perpendicular to the direction of the local magnetic field: $\mathbf{E} \cdot \mathbf{B} = \mathbf{0}$. This property is true in the linear theory, it is generalized to non-linear interactions (Knudsen 1996; Tsiklauri 2007). Therefore, $E_x = 0$, and the projection of the resulting electric field on the X axis can be derived. This derivation (provided in Mottez (2012b)) depends on the polarization of each wave (righ-handed of left-handed circular polarization). It appears that E_X depends of products of E_1E_2, of E_1^2 and of E_2^2 where E_1 and E_2 are the amplitudes (set initially) of the two waves. A second hypothesis is made at this time: we consider that the rule $\mathbf{E} \cdot \mathbf{B} = \mathbf{0}$ is true as long as it concerns the interaction of two different waves, but not

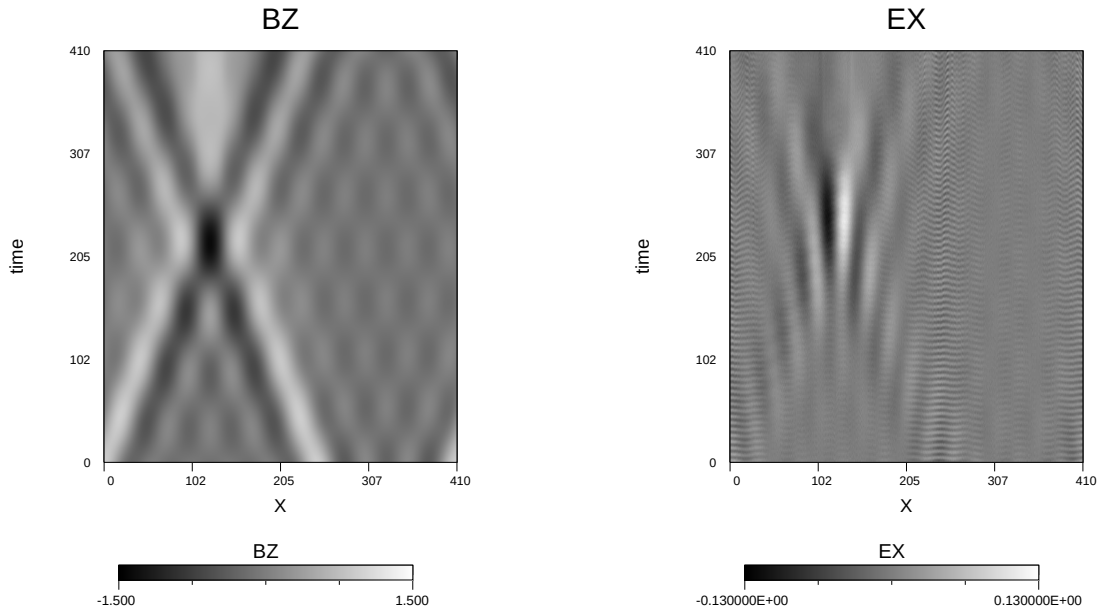

Fig. 1. Plots of electromagnetic field components as a function of position X (horizontal axis) and time t (vertical axis). **Left:** The magnetic field B_Z associated to two wave packets that propagate in opposite direction. **Right:** the parallel electric field E_X associated to the same wave packets.

of a wave with itself. (Why ? This point still needs to be clarified.) Then, in the expression of E_X, only the terms proportional to $E_1 E_2$ are kept. They perfectly match the properties found in the simulations analysis, according to the various choices of amplitudes, directions of propagation and polarisations.

5 Particle acceleration and relevance to auroral physics

The previous analysis shows that the various waves that contribute to a wave packet also interact and they contribute to a parallel electric field (even for a single wave packet). This is why E_X is not strictly null at the begining of the simulation. Figure 2 shows the phase space of the electrons at three different times in the same simulation as for Fig. 1. We can see that there is initially a perturbation of the parallel velocity of the electron associated to the initial parallel field E_X.

More interestingly, we can see that after the wave crossing, the parallel velocity is *locally* strongly enhanced, and this enhancement lasts well after the wave packets crossing, contrarily to the field E_X. This electron distribution in the phase space presents interesting similarities with those of a newly settle *strong double layer* (localized strong acceleration, well above the thermal level, with a shift of the bulk electron distribution without heating, thus ready to provide quasi mono-energetic electron beams). This is interesting, because as it was said in the introduction, these electrostatic structures (strong double layers) dominate the auroral acceleration after the phase of the Alfvénic processes.

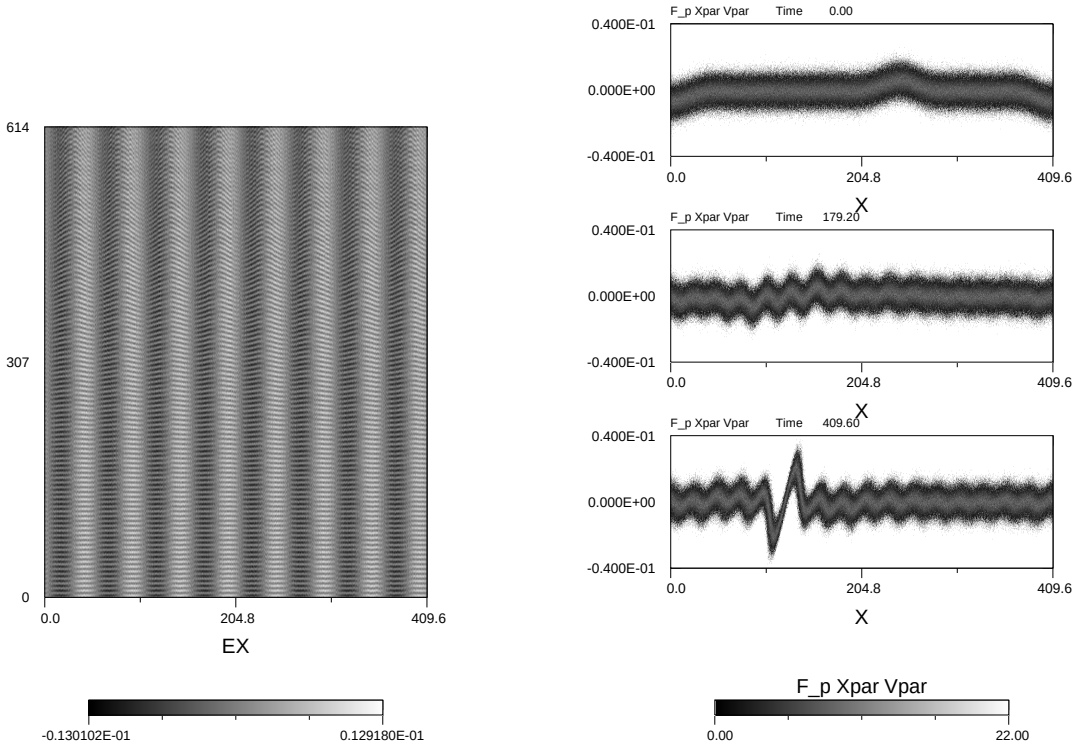

Fig. 2. Left: The parallel electric field $E_X(X,t)$ associated to a pair of monochromatic Alfvén waves that propagate in opposite directions. (Same axis as for Fig. 1). **Right:** The electron phase space density for the same simulation as for Fig. 1. The horizontal axis represents the direction X (it is parallel to the ambient magnetic field), the vertical axis represents the parallel electron velocity V_X and the grey scale is the electron density in that space.

6 Conclusion

Two Alfvén wave packets crossing each other generate an electric field in a direction X that is parallel to the average ambient magnetic field. This can be explained if we consider that the two waves interact in a way that let the wave electric field and the total magnetic field perpendicular to each other. This is a non-linear wave-wave interaction whose intensity is characterized by the intensity of each wave. The electric field E_X is favourable to electron acceleration, and the phase-space distribution of the electron keeps a signature of the two waves interaction well after the waves crossing has occurred. The influence of the accelerated electron will be the object of a further study.

The simulations presented here may provide important clues explaining the transition from the Alfvénic to the electrostatic auroral acceleration processes mentioned in the introduction.

References

Chaston, C. C., Hull, A. J., Bonnell, J. W., et al. 2007, J. Geophys. Res. (Space Physics), 112, A05215

Chust, T., Louarn, P., Volwerk, M., et al. 1998, J. Geophys. Res. (Space Physics), 103, 215

Génot, V., Louarn, P., & Mottez, F. 2000, J. Geophys. Res. (Space Physics), 105, 27611

Génot, V., Louarn, P., & Mottez, F. 2004, Annales Geophysicæ, 6, 2081

Génot, V., Mottez, F., & Louarn, P. 2001, Physics and Chemistry of the Earth C, 26, 219

Goertz, C. K. 1984, Planetary and Space Sciences, 32, 1387

Hasegawa, A. & Chen, L. 1975, Physical Review Letters, 35, 370

Hull, A. J., Wilber, M., Chaston, C. C., et al. 2010, J. Geophys. Res. (Space Physics), 115, 6211

Keiling, A., Wygant, J. R., Cattell, C., et al. 2000, Geophysical Research Letters, 27, 3169

Knudsen, D. J. 1996, J. Geophys. Res. (Space Physics), 10, 761

Louarn, P., Wahlund, J. E., Chust, T., et al. 1994, Geophys. Res. Lett., 21, 1847

Mottez, F. 2008, Journal of Computational Physics, 227, 3260

Mottez, F. 2012a, Annales Geophysicæ, 30, 81

Mottez, F. 2012b, Proceedings of "Waves and Instabilities in Space and Astrophysical Plasmas" (WISAP) Eilat, Israel, June 19th - June 24th, 2011

Mottez, F., Adam, J. C., & Heron, A. 1998, Computer Physics Communications, 113, 109

Mottez, F. & Génot, V. 2011, J. Geophys. Res., 116, A00K15

Newell, P. T., Lee, A. R., Liou, K., et al. 2010, J. Geophys. Res. (Space Physics), 115, 9226

Tsiklauri, D. 2007, New Journal of Physics, 9, 262

Volwerk, M., Louarn, P., Chust, T., et al. 1996, J. Geophys. Res. (Space Physics), 101, 13335

Zou, S., Moldwin, M. B., Lyons, L. R., et al. 2010, J. Geophys. Res. (Space Physics), 115, 12309

Session 10

Stellar physics (PNPS)

SF2A 2012
S. Boissier, P. de Laverny, N. Nardetto, R. Samadi, D. Valls-Gabaud and H. Wozniak (eds)

3D SIMULATIONS OF INTERNAL GRAVITY WAVES IN STELLAR INTERIORS

L. Alvan[1], A. S. Brun[1] and S. Mathis[1]

Abstract. We investigate the excitation and propagation of internal gravity waves by penetrative convective plumes using the 3D anelastic simulation code ASH. The study of the waves' properties is of high importance for helio- and asteroseismology and to understand how waves transport angular momentum and may establish the observed rotation profile of the solar radiative zone. After illustrating basic properties of g-modes in terms of simple ray-theory, we show that the rich field of gravity waves obtained with our 3D model is in good agreement with theoretical predictions concerning the period spacing of g-modes.

Keywords: Stars, Turbulence, Waves, Methods : Numerical

1 Introduction

Internal gravity waves (IGWs) are essential for helio- and asteroseismology to probe stellar interiors (e.g. Garcia et al. 2007). Moreover, they are of great interest in the study of angular momentum transport over large distances (Rogers & Glatzmaier 2005) and constitute an important ingredient in understanding the evolution of stellar rotation (Zahn et al. 1997; Charbonnel & Talon 2005; Mathis 2009). We here present new results obtained with the Anelastic Spherical Harmonic (ASH) code (Brun et al. 2004). Our model nonlinearly couples the convective envelope to the stable radiative interior of the Sun (Brun et al. 2011), assuming a realistic solar stratification from $r = 0.07R_\odot$ up to $0.97R_\odot$ (Brun et al. 2002). The pummeling of convective plumes at the top of the radiative zone generates perturbations which propagate in the stably stratified zone. We show that these perturbations have the characteristics of IGWs predicted by linear theory.

2 Raytracing

IGWs propagate in the solar radiative zone under the condition $\omega < N$ where ω is the waves frequency and N the Brunt-Väisälä frequency, plotted in the left panel of Fig. 1 and given by

$$N^2 = -\bar{g}\left[\frac{1}{\bar{\rho}}\frac{\partial\bar{\rho}}{\partial r} - \frac{1}{\Gamma_1\bar{p}}\frac{\partial\bar{p}}{\partial r}\right], \tag{2.1}$$

with $\bar{g}$ the mean gravity, Γ_1 the adiabatic exponent, $\bar{\rho}$ and $\bar{p}$ the mean density and pressure. The region where IGWs propagate is visible in the right panel of Fig. 1, where we have represented the path of propagation of two g-modes, using the linear dispersion relation (e.g. Christensen-Dalsgaard 2003) :

$$\begin{cases} k_r^2 = \dfrac{l(l+1)}{r^2}\left(\dfrac{N^2}{\omega^2} - 1\right), \\ k_h^2 = \dfrac{l(l+1)}{r^2}, \end{cases} \tag{2.2}$$

where l is the spherical harmonic degree and k_r and k_h the vertical and horizontal wave numbers in the WKB approximation. Oscillations are trapped in the radiative zone, between concentric spheres of radius r_1 and r_2 such as $\omega = N(r_1) = N(r_2)$.

[1] Laboratoire AIM, CEA/DSM-CNRS-Université Paris Diderot, IRFU/SAp, F-91191 Gif-sur-Yvette Cedex, France; lucie.alvan@cea.fr, allan-sacha.brun@cea.fr, stephane.mathis@cea.fr

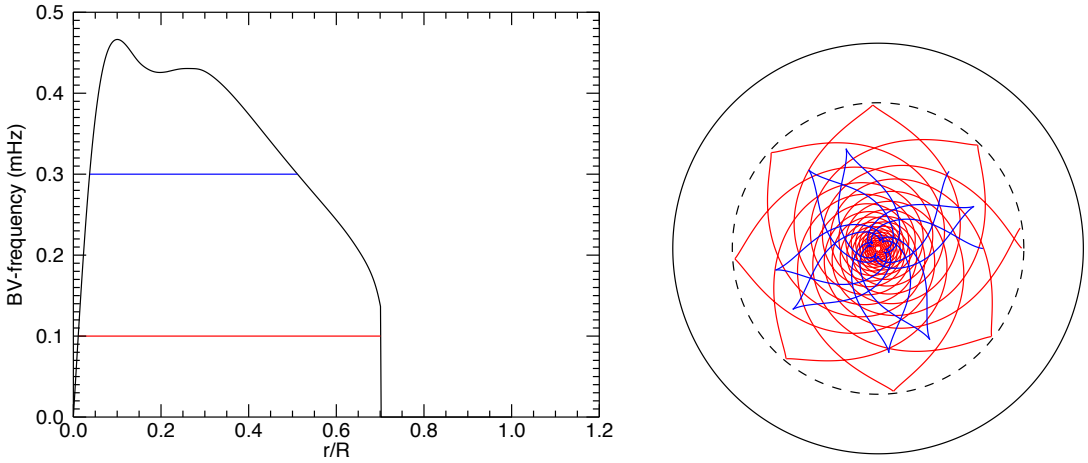

Fig. 1. Left: Radial profile of the Brunt-Väisälä frequency in the 1D solar model (Brun et al. 2002) taken as reference state for our 3D simulation (§3). The horizontal blue (resp. red) line indicates the trapping region for a g-mode with frequency $\omega = 0.3$ mHz (resp. $\omega = 0.1$ mHz). **Right:** Raypaths of gravity waves in the Sun. Waves undergo total refraction at the points where $\omega = N$. The dashed circle represents the base of the convective zone. The rays correspond to modes with frequency of 0.1 mHz (red) and 0.3 mHz (blue).

3 3D simulation

Following the work of Brun et al. (2011), we have developped a numerical 3D model of the sun coupling the convective zone with the radiative interior. As we want to focus on the propagtion of IGWs, we have chosen for this new model a lower thermal diffusivity coefficient κ. The expected effect is to decrease the radiative damping of the waves, adapted from Zahn et al. (1997) :

$$\tau_{l,m}(r) = [l(l+1)]^{3/2} \int_r^{r_c} \kappa(1+\mathrm{Pr}) \frac{N^3(r')}{[\omega + m(\Omega(r') - \Omega_c)]^4} \frac{\mathrm{d}r'}{r'^3}, \tag{3.1}$$

with $\mathrm{Pr} = \nu/\kappa$ the Prandtl number, ν the viscosity coefficient and $\Omega(r')$ and Ω_c the mean horizontally averaged angular velocity at the point r' and at the basis of the convective zone. Figure 2 shows that the amplitude of

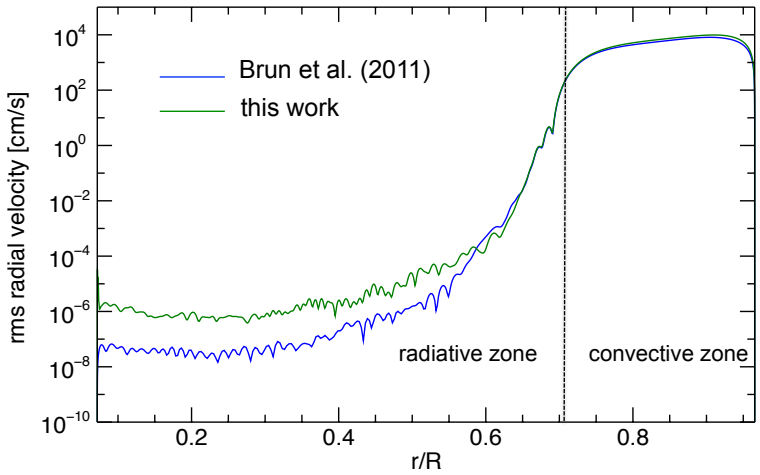

Fig. 2. Root mean square (rms) velocity as a function of the normalized radius for both models. The consequence of decreasing κ is clearly visible.

waves is indeed less attenuated in this work than in Brun et al. (2011) and hence less subject to numerical noise.

Figure 3 shows the actual displacement associated to the waves in the radiative zone. In both panels, the radial velocity v_r/v_{rms} is represented, where v_{rms} is the root mean square radial velocity at each radius. Dark blue tones (resp. red) denote downflows (resp. upflows). We clearly distinguish two regimes : a wave like pattern in the radiative zone and a large scale convection with up- and downflows in the outer convective envelope. The left panel shows phase fronts moving radially outward, which is a signature of gravity wave packets whose vertical group velocity is inward and phase velocity is outward. In the convective zone, we also note the moderate tilt of downflow lanes by the differential rotation in radius and latitude.

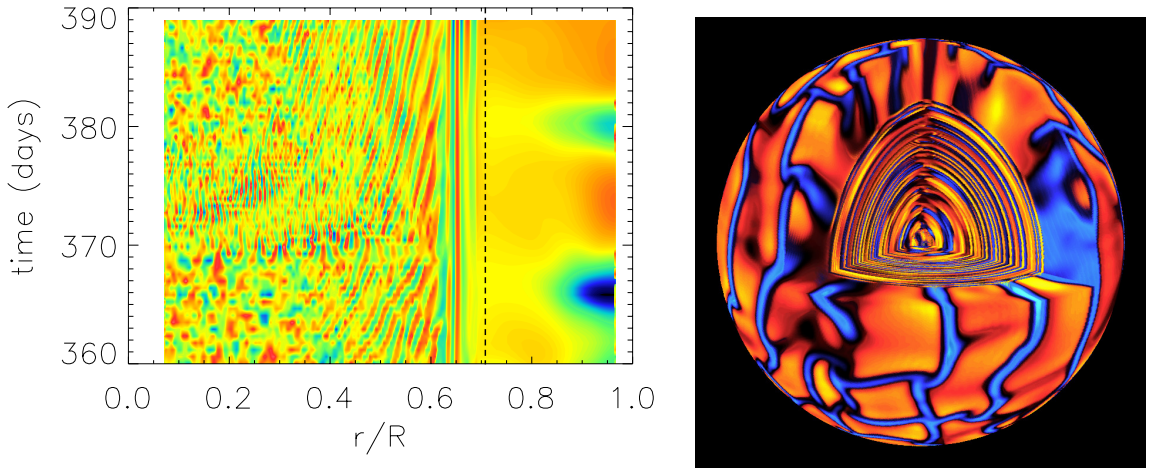

Fig. 3. Left: Radial velocity v_r/v_{rms} as a function of normalized radius and time. Dashed line mark the limit between radiative and convective zones according to the Schwarzschild criteria. **Right:** 3D rendering. An octant has been removed in order to visualize the structure within the meridional and the equatorial planes.

4 Power spectra

To study the properties of the waves in the frequential domain, we calculate the power spectrum by computing a Spherical Harmonic transform followed by a temporal Fourier transform of the waves radial velocity. Thus, we can isolate one particuliar mode (l,m). Figure 4 shows the power spectrum obtained for (l=1,m=0) and (l=2,m=0). The normalized power is plotted as function of frequency (left) and period (right). From a theoretical point of view, the frequencies of g-modes are determined for the Bore quantization rule (e.g. Kosovichev 2011):

$$\int_{r_1}^{r_2} k_r \, \mathrm{d}r = \pi(n + \alpha), \tag{4.1}$$

where r_1 and r_2 are the radii of the inner and outer turning points where $k_r = 0$, n is the radial order (integer number) and α is a phase shift which depends on the properties of the reflecting boundaries. Far from the turning points ($N \gg \omega$),

$$k_r \approx \frac{\sqrt{l(l+1)}}{r} \frac{N}{\omega}, \tag{4.2}$$

and in the asymptotic limit $n \gg l$, Gough (1993) shows that the spectrum of g modes is approximately equidistant with the period spacing

$$(\Delta \mathrm{P})_l = \frac{\pi}{\sqrt{l(l+1)} \int_{r_{\mathrm{bot}}}^{r_{\mathrm{top}}} \frac{N}{r} \, \mathrm{d}r}, \tag{4.3}$$

r_{bot} and r_{top} being the lower and upper boundaries of the radiative zone. Since we are not yet able to deal with the singularity in $r = 0$, the inner boundary of our computational domain is $r_{bot} \approx 0.07 R_\odot$. The outer boundary is $r_{top} \approx 0.71 R_\odot$. Comparing the value of $(\Delta \mathrm{P})_l$ given by Eq. (4.3) with the one measured in Fig. 4, we obtain a qualitative agreement summerized in Tab. 1.

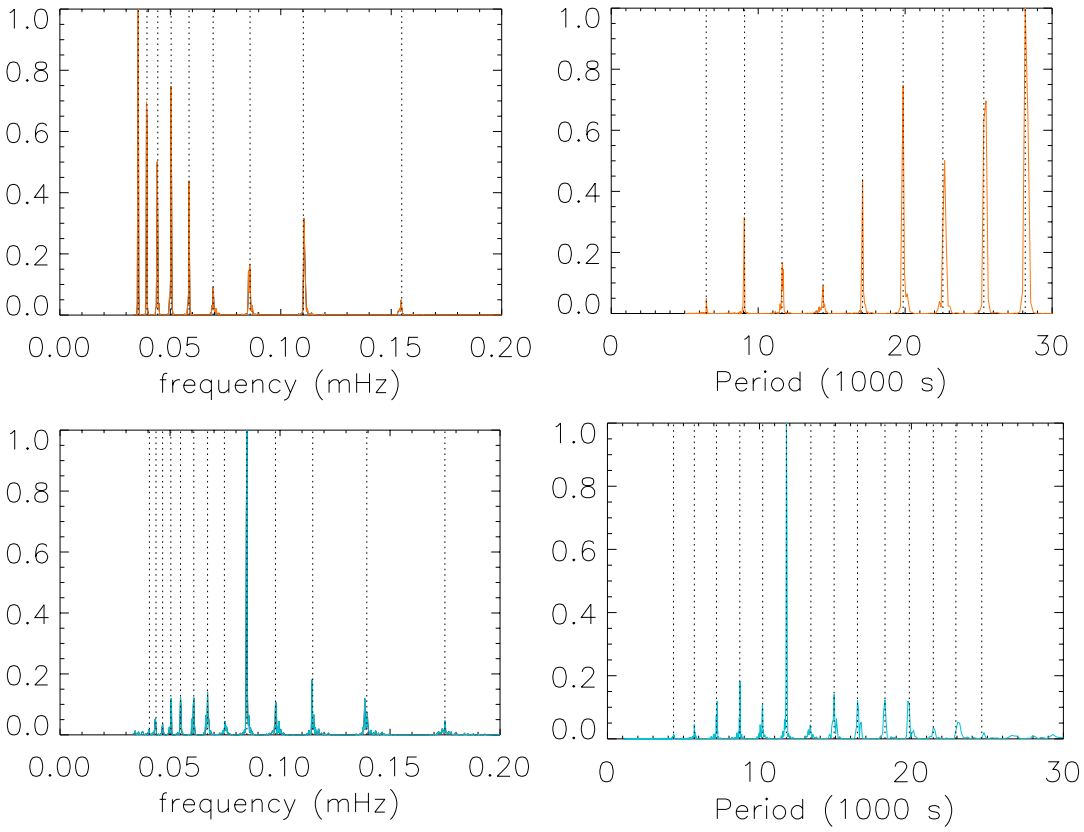

Fig. 4. Power spectra of the radial velocity for the modes (l=1,m=0) (orange) and (l=2,m=0) (blue). Vertical dashed lines mark the spacing between peaks.

Table 1. Comparison between $(\Delta P)_l$ given by Eq. (4.3) and $(\Delta P)_l$ from simulated data.

(l,m)	$(\Delta P)_l$ from Eq. (4.3)	$(\Delta P)_l$ from simulation
(1,0)	2410 s	2713 ± 96 s
(2,0)	1391 s	1560 ± 111 s

According to Eq. (4.1) and (4.2), we have

$$\omega \propto \int_{r_{\rm bot}}^{r_{\rm top}} \frac{N}{r}. \tag{4.4}$$

Since the central cut-off modifies the cavity by 10% in radius, it induces a frequency change of about 37% (due to the large area of the integral near the center). Work is in progress to model full sphere 3D solar models with our new ASH-FD code in order to improve our ability of modeling IGWs.

5 Conclusions

We here open a large field of investigation concerning detailed analysis of IGWs in 3D non-linear dynamical simulations. For example, we show only axisymmetric modes (m=0) but a comparison with other values of m will highlight the existence of a rotationnal splitting. Moreover, it is interesting to compare our results with the theoretical solutions of the eigenvalue problem. Lastly, these simulations should help to study the angular momentum transport in radiative zones and to better understand the evolution of stellar rotation. These points will be discussed in forthcoming publications.

References

Brun, A. S., Antia, H. M., Chitre, S. M., & Zahn, J.-P. 2002, A&A, 391, 725

Brun, A. S., Miesch, M. S., & Toomre, J. 2004, ApJ, 614, 1073

Brun, A. S., Miesch, M. S., & Toomre, J. 2011, ApJ, 742, 79

Charbonnel, C. & Talon, S. 2005, Science, 309, 2189

Christensen-Dalsgaard, J. 2003, Stellar Oscillations, `http://users-phys.au.dk/jcd/oscilnotes/`

Garcia, R. A., Turck-Chièze, S., Jiménez-Reyes, S. J., et al. 2007, Science, 316, 1591

Gough, D. O. 1993, in Astrophysical Fluid Dynamics - Les Houches 1987, ed. J.-P. Zahn & J. Zinn-Justin (Elsevier), 399–560

Kosovichev, A. G. 2011, Lecture Notes in Physics, ed. J.-P. Rozelot & C. Neiner, Vol. 832 (Berlin, Heidelberg: Springer)

Mathis, S. 2009, A&A, 506, 811

Rogers, T. M. & Glatzmaier, G. A. 2005, ApJ, 620, 432

Zahn, J.-P., Talon, S., & Matias, J. 1997, A&A, 322, 320

SF2A 2012
S. Boissier, P. de Laverny, N. Nardetto, R. Samadi, D. Valls-Gabaud and H. Wozniak (eds)

STARS WITH THE B[E] PHENOMENON SEEN BY LONG BASELINE INTERFEROMETRY

M. Borges Fernandes[1], O. Chesneau[2], M. Kraus[3], L. Cidale[4], A. Meilland[2], P. Bendjoya[2], A. Domiciano de Souza[2], G. Niccolini[2], I. Andruchow[4], S. Kanaan[5], P. Stee[2], F. Millour[2], A. Spang[2] and M. Curé[5]

Abstract. Thanks to the high spatial resolution provided by long baseline interferometry, it is possible to understand the complex circumstellar geometry around stars with the B[e] phenomenon. These stars are composed by objects in different evolutionary stages, like high- and low-mass evolved stars, intermediate-mass pre-main sequence stars and symbiotic objects. However, up to now more than 50% of the confirmed B[e] stars are not well classified, being called unclassified B[e] stars. From instruments like VLTI/AMBER and VLTI/MIDI, we have identified the presence of gaseous and dusty circumstellar disks, which have provided us with some hints related to the nature of these objects. Here, we show our results for two galactic stars with the B[e] phenomenon, HD 50138 and CPD 52^o9243, based on interferometric measurements.

Keywords: Stars: winds, outflows, circumstellar matter, stars:individual:HD 50138, stars:individual:CPD 52^o9243

1 Introduction

The B[e] phenomenon was defined by the presence in the optical spectra of B-type stars (Conti 1997) of strong Balmer emission lines, and permitted and forbidden emission lines of neutral and singly ionized metals, like Fe II and O I. In addition, these stars also present a strong near or mid-infrared excess due to hot circumstellar dust. Based on Lamers et al. (1998), there are different types of objects presenting the B[e] phenomenon: pre-main sequence Herbig Ae/Be stars, compact planetary nebula, symbiotic objects, hot supergiants, and unclassified objects, whose the evolutionary stage is still unknown.

Recently the optical/IR long baseline interferometry, especially with the VLTI, has become an important tool to deeply study the circumstellar environment of the brightest B[e] stars. Thanks to the field of view and the high spatial resolution of instruments, like AMBER and MIDI, it is possible to have access to information related to circumstellar medium close to the stars, allowing us to obtain sizes, shapes, and orientations, as a function of wavelength in the optical, near and mid-IR ranges.

In this paper, we present our results for two galactic stars with the B[e] phenomenon, namely HD 50138 and CPD 52^o9243, based on interferometric measurements.

2 Results

2.1 HD 50138

HD 50138 is one of the closest and brightest B[e] stars already identified in our galaxy. However its evolutionary stage is still not well known, being classified in the literature as either a classical Be or a pre main-sequence Herbig star. This object presents strong spectral variations that seem to be associated to outbursts and shell-phases. From a high-resolution spectroscopic analysis (FEROS and Narval data) and using photometric data

[1] Observatório Nacional/MCTI, Rio de Janeiro, Brazil
[2] Laboratoire Lagrange, Université de Nice Sophia-Antipolis, CNRS, Observatoire de la Côte d'Azur, France
[3] Astronomický ústav, Ondřejov, Czech Republic
[4] Universidad Nacional de La Plata, Argentina
[5] Universidad de Valparaíso, Chile

from the literature, it was found that a new shell-phase happened before 2007 (Borges Fernandes et al. 2009). In addition, spectro-polarimetric data from the literature have indicated the presence of a non-spherically symmetric circumstellar environment: probably a disk.

We obtained data from 14 baselines using MIDI, 17 using AMBER and also from 92 measurements at 10.7 μm from the KECK segment-tilting experiment (Monnier et al. 2009). We modeled these data using analytical geometrical models and the best results were found assuming a similar geometry for both near and mid-IR data: two elliptical Gaussian distributions (see Figs. 1 and 2 and Table 1).

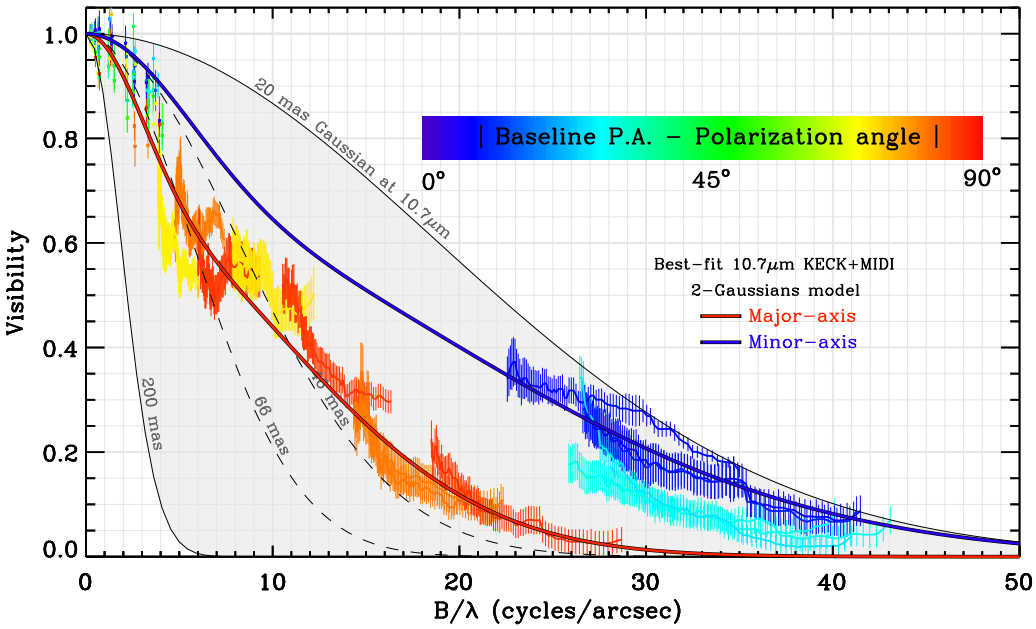

Fig. 1. VLTI/MIDI visibilities plotted as a function of the spatial frequency, B/λ, with kind permission from Borges Fernandes et al. (2011). The colors indicate the baselines position angle with respect to the polarization angle derived by Yudin & Evans (1998). The color scale (i.e., blue, cyan, green, yellow, orange, and red) goes from blue for baselines parallel to the polarization angle to red for the perpendicular ones. The dots with error bars indicate the Keck measurements. The thin solid and dashed lines represent the visibilities from Gaussian disks with different FWHM. The thick red solid line represents the model fitting aligned to the PA of the major axes of the 2-Gaussians distribution and the blue one to the PA of the minor axes.

Table 1. Parameters of the best-fit models from our analysis of interferometric data from HD 50138, assuming two elliptical Gaussian distributions, where "G1" means the first Gaussian distribution, "G2" is second one, "i" means inclination, and "θ" is the projection of the major axis onto the sky plane, see Borges Fernandes et al. (2011).

	MIDI+KECK	AMBER
Flux_{star}		0.12 ± 0.01
Flux_{G1}	0.68 ± 0.04	0.61 ± 0.06
$\text{FWHM}_{major-G1}$ (mas)	35.2 ± 1.5	
$\text{FWHM}_{major-G2}$ (mas)	131.4 ± 11.2	
$\text{FWHM}_{minor-G1}$ (mas)		3.0 ± 0.4
$\text{FWHM}_{minor-G2}$ (mas)		≥ 14.0
Flattening	1.82 ± 0.02	1.7 ± 0.3
θ (^{o})	65.9 ± 2.0	77 ± 2
i (^{o})	56.7 ± 0.4	54 ± 8
χ^2_r	1.9	13.3

Based on our results, the presence of a disk composed by gas and dust, with an inclination of $\sim 56^o$ and a projection on the sky plane of $\sim 71^o$ was confirmed (Borges Fernandes et al. 2011).

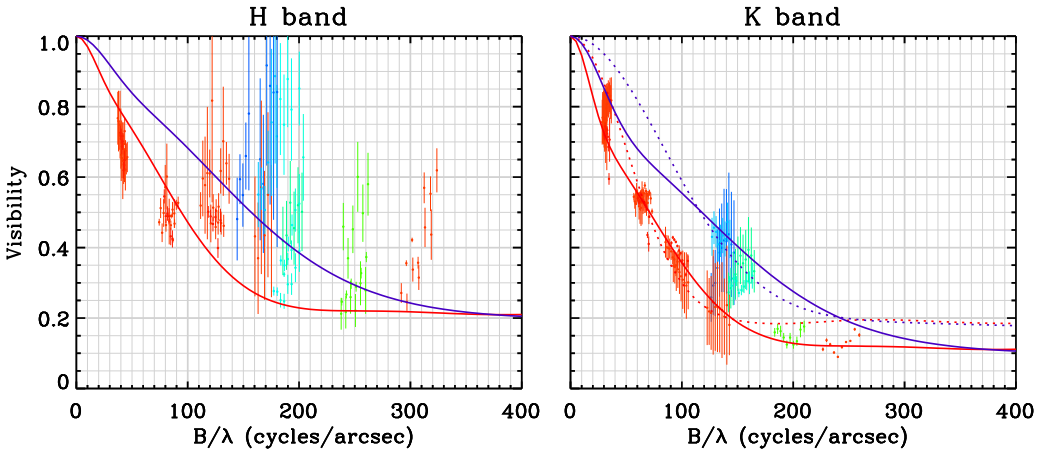

Fig. 2. Model fitting of the VLTI/AMBER data of HD 50138, with kind permission from Borges Fernandes et al. (2011), obtained using LITpro software (available at `http://www.jmmc.fr/litpro`): right panel for the K-band assuming two elliptical Gaussian distributions. The different colors follow the same description as in Fig. 1, representing the orientation of the baselines.

The formation mechanism of this disk is not clear yet, but it could be linked, as for classical Be stars, to stellar pulsations (Borges Fernandes et al. 2012).

2.2 CPD 52º 9243

CPD-52^{o}9243 is an emission-line star, which has been classified as a B[e] supergiant candidate. However, its stellar parameters are still not well known. Recently we obtained MIDI data from 4 baselines using the UTs and from an analytical geometrical modeling, we could find evidence for the presence of a dusty disk around this object (Cidale et al. 2012).

The disk has an inclination angle of 46±7 degrees, and an upper limit of its dusty inner edge of ~ 8 mas (see Fig. 3 and Table 2). Furthermore, the dusty disk surrounds a cool, detached molecular ring seen in CO band emission. The scenario for CPD-52^{o}9243 might therefore be quite similar to other B[e] supergiants, identified in close binaries, and found to have circumbinary molecular and dusty disks: HD 327083 (Wheelwright et al. 2012) and GG Car (Kraus et al. 2012).

Table 2. Parameters of our best-fitting model for VLTI/MIDI data of CPD-52^{o}9243."θ" is the projection of the major axis onto the sky plane.

FWHM major axis (mas)	16.35 ± 0.73
Flattening	0.69 ± 0.07
θ (^{o})	60.13 ± 9.57
χ^2	0.10

3 Conclusions

Optical long baseline interferometry is an ideal tool to provide information concerning the geometry and inclination of the circumstellar matter of stars with the B[e] phenomenon. These results will certainly contribute to a better comprehension of the nature of some unclassified B[e] stars and the inclusion of the B[e] phenomenon in the evolutionary tracks.

MBF acknowledges Conselho Nacional de Desenvolvimento Científico e Tecnológico (CNPq-Brazil) for the post-doctoral grant. LC acknowledges financial support from the Agencia de Promoción Científica y Tecnológica (BID 1728 OC/AR PICT 111), from CONICET (PIP 0300), and the Programa de Incentivos G11/089 of the Universidad Nacional de La Plata, Argentina. MK acknowledges financial support from GA ČR under grant number 209/11/1198. The Astronomical Institute of Ondřejov is supported

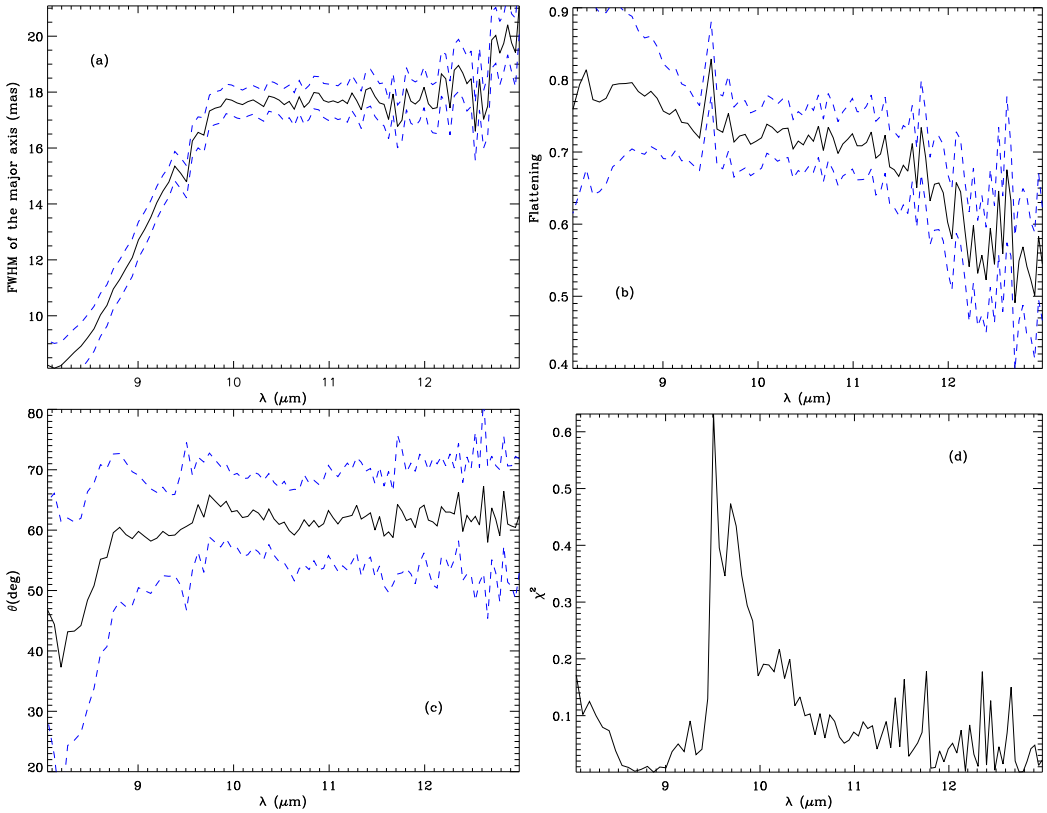

Fig. 3. The parameters provided by the best model, considering an elliptical Gaussian distribution for the circumstellar medium of CPD-52°9243, which fits the VLTI/MIDI baselines, as a function of the wavelength: (a) the FWHM of the major axis; (b) the flattening (ratio of FWHM of the minor axis and of the major axis); (c) the projection of the major axis (θ) onto the sky plane; and (d) the reduced χ^2 for each wavelength. The dashed lines indicate the errors for each parameter, as a function of the wavelength.

by the project RVO:67985815. I.A. acknowledges financial support from a posdoctoral fellow of CONICET. MC acknowledges financial support from Centro de Astrofísica de Valparaíso.

References

Borges Fernandes, M., Kraus, M., Chesneau, O., et al. 2009, A&A, 508, 309

Borges Fernandes, M., Meilland, A., Bendjoya, P., et al. 2011, A&A, 528, A20

Borges Fernandes, M., Kraus, M., Nickeler, D. H., et al. 2012, A&A, in press

Cidale, L. C., Borges Fernandes, M., Andruchow, I., et al. 2012, A&A, submitted

Conti, P. 1997, in Luminous Blue Variables: Massive Stars in Transition, eds. A. Nota, & H. J. G. L. M. Lamers, Astronomical Society of the Pacific Conference Series, vol. 120, p. 161

Kraus, M., Oksala, M. E., Nickeler, et al. 2012, A&A, submitted

Lamers, H. J. G. L. M., Zickgraf, F.-J., de Winter, D., Houziaux, L., & Zorec, J. 1998, A&A, 340, 117

Monnier, J. D., Tuthill, P. G., Ireland, M., et al. 2009, A&A, 700, 491

Wheelwright, H. E., de Wit, W. J., Weigelt, G., Oudmaijer, R. D., & Ilee, J. D. 2012, A&A, 543, A77

Yudin, R. V., & Evans, A. 1998, A&AS, 131, 401

SF2A 2012
S. Boissier, P. de Laverny, N. Nardetto, R. Samadi, D. Valls-Gabaud and H. Wozniak (eds)

CALIBRATION OF THE SURFACE-BRIGHTNESS RELATION OF B EARLY TYPE STARS: TOWARDS A VERY ACCURATE DISTANCE DETERMINATION OF LMC ECLIPSING BINARIES

M. Challouf[1,2], N. Nardetto[1], D. Mourard[1], H. Aroui[2] and O. Chesneau[1]

Abstract. The eclipsing binaries are currently used to determine the distance of the Magellanic clouds with an accuracy of 2%. Eclipsing binaries observable in the Magellanic clouds are generally composed of bright stars, with B spectral types. But there is no surface brightness relation available for stars earlier then A0, which is a limitation of the method. We propose to extent the surface brightness relation to B stars using VEGA/CHARA interferometric observations. In this paper, we present preliminary results on three stars: HD 186882, HD 176437 and HD 35468 (B2 to B9). Thirteen stars in total will be observed in a near future with VEGA/CHARA.

Keywords: angular diameters, surface brightness, distance, LMC, SMC, HD 186882, HD 176437, HD 35468

1 Introduction

The Large Magellanic Cloud (LMC) is an irregular dwarf galaxy and a companion to our own Milky Way Galaxy. Unlike spiral and elliptical galaxies, irregular galaxies lack any appearance of organized structure. Like its neighboring Small Magellanic Cloud (SMC), the LMC appears as a huge and diffuse cloud in the southern nighttime sky. The measurement of distances to the LMC in the century revolutionized our understanding of the distance scale of the Universe and provided the evidence for universal expansion. The distance to the LMC is a critical rung on the cosmic distance ladder, and numerous independent methods (utilizing, for example, RR Lyrae stars, Cepheids and red clump giant stars) have been employed to determine it. The use of eclipsing binaries in the LMC is a promising method (Pietrzyński et al. 2009; Graczyk et al. 2012). Recently, the LMC distance was determined with an accuracy of 2% using 8 eclipsing binaries (Pietrzyński et al. 2012, Nature, submitted). The method consists of combining the radii of the stars determined from spectro-photometric observations with their angular diameter derived from the surface brightness relation (hereafter SB relation). Currently, the largest limitation of the method is the uncertainty on the relationship SB. Increasing the accuracy of the SB relationship of FGK stars (by a factor 2) would allow a 1% precision on the distance of the LMC. Besides, constraining the SB relation for B stars would allow the use of brighter eclipsing binary systems, and thus helps to increase the number of distant objects detected. The aim of this work is to improve our understanding of the SB relationship (especially for B stars) using interferometry. For this, we use the interferometer VEGA on CHARA (Mourard et al. 2009). This instrument operates in the visible and benefits from bases CHARA interferometer (Ten Brummelaar et al. 2005). It has a spatial resolution of 0.3 mas, which makes it an ideal tool to determine diameters of stars. In Sect. 2, we describe the determination of angular diameter for 3 stars (δ Cyg, γ Ori, γ Lyr) and in Sect. 3, we show how these diameters are used to test the relationship of Di Benedetto (2005), which is currently widely used for the determination of the distances of eclipsing binaries in the LMC.

2 Angular diameter of δ Cyg, γ Ori and γ Lyr

Using VEGA/CHARA interferometer, we first determine the uniform disc angular diameter of the three stars in our sample.

[1] Laboratoire Lagrange, UMR 7293, UNS/CNRS/OCA, 06300 Nice, France.
[2] Laboratoire Dynamique Moléculaire et Matériaux Photoniques, UR11ES03, UT2/ESSTT, Tunis, Tunisia.

2.1 Uniform Disk (UD) angular diameter

δ Cygni (HD 186882) has a spectral type of B9.5III, a magnitude of 2.86 and its index color is 0.04. This star was observed with the VEGA instrument of the CHARA Array the 23rd and 27th of July, 2011 (refer to Table 1 for details). The visibilities have been calibrated using the procedure described in Mourard et al. (2009). We find an angular diameter of 0.764 ± 0.005 mas with a reduced χ^2 of 1.67 and an accuracy of about 0.7% (Figure 1).

Table 1. Journal of the observations of δ Cyg, γ Lyr an d γ Ori. The sequence of calibration are given with T for the target and C for the calibrators: C1=HD 185872 (0.198 ± 0.014 mas), C2=HD 184875 (0.291 ± 0.021 mas), C3=HD 178233 (0.393 ± 0.029 mas), C4=HD 34989 (0.129 ± 0.009 mas), C5=HD 37320 (0.152 ± 0.011 mas).

Star	Date	Telescope	Seq	λ [nm]	$\Delta\lambda$ [nm]	HA [h]	Base [m]	V^2 [mas]
δ Cyg	23/07/2011	E1E2W2	C1TC1	715	20	-0.160	66	$0.717_{\pm 0.035}$
						-0.262	155	$0.124_{\pm 0.032}$
						-0.262	220	–
				735	20	-0.153	66	–
							155	$0.190_{\pm 0.011}$
							220	$0.018_{\pm 0.010}$
	23/07/2011	E1E2W2	C1TC1	715	20	1.484	65	–
						1.460	154	$0.182_{\pm 0.012}$
						1.460	219	$0.022_{\pm 0.021}$
				735	20	1.491	65	$0.705_{\pm 0.038}$
						1.481	154	$0.179_{\pm 0.011}$
						1.500	219	$0.020_{\pm 0.017}$
	27/07/2011	E1E2W2	C1TC2	715	20	0.815	66	$0.726_{\pm 0.049}$
							156	$0.128_{\pm 0.013}$
							221	–
				735	20		66	$0.789_{\pm 0.049}$
							156	$0.157_{\pm 0.014}$
							221	$0.027_{\pm 0.018}$
	27/07/2011	E1E2W2	C2TC1	715	20	1.610	65	$0.771_{\pm 0.073}$
							154	$0.163_{\pm 0.014}$
							218	$0.017_{\pm 0.019}$
				735	20		65	–
							154	$0.160_{\pm 0.012}$
							218	$-0.012_{\pm 0.012}$
γ Lyr	27/07/2011	E1E2W2	C3TC3	715	20	-0.916	65	$0.796_{\pm 0.047}$
						-0.885	155	$0.181_{\pm 0.029}$
						-0.885	220	$0.022_{\pm 0.022}$
				735	20	-0.916	66	–
						-0.901	155	$0.227_{\pm 0.009}$
						-0.901	220	$-0.007_{\pm 0.070}$
	01/09/2011	E1E2W2	C3TC3	715	20	1.060	64	–
						1.065	152	$0.134_{\pm 0.018}$
						1.065	216	–
				735	20	1.060	65	$0.785_{\pm 0.047}$
						1.070	152	$0.181_{\pm 0.015}$
						1.070	216	$-0.010_{\pm 0.010}$
γ Ori	12/10/2011	E1E2W2	C4TC4	731.5	23	-2.150	150	$0.256_{\pm 0.008}$
						-2.150	214	$0.002_{\pm 0.013}$
	13/10/2011		C4TC5	731.5	23	-1.705	154	$0.221_{\pm 0.013}$
						-1.705	219	$0.019_{\pm 0.018}$

γ Lyr (HD 176437) is a giant star with a stellar classification of B9III and its index colour $V-K$ is 0.01. The measured angular diameter of this star is determined by two observations that were performed on 27th of July and 1st of September, 2011. The fit of the data are shown in Figure 1. The uniform-disk model diameter is 0.739 ± 0.007 mas with reduced χ^2 is 4.0 and with accuracy around 0.9%.

γ Ori (HD 35468) is B2III spectral type stars and its colour index is -0.70. We observed this star on 12th and 13th of October, 2011. The estimation of the angular diameter equal to 0.714 ± 0.006 mas with reduced χ^2 is 3.7 and with accuracy around 0.8%.

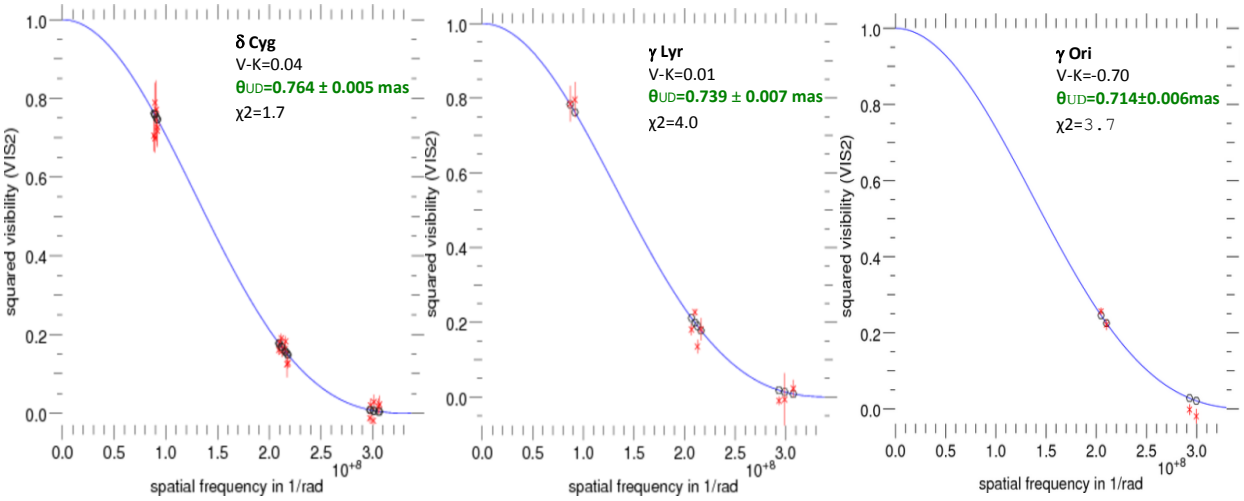

Fig. 1. The red points are the calibrated visibilities obtained with the VEGA interferometer and the solid blue line is the best model of uniform disk of the star (the angular diameter is the only parameter).

2.2 Limb-darkened (LD) angular diameter

The limb-darkening corrections (U_λ), for converting uniform-disc angular diameters to limb-darkened angular diameters, have been computed using stellar atmosphere models by Claret & Bloemen (2011), using the following stellar parameters: effective temperatures ($T_{\rm eff}$), surface gravities ($\log g$) and metallicity ($[Fe/H]$). The conversion factor between uniform and limb darkened diameters as defined by Hanbury Brown et al. (1974) is:

$$\theta_{LD}(\lambda) = \frac{\rho(\lambda)}{\theta_{UD}(\lambda)} \tag{2.1}$$

with

$$\rho(\lambda) = \left[\frac{\left(1-\frac{U_\lambda}{3}\right)}{\left(1-7\frac{U_\lambda}{15}\right)}\right]^{1/2} \tag{2.2}$$

Table 2 summarises the stellar parameters of δ Cyg, γ Lyr and γ Ori found in the literature. We finally obtain $U_R = 0.3491$, 0.3434 and 0.2211 for our three stars, respectively.

Table 2. Stellar parameters used for δ Cyg, γ Lyr and γ Ori.

Star	$T_{\rm eff}$ [K]	log g	U_R	Reference
δ Cyg	9781	3.68	0.3491	Lanz (1987)
γ Lyr	9970	3.50	0.3434	Leggett et al. (1987)
γ Ori	21580	4.20	0.2211	Code (1976)

3 The surface-brightness relation

The surface brightness relationship is a very interesting relation for determining the extragalactic distance. It simply relies on the fact that the stars are good black bodies and that there is a relation of conservation between the surface flux in a given spectral band and the color of the star. According to the formula of Stefan, the bolometric flux L is connected to the effective temperature $T_{\rm eff}$ and the bolometric radius R of the star by:

$$L \propto R^2 T_{\rm eff}^4 \tag{3.1}$$

So, the logarithm of the surface flux F defined by $F = \log(L/R^2)$ is directly related to the effective temperature of the star and thus to its colour. According to Barnes & Evans (1976), the surface flux in a given spectral band F_λ may be found from its absolute visual magnitude V_0 and true apparent angular diameter θ_{LD}:

$$S_v = V_0 + 5 \log \theta_{LD} \tag{3.2}$$

Then, the interferometric measurements of angular diameters are used to calculate the surface brightness for each star. We are therefore able to calibrate the surface brightness relation. Conversely, once calibrated, this relationship allows an estimate of the photometric angular diameter of eclipsing binaries. Combined its angular diameter photmetric with its radius, it is possible to determine the distance of the star. Di Benedetto (2005) gives a fit of this relation using 44 stars over the color range $-1 \leq (V-K)_0 \leq 3.7$:

$$S_v = [2.565 \pm 0.016] + [1.483 \pm 0.015](V-K)_0 - [0.044 \pm 0.005](V-K)_0^2 \tag{3.3}$$

Figure 2 shows a fit of the surface brightness relation using 88 stars (points of Benedetto and Boyajian) in A, F, G and K spectral types. Using all these measurement, we find a revised relation of:

$$S_v = [2.669 \pm 0.009] + [1.340 \pm 0.011](V-K)_0 - [0.007 \pm 0.003](V-K)_0^2 \tag{3.4}$$

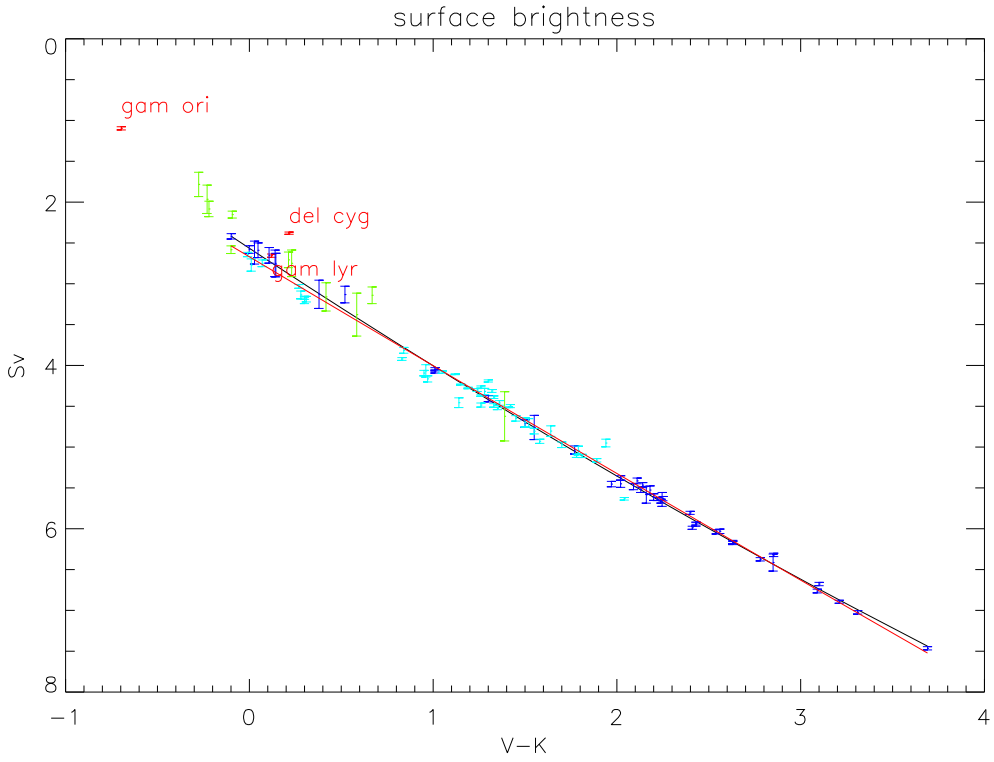

Fig. 2. The relation between visual surface-brightness parameter S_v as a function of the colour index $V-K$. The dark blue points represent the angular diameters of 44 stars that Di Benedetto (2005) established accurately. The light blue points indicate angular diameters of 44 stars determined meticulously by Boyajian et al. (2012). The black line is the fit of Di Benedetto and the red line is the fit using the points of Di Benedetto and Boyajian.

Fig. 2 also shows the VEGA measurements of Table 3 for the three stars: γ Ori, γ Lyr and δ Cyg. Eleven measurements by Hanbury Brown et al. (1974) (green dots) are shown. In the list of Hanbury Brown we removed stars in binary systems and fast rotating stars.

Table 3. VEGA/CHARA angular diameter obtained for δ Cyg, γ Lyr and γ Ori.

Star	$V-K$	θ_{UD}	θ_{LD}	S_v
δ Cyg	0.216	0.764 ± 0.005	0.785 ± 0.005	2.3682 ± 0.0013
γ Lyr	0.121	0.739 ± 0.007	0.759 ± 0.007	2.6439 ± 0.0020
γ Ori	-0.697	0.714 ± 0.006	0.728 ± 0.006	0.9552 ± 0.0020

4 Conclusion

We determined the interferometric angular diameters of three stars using the VEGA/CHARA interferometer. The capabilities of VEGA are shown with relative precision on the angular diameter of 1%. Including recent results by Boyajian et al. (2012) (44 stars), we find that the relation by Di Benedetto (2005) is slightly modified and the precision improved. However, more work is necessary to select the star carefullly depending on their class and fundamental characteristics in order to avoid any bias. In particular for B stars, the impact of a wind is not excluded and will be studied. Such study will be possible only with a larger sample of B stars. In total, we expect to observe 10 more stars with the VEGA/CHARA interferometer. Some observations are already on-going. This work, fully part of my PhD, is fundamental to improve the method of distance determination of eclipsing binaries in the LMC and SMC.

References

Barnes T.G., Evans D.S., Parsons S.B., 1976, MNRAS 174, 503
Boyajian S., McAlister A., van Belle G., 2012, ApJ 746, 101B
Claret A., Bloemen S., 2011, A&A 529, A75
Code A.D., Davis J., Bless R.E., et al., 1976, ApJ 203, 417
Di Benedetto G.P., 2005, MNRAS 357, 174
Graczyk D., Pietrzyński G., Thompson I.B., et al., 2012, ApJ 750, 144
Hanbury Brown R., Davis J., Lake R. J. W., et al., 1974, MNRAS 167, 475H
Lanz T., 1987, PhD thesis, No. 2258, Geneva University
Leggett S.K., Mountain C.M., Selby M.J., et al. , 1986, A&A 159,217
Mourard D., Clausse J. M., Marcotto A., et al., 2009, A&A 508, 1073
Pietrzyński G., Thompson Ian B., Graczyk D., et al., 2009, ApJ 697, 862
Pietrzyński G., Thompson I. B., Gieren W., et al., 2012, Nature 484, 75
Ten Brummelaar T. A., McAlister H. A., Ridgway S. T., et al., 2005, ApJ 628, 453

SF2A 2012
S. Boissier, P. de Laverny, N. Nardetto, R. Samadi, D. Valls-Gabaud and H. Wozniak (eds)

LABORATORY EXPERIMENTS OF RADIATIVE SHOCKS IN THE CONTEXT OF STELLAR ACCRETION.

U. Chaulagain[1], C. Stehlé[1], L. de Sá[1,2], J. Larour[3], P. Auvray[3], M. Kozlova[4], M. Krus[4], J. Dostal[4], J. Propupek[4], F. Suzuki-Vidal[5], P. Barroso[6], F. Reix[6], O. Acef[7] and A. Ciardi[1]

Abstract. High-energy lasers are used to simulate astrophysical phenomena in the laboratory. The PALS laser facility, with a typical irradiance of 10^{14} W.cm^{-2}, allows in particular to produce radiative shocks in high atomic number gases. The system is optimized for reaching conditions where the shock is radiative, i.e. it presents a "radiative precursor". This kind of shock is expected to occur during various astrophysical accretion processes. We present preliminary experimental results with emphasis on two diagnostics, namely the study of the laser impact on the target and an instantaneous imaging using an X - ray laser.

Keywords: Radiative shocks, Plasmas, XUV laser, Accretion.

1 Introduction

In Young Stars, the accretion rate is deduced from the photometric signatures of the accretion shocks which are generated by matter falling towards the photosphere at velocities of the order of free fall velocity ($\sim$ 300-500 km/s). These so-called radiative shocks are strong shocks (Mach number, $M >>1$) which are in a regime dominated by radiation. The shock front is heated up to high temperature, and generates intense radiation. If the optical thickness of the medium is sufficiently high, the photons are then absorbed by the unshocked cold medium, leading to an increase in its ionization and temperature, and the development of a "radiative precursor". Radiative shocks are found in many accreting systems, examples includes the initial stages of star formation (Commercon et al. 2011), in already formed Young Stars (Bouvier et al. 2007), or in black hole systems (Chakrabarti & Titarchuk 1995).
In general, the emission properties of radiative shocks and their complex structure is difficult to model, and remains to be fully understood. In this context, experimental studies under controlled conditions are an ideal tool to help unravelling their physics. The most common experimental approach to use high-energy laser installations, to generate a shock in low pressure shock tube containing Xenon gas. Shock waves at velocities of $\sim$60 km/s have been successfully achieved on several laser installations (Stehlé et al. 2010; Bouquet et al. 2004).

2 Experimental set up

The experiments were performed at the Prague Asterix Laser System (PALS). The installation is capable of delivering an energy up to 1 kJ at the fundamental wavelength of 1.315 μm, with a pulse duration of 0.4 ns. In the present experiment, the laser beam is split into two (AUX and MAIN) beams. The AUX beam (60 J) is focused on a miniaturized shock tube located in a cylindrical vacuum chamber and is used to generate the radiative shock wave. The MAIN beam (500 J) is focused on a Zinc planar target located in a spherical chamber,

[1] LERMA, Observatoire de Paris, UPMC, ENS, CNRS, Meudon, FR
[2] IRFU, CEA, Saclay, FR
[3] LPP, Ecole polytechnique, UPMC, CNRS, Palaiseau, FR
[4] Institute of Physics, Prague, Czech Republic, CZ
[5] Imperial College, London, UK
[6] GEPI, Observatoire de Paris, Universitè Paris Diderot, CNRS, Paris, FR
[7] SYRTE, Observatoire de Paris, UPMC, CNRS, LNE, Paris, FR

where it generates an X-ray laser (XRL, 3 mJ, 0.2 ns) beam at 21.2 nm (Rus et al. 2002). The XRL beam is sent towards the cylindrical chamber where it passes through the shock tube in order to image instantaneously the shock inside the tube. The delay of the XRL beam respect to AUX beam, measured at the position of the shock tube, is equal to 20 ± 0.05 ns. After travelling through the shock tube where it is absorbed by the Xe density edge located at the shock position, the XRL beam reaches a spherical mirror, which focuses it in an iron pinhole (diameter 500 μm) providing a spatial filtering of the shock self emission. Finally, the XRL beam travels through a thin Aluminium (Al) foil, which suppresses the parasitic visible light, and is recorded onto a cooled CCD (see Fig 1, left). The magnification of the CCD camera (pixel size 13.6 μm) is close to 4.

To control the focusing of the AUX beam, we used two series of diagnostics: first a keV pinhole imaging

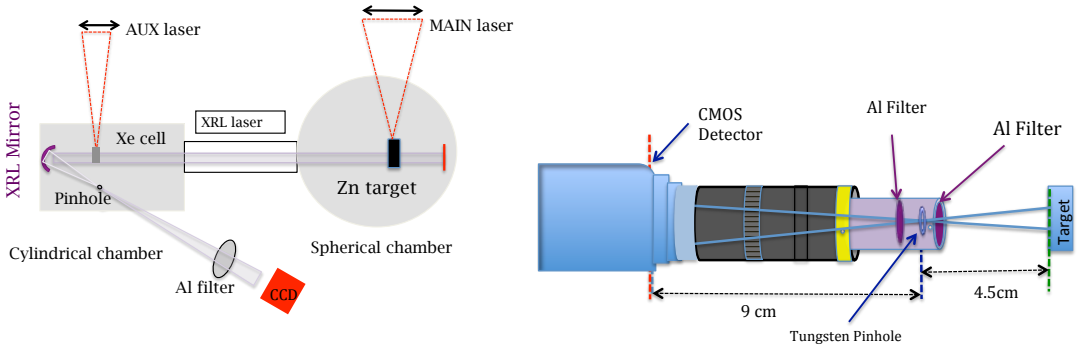

Fig. 1. Left: Schematic experimental set-up. **Right:** Principle of the keV pinhole imaging system.

(magnification 2) controls the position, the size and also the uniformity of the laser beam on the target. This diagnostic (Fig 1, right), includes a Tungsten pinhole (5 μm diameter), located in front of the naked camera CMOS detector (pixel size 6.7 μm). Two Al filters (0.4 μm and 10 μm thick) block the parasitic visible light, and allow to select the relevant keV range photons. The second diagnostics consists in using solid planar Al targets instead of the shock tube, to analyze the size of the crater created by the impact of the AUX beam on metallic surfaces (Gus'kov & Gus'kov 2001; Mora 1982).

The core of the target consists of a shock tubes, with a typical length of 6 mm, and an internal square cross

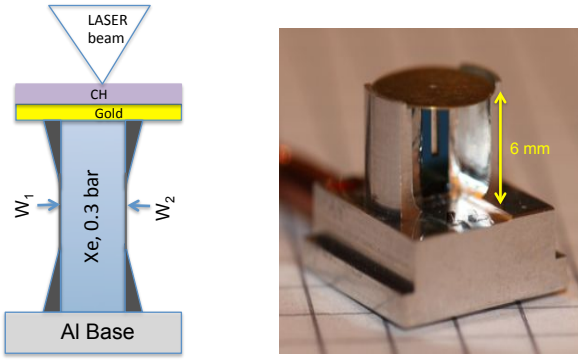

Fig. 2. Left: Target principle; W_1, and W_2 are two Si_3N_4 windows. **Right:** Image of the target.

section of 0.4×0.4 mm^2. The tube is filled in *situ* with Xenon (at a pressure of 0.3 bar). The tube is closed at one end by a 10 μm thick polystyrene (CH) foil acting as a piston, hence the ablation of the plastic by AUX launches, by rocket effect, the piston into the tube. A 0.5 μm thick gold layer is deposited on the polystyrene foil to prevent the X-rays, which are generated during the ablation phase of the polystyrene, to enter into the shock tube (Fig 2, left). The shock tube is closed laterally by two silicon nitrate windows (Si_3N_4), 0.3×0.4 mm^2, each 100 nm thick, with a net transmission of 0.015 at 21.2 nm (`http://henke.lbl.gov/optical_constants/`).

3 Results

3.1 Focusing of the laser

The intensity of the AUX laser on the target surface was modified either by translating precisely the position of the focusing lens (allowing to change the laser spot size) or by using neutral density filter to reduce the laser energy on the target. With these methods, the irradiance on the targets varied between 10^{12} to 10^{15} W.cm^{-2}. To study the crater diameter, we typically used filter with a transmission of 10%. The targets were placed in the beam waist with a reproducibility in the positioning of ± 20 μm.
The size of the craters was measured after the shot, using a high resolution microscope. The keV pinhole camera, monitoring the short duration photon burst, gives the diameter of the corresponding hot spot.
These two diagnostics indicate that the laser spot on the target was about 300 μm.

3.2 XRL imaging

Fig. 3. Snapshot of the shock probed by the XRL laser; the AUX laser coming from the right of the image. The instrumental background is subtracted.

The 21.2 nm XRL was used to probe the radiative shock (Kozlova et al. 2009) with a delay of 20 ns after the interaction between AUX and the target. The spherical mirror was manufactured using a highly polished silica substrate with a multilayer Al/Mo/B4C (theoretical reflectivity of 45% at 21.2 nm). Fig. 3 shows a typical record of a shock wave, in dark gray, propagating from right to left and a black zone which is assumed to correspond to a mixture containing residues of the piston. These results are preliminary and are under analysis.

4 Conclusions

X-ray laser radiography allows analysis of shock waves that would be nearly impossible with optical imaging, due to the expected large value of the electron density. Compared to previous similar results (Stehlé et al. 2012), this new study achieves a noticeable improvement in the quality of the imaging setup by increasing the reflectivity of the spherical mirror, and by reducing the thickness of the Si_3N_4 lateral windows. The shock image was recorded with better contrast. The sensitive keV pinhole imaging monitors not only the position of impact but also helps to estimate the shape and size of the laser beam on the target with a good precision.

The project has been funded by Observatoire de Paris, PNPS, UPMC, ANR-08-BLAN-0263-07 and LASERLAB access program. The authors acknowledge the contribution of the PALS technical staff, the target fabrication group of Observatoire de Paris, V. Petitbon (IPN) for the polystyrene manufacturing, F. Delmotte and E. Meltchakov from Institute d'optique, Graduate School, for the XUV mirror deposition.

References

Bouquet, S. et al., 2004, Phys. Rev. Lett. 92, 225001

Bouvier, J., et al., 2007, in Protostars and Planets V, by Reipurth B. et al. (eds.), (Univ. of Arizona Press), p.479.

Chakrabarti S., & Titarchuk, L. G., 1995, ApJ, 455, 623

Commercon, B. et al., A & A, 2011, 530, A13

Gus'kov, K.S. and Gus'kov, S. Yu., Quantum Electronics, 2001, 31, 305

Kozlova, M., et al., 2009, proc. of 11th Int. Con. on X-ray Lasers, Belfast 2008, Springer Proc. in Physics, 130, 417

Mora, P., 1982, Phys. Fluids, 25, 1051

Rus, B., Prag, A R., Hudecek, M., et al. 2002, Plasma Phys. Control. Fusion, 44, B207-223

Stehlé, C., et al., 2010, Laser and Particle Beams, 208, 253

Stehlé, C., et al., 2012, Opt. Comm., 285, 64.

SF2A 2012
S. Boissier, P. de Laverny, N. Nardetto, R. Samadi, D. Valls-Gabaud and H. Wozniak (eds)

HYDRODYNAMIC MODELING OF ACCRETION SHOCKS ON A STAR WITH RADIATIVE TRANSPORT AND A CHROMOSPHERIC MODEL

L. de Sá[1,2], J.-P. Chièze[1], C. Stehlé[2], I. Hubeny[3], F. Delahaye[2] and T. Lanz[4]

Abstract. The aim of the project (ANR STARSHOCK) is to understand the dynamics and the radiative properties of accretion columns, linking the circumstellar disk to the surface photosphere of Young Stellar Objects. The hydrodynamics is computed first, using a high resolution hydrodynamic 1D ALE code (ASTROLABE) coupled to radiative transfer and line cooling, along with a model for the acoustic heating of the chromospheric plasma. Spectra are then post-processed with a 1D radiative transfer code (SYNSPEC), using DFE solver and an extended atomic database covering a wavelength range from X rays to visible.

Keywords: accretion shocks, oscillations, radiative transfer, M1 closure, cooling function, dynamical chromosphere, acoustic heating

1 Introduction

One dimensional hydrodynamic models (Koldoba et al. 2008; Sacco et al. 2008, 2010) have confirmed the radiative shock origin of the soft X-ray observations of CTTSs (Testa et al. 2004; Robrade & Schmitt 2007), showing periodic variations due to radiative instabilities. Furthermore, two dimensional MHD models (Orlando et al. 2010) have stressed the dependence of the dynamics and of the stability of accretion shocks upon the plasma parameter β. However, in these simulations, cooling of the shock heated plasma is entirely attributed to optically thin line cooling, discarding radiation transfer. This may be a crude approximation in the relatively dense part of the cooling flow, which penetrates the chromosphere. The treatment of the structure of the chromosphere itself is also simplified in these simulations, although the depth at which occurs the main accretion shock, and thus its observability, depends on the pressure profile of the chromosphere.
Our aim is to show the sensitivity of the accretion shock structure on the way the radiative transfer is treated. We report here on a first attempt to include both radiative transfer and a model of stellar chromosphere heating in hydrodynamics simulations of accretion flows on stellar surfaces.

2 Physical assumptions and model

The radiatively driven evolution of an accretion flow impacting the dynamical structure of the chromosphere of a star is modelized by solving the 1D equations of hydrodynamics coupled to radiation, encompassing the optically thick to thin plasma regimes, relevant respectively to the upper photosphere and the shocked material.

2.1 Code specificities

The 1-D ASTROLABE code is a fully implicit Adaptive Lagrangian Eulerian (ALE) code with a fixed number of mesh points, which can move independently of the fluid velocity, to adapt the resolution to the flow properties (Dorfi & Drury 1987; Lesaffre et al. 2004). The accretion column is treated with a height dependent section: it may be for instance cylindrical, conical or exponential.

[1] Service d'Astrophysique, CEA Saclay, France
[2] Observatoire de Paris, CNRS, UPMC, Meudon, France
[3] University of Arizona, Tucson, USA
[4] Laboratoire JL Lagrange, OCA, CNRS, UNS, Nice, France

In the present application, the ionization fraction is calculated according to the Saha equation, which is here modified in order to encompass photoionization and Lyman α radiation trapping (Brown 1973; Sacco et al. 2008). The underlying assumption of instantaneous thermodynamical equilibrium, which is roughly satisfied for the chromosphere, is currently being studied. The variation of the adiabatic exponent is taken into account by including the ionization energy of atoms in the expression of the internal energy of the plasma.
Radiative transfer is described by the two time dependent equations for radiation energy (E_r) and momentum densities ($\mathcal{M}_r$), which are written in the comoving frame (Mihalas & Mihalas 1984; Lowrie et al. 2001). The necessary closure relation is obtained using the so-called $M1$ prescription, where the expression of the Eddington factor $f_{Edd} = P_r E_r$ is obtained by maximizing the entropy of the radiation field (Levermore 1996; Dubroca & Feugeas 1999). In regions where departures from thermodynamical equilibrium are weak, the terms which couple these two equations for E_r and $\vec{M}_r$ are:

$$\left\{ \begin{array}{rcl} S_{E_r} & = & \kappa_{_P} \rho c \, (aT^4 - E_r) \\ \vec{S}_{M_r} & = & -\kappa_{_R} \rho \, \vec{F}_r \end{array} \right. \tag{2.1}$$

where we have assumed Planck and Rosseland grey opacities, $\kappa_{_P}$ and $\kappa_{_R}$. However, in the upper, hot, low density regions, the optically thin plasma is in coronal equilibrium. This is the case in the shocked material of the accretion flow. In this case, the source term for radiative energy is $S_{E_r} = n_e n_H \Lambda(T)$, where n_e and n_H are respectively the volume densities of electrons and of hydrogen nuclei, and $\Lambda(T)$ is the plasma cooling function; in the present work we use the cooling function of Kirienko (1993). The source term of the radiation momentum vanishes: $\vec{S}_{M_r} \approx 0$.

2.2 A generic model for chromosphere

Models of stellar chromosphere generally provide temperature and density profiles in hydrostatic equilibrium, adjusted to fit the observed chromospheric spectrum. An ad hoc heating function (E_H, using the notation of Peres et al. 1982) may be derived as a function of the radius, in order to maintain the equilibrium of chromosphere. The energy input E_H mimics actual energy deposition by sound waves, Alfvén waves and electronic conduction, which, since the pioneering work of Biermann (1946) and Schwarzschild (1948), are thought to heat the chromospheric layers. However, this procedure cannot be unambiguously adopted to determine the depth of the stagnation point of the accretion flow in the chromosphere, which depends crucially on the structure of the (unsteady) pressure profile of the upper stellar atmosphere. Our first approach has been to include the acoustic, dynamical, heating of the chromosphere in the global accretion model, leaving to further 3D calculations chromospheric heating by hydromagnetic waves. The aim here is to get a self-consistent, fully hydro-radiative description of the chromospheric structure, impacted by the accretion flow.
Thus, we have investigated the behavior of acoustic waves on the structure of the outer layers of a star (we choose the Sun for comparisons with theoretical models and observations, (see e.g. Rammacher & Ulmschneider 1992; Kalkofen 2007). Mechanical energy is supplied at the base of the simulation domain (at $\tau \geq 1$), in the form of a monochromatic sinusoidal motion of the first (Lagrangian) interface. Heating of the corona is not taken into account, since the later is readily crushed by the accretion flow. Figure 1 shows the formation of travelling shocks, induced by acoustic waves. Heating of the chromosphere is the result of the time-averaged temperature structure above the photosphere.

3 First results

The main features of accretion flows, especially their periodic behavior, are conserved when they interact with a dynamic chromosphere modelized as described previously. This is illustrated by Figure 2 (left), which presents a complete cycle, with the formation of the reverse shock, followed by the cooling of the shocked material which induces the formation of a second shock in the upper chromosphere, the crushing of the whole structure on the chromosphere, and again the renewal of a reverse shock. The oscillation period is about 300 s. However, the structure of the flow at the base of the accretion column is significantly modified both by radiative transfer and by the dynamics of the chromosphere. It turns out that a crucial issue is the treatment of the transition between the collision dominated plasma (inner regions) and the non equilibrium external regions, where coronal equilibrium prevails.
The effect of radiative transfer on the global structure of the accretion shock has been explored by varying the photon absorption probability in the column, from zero (optically thin line cooling (Sacco et al. 2008)) to a finite

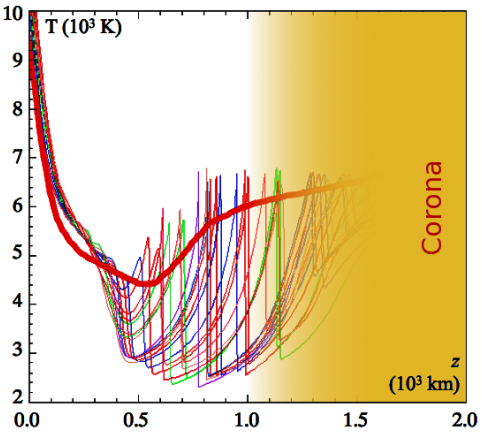

Fig. 1. Formation and propagation of shock waves induced by sound waves with initial energy flux (at $z = 0$ km) of 10^8 $erg.cm^{-2}.s^{-1}$ and a period of 60 s. The thin lines are successive snapshots of the temperature structure of the chromosphere and the thick line represents the mean temperature of the solar chromosphere (Th. Lanz, private communication). Above 500 km, acoustic waves degenerate into shocks, which strength is governed by the balance between steepening in the pressure gradient and dissipation.

value, depending on the opacity and the transverse size of the column. For example, with opacities obtained from the OP and Semenov libraries, and a column cross section of 1000 km, the accretion shock, contrary to the optically thin case, is now stationary and deeply buried in the stellar chromosphere (Figure 2, right). In view of the dramatic effects of radiation transfer, new extensive Planck and Rosseland opacity tables are currently established in the framework of an upgrade of the spectral synthesis code Synspec (Hubeny & Lanz 2011), to be used with a multigroup extension of the M1 method.

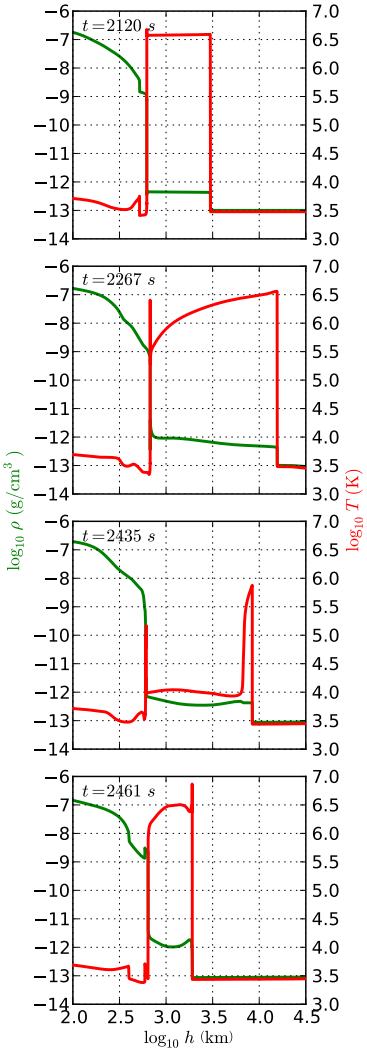

Fig. 2. Shock cycle showing snapshots of the density ρ (green line) and temperature T (red line). The gas is infalling from the right to the left on a dynamically heated chromosphere (cf. Figure 1).
Left: The accreted gas is cooled using optically thin line cooling. From top to bottom: a reverse shock forms and propagates outwards; the shocked material cools down under quasi isochoric conditions: a strong inwardly directed pressure gradient forms, which launches a second shock into the chromosphere; the whole structure is finally crushed on the chromosphere, and a new reverse shock forms. The period of this cyclic evolution is about 300 s. Cycle n°20 is shown here.
Right: In this case, the energy exchange rate between matter and radiation is not restricted to strict optically thin line cooling. According to the photon escape probability, this rate is interpolated between Eq. (2.1), through Planck and Rosseland (mean) opacities, and the optically thin regime. Enabling radiative transfer dramatically increases the cooling efficiency, so that the accretion shock turns to be stationary, apart from a periodic motion induced by the chromospheric heating.

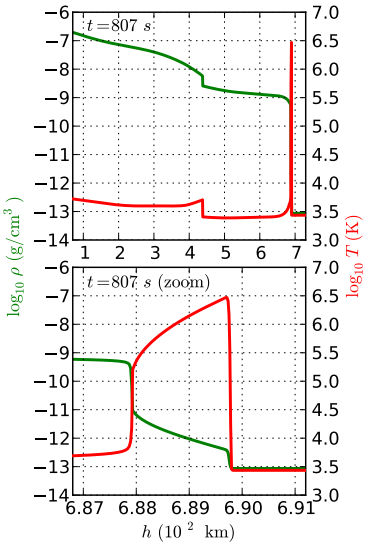

4 Conclusion

The numerical model outlined in this paper includes for the first time the treatment of the radiative transfer in the flow and a self-consistent model of the stellar chromosphere, in order to precisely characterize the thermodynamical and radiative properties of the densest part of accretion column, which is the strongest XUV emitter. In a next step, a grid of models will be calculated in order to post-process the detailed spectra emerging from these structures.

This work was supported by French ANR (grant 08-BLAN-0263-07), University Pierre et Marie Curie, Observatoire de Paris and CEA Saclay.

References

Biermann, L. 1946, Naturwissenschaften, 33, 118

Brown, J. C. 1973, Sol. Phys., 29, 421

Dorfi, E. A. & Drury, L. O. 1987, Journal of Computational Physics, 69, 175

Dubroca, B. & Feugeas, J.-L. 1999, Academie des Sciences Paris Comptes Rendus Série Sciences Mathematiques, 329, 915

Hubeny, I. & Lanz, T. 2011, Astrophysics Source Code Library, 9022

Kalkofen, W. 2007, ApJ, 671, 2154

Kirienko, A. B. 1993, Astronomy Letters, 19, 11

Koldoba, A. V., Ustyugova, G. V., Romanova, M. M., & Lovelace, R. V. E. 2008, MNRAS, 388, 357

Lesaffre, P., Chièze, J.-P., Cabrit, S., & Pineau des Forêts, G. 2004, A&A, 427, 147

Levermore, C. D. 1996, Journal of Statistical Physics, 83, 1021

Lowrie, R. B., Mihalas, D., & Morel, J. E. 2001, J. Quant. Spec. Radiat. Transf., 69, 291

Mihalas, D. & Mihalas, B. W. 1984, Foundations of radiation hydrodynamics (New York, Oxford University Press)

Orlando, S., Sacco, G. G., Argiroffi, C., et al. 2010, A&A, 510, A71

Peres, G., Serio, S., Vaiana, G. S., & Rosner, R. 1982, ApJ, 252, 791

Rammacher, W. & Ulmschneider, P. 1992, A&A, 253, 586

Robrade, J. & Schmitt, J. H. M. M. 2007, A&A, 473, 229

Sacco, G. G., Argiroffi, C., Orlando, S., et al. 2008, A&A, 491, L17

Sacco, G. G., Orlando, S., Argiroffi, C., et al. 2010, A&A, 522, A55

Schwarzschild, M. 1948, ApJ, 107, 1

Testa, P., Drake, J. J., & Peres, G. 2004, ApJ, 617, 508

SF2A 2012
S. Boissier, P. de Laverny, N. Nardetto, R. Samadi, D. Valls-Gabaud and H. Wozniak (eds)

BINSTAR, A NEW TOOL FOR THE EVOLUTION OF LOW- AND INTERMEDIATE-MASS BINARY STARS

R. Deschamps[1], L. Siess[1] and P. J. Davis[1]

Abstract. The evolution of stellar components in binary systems may be strongly influenced by their companion, for example, via Roche lobe overflow. This is particularly true for short period systems that can undergo significant mass transfer. In this paper, we present the new binary star evolution code for interacting binaries, BINSTAR. This code has been designed to consistently follow the structure and evolution of low- and intermediate-mass stars affected by mass and angular momentum transfer and spin-down mechanisms such as magnetic braking or the formation of a star-disc boundary layer. We applied BINSTAR to the study of an Algol system consisting of 6 + 3.6 $M_\odot$ stellar components with initial period $P_{\rm init}$ = 2.5 days. We find that the gainer can maintain a spin velocity below the critical Keplerian value if magnetic braking with a strong magnetic field (of about 3kG) is applied, or if star-disc boundary layer interactions is considered. However, tides only cannot prevent the gainer from reaching critical rotation during the accretion phase.

Keywords: Stars: evolution, Stars: binaries: general, Accretion: accretion disks, Stars: magnetic field

1 Introduction

The study of binary systems is relevant to many astrophysical domains. Binary stars allow a precise determination of stellar masses (the key parameter for stellar evolution) and are progenitors of many other objects for example Type Ia supernovæ, X-ray bursts and probably γ-ray bursts.

Previous numerical simulations have provided a broad understanding of short-period binaries. Although some features, for example mass transfer in circular orbits or non-conservative evolution, have been extensively studied, there is no simulation that follows all angular momentum contributions (stellar and orbital) coupled with the treatment of the star disc boundary layer (hereafter star-disc interaction). It is well-known that mass transfer is associated with exchange of angular momentum, resulting in the spin-up of the gainer star. Packet (1981) showed that so much angular momentum is transferred that the gainer's surface velocity can reach the critical Keplerian velocity $v_{*,\rm surf} = \sqrt{GM_*/R_*}$ (hereafter critically rotating accretors). Up to now, no evolutionary code consistently handles such cases. In this paper, we describe the main properties of the new code BINSTAR dedicated to the study of low- and intermediate-mass binary systems. We analyse the torques arising from star-disc interaction and magnetic fields in order to better understand the accretion of angular momentum in Algol systems.

2 The Binstar code

BINSTAR is an extension of the 1-dimensional stellar evolution code STAREVOL, that handles the simultaneous calculation of the binary orbital parameters (separation and eccentricity) and the two stellar components. The stellar input physics is the same as described in Siess (2006).

BINSTAR follows the evolution of the system angular momentum (J_Σ) which is the sum of the stellar (subscript 'd' for the donor and 'g' for the gainer) and orbital components i.e.:

$$J_\Sigma = J_{\rm d} + J_{\rm g} + J_{\rm orb}. \tag{2.1}$$

The stellar torques $\dot{J}_{\rm d,g}$ applied on each star come from tidal, mass transfers or magnetic field interactions and will be described below. A Henyey method is used to solve simultaneously the structure of the two stars and the binary parameters (separation, eccentricity), as described in Siess et al. (2013).

[1] Institut d'Astronomie et d'Astrophysique, Université Libre de Bruxelles, ULB, CP 226, 1050 Brussels, Belgium

Mass loss and associated torques There are two modes of mass loss from a star: via winds or via Roche lobe overflow (hereafter RLOF). Winds carry away a fraction of the stellar spin angular momentum so for star 'i' (i = d or g) the resulting stellar torque is:

$$\dot{J}^{\rm wind}_{\rm loss,i} = -\frac{2}{3}|\dot{M}^{\rm wind}_{\rm loss,i}|\Omega_{\rm i}R^2_{\rm i}, \tag{2.2}$$

where $\dot{M}^{\rm wind}_{\rm loss,i}$ is the wind mass loss rate and $\Omega_{\rm i}$ the stellar spin angular velocity. In this study, we assume solid rotation. During the mass transfer phase, the mass loss rate $\dot{M}^{\rm RLOF}_{\rm loss,d}$ due to RLOF is computed following the formalism given by Kolb & Ritter (1990) which differentiates between the optically thin or optically thick regime depending on the location of the Roche lobe radius inside the star. The matter leaving the star carries the donor's surface specific angular momentum, resulting in a torque for the donor:

$$\dot{J}^{\rm RLOF}_{\rm loss,d} = -|\dot{M}^{\rm RLOF}_{\rm loss,d}|\Omega_{\rm d}R^2_{\rm d}. \tag{2.3}$$

Mass accretion and associated torques In case of RLOF, only a fraction β of the matter lost from the donor may be accreted by the gainer because of the formation of a hot-spot or a circumstellar disc or ring, for example. A system is said to be conservative when the total mass and the total angular momentum (stars + orbit) are conserved ($\beta = 1$). The matter that leaves the donor at the first Lagrangian point may either directly impact the star or form an accretion disc. To determine the specific angular momentum accreted on the gainer as well as the accretion mode (direct impact or disc accretion), we compute the ballistic motion of a test particle in the gainer potential well (Flannery 1975). In case of direct impact, the resulting torque is:

$$\dot{J}^{\rm RLOF}_{\rm acc,g} = \beta|\dot{M}^{\rm RLOF}_{\rm loss,g}|\|\vec{R}\wedge\vec{v}\|, \tag{2.4}$$

where $\vec{R}$ is the radius vector between the centre of the gainer star and the particle at the point of impact, and $\vec{v}$ is the stream velocity at that location. On the other hand, if accretion occurs via a disc, the accreted specific angular momentum is equal to the Keplerian value at the surface of the star and the torque is:

$$\dot{J}^{\rm RLOF}_{\rm acc,disc} = \beta|\dot{M}^{\rm RLOF}_{\rm loss,g}|\sqrt{GM_{\rm g}R_{\rm g}}. \tag{2.5}$$

Finally, we note that part of the wind ejected from a star can be accreted by the companion (Bondi & Hoyle 1944). The accreted material carries a fraction $f_{J_{acc}}$ of the surface angular momentum of the star that expelled the wind and the torque on the wind accreting star 'i' (companion star '3-i') is:

$$\dot{J}^{\rm wind}_{\rm acc,i} = \frac{2}{3}f_{J_{\rm acc}}\dot{M}^{\rm BH}_{\rm i}\Omega_{3-{\rm i}}R^2_{3-{\rm i}}, \tag{2.6}$$

where $\dot{M}^{\rm BH}_{\rm i}$ is the Bondi-Hoyle mass accretion rate.

Magnetic wind braking If the star possesses a magnetic field, the mass ejected in the wind follows the open magnetic field lines until it reaches the Alfvèn surface (Weber & Davis 1967). At this point, the matter freely escapes the system with a higher specific angular momentum than the one available at the stellar surface. Because of this level-arm effect, the star spins down more efficiently. To determine the torque due to magnetic wind braking, we use (Dervişoğlu et al. 2010):

$$\dot{J}_W = -[(-\dot{M}_{\rm loss})^{(4n-9)}B^8_{\rm i}(2GM_{\rm i})^{-2}R^{8n}_{\rm i}]^{1/(4n-5)}\Omega_{\rm i}, \tag{2.7}$$

where n is a parameter characterizing the geometry of the magnetic field and $B_{\rm i}$ is the stellar magnetic field strength. It is a reasonable approximation to assume a dipolar magnetic field with $n = 3$ (Livio & Pringle 1992). This torque depends on the mass loss rate $\dot{M}_{\rm loss}$ (mostly winds), the stellar spin $\Omega_{\rm i}$ and the magnetic field strength $B_{\rm i}$. In our models, $B_{\rm i}$ is a free parameter and the wind mass loss rates follow standard prescriptions.

Magnetic Disc locking The dipolar stellar magnetic field anchors into the accretion disc that may form around the gainer. Since the disc does not co-rotate with the star, the stellar magnetic field lines are twisted, creating a toroidal magnetic field component. In turn, this toroidal magnetic field generates a torque on the

star. In the best case, when all the disc contributes to spin down the star, the torque writes (Dervişoğlu et al. 2010):

$$\dot{J}_{\rm disc\ locking} = -\frac{\mu^2 \Omega_{\rm i}^2}{3GM_{\rm i}}. \tag{2.8}$$

The torque depends on the stellar spin, which is not a parameter but fixed by the evolution of the system, and on the magnetic field strength through $\mu = B_{\rm i} R_{\rm i}^3$.

Tidal effects Tides are responsible for the synchronisation of the stellar spin with the orbital period. The efficiency of tidal torques increases when the orbital separation decreases. Some semi-detached binaries such as Algols are short period systems (from hours to tens of days). Therefore, we expect tides to play an important role in such systems. The tidal prescriptions of Zahn (1977) and the refinement for convective stars in short period binaries provided by Zahn (1989) are implemented in BINSTAR (for details, see Siess et al. (2013)).

Accretion disc and star-disc boundary layer BINSTAR includes the treatment of star-disc interactions. We apply the model of Paczynski (1991) which determines the accretion disc structure by assuming that the star and the disc are only one fluid. In the disc, advection of matter is driven by the outward transport of angular momentum by viscosity. By treating the star-disc boundary layer with a one fluid model, the same mechanism occurs at the surface of a critically rotating star. Viscosity processes remove angular momentum from the star, keeping it at a critical rotation rate but not exceeding it. This process allows the star to accrete large amounts of mass while giving angular momentum back to the disc. The extra stellar spin angular momentum transferred to the disc allows it to spread. Up to a certain radius, tidal forces disrupt the disc (Lin & Papaloizou 1979), and the angular momentum is given back to the orbit. For our models, we assume a disc to form as soon as the gainer reaches spin angular velocity of 0.8 the Keplerian value.

3 The case of critically rotating accretors in Algols

During the evolution of Algols, mass and angular momentum are transferred from the donor to the gainer via RLOF. The mass transfer rate can reach values as high as 10^{-4} $M_\odot$ yr^{-1}. However, only a few percent (0.12 $M_\odot$ over more than 5 $M_\odot$ transferred during the total mass transfer phase for our studied system) is sufficient to spin the gainer up to its critical rotation if no spin-down mechanism is invoked. Several scenarios have been investigated to overcome this problem. We discuss here the impact of tides, magnetic field braking and accretion via star-disc boundary layer interaction.

The tidal synchronisation time-scale is much longer than the time-scale for mass transfer ($M_{\rm g}/\dot{M}_{\rm acc,g}^{\rm RLOF}$), hence tides are inefficient to spin down the star. However, tides are likely to have an important role in spinning down the gainer star after the mass transfer episode because the tidal time-scale becomes short compared to the binary evolutionary time-scale. Also, after mass transfer stops, we do not expect the boundary layer and disc-locking mechanism to apply any longer.

The left panel of Fig. 1 shows the time evolution of the surface angular velocity (normalized to the critical velocity) of our system for different magnetic field strengths compared to a standard case (termed 'Free-rotation') where the evolution of the rotational velocity is not constrained. Only a strong magnetic field of around 3 kG can prevent the gainer from reaching the critical Keplerian velocity.

Irrespective of how much matter is transferred, the boundary layer mechanism keeps the star at the critical velocity. As the specific angular momentum accreted differs between spin-down mechanisms, the stellar spin angular momentum and in turn the orbital angular momentum change, subsequently affecting the separation of the system. The right panel of Fig. 1 displays the evolution of the separation for three models ('Free-rotation', magnetic field (3 kG), star disc boundary layer) for our considered system. We clearly see that the spin-down mechanism has a large impact on the binary separation, producing shorter period systems for the boundary-layer model. This variation will then impact on the subsequent long term evolution of the binary system, leading to different objects, for example detached binaries or contact systems.

4 Conclusions

In this study, we performed the first binary evolution that consistently takes into account the torques arising from magnetic field and star-disc interactions in an Algol system with a critically rotating accretor. Strong magnetic fields (of about 3 kG for our standard 3 + 6 $M_\odot$ case with $P_{\rm init} = 2.5$ days) and star-disc interactions

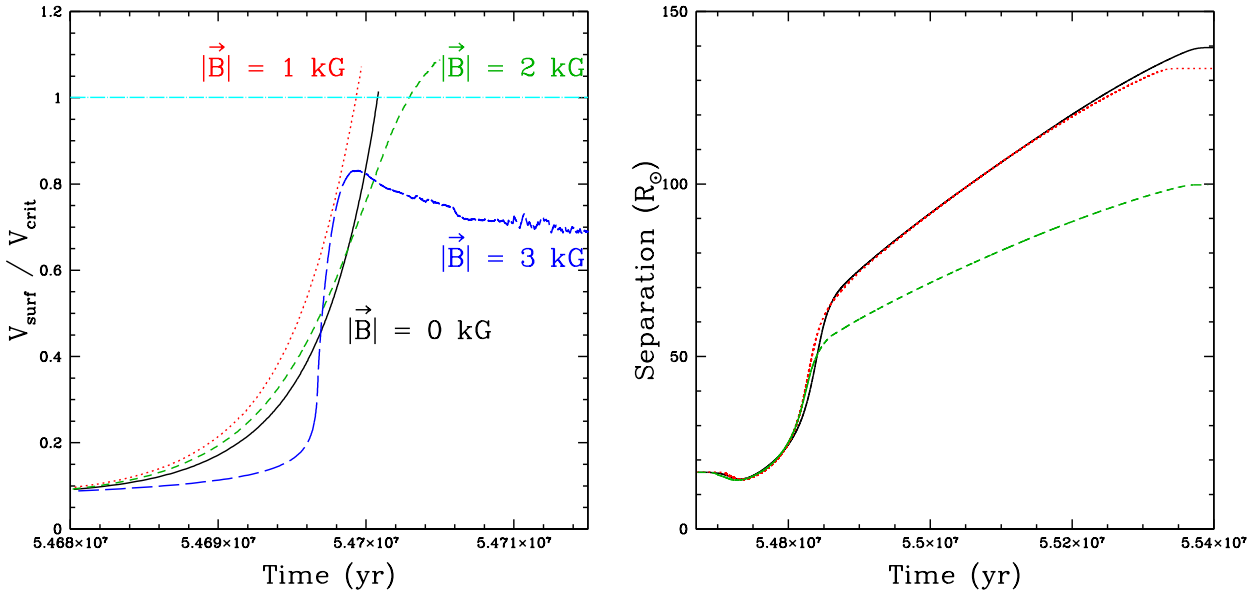

Fig. 1. Left: Evolution of the surface velocity (gainer only, normalized to the critical velocity) for different magnetic field strengths for a 6 + 3.6 $M_\odot$ system with initial period $P_{\rm init}$ = 2.5 days. Solid black line: $|\vec{B}_{\rm s}|$ = 0 kG; dotted red line: $|\vec{B}_{\rm s}|$ = 1 kG; dashed green line: $|\vec{B}_{\rm s}|$ = 2 kG; long-dashed blue line: $|\vec{B}_{\rm s}|$ = 3 kG. The dot-dashed magenta straight line represents the critical angular rotation of the star. All simulations are stopped when $v_{\rm surf} \approx v_{\rm crit}$. Only the simulation with a strong enough magnetic field avoids the critical rotation. **Right:** Evolution of the binary separation for three different configurations for the same system. Solid black line: rotation not treated ('Free-rotation'); dotted red line: magnetic field 3 kG; dashed green line: star-disc boundary layer treatment. The final separation (after the end of the mass transfer phase at $t \approx 5.535 \times 10^7$ yr) strongly depends on the treatment of the braking mechanism. In the 'Free-rotation' model, the final separation is larger than in a system accounting for rotation.

can sufficiently spin down the accretor to avoid any super-critical rotational velocities. On the other hand, tides are not efficient enough, although they are not excluded to be at work to slow down the gainer after the mass transfer phase. We show that the overall evolution of the system and especially the final separation depends sensitively on the spin-down mechanism which may lead to different subsequent evolution of the binary system.

RD and PJD acknowledge support from the Communauté française de Belgique – Actions de Recherche Concertées. LS is an FNRS Researcher.

References

Bondi, H. & Hoyle, F. 1944, MNRAS, 104, 273
Dervişoğlu, A., Tout, C. A., & Ibanoğlu, C. 2010, MNRAS, 406, 1071
Flannery, B. P. 1975, MNRAS, 170, 325
Kolb, U. & Ritter, H. 1990, A&A, 236, 385
Lin, D. N. C. & Papaloizou, J. 1979, MNRAS, 186, 799
Livio, M. & Pringle, J. E. 1992, MNRAS, 259, 23P
Packet, W. 1981, A&A, 102, 17
Paczynski, B. 1991, ApJ, 370, 597
Siess, L. 2006, A&A, 448, 717
Siess, L., Izzard, R., Davis, P., & Deschamps, R. 2013, A&A, submitted
Weber, E. J. & Davis, Jr., L. 1967, ApJ, 148, 217
Zahn, J. 1989, A&A, 220, 112
Zahn, J.-P. 1977, A&A, 57, 383

SF2A 2012
S. Boissier, P. de Laverny, N. Nardetto, R. Samadi, D. Valls-Gabaud and H. Wozniak (eds)

CALCULATING MASS TRANSFER IN ECCENTRIC BINARIES USING THE BINARY EVOLUTION CODE BINSTAR

P. J. Davis[1], L. Siess[1] and R. Deschamps[1]

Abstract. We present calculations of mass transfer via Roche lobe overflow for a $1.50 + 1.40$ $M_\odot$ main sequence binary system with an eccentricity of 0.25 and orbital period of approximately 0.7 d using the state-of-the-art binary evolution code `BINSTAR`. We consider the effect of eccentricity and an asynchronously rotating donor star on the Roche lobe radius, and investigate their impact on the mass transfer rate.

Keywords: Binaries: close, stars: evolution, methods: numerical

1 Introduction

Studies of interacting binaries typically assume that the orbit is circular and that the donor is rotating synchronously with the orbit by the time Roche-lobe overflow (RLOF) commences, as a result of the short timescales over which tidal forces act (Zahn 1977). However, such assumptions have been challenged by observations of ellipsoidal variables with confirmed significant eccentricities (Nicholls & Wood 2012). Furthermore, Sepinsky et al. (2007b, 2009) found that mass transfer via RLOF in eccentric binaries may act to increase the eccentricity on a shorter timescale than the tidal circularization timescale which acts to decrease it.

In an accompanying paper, Sepinsky, Willems, & Kalogera (2007a) found that the Roche lobe radius for a donor star, which is rotating super-synchronously compared with the orbital motion at periastron is smaller than the radius calculated using the standard Eggleton (1983) prescription. These effects, of eccentricity and asynchronism, directly affect the RLOF mass transfer rate, and have been modelled using the state-of-the-art binary evolution code `BINSTAR`.

Here, we consider a 1.50+1.40 $M_\odot$ binary, with an eccentricity of 0.25, and an initial period $P_{\rm orb} \approx 0.7$ d. The impact of asynchronous rotation and eccentricity on the mass transfer rate are investigated, as well as the response of the structure of the donor and accretor. In Sect. 2, we describe the `BINSTAR` code, and the key input physics. Calculated mass transfer rates are presented in Sect. 3, while the reaction of the stars to mass transfer is discussed in Sects. 4 and 5. A summary is given in Sect. 6.

2 Computational method

`BINSTAR` is designed for the evolution of low- and intermediate-mass binaries. It is an extension of the 1-dimensional, single star evolution code `STAREVOL` (see Siess 2010, and references therein). Briefly, `BINSTAR` simultaneously solves for the orbital eccentricity and separation, and the two stars. `BINSTAR` also handles semi-convection, thermohaline mixing and diffusive overshooting and includes a nuclear network of 53 species (up to ^{37}Cl). For further details of the binary input physics, see Siess et al. (2013).

2.1 The initial binary model

We consider a main sequence binary consisting of a donor star of mass $M_{\rm d} = 1.50$ $M_\odot$ with a gainer of mass $M_{\rm g} = 1.40$ $M_\odot$, with radii $R_{\rm d} = 1.44$ $R_\odot$ and $R_{\rm g} = 1.23$ $R_\odot$ respectively. The stars have an age of approximately 1.3 Gyr and a metallicity of $Z = 0.001$, and we use a convection mixing length of $\alpha_{\rm MLT} = 1.71$. We do not consider convective overshooting. The binary has an eccentricity $e = 0.25$ and a semi-major axis $a = 4.80$ $R_\odot$.

[1] Institut d'Astronomie et d'Astrophysique, Université Libre de Bruxelles, Boulevard du Triomphe, Brussels 1050, Belgium

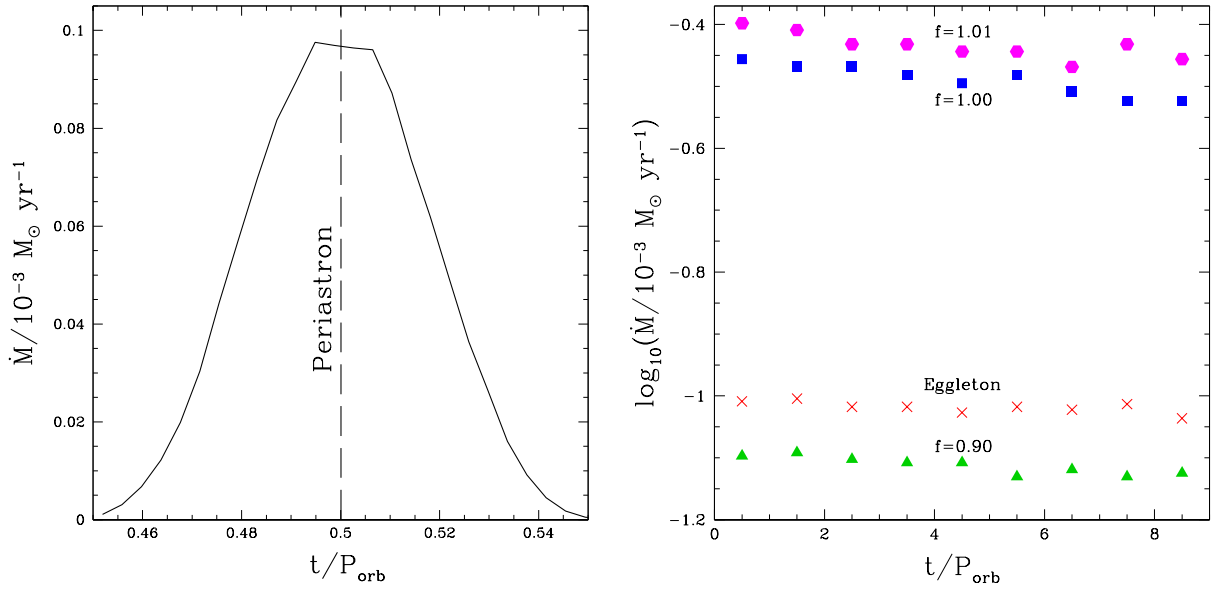

Fig. 1. Left: Mass transfer rate as a function of time since apastron, where time is in units of the orbital period, and the standard Roche formalism is used (Eq. 2.1). The dashed, vertical line indicates periastron. **Right:** Periastron mass transfer rate during 9 consecutive orbits for the standard Roche formalism (red crosses), $f = \Omega/\omega_{\rm peri} = 0.90$ (green triangles), $f = 1.00$ (blue squares) and $f = 1.01$ (magenta hexagons).

2.2 *Roche lobe radius*

For an eccentric binary in synchronous rotation where the separation between the two stars is D, the Roche lobe radius of the donor star, $R_{\mathcal{L}_1}$, is

$$R_{\mathcal{L}_1} = \frac{0.49q^{2/3}}{0.6q^{2/3} + \ln(1+q^{1/3})} D, \tag{2.1}$$

where $q = M_{\rm d}/M_{\rm g}$ and we have modified the expression for $R_{\mathcal{L}_1}$ given by Eggleton (1983) by replacing a with D. For brevity, we henceforth term this as the 'standard Roche formalism'.

We also follow Sepinsky et al. (2007a) and calculate $R_{\mathcal{L}_1}$ by taking into account the eccentricity of the orbit, and any asynchronism of the donor star. The potential in this case (normalized to the gravitational potential of the accretor), is given by

$$\Psi = -\frac{q}{(x^2+y^2+z^2)^{\frac{1}{2}}} - \frac{1}{[(x-1)^2+y^2+z^2]^{\frac{1}{2}}} - \frac{1}{2}\frac{f^2(1+e)^4}{(1+e\cos\nu)^3}(1+q)(x^2+y^2) + x, \tag{2.2}$$

where the x-axis lies along the line joining the centers of mass of the two stars, in the direction from the donor to the accretor, the z-axis is perpendicular to the plane of the orbit and is parallel to the spin angular velocity vector of the donor, and the y-axis is perpendicular to the x- and z-axes, and completes a right-handed coordinate set. All coordinates are given in units of D. We use a Monte-Carlo integration technique to calculate $R_{\mathcal{L}_1}$ from Eq. (2.2). In Eq. (2.2) f is the spin angular speed of the donor star in units of the orbital angular speed at periastron, i.e.

$$f = \frac{\Omega}{\omega_{\rm peri}}. \tag{2.3}$$

2.3 *Calculating mass transfer rates*

We consider a donor star of mass $M_{\rm d}$, radius $R_{\rm d}$, effective temperature $T_{\rm eff,d}$, and with a mean molecular weight and density at the photosphere, $\mu_{\rm ph,d}$ and $\rho_{\rm ph,d}$ respectively. The mass transfer rate, $\dot{M}_{\rm d}$, in the case where

material is removed from the optically thin region of the donor's atmosphere (i.e. where the optical depth is $\tau \leq \frac{2}{3}$) is calculated using

$$-\dot{M}_{\rm d} = \dot{M}_0 \exp\left(\frac{R_{\rm d} - R_{\mathcal{L}_1}}{\hat{H}_{\rm P}}\right), \tag{2.4}$$

(Ritter 1988) where $\hat{H}_{\rm P}$ is the pressure scale height of the donor at the location of the inner Lagrangian point $\mathcal{L}_1$, and $\dot{M}_0$ is the mass transfer rate if the donor star exactly fills its Roche lobe. Equation. (2.4) is only valid if the donor star is slightly over- or under-filling its Roche lobe. If this is not the case, then mass is also lost from the optically thick layers of the star (where $\tau \geq 2/3$). The mass transfer rate is therefore given by

$$-\dot{M}_{\rm d} = \dot{M}_0 + 2\pi F(q)\frac{R_{\mathcal{L}_1}^3}{GM_{\rm d}}\int_{R_{\mathcal{L}_1}}^{R_{\rm ph}} \Theta(\Gamma_1)\frac{Gm(P\rho)^{\frac{1}{2}}}{r^2}\,{\rm d}r, \tag{2.5}$$

(Kolb & Ritter 1990) where $F(q)$ is determined from the area of the equipotential surface which intersects with the $\mathcal{L}_1$ point. Also, P, T, μ and m are the pressure, temperature, mean molecular weight and the mass of the donor star respectively at the radial coordinate r. Next, $\Theta(\Gamma_1)$ is a function of the adiabatic exponent, $\Gamma_1 = ({\rm dln}P/{\rm dln}\rho)_{\rm ad}$ (see Kolb & Ritter 1991 for further details). The integral in Eq. (2.5) is evaluated numerically from the $\mathcal{L}_1$ point to the photosphere (subscript 'ph').

3 Calculated mass transfer rates

The left panel of Fig. 1 shows that $|\dot{M}_{\rm d}|$ rises as the stars approach periastron (dashed vertical line), reaching about 10^{-4} M$_\odot$ yr^{-1} for the standard Roche formalism. This behaviour is due to the fact that $R_{\mathcal{L}_1}$ decreases as D decreases (Eq. 2.1) causing a corresponding rise in the amount that the star overfills its Roche lobe, $R_{\rm d} - R_{\mathcal{L}_1}$, and therefore in $|\dot{M}_{\rm d}|$ (Eqs. 2.4 and 2.5). At periastron, $R_{\rm d} - R_{\mathcal{L}_1}$ is maximum. Away from periastron, $R_{\mathcal{L}_1}$ and $R_{\rm d} - R_{\mathcal{L}_1}$ decline causing a drop in $|\dot{M}_{\rm d}|$.

The right panel of Fig. 1 shows that $|\dot{M}_{\rm d}|$ at a given periastron passage increases as f is increased. Indeed, $|\dot{M}_{\rm d}|$ increases from approximately 7×10^{-5} M$_\odot$ yr^{-1} for the sub-synchronous ($f = 0.90$) case to about 4×10^{-4} M$_\odot$ yr^{-1} for the super-synchronous case ($f = 1.01$). If f is increased (causing a corresponding increase in the centrifugal acceleration), then the location of $\mathcal{L}_1$ must be situated closer to the donor star so that a net zero-acceleration is re-established. Since the Roche equipotential surface passes through the $\mathcal{L}_1$ point, an increasing value of f means that both the volume and $\mathcal{L}_1$ will shrink.

4 Reaction of the donor

The inset in Fig. 2 shows that the donor's surface luminosity, $L_{\rm d}$, initially rises at the start of mass loss, due to its small surface convection zone. Mass loss from this layer releases gravo-thermal energy causing $L_{\rm d}$ to briefly increase. However, subsequent reaction is dominated by the extended radiative envelope of the donor. The action of removing mass from the radiative layers absorbs gravo-thermal energy, causing them to be under-luminous compared to an unperturbed star of the same mass. Hence, $L_{\rm d}$ decreases, and the energy deficit within the surface layers causes them to contract (Fig. 2).

Once mass transfer shuts off, the donor radius, $R_{\rm d}$ and $L_{\rm d}$ rise again as energy flows from the donor's interior to fill the luminosity deficit in the outer surface layers as it restores thermal equilibrium. However, the donor does not fully re-establish thermal equilibrium by the time mass transfer resumes at the next periastron passage; the donor is still under-sized and under-luminous (main panel of Fig. 2). As $R_{\rm d}$ shrinks, $R_{\rm d} - R_{\mathcal{L}_1}$ becomes smaller with each successive periastron passage, and the mass transfer rate during periastron will decrease with time. This can be seen in the right panel of Fig. 1.

5 Reaction of the accretor

Towards periastron and in contrast to the donor star, the accretor's surface convection zone continues to play a role in response to mass addition. Mass accretion causes the gainer's surface convection zone to grow in size (see Davis, Siess, & Deschamps 2013, for details), and subsequent addition of mass to the convection zone absorbs gravo-thermal energy. These layers become under-luminous (inset of Fig. 2) and as a result, they contract.

Beyond periastron, with the decline in $|\dot{M}_{\rm d}|$, the surface layers re-expand and the luminosity increases as energy from the accretor's interior flows outwards to the under-luminous layers. Once mass transfer shuts off,

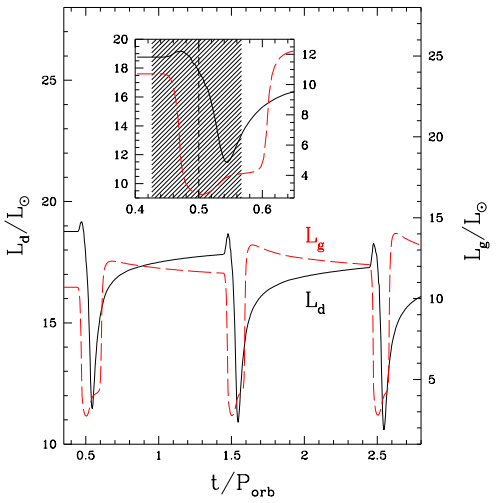

Fig. 2. Time evolution of the donor's luminosity, $L_{\rm d}$ (left axis, solid black curve), and accretor's luminosity, $L_{\rm g}$ (right axis, dashed red curve), during mass transfer using the standard Roche formalism. The inset shows a close-up of the first periastron passage. The shaded region gives the duration of mass loss, while the dotted vertical line indicates periastron.

the expansion of the surface layers continue. However, once the excess energy originally created by the accretion phase has been radiated away, both the radius and surface luminosity start to slowly decrease.

6 Summary

We present the first calculations of mass transfer in an eccentric binary system using a detailed stellar and binary evolution code, called `BINSTAR`. The evolution of the mass transfer rate has a Gaussian-like profile, with mass transfer commencing (ending) just before (after) periastron, in agreement with recent smooth particle hydrodynamical simulations (Lajoie & Sills 2011; Davis et al. 2013). The mass transfer rate is maximum at periastron, and using the standard Eggleton (1983) formalism it peaks at about 10^{-4} $M_\odot$ yr^{-1}. This is about a factor of 3 smaller than the synchronous $f = 1.00$ case (which includes the effects of eccentricity), highlighting the need to account for the non-circular nature of the orbit when determining the Roche lobe radius. During mass transfer, the donor's radius and luminosity decline due to its substantial radiative envelope. As a result of the accretor's growing surface convection zone during accretion, its radius and surface luminosity initially shrink until periastron, after which they rise. Both stars do not fully re-establish thermal equilibrium by the time mass transfer re-commences.

PJD acknowledges financial support from the Communauté Française de Belgique - Actions de recherche Concertées, from the Université Libre de Bruxelles and from an FNRS Fellowship (Chargé de Recherches 2011). LS is a FNRS research associate.

References

Davis, P. J., Siess, L., & Deschamps, R. 2013, A&A (submitted)
Eggleton, P. P. 1983, ApJ, 268, 368
Kolb, U. & Ritter, H. 1990, A&A, 236, 385
Lajoie, C.-P. & Sills, A. 2011, ApJ, 726, 67
Nicholls, C. P. & Wood, P. R. 2012, MNRAS, 421, 2616
Ritter, H. 1988, A&A, 202, 93
Sepinsky, J. F., Willems, B., & Kalogera, V. 2007a, ApJ, 660, 1624
Sepinsky, J. F., Willems, B., Kalogera, V., & Rasio, F. A. 2007b, ApJ, 667, 1170
Sepinsky, J. F., Willems, B., Kalogera, V., & Rasio, F. A. 2009, ApJ, 702, 1387
Siess, L. 2010, A&A, 512, A10
Siess, L., Izzard, R. G., Davis, P. J., & Deschamps, R. 2013, A&A (submitted)
Zahn, J.-P. 1977, A&A, 57, 383

SF2A 2012
S. Boissier, P. de Laverny, N. Nardetto, R. Samadi, D. Valls-Gabaud and H. Wozniak (eds)

CHARRON: CODE FOR HIGH ANGULAR RESOLUTION OF ROTATING OBJECTS IN NATURE*

A. Domiciano de Souza[1], J. Zorec[2] and F. Vakili[1]

Abstract. Rotation is one of the fundamental physical parameters governing stellar physics and evolution. At the same time, spectrally resolved optical/IR long-baseline interferometry has proven to be an important observing tool to measure many physical effects linked to rotation, in particular, stellar flattening, gravity darkening, differential rotation. In order to interpret the high angular resolution observations from modern spectro-interferometers, such as VLTI/AMBER and VEGA/CHARA, we have developed an interferometry-oriented numerical model: CHARRON (Code for High Angular Resolution of Rotating Objects in Nature). We present here the characteristics of CHARRON, which is faster ($\simeq 10-30$ s per model) and thus more adapted to model-fitting than the first version of the code presented by Domiciano de Souza et al. (2002).

Keywords: Stars: rotation, Methods: observational, Methods: numerical, Techniques: interferometric, Techniques: high angular resolution

1 Introduction

Many recent observations and theories show that rotation (or angular momentum) is a key ingredient in stellar physics (e.g. Maeder & Meynet 2012; van Belle 2012; Maeder & Meynet 2000). Rotation modifies several aspects of the stellar physical structure (geometircal shape, temperature and luminosity distribution, convective and radiative zones, etc) and evolution (lifetimes, evolutionary tracks, chemical abundances, final stellar masses, rotation periods of pulsars).

Since the beginning of the 21st century, optical/IR long-baseline spectro-interferometry (OLBSI) has been providing crucial observations that greatly improve our understanding of rotating stars. By spatially resolving the stellar surface, OLBSI directly proved that fast rotating stars are flattened (rotationally distorted photospheres; e.g. van Belle et al. 2001; Domiciano de Souza et al. 2003) and and gravity darkened (poles hotter than the equator; e.g. Domiciano de Souza et al. 2005; Che et al. 2011). These important results were obtained from spectro-interferometric observables like visibility amplitudes and closure phases. Recently, Domiciano de Souza et al. (2012)showed that the differential phases (an still under-exploited observable) allow to measured measure angular diameters, rotation velocities, and orientation of stellar rotation axes.

In order to interpret the OLBSI observations and constraint the physical parameters of rotating stars, it is important to develop models including the main physical effects caused by high rotation rates. In this work we describe the IDL-based model CHARRON[i] (Code for High Angular Resolution of Rotating Objects in Nature), which is dedicated to the interpretation and analysis of spectro-interferometric observations of rotating stars.

2 Basic equations of stellar rotation

As discussed by Zorec et al. (2011), the gravitational potential of rotating centrally condensed objects is, in most realistic cases, well described (better than $\sim 5\%$) by a simple central-field expression (Roche approximation):

$$\Phi_{\rm G}(\theta) = -GM/R_{\rm s}(\theta)\ , \tag{2.1}$$

[1] Laboratoire J.-L. Lagrange, UMR 7293, OCA-UNS-CNRS, Boulevard de l'Observatoire, BP 4229, 06304 Nice Cedex 4, France
[2] UPMC Univ. Paris 06, UMR7095, Institut d'Astrophysique de Paris, 98bis Bd. Arago, 75014 Paris, France
[i] Name of an ancient profession (from Wikipedia french webpage: *spécialiste du bois, maître de tout ce qui tourne et roule, de la brouette à la charrette*).

where θ is the colatitude, $R_{\rm s}(\theta)$ is the stellar surface radius, and the other symbols have their usual meanings. This is equivalent to the potential that we would have if the whole mass was concentrated at the center of the star.

Many works showed the presence of differential rotation law in the surface of stars (e.g. Reiners & Royer 2004; Ammler-von Eiff & Reiners 2012; Zorec et al. 2012). Most of these works adopt a solar-like surface velocity (Maunder formula)

$$\Omega(\theta) = \Omega_{\rm e}(1 + \alpha \cos^2 \theta) \ , \tag{2.2}$$

where $\Omega_{\rm e}$ is the equatorial angular velocity and α is the differential rotation parameter, corresponding to the excess of polar angular velocity ($\Omega_{\rm pol}$) relative to $\Omega_{\rm e}$, i.e., $\alpha = (\Omega_{\rm pol} - \Omega_{\rm e})/\Omega_{\rm e}$.

Equation 2.2 is a non-conservative rotation law, which implies that the shape of the star cannot be obtained from an effective rotational potential. It is instead defined from the surface resulting in a zero work done by the effective gravity $\mathbf{g}_{\rm eff}$ for an arbitrary displacement $d\mathbf{s}$ (Maeder 2009):

$$\mathbf{g}_{\rm eff}.d\mathbf{s} = 0 \ . \tag{2.3}$$

From the equation above and following Zorec et al. (2011), the surface of a star in the Roche approximation rotating with a Maunder-like non-conservative law is given by

$$\frac{R_{\rm s}(\theta)}{R_{\rm e}} = \frac{1}{1 + \eta_o[I(\pi/2) - I(\theta)]} \ , \tag{2.4}$$

where

$$I(\theta) = \frac{1}{2}\int_0^\theta \left[\frac{\Omega_{\rm s}(\theta)}{\Omega_{\rm e}}\right]^2 \left(\frac{d\varpi^2}{d\theta}\right) d\theta \ , \tag{2.5}$$

and

$$\varpi(\theta) = R_{\rm s}(\theta)\sin\theta \ . \tag{2.6}$$

The parameter η_o is the ratio of centrifugal to the gravitational acceleration in the equator

$$\eta_o = \frac{\Omega_{\rm e}^2 R_{\rm e}^3}{GM} \ . \tag{2.7}$$

The shape of the star $R_{\rm s}(\theta)$ is obtained by iteration using the equations above. Uniform rotation ($\Omega(\theta) = \Omega_{\rm e}$ constant) is a special case of this model, where shape of the star is given by the classical Roche model (e.g. Kopal 1987).

The surface effective gravity (gravitational plus centrifugal accelerations) is given by

$$\mathbf{g}_{\rm eff} = g_{{\rm eff},r}\hat{r} + g_{{\rm eff},\theta}\hat{\theta} = \left[-GM/R_{\rm s}^2(\theta) + \Omega(\theta)^2 R_{\rm s}(\theta)\sin^2\theta\right]\hat{r} + \left[\Omega(\theta)^2 R_{\rm s}(\theta)\sin\theta\cos\theta\right]\hat{\theta} \ . \tag{2.8}$$

The surface effective temperature is linked to $g_{\rm eff}$ through the gravity darkening effect (von Zeipel effect; von Zeipel 1924). We adopt the commonly used expression for the gravity darkening effect

$$T_{\rm eff}(\theta) = C_{\rm gd}\, g_{\rm eff}^{\beta}(\theta) \ , \tag{2.9}$$

where the gravity darkening parameter β depends on the surface temperature and internal physical conditions. The gravity darkening constant $C_{\rm gd}$ is obtained from

$$C_{\rm gd} = \left(\frac{\overline{T}_{\rm eff}^4 S}{\int g^{4\beta} ds}\right)^{1/4} = \left(\frac{L}{\sigma \int g^{4\beta} ds}\right)^{1/4} \ . \tag{2.10}$$

The stellar luminosity L, surface area S, and mean surface effective temperature are related by

$$L = S\sigma\overline{T}_{\rm eff}^4 \ , \tag{2.11}$$

σ being the Stefan-Boltzmann constant.

We note that in the equations above we are ignoring the Eddington factor, which changes the effective gravity but is significant only for very massive stars (above ~ 20 M$_\odot$).

3 CHARRON description and application example

The equations given in the previous section are implemented in CHARRON to define the physical structure of the rotating star in terms of shape, mass, luminosity, rotation rate, and local effective temperature and gravity. CHARRON is written in IDL[ii] and makes use of the fast vector operations provided by this language.

The numerical implementation of the physical equations and the discretization procedure of the stellar surface into thousands ($\simeq 50\,000$) small surface area elements are similar to those used in the code BRUCE (Townsend 1997) and in the interferometry-oriented code presented by Domiciano de Souza et al. (2002).

To obtain monochromatic intensity maps of the stellar photosphere a local spectrum, Doppler shifted by the local rotation velocity projected onto the observer's direction, is assigned each visible surface area element. This local photospheric spectrum, provided by the user, can be given as an analytical equation (including continuum, spectral line, limb darkening) or as the output of stellar atmosphere models calculated with radiative transfer codes. These local spectra can depend on different physical parameters, in particular the local effective temperature and gravity. CHARRON calculates the Fourier transform of the monochromatic intensity maps to obtain spectro-interferometric observables, in particular spectra, absolute and differential visibilities, differential phases, and closure phases.

A set of input parameters is required by CHARRON to define the stellar rotation model and spectro-interferometric observables. A useful set of input parameters is equatorial radius $R_{\rm e}$, equatorial rotation velocity $V_{\rm e}$, differential rotation parameter α, mass M, inclination i, distance d, gravity darkening parameter β, orientation of the rotation axis on the sky plane, and local profile.

Figure 1 shows examples of monochromatic intensity maps and differential phases $\phi_{\rm diff}(\lambda)$ of the fast rotating Be star Achernar calculated with CHARRON to interpret VLTI/AMBER $\phi_{\rm diff}(\lambda)$ observations of this star performed in the Br γ line at spectral resolution 12 000. The full results of the VLTI/AMBER data analysis and interpretation with CHARRON are given by Domiciano de Souza et al. (2012).

4 Conclusion and futur prospects

CHARRON, presented in this work, was shown to be well adapted to interpret spectro-interferometric observations of fast rotating stars. This code will be used to analyze the observations from several on-going observing programs on rotating stars, which have been proposed by our team on modern spectro-interferometers, in particular VLTI/AMBER and CHARA/VEGA.

References

Ammler-von Eiff, M. & Reiners, A. 2012, A&A, 542, A116

Che, X., Monnier, J. D., Zhao, M., et al. 2011, ApJ, 732, 68

Domiciano de Souza, A., Hadjara, M., Vakili, F., et al. 2012, A&A, 545, A130

Domiciano de Souza, A., Kervella, P., Jankov, S., et al. 2003, A&A, 407, L47

Domiciano de Souza, A., Kervella, P., Jankov, S., et al. 2005, A&A, 442, 567

Domiciano de Souza, A., Vakili, F., Jankov, S., Janot-Pacheco, E., & Abe, L. 2002, A&A, 393, 345

Kopal, Z. 1987, Ap&SS, 133, 157

Maeder, A. 2009, Physics, formation and evolution of rotating stars, 1st edn., Astronomy and Astrophysics Library (Springer-Verlag)

Maeder, A. & Meynet, G. 2000, ARA&A, 38, 143

Maeder, A. & Meynet, G. 2012, Reviews of Modern Physics, 84, 25

Reiners, A. & Royer, F. 2004, A&A, 415, 325

Townsend, R. H. D. 1997, MNRAS, 284, 839

van Belle, G. T. 2012, A&A Rev., 20, 51

van Belle, G. T., Ciardi, D. R., Thompson, R. R., Akeson, R. L., & Lada, E. A. 2001, ApJ, 559, 1155

von Zeipel, H. 1924, MNRAS, 84, 665

Zorec, J., Frémat, Y., Domiciano de Souza, A., et al. 2011, A&A, 526, A87

Zorec, J., Frémat, Y., Semaan, T., et al. 2012, submitted

[ii] Interactive Data Language

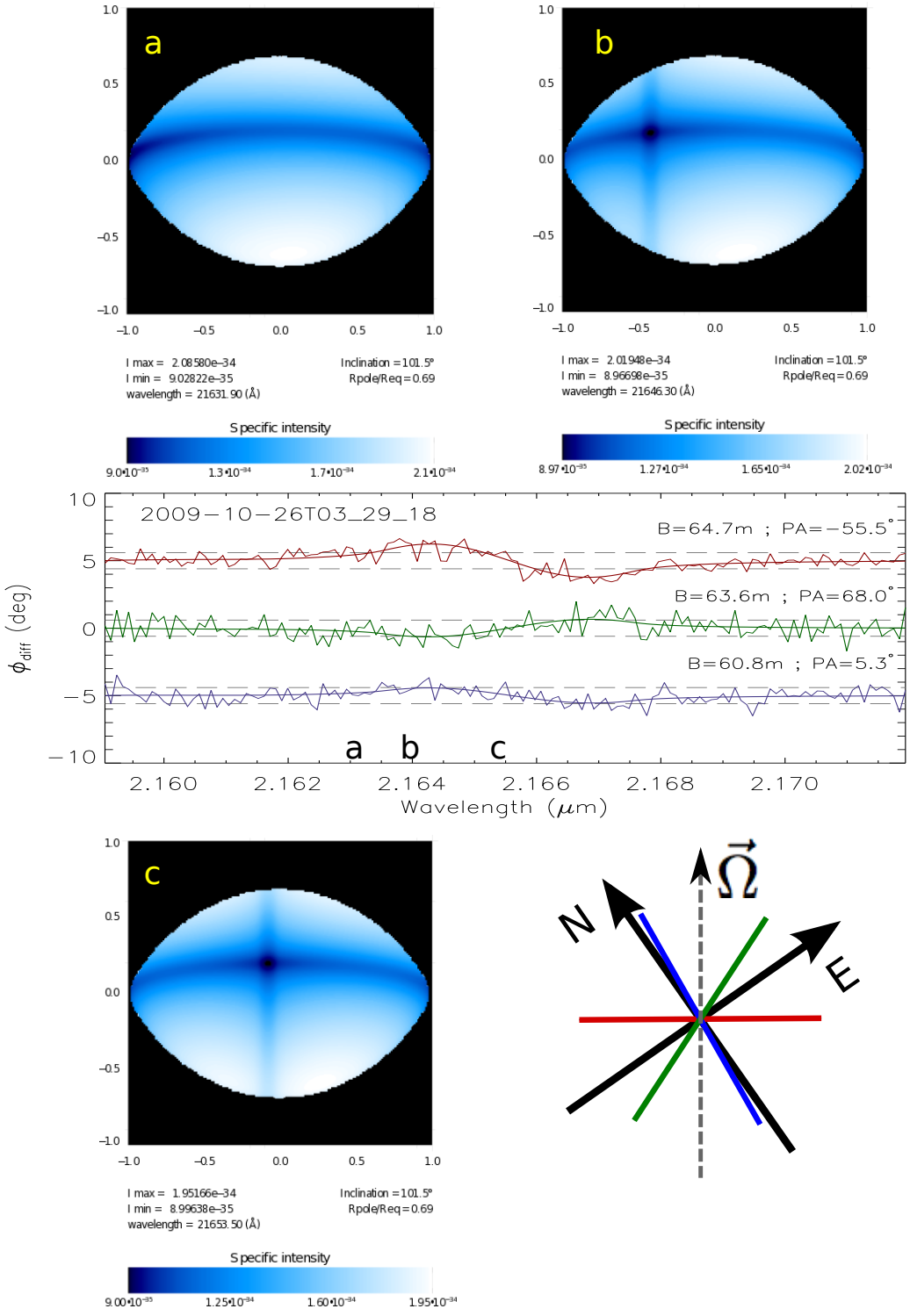

Fig. 1. Top: Monochromatic intensity maps calculated with CHARRON for three wavelengths λ (panels a, b, and c) close-to and inside the Brγ line. These maps show the influence of gravity darkening, flattening, and Doppler shifts due to fast rotation. **Middle:** Example of differential phase $\phi_{\rm diff}(\lambda)$ observed with the VLTI/AMBER interferometer on the Be star Achernar around the Br γ line. The curves show three $\phi_{\rm diff}(\lambda)$ observed at a given date and time with three different baselines (lengths and position angles). The dashed gray horizontal lines indicate the median uncertainty $\pm\sigma_\phi = \pm 0.6$ deg of all AMBER observations. The smooth curves superposed to the observations are the best-fit $\phi_{\rm diff}$ model obtained with CHARRON. The model $\phi_{\rm diff}$ correspond to the intensity maps shown in the figure. The whole set of $\phi_{\rm diff}(\lambda)$ curves are given by Domiciano de Souza et al. (2012). **Bottom:** Projection onto the sky plane (relative to the North and East directions) of the stellar rotation-axis ($\vec{\Omega}$) and of the three VLTI baselines.

SF2A 2012
S. Boissier, P. de Laverny, N. Nardetto, R. Samadi, D. Valls-Gabaud and H. Wozniak (eds)

PLANETARY NEBULAE: GETTING CLOSER TO AN UNBIASED BINARY FRACTION

D. Douchin[1,4], O. De Marco[1], G. H. Jacoby[2], T. C. Hillwig[3], D. J. Frew[1], I. Bojicic[1], G. Jasniewicz[4] and Q. A. Parker[1]

Abstract. Why 80% of planetary nebulae are not spherical is not yet understood. The *Binary Hypothesis* states that a companion to the progenitor of the central star of a planetary nebula is required to shape the nebula and even for a planetary nebula to be formed at all. A way to test this hypothesis is to estimate the binary fraction of central stars of planetary nebula and to compare it with the main sequence population. Preliminary results from photometric variability and infrared excess techniques indicate that the binary fraction of central stars of planetary nebulae is higher than that of the putative main sequence progenitor population, implying that PNe could be preferentially formed via a binary channel. This article briefly reviews these results and future studies aiming to refine the binary fraction.

Keywords: ISM: planetary nebulae: general, Stars: binaries: general, Stars: evolution, Infrared: stars

1 Introduction

Planetary nebulae (PNe) are presumed to be ejected by all $\simeq$ 1-8 $M_\odot$ stars, however when the observed PN population is compared with the theoretically expected population, a discrepancy in the number of objects appears: there are less PNe in the Galaxy than there should be (Moe & De Marco 2006). This could imply that only a subset of the parent population is actually forming PNe. This subset could be the binary progenitors (Moe & De Marco 2012). Indeed, more than 80% of PNe are non-spherical (Parker et al. 2006; Jacoby et al. 2010), showing structures such as lobes and jets that give an axisymmetric, point-symmetric or asymmetric shape to the nebula. The hypothesis traditionally used to account for these shapes has been the action of a magnetic field of the AGB star during the super wind phase upon the gas being ejected. However, this hypothesis has been disputed by Soker (2006) and Nordhaus et al. (2007), who showed that the magnetic field cannot be sustained for long enough on a whole-star scale due to the coupling between the magnetic field and the stellar rotation. Another hypothesis to account for the non-spherical shapes of PNe is the presence of a companion (e.g. Soker 1997). The hypothesis according to which a companion is required to shape an axisymmetric PN has been dubbed the *Binary Hypothesis* (De Marco 2009). To test it, it is necessary to estimate the binary fraction of central stars of planetary nebulae (CSPNe). If the observed binary fraction of CSPNe population is superior to that of the putative parent population (the main sequence (MS) stars with mass $\simeq$ 1-8 $M_\odot$, Moe & De Marco 2006), this indicates that PNe are preferentially a binary phenomenon (see De Marco (2009) for a detailed review). This paper describes briefly current efforts aimed at estimating an unbiased binary fraction of CSPN.

[1] Astronomy, Astrophysics and Astrophotonics Research Center and Department of Physics and Astronomy, Macquarie University, Sydney, NSW 2122, Australia

[2] GMTO Corp, Pasadena, CA 91101, USA

[3] Dept. of Physics and Astronomy, Valparaiso University, Valparaiso, IN 46383, USA

[4] Laboratoire Univers et Particules de Montpellier (LUPM), UMR 5299 - CC72, Université Montpellier 2, Place Eugène Bataillon, 34 095 Montpellier Cedex 5, France

2 The binary fraction obtained using photometric variability

Photometric variability of a binary CSPN can be due to an irradiation effect from the hot CSPN onto the companion, tidal deformations and eclipses (Bond 2000; Miszalski et al. 2009). The advantage of detecting bniaries using photometric variability is that it simply requires repeated observations of targets in average observing weather conditions and from the ground. For this reason, it is a reliable method and provides constantly new results (e.g. Hillwig et al. 2010). The main drawback of this method is that it is biased to small separations as irradiation effect, tidal deformations and eclipses all increase in intensity or frequency with decreasing separations, therefore it only gives access to the short period binary fraction.
Bond (2000) and Miszalski et al. (2009) already estimated close binary fractions (P $\lesssim$ 3 days) of CSPNe of 10-15% and 12-21% respectively. Although these fractions are lower limits, comparing them with the MS stars binary fraction at appropriately small separations i.e. 5-7% (Duquennoy & Mayor 1991; Raghavan et al. 2010; De Marco et al. 2012 reveals that more PNe are formed around binaries.

Hillwig et al. (these proceedings) are monitoring targets from the 2.5 kpc volume-limited sample of Frew (2008) to estimate a new close binary fraction. Although the method is similar, the sample is less biased than the previously used magnitude-limited samples and also deeper (V $<$ 21). In a similar experiment, Jacoby et al. (2012) are monitoring 5-6 CSPNe within the Kepler satellite field of view, to estimate an independent binary fraction. The sample is statistically small ; however, the CSPNe are observed with a precision never reached before ($\lesssim$ 1 mmag).

3 The binary fraction obtained using red and infrared excess

The red/IR excess technique aims to detect the signature of a cool, unresolved companion by measuring the absolute photometry of the CSPN. To do so, high precision absolute photometry needing photometric weather conditions in the B, V and I or J bands is required. This technique is fully described in De Marco et al. (2012). The measured $B-V$ color is compared to the expected $B-V$ for the single CSPN temperature according to atmospheric stellar models (e.g. Rauch & Deetjen 2003) and allows reddening to be determined whereas the $V-I$ or $V-J$ color allows the measurement of the red/IR excess, which is the difference between the $V-I$ or $V-J$ expected for a single star at the CSPN temperature and the measured one. If this difference is greater than the error on the photometric measurement, it is a binary detection. Since companions cooler than $\simeq$ M0-5 are faint, we need excellent photometric precision. Once a binary fraction has been estimated, it can be compared to the MS one (Raghavan et al. 2010) only after undetected systems are accounted for. Using the J-band allows to detect colder companions, while still not being contaminated by hot dust, although it requires a separate NIR observing run and is therefore time demanding.
Frew & Parker (2007) have used the photometry from the 2MASS and DENIS NIR surveys to determine a binary fraction ¿ 54% but the detection bias was poorly quantified. De Marco et al. (2012) have used the method described above on a sample of 27 CSPNe and have found a debiased fraction ¿ 30% from I-band data and of ¿ 54% from J-band data of a subset of 11 CSPNe in line with Frew & Parker (2007) J-band results. These preliminary results will be confronted by the study of an additional 23 objects for which optical absolute photometry has been acquired at the NOAO 2.1m telescope in March 2011 as well as $\simeq$ 30 objects for which J and H-band photometry has been obtained at the AAT 4m telescope in 2011 and the ANU 2.3m telescope in 2012. These new measurements should bring the sample to a statistically significant size and considerably reduce the error bars on the binary fraction. Recent surveys including J-band photometry will be analysed as well to extract the IR excess of other targets from the sample of Frew (2008).

4 Conclusion

Estimating an unbiased binary fraction of CSPNe is crucial to understanding whether companions play a key role in shaping PNe. Photometric variability has allowed us to determine a close binary fraction of 15-20% and is still being refined using a new, less biased sample to understand the biases inherent to the method. The red/IR excess technique has allowed us to obtain a CSPN binary fraction of 70-100%, much larger than for the MS population. However, this number carries a large uncertainty for the moment due to the small sample size. Current studies based on optical and NIR photometry as well as the use of recent NIR surveys will double the sample size to constrain the CSPN binary fraction precisely enough to support or refute the hypothesis that PNe could emerge preferentially from binary star evolution.

References

Bond, H. E. 2000, in Astronomical Society of the Pacific Conference Series, Vol. 199, Asymmetrical Planetary Nebulae II: From Origins to Microstructures, ed. J. H. Kastner, N. Soker, & S. Rappaport, 115

De Marco, O. 2009, PASP, 121, 316

De Marco, O., Passy, J.-C., Frew, D. J., Moe, M. M., & Jacoby, G. H. 2012, MNRAS

Duquennoy, A. & Mayor, M. 1991, A&A, 248, 485

Frew, D. J. 2008, PhD thesis, Department of Physics, Macquarie University, NSW 2109, Australia

Frew, D. J. & Parker, Q. A. 2007, in Asymmetric Planetary Nebulae 4 conference, APN IV Conference Proceedings, 475

Hillwig, T. C., Bond, H. E., Afşar, M., & De Marco. 2010, AJ, 140, 319

Jacoby, G., De Marco, O., Howell, S., & Kronberger, M. 2012, in American Astronomical Society Meeting Abstracts, Vol. 219, American Astronomical Society Meeting Abstracts #219

Jacoby, G. H., Kronberger, M., Patchick, D., et al. 2010, PASA, 27, 156

Miszalski, B., Acker, A., Moffat, A. F. J., Parker, Q. A., & Udalski, A. 2009, AA, 496, 813

Moe, M. & De Marco, O. 2006, ApJ, 650, 916

Moe, M. & De Marco, O. 2012, in IAU Symposium, Vol. 283, IAU Symposium, 111–114

Nordhaus, J., Blackman, E. G., & Frank, A. 2007, MNRAS, 376, 599

Parker, Q. A., Acker, A., Frew, D. J., et al. 2006, MNRAS, 373, 79

Raghavan, D., McAlister, H. A., Henry, T. J., et al. 2010, ApJS, 190, 1

Rauch, T. & Deetjen, J. L. 2003, in Astronomical Society of the Pacific Conference Series, Vol. 288, Stellar Atmosphere Modeling, ed. I. Hubeny, D. Mihalas, & K. Werner, 103

Soker, N. 1997, ApJS, 112, 487

Soker, N. 2006, ApJl, 645, L57

SF2A 2012
S. Boissier, P. de Laverny, N. Nardetto, R. Samadi, D. Valls-Gabaud and H. Wozniak (eds)

PULSATIONS-CONVECTION COMBINATION IN STARS

S. Félix[1], E. Audit[1] and B. Dintrans[2]

Abstract. The κ-mechanism and the Cepheids' instability band have been studied and modeled in 1D and 2D cartesian boxes with the Pencil code (Thomas Gastine's thesis work and papers). We intend to extend this work to 3D simulations with the hydrodynamic code Heracles. First step is getting hydrostatic equilibrium with sufficient precision so that future added features will be correctly performed. 1D and 2D cases are explored, both with isothermal and ideal gas evolutions with Heracles. Those equilibria are then perturbated by an overdensity. First results show that we manage to get a fairly good equilibrium profile with negligible residual velocities.

Keywords: hydrostatic equilibrium, simulations, Heracles, Cepheid, κ-mechanism

1 Introduction

Cepheids are variable stars from the instability strip of the Hertzsprung-Russel diagram. They have a variable luminosity (and radius) linked to the famous period-luminosity relationship used to calculate star's distances. These periodic variations were explained by Eddington (1917) through the κ-mechanism, an excitation mechanism of stellar oscillations that is related to the opacity in ionisation regions.

The blue edge of the classical instability strip (where stars have higher surface temperature) is rather well-known and explained (Chiosi et al. (1993); Beaulieu et al. (1995)) but cold Cepheids close to the red edge present a convective zone at their surface that affects their pulsation properties.

These cold Cepheids were poorly described by complex models with a large number of unconstrained (if not degenerate) free parameters (Yecko et al. (1998); Buchler (2009); Gastine & Dintrans (2011a)), until Thomas Gastine performed 1D and 2D direct numerical simulations that correctly took into account the nonlinearities involved in the convection-pulsation coupling (Gastine & Dintrans (2011b)), using the Pencil Code.

Among other things, he showed that, for a given position in the layer, the hollow amplitude and width of the conduction profile stand out as the key parameters governing the occurrence of unstable modes driven by the κ-mechanism (Gastine & Dintrans (2008)).

These authors then studied the physical conditions needed to lead to a quenching of oscillations by convection. Indeed, in cold Cepheids, a coupling occurs between the acoustic oscillations and the convective motions close to the surface: hence, the surface convective zone stabilises the radial oscillations excited by the κ-mechanism. It was shown that a larger stratification in density leads to smaller convective plumes that do not affect the purely radial modes much, while large-scale vortices may quench the oscillations.

But the convection is an intrinsically 3D phenomenon so it is necessary to get to know what happens in 3D simulations. In order to do that, we are using the Heracles hydrodynamic simulation code from CEA, France. The first step is to reproduce Thomas Gastine's results obtained in 1D and 2D with this code and, first of all, constructing 1D and 2D hydrostatic equilibrium for isothermal or ideal gas.

First results are shown here, for isothermal and ideal gas, first for 1D and then for 2D equilibrium.

2 Hydrostatic equilibrium with Heracles

Heracles is a 3D hydrodynamical code used to simulate astrophysical fluid flows. It uses a finite volume Godunov method on a fixed grid to solve, in our first simple study case, the equations of hydrodynamics and gravity. We are using a 1D or 2D cartesian grid of physical size $l \times L$.

[1] CEA - Maison de la Simulation (USR3441), Gif-sur-Yvette, France.
[2] IRAP, CNRS/Université de Toulouse (UMR5277), 14 av. Edouard Belin, F-31400 Toulouse, France

2.1 1D equilibrium

We ran first isothermal ($\gamma = 1$) then ideal gas ($\gamma = \frac{5}{3}$) 1D simulations, using a 1D "box" $l = 1$, divided in a grid of constant spacing Δx.

Initial conditions are taken so as to reproduce hydrostatic equilibrium with a uniformed temperature: density is the usual theoretical integrated exponential profile

$$\rho_i = \frac{1}{\Delta x}\int_{x_i}^{x_{i+1}} \rho_0 \exp(-x/h)\mathrm{d}x = \rho_0 \frac{h}{\Delta x}\left[\exp(\Delta x/h) - 1\right]\exp(-i\Delta x/h), \tag{2.1}$$

so that ρ_i is the mean value of ρ over the grid cell i located at $x_i = (i-1)\Delta x$. Sound speed is $c_s = 1$ and gravity is $|g| = 1/2$, constant and directed along the x axis, towards negative values. Hence, the pressure height is $h = c_s^2/(\gamma|g|) = 2$. Finally, 1D fluid velocity is null everywhere, so that energy is only $E = P/(\gamma - 1)$ where P is the gas pressure.

The important part is boundary conditions. We have two fictive zones at each side of the domain. Hydrostatic equilibrium at constant temperature is prolonged for density and energy at each side of the domain and reflexive velocity conditions are imposed (i.e. mass flux is null at the external interfaces). Finally we are also using logarithm slopes for density and energy calculations, to get more precise results.

We obtain the following results first for an isothermal equation of state (left column of Figure 1) and then for an ideal gas (right column). In both cases, density profiles (upper panels are theoretical and simulated density profiles and middle panels are the difference between those two densities) are quite satisfying. Velocities (lower panels) should be exactly zero, as we reached hydrostatic equilibrium. Nevertheless, some residual velocities might appear due to inevitable computational approximations (rounding errors...) but are quite small (at most 10^{-6} smaller than the sound speed, that is way smaller than the fluctuations we will later be interested in) and thus negligeable.

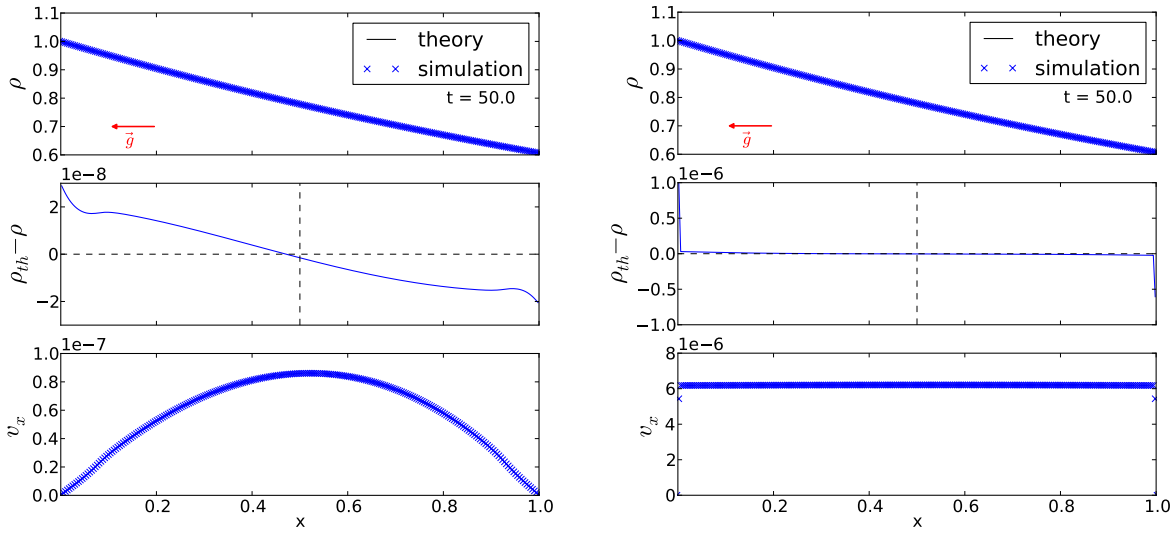

Fig. 1. Results of Heracles code for an isothermal (**Left column**) and ideal gas (**Right column**) 1D hydrostatic equilibrium at final time $t = 50.0$. **Upper panels:** simulated and theoretical densities $\rho(x)$. **Middle panels:** difference between theoretical and simulated densities $\rho_{th} - \rho$. **Lower panels:** velocity profiles along x-axis. The arrow $\vec{g}$ indicates the used gravity vector.

When a perturbation is added to the previous (isothermal or adiabatic) equilibrium, such as a smooth overdensity (later referenced to as a "density bubble", Figure 2), acoustic oscillations in density profile are expected until the fluid reaches equilibrium, after a characteristic time of $\tau_{\mathrm{dyn}} \sim 1/\sqrt{G < \rho >}$ where $< \rho >$ is the mean density value (e.g. Dintrans & Brandenburg 2004). This is obviously a new equilibrium since the box contains more mass now: the red line in Figure 2 is above the initial blue line. From these oscillations, a characteristic Fourier decomposition of the velocity is computed and results are given in Figure 3 upper panel

for the isothermal case. The frequencies of these oscillations can be computed analytically and this figure shows that our simulations are in good agreement with theoretical values $\omega_n = c_s\sqrt{k_z^2 + 0.25/h^2}$, with $k_z = (n+1)\pi$ and n the radial order of the acoustic mode.

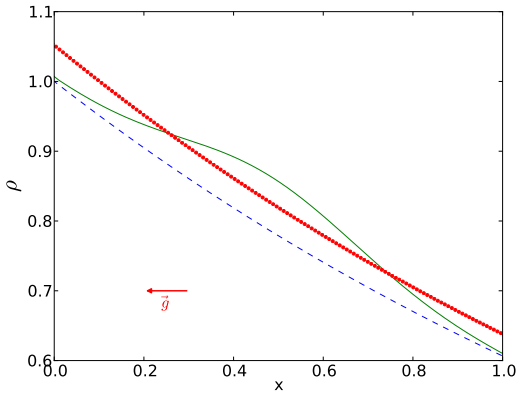

Fig. 2. Results of Heracles code for an isothermal 1D hydrostatic equilibrium perturbated by a density bubble: the dashed blue line is the density profile at equilibrium before the addition of the bubble ; the continuous green line is the density profile at the timestep when the bubble is added and the dotted red line shows the density profile at the end of the simulation when a new equilibrium has been reached. The arrow $\vec{g}$ indicates the used gravity vector.

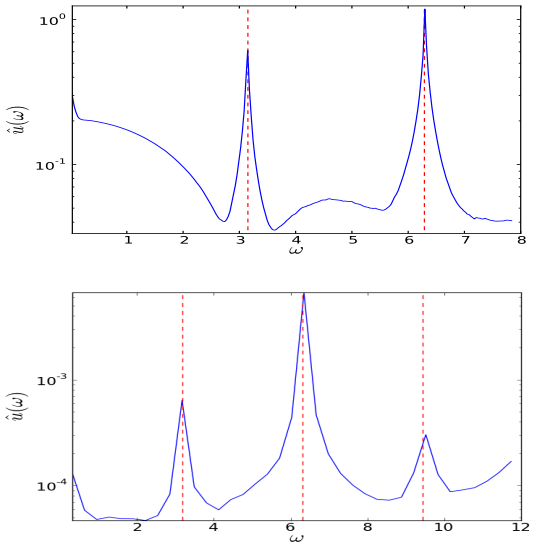

Fig. 3. Fourier spectra obtained for the 1D (**Upper panel**) and 2D (**Lower panel**) isothermal case with a bubble: theoretical frequencies are shown in red dashed lines.

2.2 2D equilibrium

In this case, we perform 2D isothermal and ideal gas simulations with the same options as in 1D simulations, except the following 2D features:

- Parameters: 2D box with $l = 1,\ L = 1$, divided in a grid of constant spacing $\Delta x \times \Delta y$.
- Initial conditions: on the x-axis, we get the same exponential profile for all the points of the y-axis.
- Boundary conditions: on the y-axis, boundary conditions are periodic.

The hydrostatic equilibrium is stable in both cases and, as in 1D equilibrium, residual velocities are negligeable. Figure 4 upper row shows an unperturbated isothermal 2D hydrostatic equilibrium: we can see that 2D equilibrium behaves like a juxtaposition of 1D equilibria.

When a density perturbation is added to the previous equilibrium (Figure 4 middle row), oscillations develop until the fluid reaches equilibrium again (again, it is a new equilibrium with more mass, as shown in Figure 4 lower row). The Fourier decomposition is also in good agreement with theoretical frequencies, as the lower panel in Figure 3 shows.

3 Conclusions

With HERACLES, we obtain a fairly good hydrostatic equilibrium with very small residual velocities. Theoretical frequencies are found if the equilibrium is perturbated by a density bubble and a new equilibrium is reached after some time. This will be quite important since we are going to implement complex conduction profiles and instabilities. We aim at extending these studies to a 3D cartesian box with HERACLES.

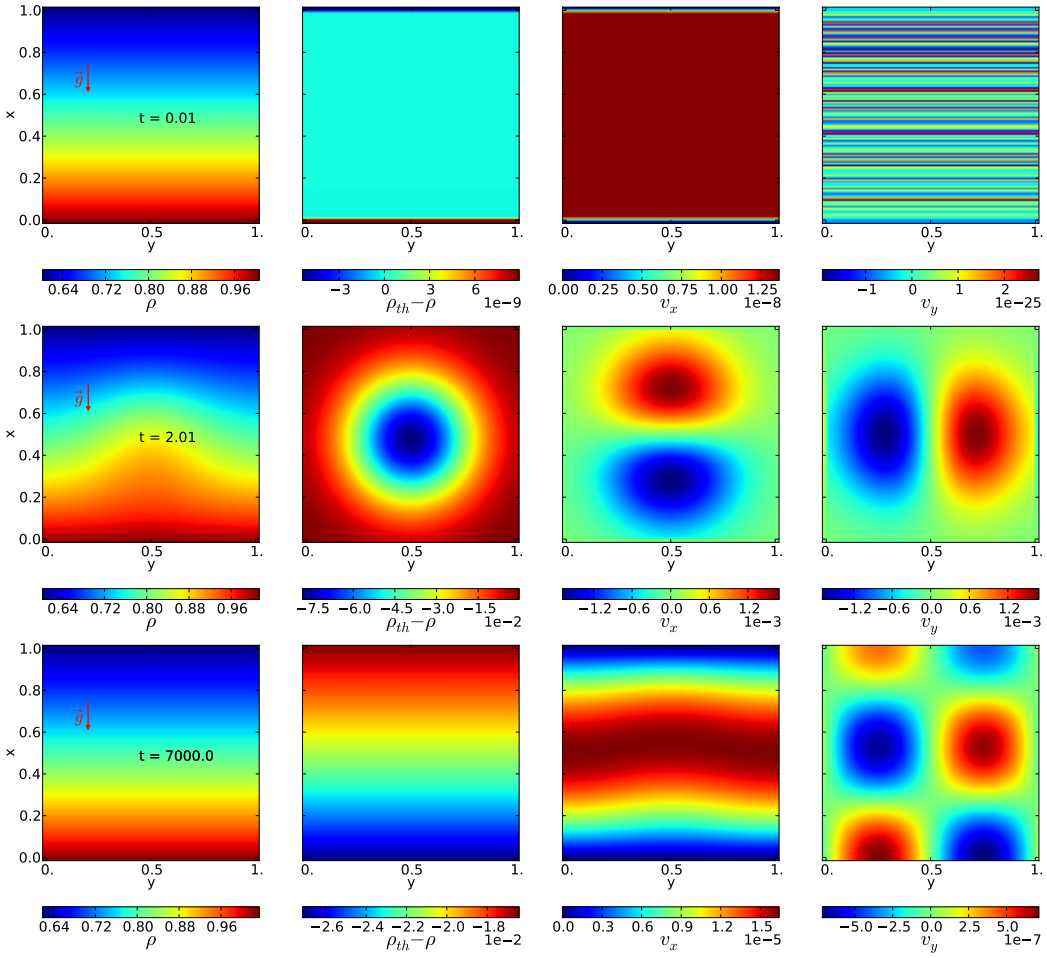

Fig. 4. Results of Heracles code for an isothermal 2D hydrostatic equilibrium before a bubble is added (**Upper row**, time 0.01), at the timestep the bubble is added (**Middle row**, time 2.0) and when the new equilibrium is reached (**Lower row**, final time 7000). **From left to right, first column:** density profile $\rho(x, y)$; **second column:** difference between theoretical (without perturbation) and simulated densities $\rho_{th} - \rho$; **third column:** velocity profile along x-axis $v_x(x, y)$; **fourth column:** velocity profile along y-axis $v_y(x, y)$. The arrow $\vec{g}$ indicates the used gravity vector.

References

Beaulieu, J. P., Grison, P., Tobin, W., et al. 1995, A&A, 303, 137

Buchler, J. R. 2009, in American Institute of Physics Conference Series, Vol. 1170, American Institute of Physics Conference Series, ed. J. A. Guzik & P. A. Bradley, 51–58

Chiosi, C., Wood, P. R., & Capitanio, N. 1993, ApJS, 86, 541

Dintrans, B. & Brandenburg, A. 2004, A&A, 421, 775

Eddington, A. S. 1917, The Observatory, 40, 290

Gastine, T. & Dintrans, B. 2008, in SF2A-2008: Proceedings of the Annual meeting of the French Society of Astronomy and Astrophysics, ed. C. Charbonnel, F. Combes, & R. Samadi, 471–474

Gastine, T. & Dintrans, B. 2011a, A&A, 530, L7

Gastine, T. & Dintrans, B. 2011b, in SF2A-2011: Proceedings of the Annual meeting of the French Society of Astronomy and Astrophysics, ed. G. Alecian, K. Belkacem, R. Samadi, & D. Valls-Gabaud, 215–219

Yecko, P. A., Kollath, Z., & Buchler, J. R. 1998, A&A, 336, 553

SF2A 2012
S. Boissier, P. de Laverny, N. Nardetto, R. Samadi, D. Valls-Gabaud and H. Wozniak (eds)

A POSSIBLE IMPACT NEAR THE MILKY WAY OF A FORMER MAJOR MERGER IN THE LOCAL GROUP

S. Fouquet[1], F. Hammer[2], Y. Yang [1,3], M. Puech[2] and H. Flores[2]

Abstract. The Milky Way (MW) dwarf system presents two exceptional features, namely it forms a thick plane called the Vast Polar Structure (VPOS), and the two biggest dwarves, the Magellanic Clouds (MCs), are irregular galaxies that are almost never seen at such a proximity from a luminous, L* galaxy. Investigating from our modelling of M31 as a result of a former gas-rich major merger, we find that one of the expected tidal tail produced during the event may have reached the MW. Such a coincidence may appear quite exceptional, but the MW indeed lies within the small volume delineated by the tidal tail at the present epoch.

In our scenario, most of the MW dwarves, including the MCs, may have been formed within a tidal tail formed during the former merger in the Local Group. It leads to a fair reproduction of the VPOS as well as to a simple explanation of the MCs proximity to the MW, i.e. accounting for both exceptional features of the MW dwarf distributions. However this scenario predicts dark-matter free MW dwarves, which is in apparent contradiction with their intrinsically large velocity dispersions. To be established or discarded, this requires to further investigate their detailed interactions with the MW potential.

Keywords: Local Group, major merger, tidal dwarf galaxies, LMC, DoS

1 Introduction

The anisotropy of the MW satellites spatial distribution had led Lynden-Bell (1976) to suggest that the MCs, Draco, Scuptor and Ursa Minor may form a stream. More recently, Kroupa et al. (2005) and Metz et al. (2007, 2009); Fouquet et al. (2012) found that the classical dwarf galaxies have their locations and orbital motions inscribed into a thick plane, named the VPOS (Pawlowski et al. 2012), which could provide an important challenge for the ΛCDM cosmological simulations (Kroupa et al. 2005). Realisations of recent simulations show that the VPOS is much thinner than expected (Wang et al. 2012), and this leads to a general consensus that progenitors of MW dwarves should have reached the MW in an organised motion, either from a very compact group or from a tidal tail (Pawlowski et al. 2011). Both issues have their pros and cons, because such a compact group seems unlikely (Metz et al. 2009) or because tidal dwarves (TDGs) are dark-free in contradiction with measurements of their velocity dispersion (Walker et al. 2009).

Perhaps the above problem is related to the MCs proximity to the MW (50kpc), which is also an enigma given the fact that no similar configuration is found in the nearby Universe. Indeed, the probability to find two massive ($> 10^8$ $M_\odot$) dwarf irregular galaxies close (< 60 kpc) to their host L* galaxies is very small (< 0.4 %, Robotham et al. 2012), and the only examples found are in groups made by two L* galaxies, such as M31 and the MW in the Local Group.

The present work investigates a new scenario linking together the formation of the VPOS and the position of the MCs. Following Pawlowski et al. (2011), we suggest that the 11 classical dwarves could be ancient TDGs, formed due to a major merger. The difference with the Pawlowski et al. (2011)' scenario comes from our assumption that it is linked to the M31 tumultuous past history, instead of that of the MW. Our scenario investigates whether the VPOS could be the result of the interaction between a tidal tail linking M31 to the MW, while the exceptional MCs proximity to the MW would simply reflect the tiny probability for a tidal tail send by M31 to interact with the MW.

[1] Univ Paris Diderot, Sorbonne Paris Cité, GEPI, UMR 8111, F-75205 Paris, France
[2] Laboratoire GEPI, Observatoire de Paris, CNRS-UMR8111, Univ Paris Diderot, Sorbonne Paris Cité, 5 place Jules Janssen, 92195 Meudon France
[3] National Astronomical Observatoires, Chinese Academy of Sciences, 20A Datun Road, Chaoyang District, Beijing 100012, China

2 TDGs within a tidal tail ejected by M31 towards the MW

According to Hammer et al. (2010), M31 could be the result of a gas-rich major merger (mass ratio $\sim 3 \pm 0.5 : 1$, $r_{pericenter} \sim 25 \pm 5$), with a first passage 8-9 Gyrs ago and a fusion time 5-6 Gyr ago, providing the formation of several tidal tails. At the present-time in the simulations, the tidal tail generated during the first passage is presently long enough (>1.5 Mpc) to reach the Milky Way (785 kpc from M31). However, it could have been ejected towards different directions. In fact, the angular momentum of a tidal tail in a major merger follow the orbital angular momentum which is within $\pm$ 25° to that of the remnant disk. As the M31 disk is nearly edge-on (77°) for a MW observer, the tidal tail must be in a thick plane aligned to the M31 disk and that includes the MW. An additional constrain is provided by the Giant Stream (with an angular uncertainty of 20°) that is also reproduced by the Hammer et al. (2010) simulations. Consequently, the tidal tail must lie in a quite small solid angle representing only 5% of the 4π steradian sphere (see Fig. 1). It is quite an exceptional coincidence (Fouquet et al. 2012) that the MW also lies in this small solid angle (see Fig. 1, right panel), that strengthens the possibility of an encounter between the MW and a tidal tail originated from M31. Perhaps this is a reminiscence of the investigations of Robotham et al. (2012) in the local volume.

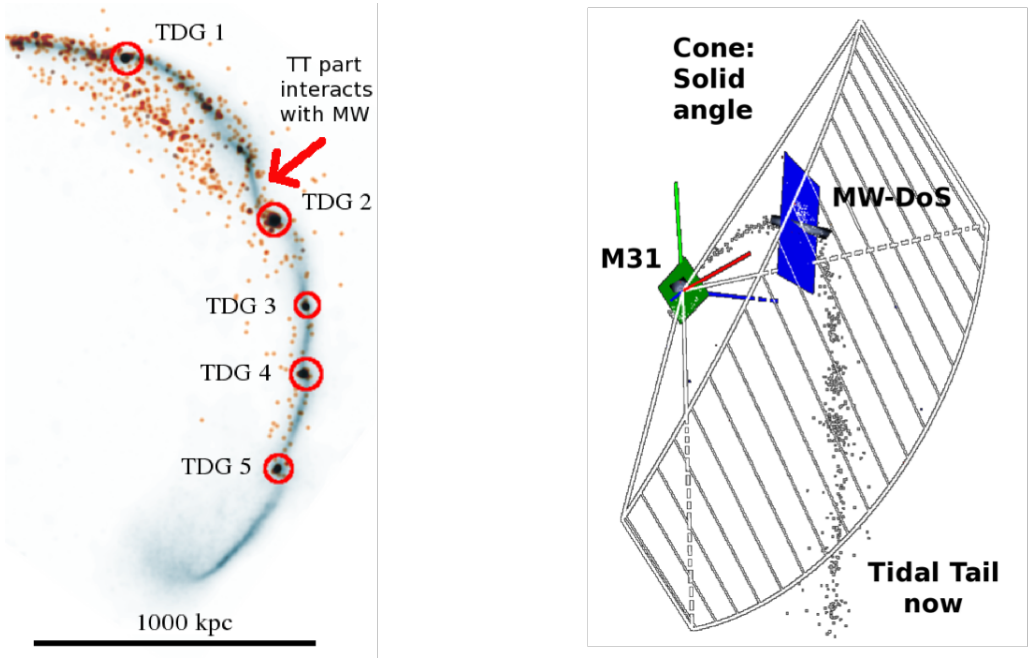

Fig. 1. Left: An example of first tidal tail at the present-time with five formed TDGs. The blue color code for the gas density, and the orange one for the stars. **Right:** the tidal tail interacting with the MW. The solid angle represents the space where the tidal tail is constrained to move.

The left panel of Fig. 1 shows the tidal tail which could interact with MW at the present time. It is extracted from a GADGET2 simulation whose the number of particles exceeds 2 millions. The five overdensities are TDGs resulting of gas and baryonic matter collapse due to gravitational instability and gas cooling (Wetzstein et al. 2007). Their baryonic masses are larger than 10^8 $M_\odot$ and for the most massive one (TDG 2), its mass is close to 10^9 $M_\odot$, one third of the baryonic LMC mass. The high mass of the TDG2 and its position at the center of the tidal tail and not at the top of it is apparently discrepant from the Bournaud & Duc (2006) results. This could be caused by the high fraction of gas of the progenitors galaxies (>60%) that is assumed in our study, which make easier the formation of high mass TDG formation (Wetzstein et al. 2007).

3 Reproduction of the VPOS by the MW-tidal tail encounter

From the work made by Hammer et al. (2010), we confirm that a tidal tail including several TDGs, could interact with the MW. Then, we have developped a simple formalism to simulate the interaction between the simulated tidal tail with a MW analytic mass profile model to verify whether or not it could reproduce the

VPOS (Fouquet et al. 2012).

We have first tried to match the LMC position and its trajectory to that of the tidal tail. We have treated the LMC case alone because its position and proper velocity are the best known among the MW dwarf galaxies. Tracing back the LMC depends on the current position and velocity of the LMC, the MW and M31, and on their total masses (Yang & Hammer 2010). Observations let significant freedom in establishing the total mass of massive galaxies and even more for the M31 transversal motion. Here we adopt $M_{baryonic}/M_{DM} = 20\%$, instead of half this value from Yang & Hammer (2010). We derive proper motions for which the LMC trajectory and velocity match well the trajectory of the tidal tail for M31, assuming a M31 motion close to that derived by van der Marel et al. (2012).

Then, we have performed N-body simulations to investigate the encountering between the tidal tail and the MW, leading to a reasonable fit of both spatial and orbital motion distributions of the dwarf galaxies that lie in the VPOS, within the measurement uncertainties (see Fig. 2 and Fouquet et al. (2012) for the orbital motions).

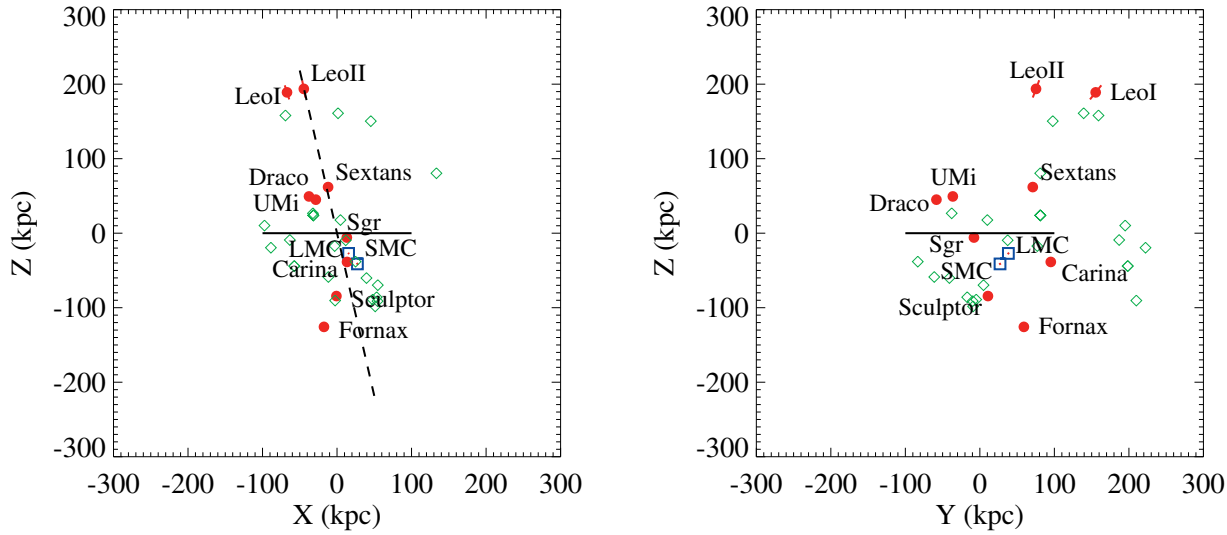

Fig. 2. Spatial distribution of the dwarf galaxies and of the simulated particles (the green diamonds). The blue squares represent the Magellanic Clouds, the red dots the dwarf spheroidals and the red lines their uncertainties. On the two panels, the MW (the solide line) is viewed edge-on. **Left:** the VPOS (the dashed line) is viewed edge-on. **Right:** the VPOS is rotated from the position of the left panel by 90° along the MW disk axis.

4 Conclusion and prospectives

The suggested scenario has the advantages to be consistent with the hierarchical model, for which a significant part of gas-rich major mergers forming disks have occured at z $\sim$ 0.4-0.8 Hammer et al. (2009), as it could be also the case for M31. Moreover it naturally explains within a single scheme the two exceptional features in MW dwarf galaxies, i.e., the VPOS and the proximity of the MCs to the MW.

However, it remains speculative with respect to the large velocity dispersions of the MW dwarf galaxies. Indeed, if they were formed in a tidal tail, they must contain a very small fraction of dark matter providing small M/L ratio, while their M/L ratio deduced from their velocity dispersions are reaching very large values (Walker et al. 2009). Perhaps the MW dwarf galaxies are not virialised and former numerical studies have shown that a dwarf galaxy in interaction with its host galaxy could show apparently large M/L values if it is assumed stable whereas it is not (Kroupa 1997). Further studies are needed to investigate this important issue as well as to understand how the gas may have been stripped during such an interaction to form spheroidal dwarves .

References

Bournaud, F. & Duc, P.-A. 2006, A&A, 456, 481
Fouquet, S., Hammer, H., Yang, Y., Puech, M., & Flores, H. 2012, MNRAS, arXiv:1209.4077
Hammer, F., Flores, H., Puech, M., et al. 2009, A&A, 507, 1313
Hammer, F., Yang, Y. B., Wang, J. L., et al. 2010, ApJ, 725, 542
Kroupa, P. 1997, New A, 2, 139
Kroupa, P., Theis, C., & Boily, C. M. 2005, A&A, 431, 517
Lynden-Bell, D. 1976, MNRAS, 174, 695
Metz, M., Kroupa, P., & Jerjen, H. 2007, MNRAS, 374, 1125
Metz, M., Kroupa, P., & Jerjen, H. 2009, MNRAS, 394, 2223
Pawlowski, M. S., Kroupa, P., & de Boer, K. S. 2011, A&A, 532, A118
Pawlowski, M. S., Pflamm-Altenburg, J., & Kroupa, P. 2012, MNRAS, 423, 1109
Robotham, A. S. G., Baldry, I. K., Bland-Hawthorn, J., et al. 2012, MNRAS, 424, 1448
van der Marel, R. P., Fardal, M., Besla, G., et al. 2012, ApJ, 753, 8
Walker, M. G., Mateo, M., Olszewski, E. W., et al. 2009, ApJ, 704, 1274
Wang, J., Frenk, C. S., & Cooper, A. P. 2012, ArXiv e-prints (1206.1340)
Wetzstein, M., Naab, T., & Burkert, A. 2007, MNRAS, 375, 805
Yang, Y. & Hammer, F. 2010, ApJ, 725, L24

SF2A 2012
S. Boissier, P. de Laverny, N. Nardetto, R. Samadi, D. Valls-Gabaud and H. Wozniak (eds)

THE BAADE-WESSELINK PROJECTION FACTOR OF THE δ-SCUTI STARS AI VEL AND β CAS

G. Guiglion[1], N. Nardetto[1], A. Domiciano de Souza[1], P. Mathias[2], D. Mourard[1] and E. Poretti[3]

Abstract. The Baade-Wesselink method of distance determination is based on the oscillations of pulsating stars. After determining the angular diameter and the linear radius variations, the distance is derived by a simple ratio. The linear radius variation is measured by integrating the pulsation velocity (hereafter $V_{\rm puls}$) over one pulsating cycle. However, from observations we have only access to the radial velocity ($V_{\rm rad}$) because of the projection along the line-of-sight. The projection factor, used to convert the radial velocity into the pulsation velocity, is defined by: $p = V_{\rm puls}/V_{\rm rad}$. We aim to derive the projection factor for two δ-Scuti stars, the high amplitude pulsator AI Vel and the fast rotator β Cas. The geometric component of the projection factor is derived using a limb-darkening model of the intensity distribution of AI Vel, and a fast rotator model for β Cas. Then, by comparing the radial velocity curves of several spectral lines forming at different levels in the atmosphere, we derive directly the velocity gradient (in a part of the atmosphere of the star) using SOPHIE/OHP data for β Cas and HARPS/ESO data for AI Vel, which is used to derive a dynamical projection factor for both stars. We find $p = 1.44 \pm 0.05$ for AI Vel and $p = 1.41 \pm 0.25$ for β Cas. By comparing Cepheids and δ-Scuti stars, these results bring valuable insights into the dynamical structure of pulsating star atmospheres.

Keywords: δ-Scuti, projection factor, spectroscopy, modelling

1 Introduction

Determining distances in the Universe is not a trivial task. From our Galaxy to the Virgo Cluster, distances can be derived using the Period-Luminosity relation (PL) relation of Cepheids (Riess et al. 2009a,b). However, this relation has to be calibrated using for instance the Baade-Wesselink method of distance determination (Storm et al. 2011a,b). The principle of this method is simple: after determining the angular diameter and the linear radius variations of the star, the distance is derived by a simple ratio. Angular diameter variations can be measured using interferometry (Kervella et al. 2004) or using the infrared surface brightness relation (Gieren et al. 1998, 2005). When determining the linear radius variation of the Cepheid by spectroscopy, one has to use the so-called projection factor in order to convert the radial velocity into pulsation velocity. There are in principle three sub-concepts involved in the Baade-Wesselink projection factor: (1) the geometric projection factor p_0 directly related to the limb-darkening of the star (see Section 3), (2) the correction $f_{\rm grad}$ due to the velocity gradient between the spectral line forming region and the photosphere -this quantity can be derived directly from observations by comparing different lines forming at different level in the atmosphere- (see Sections 2 and 4) and (3) the correction $f_{\rm og}$ due to the relative motion between the *optical* and *gas* layers associated to the photosphere (see Section 5). For a detailed analysis of the p-factor decomposition refer to Nardetto et al. (2007). The projection factor is then defined by $p = p_0 f_{\rm grad} f_{\rm o-g}$. In the following, we apply this decomposition of the projection factor (originally developed for Cepheids) to the δ Scuti stars AI Vel and β Cas (Guiglion et al., 2012, A&A, to be submitted). The determination of the projection factor is very pertinent to the study of this class of variable stars since it follows a PL relation (McNamara et al. 2007; Poretti et al. 2008).

[1] Laboratoire Lagrange, UMR 7293, Université de Nice Sophia Antipolis, CNRS, Observatoire de la Côte d'Azur, BP 4229, 06304 Nice Cedex 4, France
[2] Institut de Recherche en Astrophysique et Planétologie, UMR 5277, 57 avenue d'Azereix, 65000 Tarbes, France
[3] INAF-Osservatorio Astronomico di Brera, Via E. Bianchi 46, 23807 Merate, Italy

2 Spectroscopic observations of δ Scuti stars

AI Vel (HD 69213, A9IV/V) is a multi-periodic high-amplitude δ-Scuti star with $T_{\rm eff} = 7\,430$ K, $\log g = 3.72$ and is located at $d = 98$ pc according to the Hipparcos catalogue (van Leeuwen 2007). Its fundamental pulsation period is $P = 0.111574$ days (Walraven et al. 1992). According to the same study, AI Vel oscillations are characterized by 2 radial modes and 3 non-radial modes. We observed AI Vel during 4 nights in January 2011 (9th, 10th, 11th, 12th) using the HARPS[i] spectrograph of the La Silla 3.6 meters telescope (ESO). Our set is composed of 104 high resolution spectra, with a mean S/N of 140, a resolution R = 80 000 and a wavelength domain from 3 780 to 6 910 Å. We identified 53 metallic unblended spectral lines relevant for the determination of radial velocities.

β Cas (HD 432) is a low-amplitude δ-Scuti star with a spectral type of F2III/IV (Rhee et al. 2007). The star is located at $d = 16.8$ pc (van Leeuwen 2007). In the literature, the rotational velocity $v \sin i$ is found to be from 71 to 85 km s^{-1} (Bernacca & Perinotto 1970; Uesugi & Fukuda 1970; Schröder et al. 2009). The effective temperature ranges from 6 877 K to 7 178 K (Gray et al. 2001; Rachford & Foight 2009). Riboni et al. (1994) measured the period using photometry: $P = 0.101036676 \pm 0.000000053$ days. We observed β Cas with the OHP 1.93 meter telescope (SOPHIE[ii]) during one night in september 2011 (30th). We collected 241 high resolution spectra with a mean S/N of 100, a resolution R = 75 000 and a wavelength domain from 3 872 to 6 943 Å. We identified only 8 unblended spectral lines relevant for the spectral analysis because of the strong broadening of the lines.

For both stars, the centroid radial velocity $RV_{\rm c}$ (or the first moment radial velocity) and the line depth D are derived as a function of the pulsation phase for each selected spectral line. These observations are used in Section 4 to apply a dynamical correction to the geometric projection factor. In the following we assume that the non-radial modes for both stars have an negligible impact on the projection factor. A detailed analysis of this assumption will be done in a following paper.

3 The geometric projection factor p_0

In the case of a limb-darkened pulsating star in rotation with a one-layer atmosphere, the projection factor is purely geometric and we have $p = \frac{V_{\rm puls}}{V_{\rm rad}} = p_0$. The radial velocity is then defined by:

$$V_{\rm rad} = \frac{1}{\pi {\rm R}^2} \int_{x,y \in {\rm D_R}} I(x,y,\lambda) \cdot V_{\rm puls} \cdot \sqrt{1 - \frac{(x^2+y^2)}{{\rm R}^2}}\, dxdy, \tag{3.1}$$

where $\rm D_R$ is the surface of the stellar disc of linear radius R and $I(x,y,\lambda)$ the limb-darkened intensity distribution considered at the wavelength of observation λ defined by $I(x,y,\lambda) = I_0(1 - u_\lambda + u_\lambda \sqrt{1-(x^2+y^2)})$ where u_λ is the linear limb-darkening coefficient from Claret & Bloemen (2011). We assume that the projection factor is constant with the pulsating phase. In other words, the geometric projection factor can be calculated at any pulsation phase, whatever the pulsation velocity considered (one can consider for instance $V_{\rm puls} = 1$). Considering $T_{\rm eff} = 7\,400$ K and $\log g = 3.5$, we find $u_{\rm R} = 0.474 \pm 0.025$ in the R-band. We deduce the value of the geometric projection factor for AI Vel: $p_0 = 1.43 \pm 0.01$. This value is larger compared to Cepheids (typically 1.36 to 1.41, see Fig.1 (left)).

Concerning β Cas, its high rotation rate leads to a distortion of its intensity distribution and of its geometrical shape. The geometric projection effect depends on the inclination of the rotation axis of the star compared to the line-of-sight. If the rotation axis of the star is along the line-of-sight ($i = 0°$), the star is pole-on and is seen as a circle. For $i > 0°$ the star has an ellipsoidal shape. Using the fundamental parameters from Che et al. (2011) and the rotating stars model by Domiciano de Souza et al. (2002, 2012), we derive the intensity distribution in the continuum for different inclinations of the star (from $i = 0°$ to $i = 90°$ with a step of 5°) and for three wavelengths: $\lambda = 6\,000, 6\,500$ and $7\,000$ Å. Using these intensity maps, we can easily calculate the

[i] High Accuracy Radial velocity Planetary Search project developed by the European Southern Observatory (ESO).

[ii] Spectrographe pour l'Observation des Phénomènes des Intérieurs stellaires et des Exoplanètes developed by the Observatoire de Haute Provence (OHP).

geometric projection factor. Indeed, for an ellipsoid, $V_{\rm rad}$ is then defined by:

$$V_{\rm rad} = \frac{1}{\pi {\rm R}^2} \int_{x,y \in {\rm D_R}} I(x,y,\lambda) \cdot \sqrt{1 - \left(\frac{x^2}{{\rm a}^2} + \frac{y^2}{{\rm b}^2} \right)} dxdy, \tag{3.2}$$

where a and b are the semi-major and semi-minor axis of the ellipse, respectively. In Figure 1 (right), we show the geometric projection factor (p_0) as a function of i. This relation is extremely interesting because it shows that the inclination of a fast rotating star can have an impact of more than 10% on the projection factor. Of course, it depends also on the rotation velocity of the star: the larger the rotation velocity (for a given inclination), the lower the projection factor. Using the inclination found by Che et al. (2011), $i = 19.9 \pm 1.9°$, we finally find a geometric projection factor for β Cas of $p_0 = 1.41 \pm 0.02$ (averaged over the three wavelengths considered).

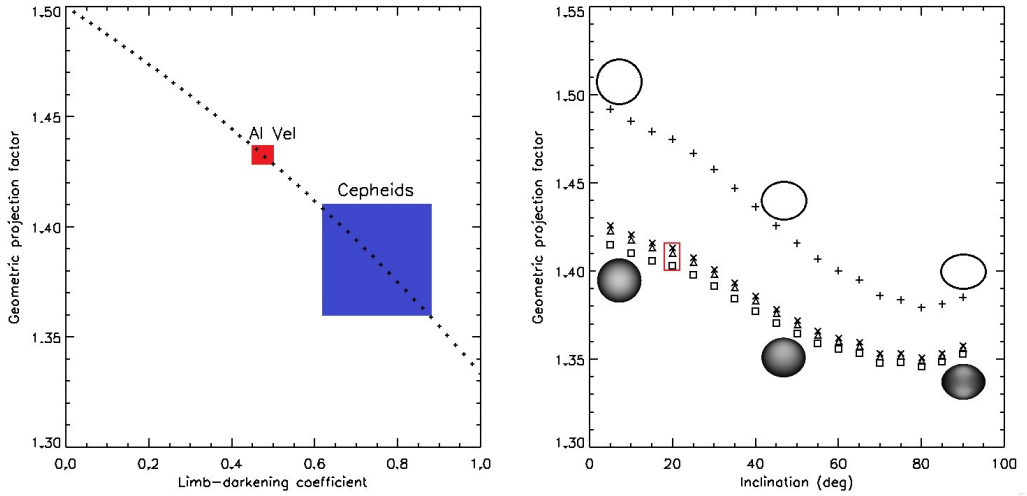

Fig. 1. Left: p_0 as a function of the limb-darkening parameter u_λ. The red box indicates the uncertainty on p_0 for the δ Scuti AI Vel. The blue box indicates the typical values of u_λ and p_0 for Cepheids. The dots corresponds to the relation provided by Nardetto et al. (2006). **Right:** p_0 as a function of the inclination of the fast rotating star β Cas for three different wavelength ($\lambda = 6\,000$ Å ($\square$), $\lambda = 6\,500$ Å ($\triangle$), and $\lambda = 7\,000$ Å ($\times$)). The red box indicates the uncertainty on p_0 for β Cas. The case of an uniform elonged disc is over-plotted (+) and we find that $p_0 = 1.5$ for $i = 0°$ as expected for a circular uniform disc.

4 The dynamical structure of δ-Scuti stars

By comparing the 2K-amplitude (defined as the amplitude of the first moment radial velocity curve, hereafter $\Delta RV_{\rm c}$) with the depth of the 53 spectral lines selected in the case of AI Vel, one can measure directly the atmospheric velocity gradient in the part of the atmosphere where the spectral line are formed. Note indeed, that in order to quantify the impact of velocity gradient on the projection ($f_{\rm grad}$) we do not need to derive the velocity gradient over the whole atmophere, but only at the location of the forming regions of the spectral lines used to derive the distance of the star.

In order to find a relation between $\Delta RV_{\rm c}$ and D, we consider the second night of observation for which we have almost a complete cycle (Figure 2, top left). We perform a linear regression according to the relation $\Delta RV_{\rm c} = a_0\, D + b_0$. We obtain $\Delta RV_{\rm c} = [-0.40 \pm 0.53] D + [32.87 \pm 0.23]\,{\rm km\,s^{-1}}$ (Figure 2, top right). In principle, $f_{\rm grad}$ depends on the spectral line considered (Nardetto et al. 2007): $f_{\rm grad} = b_0/(a_0 D + b_0)$. Here, we find that $f_{\rm grad}$ is typically the same for all spectral lines ($f_{\rm grad} = 1.01 \pm 0.01$) which is consistent with no correction of the projection factor due to the velocity gradient.

Figure 2 (bottom left) presents the interpoled $RV_{\rm c}$ curve of β Cas in the case of the FeI spectral line ($\lambda = 4\,508.288$ Å). We clearly see an increase of the amplitude of the radial velocity curve ($\sim 4.6 \pm 0.9\%$ per cycle). Moreover the radial velocity curves have several minima and maxima and we can easily deduce a period of pulsation. We find $P = 0.10046 \pm 0.00054$ days. Our value is in a good aggrement with Riboni et al. (1994).

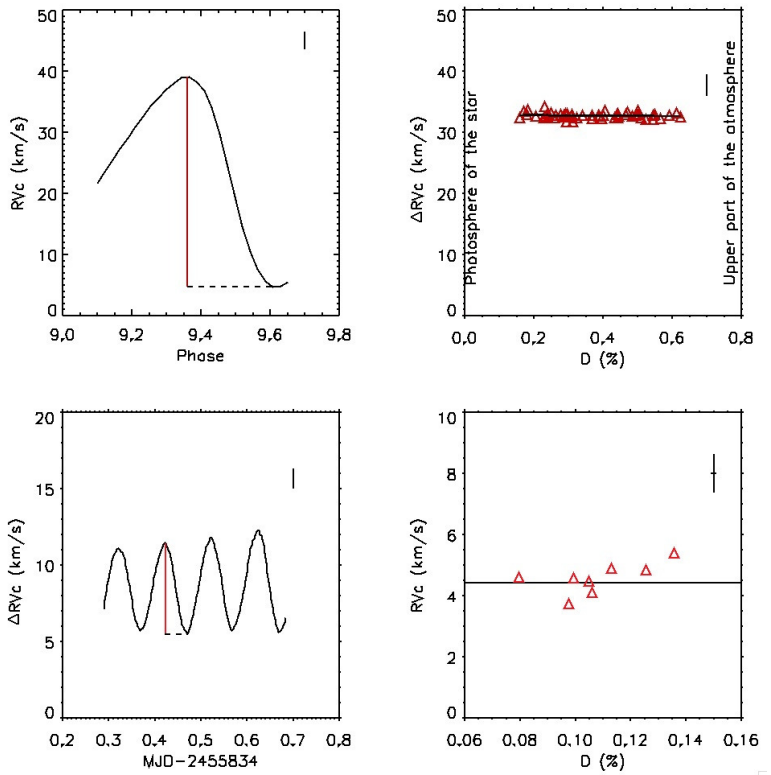

Fig. 2. Top: RV_c as a function of the pulsation phase for the night 2 (FeII spectral line, 5 234.625 Å) and amplitude of RV_c curves as a function of the spectral line depth. **Bottom:** Interpoled RV_c *vs.* MJD for the FeI spectral line $\lambda = 4\,508.288$ Å and ΔRV_c *vs.* D with corresponding statistical uncertainties. The solid line corresponds to the average of the values.

As for AI Vel, we need to consider several spectral lines forming at different levels in the atmosphere. In Figure 2 (bottom right), ΔRV_c is plotted as a function of D (see the vertical red line on the figure). Contrarily to AI Vel for which we had many spectral lines, the case of β Cas is more difficult: most of the spectral lines, broadened by the large rotation velocity of the star, are indeed blended. As a consequence, we cannot estimate properly the actual $f_{\rm grad}$ correction for β Cas: If we measure the velocity gradient as we did for AI Vel, we find $f_{\rm grad} = 0.64 \pm 0.82$. This value is simply to small to be relevant compared to what we know from Cepheids ($f_{\rm grad} \sim 0.95$) and what we obtain for AI Vel ($f_{\rm grad} \sim 1.00$). It would imply indeed, a huge velocity gradient in the atmosphere of the star which is not reasonnable. However, our data are consistent with a constant (no velocity gradient). If we make the assumption that $f_{\rm grad} = 1$ (or $a_0 = 0$) as for AI Vel, we obtain $b_0 = 4.07 \pm 0.25$ with a reduced χ^2 of 1.0, which provides us an uncertainty on $f_{\rm grad}$ of 0.14.

5 The $f_{\rm o-g}$ correction

The $f_{\rm o\text{-}g}$ correction, which is the last component of the projection factor decomposition, cannot be measured from observations. To estimate the differencial velocity between the *optical* and *gas* layers at the photosphere of the star, we need an hydrodynamic model. However, modelling the pulsating atmosphere of δ Scuti stars is not simple because of: (1) cycle-to-cycle variations, (2) non-radial modes and (3) fast rotation in some cases (like for β Cas). However, $f_{\rm o\text{-}g}$ have been studied intensively in the case of Cepheids (Nardetto et al. 2004, 2007, 2011), and it seems that there is a linear relation between $f_{\rm o\text{-}g}$ and $\log P$: $f_{\rm o\text{-}g} = [-0.023 \pm 0.005] \log P + [0.979 \pm 0.005]$. Moreover, we have a theoretical value of $f_{\rm o\text{-}g}$ for the short-period β-Cepheid α Lup ($P = 0.2598$), $f_{\rm o\text{-}g} = 0.99 \pm 0.01$, which seems to be consistent with the $\log P$-$f_{\rm o\text{-}g}$ relation of Cepheids (Nardetto et al. 2012, in preparation). For our study, we propose to extend this law for the δ-Scuti β Cas and AI Vel. Considering $P = 0.11157$ days for AI Vel and $P = 0.10046 \pm 0.00054$ days for β Cas (from this paper), we find $f_{\rm o\text{-}g} = 1.00 \pm 0.02$ for both stars.

6 Conclusion

We can now calculate the final projection factor p, using the relation $p = p_0 f_{\rm grad} f_{\rm o\text{-}g}$. We find $p = 1.44 \pm 0.05$ for AI Vel and $p = 1.41 \pm 0.25$ for β Cas. These results are consistent with the Pp relation $p = [-0.071 \pm 0.020] \log P + [1.311 \pm 0.019]$ from Laney & Joner (2009) applyed for classical and dwarf Cepheids (It corresponds to $p = 1.38 \pm 0.02$ for AI Vel and β Cas). To derive these values, they simply compared the distance of the stars derived from the PL relation with the ones obtained from the photometric version of the Baade-Wesselink method. The fact that our values of the projection factor are consistent at $1\,\sigma$ with the independant determinations by Laney & Joner (2009) strongly suggests that our assumptions are acceptable, namely (1) the projection factor decomposition can be applied to δ Scuti stars (at least AI Vel and β Cas), (2) the non-radial modes have a negligible impact on the projection factor and (3) the $f_{\rm o\text{-}g}$ we have considered is probably acceptable in the case of short period pulsating stars.

Interestingly, if we use the Pp obtained for classical Cepheids by Nardetto et al. (2007): $p = [-0.064 \pm 0.020] \log P + [1.376 \pm 0.023]$ in order to derive the projection factors of the two δ Scuti stars, we find $p = 1.44 \pm 0.01$, which is consistent with our values. This seems to show that the period-projection factor relation provided by Nardetto et al. (2007) is also applicable to short period pulsating stars and in particular to δ-Scuti.

References

Bernacca, P. L. & Perinotto, M. 1970, Contributions dell'Osservatorio Astrofisica dell'Universita di Padova in Asiago, 239, 1

Che, X., Monnier, J. D., Zhao, M., et al. 2011, ApJ, 732, 68

Claret, A. & Bloemen, S. 2011, VizieR Online Data Catalog, 352, 99075

Domiciano de Souza, A., Vakili, F., Jankov, S., Janot-Pacheco, E., & Abe, L. 2002, A&A, 393, 345

Domiciano de Souza, A., Zorec, J., & Vakili, F. 2012, in SF2A, these proccedings

Gieren, W., Storm, J., Barnes, III, T. G., et al. 2005, ApJ, 627, 224

Gieren, W. P., Fouque, P., & Gomez, M. 1998, ApJ, 496, 17

Gray, R. O., Graham, P. W., & Hoyt, S. R. 2001, AJ, 121, 2159

Kervella, P., Bersier, D., Mourard, D., Nardetto, N., & Coudé du Foresto, V. 2004, A&A, 423, 327

Laney, C. D. & Joner, M. D. 2009, in American Institute of Physics Conference Series, Vol. 1170, American Institute of Physics Conference Series, ed. J. A. Guzik & P. A. Bradley, 93–95

McNamara, D. H., Clementini, G., & Marconi, M. 2007, AJ, 133, 2752

Nardetto, N., Fokin, A., Fouqué, P., et al. 2011, A&A, 534, L16

Nardetto, N., Kervella, P., Mourard, D., Bersier, D., & Coudé du Foresto, V. 2004, in Astronomical Society of the Pacific Conference Series, Vol. 310, IAU Colloq. 193: Variable Stars in the Local Group, ed. D. W. Kurtz & K. R. Pollard, 520

Nardetto, N., Mourard, D., Kervella, P., et al. 2006, A&A, 453, 309

Nardetto, N., Mourard, D., Mathias, P., Fokin, A., & Gillet, D. 2007, A&A, 471, 661

Poretti, E., Clementini, G., Held, E. V., et al. 2008, ApJ, 685, 947

Rachford, B. L. & Foight, D. R. 2009, ApJ, 698, 786

Rhee, J. H., Song, I., Zuckerman, B., & McElwain, M. 2007, ApJ, 660, 1556

Riboni, E., Poretti, E., & Galli, G. 1994, A&AS, 108, 55

Riess, A. G., Macri, L., Casertano, S., et al. 2009a, ApJ, 699, 539

Riess, A. G., Macri, L., Li, W., et al. 2009b, ApJS, 183, 109

Schröder, C., Reiners, A., & Schmitt, J. H. M. M. 2009, A&A, 493, 1099

Storm, J., Gieren, W., Fouqué, P., et al. 2011a, A&A, 534, A94

Storm, J., Gieren, W., Fouqué, P., et al. 2011b, A&A, 534, A95

Uesugi, A. & Fukuda, I. 1970, Memoirs Faculty of Sciences University of Kyoto, 33, 205

van Leeuwen, F. 2007, A&A, 474, 653

Walraven, T., Walraven, J., & Balona, L. A. 1992, MNRAS, 254, 59

SF2A 2012
S. Boissier, P. de Laverny, N. Nardetto, R. Samadi, D. Valls-Gabaud and H. Wozniak (eds)

MODELING PERIODIC MEDIA WITH THE THREE-DIMENSIONAL RADIATIVE TRANSFER CODE IRIS

L. Ibgui[1], I. Hubeny[2], T. Lanz[3] and C. Stehlé[1]

Abstract. We describe the implementation in our generic three-dimensional radiative transfer code, IRIS, of an algorithm that allows the modeling of periodic infinite media. We show how this algorithm has been validated by comparison with well-established 1D plane-parallel models. A particularly interesting astrophysical application will be the calculation of synthetic spectra of the fully three-dimensional solar atmosphere.

Keywords: methods: numerical, radiative transfer

1 Introduction

Radiation is a major component of many astrophysical objects, as a probe of the physical state of the medium, but also as a contributor to the momentum and energy budget of the medium. An accurate modeling of the radiative transfer is, therefore, a key element for the determination of the composition and the physical properties of such objects. To this end, we have developed a generic 3D radiative transfer code, IRIS, that post-processes radiation magnetohydrodynamics simulations, in order to provide spectroscopic signatures.

Although the code can be applied to a wide range of astrophysical objects, we focus here on the specific case of infinite media with double periodicity in one plane. This is typically the case for the solar atmosphere, for which the code will be able to provide synthetic spectra from hydrodynamic simulations, and for cosmological simulations.

The main characteristics of IRIS are summarized in § 2. In § 3, we explain the method of taking into account the periodic boundary conditions. We show how our approach has been validated through comparison with results obtained with a specific horizontally periodic medium: the 1D plane-parallel medium.

2 Overview of IRIS code

IRIS is a new generic three-dimensional radiative transfer code (Ibgui et al. 2011, 2012). Its purpose is to post-process 3D (radiation) (magneto)hydrodynamics (RMHD) simulations, in order to provide spectroscopic signatures of a given astrophysical object. It solves the exact monochromatic 3D static radiative transfer equation (RTE), in a Cartesian grid that is nonuniform in each direction. The thermodynamic properties (temperature, density, velocity) are determined from the RMHD simulations. We assume local thermodynamic equilibrium (LTE). This restriction will be removed in the future. The opacities are defined at each grid point for a grid of frequencies. The specific intensity is calculated for all the frequencies at each grid point, with the short-characteristics method (Kunasz & Auer 1988). The latter is coupled with an efficient interpolation technique that uses piecewise cubic, locally monotonic, polynomials. Such interpolants drastically restrain the known numerical diffusion effect of the short-characteristics method. The code determines the following quantities, which are functions of the frequency ν and the position (x, y, z): the mean intensity J, the three components of the radiation flux vector F_x, F_y, F_z, the six components of the radiation pressure tensor P_{xx}, P_{yy}, P_{zz}, P_{xy}, P_{xz}, P_{yz}. Many more details are provided in the paper by Ibgui et al. (2012). The user can fully specify the boundary conditions for a well-delimited medium. This is not possible in the case of a horizontally periodic infinite medium as we explain below.

[1] LERMA, Observatoire de Paris, CNRS, UMPC, 5, place J.Janssen, 92195 Meudon Cedex, France
[2] Department of Astronomy, Steward Observatory, The University of Arizona, 933 N.Cherry Ave, Tucson, AZ 85721-0065, USA
[3] Laboratoire J.-L. Lagrange, Université de Nice Sophia Antipolis, CNRS, Observatoire de la Côte d'Azur, Boulevard de l'Observatoire, B.P. 4229, 06304 Nice Cedex 4, France

3 Boundary Conditions for Horizontally Periodic Media

3.1 Method

We consider a three-dimensional medium with an infinite extension in the horizontal plane (x, y), and a finite extension along the vertical z-axis between its lower boundary $z_{\min}$ and its upper boundary $z_{\max}$. We assume that this medium has a double periodicity, one in x-direction, one in y-direction. Boundary conditions are known at $z_{\min}$ and $z_{\max}$. For example, we may consider a non-irradiated stellar atmosphere with no incoming radiation at the outer surface $z_{\max}$ and a black body radiation at its inner surface $z_{\min}$. The computational grid ranges from $z_{\min}$ to $z_{\max}$ in vertical direction, from $x_{\min}$ to $x_{\max}$, and from $y_{\min}$ to $y_{\max}$ in the horizontal plane, so that $(x_{\max} - x_{\min})$ defines a period in x-direction and $(y_{\max} - y_{\min})$ defines a period in y-direction. Now, we remind that the short-characteristics method consists in solving the integral form of RTE by propagating the rays from one upwind boundary in which the specific intensity is known, throughout the computational domain, down to the downwind boundary. For periodic media, while the vertical boundary conditions are explicitly defined (see above), the lateral boundary conditions are implicitly defined, such as, for any physical quantity $f(\nu, x, y, z)$ we have the following relations:

$$f(\nu, x_{\max}, y, z) = f(\nu, x_{\min}, y, z), \qquad \text{for any } y, z, \tag{3.1}$$

$$f(\nu, x, y_{\max}, z) = f(\nu, x, y_{\min}, z), \qquad \text{for any } x, z. \tag{3.2}$$

Consequently, when the upwind edge of a short-characteristic intersects a lateral boundary (see Fig. 1), we prolong this characteristic, which becomes a long-characteristic, until it intersects a horizontal face, following the suggestions by Auer et al. (1994) and Fabiani Bendicho (2003). For a given direction of propagation, and for each z-layer, this treatment affects only the cells in the first x-row and first y-row, i.e., the boundary rows. Since the medium is horizontally periodic, we can start the propagation of the rays at any x-row and any y-row, provided that we span the whole period in x and the whole period in y. In order to minimize the number of cells that are intersected by the long-characteristics, which saves cpu time, we define our first x-row as the one for which the corresponding cell size Δx is the largest, and, in the same vein, our first y-row as the one for which Δy is the largest. Once these two rows have been treated, we resume the short-characteristics method for the next rows of the current z-layer.

3.2 Comparison with 1D plane-parallel models

This method has been tested by comparison with the results provided by well-tested 1D methods in the case of a 1D plane-parallel medium. The test case is a simulation of an experimental radiative shock, generated in a tube full of Xenon, assumed to be a perfect gas, with the following upstream conditions: fluid velocity = 60 km s^{-1}, pressure = 7 bar, temperature = 1 eV. The hydrodynamics results are provided by Matthias González[i] with the code HERACLES (González et al. 2007). The opacities are from Michaut et al. (2004). Figure 2 shows results provided by IRIS, in comparison with the results from a 1D solver. By way of example, we show, at the frequency $h\nu = 296$ eV ($h\nu = 4.19\ nm$), the radiation flux in z-direction, $F_z(z)$, and the components $P_{zz}(z)$, $P_{xx}(z)$, and $P_{yy}(z)$ of the radiation pressure tensor. The results obtained by IRIS and by the 1D code perfectly match. In addition, IRIS verifies the following properties of a 1D plane-parallel medium, valid for any frequency: F_z does not depend on x and y, $F_x = F_y = 0$, $P_{xy} = P_{xz} = P_{yz} = 0$, and $P_{xx} = P_{yy}$ for any (x, y, z). Above all, we have validated the calculation of the specific intensity for all the 8 octants and verified that I is independent of the azimuthal angle φ.

4 Conclusion

The three-dimensional radiative transfer code, IRIS, which solves the monochromatic 3D radiative transfer equation, can take into account any medium with a horizontal periodicity. Obtaining synthetic spectra from 3D hydrodynamic simulations of the solar atmosphere, as well as for cosmological simulations, is one of our primary objectives.

[i] AIM, CEA/DSM/IRFU, CNRS, Université Paris Diderot, 91191 Gif-sur-Yvette, France

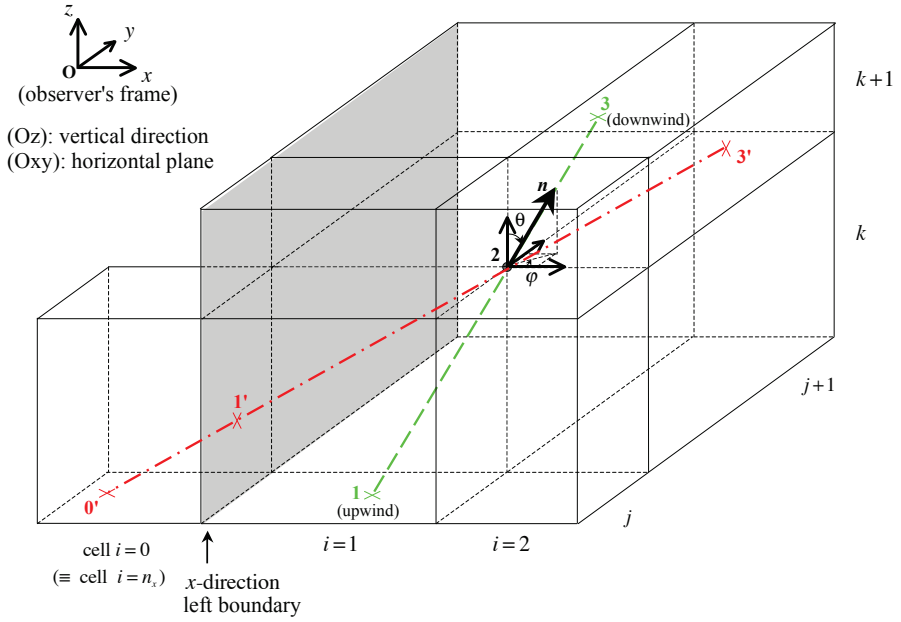

Fig. 1. Horizontally periodic medium. The upwind specific intensity is known at point 1 (that lies on a horizontal face) for the short-characteristic (1,2,3). The upwind specific intensity is not known at point 1' (lateral boundary of the grid) for the short-characteristic (1',2,3'). The latter is therefore prolonged until it intersects a horizontal face.

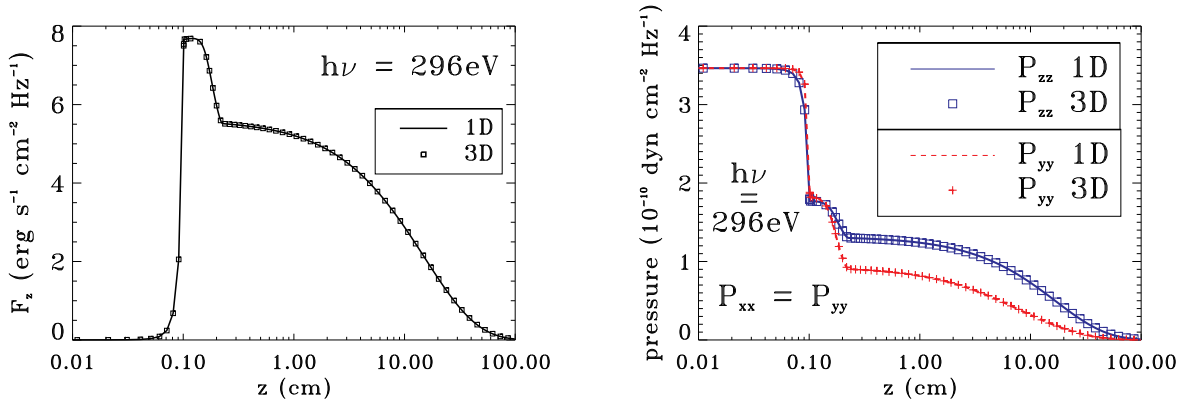

Fig. 2. Results from IRIS with periodic boundary conditions, and from a 1D solver, for a 1D plane-parallel medium, at $h\nu = 296$ eV. **Left:** radiation flux $F_z(z)$, **Right:** radiation pressure $P_{zz}(z)$, $P_{xx}(z) = P_{yy}(z)$.

The authors are grateful to Matthias González (AIM, CEA/DSM/IRFU, CNRS, Université Paris Diderot, 91191 Gif-sur-Yvette, France) for providing the 3D hydrodynamics results of the ideal gas shock wave simulation, which were used as an input for the radiative transfer code IRIS. The work is supported by French ANR, under grant 08-BLAN-0263-07. IH acknowledges the travel support from the Observatoire de Paris.

References

Auer, L., Bendicho, P. F., & Trujillo Bueno, J. 1994, A&A, 292, 599

Fabiani Bendicho, P. 2003, in Astronomical Society of the Pacific Conference Series, Vol. 288, Stellar Atmosphere Modeling, ed. I. Hubeny, D. Mihalas, & K. Werner, 419

González, M., Audit, E., & Huynh, P. 2007, A&A, 464, 429

Ibgui, L., Hubeny, I., Lanz, T., & Stehlé, C. 2011, in SF2A-2011: Proceedings of the Annual meeting of the French Society of Astronomy and Astrophysics, ed. G. Alecian, K. Belkacem, R. Samadi, & D. Valls-Gabaud, 485–489

Ibgui, L., Hubeny, I., Lanz, T., & Stehlé, C. 2012, submitted to A&A

Kunasz, P. & Auer, L. H. 1988, J. Quant. Spec. Radiat. Transf., 39, 67

Michaut, C., Stehlé, C., Leygnac, S., Lanz, T., & Boireau, L. 2004, European Physical Journal D, 28, 381

SF2A 2012
S. Boissier, P. de Laverny, N. Nardetto, R. Samadi, D. Valls-Gabaud and H. Wozniak (eds)

3D NUMERICAL SIMULATIONS OF LABORATORY MODELS OF ACCRETION SHOCKS IN YOUNG STELLAR OBJECTS

L. Ibgui[1], I. Hubeny[2], T. Lanz[3], C. Stehlé[1], M. González[4] and J.-P. Chièze[4]

Abstract. We show preliminary results of our numerical simulations of laboratory experiments of radiative shocks. Such experiments aim at understanding accretion shocks in young stellar objects. Three-dimensional non-stationary radiation hydrodynamics calculations were performed with the code HERACLES. X-UV spectra were then generated with the new three-dimensional radiative transfer code IRIS.

Keywords: Accretion, accretion disks, Radiative transfer, Hydrodynamics, Shock waves, Atomic processes

1 Introduction

Understanding the physics of radiative shocks in accretion columns is a prerequisite for a correct modeling of the accretion around young stellar objects. Now, it is possible to generate radiative shocks in laboratory. With such an asset, we can explore in detail various aspects of this physical phenomenon. We present a new generic 3D radiative transfer code, IRIS (Ibgui et al. 2012), that post-processes (radiation) (magneto) hydrodynamics (R)(M)HD simulations, in order to provide spectroscopic diagnostic information of a studied astrophysical object or structure, but also of laboratory generated structures. The main characteristics of IRIS are summarized in § 2. In § 3, we show a few preliminary results of our numerical simulations of experimentally generated radiative shocks. The RHD calculations are made with the well-tested code HERACLES (González et al. 2007).

2 IRIS: numerical schemes and capabilities of the code

IRIS is a new generic three-dimensional spectral radiative transfer code (Ibgui et al. 2011, 2012), which generates synthetic spectra or images, by post-processing snapshots provided by 3D (R)(M)HD simulations. IRIS solves the static 3D monochromatic radiative transfer equation (RTE) in the observer's frame, and in a nonuniform Cartesian grid. For any snapshot identified by instant t, the code determines the specific intensity $I(\boldsymbol{r}, \boldsymbol{n}, \nu, t)$ for any specified position $\boldsymbol{r}$, photon direction $\boldsymbol{n}$, and frequency ν. The current version of the code assumes local thermodynamic equilibrium (LTE).

The solver employs the short-characteristics method (Mihalas et al. 1978; Olson & Kunasz 1987; Kunasz & Auer 1988; Kunasz & Olson 1988). The RTE is solved in its integral form that is discretized along each short-characteristic. The physical quantities at the intersections of the short-characteristic with the faces of the grid cells are determined by piecewise cubic locally monotonic interpolations. The variations of these quantities along a short-characteristic are approximated by the same type of interpolants. The interpolation scheme consists of a cubic Hermite polynomial combined with weighted harmonic mean node derivatives (Brodlie 1980; Fritsch & Butland 1984; Auer 2003).

IRIS can handle the effects of the macroscopic (non-relativistic) velocities: where necessary, the code subdivides a short-characteristic, in order to correctly deal with the Doppler shift of photon frequency due to velocity

[1] LERMA, Observatoire de Paris, CNRS, UMPC, 5, place J. Janssen, 92195 Meudon Cedex, France
[2] Department of Astronomy, Steward Observatory, The University of Arizona, 933 N. Cherry Ave, Tucson, AZ 85721-0065, USA
[3] Laboratoire J.-L. Lagrange, Université de Nice Sophia Antipolis, CNRS, Observatoire de la Côte d'Azur, Boulevard de l'Observatoire, B.P. 4229, 06304 Nice Cedex 4, France
[4] AIM, CEA/DSM/IRFU, CNRS, Université Paris Diderot, 91191 Gif-sur-Yvette, France

gradient between two positions. The code also computes the monochromatic radiation moments (mean intensity, radiation flux vector, and radiation pressure tensor), by angular integration of the specific intensity. IRIS can deal with periodic boundary conditions in the case of a medium with an infinite extension in its horizontal plane, such as a stellar atmosphere or an accretion disk. For detailed explanations of all the related algorithms, we refer the reader to the paper by Ibgui et al. (2012).

3 3D numerical simulations of laboratory shocks: preliminary results

3.1 Brief description of the experimental case

Radiative shocks, i.e., shocks that are structured by radiation within a plasma, appear in accretion columns around young stellar objects, and have a strong contribution to the spectral signature of these objects. This is why it is important to have a good understanding of the physics of these shocks. Now, it is possible to perform laboratory experiments that simulate radiative shocks. Laser driven shocks were recently produced in the PALS (Prague Asterix Laser System) facility in Prague (Bouquet et al. 2004; Reighard et al. 2006; Stehlé et al. 2010, 2012). The experimental target consists of a 6 mm long shock-tube with a uniform 0.4×0.4 mm^2 section. The tube is full of pure xenon, initially at room temperature, under pressure of typically 0.2 to 0.3 bar (order of magnitude of the density: 10^{-3} g cm^{-3}). The laser hits a piston at the base of the tube. The resulting motion of the piston (at constant velocity of 60 km s^{-1} relative to the laboratory frame) generates a non-stationary flow with a radiative shock. For further details, the reader is referred to the above papers. We have simulated the flow in the shock-tube, along with the spectra emitted by the flow, as presented in § 3.2 and § 3.3 below.

3.2 Radiation hydrodynamics simulation with HERACLES

HERACLES is a three-dimensional radiation hydrodynamics code whose radiative equations, described by the M_1 model (Levermore 1996; Dubroca & Feugeas 1999), are solved with a second-order Godunov type algorithm (González et al. 2007). The influence of the radiation on the shock structure was demonstrated by previous two-dimensional simulations with HERACLES (González et al. 2009).

For the present study, three-dimensional simulations of the flow in the shock-tube were performed. In Fig. 1, left panel, the piston is represented by the hatched face, and the shock propagates in positive z-direction. The lateral walls and the base on the right have a zero albedo, which means that there is no wall reflexion: the photons can freely escape. In addition, there is no photon incoming from the outside through these five faces. As for the base on the left, i.e., the piston, we assume that it radiates like a black body at the local temperature of the plasma.

HERACLES uses a perfect gas equation of state that includes the mean ionization stage of the plasma. The code uses grey opacities (Mirone et al. 1997). We present here some preliminary results. Fig. 2, left panel, displays the variation of the density and the temperature along the central axis of the shock-tube, for a snapshot defined at time $t = 4$ ns after the piston launch. Along axis, the distance between the shock front and the piston is $z_{\rm shock} = 0.019$ mm. The gas is heated upstream (large z values) by the photons generated by the shock: this part of the flow is the radiative precursor (Mihalas & Mihalas 1984). Fig. 2, right panel, displays a map of the temperature distribution over a cross-section (x, y) of the shock-tube, in the precursor at $z = 0.066$ mm. This figure shows evidence of the three-dimensional nature of the flow. Detailed descriptions of the results will be provided in a future paper (Ibgui et al. 2012, in preparation).

3.3 X-UV Spectra obtained with IRIS: some early results

With IRIS, we post-processed the results provided by HERACLES. We used xenon monochromatic opacities calculated by the Screened Hydrogenic Model (Eidmann 1994; Michaut et al. 2004). They include bound-bound, bound-free, and free-free processes. Fig. 1, left panel, defines our notations. (O, x, y, z) is a coordinate system that is linked to the piston's frame. The position of a given point M in the flow is identified by its coordinates (x, y, z). The direction of propagation of the radiation, $\boldsymbol{n}$, is defined with respect to the basis $(\boldsymbol{e_x}, \boldsymbol{e_y}, \boldsymbol{e_z})$, by the polar angle θ between $\boldsymbol{n}$ and $\boldsymbol{e_z}$, and by the azimuthal angle φ, between $\boldsymbol{e_x}$ and the projection of $\boldsymbol{n}$ on the $x-y$ plane. To be consistent with the radiation boundary conditions adopted by HERACLES (see Section 3.2), we assume a null incoming specific intensity from the lateral walls and from the base on the right. In addition, the incoming specific intensity from the piston (base on the left) equals the Planck function at the local temperature of the plasma. Finally, there is no wall reflexion, so that the photons can freely escape.

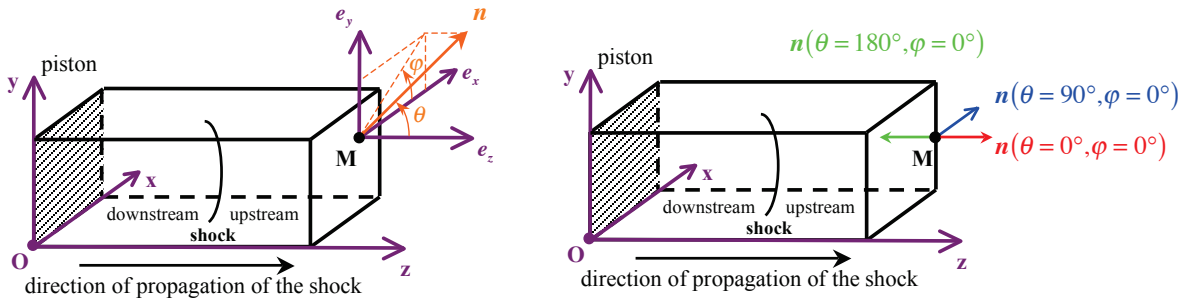

Fig. 1. Xenon filled tube, in which the radiative shock is generated by the motion of the piston in positive z-direction. **Left:** position of a given point M and a direction $\boldsymbol{n}$ of propagation of the radiation. **Right:** position M and three directions for which we show spectra in § 3.3.

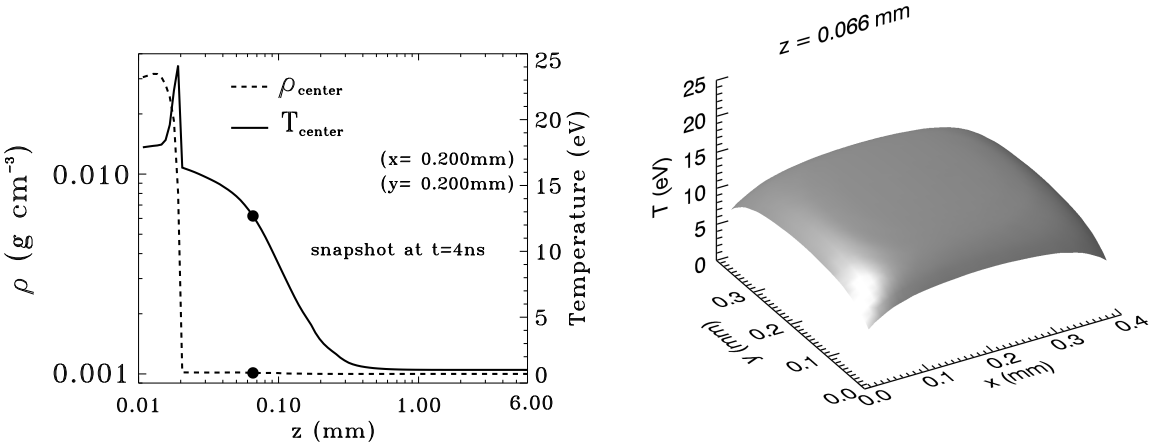

Fig. 2. Left: Density (g cm^{-3}) and temperature (eV, where 1 eV corresponds approximately to 11604.5 K) at the center of the shock-tube versus distance z from the piston, at a given instant $t = 4$ ns. **Right:** Temperature distribution over the (x, y) cross-section at position $z = 0.066$ mm that is represented by the thick dots in the left panel.

Fig. 3 shows X-UV spectra of specific intensities that emerge from the flow at point M in the border (lateral) face defined by $x = 0.40$ mm, $y = 0.20$ mm, and $z = 0.011$ mm. The curves in the figure represent the specific intensities in three directions defined by $\varphi = 0°$, and, $\theta = 0°$ (red), $\theta = 90°$ (blue), and $\theta = 180°$ (green). Fig. 1, right panel, clarifies the position of M and the directions of the radiation. The temperature profile along z-axis to which M belongs is depicted by the solid line in the right panel of Fig. 3. Note that the temperature profile differs for each different z-axis. For comparison, we plot with a dashed line the profile for the central z-axis. The peak of the temperature, which corresponds to the position of the shock, is, for the central profile, ahead of the peak for the border profile. This is consistent with the curved shape of the temperature map shown in Fig. 2, right panel. M is in the shocked part of the flow.

The spectra clearly show the anisotropy of the radiation downstream of the shock. The specific intensity $I_\nu(\theta = 0°)$ fits the Planck function at the local temperature of the plasma. This value of the intensity is mainly due to the emission from the piston. The specific intensity in the perpendicular direction $I_\nu(\theta = 90°)$ is close to the Planck function, but we see emission and absorption lines contributions. The specific intensity in the opposite direction $I_\nu(\theta = 180°)$ is very different from the two preceding ones. Since there is no photon incoming from the base on the right of the tube, the emission here is mainly due to the photon emitted in the shock and, to a lesser extent, to the photons emitted in the precursor region. For the three directions, the emission in the X-rays ($\lambda \leq 10$ nm, $h\nu \geq 124$ eV) is weaker than the emission in the UV domain. For $I_\nu(\theta = 180°)$, the largest emission peaks are between 55 eV (22.5 nm) and 115 eV (10.8 nm). In a future paper (Ibgui et al. 2012, in preparation), we will present results for more positions, specifically around the shock and in the precursor.

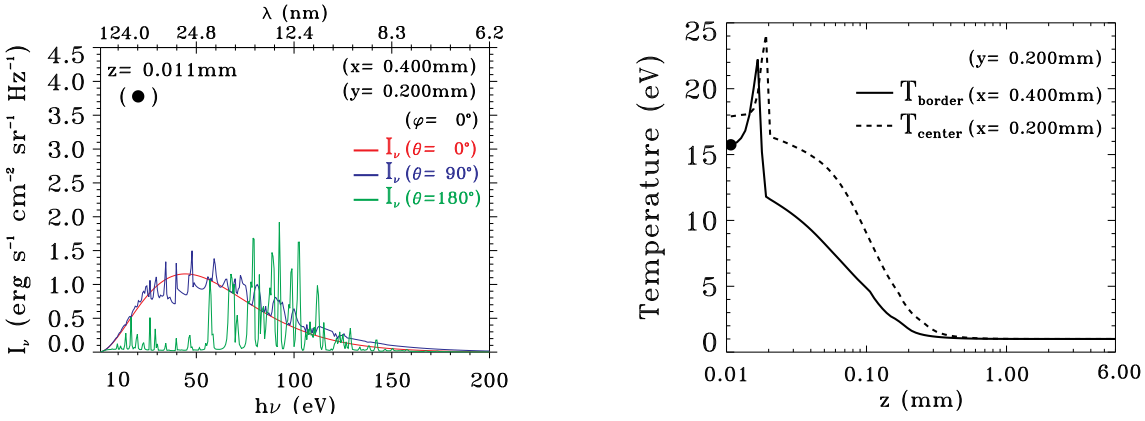

Fig. 3. Left: spectral specific intensities emerging from the shock tube at $(x, y, z) = (0.400, 0.200, 0.011)$ mm. Intensities in three directions are represented: $\varphi = 0°$, and $\theta = 0°$ (red), $\theta = 90°$ (blue), and $\theta = 180°$ (green). **Right:** temperature profiles along two z-axes: a border axis $x = 0.400$ mm, the central axis $x = 0.200$ mm. For both, $y = 0.200$ mm. $z = 0.011$ mm position is represented by a thick dot in the profile. See § 3.3 for explanations.

4 Conclusion

Preliminary results of three-dimensional non-stationary radiation hydrodynamics simulations with HERACLES, along with spectra simulated by IRIS prove the three-dimensional nature of a radiative shock, the anisotropy of the radiation, and the strong dependence of the radiation with the frequency. Further results will be detailed in a paper, Ibgui et al. (2012), in preparation.

The work is supported by French ANR, under grant 08-BLAN-0263-07. IH acknowledges the travel support from the Observatoire de Paris.

References

Auer, L. 2003, in Astronomical Society of the Pacific Conference Series, Vol. 288, Stellar Atmosphere Modeling, ed. I. Hubeny, D. Mihalas, & K. Werner, 3

Bouquet, S., Stéhlé, C., Koenig, M., et al. 2004, Physical Review Letters, 92, 225001

Brodlie, K. W. 1980, in Mathematical Methods in Computer Graphics and Design, K. W. Brodlie ed., Academic Press, London, 1

Dubroca, B. & Feugeas, J. 1999, Academie des Sciences Paris Comptes Rendus Serie Sciences Mathematiques, 329, 915

Eidmann, K. 1994, Laser and Particle Beams, 12, 223

Fritsch, F. N. & Butland, J. 1984, SIAM J. Sci. Stat. Comput., 5, 300

González, M., Audit, E., & Huynh, P. 2007, A&A, 464, 429

González, M., Audit, E., & Stehlé, C. 2009, A&A, 497, 27

Ibgui, L., Hubeny, I., Lanz, T., & Stehlé, C. 2011, in SF2A-2011: Proceedings of the Annual meeting of the French Society of Astronomy and Astrophysics, ed. G. Alecian, K. Belkacem, R. Samadi, & D. Valls-Gabaud, 485–489

Ibgui, L., Hubeny, I., Lanz, T., & Stehlé, C. 2012, submitted to A&A

Kunasz, P. & Auer, L. H. 1988, J. Quant. Spec. Radiat. Transf., 39, 67

Kunasz, P. B. & Olson, G. L. 1988, J. Quant. Spec. Radiat. Transf., 39, 1

Levermore, C. D. 1996, Journal of Statistical Physics, 83, 1021

Michaut, C., Stehlé, C., Leygnac, S., Lanz, T., & Boireau, L. 2004, European Physical Journal D, 28, 381

Mihalas, D., Auer, L. H., & Mihalas, B. R. 1978, ApJ, 220, 1001

Mihalas, D. & Mihalas, B. W. 1984, Foundations of radiation hydrodynamics

Mirone, A., Gauthier, J. C., Gilleron, F., & Chenais-Popovics, C. 1997, J. Quant. Spec. Radiat. Transf., 58, 791

Olson, G. L. & Kunasz, P. B. 1987, J. Quant. Spec. Radiat. Transf., 38, 325

Reighard, A. B., Drake, R. P., Dannenberg, K. K., et al. 2006, Physics of Plasmas, 13, 082901

Stehlé, C., González, M., Kozlova, M., et al. 2010, Laser and Particle Beams, 28, 253

Stehlé, C., Kozlová, M., Larour, J., et al. 2012, Optics Communications, 285, 64

SF2A 2012
S. Boissier, P. de Laverny, N. Nardetto, R. Samadi, D. Valls-Gabaud and H. Wozniak (eds)

ABUNDANCE ANALYSIS OF B, A AND F DWARFS IN THE M6 OPEN CLUSTER: SPECTRUM SYNTHESIS METHOD

T. Kılıçoğlu[1], R. Monier[2,3] and L. Fossati[4]

Abstract. The chemical abundances of 10 stars in the M6 open cluster (∼100 Myr) were derived using spectrum synthesis. The stars were observed using the FLAMES/GIRAFFE spectrograph. We found star-to-star variations in abundances for A type stars. General enrichment of Si, Cr, and Y were obtained for the cluster.

Keywords: Stars: abundances , open clusters and associations: individual: M6

1 Introduction

M6 is a young (∼100 Myr) open cluster located in the constellation of Scorpius. The distance to the cluster can be adopted as 500 ± 70 pc from the published values (i.e. Vleeming 1974, Paunzen et al. 2006, and WEBDA Database). Differences in chemical compositions among main sequence late-B, A and F type stars within a given cluster are probably due to differences in their masses, rotation and various kind of mixing mechanisms. These star-to-star abundance differences were previously investigated by Monier (2005), Gebran & Monier (2008), Gebran et al. (2008), Fossati et al. (2008), Fossati et al. (2011), and Gebran et al. (2010). Here, our aim is to continue to test evolutionary models via abundance determinations of the members of M6.

2 Observations

The spectra of the program stars were observed using the FLAMES/GIRAFFE spectrograph with MEDUSA, mounted at UT2 (Kueyen), the 8 meter class VLT telescope in May and June, 2007. The spectral regions cover three wavelength intervals: 4500-5100 Å, 5140-5350 Å, and 5590-5840 Å at resolving powers of about 7500, 25900, 24200, respectively.

3 Abundance Analysis

The initial atmospheric parameters of the 10 stars were derived by using Geneva 7color Photometry together with Kunzli et al. (1997)'s calibrations (CALIB code, North, P., private communication). We then used Hβ line models to derive more accurate effective temperatures and surface gravities. In order to calculate model atmospheres, we used Linux version of ATLAS9 code assuming plane-parallel geometry, a gas in hydrostatic and radiative equilibrium and LTE (Kurucz 1993, Sbordone et al. 2004, Sbordone 2005). ATLAS9 models were computed adopting Grevesse & Sauval (1998)'s solar chemical abundances and new ODFs (Castelli & Kurucz 2003). Synthetic spectra were obtained by using SYNSPEC48 with its SYNPLOT interface (Hubeny & Lanz 1992). Chemical abundances were derived by adjusting synthetic spectra with observed spectra (Fig. 1). The abundances of the elements used to compute synthetic spectra of the stars were adjusted manually to minimize chi-squares.

[1] Ankara University, Faculty of Science, Department of Astronomy and Space Sciences, 06100, Tandoğan, Ankara, Turkey
[2] Laboratoire Lagrange, Université de Nice - Sophia Antipolis, 06108 Nice Cedex 2, France
[3] LESIA Observatoire de Paris Meudon, 5 Place J. Janssen, 92195, Meudon
[4] Department of Physics and Astronomy, Open University, Walton Hall, Milton Keynes MK7 6AA, UK.

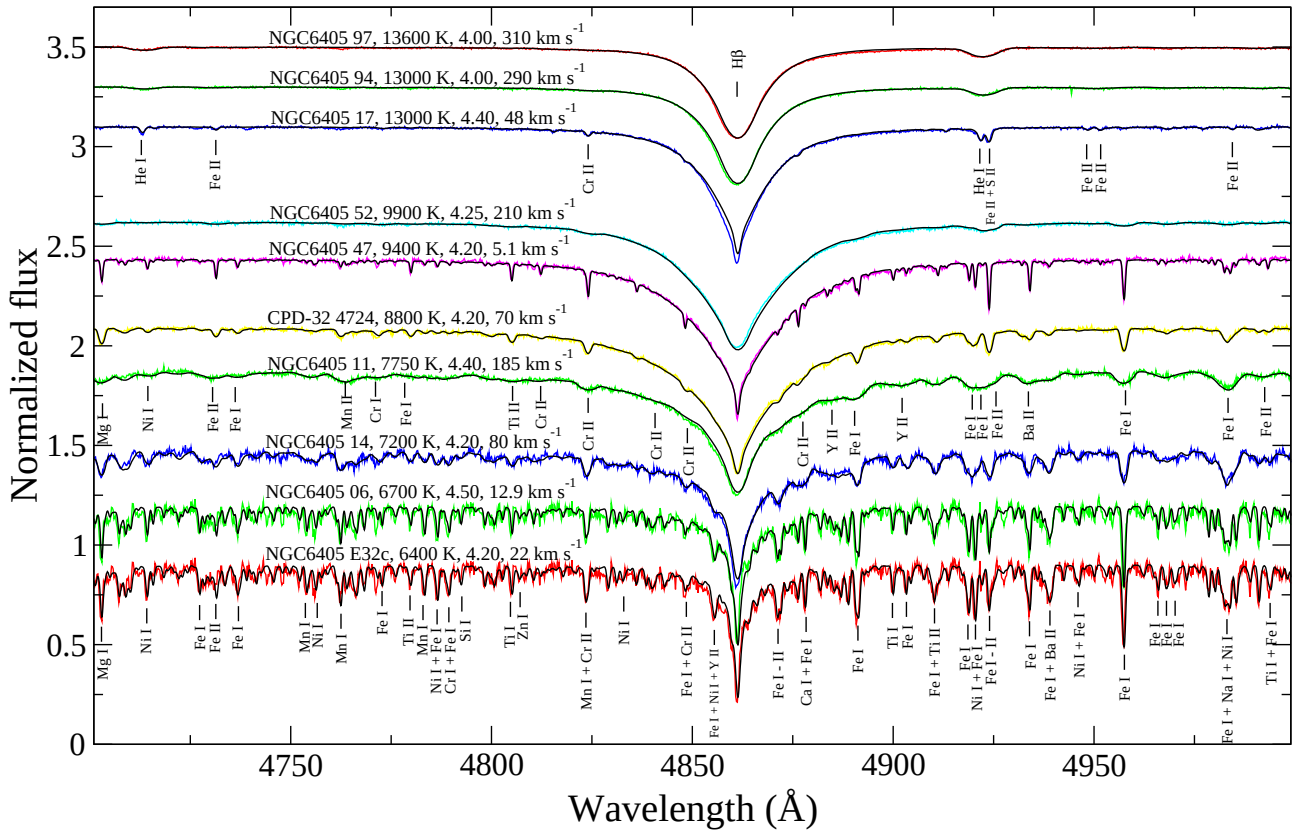

Fig. 1. The low resolution (R=7500) spectra of the cluster members (colored lines) with their final synthetic spectra (black lines) computed by using SYNSPEC48. The strongest lines are identified. The names, effective temperatures, logarithms of the surface gravities, and rotational velocities of the stars are collected above each spectrum. The normalized spectra have been shifted by an arbitrary amount in y-axis for display purpose.

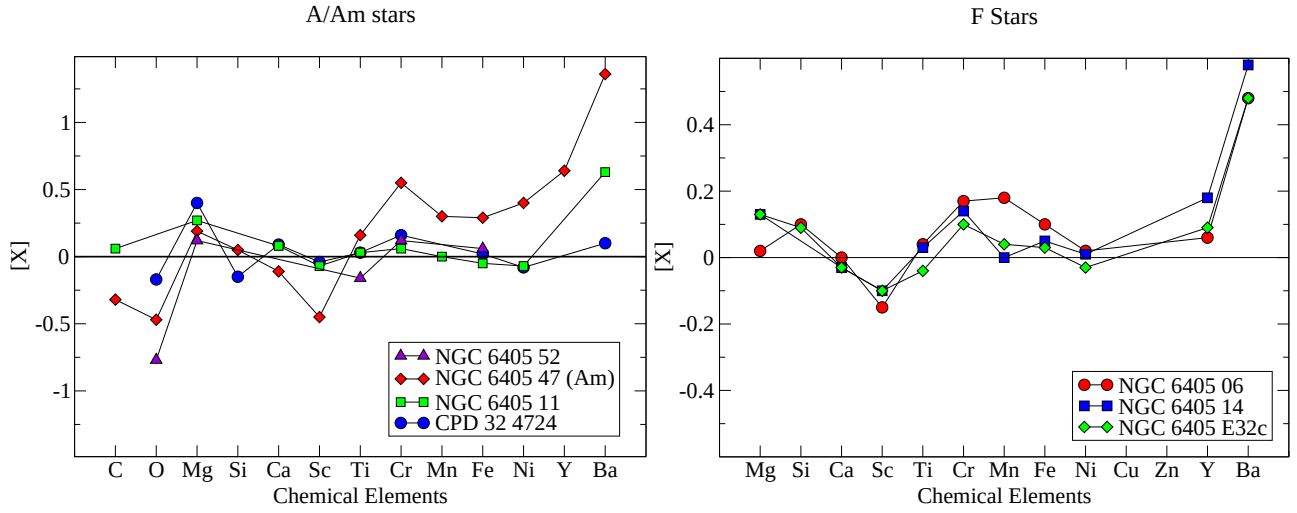

Fig. 2. Left: The derived abundances relative to the Sun for A type members. **Right:** Same for the F stars.

4 Results

We derived the chemical abundances of up to 16 chemical elements of 10 B, A, and F type dwarfs of the young open cluster M6 (Fig. 2). Gebran et al. (2008) reported a large star-to-star abundance variations for

A stars in Coma Berenices. These variations are present for C, O, Na, Sc, Ti, Mn, Fe, Ni, Sr, Y, Zr and Ba elements. Monier (2005), Gebran & Monier (2008), and Gebran et al. (2010) found similar variations for A stars in Hyades and Pleiades open clusters. Gebran et al. (2008) theorize that this peculiar behavior is a signature of the occurrence of transport processes competing with radiative diffusion. The normal A-type stars in M6 also display star-to-star variations, particularly for Mg, Ti and Ba. In contrast, the abundance patterns of the F type stars in the cluster differ little from each other, except for Mg and Mn. The chemical abundances of F stars suggest an initial enrichment of M6 in Si, Cr, Y, and particularly Ba. Analysis of a larger sample of stars having different atmospheric parameters in this cluster will help us to elucidate the mechanisms of mixing at play in the interiors of these main-sequence stars.

We kindly thank Pierre North for making his code CALIB available. This research has been supported by the Scientific and Technological Research Council of Turkey (TUBITAK, Research Fellowship of 2214), and has used SIMBAD, WEBDA, VALD, and NIST databases.

References

Castelli, F. & Kurucz, R. L. 2003, in IAU Symposium, Vol. 210, Modelling of Stellar Atmospheres, ed. N. Piskunov, W. W. Weiss, & D. F. Gray, 20P

Fossati, L., Bagnulo, S., Landstreet, J., et al. 2008, A&A, 483, 891

Fossati, L., Folsom, C. P., Bagnulo, S., et al. 2011, MNRAS, 413, 1132

Gebran, M. & Monier, R. 2008, A&A, 483, 567

Gebran, M., Monier, R., & Richard, O. 2008, A&A, 479, 189

Gebran, M., Vick, M., Monier, R., & Fossati, L. 2010, A&A, 523, A71

Grevesse, N. & Sauval, A. J. 1998, Space Sci. Rev., 85, 161

Hubeny, I. & Lanz, T. 1992, A&A, 262, 501

Kunzli, M., North, P., Kurucz, R. L., & Nicolet, B. 1997, A&AS, 122, 51

Kurucz, R. 1993, ATLAS9 Stellar Atmosphere Programs and 2 km/s grid. Kurucz CD-ROM No. 13. Cambridge, Mass.: Smithsonian Astrophysical Observatory, 1993., 13

Monier, R. 2005, A&A, 442, 563

Paunzen, E., Netopil, M., Iliev, I. K., et al. 2006, A&A, 454, 171

Sbordone, L. 2005, Memorie della Societa Astronomica Italiana Supplementi, 8, 61

Sbordone, L., Bonifacio, P., Castelli, F., & Kurucz, R. L. 2004, Memorie della Societa Astronomica Italiana Supplementi, 5, 93

Vleeming, G. 1974, A&AS, 16, 331

SF2A 2012
S. Boissier, P. de Laverny, N. Nardetto, R. Samadi, D. Valls-Gabaud and H. Wozniak (eds)

DETECTION OF A NEW PHOSPHORUS RICH STAR IN THE OPEN CLUSTER M6

T. Kılıçoğlu[1], R. Monier[2,3] and L. Fossati[4]

Abstract. We present the first spectroscopic analysis of HD318101, a member of the M6 (NGC 6405, age 100 Myr) open cluster, using low and high resolution (R∼7500, R∼25000) spectra stretching from 4500 to 5840 Å. The atmospheric parameters of the star were determined from Geneva photometry and hydrogen line modeling (T_e = 15400 ± 500 K, log g = 4.0 ± 0.25). The abundances of 8 elements were determined by fitting synthetic spectral lines to the observed ones. We derived a strong overabundance of phosphorus (+1.69 dex, relative to the Sun) from several P II lines. We also found helium to be underabundant (-0.37 dex). These abundance anomalies suggest that HD318101 could be a He-weak PGa type star (CP4).

Keywords: Stars: abundances, Stars: chemically peculiar, Stars: individual: HD318101

1 Introduction

Non-magnetic chemically peculiar stars are divided into four main groups (Kurtz 2000): λ Boo (7000-10000 K, metal poor), Am (7000-10000 K, metal rich), HgMn (10000-14000 K), and He-weak PGa (13000 - 18000 K). Elemental diffusion can be the cause of these elemental peculiarities. For B stars, stellar winds might also cause some chemical peculiarities. Detailed discussions of peculiar B and A stars can be found in Alecian (1996), Kudritzki & Puls (2000), Krticka & Kubat (2004), and Gebran & Monier (2008).

HD318101 (NGC 6405 20) is one of the brightest member of the M6 open cluster. Nesterov et al. (1995) ascribed this star a spectral type B9. Johnson UBV, Strömgren *uvby*, and Geneva 7color photometric measurements of the star were published by Talbert (1965), Schneider (1985), and in the WEBDA, respectively.

2 Observations

The spectrum of HD 318101 was acquired with FLAMES/GIRAFFE spectrograph with MEDUSA, mounted at UT2 (Kueyen), the 8 meter class VLT telescope in May and June, 2007. The spectral regions cover three wavelength intervals: 4500-5100 Å, 5140-5350 Å, and 5590-5840 Å at resolving powers of about 7500, 25900, 24200, respectively.

3 Abundance Analysis

The color B-V = -0.03 is calculated from Kharchenko & Roeser (2009). We derived an effective temperature (T_e) of 15950 K using Cox (2000)'s calibrations and an averaged color excess of the cluster: E(B-V) = 0.15 ± 0.01. We used Geneva 7color photometry as a second indicator and derived T_e = 15864 K and log g = 4.04 from Kunzli et al. (1997)'s calibrations (CALIB code). We also used synthetic profiles of the Hβ line to obtain more accurate atmosphere parameters, and derived T_e = 15400 ± 500 K and log g = 4.00 ± 0.25. Model atmospheres were calculated using ATLAS9 on Linux (Kurucz 1993, Sbordone et al. 2004, Sbordone 2005). The linelist was first constructed from Kurucz's gfall.dat, and then updated with VALD and NIST. Synthetic spectra were computed using SYNSPEC48 (Hubeny & Lanz 1992), assumming Grevesse & Sauval (1998)'s solar chemical composition.

[1] Ankara University, Faculty of Science, Department of Astronomy and Space Sciences, 06100, Tandoğan, Ankara, Turkey
[2] Laboratoire Lagrange, Université de Nice - Sophia Antipolis, 06108 Nice Cedex 2, France
[3] LESIA Observatoire de Paris Meudon, 5 Place J. Janssen, 92195, Meudon
[4] Department of Physics and Astronomy, Open University, Walton Hall, Milton Keynes MK7 6AA, UK.

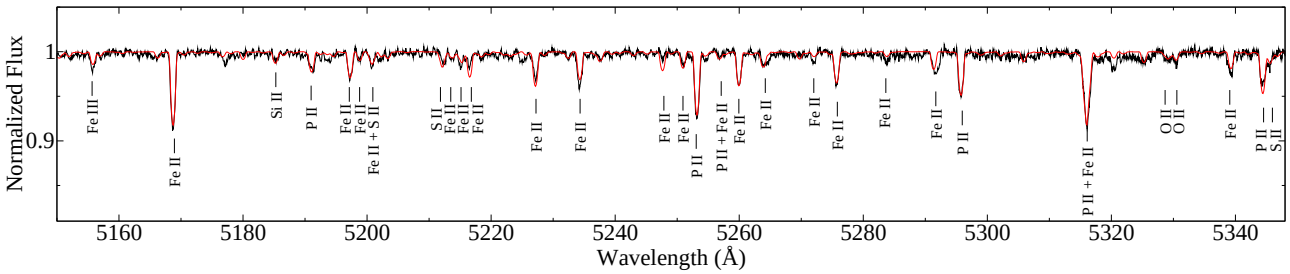

Fig. 1. The high resolution (R=25900) GIRAFFE spectrum of HD 318101 (black) and its synthetic spectrum (red).

4 Results and Discussion

Abundances for 8 chemical elements were determined by looking for the best fit between the observed spectrum and theoretical one (Fig. 1). The comparison of synthetic and observed spectra showed that Phosphorus overabundance of HD 318101 should be 1.7 ± 0.4 dex, with respect to the Sun (∼50 times more than solar) while iron abundance is solar. We also noticed an underabundance in Helium (-0.37 dex). A detailed NLTE study for O and B type stars (15000 K-35000 K) were performed by Przybilla et al. (2011). According to their comparison of LTE and NLTE models at the temparature of 22000 K, NLTE models form similar or sometimes deeper lines than LTE models for He I lines. A NLTE analysis could reduce the He abundance for this star. We failed to find Ga II lines in the range from 4500 to 5840 Å. New observations at high resolution including ultraviolet region are necessary to derive the abundances of the other elements.

The overabundance of phosphorus and the underabundance of helium suggest that HD 318101 may be a Helium-weak star, and possible a PGa (CP4) star. More accurate fundamental parameters, Iron and Gallium abundances are necessary to confirm that HD318101 is indeed a PGa star.

We kindly thank Pierre North for making his code CALIB available. This research has been supported by the Scientific and Technological Research Council of Turkey (TUBITAK, Research Fellowship of 2214), and has used the SIMBAD, WEBDA, VALD, and NIST databases.

References

Alecian, G. 1996, A&A, 310, 872

Cox, A. N. 2000, Allen's astrophysical quantities (New York: AIP Press; Springer)

Gebran, M. & Monier, R. 2008, A&A, 483, 567

Grevesse, N. & Sauval, A. J. 1998, Space Sci. Rev., 85, 161

Hubeny, I. & Lanz, T. 1992, A&A, 262, 501

Kharchenko, N. V. & Roeser, S. 2009, VizieR Online Data Catalog, 1280, 0

Krticka, J. & Kubat, J. 2004, in Magnetic Stars, ed. N. Arkhyz, Y. V. Glagolevskij, I. I. Kudryavtsev, & I. I. Romanyuk, 234–240

Kudritzki, R.-P. & Puls, J. 2000, ARA&A, 38, 613

Kunzli, M., North, P., Kurucz, R. L., & Nicolet, B. 1997, A&AS, 122, 51

Kurtz, D. W. 2000, in Astronomical Society of the Pacific Conference Series, Vol. 210, Delta Scuti and Related Stars, ed. M. Breger & M. Montgomery, 287

Kurucz, R. 1993, ATLAS9 Stellar Atmosphere Programs and 2 km/s grid. Kurucz CD-ROM No. 13. Cambridge, Mass.: Smithsonian Astrophysical Observatory, 1993., 13

Nesterov, V. V., Kuzmin, A. V., Ashimbaeva, N. T., et al. 1995, A&AS, 110, 367

Przybilla, N., Nieva, M.-F., & Butler, K. 2011, Journal of Physics Conference Series, 328, 012015

Sbordone, L. 2005, Memorie della Societa Astronomica Italiana Supplementi, 8, 61

Sbordone, L., Bonifacio, P., Castelli, F., & Kurucz, R. L. 2004, Memorie della Societa Astronomica Italiana Supplementi, 5, 93

Schneider, H. 1985, A&AS, 61, 45

Talbert, F. D. 1965, PASP, 77, 19

SF2A 2012
S. Boissier, P. de Laverny, N. Nardetto, R. Samadi, D. Valls-Gabaud and H. Wozniak (eds)

SPECTRAL CHARACTERISATION OF THE CARMENES INPUT CATALOGUE

A. Klutsch[1], F. J. Alonso-Floriano[1], J. A. Caballero[2], D. Montes[1], M. Cortés-Contreras[1], J. López-Santiago[1], J. C. Morales[3], A. Quirrenbach[4], P. J. Amado[5], I. Ribas[3], A. Reiners[6], R. Mundt[7] and the CARMENES Consortium

Abstract. CARMENES (Calar Alto high-Resolution search for M dwarfs with Exoearths with Near-infrared and optical Échelle Spectrographs) is the future exoplanet hunter for the 3.5-m Calar Alto telescope. Its first light is expected to be in early 2014. For a sample of 312 M-type stars, we performed their spectral-type classification by comparing their low-resolution spectra with those of spectral-type standard stars acquired during the same observing runs, and using spectral indices well-calibrated for M dwarfs, such as, TiO5, CaH2 and CaH3. We also derived chromospheric activity indicators and relative metallicities. All these data were included in our "input catalogue", CARMENCITA (CARMENES Cool star Information and daTa Archive), which will be the most comprehensive catalogue on M dwarfs ever built. This database currently comprises the over 1300 brightest, latest M dwarfs northern of δ = -23 deg. Among them, we will select carefully the 300 most promising candidates that will be surveyed for low-mass planet companions by means of the analysis of high accuracy radial velocity measurements. Our URL: `http://carmenes.caha.es/`

Keywords: stars: low-mass, stars: planetary systems, instrumentation: spectrographs, stars: fundamental parameters

1 Introduction

M dwarfs are the most common stellar population in the solar neighborhood. As their habitable zones are closer than those of F, G, and K stars, the radial-velocity signature of an Earth-like planet located in the habitable zone and the probability of showing transits are much larger. But, because of their faintness in the optical, few searches for exoplanets around M dwarfs with the radial-velocity method have been performed in comparison to Solar-like main-sequence stars. For these reasons, our consortium is building a near-infrared spectrograph with a radial velocity accuracy on the m s^{-1} level for the Calar Alto Astronomical Observatory. Such an instrument would be more efficient to detect terrestrial planets around low-mass stars. Before that, we must have chosen carefully the sample of 300 M dwarfs to which CARMENES will look for low-mass exoplanets under guaranteed time. This task implies a deep understanding of their stellar parameters.

2 Sample selection and observations

All our sources were taken from the CARMENCITA (CARMENES Cool star Information and daTa Archive) database, which results from the compilation of previous and on-going M-dwarf catalogues and surveys (e.g., Ross, Luyten, Gliese, Palomar/Michigan State University –PMSU–, Lépine & Gaidos). Caballero et al. (2012) gave an exhaustive list of information already collected for all the selected sources.

[1] Universidad Complutense de Madrid, Departamento de Astrofísica, Facultad de Ciencias Físicas, E-28040 Madrid, Spain
[2] Centro de Astrobiologia (CSIC-INTA), PO Box 78, E-28691 Villanueva de la Cañada, Madrid, Spain
[3] Institut de Ciències de l'Espai (CSIC-IEEC), Campus UAB, Facultat de Ciències, Torre C5 parell, E-08193 Bellaterra, Spain
[4] Landessternwarte Königstuhl (ZAH), Königstuhl 12, D-69117 Heidelberg, Germany
[5] Instituto de Astrofísica de Andalucía (CSIC), PO Box 3004, E-18080 Granada, Spain
[6] Institut für Astrophysik Göttingen, Physik Fakultät, Friedrich-Hund-Platz 1, D-37077 Göttingen, Germany
[7] Max Planck Institute für Astronomy, D-69117 Heidelberg, Germany

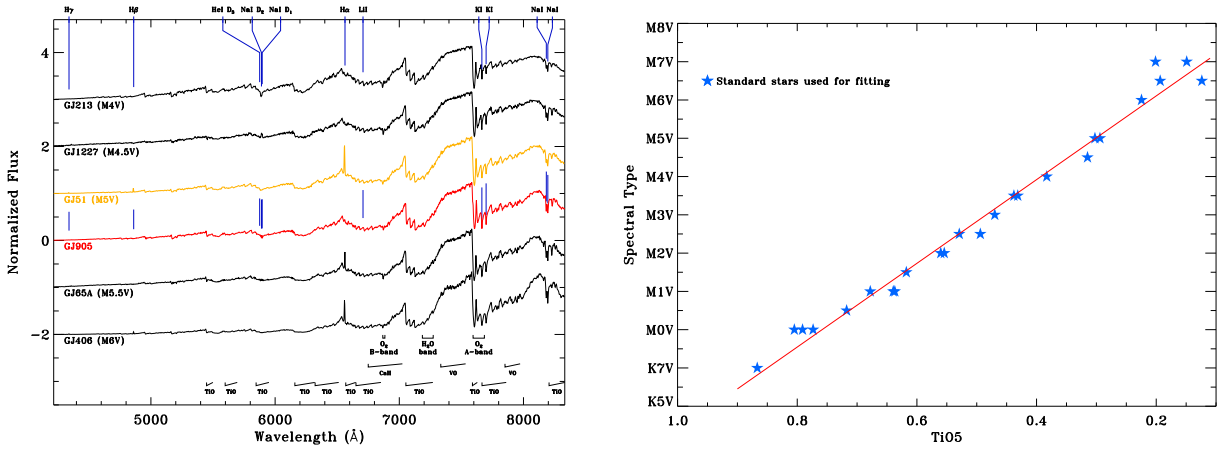

Fig. 1. Spectral type determination of our sources. **Left:** Example of least-square minimisation of an M5.0V star (GJ 905). In red, target spectrum; in orange, the best match; in black, other standard spectra. We also display the locus of molecular and telluric bands listed by Kirkpatrick et al. (1991). **Right:** Calibration of the spectral type from the TiO5 index.

From November 2011 to March 2012, we conducted an observing programme on a first sample of 312 sources. Their long-slit low-resolution spectra (spectral resolution R $\sim$ 1500) were taken with the Calar Alto Faint Object Spectrograph (CAFOS) mounted on the 2.2 m telescope of the German-Spanish Calar Alto Observatory (`http://www.caha.es/`, Almería, Spain). Another sets of sources will be observed in forthcoming CAFOS runs.

3 Spectral typing

During these observations, we also included about 50 standard stars with spectral types from K5 to M7 for both dwarf and giant classes. By comparing with the archive of M-type star spectra from the PMSU survey (Reid et al. 1995; Hawley et al. 1996), we only retained those whose spectra were the most representative of one given spectral type in order to build our own library of standard stars.

Our spectral characterisation of every target relied on the comparative analysis of the full spectral range of its normalised spectrum and of our standards. For this work, we discarded the wavelength ranges contaminated by strong telluric lines or by any activity indicators (e.g., the Balmer lines). By means of a least-square minimisation technique, we looked for best matches (see the left panel of Fig. 1)

Alonso-Floriano et al. (2012) used calibrations with the spectral indices to derive the spectral type of our stars by interpolating the relation between one given spectral index and the spectral type (e.g., the TiO5 index, see the right panel of Fig. 1). So far, we were studied the TiO1–5, CaH1–3, CaOH and Hα indices as defined by Reid et al. (1995). However more indices will come later (e.g., from Lépine et al. 2003).

Our results show that these two independent methods of classification are fairly consistent. The spectral types of the 312 targets mainly range from M2.5V to M5.0V (Fig. 2). The spectral typing of all our targets was performed with an accuracy of about $\pm$0.5 subtypes.

We also compared our results with those derived from both photometric and/or spectroscopic data. Most of the standard stars, which are both in PMSU catalogue and in our sample, have the same spectral type, with an accuracy of $\pm$0.5 subtypes. However, we found that the spectral types estimated from optical to near-infrared colours by Lépine & Gaidos (2011) are mainly 1–2 subtypes later than those derived from our spectroscopic data and over 5 subtypes for some M dwarfs (Fig. 2).

4 Chromospheric activity and metallicity

Some spectral indices are more sensitive to activity, metallicity or gravity. Alonso-Floriano et al. (2012) focused on the chromospheric activity and relative metallicity of all the observed stars.

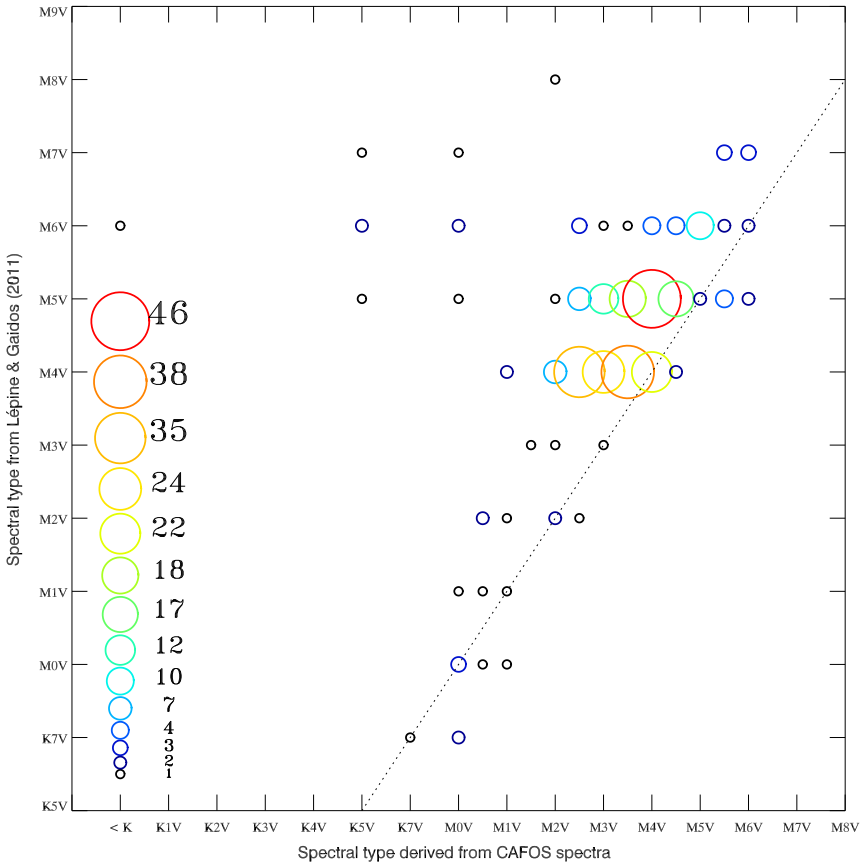

Fig. 2. Comparison between spectral types estimated by Lépine & Gaidos (2011) from photometric data and from our spectroscopic observations of stars in common. The size and colour of symbols indicate the number of sources in each bin. The dotted line shows the one-to-one relation.

By determining the Hα index, we enabled to make a preliminary identification of chromospherically active stars in our sample. The most active stars have a spectral type between M3.0V and M5.0V (Fig. 3, left panel). A more detailed analysis of the Hα and Hβ behaviours will give us a better characterisation of their activity.

We determined relative metallicity index ζ = [1-TiO5]/[1-TiO5$_\odot$] following the method described by Lépine et al. (2007). Our fit of TiO5 index as a function of the sum of CaH2 and CaH3 indices (Fig. 3, right panel) is rather consistent with that presented recently by Lépine et al. (2012). We found a difference between these two calibrations for the latest M dwarfs only. None of our targets are classified as subdwarfs.

Montes et al. (2012) investigated some M dwarfs in wide-binary systems with FGK primaries to which we already performed abundance analysis from our high-resolution spectra using the code StePar (Tabernero et al. 2012). We showed that the relation between the TiO5 and CaH2+CaH3 indices could be calibrated using the [Fe/H] abundances of the FGK companions.

5 Conclusions

We performed the spectral-type classification of 312 M-type dwarfs by means of a least-square minimisation technique applied on the full spectral range of normalised spectra, and using spectral indices well-calibrated for M dwarfs, such as, TiO5, CaH2 and CaH3. These two methods provide the same classification with an accuracy of about $\pm$0.5 subtypes. We also derived chromospheric activity indicators and relative metallicities. We included all these parameters, derived from our data, in the CARMENCITA database. This catalogue will be the centrepiece for choosing the 300 most promising planet candidates that will be surveyed during a five-year survey with the CARMENES spectrograph under guaranteed time (Quirrenbach et al. 2010, 2012). We expect to detect super-Earths of 5 M$_\odot$ or less, some of which may be in the habitable zone or transiting.

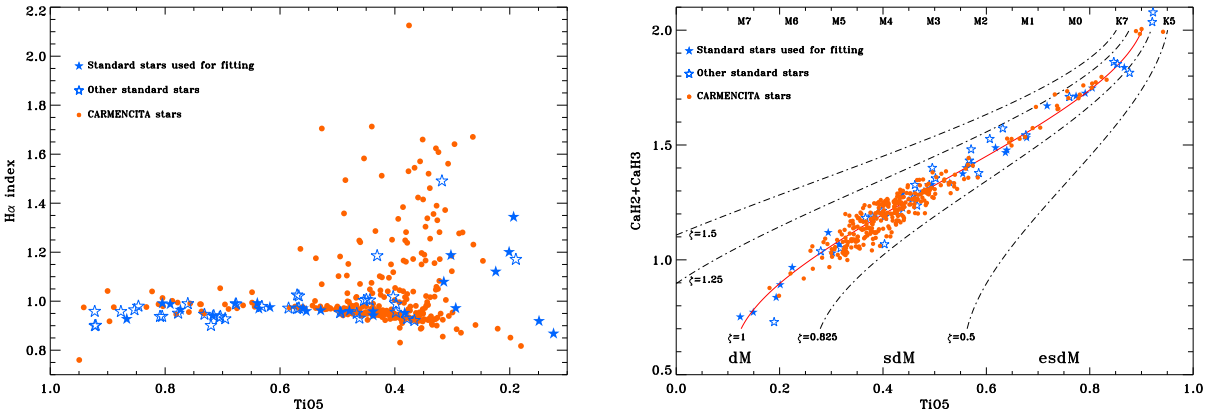

Fig. 3. Distribution of the Hα (**left panel**) and CaH2+CaH3 (**right panel**) index values as a function of the TiO5 one. On the right panel, we display the iso-ζ contours (1.5, 1.25, 1.0, 0.825, and 0.5 from top to bottom). The two last values correspond to the separators between the metallicity classes of M-type stars as defined by Lépine et al. (2007): dwarf (dM), subdwarf (sdM), and extreme subdwarf (esdM).

This work was supported by Universidad Complutense de Madrid, AstroMadrid (CAM S2009/ESP-1496), and the Spanish Ministerio de Economía y Competitividad (MINECO), under grants AYA2011-30147-C03-02, AP2009-0187, and AYA2011-29754-C03-03.

References

Alonso-Floriano, F. J., Montes, D., Caballero, J. A., et al. 2012, in the 17th Cambridge Workshop on Cool Stars, Stellar Systems and the Sun, P01.6.4

Caballero, J. A., Cortés-Contreras, M., López-Santiago, J., et al. 2012, in the 17th Cambridge Workshop on Cool Stars, Stellar Systems and the Sun, P05.1.5

Hawley, S. L., Gizis, J. E., & Reid, I. N. 1996, AJ, 112, 2799

Kirkpatrick, J. D., Henry, T. J., & McCarthy, Jr., D. W. 1991, ApJS, 77, 417

Lépine, S. & Gaidos, E. 2011, AJ, 142, 138

Lépine, S., Hilton, E. J., Mann, A. W., et al. 2012, AJ submitted, eprint arXiv:1206.5991

Lépine, S., Rich, R. M., & Shara, M. M. 2003, AJ, 125, 1598

Lépine, S., Rich, R. M., & Shara, M. M. 2007, ApJ, 669, 1235

Montes, D., Alonso-Floriano, F. J., Caballero, J. A., et al. 2012, in the 17th Cambridge Workshop on Cool Stars, Stellar Systems and the Sun, P01.3.12

Quirrenbach, A., Amado, P. J., Mandel, H., et al. 2010, SPIE, 7735, E37

Quirrenbach, A., Amado, P. J., Seifert, W., et al. 2012, SPIE, 8446, 25

Reid, I. N., Hawley, S. L., & Gizis, J. E. 1995, AJ, 110, 1838

Tabernero, H. M., Montes, D., & González Hernández, J. I. 2012, A&A, in press, eprint arXiv:1205.4879

SF2A 2012
S. Boissier, P. de Laverny, N. Nardetto, R. Samadi, D. Valls-Gabaud and H. Wozniak (eds)

CHARACTERIZATION OF YOUNG FIELD STARS IN THE VICINITY OF THE CO CEPHEUS VOID

A. Klutsch[1], D. Montes[1], P. Guillout[2], A. Frasca[3], F.-X. Pineau[2], N. Grosso[2], E. Marilli[2] and J. López-Santiago[1]

Abstract. After mixing in the Galactic plane, young stars are barely discernible from old ones. Nonetheless, the characterization of stars in the *RasTyc* sample has led to the discovery of several sources whose lithium content is higher than that of the Pleiades cluster members. In the locus of the CO Cepheus void, we identified four comoving T Tauri stars within a few degrees. They likely form a new young association. Looking for the presence of further members, we performed selections through multivariate analysis. We focused on the late-type stars in the field, which are identified as the optical and infrared counterparts of ROSAT All-Sky Survey/XMM-Newton X-ray sources and are in a 30°-wide region encompassing this new moving group. Based on our spectroscopic observations of this dataset, we identified two distinct populations of lithium-rich stars that are spatially and kinematically separated. While the sources having the same lithium content as the members of the Pleiades cluster are mostly projected in front of the Galactic plane, the youngest stars are mainly located towards the sky area surrounding the CO Cepheus void. The latter stars have an age of about $5 - 15$ Myr, which is rather similar to that derived for the four comoving T Tauri stars previously found in this region. The discovery and characterization of all the young stars in the field are of great importance to have new insights into the process of stellar formation outside the typical star-forming regions. The Gaia mission will certainly shed light on this issue and on the origin of this group that could be related to the Cepheus-Cassiopeia complex.

Keywords: stars: fundamental parameters, stars: pre-main sequence, stars: formation, stars: kinematics and dynamics, stars: late-type, X-rays: stars

1 Introduction

In the optically bright sample of ROSAT All-Sky Survey/Tycho (*RasTyc*) sources, Guillout et al. (2009) identified 5 pre-main-sequence stars that appear to be unrelated to any known star-forming region. Analysing our first observations of the optically faint sources (Klutsch 2008), we discovered a group of four lithium-rich stars near the Cepheus-Cassiopeia complex, which is rich in CO molecular regions (Dame et al. 2001) and dark clouds (Dobashi et al. 2005; Kiss et al. 2006). Although this sky area is known as an active star-forming region (Kun 2008; Kun et al. 2008, 2009; Kirk et al. 2009), this concentration of young stars is projected in front of one of the sky areas devoid of interstellar matter listed by Kiss et al. (2006). Guillout et al. (2010) showed that they form a homogeneous group of T Tauri stars with a common origin. From all the observations of the faintest targets, Frasca et al. (2012) found more than 10 new sources displaying a lithium content larger than that of the Pleiades cluster members. Two of them (crosses in Fig. 1) are located in the same sky area as the four comoving T Tauri stars (asterisks in Fig. 1).

[1] Universidad Complutense de Madrid, Departamento de Astrofísica, Facultad de Ciencias Físicas, E-28040 Madrid, Spain

[2] Observatoire Astronomique de Strasbourg, Université de Strasbourg, CNRS, UMR 7550, 11 rue de l'Université, F-67000 Strasbourg, France

[3] INAF - Osservatorio Astrofisico di Catania, via S. Sofia, 78, I-95123 Catania, Italy

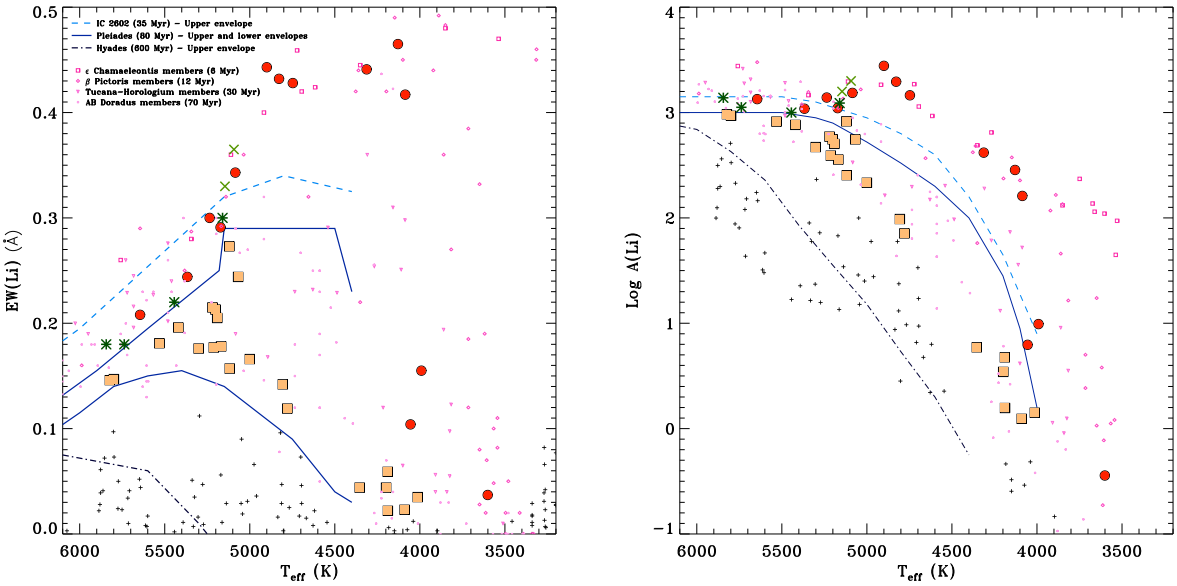

Fig. 1. Left: Li I λ6707.8 line equivalent width versus the effective temperature of our young star candidates. **Right:** Lithium abundance versus the effective temperature of targets. On both panels, we highlight the stars whose lithium content is larger than the Pleiades cluster members (circles), and the Pleiades-like ones (squares). We use plus symbols for the other candidates. We show the locus of the four comoving T Tauri stars (asterisks), and the two lithium-rich stars (crosses) discovered by Frasca et al. (2012). We also overplot the envelopes of three young clusters (various lines) and the distribution of members for 4 young associations (various small pink symbols) taken from da Silva et al. (2009).

2 Young star candidates: Selection, observations and analysis

Looking for new members of this association, we adopted the innovative analysis methods of Pineau et al. (2011) for building a sample of 162 young star candidates (see Klutsch et al. 2011, for details on our selection criteria). Tachihara et al. (2005) also discovered several T Tauri stars in this sky area. We included them in our candidate list to establish if they could be members of this young moving group. Between September 2009 and November 2010, we acquired intermediate- and high-resolution spectra (IDS@INT, FOCES@2.2m, and Sophie@T193), deriving their spectral type, physical parameters and radial velocities. Finally, we studied the age, kinematics, and chromospheric activity of all the observed targets.

3 Properties of pre-main-sequence sources and Pleiades-like stars

We found 14 young sources (circles in Fig. 1) for which the estimated age is rather similar to that of the four comoving T Tauri stars (asterisks), and 22 "older" Pleiades-like sources (squares). They form two distinct stellar populations located in different areas (Fig. 2, left panel). The youngest sources (including the six *RasTyc* sources), for which the lithium content ranges between that of the members of the ϵ Chamaeleontis (6 Myr) and Tucana-Horologium (30 Myr) associations, are mostly projected in front of the CO Cepheus void, in the Cepheus Flare region. The Pleiades-like sources are mainly located towards the Galactic plane. We also bring out a smaller concentration (inside the big open square in Fig. 2, right panel) composed of three young multiple systems. Up to now, these sources are identified as being one spectroscopic binary, one visual binary and one visual binary whose primary component is a spectroscopic binary (Klutsch et al. 2011).

With an estimated age of $5 - 15$ Myr and an average radial velocity of -8 ± 2 km s^{-1}, all the youngest stars newly discovered in the CO Cepheus void show the same properties as the four comoving T Tauri stars already found by us in this region. In particular, they all display very similar proper motions, both those with and without radial velocity data (hexagons and circles, respectively, in the right panel of Fig. 2 and the lower panel of Fig. 3). All these properties support the assumption that they likely have a common origin.

We selected all the sources brighter than $K_s = 10$ mag (dots in the lower panel of Fig. 3) from the PPMXL

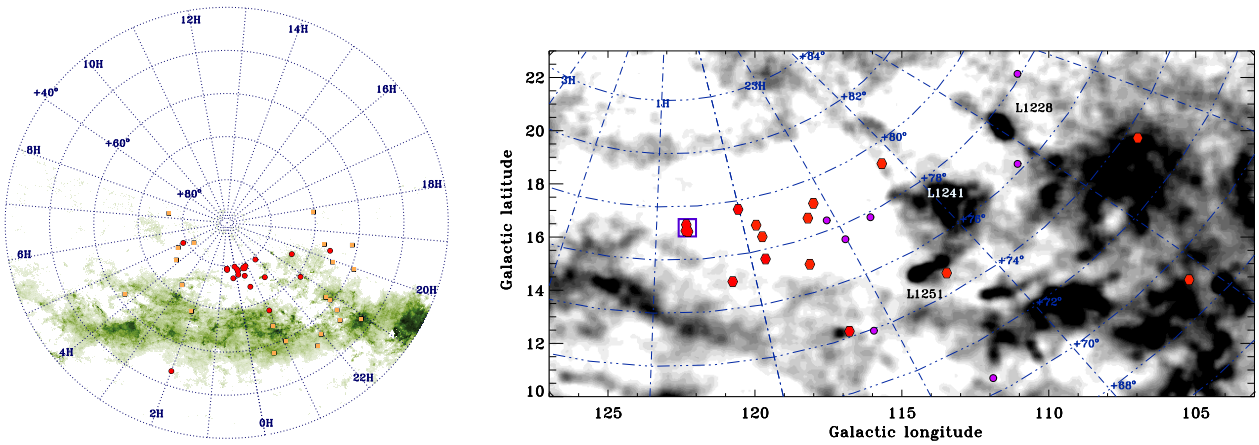

Fig. 2. Left: Spatial distribution of the young stars highlighted in Fig. 1, overplotted on the extinction (A_v) map of Dobashi et al. (2005). **Right:** Zoom on the CO Cepheus void. We plot all the young stars, both with (hexagons) and without (circles) accurate radial velocity measurements. Note that all the sources for which the information on radial velocity is missing were classified as T Tauri stars by Tachihara et al. (2005). On both panels, the six *RasTyc* sources are included in the list of the youngest stars with radial velocity data (red symbols).

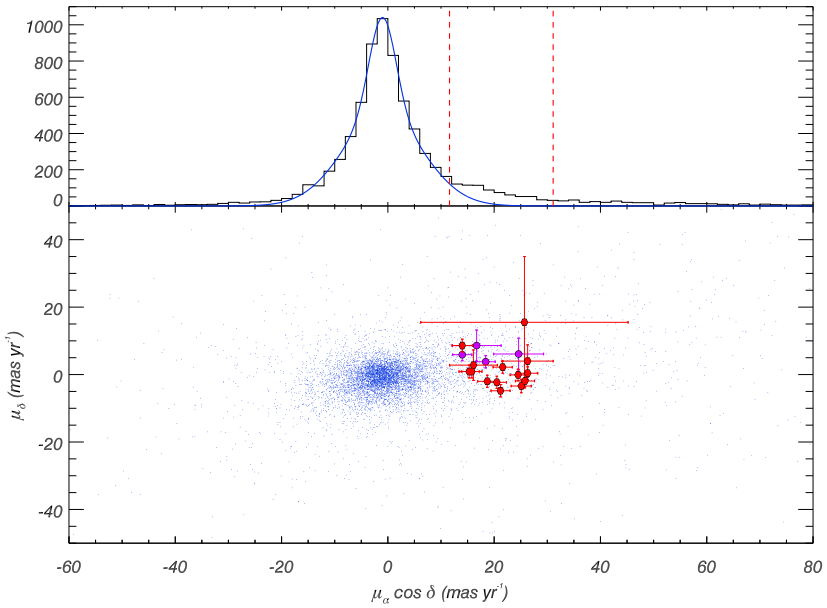

Fig. 3. Top: Histogram of the proper motions in right ascension for all the stars in the CO Cepheus void that are brighter than $K_s = 10$ mag. The curve correspond to the fit of this distribution, and the two vertical lines delimit the range of proper motions of our candidates. **Bottom:** Distribution of proper motion values of all the selected stars (dots). We also overplot the proper motions (and associate errors) of all young stars towards the CO Cepheus void, both with (hexagons) and without (circles) radial velocity measurements.

catalog (Roeser et al. 2010), using a cone search (radius = 5°) that covers all the sky area devoid of interstellar matter. The comparison between the distribution of the proper motions in right ascension and its fit emphasized an excess of sources within the range of proper motions of our candidates (delimited by two vertical lines in the upper panel of Fig. 3), which are slightly larger than the average value derived from the field stars. About 10% of the selected PPMXL sources display such a characteristic, while only a few are identified as young stars. This could be the result of the unknown supernova shock expected to be at the origin of this CO void (Grenier et al. 1989), or larger dynamical process(es) in the Galaxy.

One of the youngest sources, located outside the Cepheus area (see Fig. 2, left panel), was already rejected from the list of likely candidates of the association. Among the five remaining targets, 4 are fast rotators ($v \sin i > 20$ km s^{-1}), but we cannot exclude that they are spectroscopic binaries seen close to conjunction.

4 Conclusions

We present the latest findings of our work aiming at the identification of new members of the young moving group recently discovered towards the CO Cepheus void. Thanks to our spectroscopic observations, we identified two distinct populations of lithium-rich stars that are spatially and kinematically separated. Sources with a lithium abundance similar to that of the Pleiades cluster members are mostly projected towards the Galactic plane, while the youngest stars (age = 5 – 15 Myr) are mainly located in the sky area surrounding the CO Cepheus void. The latter stars have properties (age, proper motions, radial velocity, ...) rather similar to those derived for the four comoving T Tauri stars already found in this region.

During the last decade, several young stars (age $<$ 50 Myr) were discovered and they mainly belong to young associations and moving groups visible from the southern hemisphere. Though few members of the β Pictoris and AB Dor moving groups are located in the northern hemisphere, this new concentration of young comoving stars in front of the CO Cepheus void likely forms the first young association found northward of $\delta = +30$ deg.

This group is located in the vicinity of the Cepheus-Cassiopeia complex, which is an active star-forming region. Additional data, such as those from the future Gaia mission, will certainly shed light on an eventual link between these two structures and on the process of stellar formation outside the typical star-forming regions.

This work was supported by Universidad Complutense de Madrid, AstroMadrid (CAM S2009/ESP-1496), and the Spanish Ministerio de Economía y Competitividad (MINECO), under grants AYA2011-30147-C03-02 and AYA2011-29754-C03-03. Part of this study is supported by the Italian Ministero dell'Istruzione, Università e Ricerca (MIUR), and the Région Alsace.

References

da Silva, L., Torres, C. A. O., de La Reza, R., et al. 2009, A&A, 508, 833

Dame, T. M., Hartmann, D., & Thaddeus, P. 2001, ApJ, 547, 792

Dobashi, K., Uehara, H., Kandori, R., et al. 2005, PASJ, 57, 1

Frasca, A., Guillout, P., Klutsch, A., et al. 2012, in preparation

Grenier, I. A., Lebrun, F., Arnaud, M., Dame, T. M., & Thaddeus, P. 1989, ApJ, 347, 231

Guillout, P., Frasca, A., Klutsch, A., Marilli, E., & Montes, D. 2010, A&A, 520, A94

Guillout, P., Klutsch, A., Frasca, A., et al. 2009, A&A, 504, 829

Kirk, J. M., Ward-Thompson, D., Di Francesco, J., et al. 2009, ApJS, 185, 198

Kiss, Z. T., Tóth, L. V., Krause, O., Kun, M., & Stickel, M. 2006, A&A, 453, 923

Klutsch, A. 2008, PhD thesis, Observatoire de Strasbourg, Universié Louis Pasteur

Klutsch, A., Montes, D., Guillout, P., et al. 2011, in ASP Conference Series, Vol. 448, 16th Cambridge Workshop on Cool Stars, Stellar Systems, and the Sun, ed. C. Johns-Krull, M. K. Browning, & A. A. West, 661

Kun, M. 2008, in Handbook of Star Forming Regions, Volume I, ed. Reipurth, B. (ASP Monograph Publications), 240

Kun, M., Balog, Z., Kenyon, S. J., Mamajek, E. E., & Gutermuth, R. A. 2009, ApJS, 185, 451

Kun, M., Kiss, Z. T., & Balog, Z. 2008, in Handbook of Star Forming Regions, Volume I, ed. Reipurth, B. (ASP Monograph Publications), 136

Pineau, F.-X., Motch, C., Carrera, F., et al. 2011, A&A, 527, A126

Roeser, S., Demleitner, M., & Schilbach, E. 2010, AJ, 139, 2440

Tachihara, K., Neuhäuser, R., Kun, M., & Fukui, Y. 2005, A&A, 437, 919

SF2A 2012
S. Boissier, P. de Laverny, N. Nardetto, R. Samadi, D. Valls-Gabaud and H. Wozniak (eds)

AUTOMATIC COMPARISON BETWEEN OBSERVED AND COMPUTED STELLAR SPECTRA WITH TOOLS AND PROTOCOLS FROM THE VIRTUAL OBSERVATORY

A. Lèbre[1], A. Palacios[1], M. Sanguillon[1] and P. Maeght [2]

Abstract. We present - through a *demo* - the VOSPECFLOW application that intends to make easier - with the use of protocols from the Virtual Observatory - the comparison between observed stellar spectra (stored in the TBLegacy archive) and high resolution synthetic spectra (stored in the POLLUX database).

Keywords: Techniques: photometric, Astronomical databases: miscellaneous, Virtual observatory tools

1 Introduction

Synthetic spectra computed over a large spectral range (300 - 1 200 nm) and at high resolution (R = 150 000), such as the ones distributed in the POLLUX database (Palacios et al. 2010) can not be directly nor easily confronted to observational data, such as stellar spectra stored in telescope's archives. Indeed the imprint of the instrument involved to collect the data, as well as some stellar properties such as macroturbulence or surface rotation, have to be taken into account through adequate modifications of the synthetic spectrum to transform it into an optimized simulation of an observed spectrum. Moreover, even if the Virtual Observatory (V.O.) facilitates the access to interoperable data distributed in a somehow homogenized file format (mainly VOTable or FITS format), observed and computed stellar spectra often present different file structures (different number of columns, different units for columns of the same meaning, presence or not of a normalized flux column, ...). Finally, observed and theoretical stellar spectra are generally accessible, within the V.O., through different dedicated protocols, the Simple Stellar Access protocol (SSAP) and the Theoretical Stellar Access Protocol (TSAP), respectively. Each of these protocols involves very specific keywords to request a V.O. compliant service. For example a telescope's archive will be queried through the IDENT and POSITION of a specific star (of often unknown stellar parameters), while theoretical spectra stored in a database will be queried through stellar parameters (Teff, log g, [Fe/H], ...). All of these subtle differences between observed and computed stellar spectra (regarding their structure and storage) really prevent their direct confrontation through any *quicklook* basic tool. For that reason, along the development of the POLLUX database and within the large collaboration OV-GSO (Observatoire Virtuel du Grand Sud Ouest), we have defined the VOSPECFLOW application that we present below.

2 VOSPECFLOW : How it works and what it aims at

The VOSPECFLOW application aims at making easier the comparison between observed and computed stellar spectra. In its present version, it involves observations stored in the TBLegacy archive (`http://tblegacy.bagn.obs-mip.fr/`) and high resolution synthetic spectra stored in the POLLUX database (`http://pollux.graal.univ-montp2.fr/`). Using V.O. protocols and starting from the name of a given star (e.g., HD 232 862), VOSPECFLOW automatically performs successive requests to various services (Fig. 1) such as :

- SIMBAD &VizieR, to retrieve respectively the position informations of the star and its stellar parameters
- TBLegacy, to retrieve - with the position informations obtained from the request addressed to SIMBAD- a list of observations of the star, collected with the Narval spectropolarimeter (Fig. 2)

[1] LUPM, Université de Montpellier and CNRS, Place E. Bataillon, 34090 Montpellier, France
[2] UPS-OMP, Université de Toulouse and CNRS, 57, Ave. d'Azereix, 65 000 Tarbes, France

- POLLUX, to retrieve - with the stellar parameters obtained from the request addressed to VizieR - a list of synthetic spectra the parameters of which best comply with those of the actual star as returned by VizieR.

Then, onto a limited portion (10 nm large) of a synthetic spectrum selected among the proposed POLLUX spectra, VOSPECFLOW allows the user to perform - *on the fly* - up to three successive convolutions so as to mimic the instrumental profile, macroturbulent and rotational effects (Fig. 3). This aims at transforming the synthetic spectrum into an optimized simulation of an observation. To take into account the stellar properties, macroturbulence and surface rotation effects can be introduced respectively with a radial-tangent profile and with a rotational profile, the width of these functions being macroturbulent veocity and vsini, respectively. Then, the instrumental profile can be applied through a gaussian function with a fixed full width half maximum. The result of these operations as well as the initial spectra retrieved from TBLegacy or POLLUX can be visualized within a dedicated graphic interface (Fig. 4), these data being temporarily stored in a VOSPECFLOW space.

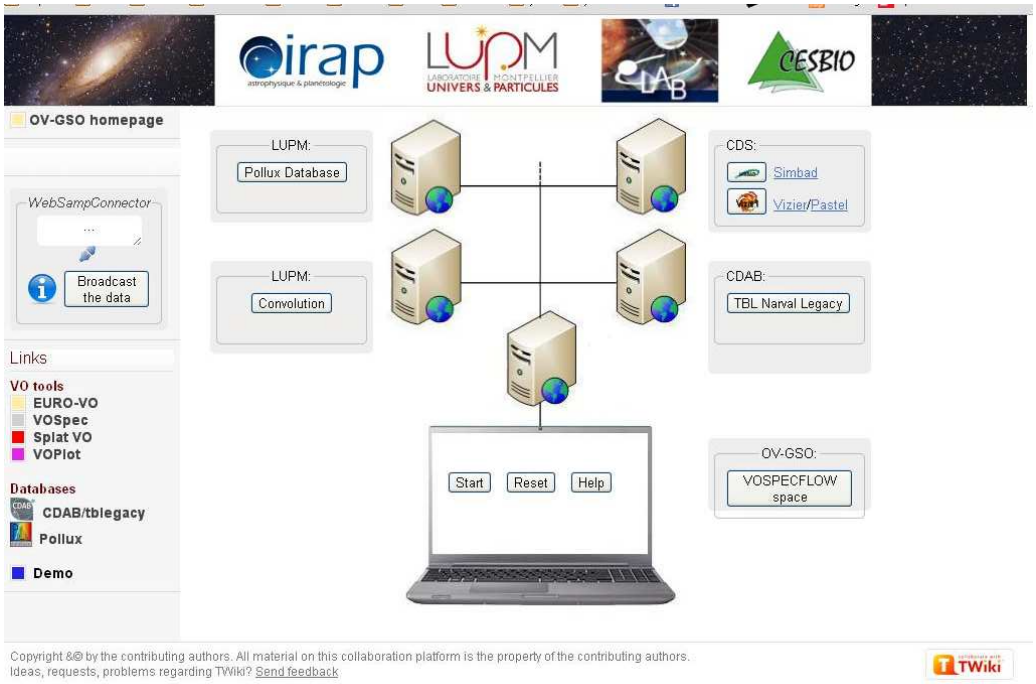

Fig. 1. VOSPECFLOW global view. In the central panel, the different remoted services are indicated (SIMBAD and VizieR at CDS ; TBLegacy at CDAB ; POLLUX at LUPM). The SAMP connexion to VO tools (such as VOspec) is located on the right side and allows broadcast (to other V.O. services / tools) of data temporarily stored in the space VOSPECFLOW at OV-GSO

3 VOSPECFLOW and other V.O. tools

On the left side of VOSPECFLOW main page, a WebSAMPConnector is present (see Fig. 1). When connected, this client toolkit enables our VOSPECFLOW service to interoperate and communicate with VO softwares and to perform, for example, data transfer. At that stage, into any V.O. tool, such as VOSpec, it is thus possible to broadcast any of the data that the user has been storing in the VOSPECFLOW space, such as the portion of synthetic spectrum resulting from convolution operations. Then the visualization and further spectral analysis can be performed directly through the selected V.O. tool (Fig. 5).

4 Conclusions

The application VOSPECFLOW mainly offers facilities like access to data, transformation of a high resolution synthetic spectrum into an optimized simulation of observation, *quicklook* graphic display. However in its present

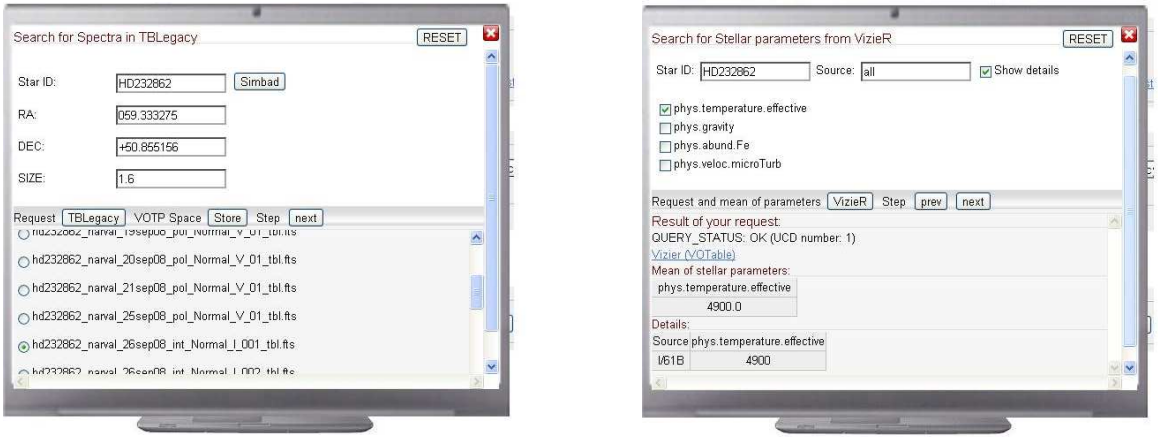

Fig. 2. Left: Request to SIMBAD, to retrieve position informations : RA and DEC. From them, request to TBLegacy to retrieve observations of HD 232 862. **Right:** Request to VizieR, to retrieve stellar parameters from various catalogs.

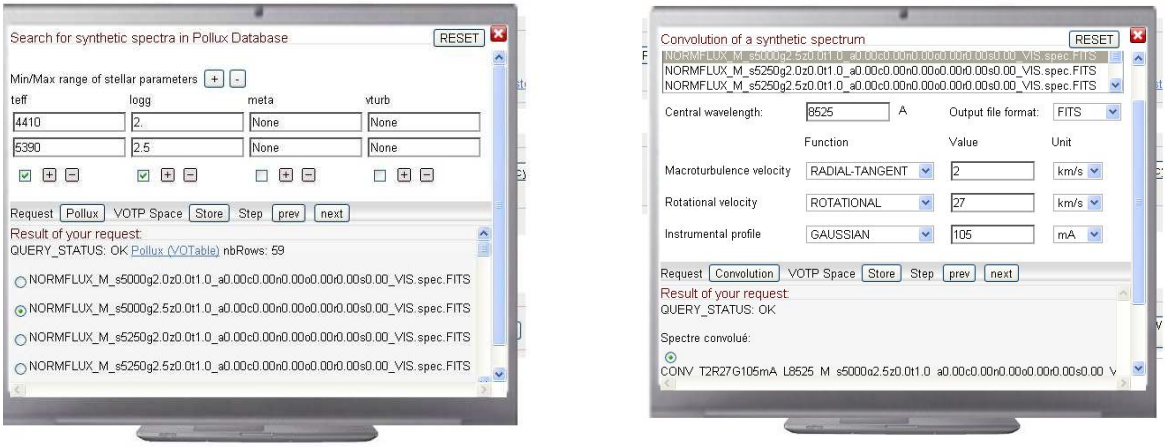

Fig. 3. Left: From stellar parameters retrieved from VizieR, request to POLLUX, to retrieve synthetic spectra with nearest values for parameters (Teff, log g, [Fe/H]). **Right:** Convolution operations applied to a theoretical POLLUX spectrum so as to turn it into an optimized simulation of an observation.

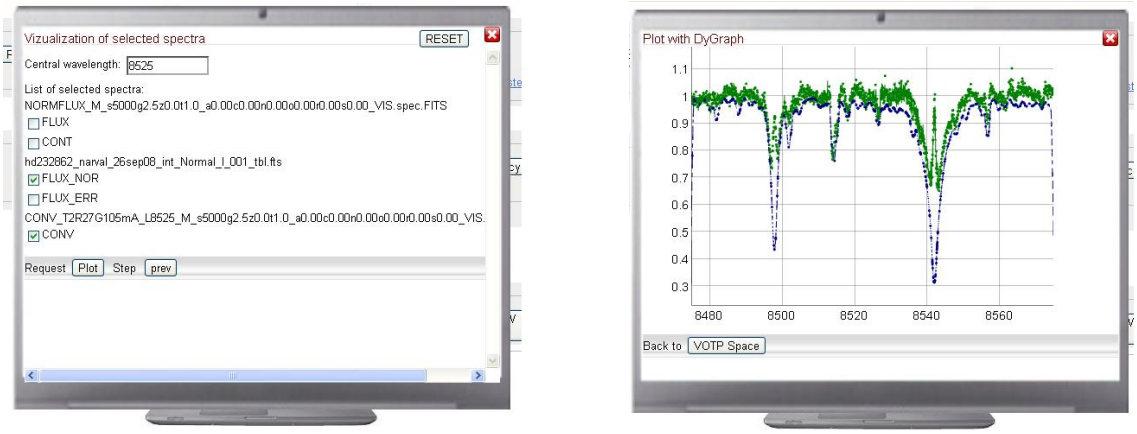

Fig. 4. Left: Selection of (portion of) spectra to be visualized. **Right:** Convolution operations applied to a theoretical POLLUX spectrum so as to turn it into an optimized simulation of an observation.

form, this tool should be used with caution. In particular, it is not designed to produce scientific results such as determination of precise stellar parameters or measurement of chemical abundances. Only diagnostics onto stellar parameters (i.e., determination of a range of values) or qualitative information onto the presence/absence of any element into a stellar atmosphere can be inferred from the use of VOSPECFLOW that is mainly designed to help the user well upstream of a more complete and classical analysis of the spectra.

The first version of VOSPECFLOW presented here relies only on the TBLegacy archive and on the POLLUX database, being respectively observational and theoretical data providing V.O. services. Its extension toward other V.O. services, such as other telescope's archives or computed spectra distributed from V.O. compliant databases is foreseen.

VOSPECFLOW will be opened to the community at the beginning of the year 2013, and the information of its url will be spread through SF2A communication channel. Besides, the module allowing convolution operations onto a synthetic spectrum will be implemented in the POLLUX website before the end of 2012.

This research was achieved using the POLLUX database (`http://pollux.graal.univ-montp2.fr`) operated at LUPM (Université Montpellier II - CNRS, France with the support of the PNPS and INSU.

References

Palacios, A., Gebran, M., Josselin, E., et al. 2010, A&A 516, A13

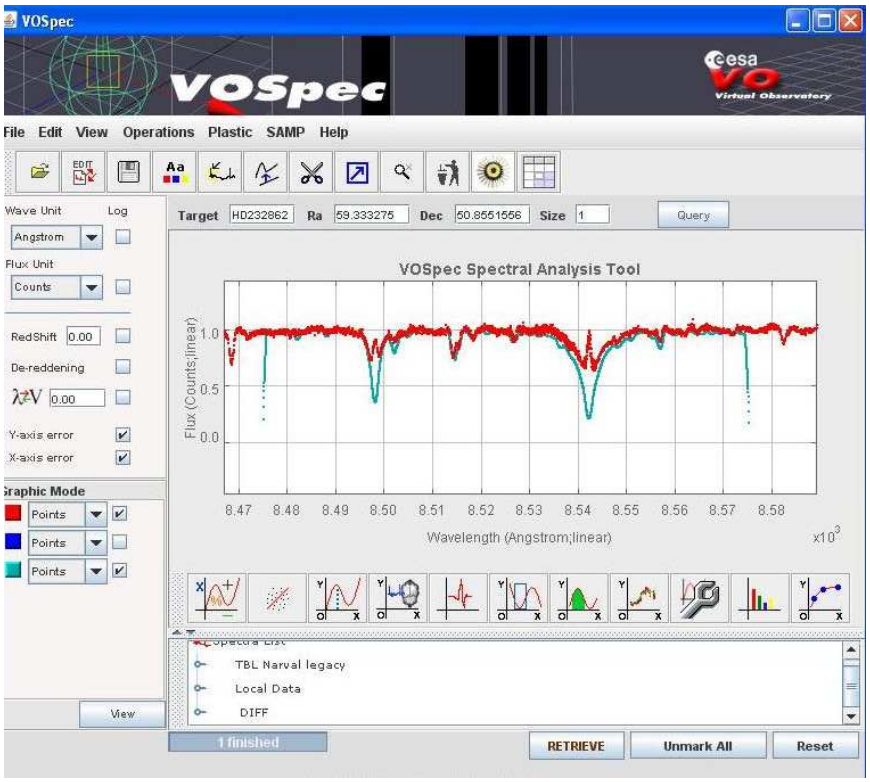

Fig. 5. Final visualization through VOSpec, using the broadcast data through the SAMP protocol.

SF2A 2012
S. Boissier, P. de Laverny, N. Nardetto, R. Samadi, D. Valls-Gabaud and H. Wozniak (eds)

IMPACT OF NON-LTE EFFECTS ON THE IR CA II TRIPLET AND THE MG I 8736 Å EQUIVALENT WIDTHS IN LATE-TYPE GIANT AND SUPER-GIANT STARS

T. Merle[1], F. Thévenin[1], B. Pichon[1] and L. Bigot[1]

Abstract. Calcium and magnesium are key α-elements to study stellar populations in galaxies. Classical stellar abundances analyses rely on the local thermodynamic equilibrium (LTE) assumption which is not always appropriate, in particular for metal-poor and/or evolved stars. To better understand these stars and apprehend their impacts on the chemical enrichment of the Galaxy, it is necessary to use a Non-LTE (NLTE) description which is more realistic but also more complex to build up. For the calcium (Ca) and magnesium (Mg) lines in the RVS@Gaia, we computed theoretical NLTE corrections to apply to the measured equivalent widths of these lines using very complete model atoms of Mg and Ca. These corrections can be used by the automated abundance analysis methods based on equivalent widths for current and forthcoming large surveys.

Keywords: line: formation, radiative transfer, stars: abundances, stars: late-type

1 Why the Ca II IR triplet and the Mg I 8736 Å lines are important?

These lines are important because they represent lines of α-elements useful for derive abundances of magnesium, calcium and iron, and study the galactic enrichment. The IR ionized calcium triplet (CaT) is important since it allows us to determine the metallicity of red giant stars belonging to globular clusters (Armandroff & Da Costa 1991) and to dwarf spheroidal galaxies (Battaglia et al. 2008; Starkenburg et al. 2010) thanks to the measure of their equivalent widths at low resolution. The Mg I 8736 Å line is the only Mg I useful line at the resolution of the RVS[i]. It is a weak and unblended line not visible at metallicity lower than [Fe/H] ~ -2. Fig. 1 shows an example of spectra in the RVS (Radial Velocity Spectrometer) wavelength range for the Sun (integrated flux) where the CaT and the Mg I 8736 Å lines are labeled. Theoretical (red line) and observed (black line) spectra are compared at resolution of $R = 8500$. Theoretical LTE spectra is from MARCS model (Edwardsson, private communication) and observations are from Brault & Neckel (1987). The synthetic spectra reproduce well the observations except for few very weak lines for which the oscillator strengths are badly known and for the cores of the CaT which are formed in Non-LTE (NLTE) in the chromosphere, not included in the MARCS models.

2 How to compute line profile in Non-LTE?

As underlined by Asplund (2005), *"In non-LTE, in principle everything depends on everything else, everywhere else."*. This means that to compute line profile in NLTE, we need a huge amount of supplementary atomic data, concerning the element considered. In LTE, the line source function and the line opacity depend on the temperature, the free electron density and the LTE population number densities (governed by the Boltzmann and Saha's laws). In NLTE, the line source function and the line opacity depend on the NLTE population number densities of the element on which the line belongs, governed by the statistical equilibrium equations. To reach a better NLTE description a complete model atom in then required.

We used a modified version of the 1D NLTE radiative transfer code MULTI (Carlsson 1986). The radiative transfer and the statistical equilibrium equations are solve consistently using a theoretical MARCS model atmosphere (Gustafsson et al. 2008) for one element at a time. This element is considered as a trace element, i.e. is assumed to not disturb the structure of the model atmosphere. We constructed model atoms of Mg I and

[1] Laboratoire Lagrange, UMR7293, Université de Nice Sophia-Antipolis, CNRS, Observatoire de la Côte d'Azur, 06300 Nice, France
[i] whereas there is also a line at 8473 Å and a triplet at 8710, 8712 and 8717 Å.

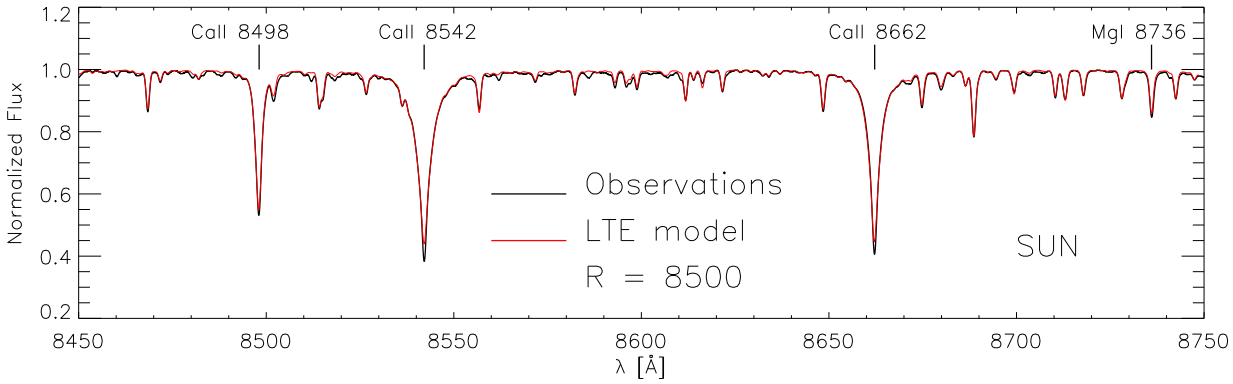

Fig. 1. Solar spectra in the RVS wavelength range.

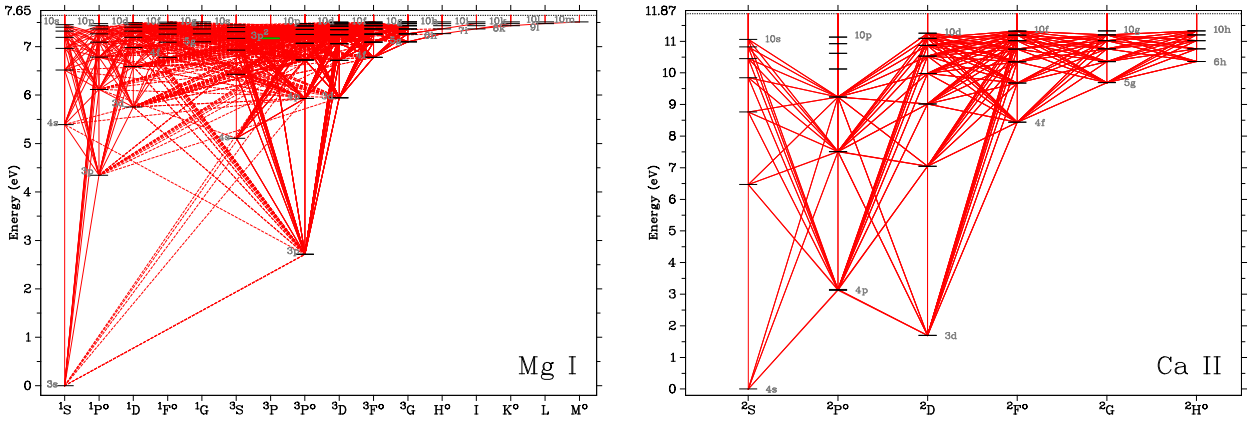

Fig. 2. Grotrian diagrams of Mg I (**left panel**) and Ca II (**right panel**). Solid red lines are the radiative transitions and dashed red lines (only for the Mg I model atom) are the semi-allowed transitions included in the models.

Ca II using the FORMATO code (Merle et al. 2011) which enables flexibility and modularity. Grotrian diagrams of model atoms of Mg I and Ca II are shown in Fig. 2. Energy levels until $n = 10$ are included. Fine structure is taken into account but not visible at this scale. The sources of atomic data are given in Merle et al. (2011). Oscillator strengths for the CaT are from Meléndez et al. (2007) and for Mg I 8736 Å line from VALD (Kupka et al. 2000). Inelastic collisions with neutral hydrogen were neglected since no reliable collision strengths with H were available until very recently for Mg I (Barklem et al. 2012).

3 What about the results?

We computed departure coefficients $b_i = n_i/n_i^*$ and NLTE/LTE equivalent width ratios W/W^* for a grid of atmospheric parameters:

- $3500\ \mathrm{K} \leq T_{\mathrm{eff}} \leq 5500\ \mathrm{K}$ with a step of 200 or 250 K;
- $0.5 \leq \log g \leq 2.0$ with a step of 0.5 dex;
- $-4.0 \leq [\mathrm{Fe/H}] \leq +0.5$ with a step of 0.5 dex in $[-4.0, -1]$ and 0.25 in $[-1.0, +0.5]$;

for a galactic enrichment in α-elements (i.e. $[\alpha/\mathrm{Fe}] = 0.0$ in a metallicity range of $[0.0, +0.5]$, $[\alpha/\mathrm{Fe}] = -0.4[\mathrm{Fe/H}]$ in $[-1.0, 0.0]$ and $[\alpha/\mathrm{Fe}] = +0.4$ in $[-4.0, -1.0]$). The MARCS models with a mass of $M = 1M_{\odot}$ and a constant microturbulent velocity fields of $\xi = 2$ km s^1 are adopted. We will discuss, hereafter, only the case of the CaT and the Mg I 8736 Å lines. Due to the importance of these lines for the Gaia mission, we computed

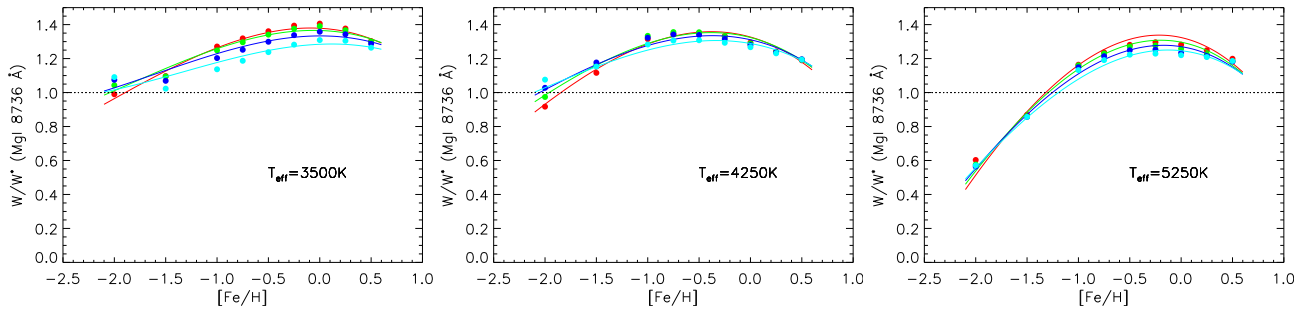

Fig. 3. W/W^* for the Mg I 8736 Å line as function of metallicity for three $T_{\rm eff}$. Each colour corresponds to a surface gravity (red, green, blue and cyan for $\log g = 0.5$, 1.0, 1.5 and 2.0 dex respectively). Dots represent theoretical results and full lines third order polynomial fits as a function of atmospheric parameters. The dotted line ($W/W^* = 1$) stands for no deviation from LTE.

fits of the W/W^* as a multivariable polynomial, using the LSQ package of Miller (1992). For each line of Mg I and Ca II in the RVS wavelength range, the W/W^* fit depends on $T_{\rm eff}$, $\log g$ and [Fe/H]. Theses fits can be used to estimate W/W^* with an accuracy better than 10 % in the range of stellar parameter considered. For more details on the other lines of these two α-elements see Merle et al. (2011).

The Mg I 8736 Å line, which is the most visible Mg I line in this RVS@Gaia range, is not visible under [Fe/H] ~ 2. Variations of W/W^* with atmospheric parameters are shown on the Fig. 3. Each panel represents the W/W^* of a given $T_{\rm eff}$ as a function of the metallicity [Fe/H]. Each colour represents a surface gravity (red, green, blue and cyan for $\log g = 0.5$, 1.0, 1.5 and 2.0 dex respectively). Dots are the computed values and full lines the polynomial fit. Its W/W^* is larger than one for a large range of stellar parameters and can reach $W/W^* = 1.4$ at solar metallicity. Positive values of W/W^* lead to a negative abundance correction, i.e., to an over-estimation of the Mg I abundance in LTE for this line. To our knowledge, there is only one previous study of the Mg I 8736 Å line in NLTE by Shimanskaya et al. (2000, and private communication). Their NLTE corrections for this line are lower due to the use of a semi-empirical formula to treat inelastic collisions with hydrogen.

The variation of W/W^* with [Fe/H] of the CaT (left panel of Fig. 4) can be explained with the variations of the departure coefficients presented in the right panel of Fig. 4. As the stimulated emission can be neglected for optical and near IR lines, the line source function relative to the Planck function S^l_ν/B_ν follows the departure coefficient ratio b_j/b_i (i and j are the lower and upper levels respectively). W/W^* depends on the values of b_i relative to b_j and on the deviation between them. In a metal-rich model (bold lines in right panel of Fig. 4), the levels are over-populated due to the over-ionization of Ca I and $b_i < b_j$ that implies $S^l_\nu > B_\nu$, and the emergent intensity is strengthened in the line compared to LTE intensity. Thus the EW in NLTE is lower than the EW in LTE. This explains why $W/W^* \leq 1$ for models with $-1 \leq$[Fe/H]$\leq +0.5$ in left panel of Fig. 4. For a metal-poor model (thin lines in right panel of Fig. 4), the mechanism is the opposite due to the change in the relative values of b_i and b_j. For metallicities lower than -1, $b_i > b_j$ if $\tau_{5000} \leq -1.7$ and then $S^l_\nu < B_\nu$. This implies a reduction of the emergent intensity in the line and then a larger value of EW in NLTE relative to the LTE. This explains why $W/W^* > 1$ for models with [Fe/H] ≤ -1 in left panel of Fig. 4.

The fine structure of the levels follows the same trends but level population differences increase with decreasing $\log \tau_{5000}$. The Ca II IR 8498 Å line has the greater NLTE effects relative to the two other lines because it has the largest amplitude on the deviation between the lower coefficient b_i ($3d\ ^2D_{3/2}$, blue dotted line) and the upper coefficient b_j ($4p\ ^2P^o_{3/2}$, red dashed line) as seen in right panel of Fig. 4. The CaT lines are dominated by their wings even at [Fe/H] $= -2$ as shown in fig. 1 of Starkenburg et al. (2010). These wings are formed in the deep photosphere in LTE conditions. Therefore the EW are weakly influenced by the NLTE effects at solar metallicity and can become very large for the most metal-poor stars (20-30% at [Fe/H] $= -3$). These results are in quite good agreement with those of previous investigations with the same stellar parameters (e.g. Jorgensen et al. 1992, Andretta et al. 2005).

We also compared the NLTE effects on CaT computed by Starkenburg et al. (2010) and found a clear discrepancy at low metallicity. They provided a 2D polynomial fit of $W^*/W = f(T_{\rm eff}, [{\rm Fe/H}])$ for the lines at 8542 Å and 8662 Å, considering that these ratios are insensitive to the surface gravity ($1 \leq \log g \leq 2$). We plotted in the left panel of Fig. 4 their polynomial fit for the 8662 Å line. The discrepancies between our

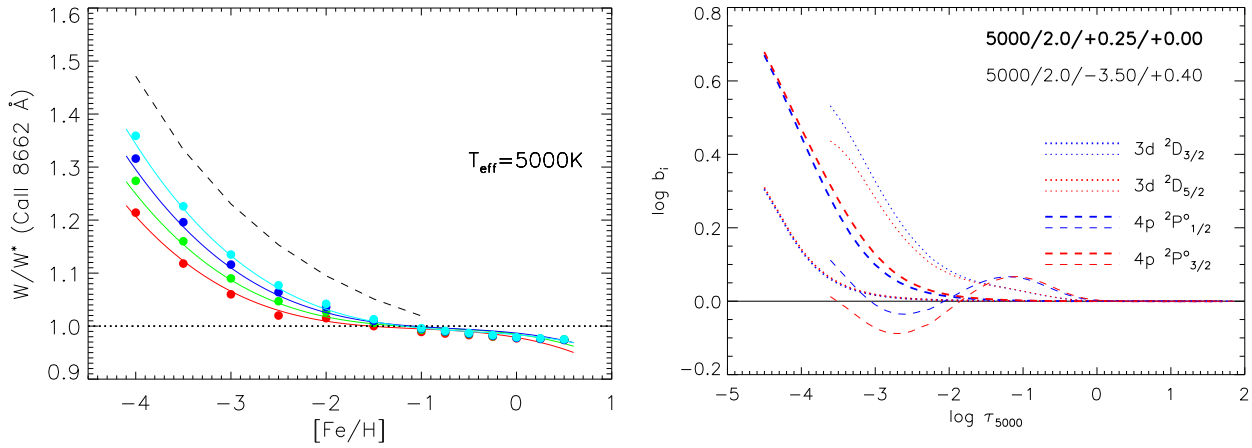

Fig. 4. Left: W/W^* for one of the component of the CaT at 8662 Å as function of metallicity. Colours have the same meaning than in Fig. 3. Dashed line represents the W/W^* fit obtained by Starkenburg et al. (2010). **Right:** Population number densities of the levels of Ca II involved in the CaT as a function of the radial optical depth in the continuum at 5000 Å $\log \tau_{5000}$ for a metal-rich (in bold) and a metal-poor model.

W/W^* and theirs, at a given $T_{\rm eff}$, increase with decreasing metallicity and with decreasing surface gravity. At [Fe/H] $= -4$, the deviation is about 10% for $\log g = 2$ and about 18% for $\log g = 1$. These differences may come from the fact that they used a different geometry (plane-parallel) in their study. We checked that the use of the scaling factor $S_H = 1$ for the collisions with neutral hydrogen cannot compensate this difference.

4 What can be learn from all of this?

We have performed NLTE computations for the Mg I and Ca II model atoms. We provide computed W/W^* for a grid of 453 MARCS model atmospheres of late-type giants and supergiants[ii]. The inclusion of fine structure in the model atoms do not affect strongly NLTE results since the W/W^* of the components of a multiplet are very similar but permit a consistent representation of the physics. The departures from LTE for the Mg I 8736 Å line are not negligible and must be taken into account to correctly estimate the magnesium abundance. The CaT lines are mainly formed in LTE if [Fe/H] ≥ -2. The NLTE effects increase with a decrease of the metallicity and with an increase of the surface gravity. We show that the W/W^*(CaT) can increase by 20% for $\log g$ varying from 0.5 to 2.0. In the context of large surveys as Gaia, the W/W^* tables and the polynomial fits (given in Merle et al. 2011) can be extensively used to remove the NLTE effects of the measured equivalent widths in the classical LTE abundance analysis using equivalent width fitting method.

References

Andretta, V., Busà, I., Gomez, M. T., & Terranegra, L. 2005, A&A, 430, 669
Armandroff, T. E. & Da Costa, G. S. 1991, AJ, 101, 1329
Asplund, M. 2005, ARA&A, 43, 481
Barklem, P. S., Belyaev, A. K., Spielfiedel, A., Guitou, M., & Feautrier, N. 2012, A&A, 541, A80
Battaglia, G., Irwin, M., Tolstoy, E., et al. 2008, MNRAS, 383, 183
Brault, J. & Neckel, H. 1987, ftp://ftp.hs.uni-hamburg.de/pub/outgoing/FTS-Atlas
Carlsson, M. 1986, Uppsala Astronomical Observatory Reports, 33
Gustafsson, B., Edvardsson, B., Eriksson, K., et al. 2008, A&A, 486, 951
Jorgensen, U. G., Carlsson, M., & Johnson, H. R. 1992, A&A, 254, 258
Kupka, F. G., Ryabchikova, T. A., Piskunov, N. E., Stempels, H. C., & Weiss, W. W. 2000, Baltic Astronomy, 9, 590
Meléndez, M., Bautista, M. A., & Badnell, N. R. 2007, A&A, 469, 1203

[ii] available on VizieR at CDS (J/MNRAS/418/863/grid) or upon request to the authors.

Merle, T., Thévenin, F., Pichon, B., & Bigot, L. 2011, MNRAS, 418, 863
Miller, A. J. 1992, Appl. Statist., 41, 458
Shimanskaya, N. N., Mashonkina, L. I., & Sakhibullin, N. A. 2000, Astronomy Reports, 44, 530
Starkenburg, E., Hill, V., Tolstoy, E., et al. 2010, A&A, 513, A34

SF2A 2012
S. Boissier, P. de Laverny, N. Nardetto, R. Samadi, D. Valls-Gabaud and H. Wozniak (eds)

UVMAG: A UV+VISIBLE SPECTROPOLARIMETER TO STUDY STELLAR MAGNETOSPHERES

C. Neiner[1] and the UVMag consortium

Abstract. In the last decade magnetic fields have been detected in basically all types of stars. These discoveries gave rise to innovative studies on the mapping of magnetic fields and on their impact on stellar environment. To go even further, the UVMag international consortium proposes to combine UV and visible spectropolarimetry. The UV domain allows us to study stellar winds, while the optical domain allows us to study the stellar surface. With UV and visible spectropolarimetry we can then study magnetospheres as a whole and do this over a complete stellar rotation period thanks to a space mission. UV and visible spectropolarimetry can of course also address many other stellar physics issues.

Keywords: ultraviolet, spectropolarimetry, magnetospheres, stellar winds

1 The UVMag consortium

The UVMag consortium has been created in 2010 to discuss, design and promote space UV and visible spectropolarimetry. The goal is to propose a mission dedicated to stellar physics and in particular magnetospheres. The idea is based on the recent success of ground-based optical spectropolarimeters combined with the use of archival UV data. The consortium is led by France, with collaborations from Belgium, Brazil, Canada, Germany, Ireland, the Netherlands, Sweden, Switzerland and the USA.

2 Science drivers: stellar physics

We propose to study the formation, structure, evolution and environment of all types of stars in particular through the measurement of their magnetospheres, i.e. through the association of spectropolarimetry and spectroscopy in the UV and visible domains. The UV domain is crucial in stellar physics because it is particularly rich in atomic and molecular transitions, and covers the region in which the intrinsic spectral distribution of hot stars peaks. The UV lines are the least influenced by non-LTE effects in stellar photospheres and are thus most useful e.g. for quantitative abundance determinations. The lower levels of these lines are less likely to depopulate in low density environments such as chromospheres, circumstellar shells, stellar winds, nebulae and the interstellar medium, and so remain the only useful diagnostics in most of these environments. Another advantage of observing in the UV is the extreme sensitivity of the Planck function to the presence of small amounts of hot gas in dominantly cool environments. This allows the detection and monitoring of various phenomena that would otherwise be difficult to observe: accretion continua in young stars, magnetic activity, chromospheric heating, corona, starspots on cool stars, and intrinsically faint, but hot, companions of cool stars. The UV domain is also the one where Sun-like stars exhibit their hostility (or not) to Earth-like life, population 0 stars must have shone the brightest, accretion processes convert much kinetic energy into radiation which strongly impacts stellar formation and evolution, the "Fe curtain" features respond to changes in local irradiation, etc.

In addition, most of cool stars and a fraction of hot stars are magnetic and their magnetic field interacts with their wind and environment, modifies their structure and surface abundances, and contributes to the transport of angular momentum. With spectropolarimetry, one can address with unprecedented detail these important

[1] LESIA, UMR 8109 du CNRS, Observatoire de Paris, UPMC, Univ. Paris Diderot, 5 place Jules Janssen, 92195 Meudon Cedex, France

issues in stellar physics, from stellar magnetic fields to surface inhomogeneities, surface differential rotation to activity cycles and magnetic braking, from microscopic diffusion to turbulence, convection and circulation in stellar interiors, from abundances and pulsations in stellar atmospheres to stellar winds and accretion disks, from the early phases of stellar formation to the late stages of stellar evolution, from extended circumstellar environments to distant interstellar medium. Moreover, measuring polarization directly in the UV wind-sensitive lines has never been done, and would be extremely useful in order to trace the polarization along the field lines. Finally, polarimetry is not restricted to magnetic fields only. The scope of stellar polarimetry is much broader, in particular with respect to circumstellar processes.

The spectropolarimetric capability, both in the UV and visible wavelength domains, will therefore nicely complement the spectrograph to multiply tenfold the capabilities of extracting information on magnetospheres, winds, disks, and magnetic fields. The UV+visible spectropolarimeter will consequently provide a very powerful and unique tool to study most aspects of stellar physics in general and in particular for stellar formation, structure and evolution as well as for stellar environment.

The long-standing as well as new questions in stellar physics will be answered by studying various types of stars: O stars which exhibit very strong clumpy winds, Of?p stars which have very specific spectral characteristic probably related to their magnetic field, active B stars which associate various extreme physical processes, Be stars which are very rapidly rotating and undergo outbursts producing a circumstellar disk, γ Cas stars which emit unexplained variable X-ray flux, Ap/Bp stars which host very strong fossil magnetic fields, A stars that are very weakly magnetized, δ Scu and γ Dor stars which pulsate, roAp stars in which magnetic field and pulsations interact strongly, Herbig Ae/Be stars which are the precursor of main sequence Ap/Bp stars, intermediate-mass T Tauri stars which cover the transition from a fully convective star to a radiative star, classical T Tauri stars which are still accreting mass, weak-lined T Tauri stars which have stopped accreting but have not yet reach the main sequence, solar-type stars with dynamo magnetic fields, young and old Suns to be compared with our Sun, cool supergiants which offer the possibility to study small-scale dynamos, M dwarfs which exist on both side of the full-convection threshold, red giants, planetary nebulae and post-AGB stars which represent later stages of stellar evolution, stars in the Magellanic Clouds which are in a different environment in terms of metallicity, and binaries which probe additional ingredients in stellar evolution and undergo tidal effects.

In addition to stellar physics, several additional science topics could be investigated with no or little changes in the proposed project. This includes for example studies of the ISM, white dwarfs, or novae. Moreover, our project could be enhanced to also study other topics, e.g. exoplanetary magnetospheres. In this example, polarization signals of the order of 10^{-4} (for hot Jupiters) or less (down to 10^{-11} for Earth-like planets around solar-like stars) would be required, i.e. a very high signal-to-noise and very low instrumental polarization.

3 The space mission

3.1 Concept

To observe in the UV domain, as well as to reach faint stars and weak magnetic fields, it is necessary to collect the requested observations from space. In addition, we wish to obtain long continuous spectropolarimetric time series of a number of targets, which is hampered from the ground when the variability period is close to 1 day or a fraction/multiple of 1 day or when the weather does not cooperate over long periods of time (rotation periods can be up to several weeks). Finally, simultaneous spectropolarimetric observations in the UV and visible domains would provide information on the wind and polarization properties at the same time, providing new insights into certain phenomena such as magnetospheric confinement or chromospheric activity. We therefore propose to study a concept of a space spectropolarimeter working in the UV and visible domains. It could be installed either on a medium-size space mission dedicated to solving a number of stellar physics issues and available for long-term monitoring of stars, or on a Large UV and Visible space Observatory (LUVO) with which better statistics could be reached and the spectropolarimeter could benefit other science topics besides stellar physics. However, more instrumental flexibility and complexity might then be needed, e.g. a MOS/IFU mode or an imaging mode, and the instrument availability might not allow as many long time series as a dedicated mission would.

3.2 Scientific requirements for the instrument

The scientific requirements currently considered for the instrument are summarized in Table 1.

Table 1. Basic scientific specifications currently considered for the instrument. The minimal requirement is given, as well as the objective.

Specification	Requirement	Goal
Spectral range	117-320 + 390-870 nm	90-1000 nm
UV resolution	25000	100000 and 2000
Optical resolution	35000	80000
UV S/N	100	200
Optical S/N	100	300
Polarization	V in lines	QUV in lines + continuum
Instrumental polarization	3%	1%
Accuracy in radial velocity	1 km s^{-1}	0.3 km s^{-1}
Target magnitude	$V = 3 - 10$	$V = 2 - 15$
Targeted stars	50	100
Time per targeted star	4 weeks	6 weeks (4+1+1)
Survey stars	4000	8000
Time per survey star	20 min	30 min
Mission duration	4 years	12 years

Table 2. Number of available targets per spectral type, according to Simbad (CDS). An estimate of the number of magnetic stars is also given, according to the approximate statistical occurrence of magnetic fields in each type of targets. Numbers are also given for some examples of rare types of objects. The numbers are given for the minimal magnitude requirement and goal.

Spectral type	$V = 3 - 10$	$V = 2 - 15$	Magnetic rate	Magnetic $V = 3 - 10$	Magnetic $V = 2 - 15$
O	428	1823	6%	26	109
B	19940	42891	6%	1196	2573
A	53143	102442	20%	10629	20488
F	61867	105487	50%	30934	52744
G	55780	97365	50%	27890	48683
K	88358	121052	50%	44179	60526
M	10276	18367	50%	5138	9184
Be stars	1225	1705	1%	12	17
Herbig Ae/Be	44	60	10%	4	6
M dwarfs	94	693	50%	47	347

To measure the line and Stokes profiles, we should obtain spectropolarimetric data with a high resolution. In addition, to fulfill our goals we need to reach a high signal-to-noise ratio and therefore to observe bright stars. We also wish to reach fainter stars to be able to observe certain rare classes of stars (such as M dwarfs or Herbig Ae/Be stars) and to probe other environments, e.g. the Magellanic Clouds. Thus our dynamical range needs to be very large.

Moreover, we would like to point in any direction in the sky, to reach any interesting target. We wish to observe once several thousands of stars of all types forming a statistical survey. We also require to be able to remain stably pointed on a shorter list of stars (targeted objects) continuously for 2 rotation cycles. Such time series document phenomena on stars that can be impulsive (flares, infall), periodic (pulsations, rotational migration of spots, corotating clouds), quasi-periodic (evolution of blobs from hot winds), and gradual (evolution of spots). While some hot stars rotate very fast (of the order of 1 day), other targets have rotation periods of several weeks. In Table 2 we considered that on average the rotation period is 2 weeks. The mission duration derives from this mean rotation period and the number of targets, at least 4 years. A mission of 12 years would not only allow to study 2 times more targeted and survey objects but to probe stellar magnetic cycles (similar to the 22-year solar cycle).

Precise radial velocity is requested for example for Doppler Imaging of active binary systems or probing the

redshifts of high temperature emission lines in the subcoronal atmospheres of cool stars.

Polarization in Stokes V in spectral lines is the minimum requirement to be able to infer magnetic properties. However, polarization in QUV would allow full 3D mapping of the magnetospheres and linear polarization (QU) would also allow us to measure other physical processes such as depolarization from a circumstellar disk, probing scales well beyond what is feasible with interferometry. In addition, polarization of the continuum would be very useful to study dusty environments, providing important information about e.g. star forming regions or protostars.

4 Ongoing activities

Previous UV instruments (e.g. IUE, STIS or FUSE), combined to ground-based optical spectropolarimetry, have provided valuable data for the first studies of stellar magnetospheres. HIRDES on the future WSO would also provide the instrumental capabilities needed to address the scientific rationale exposed here. However, these instruments are either unavailable anymore or available for too short periods of time to perform a time series over a full stellar rotation cycle. This is why we need a new UV spectrograph.

In addition, ground-based optical spectropolarimeters provide important datasets for all types of bright stars. However, there are no space high-resolution stellar spectropolarimeters, to reach fainter targets and to obtain continuous timeseries. Moreover, UV spectropolarimetry cannot be achieved from the ground. There are already several ongoing projects in this field in the optical (e.g. for SST, Solar Orbiter or SPEX), but not in the UV. Therefore, in the frame of UVMag, a Research & Technology (R&T) study funded by the French space agency CNES has just started at the IRAP and LESIA laboratories, to design a space-based high-resolution UV and visible spectropolarimeter.

5 Conclusions

The UVMag consortium has set the basic requirements for a space mission to study the magnetospheres and winds of all types of stars. Simultaneous UV and visible spectropolarimetry over long periods of time is indeed the only way to comprehend the full interaction between the stellar magnetic field and stellar wind. This is the next step to progress on the characterization and modeling of the formation, structure, evolution and environments of stars.

The UVMag project is described in the more detailed documents available on the UVMag website[i].

We thank CNES for their financial and technical support for the UVMag R&T study.

[i] http://lesia.obspm.fr/UVMag

SF2A 2012
S. Boissier, P. de Laverny, N. Nardetto, R. Samadi, D. Valls-Gabaud and H. Wozniak (eds)

TURBULENT MIXING IN STELLAR RADIATIVE ZONES

V. Prat [1, 2] and F. Lignières [1, 2]

Abstract. Macroscopic and turbulent motions created by rotation can significantly affect internal structure and evolution of stars in a way that is currently not well understood. In particular, turbulent mixing coefficients that are currently taken into account in many stellar evolution codes have been derived on phenomenological arguments and have not been tested through numerical simulations or laboratory experiments.

Our purpose is to test the vertical turbulent diffusion coefficient generated by radial differential rotation of Zahn (1992) with 3D local direct numerical simulations of stably-stratified homogeneous stationary sheared turbulence. To reach the high thermal diffusivity regime found in stellar radiative zones, we use an asymptotic development of the Boussinesq equations in the domain of the small Péclet numbers.

We present the results of simulations performed at different turbulent Péclet numbers (including one within the small-Péclet-number approximation). These results show that the form of the vertical turbulent diffusion coefficient initially proposed by Zahn is valid for Péclet numbers smaller than one. We also give a first quantitative estimate of this coefficient through numerical simulations.

Keywords: diffusion, hydrodynamics, rotation, stellar interiors, stars

1 Introduction

Macroscopic motions induced by rotation like meridional circulation or differential rotation actively contribute to chemical mixing by forcing turbulent motions. Such a mixing has an influence on the internal structure and the evolution of a star, notably by providing fresh combustible to the core, which increases the lifetime of the star. For more information about the effects of rotation on stellar evolution, see the recent review by Maeder & Meynet (2012).

Turbulent motions involved in rotating stars are full 3D motions and thus cannot be resolved by 1D or 2D star models. To make stellar evolution models more realistic, it is therefore crucial to reliably model these motions so that they can be integrated in such evolution models. Many stellar evolution codes currently use prescriptions for turbulent mixing based on Zahn (1992) which introduces various turbulent diffusion coefficients.

Among them is the vertical turbulent diffusion coefficient D_v defined by:

$$D_\mathrm{v} = \frac{1}{3}\kappa Ri_\mathrm{cr}\left(\frac{r\sin\theta}{N_\mathrm{T}}\frac{\mathrm{d}\Omega}{\mathrm{d}r}\right)^2 , \tag{1.1}$$

which can be put in the form:

$$D_\mathrm{v} = \frac{1}{3}\kappa\frac{Ri_\mathrm{cr}}{Ri} , \tag{1.2}$$

where κ is the thermal diffusivity of the fluid, Ri the Richardson number which compares the effects of stratification (through the Brunt-Väisälä frequency N_T) and vertical shear ($r\sin\theta\mathrm{d}\Omega/\mathrm{d}r$ in spherical geometry with a rotation profile $\Omega(r)$). Ri_cr is the critical Richardson number for which the flow is marginally stable. The purpose of this work is to test the form of this coefficient in the domain of high thermal diffusivities present in stellar radiative zones and possibly propose a model of turbulent mixing to be included in stellar evolution codes. To achieve this, we performed 3D local direct numerical simulations (DNS) of a stably-stratified sheared flow.

[1] CNRS, IRAP, 14, avenue Édouard Belin, F-31400 Toulouse, France
[2] Université de Toulouse, UPS-OMP, IRAP, Toulouse, France

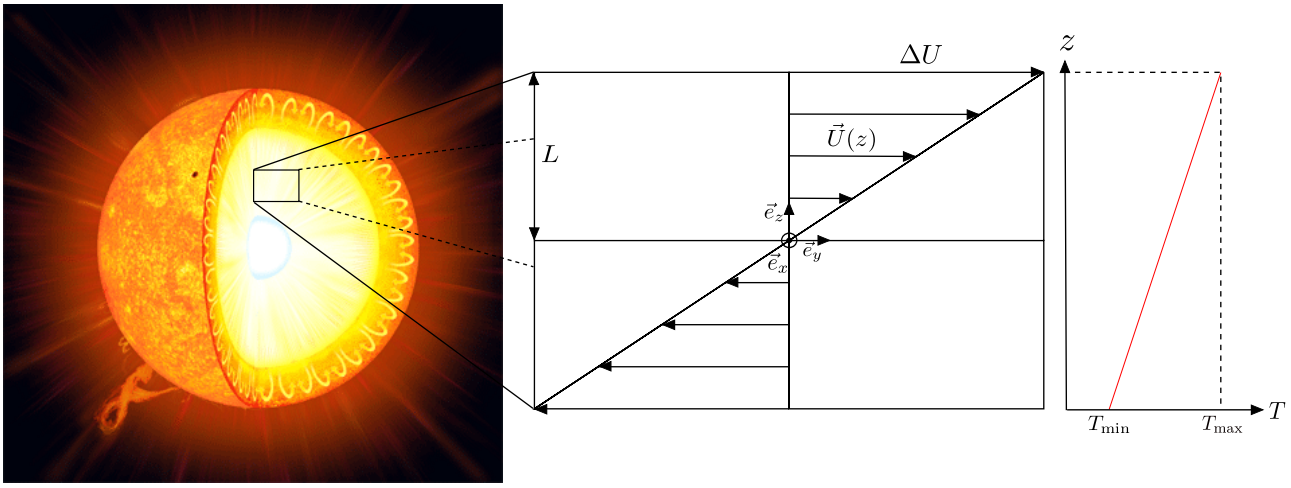

Fig. 1. Sketch of the flow

2 Theoretical framework

Figure 1 shows our cartesian numerical domain in which the local effect of differential rotation is represented by a uniform forced mean vertical shear and a stable uniform forced mean temperature gradient mimics the stable entropy stratification typical of radiative zones. Indeed, temperature and entropy are equivalent in the Boussinesq formalism. The non-dimensional governing equations read:

$$\vec{\nabla}\cdot\vec{v} = 0 \tag{2.1}$$

$$\frac{\partial\vec{v}}{\partial t}+\vec{v}\cdot\vec{\nabla}\vec{v} = -\vec{\nabla}p+Ri\theta\vec{e}_z+\frac{1}{Re}\Delta\vec{v}+\vec{f}_{\rm v} \tag{2.2}$$

$$\frac{\partial\theta}{\partial t}+\vec{v}\cdot\vec{\nabla}\theta+v_z = \frac{1}{Pe}\Delta\theta+f_{\rm T} \tag{2.3}$$

where we use L, ΔU and $\Delta T=(T_{\max}-T_{\min})/2$ as respectively length, velocity and temperature scales (see Fig. 1). Velocity of the flow is noted $\vec{v}$, pressure deviation from equilibrium p and temperature deviation from the mean profile θ. Forcing terms $f_{\rm v}$ and $f_{\rm T}$ are used to impose the mean velocity and temperature profiles.

Three non-dimensional parameters appear in these equations including the already presented Richardson number and two others: the Reynolds number $Re=UL/\nu$ and the Péclet number $Pe=UL/\kappa$ where ν is the viscosity of the fluid.

The high thermal diffusivity present in stellar radiative zones creates a huge gap between the dynamical time $\tau_{\rm dyn}=L/\Delta U$ and the diffusive one $\tau_{\rm diff}=L^2/\kappa$. It is therefore impossible to perform simulations in such conditions without some sort of approximation. Nevertheless, an asymptotic version of the Boussinesq equations can be derived using a Taylor-expansion of all variables at first order in Pe (Lignières 1999). Equations (2.2) and (2.3) then become:

$$\frac{\partial\vec{v}}{\partial t}+\vec{v}\cdot\vec{\nabla}\vec{v} = -\vec{\nabla}p+RiPe\psi\vec{e}_z+\frac{1}{Re}\Delta\vec{v}+\vec{f}_{\rm v} \tag{2.4}$$

$$v_z = \Delta\psi \tag{2.5}$$

with $\psi=\theta/Pe$. This is called the small-Péclet-number (SPN) approximation. There are two non-dimensional parameters left in the new equations: the Reynolds number and the product of the Richardson and Péclet numbers. It means that stratification and thermal diffusion are merged into a single physical effect.

3 Simulations of turbulent transport

In order to obtain an homogeneous and stationary turbulence, as implicitely assumed in the derivation of Eq. (1.1), it is necessary to determine the value of the critical Richardson number for each considered value of the Péclet number. Then, we use two approaches to study the turbulent transport: one Lagrangian and the other Eulerian.

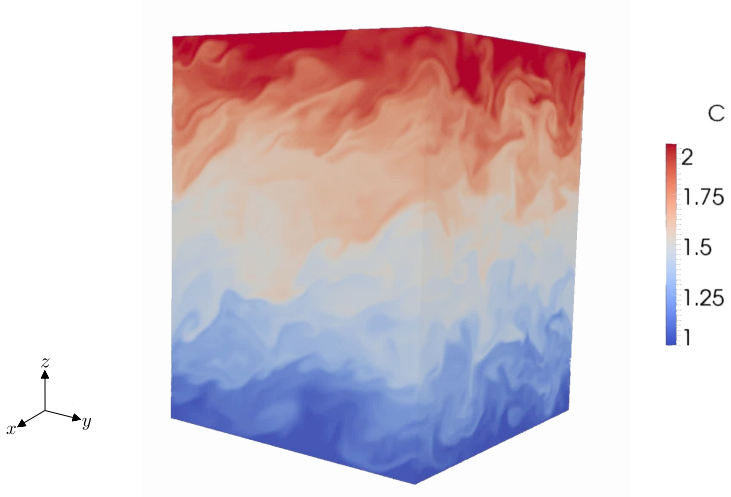

Fig. 2. Snapshot of the concentration field

3.1 Lagrangian approach

The principle of this approach is to put particles uniformly in the fluid at a given time and to follow their trajectories under the effect of the velocity field. The Eulerian homogeneity and the stationarity of our turbulence ensures its Lagrangian homogeneity, which means that the particles see the same turbulent properties during the whole simulation. In this case, Taylor (1921) shows that for times much greater than the turbulent correlation time, the transport is diffusive, the vertical mean square displacement of particles is then linear in time:

$$\left\langle [z(t) - z(0)]^2 \right\rangle = 2D_{\rm t}t \tag{3.1}$$

and the theory also gives an explicit expression for the diffusion coefficient:

$$D_{\rm t} = \int_0^{+\infty} \langle v_z(t) v_z(t+\tau) \rangle {\rm d}\tau = \langle {v_z}^2 \rangle T_{\rm L} \tag{3.2}$$

3.2 Eulerian approach

This method consists in solving an advection/diffusion equation for a passive scalar field (a concentration c) which presents a uniform mean vertical gradient Γ:

$$\frac{\partial c}{\partial t} + \vec{v} \cdot \vec{\nabla} c = D_{\rm m} \Delta c + f_{\rm c} \tag{3.3}$$

where $D_{\rm m}$ is the molecular diffusivity and $f_{\rm c}$ a forcing term. The vertical turbulent diffusion coefficient $D_{\rm t}$ is then determined *via* the relation:

$$D_{\rm t} = -\frac{\langle c v_z \rangle}{\Gamma} \tag{3.4}$$

An example of simulation with such a concentration field is shown in Fig. 2.

3.3 Comparison of the methods

The values of $D_{\rm t}$ obtained using the different methods are found to be similar, but show a significant dispersion ($\pm 20\%$). This dispersion appears to be due to temporal fluctuations of the physical properties of the flow. It is therefore natural to want to study the turbulent transport for a longer time in order to reduce these fluctuations. Whereas in the Lagrangian approach the integration time is limited by the presence of the lower and upper boundaries of the fluid, it can be arbitrarily fixed in the Eulerian approach, which makes it more appropriate.

Table 1. Results of the different runs ($S = \Delta U/L = \mathrm{d}U/\mathrm{d}z$)

Pe_ℓ	Re_ℓ	Ri_{cr}	$(RiPe_\ell)_{\mathrm{cr}}$	ST_{L}	$\langle {v_z}^2 \rangle / \Delta U^2$	$D_{\mathrm{t}}/(SL^2)$	$\beta = D_{\mathrm{t}}/(u\ell)$
52	260	0.124	6.45	0.771	0.00350	0.00270	0.104
0.34	340	1.27	0.432	0.825	0.00573	0.00473	0.138
$\ll 1$	335	–	0.426	0.816	0.00543	0.00443	0.131

4 Results

We performed simulations at three different turbulent Péclet numbers $Pe_\ell = u\ell/\kappa$ (based on turbulent velocity and length scales u and ℓ): 52, 0.34 and $\ll 1$ (using the SPN approximation). Table 1 shows the values of various physical parameters, including the turbulent diffusion coefficient.

Focusing on the two latter simulations, one can see that the two values of the product of the Richardson and Péclet numbers are very close to each other with a relative difference of 1.4%. This proves that for Péclet numbers smaller than 0.34, the stationary regime of turbulence is characterized by the critical turbulent "Richardson-Péclet" number $(RiPe_\ell)_{\mathrm{cr}}$ which is independent of the Péclet number.

Besides, since the two latter values of the β number are also very similar (relative difference of 5.3%), we can write the vertical turbulent diffusion coefficient in the form:

$$D_{\mathrm{t}} = \beta \kappa Ri^{-1} (RiPe_\ell)_{\mathrm{cr}} \tag{4.1}$$

with a constant β in the $Pe_\ell \leq 0.34$ domain.

Comparing Zahn's prescription (1.1) with our newly derived expression (4.1), the most obvious is that we recover the fact that D_{t} is proportional to κRi^{-1}. Moreover, our simulations provide a first quantitative determination of the proportionality coefficient $\beta(RiPe_\ell)_{\mathrm{cr}} = 0.0558$ which is not far from the order of magnitude estimate proposed by Zahn (1992) $Ri_{\mathrm{cr}}/3 \simeq 0.0833$.

5 Conclusions

We have validated Zahn's prescription for the vertical turbulent diffusion coefficient in the small-Péclet-number regime, including its dependence on thermal diffusivity, but all considered simulations have been performed with a fixed Reynolds number. The dependence of β and $(RiPe_\ell)_{\mathrm{cr}}$ on viscosity is still unexplored.

A future improvement could be to take into account the feedback of the concentration on the flow through molecular weight stratification in order to constrain more complex models (see for example Maeder & Meynet 1996; Talon & Zahn 1997).

Other linked problems would be interesting, like comparing the vertical diffusion coefficient due to a vertical shear (our D_{t}, called D_{v} in Zahn 1992) to the horizontal diffusion coefficient D_{h} due to an horizontal shear or varying the angle between shear and stratification. A more complete determination of the dependence of D_{t} on thermal diffusivity is also in progress, with a particular focus on the parameter domain between $Pe_\ell = 52$ and the asymptotic regime.

We acknowledge the CALMIP program of the Université de Toulouse for its numerical support.

References

Lignières, F. 1999, A&A, 348, 933

Maeder, A. & Meynet, G. 1996, A&A, 313, 140

Maeder, A. & Meynet, G. 2012, Rev. Mod. Phys., 84, 25

Talon, S. & Zahn, J.-P. 1997, A&A, 317, 749

Taylor, G. I. 1921, in Proc. London Math. Soc., 196–212

Zahn, J.-P. 1992, A&A, 265, 115

SF2A 2012
S. Boissier, P. de Laverny, N. Nardetto, R. Samadi, D. Valls-Gabaud and H. Wozniak (eds)

STELLAR PARAMETERS OF M DWARFS FROM LOW AND HIGH-RESOLUTION SPECTRA TOGETHER WITH NEW MODEL ATMOSPHERES

A. S. Rajpurohit[1], C. Reylé[1], M. Schultheis[1], F. Allard[2], R. Scholz[3] and D. Homeier[2]

Abstract. We present an optical spectral atlas of stars covering the whole M-dwarf sequence. It consists of 95 M dwarfs at solar metallicity observed at low-resolution with EMMI@NTT and 21 M-subdwarfs, extreme-subdwarfs and ultra-subdwarfs observed at high resolution with UVES@VLT. Using the most recent PHOENIX BT-Settl stellar model atmospheres we perform a detailed comparison with our observed spectra using χ^2 minimization technique. We confront the models with low-resolution spectra of M dwarfs at solar metallicity and we assign effective temperatures to the M dwarfs. We present temperature versus spectral type and colour relations and their comparison with others found in the literature. We also present our high-resolution spectra of the subdwarfs (sdM, esdM, usdM) and compare them to the newest grid of the BT Settl models which uses the revised solar abundances of Caffau et al (2011). This comparison allows us to study the spectral details of cool atmospheres, to determine precise [Fe/H] values for our objects, and to investigate the effect of metallicity on cool dwarf atmospheres. This study also helps to validate the atmosphere models and improve them by determining new constants on molecular opacities, dust cloud formation etc.

Keywords: stars: atmospheres, stars: fundamental parameters, stars: low-mass-brown dwarfs

1 Introduction

Low-mass stars ($0.08M_\odot$ to $0.6M_\odot$ depending on the metallicity) ,in particular M dwarfs, are the dominant stellar component of the Milky Way. They constitute 70% of all stars (Bochanski et al. 2010; Gould et al. 1996; Henry 1998) and nearly half (40%) of the total stellar mass of the galaxy. Our understanding of the Galaxy therefore relies upon the description of this faint component. Whereas subdwarfs (sdM, esdM, usdM) are among the faintest and coolest stellar objects. The locus of subdwarfs in the H-R diagram deviates from most of the field stars due to the metallicity difference that, that translates in different opacities compared to those of regular dwarfs. subdwarfs are sometimes called low metallicity halo stars or galactic thick disk stars based on their spectroscopic features, kinematics and ages. M dwarfs and subdwarfs have been employed in several Galactic studies as they carry the fundamental information regarding the stellar physics, Galactic structure, formation and dynamics. Thus the determination of accurate fundamental parameters for M dwarfs and subdwarfs has relevant implications for both stellar and Galactic astronomy. Because of their intrinsics faintness and a homogeneous sample with respect to age and metallicity has not yet been built. The energy distribution in M dwarfs and subdwarfs is governed by the presence of various molecular absorption bands such as TiO, VO and metal hydrides in the visual ($\geq$ 4000) to near-infrared ($\leq 1.3\mu$m). However because of the decreasing metallicity for subdwarfs, the TiO bands are less strong, and the pseudo-continuum brighter as a result. But this increases the contrast to the other opacities such as hydride bands and atomic lines which feel the higher pressures of the deeper layers where they emerge from. We see therefore these molecular bands with more details than for M dwarfs and under more extreme gas pressure conditions. This often reveals the inaccuracy or incompleteness of the opacities used in the model. Thus the presence of these molecular bands reduces the strength of atomic lines and the spectral contrast. This makes the complexity of stellar atmosphere

[1] Observatoire de Sciences de l'Univers THETA de Franche-Comté, Université de Franche-Comté, Institut Utinam, UMR CNRS 6213, BP 1615, 25010 Besançon Cedex, France

[2] CRAL (UMR 5574 CNRS), École Normale Supérieure, 69364 Lyon Cedex 07, France

[3] Leibniz-Institut für Astrophysik Potsdam (AIP)

of subdwarfs increasing significantly with decreasing effective temperature. The effective temperature (T_{eff} < 4000 K) and pressures in M dwarfs atmospheres allow for the widespread formation of the molecules. In dwarfs of spectral type later than M6 the outermost temperature falls below the condensation temperature of silicates which give rise to the formation of dust clouds (Tsuji et al. 1996b,a; Allard et al. 1997; Ruiz 1997; Allard et al. 1998). These processes complicate the understanding of these cool atmospheres. This means that the model atmosphere for low-mass stars has to take into account the formation of dust clouds and a variety of sometimes little studied molecules with large opacities, each affecting the abundance of the parent atomic population.

2 Model Atmosphere

In this study, we have used the recent new BT-Settl models (Allard et al. 2012) for our analysis of both low and high-resolution spectra. Theses model atmospheres are computed with the PHOENIX code using hydrostatic equilibrium, convection using the Mixing Length Theory and a mixing length of 1/Hp=2.0 according to results of radiation hydrodynamics (Ludwig et al. 2006), spherically symmetric radiative transfer, departure from LTE for all elements up to iron, the latest solar abundances by Asplund et al. (2009) and Caffau et al. (2011) equilibrium chemistry, an important database of the latest opacities and thermochemical data for atomic and molecular transitions, and monochromatic dust condensates refractory indexes. Grains are assumed spherical and non-porous, and their Rayleigh and Mie reflective and absorptive properties are considered. The diffusive properties of grains are treated based on 2-D radiation hydrodynamic simulations, including forsterite cloud formation to account for the feedback effects of cloud formation on the mixing properties of these atmospheres (Freytag et al. 2010). For this paper, we use the model grid described as follows: T_{eff} from 2000 K to 4000 K with 100 K step, log g = 5.0 dex, 5.5 dex, M/H = -2.0 dex to +0.5 dex with 0.5 dex step[i].

3 Comparison between atmosphere models with M-dwarf spectra

3.1 With low resolution EMMI@NTT

We compared 95 M dwarfs (from M0 to M9) low resolution spectra with optical spectroscopic classification (Reylé et al. 2006) with the most recent PHOENIX stellar atmosphere model BT-Settl (Allard et al. 2012). Both theory and observation indicate the dwarfs having log g = 5.0±0.2 (Gizis 1996) and we therefore restrict our analysis to log g = 5.0-5.5 models. We have determined the T_{eff} by assuming solar metallicity for our low resolution sample. We confirmed the solar metallicity for all our objects by comparing them with isochrones at different metallicity (see Fig. 1) generated from BT-Settl model atmosphere. The fits of BT-Settl models to the low resolution spectra is shown in Fig. 2. The best fit spectra reproduce very well the TiO band which is very sensitive to temperature cooler than 4000 K as well as most of the spectral features, and also the overall shape of the optical to near IR spectra across the M dwarfs regime. The purpose of this fit was to determine the effective temperature by fitting the overall shape of the optical spectra which is dominated by molecular absorption. No attempt has been made to fit the individual atomic lines such as K I resonance doublet or Na I doublet for the low resolution spectra. Some discrepancies remain in the strength of some absorption bands such as the TiO absorption around 6500 Å,7000 Å, CaH absorption around 6400 Å. The cause could be inaccurate atomic parameters and or missing molecular opacities.

3.2 With high resolution UVES@VLT spectra

We compared 21 high-resolution spectra of subdwarfs (sdM,esdM,usdM) with the most recent PHOENIX stellar atmosphere model BT-Settl. The TiO bands at 7053 Å, 7589 Å, 7666 Å, 8432 Å, and 8859 Åand VO bands at 7334 Å,7851 Åand 8521 Åare very well recovered by the models and get weaker towards cooler temperature due to condensation into dust species like perovskite ($CaTiO_3$), solid titanium oxide and vanadium oxides. The strongest atomic absorption lines in the spectra of usdM are the massively pressure broadened alkali lines, i.e. elements with only one electron in their outer shell, which can get excited even at very low temperatures. All alkali elements Ca I, Fe I, Ti I, K I, Na I have strong lines in the observed wavelength region. KI and Na I lines in early and mid M subdwarfs is well matched by the model but they become stronger and wide towards

[i]http://phoenix.ens-lyon.fr/simulator/index.faces

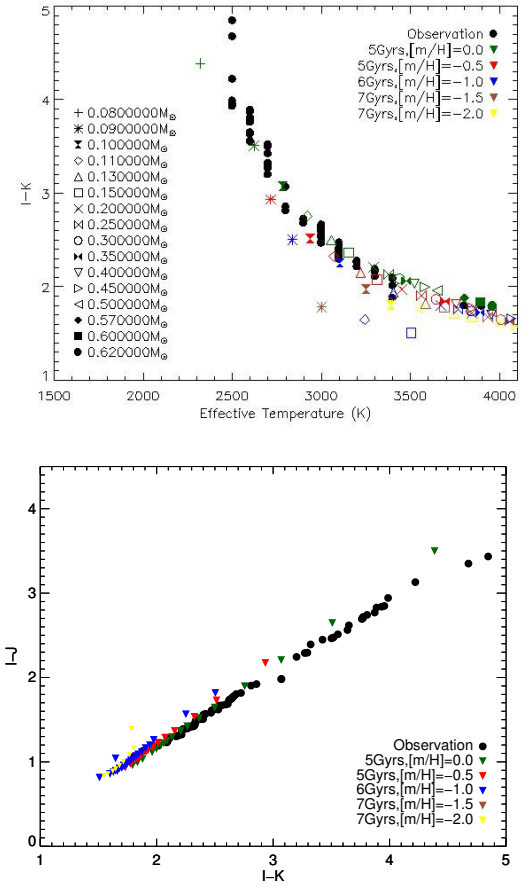

Fig. 1. Estimated T_{eff} and I-K color (**top panel**) and color-color plot (**bottom panel**) for observed M dwarfs (red) compared to the BT- Settl isochrones for 5,6 and 7 Gyrs (Baraffe et al. 1998) using BT-Settl model atmosphere.

lower temperature. The detailed analysis of these high-resolution spectra with the synthetic spectra will allow us to determine the metallicity of these subdwarfs and also helps to determine the strengths of molecular bands and atomic lines as well as damping constant of various features seen in these spectra. Figures 3 shows such comparison with the model atmosphere. The uncertainty from the fitting procedure are the grid spacing of 0.5 in [m/H] and 100 K in T_{eff}. Compared to Gizis (1996) our fits give somewhat 100K higher temperatures. The subdwarfs and extreme subdwarf have the best fit at [m/H]=-1.0 to [m/H]=-2.0.

4 Effective temperature scale of M dwarfs

As photospheric temperatures decrease, atoms combine to form molecules; upon still further cooling, atoms and molecules may coagulate to form dust grains. Dust formation can change the atmospheric spectral characteristics in various ways. For example, grains can warm the photosphere by backwarming, making the spectral distribution redder while weakening molecular lines (example H_2O and TiO) (Tsuji et al. 1996a). Dust formation decreases the photo-spheric gas phase abundance of the atoms that form dust (example Ti, Ca, Al, Mg, Si, Fe). Furthermore, with decreasing temperature, dust grains can become larger and gravitationally settle below the photosphere (Allard et al. 1998). Thus, in any attempt to assign effective temperatures to cool photospheres, we must make use of models that take dust formation and its behavior into account. The extreme temperature sensitivity of these metal oxide bands can be utilized for spectral classification and they are the primary temperature indicator of the cool stars.

The effective temperature is an important parameter to understand the cool atmosphere of low mass stellar and substellar objects. Many efforts have been made to derive a well secure effective temperature scale of M dwarfs but the scale is still uncertain because of the difficulty to accurately model the complex M dwarf spectra. The construction of T_{eff} sequences has been attempted in recent years by comparing the spectra of these objects

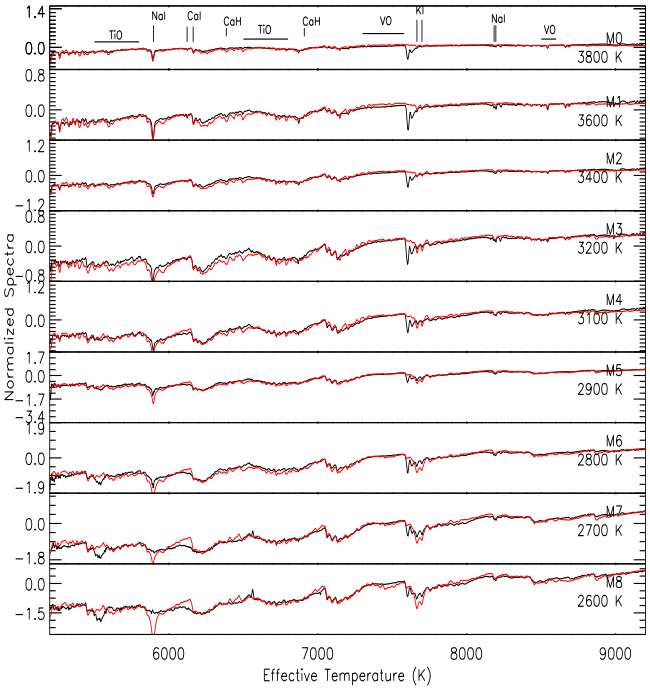

Fig. 2. Comparison of Observed spectral sequence of M dwarfs (black) with the best fit BT-Settl model (red). The main atomic and molecular features are indicated in the upper panel. The strong line at 7600 Åis telluric

to synthetic ones generated by atmospheric models (Reylé et al. 2011; Rajpurohit et al. 2011). In practice, the temperature derived from fitting to model spectra (Kirkpatrick et al. 1993) are systematically $\sim$ 300 K warmer than those estimated by empirical methods which is often wrong because they are based on using extrapolation of the Rayleigh jeans tails using historically the blackbody curve. Rajpurohit et al. (2011) and Reylé et al. (2011) used observed optical low resolution spectra to compare with the recent BT-Settl models which includes cloud physics and dust in it. Leggett et al. (1996) used observed infrared low resolution spectra and photometry to compare with NextGen models. They found radii and effective temperatures which are consistent with the estimates based on photometric data. Their study shows that these updated models should provide, for the first time, a realistic temperature scale of M dwarfs and subdwarfs. They found that the new model provides reasonable representations of the overall spectral features, with realistic strength variations induced by changes in stellar parameters. The adopted SpT (black) (figure 4) is the average from TiO_5, CaH_2 and CaH_3 spectral indices. The relation is compared to others found in the literature

5 Conclusions

We have presented the effective temperature scale for the stars in our sample by comparing the observed spectra with synthetic spectra obtained with the most recent PHOENIX BT-Settl stellar model atmospheres (Allard et al. 2012). Our proposed effective temperature scale extended down to 2500 K where the dust and cloud in their atmosphere start forming. We found that the slope of the optical to near IR spectra is well reproduced by the models for both high and low resolution spectra, while some discrepancies remain in the strength of some absorption bands and atomic lines. The quality of the fit deteriorates as one goes from the early M to the late M. Our comparison to the observed spectra with most recent model atmosphere showed that the general features are understood and that probably most of the species and their spectral effects are taken into account. There are still improvements to be made in the models. There are important opacity sources for which laboratory data are needed such as oscillator strengths for hydrides for example. In extreme cool M dwarfs (esdM) and ultra-cool M dwarfs (usdM), it is necessary to achieve a very good fit to all the absorbers in order to determine atmospheric properties and to understand the effect of the chemical composition on their cool atmosphere.

We acknowledge financial support from Programme National de Physique Stellaire (PNPS) of CNRS/INSU, France.

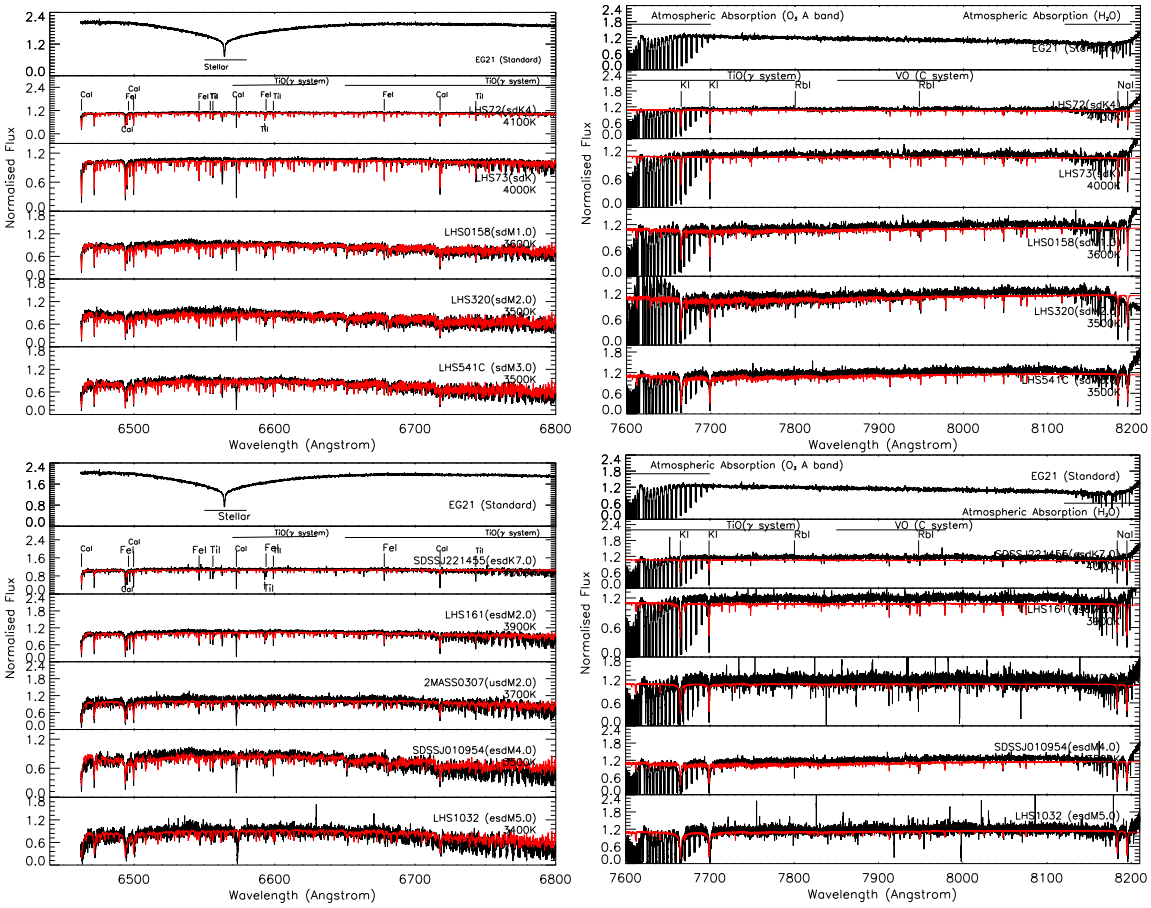

Fig. 3. Comparison of observed spectral sequence of sdM (**top**) and esdM (**bottom**) in black with the best fit BT-Settl model in red. The **left** and **right** panels show the different wavelength regime of UVES spectra.

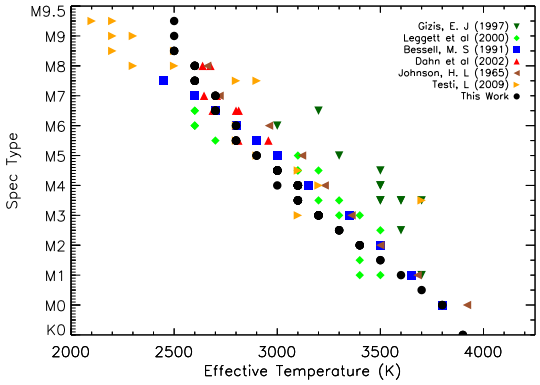

Fig. 4. Our adopted spectral type - T_{eff} relation (black) compared to relations from Leggett et al. (2001); Bessell (1991); Dahn et al. (2002).

References

Allard, F., Alexander, D. R., & Hauschildt, P. H. 1998, in Astronomical Society of the Pacific Conference Series, Vol. 154, Cool Stars, Stellar Systems, and the Sun, ed. R. A. Donahue & J. A. Bookbinder, 63

Allard, F., Hauschildt, P. H., Alexander, D. R., & Starrfield, S. 1997, ARA&A, 35, 137

Allard, F., Homeier, D., & Freytag, B. 2012, Royal Society of London Philosophical Transactions Series A, 370, 2765

Asplund, M., Grevesse, N., Sauval, A. J., & Scott, P. 2009, ARA&A, 47, 481

Baraffe, I., Chabrier, G., Allard, F., & Hauschildt, P. H. 1998, A&A, 337, 403

Bessell, M. S. 1991, AJ, 101, 662

Bochanski, J. J., Hawley, S. L., Covey, K. R., et al. 2010, AJ, 139, 2679

Caffau, E., Ludwig, H.-G., Steffen, M., Freytag, B., & Bonifacio, P. 2011, Sol. Phys., 268, 255

Dahn, C. C., Harris, H. C., Vrba, F. J., et al. 2002, AJ, 124, 1170

Freytag, B., Allard, F., Ludwig, H.-G., Homeier, D., & Steffen, M. 2010, A&A, 513, A19

Gizis, J. E. 1996, in Astronomical Society of the Pacific Conference Series, Vol. 109, Cool Stars, Stellar Systems, and the Sun, ed. R. Pallavicini & A. K. Dupree, 683

Gould, A., Bahcall, J. N., & Flynn, C. 1996, ApJ, 465, 759

Henry, T. J. 1998, in Astronomical Society of the Pacific Conference Series, Vol. 134, Brown Dwarfs and Extrasolar Planets, ed. R. Rebolo, E. L. Martin, & M. R. Zapatero Osorio, 28

Kirkpatrick, J. D., Kelly, D. M., Rieke, G. H., et al. 1993, ApJ, 402, 643

Leggett, S. K., Allard, F., Berriman, G., Dahn, C. C., & Hauschildt, P. H. 1996, ApJS, 104, 117

Leggett, S. K., Allard, F., Geballe, T. R., Hauschildt, P. H., & Schweitzer, A. 2001, ApJ, 548, 908

Ludwig, H.-G., Allard, F., & Hauschildt, P. H. 2006, A&A, 459, 599

Rajpurohit, A. S., Reylé, C., Schultheis, M., Leinert, C., & Allard, F. 2011, in SF2A-2011: Proceedings of the Annual meeting of the French Society of Astronomy and Astrophysics, ed. G. Alecian, K. Belkacem, R. Samadi, & D. Valls-Gabaud, 339–343

Reylé, C., Rajpurohit, A. S., Schultheis, M., & Allard, F. 2011, in Astronomical Society of the Pacific Conference Series, Vol. 448, 16th Cambridge Workshop on Cool Stars, Stellar Systems, and the Sun, ed. C. Johns-Krull, M. K. Browning, & A. A. West, 929

Reylé, C., Scholz, R.-D., Schultheis, M., Robin, A. C., & Irwin, M. 2006, MNRAS, 373, 705

Ruiz, J. 1997, Earth Moon and Planets, 77, 99

Tsuji, T., Ohnaka, K., & Aoki, W. 1996a, A&A, 305, L1

Tsuji, T., Ohnaka, K., Aoki, W., & Nakajima, T. 1996b, A&A, 308, L29

SF2A 2012
S. Boissier, P. de Laverny, N. Nardetto, R. Samadi, D. Valls-Gabaud and H. Wozniak (eds)

ROTATIONAL VELOCITY DISTRIBUTION OF A STARS: SEARCHING FOR INTRINSIC SLOWLY ROTATING NORMAL A0-A1 STARS

F. Royer[1], M. Gebran[2], R. Monier[3,4], Y. Caraty[1], T. Kılıçoğlu[5], O. Pintado[6], S. Adelman[7], B. Smalley[8], A. Reiners[9], G. Hill[10] and A. Gulliver[11]

Abstract. Royer et al. (2007) showed that the distribution of rotational velocities for A0-A1 stars is bimodal although all known peculiar and/or binary stars had been excluded from their sample. We present here the preliminary results of the abundance analysis for 47 A0-A1 "normal" main sequence stars selected with $v \sin i$ slower than 65 km s^{-1}. These high signal-to-noise spectra collected with ÉLODIE and SOPHIE (OHP) will allow us to obtain a clean sample of low $v \sin i$ normal A0-A1 stars and search for intrinsic slow rotators.

Keywords: Stars: early-type, Stars: rotation

1 Introduction

Normal A-type stars are fast rotators on average, and the distributions of their equatorial velocities display a mode between 150 and 220 km s^{-1} (Abt & Morrell 1995; Royer et al. 2007). The bimodality of the equatorial velocity distribution observed for A0-A1-type stars is argued to be due to binaries and chemically peculiar stars (Abt & Morrell 1995). Nonetheless Royer et al. (2007) showed a pronounced double peaked distribution of rotational velocities for A0-A1 stars, although all known peculiar and/or binary stars had been excluded from their sample. Abt (2009) suggested that slowly rotating normal stars could be Ap stars that already underwent a magnetic braking but do not show chemical peculiarity yet.

We present here the preliminary results of an observation programme aimed at understanding these A0-A1 slow rotators. High signal-to-noise spectra were collected with ÉLODIE and SOPHIE (OHP) for 47 A0-A1 "normal" main sequence stars selected from Royer et al.'s sample with $v \sin i < 65$ km s^{-1}. Binary stars and chemically peculiar stars (hereafter CP) are discarded on the basis of spectral synthesis. Signatures of gravity darkening are searched for to disentangle v and i from the projected rotational velocities, and sort out pole-on stars, like Vega (Gulliver et al. 1994), from intrinsic slowly rotating stars.

2 Data

The sample is selected from Royer et al. (2007), using A0-A1 main-sequence stars, not already known as binary or CP stars, with a low $v \sin i < 65$ km s^{-1}. The sample is limited to targets observable from Observatoire de Haute-Provence ($\delta > -15$ °). Six nights were allocated on ÉLODIE (2005, 2006) and four nights on SOPHIE (2009, 2011, 2012). Additional spectra were fetched from the ÉLODIE archive (Moultaka et al. 2004) and the SOPHIE archive.

[1] GEPI – Observatoire de Paris
[2] Notre Dame University-Louaize, Lebanon
[3] Lagrange – Université de Nice
[4] LESIA – Observatoire de Paris
[5] Ankara University, Turkey
[6] INSUGEO, CONICET, Argentina
[7] The Citadel, SC, USA
[8] Keele University, UK
[9] Universität Göttingen, Germany
[10] University of Auckland, New Zealand
[11] Brandon University, Canada

3 Classification: selecting normal stars

3.1 Spectroscopic binaries

Radial velocities are derived from the cross-correlation of the observed spectra with a synthetic template ($T_{\rm eff}$ = 9500 K and $\log g = 4$ dex). The variation of the radial velocity (for targets with several spectra) and the shape of the cross-correlation permitted the detection of several spectroscopic binaries: HD6530, HD40446, HD50931 and HD217186.

3.2 Atmospheric parameters and abundance analysis

Effective temperature and surface gravity have been determined for the remaining stars using the calibration of Strömgren photometry from Napiwotzki et al. (1993). An abundance analysis, based on Takeda (1995) minimization procedure, has been carried out to determine the abundances of 16 elements (C, O, Na, Mg, Si, Ca, Sc, Ti, Cr, Mn, Fe, Ni, Sr, Y, Zr and Ba).

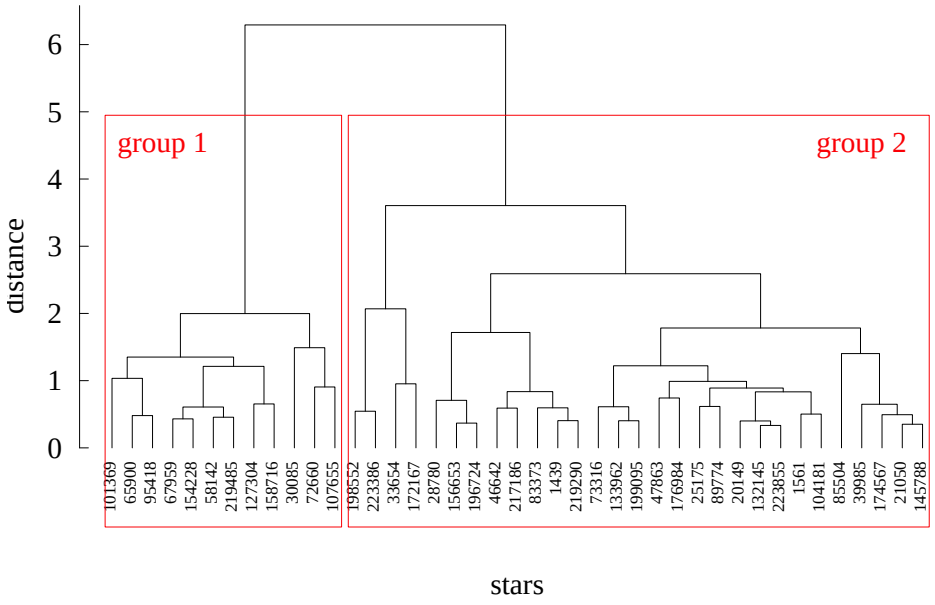

Fig. 1. Dendogram plot of the hierarchical tree resulting from the cluster analysis of the 14-species chemical abundances of the sample. The x-axis gives the HD numbers of the stars and the y-axis represents the Euclidean distance, in the normalized abundance space, between subgroups. The two main groups are identified by the labeled boxes.

3.3 Cluster analysis

These abundances (Na and Mn are only available for a few stars and not taken into account) have been used to perform a hierarchical classification of the sample (Cowley & Bord 2004) into two different groups (Fig. 1). The abundance patterns (medians and standard deviations) of both groups are shown in Fig. 2, confirming that group 1 corresponds to CP stars and group 2 to normal stars.

4 A closer look at HD30085

HD30085, classified as a normal A0 IV by Cowley et al. (1969), is part of our CP group and turns out to be Mn-rich star, possibly a HgMn CP star. We derived a temperature of 11300 K and a surface gravity of 3.95 dex

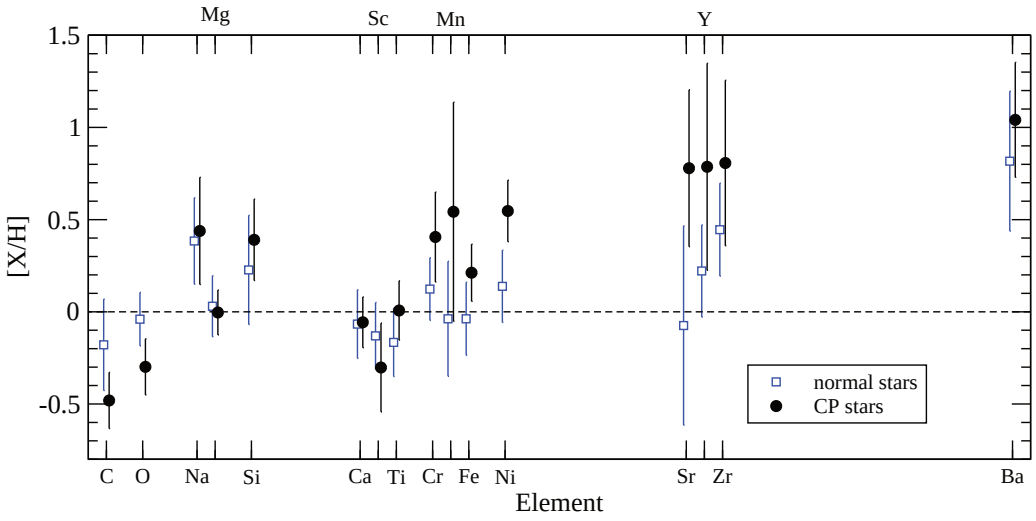

Fig. 2. Abundance pattern for the two groups. For each element, the median abundance is plotted and the error bar corresponds to the dispersion around the median value.

using Napiwotzki et al.'s calibration of Strömgren photometry, which suggests a spectral type reassessment to B8-B9 V.

By iteratively adjusting LTE synthetic spectra to the observed normalized spectrum of HD30085, we have found large overabundances for Mn (Fig. 3.a), Y, Zr (Fig. 3.b), and Sr, about two orders of magnitude larger than solar abundances. Helium is underabundant (−1.1 dex) which appears to be the case in most HgMn stars (Alecian et al. 2009).

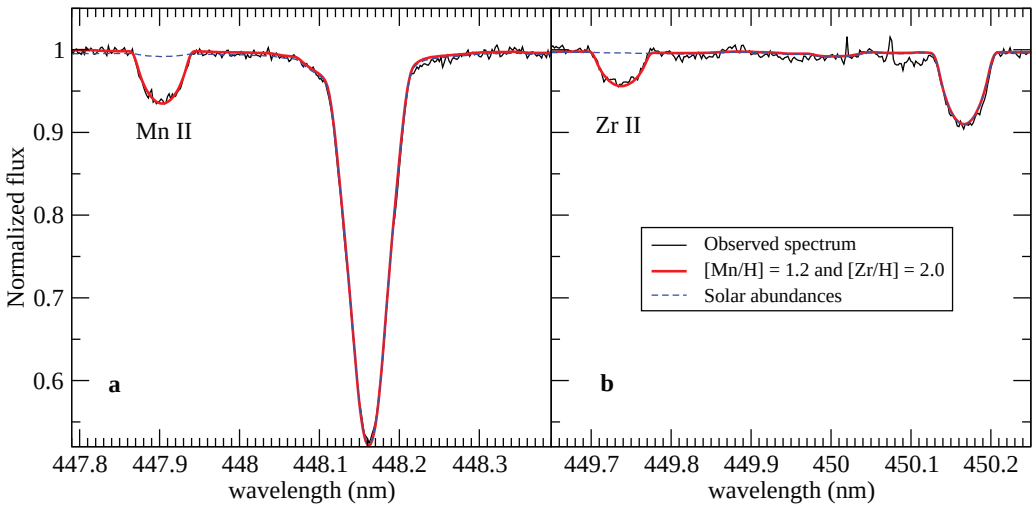

Fig. 3. Spectrum of HD30085 (thin solid line) superimposed to synthetic spectra with different abundances: **(a)** [Mn/H] = 0 dex (dashed line) and [Mn/H] = 1.2 dex (thick solid line), **(b)** [Zr/H] = 0 dex (dashed line) and [Zr/H] = 2.0 dex (thick solid line).

5 Pole-on candidates

The normal group resulting from the aforementioned classification is being carefully studied to disentangle the projection effect from the true equatorial velocity. The spectral signature of fast rotators seen pole-one, due to gravity darkening, can be detected on faint lines. Such features have been detected in the spectrum of Vega by Gulliver et al. (1994), and since, many authors studied the star by spectroscopy (Takeda et al. 2008; Yoon et al.

2008; Hill et al. 2010) and interferometry (Peterson et al. 2006). Using a spectrum of Vega, Takeda et al. (2008) found that, whereas ionized element lines show classical profiles on average, neutral element lines display very characteristic profiles: from flat-bottomed to reversed profiles, due to the effective temperature gradient from the pole to the equator. The quality of our data ($R = 75\,000$; SNR $\sim$ 250–400) does not reach that obtained for Vega by Takeda et al. (2007): $R \sim 100\,000$, SNR $\sim$ 1000–3000. Then we decided to investigate the line profiles globally, using a Least-Square Deconvolution method (Donati et al. 1997; Kochukhov et al. 2010) to enhance the signal and recover the broadening function. Using the line list from Takeda et al. (2008), broadening functions for Fe II lines and Fe I lines separately have been determined for our normal stars. A few among our targets show the characteristic profiles expected for fast pole-on rotators (Fig. 4), i.e. classical shape for Fe II and flat or reversed bottom for Fe I broadening functions.

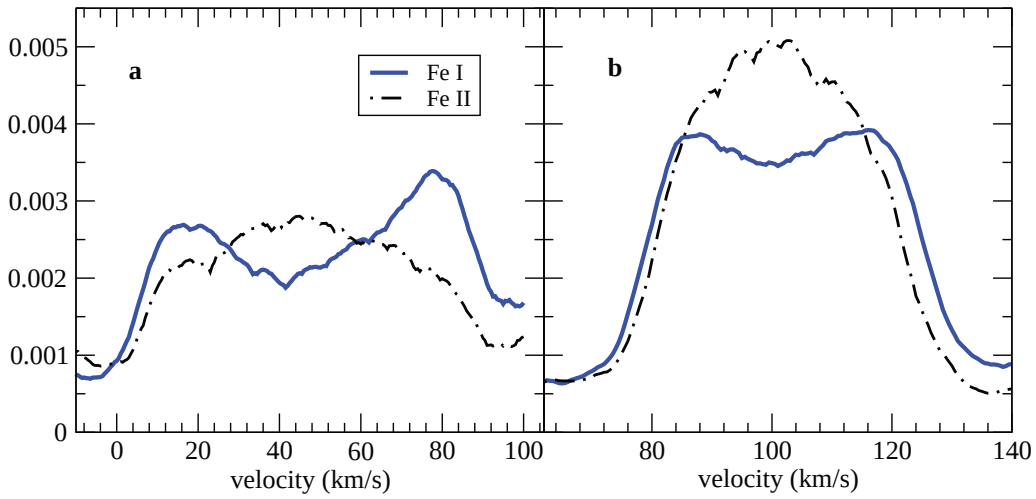

Fig. 4. Broadening functions extracted from Fe II (thick solid line) and Fe I lines (dashed line) for two pole-on candidates in our sample (**a** and **b**).

References

Abt, H. A. 2009, AJ, 138, 28

Abt, H. A. & Morrell, N. I. 1995, ApJS, 99, 135

Alecian, G., Gebran, M., Auvergne, M., et al. 2009, A&A, 506, 69

Cowley, A., Cowley, C., Jaschek, M., & Jaschek, C. 1969, AJ, 74, 375

Cowley, C. R. & Bord, D. J. 2004, in The A-Star Puzzle, IAU Symp. 224, ed. J. Zverko, J. Žižňovský, S. J. Adelman, & W. W. Weiss, 265–281

Donati, J.-F., Semel, M., Carter, B. D., Rees, D. E., & Collier Cameron, A. 1997, MNRAS, 291, 658

Gulliver, A. F., Hill, G., & Adelman, S. J. 1994, ApJ Lett., 429, L81

Hill, G., Gulliver, A. F., & Adelman, S. J. 2010, ApJ, 712, 250

Kochukhov, O., Makaganiuk, V., & Piskunov, N. 2010, A&A, 524, A5

Moultaka, J., Ilovaisky, S. A., Prugniel, P., & Soubiran, C. 2004, PASP, 116, 693

Napiwotzki, R., Schoenberner, D., & Wenske, V. 1993, A&A, 268, 653

Peterson, D. M., Hummel, C. A., Pauls, T. A., et al. 2006, Nat, 440, 896

Royer, F., Zorec, J., & Gómez, A. E. 2007, A&A, 463, 671

Takeda, Y. 1995, PASJ, 47, 287

Takeda, Y., Kawanomoto, S., & Ohishi, N. 2007, PASJ, 59, 245

Takeda, Y., Kawanomoto, S., & Ohishi, N. 2008, ApJ, 678, 446

Yoon, J., Peterson, D. M., Zagarello, R. J., Armstrong, J. T., & Pauls, T. 2008, ApJ, 681, 570

SF2A 2012
S. Boissier, P. de Laverny, N. Nardetto, R. Samadi, D. Valls-Gabaud and H. Wozniak (eds)

TIME-IMPLICIT HYDRODYNAMICAL SIMULATIONS OF STELLAR INTERIORS: APPLICATION TO TURBULENT CONVECTION

M. Viallet[1]

Abstract. The talk described the first results on turbulent convection in the envelope of a red giant star obtained with the MUSIC code, a new multi-dimensional time-implicit code devoted to stellar interiors (Viallet, Baraffe & Walder, A&A, 2011). Currently, most of our physical understanding of stellar interiors and evolution largely relies on one-dimensional calculations. The description of complex physical processes like time-dependent turbulent convection, rotation or MHD processes mostly relies on simplified, phenomenological approaches, with a predictive power hampered by the use of several free parameters. These approaches have now reached their limits in the understanding of stellar structure and evolution. The development of multi-dimensional hydrodynamical simulations becomes crucial to progress in the field of stellar physics and to meet the enormous observational efforts aimed at producing data of unprecedented quality (COROT, Kepler GAIA). The MUSIC code solves the hydrodynamical equations in spherical geometry and is based on the finite volume method. The talk presented implicit large eddy simulations of the turbulent convection in a cold giant envelope both in 2D and 3D and covering 80% in radius of the stellar structure. The computational domain includes both the convective envelope and a significant fraction of the radiative zone, allowing for convective penetration. These simulations provide valuable insight to improve the description of turbulent convection in 1D models.

Keywords: Convection, Stars:interiors, Turbulence

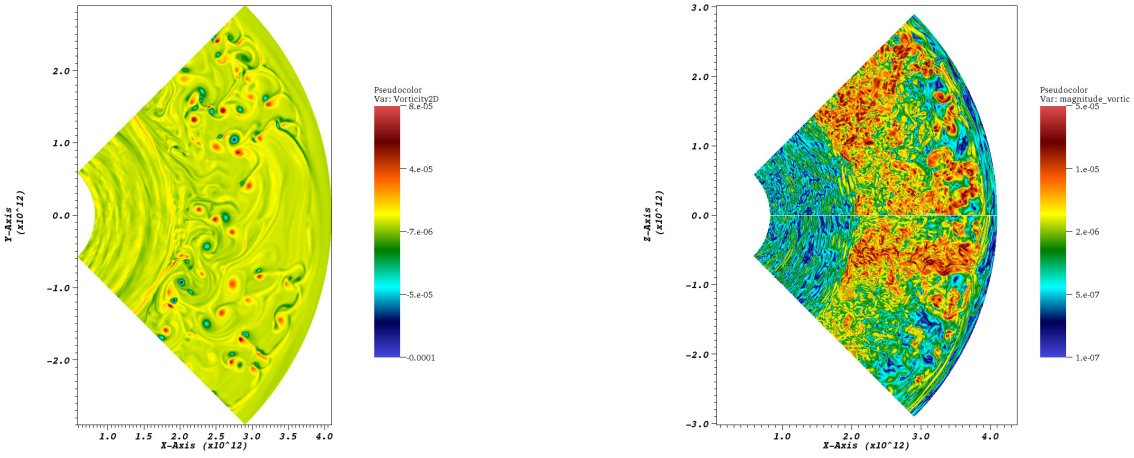

Fig. 1. Snapshots of the computational domain for the 2D and 3D red giant models. The left panel shows the vorticity field ω in a 432×512 simulation, the right panel shows the magnitude of the vorticity $||\vec{\omega}||$ in a 432×256^2 simulation (the figure shows two perpendicular cuts in the vertical direction side by side).

MV acknowledges support from an International Newton Fellowship from the Royal Society.

[1] School of Astronomy And Physics, University Of Exeter, Stocker Road, EX4 4QL Exeter, UK

SF2A 2012
S. Boissier, P. de Laverny, N. Nardetto, R. Samadi, D. Valls-Gabaud and H. Wozniak (eds)

ELEMENTAL ABUNDANCES IN RGB STARS OF THE LARGE MAGELLANIC CLOUD

M. Van der Swaelmen[1], V. Hill[1] and F. Primas[2]

Abstract. The present work is based on a high-resolution spectroscopic survey of two LMC fields located in the bar and the inner disc, observed at ESO/VLT with FLAMES/GIRAFFE. Three setups were used to cover about 1000 Å and enable the measurement of numerous elemental abundances. We confront the results in the inner disc and bar fields and discuss their similarities/differences in the light of the origin of the LMC bar. Both fields show that the LMC has a SFH slower than the MW, resulting in a chemical evolution dominated by SNIa and metal-poor AGB winds. Chemical anomalies for Eu, Ba and La are detected in the most metal-rich field stars, as it has been before in LMC GC stars, and cannot be explained by canonical nucleosynthesis processes.

Keywords: Abundances, Magellanic Clouds, Galaxy: evolution

1 Introduction

Despite decades of intensive observational and theoretical works, we are still far from a complete and clear understanding of our close universe, the Milky Way (MW) and its neighbours. Among the satellites of the MW, the Small and the Large Magellanic Clouds (SMC, LMC) are of particular interest since it is the closest example of galaxies in gravitational (systems: SMC+LMC, SMC+LMC+MW) and chemical interactions (Magellanic Bridge between the clouds, made of stars and gas). Therefore it is a unique laboratory to study the effect of gravitational tides and matter exchange on the chemical evolution and the star formation history of a galaxy. The LMC is an almost face-on, gas-rich galaxy with regions of active stellar formation (distance: 50 kpc (Alves 2004), mass: 10^{10}M$_\odot$ (van der Marel et al. 2002)). The young population exhibits an irregular morphology, likely the stigmata of the very recent interaction with the SMC. The old and intermediate-age population are located within a regular disc and a prominent and luminous off-centre bar. The morphology of the LMC is not well understood and, in particular, we still do not know the origin and the true nature of the bar-like structure: is it a dynamical bar driven by disc instabilities like the one found at the centre of the MW or is it a stellar overdensity? was the formation of the bar driven by a close encounter with the SMC (Subramaniam & Subramanian 2009; Zaritsky 2004; Bekki 2009)? Smecker-Hane et al. (2002) have derived from deep colour-magnitude diagram (CMD) the star formation histories for field stars located in the LMC bar and the inner part of the LMC disc. They found that the LMC field stars do no exhibit an age gap, unlike the stars of the LMC globular clusters (GC), hence their usefulness to probe the epoch 3 to 13 Gyr (see also Cole et al. 2005). Moreover they show that the star formation history (SFH) of the bar and the inner disc were similar at old epochs (between 7 and 14 Gyr); but while the SFH of the inner disc has remained rather constant, the bar has experienced a dramatic increase of its SFH, 4 to 6 Gyr ago. Interestingly, it corresponds to the epoch of the formation of the bar. This work aims at investigating the chemical history of and the relation between the bar and the disc via a detailed chemical analysis of Red Giant Branch (RGB) stars located in the bar and in the inner disc.

[1] Laboratoire Lagrange, UMR 7293, Université de Nice Sophia-Antipolis, Observatoire de la Côte d'Azur, BP4229, 06304, Nice Cedex 4, France

[2] European Southern Observatory, Karl Schwarzschild Str. 2, 85748 Garching b. München, Germany

2 Data and methods

Cole et al. (2005) observed 373 RGB stars in the field of the LMC bar and derived radial velocities and metallicities for their stars. We used their metallicity distribution to select 113 RGB stars belonging to the LMC bar, taking care to sample each metallicity bin from $[\mathrm{Fe/H}]_{\mathrm{CaT}} = -1.69\,\mathrm{dex}$ to $[\mathrm{Fe/H}]_{\mathrm{CaT}} = 0.14\,\mathrm{dex}$. We obtained high resolution spectra ($R \sim 20,000$) of our 113 stars at VLT/ESO with the FLAMES/GIRAFFE multifibre spectrograph (Pasquini et al. 2002). In order to measure numerous elemental abundances, we used three setups HR11, HR13 and HR14, covering a total of $\approx 1000\,\mathrm{\AA}$. The spectra thus cover lines belonging to the α- (Ca, O, Mg, Ti, Si), iron-peak (Sc, V, Cr, Co, Ni, Cu), s-process and r-process elements (Ba, La, Zr, Y, Eu). This complements a similar dataset in the LMC disc, located at $\sim 2\,\mathrm{kpc}$ from the centre (Pompéia et al. 2008). We carried out the data reduction with the help of the ESO GIRAFFE pipeline (built upon the Geneva Giraffe pipeline described in Blecha et al. 2000), part of the *esorex* framework. The reduction steps include the dark current correction, wavelength calibration (using a Th-Ar lamp), spectrum extraction and flat fielding. As the pipeline does not support sky subtraction nor radial velocity correction, we carried out those operations separately. Once all exposures of the same star were sky-subtracted and in the same frame, we averaged them with k-σ clipping rejection (over the fluxes at a given wavelength) to clean for cosmic rays and increase the signal-to-noise ratio (SNR). We ended with a typical final SNR of around 25 for HR11, 40 for HR13 and 48 for HR14.

3 Stellar parameters and abundances

To derive the stellar parameters of our LMC stars (the temperature $\mathrm{T_{phot}}$, the gravity $\log g$, the overall metallicity [M/H] and the microturbulent velocity ξ_{micro}), we used a combination of photometric and spectroscopic methods. For our stars, visible (V and I magnitude, from the OGLE catalogue Udalski et al. 1997, 2000; Szymanski 2005) and infrared (J, H and K magnitude, from the 2MASS catalogue Skrutskie et al. 2006) photometry is available. We used the Ramírez & Meléndez (2005a,b) photometric calibrations for giants to compute four scales of photometric temperatures, using four de-reddened colour indices. The surface gravities $\log g$ were derived using the Bayesian estimation algorithm of stellar parameters of da Silva et al. (2006), based on evolutionary tracks. The overall metallicity and the microturbulent velocity were derived simultaneously by requiring that different FeI lines of different equivalent widths (EW) give the same iron abundance [FeI/H].

We used the two traditional methods to measure the chemical abundances: EW and fitting of absorption profiles. For the first method, we used the automated tool DAOSPEC (Stetson & Pancino 2008) to measure the EW and we converted them into abundances with *turbospectrum* (*turbospectrum* is described in Alvarez & Plez 1998 and improved along the years by B. Plez) together with the grid of OSMARCS spherical model atmospheres (Gustafsson et al. 2008). The spectrum syntheses, computed by *turbospectrum*, are in spherical geometry, with LTE spherical radiative transfer. The second method, the fitting of absorption profile, consists in computing a grid of theoretical spectra by varying the abundance of an element and comparing them to an observed absorption line of this specific element. We used a χ^2 minimisation to find the best fitting, which gives the value of the elemental abundance. We re-analysed (stellar parameters+abundances) the sample of LMC disc stars of (Pompéia et al. 2008), in exactly the same fashion to insure a homogeneous comparison of bar and disc fields and we used Arcturus as a reference star to determine the zero-point of our chemical abundances scale. The abundances we derived for Arcturus are in good agreement with the literature (Ramírez & Allende Prieto 2011; Worley et al. 2009). The tests we performed on noisy Arcturus spectra (at the same SNR level of GIRAFFE spectra) allowed us to derive typical error bars for our LMC stars.

4 Results

In this section, we present the results for some key elements: O, Mg, Si (α elements), Ba, La and Eu (s- and r-elements). Figure 1 (left panel) shows the [α/Fe] trend (mean of O, Mg and Si ratios) for the LMC bar and disc stars, as well as that of the MW. α elements are thought to be produced in massive stars interiors dying as type II supernovae (SNII) while iron is mainly produced in type Ia supernovae (SNIa). Therefore, the ratio [α/Fe] can track the epoch when SNIa start to dominate the chemical enrichment of a galactic environment. Metal-poor ($[\mathrm{Fe/H}] \leq -1.1\,\mathrm{dex}$) LMC stars possess alpha abundances similar to those of MW halo stars, but we note that stars with higher metallicity have α ratios smaller than that of the MW. Unlike for the MW, we do not see a clearly defined plateau in the LMC trends in the low metallicity regime; but despite the paucity of data, we can

suspect that the transition between the SNe II-dominated regime and SNe Ia-dominated regime seems to occur at a lower metallicity in the LMC bar than in the MW. This tells us that the LMC bar has experienced a chemical enrichment different from that of the Milky Way, with a slower SFH. The LMC bar and disc do not exhibit strong differences, though a larger scatter of $[\alpha/\mathrm{Fe}]$ is observed for the bar for $-1\,\mathrm{dex} \leq [\mathrm{Fe/H}] \leq -0.5\,\mathrm{dex}$. Remarkably, we found an excellent agreement between globular clusters (Mucciarelli et al. 2008, 2010) and field stars at both low and high metallicities (we do not have stars at the metallicity of the metal-poor GC but the level of their $[\alpha/\mathrm{Fe}]$ is compatible with that of the most metal-poor field stars).

Figure 1 (right panel) shows the [Eu/Fe] trend for the LMC bar and disc stars, and the MW stellar populations. According to chemical composition of the Sun, europium is thought to be an element mainly produced by the r-process occurring during SNII explosive nucleosynthesis. Therefore, we expect it to follow a pattern similar to that of the $[\alpha/\mathrm{Fe}]$. At low metallicity, we have enhanced [Eu/Fe] for the LMC as expected, but we have also enhanced ratios at high metallicities. For the low metallicity regime, the abundance ratios of the LMC and the MW overlap, while for $[\mathrm{Fe/H}] \geq -1\,\mathrm{dex}$ the LMC trend is above the MW's. This chemical anomaly cannot be understood in the canonical nucleosynthesis picture recalled before. To explain it, we may invoke another source of Eu. Asymptotic Giant Branch (AGB) stars may be candidates: they are the place of s-process nucleosynthesis, and so, can produce Eu. Nevertheless, it is not clear whether the production of Eu would be efficient enough to reach such high [Eu/Fe]. Here again, we found an excellent agreement between LMC field and LMC GC stars. It is worth mentioning that this enhancement at high metallicity is not an artifact of our abundance analysis since we found the expected value for Arcturus.

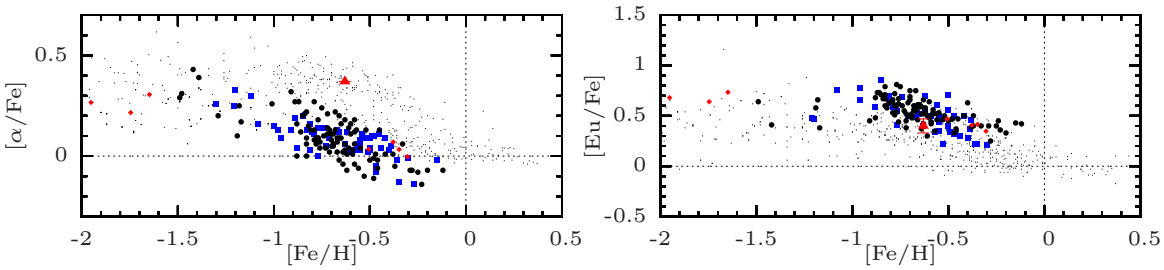

Fig. 1. Left: $[\alpha/\mathrm{Fe}]$ vs $[\mathrm{Fe/H}]$. **Right:** [Eu/Fe] vs [Fe/H]. Legend for both: black dots: LMC bar (this study), blue squares: LMC disc (re-analysis of Pompéia et al. 2008), red diamonds: LMC GC (Mucciarelli et al. 2008, 2010), red triangle: Arcturus (reference star of this study), black tiny points: MW thin and thick disc (Bensby et al. 2005; Reddy et al. 2003, 2006), MW halo (Fulbright 2000; Stephens & Boesgaard 2002).

Figure 2 (left panel) shows the [Ba, La/Eu] trend. Ba and La are s- and r-elements, produced by AGB and SNII; the [Ba, La/Eu] allows to track the relative importance of SNII and AGB in the chemical enrichment. For a pure r-process, Arlandini et al. (1999) predict $[\mathrm{Ba/Eu}] = -0.67\,\mathrm{dex}$. This value is reached for the metal-poor stars of LMC GC. The s-process starts to dominate from a metallicity of about $-1\,\mathrm{dex}$ in the LMC bar and disc. Moreover, the [Ba/Eu] and [La/Eu] increase is steeper in the LMC than in the MW: it proves that AGB played a stronger role in the chemical enrichment of the LMC, compared to the MW. Figure 2 (right panel) shows the [Ba/Fe] trend (similar pattern is observed for [La/Fe]). A very steep increase of LMC [Ba/Fe] is observed from $[\mathrm{Fe/H}] \approx -1.1\,\mathrm{dex}$, while the LMC and MW ratios overlap for lower metallicities. This dramatic increase is not expected in the canonical nucleosynthesis picture and clearly contrasts with what is observed for the MW. This is another chemical anomaly, shared by the dwarf galaxies like Fornax or Sagittarius, two galaxies also dominated by intermediate-age stellar populations. We may explain this with very efficient AGB winds.

5 Discussion and conclusion

We performed a detailed chemical analysis of LMC field stars located in the bar and the disc and compared it to LMC GC stars and MW field stars. We found that the LMC had a chemical history different from that of the MW: the SFH of the LMC was slower and the chemical enrichment was dominated by SNIa (α trend) and AGB winds ([Ba, La/Eu] vs [Fe/H]). We found chemical anomalies for Ba, La and Eu compared to the Galactic trends. Those trends are the results of a chemical enrichment occurring in a metal-poor environment and cannot be completely apprehended in the current chemical evolution scheme: they recall the importance of studying external galaxies that followed different enrichment path in order to perfect our understanding of the

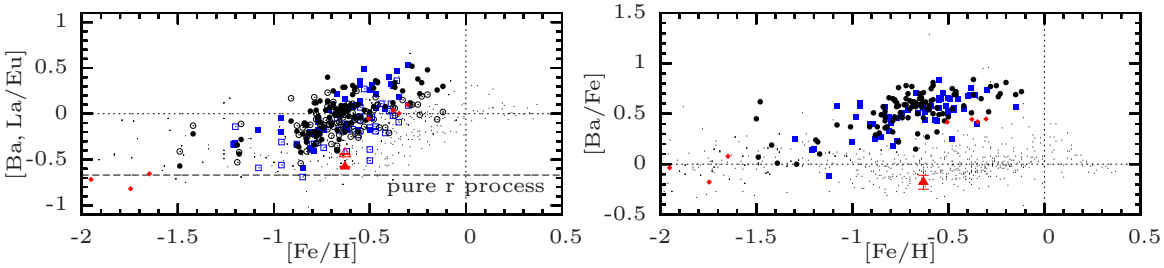

Fig. 2. Left: [Ba/Eu] vs [Fe/H] (filled symbols), [La/Eu] vs [Fe/H] (empty symbols). **Right:** [Ba, La/Fe] vs [Fe/H]. Same legend as Figure 1.

details of galactic chemical evolution. The two LMC fields do not exhibit strong differences in their abundance patterns, except for the α. For the α elements, a larger scatter is observed for the bar stars in the metallicity range $[-1, -0.5]$ and maybe related to the formation of the bar: the start of a new episode of star formation will increase the number of massive stars, in which the α elements originate, and therefore will enrich the interstellar medium with freshly formed α. If this scatter is true, then it is a proof that the bar is a stellar overdensity and not a dynamical structure. We found similar abundance ratios for the LMC field and GC populations, which is rather intriguing since we should expect a different chemical history (no GC formation between ~ 10 and 3 Gyr ago, while the field star formation has never stopped).

References

Alvarez, R. & Plez, B. 1998, A&A, 330, 1109
Alves, D. R. 2004, New A Rev., 48, 659
Arlandini, C., Käppeler, F., Wisshak, K., et al. 1999, ApJ, 525, 886
Bekki, K. 2009, MNRAS, 393, L60
Bensby, T., Feltzing, S., Lundström, I., & Ilyin, I. 2005, A&A, 433, 185
Blecha, A., Cayatte, V., North, P., Royer, F., & Simond, G. 2000, in SPIE Conference Series, Vol. 4008, Society of Photo-Optical Instrumentation Engineers (SPIE) Conference Series, ed. M. Iye & A. F. Moorwood, 467–474
Cole, A. A., Tolstoy, E., Gallagher, III, J. S., & Smecker-Hane, T. A. 2005, AJ, 129, 1465
da Silva, L., Girardi, L., Pasquini, L., et al. 2006, A&A, 458, 609
Fulbright, J. P. 2000, AJ, 120, 1841
Gustafsson, B., Edvardsson, B., Eriksson, K., et al. 2008, A&A, 486, 951
Mucciarelli, A., Carretta, E., Origlia, L., & Ferraro, F. R. 2008, AJ, 136, 375
Mucciarelli, A., Origlia, L., & Ferraro, F. R. 2010, ApJ, 717, 277
Pasquini, L., Avila, G., Blecha, A., et al. 2002, The Messenger, 110, 1
Pompéia, L., Hill, V., Spite, M., et al. 2008, A&A, 480, 379
Ramírez, I. & Allende Prieto, C. 2011, ApJ, 743, 135
Ramírez, I. & Meléndez, J. 2005a, ApJ, 626, 446
Ramírez, I. & Meléndez, J. 2005b, ApJ, 626, 465
Reddy, B. E., Lambert, D. L., & Allende Prieto, C. 2006, MNRAS, 367, 1329
Reddy, B. E., Tomkin, J., Lambert, D. L., & Allende Prieto, C. 2003, MNRAS, 340, 304
Skrutskie, M. F., Cutri, R. M., Stiening, R., et al. 2006, AJ, 131, 1163
Smecker-Hane, T. A., Cole, A. A., Gallagher, III, J. S., & Stetson, P. B. 2002, ApJ, 566, 239
Stephens, A. & Boesgaard, A. M. 2002, AJ, 123, 1647
Stetson, P. B. & Pancino, E. 2008, PASP, 120, 1332
Subramaniam, A. & Subramanian, S. 2009, ApJ, 703, L37
Szymanski, M. K. 2005, Acta Astron., 55, 43
Udalski, A., Kubiak, M., & Szymanski, M. 1997, Acta Astron., 47, 319
Udalski, A., Szymanski, M., Kubiak, M., et al. 2000, Acta Astron., 50, 307
van der Marel, R. P., Alves, D. R., Hardy, E., & Suntzeff, N. B. 2002, AJ, 124, 2639
Worley, C. C., Cottrell, P. L., Freeman, K. C., & Wylie-de Boer, E. C. 2009, MNRAS, 400, 1039
Zaritsky, D. 2004, ApJ, 614, L37

Session 11

Stellar and solar magnetism

SF2A 2012
S. Boissier, P. de Laverny, N. Nardetto, R. Samadi, D. Valls-Gabaud and H. Wozniak (eds)

THE MAGNETISM IN MASSIVE STARS (MIMES) PROJECT: FIRST HARPSPOL DISCOVERIES

E. Alecian[1], R. Peralta[1], M. E. Oksala[2], C. Neiner[1] and the MiMeS collaboration

Abstract. In the framework of the Magnetism in Massive Stars (MiMeS) project, a HARPSpol Large Program at the 3.6m-ESO telescope has recently started to collect high-resolution spectropolarimetric data of a large number of Southern massive OB stars in the field of the Galaxy and in many young clusters and associations. In this contribution, we present details of the HARPSpol survey, the first HARPSpol discoveries of magnetic fields in massive stars, and the magnetic properties of two previously known magnetic stars.

Keywords: Stars: massiv, Stars: magnetic field, Stars: chemically peculiar, Stars: individual: HD 64740, HD 96446, HD 122451, HD 105382, HD 130807, HD 121743, HD 66765, HD 67621, HD 156324, HD 156424

1 The MiMeS project

The Magnetism in Massive Stars[i] (MiMeS) project aims at understanding magnetism in massive stars and its effect on the stellar evolution, interior and close environment. The project is led by G. Wade in Canada and C. Neiner in France. The main scientific objectives are: understanding the origin of magnetic fields in massive stars, and in particular the physics of fossil fields, studying the physics of atmospheres, winds, envelopes and magnetospheres of hot stars, the rotational evolution and magnetic braking, and the evolution of magnetic OB stars and origin of neutron star magnetic fields.

The main observational part of this project is the compilation of a large number of high-resolution spectropolarimetric observations that we have been acquiring since 2008 with ESPaDOnS, Narval and HARPSpol, thanks to three Large Programmes coordinated by G. Wade, C. Neiner, and E. Alecian, respectively. The observing sample has been divided into two sub-samples: the survey component (SC) and the targeted component (TC). The SC sample is intended to search for new magnetic stars among about 400 OB stars and to establish the basic statistics of magnetic fields in massive stars (e.g. incidence of the fields in massive stars, per spectral type, per mass bins, ..., as well as fields properties as a function of mass, age, ...). This sample includes about 200 OB stars that have been observed with the International Ultraviolet Explorer (IUE), which provides us with information on the stellar wind, since the shape and strengths of some resonance lines are sensitive to the wind. The TC sample contains about 40 stars that were previously known to be magnetic, or that were part of the SC sample and have been discovered to be magnetic. We intend to acquire a large number of spectropolarimetric observations well sampled over the rotating phase of the TC stars, to study in detail their magnetic fields and circumstellar environment (Wade et al. 2009; Oksala et al. 2011).

The HARPSpol part of the MiMeS observations contains 4 TC stars, about 50 IUE OB stars to complete the ESPaDOnS and Narval samples, and about 150 OB stars in 7 clusters of different ages (from 4 to 100 Myr) to study the impact of the initial conditions of formation, and age on the fields.

Based on observations collected at the European Southern Observatory, Chile (Program ID 187.D-0917)

[1] LESIA-Observatoire de Paris, CNRS, UPMC, Univ. Paris-Diderot, 5 place Jules Janssen, F-92195 Meudon Principal Cedex, France
[2] Astronomický ústav, Akademie věd České republiky, Fričova 298, 251 65 Ondřejov, Czech Republic
[i] `http://www.physics.queensu.ca/~wade/mimes`

2 First results of the HARPSpol large program

2.1 The Survey Component of the HARPSpol sample

The observations started in May 2010 and will end in February 2013. About 75% of the observing time has been executed so far, resulting in 224 observations of 119 stars, with a resolving power of about 110 000. We use a modified version of the REDUCE package (Piskunov & Valenti 2002) to reduce the data. The Least-Square-Deconvolution (LSD, Donati et al. 1997) technique has been applied to the data to increase the signal-to-noise ratio (SNR), and hence increase the chance of magnetic detection. This technique requires the use of spectral masks (see Donati et al. 1997) that have been computed using Kurucz (1993) ATLAS 9 atmospheric models of appropriate effective temperature and surface gravity for each star. The LSD method results in mean Stokes I and V profiles. A diagnostic N profile is also computed in order to check that no spurious polarised signal is present in our data (see Donati et al. 1997). Fig. 1 illustrates the LSD profiles obtained with HARPSpol in both magnetic and non-magnetic stars. Note that the flat N profiles in all of our data indicate that no spurious signal is present, and that the Zeeman signatures in V, if present, are real.

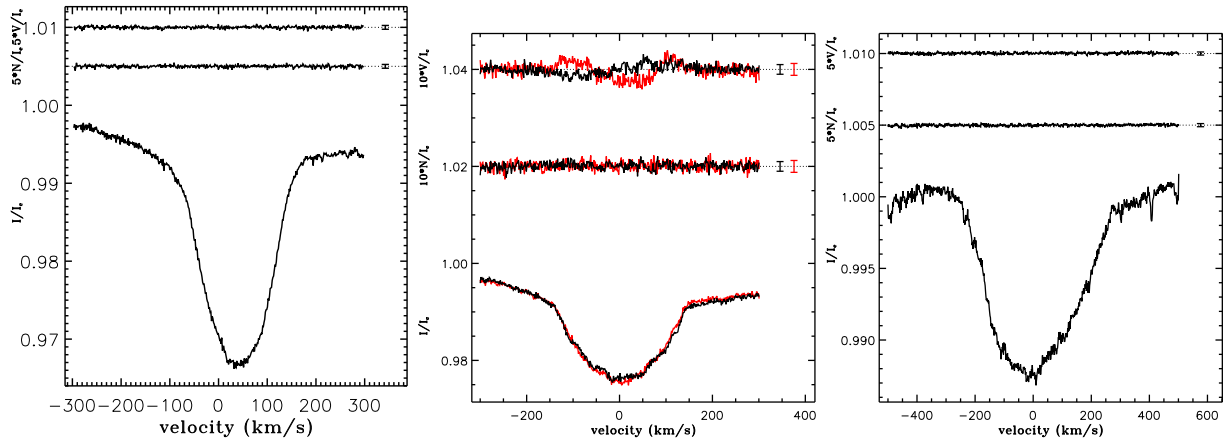

Fig. 1. Examples of LSD I (bottom), V (top) and diagnostic N (middle) profiles of HARPSpol targets. The observations of θ Car (left) and Achernar (right) illustrate the low upper limits on magnetic fields that we can obtain with HARPSpol. Multiple observations of the TC target HD 64740 (middle panel) are superimposed (Peralta et al. in prep.).

The HARPSpol observations have produced 7 new magnetic stars: HD 122451, HD 130807 and HD 121743 in the Sco-Cen association, HD 66765 and HD 67621 in Vel OB2, and HD 156324 and HD 156424 in Sco OB4 (Fig. 2, Alecian et al. 2011, Alecian et al. in prep.), and to confirm the magnetic field in one previously suspected magnetic star (HD 105382 of the Sco-Cen association). So far, the complete sample of OB stars has been observed for 2 out of the 7 clusters (NGC 6530 and Vel OB2). While no magnetic field has been detected among the 8 OB stars of NGC 6530, 2 magnetic stars have been detected among the 10 OB stars of Vel OB2. These results will be analysed once the whole data set of cluster stars has been acquired.

2.2 The He-strong star HD 64740

With HARPSPol, we have acquired 12 observations of the TC star HD 64740, well sampled over the rotation period previously determined by Bohlender et al. (1987, $P_{\rm rot} \sim 1.33026$ d). We estimated the surface averaged longitudinal magnetic fields (B_ℓ) using the first moment technique (e.g. Wade et al. 2000). The B_ℓ are plotted with green asterisks in Fig. 3 together with the historic data of Borra & Landstreet (1979) and Bohlender et al. (1987), phased using the rotation period and the HJD at B_ℓ minimum of Bohlender et al. (1987). We observe a shift of about 0.5 in phase between the old and new data indicating that the rotation period is not accurate enough. Using the new and old data, we have improved the rotation period determination. The new values of the period and HJD at minimum are

$$\mathrm{JD}(B_\ell \text{ min}) = 2455901.61503 + E1.330200(12). \quad (2.1)$$

The He I lines of HD 64740 are stronger than the prediction from models with a solar abundance, and vary in phase with the rotation period, confirming the He-strong nature of this star. Two patches of overabundance of

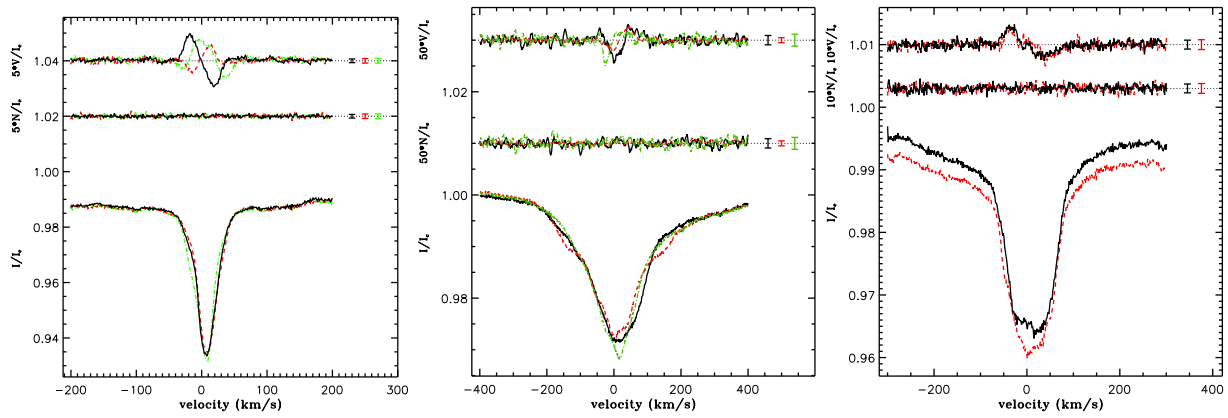

Fig. 2. LSD I (bottom), V (top) and diagnostic N (middle) profiles of some of the new magnetic stars detected with HARPSpol (Alecian et al. 2011, Alecian et al. in prep.). From left to right: HD 130807, HD 122451, HD 121743. Multiple observations are superimposed for each star.

helium are observed close to the magnetic poles, as usually observed in other He-strong stars.

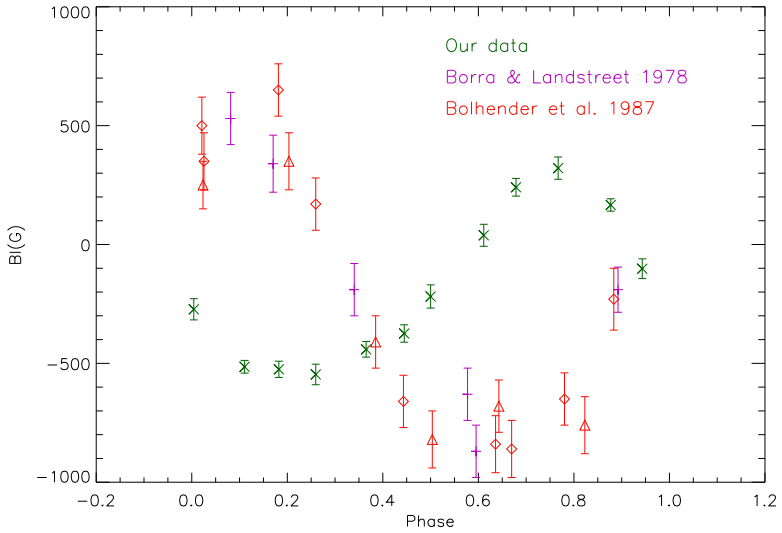

Fig. 3. Longitudinal magnetic fields (B_ℓ) vs phase of HD 64740, using the period of Bohlender et al. (1987, BB87). Asterisks: measured on the HARPSpol spectra. Other symbols: published data of Borra & Landstreet (1979) and BB87. The phase shift of our data is due to a lack of precision on the period. Our data show an asymmetry indicating that a quadrupolar component (in addition to the dipolar component) is present at the surface of the star (Peralta et al. in prep.).

Using the oblique rotator model of Alecian et al. (2008a), we modelled the Stokes V profiles of HD 64740 in order to characterise its magnetic field. We find that a dipole field of 30 kG at the North pole, inclined by about 20 degrees with respect to the rotation axis, and displaced by about 0.06 R_* from the centre of the star reproduce the data well (Peralta et al. in prep).

The wings of the Hα profile of HD 64740 are superimposed with variable emission of circumstellar (CS) origin. This emission varies in phase with the rotation period and seems to be localised in two opposite clouds situated at about 3 stellar radii (Peralta et al. in prep.). These clouds are likely the result of centrifugally supported wind material trapped within the co-rotating magnetosphere, located at the intersection of the magnetic and rotational equators. This type of rigidly rotating magnetosphere (RRM) is observed in several other magnetic OB stars (Townsend & Owocki 2005; Oksala et al. 2012; Petit et al. 2012).

2.3 The magnetic field of HD 96446

We also obtained four observations of the TC star HD 96446 over 6 days, then, a year later, 6 observations over 10 days. HD 96446 is a well known magnetic He-strong star (Borra & Landstreet 1979) with a published photometric rotation period of 0.85137 d (Matthews & Bohlender 1991). The data exhibits only negative Zeeman signatures, and show faint variations from one observation to the other, indicating that only the negative pole is visible. Together with a low $v \sin i$ (~ 3 km s^{-1}), this implies that the inclination of the rotation axis is small (3-15°, Neiner et al. 2012). Neiner et al. (2012) have analysed the first set of HARPSPol observations and find that the field of HD 96446 is very likely dipolar with a polar strength of 5 to 10 kG. Thanks to the high spectral resolution of HARPS they are able to measure the Zeeman splitting inside the spectral lines, and find values of the field modulus compatible with a dipolar field of 5 to 10 kG. Neiner et al. conclude that while this star is very similar to σ Ori E, the prototype for the RRM model (Townsend & Owocki 2005), HD 96446 displays no hints of circumstellar emission in Hα. The authors propose that either the rotation period of this star should be revised significantly ($P_{\rm rot} \sim 10 - 20$ d), or that the RRM model should be improved to include e.g. a leakage mechanism, to reproduce the observations of HD 96446.

3 Conclusions

HARPSpol provides us with very high quality spectropolarimetric data similar to Narval and ESPaDOnS, allowing us to reach upper limits on magnetic fields lower than 100 G on average. The very high resolution power (∼110 000) allowed us to detect the Zeeman splitting inside the intensity lines of HD 96446, providing us with additional constraints on its magnetic field. Three magnetic stars among 34 have been detected in ScoCen, while 2 magnetic stars among 10 have been detected in Vel OB2. Both associations having similar ages, these first results are statistically surprising but preliminary. Serious conclusions will only be derived once the whole data set of the 7 clusters is acquired.

We wish to thank the Programme National de Physique Stellaire (PNPS) for their support.

References

Alecian, E., Catala, C., Wade, G. A., et al. 2008a, MNRAS, 385, 391

Alecian, E., Kochukhov, O., Neiner, C., et al. 2011, A&A, 536, L6

Bohlender, D. A., Landstreet, J. D., Brown, D. N., & Thompson, I. B. 1987, ApJ, 323, 325

Borra, E. F. & Landstreet, J. D. 1979, ApJ, 228, 809

Donati, J.-F., Semel, M., & Carter, B. D., e. a. 1997, MNRAS, 291, 658

Kurucz, R. 1993, Opacities for Stellar Atmospheres: [-3.5],[-4.0],[-4.5]. Kurucz CD-ROM No. 7. Cambridge, Mass.: Smithsonian Astrophysical Observatory, 1993., 7

Matthews, J. M. & Bohlender, D. A. 1991, A&A, 243, 148

Neiner, C., Landstreet, J. D., Alecian, E., et al. 2012, A&A, 546, A44

Oksala, M. E., Wade, G. A., Townsend, R. H. D., et al. 2012, MNRAS, 419, 959

Oksala, M. E., Wade, G. A., Townsend, R. H. D., et al. 2011, ArXiv e-prints

Petit, V., Owocki, S. P., Wade, G. A., et al. 2012, MNRAS, submitted

Piskunov, N. E. & Valenti, J. A. 2002, A&A, 385, 1095

Townsend, R. H. D. & Owocki, S. P. 2005, MNRAS, 357, 251

Wade, G. A., Alecian, E., Bohlender, D. A., et al. 2009, in IAU Symposium, Vol. 259, 333–338

Wade, G. A., Donati, J.-F., Landstreet, J. D., & Shorlin, S. L. S. 2000, MNRAS, 313, 851

SF2A 2012
S. Boissier, P. de Laverny, N. Nardetto, R. Samadi, D. Valls-Gabaud and H. Wozniak (eds)

HOW THE PLANETARY RESEARCH HELPS TO THE STELLAR DYNAMO UNDERSTANDING

I. Boisse[1], M. Oshagh[1,2], C. Lovis[3], N. C. Santos[1,2], X. Dumusque[1,3], X. Bonfils[4], M. Montalto[1] and G. Boué[1]

Abstract. Most of the exoplanet science is dependent on the stellar knowledge. One of them that has to be understood is the magnetic activity when we search for planets with radial velocity or photometry measurements. The main shape of stellar activity and spots properties have to be understood, for example, to choose the best targets to search for low-mass planets in the habitable zone or to derive the accurate parameters of a planetary system. With that aim, we show in this presentation how these studies lead to give clues on spots latitudes and on the long term variation of stellar activity. The properties of magnetic activity on the low rotators solar-type stars are not easily reachable by other techniques (spectropolarimetry or Doppler imaging) and these studies should be used to constrain theories of stellar dynamo.

Keywords: Techniques: radial velocities, photometry, Stars: activity, Dynamo, Planetary system

1 Why planetary researchers are worried about stellar activity ?

Up to now, more than 800 planets were discovered and characterized, most of them thanks to the radial-velocity (RV) technique. However, this efficient method is indirect as well as the photometric transit and astrometry techniques. One of the problems with this is the fact that RV variations can in some cases be caused by other mechanisms that are not related to the presence of low-mass companions. Even if RV surveys could reject very active targets, all stars present variability at different level (from few cm^{-1} to hundreds of m^{-1}). Moreover, mainly RV is needed to establish the planetary nature and measure the mass of a transiting candidate (and stellar activity is less determinant for transit detection).

RV values are derived from the measurement of position in wavelength of thousands of spectral lines. Unfortunately, the measurement is not only sensitive to Doppler shift due to gravitationally bounded companion but also to line profile deformations. Especially, apparition and disappearance of spots from the observer view due to the stellar rotation, or change of the convection pattern with magnetic cycle induce a distortion of the line that changes with time. The jitter that results in RV measurement may hamper planet discovery or degrade the orbital parameters estimation. They may also give false candidates, if they produce a stable periodic signal (e.g. Queloz et al. 2001). An essential work is then needed to understand all phenomena caused by stellar variability, and to characterize their impact on RV and photometry to be able to distinguish between these and real planetary signatures.

2 How planetary researchers track stellar activity ?

Phenomena such as stellar pulsation or inhomogeneous convection could be averaged by specific observational strategy (Dumusque et al. 2011). Because the typical timescale of those oscillations is less than fifteen minutes, an exposure time of fifteen minutes or larger reduces greatly the oscillation noise. In the same way, the timescale of granulation is less than 30 hours, therefore taking several measurements per night allows a reduction of the

[1] Centro de Astrofísica, Universidade do Porto, Rua das Estrelas, 4150-762 Porto, Portugal
[2] Departamento de Física e Astronomia, Faculdade de Ciências, Universidade do Porto, 4169-007 Porto, Portugal
[3] Observatoire de Genève, Université de Genève, 51 Ch. des Maillettes, 1290 Sauverny, Switzerland
[4] UJF-Grenoble1/CNRS-INSU, Institut de Planétologie et d'Astrophysique de Grenoble, UMR 5274, Grenoble, F-38041, France

RV contribution of granulation. These methods have already been used (Pepe et al. 2011) and showed good efficiency (e.g. Santos et al. 2004, , that averaged asteroseismologic data to detect one of the first low-mass planet).

In the following, we focus on stellar activity, mainly dark spots and bright plages on stellar surface, and on magnetic cycle. These phenomenon are assumed to be part of the stellar dynamo process, that generates stellar magnetic field. To identify stellar activity, we can monitor the bisector span (BIS), the width and the depth of the mean line of the spectrum, and also to calculate the chromospheric emission ratio, $\log R'_{HK}$ from the CaII H&K lines and to monitor other lines sensitive to active features: Hα, HeI, NaI. However the behavior of these parameters is not yet understood properly, moreover because they depend on stellar parameters (Desort et al. 2007; Boisse et al. 2011, 2012). For example, Bonfils et al. (2007) has to compared RV and stellar activity index, because the BIS becomes inefficient as an indicator of activity when the star rotates too low.

SOAP: a tool for the fast computation of the stellar spots impact[i]

SOAP is an online software that simulates the effect of stellar spots and plages on RV and photometry (Boisse et al. 2012). This numerical model centers the visible stellar disk on a grid of several tens of thousands of resolution elements. The typical line of the emerging spectrum of the star is modeled by a Gaussian for each grid cell (equivalent to the spectrum cross-correlation function that can be seen as a weighted average of all the spectral lines convolved with a rectangular function). Each Gaussian (in a given stellar position) is Doppler-shifted according to the projected rotational velocity and weighted by a linear limb-darkening law. SOAP calculates the position of the surface inhomogeneities defined by their latitudes, longitudes, and sizes. The cells inside the spots are modeled by the same Gaussian as for the stellar disk, but are weighted by their brightness. The code then removes (for dark spot) or adds (for bright plage) the Gaussian and flux of the inhomogeneities to those of the non-spotted star. Finally, SOAP delivers the integrated spectral line, the flux, the RV, and the bisector span as a function of the stellar rotational phase.

SOAP-T is an improved version that includes the impact of a transiting planet in RV and photometry (Oshagh et al. 2012).

3 What we learnt about stellar activity ?

Monitoring and determining properties of active regions

Boisse et al. (2009) monitored HD189733 simultaneously in RV with SOPHIE and in photometry with the MOST satellite. They showed the presence of an active region on the stellar surface. The plage was tracked by Hα emission, but in photometry the dark spot dominates the signal. The spots temperature were constrained from the crossing of the transiting planet observed by HST (Pont et al. 2007). The ratio of the covered surface by dark spots and bright plages, and their contrast in temperature with the stellar photosphere, are key parameters to model activity, mainly to analyze photometric rotational modulations from Kepler and CoRoT lightcurves (e.g. Lanza et al. 2011; Kipping 2012).

Long-term RV and $\log R'_{HK}$ variations: Characterizing photospheric modifications with magnetic field evolution

RV surveys searching for planets monitor primarily main-sequence stars of spectral-type from A-F to M. Some database reach now a time coverage of more than 15 years. Even if the sampling of the observation and the target selection are not optimized for activity monitoring, results can be drawn about long term variations.

Lovis et al. (2011) studied 304 FGK stars, mainly dwarfs, from the HARPS sample. They searched for long term variability with period greater than 2 years. They computed the activity index, $\log R'_{HK}$, from the CaII H&K lines. They compared its variability with the one of the RV, BIS and parameters of the mean spectral line. We would like to point out three of their results. They detected variability periods shorter than the 11 yrs of the Sun cycle. It may be a sign of multiperiodism in other stars. They found few F stars present periodicity. But we could also argue that magnetic cycle measured in F stars (Tau Boo Farès et al. 2009) (Iota Hor Metcalfe et al. 2010) present periods shorter than 2 years. The last point is the dependence of the correlation slope between RV and R'_{HK}, as a function of effective temperature (see Fig. 1). This indicate that for a same variation in the $\log R'_{HK}$, the impact in RV will be 2-3 times greater for a G dwarf than for a late K star. Which phenomena

[i]The tool is available at `http://www.astro.up.pt/soap`

(or composition of phenomena) is responsible for this is still an open question. It could be due to a different modification of the convection pattern with activity level or to a distinct filling factor of plages compared to spots with spectral types.

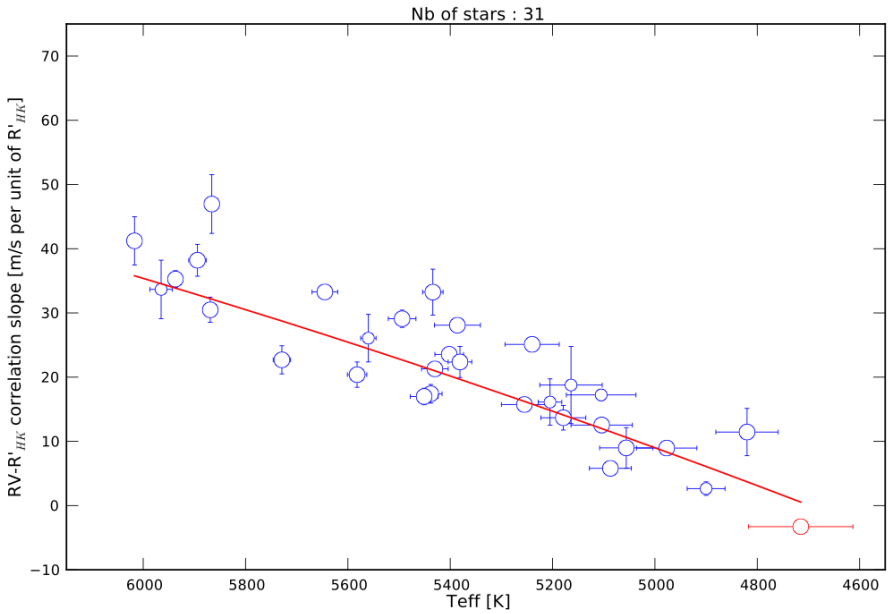

Fig. 1. Correlation slope between RV and $R^{'}_{\mathrm{HK}}$, as a function of effective temperature (from Lovis et al. (2011)).

Track the spots with planetary transits

A planet transiting its host-star could overlap with active zones on the stellar surface. It will generate anomalies (bumps) inside the transit light-curve (see Fig. 2). The evolution of these anomalies can be tracked if long-term and continuous observations are accessible (e.g. CoRoT and Kepler). It could allow to determine the spin-orbit angle, the inclination of the stellar spin axis, and the configuration of the spots on the stellar surface (e.g. Nutzman et al. 2011; Désert et al. 2011; Sanchis-Ojeda et al. 2011).

Sanchis-Ojeda & Winn (2011) detected two bumps in the folded Kepler light-curve of 26 transits of HAT-P-11. They interpreted these peaks as evidence of long lived spot belt regions, and derived two possible scenario for the planet orbit, stellar spin axis and spots positions. Using SOAP-T and the out-of-transit light curve, Oshagh et al. (2012) showed that the most probable scenario of the previous study is the one that presents two active belts at $\sim \pm 20°$, comparable to what is observed on the Sun but at lower latitude. Kepler will continue to monitor the star during several years. In analogy to what is seen on the Sun, we could expect to observe a change in the spots latitude with time if HAT-P-11 has a magnetic cycle.

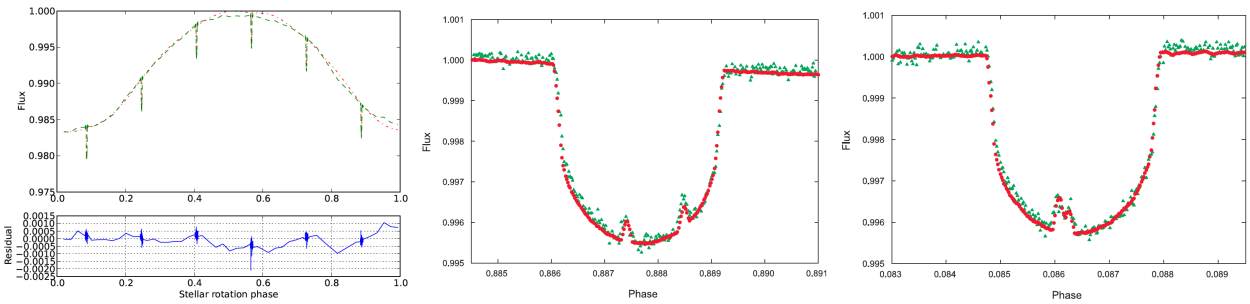

Fig. 2. Left: Kepler observation of HAT-P-11 (green) and SOAP-T fit (red) of HAT-P-11 during one stellar rotation. Blue are the residuals. **Middle and right:** Zooms on two transits of the left figure. The flux values are normalized to one. Figures from Oshagh et al. (2012).

4 Future

SOAP simulates the photometric effect due to inhomogeneities on the stellar surface. However, it does not consider the effect that they also block the convection pattern. Moreover, spots and plages are not only areas darker or brighter, but have a different temperature (then a different spectra) than the stellar photosphere.

The wavelength dependency of spots must be taken into account because, if most of the accurate spectrographs are now in the optical, soon near-infrared instruments will be available, a wavelength domain in which the amplitude of RV variation due to activity is smaller (e.g. Huélamo et al. 2008). Stellar magnetic fields might be monitored by polarimetry of the stellar lines induced by Zeeman effect with instruments such as ESPADONS@CFHT, Narval@TBL, HARPSPol@ESO, or soon SPIRou@CFHT also dedicated to the search of planets around low-mass stars.

Dedicated observations of active stars are therefore needed, if possible simultaneously, in RV, photometry, and polarimetry to characterize the different level of stellar variability, to understand the correlation between the different proxies, and to constrain the simulations. The release of thousands of light curves from the space missions CoRoT and Kepler dedicated to asteroseismology and the search for planets via transit will help us to understand statistically the photometric variability of these stars.

IB, MO, NCS, MM, and GB acknowledge the support of the European Research Council/ European Community under the FP7 through a Starting Grant, as well from Fundaccao para a Ciência e a Tecnologia (FCT), Portugal, through SFRH/BPD/81084/2011 and the project PTDC/CTE-AST/098528/2008.

References

Boisse, I., Moutou, C., Vidal-Madjar, A. et al. 2009, A&A, 495, 959
Boisse, I., Bouchy, F., Hébrard, G. et al. 2011, A&A, 528, A4
Boisse, I., Bonfils, X. & Santos, N.C. 2012, A&A, 545, 109
Bonfils, X., Mayor, M., Delfosse, X. et al. 2007, A&A, 474, 293
Désert, J.-M., Charbonneau, D., Demory, B.-O. et al. 2011, ApJS, 197, 14
Desort, M., Lagrange, A;-M., Galland, F., Udry, S. and Mayor, M. 2007, A&A, 473, 983
Dumusque, X., Udry, S., Lovis, C., Santos, N.C. and Monteiro, M. 2011, A&A, 525, 140
Farès, R., Donati, J.-F., Moutou, C. et al. 2009, MNRAS, 398, 1383
Huélamo, N., Figueira, P., Bonfils, X. et al. 2008, A&A, 489, L9
Kipping , D., 2012, arXiv: 1209.2985
Lanza, A.F., Boisse, I., Bouchy, F., Bonomo, A.S. and Moutou, C. 2011, A&A, 533, 44
Lovis, C., Dumusque, X., Santos, N.C. et al. 2011, arXiv:1107.5325
Metcalfe, T.S., Basu, S., Henry, T.J. et al. 2010, ApJ, 723, 213
Nutzman, P.A., Fabrycky & Fortney 2011, ApJ, 740, L10
Oshagh, M., Boisse, I., Boué, G. et al. 2012, A&A, in press
Pepe, F., Lovis, C., Ségransan, D. et al. 2011, A&A, 534A, 58P1
Pont, F., Gilliland, R.L., Moutou, C. et al. 2007, A&A, 476, 1347
Queloz, D., Henry, G.W., Sivan, J.-P. et al. 2001, A&A, 379, 279
Sanchis-Ojeda, R., Winn, J.N., Holman, M. et al. 2011, ApJ, 733, 127
Sanchis-Ojeda, R. & Winn, J.N. 2011, ApJ, 743, 61
Santos, N.C., Bouchy, F., Mayor, M. et al. 2004, A&A, 426L, 19

SF2A 2012
S. Boissier, P. de Laverny, N. Nardetto, R. Samadi, D. Valls-Gabaud and H. Wozniak (eds)

TWISTED MAGNETIC STRUCTURES EMERGING FROM BUOYANCY INSTABILITIES

L. Jouve[1], L.J. Silvers[2] and M.R.E. Proctor[3]

Abstract. We here report calculations of magnetic buoyancy instabilities of a sheared magnetic layer where two separate zones are unstable. The idea is to study the possible generation of large-scale helical structures which could then rise through a stellar convection zone and emerge at the surface to create active regions. The calculations shown here are a follow-up of the work of Favier et al. (2012) where the instability developed in a weakly magnetized atmosphere, consisting of a uniform field oriented in a different direction from the unstable layer below. Here, the top layer representing the atmosphere is itself unstable to buoyancy instabilities and thus quickly creates a more complex magnetic configuration with which the layer below will interact. We also find in this case that the accumulation of magnetic tension between the two unstable layers favors the creation of large-scale helical structures.

Keywords: Sun, magnetic field, instabilities, MHD

1 Introduction

The idea of this work is to study the onset and development of magnetic buoyancy instabilities of a sheet of field in a configuration where large scale helical magnetic structures may emerge. Detailed calculations were performed by Favier et al. (2012), in which the buoyancy instability develops in a weakly magnetized atmosphere where the direction of the field varies with respect to the direction of the strong unstable field below. The idea was to understand how coherent structures could be created at the base of a stellar convection zone where a large-scale shear produces a strong toroidal magnetic field associated with a small poloidal component. The authors showed that from small-scale interchange instability, large-scale helical coherent magnetic structures could be created, thus giving a possible explanation for the coherent rise of magnetic flux from the base of the convection zone to the surface where bipolar active regions emerge.

Here, we investigate the case where the atmosphere above is itself unstable to buoyancy instabilities and naturally creates a more complex field configuration. The idea here is to study the possibility of the spontaneous creation of similar coherent structures when the atmospheric field is less idealized and organized at smaller scales. The calculation thus starts with an initial magnetic layer oriented in the x-direction, complemented with a transverse field B_y such that two zones are initially made unstable to 2D and 3D perturbations.

2 Model set up

2.1 Governing equations

The evolution is governed by the compressible MHD equations, with heat transfer treated in the diffusion approximation. The polytropic atmosphere is considered to be convectively stable so as to focus on the instabilities driven by the magnetic field. Those equations are solved in a Cartesian domain in the same way as Matthews et al. (1995). In particular, the following dimensionless parameters are used:

[1] Université de Toulouse, UPS-OMP, Institut de Recherche en Astrophysique et Planétologie, Toulouse, France
[2] Department for Mathematical Science, City University London, Northampton Square, London, EC1V 0HB, UK
[3] Department of Applied Mathematics and Theoretical Physics, University of Cambridge, Centre for Mathematical Sciences, Wilberforce Road, Cambridge CB3 0WA, UK

$$\sigma = \frac{\mu C_p}{K} \quad , \quad \zeta = \frac{\eta \rho_0 C_p}{K} \quad , \quad \theta = \Delta d / T_0 \quad , \quad m = \frac{g}{R\Delta} - 1 \quad , \quad F = \frac{B_0^2}{p_0 \mu_0} \quad , \quad C_k = \frac{K}{\rho_0 C_p (R T_0)^{1/2}}$$

where p_0, ρ_0 and T_0 being the pressure, density and temperature at $z = 0$, μ_0 the magnetic permeability, C_p the specific heat at constant pressure, R the gas constant, g the gravitational acceleration, Δ is the temperature gradient and d is the depth of the box. The thermal conductivity K, viscosity ν and magnetic diffusivity η are all assumed to be constant.

The equations then read:

$$\frac{\partial \rho}{\partial t} = -\nabla \cdot (\rho \mathbf{u}) \tag{2.1}$$

$$\frac{\partial \rho \mathbf{u}}{\partial t} = -\nabla (p + F B^2/2) + \nabla \cdot (F \mathbf{B}\mathbf{B} - \rho \mathbf{u}\mathbf{u} + \sigma C_k \tau) + (m+1)\theta \rho \mathbf{z} \tag{2.2}$$

$$\frac{\partial \mathbf{B}}{\partial t} = \nabla \times (\mathbf{u} \times \mathbf{B} - \zeta C_k \nabla \times \mathbf{B}) \tag{2.3}$$

$$\frac{\partial T}{\partial t} = -\mathbf{u} \cdot \nabla T - (\gamma - 1) T \nabla \cdot \mathbf{u} + \frac{\gamma C_k}{\rho} \nabla^2 T + \frac{C_k (\gamma - 1)}{\rho} (\sigma \tau^2/2 + F \zeta J^2) \, , \tag{2.4}$$

where τ is the stress tensor and where the ideal gas law is used. The boundary conditions used are impermeable and stress-free at top and bottom, vertical magnetic field at top and bottom and constant flux at the bottom for the temperature.

2.2 Initial field configuration

The initial magnetic field configuration consists in a layer of magnetic field in which two spatially separated zones will be unstable with respect to buoyancy instabilities. The magnetic layer is located between $z = 0.6$ and $z = 0.8$ (the top of the domain being located at z=0). As shown by Newcomb (1961), the criteria for 2D and 3D instabilities respectively read

$$\rho \, |\mathbf{B}| \, \frac{\partial}{\partial z} \left(\frac{|\mathbf{B}|}{\rho} \right) > \rho^\gamma \frac{\partial}{\partial z} \left(\frac{T}{\rho^{\gamma - 1}} \right) \tag{2.5}$$

and

$$|\mathbf{B}| \frac{\partial |\mathbf{B}|}{\partial z} > \rho^\gamma \frac{\partial}{\partial z} \left(\frac{T}{\rho^{\gamma - 1}} \right) \, . \tag{2.6}$$

The profile of the transverse field is chosen here so as to make the left-hand sides of Eq 2.5 and 2.6 positive in two different locations between $z = 0.6$ and $z = 0.8$. As a consequence, both the overlying atmospheric field and the layer below (possessing different field inclinations) will be unstable to buoyancy instabilities.

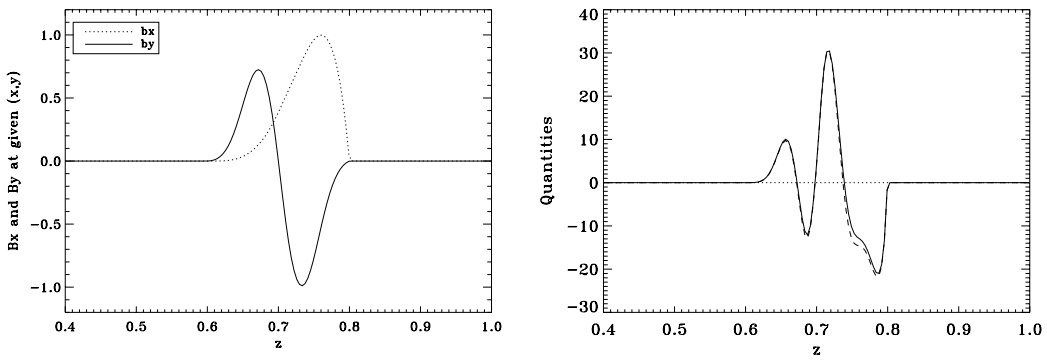

Fig. 1. Left: initial profiles of B_x and B_y. **Right:** initial values of the right hand side and left-hand sides of Eqs 2.5 and 2.6.

As initial profiles for the magnetic field we choose the following:

$$B_x = B_0 (z-0.6)^4 (z-0.8) \tag{2.7}$$

$$B_y = B_{0y} (z-0.6)^{3/2} (z-0.8) \exp\left(-\frac{(z-0.7)^2}{0.05^2}\right) . \tag{2.8}$$

Figure 1 shows the initial magnetic field profile as well as the characteristic quantities for the onset of magnetic buoyancy instabilities. It is clearly visible on the right panel of this figure that the magnetic field profile is made unstable at 2 different locations within the layer, without any interaction between them at the initial state. The profiles of B_x and B_y are smooth, the longitudinal field keeps the same sign within the whole layer while B_y changes sign at $z = 0.7$. Of course, in this case, the top unstable layer is dominated by a field in the y-direction, which would correspond to an almost entirely poloidal field at the base of the convection zone, and thus probably unlikely. Nevertheless, we are interested in the effect of a transverse field varying with depth and this configuration will thus capture the largest possible effects of this situation.

The dimensionless numbers used in this simulation are the following: $\gamma = 5/3$, $m = 1.6$,$\theta = 2$, $C_k = 1.25 \times 10^{-2}$, $\sigma = 2 \times 10^{-2}$ for the hydro numbers and $F = 1$, $\zeta = 2 \times 10^{-3}$ for the magnetic quantities. The resolution used is $N_x = 256$, $N_y = 128$ and $N_z = 260$.

3 Results

3.1 Layer interaction

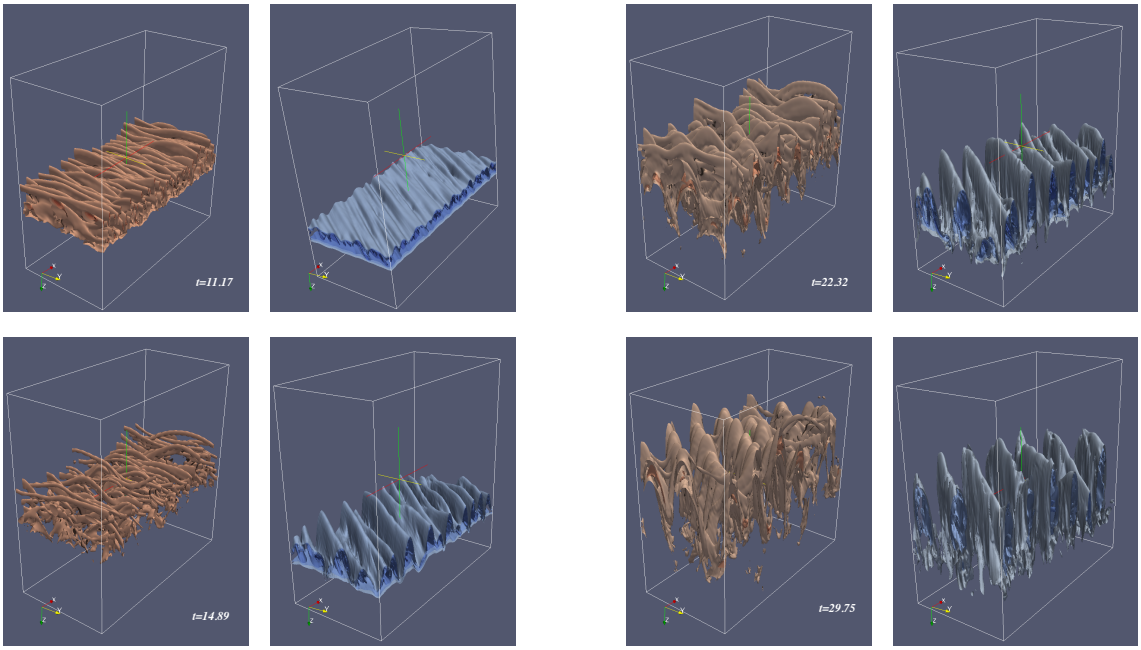

Fig. 2. Evolution of B_y in the two unstable zones within the domain. B_y is positive in the top layer (**left panels**) and negative in the bottom layer (**right panels**). The isosurfaces have dimensionless values between -0.6 and 0.6, with a distance of 0.1 between them. The colour scale is thus kept the same for all snapshots, allowing us to see the effect of magnetic diffusion on the rising layers.

Figure 2 shows isosurfaces of the two unstable layers in this case. We focus on each unstable zone separately, in order to have a clearer idea of what the orientation of the field is in each layer and how the instability sets in. The two different orientations of the field appear clearly in this picture. We note that the positive B_y zone (the top unstable layer) gets unstable before the other layer and very narrow flux tubes start to emerge. This is consistent with the linear analysis of Cattaneo et al. (1990) and Favier et al. (2012) which showed that the presence of an overlying atmosphere with inclined field lines reduces the growth rate of the instability of a magnetic layer.

The two layers then interact and create 3D structures. At $t = 14.89$, the structure of the top unstable layer is very interesting, small arched flux tubes are created and tend to maintain good coherence, a configuration which is quite favorable for the emergence of twisted structures. This is indeed what happens, as will be shown in the next subsection. Both layers now emerge with different speeds and rise towards the top of the layer. We find here that the top unstable layer rises on average more slowly than the bottom one. It is indeed affected more quickly both by viscosity and magnetic diffusion since the instability grows faster and since the flux ropes are smaller scale. As a consequence, at around 20-30 sound crossing times, the unstable modes of the bottom layer start to interact with those of the upper layer and the imprint of the preferred orientation of the modes of the blue layer can be seen on the red layer (top one). There is thus a strong interaction between the modes of various orientations and this will have consequences on the field line structure.

It is worth noticing that the whole layer gets completely disrupted by the magnetic buoyancy instabilities in this case, even though the resonant layer is located in the middle of the magnetic domain (see discussion on the resonant layer by Cattaneo et al. 1990). The vertical velocity (not shown here) indeed shows that downward motions are very strong, concentrated on narrow bands and penetrate very deep into the magnetic domain. It thus results in the complete disruption of the magnetized zone after a few tens of sound crossing times.

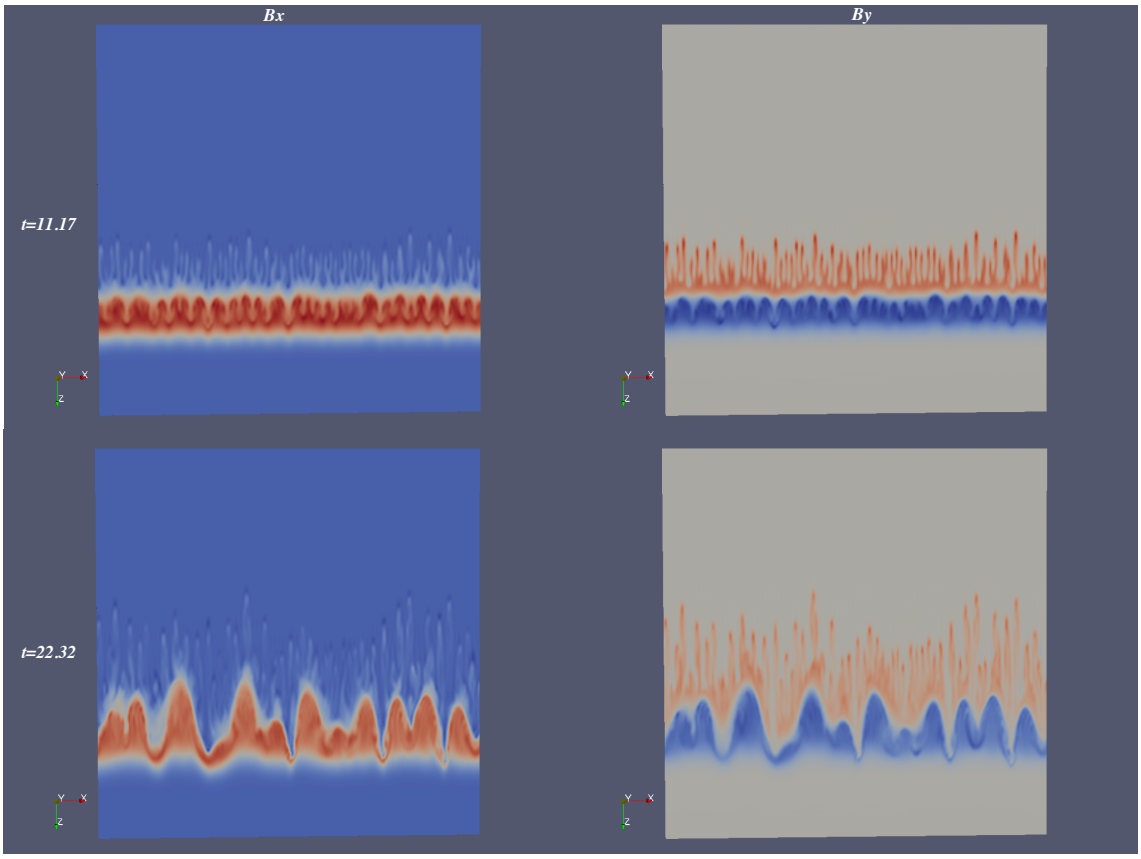

Fig. 3. Cuts at $y = cst$ of the magnetic field components B_x and B_y. For B_x, the colour scale ranges between 0 and 0.8 and for B_y, the range is $-0.6/0.6$. Large-scale magnetic structures are clearly visible on both snapshots.

Figure 3 shows cuts at $y = cst$ and at two specific times of the x and y components of the magnetic field. This picture shows the interaction between the very small scales emanating from the interchange instability of the top layer and the much larger scales below. As shown by Favier et al. (2012) in their more idealized atmosphere, the magnetic tension lying at the interface between the two unstable layers promotes the merging between small-scale structures in the bottom magnetic layer. It is indeed quite clear that between $t = 11.17$ and $t = 22.32$, the top layer has been completely disrupted into small-scale features when the bottom layer has built much larger scales.

As a consequence, large-scale coherent structures are also generated in this less idealized case and could in principle rise through a large number of pressure scale heights before being diffused away or reprocessed by

convective flows in a real stellar convection zone.

3.2 Generation of twisted flux ropes

Finally, since our initial goal was to study the possible generation of twisted flux ropes in these calculations, we focus on the field line configurations, especially on the small unstable structures emerging in this simulation at the top of our magnetic domain. Figure 4 shows some rendering of magnetic field lines around current helicity concentrations in this calculation. As also shown by Favier et al. (2012), the initial configuration chosen here not only favors the generation of large-scale magnetic features from small-scale magnetic buoyancy instabilities but also promotes the creation of twisted flux ropes. Those helical fluxtubes should evolve in the polytropic atmosphere keeping much more coherence than the magnetic structures which are produced in a purely horizontal field case. Indeed, it was shown in multi-dimensional simulations of the dynamics of magnetic flux ropes (e.g. Emonet & Moreno-Insertis 1998) that a certain amount of twist of the field lines was necessary for concentrations of magnetic field to compete against the gravitational torque exerted on the rope during its emergence. Figure 4 shows that in these calculations, helical magnetic structures naturally emerge from the buoyancy instability in an initial configuration where both a longitudinal and a transverse field are present.

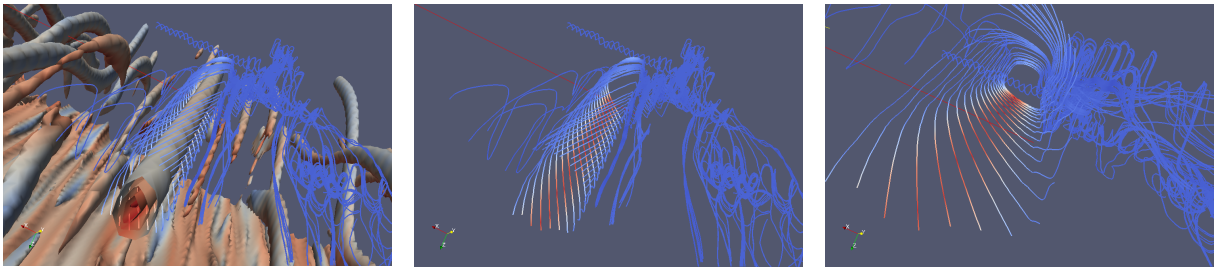

Fig. 4. Field line tracing around small flux ropes created in this simulation through the instability of a magnetically sheared layer.

4 Conclusion

In this work, we studied the development of magnetic buoyancy instabilities of a magnetic layer in which two zones with different orientations of the field lines become unstable. The top layer becomes unstable first, in agreement with linear theory, and the two layers quickly interact, creating large-scale helical structures at the interface where magnetic tension and twist accumulate. The outcome of those calculations is similar to the case studied by Favier et al. (2012) where a layer of field becomes unstable and interacts with a weakly magnetized (and thus stable) atmosphere. We thus show here that despite the more complex configuration of the atmosphere above (created here by the unstable top layer), twisted large-scale magnetic structures can still naturally emerge from buoyancy instabilities. This could in principle explain how strong concentrations of field created at the base of the solar (and stellar) convective zones are able to rise coherently to the surface to create the observed active regions.

We wish to thank S. Brun and B. Dintrans for the organization of Section 11 "Dynamo et magnétisme solaire et stellaire" of the SF2A 2012. We are also thankful to CALMIP for providing us with CPU time with which the calculations presented here were performed.

References

Cattaneo F., Chiueh T. & Hughes D. W. 1990, J. Fluid Mech., 219, 1

Emonet T. & Moreno-Insertis F. 1998, Astrophys. J., 492, 804

Favier, B., Jouve, L., Edmunds, W., Silvers, L.J. & Proctor, M.R.E., 2012, MNRAS, in press

Matthews, P. C., Hughes, D. W. & Proctor, M. R. E. 1995, ApJ, 448, 938

Newcomb, W. A. 1961 Phys. Fluids, 4, 391.

SF2A 2012
S. Boissier, P. de Laverny, N. Nardetto, R. Samadi, D. Valls-Gabaud and H. Wozniak (eds)

DOES INERTIA DETERMINE THE MAGNETIC GEOMETRY OF LOW-MASS STARS?

J. Morin[1], T. Gastine[2], L. Duarte[2], A. Reiners[1], U. R. Christensen[2] and J. Wicht[2]

Abstract. M dwarfs are of prime interest for stellar dynamo theories. They indeed span a wide range of parameters, in terms of relative depth of the convection zone (the lowest-mass M dwarfs being fully convective) and rotation. The number of magnetic field measurements on M dwarfs has been rapidly growing in the past few years, trends are emerging and now need to be understood in the framework of dynamo theory. We detail the analogy between latest anelastic dynamo simulations by Gastine et al. and observations of M-dwarf magnetism, focusing on field geometries derived from spectropolarimetric observations. In geodynamo models, the relative importance of inertia in the force balance is known to have a strong impact on the magnetic field geometry. This can be quantified by the so-called "local Rossby number", which has been found to be a rather universal quantity that allows to separate dipolar and multipolar dynamo models. We discuss its relevance in setting the field geometry of M dwarfs and the transition towards a bistable regime.

Keywords: Dynamo, Stars: magnetic field, Stars: rotation, Stars: low-mass

1 Introduction

M dwarfs – the lowest-mass stars of the main sequence – are of prime interest to study stellar dynamos operating in physical conditions quite remote from the solar case. During the past few years, their surface magnetic fields have been investigated using two complementary approaches: spectroscopy in unpolarized light from which the average magnetic field strength can be derived, and spectropolarimetry which provides a constraint on the geometry of the field at large and intermediate scales (for recent reviews see Donati & Landstreet 2009; Reiners 2012). Using the latter approach combined with Zeeman-Doppler imaging (ZDI, Semel 1989), the study of a sample of about 20 M0-M8 dwarfs points towards a broad variety of magnetic field geometries: partly-convective stars as well as a few fully-convective ones feature complex magnetic structures (Donati et al. 2008; Morin et al. 2010), while most fully-convective ones host a strong axial dipole component (Morin et al. 2008a,b). Explaining such a diversity in the magnetic field geometry is one of the main goals of stellar dynamo theory.

In geodynamo models, the "local Rossby number" – defined by $\mathrm{Ro}_l = u_{\mathrm{rms}}/\Omega l$, l being the typical flow lengthscale – which measures the relative contribution of inertia and Coriolis force in the global balance, has been found to be a rather universal quantity that allows to separate dipolar and multipolar dynamo models. A sharp transition between these two types of dynamo indeed occurs around $\mathrm{Ro}_l \simeq 0.1$ (Christensen & Aubert 2006). However, recent studies employing stress-free mechanical boundary conditions (more appropriate when modelling stellar dynamos) question this view as they found that a dipolar and a multipolar magnetic field can coexist at the same parameter regime depending on the initial condition (e.g. Busse & Simitev 2006), leading to multipolar solutions even for $\mathrm{Ro}_l < 0.1$ (Schrinner et al. 2012). Although most of these studies have been conducted under the Boussinesq approximation (i.e. assuming constant reference state), the parametric study of Gastine et al. (2012) shows that these results remain valid when the effect of moderate density stratification are taken into account.

Several recent studies have shown that dynamo action in planets and low-mass stars share a number of similarities (e.g. Goudard & Dormy 2008; Christensen et al. 2009). Here we discuss the analogy between the anelastic dynamo models of Gastine et al. (2012) and spectropolarimetric observations of M dwarfs (see Morin et al. 2010, and references therein), thereby extending the discussion on possible bistability among very-low-mass stars of Morin et al. (2011a).

[1] Institut für Astrophysik, Georg-August-Universität Göttingen, Friedrich-Hund Platz, 37077 Göttingen, Germany
[2] Max Planck Institut für Sonnensystemforschung, Max-Planck-Straße 2, 37191 Katlenburg Lindau, Germany

2 The dynamo model

We consider MHD simulations of a conducting anelastic fluid in spherical shells rotating at a constant rotation rate Ω about the z-axis. Following Gilman & Glatzmaier (1981), the governing MHD equations are non-dimensionalised using the shell thickness $d = r_o - r_i$ as the reference lengthscale and Ω^{-1} as the time unit. Our dynamo model results are then characterised by several dimensionless diagnostic parameters. The rms flow velocity for instance is given by the Rossby number $\mathrm{Ro} = u_{\mathrm{rms}}/\Omega d$. Following Christensen & Aubert (2006), we also employ the aforementioned local Rossby number $\mathrm{Ro}_l = \mathrm{Ro}\,\bar{\ell}_u/\pi$, that is known to be a more appropriate measure to quantify the impact of inertia on the magnetic field geometry. The mean spherical harmonic degree $\bar{\ell}_u$ is obtained from the kinetic energy spectrum and relates to the typical flow lengthscale l through:

$$l = \pi\, d/\bar{\ell}_u \quad \text{with} \quad \bar{\ell}_u = \sum_{\ell} \ell \frac{\langle \vec{u}_\ell \cdot \vec{u}_\ell \rangle}{\langle \vec{u} \cdot \vec{u} \rangle}, \tag{2.1}$$

where $\vec{u}_\ell$ is the flow velocity at a given spherical harmonic degree ℓ and the brackets correspond to an average over time and radius. The magnetic field strength is measured by the Elsasser number $\Lambda = B_{\mathrm{rms}}^2/\rho\mu\lambda\Omega$, where ρ is the density, and μ and λ are the magnetic permeability and diffusivity. The geometry of the surface field is quantified by its dipolarity f_{dip} that measures the ratio of the magnetic energy of the dipole to the magnetic energy contained in spherical harmonic degrees up to $\ell_{\mathrm{max}} = 11$. The dimensionless MHD equations are advanced in time with the spectral code MagIC (Wicht 2002; Gastine & Wicht 2012) that uses the anelastic formulation of Lantz & Fan (1999) and has been validated against several dynamo benchmarks (Jones et al. 2011). We rely in the following on the results of the parameter study of Gastine et al. (2012).

3 Spectropolarimetric observations

Spectropolarimetric observations of 23 active M0-M8 dwarfs with rotation periods ranging from 0.4 to 19 days have been carried out. For each star at least one time-series of unpolarized and circularly polarized spectra sampling a few rotation periods has been obtained. The data reduction and analysis is detailed by Donati et al. (2006, 2008) and Morin et al. (2008a,b, 2010).

The relative importance of inertia with respect to the Coriolis force in the convection zone of these stars is assessed through an empirical Rossby number given by

$$\mathrm{Ro}_{\mathrm{emp}} = \frac{P_{\mathrm{rot}}}{\tau_{\mathrm{conv}}}, \tag{3.1}$$

where τ_{conv} is the empirical turnover timescale of convection based on the rotation-activity relation (Kiraga & Stepien 2007). This Rossby number misses explicitly the flow lengthscale l involved in Ro_l. However, as τ_{conv} is based on the average convective turnover time it encompasses this scale information to some extent. We thus use $\mathrm{Ro}_{\mathrm{emp}}$ as our best available proxy for Ro_l.

For each obtained spectrum, an average line profile with increased signal-to-noise ratio is computed using the least-squares deconvolution technique (LSD, Donati et al. 1997). Each time-series of LSD profiles is modelled with ZDI, resulting in a map of the large-scale component of the surface magnetic field vector that satisfies a maximum-entropy criterion. The large-scale magnetic fields of most of these stars fall into two distinct groups: one is dominated by a strong axial dipole and the other by a much weaker and non-axisymmetric field.

Similarly to Morin et al. (2011b), we define an Elsasser number based on the averaged unsigned large-scale magnetic field $\langle \mathrm{B_V} \rangle$ which roughly characterises the ratio of the Lorentz and Coriolis forces. We also consider the fraction of the magnetic energy that is recovered in the axial dipole mode in ZDI maps. The spatial resolution of such maps mostly depends on $v \sin i$ and the actual degree ℓ_{max} up to which the reconstruction can be performed ranges from 4 to 10, although very little energy is recovered in modes with $4 < \ell \leq 10$. We therefore directly compare this quantity to the dipolarity employed in numerical models and term them both f_{dip}. We however note that in simulations, f_{dip} does not strongly depend on the chosen ℓ_{max}, whereas for the observation-based dipolarity, considering the ratio of magnetic energy in the axial dipole relative to the total magnetic energy derived from unpolarized spectroscopy (instead of the large-scale magnetic energy derived from spectropolarimetric data with ZDI) would lead to much lower values of f_{dip} (cf. Reiners & Basri 2009). We attribute this difference to the low magnetic Reynolds number ($\mathrm{Rm} \sim 100 - 500$) accessible by numerical simulations which does not allow for a significant small-scale field to be generated – hence the weak dependence of f_{dip} on ℓ_{max} – while in stellar interiors large-scale and small-scale dynamo action likely coexist (e.g. Cattaneo & Hughes 2009).

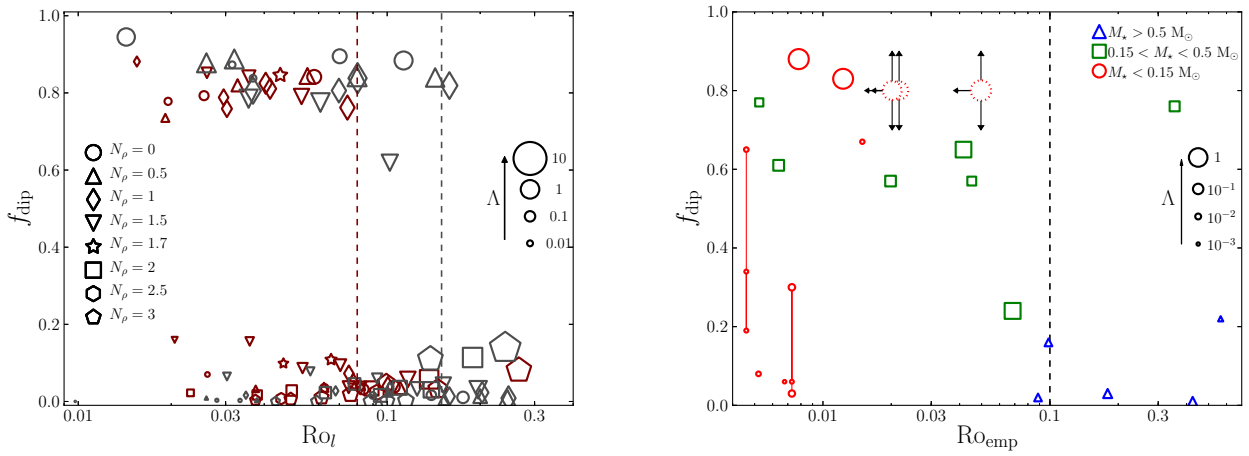

Fig. 1. Left: Relative dipole strength plotted against Ro_l in anelastic dynamo models. Red (grey) symbols correspond to simulations in thick (thin) shells ($r_i/r_o = 0.2$ and $r_i/r_o = 0.6$, respectively) and their size is scaled according to the value of the surface field, expressed in units of the square root of the Elsasser number. Each type of symbols corresponds to a given density contrast. The vertical lines mark the tentative limits for dipolar dynamos. **Right:** Relative dipole strength plotted against $\mathrm{Ro}_{\rm emp}$. Symbol sizes scale with the Elsasser number based on the average large-scale magnetic field derived from spectropolarimetric observations. The vertical dashed line marks the tentative limit for the dipolar regime. For the two stars exhibiting the largest temporal variations, the individual epochs are shown and connected by a vertical red line. Dotted red circles with black arrows correspond to stars from Morin et al. (2010) for which ZDI reconstruction could not be achieved, only upper limit for the rotation period and an estimate of dipolarity were derived.

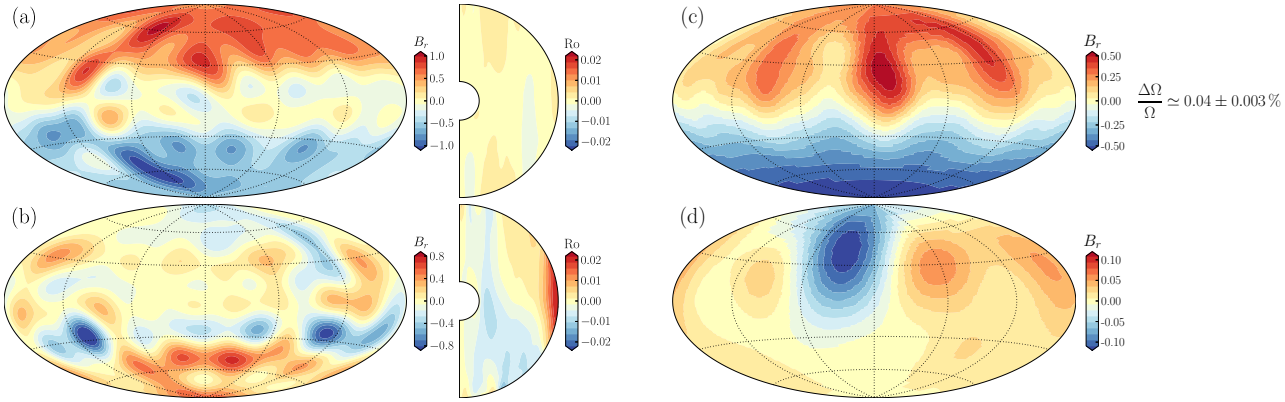

Fig. 2. Left: Radial component of the surface magnetic field $B_r(r = r_0)$ and axisymmetric zonal flows $\overline{u_\phi}$ for a dipolar dynamo model (**a**) and a multipolar one (**b**) with similar density contrast $N_\rho \simeq 2$. The maps of B_r have been low-pass filtered up to $\ell_{\rm max} = 10$. Magnetic fields are expressed in units of the square root of the Elsasser number and velocities in units of the Rossby number. **Right:** Radial component of the surface magnetic field of V374 Peg (**c**) and GJ 1245 B (**d**) recovered with ZDI from spectropolarimetric observations of Donati et al. (2006) and Morin et al. (2010), respectively. The field has been reconstructed up to $\ell_{\rm max} = 10$ (4) for V374 Peg (GJ 1245 B). Surface differential rotation of V374 Peg has been derived by Morin et al. (2008b) from spectropolarimetric observations, while this was not possible for GJ 1245 B. Magnetic fields are expressed in units of the square root of the Elsasser number.

4 Results and conclusions

Spectropolarimetric observations of active M dwarfs and dynamo models show a broad variety of magnetic geometries (see Gastine et al. 2012; Morin et al. 2010, and references therein). In both cases, dipolar and multipolar large-scale magnetic fields are found to coexist at low Rossby numbers. Here we briefly discuss the analogy between these two results, the reader is referred to Gastine et al. (submitted) for more details.

We derive observation-based quantities aimed to reflect the diagnostic parameters employed in the numerical

models (Ro_l, Λ and f_{dip}), although these crude proxies are not expected to provide a direct quantitative match. Within these limits, we draw an interesting analogy between the observational parameters and their numerical counterparts: for large values of the Rossby numbers multipolar fields are found, while below a critical value around $\mathrm{Ro}_l \sim \mathrm{Ro}_{\mathrm{emp}} \sim 0.1$, a bistable region exists where both dipolar and multipolar fields can be generated (see Fig. 1, 2). Several limitations must be noted though. *(i)* The spectropolarimetric sample is biased as all stars at high (low) $\mathrm{Ro}_{\mathrm{emp}}$ are partly (fully) convective. Thus it is not yet clear if the change in f_{dip} observed around $\mathrm{Ro}_{\mathrm{emp}} \sim 0.1$ can be attributed to a threshold in Ro_l or rather to the drastic changes in stellar structure occurring at the fully-convective transition. *(ii)* As the numerical models of Gastine et al. (2012) do not attempt to model a tachocline, they might miss some important features of early M dwarfs magnetism. However this issue does not question the validity of the agreement between observations and simulations regarding the existence of a bistable dynamo regime at low Ro_l for fully-convective stars. *(iii)* In numerical models, the dipolar branch only exists for moderate density contrasts ($N_\rho \leq 2$), much below the stratification of stellar interiors. Different assumptions from those considered by Gastine et al. (2012) could possibly extend the dipolar regime towards higher stratifications, for instance by using different values of Prandtl numbers (Simitev & Busse 2009) or radius-dependent properties (e.g. thermal and ohmic diffusivities).

The analogy between numerical models and magnetic properties of M dwarfs can be further assessed with additional observations, as it implies that: *(i)* stars with multipolar fields can be found over the whole parameter range where also dipole-dominated large-scale fields are observed; *(ii)* in the bistable domain, stars on the multipolar branch have a much stronger surface differential rotation than those on the dipolar branch.

We thank A. S. Brun, B. Dintrans and Y. Ponty for giving us the opportunity to present these results during the session "Dynamos and solar/stellar magnetism". JM acknowledges funding as a postdoctoral fellow of the Alexander von Humboldt foundation. TG and LD are supported by the Special Priority Program 1488 (PlanetMag, `http://www.planetmag.de`) of the German Science Foundation.

References

Busse, F. H. & Simitev, R. D. 2006, GAFD, 100, 341

Cattaneo, F. & Hughes, D. W. 2009, MNRAS, 395, L48

Christensen, U. R. & Aubert, J. 2006, GJI, 166, 97

Christensen, U. R., Holzwarth, V., & Reiners, A. 2009, Nature, 457, 167

Donati, J.-F., Forveille, T., Cameron, A. C., et al. 2006, Science, 311, 633

Donati, J.-F. & Landstreet, J. D. 2009, ARA&A, 47, 333

Donati, J.-F., Morin, J., Petit, P., et al. 2008, MNRAS, 390, 545

Donati, J.-F., Semel, M., Carter, B. D., et al. 1997, MNRAS, 291, 658

Gastine, T., Duarte, L., & Wicht, J. 2012, A&A, 546, A19

Gastine, T. & Wicht, J. 2012, Icarus, 219, 428

Gilman, P. A. & Glatzmaier, G. A. 1981, ApJS, 45, 335

Goudard, L. & Dormy, E. 2008, Europhysics Letters, 83, 59001

Jones, C. A., Boronski, P., Brun, A. S., et al. 2011, Icarus, 216, 120

Kiraga, M. & Stepien, K. 2007, Acta Astronomica, 57, 149

Lantz, S. R. & Fan, Y. 1999, ApJS, 121, 247

Morin, J., Delfosse, X., Donati, J.-F., et al. 2011a, in SF2A-2011: Proceedings of the Annual meeting of the French Society of Astronomy and Astrophysics, ed. G. Alecian, K. Belkacem, R. Samadi, & D. Valls-Gabaud, 503–508

Morin, J., Donati, J., Petit, P., et al. 2008a, MNRAS, 390, 567

Morin, J., Donati, J.-F., Forveille, T., et al. 2008b, MNRAS, 384, 77

Morin, J., Donati, J.-F., Petit, P., et al. 2010, MNRAS, 407, 2269

Morin, J., Dormy, E., Schrinner, M., & Donati, J.-F. 2011b, MNRAS, 418, L133

Reiners, A. 2012, Living Reviews in Solar Physics, 9, 1

Reiners, A. & Basri, G. 2009, A&A, 496, 787

Schrinner, M., Petitdemange, L., & Dormy, E. 2012, ApJ, 752, 121

Semel, M. 1989, A&A, 225, 456

Simitev, R. D. & Busse, F. H. 2009, Europhysics Letters, 85, 19001

Wicht, J. 2002, Physics of the Earth and Planetary Interiors, 132, 281

SF2A 2012
S. Boissier, P. de Laverny, N. Nardetto, R. Samadi, D. Valls-Gabaud and H. Wozniak (eds)

ON CLOSE-IN MAGNETIZED STAR-PLANET INTERACTIONS

A. Strugarek[1], A. S. Brun[1] and S. Matt[1]

Abstract. We present 2D magnetohydrodynamic simulations performed with the PLUTO code to model magnetized star-planet interactions. We study two simple scenarios of magnetized star-planet interactions: the *unipolar* and *dipolar* interactions. Despite the simplified hypotheses we consider in the model, the qualitative behavior of the interactions is very well recovered. These encouraging results promote further developments of the model to obtain predictions on the effect and the physical manifestation of magnetized star–close-in planet interactions.

Keywords: Stars: winds, Stars: planetary systems, Stars: coronae

1 Introduction

More than 830 exo-planets have been presently discovered[i]. The interactions between stars and their orbiting planets can be distinguished between *distant* gravitational (orbital motions, tides) and *direct* (hydro-)magnetic (stellar wind, radiation) interplays. Both interactions are likely to play a major role in determining habitability zones and in understanding planet dynamics. In addition, close-in giant planets may also impact the rotation and magnetic properties of their host stars (Donati et al. 2008; Bolmont et al. 2012). Finally, the magnetized interactions can yield enhanced localized emissions in the chromospheres of their host stars (Shkolnik et al. 2005). For these reasons, a better characterization of star-planet interactions (SPIs) would be highly valuable (Cuntz et al. 2000; Ip et al. 2004; Lanza 2009). In this paper, we focus on basic mechanisms that underly the *direct* magnetized SPIs.

Magnetized SPIs can be separated into two classes: the so-called *unipolar* (magnetized wind, unmagnetized planet) and *dipolar* (magnetized wind and planet) interactions (Zarka 2007). They were initially studied in the context of satellites orbiting in the magnetosphere of giant planets (Kivelson et al. 2004). The space plasma in the upper magnetospheres of planets and in stellar winds is characterized by a Knudsen number (mean free path over characteristic size of the system) much greater than unity. Hence, the fluid approximation does not hold because there is *a priori* no reason to consider that the plasma is locally thermally equilibrated: a kinetic modeling should be used to accurately represent it (Marsch 2006). Because of limited computation resources, the large scales involved in magnetized SPIs prevent us to use a global kinetic modeling. Magnetohydrodynamic (MHD) models (which are less expensive to simulate) have been therefore widely used instead. Such models are able to recover the global properties of stellar winds (Goldstein et al. 1995) and have been used either by fitting the equation of state to recover the exact solar wind (Wang & Sheeley 1990; Arge & Pizzo 2000), or by conducting parametric studies to derive general scaling laws (Washimi & Shibata 1993; Matt et al. 2012, and references therein). Cohen et al. (2011) simulated magnetized SPIs based on the former kind of modeling (using the so-called *WSA* model). In this paper, we base our study on the latter modeling approach, which will allow us to derive robust scaling laws for magnetized SPIs.

We develop in section 2 the method we use to study magnetized SPIs. Then, we apply our setup to the two basic cases of the unipolar and diploar interactions in section 3. We validate the modeling choices we made and are able to predict the action of a close-in planet on the stellar surface flows. Finally, we give the perspectives of this preliminary work in section 4.

[1] Laboratoire AIM Paris-Saclay, CEA/Irfu Université Paris-Diderot CNRS/INSU, F-91191 Gif-sur-Yvette.
[i] `http://exoplanet.eu`

2 Modeling magnetized star-planet interactions

The magnetized SPIs consists of the interaction between the magnetized wind of the host star and the magnetized or unmagnetized planet. Any modeling tackling these interactions have to treat plasmas associated with both the wind and the planet.

2.1 Wind modeling

Following numerous previous studies (*e.g.*, Ustyugova et al. 1999), we use standard MHD wind theory that characterizes magnetized steady-state flows anchored at the surface of a rotating star. The exact wind driving mechanism is still debated today, its details should not matter for the purpose of this paper. Hence we make the assumption that it is driven by the thermal pressure of the coronal plasma (which is a common basic assumption, *e.g.*, in the case of the solar wind).

We use the PLUTO code (Mignone et al. 2007) to calculate steady-state winds using the ideal compressible MHD equations (written here in their primitive formulation for simplicity)

$$\partial_t \rho + \boldsymbol{\nabla}\cdot(\rho\mathbf{v}) = 0\,, \tag{2.1}$$

$$\partial_t \mathbf{v} + \mathbf{v}\cdot\boldsymbol{\nabla}\mathbf{v} + \frac{1}{\rho}\boldsymbol{\nabla}P + \frac{1}{\rho}\mathbf{B}\times\boldsymbol{\nabla}\times\mathbf{B} = \mathbf{g}\,, \tag{2.2}$$

$$\partial_t P + \mathbf{v}\cdot\boldsymbol{\nabla}P + \rho c_s^2\boldsymbol{\nabla}\cdot\mathbf{v} = 0\,, \tag{2.3}$$

$$\partial_t \mathbf{B} - \boldsymbol{\nabla}(\mathbf{v}\times\mathbf{B}) = 0\,, \tag{2.4}$$

where ρ is the density, $\mathbf{v}$ the velocity, P the gas pressure, $\mathbf{B}$ the magnetic field, $\mathbf{g}$ the gravitational acceleration, ∂_t the derivative with respect to time and $c_s = \sqrt{\gamma\,P/\rho}$ the sound speed (γ is the polytropic index of the plasma). We use an ideal gas equation of state.

We use the following options in PLUTO to run our simulations. A minmod limiter on all the variables and a *hll* (Harten, Lax, Van Leer) solver to compute the intercell fluxes. A second order Runge-Kutta scheme is used for the time evolution. The solenoidality of the magnetic field ($\boldsymbol{\nabla}\cdot\mathbf{B} = 0$) is ensured with a *constrained transport* (CT) method (*e.g.*, Gardiner & Stone 2005).

We initialize our simulation with the spherically symmetric hydrodynamic Parker solution (Parker 1958). We add a dipolar magnetic field characterized by the ratio $v_A/v_{\rm esc} = 0.32$ at the surface of the star ($v_A = B/\sqrt{4\pi\rho}$ is the Alfvèn speed and $v_{\rm esc} = \sqrt{2GM_\star/R_\star}$ is the escape speed). We developed special boundary conditions (Matt & Pudritz 2008; Zanni & Ferreira 2009) that ensure the conservation of the five quantities theoretically conserved along field lines that were identified by Lovelace et al. (1986) and Keppens & Goedbloed (2000). The parameters and characteristics of the simulated wind are given in table 1. The wind exhibits a large dead zone (closed field lines and very slow motions region) inside its alfvenic surface that extends up to $r \sim 7\,R_\star$ at the equator. We develop hereafter the methodology we use to simulate an orbiting planet.

Table 1. Parameters and deduced characteristics of the simulated stellar wind. The parameter $v_{\rm rot}/v_{\rm esc}$ sets the rotation rate of the star. The mass loss rate is normalized to $\rho_\star v_{\rm esc} R_\star^2$ and the angular momentum loss rate to $\rho_\star v_{\rm esc}^2 R_\star^3$. The ratio between opened and closed field lines is given by $\Psi_{\rm o}/\Psi_\star$ ($1-\Psi_{\rm o}/\Psi_\star$ gives the size of the dead zone, with $\Psi_{\rm o} \equiv \oint \mathbf{B}\cdot{\rm d}\mathbf{A}$). Finally, we give the typical poloidal velocity of the wind at ($r = 15\,R_\star, \theta = 45°$).

Parameters	γ	$c_{\rm s}/v_{\rm esc}$	$v_{\rm rot}/v_{\rm esc}$	$v_{\rm A}/v_{\rm esc}$
	1.05	0.2220	0.00303	0.3183
Characteristics	$\dot{m}$	$\Psi_{\rm o}/\Psi_\star$	$\dot{j}$	$v_{\rm p}/v_{\rm esc}$ ($15r_*$, 45°)
	6.48 10^{-4}	0.251	7.12 10^{-4}	0.250

2.2 Planet modeling

We introduce a planet as a boundary condition inside the computational domain. We choose to study only close-in planets in this paper, *i.e.* planets which are *inside* the dead-zone of the stellar wind. Hence, we introduce a very close planet at $r_{\rm orb} = 2.5\,R_\star$. The type of interaction between the two bodies is determined by the topology of the planetary magnetic field. We choose a heavy Jupiter-like planet such that $r_P = 0.1\,R_\star$ ($R_J \sim 0.1\,R_\odot$) and $m_p = 0.01\,M_\star$ ($M_J = 0.001\,M_\odot$). We design a stretched grid such that the typical resolution is of the order

of $r_P/32$ at the planet surface and of $R_\star/64$ at the stellar surface. We ensured the numerical convergence of our results when increasing the resolution by a factor two.

The initialization of the planet in the steady-state wind creates a transient evolution that is rapidly forgotten. Because we use an idealized axisymmetric configuration (the so-called 2.5D approximation, *i.e.*, we study the 3D fields only on an axisymmetric poloidal plane), the planet we simulate has the shape of a torus circling the star, rather than a sphere. As a consequence, the orbital motion does not introduce any time-variability in the orbital direction and a new steady-state can be obtained. Even if this situation is far from reality, it constitutes a first step towards the realistic modeling of magnetized SPIs (see perspectives in section 4).

3 Basic interactions

As mentioned in the introduction, the magnetized SPIs can be decomposed into *unipolar* and *dipolar* interactions (Zarka 2007). We successively simulate the two situations in the following, which are very well recovered by our model.

– **Unipolar interaction** – We introduce a unmagnetized rotating planet in the dead zone of the simulated wind (section 2.1). This system is equivalent to the well known interaction of Io in the magnetosphere of Jupiter. The unmagnetized planet drags the poloidal magnetic field lines and current sheets establish along the poloidal field lines connecting the planet to the host star (Goldreich & Lynden-Bell 1969). We indeed observe a current loop in figure 1(a) that connect the planet and the star together (the black arrows represent the current density $\mathbf{J} = \boldsymbol{\nabla} \times \mathbf{B}$). An azimuthal component of the magnetic field (B_φ) is also naturally created through an effective 'Omega'-effect generated by the orbital motion of the planet. A steady state situation is achieved when the numerical diffusion of the magnetic field in the azimuthal direction is balanced by the continuous twisting action of the differential rotation between the star and planet orbit. A steady state return flow from the planet to the star is then associated with the magnetic flux-tube. The magnetic connection between the star and the planet implies the existence of a torque between the two objects. The planet orbits at the keplerian velocity (such that its orbital motion compensates the stellar gravitational pull), hence it rotates much faster than the stellar surface (*i.e.*, the co-rotation radius is larger than the orbital radius of the planet). The planet exerts consequently a torque localized in latitude which is approximately 4 times larger (and of opposite sign) than the overall torque exerted by the stellar wind when no planet is taken into account. The exact value of the torque is likely to depend on both *(i)* the fact that we are considering a 2D setup and *(ii)* the amount of numerical diffusivity.

– **Dipolar interaction** – We also perform the exact same simulation with a *magnetized* planet. We choose a dipolar planetary magnetic field anti-aligned with the initial stellar dipole (we choose its original amplitude such that the initial planetary magnetosphere is of the order of $2\,r_p$). As a consequence, the closed magnetic field lines of the wind naturally connect at the poles of the planet, and magnetic reconnection occur at the equator where the magnetic field lines of the wind and of the planet are anti-aligned. We also note here that the planetary field only resembles a dipole in the poloidal plane but was slightly modified to preserve $\boldsymbol{\nabla} \cdot \mathbf{B} = 0$ in an axisymmetric geometry. We display in figure 1(b) the interaction between the magnetized planet and the stellar wind.

Reconnections of the magnetic field lines occur at the equator and are labeled by the dashed white line. We see that the field lines connect together the planet and the stellar surfaces (dashed red line). Because these field lines are close to the closed-opened field lines boundary, they tend to be advected by the stellar wind and are stretched away from the planet (yellow dashed line). Reconnection then occur again and the magnetic field lines close in the magneto-tail of the planetary magnetosphere (black dashed line). This process is very similar to the basic reconnection mechanism developed to explain the structure of the magnetosphere of the planets of the solar system (Gombosi 1998).

We recall here that these numerical experiments are done in the framework of ideal MHD. Hence, any reconnection occurring in the simulations is controlled by the effective diffusion introduced by the numerical techniques we use. In order to quantitatively characterize the reconnection process we observe, a better control of the ohmic diffusion is mandatory and will be adressed in future work.

Finally, the magnetic connection between the two objects is stronger than in the unipolar case and the torque exerted by the planet on the stellar surface is roughly twenty times larger (and of opposite magnitude) than the torque exerted by the stellar wind.

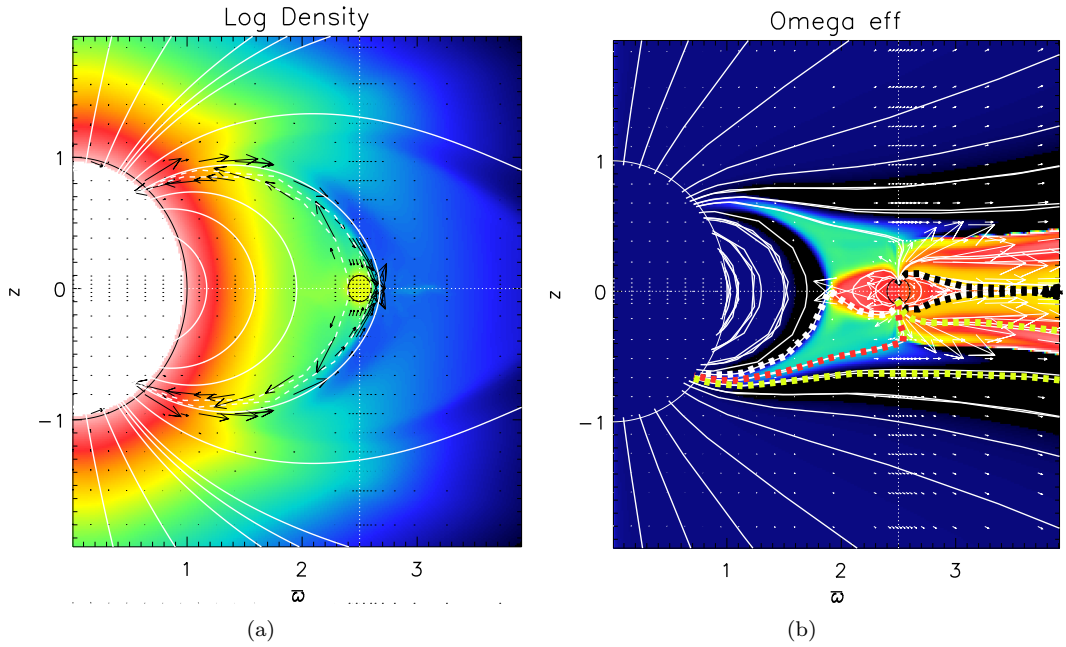

Fig. 1. Left: Simulation of the unipolar interaction. The color map represents the logarithm of density (blue/black is low density, red/white high density) and the black arrows are the current density **J**. **Right:** Simulation of the dipolar interaction. The colormap represent the effective rotation rate $\Omega_{\rm eff} = \frac{1}{\varpi}\left(v_\varphi - \frac{\mathbf{v}_p\cdot\mathbf{B}_p}{B_p^2}B_\varphi\right)$, where (ϖ, φ, z) are the cylindrical coordinates and the subscript p denotes the poloidal (ϖ, z) component of the field. The rotation rate of the star is blue. The white arrows are the velocity field.

4 Conclusions and perspectives

In this paper, we demonstrated that ideal MHD simulations in 2D axisymmetric geometry could well capture the basic magnetized SPIs involving a close-in giant planet orbiting inside the alfvenic surface of its host star. We tested both the unipolar (unmagnetized planet) and dipole (magnetized planet) interactions and showed that the former were likely to exert a greater torque on the stellar surface. Because the planet orbital motion and the rotation rate of the star are fixed, the applied torque does not modify the surface rotation nor the planet orbit. Fixing them is legitimate here since approximately 10^{14} orbits would be required to change the orbital radius by $0.1\,R_\star$ in the unipolar case (based on the observed torque in the simulations). This picture may drastically change when varying the wind and planet parameters.

We established a modeling framework that will allow us to develop a complete numerical analysis of magnetized SPIs. The obvious next step consist naturally in simulating the star-planet pairs in 3D in order to let the interaction develop in the correct geometry. Then, we will be able to explore the various interaction regimes depending on the magnetic topologies and time-variability of the stellar and planetary fields, and on the position of the planetary orbit in the stellar wind. Finally, we also intend to develop tools to determine the expected level of emissions resulting from the magnetized SPIs (*e.g.*, see Vidotto et al. 2012). This work will lead to reliable scaling laws on the effect of magnetized SPIs that will be useful to explain and guide exoplanet observations, but also to test fundamental ideas explaining the physical processes underlying these interactions.

The authors thank N. Bessolaz, R. Pinto and C. Zanni for very helpful discussions at the origin of this work.

References

Arge, C. N. & Pizzo, V. J. 2000, JGR, 105, 10465
Bolmont, E., Raymond, S. N., Leconte, J., & Matt, S. P. 2012, A&A, 544, 124
Cohen, O., Kashyap, V. L., Drake, J. J., et al. 2011, ApJ, 733, 67
Cuntz, M., Saar, S. H., & Musielak, Z. E. 2000, ApJ, 533, L151

Donati, J.-F., Moutou, C., Fares, R., et al. 2008, MNRAS, 385, 1179
Gardiner, T. A. & Stone, J. M. 2005, JCP, 205, 509
Goldreich, P. & Lynden-Bell, D. 1969, ApJ, 156, 59
Goldstein, M. L., Roberts, D. A., & Matthaeus, W. H. 1995, Annual Review of A&A, 33, 283
Gombosi, T. I. 1998, Physics of the space environment (Physics of the space environment / Tamas I. Gombosi. Cambridge ; New York : Cambridge University Press)
Ip, W.-H., Kopp, A., & Hu, J.-H. 2004, ApJ, 602, L53
Keppens, R. & Goedbloed, J. P. 2000, ApJ, 530, 1036
Kivelson, M. G., Bagenal, F., Kurth, W. S., et al. 2004, In: Jupiter. The planet, 513
Lanza, A. F. 2009, Astronomy and Astrophysics, 505, 339
Lovelace, R. V. E., Mehanian, C., Mobarry, C. M., & Sulkanen, M. E. 1986, ApJ Supp. Series, 62, 1
Marsch, E. 2006, Living Review on Solar Physics, 3, 1
Matt, S. & Pudritz, R. E. 2008, ApJ, 678, 1109
Matt, S. P., MacGregor, K. B., Pinsonneault, M. H., & Greene, T. P. 2012, ApJ Letters, 754, L26
Mignone, A., Bodo, G., Massaglia, S., et al. 2007, ApJ Supp. Series, 170, 228
Parker, E. N. 1958, ApJ, 128, 664
Shkolnik, E. L., Walker, G. A. H., Bohlender, D. A., Gu, P. G., & Kürster, M. 2005, ApJ, 622, 1075
Ustyugova, G. V., Koldoba, A. V., Romanova, M. M., Chechetkin, V. M., & Lovelace, R. V. E. 1999, ApJ, 516, 221
Vidotto, A. A., Fares, R., Jardine, M., et al. 2012, arXiv: 1204.3843
Wang, Y.-M. & Sheeley, N. R. J. 1990, ApJ, 355, 726
Washimi, H. & Shibata, S. 1993, MNRAS, 262, 936
Zanni, C. & Ferreira, J. 2009, A&A, 508, 1117
Zarka, P. 2007, Planetary and Space Science, 55, 598

Session 12

Baryon Acoustic Oscillations (BAO)

SF2A 2012
S. Boissier, P. de Laverny, N. Nardetto, R. Samadi, D. Valls-Gabaud and H. Wozniak (eds)

THE ELG TARGET SELECTION WITH THE BOSS SURVEY

S. Escoffier[1], J. Comparat[2], A. Ealet[1], J.-P. Kneib[2], J. Zoubian[2] and F. Lamareille[3]

Abstract. The Baryon Acoustic Oscillation (BAO) feature in the power spectrum of galaxies can be used as a standard ruler to probe the accelerated expansion of the Universe. In this paper, we study several galaxy selection schemes aiming at building an emission-line galaxy (ELG) sample in the redshift range $0.6 < z < 1.7$, that would be suitable for future BAO studies using the Baryonic Oscillation Spectroscopic Survey (BOSS) spectrograph on the Sloan Digital Sky Survey (SDSS) telescope. We explore two different color selections using both the SDSS and the Canada-France-Hawaii Telescope Legacy Survey (CFHTLS) photometry in the u, g, r, i bands and evaluate their performance for selecting bright ELG. This study confirms the feasibility of massive ELG surveys using the BOSS spectrographs on the SDSS telescope for a BAO detection at redshift $z \sim 1$, in particular for the proposed eBOSS experiment.

Keywords: BOSS, Emission Line Galaxies (ELG), target selection

1 Introduction

The evidence for the acceleration of the expansion of the Universe (Riess et al. 1998; Perlmutter et al. 1999) led to the existence of a new, enigmatic dark energy that opposes the self-attraction of matter. Even though the ΛCDM model, which consists of an inflationary cold dark matter model with a cosmological constant, is strongly favored, other interpretations have been suggested to explain cosmic acceleration. Alternatives involve scalar field models as quintessence, modification of the General Relativity itself on cosmological scales or extra dimensions of space-time. There is no doubt that understanding the nature of dark energy is one of the most important puzzles nowadays in cosmology.

Observational exploration is crucial to provide clues to the energy content of the Universe. One of the leading methods for measuring the expansion history is to use the Baryon Acoustic Oscillations feature (BAO) in the clustering of galaxies as a standard ruler (Seo & Eisenstein 2003). The BAO refer to the imprint of acoustic waves in the early Universe frozen after the decoupling of baryons and photons. Anticipated as a potential effect of the CMB as early as 1970s (Peebles & Yu 1970; Sunyaev & Zeldovich 1970), the first convincing BAO detections came in 2005 from the SDSS Data Release 3 (DR3) and the final 2dFGRS samples (Eisenstein et al. 2005; Cole et al. 2005). Recently, new BAO detections have been reported. Beutler et al. (2011) reported a 4.5% distance measurement at low redshift $z \sim 0.1$ with the 6dFGRS sample, and the acoustic scale has been measured in the redshift range $0.16 < z < 0.47$ by the final SDSS-II sample (DR7) with a distance precision of 2.7% (Percival et al. 2010; Kazin et al. 2010). Steping beyond $z = 0.5$, BAO feature has been measured in the SDSS-III Baryon Oscillation Spectroscopic Survey (BOSS;(Dawson et al. 2012)) (DR9) with a sample of higher redshift luminous red galaxies (LRG) in the redshift range $0.43 < z < 0.7$ (Anderson et al. 2012). Adding to these data, the WiggleZ Dark Energy Survey has quantified BAO by targeting bright emission-line galaxies (ELG) in the range $0.3 < z < 0.9$ (Blake et al. 2011).

In summary, the BAO peak has been detected in several galaxy samples to $z < 1$, and there are strong motivations for extending these large-scale structure measurements to higher redshifts. The BAO method measures the cosmic distance in both radial and transverse directions, giving the Hubble parameter $H(z)$ and the angular diameter distance $D_A(z)$, respectively. Beyond the BAO, the full shape of the galaxy power spectrum

[1] CPPM, Aix-Marseille Université, CNRS/IN2P3, Marseille, France
[2] Aix Marseille Université, CNRS, LAM (Laboratoire d'Astrophysique de Marseille) UMR 7326, 13388, Marseille, France
[3] Université de Toulouse, UPS-OMP, IRAP, Toulouse, France

provides useful information to constrain cosmological parameters and even to test deviations from Einstein's theory of gravity (White et al. 2009). Thought to be the cosmological probe the least affected by systematic uncertainties according to the Dark Energy Task Force (DETF;(Albrecht et al. 2006)), the BAO probe requires to map very large cosmic volumes to achieve a precise distance measurement (as baryons comprise only a small fraction of matter, the amplitude of the BAO peak is small). In addition, resolving the features of BAO along the line-of-sight motivates the need for spectroscopic redshift surveys. The next generation of cosmological surveys (the stage IV facilities as defined in the DETF report) plans to map the high redshift Universe in the range $0.6 < z < 2$. On the ground, BigBOSS would carry out spectroscopic surveys of 10 million galaxies by targeting LRG to $z = 1$ and ELG to $z = 1.7$ (Schlegel et al. 2011). In space, the ESA's Euclid mission plans to measure redshifts of 50 million strong Hα emitters in the redshift range $0.7 < z < 2$ (Laureijs et al. 2011).

Motivated by future BAO surveys as eBOSS[i] or BigBOSS, this paper deals with a galaxy target selection to identify ELG in the redshift range $0.6 < z < 1.7$. Section 2 describes the color selection using imaging data from the Sloan Digital Sky Survey (SDSS) and the Canada-France-Hawaii Telescope Legacy Survey (CFHTLS). In section 3 we describe the simulation of ELG spectra using the Cosmos Mock Catalog as well as the expected redshift success rate when spectra are observed with the BOSS spectrograph. Section 4 concludes with the visual inspection of $2,000$ spectra observed during an ancillary program of BOSS dedicated to this study.

2 The ELG color selection

At lower redshift, luminous red galaxies are good candidates for spectroscopic surveys as they have strong absorption features like the 4000 break. However, from $z > 1$, the 4000 break moves into the infrared and, as red galaxies become very faint, long exposure time is required. Moreover density of LRG targets falls dramatically at $z > 1$ as shown in Fig. 1. At high redshift near $z \sim 3$, a challenging option is to target quasars (QSOs). By instance, one of the key goals of the BOSS project is to study BAO features using Lyman-α forest absorption spectra of distant quasars in the range $2.2 < z < 3.5$ (McDonald & Eisenstein 2007; Ross et al. 2012). When working at $z \sim 1$, a relevant choice is emission-line galaxies, including both strongly star-forming galaxies and emission-line QSOs. In this paper, we only consider star-forming emission-line galaxies that we call ELG. One of the advantages of ELG is that emission lines can be detected even when the continuum is weak. The redshift extraction is based on identification of emission lines, with the detection of the [OII] λ3727 doublet for $0.6 < z < 1.6$.

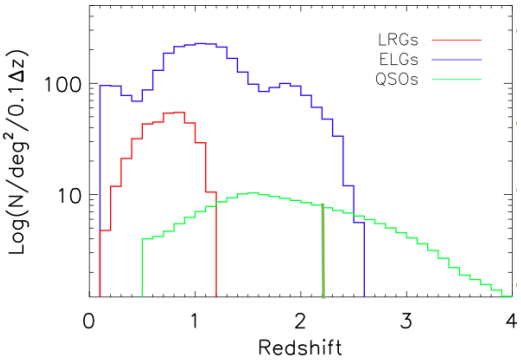

Fig. 1. Density of luminous red galaxies (LRG), emission-line galaxies (ELG) and quasars (QSO) as a function of redshift.

The aim of this work is to apply selection criteria to BOSS that uses the 2.5-m SDSS telescope at Apache Point Observatory (Gunn et al. 2006). The SDSS photometric survey, delivered under the data release 8 (DR8, (Aihara et al. 2011)), covers $14,555$ square degrees in the 5 photometric bands u, g, r, i, z. The 3σ magnitude depths are: $u = 22.0$, $g = 22.2$, $r = 22.2$, $i = 21.3$. The magnitudes we use are corrected from galactic extinction. In addition, we use the CFHTLS photometric redshift catalog (Ilbert et al. 2006; Coupon et al. 2009). The CFHTLS covers 155 square degrees in the u, g, r, i, z bands, with transmission curves of filters slightly different from SDSS. The 3σ magnitude depths are: $u = 25.3$, $g = 25.5$, $r = 24.8$, $i = 24.5$, thus the CFHTLS photometry

[i] extendedBOSS is part of a proposed program of post-2014 surveys on the Sloan telescope.

is much deeper than SDSS DR8, however the CFHTLS covers only a small fraction of the SDSS field of view. The photometric redshift accuracy is estimated to be $\sigma_z < 0.04\,(1+z)$ for $g < 22.5$.

In this paper we explore two color selections based on *ugr* and *gri* color-color diagrams.

The *ugr* color selection is defined by $-1 < u-r < 0.5$ and $-1 < g-r < 0.5$ that selects strongly star-forming galaxies at $z > 0.6$. An additional cut $-1 < u-g < 0.5$ removes all low-redshift galaxies ($z < 0.3$). For this selection, the bright sample is defined for the g magnitude between $20 < g < 22.5$ and the faint sample for $g < 23.5$ (Fig. 2 Left). The *ugr* color selection avoids the stellar sequence, but not the quasar sequence. Hence, the contamination of the *ugr* selection by point-source objects is expected to be due to quasars. The selection is centered to $z \sim 1.3$.

The bright sample of the *gri* color selection is defined by the magnitude cut $19 < i < 21.3$, where in addition blue galaxies at $z \sim 0.8$ are selected with $0.8 < r-i < 1.4$ and $-0.2 < g-r < 1.1$ (Fig. 2 Right). In the faint range defined as $21.3 < i < 23$, we tilt the selection to select higher redshifts with $-0.4 < g-r < 0.4$, $-0.2 < r-i < 1.2$ and $g-r < r-i$. The *gri* selection avoids both the stellar sequence and the quasar sequence. Thus the contamination from point-sources should be minimal. The selection is centered to $z \sim 0.8$ (bright) and $z \sim 1$ (faint).

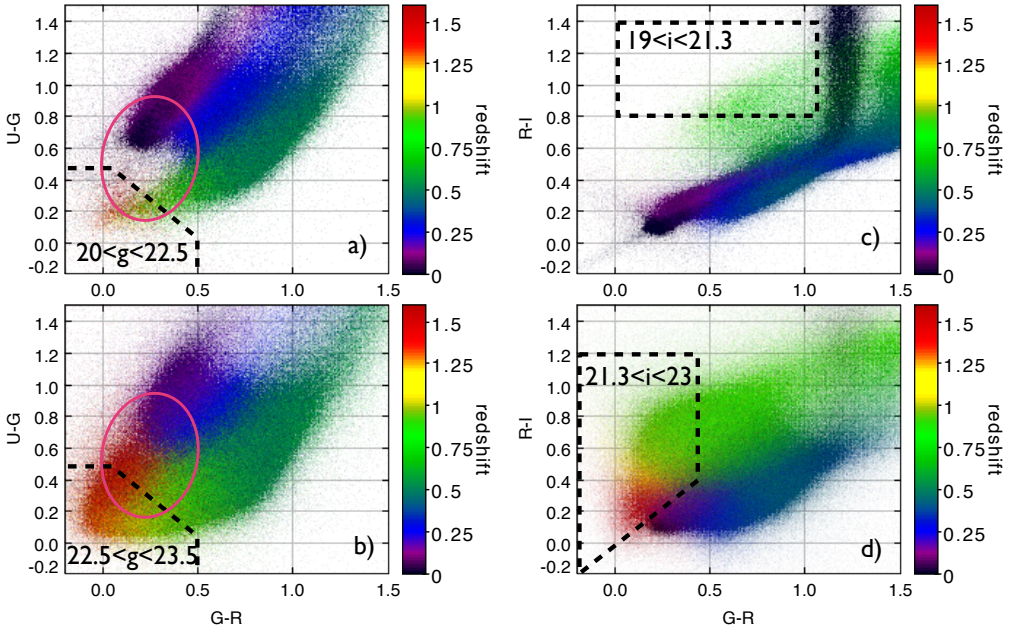

Fig. 2. Color-color diagrams in the CFHTLS photometric database. **Left:** The *ugr* selection for the bright (top) and the faint (bottom) samples. **Right:** The *gri* selection for the bright (top) and the faint (bottom) samples.

3 Validation using simulations

In order to be able to evaluate the color selection efficiency, we need for a spectro-photometric catalog with a large sample of galaxy spectra. In this aim, we use the COSMOS Mock Catalog (CMC) based on the COSMOS photometric catalog (Ilbert et al. 2009). The CMC contains about 280,000 galaxies, in which each simulated galaxy has a photo-z and a best-fit template (Jouvel et al. 2009). In addition, with each galaxy of the CMC is associated a simulated spectrum, for which emission lines have been added using Kennicutt calibration laws (Kennicutt 1998; Ilbert et al. 2009) and calibrated using zCOSMOS (Lilly et al. 2009) as described in (Zoubian et al. 2012). The strength of [OII] emission lines was confirmed using DEEP2 and VVDS DEEP luminosity functions (Le Fèvre et al. 2005; Zhu et al. 2009). Finally a host galaxy extinction law is applied to each spectrum. From the CMC, two simulated galaxy catalogs were built, one for each color selection function (*ugr* and *gri*), for $0.6 < z < 1.7$. Each synthetic spectrum was affected by sky and photon noise as if observed by the BOSS spectrographs (Smee et al. 2012), by using the *specsim1d* software. We simulated a set of four exposures of 900 seconds each.

To extract the spectroscopic redshift, the resulting simulated spectra were then analyzed by the two redshift codes of the BOSS pipeline software, the idlspec2d software (Bolton et al. 2012) and a modified version of the Zcode Fortran program, initially developed by (Sutherland 1999) and made available to the BOSS community. While the former, primarily designed for LRG targets, is based on a least-squares minimization using galaxies templates, the latter performed also a redshift estimate based on fitting discrete emission line templates in Fourier space over all z. In a further step we address the flux measurement of emission lines, conducted using the Platefit Vimos software developed by (Lamareille et al. 2009). This software was developed to measure the flux of all emission lines after removing the stellar continuum and absorption lines from lower resolution and lower signal-to-noise ratio spectra (Lamareille et al. 2006).

Finally we define a successful redshift measurement if $\delta z/(1+z) < 0.004$. The redshift success rate (RSR) of the *ugr* selection is shown in Fig. 3 for the two redshift codes of the BOSS pipeline, using galaxies templates (in red) and emission lines templates (in blue). The redshift extraction is not meaningful below $z < 0.6$ due to the lack of statistics. The RSR is higher than 70% for $z < 1.5$, and is about 90% for the n(z) distribution between $0.6 < z < 1.6$. For $z > 1.6$, the redshift extraction always fails, and some catastrophic failures ($\delta z/(1+z) > 0.01$) remain for $1 < z < 1.6$, essentially due to the bad identification of the [OII] emission line view as the $H\alpha$ line.

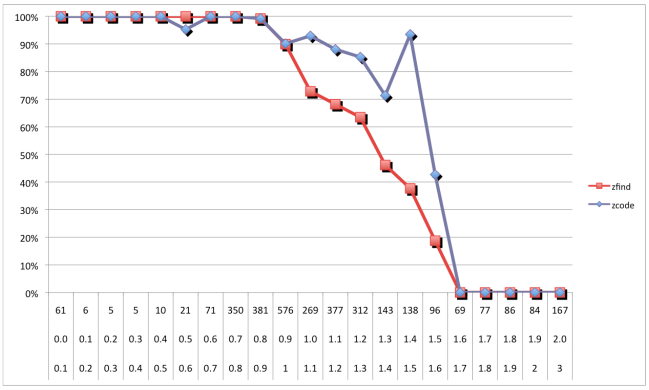

Fig. 3. Redshift success rate of the *urg* sample with the two redshift codes of the BOSS pipeline.

4 Validation using ancillary observations

To test the reliability of both the bright *ugr* and *gri* color selections, we have conducted a set of dedicated observations, as part of the Emission Line Galaxy SDSS-III/BOSS ancillary program. The observations were conducted between Autumn 2010 and Spring 2011 using the SDSS telescope with the BOSS spectrograph. A total of $\sim 2,000$ spectra, observed four times of 15 minutes, were taken in different fields: in the Stripe 82 (using single epoch SDSS photometry for color selection) and in the CFHTLS W1, W3 and W4 wide fields (using CFHT-LS photometry). This data set has been released in the SDSS-III DR9 (Ahn et al. 2012).

All these observed spectra were visually inspected to confirm or correct the redshifts produced by two different pipelines. To classify the observed objects, we have defined sub-categories, one with secure redshifts and the other with unreliable redshifts. For the targets selected using the SDSS photometry and the *ugr* color selection : 32% are ELGs at z > 0.6, and 32% are ELGs at $z < 0.6$. Besides, 20% are flagged as bad data, and QSOs are 10% of the selected targets. Within the *gri* selection, 50% of targets are ELGs at $z > 0.6$.

Using the CFHTLS photometry, 46% of targets are ELGs at z > 0.6 and 14% are QSOs with the *ugr* selection. Within the *gri* selection, 61% are ELGs at $z > 0.6$, 12% are red galaxies with a strong continuum, and only 1% of targets are QSOs. For both bright and faint samples, 18% of spectra are bad data (for a complete description, see Comparat et al. (2012).

5 Conclusions

We present an efficient emission-line galaxy selection that could provide a sample from which the BAO feature could be measured in the 2-point correlation function at $z > 0.6$. Using such deeper photometric surveys and improved pipelines, it should be possible to probe BAO to $z = 1.2$ in the next 6 years, e.g. by the eBOSS experiment, and to $z = 1.7$ in the next 10 years, e.g. by PFS-SuMIRE or BigBOSS experiment.

Funding for SDSS-III has been provided by the Alfred P. Sloan Foundation, the Participating Institutions, the National Science Foundation, and the U.S. Department of Energy Office of Science. The SDSS-III web site is `http://www.sdss3.org/`. Based on observations obtained with MegaPrime/MegaCam, a joint project of CFHT and CEA/DAPNIA, at the Canada-France-Hawaii Telescope (CFHT) which is operated by the National Research Council (NRC) of Canada, the Institut National des Science de lÕUnivers of the Centre National de la Recherche Scientifique (CNRS) of France, and the University of Hawaii. This work is based in part on data products produced at TERAPIX and the Canadian Astronomy Data Centre as part of the Canada-France-Hawaii Telescope Legacy Survey, a collaborative project of NRC and CNRS. This work was supported by the ANR grant ANR-08-BLAN-0222.

References

Ahn, C. P. et al. 2012, arXiv:1207.7137 [astro-ph.IM]
Aihara, H. et al. 2011, ApJS, 193, 29
Albrecht, A., Bernstein, G., Cahn, R., et al. 2006, arXiv:astro-ph/0609591
Anderson, L., Aubourg, E., Bailey, S., et al. 2012, arXiv:1203.6594 [astro-ph.CO]
Beutler, F., Blake, C., Colless, M., et al. 2011, MNRAS, 416, 3017
Blake, C., Davis, T., Poole, G., et al. 2011, MNRAS, 415, 2892
Bolton, A. S., Schlegel, D. J., Aubourg, E., et al. 2012, arXiv:1207.7326 [astro-ph.CO]
Cole, S. et al. 2005, MNRAS, 362, 505
Comparat, J., Kneib, J.-P., Escoffier, S., et al. 2012, arXiv: 1207.4321 [astro-ph.CO]
Coupon, J., Ilbert, O., Kilbinger, M., et al. 2009, A&A, 500, 981
Dawson, K. S. et al. 2012, arXiv:1208.0022 [astro-ph.CO]
Eisenstein, D. J. et al. 2005, ApJ, 633, 560
Gunn, J. E. et al. 2006, AJ, 131, 2332
Ilbert, O., Arnouts, S., McCracken, H., et al. 2006, A&A, 457, 841
Ilbert, O., Capak, P., Salvato, M., et al. 2009, ApJ, 690, 1236
Jouvel, S., Kneib, J.-P., Ilbert, O., et al. 2009, A&A, 504, 359
Kazin, E. A. et al. 2010, ApJ, 710, 1444
Kennicutt, Robert C., J. 1998, ARA&A, 36, 189
Lamareille, F., Brinchmann, J., Contini, T., et al. 2009, A&A, 495, 53
Lamareille, F., Contini, T., Le Borgne, J.-F., et al. 2006, A&A, 448, 893
Laureijs, R., Amiaux, J., Arduini, S., et al. 2011, arXiv:1110.3193 [astro-ph.CO]
Le Fèvre, O., Vettolani, G., Garilli, B., et al. 2005, A&A, 439, 845
Lilly, S. J., Le Brun, V., Maier, C., et al. 2009, ApJS, 184, 218
McDonald, P. & Eisenstein, D. 2007, Phys. Rev., D76, 063009
Peebles, P. & Yu, J. 1970, ApJ, 162, 815
Percival, W. J. et al. 2010, MNRAS, 401, 2148
Perlmutter, S., Aldering, G., Goldhaber, G., et al. 1999, ApJ, 517, 565
Riess, A. G., Filippenko, A. V., Challis, P., et al. 1998, AJ, 116, 1009
Ross, N. P., Myers, A. D., Sheldon, E. S., et al. 2012, ApJS, 199, 3
Schlegel, D. et al. 2011, arXiv:1106.1706 [astro-ph.IM]
Seo, H.-J. & Eisenstein, D. J. 2003, ApJ, 598, 720
Smee, S., Gunn, J. E., Uomoto, A., et al. 2012, arXiv:1208.2233 [astro-ph.IM]
Sunyaev, R. & Zeldovich, Y. 1970, Astrophys. Space Sci., 7, 3
Sutherland, W. J. 1999, The 2dF Redshift Code - User Guide
White, M., Song, Y.-S., & Percival, W. J. 2009, MNRAS, 397, 1348
Zhu, G., Moustakas, J., & Blanton, M. R. 2009, ApJ, 701, 86
Zoubian, J. et al. 2012, in preparation

Session 13

Clusters in the cosmic web

SF2A 2012
S. Boissier, P. de Laverny, N. Nardetto, R. Samadi, D. Valls-Gabaud and H. Wozniak (eds)

MULTIFREQUENCY SURVEYS OF THE VIRGO CLUSTER: ALFALFA, HEVICS, SMAKCED, NGVS, GUVICS

A.Boselli[1] and the ALFALFA, HeViCS, SMAKCED, NGVS, GUViCS teams

Abstract. The Virgo cluster, the largest nearby concentration of galaxies, is the target of several multifrequency surveys aimed at studying the effects of the environment on galaxy evolution. These blind or pointed surveys are: the Arecibo Legacy Fast ALFA Survey (ALFALFA; PI. R. Giovanelli), the Herschel Virgo Cluster Survey (HeViCS; PI J. Davies), the Stellar content, MAss and Kinematics of Cluster Early-type Dwarfs (SMAKCED, PI T. Lisker), the Next Generation Virgo Cluster Survey (NGVS; PI L. Ferrarese) and the GALEX UV Virgo Cluster Survey (GUViCS; PI A. Boselli). I briefly describe the surveys mentioning some of the most interesting results obtained so far.

Keywords: galaxies: clusters: individual: Virgo, galaxies: evolution; radio lines: galaxies; infrared: galaxies; ultraviolet: galaxies;

1 Introduction

A complete understanding of the matter cycle in galaxies, i.e. of the process that transforms the primordial atomic gas into molecular clouds where stars are formed, and of the metal production and the formation of dust grains requires a multifrequency analysis. Indeed, the atomic gas can be directly observed using the 21 cm emission line, while the molecular component is generally traced through the emission of carbon monoxide emission lines. Star formation can be quantified under some assumptions through the observations of the ionised hydrogen or of the UV stellar continuum emitted by the youngest stellar populations. Dust, formed by the aggregation of metals produced in the final phases of stellar evolution and injected into the interstellar medium by stellar winds and supernovae explosions, absorbs the stellar radiation and re-emits the acquired energy in the infrared domain (e.g. Boselli (2011)).
In cluster galaxies this matter cycle can be easily modified by the perturbations induced by the hostile environment in which galaxies reside (e.g. Boselli & Gavazzi (2006)). The atomic gas, distributed on a disc of size $\sim$ two times more extended than the optical disc, is easily perturbed by the interaction either with the hot intergalactic medium (ram pressure stripping, Gunn & Gott (1972); thermal evaporation, Cowie & Songaila (1977); viscous stripping, Nulsen (1982)), or by the flyby encounters with other cluster members (galaxy harassment, Moore et al. (1998)). These perturbations might induce nuclear gas infall (Kennicutt et al. 1987) or the truncation of the gaseous disc with, as a consequence, a radial decrease of the star formation activity (Boselli et al. 2006). In dwarf galaxies the gas can be totally removed, and the star formation activity totally stopped, transforming gas rich, late-type systems into quiescent dwarf ellipticals (Boselli et al. (2008a), Boselli et al. (2008b)). Frozen in the interstellar medium, the dust component can be also removed during the interaction with the hostile environment (Cortese et al. (2010a), Cortese et al. (2010b), Cortese et al. (2012)).
With the aim of gathering a complete and coherent view on the different processes acting on galaxies in high density environments we have recently undertaken several blind surveys of the Virgo cluster, the largest concentration of galaxies within 35 Mpc. There are several reasons why Virgo has been chosen for these studies: it is a close, rich cluster, whose distance (16.5 Mpc, Gavazzi et al. (1999); Mei et al. (2007)) is such that galaxies spanning a wide range in morphology and luminosity can be studied, from giant spirals and ellipticals down to dwarf irregulars, blue compact dwarfs (BCDs) and dwarf ellipticals (dE) and spheroidals (dS0). Furthermore, Virgo is still in the process of being assembled, so that a wide range of processes (ram-pressure stripping, tidal

[1] Aix Marseille Université, CNRS, LAM (Laboratoire d'Astrophysique de Marseille) UMR 7326, 13388, Marseille, France

interactions, harassment and pre-processing) are still taking place. The blind surveys that i describe are: the 21 cm Arecibo Legacy Fast ALFA survey (ALFALFA, Giovanelli et al. (2005)), the far infrared Herschel Virgo Cluster Survey (HeViCS, Davies et al. (2012)), the optical Next Generation Virgo Cluster Survey (NGVS, Ferrarese et al. (2012)), and the UV GALEX ultraviolet Virgo Cluster Survey (GUViCS, Boselli et al. (2011)). I also briefly describe the Stellar content, MAss and Kinematics of Cluster Early-type Dwarfs (SMAKCED, Janz et al. (2012)), a near infrared and kinematical survey of dwarf early-type galaxies in the Virgo cluster.

2 The Virgo cluster surveys

2.1 ALFALFA: the Arecibo Legacy Fast ALFA survey

The Arecibo Legacy Fast ALFA survey (ALFALFA)[i] is a blind HI survey covering 7000 deg^2 in the declination range $0^o <$ dec$< 32^o$ and velocity range -1600$< vel <$ 18000 km s^{-1} with a spectral resolution of 5 km s^{-1} down to a sensitivity limit of 2.4 mJy, corresponding to $\sim 10^{7.5}$ M$\odot$ at the distance of Virgo (Giovanelli et al. (2005)). The survey, which has already completed the Virgo cluster region, has been designed to provide the basis for studies of the dynamics of galaxies within nearby superclusters, allow measurement of the HI diameter and mass function, and enable a first wide-area blind search for local HI tidal features and HI absorbers. The first catalogue of data has been published in Giovanelli et al. (2007), Kent et al. (2008) and Haynes et al. (2011). The analysis of the data done so far revealed, for instance, that the HI cloud without optical counterpart observed by Minchin et al. (2005) is atomic gas stripped from NGC 4254 through an harassment process (Haynes et al. (2007)). It also allowed the detection of other HI clouds without optical counterparts (Kent et al. (2007)). Combined with an Hα imaging survey of HI detected galaxies, we have also studied the statistical properties, including the present day star formation activity, of HI selected objects in Virgo and in the field (Gavazzi et al. 2008, 2012)).

2.2 HeViCS: the Herschel Virgo Cluster Survey

The Herschel Virgo Cluster Survey (HeViCS)[ii] (Davies et al. (2012)) is a blind far-IR survey of 60 deg^2 in five photometric bands from 100 to 500 μm with PACS and SPIRE on the Herschel Space Observatory down to the confusion limit (at 250 μm; 286 hrs allocated as an open time key program on Herschel). The HeViCS project is done in tight collaboration with the Herschel Reference Survey (Boselli et al. (2010b); HRS), a similar project aimed at studying relatively isolated galaxies at the same distance than Virgo ideally selected for comparison in environmental studies. Figure 1 shows the surveyed region, and the infrared image obtained using the Herschel data. The bright point like sources are mainly Virgo cluster galaxies, while the filamentary structures are Galactic cirri. Data for the bright infrared galaxies can be found in Davies et al. (2012) and Ciesla et al. (2012), this last paper including also HRS galaxies.

The goal of this survey is to study the dust properties of cluster galaxies, including the extended dust distributed around galactic discs or associated with tidal debris and low surface brightness galaxies, and to reconstruct the far-IR luminosity function as well as to detect dust in the intra cluster medium. The preliminary analysis of the data has already brought to very interesting and new results: it has indeed shown for the first time that cluster galaxies are stripped of their dust content because of both gravitational interactions and ram pressure stripping (Cortese et al. (2010a), Cortese et al. (2010b)). It has also shown the existence of dust in metal poor BCD (Grossi et al. (2010)) and dwarf elliptical galaxies (de Looze et al. (2010)), as well as the existence of massive ellipticals with a far infrared emission dominated by synchrotron (Baes et al. (2010); Boselli et al. (2010a)). Other works were focused on the study of the relation between the gas and the dust content and the metallicity of resolved and unresolved objects (Smith et al. (2010); Magrini et al. (2011); Corbelli et al. (2012)), while the study of the far infrared colours of late-type systems is presented in Boselli et al. (2012).

[i] http://egg.astro.cornell.edu/alfalfa/
[ii] http://www.hevics.org/

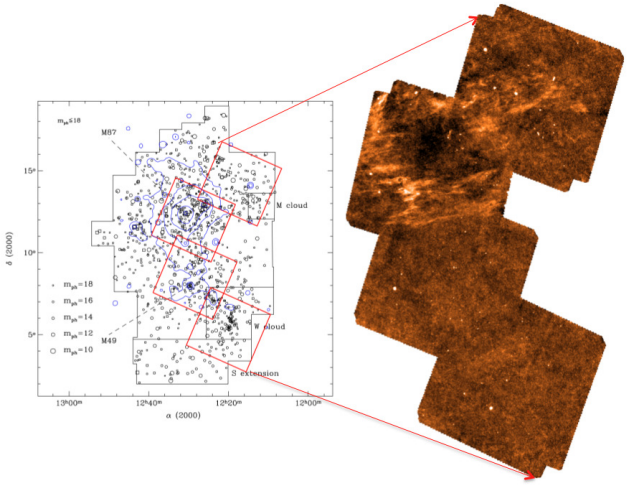

Fig. 1. The Virgo region observed by Herschel (red solid squares) compared to that observed by Binggeli et al. (1985) (black solid) (left). The *Herschel* PACS image at 250 μm (right) (adapted from Davies et al. (2012)).

2.3 SMAKCED: the Stellar content, MAss and Kinematics of Cluster Early-type Dwarfs

The Stellar content, MAss and Kinematics of Cluster Early-type Dwarfs (SMAKCED)[iii] is a pointed near infrared photometric and optical high resolution spectroscopic survey of selected dwarf elliptical galaxies in the Virgo cluster (see Janz et al. (2012)). Near infrared data are necessary to trace the distribution of the bulk of the stellar component within galaxies, and thus determine different structural parameters. High resolution spectroscopy is used to measure the kinematical properties of the observed galaxies, including velocity dispersion and rotational velocity. Combined, these data will be used to study and compare the main scaling relations of dwarf ellipticals to those of massive systems or spiral galaxies with the aim of understanding whether this particular category of objects might result from the transformation of gas rich, late-type systems recently perturbed by the interaction with the hostile cluster environment. The first results indeed confirm this scenario: a large fraction of early-type dwarf galaxies are supported by rotation. These dE are characterised by relatively young stellar populations and are located at the peryphery of the Virgo cluster. Their rotation curve is similar to that of late-type systems of similar mass (Toloba et al. (2009); Toloba et al. (2011)).

2.4 NGVS: the Next Generation Virgo Survey

The Next Generation Virgo Survey (NGVS)[iv] (Ferrarese et al. (2012)) is an optical (*ugriz*) survey covering 104 deg^2 of the Virgo cluster with MegaPrime on the CFHT to a point-source depth of $g \sim 25.7$ mag and a corresponding surface brightness of $\mu_g \sim 29$ mag arcsec^{-2}. The survey has detect $\sim 3\ 10^7$ sources, including low surface brightness Virgo cluster members, globular clusters associated to the massive galaxies and background objects. Due to a dome failure in the spring 2012 semester, the survey still has to be completed in the u and r bands (123 hours required). Figure 2 illustrates the sky region covered by the NGVS survey (solid red line) and the overlap with several other programs that have targeted the Virgo cluster.

The goals of the NGVS are the study of faint end slope of the galaxy luminosity function, the characterization of galaxy scaling relations over a dynamic range of 7 orders of magnitude in mass, and the study of the diffuse and discrete intracluster population.

[iii] `http://smakced.ned/`
[iv] `https://www.astrosci.ca/NGVS/The_Next_Generation_Virgo_Cluster_Survey/Home.html`

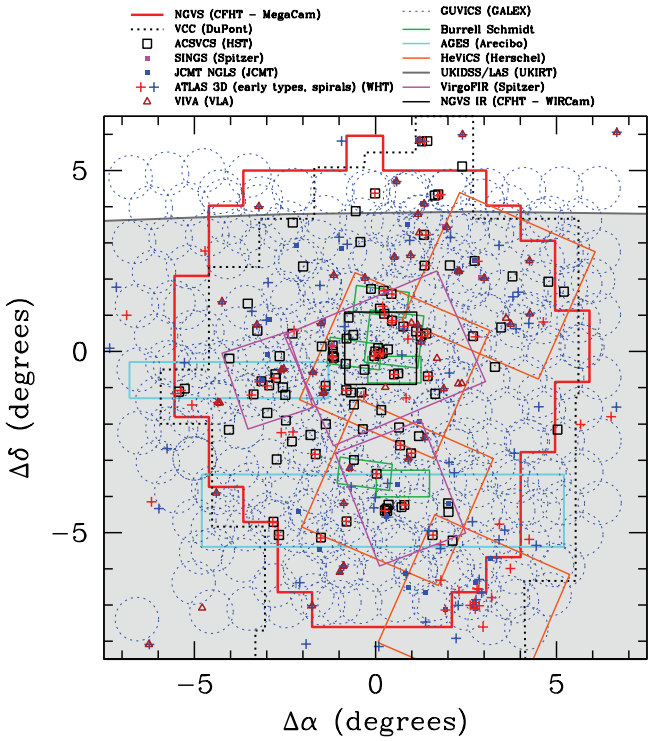

Fig. 2. NGVS survey area, shown in heavy red, compared to the regions covered by a number of multi-wavelength surveys of the Virgo cluster (primarily at non-optical wavelengths), taken from Ferrarese et al. (2012). The different surveys are indicated in the legend at the top of the figure.

2.5 GUViCS: the GALEX UV Virgo Cluster Survey

The GALEX UV Virgo Cluster Survey (GUViCS)[v] Boselli et al. (2011) is an ultraviolet survey of the Virgo cluster in the NUV (2316 Å) and FUV (1539 Å) bands. The data were obtained as part of the mission surveys on one hand, during GI open time proposals (Boselli et al. (2005b)), and especially during a cycle 6 proposal that will extend the coverage to the whole area of the cluster with 94 new pointings, for a total of 121.5 ksec. The surveyed region, as depicted in Fig. 3, covers $\sim$ 40 sq. deg. in the FUV and $\sim$ 120 sq. deg. in the NUV at a sensitivity of $\simeq$ 27.5-28 mag arcsec^{-2} in surface brightness and a detection limit for point sources of $\sim$ 21.5 AB mag. This survey detected $\sim$ 1.4 10^6 sources in the NUV band, and $\sim$ 2 10^5 in the FUV.

The UV observations are of paramount importance for a large number of studies. In star forming galaxies, the present day star formation activity can be measured from the UV flux emitted by the youngest stellar population (Kennicutt (1998); Boselli et al. (2001), Boselli et al. (2009)), provided that dust extinction can be accurately determined (e.g. using the far-IR to UV flux ratio, Cortese et al. (2006), Cortese et al. (2008)). In quiescent galaxies, the level emission can help to date the last generation of stars (on a few 100 Myr timescale) or be related to very old populations (UV upturn; Boselli et al. (2005a)).

The analysis of these GALEX data allowed us to detect low surface brightness features associated with tidally perturbed galaxies (Boselli et al. (2005a); Arrigoni Battaia et al. (2012)) or study the star formation history at galactic scales in NGC 4569, a prototypical massive spiral undergoing a ram pressure stripping event (Boselli et al. (2006)). We also determined the UV luminosity function of galaxies in the core of the cluster in the NUV and FUV bands and separately for early- and late-type systems (Boselli et al. (2011)). Among the works done so far, however, the most important is probably the study of the origin of dwarf elliptical galaxies in Virgo. Our analysis has convincingly shown that this population of objects probably results from the transformation of low luminosity, star forming systems which recently entered the hostile cluster environment and rapidly ($\leq$ 100 Myr) lost their gasous content, quenching their star formation activity (Boselli et al. (2008a), Boselli et al. (2008b)).

[v] http://galex.oamp.fr/guvics/index.html

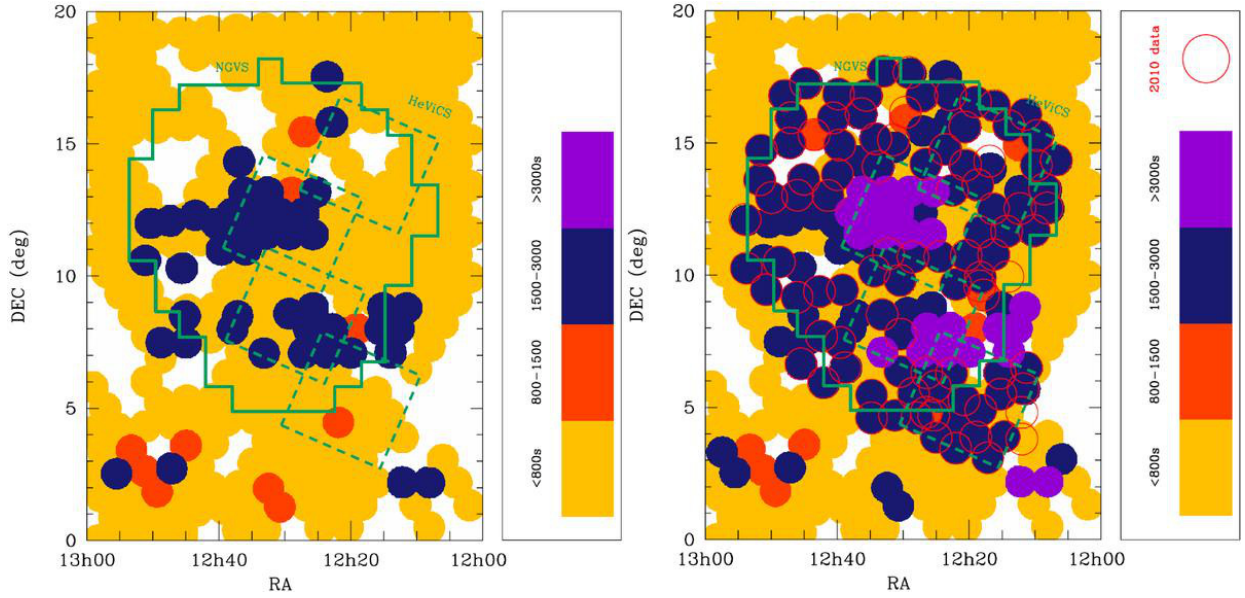

Fig. 3. The Virgo cluster region observed by GALEX in the FUV (**left**) and NUV (**right**) bands, from Boselli et al. (2011).

I also take the opportunity to advertise the long term effort that our team has done during these last years to obtain, reduce and homogeneise imaging and spectroscopic data for galaxies in the Virgo cluster at almost all frequencies, all made available to the community through our dedicated database GOLDMine [vi] (Gavazzi et al. (2003)). This includes Hα narrow band (Boselli & Gavazzi (2002), Boselli et al. (2002a), Gavazzi et al. (2002), Gavazzi et al. (2006)), optical (Boselli et al. (2003a), Gavazzi et al. (2005b)), near infrared (Boselli et al. (1997), Boselli et al. (2000), Gavazzi et al. (2000b), Gavazzi et al. (2001)) and mid infrared imaging (Boselli et al. (2003b)), 2.6 mm CO (Boselli et al. (1995), Boselli et al. (2002b)) and 21 cm HI data (Gavazzi et al. (2005a)), radio continuum data (Gavazzi & Boselli (1999)), as well as optical spectroscopy (Gavazzi et al. (2000a), Gavazzi et al. (2004)). This unique set of data is at the origin of the review paper on the effects of the environment on galaxy evolution that we published a few years ago (Boselli & Gavazzi (2006)) as well as of many others publicarions.

This publication is done on behalf of the ALFALFA, HeViCS, NGVS, SMAKCED and GUViCS teams. I am greateful to the PI of the different projects, R. Giovanelli, J. Davies, L. Ferrarese and T. Lisker, for providing me with all the information necessary to write this communication.

References

Arrigoni Battaia, F., Gavazzi, G., Fumagalli, M., et al. 2012, A&A, 543, A112

Baes, M., Clemens, M., Xilouris, E. M., et al. 2010, A&A, 518, L53

Binggeli, B., Sandage, A., & Tammann, G. A. 1985, AJ, 90, 1681

Boselli, A. 2011, A Panchromatic View of Galaxies (Wiley-VCH Verlag GmbH & Co. KGaA)

Boselli, A., Boissier, S., Cortese, L., et al. 2009, ApJ, 706, 1527

Boselli, A., Boissier, S., Cortese, L., & Gavazzi, G. 2008a, ApJ, 674, 742

Boselli, A., Boissier, S., Cortese, L., & Gavazzi, G. 2008b, A&A, 489, 1015

Boselli, A., Boissier, S., Cortese, L., et al. 2005a, ApJ, 623, L13

Boselli, A., Boissier, S., Cortese, L., et al. 2006, ApJ, 651, 811

Boselli, A., Boissier, S., Heinis, S., et al. 2011, A&A, 528, A107

Boselli, A., Casoli, F., & Lequeux, J. 1995, A&AS, 110, 521

[vi] http://goldmine.mib.infn.it/

Boselli, A., Ciesla, L., Buat, V., et al. 2010a, A&A, 518, L61
Boselli, A., Ciesla, L., Cortese, L., et al. 2012, A&A, 540, A54
Boselli, A., Cortese, L., Deharveng, J. M., et al. 2005b, ApJ, 629, L29
Boselli, A., Eales, S., Cortese, L., et al. 2010b, PASP, 122, 261
Boselli, A. & Gavazzi, G. 2002, A&A, 386, 124
Boselli, A. & Gavazzi, G. 2006, PASP, 118, 517
Boselli, A., Gavazzi, G., Donas, J., & Scodeggio, M. 2001, AJ, 121, 753
Boselli, A., Gavazzi, G., Franzetti, P., Pierini, D., & Scodeggio, M. 2000, A&AS, 142, 73
Boselli, A., Gavazzi, G., & Sanvito, G. 2003a, A&A, 402, 37
Boselli, A., Iglesias-Páramo, J., Vílchez, J. M., & Gavazzi, G. 2002a, A&A, 386, 134
Boselli, A., Lequeux, J., & Gavazzi, G. 2002b, A&A, 384, 33
Boselli, A., Sauvage, M., Lequeux, J., Donati, A., & Gavazzi, G. 2003b, A&A, 406, 867
Boselli, A., Tuffs, R. J., Gavazzi, G., Hippelein, H., & Pierini, D. 1997, A&AS, 121, 507
Ciesla, L., Boselli, A., Smith, M. W. L., et al. 2012, ArXiv e-prints
Corbelli, E., Bianchi, S., Cortese, L., et al. 2012, A&A, 542, A32
Cortese, L., Bendo, G. J., Boselli, A., et al. 2010a, A&A, 518, L63
Cortese, L., Boselli, A., Buat, V., et al. 2006, ApJ, 637, 242
Cortese, L., Boselli, A., Franzetti, P., et al. 2008, MNRAS, 386, 1157
Cortese, L., Ciesla, L., Boselli, A., et al. 2012, A&A, 540, A52
Cortese, L., Davies, J. I., Pohlen, M., et al. 2010b, A&A, 518, L49
Cowie, L. L. & Songaila, A. 1977, Nature, 266, 501
Davies, J. I., Bianchi, S., Cortese, L., et al. 2012, MNRAS, 419, 3505
de Looze, I., Baes, M., Zibetti, S., et al. 2010, A&A, 518, L54
Ferrarese, L., Côté, P., Cuillandre, J.-C., et al. 2012, ApJS, 200, 4
Gavazzi, G., Bonfanti, C., Pedotti, P., Boselli, A., & Carrasco, L. 2000a, A&AS, 146, 259
Gavazzi, G. & Boselli, A. 1999, A&A, 343, 86
Gavazzi, G., Boselli, A., Cortese, L., et al. 2006, A&A, 446, 839
Gavazzi, G., Boselli, A., Donati, A., Franzetti, P., & Scodeggio, M. 2003, A&A, 400, 451
Gavazzi, G., Boselli, A., Pedotti, P., Gallazzi, A., & Carrasco, L. 2002, A&A, 396, 449
Gavazzi, G., Boselli, A., Scodeggio, M., Pierini, D., & Belsole, E. 1999, MNRAS, 304, 595
Gavazzi, G., Boselli, A., van Driel, W., & O'Neil, K. 2005a, A&A, 429, 439
Gavazzi, G., Donati, A., Cucciati, O., et al. 2005b, A&A, 430, 411
Gavazzi, G., Franzetti, P., Scodeggio, M., et al. 2000b, A&AS, 142, 65
Gavazzi, G., Fumagalli, M., Galardo, V., et al. 2012, ArXiv e-prints
Gavazzi, G., Giovanelli, R., Haynes, M. P., et al. 2008, A&A, 482, 43
Gavazzi, G., Zaccardo, A., Sanvito, G., Boselli, A., & Bonfanti, C. 2004, A&A, 417, 499
Gavazzi, G., Zibetti, S., Boselli, A., et al. 2001, A&A, 372, 29
Giovanelli, R., Haynes, M. P., Kent, B. R., et al. 2005, AJ, 130, 2598
Giovanelli, R., Haynes, M. P., Kent, B. R., et al. 2007, AJ, 133, 2569
Grossi, M., Hunt, L. K., Madden, S., et al. 2010, A&A, 518, L52
Gunn, J. E. & Gott, III, J. R. 1972, ApJ, 176, 1
Haynes, M. P., Giovanelli, R., & Kent, B. R. 2007, ApJ, 665, L19
Haynes, M. P., Giovanelli, R., Martin, A. M., et al. 2011, AJ, 142, 170
Janz, J., Laurikainen, E., Lisker, T., et al. 2012, ApJ, 745, L24
Kennicutt, Jr., R. C. 1998, ARA&A, 36, 189
Kennicutt, Jr., R. C., Roettiger, K. A., Keel, W. C., van der Hulst, J. M., & Hummel, E. 1987, AJ, 93, 1011
Kent, B. R., Giovanelli, R., Haynes, M. P., et al. 2008, AJ, 136, 713
Kent, B. R., Giovanelli, R., Haynes, M. P., et al. 2007, ApJ, 665, L15
Magrini, L., Bianchi, S., Corbelli, E., et al. 2011, A&A, 535, A13
Mei, S., Blakeslee, J. P., Côté, P., et al. 2007, ApJ, 655, 144
Minchin, R., Davies, J., Disney, M., et al. 2005, ApJ, 622, L21
Moore, B., Lake, G., & Katz, N. 1998, ApJ, 495, 139

Nulsen, P. E. J. 1982, MNRAS, 198, 1007
Smith, M. W. L., Vlahakis, C., Baes, M., et al. 2010, A&A, 518, L51
Toloba, E., Boselli, A., Cenarro, A. J., et al. 2011, A&A, 526, A114
Toloba, E., Boselli, A., Gorgas, J., et al. 2009, ApJ, 707, L17

SF2A 2012
S. Boissier, P. de Laverny, N. Nardetto, R. Samadi, D. Valls-Gabaud and H. Wozniak (eds)

LENSING IN CLUSTERS

R. Cabanac[1]

Abstract. This review is based on the paper of Kneib & Natarajan (2011). I briefly review the strong lensing methods and presents the main results Strong Lensing studies achieved in recent years in the domain of clusters of galaxies.

Keywords: Gravitational lensing: strong, Galaxies:clusters:general

1 Introduction

In recent years, the release of large and deep imaging and spectroscopic surveys has increased the use of large samples of strong lensing candidates to study the dark components of the universe. In turn, this has triggered the community to improve modelling tools and better understand systematics, which are a chief concern of strong lensing cosmological studies. Section one outlines the methods used in lensing, Section two presents studies on mass distribution in clusters, Section three and four compares observed properties with theoretical predictions, and Section five introduces the coming ground-based and space borne instruments.

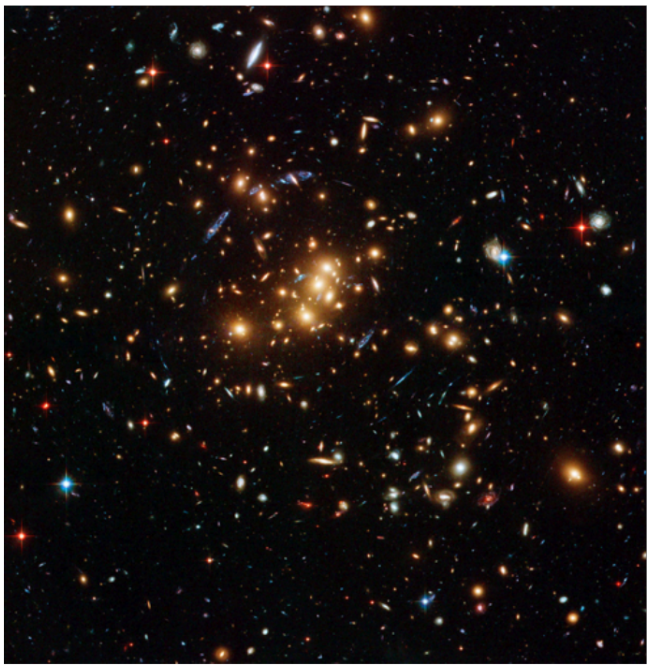

Fig. 1. Strong Lensing arcs in cluster Cl0024+1654 at redshift z=0.395 (HST ACS imaging)

[1] OMP, 57 Ave d'Azereix, 65000, Tarbes, France

2 Contraining cluster mass distributions with lensing

The General Relativity theory provides an elegant interpretation of large arcs witnessed in deep imaging of some clusters, the theory has been described in Schneider, Ehlers & Falco (Schneider et al. 1992), interested readers are refered to their monography. In summary, Lensing effects are space-time deformations induced by massive over-densities

We will focus on the application to massive clusters at redshifts $z \sim 0.2$-0.5, which are well approximated as single-plane lenses. Lensing effect actually probes the 2-D Newton potential $\phi(x, y)$ from a 3-D density distribution $\rho(x, y, z)$. The projected surface mass density is $\Sigma(x, y) = \frac{\nabla^2\phi(x,y)}{4\pi G}$.

Lensing effect maps a source plane into a image plane and is usually parametrized in terms three vectors: convergence κ, shear γ and deflection angles $\overrightarrow{\alpha}$

$\overrightarrow{\alpha}(\overrightarrow{\theta}) = \overrightarrow{\nabla}_{\overrightarrow{\theta}}\varphi(\overrightarrow{\theta})$, $\kappa(\overrightarrow{\theta}) = \frac{1}{2}\left(\frac{\partial^2\varphi}{\partial\theta_1^2} + \frac{\partial^2\varphi}{\partial\theta_2^2}\right)$, $\gamma^2(\overrightarrow{\theta}) = \| \gamma(\overrightarrow{\theta}) \|^2 = \frac{1}{4}\left(\frac{\partial^2\varphi}{\partial\theta_1^2} - \frac{\partial^2\varphi}{\partial\theta_2^2}\right)^2 + \left(\frac{\partial^2\varphi}{\partial\theta_1\partial\theta_2}\right)$.

2.1 Strong lensing modeling

Modeling approaches : Two methods of modelling are used in the community. Parametric modelling is physically motivated and uses small number of clumps to describe the mass density potential (Kneib et al. 1996; Natarajan & Kneib 1996). Non-parametric methods use tesselated (pixelized) mass distributions with no prior (Saha & Williams 1997; Diego et al. 2005; Coe et al. 2010). The two methods are complementary and usually converge towards similar results.

From simple to more complex : The fundamental parameter that lensing events tell the observer is the total mass contained within the Einstein radius, given by: $M(< \theta_E) = \pi\Sigma_{crit}D_{OL}^2\theta_E^2$, where θ_E is the location of the tangential critical line for a circular mass distribution, usually approximated by the tangential arc radius, Σ_{crit} is the critical density, D_{OL} is the angular distance between the observer and the lens.
For non-circular distributions and profiles additional constraints are used, for instance, arcs at different radii are very useful to probe the shape of dark matter profiles. In particular, radial arcs are unique probe to the center surface density (Fort et al. 1992; Smith et al. 2001; Sand et al. 2005; Gavazzi et al. 2003)
The proper way (commonly used in the community) to accurately constrain the mass in cluster cores is thus to use multiple-images with preferably measured spectroscopic redshifts to absolutely calibrate the mass. To do this, one generally denes a likelihood $\pounds$ for the observed data D and parameters p of the model, N systems, n_i images: $\pounds = Pr(D|p) = \prod_{i=1}^{N} \frac{1}{\prod_{j=1}^{n_i}\sigma_{ij}\sqrt{2\pi}} exp^{-\chi^2/2}$ and each image contributes to $\chi_i^2 = \sum_{j=1}^{n_i} \frac{(\theta_{obj}^j - \theta_p^j)^2}{\sigma_{ij}^2}$. θ_p^j is the position predited by model p, and σ_{ij}^2 are errors. For extended arc images, non-parametric pixellated modelling is the only way to take into account the S/N of each image (Dye & Warren 2005; Suyu et al. 2006), but rather combersome for clusters because many images are often involved over large areas. Finally, selecting lensed images is an iterative process, which must be done by humans, a physically motivated mass speed up the process.

Parametric modeling of the various cluster mass components : A good cluster lens model must have Dark Halo(s) for the cluster component(s) ϕ_{c_i} (DM + intracluster gas), Dark halos around massive galaxies (truncated because of tidal stripping) ϕ_{p_j}, the total potentiel being the sum of all components, $\phi_{tot} = \sum_i \phi_{c_i} + \sum_i \phi_{p_j}$. A popular model for galaxies is the physically motivated PIEMD (Brainerd et al. 1996), that allows probing trucation and various mass/light ratio (Limousin et al. 2008; Leauthaud et al. 2011, in COSMOS).

Bayesian modeling : State-of-the-art parametric modelling (LENSTOOL, `http://www.oamp.fr/cosmology/lenstool/`, (Jullo et al. 2007)) is performed using Bayesian inference. The Bayesian approach allows a better parameter exploration and model comparison under the intrinsic degeneracies of lens modeling.

$Pr(p|D, M) = \frac{Pr(D|p,M)Pr(p|M)}{Pr(D|M)}$

Probing the radial profile of the mass in cluster cores : As already mentionned strong lensing arcs are the only observable able to probe the inner profile of DM at the center of clusters. It is important because DM only simulations predict cluster core shapes $\rho_{DM} \propto r^{-\beta}$ and $\beta = -1$ NFW or $\beta = -1.5$ (Moore et al. 1998). Most precise techniques combine stellar dynamics in triaxial halo with lensing to compute independent profiles for DM and Baryonic matter. All recent results on Abell 383 point towards a DM $\beta < -1$. A lot of work is ongoing

for other clusters.

Recent non-parametric strong lensing modeling: With advent of very high-quality data set. Non-parametric modelling is becoming popular (Coe et al. 2010; Zitrin et al. 2010). Non-parametric models replace profiles by pixel (or radial basis function) maps. Due to a large number of degrees of freedom, non-parametric models lead to more flexibility to probe a wide range of mass distributions (Bradač et al. 2005, Bullet cluster). A drawback is that non-parametric model are difficult to interpret and do not take into account known components (e.g. galaxy scale clumps). Hybrid schemes partially solving this problem (mixing parametric and non-parametric techniques are promising (Jullo & Kneib 2009).

2.2 Cluster weak lensing modeling

At larger radii from cluster centers, in subcritical areas, the only available lensing signal is weak lensing. Weak lensing signal in outskirks of clusters must be treated statistically ($\sim$ percent level) and is prone to strong observational errors (PSF variations, foreground contamination). Reconstruction methods are not straitghtforward, but the large number of lensed objects make it useful. A lot of observations are now available either from space with Hubble Space Telescope, and ground with CFHT12K (Bardeau et al. 2007; Hoekstra 2007), Megacam (Gavazzi & Soucail 2007) (Shan et al. 2010), SuprimeCam (Okabe et al. 2010). A lot of progress has also been done on the measurements of galaxy shapes: using a clean sample, the direct method is IMCAT (Kaiser et al. 1995), (Rhodes et al. 2000; Hoekstra 2000), reverse method IM2SHAPE (Bridle et al. 2002), LENSFIT (Kitching et al. 2008) and SHAPELETS (Refregier & Bacon 2003). The best methods have improved through challenges STEP, GREAT8 and 10 (Bridle et al. 2010; Kitching et al. 2012).
Measuring total mass and mass profiles: Direct methods to extract weak lensing signals are aperture mass densitometry (Fahlman et al. 1994). Clowe (1998) proposes to sum up tangential weak shear within a radius θ_1. $M(<\theta) = \pi D_{OL}^2 \theta^2 \Sigma_{crit} \zeta(\theta)$ (Hetterscheidt et al. 2005; Hoekstra 2007; Okabe et al. 2010, e.g.), that method assumes that all background galaxies are at same redshift. Semi-direct methods use surface density estimator (Mandelbaum et al. 2005) : $\Delta\Sigma(r)$, this estimator is then computed directly from parametrized models (Gruen et al. 2011).Finally, one can use a parametric method by fitting directly the weak lensing signal with a parametric model (following strong lensing methods). (Metzler et al. 1999, 2001; King et al. 2001).
Cluster triaxiality: Spherical symetry is not a good approximation for clusters. Triaxial cluster can explain observed discrepancy between the high concentration measured in lensing clusters with regard to DM simulations. (Gavazzi 2005). This is the case fro A1689 (Andersson & Madejski 2004; Lemze et al. 2008; Peng et al. 2009). Combining X-rays, Sunyaev-Zeldovich (SZ) and lensing analyses allows us to probe triaxiality (Mahdavi et al. 2007, on A478). Morandi et al. (2010) Study on MACS J1423.8+2404 shows a triaxial halo with axial ratio 1.53±0.15 (plane of sky) and 1.44±0.07 (line of sight).

3 Mass distribution of cluster samples

Compare lensing analysis of cluster samples with X-ray luminosity, temperature, velocity dispersions, SZ effect. Are cluster relaxed? How much substructure in clusters? How triaxial are they? What are the signatures of merger events? How important are projections? Observations can be compared to numerical simulations in order to test formation paradigm. The challenge is to define and collect a statistically significant dataset spanning a range of spatial scales. Early work: Luppino et al. (1999); Dahle et al. (2002); Smith et al. (2003). Lensing clusters imaged by HST are likely to be biased toward massive end at all redshifts. (+ projection effects). X-ray selection is less biased $\propto$ ICM electron density^2, Smith et al. (2005) finds in 12 clusters $z \sim 0.2$ $L_X > 8 \times 10^{44}$erg/s (0.1-2.4 keV) from XBACS catalog. 70% of that sample shows strong lensing signal. Smith et al. define dynamical relaxation as: a dominant core ($M_{core}/M_{tot} > 0.95$), a dominant central galaxy, and alignment between x-ray and mass distrib. 7 clusters are disturbed, bi or tri modal implying recent merging activities. In contrast, Bardeau et al. (2007) did not see such a difference using CFHT12K imaging. New samples are very much needed but hard to build, work using 50 X-ray clusters is ongoing Hoekstra et al. (2012, Canadian Cluster Comparison Project).

3.1 On-going and future cluster lensing surveys

4 techniques are used to search for clusters; (i) photometric searches : Red-sequence surveys (Gladders 2002), CFHTLS, new surveys starting VST KIDS, Dark Energy Survey (DES). (ii) X-ray selected cluster: ROSAT

based MAssice Cluster Survey (MACS Ebeling et al. 2001; Böhringer et al. 2004, REFLEX) dedicated search WARPS, SHARC, ROSAT deep cluster survey, XMM DCS, XMM LSS (Scharf et al. 2005; Rosati et al. 2002). (iii) SZ search: Atacama Cosmology Telescope Cluster survey (Marriage et al. 2011). South Pole Telescope Cluster survey (Plagge et al. 2010), and Planck. (iv) Weak and strong lensing searched based on photometric surveys or follow-up of x-ray and SZ clusters.

3.2 Targeted cluster surveys

The Local Cluster Substructure Survey (LoCuSS): extend Smith et al. (2005) goals: get mass, structure and thermodynamics of a volume of ~ 80 clusters $0.15 < z < 0.3$ limited sample (Richard et al. 2010), weak lensing of 30 clusters. Principal results: NFW profiles confirmed, Mass concentration relation consistent with ΛCDM (contrary to previous work on large Einstein radius clusters!). First SZ-WL results on 18 clusters, seems to confirm a projection bias for WL prolate undisturbed clusters compared to disturbed clusters (Okabe et al. 2010; Zhang et al. 2010; Marrone et al. 2012).
The MAssive Cluster Survey: 124 X-ray luminous clusters $0.3 < z < 0.7$: many are strong lenses (Zitrin et al. 2011, 12 clusters HST follow-up $z > 0.5$). Many clusters being studied (Limousin et al. 2010, 2012; Morandi et al. 2010). MACSJ0717.5+3745 shows a merger of four structures (Jauzac et al. 2012) weak lensing measurement using 18 pointings HST). MACS sample is significantly richer in arcs than RCS.
ESO distant cluster survey: $z > 0.6$ optical selection of 20 fields of Las Campanas Distant Cluster Survey. Spectroscopy and photomery follow-ups on the most distants clusters. Clowe et al. (2006b) compare mass measurements of 13 EDiSC clusters with luminosities and finds dependence of cluster mass-to-light ratio with redshift.
Red-sequence cluster survey (Gladders 2002). RCS2 1000 deg^2, among 10^4 cluster sample, a small sub-sample show strong lensing events. Appart from identifying them nothing was done yet on them.
The Multi-Cluster Treasury: ongoing CLASH survey, Postman et al. HST follow-up of 20 X-ray clusters.

3.3 Cluster lenses in wide cosmological surveys

Non targeted surveys are rich source of lenses at all scales. They triggered new automated detection procedures and are much need to prepare massive data from EUCLID. The SDSS, although not optimized for lens search (too shallow, poor seeing). Henawi et al. discovers 16 lenses, 21 candidates among 240 clusters. Those samples are statistically clean, will help defining selection functions. Kubo et al. (2009) identify 10 strong lenses in the Sloan Bright Arc Survey. Bayliss et al. (2011); Bayliss (2012) follow-up 26 Strong lensing cluster among SDSS/RCS. The CFHTLS: SL2S (Cabanac et al. 2007; More et al. 2012), 40 group scale, 120 candidates. Limousin et al. (2009) studied mass and light distribution of 13 groups, encovering redshift trends in mass and groups luminosities. Group lensing is a niche for flexion analysis. First large-scale structure maps of lenses. CFHTLS: weak lensing on Deep fields (Gavazzi & Soucail 2007). First maps of weak lensing peaks. Catalog of lensing selected clusters (Shan et al. 2012). Bergé et al. (2008) combined analysis of XMM-LSS and CFHTLS , contrained $\sigma_8 = 0.92^{+0.26}_{-0.30}$. COSMOS: very deep, allows probing fainter clusters at higher redshift. Faure et al. (2008, 2009, 2011), Strong Lensing map of COSMOS $z < 2$ no correlation between lens loci and COSMOS large structures. Leauthaud et al. (2010): weak lensing study of 200 x-ray groups.

4 Comparison of observed lensing cluster properties with theoretical predictions

Internal structure of cluster halos Cosmological DM-only simulations predict NFW profiles for clusters over a large range of range of scales.
On the observational side, lensing analyses probe total mass in the inner 0.1-5 Mpc and tend to show various inner concentrations. Plausible errors in lensing explaining such difference between predictions and observations are contaminations of other structure line of sight, projection biases, and physical feedback of baryons over DM (Comerford & Natarajan 2007).
Mass function of substructure in cluster halos No substructure crisis in clusters between ΛCDM (Springel et al. 2005, Millenium) and galaxy-galaxy lensing analyses in clusters. (Natarajan et al. 2007). Substructure crisis at galaxy scales must come from evolutionary reasons (e.g. baryonic feedback). Group-scale analyses shall also be interesting!

Does Dark Matter exist? The bullet cluster and other clusters showing different distributions between WL and ICM are convincing (Bradač et al. 2006; Clowe et al. 2006a).

5 Future prospects

Space missions: JWST, EUCLID, WFIRST(?) and ground-based project (LSST, DES, TMT?, E-ELT) will bring lensing studies into a distinct new level.
Radio observations: ALMA (SKA?) is expected to boost the field of lensed galaxy combining velocity field data and galaxy shapes.

References

Andersson, K. E. & Madejski, G. M. 2004, ApJ, 607, 190
Bardeau, S., Soucail, G., Kneib, J.-P., et al. 2007, A&A, 470, 449
Bayliss, M. B. 2012, ApJ, 744, 156
Bayliss, M. B., Gladders, M. D., Oguri, M., et al. 2011, ApJ, 727, L26
Bergé, J., Pacaud, F., Réfrégier, A., et al. 2008, MNRAS, 385, 695
Böhringer, H., Schuecker, P., Guzzo, L., et al. 2004, A&A, 425, 367
Bradač, M., Clowe, D., Gonzalez, A. H., et al. 2006, ApJ, 652, 937
Bradač, M., Erben, T., Schneider, P., et al. 2005, A&A, 437, 49
Brainerd, T. G., Blandford, R. D., & Smail, I. 1996, ApJ, 466, 623
Bridle, S., Balan, S. T., Bethge, M., et al. 2010, MNRAS, 405, 2044
Bridle, S. L., Kneib, J.-P., Bardeau, S., & Gull, S. F. 2002, in The Shapes of Galaxies and their Dark Halos, ed. P. Natarajan, 38–46
Cabanac, R. A., Alard, C., Dantel-Fort, M., et al. 2007, A&A, 461, 813
Clowe, D., Bradač, M., Gonzalez, A. H., et al. 2006a, ApJ, 648, L109
Clowe, D., Schneider, P., Aragón-Salamanca, A., et al. 2006b, A&A, 451, 395
Clowe, D. I. 1998, PhD thesis, UNIVERSITY OF HAWAII
Coe, D., Benítez, N., Broadhurst, T., & Moustakas, L. A. 2010, ApJ, 723, 1678
Comerford, J. M. & Natarajan, P. 2007, MNRAS, 379, 190
Dahle, H., Kaiser, N., Irgens, R. J., Lilje, P. B., & Maddox, S. J. 2002, ApJS, 139, 313
Diego, J. M., Protopapas, P., Sandvik, H. B., & Tegmark, M. 2005, MNRAS, 360, 477
Dye, S. & Warren, S. J. 2005, ApJ, 623, 31
Ebeling, H., Edge, A. C., & Henry, J. P. 2001, ApJ, 553, 668
Fahlman, G., Kaiser, N., Squires, G., & Woods, D. 1994, ApJ, 437, 56
Faure, C., Anguita, T., Alloin, D., et al. 2011, A&A, 529, A72
Faure, C., Kneib, J.-P., Covone, G., et al. 2008, ApJS, 176, 19
Faure, C., Kneib, J.-P., Hilbert, S., et al. 2009, ApJ, 695, 1233
Fort, B., Le Fevre, O., Hammer, F., & Cailloux, M. 1992, ApJ, 399, L125
Gavazzi, R. 2005, A&A, 443, 793
Gavazzi, R., Fort, B., Mellier, Y., Pelló, R., & Dantel-Fort, M. 2003, A&A, 403, 11
Gavazzi, R. & Soucail, G. 2007, A&A, 462, 459
Gladders, M. D. 2002, PhD thesis, Department of Astronomy and Astrophysics, University of Toronto
Gruen, D., Bernstein, G. M., Lam, T. Y., & Seitz, S. 2011, MNRAS, 416, 1392
Hetterscheidt, M., Erben, T., Schneider, P., et al. 2005, A&A, 442, 43
Hoekstra, H. 2000, PhD thesis, Kapteyn Astronomical Institute, Groningen, The Netherlands
Hoekstra, H. 2007, MNRAS, 379, 317
Hoekstra, H., Mahdavi, A., Babul, A., & Bildfell, C. 2012, ArXiv e-prints (1208.0606)
Jauzac, M., Jullo, E., Kneib, J.-P., et al. 2012, ArXiv e-prints (1208.4323)
Jullo, E. & Kneib, J.-P. 2009, MNRAS, 395, 1319
Jullo, E., Kneib, J.-P., Limousin, M., et al. 2007, New Journal of Physics, 9, 447
Kaiser, N., Squires, G., & Broadhurst, T. 1995, ApJ, 449, 460

King, L. J., Schneider, P., & Springel, V. 2001, A&A, 378, 748
Kitching, T. D., Balan, S. T., Bridle, S., et al. 2012, MNRAS, 423, 3163
Kitching, T. D., Miller, L., Heymans, C. E., van Waerbeke, L., & Heavens, A. F. 2008, MNRAS, 390, 149
Kneib, J.-P., Ellis, R. S., Smail, I., Couch, W. J., & Sharples, R. M. 1996, ApJ, 471, 643
Kubo, J. M., Allam, S. S., Annis, J., et al. 2009, ApJ, 696, L61
Leauthaud, A., Finoguenov, A., Kneib, J.-P., et al. 2010, ApJ, 709, 97
Leauthaud, A., Tinker, J., Behroozi, P. S., Busha, M. T., & Wechsler, R. H. 2011, ApJ, 738, 45
Lemze, D., Barkana, R., Broadhurst, T. J., & Rephaeli, Y. 2008, MNRAS, 386, 1092
Limousin, M., Cabanac, R., Gavazzi, R., et al. 2009, A&A, 502, 445
Limousin, M., Ebeling, H., Ma, C.-J., et al. 2010, MNRAS, 405, 777
Limousin, M., Ebeling, H., Richard, J., et al. 2012, A&A, 544, A71
Limousin, M., Richard, J., Kneib, J.-P., et al. 2008, A&A, 489, 23
Luppino, G. A., Gioia, I. M., Hammer, F., Le Fèvre, O., & Annis, J. A. 1999, A&AS, 136, 117
Mahdavi, A., Hoekstra, H., Babul, A., et al. 2007, ApJ, 664, 162
Mandelbaum, R., Hirata, C. M., Seljak, U., et al. 2005, MNRAS, 361, 1287
Marriage, T. A., Acquaviva, V., Ade, P. A. R., et al. 2011, ApJ, 737, 61
Marrone, D. P., Smith, G. P., Okabe, N., et al. 2012, ApJ, 754, 119
Metzler, C. A., White, M., & Loken, C. 2001, ApJ, 547, 560
Metzler, C. A., White, M., Norman, M., & Loken, C. 1999, ApJ, 520, L9
Moore, B., Governato, F., Quinn, T., Stadel, J., & Lake, G. 1998, ApJ, 499, L5
Morandi, A., Pedersen, K., & Limousin, M. 2010, ApJ, 713, 491
More, A., Cabanac, R., More, S., et al. 2012, ApJ, 749, 38
Natarajan, P., De Lucia, G., & Springel, V. 2007, MNRAS, 376, 180
Natarajan, P. & Kneib, J.-P. 1996, MNRAS, 283, 1031
Okabe, N., Takada, M., Umetsu, K., Futamase, T., & Smith, G. P. 2010, PASJ, 62, 811
Peng, E.-H., Andersson, K., Bautz, M. W., & Garmire, G. P. 2009, ApJ, 701, 1283
Plagge, T., Benson, B. A., Ade, P. A. R., et al. 2010, ApJ, 716, 1118
Refregier, A. & Bacon, D. 2003, MNRAS, 338, 48
Rhodes, J., Refregier, A., & Groth, E. J. 2000, ApJ, 536, 79
Richard, J., Smith, G. P., Kneib, J.-P., et al. 2010, MNRAS, 404, 325
Rosati, P., Borgani, S., & Norman, C. 2002, ARA&A, 40, 539
Saha, P. & Williams, L. L. R. 1997, MNRAS, 292, 148
Sand, D. J., Treu, T., Ellis, R. S., & Smith, G. P. 2005, ApJ, 627, 32
Scharf, C. A., Zurek, D. R., & Bureau, M. 2005, ApJ, 633, 154
Schneider, P., Ehlers, J., & Falco, E. E. 1992, Gravitational Lenses (Berlin: Springer-Verlag)
Shan, H., Kneib, J.-P., Tao, C., et al. 2012, ApJ, 748, 56
Shan, H. Y., Qin, B., & Zhao, H. S. 2010, MNRAS, 408, 1277
Smith, G. P., Edge, A. C., Eke, V. R., et al. 2003, ApJ, 590, L79
Smith, G. P., Kneib, J.-P., Ebeling, H., Czoske, O., & Smail, I. 2001, ApJ, 552, 493
Smith, G. P., Kneib, J.-P., Smail, I., et al. 2005, MNRAS, 359, 417
Springel, V., White, S. D. M., Jenkins, A., et al. 2005, Nature, 435, 629
Suyu, S. H., Marshall, P. J., Hobson, M. P., & Blandford, R. D. 2006, MNRAS, 371, 983
Zhang, Y.-Y., Okabe, N., Finoguenov, A., et al. 2010, ApJ, 711, 1033
Zitrin, A., Broadhurst, T., Barkana, R., Rephaeli, Y., & Benítez, N. 2011, MNRAS, 410, 1939
Zitrin, A., Broadhurst, T., Umetsu, K., et al. 2010, MNRAS, 408, 1916

SF2A 2012
S. Boissier, P. de Laverny, N. Nardetto, R. Samadi, D. Valls-Gabaud and H. Wozniak (eds)

GAMMA-RAY EMISSION IN GALAXY CLUSTER FROM DARK MATTER ANNIHILATION

C. Combet[1]

Abstract. Clusters of galaxies are potentially important targets for indirect detection of dark matter (DM) in γ-rays, be it from DM annihilation or decay. Here we summarise the results of three recent papers, where we reassessed DM indirect detection prospects in massive halos making use of the recently-released Meta-Catalogue of X-ray Clusters. In particular, we find a stacking strategy to be marginally beneficial for space-borne γ-ray observatories while completely redhibitory for ground-based instruments.

Keywords: Galaxies:clusters:general, Dark matter, Gamma-rays:general

1 Introduction

The annihilation (or decay) of dark matter (DM) particles into $\gamma-$rays has been flagged as one of the most promising channels for indirect detection. While the Galactic centre is the most obvious target (Silk & Bloemen 1987), its large astrophysical $\gamma-$ray background makes identification of an exotic signal challenging (e.g., Aharonian et al. 2004). A good alternative lies with dwarf spheroidal galaxies (dSphs), which are background-free, relatively close by and with DM density profiles that can be constrained from their internal kinematics (e.g., Evans et al. 2004; Walker et al. 2011; Charbonnier et al. 2011; Ackermann et al. 2011).

Due to their huge DM content, clusters of galaxies have also been investigated for indirect detection studies. Although strong constraints have already been derived from X-ray and gravitational lensing studies on the DM distribution in clusters (Pointecouteau et al. 2005; Vikhlinin et al. 2006; Buote et al. 2007; Shan et al. 2010; Pastor Mira et al. 2011; Ettori et al. 2011), obtaining a clear picture of their inner DM distribution is still a challenging task. The standard approach is then to assume NFW (Navarro, Frenk & White 1997) or Einasto (e.g., Merritt et al. 2006) profiles for these objects. Doing so, Fornax, Coma or Perseus have been identified as the best targets for DM emission (Jeltema et al. 2009; Pinzke et al. 2011) when using parameters from 170 clusters of the HIFLUGCS catalogue (Reiprich & Böhringer 2002; Chen et al. 2007).

In three recent papers (Combet et al. 2012; Maurin et al. 2012; Nezri et al. 2012) we make use of the new Meta-Catalogue of X-ray detected Clusters (1743 objects), MCXC (Piffaretti et al. 2011), to i) provide a new ranking of best targets using the MCXC cluster parameters, ii) quantify the improvement of a stacking approach over a single-source analysis and iii) find new directions to discriminate between astrophysical and exotic signals. In this proceeding, we only summarise the first two items in the case of DM annihilation.

2 Modelling DM annihilation γ-ray emission

The γ-ray flux Φ_γ from dark matter annihilations (cm^{-2} s^{-1} sr^{-1} GeV^{-1}) received on Earth in a solid angle $\Delta\Omega$ is generically written as

$$\frac{d\Phi_\gamma}{dE_\gamma} = \frac{1}{4\pi}\frac{\langle\sigma_{\rm ann}v\rangle}{2m_\chi^2}\cdot\frac{dN_\gamma}{dE_\gamma}\times J(\Delta\Omega), \tag{2.1}$$

where m_χ is the particle mass, $\langle\sigma_{\rm ann}v\rangle$ is the velocity-averaged annihilation cross section and dN_γ/dE_γ is the energy spectrum of annihilation products. The dN_γ/dE_γ term depends on the particle physics model and

[1] Laboratoire de Physique Subatomique et de Cosmologie, Université Joseph Fourier Grenoble 1/CNRS/IN2P3/INPG, 53 avenue des Martyrs, 38026 Grenoble, France

is discussed here. Instead, we focus solely on the so-called astrophysics factor J which corresponds to the integration along the line of sight of the dark matter density squared,

$$J(\Delta\Omega) = \int_{\Delta\Omega} \int \rho^2(l,\Omega)\, dl d\Omega \,. \tag{2.2}$$

The latter is computed with the CLUMPY code (Charbonnier et al. 2012), that has been designed to perform this integral in a variety of setups and with large versatility (Milky-way DM halo or external halo, user-defined dark matter profiles, different concentration prescriptions, inclusion of substructures, integration angle, etc.).

For the DM halo smooth profile, we use an NFW (Navarro, Frenk & White 1997)

$$\rho(r) = \frac{\rho_s}{\left(\frac{r}{r_s}\right)\left(1+\frac{r}{r_s}\right)^2} \,, \tag{2.3}$$

where r_s is the scale radius and ρ_s is the normalisation. We note that Einasto profiles (Merritt et al. 2006) give slightly more 'signal' than NFW halos, making our conclusions on detectability conservative.

Cold DM N-body simulations show a high level of clumpiness in the DM distribution (e.g., Diemand et al. 2007; Springel et al. 2008). These substructures boost the signal in the outer parts of the DM halos and should be properly taken into account. The substructure modelling goes as follows: i) the mass distribution is $dN_{\rm subs}/dM \propto M^{-1.9}$ with a mass fraction $f = 10\%$ in substructures (Springel et al. 2008), a minimal and maximal mass of $10^{-6}\ M_\odot$ and $10^{-2} M_{\rm cluster}$ respectively, and the Bullock et al. (2001) concentration (down to the minimal mass); ii) the substructure spatial distribution $dN_{\rm subs}/dV$ follows the host halo smooth profile. With this as our reference configuration, we obtain boost factors of $\sim 10-20$ for the MCXC galaxy clusters. Note that the value of the boost can vary by one or two orders of magnitude depending on the modelling (see sec. 3.4 and figure 4 of Nezri et al. 2012) but that our chosen configuration gives a rather conservative estimate.

3 Results

The 1743 clusters of the MCXC catalogue are processed using the above modelling. The normalisation of each cluster profile (i.e. ρ_s and r_s) is obtained using the M_{500} and R_{500}[i] provided in the catalogue.

The symbols in figure 1 give the J-factor of all the MCXC clusters as a function of their angle ϕ to the Galactic centre, for integration angles $\alpha_{\rm int} = 0.1°$ (left panel) and $\alpha_{\rm int} = 0.5°$ (right panel). The brightest halos are identified with specific symbols. The solid black line corresponds to the total (smooth and substructures) exotic background of the Milky-way halo, peaking at the Galactic centre. The number of halos lying below the Galactic background depends on the integration angle, the contrast $J_{\rm cluster}/J_{\rm Gal}$ increasing as the integration angle is decreased because of the concentrated emission in clusters. Online material of Nezri et al. (2012) gathers the J-values of all MCXC clusters which can readily be used by others. Our new ranking of 'best' targets differs slightly from results based on the HIFLUGCS catalogue (Jeltema et al. 2009; Pinzke et al. 2011) because of the different gas density model used in the MCXC; the results are nonetheless in overall agreement (see Appendix B in Nezri et al. 2012).

The shear number of clusters with significant J-factors (fig. 1, left) had us considering stacking as a viable option to improve the limit of indirect detection. The $\log J - \log N$ histogram (not shown here) has a slope of ~ -2, which is a first indication of the potential of stacking: in the absence of background noise, stacking ten times more objects increases the flux by a factor 100. This is however a too naive view and the signal-to-noise ratio must be considered before any conclusion can be reached.

The left panel in figure 2 shows the evolution of the S/N ratio when stacking cluster signals (in decreasing order of J) for several integration angles (colours). The signal-to-noise ratio goes through a maximum corresponding to a given number of stacked clusters. Stacking more objects increases the noise faster than the signal and becomes pointless. The optimal number of objects to stack increases with decreasing integration angle, once again because of the very centrally-located emission in cluster of galaxies.

Finally, realistic instrumental responses and observational strategies must be considered. For an all-sky γ-ray instrument as Fermi-LAT, all sources are naturally observed the same amount of time. Conversely, for a given granted observation time at a ground-based facility – like the future Cerenkov Telescope Array (CTA)–, a

[i]The radius R_{500} is defined as the radius within which the average density is 500 times the critical density of the Universe (at a given redshift), and M_{500} is the mass within R_{500}.

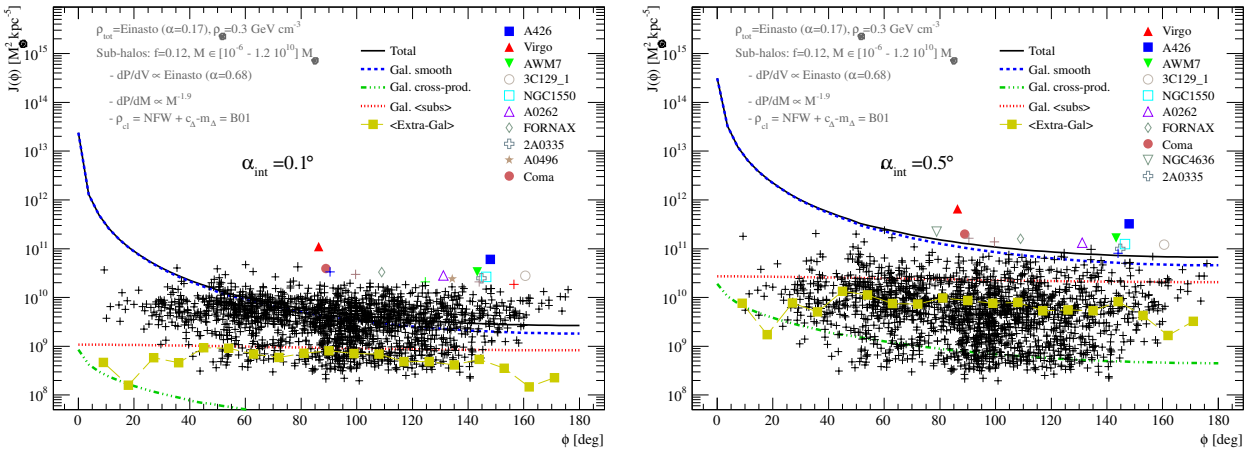

Fig. 1. Computed J-factors for the MCXC sources (the 10 highest-contrast clusters are highlighted, the remaining are shown with a '+' symbol) vs Galactic DM background (total is the sum of smooth, sub-halos, and cross-product|see details in Charbonnier et al. 2012). The yellow filled square symbols are evaluated from the cumulative of the cluster signal in different ϕ bins: this can be interpreted as a lower limit for the extra-galactic DM annihilation signal. **Left panel:** integration angle $\alpha_{\rm int} = 0.1°$. **Right panel:** $\alpha_{\rm int} = 0.5°$.

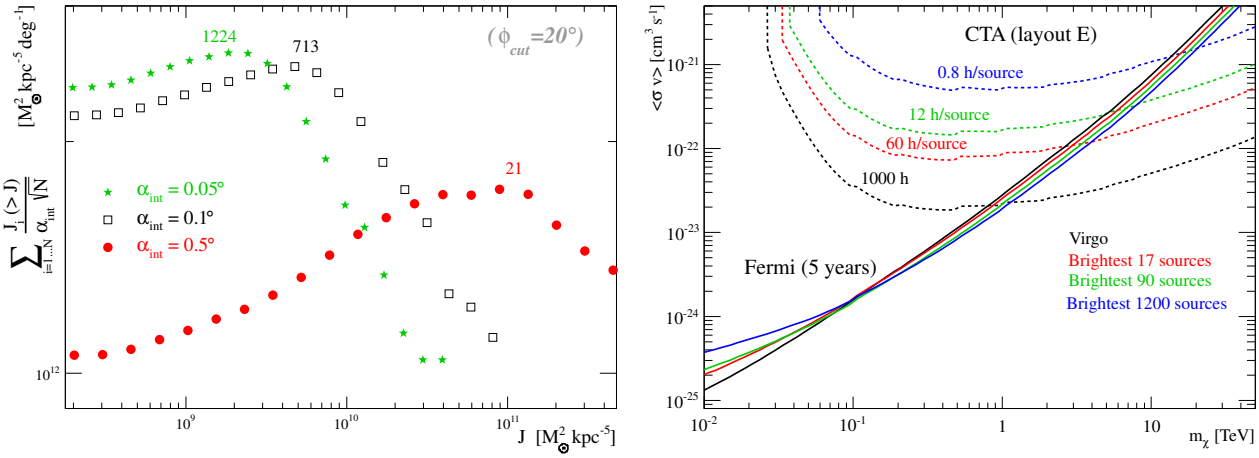

Fig. 2. Left panel: $\sum_i J_i(>J)/\alpha_{\rm int}\sqrt{N}$ (proportional to the cumulative signal-to-noise for a fixed integration angle) as a function of J for the same integration angles. **Right panel:** The 5σ sensitivity of Fermi-LAT (5 years exposure) (solid curves) and CTA (1000 hours total exposure) for stack sizes of the optimum number of sources for a 0.1° (1200) (blue), 0.5° (90) (green) and 1° (17) (red) PSF. Virgo alone is shown in black. For CTA the 1000 hour exposure is divided equally over the number of sources in the stack.

choice must be made between observing one source for the all duration, or attempting to stack several objects, hence dividing-up the observation time. The summary of these considerations is given in fig. 2 (right). This shows in the mass-cross section plane (see eq.(2.1)) the limits that can be achieved using either 5 years of Fermi-LAT data, or 1000 h with CTA. Different colours correspond to stacking different number of objects (with the appropriate integration angle to make stacking optimum for that number of object).

For Fermi-LAT, the stacking strategy yields a marginal improvement (about $\times 2$) above $M_\chi \sim 0.1$ TeV. Below this value, the instrument is in background-limited regime, with poor angular resolution: stacking actually worsens the limit at low energies. For ground-based instruments like CTA, the observation time must be divided up among sources which leads to much less constraining exclusion limits: for ground-based instruments, the best strategy is to look at the supposedly brightest object for as long as possible.

We mentioned in the introduction that dwarf spheroidal galaxies are also very interesting targets for indirect detection. In recent works (Charbonnier et al. 2011; Walker et al. 2011), we have studied the detectability of

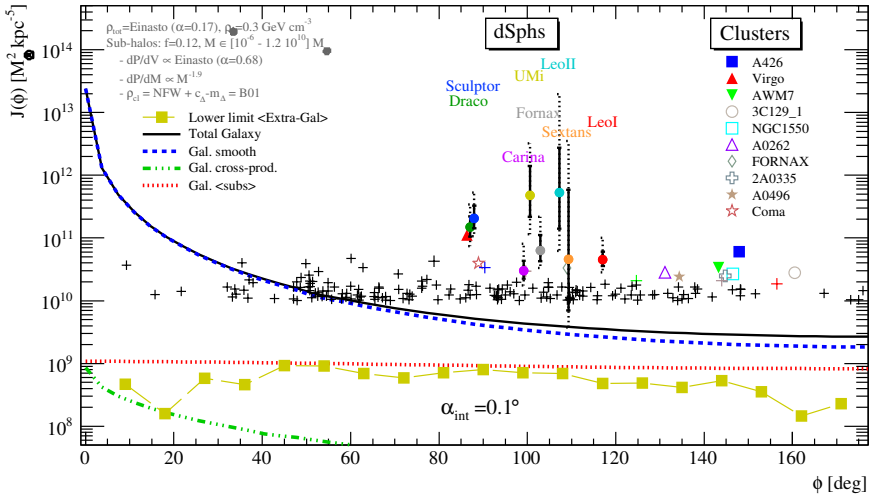

Fig. 3. Same as fig. 1 (left). Symbols with errors bars correspond to J-factors of dSph as evaluated by Charbonnier et al. (2011). Symbols without error bars correspond to the clusters of this study (not all 1743 clusters have been plotted here.).

these objects with Fermi-LAT and CTA. In figure 3, we finally compare the J-factors of the MCXC galaxy clusters to that of dSph galaxies. The brightest clusters have similar J values to the faintest dSph galaxies. Despite large error bars, some of the latter (like Leo II or Ursa Minor) are significantly brighter, making them *a priori* more favourable targets. The lack of cosmic ray induced $\gamma-$ray emission in dSph galaxies is another argument is their favour. As discussed in Maurin et al. (2012), this astrophysical signal is present in galaxy clusters and makes the identification of an exotic signal a more difficult task. Note however that the large uncertainty linked to the substructure boost in clusters prevent making too strong a conclusion.

4 Conclusions

We have evaluated the J-factor of DM annihilation for the 1743 galaxy clusters of the MCXC catalogue. The values we find are in overall agreement with previous studies but differ because of the more robust gas modelling used in the MCXC. In studying the benefit of stacking, we find it is marginally worthwhile for all-sky instruments but completely redhibitory for ground-based telescopes. A benefit of stacking lies nonetheless in the fact that it is a way to wash out the large modelling uncertainties of the dark matter halo in galaxy clusters. In comparing the detection prospect in galaxy clusters to that of dSph galaxies, we conclude that dSph remain a safer option given the clean γ-ray environment they host and the stronger observational constraints that can be put on their dark matter profiles.

References

Ackermann, M. et al. 2011, Physical Review Letters, 107, 241302
Aharonian, F. et al. 2004, A&A, 425, L13
Bullock, J. S., Kolatt, T. S., Sigad, Y., et al. 2001, MNRAS, 321, 559
Buote, D. A., Gastaldello, F., Humphrey, P. J., et al. 2007, ApJ, 664, 123
Charbonnier, A., Combet, C., Daniel, M., et al. 2011, MNRAS, 418, 1526
Charbonnier, A., Combet, C., & Maurin, D. 2012, Computer Physics Communications, 183, 656
Chen, Y., Reiprich, T. H., Böhringer, H., Ikebe, Y., & Zhang, Y.-Y. 2007, A&A, 466, 805
Combet, C., Maurin, D., Nezri, E., et al. 2012, Phys. Rev. D, 85, 063517
Diemand, J., Kuhlen, M., & Madau, P. 2007, ApJ, 657, 262
Ettori, S., Gastaldello, F., Leccardi, A., et al. 2011, A&A, 526, C1
Evans, N. W., Ferrer, F., & Sarkar, S. 2004, Phys. Rev., D69, 123501
Jeltema, T. E., Kehayias, J., & Profumo, S. 2009, Phys. Rev. D, 80, 023005

Maurin, D., Combet, C., Nezri, E., & Pointecouteau, E. 2012, ArXiv e-prints: 1203.1166, A&A accepted
Merritt, D., Graham, A. W., Moore, B., Diemand, J., & Terzić, B. 2006, AJ, 132, 2685
Navarro, Frenk & White. 1997, ApJ, 490, 493
Nezri, E., White, R., Combet, C., et al. 2012, MNRAS, 425, 477
Pastor Mira, E., Hilbert, S., Hartlap, J., & Schneider, P. 2011, A&A, 531, A169
Piffaretti, R., Arnaud, M., Pratt, G. W., Pointecouteau, E., & Melin, J.-B. 2011, A&A, 534, A109
Pinzke, A., Pfrommer, C., & Bergström, L. 2011, Phys. Rev. D, 84, 123509
Pointecouteau, E., Arnaud, M., & Pratt, G. W. 2005, A&A, 435, 1
Reiprich, T. H. & Böhringer, H. 2002, ApJ, 567, 716
Shan, H., Qin, B., Fort, B., et al. 2010, MNRAS, 406, 1134
Silk, J. & Bloemen, H. 1987, ApJ, 313, L47
Springel, V., Wang, J., Vogelsberger, M., et al. 2008, MNRAS, 391, 1685
Vikhlinin, A., Kravtsov, A., Forman, W., et al. 2006, ApJ, 640, 691
Walker, M. G., Combet, C., Hinton, J. A., Maurin, D., & Wilkinson, M. I. 2011, ApJ, 733, L46

SF2A 2012
S. Boissier, P. de Laverny, N. Nardetto, R. Samadi, D. Valls-Gabaud and H. Wozniak (eds)

MASS-SIZE RELATION AT HIGH REDSHIFT IN DIFFERENT ENVIRONMENTS

L. Delaye[1,2], M. Huertas-Company[1] and S. Mei[1]

Abstract. We study cluster early-type galaxies (ETGs) from the HAWK-I cluster survey in the redshift range $0.8 < z < 1.5$. Comparing them to a sample of field ETGs, we are able to analyze the environmental dependence of the mass-size relation and size evolution of passive ETGs. We find no evidence for an environmental effect within 1σ level for passive ETGs with stellar masses above 3×10^{10} $M_{\odot}$.

Keywords: Galaxies: elliptical, Galaxies: clusters: general, Galaxies: evolution, Galaxies: high redshift

1 Introduction

Many studies have already shown that massive passive galaxies at high redshift ($z \sim 2$) are more compact than their local counterpart at low redshift (Daddi et al. 2005; Trujillo et al. 2006; Buitrago et al. 2008; van Dokkum et al. 2008; Saracco et al. 2011; Newman et al. 2012, and references therein). Even if those results have been controversial for a few years, they are now well established because of independent measurements. Martinez-Manso et al. (2011); van de Sande et al. (2011) and Newman et al. (2012) have confirmed the compact nature of high redshift galaxies through dynamical mass measurements.

Two main mechanisms can theoretically explain this growth in size. One involves dry mergers (Naab et al. 2009; Shankar et al. 2012, and references therein) which allow the galaxy to increase its size by spreading stars in the outer parts after a merger event. The other involves AGN feedback and is called the puffing-up scenario (Fan et al. 2008, 2010): AGN expulses gas from the galaxy and the stars rearrange themselves thus increasing the radius. According to the hierarchical model, galaxies populating the most massive halos, experience on average more mergers and thus are expected to be larger by a factor of a few (Shankar et al. 2012, and 2013, in preparation). So, if the merger scenario is correct, we could observe a different evolution in different environments such as clusters and the field: cluster galaxies are expected to be more evolved, hence larger.

From the observational point of view, there are still some controversies. Papovich et al. (2012) and Cooper et al. (2012) found larger galaxies in cluster environment whereas Raichoor et al. (2012) found the opposite trend. Other studies do not find any trend with the environment (Maltby et al. 2010; Rettura et al. 2010; Huertas-Company et al. 2012). However, these results have been obtained at different redshifts, with different galaxy selection criteria (such as morphology, color, star formation activity, masses threshold...), with different way to measure the environment and with low statistics so that it might explain the differences.

In this work, we study the dependence of the mass-size relation of passive early-type galaxies (ETGs) on environment at $z = 0.8 - 1.5$, an epoch where massive cluster galaxies are assembling (Rettura et al. 2010; Lidman et al. 2012).

2 Data and Sample selection

2.1 Cluster selection

We selected nine clusters having at least 10 spectroscopically confirmed cluster members, beyond $z = 0.8$ and covering a broad redshift interval, imaged with the *Advanced Camera for Surveys* (ACS) on the *Hubble Space Telescope* (HST) in at least two bands and having deep ground-based images in the the near-IR.

[1] GEPI, Paris Observatory, 77 av. Denfert-Rochereau, 75014 Paris, France
[2] IRFU/SAp, CEA Saclay, Orme des Merisiers, 91191 Gif-sur-Yvette, France

Eight of the nine clusters in this paper were targeted in the HAWK-I[i] cluster survey (HCS: Lidman et al. in prep). The HCS is a near-IR imaging survey that targeted nine well known high redshift galaxy clusters between $z = 0.8$ and 1.5. The aim of the survey was to obtain deep, high-resolution images of a sample of clusters for the purpose of studying the impact of environment on the evolution of cluster members. The ninth cluster in our sample, RDCS J1252-2827, was imaged with ISAAC (Infrared Spectrometer And Array Camera, Lidman et al. 2004). For some clusters, we add J-band data from SofI[ii].

2.2 Analysis

We use GALAPAGOS (Barden et al. 2005) to estimate sizes the ACS/HST z_{850}-band which is the closest available to the B rest-frame filter at the redshifts we consider. This code uses GALFIT (Peng et al. 2002) to model the galaxy light profile using a 2D Sersic profile with a fixed sky value previously estimated. The accuracy of our size estimates is assessed through extensive simulations in which we drop mock galaxies in real background images. Sizes can be recovered with a systematic error lower than 0.1 and a dispersion lower than 0.30 up to $z_{850} = 24$ AB mag (see Delaye et al. 2012, in prep).

We estimate stellar masses through spectral energy distribution (SED) fitting using the spectral library of Bruzual & Charlot (2003) (hereafter, BC03) and the LePhare code (Arnouts et al. 1999; Ilbert et al. 2006). The models were generated using a Chabrier (2003) IMF, three different metallicities ($Z = [0.004, 0.008, 0.02$ (solar)]), exponentially declining star formation histories $\psi(t) \propto e^{-t/\tau}$ with a characteristic time $0.1 \leq \tau$ (Gyr) ≤ 30, and no dust extinction. We fixed the redshift at the cluster redshift to better constrain the stellar mass (see Delaye et al. in prep).

To determine the morphology, we use GalSVM, a non-parametric code based on support-vector machines (Huertas-Company et al. 2008, 2009, 2011) on the HST/ACS F850LP images. The local training sample used is a catalogue from the SDSS DR7 of about 14,000 galaxies visually classified (Nair & Abraham 2010). We define as ETGs the galaxies having a probability greater than 0.5 of being early-type (see Huertas-Company et al. 2012, and Delaye et al. (in prep) for details). We also made a visual classification to confirm our results.

2.3 Sample selection

This work is focused on red-sequence massive ETGs. We consider only galaxies with $z_{850} < 24$ AB mag in order to have accurate size estimates and morphologies and make several further selections to build our final sample of cluster members. For each cluster, we perform an iterative sigma-clipping fit to the red sequence in the $(i_{775} - z_{850})$-z_{850} plane, using only spectroscopically confirmed members and then select objects within 3σ of the best fit.

Among the selected red-sequence population, we select ETGs based on our automated morphological classification. We remove from the final sample, objects for which the Sersic fits did not converge (only 5 for the whole sample). We consider that the fitting procedure has converged if z_{850} brighter than 24 mag, $0.1'' < R_{\rm eff} < 1.6''$ and $1 < n < 8$. Finally, we keep only ETGs more massive than the completeness limit, $M_{\rm lim} = 3 \times 10^{10}$ M$_\odot$.

3 Field comparison sample

In order to measure the environmental effects on the size evolution of passive ETGs, we define a field sample from a combination of four different datasets to be compared with our main clusters sample.

A first set of galaxies is built by putting together all foreground and background galaxies detected in the cluster fields with spectroscopic redshifts ($z - z_{cl} > 0.02$). We apply the same color selection than for cluster galaxies and all derived quantities (stellar masses, sizes and morphologies) are obtained with the same methods described for the cluster sample.

We add a sample of galaxies from the COSMOS survey (Schinnerer et al. 2007; Bondi et al. 2008) with photometric redshifts between $z = 0.7$ and $z = 1.6$ taken from the catalog described in Huertas-Company et al. (2012) and Georges et al. (2012). Passive galaxies are selected using the color selection NUV $- R > 3.5$ (Ilbert et al. 2010) corrected from dust extinction. Sizes are estimated using GALAPAGOS on the HST/ACS F814W images. Stellar masses were estimated using the LePhare code with BC03 library, a Chabrier IMF and the

[i] High Acuity Wide-field K-band Imager
[ii] Son of ISAAC

30 available filters in COSMOS field. Finally morphologies were derived automatically (see Huertas-Company et al. 2012, for a detailed description).

Twenty-four additional field galaxies in the redshift range $1.1 < z < 1.4$ with published sizes, stellar masses and morphologies (Raichoor et al. 2012) from the GOODS-CDF-S field (Giavalisco et al. 2004) are also considered. Stellar masses were measured with an SED fitting code (different from LePhare) using BC03 models and a Salpeter IMF ($\log(M_{\rm Chabrier}) = \log(M_{\rm Salpeter}) - 0.25$, Bernardi et al. 2010). Sizes were computed on the HST/ACS F850LP image using GALFIT with a fixed sky value. Galaxies were visually classified in the F850LP images (see Raichoor et al. 2011, for a detailed description).

Finally, we add galaxies in the redshift range $0.7 < z < 1.6$ from the CANDELS survey with published stellar masses and sizes by (Newman et al. 2012). Galaxy sizes are also derived with GALFIT (see Newman et al. 2012, for detail) in the optical rest-frame band. Stellar masses were computed through SED fitting using Bruzual (2007) models and a Salpeter IMF. To convert into Chabrier IMF, we applied the same correction than above and to convert from CB07 to BC03 models, we applied: $\log(M_{\rm BC03}) = \log(M_{\rm CB07}) + 0.05 \times z$ (Newman, private communication) where z is the redshift. Galaxies in this sample were selected to be quiescent with SSFR< 0.02 Gyr^{-1} and no detection in the MIPS 24μm channel (Newman et al. 2012), but no morphological information is provided.

4 Mass-size relation and size evolution

In the following, we gather all passive ETGs in clusters and all passive ETGs in the field in 3 redshift bins ($0.7 \leq z < 0.9$, $0.9 \leq z < 1.1$ and $1.1 \leq z < 1.6$).

In Figure 1, we show the mass-size relation (MSR) of passive ETGs in clusters and in the field in the three different redshift bins as well as the best fit power law models. Slopes of the MSRs of ETGS in clusters and in the field are consistent within 1σ at all redshifts between 0.7 and 1.6.

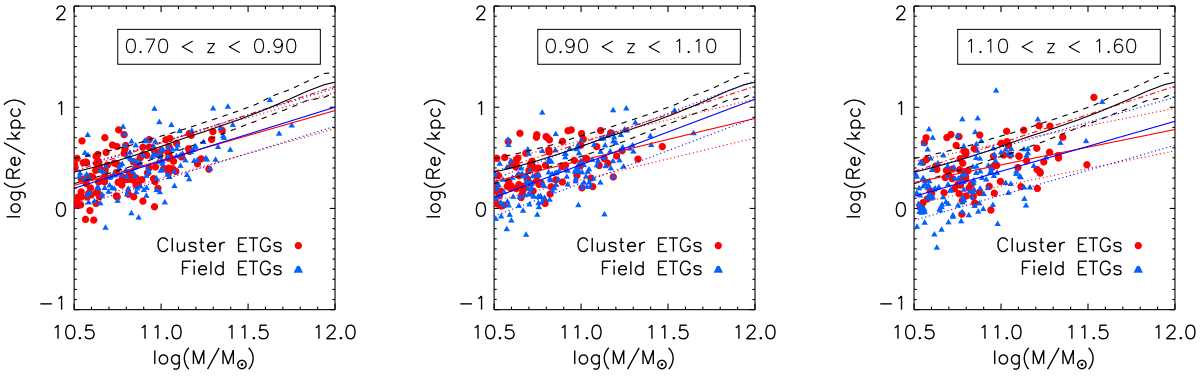

Fig. 1. Mass-size relation of passive field (blue triangles) and cluster (red circles) early-type galaxies. Blue and red lines correspond respectively to the best fit for field and cluster MSR $\pm 1\sigma$ (dotted lines). The local MSR of Bernardi et al. (2010) is in black lines.

To study the size evolution, we compute the mean mass-normalized ($R_e/M_{11}^{0.57}$ with $M_{11} = 10^{11}$ M$_\odot$, Newman et al. (2012); Cimatti et al. (2012)) radius in each of the 3 redshift bins. Mean sizes are estimated by fitting a gaussian function on the size ratio distribution; so that the reported values are the positions of the peaks of the best-fit. Errors are estimated through bootstrapping. Results do not change if we consider a median or a 3-sigma clipped average.

We include a local comparison sample from the SDSS built by cross-correlating the morphological catalog by Huertas-Company et al. (2010) with the group catalog by Yang et al. (2007) updated to the DR7. Sizes come from Sersic fits performed by Meert et al. (2012, submitted). We selected ETGs ($P(ETG) > 0.7$) and divided the sample in field ($\log M_h < 12.5$) and clusters ($\log M_h > 14$).

Figure 2 represents the mass normalized radius evolution of passive ETGs in cluster and in the field for masses above 3×10^{10} M$_\odot$. No significant differences are observed in the size evolution. Field ETGs follow $R_e/M_{11}^{0.57} \propto (1+z)^\alpha$ with $\alpha = -1.05 \pm 0.04$ and cluster ETGs have a similar α value ($\alpha = -1.02 \pm 0.06$). Our

results are consistent with size evolution found by Newman et al. (2012); Cimatti et al. (2012); Damjanov et al. (2011).

Finally, we can conclude that, with $M \geq 3 \times 10^{10}$ $M_{\odot}$, field and cluster passive ETGs evolve in the same way taking into account the large uncertainties.

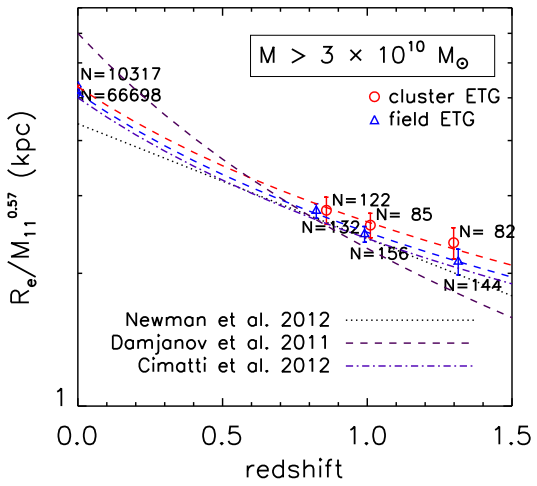

Fig. 2. Size evolution in function of redshift for passive ETGs with $\log(M/M_{\odot}) \geq 10.5$ in clusters (red circles) and in the field (blue triangles). Radius are normalized to $M_{\star} = 10^{11}$ $M_{\odot}$ using the slope $R_e \propto M_{\star}^{0.57}$. Black dotted line corresponds to the fit of Newman et al. (2012). Dashed line is the size evolution fit of Cimatti et al. (2012) and dash-dotted line the one of Damjanov et al. (2011).

5 Conclusion

We have studied a large sample of cluster and field passive early-type galaxies between $z = 0.7$ and $z = 1.6$. We estimated the stellar masses with SED fitting method using BC03 stellar population model and sizes fitting a 2D Sersic profile to the HST/ACS F850LP images. Comparing these two environments, we do not find differences in the mass-size relation and size evolution of passive ETGs at 1σ level. The size evolution we found for both environment is consistent with previous works of Damjanov et al. (2011); Newman et al. (2012) and Cimatti et al. (2012). These results might depend on morphology and galaxy mass range as discussed in Huertas-Company et al. (2012). We will discuss this in our paper Delaye et al. (in prep) as well as a comparison with hierarchical model predictions.

References

Arnouts, S., Cristiani, S., Moscardini, L., et al. 1999, MNRAS, 310, 540

Barden, M., Rix, H.-W., Somerville, R. S., et al. 2005, ApJ, 635

Bernardi, M., Shankar, F., Hyde, J. B., et al. 2010, MNRAS, 404, 2087

Bondi, M., Ciliegi, P., Schinnerer, E., et al. 2008, ApJ, 681, 1129

Bruzual, G. 2007, in Astronomical Society of the Pacific Conference Series, Vol. 374, From Stars to Galaxies: Building the Pieces to Build Up the Universe, ed. A. Vallenari, R. Tantalo, L. Portinari, & A. Moretti, 303

Bruzual, G. & Charlot, S. 2003, MNRAS, 344, 1000

Buitrago, F., Trujillo, I., Conselice, C. J., et al. 2008, ApJL, 687, L61

Chabrier, G. 2003, ApJL, 586, L133

Cimatti, A., Nipoti, C., & Cassata, P. 2012, MNRAS, 422, L62

Cooper, M. C., Griffith, R. L., Newman, J. A., et al. 2012, MNRAS, 419, 3018

Daddi, E., Renzini, A., Pirzkal, N., et al. 2005, ApJ, 626, 680

Damjanov, I., Abraham, R. G., Glazebrook, K., et al. 2011, ApJL, 739, L44

Fan, L., Lapi, A., Bressan, A., et al. 2010, ApJ, 718, 1460
Fan, L., Lapi, A., De Zotti, G., & Danese, L. 2008, ApJL, 689, L101
Giavalisco, M., Ferguson, H. C., Koekemoer, A. M., et al. 2004, ApJL, 600, L93
Huertas-Company, M., Aguerri, J. A. L., Bernardi, M., Mei, S., & Sanchez Almeida, J. 2010, VizieR Online Data Catalog, 352, 59157
Huertas-Company, M., Aguerri, J. A. L., Bernardi, M., Mei, S., & Sánchez Almeida, J. 2011, A&A, 525, A157
Huertas-Company, M., Foex, G., Soucail, G., & Pelló, R. 2009, A&A, 505, 83
Huertas-Company, M., Mei, S., Shankar, F., et al. 2012, ArXiv e-prints
Huertas-Company, M., Rouan, D., Tasca, L., Soucail, G., & Le Fèvre, O. 2008, A&A, 478, 971
Ilbert, O., Arnouts, S., McCracken, H. J., et al. 2006, A&A, 457, 841
Ilbert, O., Salvato, M., Le Floc'h, E., et al. 2010, ApJ, 709, 644
Lidman, C., Rosati, P., Demarco, R., et al. 2004, A&A, 416, 829
Lidman, C., Suherli, J., Muzzin, A., et al. 2012, ArXiv e-prints (1208.5143)
Maltby, D. T., Aragón-Salamanca, A., Gray, M. E., et al. 2010, MNRAS, 402, 282
Martinez-Manso, J., Guzman, R., Barro, G., et al. 2011, ApJL, 738, L22
Naab, T., Johansson, P. H., & Ostriker, J. P. 2009, ApJL, 699, L178
Nair, P. B. & Abraham, R. G. 2010, ApJS, 186, 427
Newman, A. B., Ellis, R. S., Bundy, K., & Treu, T. 2012, ApJ, 746, 162
Papovich, C., Bassett, R., Lotz, J. M., et al. 2012, ApJ, 750, 93
Peng, C. Y., Ho, L. C., Impey, C. D., & Rix, H. 2002, AJ, 124, 266
Raichoor, A., Mei, S., Nakata, F., et al. 2011, ApJ, 732, 12
Raichoor, A., Mei, S., Stanford, S. A., et al. 2012, ApJ, 745, 130
Rettura, A., Rosati, P., Nonino, M., et al. 2010, ApJ, 709, 512
Saracco, P., Longhetti, M., & Gargiulo, A. 2011, MNRAS, 412, 2707
Schinnerer, E., Smolčić, V., Carilli, C. L., et al. 2007, ApJS, 172, 46
Shankar, F., Marulli, F., Bernardi, M., et al. 2012, ArXiv e-prints
Trujillo, I., Förster Schreiber, N. M., Rudnick, G., et al. 2006, ApJ, 650, 18
van de Sande, J., Kriek, M., Franx, M., et al. 2011, ApJL, 736, L9
van Dokkum, P. G., Franx, M., Kriek, M., et al. 2008, ApJL, 677, L5
Yang, X., Mo, H. J., van den Bosch, F. C., et al. 2007, ApJ, 671, 153

SF2A 2012
S. Boissier, P. de Laverny, N. Nardetto, R. Samadi, D. Valls-Gabaud and H. Wozniak (eds)

THE EXTRAORDINARY CLUSTER OF GALAXIES ABELL 3376: AN OPTICAL VIEW

F. Durret[1], C. Perrot[2], G. B. Lima Neto[3], C. Adami[4] and J. Bagchi[5]

Abstract. Abell 3376 is a merging cluster of galaxies at redshift $z = 0.046$. It is famous mostly for its giant radio arcs, and shows an elongated and highly substructured X-ray emission, but has not been analysed in great detail at optical wavelengths. We have obtained deep images of Abell 3376 in the B and R bands and present here preliminary results on the B band galaxy luminosity function.

Keywords: Galaxies: clusters: individual: Abell 3376, Galaxies: luminosity function, mass function

1 Introduction

Abell 3376[i] is a merging cluster of galaxies at redshift $z = 0.046$. Its most remarkable feature is the existence of giant ($\sim$2 Mpc $\times$ 1.6 Mpc) ring-shaped nonthermal radio-emitting structures discovered by Bagchi et al. (2006, see their Fig. 1). These structures can be naturally explained by the acceleration of electrons due to the merger of two clusters.

The fact that it is a merging structure is indeed confirmed in X-rays. The XMM-Newton image of Abell 3376 is strongly elongated along the northeast-southwest axis joining the two giant radio arcs, and the temperature and metallicity maps of the X-ray gas show strong inhomogeneities (see Bagchi et al. 2006, Fig. 2). Recent numerical simulations by Machado & Lima Neto (2012) based on the parallel SPH code Gadget-2 have been able to reproduce the X-ray emissivity map, and suggest an approximately head-on collision with a mass ratio of about 3:1, observed about 0.2 Gyr after the instant of central passage, and taking place very close to the plane of the sky. Still another proof for merging resides in the fact that the brightest cluster galaxy is far from the region with strong X-ray emission, as seen in Fig. 1.

Note that Abell 3376 is part of the WINGS survey (Fasano et al. 2006) and its galaxy spatial distribution confirms the existence of substructures (Ramella et al. 2007). We retrieved from the NED data base a catalogue of galaxies with V band magnitudes within a radius of 40 arcmin around the cluster.

2 New optical data

We have obtained deep optical images in the B and R bands with the Cerro Tololo 4m telescope and the MOSAIC2 camera. Individual exposure times were 300 s in B and 2000 s in R. In total, we obtained 4 images in B and 4 images in R, in each of two adjacent regions covering the east and west parts of the cluster.

Since the cluster was observed during a single entire night, the airmass variations were important, so the images were extinction corrected individually after the usual bias and flat field corrections. They were then assembled into two large images, one in B and one in R, using the SCAMP and SWARP softwares developed by E. Bertin (`http://www.astromatic.net/`). These images cover $1.16065 \times 0.5947 = 0.69028$ deg^2 (scale 0.266 arcsec/pixel). Note that since the individual exposures in the R band were long, objects brighter than R$\sim$ 19 are saturated and will not be considered for scientific purposes.

[1] UPMC Université Paris 06, UMR 7095, Institut d'Astrophysique de Paris, 98bis Bd Arago, F-75014, Paris, France
[2] Observatoire de Paris-Meudon, France
[3] IAG, USP, R. do Matão 1226, 05508-090, São Paulo/SP, Brazil
[4] Aix Marseille Université, CNRS, LAM (Laboratoire d'Astrophysique de Marseille) UMR 7326, 13388, Marseille, France
[5] IUCAA, Pune University Campus, Post Bag 4, Pune 411007, India
[i] Based on observations taken with the CTIO Blanco and SOAR telescopes. This research has made use of the NED data base.

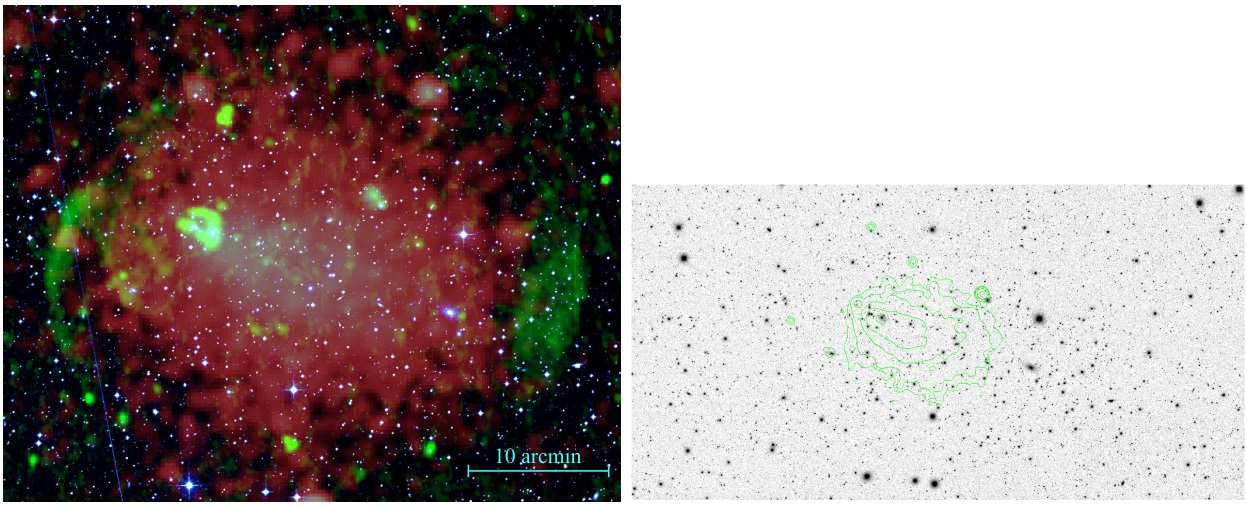

Fig. 1. Left: image of Abell 3376 with the radio (VLA, 1.4 GHz) and X-ray (XMM-Newton) emissions superimposed on the optical one, in green and red respectively. **Right:** optical image obtained with the CTIO/Blanco telescope with XMM-Newton X-ray contours superimposed. North is top and east to the left.

In order to obtain a photometric calibration of these images, since no standard stars had been taken, we reobserved the central region of Abell 3376 the following year with the SOAR telescope in the same bands. These images were taken in photometric conditions with respective exposure times of 600 s and 300 s in B and R, and covered a region of $0.084125 \times 0.08075 = 0.0067931$ deg^2 (scale 0.15 arcsec/pixel). We calibrated these images photometrically with Landolt standard stars, cross-identified objects present in the Blanco and SOAR images, and thus calibrated the Blanco images in B and R.

We now concentrate only on the deep large Blanco images.

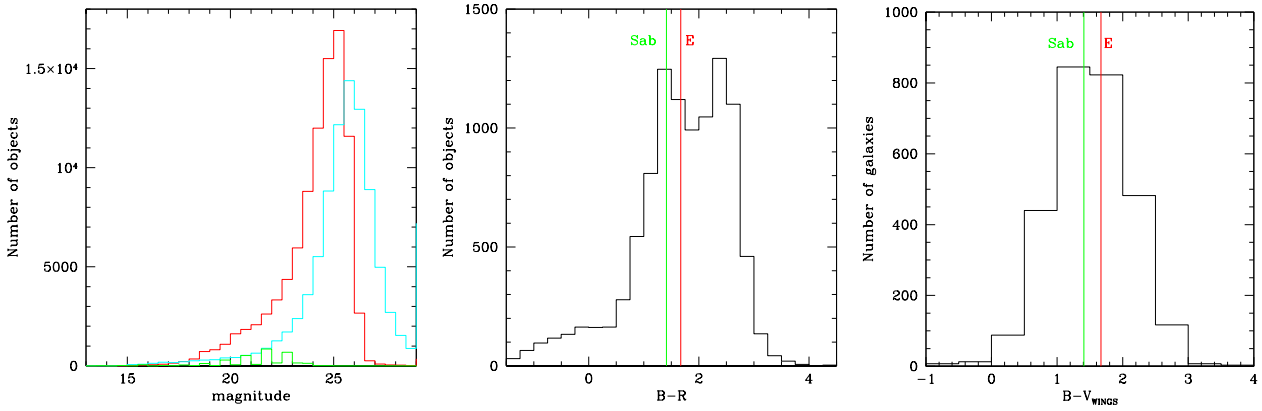

Fig. 2. Left: magnitude histograms for all the objects (stars+galaxies) detected in our images in the B (cyan) and R (red) bands. The green histogram shows the *galaxy* counts in the V band from the WINGS survey. **Middle:** (B-R) histogram, with typical values for elliptical and Sab galaxies indicated as red and green lines respectively (taken from Fukugita et al. 1995). **Right:** (B-V$_{\rm WINGS}$) histogram, with typical values for elliptical and Sab galaxies indicated as red and green lines.

Magnitude histograms in the B and R bands, together with the (B-R) histogram are displayed in Fig. 2 for all the objects of our images (stars + galaxies). In order to confirm the quality of our photometric calibration, we also show in this figure the histogram of the (B-V$_{\rm WINGS}$) colour.

The star-galaxy separation was based on the maximum surface brightness $\mu_{max,R}$ versus R band magnitude diagram.

3 The galaxy luminosity function in the B band

Two methods are usually applied to compute galaxy luminosity functions. The first one is to draw a colour-magnitude diagram, to superimpose on this diagram the positions of galaxies having a spectroscopic redshift in the cluster in order to define the position of the red sequence as well as possible, and to extract the galaxies belonging to the cluster along this red sequence. The second method is to count all the galaxies in magnitude bins and subtract statistically the contribution of background galaxies, using field galaxy counts.

In view of the saturation problems in the R band image, the first method cannot be applied, since we cannot define the red sequence for galaxies brighter than R∼19, which are those with spectroscopic redshifts. We shall therefore apply the second method, and subtract the field galaxy counts per square degree taken by McCracken et al. (2003) in the same filters.

Since more tests are necessary to test the quality of our R band data, we will present here only our results in the B band.

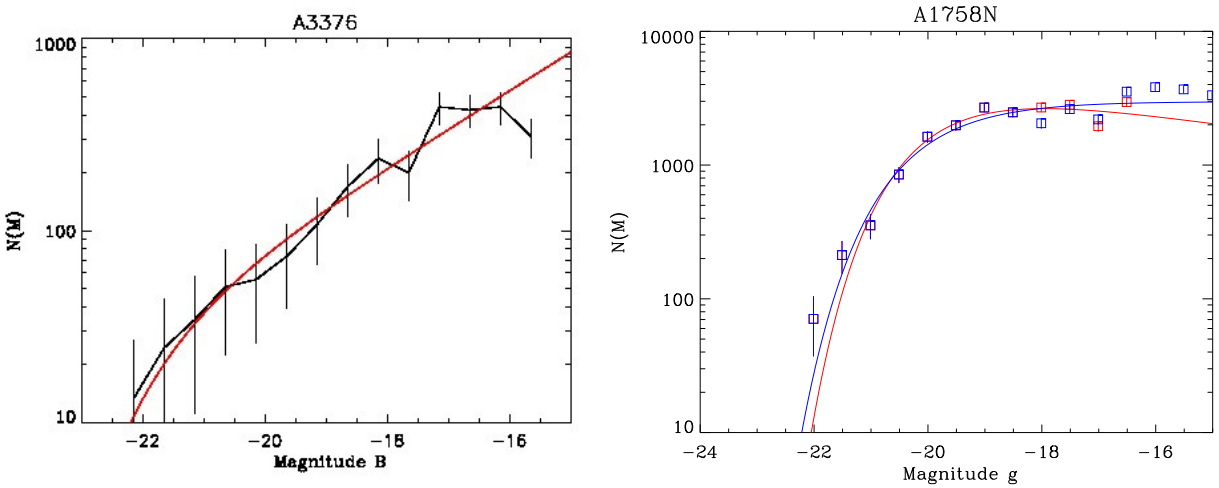

Fig. 3. Left: Galaxy luminosity function of Abell 3376 in the B band. **Right:** Galaxy luminosity function of the merging cluster Abell 1758 in the g band. The blue and red points correspond to the two methods to select galaxies described in the text, and the best Schechter function fits are drawn with the same colours as the corresponding points. At bright magnitudes the points exactly coincide, and because the blue points were plotted after the red ones, they appear blue.

The galaxy luminosity function in the B band (as a function of absolute magnitude, to make the comparison easier with other clusters, assuming a distance modulus of 36.40 for Abell 3376) is shown in Fig. 3. It was fit by a Schechter function:

$$S(M) = 0.4 \ln 10 \, \phi^* \, y^{\alpha+1} \, e^{-y}$$

with $y = 10^{0.4\,(M^*-M)}$.

The parameters of the Schechter function fit are $M^* = -20.59 \pm 0.23$ and $\alpha = -1.33 \pm 0.25$ in the $[-22.15, -15.65]$ B band absolute magnitude interval. Note that the faint end slope depends on the limit set at faint magnitudes.

In order to check down to which magnitude we could reasonably fit the GLF, we performed simple simulations to estimate the completeness of our galaxy catalogue as a function of magnitude. Our method is to add "artificial stars" (i.e. 2D Gaussian profiles with the same full-width-at-half-maximum as the average image point spread function) of different magnitudes to the CCD images and attempted to recover them by running SExtractor again with the same parameters used for object detection and classification on the original images. In this way, the completeness was measured on the original images.

These simulations give a completeness percentage for stars. This is obviously an upper limit for the completeness level for galaxies, because stars are easier to detect than galaxies. However, we have shown that this method yields a good estimate of the completeness for normal galaxies if we apply a shift of ~ 0.5 mag (see Adami et al. 2006). Results are shown in Fig. 4.

From these simulations, and taking into account the fact that the results are worse by ~ 0.5 mag for mean galaxy populations than for stars, we can consider that our galaxy catalogue in the B band is complete to better than 90% for B$\leq$ 24.5.

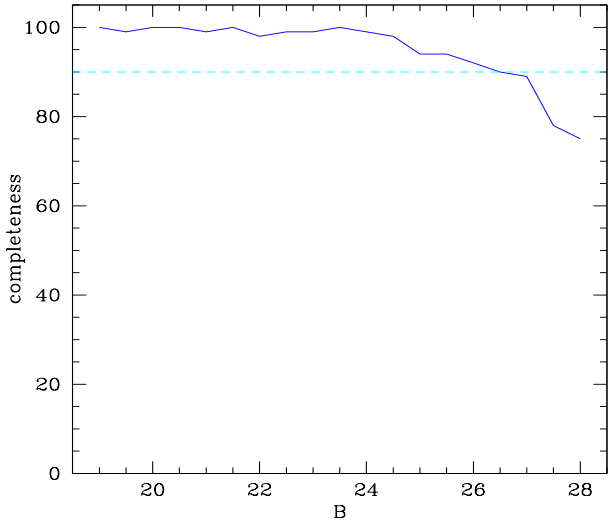

Fig. 4. Completeness as a function of magnitude in percentages in the B band for point–like objects. A shift of ~ 0.5 mag gives a good estimate of the completeness for galaxies (see text). The dashed line shows the 90% completeness level (for stars).

The faint end slope of the galaxy luminosity function has therefore been estimated in a magnitude interval where the completeness is still higher than 90%, and can therefore be considered as reliable.

4 Conclusions

The best fit parameters for the galaxy luminosity function in the B band for Abell 3376 can be compared to another merging cluster, Abell 1758 North, which we recently analysed using exactly the same method (Durret et al. 2011). We derived for this cluster a galaxy luminosity function in the g band and found a faint end slope $\alpha = -1.00 \pm 0.02$ (Durret et al. 2011). This slope is notably flatter than the one we estimated for Abell 3376, as clearly seen in Fig. 3.

An explanation could be that the mergers in these two clusters do not have the same age and that the faint end slope varies with time. We are in the process of analysing galaxy luminosity functions in a sample of clusters at redshifts up to 0.9 in all stages of merging, from relaxed to strongly substructured. This should shed light on the influence of mergers on the galaxy distributions in clusters.

We thank Emmanuel Bertin for his help and advice on his software. We acknowledge financial support from CNES and CAPES/COFECUB program 711/11.

References

Bagchi J., Durret F., Lima Neto G.B., Paul S. 2006, Science 314, 791
Durret F., Laganá T., Haider M. 2011, A&A 529, 38
Fasano G., Marmo C., Varela J. et al. 2006, A&A 445, 805
Fukugita M., Shimasaku, K., Ichikawa T. 1995, PASP 107, 945
Machado R.E.G. & Lima Neto G.B. 2012, arXiv:1209.0632
McCracken H.J., Radovich M., Bertin E. et al. 2003, A&A 410, 17
Ramella M., Biviano A., Pisani A. et al. 2007, A&A 470, 39

SF2A 2012
S. Boissier, P. de Laverny, N. Nardetto, R. Samadi, D. Valls-Gabaud and H. Wozniak (eds)

X-RAY ASPECTS OF THE DAFT/FADA CLUSTERS

L. Guennou[1], F. Durret[2], G. B. Lima Neto[3] and C. Adami[1]

Abstract. We have undertaken the DAFT/FADA survey with the aim of applying constraints on dark energy based on weak lensing tomography as well as obtaining homogeneous and high quality data for a sample of 91 massive clusters in the redshift range [0.4,0.9] for which there are HST archive data. We have analysed the XMM-Newton data available for 42 of these clusters to derive their X-ray temperatures and luminosities and search for substructures. This study was coupled with a dynamical analysis for the 26 clusters having at least 30 spectroscopic galaxy redshifts in the cluster range. We present preliminary results on the coupled X-ray and dynamical analyses of these clusters.

Keywords: Cosmology, Galaxy clusters, Survey, Substructures

1 Introduction

It has been half a century since the observation of the first X-ray source outside the Solar System. Since then, X-ray astronomy never ceased to provide new means of study for large scale structures as well as for point sources, and space instruments have been steadily improving, with increasing sensitivity and spatial resolution, allowing ever deeper and more accurate observations. Today, the three main X-ray satellites are XMM-Newton, Suzaku and Chandra, and we used primarily data from XMM-Newton to try detecting substructures in all the clusters of the DAFT/FADA survey for which such data were available (about half of the sample).

The DAFT/FADA survey (PIs: M. Ulmer, C. Adami, and D. Clowe) is based on the study of 91 rich (masses $> 10^{14} M_{\odot}$) and distant (redshifts $0.4 < z < 0.9$) clusters, all with HST data available. This survey has two main objectives. The first one is to constrain dark energy using weak lensing tomography on galaxy clusters. The second one is to build a database of rich distant clusters to study their properties.

The chosen redshift range is interesting in the study of galaxy clusters because it is situated just after the predicted end of the galaxy cluster formation (estimated around $z = 1.0$ within the current cosmological concordance model). At this redshift, the galaxy cluster formed and the groups that it has accreted have different scales, implying different mechanisms than during initial cluster formation. The dynamical state of clusters can be probed by detecting substructures, either in the galaxy distribution or in the intra cluster medium (ICM). The search for substructures in this redshift range will thus allow us to search for traces of this accretion mechanism inside galaxy clusters. First results of the DAFT/FADA survey can be found in Guennou et al. (2010).

In this framework, we applied the Sherpa tools to the X-ray images to bring out substructures detected in XMM-Newton data, and we used the Serna & Gerbal (1996) hierarchical program (based on spectroscopic redshifts and V band magnitudes) to detect optical substructures. This double detection will allow us to ascertain the existence (or not) of substructures in the galaxy clusters considered. We present hereafter in section 2 the data and methods used in this study, followed in section 3 by the results and discussion.

[1] Aix Marseille Université, CNRS, LAM (Laboratoire d'Astrophysique de Marseille) UMR 7326, 13388, Marseille, France
[2] UPMC Université Paris 06, UMR 7095, Institut d'Astrophysique de Paris, 98bis Bd Arago, F-75014, Paris, France
[3] IAG, USP, R. do Matão 1226, 05508-090, São Paulo/SP, Brazil

2 Data and method

We retrieved XMM-Newton data from the archive and kept the 42 clusters with data of sufficient quality. We also obtained deep optical imaging for most of the 91 clusters in several bands, with various telescopes, reaching a total of around 70 nights of observing time on 4m to 10m telescopes (Blanco, WIYN, GTC, Gemini, SOAR). We retrieved all the galaxy redshifts available in NED in a 5 arcmin region around each cluster center, and added some redshifts that we obtained during several observing runs with 8m telescopes (42 redshifts obtained with GMOS on the GEMINI telescope and 27 obtained with FORS2 on the VLT).

The XMM-Newton data were analysed using the SAS (Science Analysis System from XMM-Newton team) tool from the Heasarc package to do the main part of the reduction. After this we applied the program created by Andy Read to remove flares, using a 3σ clipping technique, and calibrated the images. The X-ray images, with a pixel size of 4.1", were then fit with an azimuthally symmetric elliptical β-model, representing a simulated relaxed cluster with a homogeneous gravitational potential, applying the Sherpa tool from CIAO. The residuals were computed as the difference between the image and the fit, allowing us to bring out any perturbations from a homogeneous gravitational potential due to the substructures that are not completely merged with the cluster yet. An example is displayed in Fig. 1, showing the case of LCDCS 504 (z=0.7943).

Note that in some residual images it was difficult to distinguish substructures from point sources. In order to check this point, we plan to use Chandra data when available and/or to perform optical spectroscopy on the objects as shown in Fig. 2.

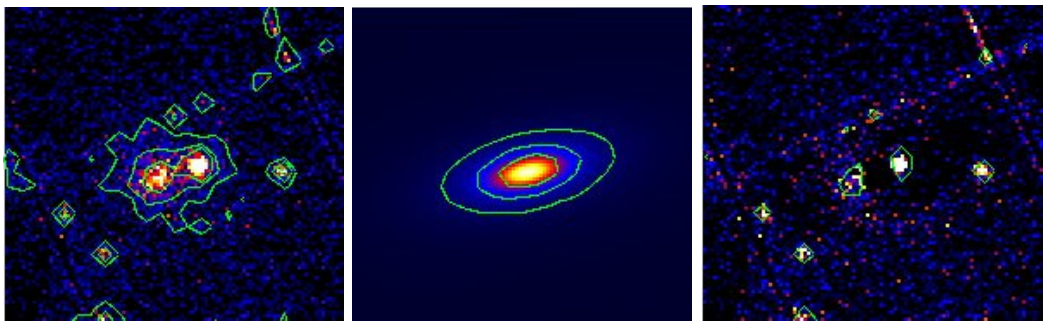

Fig. 1. Example of the method used to detect substructures using Sherpa on X-ray data for LCDCS 504. The let panel shows the cluster image, the middle panel shows the azimuthally averaged $\beta-$model applied, and the right panel shows the residual image obtained when we subtract the model from the cluster.

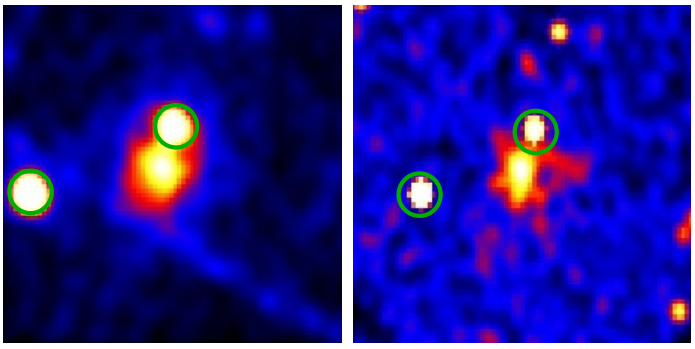

Fig. 2. An example of the help Chandra will provide in the detection of point source objects. The left panel shows the image obtained with XMM. The right panel shows the image obtained with Chandra. We can see that the point sources circled in green can be detected more easily with Chandra.

For each cluster with more than 30 galaxy redshifts available in the cluster range, we applied the Serna & Gerbal (1996) analysis to search for substructures. This method calculates the relative binding energy between galaxies and allows us, from the galaxy positions, redshifts and magnitudes, to detect and characterize

substructures on a line of sight. A dendogram is created, representing the binding potential energy between galaxies (see Fig. 3). The number of substructures and their corresponding masses can thus be estimated, assuming a value for the mass to luminosity ratio.

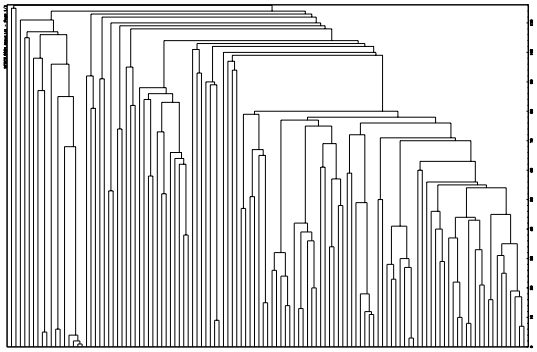

Fig. 3. Dendogram obtained by the Serna & Gerbal (1996) method applied to the optical spectroscopic redshifts and V magnitudes of LCDCS 504. Each vertical line represents a galaxy, and the scale on the vertical axis corresponds to the relative binding energy between galaxies (in arbitrary units). Several substructures are clearly visible.

An important question concerning the application of the Serna & Gerbal (1996) method is how the incompleteness in the galaxy optical spectroscopy can affect the results. In order to estimate how important this problem is, we considered a well observed cluster, Abell 851, for which 194 spectroscopic redshifts are available in the cluster redshift range, and we observed the changes in the results depending on the completeness of the input catalogue. To perform this task, we considered between 100% and 10% of the complete catalog and for each step we ran the Serna-Gerbal and checked the results to detect differences as the incompleteness grew. In this way, we can observe the impact of the incompleteness on our results and its damages on the results depending on the richness of the substructures. Results are shown in Fig. 4, where we observe that substructures with few members quickly disappear when the incompleteness increases, and the mass of these "light" substructures also strongly varies. On the other hand, substructures with many members (i.e. large substructures), remain visible even with a high incompleteness, and their mass remains quite constant. In short, the heaviest and biggest substructures are still detected, even with a low completeness, while smaller substructures disappear.

These tests allow us to think that the large and massive substructures will still be detected by the Serna-Gerbal program, even if we cannot estimate accurately the completeness of our redshift catalogs. Since we are also using X-ray data, where large substructures are primarily detected using the Sherpa tools, we are confident that we can apply both methods and assess in two different ways the presence or absence of substructures in these clusters.

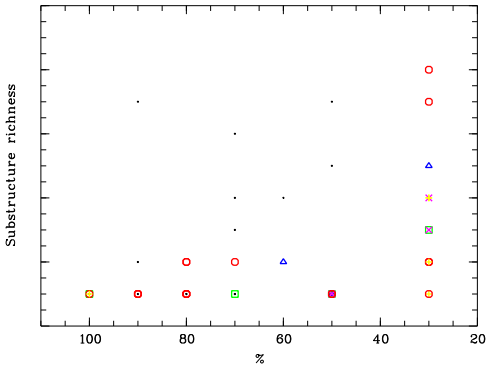

Fig. 4. Effects of the incompleteness of the input spectroscopic catalogue on the Serna & Gerbal (1996) method. The points show the richness of the galaxy group versus the percentage of completeness until which the group exists for 6 clusters, each represented with a different symbol and color.

3 Results and discussion

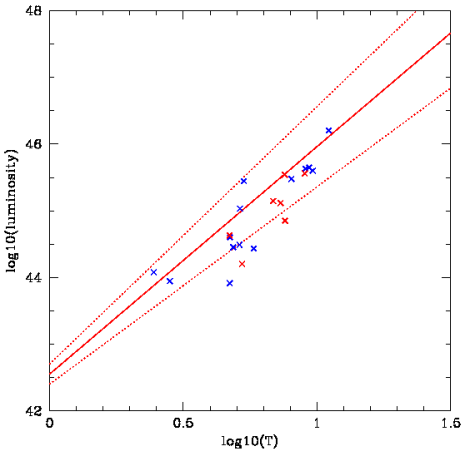

Fig. 5. Relation between temperature and luminosity for our clusters. The red line represents the $L_X - T_X$ relation found by Takey et al. (2011). The blue and red points represent galaxies with redshifts respectively lower and higher than 0.6.

Out of our initial sample of 42 DAFT/FADA clusters with XMM-Newton data, we were able to analyse spatially 30 clusters, to which we applied the Sherpa tools to detect possible substructures inside the clusters. Out of these 30 clusters, only 23 had deep enough X-ray data for a robust analysis. Out of these 23, we find that only 6 clusters clearly possess substructures, while 13 may have some and only 4 clusters seem completely relaxed.

We also assessed the quality of our X-ray data and analysis by plotting an $L_X - T_X$ diagram for our clusters (see Fig. 5) and comparing our data with the $L_X - T_X$ relation found by Takey et al. (2011) for clusters with a redshift smaller than 0.6. For this purpose, we modified our energy interval, initially chosen between 0.5 and 8.0 keV, to the one used by Takey et al. (2011), by applying the PIMMS software, and considered the r_{500} spatial zone. We can see that our points roughly agree with the relation found by Takey et al. (2011).

We also compared the substructures detected in X-rays with those detected with the hierarchical method to confirm or invalidate the existence of substructures inside the clusters. The analysis of all the clusters for which sufficient data are available will be the subject of a future paper (Guennou et al., in preparation).

We acknowledge financial support from CNES and CAPES/COFECUB program 711/11.

References

Guennou L., Adami C., Ulmer M. P. et al. 2010, A&A 523, 21
Serna, A., & Gerbal, D. 1996, A&A, 309, 65
Takey A., Schwope A., Lamer G. 2011, A&A 534, 120

SF2A 2012
S. Boissier, P. de Laverny, N. Nardetto, R. Samadi, D. Valls-Gabaud and H. Wozniak (eds)

A SURVEY FOR FE II EMISSION TOWARD A LARGE QUASAR GROUP AT $Z \sim 1.2$

K.A. Harris[1,2], R.G. Clowes[2], G.M. Williger[1,3], L.G. Haberzettl[3] and L.E. Campusano[4]

Abstract. We present 14 quasars which show evidence of strong and ultra-strong UV Fe II emission. The quasars are all within an area of two deg^2 covering a portion of the Clowes-Campusano Large Quasar Group (CCLQG) ($\langle z \rangle = 1.28$). This area is noteworthy for the high densities of quasars at several redshifts, spanning a redshift range of $1.11 < z < 1.67$. The distribution of Fe II emission has been compared to a control sample and there is a highly significant relative excess at higher emission levels. This indicates either a special environment within a LQG or suggests that a large number of quasars within a LQG are in a particular stage of their evolution.

Keywords: quasars, large quasar groups, iron emission

1 Introduction

Iron emission can be seen in Active Galactic Nuclei (AGN) and quasars in the optical and ultra-violet at varying levels. Few quasars in the literature have been measured to be strong or ultra-strong UV Fe II emitters, suggesting this strength of emission is rare. All of these show ultra-strong Fe II emission in the rest-frame region between 2255 Å and 2650 Å. The most notable ultra-strong UV Fe II emitters are:

- IZw1, a Seyfert galaxy (Bruhweiler & Verner 2008; Vestergaard & Wilkes 2001),
- 2226-3905 (Graham et al. 1996),
- 0335-336 from Weymann et al. (1991), and
- Mrk 376 and Mrk 486 (Seyfert galaxies) (e.g. Osterbrock 1976).

It is important to gain accurate measurements of the Fe abundance as a function of cosmic time, especially for high redshift quasars, as this will provide constraints on and verify cosmological parameters (e.g. Hamann & Ferland 1993). Simulations of Fe II emitting regions have suggested that the Fe II abundance alone, though still important, may not be the main factor influencing the strength of the UV Fe II emission (Sigut & Pradhan 2003; Baldwin et al. 2004). The observed UV Fe II emission is most likely caused by the interplay of different mechanisms (Elitzur & Netzer 1985; Sigut et al. 2004; Osterbrock & Ferland 2006). Collisional excitation can excite the Fe II to a few eV above ground level, whereas resonance fluorescence (from both the continuum and Lyα) can excite Fe II to 5–10 eV above ground level.

2 The Clowes-Campusano Large Quasar Group

Large Quasar Groups (LQGs) are some of the largest structures seen in the Universe and can span 50–200 h^{-1} rest-frame Mpc. These clusters of quasars exist at high redshifts, presumably trace the mass distribution, and are potentially the precursors of the large structures seen at the present epoch, such as super-clusters (Komberg et al. 1996; Wray et al. 2006). The Clowes-Campusano Large Quasar Group (CCLQG, Fig. 1) contains 34 quasars at $1.18 < z < 1.43$ (Clowes et al. 2012, and references therein). The field covers ~ 20 deg^2 (1° is ~ 30 local Mpc at $z \sim 1.3$) The CCLQG is associated with an overdensity of strong Mg II absorbers which are likely produced by galaxy haloes (Williger et al. 2002).

[1] Observatoire de la Côte d'Azur, Université de Nice, 06108 Nice Cedex 2, France
[2] University of Central Lancashire, Preston, England
[3] University of Louisville, Kentucky, USA
[4] Universidad de Chile, Santiago, Chile

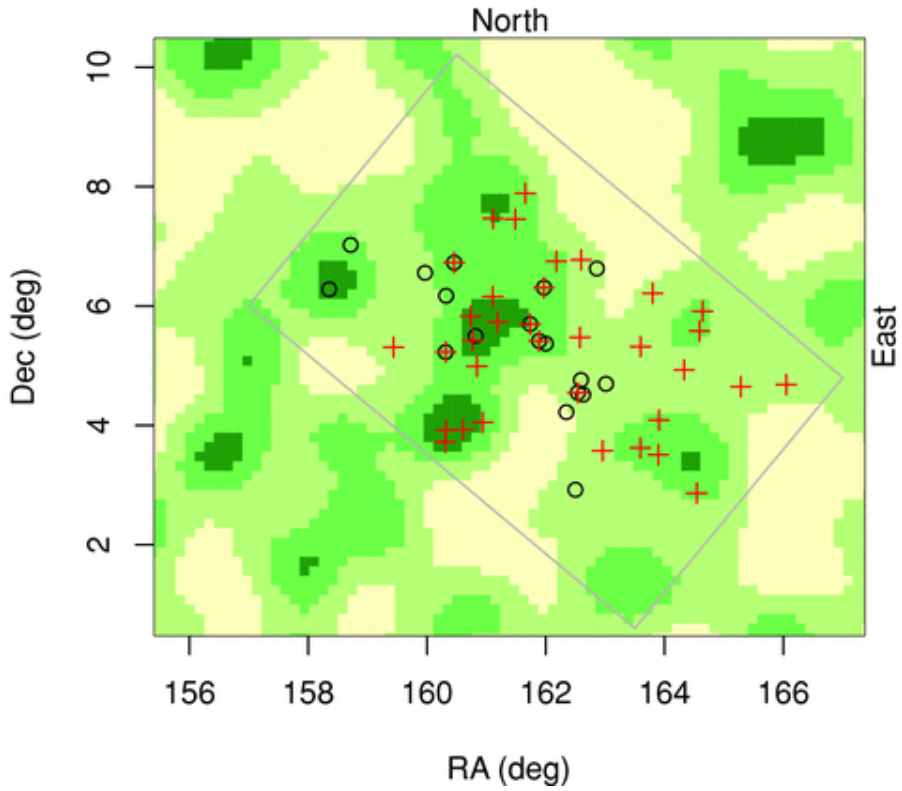

Fig. 1. From Clowes et al. (2012). Sky distribution of 34 quasars at $\langle z \rangle = 1.28$ (crosses) connected with original 18 LQG members (circles). Superimposed on these distributions is a kernel-smoothed intensity map of all quasars at $1.18 < z < 1.42$.

3 Observations/Data

We took data from the 6.5m MMT+Hectospec, supplemented with Sloan Digital Sky Survey (SDSS) spectra.

Hectospec: We observed 17 quasars over Feb–Apr 2010, taken from the SDSS DR6 photo-z catalogue (Richards et al. 2009), selecting for $r < 20.1$, covering 3900–9100 Å (see Fig. 2 for an example), targeting quasars with redshifts $1.1 < z < 1.6$. Our observations had ~ 4 Å resolution and 1.2 Å/pixel dispersion.

SDSS: We took data from 30 quasars in CCLQG field, from the DR7 spectroscopic catalogue (Schneider et al. 2010), selecting for $i < 19.1$, with resolution $R \sim 2000$, and covering 3800–9200 Å.

Controls: We also selected as a control sample ~ 400 quasars from Stripe 82 of the SDSS DR7 catalogue, which have higher signal to noise ratio (SNR) than the general SDSS data set.

4 Fe II Equivalent Widths and Discussion

We used the Fe II measurement convention of Weymann et al. (1991) for both the CCLQG field sample and the Stripe 82 control sample. The Fe II 2400 Å rest equivalent width (EW) distribution (W2400) is shown in Fig. 3, with Poissonian errors for illustration. We divide the sample into 3 categories: WEAK: W2400 < 30 Å, STRONG: 30 Å $<$ W2400 < 45 Å, and ULTRA-STRONG: W2400 > 45 Å. Typical W2400 errors are ± 5 Å for spectra with SNR > 5/pixel, and ± 3 Å for SNR > 10/pixel.

A one-sided Mann-Whitney test was used, with a confidence level of 95%, to estimate the p-value as 4.7×10^{-5} and a shift in median compared to the control as 10.4 Å. The alternative hypothesis for this test was that the distribution of the LQG field quasars is shifted to greater W2400 values than the control sample. The errors on

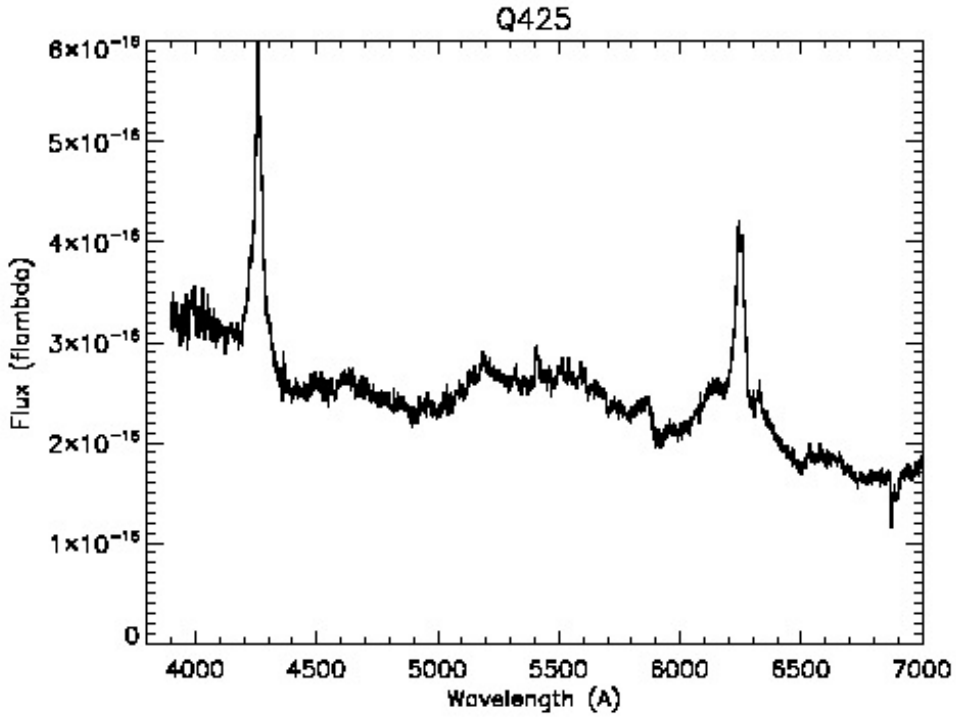

Fig. 2. Quasar 425 in our sample (1048+0522, $z_Q = 1.230$). The redshifted broad FeII emission bump is clearly visible at 5200–5800 Å (ultra-strong, rest EW = 56 Å).

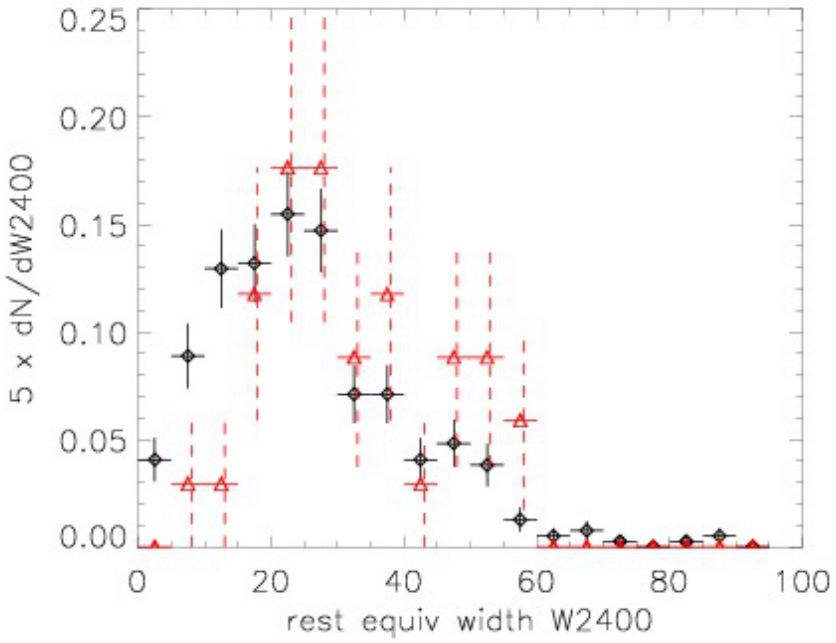

Fig. 3. Fe II 2400 Å rest equivalent width distribution for CCLQG field sample (red) and SDSS Stripe 82 control sample (black). Errors are Poissonian.

the W2400 measurements were estimated using repeat measurements of the EW, and the Mann-Whitney test was repeated to create a range of p-values. We obtain a range for the p-value of $4.8 \times 10^{-9} - 6.3 \times 10^{-4}$. Even taking the largest p-value, the null hypothesis (that the distributions are the same) can be discarded in favour of the alternative hypothesis, with an increase in the general emission strength of W2400 for the LQG sample of ~ 9 Å compared to the controls.

Further details are in Harris et al. (2012, MNRAS, submitted).

KAH would like to acknowledge and thank British STFC, the University of Central Lancashire and the Obs. de la Côte d'Azur for their funding, and hospitality. LEC received partial support from Center of Excellence in Astrophysics and Associated Technologies (PFB 06). We thank the MMT staff for observing support, and acknowledge use of the Sloan Digital Sky Survey, funded by the Alfred P. Sloan Foundation, the Participating Institutions, the National Science Foundation, the US Dept. of Energy, NASA, the Japanese Monbukagakusho, the Max-Planck-Gesellschaft, and the Higher Education Funding Council for England.

References

Baldwin, J. et al. 2004, ApJ, 615, 610
Bruhweiler, F. & Verner, E. 2008, ApJ, 675, 82
Clowes, R. et al. 2012, MNRAS, 419, 556
Elitzur, M. & Netzer, H. 1985, ApJ, 291, 464
Graham, M. et al. 1996, MNRAS, 279, 1349
Hamann, F. & Ferland, G. 1993, ApJ, 418, 11
Komberg, B. et al. 1996, MNRAS, 282, 713
Osterbrock, D. 1976, ApJ, 203, 329
Osterbrock, D. & Ferland, G. 2006, Astrophysics of Gaseous Nebulae (Mill Valley: University Science Books)
Richards, G. et al. 2009, ApJS, 180, 67
Sigut, T. & Pradhan, A. 2003, ApJS, 145, 15
Sigut, T. et al. 2004, ApJ, 611, 81
Vestergaard, M. & Wilkes, B. 2001, ApJS, 134, 1
Weymann, R. et al. 1991, ApJ, 373, 23
Williger, G. et al. 2002, ApJ, 578, 708
Wray, J. et al. 2006, ApJ, 652, 907

SF2A 2012
S. Boissier, P. de Laverny, N. Nardetto, R. Samadi, D. Valls-Gabaud and H. Wozniak (eds)

EVOLUTION OF THE DISTRIBUTION OF BARYONS IN A SIMULATED LOCAL GROUP UNIVERSE

S. Peirani[1]

Abstract. Using hydrodynamical zoom simulations in the standard ΛCDM cosmology, we have investigated the evolution of the distribution of baryons (gas and stars) in a local group-type universe. We found that physical mechanisms able to drive the gas out of the virial radius at high redshifts (such as AGN) will have a stronger impact on the deficit of baryons in the mass budget of Milky Way type-galaxies at present times than those that expel the gas in the longer, late phases of galaxy formation.

Keywords: Galaxies: Local Group, Galaxies: haloes, Dark matter, Methods: N-body simulations

1 Introduction

In the traditional picture of galaxy formation, galaxies are supposed to form when baryonic gas falls into the gravitational potential of their host dark matter halo, the distribution of dark matter is therefore expected to faithfully trace that of the baryons. However on galactic scales, observations tend to suggest that the spatial distributions of dark matter and baryons (especially in the form of gas) may display some substantial differences. In particular, it has been shown that galaxies are missing most of their baryons, – most galaxies are severely baryons-depleted relative to the cosmological fraction (see for instance Bell et al. 2003; Hoekstra et al. 2005; McGaugh 2010).

This so-called "missing baryons problem" (see Bregman 2007 for a complete review), if *real*, calls for two alternative scenarios. Either a significant part of the gas never collapsed into the gravitational potential wells of protogalaxies in the first place, or some of the gas has been expelled by galaxy formation feedback processes such as supernova winds. Hence solving the missing baryon problem may prove to be central in order to constrain galaxy formation models.

In Peirani et al. (2012), we made use of cosmological "zoom" simulations with an extended treatment of the physics of baryons to study the formation of Milky Way-like galaxies. Our aim was to characterise the relative role of supernova feedback to accretion and mergers in the evolution of the distribution of baryons for objects of such masses. But we have also tested scenarios in which a significant fraction of gas in progenitors is expelled at high redshift by more powerful sources of feedback, such as AGN associated with massive black holes. This allowed us to quantify two distinct processes which may allow us to address the so-called missing baryon problem, should it persist. The simulation of local group universe also allowed us to study the problem of the "cold" Hubble flow (see for instance Peirani 2010; Peirani & Pacheco 2006, 2008) as well as possible indirect detection of neutralino, through its γ-ray annihilation product, by FERMI satellite from our galactic halo or M31 and the dwarf galaxies (see for instance Peirani, Mohayaee & Pacheco 2004b) and theoretical models of the formation of a disc galaxy similar to the Milky Way (Peirani, Mohayaee & Pacheco 2004a).

2 Numerical Modelling

The numerical methodology used in the present paper is described in detail in Peirani et al. (2012) to which we refer the reader for more information. For the sake of clarity, we summarize the main steps below.

We analyse three cosmological zoom simulations for a ΛCDM universe using WMAP5 parameters (Komatsu et al. 2009), namely $\Omega_{\rm M} = 0.274$, $\Omega_\Lambda = 0.726$, $\Omega_b = 0.0456$, $H_0 = 70.5$ km/s/Mpc, $n = 0.96$ and $\sigma_8 = 0.812$.

[1] Institut d'Astrophysique de Paris (UMR 7095: CNRS & UPMC), 98 bis Bd Arago, 75014 Paris, France

Each simulation was performed in a periodic box of side $100\,h^{-1}$ Mpc with 2×2048^3 effective dark matter and gas particles in the highest resolution region (a sphere of $7\,h^{-1}$ Mpc of radius).

The three simulations have common initial conditions whose phases are consistent with the local group but essentially differ in the quantity of energy released by SN derived from star particles i (E_i). As mentioned in Peirani et al. (2012), we consider that a fraction γ of this energy is deposited in the j^{th} neighbour gas particle by applying a radial kick to its velocity with a magnitude $\Delta v_j = \sqrt{(2 w_j \gamma E_i / m_j)}$, where w_j is the weighting based on the smoothing kernel and m_j is the mass of gas particle j. The first simulation Sim1a uses the standard value of $\gamma = 0.1$ while in the second one, Sim1b, we have considered a higher efficiency $\gamma = 1.0$ in order to investigate how our results would be affected. In the third simulation (Sim2), our aim is to study the effects of earlier high energy ejection to the ISM induced either by intermediate mass black holes or other high energy processes such as hypernovae events. For this purpose, a simple modelling was used in which a much higher efficiency ($\gamma = 50$) was considered during a very short ($\Delta t \sim 45\,$Myr) at earlier times ($z \sim 8.0$) and $\gamma = 0.1$ otherwise.

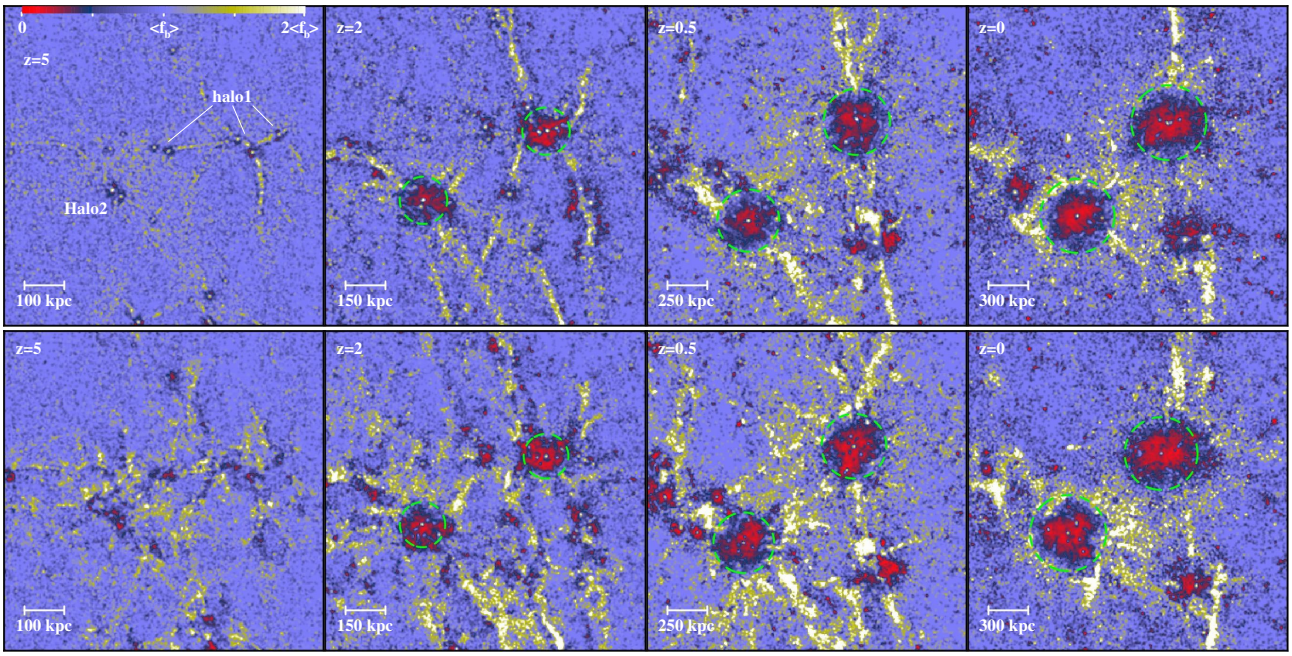

Fig. 1. The projected baryonic fraction at $z = 5$ (first column) $z = 2$ (second column), $z = 0.5$ (third column) and $z = 0$ (fourth column) from Sim1b (first line) and Sim2 (second line). Dashed circles show virial radii. High f_b value regions are clearly visible around galaxies (or proto-galaxies) and in the filaments. This trend seems to be more pronounced in $Sim2$ although the difference between the two simulations is vanishing at low redshift.

3 Spatial distribution in the simulated LG

Fig. 1 shows the projected distribution of baryons in our LG type universes derived from Sim1b and Sim2 and at four specific epochs (i.e. $z = 5, 2, 0.5$ and 0). We clearly see that the evolution of the distributions of baryons and dark matter do not follow the same trend. Indeed, the regions of the universe in red and dark blue correspond to regions where the baryonic fraction is lower than the universal value. And those specific regions are mainly located around the forming protogalaxies or galaxies at each redshift, while in the very inner part of dark matter haloes, f_b is higher. This is an expected result: due to cooling, the gas collapses to the center of haloes where stars can be formed. However, note that the size of these "red" cavities increases over time which suggests that the fraction of gas that has collapsed to the center of the halo is not immediately replaced by some fresh gas from its vicinity.

Note also, at high and low redshift, the existence of relative high baryon content regions which are located either in the filaments or beyond the virial radii. Such anisotropic distribution seems to be more pronounced in Sim2 relative to Sim1b. If the high baryon fractions in filaments can be understood by the dissipative nature

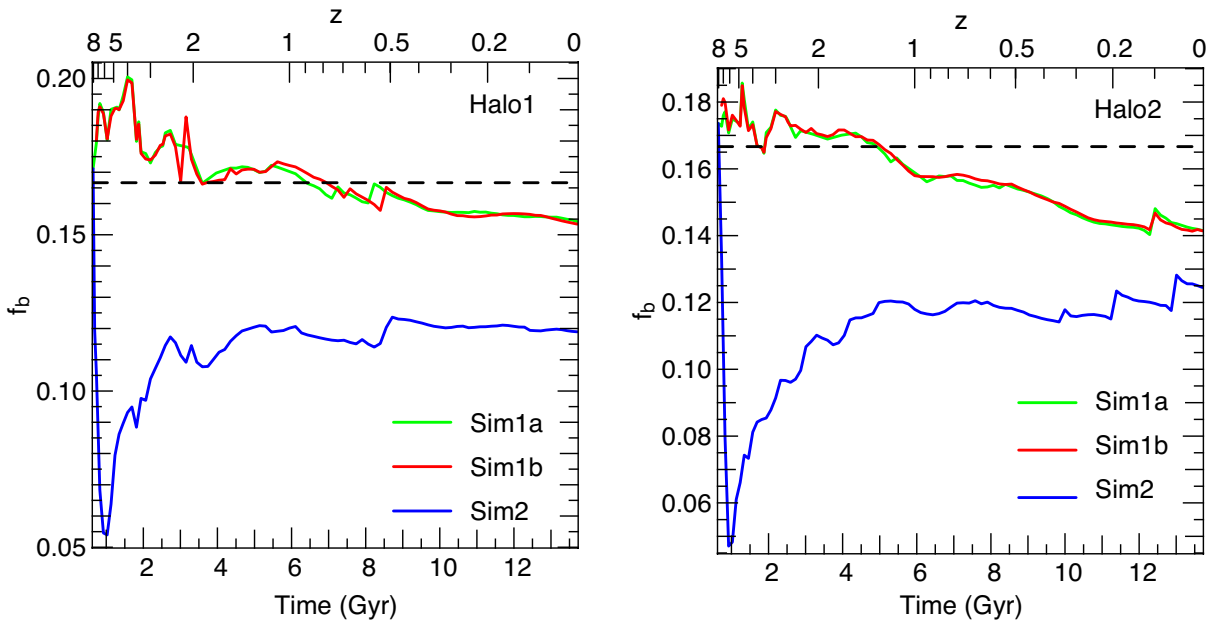

Fig. 2. The evolution of the baryonic fraction f_b estimated at the virial radius for HALO1 (left panel) and HALO2 (right panel) as a function of cosmic time. In each panel, red, green and blue lines correspond to values derived from SIM1*a*, SIM1*b* and SIM2 respectively. The horizontal dashed line corresponds to the universal fraction. Note that the early feedback model induces a lower ($f_b \sim 0.12$) baryon fraction at present time.

of gas, allowing it to cool to the dense filaments, it is crucial to characterise the mechanisms that drive high baryon content regions beyond the virial radii.

4 Cosmic evolution of fb

4.1 The effects of feedback at low redshift

The cosmic evolution of the baryonic fraction f_b estimated at the virial radius for the two main haloes is shown in Figure 2. In each of these two simulations, they follow the same trend. At high redshift, f_b is close to the universal value and sometimes is slightly higher. Cold flows provides gas to form stars. From $z \sim 3$, f_b is decreasing with cosmic time until it reaches the values of ~ 0.15 and ~ 0.14 at $z = 0$ for HALO1 and HALO2 respectively. More interestingly, no particular differences are seen in the evolution of f_b between SIM1*a* and SIM1*b*. This suggests that higher SN feedback can reduce the star formation rate (and therefore the final stellar mass) but is rather inefficient in expelling the gas outside the virial radius at high and low redshifts for massive galaxies.

4.2 The effects of feedback at high redshift

In SIM2 however, due to earlier and important eviction of gas from other potential sources of feedback (AGN, hypernovae,...) f_b reaches its lowest value $f_b \sim 0.05$ at $z \sim 6$, then increases until $z \sim 1.5$ and becomes nearly constant ($f_b \sim 0.12$) until the present time. This strongly suggests that sources of feedback acting at high redshift, even for a very short period, can have a stronger impact on the final mass budget of massive galaxies than those acting in the later and longer phases of galaxy formation.

4.3 The role of accretion of matter

The evolution of the mean baryonic fraction value f_b at the virial radius is essentially governed by the relative efficiency at which the dark matter and baryons are accreted. Indeed, the evolution of the accreted mass of both dark matter and baryons follows two different regimes: a rapid growth at high redshifts ($z \geq 1.5$) and a slower

one at lower redshifts. The high f_b values at high redshift derived from SIM1a and SIM1b can be explained by the accretion of high gas-to-dark matter ratio from dense region such as filament via cold flows. But at lower redshift, f_b is decreasing due to the accretion of low gas-to-dark matter ratio material, in particular from the diffuse region. Indeed, we found that the baryonic fraction of the diffuse accreted matter (namely $f_b \sim 0.11-0.14$) is on the average much lower than the universal value: as the haloes become more massive, the temperature at the virial radius increases and the gas is shock-heated and this process slows down its accretion onto the halo. For SIM2, f_b reaches its lowest value ($f_b \sim 0.05$) at $z \sim 5$ right after some significant expulsion of gas. After that, there is a short phase where f_b increases because the accreted matter has a higher baryonic content (but not necessarily higher than the universal value). Then, in the late phase of evolution of each halo, f_b tends to be constant ($f_b \sim 0.12$) because the average accreted matter tends to have the same baryonic fraction value as the mean value inside virial radii.

5 Conclusions

In summary, our study indicates that in order to reach lower f_b values at $z = 0$ for Milky Way type galaxies, the eviction of cold gas by feedbacks during the first phase of galaxy formation at high redshifts proves to be crucial. If such statement is correct, numerical and observational efforts have to be focused towards characterising the respective role of each feedback process on the IGM at high redshift. But in order to achieve this goal, one must first improve the constraints of the expected energy injection to the IGM from SN, AGN, UV background (etc...) via observations.

I am grateful to the SF2A organising committee and to the Observatoire de la Côte d'Azur for the excellent organisation of the workshop. I warmly thank the chef Khaled and his wonderful team, P. de Laverny, A. Recio-Blanco, N. Nardetto and A. Crida.

References

Bell, E. F., McIntosh, D. H., Katz, N., & Weinberg, M. D. 2003, ApJS, 149, 289

Bregman, J. N. 2007, ARA&A, 45, 221

Hoekstra, H., Hsieh, B. C., Yee, H. K. C., Lin, H., & Gladders, M. D. 2005, ApJ, 635, 73

Komatsu, E., Dunkley, J., Nolta, M. R., et al. 2009, ApJS, 180, 330

McGaugh, S. S., Schombert, J. M., de Blok, W. J. G., & Zagursky, M. J. 2010, ApJ, 708, L14

Peirani, S., Mohayaee, R., & de Freitas Pacheco, J. A. 2004a, MNRAS, 348, 921

Peirani, S., Mohayaee, R., & de Freitas Pacheco, J. A. 2004b, Phys. Rev. D, 70, 043503

Peirani, S., & de Freitas Pacheco, J. A. 2006, New A, 11, 325

Peirani, S., & de Freitas Pacheco, J. A. 2008, A&A, 488, 845

Peirani, S. 2010, MNRAS, 407, 1487

Peirani, S., Jung, I., Silk, J., & Pichon, C. 2012, `http://arxiv.org/abs/1205.4694`

SF2A 2012
S. Boissier, P. de Laverny, N. Nardetto, R. Samadi, D. Valls-Gabaud and H. Wozniak (eds)

MORPHOLOGY OF GALAXY CLUSTERS IN LARGE OPTICAL GALAXY SURVEYS

F. Rostagni[1], C. Benoist[1] and S. Maurogordato[1]

Abstract. We present a quantitative morphological classification of a sample of low redshift galaxy clusters extracted from the SDSS C4 cluster catalogue. Based on a wavelet analysis of both the galaxy velocity distribution and projected distribution, four morphological classes have been defined: regular, major multimodal, minor multimodal and irregular unimodal clusters. The method is applied to a subsample of 224 C4 clusters: 79 clusters (35%) are classified as regular, 51 (23%) as major multimodal, 16 (7%) as minor multimodal and 78 (35%) as irregular unimodal clusters.

Keywords: Galaxies: clusters: general, large scale structure of Universe

1 Introduction

Galaxy clusters are the largest gravitationally bound systems of the universe. According to the standard model of cosmology they formed recently through a hierarchical growth in which smaller units, galaxies and groups of galaxies, assemble together. Numerous observations in X-rays (Jones & Forman 1999) as well as in optical (Geller & Beers 1982; Dressler & Shectman 1988) show that there are substructures in a non negligible fraction of clusters, suggesting that clusters are currently in a non relaxed dynamical state. These results show that when using large cluster samples for statistical studies it is of prime importance to characterize systematically clusters' structural properties. Neglecting that a significant fraction of clusters can be far from relaxation could indeed bias severely any statement on the evolution of clusters or some of their scaling relations. It could in particular affect artificially the scatter of the mass-richness relation that is central to the use of cluster counts for constraining cosmological scenarios. In order to fully address the dynamical state of a cluster, one needs to trace both the gas and galaxies. In the present work we focus on the optical morphology.

Several works were performed in order to establish cluster morphological classifications. First, the cluster galaxy content was used to classify clusters (Bautz & Morgan 1970; Rood & Sastry 1971). In the eighties, with the advent of the X-ray astronomy, several powerful statistical tools were developed to analyze the cluster X-ray morphology. Mohr et al. (1993) used the centroid shift to constrain the dynamical state of 5 clusters observed with the *Einstein Observatory*. This technique was also used on more clusters (Jones & Forman 1999; Schuecker et al. 2001). Buote & Tsai (1996) developed the power ratio method, consisting in measuring the ratio between statistical moments of cluster X-ray luminosity. Cluster ellipticity was also used to assess cluster dynamical state (Kolokotronis et al. 2001; Melott et al. 2001; Plionis 2002).

Thanks to the development of multi-object spectroscopy, large redshift surveys were completed enabling to disentangle piled up structures along the line of sight. Numerous statistical tools were developed to evaluate cluster properties along the line of sight (Beers et al. 1990) and to check the Gaussianity of their redshift distribution (Ashman et al. 1994). In parallel, analyses of galaxy projected distribution were performed to detect substructures. Such studies were based on, for instance, adaptive kernels (Ramella et al. 2007) or wavelet analysis (Ferrari et al. 2005; Flin & Krywult 2006).

The aim of the present analysis is to establish a new optical cluster classification. In this analysis, galaxy positions and redshifts are used to characterize cluster optical morphology on a large homogeneous sample of nearby clusters: the C4 clusters catalog extracted from the SDSS, whose median redshift is 0.08. The classification method and the morphology indicators are explained in section 3 and the application to the sample is described in section 4.

In this paper, physical distances are computed assuming a flat universe with $H_0 = 70\text{km.s}^{-1}$, $\Omega_M = 0.3$ and $\Omega_\Lambda = 0.7$.

[1] Laboratoire Lagrange, OCA, CNRS, UNS, boulevard de l'Observatoire 06304 Nice Cedex, France

2 Data description

Currently the Sloan Digital Sky Survey (York et al. 2000) is the sky survey best suited for analyzing the local universe. Miller et al. (2005) developed the C4 cluster finder algorithm and detected 749 clusters in SDSS DR2 (Abazajian et al. 2004). C4 clusters are the baseline of the present analysis. Photometric and spectroscopic information of all galaxies falling within 5Mpc from C4 cluster centers have been extracted into regions named *C4 fields* in the following. To assure a high degree of spectroscopic completeness, galaxies were selected to be brighter than $r = 17.77$. However, for geometrical reasons, the densest fields, that correspond to galaxy clusters, were not achieved with the same nominal completeness rate. To trace clusters and their potential substructures with enough accuracy, only fields with (i) a completeness larger than 50% and (ii) a central cluster core containing enough galaxies are kept. These two criteria plus the removal of clusters close to SDSS edges reduced the cluster sample from 749 to 237 clusters. Cluster coordinates (α, δ, z) were refined and only the main cluster among clusters closer than 2Mpc from each other was kept, leading to a final sample of 224 clusters. Clusters of this sample have redshifts ranging from 0.03 to 0.14, the median being 0.08, and velocity dispersions between 150 and 2500km.s^{-1}.

3 Morphological classification

In the present study, four categories of galaxy clusters are defined: regular, major multimodal, minor multimodal and irregular unimodal clusters. Regular clusters are defined as clusters having a Gaussian velocity distribution and characterized by an unique structure in projection on the plane of the sky with a spherical profile. Major multimodal clusters are defined as clusters presenting at least two close components with mass ratio greater than 1:5; minor multimodal clusters as clusters having one or more close components with mass ratio smaller than 1:5 and irregular unimodal clusters as clusters with one non Gaussian peak and/or one elliptical isolated clump.

Along the line of sight, the velocity distribution of clusters is fitted by a Gaussian mixture to search for multimodality and normality tests are performed. In projection, density maps are computed based on a multi-scale approach (see Ferrari et al. 2005, for a detailed description) and considering the scales corresponding to the typical cluster sizes: from 0.5Mpc to 2Mpc. Overdensities are then extracted from the image, their position (α, δ) and their properties (ellipticity and richness) are measured. Here, the multimodality is defined by the presence of overdensities within 2Mpc from the cluster. The type of multimodality is then defined by the richness ratio: overdensities with richness greater than a fifth of the one of the cluster are considered as major multimodals, while others are minor multimodals. The ellipticity of the main cluster is also used to classify isolated clusters: the ellipticity threshold was set to 0.3 to separate regular clusters ($\epsilon \leq 0.3$) from irregular unimodal clusters ($\epsilon > 0.3$).

4 Application to C4 clusters

In this section, the classification is applied to the subsample of 224 C4 clusters with the properties described in section 2. For each cluster, we defined a redshift range in order to optimize the selection of cluster members while minimizing contamination by interlopers. The cluster redshift distribution function (hereafter RDF) is computed using again a multi-scale approach in an aperture corresponding to an angular size of 1Mpc at the cluster C4 redshift. The cluster redshift is defined as the RDF mode and the redshift range is defined as the region in which the RDF is greater than 5% of its maximum value. Examples of RDFs are shown in left panels of fig. 1, with the C4 cluster redshift indicated in red and the redshift range in green.

After selecting galaxies within this redshift range, the redshift distribution is fitted by a Gaussian mixture and normality tests are performed. The decomposition into a Gaussian mixture is performed with EMMIX software (McLachlan & Peel 1999) and the normality tests with ROSTAT software (Beers et al. 1990). Furthermore to assess the quality of fits, the χ^2 was computed between the best fit (ROSTAT fit for single Gaussian peak clusters and EMMIX fit for the others) and the RDF computed with the wavelet analysis. The value of 0.2 is chosen to separate Gaussian $\left(\chi^2 \leq 0.2\right)$ from non Gaussian distributions $\left(\chi^2 > 0.2\right)$.

In order to study the projected distribution of galaxies, density maps have been computed as described in section 3 using all galaxies of the whole *C4 field* and within the previously defined redshift range. SExtractor software (Bertin & Arnouts 1996) was used to detect overdensities in the density maps. The flux measured by SExtractor corresponds to a richness, *i.e.* the number of galaxies in an overdensity with $r \leq 17.77$. For

the present analysis, only overdensities with richness greater than 5 are kept as relevant. Physical projected distances (at the cluster redshift) are computed between overdensities and the main cluster (at the center) and richness ratios are computed. Examples of density maps are shown in right panels of fig. 1 with the detected overdensities (red ellipses) and the 2Mpc radius represented by the green circle around the main cluster.

Finally, the 224 clusters have been classified into the four morphological categories previously defined: 79 clusters (35%) are classified as regular clusters, 51 (23%) as major multimodal clusters with mass ratio greater than 1:5, 16 clusters (7%) as minor multimodal clusters with mass ratio smaller than 1:5 and the remaining 78 clusters (35%) as irregular unimodal clusters, without substructure. An example of each class is shown in figure 1. The C4 cluster 0007 (top panels of fig. 1) is a regular cluster: its velocity distribution is Gaussian with $\chi^2 = 0.045$, it has no neighbour within 2Mpc and it has a small ellipticity $\epsilon = 0.19$. On the second line of figure 1, the C4 cluster 0082 is a major multimodal cluster in projection: its velocity distribution is Gaussian $\left(\chi^2 = 0.09\right)$ but a rich neighbour (richness ratio 1:1.6) lies within 2Mpc. On the third line, the C4 cluster 0126 is an example of minor multimodal clusters with a Gaussian velocity distribution $\left(\chi^2 = 0.18\right)$ and a neighbour with richness ratio of 1:6 within 2Mpc. The C4 cluster 0017 (bottom panels) is an irregular unimodal cluster with a Gaussian velocity distribution $\left(\chi^2 = 0.09\right)$, without neighbour and with high ellipticity ($\epsilon = 0.51$).

5 Conclusion

This work presents a new optical approach to classify galaxy clusters using both galaxy velocity distribution and galaxy projected distribution. A fraction of 65% of non regular clusters is found, which is in good agreement with previous studies: at least 40% (Geller & Beers 1982; Kolokotronis et al. 2001) and up to 70% of clusters present substructures in the local universe (Dressler & Shectman 1988; Girardi et al. 1997; Einasto et al. 2012).

This classification provides a statistical sample of clusters to study environment effects on galaxies according to their cluster dynamical state. It will also be used as a reference for a similar study based on photometric redshifts and/or at higher redshifts (CFHT-LS, EUCLID, DES, etc.).

References

Abazajian, K., Adelman-McCarthy, J. K., Agüeros, M. A., et al. 2004, AJ, 128, 502
Ashman, K. M., Bird, C. M., & Zepf, S. E. 1994, AJ, 108, 2348
Bautz, L. P. & Morgan, W. W. 1970, ApJ, 162, L149
Beers, T. C., Flynn, K., & Gebhardt, K. 1990, AJ, 100, 32
Bertin, E. & Arnouts, S. 1996, A&AS, 117, 393
Buote, D. A. & Tsai, J. C. 1996, ApJ, 458, 27
Dressler, A. & Shectman, S. A. 1988, AJ, 95, 985
Einasto, M., Vennik, J., Nurmi, P., et al. 2012, A&A, 540, A123
Ferrari, C., Benoist, C., Maurogordato, S., Cappi, A., & Slezak, E. 2005, A&A, 430, 19
Flin, P. & Krywult, J. 2006, A&A, 450, 9
Geller, M. J. & Beers, T. C. 1982, PASP, 94, 421
Girardi, M., Escalera, E., Fadda, D., et al. 1997, ApJ, 482, 41
Jones, C. & Forman, W. 1999, ApJ, 511, 65
Kolokotronis, V., Basilakos, S., Plionis, M., & Georgantopoulos, I. 2001, MNRAS, 320, 49
McLachlan, G. & Peel, D. 1999, Journal of Statistical Software, 4, 1
Melott, A. L., Chambers, S. W., & Miller, C. J. 2001, ApJ, 559, L75
Miller, C. J., Nichol, R. C., Reichart, D., et al. 2005, AJ, 130, 968
Mohr, J. J., Fabricant, D. G., & Geller, M. J. 1993, ApJ, 413, 492
Plionis, M. 2002, ApJ, 572, L67
Ramella, M., Biviano, A., Pisani, A., et al. 2007, A&A, 470, 39
Rood, H. J. & Sastry, G. N. 1971, PASP, 83, 313
Schuecker, P., Böhringer, H., Reiprich, T. H., & Feretti, L. 2001, A&A, 378, 408
York, D. G., Adelman, J., Anderson, Jr., J. E., et al. 2000, AJ, 120, 1579

(a) C4 cluster 0007

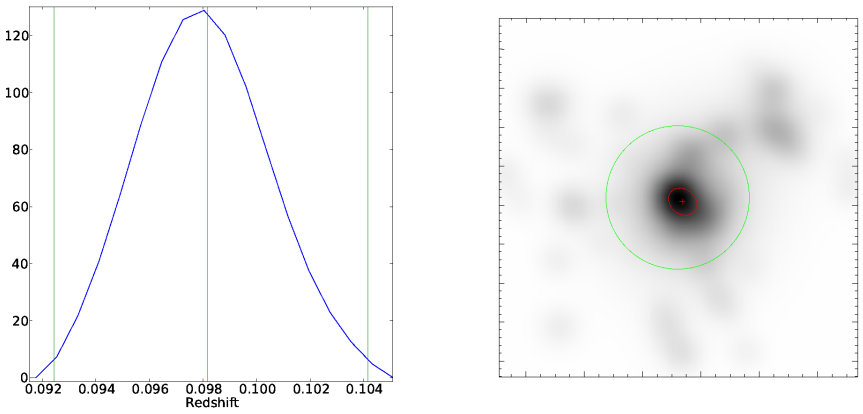

(b) C4 cluster 0082

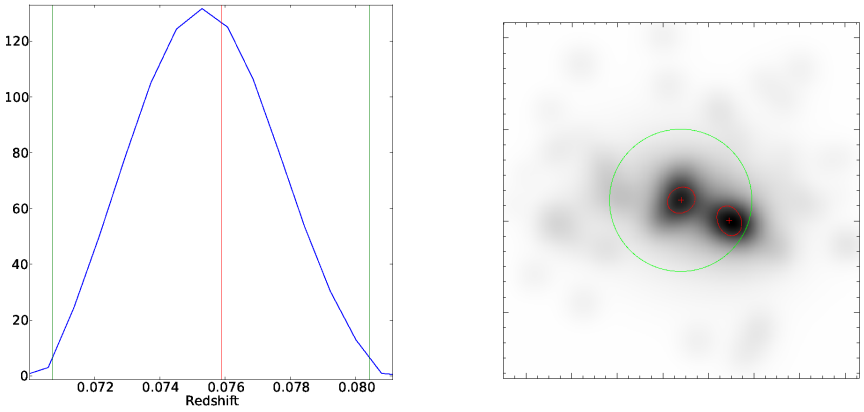

(c) C4 cluster 0126

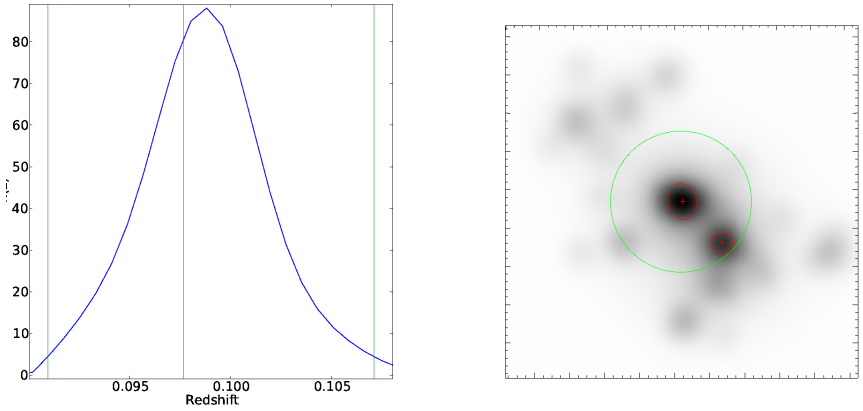

(d) C4 cluster 0017

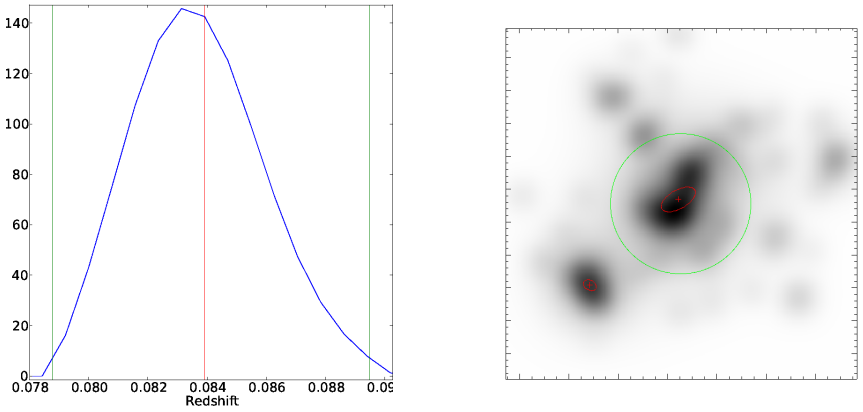

Fig. 1. Examples of the four cluster morphologies. **Left panels**: cluster redshift distribution function (RDF) with C4 cluster redshift (red) and the redshift interval used to build the cluster density map (green). **Right panels**: density maps with detected overdensities indicated by the red ellipses and the green circle represents the distance of 2Mpc from the main cluster (at the center). Panels (a): example of a regular cluster. Panels (b): example of a major bimodal cluster. Panels (c): example of a minor multimodal cluster. Panels (d): example of an irregular unimodal cluster.

SF2A 2012
S. Boissier, P. de Laverny, N. Nardetto, R. Samadi, D. Valls-Gabaud and H. Wozniak (eds)

OPTICAL GALAXY REDSHIFT SURVEYS

L. Sodré Jr.[1]

Abstract. Galaxy redshift surveys are a major tool to address the most challenging cosmological problems of contemporary cosmology, like the nature of dark energy and properties of dark matter. These surveys, besides their interest for cosmology, are useful for a much larger variety of scientific applications, from the study of small bodies in the solar system, to properties of tidal streams in the Milky Way halo, galaxy clusters, and galaxy formation and evolution. Here I briefly discuss what is a redshift survey and how it can be used to attack astrophysical and cosmological problems. I finish with a brief description of two new surveys: the Javalambre Physics of the Accelerating Universe Astrophysical Survey (JPAS) and the Subaru Prime Focus Spectrograph (PFS) survey.

Keywords: Cosmology: observations, Galaxies: general, Galaxies: evolution

1 Introduction

Galaxy redshift surveys on large areas of the sky are nowadays the astrophysical equivalent of large high-energy physics collaborations, like those built around the Large Hadron Collider at CERN to probe the realm of elementary particles. They aim to build 3-D maps of the galaxy distribution, since many astrophysical and cosmological process let their imprint in the spatial structure traced by galaxies.

Here I briefly review what galaxy redshift surveys are and what science they can address. I conclude presenting the main characteristics of two new surveys: JPAS, conducted by a Spanish-Brazilian collaboration from 2014 on, and PFS, a survey based in a new massively-multiplexed fiber-fed optical and near-infrared spectrograph under construction for the Subaru telescope and with first light predicted for late 2017.

2 The large scale structure

The knowledge of the galaxy distribution at the largest scales is a major achievement of redshift surveys like the 2dF Galaxy Redshift Survey (Colless et al. 2001) and the Sloan Digital Sky Survey (e.g., Abazajian et al. 2005). They have demonstrated that galaxies are distributed in a network of filaments and walls with galaxy clusters at their intersection. This network also contains large voids embedded, with diameters of a few tens Mpc (e.g., Costa-Duarte, Sodré & Durret 2011).

But galaxies are just the visible tracers of the dominant mass component of the universe: cold dark matter. Cold means that the velocity of the dark matter particles is non-relativistic when they were formed, just after the Big Bang. A major reason for the CDM paradigm is the strong resemblance between the observed galaxy distribution with the large scale distribution of dark matter established by numerical N-body simulations (e.g., Springel, Frenk & White 2006). Indeed, the type of dark matter has a profound effect on the appearance of the large scales (e.g., Ostriker & Steinhardt 2003). Cold particles allow the collapse of very small structures, whereas if the universe was dominated by hot dark matter (e.g., massive neutrinos), only large objects, like superclusters and clusters, would be initially formed, and galaxies would appear later through the fragmentation of large objects.

The difference between the expected appearance of the universe in its largest scales predicted by different models actually shows how powerful is the study of galaxy distribution for unveiling some of the universe deepest mysteries.

[1] Instituto de Astronomia, Geofísica e Ciências Atmosféricas, Universidade de São Paulo - CEP 05508-090, São Paulo, SP, Brazil

Galaxy redshift surveys are an important tool of contemporary astrophysics and observational cosmology. Their objective is to map the universe as traced by galaxies, obtaining a 3-D map of the galaxy distribution. The reason is that the cosmological parameters are imprinted in these 3-D maps, and their analysis is considered the most powerful way to address the nature of dark energy and other problems (Albrecht et al. 2006).

To make these 3-D maps we need to determine the cosmological distances of galaxies. This is usually done by measuring their spectral deviation z. For a given (homogeneous and isotropic) cosmological model, distances are a function of z, only.

The overall, uniform, expansion of the universe is known as the Hubble flow. But z is also affected by the peculiar velocities, the movements produced by the gravitational interaction between a galaxy and its neighbors, affecting the distance estimation of nearby galaxies. It is worth mentioning that galaxies are a biased tracer of dark matter, and studies of the peculiar velocity field (e.g., through redshift space distortions; Lahav & Suto 2004) are a powerful way to measure this bias.

There are two ways to obtain z: spectroscopy and photometry. In the first case, the measured spectrum allows the measurement of the spectral deviation of a galaxy with high accuracy (rms error $\sigma_z \sim 3 \times 10^{-4}$). In the case of photometric redshifts, the fluxes in a few filters (5 for SDSS) are used as proxies for the galaxy spectrum, and typical errors are much larger (e.g., $\sigma_z \sim 0.02(1+z)$ for SDSS/DR7; O'Mill et al. 2012). Each method has its pros and cons: photometric redshifts are much cheaper in terms of telescope time and consequently photometric surveys can go wider and deeper than spectroscopic surveys. Spectroscopic surveys, on the other side, besides their accuracy and superiority for several cosmological applications (e.g., measurement of redshift space distortions, radial baryon accoustic oscillations), also provide detailed galaxy SEDs, very useful for evaluating galaxy properties.

3 Cosmology with large scale probes

The prime objective of most galaxy redshift surveys is to investigate the nature of dark energy, mainly by constraining its equation of state, $p_{DE} = w\rho_{DE}c^2$. The value $w = -1$ corresponds to a cosmological constant, which provides a good fit to the current data (Komatsu et al. 2011). But is this indeed a good model for the behavior of dark energy or does its properties vary with redshift?

There are several probes to address dark energy properties, either based on distance-redshift relations or on the growth rate of cosmic structures. Indeed, the existence of dark energy was established though the luminosity distance-redshift relation of type Ia supernovae. Other canonical probes include the baryon acoustic oscillations (BAOs), cosmic shear, and the abundance of galaxy clusters. These probes, when combined with information obtained from the analysis of the temperature fluctuations of the cosmic microwave background (CMB), are able to impose stringent constraints on cosmological parameters (Eisenstein, Hu & Tegmark 1999).

Baryon acoustic oscillations (BAOs) are acoustic waves produced during the radiative era by the interaction of the photon-baryon plasma with dark matter. These waves stop propagating at recombination, when the rate of Compton scattering between electrons and photons becomes too low, and have their size frozen and equal to the size of the sound horizon at that epoch, $l_{BAO} \sim 150h^{-1}$ Mpc (Eisenstein & Hu 1998). Since BAOs are associated with a density enhancement, they increase the probability of finding a galaxy at l_{BAO} of other galaxies, and can be observed as a small excess ($\sim 1\%$) in the galaxy correlation function (e.g., Percival et al. 2010). Analysis of SDSS luminous red galaxies with an algorithm that takes in to account the effects of the peculiar velocity field (Padmanabhan et al. 2012) provides a 2% accuracy in l_{BAO} in the local universe, $z = 0.35$. The measurement of this scale as a function of z is a powerful cosmological probe and a major objective of future surveys. It is worth mentioning that the BAO features can be measured either in the transverse or radial directions and that each of these measurements bring different cosmological information: radial BAO is directly sensitive to the Hubble parameter $H(z)$, whereas transverse BAO is a probe of the distance-redshift relation. Photometric redshift surveys are more sensitive to transverse BAOs, since photometric redshift errors tend to blur the radial information.

In a ΛCDM universe structures grow from small density fluctuations due to their gravitational attraction. The largest virialized (or quasi) structures formed are the galaxy clusters and it is assumed that their material composition is representative of the universe as a whole. The number of clusters in a given redshift and the cluster spatial correlations are strong functions of the cosmological parameters, and the cluster mass function- the number of clusters at a given redshift with mass in a certain interval- is then a powerful cosmological probe, since it depends directly on the element of volume and on the growth of structures. Massive clusters can be found in the galaxy distribution through a variety of techniques (e.g., Wen, Han & Liu 2012). An important

difficulty with this approach is the estimation of cluster masses from the photometric information (richness and/or luminosity) available in these surveys. This can be overcomed through multiwavelength observations (e.g., X-rays) and/or self-calibration of the mass function (Lima & Hu 2007) in combination with external mass inferences. Nevertheless, the results obtained up to now are consistent and highly complementary to those obtained by other probes (e.g., Vikhlinin et al. 2009).

Density fluctuations can also be studied through gravitational lensing. The ellipticities of background galaxies change as their light travels towards the observer due to the gravitational deflection by the mass distribution along the line of sight. These optical distortions are highly correlated and are the signature of cosmic shear. The study of the cosmic shear as a function of redshift is called lensing tomography and is sensitive to cosmic expansion through both geometry and the growth rate of structures (e.g., Hu 2002).

Gravity affects both the overall expansion and the formation and evolution of structures, but in completely different ways, what allows to use observations of the 3-D galaxy distribution to test the gravitational theory in cosmological scales. Recently, the combination of cosmic shear, galaxy clustering and structure growth rate allowed the comparison between general relativity and modified gravity theories, suggesting that general relativity is a better descriptor of the behavior of gravitation theory in large scales than some versions of alternative gravity theories (Reyes et al. 2010).

Massive neutrinos also let their imprint on the galaxy distribution. They are a kind of hot dark matter, since they were relativistic when formed. Consequently, they escape from density fluctuations and, since they carry mass, they dissipate small density fluctuations. This process, called "free streaming", produces a cut-off in the number density of small fluctuations that can be detected in the power spectrum of the galaxy distribution and, in combination with other probes, provides strong constraints on the sum of the mass of neutrinos species. For example, analysis of the Canada-France-Hawaii Telescope Legacy Survey Wide Fields combined with WMAP7 data and a prior on the Hubble constant gives a very stringent upper limit on the sum of mass of neutrino species equal to 0.29 eV (Xia et al. 2012).

Another major scientific contribution from large scale redshift surveys is on our knowledge on how galaxies form and evolve. The reason is that the spectra or colors collected are useful to investigate the stellar populations and other galaxy properties (Cid Fernandes et al. 2005). Thanks mainly to SDSS photometric and spectroscopic surveys, much is known about the galaxy populations (e.g., stellar mass, luminosity, size, stellar populations, mean stellar ages and metallicities) and their relation with the environment, but big uncertainties remain. With CDM we expect that structures grow hierarchically, with merger of structures producing larger structures. But how does it work? Why the star formation rate start decreasing since $z \sim 1-2$? How massive black holes interact with their host galaxy? In the case of Milk Way, SDSS lead to the discovery of many satellite galaxies (e.g., Belokurov et al. 2010) and tidal tails, which are snapshots of merging activity. We hope that most of these questions will be addressed by surveys like those we describe in the next section.

4 JPAS and PFS

The Javalambre Physics of the Accelerating Universe Astrophysical Survey (JPAS) is a collaboration between Spain and Brazil aiming to conduct a survey on $\sim$ 8000 square degrees with 54 narrow band filters and two broad band filters over the range $\sim$ 3500Å to $\sim$ 10000Å, with photometric depth $I < 22.5$. This innovative filter system actually provides a low resolution spectrum at each pixel on the sky and was designed to produce photometric redshifts with accuracy $\sim 0.003(1+z)$, about ten times better than that possible with SDSS (Benitez et al. 2009). This survey should start in 2014 and its main part should be concluded by 2018. The survey will be conducted from the Javalambre Astrophysical Observatory (JAO), which is being built on Pico del Buitre, near the city of Teruel, in Spain. The Sierra de Javalambre is amongst the darkest regions in Europe and has an excellent seeing, with a median of 0.71 arcsec (Moles et al. 2010). The main telescope, T250, has diameter of 2.5m and a very large field of view, $\sim$5 square degrees. It will be equipped with a 1.2 Gigapixel camera which will be a mosaic of 14 10k x 10 k CCDs, with the 56 filters mounted in 4 trays. OAJ will also have a smaller telescope, T80, with diameter of 80cm and equipped with a 2 square degree camera for calibration of the photometric system of the survey.

The JPAS expected accuracy in photometric redshifts is enough to allow measuring BAO features also in the radial direction, what makes this photometric survey very competitive, with a DETF figure of merit above 100. We plan to measure the BAO scale above that allowed by galaxies ($z \sim 1.3$) by using quasars (Abramo et al. 2012); these probes have number densities large enough to allow measuring BAOs up to $z \sim 3-4$. Besides cosmology, JPAS will provide scientific results in many other areas: small bodies in the solar system, Galaxy

archeology, galaxy evolution, quasars, clusters of galaxies. An absolutely unique aspect of JPAS is that it will allow us for the first time to do an all-sky IFU (for integral field unit) science, since JPAS will measure a low resolution spectrum at each pixel on the sky. This opens immense opportunities for studies on galaxy structure and evolution. But, besides these very competitive scientific perspectives we are pursuing, maybe the most compelling results of JPAS are still unknown, as always happens when new windows are open.

The Prime Focus Spectrograph (PFS) survey will be carried on from the Subaru Telescope by using a new optical to near-infrared spectrograph equipped with 2400 optical fibers and which is under construction by an international collaboration under the leadership of Kavli IPMU (Ellis et al. 2012). The survey will be conducted as a Subaru Strategic Program of ∼300 nights and aims to constrain the nature of dark energy in the redshift range $0.8 < z < 2.4$ by measuring accurate (3%) cosmological distances through BAOs, as well as using redshift space distortions to constrain the structure growth factor to 6% precision. The survey will also complement the goals of Gaia mission by the measurement of velocities and metallicities for $\sim 10^6$ Milky Way stars, and will also target red giant branch stars in M31. The survey will also probe galaxy evolution at large redshift through the observation of galaxies, quasars, Lyman break galaxies and Lyman-α emitters, quantifying galaxy evolution from $z = 0$ to close the reionization epoch. PFS will be probably, the most powerful spectrograph during the Euclid era.

I acknowledge the support of FAPESP and CNPq to this work.

References

Abazajian, K., et al., 2005, ApJ, 625, 613
Abramo, L. R. W., et al., 2012, MNRAS, 423, 3251
Albrecht, A., et al., 2006, Report of the Dark Energy Task Force (astro-ph/060959)
Belokurov, V., et al., 2010, ApJ, 712, L103
Benitez, N., et al., 2009, ApJ, 691, 241
Cid Fernandes, R., et al., 2005, MNRAS, 358, 363
Colless, M., et al., 2001, MNRAS, 328, 1039
Costa-Duarte, M. V.; Sodré, L., Jr.; Durret, F., 2011, MNRAS, 411, 1716
Eisenstein, D. J.; Hu, W.; Tegmark, M., 1999, ApJ, 518, 2
Eisenstein, D. J.; Hu, W., 1998, ApJ, 496, 605
Ellis, R., et al., 2012, arXiv:1206.0737
Hu, W., 2002, Phys. Rev. D, 66, 083515
Komatsu, E., 2011, ApJS, 192, 18
Lahav, O.; Suto, Y., 2004, Living Rev. Relativity, 7, 8
Lima, M.; Hu, W., 2007, Phys. Rev. D, 76, 123013
Moles, M., et al., 2010, PASP, 122, 363
O'Mill, A. L., et al., 2012, MNRAS, 421, 1897
Ostriker, J.; Steinhardt, P., 2003, Science, 300, 1909
Padmanabhan, N., et al., 2012, arXiv:1202.0090
Percival, W. J., et al., 2010, MNRAS, 401, 2148
Reyes, R., et al., 2010, Nature, 464, 256
Springel, V.; Frenk, C.; White, S. D., 2006, Nature, 440, 1137
Vikhlinin, A. M., et al., 2009, ApJ, 692, 1033
Wen, Z. L.; Han, J. L.; Liu, F. S., 2012, ApJSS, 199, 34
Xia, J.-Q., et al., 2012, arXiv:1203.5105

SF2A 2012
S. Boissier, P. de Laverny, N. Nardetto, R. Samadi, D. Valls-Gabaud and H. Wozniak (eds)

A MULTI-BAND SURVEY FOR LBGS AND $Z < 2$ QUASARS IN THE EXTENDED HDF-S

G.M. Williger[1,2], L.G. Haberzettl[2], R.G. Clowes[3], L.E. Campusano[4] and P.J. Francis[5]

Abstract. We present new observations in the UV and R-band of the extended (E)HDF-S, to enable searches for Lyman break galaxies (LBGs) at $z \sim 1-2$ and quasars at $z \lesssim 2$. This will pave the way for tracing large scale structure (LSS) in the region via galaxy filaments and also permit tomography via quasar absorbers. The EHDF-S is the southernmost public deep field: (1) the mostly easily accessible from planned Antarctic facilities, and (2) one of the few in the HST continuous viewing zone (CVZ). Continued surveys in the region will also prepare for future exploitation with ALMA, SKA etc.

Keywords: quasars, deep fields, Lyman break galaxies, surveys

1 Introduction

The HDF-S was chosen to complement the HDF-N, to help characterise cosmic variance, and to provide a deep field for southern observatories. ADS in June 2012 shows at least 339 refereed papers with HDF-S in the abstract. HST coverage spans a few arcmin each for STIS, NICMOS, WFPC2 etc. A number of wide-field imaging observations have been done of the EHDF-S, from *FUV* to 20 cm (Table 1). In addition, there are ~ 500 spectroscopic or photometric redshifts available e.g. Sawicki et al. (2003) and Glazebrook et al. (2006), which show redshift spikes at $z \sim 0.50$ and 0.57.

Table 1. Selected Wide-field Observations: EHDF-S

study	size	bands	depth	ref
BTC	$45'$	UBVRI	AB$\sim 24-26$	Palunas et al. (2000)
MUSYC	$35'$	UBVRIz	AB$\sim 24-26$	Gawiser et al. (2006)
MUSYC	$10' \times 20'$	JHK	$\sim 21-22.5$ Vega	Quadri et al. (2007)
MUSYC	$10' \times 20'$	$3.6-8$; 24 μm	$\sim 22-25$ AB; $12-30$ μJy	Huynh et al. (2010); Marchesini et al. (2009)
GALEX	$70'$	FUV, NUV, NUV-grism	AB~ 24	Haberzettl et al. (2009); prop GI5-041
ATCA	$68'$	3,6,11,20 cm	$11-16$ μJy	Norris et al. (2005)

2 Observations

GALEX: We combined GALEX EHDF-S data from our program with images from MAST. Altogether, we have 12 ksec of *FUV* images, 25 ksec of *NUV* images and 45 ksec of *NUV* slitless spectroscopy. We find 17 *NUV*-bright quasars with $0.4 < z < 1.3$ (see Fig. 1 for an example).

[1] Obs. de la Côte d'Azur, U. de Nice, 06108 Nice-Cedex 2, France
[2] U. Louisville, Louisville KY, USA
[3] U. Central Lancashire, Preston, England
[4] U. de Chile, Santiago, Chile
[5] Australian National Univ., Canberra, Australia

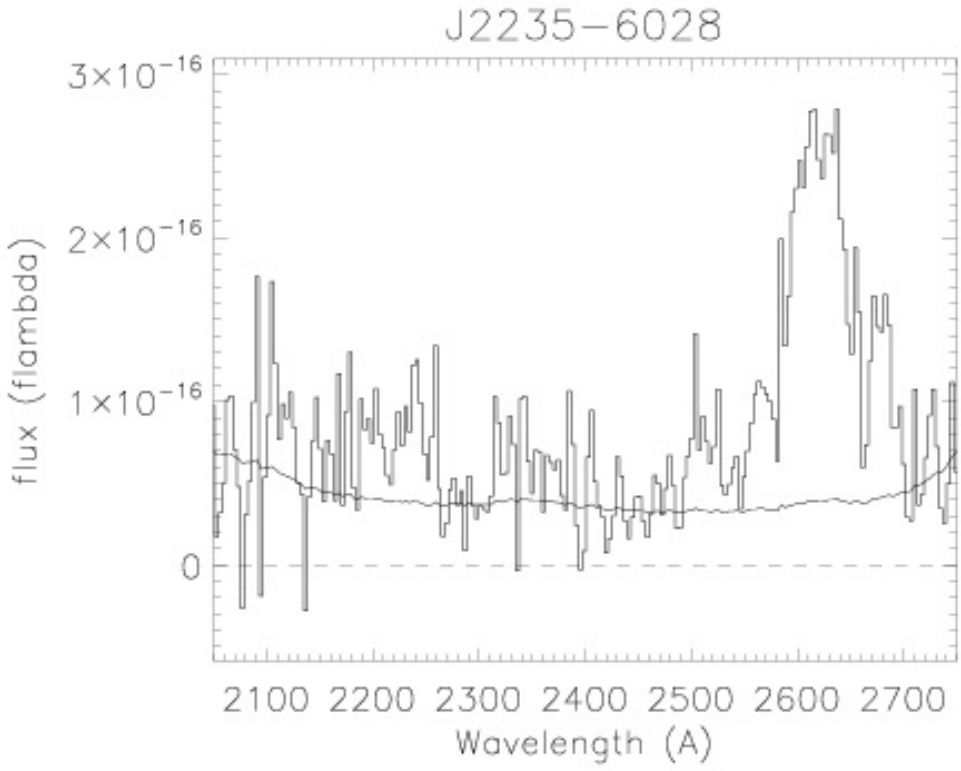

Fig. 1. Sample NUV slitless spectrum from GALEX for quasar with $z = 1.16$. Note strong absorption at 2290 Å, possibly damped Lyα at $z = 0.88$.

LCO R-images: About half our NUV-bright quasars are outside the BTC/MUSIC fields. We used the Las Campanas 2.5 m Dupont + WFCCD to image 4x25′diameter fields in R-band over 2011 Dec 28–30 to $R \sim$25 ($\sim$ 1.1 Å FWHM).

SALT, Warsaw Telescope Observations: We have obtained $\sim$ 8 hours on SALT multi-object spectroscopy for quasar confirmation, and 3 nights of Warsaw 1.3 m telescope time for deep VI imaging over 1.2°, in 2012 Jun–Sep (Fig. 2).

3 Results and Discussion

UV-Optical Quasar Candidates: We used $FUV - NUV - u - g - r$ transformed colours from Hutchings & Bianchi (2010) and Hutchings (2012 private comm.) to isolate on the order of at least 1000 $z < 2$ quasar candidates with $R < 22.5$ from the stellar and galactic loci in the BTC and MUSYC fields.

$z \sim 1$ Lyman Break Galaxies: We identified $\sim$ 1900 FUV dropouts ($FUV - NUV \gtrsim 1.5$, $R <$ 22.5) in the BTC and MUSYC fields. We are calculating their 7-band photometric redshifts to identify any concentrations/indications of structures, similar to Haberzettl et al. (2009).

Future Exploitation: A number of southern/Antarctic facilities are coming online in the near future. ALMA and SKA will revolutionise mm and radio astronomy. Several Antarctic observatories are proposed/planned to profit from the superior seeing and low water column:

- China: 4 m KDUST IR and 10 m submm
- France/Italy: 2.5 m Polar Large Telescope
- Japan/China: 2.5 m PLATO-type telescope

See Burton (2010) for details. The HDF-S remains a field with unique potential due to its accessibility from Antarctica, and its potential for doubly efficient HST observations in the CVZ.

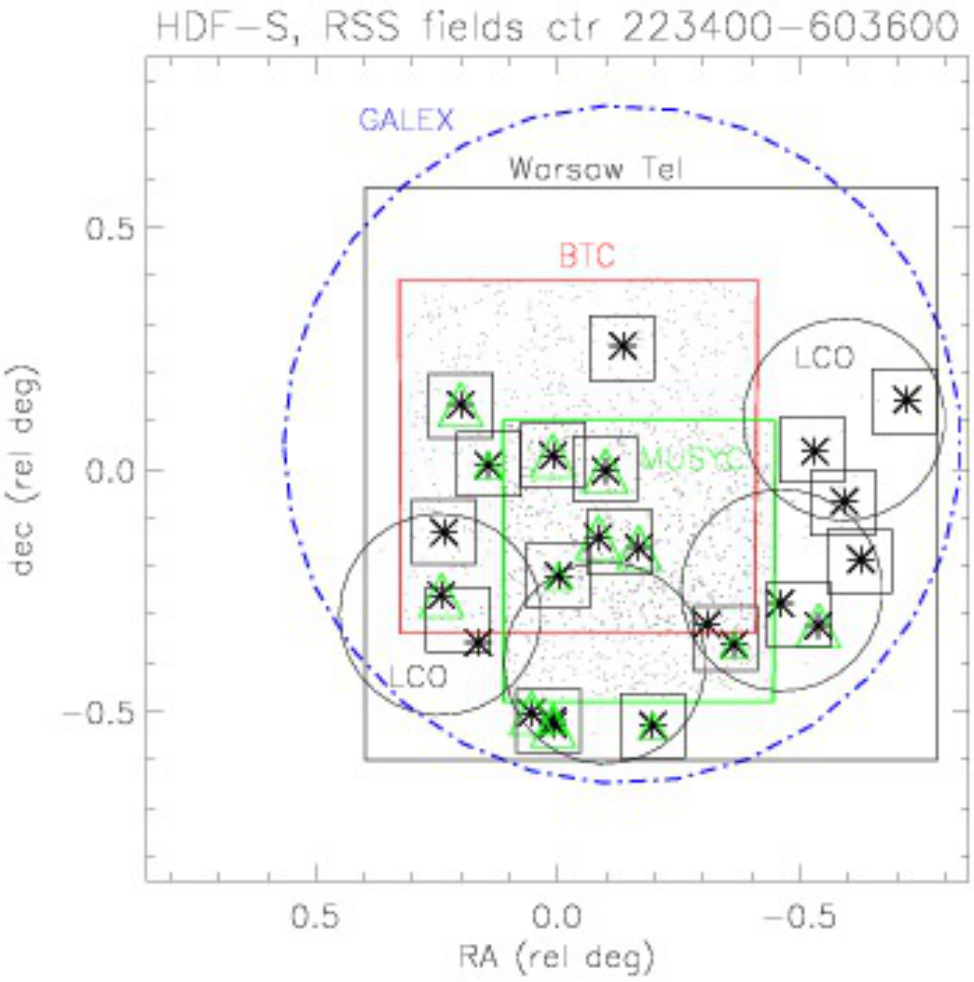

Fig. 2. Map of the EHDF-S labelled with fields for GALEX (large circle), the Warsaw Telescope, BTC, MUSYC fields (large boxes), the LCO Dupont 2.5 m (4 medium circles), 17 SALT RSS multislit spectroscopic fields (small boxes), NUV-bright quasars (asterisks), $z < 1.5$ Lyα absorbers (green triangles, large=high probability, small=candidate) and FUV dropouts (black dots).

We acknowledge support from a NASA GALEX grant for proposal G5-041, and appreciate observing planning and support from the SALT and Las Campanas staffs, and A. Udalski, M. Szymanski and the Warsaw Telescope team.

References

Burton, M. G. 2010, A&A Rev., 18, 417
Gawiser, E. et al. 2006, ApJS, 162, 1
Glazebrook, K. et al. 2006, AJ, 131, 2383
Haberzettl, L. et al. 2009, ApJ, 702, 506
Hutchings, J. & Bianchi, L. 2010, AJ, 140, 1987
Huynh, M. et al. 2010, ApJ, 723, 1110
Marchesini, D. et al. 2009, ApJ, 701, 1765
Norris, R. et al. 2005, AJ, 130, 1358
Palunas, P. et al. 2000, ApJ, 543, 61
Quadri, R. et al. 2007, AJ, 134, 1103
Sawicki, M. et al. 2003, AJ, 126, 1208

Session 14

Solar coronagraphy: New techniques, new questions

SF2A 2012
S. Boissier, P. de Laverny, N. Nardetto, R. Samadi, D. Valls-Gabaud and H. Wozniak (eds)

ANALYTICAL EXPRESSIONS AND NUMERICAL SIMULATIONS FOR AN EXTERNAL CIRCULAR OCCULTER CORONAGRAPH

C. Aime[1], A. Carlotti[2] and Y. Rabbia[1]

Abstract. We give in this study an analytical expression for the Fresnel diffraction of a circular occulter and compare it to numerical computations. The analytical expression uses Lommel series. Two different series are needed, whether the inside or the outside of the occulter's geometric shadow is considered. These series are infinite sums of Bessel functions which converge more or less rapidly depending on the experimental parameters and the position in the shadow. Numerical computations require thousands of points. The calculations given here are valid for an incoming plane wave, i.e. a point-like source. This is the necessary first step to a generalization to solar studies. The good consistency observed between numerical computations and analytical calculations makes it possible to generalize the numerical computations to different forms of occulters, and an example is given for a serrated edge disk. Simple considerations suggest that shaped apertures are required for exoplanet detection while mere circular occulters are convenient for solar coronal studies.

Keywords: Sun, exoplanets, coronagraph, external occulter

1 Introduction

The problem of observing the solar corona has been addressed by solar astronomers since the fundamental experiment of Lyot (1939) and the first use of external occulter by Evans (1948). An extremely well documented description of the methods of observation of these techniques, and the history of solar coronagraphy can be found in Koutchmy (1988). Some of the ideas described in this review paper (for example shaped occulters) are now considered for the detection of exoplanets (see for example Arenberg et al. (2007)). Shaped occulters have been proposed independently for solar and extrasolar studies the same year (Spitzer 1962; Purcell & Koomen 1962).

The problems are technically much more difficult for the exoplanet case than for the solar case, but from a computational point of view, the difficulties are inverted. For the exoplanet study, the star is considered as an unresolved point-like source. If the objective is to see an Earth-like planet at 10 parsecs, then the occulter as seen from the telescope must create a shadow with an angle of 0.2". From this constraint, and for a 4-m telescope, external occulters must have a 10 to 50 m diameter and be kept at a distance of 10 000 to 80 000 km.

For solar observations, the angle of the shadow is that of the entire solar disk, 1/100 rd, about 10 000 times larger than for an exoplanet. The occulter diameter becomes 1 to 1.5 m., and it must be kept at 100 to 150 m from a small telescope, as described in Lamy et al. (2010). These conditions correspond to a large number of Fresnel zones on the occulter, and the diffraction is much more difficult to compute. Another major difficulty is the fact that the Sun is an extended source and that it is necessary to sum contributions coming from all parts of the solar disk to obtain the resulting intensity at the position of the corona.

We consider here the case of a point-like source, a preliminary step that is required to compute the actual performance of a solar occulter. Nevertheless, interesting inferences can be already obtained from this first work.

[1] Université de Nice Sophia-Antipolis, Centre National de la Recherche Scientifique, Observatoire de la Côte d'Azur, UMR7293 Lagrange, Parc Valrose, 06108 Nice, France

[2] Princeton University, Mechanical & Aerospace Engineering, Olden street, Princeton, 08544 NJ, USA

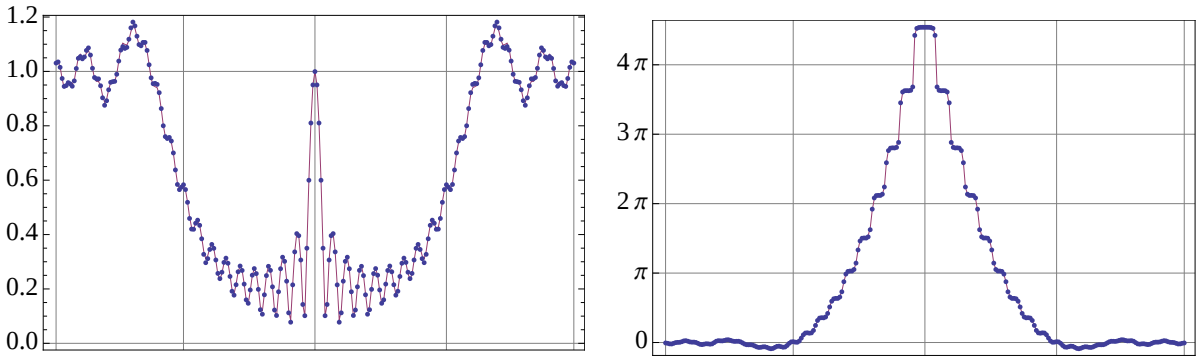

Fig. 1. Modulus (**left**) and unwrapped phase (**right**) produced by a circular occulter of diameter 10 m set at 10 000 km for an incident wave plane. The wavelength is $0.55\mu m$. The Arago spot is dominant in this configuration. The two vertical lines gives the geometrical position of the edges of the occulter. Continuous curves correspond to Eq. 2.3 while dots are the result of a numerical simulation making use of the spatial filtering.

2 Analytic expressions for the Fresnel diffraction of a circular occulter.

The shadow produced at the telescope entrance aperture by an external occulter is a typical problem of Fresnel diffraction, i.e. the free-space propagation of a coherent wave between two planes over a finite distance. Let us briefly recall some fundamentals equations.

If we denote $f_0(x, y)$ the complex amplitude of a wave in the plane $z = 0$ (the plane of the occulter in our problem), its expression $f_z(x, y)$ at the distance z (the entrance aperture of the telescope) can be obtained by any of the equivalent equations:

$$\begin{aligned} f_z(x,y) &= \frac{1}{i\lambda z} \iint f_0(\xi,\eta) \exp\frac{i\pi(\xi^2+\eta^2)}{\lambda z} \exp(-2i\pi\frac{\xi x+\eta y}{\lambda z})\, d\xi\, d\eta \\ &= f_0(x,y) * \frac{1}{i\lambda z} \exp\frac{i\pi(x^2+y^2)}{\lambda z} \\ f_z(x,y) &= \Im^{-1}\left[\hat{f}_0(u,v)\exp(-i\pi\lambda z(u^2+v^2))\right] \end{aligned} \tag{2.1}$$

where λ is the wavelength of the light, the symbol $*$ stands for the 2D convolution, $\hat{f}_0(u, v)$ is the 2D Fourier transform of $f_0(x, y)$ for the spatial frequencies (u, v), and $\Im^{-1}$ denotes the operation of inverse 2D Fourier transform.

The first relation is the mathematical formulation of the Huygens-Fresnel principle, which can be written as a convolution relationship. The integral will be used for the derivation of the analytical expression of the Fresnel diffraction of a circular occulter. The inverse filtering formula is suitable for numerical computation, because it allows the use of fast Fourier transforms. A numerical difficulty arises because of the very high sampling required either by the quadratic phase term filter $\exp(-i\pi\lambda z(u^2 + v^2))$ or by $\hat{f}_0(u, v)$.

The transmission of a circular occulter of diameter D can be written as $1 - \Pi(r/D)$, where $r = \sqrt{x^2 + y^2}$, and $\Pi(r)$ is the top-hat function of transmission 1 for $|r| < 1/2$, and 0 elsewhere. Making use of the first expression of Eq. 2.1, the amplitude $\Psi(r)$ of the wave produced by the Fresnel diffraction of the occulter at the distance z can be written as:

$$\Psi(r) = A - \frac{A}{i\lambda z}\exp(i\pi\frac{r^2}{\lambda z})\int_0^{D/2} 2\pi\xi \exp(i\pi\frac{\xi^2}{\lambda z}) J_0(2\pi\frac{\xi r}{\lambda z}) d\xi \tag{2.2}$$

where $J_0(r)$ is the Bessel function of the first kind and A stands for $A\exp(2i\pi z/\lambda)$. As we can see, for a wave of unit amplitude ($A = 1$), the Fresnel diffraction of the occulter writes as 1 minus the Fresnel diffraction of the hole. In the literature, it is often inadequately made reference to the Babinet theorem for this property.

Obtaining the complete expression of the wave for any r value is not straightforward. It is easy to show that, at the center of the shadow ($r = 0$), there is a bright spot, of the same intensity level as if the occulter was not present, and which is the famous Arago spot, experimental corner stone of Fresnel's theory. The integral in Eq. 2.2 is a Hankel transform that does not have a simple analytical solution for $r \neq 0$.

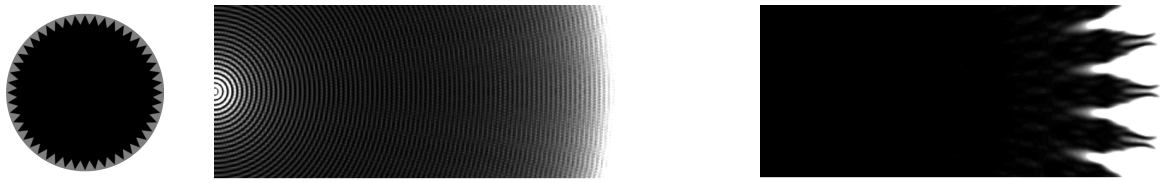

Fig. 2. Left: the circular occulter and the serrated edge outlined inside. Center: the shadow produced by the circular occulter. **Right:** the shadow produced by the serrated edge occulter. The figure is for illustration only, the parameters (occulter of 10 cm at 100 m) being chosen for computational constraints and easiness of representation.

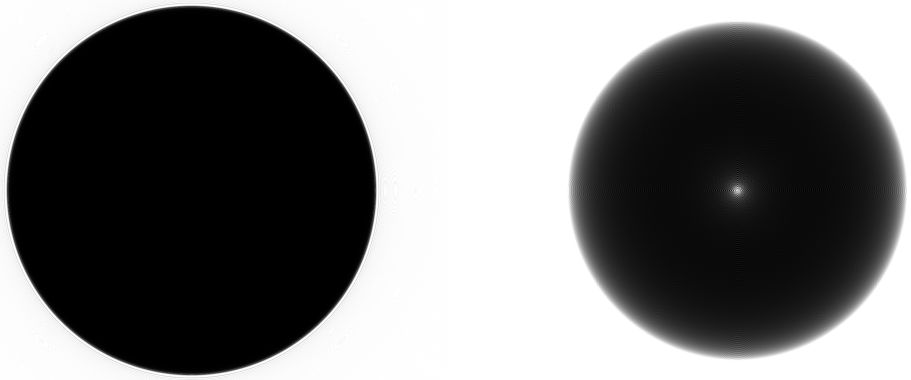

Fig. 3. Shadow produced by a circular occulter of diameter 1 m set at 100 m for an incident wave plane. **Left:** direct representation. **Right:** Same as left panel with the intensity multiplied by 1000.

A similar problem is found in the three-dimensional light distribution near focus, described in Born & Wolf (2006). It makes use of Lommel series. We have used this approach to obtain the Fresnel diffraction of a circular occulter. After some calculations, we obtain the simplified expressions for a circular occulter of diameter D at the distance z:

$$\begin{aligned}
&\text{for } r < D/2: \quad \Psi(r) = A\exp(i\frac{\pi r^2}{\lambda z})\exp(i\frac{\pi D^2}{4\lambda z}) \times \sum_{k=0}^{\infty}(-i)^k(\frac{2r}{D})^k J_k(\frac{\pi D r}{\lambda z}) \\
&\text{for } r = D/2: \quad \Psi(\frac{D}{2}) = \frac{A}{2}(1+\exp(i\frac{\pi D^2}{2\lambda z})J_0(\frac{\pi D^2}{2\lambda z})) \\
&\text{for } r > D/2: \quad \Psi(r) = A - A\exp(i\frac{\pi r^2}{\lambda z})\exp(i\frac{\pi D^2}{4\lambda z}) \times \sum_{k=1}^{\infty}(-i)^k(\frac{D}{2r})^k J_k(\frac{\pi D r}{\lambda z})
\end{aligned} \tag{2.3}$$

To the authors' knowledge, these expressions have not yet been published in the literature.

The two series, for the inner ($r < D/2$) and outer ($r > D/2$) zones of diffraction, converge to the correct value for $r = D/2$. However, in practice, the series are limited to a finite number of terms and the convergence of the series is more difficult to obtain near the transition zone than far away from it. In practice, we used up to 400 terms for the series, which corresponds to a reasonable computing time and a precise result. All computations were made using *Mathematica*[i].

In Fig. 1 we have represented the modulus and the (unwrapped) phase of the shadow produced by an incoming plane wave occulted by a 10m. circular occulter located at 10 000 km from the telescope, parameters

[i] *Mathematica* 2012, Wolfram Research, Inc., Champaign, IL

corresponding to the observation of an exoplanet. The continuous lines are obtained from the Lommel series (100 terms) and the dots are from a numerical computation. The behavior of the phase in the Fresnel diffraction of the occulter is particular. Although the phase term is almost zero in the bright part outside the disk, it becomes highly perturbed in the shadow behind the screen. For the detection of an exoplanet, this means that the telescope response will be quite different for the star and the planet, and the question of a wavefront correction in the form of a multi-object adaptive optics system may be raised.

As it can be seen in the figure, the shadow is not dark enough to suppress the starlight, and the Arago spot is very bright. This is the reason why much larger occulters (for example 50 m. at 80 000 km) are considered. Moreover, occulters with a shaped contour will be preferred to circular ones for exoplanet detection. They have the advantage of producing a much darker central region. An illustration of that is given in Fig. 2 for a serrated edge occulter, similar to the one described in Koutchmy (1988).

Such occulters, that are excellent for the detection of an exoplanet, are probably inappropriate for the Sun that is an extended source. Each point of the solar surface will produce a shifted shadow on the telescope aperture. The goal is to cancel the light coming from the solar disk without attenuating the light coming from the corona. Creating a dark shadow at the center of the figure is not as crucial as having a sharp transition between the dark and bright areas. As it is clearly visible in the figure, a serrated edge occulter does not induce a sharp transition between the dark and the bright regions. However, this was not the conclusion of Fort et al. (1978) considering an occulter with very small teeth, and further studies of these kind of occulters are needed.

The use of a circular occulter in the case of solar observations is nevertheless a possible solution. In Fig. 3 (left) we have represented the intensity produced by an incoming plane wave on a circular occulter with a diameter that ranges from 1 m to 100 m, parameters corresponding to the shadow produced by a point source of the solar disk. The Arago spot is no more visible in this figure, but remains visible in Fig. 3 (right) where the intensity level has been multiplied by a thousand. The geometry of the two figures are the same, which means that the edges of the dark zone, that appeared sharp in the left figure are indeed somewhat smooth on that scale. Using larger occulters at larger distances will make it possible to obtain edges more and more sharp.

One last point favors circular occulter for solar studies. The central part of the shadow corresponding to the Arago spot is fairly described by the only non-zero term of the Lommel series, the simple Bessel function $J_0(\pi r D/\lambda z)$. The diameter of the Arago spot can then be approximately written as $1.53\lambda/\alpha$, where $\alpha = D/z$ is the apparent diameter of the occulter as seen from the telescope's aperture. As a consequence, the Arago spot extends over a width 10 000 times smaller in the solar case than in the case of a exoplanet observation.

Thanks are due to Marcel Carbillet and Andrea Ferrari for constructive remarks.

References

Arenberg, J.W., Lo, A.S., Glassman, T.M. & Cash,W., 2007, C.R. Physique, 8, 438

Born, M., & Wolf, E. 2006, Principles of Optics, 7th Ed. (Cambridge University Press, 2006), 484

Evans, J.W. 1948, J.Opt.Soc.Am., 88,1083

Fort, B., Morel, C. & Spaak, G. 1978, A & A, 63, 243

Koutchmy, S. 1988, Space Sci. Rev., 47, 95

Lamy, P. , Damé, L. , Vivès, S. & Zhukov, A. , 2010, SPIE, 7731, 18

Lyot, B. 1939, Mon. Not. R. Astron. Soc., 99, 580

Purcell, J.D. & Koomen, M.J.. 1962, J.Opt.Soc.Am., 52, 596

Spitzer, L. 1962, American Sci., 50, 473

SF2A 2012
S. Boissier, P. de Laverny, N. Nardetto, R. Samadi, D. Valls-Gabaud and H. Wozniak (eds)

ABOUT THE SOLAR EDGE AND SOLAR DIAMETER VARIATION STUDIES

C. Bazin[1], S. Koutchmy[1] and P. Rocher[2]

Abstract. Without spurious effects due to instrumental and/or Earth atmospheric parasitic light, the true solar edge can only be correctly analyzed at the time of solar total eclipses. We discuss the problems occurring when using solar diameter measurements made outside of solar total eclipses, including the possible limb effects related to different sources of solar activity. Effects due to the PSF and to the scattered light should be discussed with reference to coronagraphic methods used to reduce the ultimate sources of parasitic light.

Keywords: sun:corona, sun:fundamental parameters, Eclipses

1 Introduction

The variation of the solar diameter was discussed a long time ago, with also some interrogations on indirect effects on the Earth climate of long time period solar variabilities associated with the Total Solar Irradiance - TSI. This energy can be also evaluated by considering the solar diameter measurements, as described in Nesmes-Ribes and Thuillier 1966. They suggested that the solar diameter could change over centuries, and this could be measured in space, free of Earth atmospheric turbulence, distortion and refraction, thanks to the Picard space mission designed by the French Space Agency CNES. These solar diameter measurements are performed in space but outside of eclipse conditions. The variations of the Total Solar Irradiance (TSI) S can be analyzed assuming a simple model:

$S = \frac{\pi * R^2 * \sigma * T_{eff}^2}{A^2}$

A is the distance Sun-Earth (an average value over 1 Year is evidently considered) equal to the astronomical unit (constant) in average (also called the A.U.) while variations over the solar disk are neglected. The variations of S can then be due to the changes of the solar radius Ro or/and of the effective temperature T of the photosphere (possibly a consequence of global processes occurring deep inside the Sun) assuming A is constant:

$\frac{\delta S}{S} = 2 * \frac{\delta R_0}{R_0} + 4 * \frac{\delta T_{eff}}{T_{eff}}$

The relative variations of the TSI, S, during a solar cycle is less than +/- 0.001. Then the relative variation of the solar radius cannot be more than +/- 0.4 arcsecond and indeed, it is considerably smaller. It could be as small as 10 milli-arcsec, taking into account the variations of the effective temperature of the photosphere, which seems not correlated with the solar cycle and the magnetic activity based on the Kitt Peak 35 Years long series of precise measurements of the equivalent width of selected solar spectral lines (Livingston et al. 2004).

2 Methods for the solar diameter measurements

Several methods have been or are still used to measure the solar diameter (Koutchmy et al 2011). Special heliometers were designed for more than 100 years. They were visually operated instruments and a large (1.55 arcseconds) correction for irradiation effect should be introduced. Also the analysis of Mercury and Venus transits can be used for measuring the solar diameter. Solar Astrolabes working at the same almucantarat for both limbs allow long acquisitions series, without a need of correction for refraction effect. Small apertures were used. Solar transit measurements can be made with stationary ground based telescopes measuring also at the

[1] Institut d'Astrophysique de Paris- UMR 7095- CNRS and UPMC
[2] IMCCE-Observatoire de Paris-UMR 8028-CNRS

same almucantarat. The analysis of solar disk images are actually made in Space with MDI of SoHO, AIA of SDO and the dedicated Picard mission. Finally, Solar Total Eclipses allow an accurate timing of the contact instants determined by the value of the solar diameter and the invariable diameter of the Moon and of the distance Earth- Moon. Eclipses observations seem to be a good way to measure the solar diameter, the Sun is covered by the Moon, our celestial body, at a distance of about 400000 km. The phenomenon allows defining as well and importantly the true solar edge, thanks to the use of slit less flash spectra, separating the continuum at the solar edge and the faint low excitation emission lines, which could indeed be associated with the local magnetic field. The inconveniences are that the solar total eclipses occurs in average at approximately one per two years, in different locations on Earth, and the contact duration is a few seconds and this is very short.

3 Advantages of Eclipse Observations

Solar eclipse observations are performed on the ground with economic, small portable equipment, including new technology fast CCD cameras and light PC computers. Total solar eclipses are free of seeing effects because the occultation occurs in space, this is a fundamental advantage, and there are no spurious effects due to the scattered and parasitic light coming from the disk which is fully occulted in Space. It is a differential method where the immutable lunar disk is used as a reference and magnified by a factor of more than 1:30. Additional advantages come from the use of precise timing and positioning GPS devices and spectrally resolved time series. Precise lunar profiles are available from stellar occultation. The classical Watts profiles and those from the Kaguya space mission are indeed used. The following figure 1 shows how could be defined the true solar edge during the last total solar eclipse of 11th July 2010 in French Polynesia, using slitless flash spectra, by analyzing the true continuum seen between the many faint emission lines.

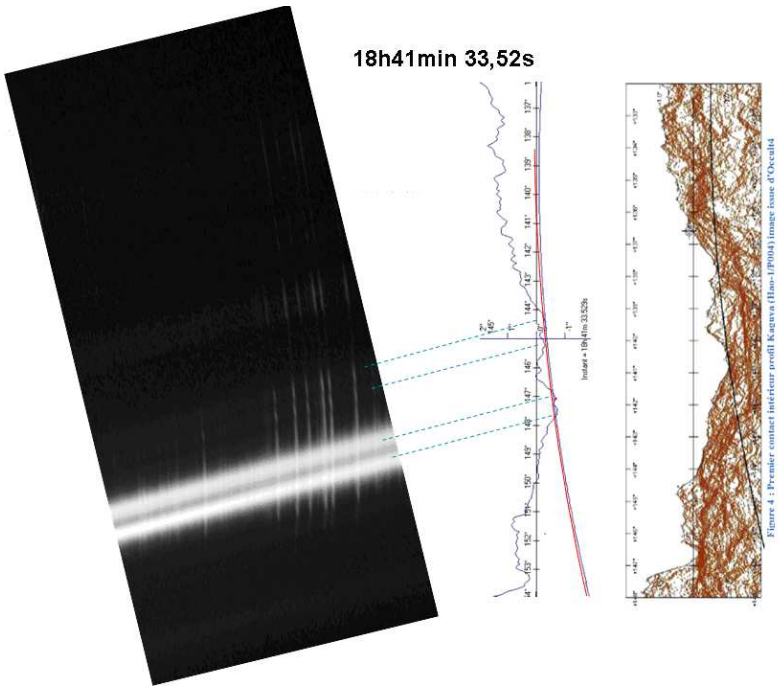

Fig. 1. Extract of 11th July 2010 total eclipse flash spectra, fitting with the Kaguya lunar limb profile. This shows how the lunar mountains and valleys modulate the solar lines, the continuum of the flash spectra, and the modulation of the Baily bead spectra.

The disadvantage of the method is that there are irregularities due to lunar mountains and valleys, which give more difficulties to measure the contacts by the use of a chrono-datation. There is also the question of the optical global Moon shape and geometry, but this point is beyond the scope of this contribution, and further analysis should be performed. To avoid these defects, we also tried to look (first, at ground based) at a diffracted solar limb using the linear edge of a metallic wall situated at a distance of 150 meters to simulate future observations with the proposed space borne mission Aspiics/Proba3 (Vives et al 2005).

4 Outside of eclipse groundbased experiments for studying the solar edge using external occultation coronographic methods

These diffraction experiments were done in the context of the Aspiics/Proba3 space mission, consisting of an artificial occultation to try to reproduce solar total eclipses conditions using two satellites, one with the observing instruments, and the other with an occulting disk of 1.5 m of diameter, separated by a distance of 150 meters. Figure 2 shows the schematic we used for performing the acquisitions of the rising Sun occulted by a vertical wall images. The next figure 3 shows typical results we obtained, by taking four images per second during the

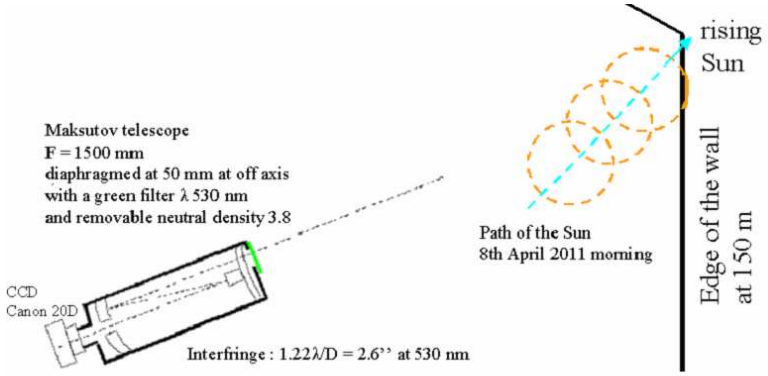

Fig. 2. Schematic of the experiment using a Maksutov imaging telescope, situated at 150 m from the edge of the wall when the rising Sun limb begins to appear

appearance of the solar limb, when it rises in the vicinity of the vertical wall edge situated at 150 m. This method

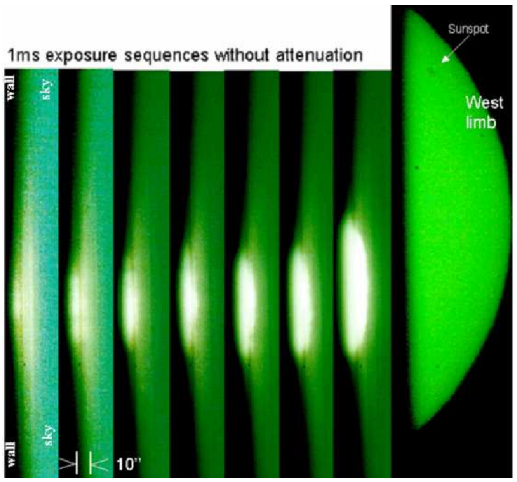

Fig. 3. Time sequences performed the 8th April 2011 at 6h15 UTC, at the time of the rising Sun, taken using a 4 frames/s cadence, 1ms of exposure time at 200 ISO, to show the diffraction patterns from a vertical wall edge. A large band green filter is placed in front of an F = 1500 mm Maksutov telescope, diaphragmed at 50 mm, see Fig. 2. The focusing was put at infinity. The edge of the vertical wall was situated at 150 meters. Image visualizations were adjusted in Log scale. An Astrosolar ND 3.8 neutral density filter was used after for the 5 ms exposure image of the disk shown at right at same scale for orientation and calibration.

supposedly allows evaluating at groundbased the extension of the scattered light, including the instrument PSF, closed to the solar limb, during a grazing occultation. The diffraction of the Sun light by the edge of the wall should be seen at the beginning just before the extreme solar limb appears. It apparently produces a total extension of at least 10 arcseconds. The aperture of the Maksutov telescope produces small diffraction minima and maxima when illuminated by the very small crescent of the solar limb and the measured distance between

two maxima was estimated to be 3 +/- 0.5 arcseconds. Because the apparent path of the rising Sun in the sky is not strictly vertical like the wall edge, the contact corresponding to a less than 3 arcseconds crescent is rather short. These sequences allowed evaluating the solar aureola which is more than ten times more extended than the diffraction pattern, and it overlaps the Earth atmosphere scattering and the effect of the PSF. This shows the possibilities, without aureola in space, to observe very near the solar limb with Aspiics/Proba 3. Indeed, there will be much less parasitic scattered light in Space than at ground based, especially with a low Sun. The day of the 8th April 2011 was however very clear, without clouds and the seeing was fair. We also looked at the diffraction of the wall using the rising Sun, without green filter when focussing at 150 m. The following figure 4 shows two images we obtain with the defocused image of the Sun and the extension of the diffracted light by the wall.

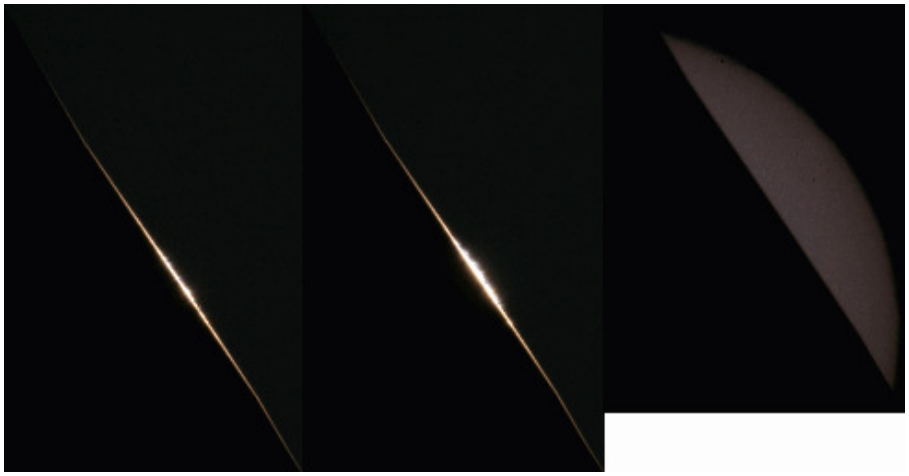

Fig. 4. Fringes with the occulted rising Sun while focusing on the wall at 150 m and a 0.25 ms exposure at 200 iso without ND; the solar disk at the same scale with a ND 3.8 and 5 ms exposure.

5 Conclusion

From the previous solar limb images obtained without an occultation in Space, we deduced that the solar light seen beyond the limb was due to the aureola effect (Earth atmospheric scattering and/or the instrumental PSF including extended wings) and in a lower extend, by diffraction fringes when a 50 mm aperture imaging telescope is used. The total diffraction extension obtained with tests with a linear wall edge had an extension of approximately 10 arcseconds, mainly due to the effect of the Earth atmosphere. We expect very much less parasitic scattered and diffracted light with the Aspiics/Proba 3 space mission. There will be no aureola. It will also be possible to observe close to the limb, for analysing the transition region and the low corona. From the total solar eclipse conditions, the solar edge is much better defined, while using high cadence flash spectra imaging, and this will continue to be the best method to be developed in the near future for studying the solar diameter.

References

Bazin, C., Koutchmy, S., & Tavabi, E. 2010, IAGA Symp. in Cairo, Proc. 2011, L. Dame and A. Hady Editors

Bazin, C., Koutchmy, S, Lamy, P., & Sevre, F. 2010, First Picard Workshop of the 8 - 9 March 2010, IAP-Paris France, http://irfu.cea.fr/Projects/COAST/ConferencePICARD/2010_21_PICARD_Bazin.pdf

Koutchmy, C., Bazin, C., Prado, J-Y., Lamy, P., & Rocher, P. 2011, Conference Proceedings MTPR-10, Lotfia El Nadi Ed. 15 p.

Livingston, W., Gray, D., Wallace, L. & White, O.R., 2004 ASP Conference Series, Vol 346, 353

Nisme-Ribes, E. & Thuillier, G. 1966 Histoire solaire et climatique, Belin Ed.

Venet, M., Bazin C., Koutchmy S. & Lamy P. 2010 ESA/ESTEC conference

Vives, S., Lamy, P., Auchere, F., et al. 2005 SPIE, Vol. 5901, 305-315

SF2A 2012
S. Boissier, P. de Laverny, N. Nardetto, R. Samadi, D. Valls-Gabaud and H. Wozniak (eds)

CORONAGRAPHY AT PIC DU MIDI: PRESENT STATE AND FUTURE PROJECTS

L. Koechlin[1]

Abstract. The Pic du Midi coronagraph (CLIMSO) is a group of four instruments in parallel, taking images of the whole solar photosphere and low corona. It provides series of 2048*2048 pixels images taken nominally at 1 minute time intervals, all year long, weather permitting. A team of $\simeq 60$ persons, by groups of 2 or 3 each week, operate the instruments. Their work is programmed in collaboration with Institut de Recherches en astrophysique et planétologie (IRAP) of Observatoire Midi Pyrénées (OMP), and with Programme National Soleil Terre (PNST).

The four instruments of CLIMSO (L1, C1, L2 and C2) collect images of the Sun as following: 1) L1 : photosphere in H-α (656.28 nm) ; 2) L2 : photosphere in Ca-II (393.37 nm) ; 3) C1 : prominences in H-α ; 4) C2 : prominences in He-I (1083.0 nm).

The data taken are stored in fits format images and mpeg films. They are available publicly on data bases such as BASS 2000 Meudon (`http://bass2000.obspm.fr/home.php?lang=en` and BASS2000 Tarbes (`http://bass2000.bagn.obs-mip.fr/base/sun/index.php`). Several solar studies are carried in relation with these data. In addition to the raw fits images, new images will soon be sent to the data bases: they will be calibrated in solar surface emittance, expressed in $W/m^2/nm/steradian$. Series of mpeg films for each day are presented in superposed color layers, so as to visualize the multispectral information better.

New instrumental developments are planned for the next years and already financed. They will use spectropolarimetry to measure the magnetic field and radial velocities in the photosphere and corona. The data will cover the entire solar disc and have a sample rate of one map per minute.

Keywords: Sun : corona, Techniques: polarimetric, Techniques: spectroscopic

1 Introduction

Coronagraphy started at Pic du Midi thanks to the invention by Bernard Lyot (Lyot 1930), and has continuously been developed since at that observatory. The Pic du midi site (alt 2875m) is well suited for high angular resolution and high dynamic range images, thanks to particularly clear and laminar air conditions, not all the time though: weather allows approximately 2000 hours per year of sunshine, i.e. 45%, based on charts by the French "Agence de l'Environnement et de la Maîtrise de l'Energie" (ADEME). From this clear sky percentage, a relatively large part is free from high altitude cirrus and usable for coronagraphy.

In order to cope with the increasing quality standards set by the space programs for solar observation, and to be complementary to them, the ground-based coronagraphy has evolved. Our most recent implementation of coronagraphy at Pic du Midi is a set of four instruments: CLIMSO, that consists of two 200 mm Lyot coronagraphs and two 90 mm narrowband solar telescopes. They are grouped in a standalone system held on a large equatorial table. This system has started operation in 2009, as an upgrade to the previous coronagraph (HACO) , and in complement to a still operational spectrocoronagraph on the same equatorial mount (MSCO)

This new set of instruments has been developed under the supervision of Jacques-Clair Noëns, with a particular organization regrouping two different groups of people : professional and amateur (although expert) astronomers. The differentiation here between 'professionals' and 'amateurs' holds to the fact that amateurs are not paid a salary for their contribution to Pic du Midi coronagraphs. However, these non-professionals are often working in closely related domains such as optics, computer science, high precision mechanics, and are passionate solar geeks. For example, on the non-professional side David Roumeuf (engineer at Lyon university)

[1] IRAP, CNRS, Université Paul Sabatier, 14 avenue Edouard Belin 31400 Toulouse, France

Fig. 1. The original Lyot coronagraph in the Baillaud dome at Pic du Midi. Picture taken ca. 1974.

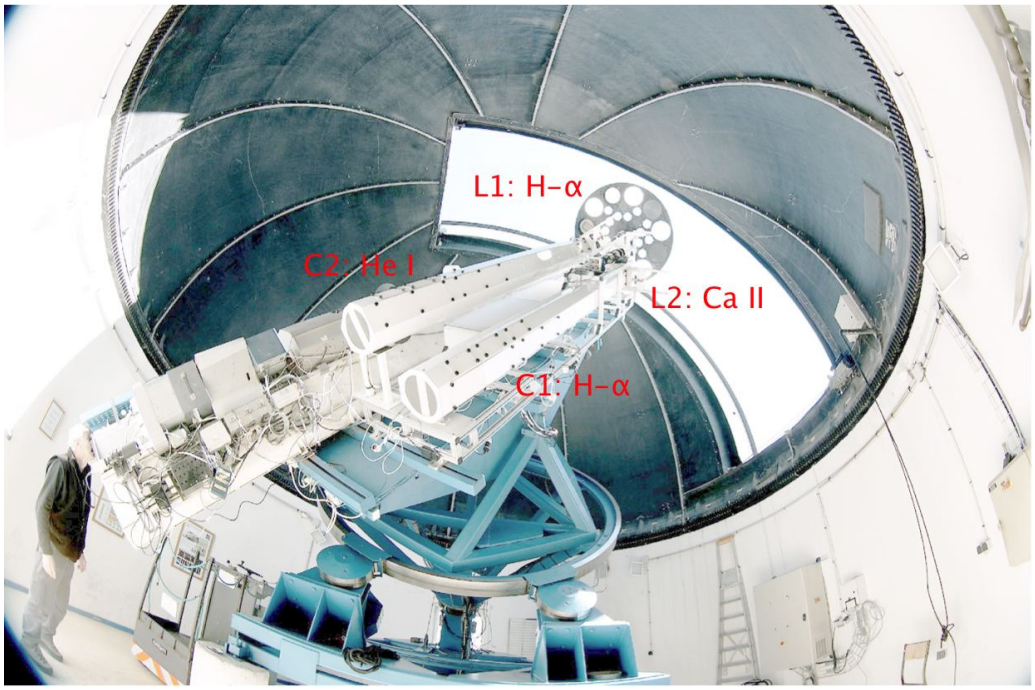

Fig. 2. The set of four instruments: CLIMSO. These two Lyot coronagraphs and two solar refractors at Pic du Midi are placed on the same equatorial table in a new dome built ca. 1999. The large instrument on the East side (left) of the equatorial table is MSCO, a spectro-coronagraph. The wheel with holes in front of CLIMSO is used for calibrations and pointing. Photo credit : OA

took in charge the overall conception and computer monitoring, Luc Dettwiller the optical design, Maurice Audejean the image processing. Many others "observateurs associés" (OA)contributed to decisive actions on the instrument, and contribute to the scientific publications.

The CLIMSO optics, computers and mechanics have been funded with large donations by Fiducial (a private

company), thanks to the action of Serge Rochain and the members of the OA non-profit organization directed presently by Franck Vaissiere.

On the "professional" side, Observatoire midi Pyrenees contributes to the project by defining the scientific program with the IRAP scientists and PNST, as well as the present data acquisition procedures and the future instrumental developments. Observatoire midi-Pyrenees is financing all the base equipment : equatorial mount, buildings and done, and pays the work of a significant number of people for their maintenance in this high altitude site.

In fact both groups are closely interacting as Observatoire Midi Pyrenees staff are involved also in the optics and mechanics, such as Raphaël Jimenez, or the image processing and data base management, such as Martine Lafon. Several science studies are carried presently using these data, see (Romeuf et al., 2007). My role as a newcomer in this field is to continue the work of astronomer J.C.Noëns: link the OA and the scientific community, contribute to the the elaboration of new science programs and instrumental developments.

The coronagraphs are also contributing the the outreach of astronomical research at Pic du Midi, as 20 to 100 persons visit the instrument each day, and hear detailed explanations on the solar studies undergone. High level education is also concerned, as groups of Master-2 students from Université Paul Sabatier in Toulouse (14 in 2011 and 15 in 2012) trained for 5 days internships at Pic du Midi. Their work includes acquisition, processing and scientific use of the coronagraphs' images.

In this paper I describe the recent developments of the instruments, their operation, the type of solar data sent to databases, the ways to retrieve them, and the planned developments in instrumentation for the next three years.

2 Design

2.1 Optics

The two photosphere telescopes are 90 mm commercial "Coronado" refractors equipped with narrowband H-α (656.28 nm) and CA-II (393.37 nm) filters respectively placed before the objective lens. The non-uniform transmission of the Coronado H-α filter across the field causes image degradations, but they can be corrected to a large extend by using the 5 flat fields taken every day. The Ca-II filter has a more uniform transmission.

The two coronagraphs are 200 mm custom designed refractors, equipped with conventional Lyot optics (i.e. adjusted field mask and pupil mask) and narrowband H-α and He-I filters respectively, placed in a parallel beam downstream.

2.2 Mechanical interface

In order to keep parallel the optical axes of both coronagraphs to a high precision, one of them has two additional degrees of freedom in rotation, and a computer controlled adjustment. Due to mechanical flexions and dilatations, this adjustment needs to be made periodically during the day, every 5 minutes on average. This adjustment is performed manually at present. The focusses of the four instruments are adjusted by remote control. They stay within good tolerances for several weeks without requiring action.

3 Operation

The instrument is operated by "Observateurs Associés": a nonprofit organization regrouping approximately 60 active members, who take turns for one or two weeks per year by groups of two. The deal is the following : non-professional astronomers are offered one week of comfortable accommodation at the Pic du Midi site, in exchange of qualified work for data acquisition. The candidates are trained for one or two weeks before being eligible to operate the instruments by themselves, and a senior member of the association is reachable (if not present) when necessary to solve technical problems that may arise.

In a coronagraph, the Lyot mask must exactly cover the photosphere, thus constraints in position and radius are strict. The set of field masks used to cover the photosphere has 0.05 mm steps, which correspond to 4 arc second increments being given the 2.478 and 2.511 m focal lengths of the H-α and Ca-II coronagraphs, respectively. These masks are changed every ten days on average (8 to 20), in order to match the variable angular diameter of the Sun, due to the ellipticity of Earth's orbit.

During the acquisition, from one hour after sunrise to one hour before sunset, weather allowing, an image every minute is taken at the four instruments. If the sky is not clear enough for the operation of coronagraphs, only the two photosphere images are stored.

The equatorial mount used at present is still the one used previously to support the original Bernard Lyot coronagraph. It's drive is precise to a few arc minutes per hour, and manual guiding is the only solution to achieving the arc second precision required. Depending on the operators skills and on the seeing conditions (atmospheric tip-tilt), this precision is reached, or not. It is one limit now for image quality, and it concerns a fraction of the images sent to the databases. This will be improved in the next future by two actions : an automatic guiding system to be ready by the end of 2012 and a sieving of images before sending them to the databases, as it is already the case for the images that are selected to make the mpeg "films of the day".These films are sent onto the BASS2000 databases daily and one of them (with extension CL12) regroups the H-α corona with a composite RGB image of the photosphere in Ca-II (green channel) and H-α (red channel).

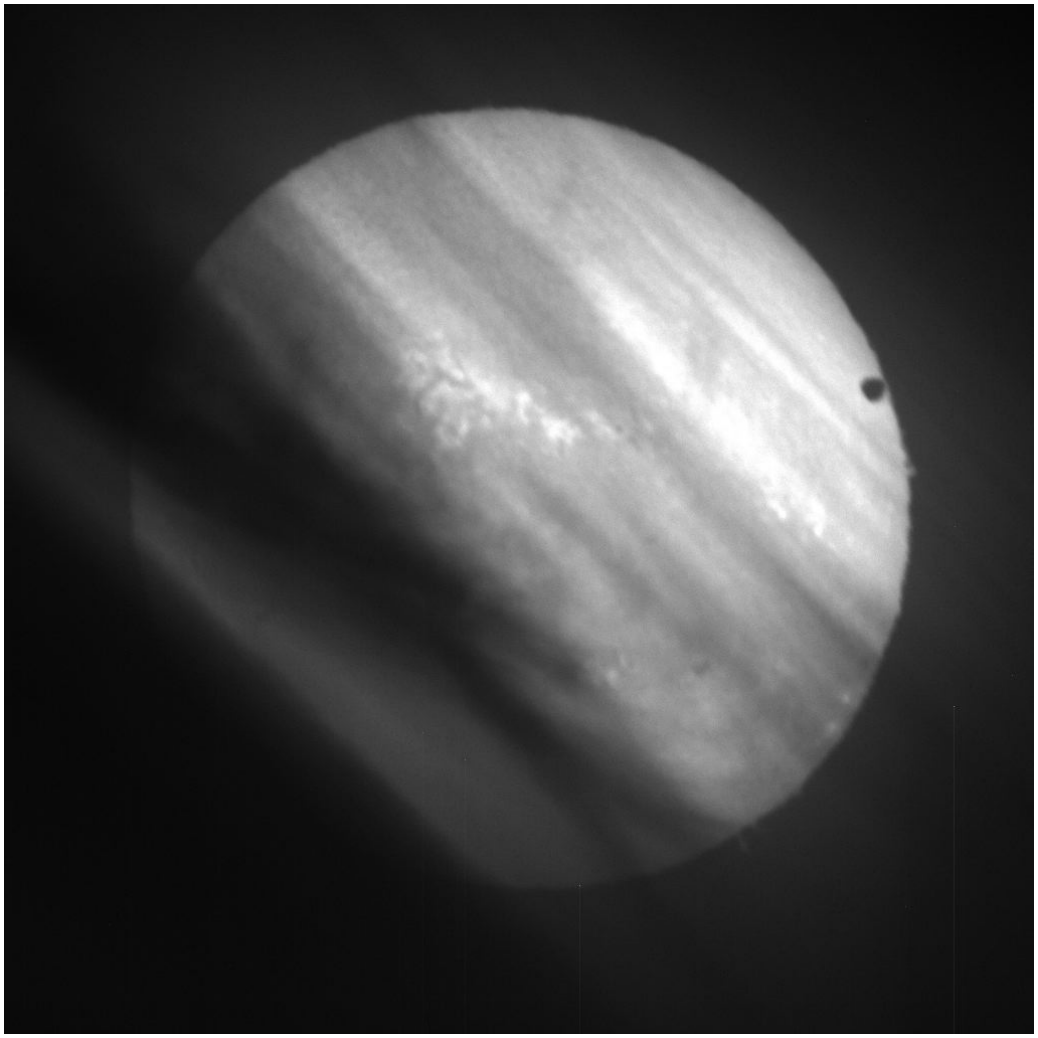

Fig. 3. Venus transit taken at Pic du Midi by the H-α telescope L1, 2012 06 06 at 04:38:28 TU. Cirrus clouds and atmospheric refraction in addition to seeing, did not allow to use the coronagraphs that morning. Photo credit : Z.Challita and P.Muller

Flat fields, darks, biasses and calibrations are taken each day in the morning. All images are stored in fits format, direct from camera reading. At present it is up to the data-base user to calibrate and reorient the images downloaded, using the references associated: series of five darks, five biasses, five flats, and two calibrations made with a relative East-West displacement, to retrieve photometry and precise field orientation. In the near future, the image orientations in the databases will be already corrected from instrumental camera disorientation.

Fig. 4. Combined image of the solar disc and prominences in H-α taken at Pic du Midi by the L1 refractor and C1 coronagraph. Additional images are available in combined colors, from L1, L2 and C1. One can notice that the the photosphere appears brighter in the lower part of the field, due to non uniform transmission (in space and in time) of the Coronado H-α filter, despite the flat fielding applied from calibrations made the same morning.

The calibrations may also be used to intercalibrate the H-α coronagraph with the H-α photosphere telescope, as the images are taken quasi-simultaneously and at the same wavelength. Knowing the solar constant for that date (which is given by satellite data and varies slowly) one can divide out the contribution of the atmosphere and instrumental transmission from the data. Although this can be computed independently since calibrations are provided, we will upload in the next few months the emittance maps computed for each image, expressed per pixel in $W/m^2/nm/steradian$ at the surface of the Sun.

4 Future improvements

For the next three years we prepare two new instruments : a larger 150 mm H-α photosphere telescope, with several narrowband channels across the H-α line, providing radial velocities, and furthermore, polarimetric data with four Stokes parameters. We aim to provide magnetic field data. The associated filters should be developed jointly by Arturo Lòpez Ariste, from Teneriffe observatory, and Silvano Fineschi, from Torino Astrophysical Observatory, in collaboration with IRAP and the OA. Once the solar telescope is tested, a new coronagraph with equal or higher spectropolarimetric performances will be built, exploring the corona in a Fe XIII line.

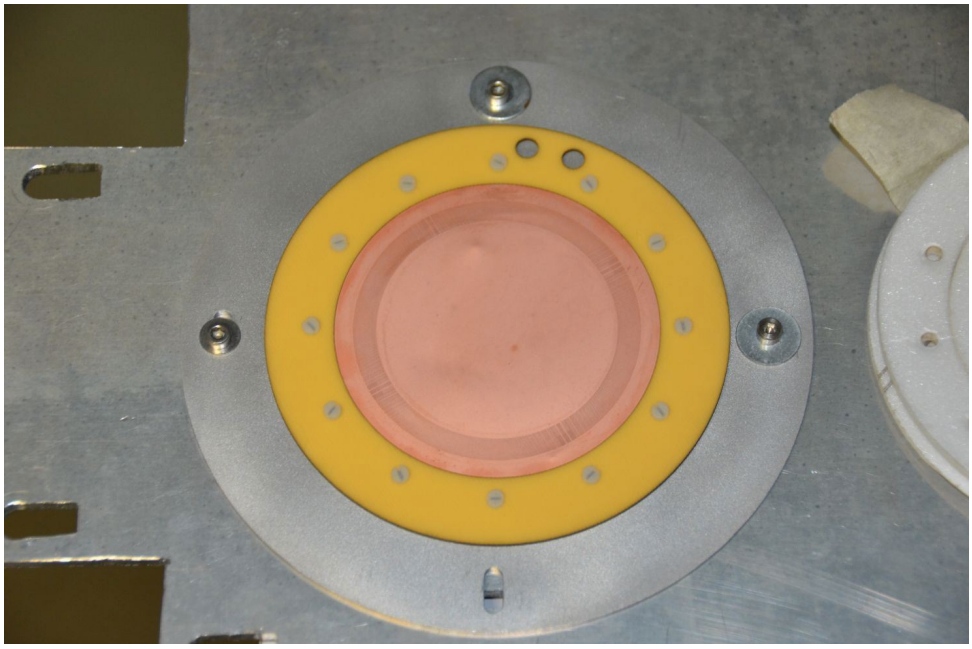

Fig. 5. The diffractive optics objective of the future autoguiding system. It is a 62 mm diameter Fresnel array carved into a thin copper foil with a large central obturation to block the order 0 of diffraction, leaving a 2.6 m focal length for the order 1 image. No chromatic correction will be necessary, as a 0.1 nm bandwidth filter is used, centered at 632.8 nm.

5 Data bases and scientific use of the data

The images taken in three spectral channels by the four instruments are sent to data bases BASS 2000 Meudon and BASS2000 Tarbes, also visible from NASA databases. The data are publicly available immediately, free of charge and with no embargo period. They can be downloaded from `http://bass2000.obspm.fr/home.php?lang=en` and `http://bass2000.bagn.obs-mip.fr/base/sun/index.php`.

The images are 2048x2048 pixels, in fits format. They are currently available as soon as they have been sent from the acquisition computer to the data base, i.e. usually the night after observation. The total amount of data per year grew from 287 Gb in 2007 to 825 Gb in 2011, and should reach 1 Tb for the year 2012. A few additional images per day are sent in quasi real-time onto `http://bass2000.obspm.fr/home.php?lang=en`.In addition to the solar studies that are under way at Observatoire Midi Pyrenees use these data (e.g. Roudier 2012), although we are not necessarily aware of all the use made of these images, we would appreciate some return information regarding their use, by mail and/or by citation in the published papers for which these data have been useful.

6 Conclusion

We presently provide images complementary to space data and to other ground based instruments. In order to improve them, we would appreciate any remark or comment that may help us improve them.

This scientific instrument and its operation are funded respectively by the Fiducial company and by French government funds through Université Paul Sabatier and Centre National de la Recherche Scientifique. A vital contribution is also the highly qualified work-power offered by the $\simeq$ 60 “Observateurs Associés” who run the instrument for image acquisition 7 days a week, almost all year long.

References

Lyot, B. 1930, Comptes rendus des séances de l’Académie des Sciences, 191, p. 834

Romeuf, D., Meunier, N., Noëns, J.C., Koutchmy, S., Jimenez, R. et al. 2007, A&A, 462, p. 731

Roudier, T., Rieutord, M., Malherbe, J. M., Renon, N., Berger, T., Frank, Z., Prat, V., Gizon, L. Švanda, M. Quasi full-disk maps of solar horizontal velocities using SDO/HMI data, 2012, Astron.&Astroph. 540, p.88, DOI: 10.1051/0004-6361/201118678

Session 16

Data reduction, analysis and visualization for spectro-imaging

SF2A 2012
S. Boissier, P. de Laverny, N. Nardetto, R. Samadi, D. Valls-Gabaud and H. Wozniak (eds)

BLIND DECOMPOSITION OF HERSCHEL-HIFI SPECTRAL MAPS OF THE NGC 7023 NEBULA

O. Berné[1], C. Joblin[1], Y. Deville[1], P. Pilleri[2], J. Pety[3], D. Teyssier[4], M. Gerin[5] and A. Fuente[2]

Abstract. Large spatial-spectral surveys are more and more common in astronomy. This calls for the need of new methods to analyze such mega- to giga-pixel data-cubes. In this paper we present a method to decompose such observations into a limited and comprehensive set of components. The original data can then be interpreted in terms of linear combinations of these components. The method uses non-negative matrix factorization (NMF) to extract latent spectral end-members in the data. The number of needed end-members is estimated based on the level of noise in the data. A Monte-Carlo scheme is adopted to estimate the optimal end-members, and their standard deviations. Finally, the maps of linear coefficients are reconstructed using non-negative least squares. We apply this method to a set of hyperspectral data of the NGC 7023 nebula, obtained recently with the HIFI instrument onboard the *Herschel* space observatory, and provide a first interpretation of the results in terms of 3-dimensional dynamical structure of the region.

Keywords: subject, verb, noun, apostrophe

1 Introduction

Telescopes keep growing in diameter, and detectors are more and more sensitive and made up of an increasing number of pixels. Hence, the number of photons that can be captured by an astronomical instrument, in a given amount of time and at a given wavelength, has raised significantly thus allowing astronomy to go *hyperspectral*. More and more, astronomers do not deal with 2D images, or 1D spectra, but with a combination of both of these media giving 3D data-cubes (2 spatial dimensions, 1 spectral dimension). The PACS, SPIRE and HIFI instruments, onboard *Herschel* all have a mode allowing spectral mapping (e.g. van Kempen et al. 2010; Habart et al. 2010; Joblin et al. 2010) in atomic and molecular lines. Owing to its high spectral resolution, HIFI allows to resolve the profiles of these lines, enabling to study the kinematics of e.g. the immediate surrounding of protostars (van Dishoeck et al. 2011), or of star-forming regions (Pilleri et al. 2012) using radiative transfer models.

Although such 3D datasets have become common, there is a lack of methods to analyze the outstanding amount of information they contain. Classical analysis methods tend to decompose the spectra by fitting them with simple functions (typically mixture of gaussians) but this has several disadvantages: 1) the assumption made by the use of a given function usually not based on physical arguments 2) if the number of parameters is high, the result of the fit may be degenerate 3) for large datasets and fitting with nonlinear functions, the fitting may be very time consuming 4) initial guesses must be provided 5) the spectral fitting is usually performed on a (spatial) pixel by pixel basis, so that the extracted components are spatially independent whereas physical components are often present at large scales on the image. Alternatively, it is possible to decompose data-cubes using Principal Component Analysis (e.g. Ungerechts et al. 1997; Brunt & Heyer 2002; Brunt et al. 2009). However this, has the disadvantage to decompose data onto an orthogonal basis, which produces components

[1] Université de Toulouse; UPS-OMP; IRAP; Toulouse, France, CNRS; IRAP; 9 Av. colonel Roche, BP 44346, F-31028 Toulouse cedex 4, France,

[2] Observatorio Astronómico Nacional (OAN), Apdo. 112, 28803 Alcalá de Henares (Madrid), Spain

[3] IRAM, 300 rue de la Piscine, 38406 Grenoble Cedex, France

[4] European Space Astronomy Centre, Urb. Villafranca del Castillo, P.O. Box 50727, Madrid 28080, Spain

[5] LERMA, Observatoire de Paris, 61 Av. de l'Observatoire, 75014 Paris, France

which are difficult to interpret directly in physical terms (e.g. spectra with negative values). An alternative analysis was proposed by Juvela et al. (1996), which consists in decomposing spectral cubes, in this case spectral maps of the pure rotational lines of carbon monoxide (CO), into the product of a small number of spectral components or "end members" and spatial "abundance" maps, with an enforcement of positivity for all the points in the decomposition. There is no assumption on spectral properties of the components, and hence this can provide deeper insights into the physical structure represented in the data, as demonstrated in this pioneering paper. This method uses the positivity constraint of the maps and spectra (all their points must be positive) combined with the minimization of a statistical criterion to derive the maps and spectral components. This method is referred to as positive matrix factorization (PMF, Paatero 1994). Although it contained the original idea of using positivity as a constraint to estimate a matrix product, this work used a classical optimization algorithm. Several years later, Lee & Seung (1999) introduced a novel algorithm to perform PMF using simple multiplicative iterative rules, making the PMF algorithm extremely fast. This algorithm is usually referred to as Lee and Seung's Non Negative Matrix Factorization (NMF hereafter) and has been widely used in a vast number of applications outside astronomy. Although some theoretical aspects of this method are still questioned (Donoho & Stodden 2003), this algorithm has proven its efficiency including in astrophysical applications (Berné et al. 2007). However, NMF has several disadvantages: 1) the number of spectra to be extracted must be given by the user and is usually hard to guess 2) the error-bars related to the procedure are not given automatically.

In this paper, we present an alternative way of performing a kinematical study of spectral maps, using a method which combines NMF to a classification algorithm and a Monte-Carlo analysis. This approach tends to discard the standard drawbacks of NMF described above, thus providing a quasi-optimal decomposition. Here we apply this method to Herschel-HIFI spectral maps of the [CII] and ^{13}CO(8-7) lines at 1900 and 881 GHz respectively. We describe the algorithms we use in Sect. 1 and the method itself in Sect. 2, and then apply it to the real data.

2 Definitions and algorithms employed by the method

2.1 Mathematical description of the data and aims

In hyperspectral astronomy, the observed data consist of a 3 D $m \times n \times l$ matrix $C(p_x, p_y, v)$ where (p_x, p_y) define the spatial coordinates and v the spectral index. We assume that all the points in $C(p_x, p_y, v)$ are positive. We call *spectrum* each vector $x(p_x, p_y, v)$ recorded at a position (p_x, p_y) over the l wavelength points. The goal of the method that we will describe here is to decompose C into the product of a few (typically < 10) spectra and weight maps using the measured noise in the data as the only input to the method and to provide an *error* estimation at each point in the extracted spectra. The main algorithms we use here are Lee & Seung's NMF and K-means which we describe hereafter.

2.2 Lee & Seung's NMF in our context

We define a new positive 2D matrix of observations X, the rows of which contain the $m \times n$, *spectra* of C arranged in any order. We now assume that each *spectrum*, x, is a linear combination of a limited number r (with $r \ll m \times n$,) of unknown *source spectra*, i.e.

$$x(p_x, p_y, v) = \sum_{i=1}^{r} a^i(p_x, p_y) s^i(v) + n(p_x, p_y, v), \tag{2.1}$$

where $s^i(v)$ are *source* spectra, i is the *source* index, $a^i(p_x, p_y)$ are the unknown "weight" coefficients and $n(p_x, p_y, v)$ is additive noise. This can be re-written in the following matrix form:

$$X = AS + N, \tag{2.2}$$

where A is the $m \times n \times r$ matrix of unknown coefficients of the linear combinations and S is an $r \times l$ matrix, the rows of which are the *source* spectra and N is the noise matrix. This is a typical blind source separation (BSS) problem (Cardoso 1998), and can be solved using multiple methods (e.g. Lee & Seung 1999, Hyvärinen et al. 2001, Gribonval & Lesage 2006). Here, we use Non-Negative matrix factorization Lee & Seung (1999) that is

applicable because A and S are positive. The objective is to find estimates of A and S, respectively W and H so that

$$X \approx WH. \tag{2.3}$$

This is done by adapting the non-negative matrices W and H so as to minimise the divergence $\delta(X|WH)$, defined as

$$\delta(X|WH) = \sum_{ij}(X^{ij} \log \frac{X^{ij}}{(WH)^{ij}} \tag{2.4}$$

$$-X^{ij} + (WH)^{ij}), \tag{2.5}$$

where the exponents i and j respectively refer to the row and column indexes of the matrices. The algorithm used to achieve the minimization of the divergence is based on the iterative update rule

$$H_{a\mu} \leftarrow H_{a\mu} \frac{\sum_i W_{ia} X_{i\mu}/(WH)_{i\mu}}{\sum_k W_{ka}},$$
$$W_{ia} \leftarrow W_{ia} \frac{\sum_\mu H_{a\mu} X_{i\mu}/(WH)_{i\mu}}{\sum_\nu H_{a\nu}}. \tag{2.6}$$

Divergence is non increasing under their respective update rules, so that starting from random W and H matrices, the algorithm will converge towards a minimum for δ. This provides the matrix H containing the r estimated *source* spectra h_i (in the following we refer to these as simply "*source* spectra"). The convergence criterion that we have used here measures the evolution of the divergence as a function of the iteration step. We have assumed that convergence is reached when

$$1 - \frac{\delta^{i+1}}{\delta^i} < \kappa, \tag{2.7}$$

where κ is small, typically 0.0001.

2.3 K-means

K-means is a standard unsupervised classification method wich aims to partition a set of vectors into k sets $\sigma = \{\sigma_1, \sigma_2, \sigma_3 \ldots \sigma_k\}$ so that within each set, a distance is minimized. In our case, this distance is 1 minus the correlation coefficient. Formally this reads:

$$argmin \sum_{i=1,k} \sum_{h_j \in \sigma_i} 1 - corr(h_j, \mu_i), \tag{2.8}$$

where *corr* stands for correlation coefficient and μ_i is the mean spectrum in cluster σ_i. Said in a simple way, *K-means* as defined here forms clusters that maximize the correlation between vectors within each cluster. The algorithm used to perform *K-means* is the one provided in Matlab.

3 Architecture of the method

This section describes how we use NMF and *K-means* as well as a Monte-Carlo (MC) analysis to build our method. The three distinct steps of this method are:

- identification of the number of *source* spectra based on the difference between the estimated power of noise and reconstruction residuals
- estimation of the *source* spectra using NMF and errors using MC analysis,
- reconstruction of the weight maps using non-negative least squares.

These steps are described in the following sections.

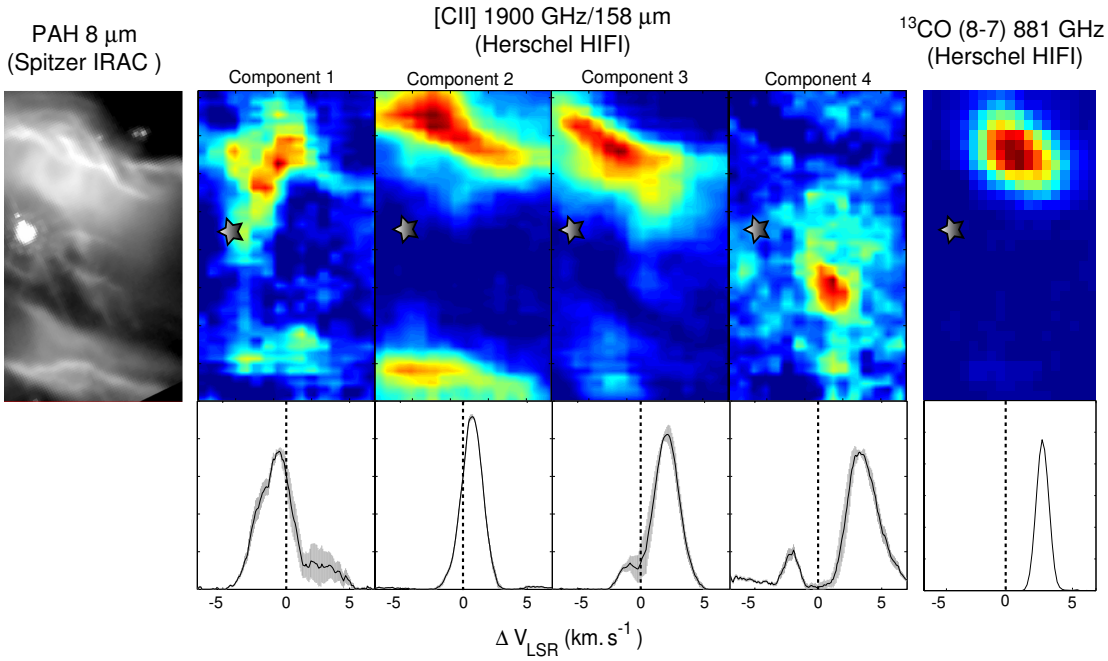

Fig. 1. Illustration of the results of our method on the *Herschel*-HIFI data of the NGC 7023 nebula. On the left, the *Spitzer*-IRAC images shows the structure of the nebula at mid-infrared wavelengths (polycyclic aromatic hydrocarbon emission). The right part of the figure shows the weight maps (upper panel) and spectral components (lower panel) extracted using the NMF-based method described in this paper. Color-scale and intensities in the spectra are in arbitrary units (due to the scale uncertainty inherent to blind signal separation methods such as NMF). The error intervals ($\epsilon(v)$) as estimated by the method for each *source* spectrum is shown with the gray envelope (which is very small in the case of the ^{13}CO line). The dashed line indicates $\Delta\ V_{LSR} = 0$.

3.1 Identification of the number of source spectra

The identification of the number of sources in our method relies on the estimation of the norm of the noise matrix N in the data. In real observations N is unknown. However, it is often possible to get an accurate estimation of the power of the noise in the data (this will be described in a subsequent paper, Berné et al. in prep.). Let us consider ν_{rms}, which is an estimation of the Frobenius norm of N:

$$\nu_{rms} \sim \|N\|_F. \tag{3.1}$$

In order to identify the number of *source* spectra, NMF as described above is applied on C starting with the minimum number of *source* spectra $r = 2$. Once NMF has converged, the matrix of approximated observations $\hat{X}$ is obtained by:

$$\hat{X} = WH. \tag{3.2}$$

The norm of residuals (i.e. the difference between original and reconstructed observations) is calculated by:

$$\Psi = \|\hat{X} - X\|_F. \tag{3.3}$$

If

$$\Psi - \hat{\nu}_{rms} \leq 0, \tag{3.4}$$

then the number of sources is $r = 2$. If the above inequality is not verified then the algorithm retries for $r = r+1$ and such until Eq. (3.4) is verified. Note that we do not bring the theoretical proof that Ψ is decreasing when r increases, however, empirical tests on several data-sets (including the one presented in this paper in Sect. 4) show that this is the case.

3.2 Monte-Carlo estimation of the *source* spectra and empirical standard deviation

Once the number of sources r has been identified we can run NMF with this value of r fixed, for p trials, with different initial random matrices for each trial. p is typically 100. For each value trail a set of r source spectra are identified. The total number of obtained spectra at the end of this process is hence $p \times r$. The algorithm uses $K-means$ to form r sets $\{\sigma_1, \sigma_2, \ldots \sigma_r\}$ each set containing $k_1, k_2, \ldots, k_r$ spectra. Each final *source* spectrum is obtained by averaging the k_n spectra in each set σ_n. The rows of a new matrix called H_* contain these r averaged vectors. The standard deviation at each wavelength v for a given *source* spectrum is obtained by

$$\epsilon_n(v) = \sqrt{\frac{1}{k_n - 1} \sum_{i=1}^{k_n} (h_i(v) - \bar{h}(v))^2}, \tag{3.5}$$

where $h_i(v)$ is the value of the source spectrum in a set at a given wavelength. $\bar{h}$ denotes the average of $h_i(v)$ in the cluster. ϵ is therefore the empirical sample standard deviation of the value of a point in a *source* spectrum within its cluster.

3.3 Reconstruction of the weight maps

The matrix of weights W_* is reconstructed by minimizing

$$\|X - W_* H_*\|. \tag{3.6}$$

This is done by using the classical non-negative least square algorithm. In the present case we have used the version of this algorithm provided in Matlab.

4 Application to Herschel observations

4.1 Data

The *Herschel* space telescope is an infrared observatory combining a 3.5 meter telescope and 3 instruments. Here we have used data from the Heterodyne Instrument for Far Infrared (HIFI) which allows spectral mapping at high spectral resolution ($v/\Delta v \sim 10^6$) and high angular resolution ($\sim 10 - 40''$) between 480-1250 GHz, and 1410-1910 GHz, as part of the open time program "Physics of gas evaporation at PDR edges" (PI C. Joblin). We have observed the NGC 7023 nebula (Fuente et al. 1996), where a massive star has blown a cavity inside the cloud where it formed. It is illuminated by the young Be star HD200775. With HIFI we have observed the fine structure line emitted by the atomic carbon ion (C^+) at 1900 GHz as well as the pure rotational line of carbon monoxide isotope ^{13}CO(8-7) at 881 GHz in spectral mapping. The resulting data consisting in a 3D matrix of 30×52 spatial positions and 201 spectral points for C^+ and 18×30 spatial positions and 143 spectral points for the ^{13}CO(8-7) spectral map.

4.2 Applying the method to our data

The spectra in this dataset are positive and we assume that non-linear radiative transfer (e.g. re-absorption) effects are not predominant which for the C^+ and ^{13}CO(8-7) line in such physical environment is acceptable. Therefore, the proposed method is applicable. We have applied the method described in Sections 2 and 3 to the dataset presented above. The whole method, implemented under Matlab runs typically in a few minutes when applied to these data. The resulting spectra and weight maps are shown in Fig. 1.

4.3 Preliminary results for C^+

Four spectra (and weight maps) are identified by the method. Each spatial and spectral component shows distinct features. For clarity, the components can be ordered from 1 to 4 based on their kinematic properties in the following way (Fig. 1):

- Component 1: lowest peak velocity (about -0.8 km s^{-1} relative to LSR)
- Component 2: mid peak velocity (about +0.8 km s^{-1} relative to LSR)
- Component 3: high peak velocity (about + 2 km s^{-1} relative to LSR)
- Component 4: double peaked, very high (+3 km s^{-1}) and very low (-2 km s^{-1}) velocity relative to LSR

4.4 Preliminary results for ^{13}CO(8-7)

For the ^{13}CO(8-7) line we are only able to find two components, one being a complete noise map, so in reality it appears as a *unique* ^{13}CO(8-7) component. This component is shown in Fig. 1.

4.5 Discussion and conclusions

A preliminary interpretation of these results can be formulated. It seems that we are observing the expansion of a roughly symmetric cavity, roughly centered at the peak position in the map of component 4. At this position, we are therefore seeing gas coming towards us and moving away from us at high velocities. The expansion velocity can be derived from this component by taking half of the velocity difference between the two peaks in the spectrum of component 4, that is about 2.5 km s^{-1}. The other 3 components seem to correspond to the other concentric shells which are expanding at the same velocity, but because of the projection effects their resulting absolute velocities as observed with *Herschel* are smaller than the expansion velocity of 2.5 km s^{-1}. The radius of the shell can be estimated using the map of component 2 and taking the distance between the emission peak in the North and the emission peak in the South. This represents an angular size of 60", that is $R = 3.5\ 10^{15}$m in physical scale using a measured distance of 430 parsec. Using this radius and the expansion velocity we can derive the age of the nebula to be 4.5×10^5 years. We also note that the center of the expanding shell does not correspond to the position of the star. This is expected since this star is known to have a large proper motion, meaning that it must have moved significantly over the expansion timescale.The exact origin of this expanding shell needs to be investigated in detail, but it is clear that its expansion is driven by the massive star that has formed within the molecular cloud (Fuente et al. 1996). Several scenarios are envisaged: winds and outflow from the star, thermal expansion under irradiation, rocket acceleration of the surrounding cloud due to photo-evaporation etc. Finally, the fact that the CO component, which traces denser regions, appear as a unique component, is compatible with the idea that the warmer gas, traced by the C^+, is subject to much more dynamical structure because of evaporation. It could also be that there is only one CO component because it traces the edge-on shell which has a higher density than the rest of the expanding shell, that can be seen in C^+. Further interpretation and modeling is required to take the best advantage of the results obtained here, however, astronomical observations in the far infrared at both high angular and high spectral resolutions, can be interpreted in terms of a linear combination of few components extracted using an NMF based method.

References

Berné, O., Joblin, C., Deville, Y., et al. 2007, A&A, 469, 575

Brunt, C. M. & Heyer, M. H. 2002, ApJ, 566, 276

Brunt, C. M., Heyer, M. H., & Mac Low, M.-M. 2009, A&A, 504, 883

Cardoso, J.-F. 1998, Proceedings of the IEEE, 86, 2009

Donoho, D. & Stodden, V. 2003, in (MIT Press), 2004

Fuente, A., Martin-Pintado, J., Neri, R., Rogers, C., & Moriarty-Schieven, G. 1996, A&A, 310, 286

Gribonval, R. & Lesage, S. 2006, in ESANN'06 proceedings - 14th European Symposium on Artificial Neural Networks (Bruges, Belgique: d-side publi.), 323–330

Habart, E., Dartois, E., Abergel, A., et al. 2010, A&A, 518, L116

Hyvärinen, A., Karhunen, J., & Oja, E. 2001, Independent component analysis, Vol. 26 (Wiley-interscience)

Joblin, C., Pilleri, P., Montillaud, J., et al. 2010, A&A, 521, L25

Juvela, M., Lehtinen, K., & Paatero, P. 1996, MNRAS, 280, 616

Lee, D. D. & Seung, H. S. 1999, Nature, 401, 788

Paatero, P. 1994, Environmetrics, 5, 11

Pilleri, P., Fuente, A., Cernicharo, J., et al. 2012, A&A, 544, A110

Ungerechts, H., Bergin, E. A., Goldsmith, P. F., et al. 1997, ApJ, 482, 245

van Dishoeck, E. F., Kristensen, L. E., Benz, A. O., et al. 2011, PASP, 123, 138

van Kempen, T. A., Kristensen, L. E., Herczeg, G. J., et al. 2010, A&A, 518, L121

SF2A 2012
S. Boissier, P. de Laverny, N. Nardetto, R. Samadi, D. Valls-Gabaud and H. Wozniak (eds)

PYOPERATORS: OPERATORS AND SOLVERS FOR HIGH-PERFORMANCE COMPUTING

P. Chanial[1] and N. Barbey[1]

Abstract.
PyOperators is a publicly available library that provides basic operators and solvers for small-to-very large inverse problems (`http://pchanial.github.com/pyoperators`). It forms the backbone of the package PySimulators, which implements specific operators to construct an instrument model and means to conveniently represent a map, a timeline or a time-dependent observation (`http://pchanial.github.com/pysimulators`). Both are part of the Tamasis (Tools for Advanced Map-making, Analysis and SImulations of Submillimeter surveys) toolbox, aiming at providing versatile, reliable, easy-to-use, and optimal map-making tools for Herschel and future generation of sub-mm instruments. The project is a collaboration between 4 institutes (ESO Garching, IAS Orsay, CEA Saclay, Univ. Leiden).

Keywords: Methods: numerical, Techniques: image processing

1 Introduction

The PyOperators and PySimulators packages provide linear and non-linear operators that can be thought as the building blocks of an instrument model H used to simulate data acquisition, and a variety of solvers to estimate the signal $\mathbf{x}$ given an observation $\mathbf{y}$ through this instrument, i.e. to solve the equation

$$\mathbf{y} = H\mathbf{x} + \mathbf{n}, \tag{1.1}$$

where $\mathbf{n}$ is the noise of covariance matrix N.

These operators can easy be combined to form block diagonal, block column and block row operators (section §3). The chaining of the operations relies on a memory manager (section §4) and has been optimised to minimise the number of memory allocations and the memory footprint, and to maximise the cache locality by relying on operator's properties such as whether or not it can perform in-place operations on its input or on its output (section §5). Solvers will be presented in section §6. The code is massively parallel and hybrid (MPI + OpenMP) (section §7). It is written in Fortran and C (for the number crunching) and Python (for the abstraction and interactivity). The Python overhead has been reduced to a mostly negligeable fraction.

2 Operators

The Operator class is a factory of multi-dimensional functions that, if linear, behave like matrices with a sparse storage footprint. Operator instances can be transposed, added, multiplied and composed in a natural way so that they can be used as the subsystems of a complex instrument acquisition model. Rules can be attached to operators through properties (such as symmetric, hermitian, involutary, orthogonal...) or through a flexible mechanism, to trigger algebraic simplifications, for additional speedups. For example, let us assume that H in Eq. 1.1 is a convolution and that the noise follows a uniform gaussian distribution $\mathbf{n} \sim \mathcal{N}(0, \sigma)$. The expression $H^{\mathrm{T}} N^{-1} H$, which is involved in the normal equation, is automatically reduced to a single convolution operator, whose Fourier-transformed kernel is the module of the initial Fourier-transformed kernel scaled by $1/\sigma^2$.

[1] Laboratoire AIM-Paris-Saclay, CEA/DSM/Irfu, CNRS, Université Paris Diderot, Saclay, 91191, Gif-sur-Yvette, France

- AdditionOperator, MultiplicationOperator, CompositionOperator
- BlockRowOperator, BlockColumnOperator, BlockDiagonalOperator
- BlockSliceOperator
- SumOperator, ProductOperator, MinOperator, MaxOperator (for reductions)
- FftOperator, ConvolutionOperator, ConvolutionTruncatedExponentialOperator
- WaveletOperator
- MPIDistributionIdentityOperator, MPIDistributionLocalOperator, MPIScatterOperator
- IdentityOperator, ZeroOperator, HomothetyOperator, ConstantOperator
- DiagonalOperator, MaskOperator
- TridiagonalOperator, BandOperator, SymmetricBandOperator
- EigendecompositionOperator (Lanczos algorithm)
- PackOperator, UnpackOperator
- RollOperator, ShiftOperator
- DiscreteDifferenceOperator
- IntegrationTrapezeWeightOperator
- NumexprOperator, DiagonalNumexprOperator, DiagonalNumexprNonSeparableOperator
- RoundOperator (6 methods)
- ClipOperator, MaximumOperator, MinimumOperator
- HardThresholdingOperator, SoftThresholdingOperator

Table 1. List of operators available in PyOperators 0.7. More operators related to data acquisition can be found in the package PySimulators.

3 Block operators

Operators can be combined to form block row, column and diagonal operators. By writing H from Eq. 1.1 as a block column matrix and N^{-1} as a block diagonal matrix:

$$H = \begin{pmatrix} H_1 \\ \vdots \\ H_n \end{pmatrix} \quad \text{and} \quad N^{-1} = \bigoplus_{i=1}^{n} N_i^{-1},$$

the product of Operators $H^{\mathrm{T}} N^{-1} H$ is automatically simplified to the expression

$$\sum_{i=1}^{n} H_i^{\mathrm{T}} N_i^{-1} H_i, \tag{3.1}$$

which handles arrays of much lesser size, better suited to take advantage of the memory cache. Currently, two schemes are supported: partitioning by stacking along a new array dimension or by chunk along an existing one.

4 Memory manager

High-level languages such as Python come with a garbage collector which operates behind the scenes with the consequence that in some cases (objects with cycling references, holding a reference to an array), temporaries may reside in memory for a period of time longer than necessary. Equally important, the sequence of freeing a buffer and soon after reallocating another one of the same size does not imply that the same memory will be used and it will result in cache line flushes. So, when manipulating very large arrays, one should be sparing about temporaries allocation, even more for supercomputers with relatively limited memory per node. This is the reason why the pyoperators package uses a lightweight memory manager designed to maximise the cache locality by reusing the memory buffers. This memory manager can serve buffers to the operators according to their specific requirements, such as contiguity or alignment (crucial for the FFTW library and other libraries that leverage on the SSE and AVX instruction sets). By relying on this memory manager, we ensure that the amount of memory used in iterative algorithms does not vary from one iteration to the next one.

5 Chaining of operations

5.1 Inplace operations

The *inplace* flag indicates that an operator can handle input and output pointing to the same memory location. This property is useful to avoid temporaries. In order to minimise the memory-cache transfers during a composition, an algorithm has been put in place to determine the intermediate variables to be extracted from the memory manager. This algorithm depends on:

- the parity of the number of out-of-place operators
- whether or not the input and the output of the composition point the same memory location (in-place or out-of-place composition)
- the size of the output, and if it is large enough to be reused in the intermediate computations.

As an example, let's consider the composition of an in-place operator `IN` by an out-of-place operator `OUT`. The out-of-place composition `(IN * OUT)(x, out=y)` requires an intermediate variable only if the size of `OUT`'s output is larger than that of variable `y`. Otherwise, `y`'s buffer is used as output for the `OUT` operator and the application of the operator `IN` is performed in-place on `y`. Concerning the in-place composition `(IN * OUT)(x, out=x)`, it is not possible to avoid the use of a temporary variable, since a buffer different from the `x` variable is required for the `OUT` operator. The application of the operator `IN` is performed out-of-place because its output has to be the `x` variable.

5.2 Inplace reductions

An operator that can do in-place reductions is an operator that can add, element-wise multiply (or else) its output to its output argument. This property can be used to further remove the need of intermediate variables. First, let's compute `(o1 + o2)(x, out=y)` assuming that the operator `o2` cannot do in-place reductions:

- the variable `y` is used as `o1`'s output,
- a temporary variable is retrieved from the memory manager and is used as `o2`'s output,
- that is then added to the `y` variable.

If we now assume that `o2` can do in-place reductions, the intermediate variable is not required anymore:

- the variable `y` is used as `o1`'s output
- `o2` updates `y` in-place.

The possibility of updating directly an operator's output also leads to a better use of the memory cache, since the temporary could otherwise flush it. Such operators are common in map-making applications where H_i^{T} from Eq. 3.1 are backprojections.

- Conjugate Gradient
- Preconditioned conjugate gradient
- Non-linear preconditioned conjugate gradient
- Variational bayesian double loop inference algorithm (Seeger et al. 2010)
- FISTA proximal gradient algorithm (Beck & Teboulle 2009)

Table 2. List of solvers available in PyOperators 0.7. Solvers from scipy.optimize and scipy.sparse.linalg can also seamlessly be used with Operators.

6 Solvers

PyOperators features solvers that can handle MPI-distributed unknowns (Table 2). These solvers are written using the flexible IterativeAlgorithm class, which in addition to managing buffer handling from one iteration to another, can be interrupted and restarted or continued in a clean state.

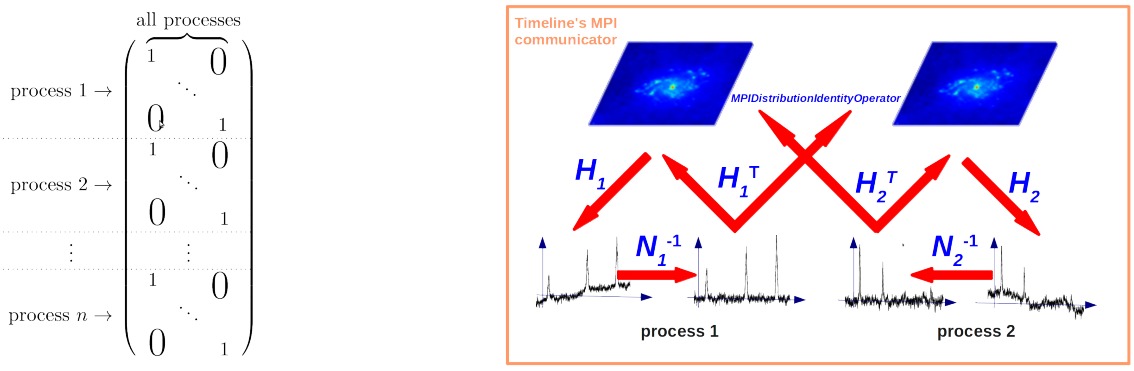

Fig. 1. Non-distributed unknown, distributed data. **Left:** Matrix representation of the operator D as MPIDistribution-IdentityOperator. **Right:** Map-making example showing the computation of $D^{\mathrm{T}}H^{\mathrm{T}}N^{-1}HD$ by two MPI processes.

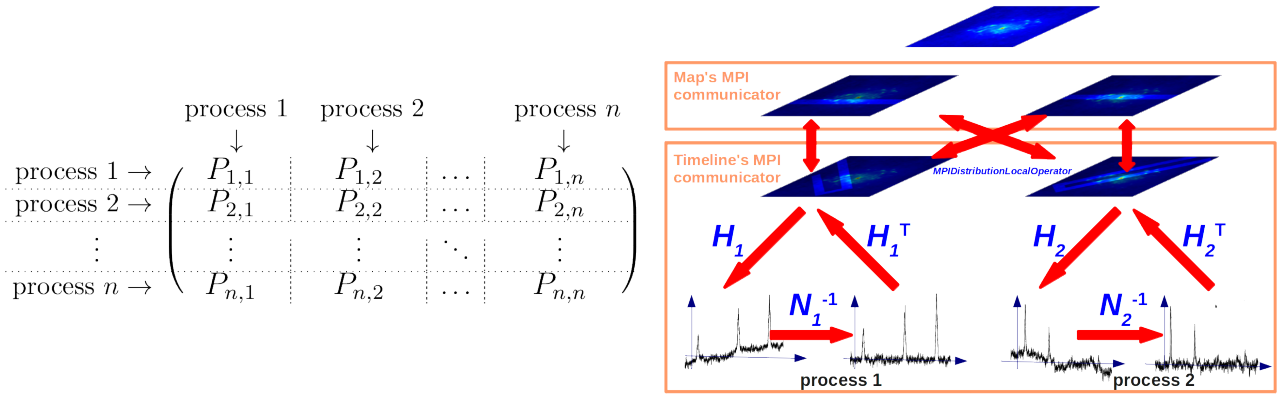

Fig. 2. Distributed unknown, distributed data. **Left:** Matrix representation of the operator D as MPIDistribution-LocalOperator. **Right:** Map-making example showing the computation of $D^{\mathrm{T}}H^{\mathrm{T}}N^{-1}HD$ by two MPI processes.

7 Parallelism

This package aims at being run on a single multicore CPU interactively (shared memory) and on clusters of CPUs (distributed memory). The first use relies on OpenMP's parallelism and the second one on MPI's. Calls

to MPI routines have been encapsulated into specific operators, so that in a distributed environment, Eq.1.1 becomes:

$$\mathbf{y} = HD\mathbf{x} + \mathbf{n} \tag{7.1}$$

where $H = H_1 \oplus H_2 \oplus \ldots \oplus H_n$ is a block diagonal operator whose blocks are handled by n MPI processes, D is the MPI distribution model, y is the distributed data and x the unknown, which can be distributed or not. Note that in a non-distributed environment, D is the identity matrix, so switching from a non-distributed environment where most of the development takes place to a distributed one where actual computations are performed is straightforward.

7.1 Non-distributed unknown, distributed data

In this scheme, the unknown is global and replicated over the nodes. In Eq. 7.1, D is an MPIDistributionIdentityOperator: a block column operator whose blocks are the identity and for which each block output is handled by an MPI process. The actual MPI all-reduction is performed by D^{T}, a block row operator whose blocks are the identity, showing up in the normal equation $D^{\mathrm{T}}H^{\mathrm{T}}N^{-1}HDx = D^{\mathrm{T}}H^{\mathrm{T}}N^{-1}y$. Fig. 1 shows D as a matrix (left) and synthesizes how the computation of $D^{\mathrm{T}}H^{\mathrm{T}}N^{-1}HD$ is performed by two MPI processes (right). Since x is the same across all the processes, the solver doesn't need any MPI communication to compute the next iteration, so that all scipy's solvers can be readily used.

7.2 Distributed unknown, distributed data

The operator MPIDistributionLocalOperator handles an input partitioned into sections across the nodes and returns to each node the packed values of the global input according to the node's global mask. The matrix representation of such operator is shown in Fig. 2 (left). The block $P_{i,j}$ is a coordinate-selection matrix, which projects the input section handled by process j onto the process i according to i's mask. When the unknown is distributed, some amount of communication is required by the solver, generally when computing dot products, and scipy solvers cannot be used.

8 Conclusions

Coupled with the package PySimulators, the PyOperators package has proven to be an efficient way to construct astronomical instruments models used to simulate data acquisition, but we stress that these tools are very general and their scope goes beyond astronomical instrumentation. The details of this aspect will be treated in a subsequent paper. This package has also already been used to process amongst the largest *Herschel*/PACS observations and the results will be the subject of a third paper.

Future ideas of development include writing a PETSc interface, offloading computation to the GPU, automatic differentiation to obtain the gradient and hessian of an operator and inclusion of rules to factorise expressions. Owing to their open-source nature, the scientific community is welcome to provide a feedback and partipate in bettering these tools.

PC and NB thank the ASTRONET consortium for funding this work through the TAMASIS and CSH projects. The HPC resources were provided by GENCI-[CCRT] grant 2011-046661 and 2012-046661. M. Sauvage and F. Bournaud are thanked for their support.

References

Beck, A. & Teboulle, M. 2009, SIAM J. Imaging Sciences, Vol. 2, No. 1, p. 183

Seeger, M., Nickisch, H, Pohmann, R. et al. 2010, Magnetic Resonance in Medicine, 63, 116

SF2A 2012
S. Boissier, P. de Laverny, N. Nardetto, R. Samadi, D. Valls-Gabaud and H. Wozniak (eds)

KNOW (BETTER) YOUR NEIGHBOUR: NEW HI STRUCTURES IN MESSIER 33 UNVEILED BY A MULTIPLE PEAK ANALYSIS OF HIGH-RESOLUTION 21-CM DATA

L. Chemin[1], C. Carignan[2], T. Foster[3] and Z. S. Kam[4]

Abstract. In our quest to constrain the dynamical and structural properties of Local Group spirals from high-quality interferometric data, we have performed a neutral hydrogen survey in the direction of Messier 33. Here we present a few preliminary results from the survey and show the benefits of fitting the HI spectra by multiple peaks on constraining the structure of the Messier 33 disk. In particular we report on the discovery of new inner spiral-like and outer annular structures overlaying with the well-known main HI disk of Messier 33. Possible origins of the additional outer annular structure are presented.

Keywords: Galaxies: individual: M33, NGC 598, Galaxies: ISM, Galaxies: kinematics and dynamics, Galaxies: structure, Local Group, Techniques: imaging spectroscopy

1 Context

The dynamical and structural properties of HI disks of nearby spirals mainly result from the analysis of the 0th and 1st moments of HI spectra obtained from single-dish and interferometric observations. Curiously more thorough analyses of HI spectra making profit from current high spectroscopic precision and sensitive cm-data remain rare.

In 2006 we have started a HI survey of the most massive spiral disks from the Local Group (except the Milky Way) to revisit their structure, kinematics and dynamics. Aperture synthesis at DRAO combined with short spacing data have been used to perform 21-cm observations of the Andromeda galaxy (Messier 31) at spectral resolution $\lesssim 5$ km s^{-1}, angular resolution ~ 300 pc ($D \sim 800$ kpc) and sensitivity down to $\sim 2 \times 10^{19}$ cm^{-2} (Chemin et al. 2009).

Since many spectra are far from being dominated by one single HI component we have shown that the moment analysis of datacubes was not appropriate (see Fig. 1 and §3.2 of Chemin et al. 2009, and left panel of Fig. 1 below). This is the reason why we developed a 'search and fit' algorithm of multiple (gaussian) components. Applied to new Messier 31 data this algorithm has allowed the detection of sometimes up to five HI significant components per profile, which had never been reported beforehand for nearby HI spirals. So many multiple peaks likely result from the combination of extreme projection effects of the warped Messier 31 disk with internal and external dynamical perturbations (spiral density wave, lagging halo, expanding gas shells, accretion of gas from the intergalactic medium or from nearby minor companions, etc). The discovery of outer HI spurs and spiral arm was also reported, as well as the characterization of the disk warp in terms of twist and tilt angles and the measurement of the most extended rotation curve for Messier 31.

We note that this kind of hyperspectral decomposition within multiple gaussian peaks is not new and has been used several times (e.g. Sicotte & Carignan 1997; Oh et al. 2008). It is nonetheless not generalized in HI studies. From a dynamical point-of-view, the multiple peak analysis has led to (marginally) different rotation velocities and inclinations than those derived with another recent and high-quality HI datacube of Messier 31 from the 0th- and 1st-moment analysis (Braun et al. 2009; Corbelli et al. 2010). Again, such differences have already been reported (see e.g. Figs. 11 and 13 of Oh et al. 2008).

[1] LAB, CNRS UMR 5804, Université de Bordeaux, F-33270, Floirac, France
[2] Dept. of Astronomy, University of Cape Town, Rondebosch 7700, South Africa
[3] Dept. of Physics and Astronomy, Brandon University, Brandon, MB R7A 6A9, Canada
[4] Dépt. de physique, Université de Montréal, Montréal, QC H3C 3J7, Canada

2 Yet another new HI survey of Messier 33

In pursuit of our project we present here very preliminary results for Messier 33, a late-type spiral whose HI disk is known to be warped (Corbelli & Schneider 1997). The 21-cm interferometric data were still obtained at DRAO (combined with the Arecibo data of Putman et al. 2009) but at a larger spectral resolution (3.3 km s^{-1}) than for Messier 31 observations. Of course it is very likely to detect multiple components with highly resolved spectra. However this does not guarantee the success of detecting *realistic* ones because noise becomes important at high resolution. Furthermore the number of components that can be fitted per spectra depends on the resolution. With more and more peaks found in an individual spectrum (as for Messier 31), it becomes less and less straightforward to interpret the data and identify for instance the component that is the most representative of the disk circular rotation to those that are caused by all abovementioned perturbing effects. The HI datacube of Messier 33 has thus been filtered to lower resolution to simplify the hyperspectral decomposition.

3 Preliminary results: evidence for new HI structures in Messier 33

Other recent HI surveys of Messier 33 have been performed at VLA and Arecibo (Thilker et al. 2002; Putman et al. 2009). The VLA data of Thilker et al. (2002) have allowed to determine for the first time the inner structure of the HI disk with unprecedented details (resolution of 20 pc). The Arecibo data of Putman et al. (2009) were more appropriate to study the nearby environment of Messier 33 at a resolution of about 1 kpc. In particular they have shown the HI disk of Messier 33 is surrounded by arc-like structures and clumps. A hint of such perturbations had been presented in another (earlier) Arecibo view of Messier 33 (Corbelli, Schneider, & Salpeter 1989). Our DRAO survey has thus an intermediate angular resolution to them.

Working with a datacube of effective spectral resolution of 10 km s^{-1} our 'search and fit' algorithm of multiple peaks identifies sometimes up to 3 significant HI components in the datacube. An example of two distinct components is shown in Fig 1 (left-hand panel). Here the components are separated by $\sim$ 45 km s^{-1}. The total integrated HI emission of Messier 33 is shown Fig 1 (central panel). The external arc-lile structure and the SW clump are clearly detected, even within our $\sim$ 300pc-resolution data, as well as the 'main' inner disk. Multiple components are not observed over the whole field-of-view, as seen in Figure 1 (right panel), but are preferentially distributed along a 'secondary' spiral-like structure in the inner disk and an annular structure in the outer regions ($r \sim 80'$ or 19 kpc). It is obvious that none of these new structures would have been identified with a moment analysis of the datacube.

A preliminary tilted-ring model has been fitted to the velocity field of the 'main' HI component shown in the left-hand panel of Fig. 2. A significant twist of the orientation of the major kinematical axis is evidenced, as well as a tilt of the HI disk (Fig. 3). This result thus confirms the warped nature of the HI disk of Messier 33. The kinematics of the external arc-like structure does not differ so much from that of the inner disk, implying that this perturbation is bound to the disk. We have not yet fitted the warp parameters for it, as shown by constant inclination and position angles at those locations ($r > 100'$, Fig. 3).

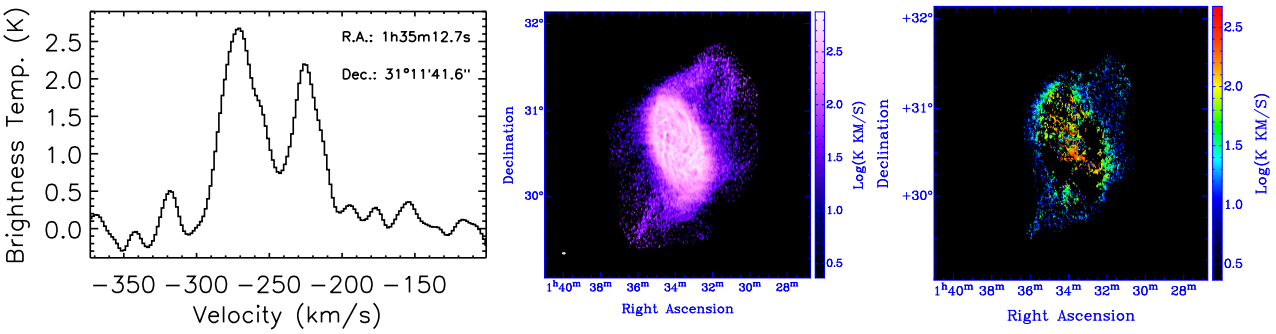

Fig. 1. Left: Illustration of a HI profile with two distinct components. **Middle**: Total integrated HI emission map of Messier 33. **Right:** HI integrated emission map of the 'secondary' fitted HI component in Messier 33. A logarithmic stretch is used for them.

The kinematics of the outer annular structure is shown in the middle panel of Fig. 2 and its residual field when subtracted from the velocity field of the 'main' HI component in the right-hand panel of Fig. 2. Differences

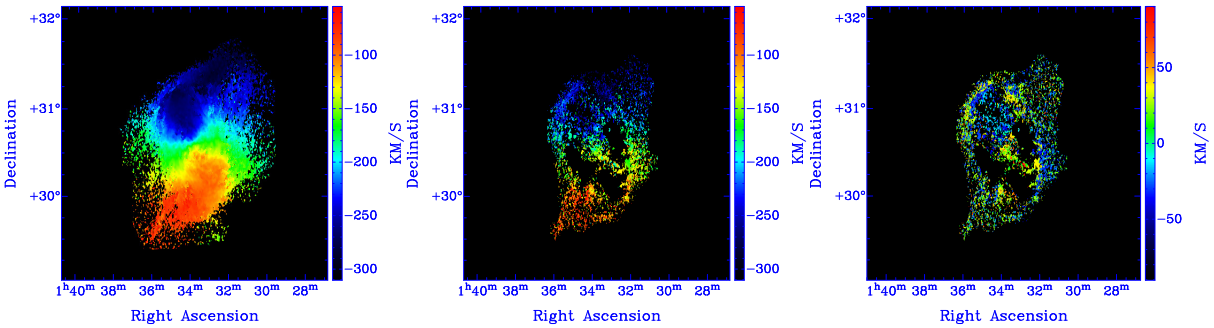

Fig. 2. Left: Velocity fields of the 'main' HI component of Messier 33. **Middle**: The secondary component. **Right:** The residual field from their mutual subtraction.

of radial velocities sometimes reach 40-50 km s^{-1} in absolute values. At this stage of our analysis it is too early to firmly identify which of the multiple components is the real tracer of the 'main' disk kinematics to that of the inner 'secondary' spiral-like structure on one hand, and to that of the outer HI annulus on another hand. Indeed the disk kinematics is strongly perturbed in those regions (warp, connection with the external arc-like structure, etc). It is also too early to constrain the exact origins of the inner 'secondary' spiral-like pattern and the outer annular structure. We retain the following hypotheses for this later:

- The annular structure has external origins to Messier 33. Gas accretion on the outer disk parts from e.g. the external arc-like strucure or the intergalactic medium could be ongoing. Messier 33 has an obvious perturbed environment, and past tidal interactions with other galaxies may not be excluded. Numerical simulations would be needed to test those assumptions.

- The annular structure is a genuine ring, with internal origins. For instance it could have been developed by gas accumulation at the outer Lindblad resonance. In this case an obvious perturbing density wave could be grand-design spiral structure of Messier 33. This hypothesis could be tested by measuring the pattern speed of the spiral density wave with a modified version of the Tremaine-Weinberg method, and by determining the locations of various Lindblad resonances.

- The annular structure is not a real ring but is only caused by a fortuitous projection effect of a peculiar warping of Messier 33 (and maybe also a disk flaring) at the periphery of the HI disk. One would need here gas orbits that have orientation angles significantly different from the constant one displayed in Fig. 3 from $r \sim 85'$ to generate a distinct structure in superimposition to the outer disk.

Noteworthy is the fact that insights for asymmetric HI profiles along a ring-like structure as caused by the warped gas orbits has been reported in Corbelli & Schneider (1997). The location of that ring-like structure found by Corbelli & Schneider (1997) corresponds with that of the external arc-like structure, but not to that of the outer HI annulus we evidence here. Furthermore the HI annulus does not share the same orientation parameters than the external arc-like structure (Fig. 1). Two different ring-like structures thus seem to coexist in the outer regions of Messier 33.

4 Conclusions

Provisional results from a new HI survey in the direction of Messier 33 performed with aperture synthesis observations at the Dominion Radio Astrophysical Observatory have been presented. Evidence for new HI structures in Messier 33 have been found from a multiple HI peak analysis of the datacube. Among them is the detection of an annular-like structure in the outer regions of the HI disk. That annulus does not correspond to the already known arc-like structure around Messier 33. Complete details of the observing campaign, the data reduction and the hyperspectral decomposition will be presented soonly (Chemin et al. 2013). Our main objectives are to revisit the structure and dynamics of Messier 33, derive an accurate and extended rotation curve for it, and model its mass distribution. With the results already obtained for the Andromeda galaxy, this new dataset should help to better constrain the evolution of massive spirals in the Local Group.

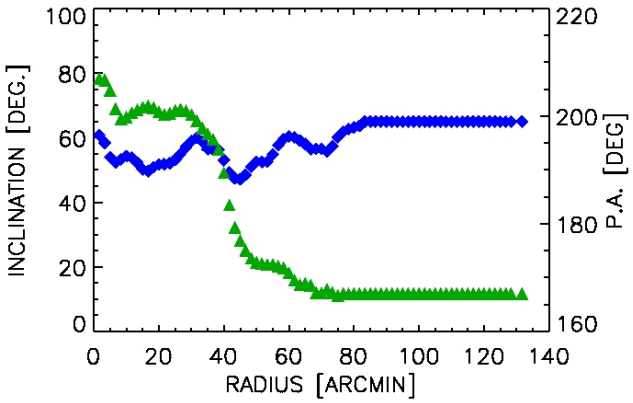

Fig. 3. Preliminary results of the tilted-ring model fitted to the 'main' HI velocity field of Messier 33 from central panel of Fig. 2. Blue squares are for the disk inclination and green triangles for the position angle of the major kinematial axis.

We are very grateful to Mary Putman and Kevin Douglas for having provided us with their single dish data.

References

Braun R., Thilker D. A., Walterbos R. A. M., & Corbelli E, ApJ, 695, 937
Chemin L., Carignan C., & Foster T., 2009, ApJ, 705, 1395
Chemin L., Carignan C., Kam Z. C., Foster T., et al., 2013, ApJ, in preparation
Corbelli E., Schneider S. E., & Salpeter E. E., 1989, AJ, 97, 390
Corbelli E., & Schneider S. E., 1997, ApJ, 479, 244
Corbelli E., Lorenzoni S., Walterbos R., Braun R., & Thilker D., 2010, A&A, 511, 89
Oh S.-H., de Blok W. J. G., Walter F., Brinks E., Kennicutt R. C. Jr., 2008, AJ, 136, 2761
Putman M. E., et al., 2009, 703, 1486
Sicotte V., & Carignan C., 1997, AJ, 113, 609
Thilker D. A., Braun R., Walterbos R. A. M., 2002, ASPC, 276, 370

SF2A 2012
S. Boissier, P. de Laverny, N. Nardetto, R. Samadi, D. Valls-Gabaud and H. Wozniak (eds)

INTEGRAL FIELD SPECTROSCOPY AND GALAXY EVOLUTION

B. Epinat [1]

Abstract. Integral field instruments have an increasing impact on our understanding of galaxy evolution mechanisms. However, these instruments are manifold and each configuration has specific capabilities adapted for different projects. This paper presents various integral field spectroscopy techniques and the main galaxy samples obtained so far, both at low and high redshift. I focus on galaxy kinematics and metallicity studies at high redshift and present their interpretations to understand the evolution of the main mass assembly processes that are merging and continuous cold gas accretion.

Keywords: 3D spectroscopy, galaxy evolution, kinematics, metallicity, high redshift, local universe

1 Introduction

Identifying the processes responsible for galaxy evolution across the cosmic time is crucial to understand the build-up of the Hubble sequence observed in the local Universe. Galaxies at $z \sim 2$ are more star forming than at $z = 0$ (e.g. Tresse et al. 2007) and they are also smaller for a given stellar mass (e.g. Dutton et al. 2011). The main processes invoked nowadays to explain galaxy evolution are mergers on the one hand (e.g. López-Sanjuan et al. 2009), and continuous cold gas accretion on the other hand (e.g. Dekel et al. 2009). In order to study the contribution of these processes along the cosmic time, integral field spectroscopy has become a widely used tool to investigate spatially resolved properties of galaxy samples both locally and at high redshift.

I present a non-exhaustive review on the achievements enabled by integral field spectroscopy on galaxy physics study. Observational constraints are put in regard to the scientific goals and emphasis on the challenges to analyse these data is given. In section 2, the uniqueness of integral field spectroscopy data is explained. Various instrumental concepts and setups that enable to study galaxy physics are also exposed. In section 3, I briefly present the main low and high redshift samples observed using integral field spectroscopy. In section 4, I focus on high redshift galaxy studies and present results obtained so far from kinematics and metallicity analysis that give some insights about galaxy evolution from $z = 3$ to $z = 1$.

2 Integral field spectroscopy techniques

Integral field spectroscopy (IFS) enables to obtain a spectrum for each spatial element of a scientific scene. Concerning galaxy physics analysis, IFS enables to avoid any assumption on the projection parameters: all directions are studied with no preference. For the kinematics, this enables to study non circular motions (e.g. Krajnović et al. 2006). It also allows to detect off axis regions in local galaxy but also companions (e.g. Epinat et al. 2012). At higher redshift, IFS will enable to detect objects with no a priori selection (e.g. MUSE).

The data processing to reconstruct the 3 dimensional information depends on the instrumental concepts. The two main kinds of concepts (in visible and near infra-red wavelengths) are the following:

- Spectral scanning instruments: this is the case of Fabry-Perot instruments (inclusing tunable filters) and Fourier transform spectrographs. Only the spectral information has to be reconstructed. The acquisition is sensitive to sky transparency variations since there is one exposure per spectral element/interferogram.

[1] Laboratoire d'Astrophysique de Marseille, Université d'Aix-Marseille & CNRS, UMR7326, 38 rue F. Joliot-Curie, F-13388 Marseille Cedex 13, France

- Image splitters: this kind of instruments uses optical slicers or microlens arrays to split the field. The field is rearranged using optics or optical fibres and the spectrum is obtain with a grating or a prism that disperse the light. The spatial information has to be reconstructed for these instruments. There can be contaminations from spectrum on a completely different position in the field. Slicers are more subject to these effects than microlens arrays, in particular at the edges of the slices. In addition, slicers are sensitive to the slit effect: the position of the object in the slit modifies slightly the position of the spectrum.

For a constant number of pixels, one has to choose a compromise between the field of view (linked to the spatial sampling) and the spectral range (linked to the spectral sampling). By construction, scanning instruments naturally have large field of view and the number of spectral elements is low whereas spatial splitters have naturally a large number of spectral elements (usually one dimension of the detector) and a smaller field of view. Such configurations have different applications for the study of galaxy physics.

3 Galaxy samples with integral field spectroscopy data

3.1 Samples in the local Universe

In the local Universe, galaxies extend over several arcminutes. IFS thus enables to study the spectral properties with a good spatial resolution (better than 1 kpc up to $z = 0.1$).

SAURON (de Zeeuw et al. 2002) and ATLAS3D (Cappellari et al. 2011) are the main samples that study early type galaxies. ATLAS3D contains 260 galaxies observed with the SAURON instrument, a spatial splitter using microlenses (Bacon et al. 2001). The field of view is around 30" with a spectral resolution around 2000 and a spectral range of $\sim$ 2000Å. These samples are mainly focused on the study of stellar populations and dynamics but the ionised gas is also studied when present in early type galaxies. For these specific data, stellar population models have been developed. These models are fit to the spectrum at each spatial element. One of the main results is the discovery of two dynamical kinds of early type galaxies, fast rotators and slow rotators (Emsellem et al. 2011).

Large samples of late-type galaxies have been built using Fabry-Perot instruments. The main ones are SINGS (Dicaire et al. 2008) and GHASP (Epinat et al. 2008). These observations are focused on gaz dynamics through the study of the Hα line, thus the spectral range is narrow (around 10 Å) but the spectral resolution is large (around 10000) and the field of view is large ($\sim$ 5'$-$10').

3.2 Samples at high redshift

From $z = 0.5$ to $z = 5$, the physical scale only varies between 6 kpc/arcsec and 8.5 kpc/arcsec. Consequently, the spatial resolution is rather low compared to local universe galaxies but galaxies fit in a much smaller field of view of several arcseconds (Fig.1). Adaptive optics enable to reach a much better resolution. However, it requires long integration times, even on 10-m class, telescope due to smaller pixels which reduces severely the sensitivity for extended regions. In addition, high redshift observations are limited to the brightest objects due to the surface brightness dimming that affects extended objects. This induces a decrease of the surface brightness proportional to $(1+z)^4$. Current IFS are not able to observe large sample of galaxies to study stellar populations at high redshift.

On the other side, it is possible to study emission lines, like [OII] in the visible or Hα and [OIII] redshifted in the near infra-red. The main samples are IMAGES ($0.4 < z < 0.8$, Yang et al. 2008), observed using GIRAFFE/VLT (multi integral field units instrument in the optical using microlenses and optical fibers), MASSIV ($0.9 < z < 1.8$, Contini et al. 2012), SINS ($1.3 < z < 2.7$, Förster Schreiber et al. 2009) and LSD/AMAZE ($2.5 < z < 4$, Gnerucci et al. 2010), the three latter observed using SINFONI/VLT (an infrared IFS using an image slicer). A sample has also been built using OSIRIS on the Keck with adaptive optics ($1.5 < z < 2.5$, Law et al. 2009; Wright et al. 2009). The typical spectral resolution of infra-red observations (SINFONI and OSIRIS) is around 2000 while the field of view is limited to around 10" with a typical resolution of 0.6" (seeing-limited observations).

These samples study the Universe across the peak of cosmic star formation activity, period when happens the morphological transition between a variety of complex systems and the well ordered Hubble sequence. However, comparing these samples is not straightforward because they result from various selection functions. Therefore, they are not exactly representative of the underlying populations in each redshift range in the same way. In particular, median SFR decreases from 72M$\odot$, 31M$\odot$ to 7M$\odot$ for SINS, MASSIV and IMAGES.

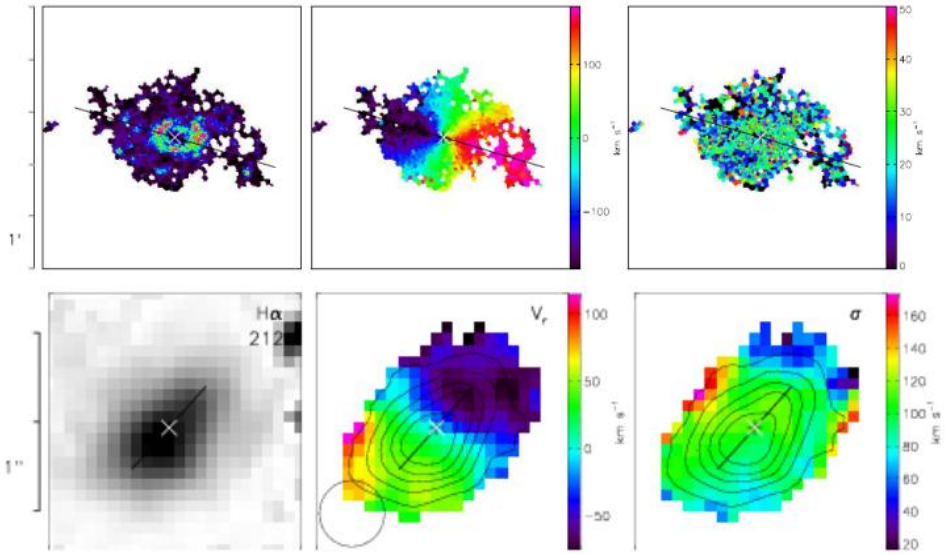

Fig. 1. Example of the comparison between local and high redshift kinematics maps deduced from IFS. Top line: UGC07901 (GHASP sample at $z \sim 0$). Bottom line: VVDS220014252 (MASSIV sample at $z \sim 1.31$). From left to right: Hα line flux map, velocity field and velocity dispersion map. The scale is indicated on the left.

4 Spatially resolved physical properties of high redshift galaxies and galaxy evolution

4.1 Kinematics

High redshift galaxy kinematics are often studied through emission line moment maps (flux, position and width) due to insufficient sensitivity to study stellar kinematics using continuum. Since the typical size of the objects is of the same order than that of spatial PSF, it is necessary to use models that take the spatial resolution into account to recover the true kinematic parameters, such as the rotation velocity and the velocity dispersion. If beam smearing is not considered, the maximum rotation velocity is underestimated and the velocity dispersion is overestimated (peak in the centre due to beam smearing). Epinat et al. (2010) has shown that such models statistically enable to recover these parameters for rotating disk galaxies: they have tested the method on 150 well studied galaxies of the local GHASP sample projected at a similar spatial resolution than SINFONI data of $z \sim 1.5$ galaxies. This method uses a disk thin rotating model convolved by the PSF. Deconvolution methods are still not fully implemented for this specific purpose but are in preparation Dahlia framework[i] for MUSE/VLT.

Kinematics have been used to make classifications of the various samples presented in section 3.2 (Yang et al. 2008; Epinat et al. 2012; Förster Schreiber et al. 2009; Gnerucci et al. 2010). Classes are slightly different among the studies but they roughly distinguish between rotators and galaxies with peculiar kinematics. In some cases, the close environment is probed, giving external indication on interactions. One result is that a large percentage of galaxies among these samples displays peculiar motions away from pure rotation. Signs of interactions are also observed in around 1/3 of each samples. The main sign of evolution is probably the observed decrease of the gaseous velocity dispersion between $\sim$ 80 km/s and $\sim$ 20 km/s from high to low redshift. This may be linked to cold gas accretion mechanism (e.g. Bournaud & Elmegreen 2009) being more efficient at high redshift. An other explanation is that this velocity dispersion is somehow linked to the star-formation regime of the samples (Lehnert et al. 2009; Le Tiran et al. 2011). This has been further supported by IFS observations of galaxies with very high star formation rates ($\sim 20 M\odot$) in the nearby Universe (Green et al. 2010; Gonçalves et al. 2010). Indeed, these local analogues also have large velocity dispersion on average. However, one issue of these studies is the lower spectral resolution ($R < 3000$) of all these observations with respect to reference studies such as GHASP ($R \sim 10000$). The impact of spectral resolution associated to low signal to noise ratio and spatial resolution on the determination of the velocity dispersion has not been studied in detail yet.

[i] https://dahlia.oca.eu/foswiki

4.2 Metallicity

It is possible to estimate metallicity from IFS data using line ratios such as $[NII]/H\alpha$ (e.g. Queyrel et al. 2012) or $[OIII]/[OII]$, $[OIII]/H\beta$ and $[NeIII]/[OII]$ (e.g. Cresci et al. 2010). Using the spatially resolved data of SINFONI, Queyrel et al. (2012) determined metallicity gradients in 29 galaxies of the MASSIV sample at $z \sim 1.3$. They found seven unambiguous positive metallicity gradients, five of them being in interaction. Therefore, they interpreted their positive gradients as the signature of fresh gas being accreted in the centre do to tidal tails, which would dilute the inner metallicity. Positive gradients of the gaseous phase have not been observed yet in the local Universe. However, e.g. Rupke et al. (2010) have shown that strongly interacting galaxies have on average flatter gradients in their gaseous phase than isolated galaxies in the local Universe, which supports the interpretation provided by Queyrel et al. (2012). At higher redshift ($z \sim 3$), Cresci et al. (2010) also observed positive metallicity gradients in three rotating galaxies of the LSD/AMAZE sample, also from SINFONI data. According to them, the fact that these galaxies do not show evidence for interaction favours a scenario in which cold flows along cosmic filaments toward the centre are diluting the inner metallicity.

These different scenarios have to be confirmed both by more observations but also from numerical simulations including metallicity evolution for interacting galaxies and cosmological inflows.

5 Instrumental perspectives

Nowadays, almost each telescope has the possibility to make IFS observations. Tunable filter instruments have recently been installed on large telescopes such as Grantecan (OSIRIS) and SALT (RSS). They have a very large field of view (>5') and a tunable spectral resolution (from a few hundreds to a few thousands). New generations of IFS are also about to be installed on the largest telescopes. MUSE/VLT, will have both a large field of view (1') and spectral range, whereas KMOS/VLT will be able to deploy small integral field units (3") over a very large field of view (7'). Therefore, they will be adapted to different observing programs. Integral field instruments are not limited to optical and visible wavelengths. Indeed, radio telescope interferometers also enable to have both spatial and spectral information. New generation instruments such as ALMA and SKA will respectively enable to observe molecular and neutral gas for a very large number of galaxies, giving new insights in galaxy evolution.

References

Bacon, R., Copin, Y., Monnet, G., et al. 2001, MNRAS, 326, 23
Bournaud, F. & Elmegreen, B. G. 2009, ApJ, 694, L158
Cappellari, M., Emsellem, E., Krajnović, D., et al. 2011, MNRAS, 413, 813
Contini, T., Garilli, B., Le Fèvre, O., et al. 2012, A&A, 539, A91
Cresci, G., Mannucci, F., Maiolino, R., et al. 2010, Nature, 467, 811
de Zeeuw, P. T., Bureau, M., Emsellem, E., et al. 2002, MNRAS, 329, 513
Dekel, A., Birnboim, Y., Engel, G., et al. 2009, Nature, 457, 451
Dicaire, I., Carignan, C., Amram, P., et al. 2008, MNRAS, 385, 553
Dutton, A. A., van den Bosch, F. C., Faber, S. M., et al. 2011, MNRAS, 410, 1660
Emsellem, E., Cappellari, M., Krajnović, D., et al. 2011, MNRAS, 414, 888
Epinat, B., Amram, P., Balkowski, C., & Marcelin, M. 2010, MNRAS, 401, 2113
Epinat, B., Amram, P., & Marcelin, M. 2008, MNRAS, 390, 466
Epinat, B., Tasca, L., Amram, P., et al. 2012, A&A, 539, A92
Förster Schreiber, N. M., Genzel, R., Bouché, N., et al. 2009, ApJ, 706, 1364
Gnerucci, A., Marconi, A., Cresci, G., et al. 2010, ArXiv e-prints
Gonçalves, T. S., Basu-Zych, A., Overzier, R., et al. 2010, ApJ, 724, 1373
Green, A. W., Glazebrook, K., McGregor, P. J., et al. 2010, Nature, 467, 684
Krajnović, D., Cappellari, M., de Zeeuw, P. T., & Copin, Y. 2006, MNRAS, 366, 787
Law, D. R., Steidel, C. C., Erb, D. K., et al. 2009, ApJ, 697, 2057
Le Tiran, L., Lehnert, M. D., Di Matteo, P., Nesvadba, N. P. H., & van Driel, W. 2011, A&A, 530, L6
Lehnert, M. D., Nesvadba, N. P. H., Le Tiran, L., et al. 2009, ApJ, 699, 1660
López-Sanjuan, C., Balcells, M., Pérez-González, P. G., et al. 2009, A&A, 501, 505

Queyrel, J., Contini, T., Kissler-Patig, M., et al. 2012, A&A, 539, A93
Rupke, D. S. N., Kewley, L. J., & Chien, L.-H. 2010, ApJ, 723, 1255
Tresse, L., Ilbert, O., Zucca, E., et al. 2007, A&A, 472, 403
Wright, S. A., Larkin, J. E., Law, D. R., et al. 2009, ApJ, 699, 421
Yang, Y., Flores, H., Hammer, F., et al. 2008, A&A, 477, 789

SF2A 2012
S. Boissier, P. de Laverny, N. Nardetto, R. Samadi, D. Valls-Gabaud and H. Wozniak (eds)

MILLIMETER RADIO SPECTRO-IMAGING

P. Gratier[1] and J. Pety[1,2]

Abstract. In recent years, the upgrade of heterodyne spectrometers at the IRAM 30m telescope has increased the instantaneous observable bandwidth by a factor 8 with spectral resolution increase of a factor 10. We here present new results using these instrument as an example of the new challenges in data reduction and analysis in millimeter radioastronomy. In the next 5 years, wide-field, wide-bandwidth imaging or spectro-imaging will become the norm at IRAM, due to new upgrades such as the arrival of multi-beam heterodyne receivers for the IRAM 30m and a large increase of the IRAM Plateau de Bure interferometer, namely the NOEMA project. New observing and data reduction methods will have to be devised to reduce and analyze the data coming from these instruments.

Keywords: Millimeter radioastronomy, spectro-imaging

1 Introduction

Millimeter radio observations differ from visible observations in several aspects. Wheras in the optical domain, the atmosphere is transparent and has a brightness temperature well below that of the observed sources, the situation is reversed in the millimeter radio domain, with source brightness temperatures much smaller than atmospheric brightness temperatures (the source brightess temperatures range from a few Kelvins to tens of milliKelvins, with typical sky temperatures of 300K). Furthermore, the atmospheric transparency in the sub(millimeter) domain can be low, especially at higher frequency, and depends strongly on the water vapor content of the atmosphere. An analogy would be that radio millimeter observation are akin to observing through a fog during daylight. For these reasons, millimeter observations are almost systematically made using differential methods, subtracting from the source signal, the data from a reference position far enough from the scientific source to be devoid of its emission but close enough to sample the same atmosphere. Typical separations from source and reference are $100''$.

2 Current observing modes

Up to recently, mostly two independent approaches have typically been used in millimeter radioastronomy: either narrow band (only one to a few molecular lines) imaging or wide band (several GHz bandwidth) single pointing spectral surveys. I will use examples of real observations to illustrate these observing methods and the associated constrains on data rates and data reduction.

2.1 Wide-field narrow-band imaging

2.1.1 Single dish telescopes

The quantity measured at the output of a single dish telescope is the convolution of the sky brightness and the antennas point source function. This PSF is well modeled by a Gaussian of FWHM $1.2\lambda/D$, where λ is the observing wavelength and D the telescope diameter. In the case of the IRAM 30m telescope for the CO(2-1) line (1.3mm) this corresponds to $11''$.

[1] Institut de Radioastronomie Millimétrique, 300 rue de la Piscine, 38406 Saint Martin d'Hères, France
[2] LERMA, UMR 8112, CNRS and Observatoire de Paris, 61 avenue de l'Observatoire, 75014 Paris, France

To map large regions of the sky, the most recent observing technique is to slew the telescope continuously while acquiring spectra regularly spaced in time. This observing mode is known as On-The-Fly observing. The full map of the triangulum galaxy M33 in CO(1-0) with the IRAM 30m telescope (Gratier et al. 2010; Druard et al. 2012) is an example of wide field mapping (see Fig. 1). The mapped field of view is $55' \times 40'$ (0.78 deg^2) with a resolution of $12''$ this corresponds to 55 000 independent beams. The spectra are composed of 512 2 MHz wide channels for a total frequency bandwidth of 1 GHz. During the 400 telescope hours needed to complete the project, $\sim 2 \times 10^6$ individual spectrum have be acquired with a data rate of 250 MB/hr.

2.1.2 Interferometric telescopes

By default, an interferometer is a mapping instrument, imaging a field of view the size of the primary beam of the antennas ($\theta_{\rm prim} = 1.2\lambda/D_{\rm prim}$) with a resolution given by the ratio of the wavelength to the largest baseline between antennas. The area mapped by an interferometer can be increased by observing successively a mosaic of pointings separated by no more than half the primary beam size. One example of a large mosaic, is the mapping of the spiral galaxy M51 by the IRAM Plateau de Bure interferometer (Project PAWS, PI: E. Shinnerer) (see Fig. 2). This mosaic is made of 60 pointings covering a 10.5 arcminute squared region with a typical resolution of $1''$. This corresponds to 36 000 independent beams. The raw data rate was 180 MB/hr.

2.2 Single pointing wide-Band spectral surveys

The second main observing mode is wide-band spectral surveys. Instantaneous frequency coverage has increased greatly in the last couple of years. At the IRAM 30m telescope for example, the combination of EMIR receivers and Fourier Transform Spectrometers increased this number by factor 8 from 2 GHz to 32 GHz while increasing the frequency resolution by a factor 10 (from 2 MHz to 200 kHz). It has become straightforward to make complete, deep surveys of the full 1mm and 3mm bands. One such example is the Horsehead WHISPER survey (PI: J. Pety, Fig. 3) which covers the full 1, 2 and, 3mm bands (more than 130 GHz total combined bandwidth) at high spectral resolution (48 kHz at 2 and 3mm, 195 kHz at 1mm). Just at 3mm, this corresponds to 750 000 frequency channels. Usual baseline subtraction techniques consisting of windowing of individual spectral lines followed by a polynomial fitting of line free channels rapidly become inadequate when facing with spectra containing several hundred thousand channels and several hundreds to thousands spectral lines. Research is ongoing inside the `GILDAS/CLASS`[i] software to devise new methods to subtract the baselines using median filtering and wavelet decomposition.

3 Future instruments and observing techniques

3.1 Heterodyne arrays

In the near future, one way of improving the mapping sensitivity of single dish telescopes will be through the use of focal plane arrays. These are sets of independent receivers bundled together, usualy in a common cryogenic assembly, in the telescope receiver cabin. IRAM is working on the development of a 25 dual-polarization beam receiver at 3mm for the 30m telescope. The beams will be distributed over a typical field of view of $6'$ and each beam will be able to observe a 4 GHz bandwidth with a typical spectral resolution of 200 kHz.

Combined with wide band spectrometers, they will have data rates of 100 GB/hr, 40 times the current narrow band imaging rate and 6 times the current wide band imaging rate. New reduction methods will have to be devised to take into account the redundancy achieved by having several independent beams recording the same position on the sky. Roussel (2012) presents such a method applied to arrays of bolometers, particularly for the Herschel instruments.

3.2 On the Fly interferometry

New millimeter interferometers such as ALMA and NOEMA will have good instantaneous uv-plane coverage thanks to their large number of baselines. On-The-Fly observing methods for interferometry are being developed for these instruments. Instead of observing discrete mosaic pointings, the antennas are continuously slewed on the sky with data being regularly acquired. In the case of NOEMA, this will lead to data rates up to 625 GB/hr.

[i] See `http://www.iram.fr/IRAMFR/GILDAS` for more information about the `GILDAS` softwares.

New imaging methods (e.g. WIfISYN, Pety & Rodríguez-Fernández 2010) are developed taking into account the specificities of On-The-Fly interferometric observations.

4 Conclusions

Technological developments in last years have increased dramatically the bandwidth coverage at high spectral resolution of heterodyne receivers. Today, spectral surveys with several tens of GHz of bandwidth are becoming routine observations at the 30m telescope. Future instruments (heterodyne receiver arrays for the IRAM 30m telescope and the NOEMA interferometer) will combine wide field and wide spectral bandwidth to enable spectro-imaging. With the increase in data rate and data volume new reduction and analysis tools (e.g. wavelets, redundancy, OTF interferometry imaging algorithm) will have to be developed.

References

Druard, C., Braine, J., Schuster, K. F. Gratier, P., et al. 2012, A&A, in prep
Gratier, P., Braine, J., Rodriguez-Fernandez, N. J., et al. 2010, A&A, 522, A3
Pety, J. & Rodríguez-Fernández, N. 2010, A&A, 517, A12
Roussel, H. 2012, ArXiv e-prints (1205.2576)

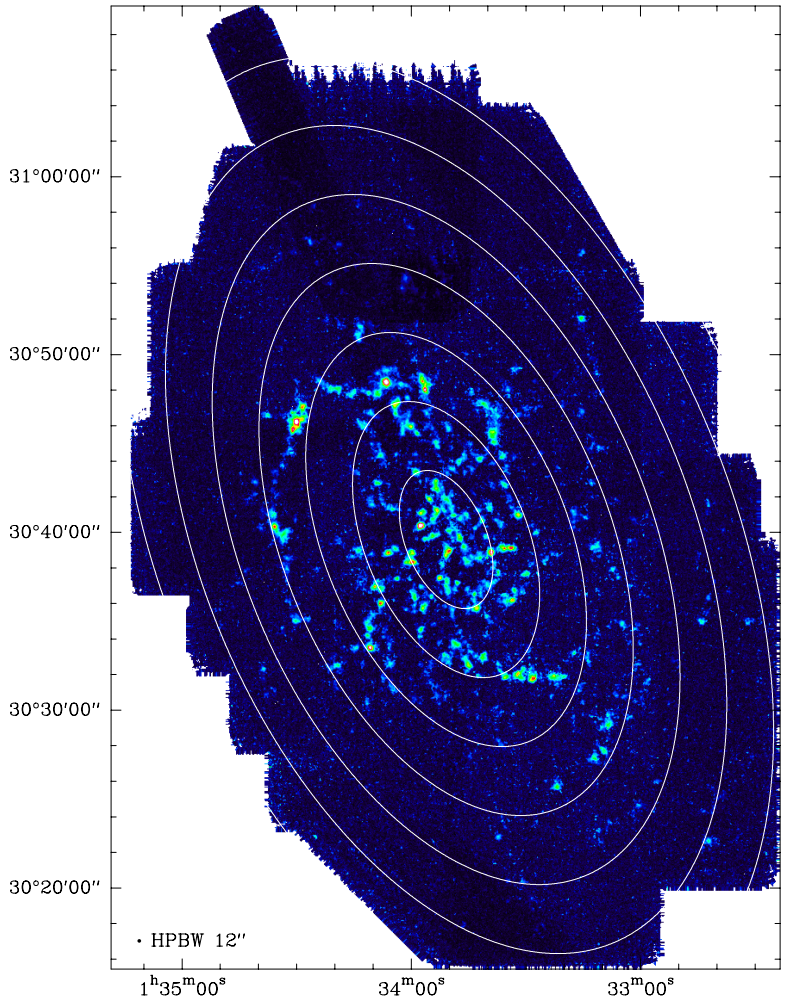

Fig. 1. CO(1-0) integrated intensity map of the M33 spiral galaxy observed with the IRAM 30m telescope. The resolution element is drawn at the bottom left. Ellipse are drawn every 1 kpc from the center of M33.

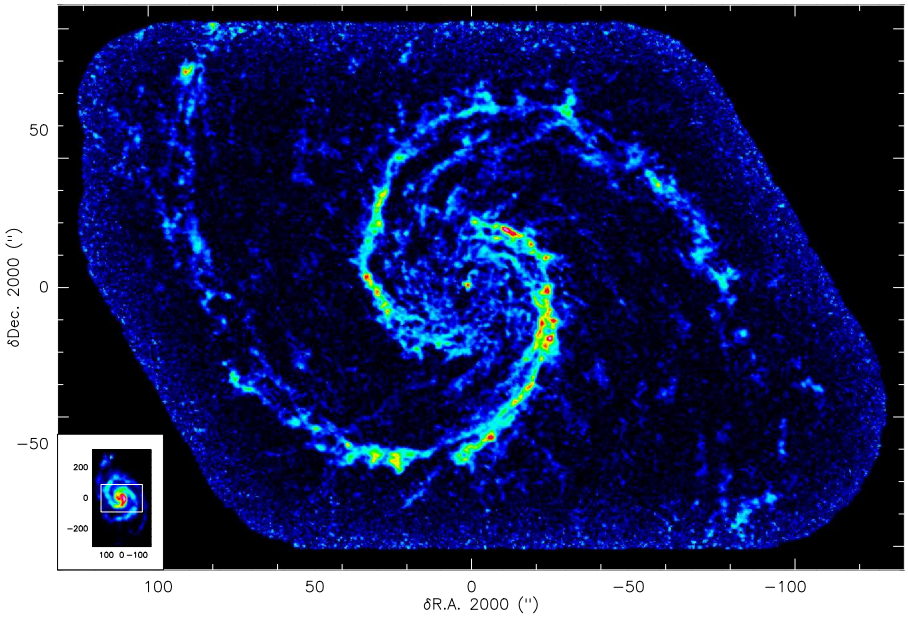

Fig. 2. ^{12}CO(1-0) integrated emission of the inner $\sim 10 \times 6$kpc of NGC 5194 (aka M51a) galaxy. The coordinate offsets are relative to the nucleus of NGC 5194. This image results from the joint deconvolution of the IRAM-30m single-dish and Plateau de Bure interferometer data sets. The image inserted at the bottom left is the ^{12}CO(1-0) integrated emission of the full M51 system (i.e., NGC 5194 + NGC 5195) as observed by the IRAM-30m telescope. The white horizontal rectangle shows the PAWS field of view. The images were scaled so that the angular resolution of both data set occupies the same size on the paper. In other words, the PAWS image shows the center of the small image zoomed by a factor 21.

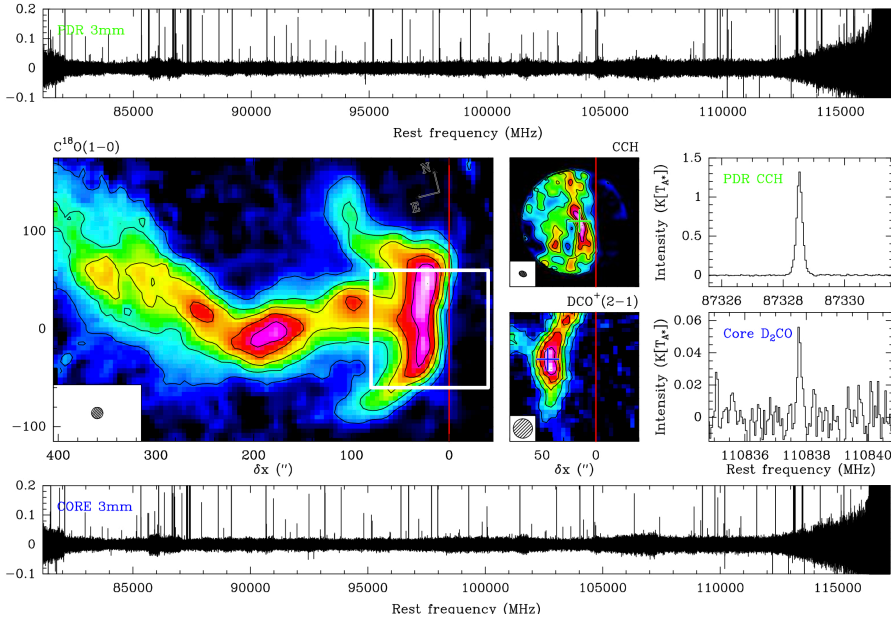

Fig. 3. The upper and lower panels display the spectra of the 3mm band at a spectral resolution of 49 kHz for two different positions in the Horsehead Nebula, obtained at the IRAM-30m with the combination of EMIR receivers and FTS backends in about 60 hours. Each spectra has 750 000 channels, as much information as in an image of 860 × 860 pixels! The median noise is about 8 mK [Ta*]. The survey positions correspond to two different environment located inside the white square on the C^{18}O(1-0) integrated emission map (wide, left image): 1) the photo-dissociation region (PDR) marked by the green cross on the CCH emission map (middle, top image from IRAM/PdBI), and 2) the dense core marked by the blue cross on the DCO$^+$ emission map (middle, bottom image from IRAM/PdBI). The middle right panels display two lines zoomed from the line surveys.

SF2A 2012
S. Boissier, P. de Laverny, N. Nardetto, R. Samadi, D. Valls-Gabaud and H. Wozniak (eds)

SCIROCCO: SIMULATION CODE OF INTERFEROMETRIC-OBSERVATIONS FOR ROTATORS AND CIRCUMSTELLAR OBJECTS

M. Hadjara[1, 2], F. Vakili [2], A. Domiciano de Souza [2], F. Millour [2] and P. Bendjoya[2]

Abstract. The VLTI (Very Large Telescope Interferometer) makes available milli-arcsecond-scale observations in the infrared. It offers new possibilities for constraining stellar structures such as polar jets, equatorial disks and rotationally-flattened photospheres of Be stars. Such constraints allows us to better estimate the stellar fundamental parameters and refine the mechanisms such as mass loss, pulsation and magnetism that govern the variability and evolution of these stars.

In this paper we present a chromatic semi-analytical model of fast rotators, which allows us to study the dynamics and the interaction between the photosphere and the wind of fast rotating stars of A, B and F spectral types. Our simple analytical model addresses the oblateness, inclination and position angle of the rotation axis of the star. It produces iso-velocity maps and intensity maps. It includes line profiles, limb-darkening and the von Zeipel effect.

SCIROCCO: **S**imulation **C**ode of **I**nterferometric-observations for **RO**tators and **C**ir**C**umstellar **O**bjects, includes all the parameters cited above in order to be a fast, powerful and light simulation tool for interpreting high angular resolution observations of rotating stars.

Keywords: Stars: rotation, Methods: numerical, Techniques: interferometric, Techniques: high angular resolution

1 Introduction

The stars with low metallicity are supposed to produce little or no magnetic field. This absence of magnetic field leads to a high spin-up during the contraction then formation of these stars (Martayan et al. 2006). This rotation rate can attain more than 80% of the critical, or breakup, velocity $v_c = \sqrt{(GM/R_c)}$ (with R_c the equatorial radius at this velocity) in some cases. These fast-rotating stars are called "fast rotators" and exhibit a number of peculiar characteristics (Domiciano de Souza et al. 2003), among which geometrical flattening, coupled with gravitational darkening von Zeipel (1924), making the poles hotter than the equator.

The models from Collins & Sonneborn (1977) indicate a two-components spectral energy distribution (SED) for these stars, with an infrared excess due to gravity darkening. Hence, it is not easy to place these stars in one single spectral classification, as the observed SED depends on its rotational velocity and inclination angle (Maeder & Peytremann 1972).

Furthermore, rapid rotation induce an additional change in the apparent spectral type and class of the star (Collins & Harrington 1966). Indeed, the full widths at half-maximum (FWHM) of UV lines are generally narrower (up 0.2 km/s) than those of the visible lines due again to gravitational darkening (Hutchings et al. 1979), since the spectral lines, depending on the temperature and gravity, are not formed uniformly on the star. This has an impact on the estimate of the inclination angle (Hutchings & Stoeckley 1977) and, hence, the estimation of the spectral type of the star. A classification based on the spectral ratio between the widths of these lines would be distorted by this effect (Collins 1974).

In addition, mechanisms such as meridional circulation and/or turbulence may affect the internal structure of the star and its evolution (Meynet 2009). Thus, fast rotators have always been considered as a physics laboratory to study stellar interiors, stellar evolution and primordial stars.

[1] Centre de Recherche en Astronomie, Astrophysique et Géophysique (CRAAG) Route de l'Observatoire, B.P. 63, Bouzareah, 16340, Alger, Algérie.; m.hadjara@craag.dz

[2] Laboratoire J.-L. Lagrange UMR 7293- Observatoire de la Côte d'Azur (OCA), Université de Nice-Sophia Antipolis (UNS), Centre National de la Recherche Scientifique (CNRS), Campus Valrose, 06108 Nice cedex 2, France.; Massinissa.Hadjara@oca.eu

In this context, spectrally-resolved long baseline interferometry offers new opportunities to observe the details of such stars with enough spatial resolution (van Belle 2012). We describe in this paper a numerical model that includes a subset of the different mechanisms described above: fast rotation, gravity darkening, and stellar pulsations. It produces intensity maps and velocity maps of the simulated star with rotationnal flatenning and several other effects, which can be compared to interferometric observations.

2 SCIROCCO

2.1 Description of the Model

SCIROCCO stands for Simulation Code of Interferometric-observations for rotators and CirCumstellar Objects. It is written in `Matlab` and make use of the following semi-analytical approach, adopting the frame depicted in Fig. 1 (shown in cartesian reference): a pixellized intensity map is computed independently from a velocity map, and both are combined into a spectrally-resolved intensity image-cube, which can be input in a later step into an interferometric simulation code.

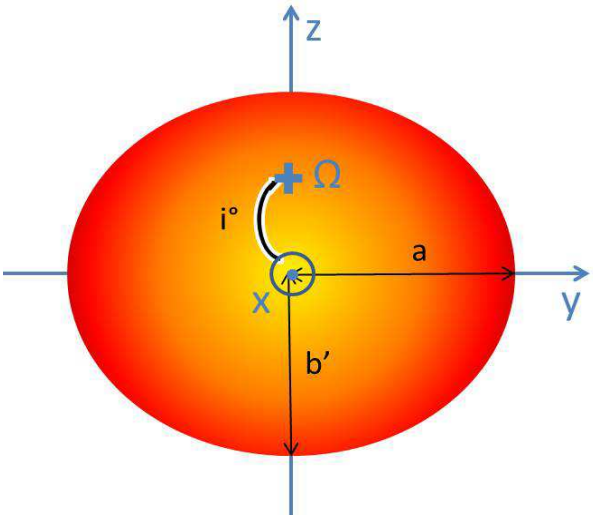

Fig. 1. Adopted reference system for a rotating star (flattened star with major axis a and minor axis b, here the apparent minor axis is $b' = ab/(a + (b - a)\cos i)$; assuming ellipsoid revolution principal/equations). The cross indicates the point where the rotation axis crosses the stellar surface. This rotation axis forms an angle i with the observer's direction (x axis) and its projection onto the sky is parallel to the z axis.

2.1.1 Intensity map

First, an intensity map of the star's photosphere is computed. We can use for example a simple limb-darkened model from (Hestroffer 1997), expressed in the geographical (co-latitude, longitude) coordinates (θ, ϕ):

$$I_c(\theta, \phi) = I_0(1 - \epsilon_\lambda(1 - \mu(\theta, \phi)) \tag{2.1}$$

where I_0 represents the flux at the center of the star, ϵ_λ is the limb darkening parameter, and $\mu(\theta, \phi)$ is the cosine of the angle between the normal to the surface at the point considered and the observer direction (Domiciano de Souza et al. 2004). The contour of the star is delimited by an ellipse with the minor axis in the direction of the rotation axis of the star. The minor-to-major axis depends on the rotation rate following the prescriptions of angle i (see Fig. 1). I_0 can serve as a weighting of the continuum flux as a function of wavelength (λ) using for example a Planck's law:

$$I_0(\lambda, T_{\rm eff}) = \frac{2hc^2}{\lambda^5} \frac{1}{e^{\frac{hc}{\lambda\sigma T_{\rm eff}}} - 1} \tag{2.2}$$

h being Planck's constant, c the speed of light, and $T_{\rm eff}$ the effective temperature of the star. I_0 can also be used to input the von Zeipel's effect into our model, by considering a co-latitude-dependent temperature in the below-mentioned local gravity field equation:

$$I_0(\theta) \propto F(\theta) = \sigma T_{\rm eff}^4(\theta) \tag{2.3}$$

with $T_{\rm eff}(\theta) \propto g^{0.25}(\theta)$, g being the local gravity field, also called the modulus of local effective surface gravity $g = \nabla\Psi(\theta)$, with $\Psi(\theta)$ is the stellar equipotential surfaces (Domiciano de Souza et al. 2004). An example of intensity map combining rotational flattening and gravity darkening is shown in Fig. 2 (left).

2.1.2 Velocity map

SCIRROCO produces a velocity map where for the moment, only rotation has been introduced:

$$V_{\rm proj}(\theta,\phi) = V_{\rm eq}\cos(\phi)(1-\alpha\sin^2(\theta))\sin(i) \tag{2.4}$$

In that equation, $V_{\rm eq}$ represent the equatorial rotation velocity, and the parameter α allows us to include a parametric differential rotation law (Domiciano de Souza et al. 2004). In the future, we also plan to include non-radial pulsations in that velocity map. An example of velocity map combining rotational flattening is shown in Fig. 2 (right).

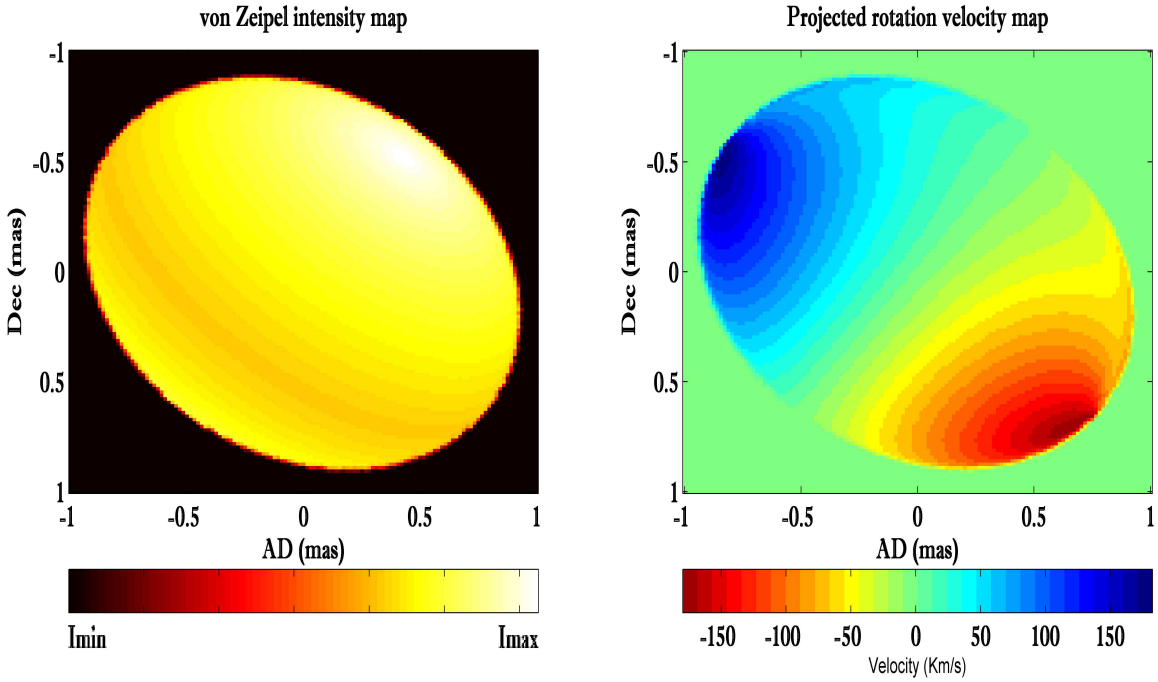

Fig. 2. Left: simulated Achernar intensity map in the continuum. The intensity at the poles is greater than at the equator. Here the velocity is around 88% of the critical velocity of the star. **Right:** velocity map of the same model (inclination 57°, orientation 39°). Here the simulated rotation is differential (the velocity of rotation at the equator is 60% larger than at the poles).

2.1.3 Spectrally-resolved image cube

The last step of the modelization process is to compute λ-dependent maps. For that, we need to model the natural line-profile of the considered line: we can assume e.g. Gaussian, Lorentzian, or Voigt profile:

$$\begin{cases} H_{\text{Gauss}}(\lambda) = 1 - H_0 \left[-\pi H_0^2 \frac{(\lambda-\lambda_0)^2}{W^2} \right] \\ H_{\text{Lorentz}}(\lambda) = 1 - \left[\frac{H_0}{1+(\frac{\lambda-\lambda_0}{W/2})^2} \right] \\ H_{\text{Voigt}}(\lambda) = (H_{Gauss} * H_{Lorentz})(\lambda) \end{cases} \tag{2.5}$$

The last step calculates the intensity maps of the star as a function of wavelength. For that, we project via the Doppler effect the velocity map (V_{proj}, Eq. 2.4) to the intensity map (I_c, Eq. 2.1), given the line profile (H, Eq. 2.5) and the work wavelength λ:

$$I(\lambda, \theta, \phi) = H\left(\lambda + \lambda_0 \frac{V_{\text{proj}}(\theta, \phi)}{c}\right) I_c(\theta, \phi) \tag{2.6}$$

We get one intensity map per wavelength of interest around the central wavelength λ_0 of the line (see Fig. 3, left). Once all intensity maps are computed, we synthesize the interferometric observables by Fourier-Transforming each map (see Fig. 3, right). This provide us spectra, visibility amplitudes, phases, and closure phases.

By comparing the observed interferometric measurements to the synthesized quantities, we can access to the parameters of the fast rotating star such as: effective temperature as a function of co-latitude, rotational rate, inclination, angular radius and flattening and, if possible the differential rotation.

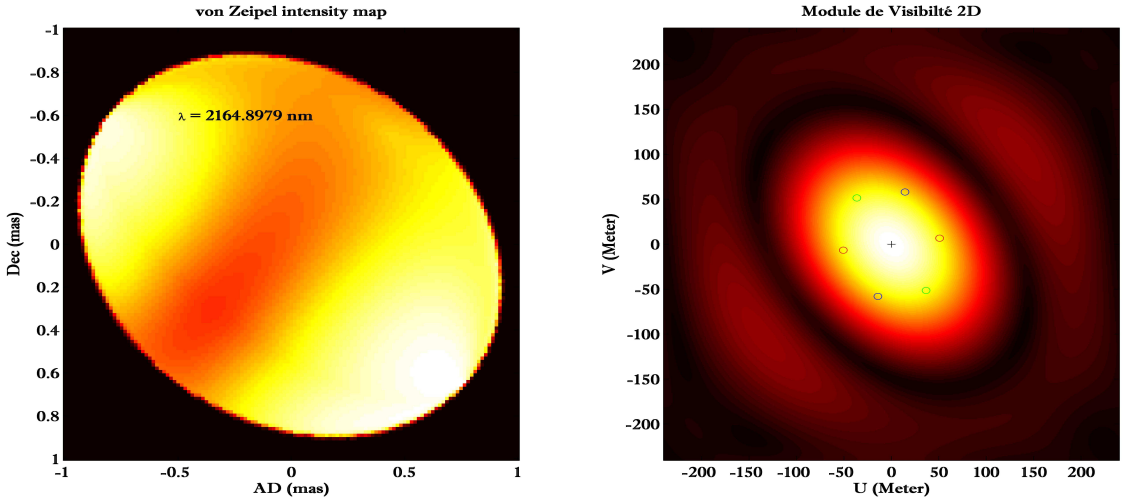

Fig. 3. Left: monochromatic intensity map for a given wavelength. **Right:** Map of corresponding 2D module visibility, which is represented on the three bases with interferometric which will make the observation (1st base small red circle, 2nd green and 3rd blue).

2.2 Simulation of interferometric observations: the example of Achernar

To illustrate this paper, we simulate the famous Be star Achernar with SCIROCCO as observed in Domiciano de Souza et al. (2003). We use the parameters detailed in the paper, which are recalled for practicity in Table 1.

Table 1. Achernar parameters (from Domiciano de Souza et al. 2003)

Star	*Achernar (α Eri)*	v/v_{crit}	*0.79-0.96*	$\mathbf{T}_{eq}$ **(K)**	*9500-14800*
Spectral type	*B3Vpe*	**Orientation (°)**	*39±1*	$\mathbf{R}_{pole}$ **(R⊙)**	*8.3-9.5*
Velocity v (km/s)	*225*	**Gravity darkening β**	*0.25*	$\mathbf{R}_{eq}$ **(R⊙)**	*12.0±0.4*
Inclination i (°)	*57*	$\mathbf{T}_{pole}$ **(K)**	*20000*	**Oblateness**	*0.348±0.10*

In addition, we introduce to our model a differential rotation coefficient ($\alpha = 0.6$) and a Voigt intrinsic line profile with a depth of 0.6 and a $FWHM = 10 * \Delta\lambda$.

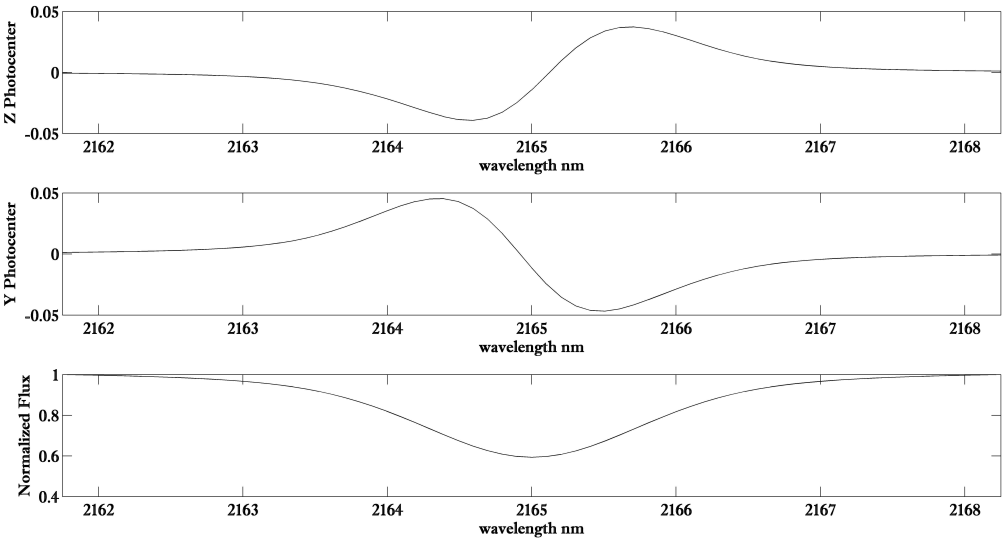

Fig. 4. Top: photo-center (or centroid: the first order term of the phase by Mac Lauren development, Jankov et al. (2001)) along the Z axis (see reference adopted Fig.1). **Middle:** photo-center by Y (note that the photo-centers are in radian). **Bottom:** normalized spectrum, we see well that our starting line has expanded and its depth was decreased (precisely because of the rotation).

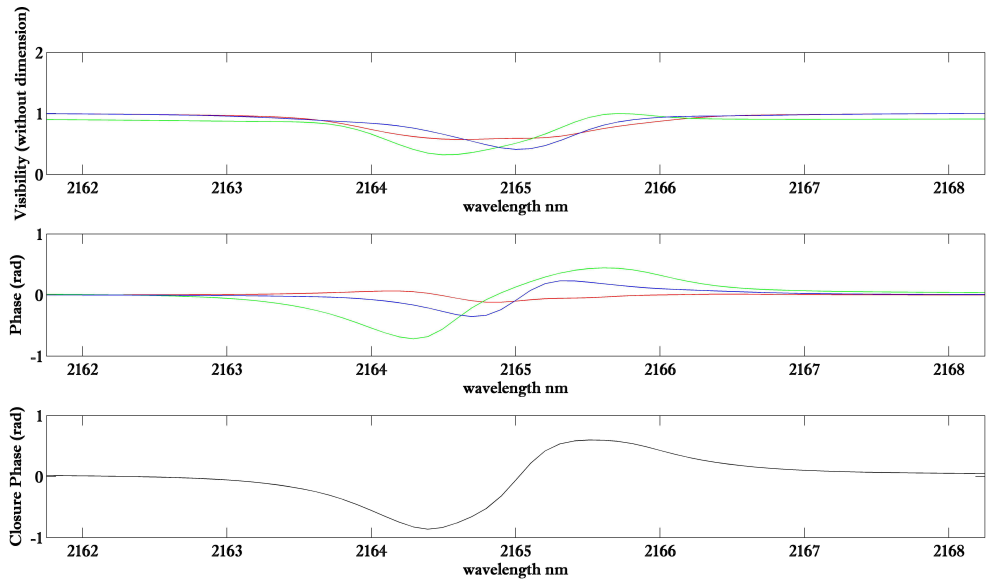

Fig. 5. Top: visibility module observed by the interferometric three bases (red, green and blue). **Middle:** the phases observed in the three interferometric bases (red, green and blue), we note that although the phase observed by the base perpendicular to the axis of rotation of the star (green) is the one that has the highest amplitude & inversely that which is along the axis of rotation (red) is the lowest. **Bottom:** the closure phase.

We choose to simulate interferometric observations with the AMBER/VLTI instrument on the 3 following interferometric baselines : G1-D0 (51.28 m, $-82.5°$), D0-H0 (63.12 m, $35.42°$), H0-G1 (59.78 m, $-13.8°$), and around the Brackett γ line (2.165μ m).

The velocity map & intensity map in the continuum continuum are shown in Fig. 2, the monochromatic intensity map at a given wavelength & corresponding 2D visibility amplitude map in Fig. 3, the photo-centers

& spectrum in Fig. 4, and finally visibilities, phases & closure phase in Fig. 5.

3 Conclusions & Discussions

We presented here a semi-analytical model of fast-rotators whose aim is to interpret interferometric datasets. We are able to produce interferometric observables using a set of physical parameters like the rotation law, gravity darkening effect, etc., while keeping the computing time reasonable (one set of visibility curves can be computed in $15s$).

The next step is to develop a "model-fitting" approach to compare real datasets with this model.

References

Chelli A., & Petrov R.G. 1995, A&A, 109, 401
Collins, G. W. 1974, ApJ, 191, 157
Collins, G. W., & Harrington J. P. 1966, ApJ, 146, 152
Collins, G. W., & Sonneborn, G. H. 1977, ApJ, 34, 41
Domiciano de Souza, A., Zorec, J., Jankov, S., Vakili, F., Abe, L. 2004, A&A 418, 781
Domiciano de Souza, A., Kervella, P., Jankov, S., Abe, L., Vakili, F. et al. 2003, A&A, 407, L47
Domiciano de Souza, A., Vakili, F., Jankov, S., Janot-Pacheco, E. & Abe, L. 2002, A&A, 393, 345
Hestroffer, D. 1997, A&A, 327, 199
Hutchings, J. B., & Stoeckley, T. R. 1977, PASP, 89, 19
Hutchings, J. B., Nemec, J. M., & Cassidy, J. 1979, PASP, 91, 313
Jankov, S., Vakili, F., Domiciano de Souza, A., & Janot-Pacheco, E. 2001, A&A, 377, 721
Maeder, A., & Peytremann, E. 1972, A&A, 21, 279
Martayan, C., Frémat, Y., Hubert, A.-M., Floquet M., Zorec J. et al. 2006, A&A, 452, 273
Meynet, G. 2009, Lecture Notes in Physics, 765, 139
van Belle, G. T. 2012, A&ARv, 20, 51
von Zeipel, H., 1924, MNRAS, 84, 665

SF2A 2012
S. Boissier, P. de Laverny, N. Nardetto, R. Samadi, D. Valls-Gabaud and H. Wozniak (eds)

HIGH ANGULAR RESOLUTION AND YOUNG STELLAR OBJECTS: IMAGING THE SURROUNDINGS OF MWC 158 BY OPTICAL INTERFEROMETRY

J. Kluska[1], F. Malbet[1], J.-P. Berger[2], M. Benisty[1], B. Lazareff[1], J.-B. Le Bouquin[1] and C. Pinte[1]

Abstract. In the course of our VLTI young stellar object PIONIER imaging program, we have identified a strong visibility chromatic dependency that appeared in certain sources. This effect, rising value of visibilities with decreasing wavelengths over one base, is also present in previous published and archival AMBER data. For Herbig AeBe stars, the H band is generally located at the transition between the star and the disk predominance in flux for Herbig AeBe stars. We believe that this phenomenon is responsible for the visibility rise effect. We present a method to correct the visibilities from this effect in order to allow "gray" image reconstruction software, like `Mira`, to be used. In parallel we probe the interest of carrying an image reconstruction in each spectral channel and then combine them to obtain the final broadband one. As an illustration we apply these imaging methods to MWC158, a (possibly Herbig) B[e] star intensively observed with PIONIER. Finally, we compare our result with a parametric model fitted onto the data.

Keywords: Instrumentation: interferometers, Methods: data analysis, Techniques: high angular resolution, Techniques: interferometric, Stars: emission-line, Be, Infrared: stars

1 Introduction

The processes that lead to the formation of exoplanets are important to understand. Stars form after a collapse of a giant cloud of dust and gas. After a million year, a protoplanetary disk is forming around the star, believed to be the birthplace of planets.

A young star is surrounded by an active environment with which it interacts. Accretion disks (Monnier & Millan-Gabet 2002), inner gaseous disks (Benisty et al. 2010; Tannirkulam et al. 2008; Eisner et al. 2009), infalling envelop renmands, winds (Cabrit et al. 2010; Dougados et al. 2005; Malbet et al. 2007; Tatulli et al. 2007) and jets (Cabrit 2003; Dougados et al. 2004) are the main components of such environments. The complexity of physical phenomenon at play requires direct observation at the astronomical unit (A.U.) scale. Optical interferometry is able to bring such informations, because it can observe both in the near infrared, where the hot dust and hot gas nearby the star are emitting, and resolve the first A.U., which correspond to milliarcsecond scale at the distance of star formation regions.

Interferometry consists in combining the light of 2 or more telescopes in order to measure the complex degree of coherence. For that purpose, the interferometer measures interference fringes. The amplitude of the fringes yields the norm, and its position the phase of a complex quantity called visibility $V(u, v)$. Thanks to the van Cittert-Zernicke theorem we know that the Fourier transform of the visibilities in the Fourier Plan (u, v) gives us the intensity distribution $I(x, y)$ of the source. Unfortunately, in the near infrared (NIR) the atmosphere blurs the phases of the visibilities. In practice, there are two interferometric measurements : the squared amplitude of the visibilities V^2 and the closure phases.

We noticed in several datasets that the visibility is higher at short wavelengths. If we plot the squared visibilities V^2 in function of B/λ, we can see (Fig. 1) that the rising curve of visibilities per base is not fitting the general trend of the data for different baselines. First, it was seen in AMBER (Petrov et al. 2007) data, but it was considered as an instrumental defect. Now, the same effect has been observed with PIONIER (Le Bouquin et al. 2011) . We try to explain this effect astrophysically, claiming that the image of the object is

[1] Institut de Planétologie et d Astrophysique de Grenoble (UMR 5274) BP 53 F-38041 GRENOBLE Cedex 9 , France
[2] ESO, Santiago Office, Alonso de Cordova 3107, Vitacura, Casilla 19001, Santiago de Chile, Chile

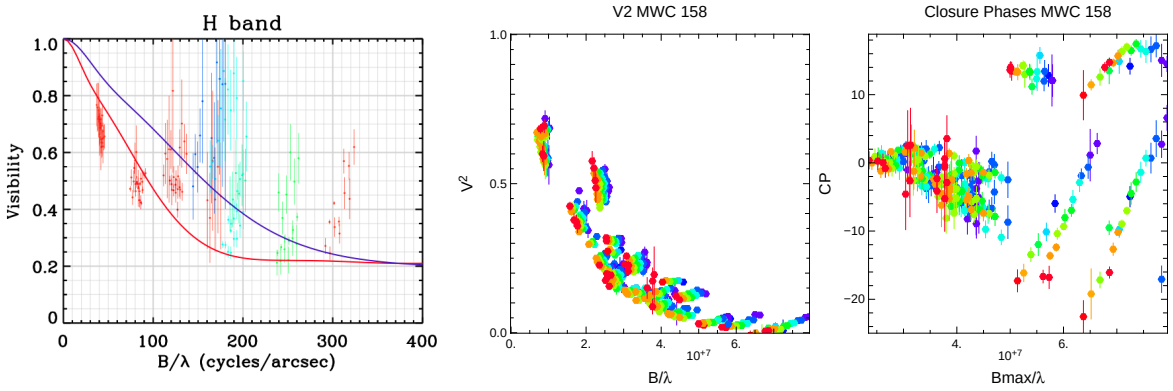

Fig. 1.
Data on MWC 158. **Left:** AMBER (Petrov et al. 2007) data from Borges Fernandes et al. (2011). **Middle:** PIONIER (Le Bouquin et al. 2011) squared visiblties. **Right:** PIONIER closure phases. For PIONIER data the color is in function of wavelength (blue : short wavelengths, red : long wavelengths).

varying through the different spectral channels inside the same spectral band, and we propose three techniques in order to take it into account and to be able to reconstruct images.

These methods will be applied to an astrophysical object. They are useful to analyze MWC158 (also known as HD50138). This star is a Be star known to have the B[e] phenomenon and presents a strong variability (Hutsemekers 1985; Andrillat & Houziaux 1991; Pogodin 1997; Borges Fernandes et al. 2009) which complexify the evolutionary stage identification of the source. Its distance is poorly constrain ($d = 500pc \pm 150pc$ van Leeuwen 2007).

In section 2 we will describe the chromatic effects in the visibilities and the section 3 will show the different methods to deal with them. Finally we will apply them to the astrophysical case of MWC 158 in the section 4.

2 Chromatism

Since interferometric instruments with spectral dispersion exist, we need to take into account the flux variations with the wavelength in order to correctly analyze the data and have access to the spectral super synthesis. In the case of Young Stellar Objects (YSOs), we noticed that the visibilities have a strong spectral dependence such as the geometrical shape of the object could not explain it.

For Herbig AeBe star, the chromatic effect explained in the section 1 exists typically for the Near Infrared interferometry. In the following, we explore the possibility that this effect is caused by a different spectral index between the central star and its surrounding media.

2.1 Modeling the effect

In order to confirm that, we made a simple model with a central star and its dusty disk.

2.1.1 The star

In our model, the star is considered to be unresolved. This hypothesis is justified for the young objects we are looking at. To simplify our model, we assume $V_{star} = 1$.

For the star we have 3 parameters : the radius (R_*), the distance (d) and the temperature (T_*). If we asumme a Herbig AeBe star with a temperature of 12000K radiating as a black body, we know that in NIR we will look on the Rayleigh-Jeans regime of a black body (see Fig. 2). That means that the spectral curve is proportional to a power law : $F_\lambda^{star} \propto \lambda^{-4}$.

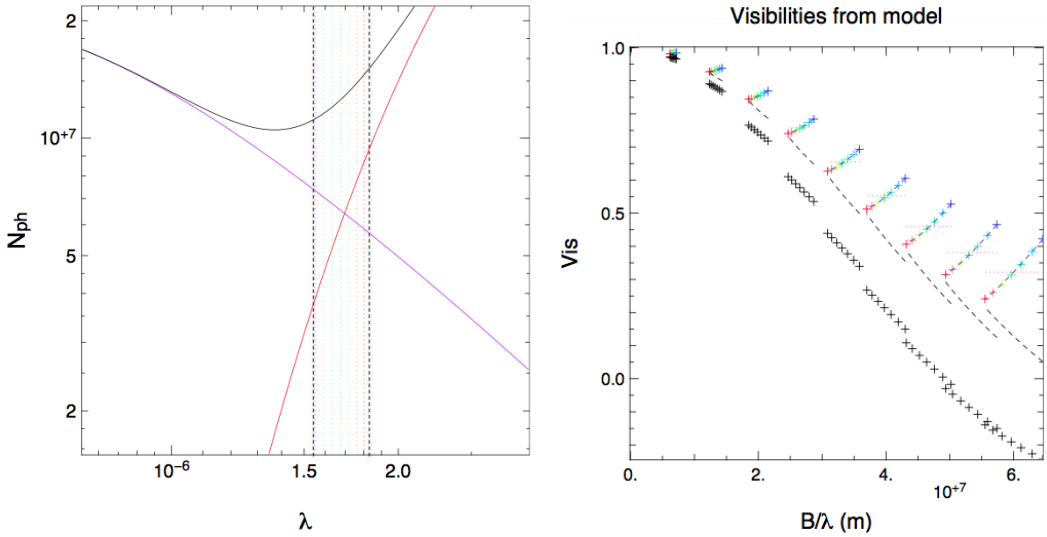

Fig. 2. Left: location of the PIONIER spectral channels on the SED of the model. We can see that they are located at the crossing between the stellar and the dust fluxes. **Right:** we can see that the chromatic phenomena is reproduced.

2.1.2 The disk

The disk model is simple : it is a geometrically thin optically thick passive disk. Its temperature is a function of the radius :

$$T(r) = T(r_0)\left(\frac{r}{r_0}\right)^{-q} \tag{2.1}$$

with :

$$q = \frac{3}{4} \tag{2.2}$$

see Lynden-Bell & Pringle (1974); Adams et al. (1988).

The disk will be sampled on several rings, each ring having its own temperature as a function of its distance to the star. The other geometrical parameters are the inclination (i), the inner and outer rims radii (R_{in}, R_{out}), and the temperature of the inner rim (T_{in}). The flux of each ring will be a black body at the temperature of the disk. The ring visibility is defined as follow (Berger 2003) :

$$V_{ring} = J_0(2\pi r\frac{B}{\lambda}) \tag{2.3}$$

To obtain the Fourier Transform of the disk we have to add the flux of each ring and sum every contributions :

$$V_{disk} = \sum^{n_{ring}} J_0(2\pi r_i\frac{B}{\lambda})2\pi r_i B_\lambda(T_i)dr_i \tag{2.4}$$

In the results shown in Fig. 2 the chromatic effect which tends to look like the data shown in Fig. 1. The visibilities have the same behavior than the data. We can conclude that the chromatic effect is not instrumental but astrophysical.

The effect is dominated by the flux ratio which is changing through the different spectral channels. If we compute the total correlated flux we have :

$$V_{\rm tot}(B/\lambda)F_{\rm tot}(\lambda) = F_*(\lambda) + V_{\rm disk}(B/\lambda)F_{\rm disk}(\lambda) \tag{2.5}$$

with :

$$F_{\rm tot}(\lambda) = F_*(\lambda) + F_{\rm disk}(\lambda) \tag{2.6}$$

If we introduce the stellar to total flux ratio f_*, we obtain the mathematical description of the chromatic phenomena :

$$V_{\rm tot}(B/\lambda) = f_*(\lambda) + V_{\rm disk}(B/\lambda)(1 - f_*(\lambda)) \tag{2.7}$$

with

$$f_*(\lambda) = \frac{F_*(\lambda)}{F_{\rm tot}(\lambda)} \tag{2.8}$$

In the next section we will discuss the different methods to overcome the chromatic effect.

3 Methods

Our goal is to be able to analyze chromatic data. We developed three complementary methods to do that : gray image reconstructions, data modification and parametric fit. The first two methods are based on image reconstruction and the last one is model fitting. We are mostly interested in the disk around the star and we are looking for informations on the resolved geometry and the strength of the chromatic effects.

3.1 Image reconstruction per spectral channel

Once we are aware of the chromatic effect, one can make image reconstructions selecting only one wavelength per reconstruction (see Fig. 3). In that case the gray image reconstruction is justified. The technique is to have one image per wavelength and to stack all the images in order to have the final broadband one.

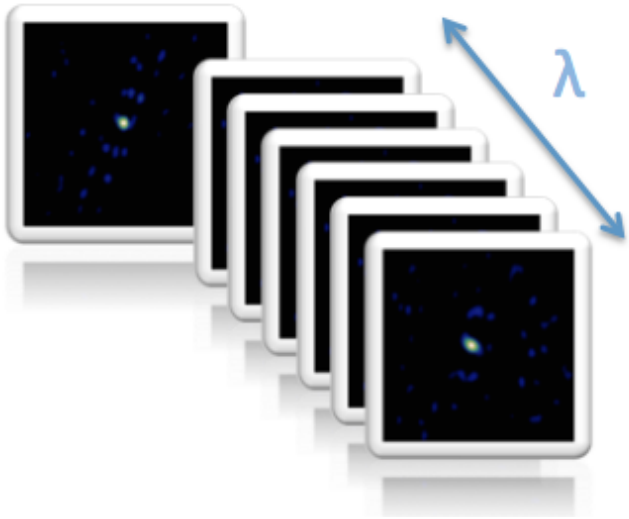

Fig. 3.
An image reconstruction is made for each spectral channel of the instrument. Then all the images are stacked together in order to obtain the final image.

The presence of various components of different spectral indexes prevents from using a gray emission approximation in the image reconstruction process. As a consequence, since we need to work on a per-spectral-channel basis the (u,v) coverage quality is severely affected.

3.2 Modification of the data

We want to have access to the disk visibilities. From the Eq. (2.7), if we know the SED and then the stellar flux ratio $f_*(\lambda)$ and its variation through the wavelengths, we can compute the disk visibilities as :

$$V_{\rm disk}(B/\lambda) = \frac{V_{\rm tot}(B/\lambda) - f_*(\lambda)}{1 - f_*(\lambda)} \tag{3.1}$$

We can apply the modification described in Eq.(3.1) to one of the interferometric measurements which is the power spectrum ($VV^* = |V|^2$). In summary, our measurements are $|V_{\rm data}|^2$ and we want to recover $|V_{disk}|^2$. Using the Eq(3.1), we have :

$$V^2_{\rm disk}(B/\lambda) = \Big(\frac{\sqrt{|V_{\rm data}(B/\lambda)|^2} - f_*(\lambda)}{1 - f_*(\lambda)}\Big)^2 \tag{3.2}$$

One of the problem is the value that we take for $\sqrt{|V_{\rm data}(B/\lambda)|^2}$; we must choose between the positive (phase $\phi = 0$) and the negative one ($\phi = \pi$). But it could be solved analyzing more precisely the data and other interferometric observables like the phase of the bispectrum (also called the closure phase).

It is not possible to retrieve the bispectrum phase of the dust from the data because we are loosing the phase of each pair of telescopes. The equations lead to a solution where we need the phase (Ragland et al. 2012).

3.3 Parametric model

In this section we have attempted to model the object. The model is geometrical and includes the chromatic effect as described in the sections 1 and 2. Our model is composed of multiple components and was developed when chromatic data was fitted.

3.3.1 Geometric part of the fit

The first component of the model is an unresolved star (a dirac in the image space) which can be shifted compared to the image photo center (that will produce a rise of closure phases). The second component is a ring. In the Fourier space the ring is defined as in Eq. (2.3) but using $\sqrt{u^2+v^2}$ for the spatial frequencies (B/λ) and their orientations that we want to solve.

We take into account the Position Angle ($P.A.$), which is defined from the North to the East, and the inclination (i). One of the parameters of this shape is the ring radius r. But this will define a ring with a infinitely small width. In order to have a Gaussian width we have to convolve the ring formulae by a Gaussian, in other words, to multiply the visibility of the ring by the visibility of the Gaussian function with the correspondent width w. Once we have the Gaussian ring, we will add some azimuthal modulations of the ring intensity to be closer to the physics of an inner rim. The modulations are functions in cosinus and sinus of the azimuthal angle (α) of the ring which starts at its major axis. We have included two sorts of modulation : one on 2 π (c_1, s_1) and the second on π (c_2, s_2). We add a gaussian width to the ring, with $r_{\rm gauss}$ being the Half Width at Half Maximum (HWHM) of the Gaussian function.

We have a model with three components : the star, the Gaussian ring and a second Gaussian ring or a Gaussian function.

The total visibilities are depending on all these components weighted by their flux.

3.3.2 Modeling the chromatism

To obtain the model visibilities we use the linearity property of the Fourier transform.

$$F_{\rm tot}V_{\rm tot} = F_*V_* + F_1V_1 + F_2V_2 \tag{3.3}$$

The fluxes are the ones recieved by the interferometric instrument. So we have :

$$F = \int_{\lambda-\frac{\Delta\lambda}{2}}^{\lambda+\frac{\Delta\lambda}{2}} F_\lambda d\lambda = \int_{\nu-\frac{\Delta\nu}{2}}^{\nu+\frac{\Delta\nu}{2}} F_\nu d\nu \tag{3.4}$$

We will use the approximation that the channel spectral width is constant and that the flux is constant in one spectral band. The flux is then equal to the value of F_λ at the central wavelength of a spectral channel. From the Eq. (3.3), we see that we can determine a flux ratios at one wavelength and to deduce the ratios on the other wavelength by the laws that we assume for each component. PIONIER is operating in the NIR in the H band. At this wavelength, we can assume that Herbig stars are in their Rayleigh-Jeans regime. That means that their flux (F_λ)is proportional to the wavelength at the power of -4. The laws for the environment are more difficult to find. We can fit a power-law in wavelength or to a black body variation if we are resolving a thermal emitting region. Since the dust temperature is supposed to be below 2000K (Dullemond & Monnier 2010), we can assume that it is in its Wien regime. Then if we assume black body regimes we obtain :

$$V_{\rm tot}(B,\lambda) = f_*^0\big(\frac{\lambda}{\lambda_0}\big)^{-4} + f_1^0\frac{B(\lambda,T_1)}{B(\lambda_0,T_1)}V_1(B,\lambda) + f_2^0\frac{B(\lambda,T_2)}{B(\lambda_0,T_2)}V_2(B,\lambda) \tag{3.5}$$

with f^0 the flux ratios at λ_0, T the temperature of a component and

$$B(\lambda,T) = \frac{2hc\lambda^{-5}}{\exp\frac{hc}{k_B\lambda T}-1} \tag{3.6}$$

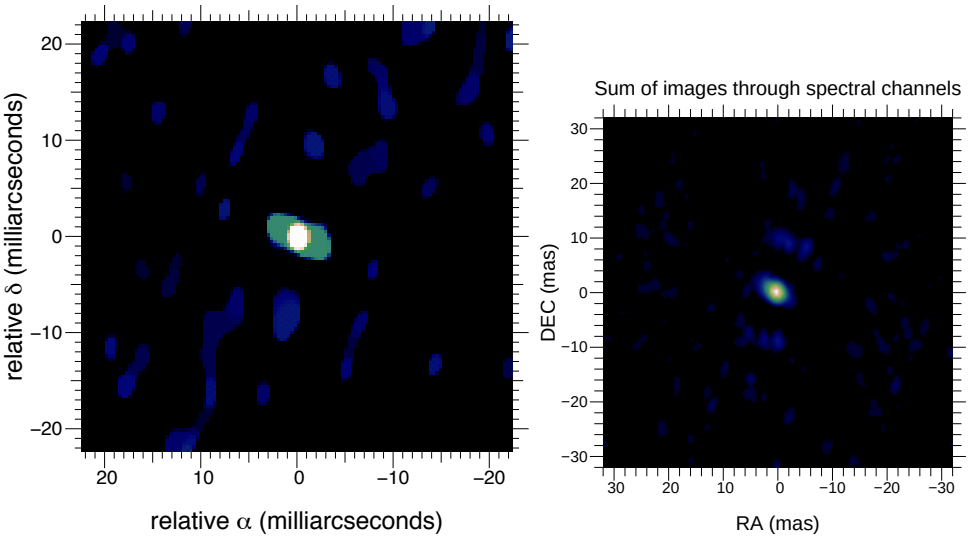

Fig. 4. Left: the stack of image reconstructions per spectral channels. **Right:** image reconstruction after modifying the squared visibilities.

is the black body function, with h the Planck constant, c the light speed, and k_B the Boltzmann constant.

The variations of the flux ratios through the observational band will build the chromatic effect that we want to take into account in our fit.

Once we get all our tools to investigate data with chromatic effect, let us apply them on an astrophysical case : MWC158.

4 The case of MWC 158

The interest on this object came with the data we get with PIONIER (Le Bouquin et al. 2011) a 4 telescopes interferometric, visitor instrument operating at the VLTI and which observe in the H band.

4.1 Image reconstructions

We were interested into this data (see Fig. 1) because it shows clearly signs of chromatism. As the (u, v)-plan is sufficiently covered we can reconstruct images. We use the `Mira` algorithm (Thiébaut 2008) , but as many image reconstruction algorithms it does not take into account the chromatism. Since it extrapolates the Fourier space, the chromatism makes him extrapolate badly and many artifacts appear. We then use the monochromatic reconstructions per spectral channel. We also use the visibility correction, not modifying the closure phases (they should be stronger). The results are showed on the Fig. 4.

We can see that there is a second resolved component. We can also see the orientation of the smallest extended component. Both of the reconstruction methods shows similar patterns. That brings us to the idea to fit two extended components.

4.2 Parametric fit

The fit bring us an idea on the geometry and the light emission from the source but with a strong a priori which is the model we want to fit. That is why we took the geometries suggested by the image reconstructions. We can see a central extended part which is composed of the star and its environment which seems to have a P.A. and an inclination.

We have begun the fit with one extended component which is a Gaussian function or a Gaussian ring. Both of the fits gave us the more or less the same inclinations and P.A. which are consistent with the image reconstructions. But the data was not entirely fitted : the short baselines indicates that there is a more extended component as showed by image reconstruction. We then add another component to our fit. In order to fit the

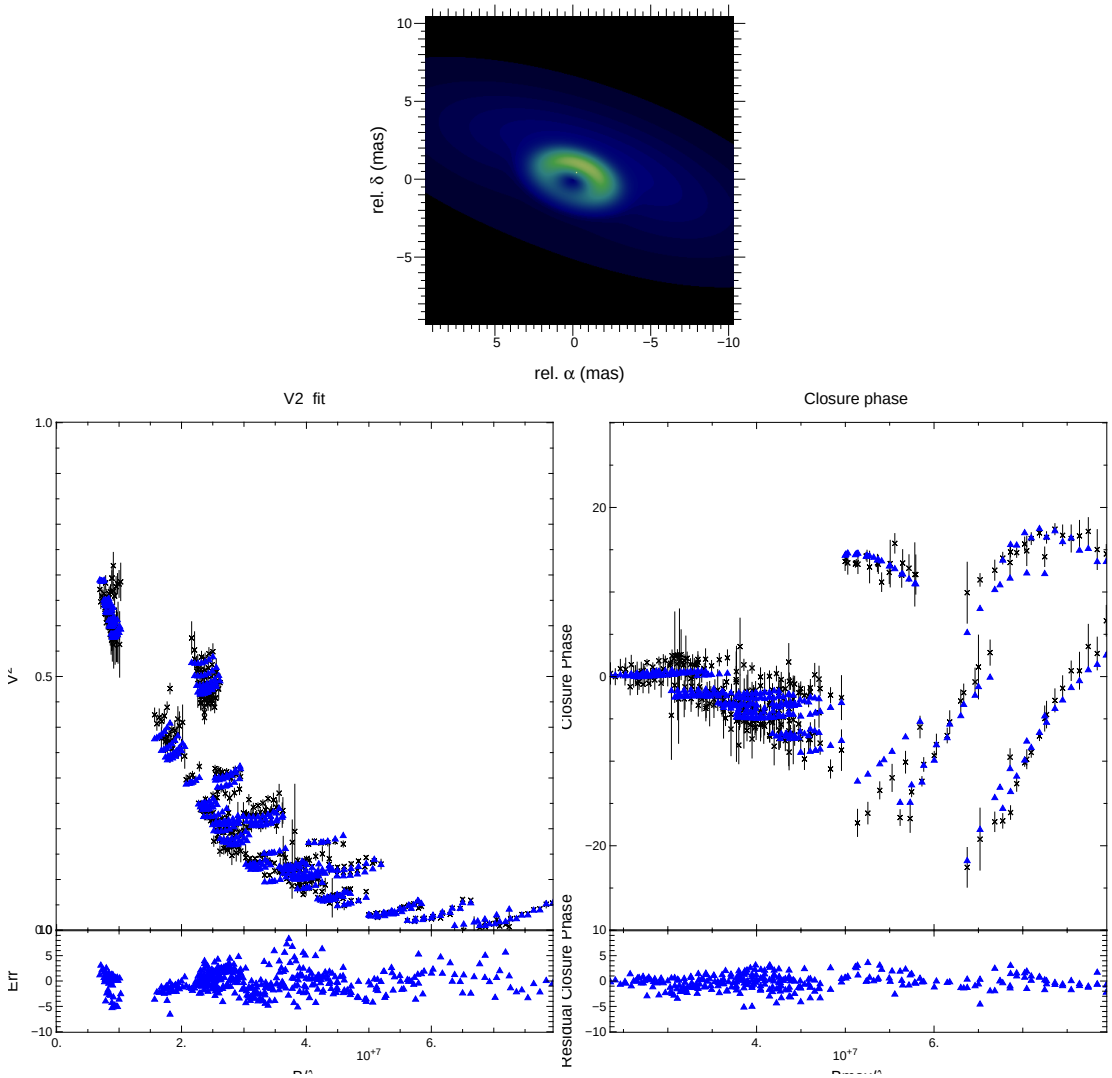

Fig. 5. The best fit results are presented. **Top:** The image corresponding to the best fit. **Right:** The fit on the V2. **Left:** The fit on the Closure Phases.

strong closure phase signal we add azimuthal modulation to the ring. It appears not to be sufficient, and the best fit was to shift the central star. It is the only solution to fit the closure phases.

In the end, and adding the different parameters, we ended with 15 parameters and a χ^2 of 3.5. In the current state of the data processing and interpretation, we believe that the best fit is presented Fig. 5. The parameters are on the Table 1. We can see that the best fit is done with two Gaussian rings.

The geometrical fit suggests a star, with a relatively close Gaussian ring (radius of 1.5 mas) with a lot of flux ($\approx 60\%$). We interpret that as the resolution of the inner rim of the dusty disk. Its azimtuhal modulation is strong in the semi minor axis direction which leads us to deduce that it is due to the inclination. Moreover, the star is shifted towards the most brilliant part of the inner rim. It indicates that the inner rim has a non-negligible height. The outer ring suggests the continuation of the disk, or a part of the disk which is not self shadowed, or a halo. The constrains are poor so we can not conclude on its origins.

The results are shown in Table 2. They are closed to the images get by reconstruction. The results are also consistent with that found with previous observations(Monnier et al. 2009; Borges Fernandes et al. 2011). The authors found similar *P.A.* with close values of the inclination of the most luminous extended object.

The fit of the chromatism, indicates us a black body temperature of the inner rim of $\approx$ 1500K (see Table 1). This is approximately the dust sublimation temperature found in the litterature (Duschl et al. 1996; Dullemond & Monnier 2010).

Table 1. The parametric fit results. The acronyms are described in the section 3.3.

χ^2	3.53							
Star			Ring 1			Ring 2		
Parameter	Value	Error	Param.	Value	Error	Param.	Value	Error
sfr_0	18.0 %	± 0.7%	$r1fr_0$	58.7%	± 1.1%	$r2fr_0$	23.3 %	± 1.8%
			T_1	1482 K	± 79 K	T_2	1326 K	± 48 K
x_*	-0.22 mas	± 0.01 mas	rr_1	1.76 mas	± 0.02mas	rr_2	3.90 mas	± 0.02 mas
y_*	0.40 mas	± 0.01 mas	w_1	1.94 mas	± 0.13 mas	w_2	13.44 mas	± 0.32 mas
			P.A.	71.67	± 0.64ą	*P.A.*	71.67ą	± 0.64ą
			i_1	52.6	± 1.3	i_2	67.7	± 1.4
			c_1	0.126	± 0.013	c_1	0.126	± 0.013
			s_1	-0.593	±0.033	s_1	-0.593	± 0.033

Table 2. The previous interferometry results on MWC 158. Some results were complete on instruments watching at longer wavelengths (10.7 or 2.2 μm). The *P.A.* are consistent and the inclinations i also.

FWHM	FWHM2	i	*P.A.*	χ^2	λ_0	Ref.
66 ±4		45	63 ± 6	1	10.7 μm	Monnier et al. (2009)
64.7 ±0.6		70.1 ± 0.7	59.1 ± 1.7	5.1	10.7 μm	Borges Fernandes et al. (2011)
35.2 ±1.5	131.4 ± 11.2	56.7 ± 0.4	65.9 ± 2.0	1.9	10.7 μm	Borges Fernandes et al. (2011)
4.4 ±0.5		54 ± 8	66 ± 9	40.8	2.2 μm	Borges Fernandes et al. (2011)
3.0 ±0.4	≥14.0	54 ± 8	77 ± 2	13.3	2.2 μm	Borges Fernandes et al. (2011)

5 Conclusions

The chromatic effect due to the flux predominances of two objects of different sizes is well understood and can be used in order to find astrophysical information of the object. In the case of Herbig AeBe stars we are able to have an approximation of the temperature of the components. If the chromatic information is given, we can perform gray disk image reconstructions. They are contributing to the astrophysical analyze of the object because they shows the P.A. and the inclinations of the disk. Moreover, in the case of MWC158 it brought us the idea of the second extended component. By the fit we were able to find the inner rim radius and its temperature and to compare what we found with the data from photometry. We bring the first confirmation of the dust sublimation temperature at the inner rim. The information taken from the NIR interferometry and the chromatic effect argue in favor of a young nature of MWC 158.

The main challenge is to be able to make chromatic Young Stellar Objects image reconstructions keeping the super spectral synthesis and without information on the total flux variation. One of the thing which is in process of testing, is the adaptation of the `Mira` algorithm to the case of young stellar object. The "gray" `mira` free parameters are the image pixels intensities. If we define the image as the image of the dust at λ_0, the start can be represented by a dirac at the center of the image. Hence, we can put the stellar flux and a stellar relative spectral power law as additional parameters to the fit. Since the regularization will tend to smooth the Fourier plan, the algorithm will favors the added parameters to fit the fixture.

We would like to thank the A.N.R. POLCA which is funding this study.

References

Adams, F. C., Lada, C. J., & Shu, F. H. 1988, ApJ, 326, 865
Andrillat, Y. & Houziaux, L. 1991, IAU Circ., 5164, 3
Benisty, M., Natta, A., Isella, A., et al. 2010, A&A, 511, A74
Berger, J.-P. 2003, in EAS Publications Series, Vol. 6, EAS Publications Series, ed. G. Perrin & F. Malbet, 23
Borges Fernandes, M., Kraus, M., Chesneau, O., et al. 2009, A&A, 508, 309
Borges Fernandes, M., Meilland, A., Bendjoya, P., et al. 2011, A&A, 528, A20
Cabrit, S. 2003, Ap&SS, 287, 259
Cabrit, S., Ferreira, J., Dougados, C., & Garcia, P. 2010, Highlights of Astronomy, 15, 261
Dougados, C., Bouvier, J., Ferreira, J., & Cabrit, S. 2005, in IAU Symposium, Vol. 226, Coronal and Stellar Mass Ejections, ed. K. Dere, J. Wang, & Y. Yan, 491–500
Dougados, C., Cabrit, S., Ferreira, J., et al. 2004, Ap&SS, 293, 45
Dullemond, C. P. & Monnier, J. D. 2010, ARA&A, 48, 205
Duschl, W. J., Gail, H.-P., & Tscharnuter, W. M. 1996, A&A, 312, 624
Eisner, J. A., Graham, J. R., Akeson, R. L., & Najita, J. 2009, ApJ, 692, 309
Hutsemekers, D. 1985, A&AS, 60, 373
Le Bouquin, J.-B., Berger, J.-P., Lazareff, B., et al. 2011, A&A, 535, A67
Lynden-Bell, D. & Pringle, J. E. 1974, MNRAS, 168, 603
Malbet, F., Benisty, M., de Wit, W.-J., et al. 2007, A&A, 464, 43
Monnier, J. D. & Millan-Gabet, R. 2002, ApJ, 579, 694
Monnier, J. D., Tuthill, P. G., Ireland, M., et al. 2009, ApJ, 700, 491
Petrov, R. G., Malbet, F., Weigelt, G., et al. 2007, A&A, 464, 1
Pogodin, M. A. 1997, A&A, 317, 185
Ragland, S., Ohnaka, K., Hillenbrand, L., et al. 2012, ApJ, 746, 126
Tannirkulam, A., Monnier, J. D., Harries, T. J., et al. 2008, ApJ, 689, 513
Tatulli, E., Isella, A., Natta, A., et al. 2007, A&A, 464, 55
Thiébaut, E. 2008, in Society of Photo-Optical Instrumentation Engineers (SPIE) Conference Series, Vol. 7013, 70131I
van Leeuwen, F. 2007, A&A, 474, 653

SF2A 2012
S. Boissier, P. de Laverny, N. Nardetto, R. Samadi, D. Valls-Gabaud and H. Wozniak (eds)

THE LARGE-SCALE ENVIRONMENT OF BETELGEUSE FROM RADIO OBSERVATIONS

T. Le Bertre[1], L. D. Matthews[2] and E. Gérard[3]

Abstract. We present H I data obtained with the Nançay Radiotelescope and with the Very Large Array (VLA) on the red supergiant α Ori (Betelgeuse). The high spectral resolution allows us to identify three components emitting in narrow spectral lines (FWHM ~ 3 km s^{-1}).

By selecting different ranges of baselines from the VLA data, it is possible to obtain images revealing different structures in the environment of α Ori. The confusion arising from the emission by the interstellar medium on the same line of sight can also be identified and thus be mitigated by filtering short spacings.

The H I data reveal a quasi-stationary detached shell of neutral atomic hydrogen $\sim 4'$ in diameter ($\sim$0.24 pc at 200 pc), and also atomic hydrogen emission associated with the $6'$ radius far-infrared arc discovered by IRAS and with a newly discovered far-ultraviolet emitting arc.

Keywords: circumstellar matter, stars: individual: α Ori , supergiants, stars: mass-loss, radio lines: stars

1 Context

Red supergiants are massive stars in a short evolutionary stage preceding a supernova explosion. They have an extended atmosphere and lose matter at a high rate. They contribute to the enrichment of the interstellar medium (ISM), directly through mass loss, and indirectly as progenitors of supernovae or Wolf-Rayet stars. However, they are rare and many processes acting in these objects are not well understood.

α Ori is the closest red supergiant (d $\sim$ 200 pc). As such it is a favorite target for detailed studies of this class of objects. The stellar surface is now resolved with interferometric techniques at near-infrared wavelengths ($\phi \sim 45$ mas, or 9 au, Hautbois et al. 2009). The ejected material has been imaged at mid-infrared wavelengths (Kervella et al. 2011). These images revealed a complex structure of the circumstellar envelope that extends from a few au to a few 10^3 au. Further away the stellar wind is seen to interact with the surrounding medium in an arc of $6'$ radius and $1'$ thickness first detected by IRAS at 60 and 100 μm (Noriega-Crespo et al. 1997).

The far-infrared arc discovered by IRAS has been resolved into several thin shells by Herschel (Cox et al. 2012). This structure has been interpreted as a bow shock resulting from the interaction of the stellar wind with the surrounding ISM. It has also been detected in the FUV by GALEX (Le Bertre et al. 2012).

2 Observations

The large-scale environment of Betelgeuse can give clues on the past history of mass loss, and on the injection of stellar matter into the ISM. Radio observations in the H I line at 21 cm can give unique information on the kinematics in this region. However the spectra at 21 cm in the direction of α Ori are dominated by the emission of interstellar matter on the same line of sight (Fig. 1, left). On the other hand, position-switched observations obtained with the Nançay Radiotelescope (NRT) have revealed an H I source of diameter $\sim 4'$, centered on α Ori. The line profile is narrow (FWHM$\sim$3 km s^{-1}) and centered on the stellar radial velocity (Fig. 1, right). Observations have also been obtained with the Very Large Array (VLA) in the C configuration (0.08 to 3.2 km baselines; Bowers & Knapp 1987) and in the D configuration (0.035 to 1.0 km baselines; Le Bertre et al. 2012).

[1] LERMA, UMR 8112, CNRS and Paris Observatory, 61 av. de l'Observatoire, F-75014 Paris, France
[2] MIT Haystack Observatory, Off Route 40, Westford, MA 01886, USA
[3] GEPI, UMR 8111, CNRS and Paris Observatory, 5 place J. Janssen, F-92195 Meudon Cedex, France

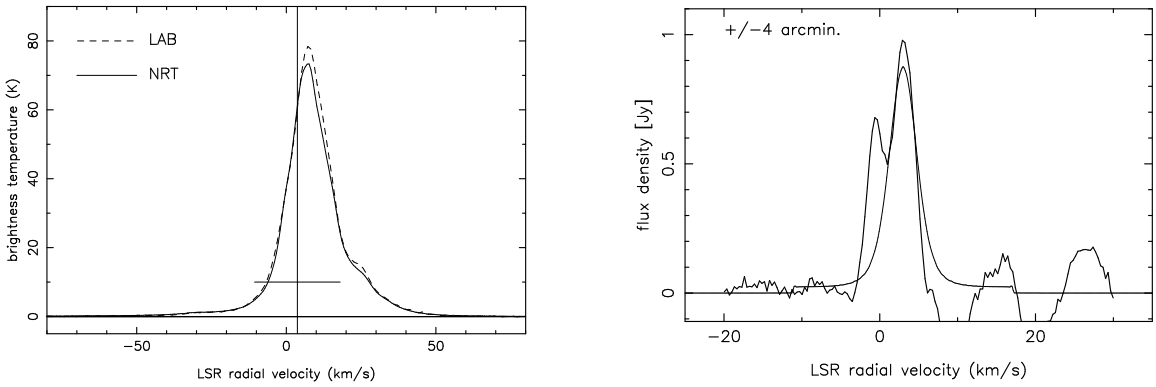

Fig. 1. Left: Frequency-switched spectrum obtained at the NRT in the direction of α Ori, compared to the spectrum from the Leiden-Argentina-Bonn (LAB) atlas (Kalberla et al. 2005). The horizontal bar represents the velocity extent of the CO emission from the α Ori stellar wind (Huggins et al. 1987), corresponding to a stellar radial velocity, $V_\star$=3.7 km s^{-1} (vertical line), and a wind expansion velocity, V_{exp}= 14.3 km s^{-1}. **Right:** Position-switched spectrum obtained at the NRT (+/− 4′) in the east-west direction. The thin line is a fit by a stationary detached shell model developed by Le Bertre et al. (2012).

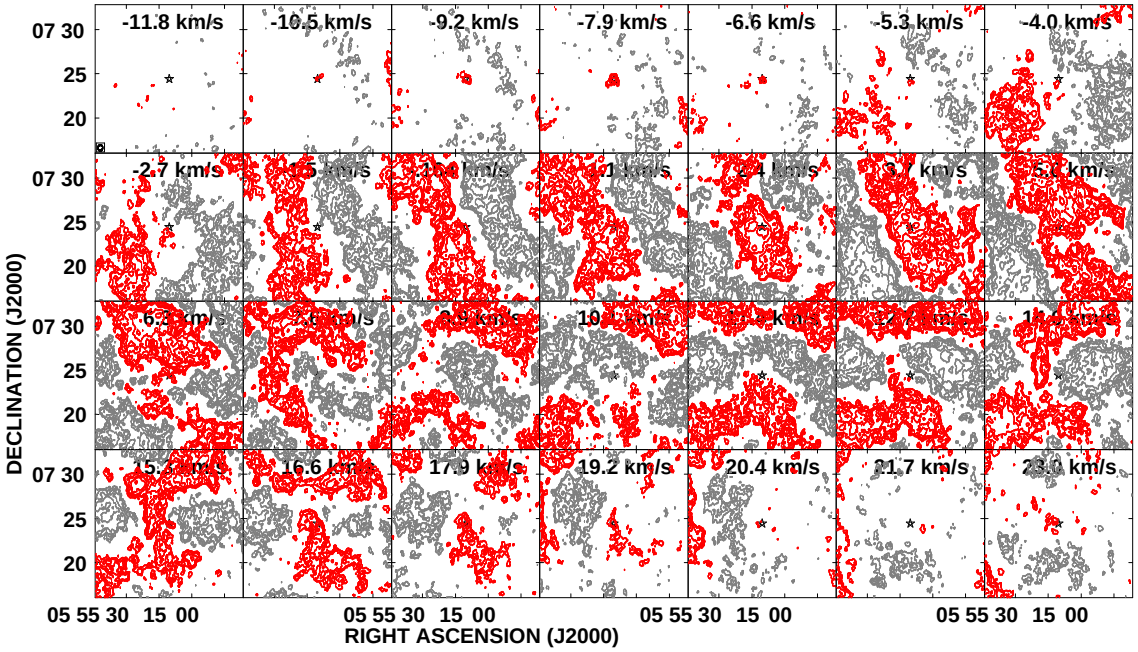

Fig. 2. VLA channel maps, all baselines. The positive contours are in red, and the negative ones in grey. The synthesized beam has a size of ∼35″. The star symbol marks the position of α Ori.

In Fig. 2 we show the result of combining the VLA C and D configuration observations. The large-scale Galactic emission is poorly spatially sampled, resulting in patterns of strong positive and negative mottling across a number of channel maps. Despite this contamination, two emission features coincident with α Ori can be seen from –9.2 to –6.6 km s^{-1} and from 17.9 to 19.2 km s^{-1}. These features correspond to the extreme velocities expected from the wind of α Ori.

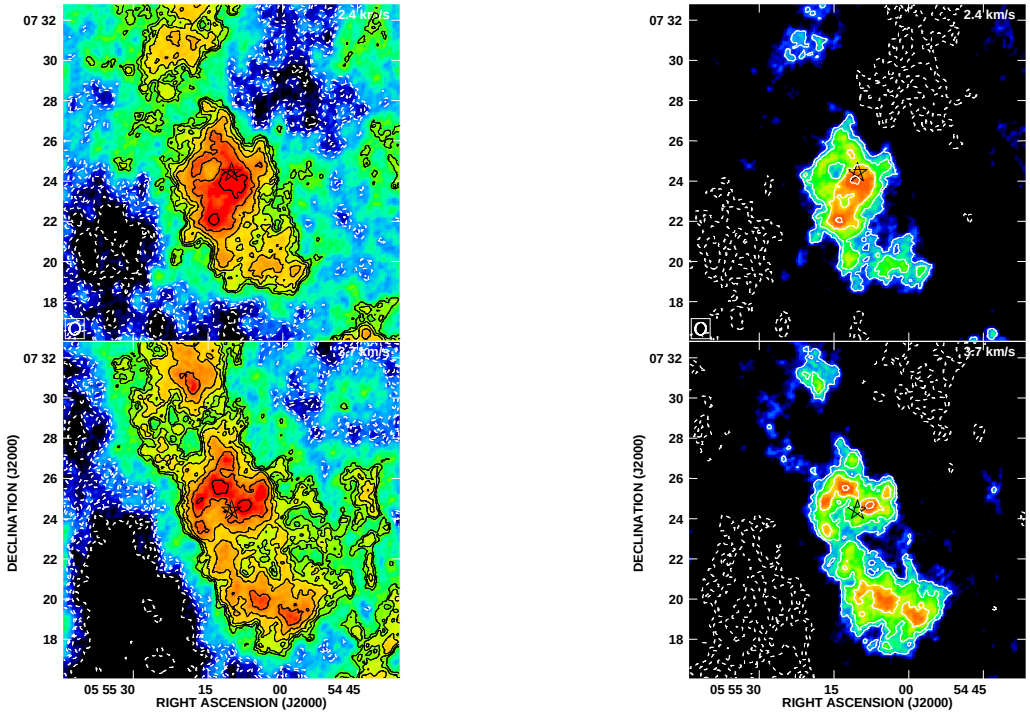

Fig. 3. Left: Channel maps at 2.4 km s^{-1} (top) and at 3.7 km s^{-1} (bottom). The dashed lines represent negative contours. **Right:** Same as on the left, but restricted to baselines larger than 0.2 kλ (0.042 km).

Furthermore, in the 2.4 and 3.7 km s^{-1} channel maps, there is a source of $\sim 4'$ (0.24 pc at a distance of 200 pc) that is better seen when the data are restricted to baselines larger than 0.2 kλ (Fig. 3), thanks to the resulting filtering of the extended interstellar emission. The line profile and the size correspond to the source detected by the NRT. Emission peaks delineate a ring around α Ori. A tail in the direction opposite to the star's space motion is also visible. This structure is similar to the quasi-stationary detached shells observed around a number of Asymptotic Giant Branch stars (e.g. Libert et al. 2007; Matthews et al. 2008).

In order to facilitate the identification of small-scale features, we have also produced channel maps by restricting the baselines to those larger than 0.4 kλ (Fig. 4). These maps reveal a clear association of the H I emission in the four channels from 6.3 to 10.1 km s^{-1} with the far-IR arc discovered by IRAS. These velocities match the peak of interstellar emission. It is thus likely that the arc discovered in the far-IR is related to the compression of the interstellar medium surrounding α Ori by its stellar wind.

On the other hand, in the 2.4 and 3.7 km s^{-1} channel maps, only the peaks of emission remain. Selecting large baselines is very efficient in reducing the confusion, by cancelling the extended interstellar emission. This allows us to discover new features hidden by the confusion. However, it also removes part of the genuine emission from the source !

3 Summary

A quasi-stationary detached circumstellar shell of $\sim 4'$ diameter ($\sim$0.24 pc) has been detected in H I emission around α Ori. The far-IR arc discovered by IRAS has also been detected in H I, but in a velocity range different

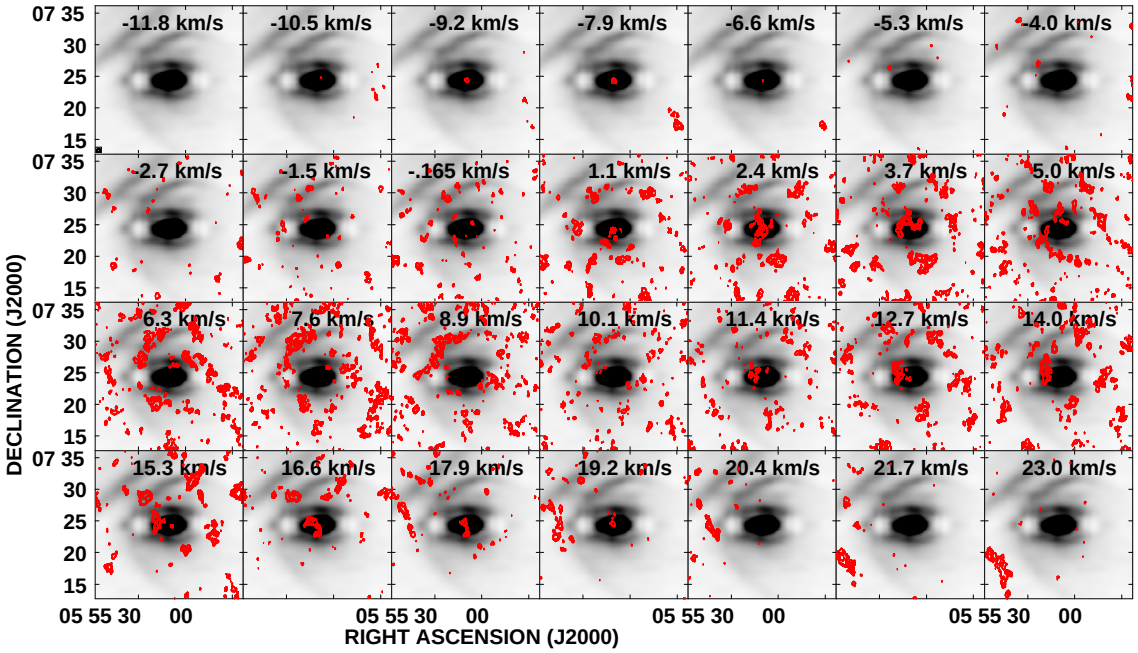

Fig. 4. VLA channel maps, restricted to baselines > 0.4 kλ (0.084 km). The negative contours have been suppressed. The background image is extracted from the IRAS survey at 60 μm. Note the association of H I emission with 60 μm emission in the four channels from 6.3 to 10.1 km s^{-1}.

from the detached shell. Multi-configuration VLA data have allowed us to uncover circumstellar H I structures on a variety of spatial scales and to disentangle emission associated with α Ori from the ISM.

The Nançay Radio Observatory is the Unité scientifique de Nançay of the Observatoire de Paris, associated as Unité de Service et de Recherche No. B704 to the French Centre National de la Recherche Scientifique (CNRS). The Nançay Observatory gratefully acknowledges the financial support of the Conseil Régional de la Région Centre in France. The VLA observations presented here are part of the NRAO programme AM1001. LDM acknowledges support from grant AST-1009644 from the National Science Foundation. This work has been supported financially by the PCMI.

References

Bowers, P. F., & Knapp, G. R., 1987, ApJ, 315, 305
Cox, N. L. J., Kerschbaum, F., van Marle, A.-J., et al., 2012, A&A, 537, A35
Haubois, X., Perrin, G., Lacour, S., et al., 2009, A&A, 508, 923
Huggins, P. J., 1987, ApJ, 313, 400
Kalberla, P. M. W., Burton, W. B., Hartmann, D., Arnal, E. M., Bajaja, E. et al., 2005, A&A, 440, 775
Kervella, P., Perrin, G., Chiavassa, A., Ridgway, S. T., Cami, J. et al., 2011, A&A, 531, A117
Le Bertre, T., Matthews, L. D., Gérard, E., & Libert, Y., 2012, MNRAS, 422, 3433
Libert, Y., Gérard, E., & Le Bertre, T., 2007, MNRAS, 380, 1161
Matthews, L. D., Libert, Y., Gérard, E., Le Bertre, T., & Reid, M. J., 2008, ApJ, 684, 603
Noriega-Crespo, A., van Buren, D., Cao, Y., & Dgani, R., 1997, AJ, 114, 837

SF2A 2012
S. Boissier, P. de Laverny, N. Nardetto, R. Samadi, D. Valls-Gabaud and H. Wozniak (eds)

REDUCTION AND ANALYSIS OF MUSE DATA

J. Richard[1], R. Bacon[1], P. M. Weilbacher[2], O. Streicher[2], L. Wisotzki[2], E. C. Herenz[2], E. Slezak[3], M. Petremand[4], A. Jalobeanu[4], C. Collet[4], M. Louys[4] and the MUSE and DAHLIA teams

Abstract. MUSE, the Multi Unit Spectroscopic Explorer, is a 2nd generation integral-field spectrograph under final assembly to see first light at the Very Large Telescope in 2013. By capturing $\sim 90,000$ optical spectra in a single exposure, MUSE represents a challenge for data reduction and analysis. We summarise here the main features of the Data Reduction System, as well as some of the tools under development by the MUSE consortium and the DAHLIA team to handle the large MUSE datacubes (about 4×10^8 pixels) to recover the original astrophysical signal.

Keywords: instrumentation, integral field spectrograph, data reduction, data analysis

1 Introduction

The Multi-Unit Spectroscopic Explorer (MUSE, Bacon et al. 2010) is a second generation instrument to be commissionned in 2013 on the Very Large Telescope (VLT, unit telescope UT4). It is an integral-field spectrograph operating in the visible wavelength range with two main modes of operation: the Wide Field Mode (1×1 arcmin field-of view, 0.2″/pixel) and the Narrow Field Mode (7.5″×7.5″, 0.025″/pixel), both with a spectral resolution of 1,800-3,600.

The instrument is specifically designed to exploit the capabilities of the VLT Adaptive Optics Telescope Facility (AO), which can use four laser guide stars and a natural guide star to apply corrections via a deformable secondary mirror. The main scientific goal of MUSE, to be carried out during the Guaranteed Time Observations, will be to study the high redshift Universe through the measurement of the Lyman-α signature in distant galaxies ($2.8 < z < 6.7$). Examples of other science topics include the study of nearby galaxies and intermediate redshift groups (up to $z = 0.8$) as well as globular clusters.

In order to fully cover such a large field-of view, the instrument is composed of 24 integral-field units, each observing in parallel a 24^{th} of the field. The light entering each unit is sliced and reimaged into 48 pseudo-slits, then propagated through a spectrograph before reaching a 4k×4k detector (Fig. 1).

In total, the data acquired by MUSE in a single exposure amounts for 86,400 optical spectra, or 3.6×10^8 pixels. A typical deep field observation with MUSE will have to combine ∼80 such exposures: this represents a challenge for data reduction and analysis.

2 MUSE data reduction

A dedicated Data Reduction System (DRS) is being developed by the MUSE consortium under supervision of AIP, and will be delivered to ESO together with the MUSE instrument. Most of the functionalities described hereafter are now fully functional or at the stage of final tests / improvements (Weilbacher et al. 2012).

The main task of the DRS is to convert the raw data coming from the 24 CCDs and create a fully calibrated datacube (in spatial, wavelength and flux coordinates), corrected for all sorts of instrumental and atmospheric effects. The system is designed to be embedded into the ESO data flow system and work as an automated

[1] CRAL, Université Lyon-1 and CNRS-UMR 5574, 9 avenue Charles André, 69561 Saint-Genis Laval Cedex, France
[2] Leibniz-Institut für Astrophysik (AIP), An der Sternwarte 16, D-14482 Potsdam, Germany
[3] Observatoire de la Côte d'Azur, Bd de l'Observatoire, BP4229, FR-06304 Nice Cedex 4, France
[4] LSIIT, UMR CNRS 7005, University of Strasbourg, B S. Brant, BP10413, 67412 Illkirch, France

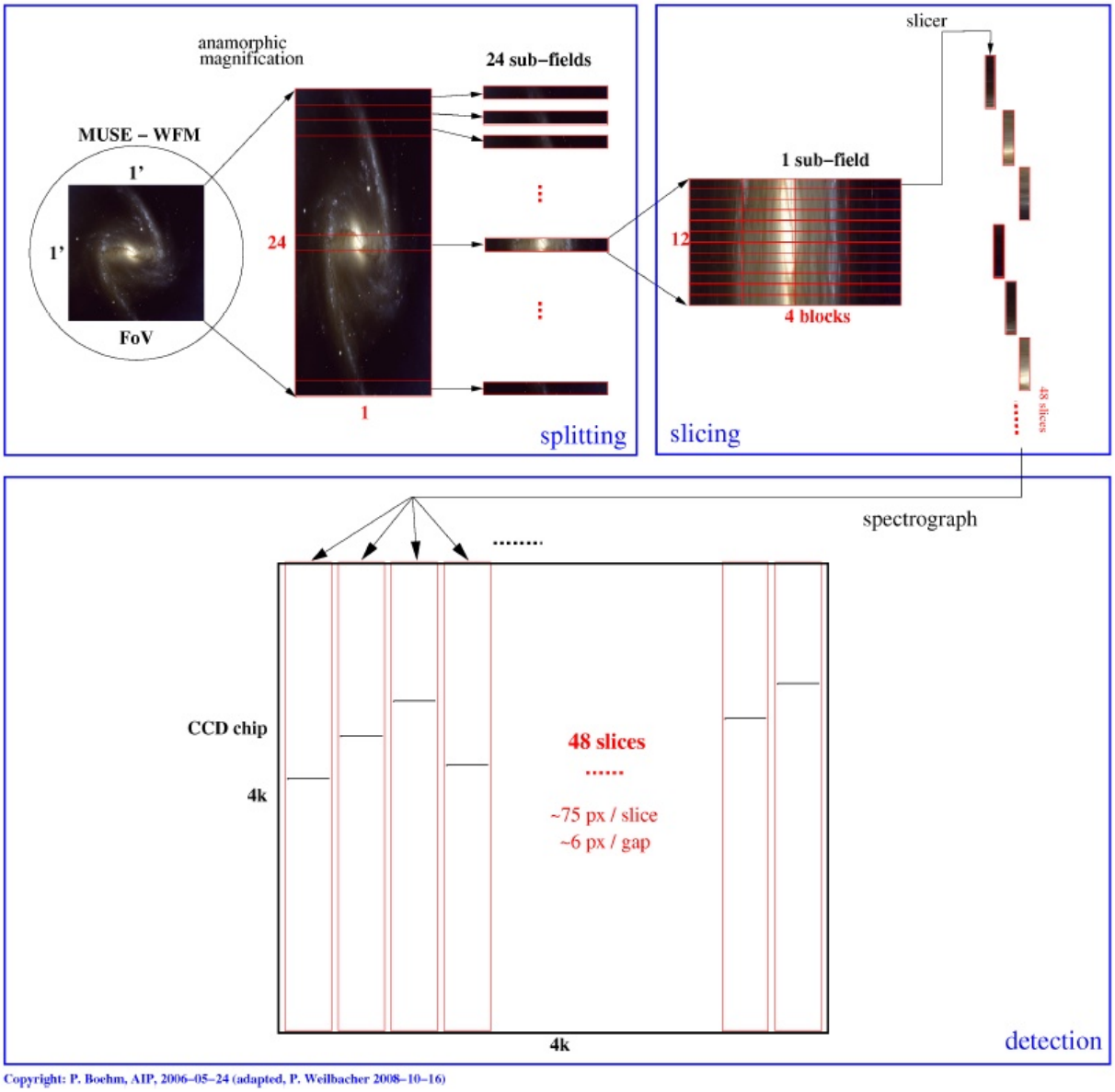

Fig. 1. Splitting of MUSE data: example given for the case of the Wide-Field Mode (WFM). The field splitter separates the $1' \times 1'$ field-of-view into 24 sub-fields (**top-left**), each entering a separate IFU and sliced into 48 pseudo-slits (top-right). The various spectra produced are imaged onto a 4k×4k detector (**bottom**). (Adapted from Weilbacher et al. 2009).

pipeline interfaced with the ESO tools esorex and gasgano, as for other second-generation instruments (e.g. XShooter). It is written in the C language using the ESO Common Pipeline Library.

In order to reach the best quality and reliability of the reduced data, only one interpolation step is performed at the end of the reduction to produce the final datacube. During the intermediate steps, the information from the 24 CCDs is propagated, for each pixel, in a master table called *pixel table*. Another important goal of the DRS is to propagate, throughout the data reduction steps, the error information corresponding to each pixel.

2.1 Data Reduction Cascade

The first steps of the DRS perform a classical reduction of each of the 24 CCDs:

- Creation of master bias, dark and flat-field frames.

- Creation of master tables for geometrical, tracing and wavelength calibrations.
- Then each science frame is corrected for bias, dark, flat and the *pixel table* is created with the pixel values and the corresponding positions and wavelengths.

In the second part of the data reduction cascade, the sky subtraction is performed on the entire pixel table, then the flux and astrometric calibrations are computed. Finally, the datacube (2 spatial axes and one wavelength axis) is constructed by a single interpolation of the pixel table.

2.2 Sky Subtraction

Sky subtraction is a very important step in the reduction of datacubes, especially in the red part of the spectrum where a large number of atmospheric emission lines dominate the background noise. This is also the region where MUSE will observe faint and distant Lyman-α emitters.

The current approach used in the DRS for sky subtraction is based on the modelling of the night sky (before resampling) into emission lines and continuum in single slices. This assumes a solid knowledge of the Line Spread Function (LSF) for each slice, which is modelled following the wavelength calibration using the brightest and most isolated lines of the arc exposures. More details on this sky subtraction method are presented in Streicher et al. (2011).

An alternative sky subtraction procedure is currently being tested. The approach used is perpendicular to the previous one, in the sense that the sky fit and subtraction is performed in the spatial (rather than the spectral) direction. Bright continuum objects, emission lines and cosmics are iteratively masked and removed from the fit. The main advantages of this classical sky subtraction is the low computing cost, and the fact that it does not depend on the knowledge of the LSF. However, it could be more vulnerable to the presence of bright objects in the case of crowded fields.

3 MUSE data analysis

3.1 Fusion of MUSE data

One of the main difficulties of the MUSE data analysis is to combine, in an optimal way, the signal obtained in multiple exposures taken under different atmospheric (seeing, transparency, sky variation) and instrumental (LSF, field location and orientation) conditions. In the DRS, this task is performed by directly interpolating multiple pixel tables into a single combined datacube during the final reduction step.

Alternatively, a more complex *fusion* task (named HyperFusion) has been developed in the DAHLIA group (Petremand et al. 2011a). A combined datacube is reconstructed by maximizing, in an optimal Bayesian context, a posterior probability built from the whole set of observations and their acquisition parameters.

Both the spatial (PSF) and spectral (LSF) responses are taken into account in this inverse problem. Compared to the "direct" approach, the *fusion* clearly improves the resolution of astrophysical sources (Figure 2), but this is a time-consuming process: combining 10 exposures take up to 5 days, compared to 2 hours with the DRS.

3.2 Visualisation of MUSE data

A dedicated tool, called *QuickViz* (Petremand et al. 2011b)[i] has been developed to help the MUSE users analyse such large datacubes. *QuickViz* is designed as a plugin for Aladin and is written in the Java language.

Specific features of *QuickViz* are the following:

- Coupled navigation between the spatial and spectral axes thanks both to calibrated cursors.
- Full use of multi-core architectures to load and handle large datacubes as well as extract spectra from.
- Data visualisation through multiple views, selections and simple processing algorithms.
- Visualisation of the associated variance to a datacube in the form of an animation.

[i] publically available at `http://lsiit-miv.u-strasbg.fr/paseo/cubevisualization.php`

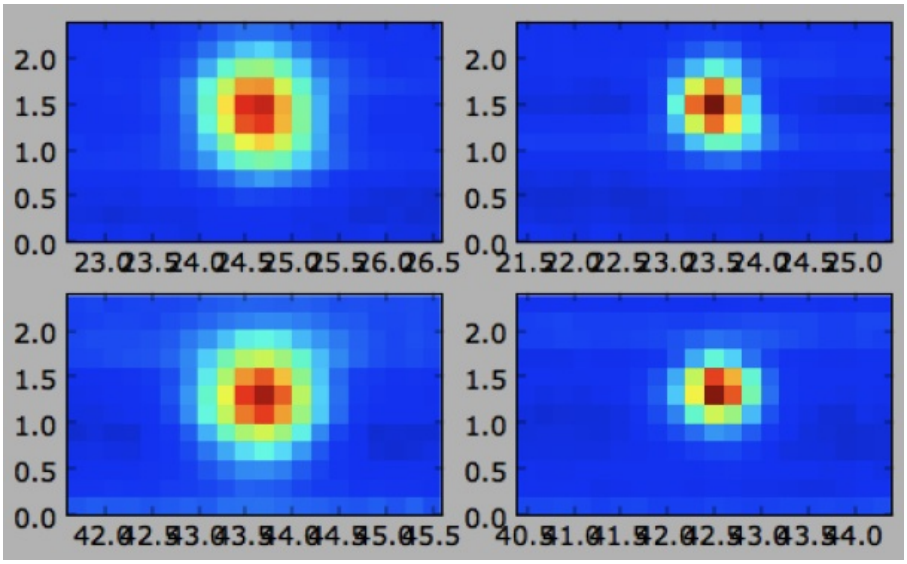

Fig. 2. Result of the fusion of MUSE datasets for 2 resolved sources using the direct method (**left** images) or the Bayesian fusion (**right** images).

3.3 Source detection and extraction

The MUSE datacubes will contain a large number of sources (up to a few thousands in the deepest fields), appearing through their spectral continuum over a large wavelength range or through emission lines (only detected on a few wavelength slices). Several data analysis tools are currently being developed in order to produce a clean catalog of all detected objects in a given datacube:

1. A classical approach uses an image analysis software (such as SExtractor) to produce a catalog of continuum sources from the *white-light* image (obtained by collapsing the full datacube) as well as emission line sources (detected on narrow-band images over a few wavelength slices).
2. A similar approach performs the fitting and subtraction of all continuum sources before searching for emission lines by cross-correlation of the full datacube with a simple line model.
3. Alternatively, more complex data mining techniques are used to "denoise" the full datacube and identify sources based on a simple dictionary of spectral shapes (Bourguignon et al. 2010, Fig. 3). These segmentation techniques can more easily de-blend overlapping sources.

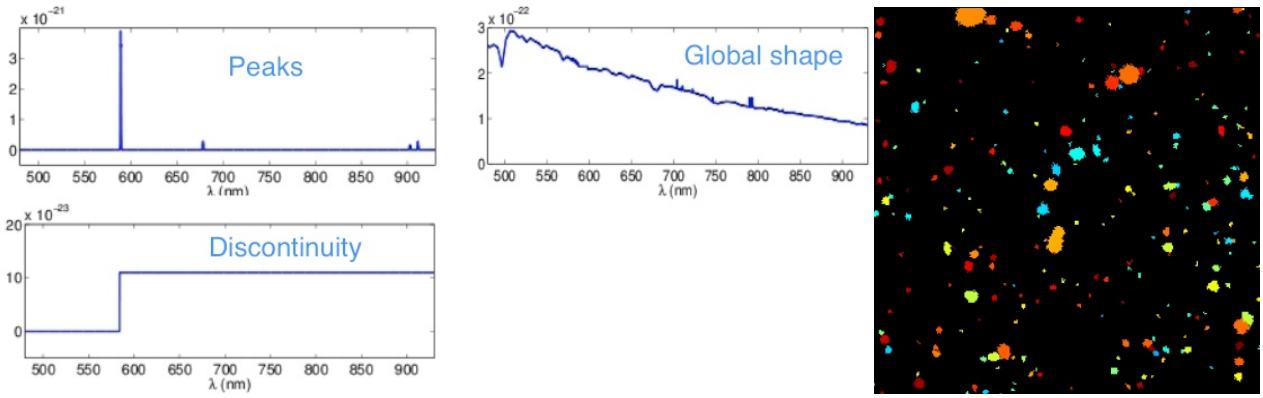

Fig. 3. Left: Example of "dictionary" of spectral shapes used in the segmentation technique: a given source spectrum is fitted by the linear combination of such shapes. **Right:** Example of datacube segmentation: sources are colored according to their spectrum.

4. Finally, a 'perpendicular' technique is the use of point marked processes (Chatelain et al. 2010) to identify sources assuming a simple morphological profile (elliptical shape, Sersíc).

This work was partially funded by the French Research Agency (ANR) through the DAHLIA project (grant ANR-08-BLAN-0253).

References

Bacon, R., Accardo, M., Adjali, L., et al. 2010, in Society of Photo-Optical Instrumentation Engineers (SPIE) Conference Series, Vol. 7735

Bourguignon, S., Mary, D., & Slezak, E. 2010, in ADA 6 - Sixth Conference on Astronomical Data Analysis

Chatelain, F., Costard, A., & Michel, O. 2010, in Acoustics, Speech and Signal Processing (ICASSP), IEEE International Conference, 3628

Petremand, M., Jalobeanu, A., & Collet, C. 2011a, in Statistical Methodology, 9

Petremand, M., Michel, L., & Louys, M. 2011b, in ASPC, Vol. 442, Astronomical Data Analysis Software and Systems XX, ed. I. N. Evans, A. Accomazzi, D. J. Mink, & A. H. Rots, 673

Streicher, O., Weilbacher, P. M., Bacon, R., & Jarno, A. 2011, in ASPC, Vol. 442, Astronomical Data Analysis Software and Systems XX, ed. I. N. Evans, A. Accomazzi, D. J. Mink, & A. H. Rots, 257

Weilbacher, P. M., Gerssen, J., Roth, M. M., Böhm, P., & Pécontal-Rousset, A. 2009, in ASPC, Vol. 411, Astronomical Data Analysis Software and Systems XVIII, ed. D. A. Bohlender, D. Durand, & P. Dowler, 159

Weilbacher, P. M., Streicher, O., Urrutia, T., et al. 2012, in Society of Photo-Optical Instrumentation Engineers (SPIE) Conference Series, Vol. 8451, 84510B

SF2A 2012
S. Boissier, P. de Laverny, N. Nardetto, R. Samadi, D. Valls-Gabaud and H. Wozniak (eds)

EXPLOITING THE REDUNDANCY IN SCANS WITH BOLOMETER ARRAYS

H. Roussel[1]

Abstract. The scanning (on-the-fly) observing mode is the most efficient for a wide range of mapping applications, but requires special processing techniques. This short article presents an algorithm designed to make use of the redundancy built in scan observations to subtract instrumental (or atmospheric) brightness drifts. Each point of the sky being scanned by several bolometers, at several times distributed over a significant fraction of the total observation duration, drifts can be extracted from the data with no a-priori knowledge of the noise characteristics and a minimal knowledge of the instrument.

Keywords: astronomical instrumentation, data processing, infrared, submillimeter

1 Introduction

Observations with bolometer arrays are affected by additive drifts, caused by low-frequency noise. If left uncorrected, the thermal part of this noise may strongly distort extended emission; the non-thermal part, visible in the form of striping, distorts compact sources and degrades the sensitivity. Since noise and signal spectral densities share the same frequency range, filtering techniques are inadequate except for point sources. The problem can be approached in two main ways: either by using a noise model and maximum-likelihood solver (Keihänen et al. 2004), or by devising an empirical tool to exploit the redundancy built in the scans.

The `Scanamorphos` public software (Roussel 2012) belongs to the second category and has been applied up to now to data from P-Artemis on APEX (André et al. 2008) and the PACS (Poglitsch et al. 2010) and SPIRE (Griffin et al. 2010) photometer arrays onboard Herschel (Pilbratt et al. 2010). The only assumption about the drifts consists in considering a minimum timescale below which they will not be corrected (ideally corresponding to their knee frequency), and the only requirement about the signal is its time invariance.

An advantage of the empirical approach is that results are immune to mismatches between noise models and realizations, and robust with respect to calibration and pointing errors. As no instrument model is relied on, an added benefit is to allow the calibration of some instrumental properties, based on science observations. In particular, `Scanamorphos` was used to calibrate the relative beam areas of the SPIRE photometer arrays (using bright extended emission from star formation regions), and provided an independent confirmation of the flat-field corrections derived by the PACS Instrument Control Center. The principles are intuitive and easy to understand, and the modularity allows subtle effects to be progressively incorporated.

The memory requirements of this class of tools induce a technical difficulty: the full history of all detectors is simultaneously needed, unless the field of view can be sliced into several blocks, then processed separately. However, the required level of redundancy is low for space observations, and several square degrees mapped with the blue array of PACS (2048 detectors) can be processed in one block with less than 48 Gb of memory.

For more details than is practical to give here, the reader is directed to the online documentation[i].

2 Principles

For Herschel, scan observations are performed as sketched in Figure 1a. In the most common case, there is an even number of scans, half in a given orientation and the other half in the perpendicular orientation, but neither the parity nor the orthogonality are mandatory. A typical weight map (number of samples weighted by the fractional area of each detector and its inverse square white noise) looks like Figure 1b. The level of redundancy per scan is of the same order for all Herschel arrays operated at the same scan speed, within a factor two.

[1] Institut d'Astrophysique de Paris, Université Pierre et Marie Curie (UPMC), CNRS (UMR 7095), 75014 Paris, France
[i] available at: `http://www2.iap.fr/users/roussel/herschel/`

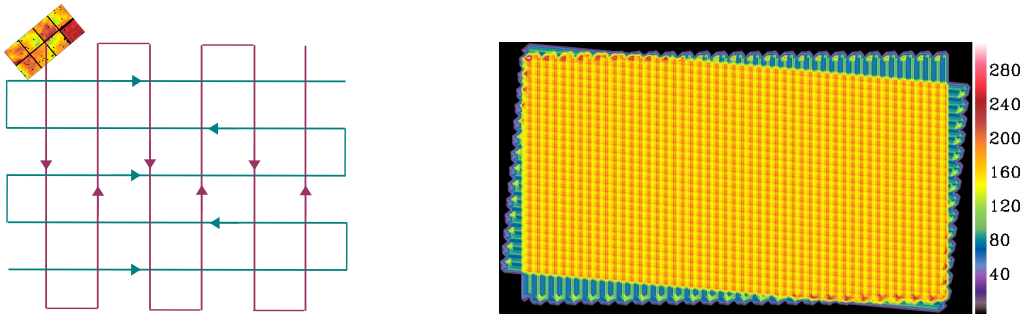

Fig. 1. Left: Schematic representation of a scan observation with the PACS blue array (made of eight 256-pixel subarrays). The colored lines show the trajectory of a detector in two orthogonal scans. There can be several repetitions of each orientation. **Right:** Weight map of a PACS observation combining 2 scans, projected on pixels of size FWHM (for the default final size of FWHM/4, the average coverage is of the order of 10 samples per pixel per scan pair).

The map size determines a boundary between long timescales (longer than the scan leg duration), that are not sampled properly by the observations, and short timescales, that do not require any assumption on the large-scale structure, contrary to the former. Drifts are first subtracted on the longest timescales (where their power spectral density is the largest), as linear baselines. The redundancy is used to determine time series that are coherent (producing the same map to first order) for all bolometers and all scans. The solution is not unique, but the aim is to preserve as well as possible genuine sky gradients. The algorithm is thus slightly different for fields containing bright extended emission, in which case the sky gradients can be comparable to the artificial gradients resulting from the thermal drift (Fig. 2). These two types of gradients can be separated owing to the strategy of scanning the sky at two very distinct scan angles. The process is iterative, building a new reference map after each step, applying an adaptive mask to the brightest sources and using robust linear fits. Once zero-order baselines have been subtracted, residual baselines are defined as the linear fit of the difference between the signal recorded by each bolometer and the signal simulated from the reference map. These residuals are subtracted from the data at each iteration, until the process converges.

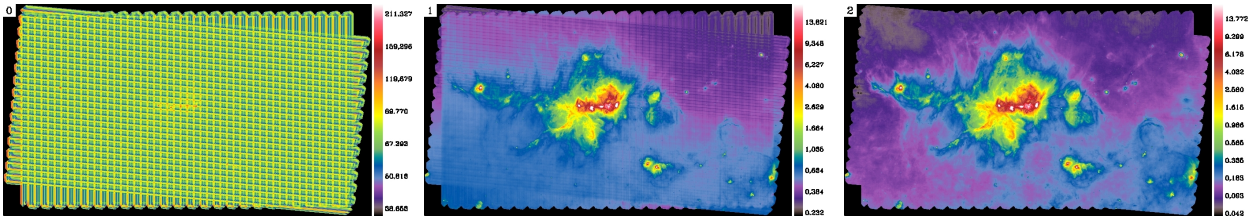

Fig. 2. Illustration of the drift subtraction on timescales above the scan leg crossing time, with the constraint of preserving genuine sky gradients. The target is the NGC 6334 star formation region (Russeil et al. 2012) from the HOBYS program (Motte et al. 2010). **Left:** Raw data. **Middle:** After subtraction of zero-order baselines (offsets). **Right:** After subtraction of linear baselines making use of the redundancy (destriping).

The correction for drifts on shorter spatial scales is based on the choice of a stability length l_s, within which the drifts are assumed constant and the signal uniform. An explicit mechanism is thus implemented to protect compact sources and sky gradients within l_s. This length is chosen equal to the average beam full width at half maximum (FWHM) by default, and increased if necessary, so that one can compute basic statistics from the samples of a bolometer crossing l_s. New spatial and temporal grids adapted to the problem are then set up, based on l_s and its crossing time T_c at the given scan speed.

Short-timescale drifts are decomposed into the drift averaged over all bolometers (abusively called thermal drift for convenience, since the latter is strongly correlated) and the individual drifts, that are uncorrelated (i.e. the flicker noise). The average drift is subtracted first, and the individual drifts subsequently. The signal recorded at time t by the bolometer b_i is described as:

$$R(t, b_i) = S(p) + \bar{D}(t) + D_{b_i}(t) + HF(t, b_i)$$

where $S(p)$ is the sky brightness in the pixel p sampled by b_i at time t, $\bar{D}$ is the average drift, D_{b_i} is the individual drift of bolometer b_i, and HF is the high-frequency noise (white noise and glitches).

In each pixel of size l_s, the contributing samples are grouped in distinct bolometer crossings, and crossings that have too few samples are rejected. A test is then applied to determine whether the assumption of signal uniformity is valid or not, by comparing the dispersion of each crossing with a noise threshold, computed from the spectral density of the relevant bolometer. If more than a predefined small fraction of the dispersions are higher than the thresholds, the pixel is likely to contain non-uniform emission, and no drift correction is computed. In the opposite case, only crossings with elevated dispersions (possibly affected by glitches) are rejected. Pointing corrections are then applied to the valid crossings, using the map built at the previous iteration, to cancel brightness differences caused by the different trajectories of the detectors within the pixel.

For the average drift, differences between pairs of crossings $\delta(t_{\mathrm{c}\,1}, t_{\mathrm{c}\,2}) = R(t_{\mathrm{c}\,1}, b_i) - R(t_{\mathrm{c}\,2}, b_j)$ are computed, and for each time pair projected on the coarse time grid $(t_{\mathrm{c}\,1}, t_{\mathrm{c}\,2})$, they are coadded regardless of the bolometers involved and the position on the sky:

$$\delta(t_{\mathrm{c}\,1}, t_{\mathrm{c}\,2}) = \bar{D}(t_{\mathrm{c}\,1}) - \bar{D}(t_{\mathrm{c}\,2}) + \mathrm{WM}_{p,i,j}\ [D_{b_i}(t_{\mathrm{c}\,1}) - D_{b_j}(t_{\mathrm{c}\,2})]$$

where WM stands for the weighted mean running on all pixels p and bolometers crossing p at times $t_{\mathrm{c}\,1}$ and $t_{\mathrm{c}\,2}$. The high-frequency noise vanishes in the coaddition and, since the individual drifts are uncorrelated, the WM term is also negligible provided the redundancy is sufficient. The coadded δ terms thus reduce to differences between the average drift at distinct times, $\bar{D}(t_{\mathrm{c}\,1}) - \bar{D}(t_{\mathrm{c}\,2})$. From the matrix of these differences, it is possible to reconstruct the absolute average drift as a function of time, using an iterative process. The solution is not unique: it is the superposition of the true average drift and an excess component, that has the same periodicity as the spatial coordinates (Fig. 3). To subtract the latter, we exploit the fact that it produces the same map for all successive scans (whereas the true drift never repeats itself), and has smoother variations.

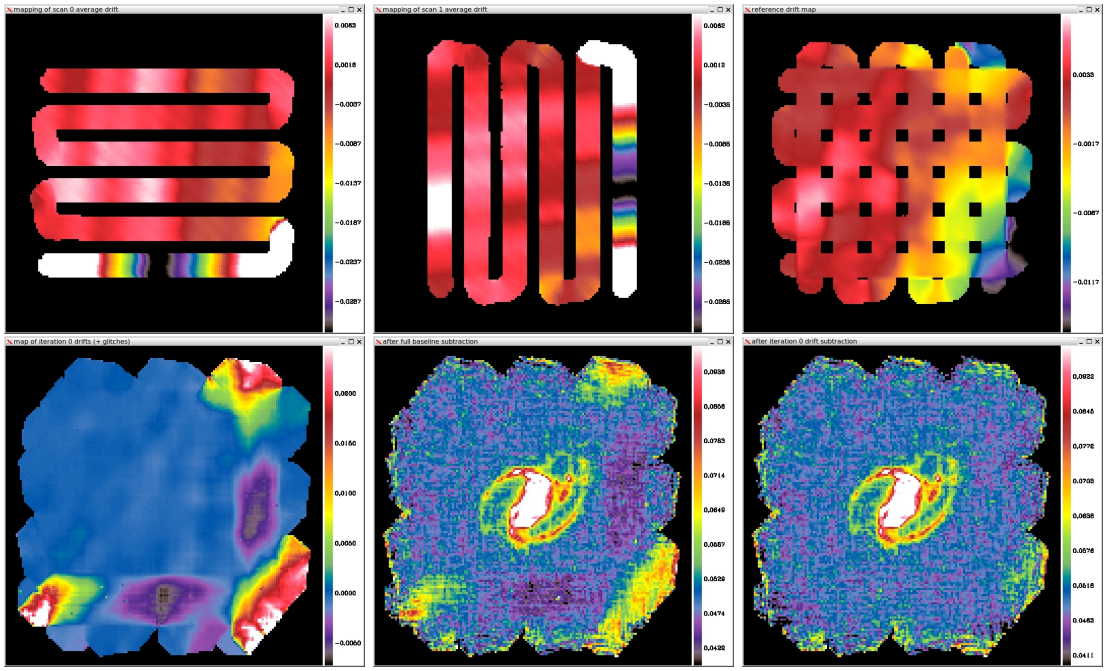

Fig. 3. Subtraction of the thermal drift, shown on an example where its effects are easy to see: a PACS observation of NGC 1097 from the KINGFISH survey (Kennicutt et al. 2011). The calibration frames taken before the scientific observations cause strong transients on two edges of the map. **Top left and middle:** Projections of the raw average drift computed from the $\bar{D}(t_{\mathrm{c}\,1}) - \bar{D}(t_{\mathrm{c}\,2})$ matrix, in the first scan (among 3) of each scanning direction. **Top right:** Projection of the excess drift. **Bottom left:** Projection of the true (raw - excess) average drift . **Bottom middle and right:** Maps of NGC 1097 before and after the average drift subtraction (on a coarse pixel grid).

For individual drifts, the difference between each crossing and the average of all valid crossings is computed:

$$\Delta(t_\mathrm{c}, b_i) = R(t_\mathrm{c}, b_i) - \mathrm{WM}_j[R(t_{\mathrm{c}\,k}, b_j)] = \bar{D}(t_\mathrm{c}) + D_{b_i}(t_\mathrm{c}) + HF(t_\mathrm{c}, b_i) - \mathrm{WM}_j[\bar{D}(t_{\mathrm{c}\,k}) + D_{b_j}(t_{\mathrm{c}\,k})]\ .$$

Since the average drift has been previously subtracted at all times, and given that the individual drifts are uncorrelated, $\Delta(t_c, b_i)$ reduces to the sum of the individual drift of bolometer b_i and its white noise binned on the coarse time grid. In practice, the redundancy is increased and the errors decreased when the corrections are first binned into much larger time intervals than T_c; the results are significantly improved in this case, as shown by Figure 4. For both the average drift and the individual drifts, the convergence is reached when the amplitude of the subtracted drifts has become smaller than the white noise for most bolometers.

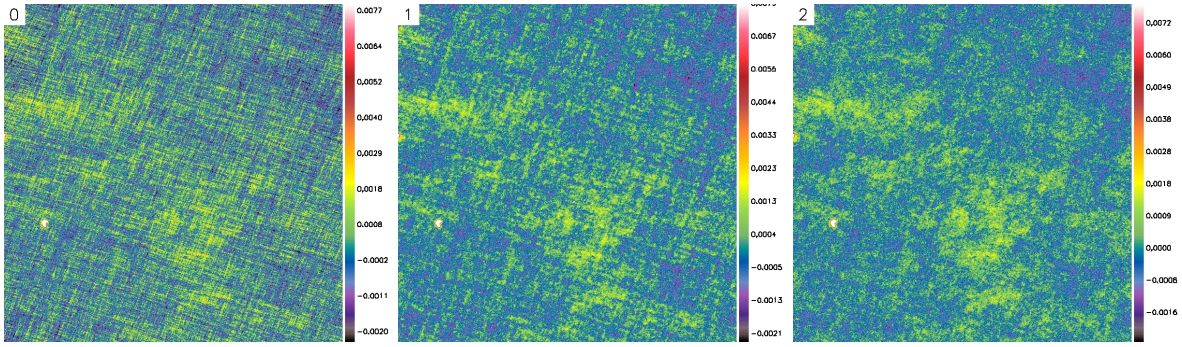

Fig. 4. Effect of performing the individual drift subtraction on various timescales, illustrated on a PACS observation from the HEVICS survey (Davies et al. 2010). The extracted image is about 2.2 degrees on a side and the displayed brightness range emphasizes very diffuse structures. **Left:** The drifts have been subtracted only on the longest timescales (above the scan leg crossing time). **Middle:** The subsequent iterations to subtract the drifts all have the minimum time step T_c . **Right:** They have successive time steps of $3^n \times T_c$, with integer $n = 3$ to 0 .

3 Example

Abundant visualizations of the different processing steps and simulation results are given in the companion paper (Roussel 2012). Let us remark that the amplitude of the individual drifts is low in SPIRE data, but of much higher amplitude with respect to the signal and white noise in PACS data. The PACS instrument is also affected by additional artefacts. The efficiency of the algorithm is thus best demonstrated on PACS data (but SPIRE data also make interesting test cases when they are affected by a so-called "cooler burp", i.e. an abrupt variation of the thermal drift slope as a function of time).

Here, we very briefly compare `Scanamorphos` with the two softwares that are fully implemented in the PACS pipeline, i.e. `PhotProject`, subtracting the low-frequency noise by means of a highpass filter applied after masking the source, and `MADmap`, a maximum-likelihood solver initially developed for CMB experiments (Cantalupo 2010), and adapted to the Herschel pipelines. We take as an example the galaxy M 82, observed as part of the Very Nearby Galaxies Survey (guaranteed time; P.I. C. Wilson). This target is chosen because its starbursting nuclear regions and dusty halo offer wide ranges of characteristic lengths and brightnesses, that are challenging for some classes of processing tools. Figure 5 shows the results and illustrates the advantages of using `Scanamorphos`. They can be succinctly summarized as follows: diffuse structures are not filtered, low-frequency noise is adequately subtracted even when superposed to an extended signal, and bright compact sources do not generate any distortions.

4 Concluding remarks

The main task of `Scanamorphos` is to correct for the brightness drifts caused by any type of additive low-frequency noise, using the redundancy built in scan observations. Other natural tasks of the same software are the masking of detector instabilities and glitches, since redundancy is necessary to distinguish these artefacts from real signal. The method outlined here is always applicable provided scans can be sliced into distinct scan legs (specifically for the destriping on the largest timescales, not for the drift subtraction on shorter timescales), and as long as there is as much redundancy as in Herschel observations (Fig. 1), even though an insignificant fraction of the field of view is covered by any single bolometer.

On the ground, the thermal drift is dominated by atmospheric fluctuations, occurring on smaller timescales than the drift originating in small temperature variations of the telescope and cryogenic bath. Consequently, the

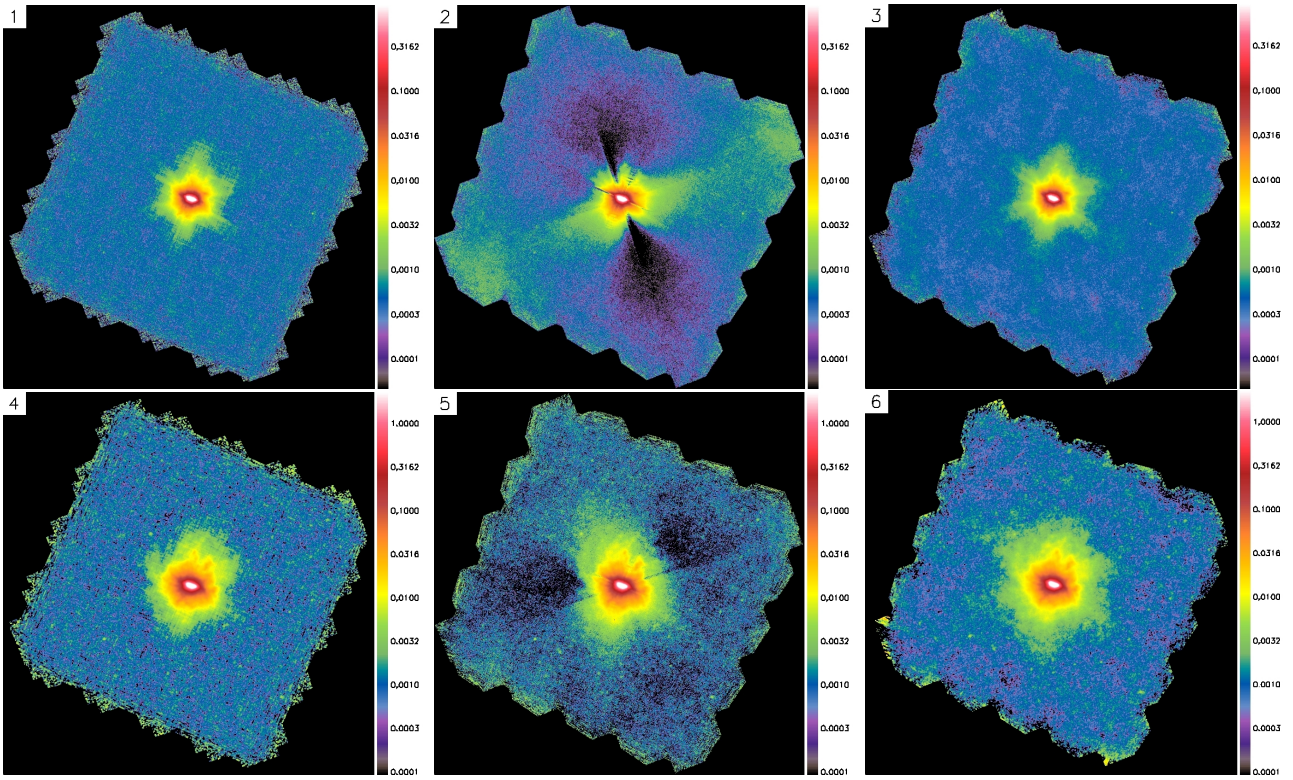

Fig. 5. Results of processing the PACS data of M 82 at 70 μm (top row) and 160 μm (bottom row) with three different tools. **Left:** PhotProject (1 and 4). **Middle:** MADmap (2 and 5). **Right:** `Scanamorphos` (3 and 6). The brightness scale (in Jy/pixel) is logarithmic and emphasizes faint structures.

method exposed above to subtract the average drift can be employed only if the sampling rate is high enough to allow a workable stability time T_c. For Herschel observations, it can take the values 5, 10 and 18.6 Hz, depending on the array and observing mode. In practice, it should be higher than a few times the knee frequency of the drift. Otherwise, either the data will remain heavily contaminated by the high-frequency component of the thermal noise, or it will be possible to restore only compact sources (i.e. much smaller than the array) by filtering the data. There is no such limitation for the uncorrelated drifts, because they are determined by detector and readout physics, and usually have smaller knee frequencies.

I am grateful to all the colleagues, too many to cite, who indirectly contributed to the continuous development of the software, by offering pieces of code to format the input data, expertise on the PACS and SPIRE instruments, test data pre-processed up to level 1, useful suggestions of new functionalities, and/or (last but not least) bug reports that were key in improving the code.

References

André, P., Minier, V., Gallais, P., et al. 2008, A&A, 490, L27
Cantalupo, C.M., Borrill, J.D., Jaffe, A.H., Kisner, T.S., & Stompor, R. 2010, ApJS, 187, 212
Davies, J.I., Baes, M., Bendo, G.J., et al. 2010, A&A, 518, L48
Griffin, M., et al. 2010, A&A, 518, L3
Keihänen, E., Kurki-Suonio, H., Poutanen, T., et al. 2004, A&A, 428, 287
Kennicutt, R.C., et al. 2011, PASP, 123, 1347
Motte, F., Zavagno, A., Bontemps, S., et al. 2010, A&A, 518, L77
Pilbratt, G.L., Riedinger, J.R., Passvogel, T., et al. 2010, A&A, 518, L1
Poglitsch, A., Waelkens, C., Geis, N., et al. 2010, A&A, 518, L2
Roussel, H. 2012, `http://arxiv.org/abs/1205.2576`
Russeil, D., Schneider, N., Anderson, L. D. et al. 2012, submitted to A&A

Session 17

High energy and cosmic phenomena (PCHE)

SF2A 2012
S. Boissier, P. de Laverny, N. Nardetto, R. Samadi, D. Valls-Gabaud and H. Wozniak (eds)

A MODEL FOR THE FLUX-R.M.S. CORRELATION IN BLAZAR VARIABILITY OR THE MINIJETS-IN-A-JET STATISTICAL MODEL

J. Biteau[1] and B. Giebels[1]

Abstract. Very high energy gamma-ray variability of blazar emission remains of puzzling origin. Fast flux variations down to the minute time scale, as observed with H.E.S.S. during flares of the blazar PKS 2155-304, suggests that variability originates from the jet, where Doppler boosting can be invoked to relax causal constraints on the size of the emission region. The observation of log-normality in the flux distributions should rule out additive processes, such as those resulting from uncorrelated multiple-zone emission models, and favour an origin of the variability from multiplicative processes not unlike those observed in a broad class of accreting systems.

We show, using a simple kinematic model, that Doppler boosting of randomly oriented emitting regions generates flux distributions following a Pareto law, that the linear flux-r.m.s. relation found for a single zone holds for a large number of emitting regions, and that the skewed distribution of the total flux is close to a log-normal, despite arising from an additive process.

Keywords: Relativistic processes, Galaxies: jets, Galaxies: active, Gamma rays: bursts

1 Introduction

The outbursts of PKS 2155-304 observed at very high energy (VHE, $E >$100 GeV) γ-rays with H.E.S.S. in July 2006 (Aharonian et al. 2007) constitute "the most dramatic [event] seen from any TeV γ-ray source" (Longair 2010) and this data-set indeed is a fantastic laboratory for the physics of blazars. Blazars are the Active Galactic Nuclei (AGN) with jets closely aligned with the line-of-sight (see e.g. Urry & Padovani 1995), they may be the best objects to probe this collimated emission of AGN, probably powered by accretion onto the central super-massive black hole (SMBH). Blazars are the prominent class of extragalactic sources detected at high energy (HE, 100 MeV$< E <$100 GeV) and VHE γ-rays. During scarce periods of high-state emission (so called "flares"), the VHE non-thermal emission can exhibit puzzling properties, the most striking of them probably being hyper-variability. The latter is characterized by an apparent violation of causality, i.e. a flux varying faster than the time needed for information to travel across the emitting region (light crossing time). For example, during the dramatic outbursts of PKS 2155-304 in July 2006, H.E.S.S. observed significant variations down to three *minutes* when the minimum size of the emitting region, bounded by the Schwarzschild radius of the SMBH, is estimated to be at least of three light-*hours*.

The commonly accepted way out this apparent violation of causality is to invoke the relativistic Doppler effect, which induces an observed variation-rate faster by a factor δ, the Doppler factor[i], than the variation time-scale in the emitting region frame. Doppler factors has large as 60 have been invoked to resolve the *minute-hour* discrepancy and to explain the optical thinness of the region to its own radiation (Begelman et al. 2008). The Doppler factor is related to the Lorentz boost and to the orientation of the emitting region, called *minijet* in the following, compared to the line-of-sight. An aligned region would then result in a maximal emission, a "flare", an the misalignment would result in sharp drop of the flux.

Several authors (Ghisellini & Tavecchio 2008; Giannios et al. 2009; Narayan & Piran 2012) have studied the flux resulting from the emission of multiple minijets, without however investigating its statistical properties. During the tremendous high-state of PKS 2155-304, its flux indeed exhibited an highly skewed distribution, interpreted in H.E.S.S. Collaboration, Abramowski et al. (2010) as log-normal[ii] and a linear correlation between the sample[iii] flux and its r.m.s. was observed.

[1] Laboratoire Leprince-Ringuet, Ecole polytechnique, CNRS/IN2P3, F-91128 Palaiseau, France

[i] The derivation of the Doppler factor is extensively discussed in the following.

[ii] If the logarithm of a variable is normally distributed then this variable has a log-normal distribution.

[iii] "Sample" refers here to quantities computed in successive time-windows within the light-curve.

2 Statistical properties of the flux of the minijets-in-a-jet

The textbook derivation of the Doppler factor δ is based on the transformation of velocities in special relativity. We hereafter exploit the fact that δ is the ratio of the observed to emitted photon energies, where the initial energy is expressed in the frame of isotropic emission. The Doppler effect does not explicitly depend on the energy of an hypothetical photon, but the use of this proxy largely simplifies the problem especially for geometries such as shown in Fig. 1, where a minijet is randomly oriented in a jet non-aligned with the line of sight.

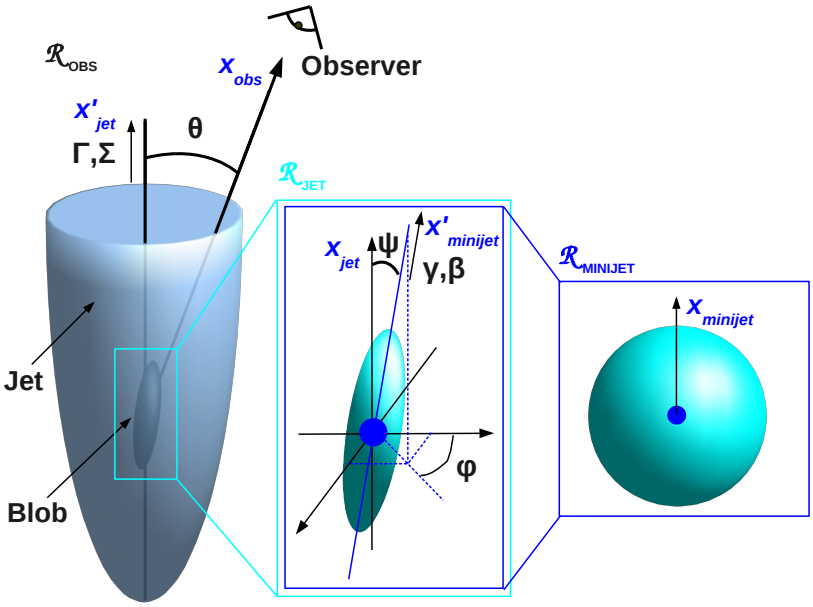

Fig. 1. Schematic view of the minijet scenario geometry. In the observer frame $\mathcal{R}_{\rm obs}$, the jet is tilted by angle θ from $x_{\rm obs}$ and is boosted by a Lorentz factor Γ (velocity Σ) along $x'_{\rm jet}$. The minijet is defined by its Lorentz factor γ (velocity β), in the jet frame $\mathcal{R}_{\rm jet}$. The minijet orientation $x'_{\rm minijet}$ is defined by the spherical angles ψ and φ, for an isotropic emission in the minijet frame $\mathcal{R}_{\rm minijet}$.

The transformation of the four-momentum, where only photons with energy E travelling along the line of sight are considered ($p_y = p_z = 0$ and $p_x = E$), is given in Eq. 2.1 :

$$\begin{bmatrix} E \\ E \\ 0 \\ 0 \end{bmatrix} = \begin{bmatrix} 1 & & & \\ & \mathrm{c}_\theta & \mathrm{s}_\theta & \\ & -\mathrm{s}_\theta & \mathrm{c}_\theta & \\ & & & 1 \end{bmatrix} \begin{bmatrix} 1 & & & \\ & \mathrm{c}_\psi & \mathrm{s}_\psi & \\ & -\mathrm{s}_\psi & \mathrm{c}_\psi & \\ & & & 1 \end{bmatrix} \begin{bmatrix} \Gamma & \Gamma\Sigma & & \\ \Gamma\Sigma & \Gamma & & \\ & & 1 & \\ & & & 1 \end{bmatrix} \begin{bmatrix} \gamma & \gamma\beta & & \\ \gamma\beta & \gamma & & \\ & & 1 & \\ & & & 1 \end{bmatrix} \begin{bmatrix} 1 & & & \\ & 1 & & \\ & & \mathrm{c}_\varphi & \mathrm{s}_\varphi \\ & & -\mathrm{s}_\varphi & \mathrm{c}_\varphi \end{bmatrix} \begin{bmatrix} E_{\rm minijet} \\ p_{x\ \rm minijet} \\ p_{y\ \rm minijet} \\ p_{z\ \rm minijet} \end{bmatrix} \tag{2.1}$$

where c and s are the cosine and sine functions.

Inverting this relation, the time-like component of the equation reads $E_{\rm minijet} = \delta^{-1}E$, with the inverse of the Doppler factor $\delta^{-1} = \gamma\Gamma(1 + \Sigma\beta\mathrm{c}_\psi - (\Sigma + \beta\mathrm{c}_\psi)\mathrm{c}_\theta) + \gamma\beta\mathrm{s}_\theta\mathrm{s}_\psi\mathrm{c}_\varphi$. In the blazar case, corresponding to a jet closely aligned with the line-of-sight, $\theta \sim 0$, the extrema of the Doppler factor in the ultra-relativistic limit are achieved for $\delta \geq \Gamma/\gamma$ and $\delta \leq 4\Gamma\gamma$.

Calling $I(E) = E\mathrm{d}N/\mathrm{d}E$ the flux intensity at the energy E, the quantity $I(E)/E^3$ is a Lorentz invariant (see, e.g., Rybicki & Lightman 1979). Note that the natural energy dependence of a non-thermal spectrum, such as observed at VHE, is a power-law model $I(E) \propto E^{-s}$, where s is the spectral index. Then, the Doppler effect impacts the intensity by a factor δ^{3+s}, which for $\theta = 0$ and $\mu = \mathrm{c}_\psi$ reads :

$$I(E) \propto \left[\gamma\Gamma(1-\Sigma)(1-\beta\mu)\right]^{-3-s} E^{-s} \equiv (4\Gamma\gamma)^{3+s} g(\mu) E^{-s} \tag{2.2}$$

where $g(\mu) = \left[(1+\Sigma)(1+\beta)/4 \ \times \ (1-\beta)/(1-\beta\mu)\right]^{3+s} \leq 1$ and with μ uniformly distributed in $[-1, 1]$, assuming an isotropic distribution of the minijets in the jet frame. The distribution of the intensity normalized to its maximum, $I_N = g(\mu)$, can easily be derived using the relation between its probability density function (PDF), $f_{\mathcal{I}}(I_N)$, and the PDF of μ, $f_{\mathcal{C}}(\mu) = 1/2$, which, by conservation of the cumulative distribution function under a change of variable, reads $f_{\mathcal{I}}(I_N) = \left|\partial g^{-1}(I_N)/\partial I\right| f_{\mathcal{C}}\left(g^{-1}(I_N)\right)$.

The PDF of the normalized distribution is then $f_{\mathcal{I}}(I_N) = (1+\Sigma)/2\beta \times \left[4\gamma^2(3+s)\right]^{-1} \times I_N^{-1-1/(3+s)}$. This power-law dependence of index $1+\alpha$, where $\alpha = 1/(3+s)$, is characteristic of Pareto distributions. Such variables are well known by geophysicists or economists (see the examples given in Newman 2005) and exhibit statistical properties of uttermost interest in the astrophysical case studied here.

First, these variables share a common feature with log-normal variables: they can be seen as the exponential of an underlying variable. Indeed, if a random variable X follows an exponential distribution $f_X(x) = \exp(-\alpha x)$, then $Y = \exp(X)$ is Paretian. Let's assume a small variation $\mathrm{d}x$ of X around x, then the resulting variation $\mathrm{d}y$ of Y around $y = h(x)$, where h is the exponential function, simply reads $(\mathrm{d}y)^2 = h'(x)^2(\mathrm{d}x)^2 = \exp(x)^2(\mathrm{d}x)^2 = y^2(\mathrm{d}x)^2$. Herein, y represents the sample flux of the source while $\mathrm{d}y$ is proportional to its r.m.s., so that the previous equation is directly the linear relation between the r.m.s. and its flux.

Secondly, ideal (i.e. un-bounded) Pareto distributions do not follow the central limit theorem (CLT). The CLT indeed relies on the hypothesis that the summed variables admit finite first and second order moments, which are undefined for Pareto distributions with $\alpha \leq 1$ and $\alpha \leq 2$ respectively. A generalized CLT can be applied in such situations and states that the sum of Pareto variables, herein the sum of the emission of minijets, tends to a maximally skewed α-stable distribution (see e.g. Zaliapin et al. 2005; Voit 2005).

As shown in the following, such heavy tailed distributions can easily be mistaken for log-normal distributions, with the limited dynamic range inherent to observations. Moreover, the tail of an α-stable distribution is a power-law of index $1+\alpha$, so that the linearity between the flux and its r.m.s. is conserved when adding the contributions of a large number of components.

3 Simulation of N minijets-in-a-jet

To generate smooth flux-distributions from Eq. 2.2, a simulation with 10^8 iterations, called hereafter time-steps, for a number of minijets $N \in \{1, 10, 30, 10^2, 3\times10^2, 10^3, 3\times10^3, 10^4\}$ is performed assuming Lorentz factors of the jet $\Gamma = 5$ and of the minijets $\gamma = 5$ (though the numerical values given in the following depend on these parameters, the qualitative results, which are the interest of this study, do not).

The distributions of the logarithm of the minijets summed flux intensities are shown in Fig. 2. For $N \geq 10^3$, the distributions exhibit a peak followed by a power-law tail of index $1+\alpha$. The right-side histograms in Fig. 2 shows the last two distributions, obtained for $N = 3\times10^3$ and $N = 10^4$ minijets, as an observer could see them. With a limited dynamic range (confusion of the low flux bins) and limited statistics or time-coverage (inability to record a significant amount of high flux points), these distributions exhibit similarities with a log-normal process, as shown by the solid black curves.

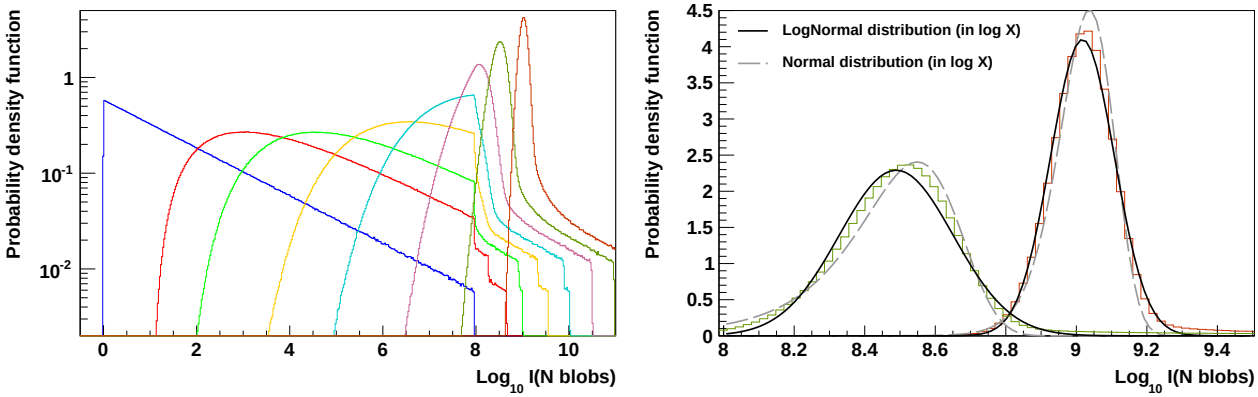

Fig. 2. Left: Distribution of the logarithm of the intensity of N independent and randomly oriented minijets. The number of minijets N increases from left to right with $N \in \{1, 10, 30, 10^2, 3\times10^2, 10^3, 3\times10^3, 10^4\}$. Even for a large number of regions, asymmetrical, tailed distributions are obtained. **Right:** Distribution of the logarithm of the flux of N minijets for $N = 3\times10^3$ (left) and $N = 10^4$ (right). The continuous black and grey dashed lines represent the best-fit with a log-normal and normal flux distributions, respectively. Note the linear y-axis.

The relation between the flux and its r.m.s. is shown for $N = 1$ and $N = 10^4$ minijets in Fig. 3. Using a simulation of 10^5 time-steps, the sample flux and its r.m.s. are computed in 10-points wide windows and are grouped in 50 bins of flux for clarity. The uncertainties on the r.m.s. are derived from the variance in each bin.

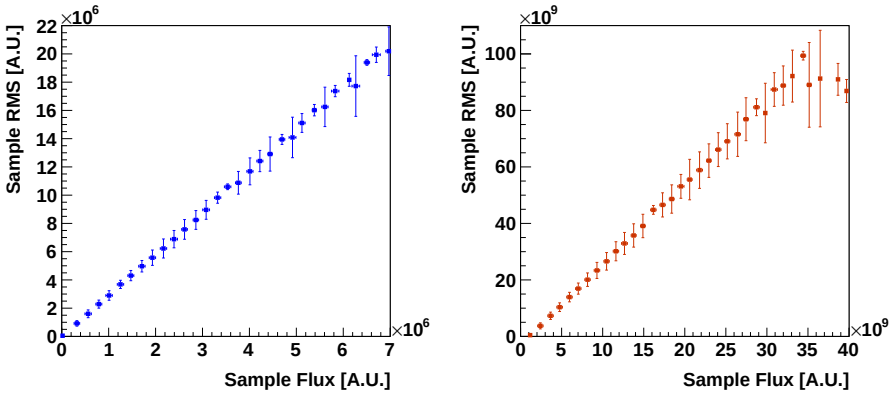

Fig. 3. Sample RMS as a function of the sample flux of $N = 1$ minijet (**left**) and the sum of $N = 10^4$ minijets (**right**). Linear relations are found in both cases, with a zero x-intercept in the first case and a positive one in the second.

While for $N = 1$, corresponding to a power-law distribution, a strict proportionality between the flux and its r.m.s. is achieved, a positive x-intercept can be seem for $N = 10^4$. This intercept corresponds to the peak of the emission shown in Fig. 2, i.e. to the flux for which the emission of the single components pile-up.

4 Conclusion

The dramatic outbursts of PKS 2155-304 constitute an extraordinary set of observables that are highly constraining for models of blazar variability. The observed statistical properties of the emission do not necessarily advocate for a multiplicative process, as could be inferred from a log-normal distribution (see e.g. Uttley et al. 2005; McHardy 2008, in the broader context of accreting objects) and these observables can be reproduced within an additive model summing Pareto variables.

We show that such a Pareto distribution of the flux of a single component is a natural consequence of minijets-in-a-jet modellings, originally developed to explain the hyper-variability, i.e. the apparent violation of causality observed in VHE light-curves. In addition to the skewed distribution of the flux, the sums of Pareto variables follow the linear flux-r.m.s. relation and are then a good representation of both temporal and statistical properties of the emission.

The potential evolutions of this model are diverse, since it can in principle be extended to any astrophysical sources where several boosted regions are involved. Remarkably, Clausen-Brown & Lyutikov (2012) recently derived a particular case ($\Gamma = 1$) of this minijets-in-a-jet statistical model to explain the flares of the Crab in the high energy domain. For this study, we did not focus on the properties of the emission in the Fourier space or as a function of energy, which would require a temporal and an energy-dependent prescriptions. Such developments will certainly be led in future studies.

References

Aharonian, F., Akhperjanian, A. G., Bazer-Bachi, A. R., et al. 2007, ApJ, 664, L71

Begelman, M. C., Fabian, A. C., & Rees, M. J. 2008, MNRAS, 384, L19

Clausen-Brown, E. & Lyutikov, M. 2012, arXiv:1205.5094

Ghisellini, G. & Tavecchio, F. 2008, MNRAS, 386, L28

Giannios, D., Uzdensky, D. A., & Begelman, M. C. 2009, MNRAS, 395, L29

H.E.S.S. Collaboration, Abramowski, A., Acero, F., Aharonian, F., et al. 2010, A&A, 520, A83

Longair, M. S. 2010, High Energy Astrophysics

McHardy, I. 2008, in Blazar Variability across the Electromagnetic Spectrum

Narayan, R. & Piran, T. 2012, MNRAS, 420, 604

Newman, M. 2005, Contemporary Physics, 46, 323

Rybicki, G. B. & Lightman, A. P. 1979, Radiative processes in astrophysics, ed. Rybicki, G. B. & Lightman, A. P. (New York: Wiley-Interscience)

Urry, C. M. & Padovani, P. 1995, PASP, 107, 803

Uttley, P., McHardy, I. M., & Vaughan, S. 2005, MNRAS, 359, 345

Voit, G. 2005, The statistical mechanics of financial markets, ed. New York : Springer

Zaliapin, I. V., Kagan, Y. Y., & Schoenberg, F. P. 2005, Pure and Applied Geophysics, 162, 1187

SF2A 2012
S. Boissier, P. de Laverny, N. Nardetto, R. Samadi, D. Valls-Gabaud and H. Wozniak (eds)

VHE GAMMA-RAY ASTRONOMY IN INDIA: STATUS OF HIGRO AND PARTICIPATION IN CTA

R. J. Britto[1], B. S. Acharya[2], J. M. Ahire[2], G. C. Anupama[3], N. Bhatt[4], P. Bhattacharjee[1], S. Bhattacharyya[4], V. R. Chitnis[2], R. Cowsik[3,5], N. Dorji[2], S. K. Duhan[2], K. S. Gothe[2], P. U. Kamath[3], R. Koul[4], P. K. Mahesh[3], P. Majumdar[1], J. Manoharan[3], A. Mitra[4], B. K. Nagesh[2], N. K. Parmar[2], T. P. Prabhu[3], R. C. Rannot[4], S. K. Rao[2], L. Saha[1], F. Saleem[3], A. K. Saxena[3], S. K. Sharma[2], A. Shukla[3], B. B. Singh[2], R. Srinivasan[3], G. Srinivasulu[3], P. V. Sudersanan[2], A. K. Tickoo[4], D. Tsewang[3], S. S. Upadhya[2], P. R. Vishwanath[3] and K. K. Yadav[4]

Abstract. Operating since 2008, HAGAR is the highest altitude gamma-ray experiment using the Cherenkov sampling technique. It is installed in the Himalayas, Nothern India, and constitutes the first phase of the Himalayan Gamma-Ray Observatory (HIGRO). HAGAR is oberving several Galactic and extragalactic sources, and results from Markarian 421 during the flare of February 2010 has been published. Results from Crab nebula are being finalised and upper limits on emission from pulsars have been presented. The second phase of HIGRO is the installation of the 21 m-diameter imaging telescope MACE in the near future, that may be followed by at least one more similar telescope. The Indian gamma-ray collaboration is also part of the Cherenkov Telescope Array (CTA) project, and is involved in site surveys in the Ladakh region (Northern India) for a possible location of CTA-North. Also, it is planned to participate in Monte Carlo simulations and calibration setup for CTA.

Keywords: gamma rays: atmospheric Cherenkov technique, methods: data analysis, R & D, telescopes: HAGAR, MACE, CTA

1 Introduction

Ground-based gamma-ray astronomy experiments in India have started as early as 1969 and these experiments were operationg in various parts of the country. Today, PACT (TIFR, located in Pachmarhi, Madhya-Pradesh) and TACTIC (BARC, located at Mont Abu, Rajasthan) are still in operation (Acharya 2005). These two experiments detect the Cherenkov light caused by relativistic particles of the gamma ray/cosmic ray induced showers, and are sensitive to the TeV domain. Another experiment, called GRAPES (located at Ooty, Tamil Nadu, South India), is a collaboration between TIFR and Osaka City University (Japan) and detect UHE gamma rays and cosmic rays through the relativistic secondary particles of the atmospheric particle/gamma-ray induced showers (Oshima et al. 2010).

2 Observations with HAGAR

Located at 4270 m amsl in the Ladakh region of the Himalayas, in Northern India (Latitude: 32°46′45″ N, Longitude: 78°58′36″ E), the HImalayan Gamma Ray Observatory (HIGRO) is the highest altitude ground-based gamma-ray observatory using the atmospheric Cherenkov technique. Phase 1 of HIGRO is the HAGAR experiment, operating fully since 2008. HAGAR is a sampling array of 7 telescopes, each one built with 7

[1] Saha Institute of Nuclear Physics, 1/AF, Bidhannagar, Kolkata 700 064, India
[2] Tata Institute of Fundamental Research, Homi Bhabha Road, Mumbai 400 005, India
[3] Indian Institute of Astrophysics, Sarjapur Road, 2^{nd} Block, Koramangala, Bangalore 560 034, India
[4] Bhabha Atomic Research Centre, Trombay, Mumbai 400 085, India
[5] Now at Washington University, St Louis, MO 63130, USA

Table 1. Summary of results obtained from Crab Nebula for event triggers generated by at least six telescopes out of seven.

Data sets	C	no. of selected pairs	duration	Count rate	N_σ	$N_\sigma/\sqrt{h}$
Crab	1	17	10.4 h	5.1 ± 0.7	7.8	2.4
	2	20	12.6 h	5.7 ± 0.6	9.5	2.7

para-axially mounted 0.9 m-diameter mirrors, giving a total reflective area of $\sim 31\ m^2$. Relative arrival time of Cherenkov shower front at each mirror is recorded using TDCs and Flash ADCs, in order to obtain a timing precision below 1 ns, to sample the Cherenkov flash. Technical details as well as analysis procedure are given in Britto et al. (2011a).

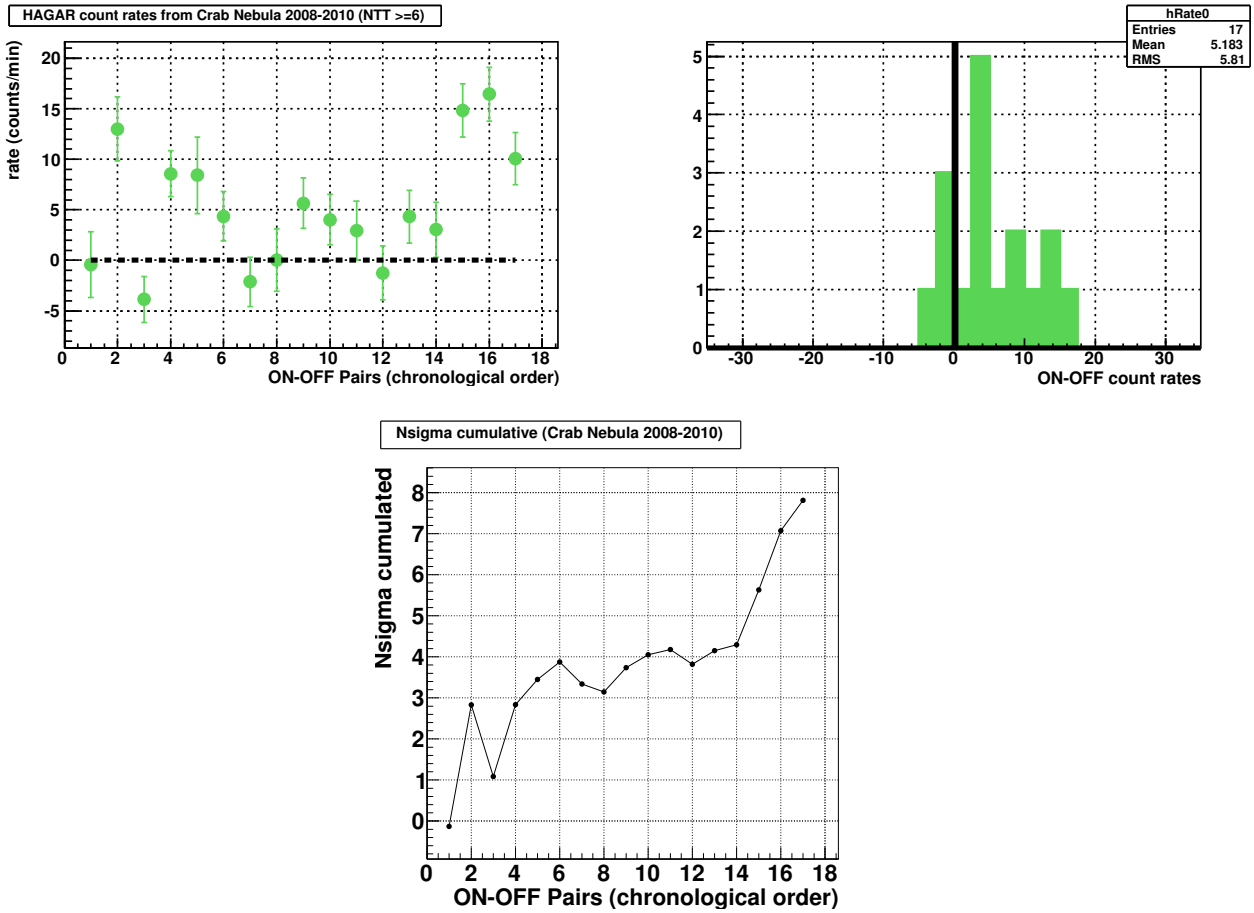

Fig. 1. Count rates of individual data sets (pairs), in chronological order, computed using C1, for the selected data set of Crab Nebula 2008-2011.

In order to remove isotropic emission due to cosmic rays, source observation region (ON) is compared with OFF-source region at same local coordinates. The analysis of data is based on the estimation of the arrival angle of the incident atmospheric shower w.r.t. the source direction. This angle – called space angle – is obtained for each event by measuring relative arrival times of the shower at each telescope. Signal is extracted after rejecting large space angle events, and following the process of normalisation of ON/OFF background events (at large space angle), to balance night sky background differences between both data samples. As the process of computing the normalisation constant 'C' is difficult due to the lack of statistics in the normalisation region, C is computed through two methods, as explained in Britto et al. (2011b). This gives the C1 and C2 values of C respectively, where C1 is the ratio of ON over OFF events in the tail of the space angles, where no gamma-ray s ignal is expected, and C2 is obtained by a more sophisticated method involving a χ^2 minimisation of the

distribution of bin-wise ON/OFF ratios of the same normalisation region in the tails of space angles.

2.1 Observations on Crab Nebula

Between September 2008 and February 2011, more than 120 hours of data have been collected from Crab Nebula. Using an event selection procedure, we performed the analysis of 10.4 hours of Crab Nebula data from the period 2008-2011 (Britto et al. 2011b). Because of the light contamination of the bright star ζ Tauri in the field-of-view of Crab nebula, results are reported for events which trigger at least six telescopes out of seven.

An excess at $7.8\,\sigma$ is reported, corresponding to 5.1 ± 0.7 *counts* min^{-1}, while computing the excess using C1. An excess of $9.5\,\sigma$, corresponding to $5.7 \pm 0.6\,\mathrm{counts\,min^{-1}}$, is obtained based on 12.6 hours of data and using the normalisation constant C2 (Fig. 1 and Table 1). Monte Carlo simulations predict $2.4\,\mathrm{counts\,min^{-1}}$ for vertical showers for a 1 Crab flux (Saha et al. 2011). However, through our current updates in the analysis method, we are getting now closer to the predicted values. The energy threshold of this analysis is expected to be around 300 GeV.

2.2 Observations on pulsars

Search for pulsed emission at the known period has been carried out for several pulsars, and preliminary analysis have been presented (Singh et al. 2011). Our first target were the Crab and Geminga pulsars. Along with these sources, we now observe J0357+3206, J0633+0632 and J2055+2539, detected by the Fermi Gamma-Ray Space Telescope, since they have high confidence pulsed emission, rotational energy loss rate and flat emission spectrum. Improvements in the analysis are going on for the search of pulsed emission.

2.3 Observations on Markarian 421 during its high activity state

HBL BL Lac AGN Markarian 421 (Mrk421, z=0.031) has been observed during its high activity state, in February-April 2010. Data analysis was performed on data with a zenith angle less than 6 degrees. We reported an excess of 13.4 ± 1.05 *count* min^{-1} at 12.7 σ based on 479 minutes of data during February 2010 (Shukla et al. 2012).

We show on Figure 2 (*Upper panel*) quasi-simultaneous light curves of Mrk 421, during February 2010, as obtained in X-ray and gamma-ray bands, using archived data from other observatories together with the present data. The light curves are plotted with one day binning (daily average) in the above figure. One zone homogeneous SSC model (Krawczynski et al. 2004) is fitted to the X-ray and gamma data to obtain the SED (Figure 2 *Lower panel*). This model assumes a spherical blob of radius R and uniform magnetic field B, moving with respect to the observer with the Lorentz Factor delta which is filled with a homogeneous non-thermal electron population. Best fit SED is obtained for the parameters given in Shukla et al. (2012).

3 Major Atmospheric Cherenkov Experiment (MACE)

Designed by the BARC group to combine the significant advantage of a high altitude and large collection dish (21 m-diameter), Major Atmospheric Cherenkov Experiment (MACE) is being contructed to enable high significance detection of gamma-ray sources above about 20 GeV (Figure 3 and Koul et al. (2005, 2011)). MACE is the second phase of HIGRO, and is expected to be installed at Hanle by 2013, next to the HAGAR array. It will have the following characteristics: a total reflective area of $\sim$330 m^2 from 356 mirror panels; f/1.2 m; FOV of $4^\circ \times 4^\circ$, a 1088 pixel camera. Detailed Monte Carlo simulations (using CORSIKA v6.735) are being carried out to understand the performance of the telescope. Simultaneous observations with HAGAR are expected, in such a way that the same event can be detected by both the experiments. MACE is expected to be operating at Hanle by 2013. We also expect at least a second similar imaging element to be installed later ne xt to the first element to perform stereoscopic observations (MACE II project).

Foundations for the first imaging telescope and building of the control room of MACE at Hanle are well advanced (Figure 3). Installation of MACE is now going on near the city of Hyderabad, South India (Figure 4). This will allow a phase of calibration and observations of Crab Nebula for a few months before the instrument is shifted to Hanle.

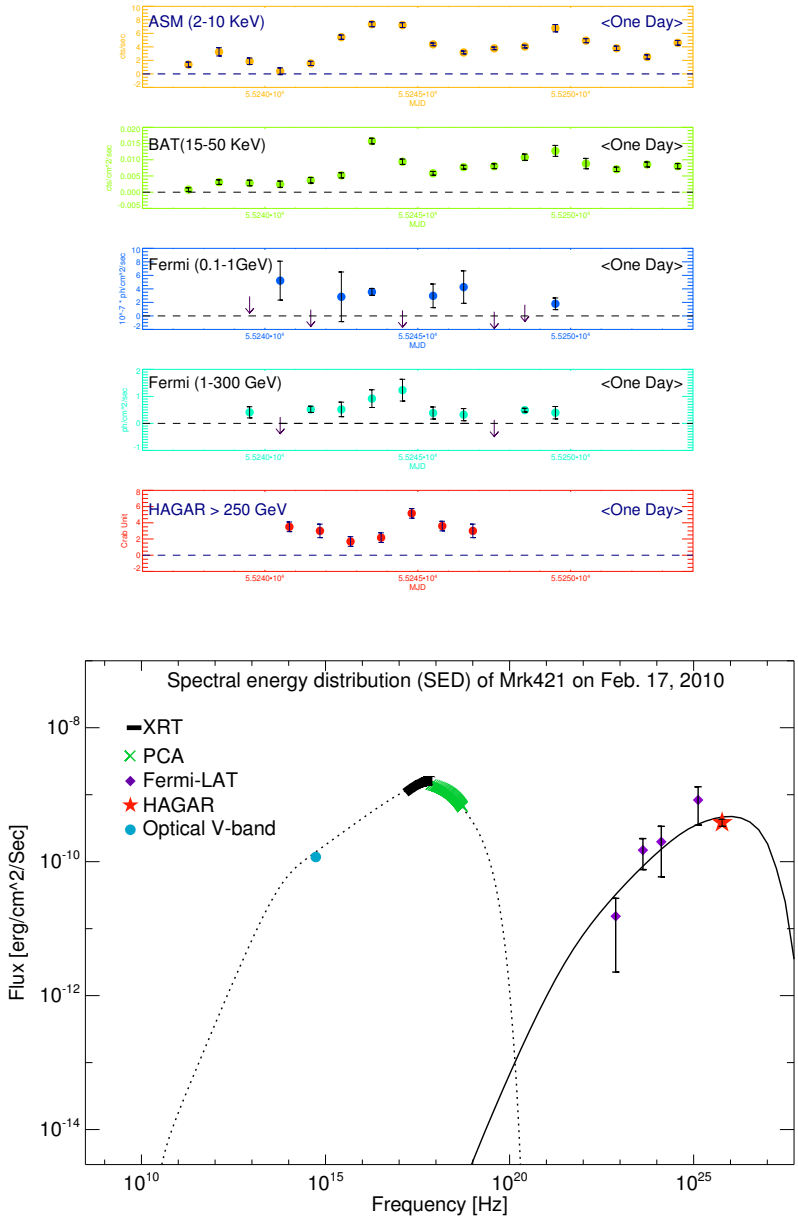

Fig. 2. Upper panel: Daily average light curve of Mrk421 during February 2010 (Shukla et al. 2011). **Lower panel:** Spectral Energy Distribution of Mrk421 of 17 February 2010 (Shukla et al. 2012).

4 Participation in CTA

The Cherenkov Telescope Array (CTA) project is an international collaboration involving 27 countries for the development of a ground-based VHE observatory of new generation imaging Cherenkov telescopes. Two arrays are expected to be installed, one for each Earth hemisphere (CTA 2010).

In 2010, India has joined the CTA collaboration, and has started to contribute with the search for a possible location of CTA-North in the Ladakh region of the Himalayas, in the State of Jammu and Kashmir, North India. We show on Figure 5 a map of the light pollution during the night, centered on North India. The site of Likir and Upshi were previously surveyed, and more recently the site of Thangchung Gari, near the village of Hanle, with better characteristics in term of night quality.

Thangchung Gari is located at 32°48′51″ N, 78°34′41″ E, altitude: 4435 m (Figure 6). Height difference of this area is 33 m for East-West, and 24 m for North-South, related to an area of more than 1.5 × 1.5 km.

Fig. 3. Left: The MACE telescope design. **Right:** Civil work at Hanle: MACE foundation and control room.

Fig. 4. Views of the ongoing installation of MACE near Hyderabad, Andra Pradesh, South India.

Obscuration by hills is within 9°. Himalayan Chandra Telescope (HCT) is operated at Hanle by Indian Institute of Astrophysics, Bangalore since 2001, at the top of a hill located few kilometres away from Thangchung Gari. At HCT, mean night sky brightness ($mag/arcsec^2$) is 22.14 ± 0.32 (U) and 22.42 ± 0.30 (B). The numbers of spectroscopic (photometric) nights are ∼ 260 (190) per year.

Beyond the site surveys, we also expect to work on Monte Carlo simulations.

5 Conclusions

We have reported preliminary results from Crab nebula with HAGAR and detection of Markarian 421 during its high state activity. Several other Galactic and extragalactic sources are continuously being observed, and new data are under process. Furthermore, improvement of the method and development of new analysis softwares are still under going. Discrepancies between MC and data are being currently looked into in details and results will be updated in a forthcoming paper. With the coming up of MACE in the near future and then CTA, high quality observations are expected. These further results would significantly constrain theoretical models for various gamma-ray emitting sources.

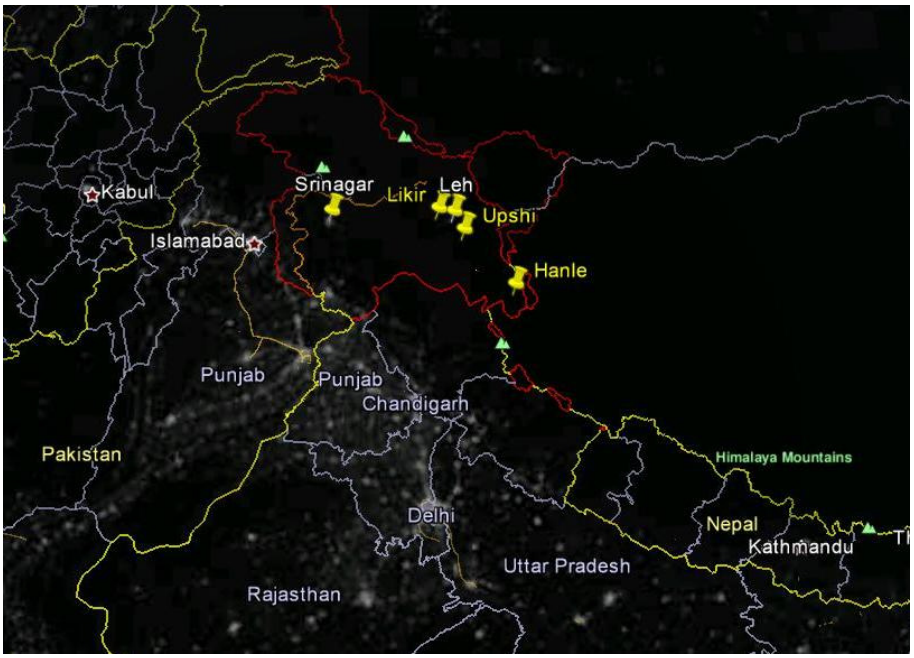

Fig. 5. Light pollution at candidate sites. Data collected by US Air Force Weather Agency, processing and image generation by NOAA's National Geophysical Center.

R. J. Britto would like to thank the PNHE group for providing waving of conference fee to attend the meeting. We thank the local staff at Hanle, and all members of our institutes and visiting students who have contributed towards the design, fabrication and testing of telescopes and data acquisition systems of HAGAR.

References

Acharya, B. S., 2005, Proceedings of the 29^{th} International Cosmic Ray Conference, Pune, 10, 271-282

Britto, R. J. et al., 2011, SF2A-2011: Proceedings of the Annual meeting of the French Society of Astronomy and Astrophysics, Eds.: G. Alecian, K. Belkacem, R. Samadi and D. Valls-Gabaud, pp.535-538

Britto, R. J. et al., 2011, Proceedings the 32^{st} ICRC, paper # 943

Koul, R., Kaul, R. K., Mitra, A. K. et al., 2005, Proceedings of the 29^{st} ICRC, Vol. 5, 243-246

Koul, R. et al, 2011, Proceedings the 32^{st} ICRC paper # 803

Krawczynski H. et al., 2004, ApJ, 601, 151

Oshima A. et al, 2010, Astroparticle Physics, 33, 2, 97-107

Saha, L. et al., 2012, submitted to Astroparticle Physics.

Shukla A. et al., 2011, Proceedings of the 32^{st} ICRC, paper # 977

Shukla A. et al., 2012, A&A, A 541, 140, 2012

Singh B. B. et al., 2011, Proceedings of the 32^{st} ICRC, paper # 276

The CTA Consortium, 2010, arXiv:1008.3703v2

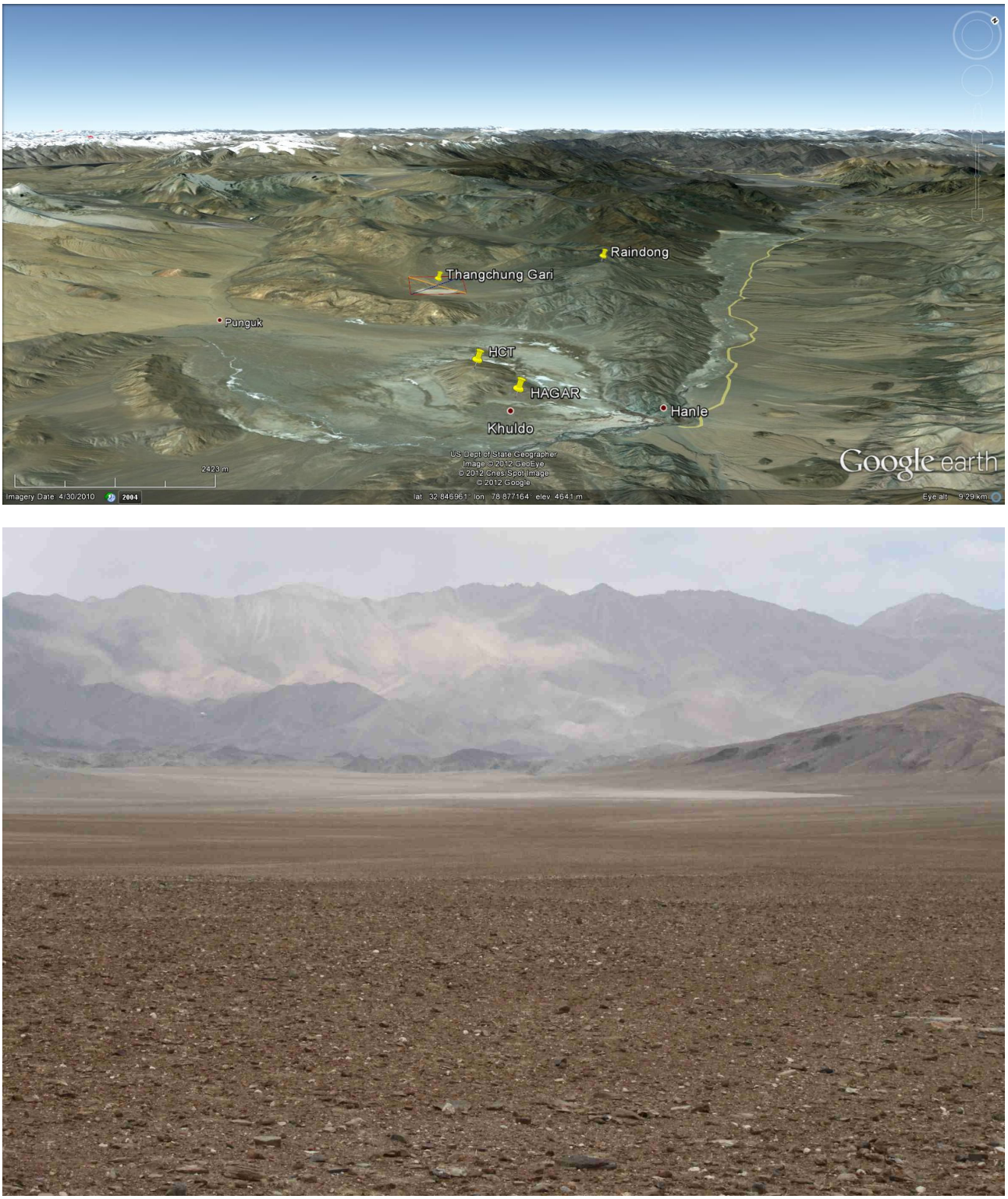

Fig. 6. Upper panel: Google Earth view of the Hanle region. **Lower panel:** photo of the site of Thangchung Gari (B.B. Singh).

SF2A 2012
S. Boissier, P. de Laverny, N. Nardetto, R. Samadi, D. Valls-Gabaud and H. Wozniak (eds)

SEARCH FOR NEUTRINO EMISSION FROM MICROQUASARS WITH THE ANTARES TELESCOPE

S. Galatà[1] and the ANTARES collaboration

Abstract. Neutrino telescopes are nowadays exploring a new window of observation on the high energy universe and may shed light on the longstanding problem regarding the origin of cosmic rays. The ANTARES neutrino telescope is located underwater 40 km offshore from the Southern coast of France, on a plateau at 2475 m depth. Since 2007 it observes the high energy (> 100 GeV) neutrino sky looking for cosmic neutrino sources. Among the candidate neutrino emitters are microquasars, i.e. galactic X-ray binaries exhibiting relativistic jets, which may accelerate hadrons thus producing neutrinos, under certain conditions. These sources are also variable in time and undergo X-ray or gamma ray outburst that can be related to the acceleration of relativistic particles witnessed by their radio emission. These events can provide a trigger to the neutrino search, with the advantage of drastically reducing the atmospheric neutrino background.

A search for neutrino emission from microquasar during outbursts is presented based on the data collected by ANTARES between 2007 and 2010. Upper limits are shown and compared with the predictions.

Keywords: Neutrinos, Quasars: general

1 Introduction

The ANTARES neutrino telescope (Ageron et al. 2011) is composed of 885 photomultiplier tubes (PMTs) hosted within pressure resistant glass spheres, referred to as optical modules (OMs), that constitute the sensitive part of the detector. The OMs are arranged on 12 lines of 480 m height each, on substructures referred to as storeys, each hosting 3 OMs, spaced by 14.5 m along each line. Lines 1-11(12) host 25(20) storeys. The detector is located 40 km offshore from the coast of Southern France and started taking physics data since January 2007, when it was composed of only five detection lines, and was finally completed to its twelve line configuration in May 2008.

High energy muon neutrinos that interact in the proximity of the detector by charged current interactions are converted into muons that produce Cherenkov light as they displace in water. The space-time distribution of the Cherenkov light signals at the OMs allows the reconstruction of the muon's trajectory which is very close to that of the originating neutrino, allowing a pointing accuracy of less than one degree. The track reconstruction algorithm is based on a likelihood maximization method and provides the direction of the incoming muons, whereas the maximized likelihood is used to define the quality cuts for the event selection. The median angular resolution to a neutrino flux $\propto E_\nu^{-2}$ is $0.5^\circ \pm 0.1^\circ$. The main particle background is due to neutrinos produced by the interaction of cosmic rays with the atmosphere. These neutrinos represent an irreducible background detected with a rate of few per day. Energetic atmospheric muons reach the detector from above giving rise to a much more intense flux of particles detected by ANTARES with a rate of few per second. For this reason, only tracks reconstructed as upgoing and with a sufficient quality are classified as neutrino candidates.

Microquasars are galactic X-ray binaries exhibiting relativistic jets (Mirabel & Rodríguez 1994). Whether hadrons are also accelerated in the jets is still an open question for most systems, since the only microquasar for which hadronic lines have been detected in the jets is SS 433 (Marshall et al. 2002). Arguments in favor of a hadronic composition of the jets can be inferred from their energetics (Heinz 2008). If a fraction of the jet power is tapped for the acceleration of hadrons, these can interact with the X-rays from the disk or the synchrotron photons within the jet and produce neutrinos up to 100 TeV (Levinson & Waxman 2001), that may potentially be detected by neutrino telescopes (Distefano et al. 2002).

[1] Centre de Physique des Particules de Marseille, 163 av. de Luminy, 13288 Marseille

Presented here is a search for neutrino emission from microquasars during X-ray or gamma ray outbursts. By restraining the neutrino search during ejection events, the background due to atmospheric neutrinos is reduced, thus increasing the probability of a discovery. The selection of the candidate microquasars and the outbursting events is presented in § 2. In § 3 the statistical search method is explained and the results are presented. Conclusions and perspectives are drawn in the last section.

2 Outburst selection

In order to define the times in which to look for neutrinos, a multi wavelength study has been performed on the sources under study using X-ray data from RXTE/ASM and Swift/BAT and, in one case, the gamma ray data from Fermi/LAT. When necessary, also results from the literature have been used. The goal is to select those times in which the source is supposed to accelerate relativistic jets, based on its known multi wavelength behaviour (X-ray, gamma and radio). In the following of this section the main selection criteria for the candidate sources are presented.

2.1 Cir X-1

This neutron star binary has an orbital period of 16.6 days (Kaluzienski et al. 1976) and undergoes regular radio flares at periastron, within the phase interval 0.09-0.21 (Murdin et al. 1980; Moin et al. 2011), which is supposed to be due to the enhanced accretion at periastron. Also, during X-ray outburst, the radio core of the source brightens and successively feeds two radio knots of an extended structure at arcsec scale (Fender et al. 2004). Following these features, the time selection for this source has been based on the presence of X-ray outbursts observed with the RXTE/ASM telescope, which have been eventually extended in order to include the periastron phase, when sufficiently close.

2.2 GX 339−4, H1743−322, IGR J17091−3624 and Cyg X-1

The time selection for these black hole binaries has been based on the known disc-jet coupling relation between X-ray and radio for this type of sources (Belloni 2010). Namely, during hard X-ray states a steady jet is normally observed with a Lorentz factor ~ 2, whereas during transitions between hard and soft states, when the source transits through the hard and soft intermediate states, a discrete ejection is observed with a higher Lorentz factor. Following this pattern, hard X-ray states and transitional states have been selected for the neutrino search. As these two cases refer to two different physical scenarios, two separate neutrino searches have been performed during hard states and transitional states respectively.

Whereas the identification of transitional states needs detailed X-ray analyses and has been based on results found in the literature, the selection of hard states has been performed by selecting X-ray outbursts in the Swift/BAT daily averaged light curve. The resulting time selection for GX 339−4 is shown in Fig. 1 as an example. The classification of X-ray states for Cyg X-1, instead, has been based on the mapping of the X-ray states with respect to the position of the source in the flux-hardness diagram of RXTE/ASM as found by (Grinberg et al. 2012).

2.3 Cyg X-3

This source has been observed emitting high energy gamma rays by both AGILE (Tavani et al. 2009) and Fermi/LAT (Abdo et al. 2009). The gamma ray emission is associated to its ultra soft X-ray states which in turn is related to giant radio outburst. The gamma ray data between 30 MeV and 30 GeV from Fermi/LAT have been analyzed using the procedure in (Abdo et al. 2009). Outbursting periods in gamma rays have been selected for the neutrino search.

3 Search in ANTARES data

An unbinned likelihood method based on a likelihood ratio test statistic has been adopted to analyze the neutrino sky maps relative to each neutrino search and define whether they are compatible with the background of atmospheric neutrinos or with the presence of a neutrino source on top of it. For each neutrino search, both the number of background events and their angular distribution have been estimated from the data. A high number of background-only pseudo experiments has been generated by randomizing the directions of the

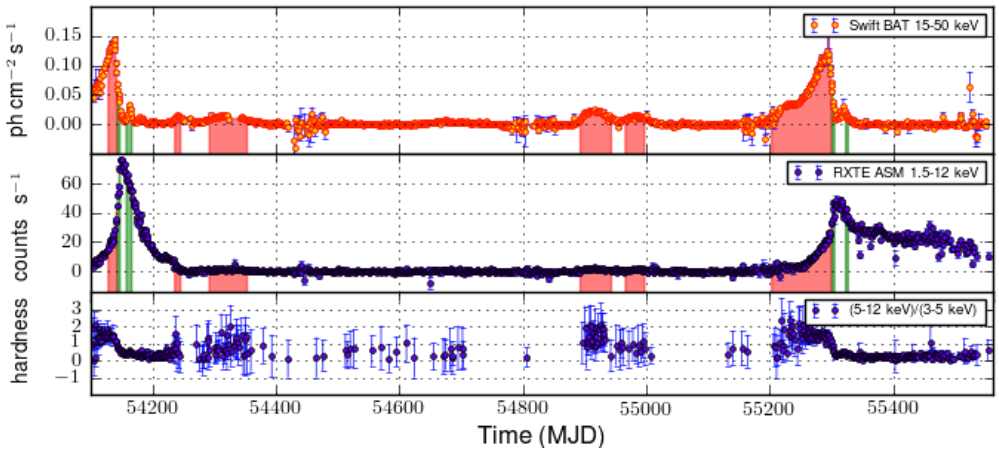

Fig. 1. X-ray light curves of GX 339−4 between 2007 and 2010, from Swift/BAT (top) and RXTE/ASM (middle). The lower panel shows the hardness ratio HR2 from ASM. The filled areas refer to the periods selected for the neutrino search: in red during the hard state and in green during the hard to soft transition. A separate neutrino search is performed on red and green areas.

selected neutrino events in the data, in order to reproduce all possible background fluctuations. Also, the effect of neutrino signals has been studied by injecting up to 30 signal events in the background only pseudo sky maps, distributed around the source according to the ANTARES point spread function. The results of the pseudo experiments have been used to optimize the quality cuts in order to maximize the probability of a discovery supposing a neutrino flux $\propto E_\nu^{-2}$. The analysis has been carried on in a blind fashion, i.e. the quality cuts and the criteria for a discovery or an evidence have been defined before looking at the actual neutrino directions in the data.

After the true neutrino directions in the data have been unveiled and the likelihood method applied on them, none of the searches ended up producing a significant result, thus the 90% confidence level upper limits on the neutrino fluences have been calculated supposing an E_ν^{-2} neutrino flux. The preliminary results are shown in Table 1. The search that was less compatible with the background-only hypothesis is the one relative to the state transitions of H1743−322. The total livetime of this search is relatively low, only 5.1 days, whereas a neutrino has been detected 2.3° away from the source, which is more than four times the detector's angular resolution, i.e. the result is compatible with the background-only hypothesis.

Table 1. Summary of the preliminary results on the neutrino searches for the outbursting microquasars under study. The columns report the values of the test statistic (TS) and the number of signals fitted by the likelihood method (n_{sig}), the livetime of the search in days, the number of selected neutrinos in the whole sky map (representing the amount of background), the distance of the closest neutrino to the source, the number of expected background neutrinos within 3° from the source and the 90% C.L. upper limit on the neutrino fluence in GeV cm^{-2}, respectively.

	TS	n_{sig}	livetime	$N_{\nu,bg}$	closest ν	$N_{bg}^{exp}(<3°)$	fluence u.l.$^{90\%\text{C.L.}}$
H1743−322(TS)	0.41	0.66	5.1	27	2.3°	0.04	30.3
Cyg X-1 (HS)	0.0016	0.08	174.4	638	1.4°	0.86	14.1
Cir X-1	0	0	100.5	256	5.7°	0.35	16.9
GX 339−4 (HS)	0	0	147.0	484	2.8°	0.66	10.9
GX 339−4 (TS)	0	0	4.9	14	11 °	0.02	19.7
H1743−322 (HS)	0	0	84.6	447	4.6°	0.61	9.1
IGR J17091−3624	0	0	8.5	40	12 °	0.05	21.3
Cyg X-1 (TS)	0	0	30.9	182	6.4°	0.27	6.0
Cyg X-3	0	0	16.6	149	6.9°	0.20	5.7

Also, the 90% upper limits on the energy flux in neutrinos have been calculated and compared with the flux predictions from (Distefano et al. 2002). To adhere the model's scenario, a neutrino flux with an exponential

cutoff at 100 TeV has been considered. This is shown in Fig. 2. The limits obtained are very close to the predictions in the cases of GX 339−4 and Cyg X-3, although it is not yet possible to constrain the model. Nevertheless, future ANTARES data and improvements in the analysis technique will allow constraints of this model at least for these two sources.

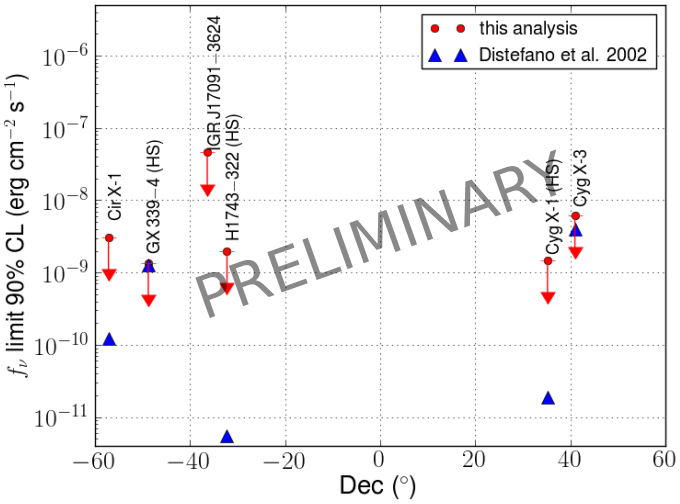

Fig. 2. Feldman-Cousins 90% confidence level upper limits on the energy flux in neutrinos f_ν obtained from this analysis, considering a flux $\propto E^{-2}\exp(-E_\nu/100$ TeV), compared with the expectations from Distefano et al. (2002). The model expectation for IGR J17091−3624 is not included in the plot since no infrared measurements were found to calculate it.

4 Conclusions

An analysis of the data collected by ANTARES between 2007 and 2010 has been presented to put in evidence a neutrino emission from outbursting microquasars. Time cuts have been defined in order to restrain the neutrino search to those periods in which the source was thought to be accelerating a relativistic jet, by using the X-ray light curves from RXTE/ASM and Swift/BAT, and the gamma ray light curve of Fermi/LAT in the case of Cyg X-3 . The analysis of ANTARES data has been performed using a likelihood method based on a likelihood ratio test, optimized for discovery. Upper limits on the neutrino fluences are shown and the comparison with the model's prediction from (Levinson & Waxman 2001) indicate that future ANTARES data will allow to put constraints on the model's parameters.

References

Abdo, A. A. et al. 2009, Science, 326, 1512
Ageron, M. et al. 2011, Nucl. Instrum. Meth., A656, 11
Belloni, T. M. 2010, in Lecture Notes in Physics, Berlin Springer Verlag, Vol. 794, Lecture Notes in Physics, Berlin Springer Verlag, ed. T. Belloni, 53
Distefano, C., Guetta, D., Waxman, E., & Levinson, A. 2002, ApJ, 575, 378
Fender, R., Wu, K., Johnston, H., et al. 2004, Nature, 427, 222
Grinberg, V. et al. 2012, to be submitted
Heinz, S. 2008, International Journal of Modern Physics D, 17, 1947
Kaluzienski, L. J., Holt, S. S., Boldt, E. A., & Serlemitsos, P. J. 1976, ApJ, 208, L71
Levinson, A. & Waxman, E. 2001, Physical Review Letters, 87, 171101
Marshall, H. L., Canizares, C. R., & Schulz, N. S. 2002, ApJ, 564, 941
Mirabel, I. F. & Rodríguez, L. F. 1994, Nature, 371, 46
Moin, A., Reynolds, C., Miller-Jones, J. C. A., et al. 2011, MNRAS, 414, 3551
Murdin, P., Jauncey, D. L., Lerche, I., et al. 1980, A&A, 87, 292
Tavani, M. et al. 2009, Nature, 462, 620

SF2A 2012
S. Boissier, P. de Laverny, N. Nardetto, R. Samadi, D. Valls-Gabaud and H. Wozniak (eds)

PULSARS, SUPERNOVAE, AND ULTRAHIGH ENERGY COSMIC RAYS

K. Kotera[1], K. Fang[2], A. V. Olinto[2] and E. S. Phinney[3]

Abstract. The acceleration of ultrahigh energy nuclei in fast spinning newborn pulsars can explain the observed spectrum of ultrahigh energy cosmic rays and the trend towards heavier nuclei for energies above 10^{19} eV as indicated by air shower studies reported by the Auger Observatory. By assuming a normal distribution of pulsar birth periods centered at 300 ms, we show that the contribution of extragalactic pulsar births to the ultrahigh energy cosmic ray spectrum naturally gives rise to a contribution to very high energy cosmic rays (VHECRs, between 10^{16} and 10^{18} eV) by Galactic pulsar births. The required injected composition to fit the observed spectrum depends on the absolute energy scale, differing considerably between the energy scale used by Auger and that used by the Telescope Array. Depending on the composition of the cosmic rays that escape the supernova remnant and the diffusion behavior of VHECRs in the Galaxy, the contribution of Galactic pulsar births can also bridge the gap between predictions for cosmic ray acceleration in supernova remnants and the observed spectrum below the ankle. Fast spinning newborn pulsars that could produce UHECRs would be born in supernovae that could present interesting specific radiative features, due to the interaction of the pulsar wind with the surrounding ejecta. The resulting supernova lightcurves could present a high luminosity plateau over a few years, and a bright X-ray and gamma-ray peak around one or two years after the onset of the explosion. If such signatures were observed, they could have important implications both for UHECR astrophysics and for the understanding of core-collapse supernovae.

Keywords: ultrahigh energy cosmic rays, neutron star, pulsar, supernova

1 Introduction

The origin of cosmic rays continues to challenge our understanding after a century of observations. Observatories on the ground have studied extensive air showers from energies 10^{15} eV up to 10^{20} eV. The bulk of the cosmic ray flux is believed to be accelerated in Galactic supernova remnants (SNR) (Baade & Zwicky 1934; Bell 1978; Blandford & Ostriker 1978). This long held notion fits well the observed spectrum up to 10^{16} eV Blasi & Amato (2012). Above these energies a new component is needed to explain the spectrum and observed composition. This new component may be Galactic, as suggested in Hillas (2006); Ptuskin et al. (2010), or extragalactic as proposed in Berezinsky et al. (2005); Lemoine (2005). The transition from Galactic to extragalactic is expected to occur well below 10^{19} eV, with models spanning the very high energy (VHE) range between 10^{16} eV and 10^{18} eV with "dip" models around 10^{17} eV (Berezinsky et al. 2005; Lemoine 2005) and "ankle" transition models around 10^{18} eV (see, e.g., Allard et al. 2005).

The study of ultrahigh energy cosmic rays (UHECRs), from 10^{18} eV to 10^{20} eV, has progressed significantly with the advent of giant airshower observatories such as the Pierre Auger Observatory (Abraham et al. 2004) and Telescope Array (TA) in Utah, USA (Tokuno et al. 2012). The spectrum, sky distribution of arrival directions, and composition indicators are well measured over a large range of energies. Differences in reports from the two major observatories include a 20% shift in absolute energy scale ($E_{\rm Auger} \simeq 0.8 E_{\rm TA}$) and the differing trends of composition indicators at higher energies. Currently the most extensive dataset on composition indicators, such as the average and the RMS of the depth of shower maximum ($X_{\rm max}$), has been published by the Auger

[1] Institut d'Astrophysique de Paris, UMR 7095 - CNRS, Université Pierre & Marie Curie, 98 bis boulevard Arago, 75014, Paris, France
[2] Department of Astronomy & Astrophysics, Kavli Institute for Cosmological Physics, The University of Chicago, Chicago, IL 60637, USA.
[3] Theoretical Astrophysics, California Institute of Technology, 1200 E California Blvd., M/C 350-17, Pasadena, CA 91125, USA

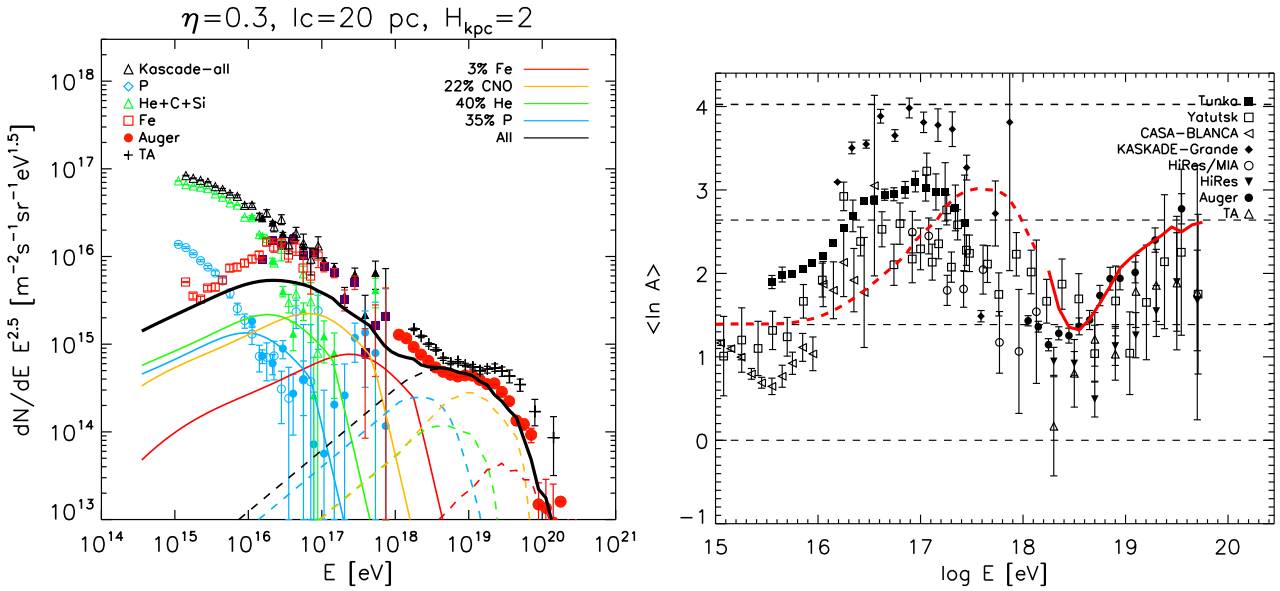

Fig. 1. Left: Total (thick solid line) UHECR spectrum produced by a population Galactic (solid) and extragalactic (dashed) pulsars with parameter distribution following Faucher-Giguère & Kaspi (2006), and with emissivity assumed to be constant over time, embedded in core-collapse SNe of ejecta mass 10 $M_\odot$ and energy 10^{51} erg. The contribution of various elements is indicated. The injection in the pulsar wind follows the ratio 35% Proton, 40% Helium, 22% CNO, and 3% Fe. **Right:** Average logarithmic mass of cosmic ray derived from Xmax measurements with non-imaging Cherenkov detectors (Tunka, Yakutsk, CASA-BLANCA) and fluorescence detectors (HiRes/MIA, HiRes, KASKADE-Grande Auger and TA) for hadronic interaction model EPOS compared with simulation predictions (red lines). Dashed lines indicate the energy range where pulsars have an underdominant contribution to the total flux and other Galactic sources, e.g., supernova remnants, also contribute.

collaboration and shows a departure from a composition consistent with lighter nuclei at 10^{18} eV to a trend towards heavier nuclei above 10^{19} eV (Abreu et al. 2011). TA reports shower behaviors consistent with protons Tameda et al. (2011). The discrepancies in composition reports and the difference in absolute energy scale make it difficult to constrain proposed models for the origin of UHECRs. Fortunately, a cross-experiment effort to understand these discrepancies is currently on-going.

2 Pulsars as sources of very high and ultrahigh energy cosmic rays

Here we show that the fast spinning pulsar birth model described in Blasi et al. (2000); Fang et al. (2012) can explain the observed spectrum (both the Auger and the TA spectra) and the composition trend described in Abreu et al. (2011). To fit these two observables we allow the freedom to vary the percentage of different elements that escape the supernova remnant divided into 4 groups: protons, Helium, Carbon group (CNO), and Iron. Although the surface of the rotating neutron star is a natural source of Iron, X-ray spectra of pulsars indicate that the top layers of their atmosphere is likely to be composed of Helium (Sanwal et al. 2002), or Carbon, Oxygen and Neon (Hailey & Mori 2002; Heinke & Ho 2010). At higher altitude, in the X-ray photosphere, one could find lighter ions (Zavlin & Pavlov 1998; Pavlov & Zavlin 2000) that could be also stripped off and accelerated in the wind. The source of UHECRs in our model are the rare, extremely fast spinning, young pulsars. The majority of pulsars will be born spinning slower and will therefore contribute to the flux of lower energy cosmic rays. The distribution of pulsar birth spin periods, $f(P = 2\pi/\Omega)$, is normal, centered at 300 ms, and with standard deviation of 150 ms, while that the initial magnetic field follows a log-normal distribution $f(\mu)$ with $\langle \log(B/\mathrm{G}) \rangle \sim 12.65$ and $\sigma_{\log B} \sim 0.55$ (Faucher-Giguère & Kaspi 2006).

In order to estimate the observed spectrum of UHECRs, after their propagation through the extragalactic medium, we used the simulation output of Kotera et al. (2010) from 10^{18} eV up to the maximum accelerator energy, $E_{\max}$, and rescaled the result to the actual spectrum injected by single pulsars. The UHECR spectrum and composition ratios for a given pulsar, after escape through the surrounding supernova ejecta, were calculated in Fang et al. (2012). The normalization of the flux is set by the factor $n_{\mathrm{Gal}}\, \nu_{\mathrm{m}}\, f_{\mathrm{s}}$. On average, the pulsar birth

rate is $\nu_s \simeq 1.6\times10^{-4}\,\mathrm{Mpc^{-3}\,yr^{-1}} = 1/60\,\mathrm{yr}\,/\mathrm{Galaxy}$(Lorimer 2008), and the galaxy density $n_{\rm Gal} \simeq 0.02\,\mathrm{Mpc^{-3}}$. f_s is an overall factor used to fit the model prediction to the measured UHECR flux. In the pulsar model, $f_s < 1$ can account for variations in the core-collapse geometry, poorer injection efficiency, or a particle density in the pulsar wind which is less than the Goldreich-Julian charge density.

The flux of cosmic rays accelerated by Galactic pulsars can be calculated as $\mathrm{d}N_{\rm Gal}/(\mathrm{d}E\,\mathrm{d}t\,\mathrm{d}A\,\mathrm{d}\Omega) = (\mathrm{d}N_{\rm i}/\mathrm{d}E)(4\pi)^{-1}\,c\,\tau_{\rm esc}V_{\rm Gal}\,\nu_s\,f_s\,(1-e^{-\nu_s\,\tau_{\rm esc}})$, where $V_{\rm Gal} = 10^{68}\,\mathrm{cm^3}$ is the volume of the Milky Way, f_s is the same scale factor introduced for the extragalactic component, and $\tau_{\rm esc}$ is the time a charged particle takes to escape the Galactic magnetic field. At energies above the knee ($\sim 10^{15}$ eV), nuclei spallation is negligible and the nuclei escape time can simply be estimated with the Leaky box model $\tau_{\rm esc}(E,Z,l_{\rm c}) = H^2/D$, where H is the height of the Galactic Halo Magnetic Field above (or below) the Galactic plane; typically $H \sim 2-8\,\mathrm{kpc}$ Mao et al. (2012). We take an empirical diffusion coefficient, D, as in Kotera & Lemoine (2008), assuming an azimuthal Galactic magnetic field of strength $3\,\mu$G, coherence length $l_c = 20\,\mathrm{pc}$, and scale height $2\,\mathrm{kpc}$.

Assuming that cosmic rays injected in the ISM by Galactic pulsars have the same composition as those from EG pulsars, we can calculate the contribution of both Galactic and extragalactic pulsars (Fig.1). To fit the Auger spectrum a balanced ratio between proton, Helium, and CNO, with a minor presence of Iron suffices, while to fit the TA spectrum a higher percentage of Iron is needed since the spectrum extends to higher energies. The composition selected by the Auger spectrum also gives a good fit to the Auger average shower maximum ($\langle X_{\rm max}\rangle$) and the fluctuations around the mean (RMS($X_{\rm max}$)). Although the end of the Galactic spectrum is highly dependent on the Galactic diffusion parameters and the history of the most recent pulsar births in the Galaxy (such that the flux in the VHE region is time dependent), these two choices of energy scales give rise to significant differences in the predictions for the Galactic component. The Auger fit implies an under dominant contribution to the flux of VHECRs, while the TA fit would imply Galactic pulsars as the main contributors to VHECRs. See Fang et al. (in prep.) for more details.

3 Signatures in the very early supernova lightcurve

While they spin down, pulsars release their rotational energy in the form of a relativistic magnetized wind. Kasen & Bildsten (2010); Dessart et al. (2012) discussed that magnetars, a sub-class of pulsars born with extremely high dipole magnetic fields of order $B \sim 10^{14-15}\,\mathrm{G}$ and millisecond spin periods, could deposit their rotational energy into the surrounding supernova ejecta in a few days. This mechanism would brighten considerably the supernova, making them appear ultra-luminous. The potential candidate sources for UHECRs that we described

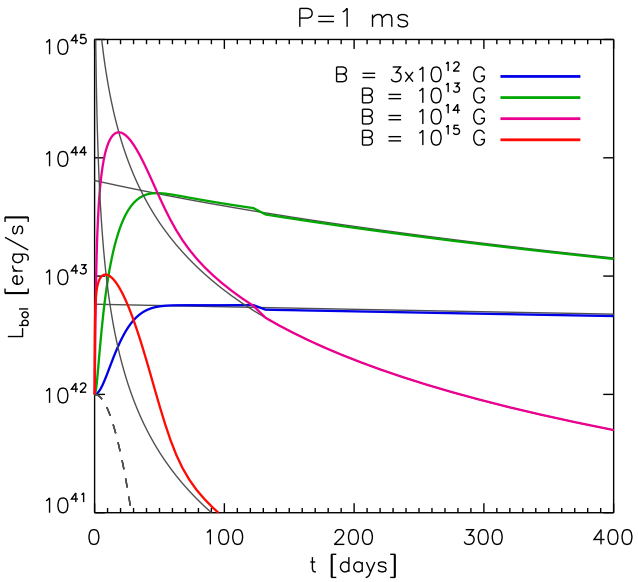

Fig. 2. Evolution of the bolometric radiated luminosity of the supernova as a function of time. The pulsar has a dipole magnetic field of increasing strength as indicated, and period $P_{\rm i} = 1\,\mathrm{ms}$. The supernova ejecta has $M_{\rm ej} = 5\,M_\odot$ and $E_{\rm ej} = 10^{51}$ erg. The gray lines give the evolution of the pulsar luminosity $L_{\rm p}$ for each initial spin period. The gray dashed lines are the contribution of the ordinary core-collapse supernova to the radiated luminosity $L_{\rm SN}$.

above and in Fang et al. (2012) are millisecond rotators at birth, and are mildly magnetized ($B \sim 10^{12-13}$ G). Higher magnetization would imply indeed a fast spin-down, and hence that lower energy particles be produced when the supernova ejecta has become diluted enough to allow their escape. Such objects are expected to inject their equally tremendous rotational energy in the supernovae ejectas, but over longer times (of order of a few years). These early emissions have never been estimated.

Using simple radiative transfer arguments, one can calculate that supernovae embedding millisecond pulsars with mild magnetic fields of order $B \sim 10^{12-13}$ G should present a high bolometric luminosity plateau over a few years (Fig. 2). More detailed calculations of the thermal and non thermal emissions, taking into account the opacity of the ejecta to the various radiations, we find that a bright X-ray or gamma-ray emission could also appear after one year from the acceleration of particles in the pulsar wind (Kotera et al. in prep.).

This study could have important implications for the understanding of core-collapse supernovae, revealing yet unidentified but highly constraining signatures. Note that direct constraints on the newly-formed remnant are scarce, epitomized by the case of SN1987A for which we do not even know the nature of the compact remnant. If this object is observable, and is actually observed by the following up of a large number of supernovae, it could be a ground-breaking discovery.

Because these objects present the ideal combination of parameters for successful production of UHECRs (Fang et al. 2012), the observation of such supernovae could be a further argument in favor of millisecond pulsars as sources of UHECRs, and a potential signature of an ongoing UHECR production.

KK acknowledges support from PNHE for this work and to attend the SF2A meeting.

References

Abraham, J. et al. 2004, Nucl. Instrum. Meth. in Phys. Res. A, 523, 50

Abreu, P. et al. 2011, 32nd International Cosmic Ray Conference, Beijing, China, arXiv:1107.4804

Allard, D., Parizot, E., Olinto, A. V., Khan, E., & Goriely, S. 2005, A&A, 443, L29

Baade, W. & Zwicky, F. 1934, Proceedings of the National Academy of Sciences of the United States of America, 20, 259

Bell, A. R. 1978, MNRAS, 182, 147

Berezinsky, V., Gazizov, A., & Grigorieva, S. 2005, Phys.Lett., B612, 147

Blandford, R. D. & Ostriker, J. P. 1978, ApJ Letters, 221, L29

Blasi, P. & Amato, E. 2012, JCAP, 1201, 010

Blasi, P., Epstein, R. I., & Olinto, A. V. 2000, ApJ Letters, 533, L123

Dessart, L., Hillier, D. J., Li, C., & Woosley, S. 2012, ArXiv e-prints

Fang, K., Kotera, K., & Olinto, A. V. 2012, The Astrophysical Journal, 750, 118

Fang, K., Kotera, K., & Olinto, A. V. in prep.

Faucher-Giguère, C.-A. & Kaspi, V. M. 2006, ApJ, 643, 332

Hailey, C. J. & Mori, K. 2002, ApJL, 578, L133

Heinke, C. O. & Ho, W. C. G. 2010, ApJL, 719, L167

Hillas, A. M. 2006, arXiv:astro-ph/0607109

Kasen, D. & Bildsten, L. 2010, ApJ, 717, 245

Kotera, K., Allard, D., & Olinto, A. V. 2010, JCAP, 10, 13

Kotera, K. & Lemoine, M. 2008, PRD, 77, 023005

Kotera, K., Phinney, E. S., & Olinto, A. V. in prep.

Lemoine, M. 2005, Phys. Rev. D, 71, 083007

Lorimer, D. R. 2008, Living Reviews in Relativity, 11

Mao, S. A., McClure-Griffiths, N. M., Gaensler, B. M., et al. 2012, ArXiv e-prints

Pavlov, G. G. & Zavlin, V. E. 2000, in Astronomical Society of the Pacific Conference Series, Vol. 202, IAU Colloq. 177: Pulsar Astronomy - 2000 and Beyond, ed. M. Kramer, N. Wex, & R. Wielebinski, 613

Ptuskin, V., Zirakashvili, V., & Seo, E. 2010, Astrophys.J., 718, 31

Sanwal, D., Pavlov, G. G., Zavlin, V. E., & Teter, M. A. 2002, ApJL, 574, L61

Tameda, Y. et al. 2011, 32nd International Cosmic Ray Conference, Beijing, China, 2

Tokuno, H., Tameda, Y., Takeda, M., et al. 2012, Nucl.Instrum.Meth., A676, 54

Zavlin, V. E. & Pavlov, G. G. 1998, A&A, 329, 583

SF2A 2012
S. Boissier, P. de Laverny, N. Nardetto, R. Samadi, D. Valls-Gabaud and H. Wozniak (eds)

UV AND OPTICAL POLARIZATION MODELING OF THERMAL ACTIVE GALACTIC NUCLEI: IMPACT OF THE NARROW LINE REGION

F. Marin[1] and R. W. Goosmann[1]

Abstract. In this research note, we start exploring the influence of the narrow line region (NLR) on the optical/UV continuum polarization of active galactic nuclei (AGN). We have upgraded our previous 3-component model of a thermal Seyfert nucleus that was composed of an equatorial, optically thin electron disc, a circumnuclear dusty torus, and a pair of collimated, optically thin electron winds. We have added a dusty extension with low optical depth to the outflows to account for continuum scattering and absorption inside the NLR. A spectropolarimetric comparison between our AGN models with and without NLR reprocessing is carried out. It turns out that the NLR can alter and even suppress the observed polarization dichotomy between type-1 and type-2 AGN. For type-2 AGN, it also significantly decreases the expected percentage of polarization and alters its spectral shape. While the NLR makes it more difficult to reproduce the observed polarization in type-1 objects, it helps to explain spectropolarimetry observations of type-2 objects. Further studies including clumpy media need to be carried out to obtain more precise constraints on the polarization dichotomy and the reprocessing geometry of AGN.

Keywords: Galaxies: active, Galaxies: Seyfert, Polarization, Radiative transfer, Scattering

1 Introduction

The unified model of active galactic nuclei (AGN) postulates that the emission of the continuum source and of the broad line region (BLR) is highly anisotropic because it is confined by the funnel of an obscuring dusty torus Antonucci (1993). A type-1 AGN has a visible BLR and is seen at a line of sight towards the central source that passes through the torus funnel. For a type-2 AGN, the view of the BLR is blocked by the torus body. The radiation from the center of the AGN can directly escape only along the polar regions of the funnel where it photo-ionizes conically shaped outflows. It was found that these winds are roughly stretched along the small scale radio-structure that is present in both radio-loud and radio-quiet AGN (Wilson & Ulvestad 1983). Beyond their sublimation radius, dust grains can form and coexist with the ionized outflow forming the so-called narrow line region (NLR). Capetti et al. (1999) showed that the NLR generally has a complex morphology consisting of filaments and compact emission knots (e.g. in NGC 4151) or narrow arcs (e.g. in Mrk 573). Due to this non-trivial geometry, it may be a difficult task to obtain accurate constraints on the NLR. However, spectropolarimetric studies of luminous AGN and numerical polarization modeling can improve our understanding if the complex radiative transfer between the various reprocessing regions is taken into account.

Goosmann & Gaskell (2007) investigated the continuum polarization induced by individual reprocessing regions, namely by dusty tori, polar outflows of various compositions, and equatorial scattering regions. Using this work as a starting point, we then modeled the optical/UV polarization emerging from a complex reprocessing system composed of three scattering components (Marin & Goosmann 2011; Marin et al. 2012b). The goal of the exhaustive study presented in Marin et al. (2012b) was to put solid constraints on the conditions that reproduce the observed polarization dichotomy between type-1 and type-2 AGN[i]. So far, we have left out the

[1] Observatoire Astronomique de Strasbourg, Université de Strasbourg, CNRS, UMR 7550, 11 rue de l'Université, 67000 Strasbourg, France. Email: frederic.marin@astro.unistra.fr

[i]Polarization is described as "parallel" when the $\vec{E}$-vector is aligned with the projected torus axis. We denote the difference between parallel and perpendicular polarization by the sign of the polarization percentage, P: a negative value of P stands for parallel polarization, a positive P for perpendicular one. Many type-1 AGN show parallel polarization while the polarization of type-2 objects is perpendicular (Antonucci 1982, 1983).

Table 1. Parameters of the individual scattering regions in our 3- and 4-component models. Note that for the polar outflow, the torus and the NLR, the half-opening angle is measured with respect to the vertical, symmetry axis of the model, while for the flared-disk the half-opening angle is taken with respect to the equatorial plane.

flared disk	dusty torus	ionized outflows	NLR
$R_{\rm min} = 3.10^{-4}$ pc	$R_{\rm min} = 0.25$ pc	$R_{\rm min} = 1$ pc	$R_{\rm min} = 20$ pc
$R_{\rm max} = 5.10^{-4}$ pc	$R_{\rm max} = 100$ pc	$R_{\rm max} = 10$ pc	$R_{\rm max} = 70$ pc
half-opening angle = 10°	half-opening angle = 30°	half-opening angle = 30°	half-opening angle = 30°
equat. optical depth = 1	equat. optical depth = 750	vertical optical depth = 0.03	vertical optical depth = 0.24
electron scattering	Mie scattering	electron scattering	Mie scattering

NLR as it is expected to decrease the total amount of parallel polarization in type-1 AGN. For more details on this we refer the reader to Marin et al. (2012b). In this short paper, we start to investigate the effects on the continuum polarization that can emerge from adding to our previously model an NLR-like polar scattering region that is filled with optically thin dust.

2 Model setup

The continuum emitting region of our thermal AGN is modeled by an isotropic, point-like source of unpolarized radiation having a power-law intensity spectrum $F_* \propto \nu^{-\alpha}$ with $\alpha = 1$. The source is closely surrounded by an electron-filled scattering ring producing the parallel polarization observed in type-1 objects (Antonucci 1984). At a larger distance and sharing the same equatorial plane, an obscuring, optically thick dusty torus blocks the radiation progressing towards edge-on directions. We assume that the torus collimates winds that are ejected from the inner accretion flow before they turn into a polar, hourglass-shaped outflow. These winds are optically thin, ionized and dominated by electron scattering. A complete description of the 3-component model can be found in Section 5 of Marin et al. (2012b). The model approximates the unified scheme of AGN and is optimized for the production of parallel polarization at a type-1 line of sight.

To study the effect of the NLR, we presently include extended, optically thin, dusty outflows sustaining the same half-opening angle and direction as the ionized winds. However, the amount of dust associated with the NLR is difficult to constrain from the observations due to 1) a complex filamentary structure between ionized gas and dust and 2) reddening corrections in the data reduction that can be a potential source of errors as the gas to dust composition is not known (Cracco et al. 2011). Taking into account that the fraction of dust in the NLR clouds must be smaller than in the circumnuclear region and in order to allow a large fraction of the radiation to escape in a polar direction, we fix the NLR opacity to a value significantly below unity (Hoenig et al. 2012). Table 1 summarizes the parameters of the reprocessing regions in our models.

We apply the latest public version of *STOKES*, a Monte Carlo radiative transfer code including a treatment of the polarization. The code was initially presented in Goosmann & Gaskell (2007) and new elements have been added by Marin et al. (2012b). The code is freely available on the Internet[ii]. It handles absorption and multiple scattering in a complex environment of emitting sources and reprocessing regions. Spectropolarimetric and polarization imaging results can be computed at any polar and azimuthal viewing angle. For more details on *STOKES* and its possible applications, we refer the reader to Marin et al. (2012b) and references therein.

3 Spectropolarimetric results

The resulting polarization percentage P and the fraction, F/F_*, of the central flux, F_*, as a function of the viewing angle for both the 3-component and the 4-component model are shown in Fig.1. As expected, the overall polarization behavior for the model including the NLR (Fig.1, top left) is different from the results obtained for the 3-component model (Fig.1, top right). When adding the NLR, the global amount of polarization in type-2 objects decreases due to a combination of effects; the polarized flux from the ionized outflows is diluted by the relatively weaker polarization of the flux coming from the NLR. Note that for our dust mixture (Mathis et al. 1977) the theoretical polarization degree produced by a single Mie scattering event reaches a maximum value of 35% at 8000 Å, while for electron scattering P is as high as 100%. The dilution from polar Mie scattering in the NLR is particularly efficient at edge-on viewing angles and P decreases by a factor of ~ 3 in comparison to the

[ii] http://www.stokes-program.info/

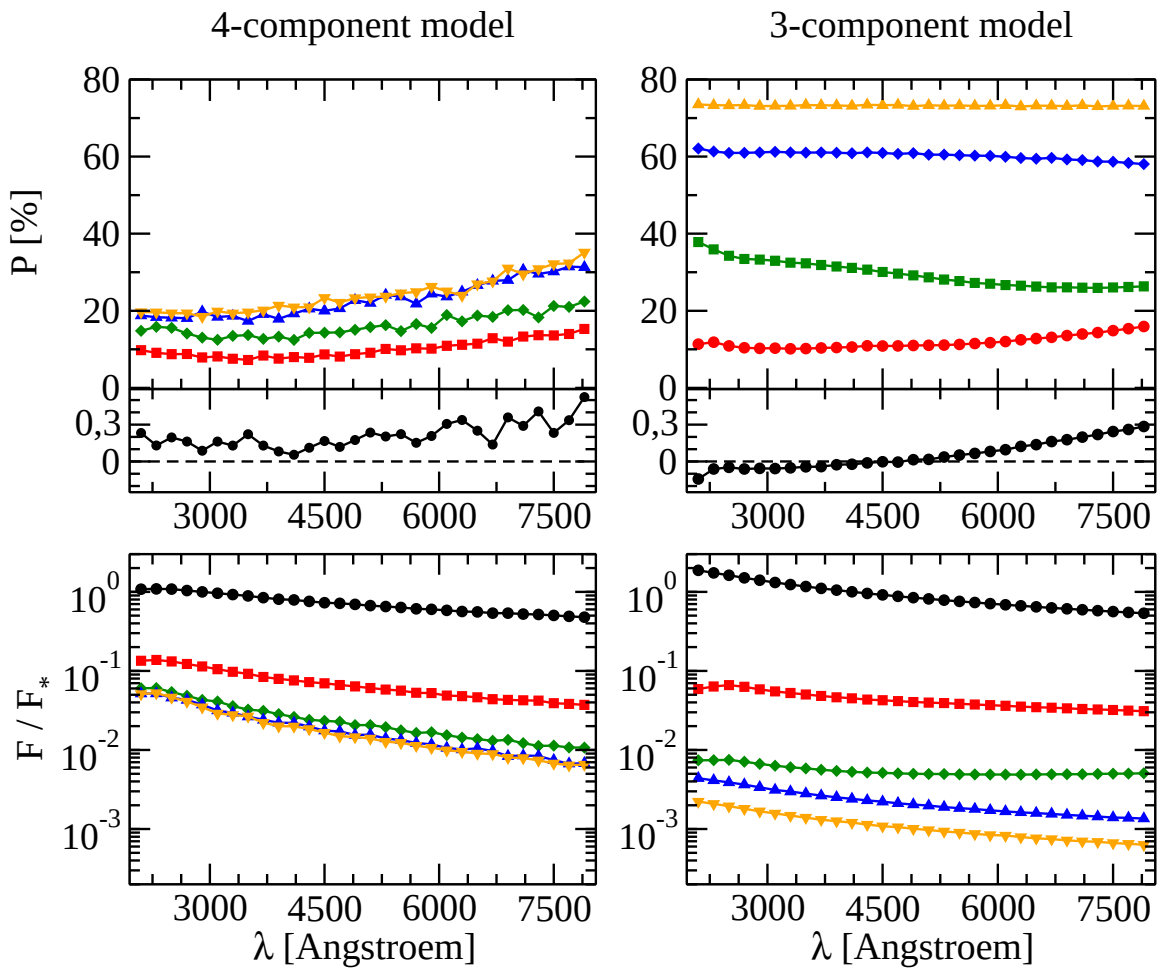

Fig. 1. Modeling the unified scheme of a thermal AGN. **Left column**: the 4-component model as described in the text. **Right column**: the 3-component model lacking the NLR region as presented in Marin et al. (2012b). Both figures show the polarization percentage, P, as a function of viewing inclination i measured from the torus axis and the fraction, F/F_*, of the central flux, F_*; Legend: $i = 84°$ (orange triangles with points to the bottom), $i = 73°$ (blue triangles with points to the top), $i = 60°$ (green diamonds), $i = 46°$ (red squares), $i = 26°$ (black circles).

3-component model. Additional depolarization occurs because the photons passing through the NLR have to undergo more scattering events before they escape from the model region. Due to the wavelength-dependence of Mie scattering, the presence of the NLR also has an effect on the spectral shape of P.

Compared to the observed optical/UV polarization of Seyfert-2 galaxies (Kay 1994, $P_{\rm obs} \leq 10\%$), our theoretical polarization is still too high, even though the presence of the NLR helps to approach the observed range of P. As discussed in Marin et al. (2012b), our model so far assumes a uniform density in all reprocessing regions. However, there are observational hints that the torus and the polar outflows should be fragmented (Nenkova et al. 2008, 2010). Preliminary modeling of such a clumpy reprocessing structure with *STOKES* indicates that the resulting polarization further decreases with respect to a uniform density model and may allow us to explain the observations of Kay (1994). Apart from the polarization, the bottom of Fig. 1 shows that the total (polarized + non-polarized) spectrum F/F_* decreases towards longer wavelengths in both models. This is another signature of the wavelength-dependent Mie scattering cross section and phase function. Also, a faint scattering feature at 2175 Å due to the carbonacious dust component is visible. When the NLR is included, the additional polar dust scattering increases the total flux scattered towards edge-on inclinations.

For type-1 objects our modeling shows that the additional dust scattering in the NLR can switch the $\vec{E}$-vector from a parallel to a perpendicular polarization state. While for the 3-component model the polar view exhibits parallel polarization below 4500 Å (Fig.1, top right, lower panel), the polarization is perpendicular across the whole wavelength range in the 4-component case (Fig.1, top left, lower panel). Given the resulting

weak percentage ($< 0.5\%$) of the perpendicular polarization, this model setup is coherent with the so-called *polar scattering dominated* AGN (Smith et al. 2002). Such type-1 AGN present a perpendicular, optical polarization rising towards the blue that Smith et al. (2002) explained by dust extinction along a line of sight passing through the upper layers of the torus material. Our model qualitatively produces a similar wavelength-dependent polarization, but at a much lower viewing angle. However, the relatively low optical depth of the polar dust scattering does not reproduce the full extend of the observed rise in P towards the blue end of the spectrum.

4 Summary and conclusions

To study the impact of the NLR on the polarization spectra in the optical/UV, we presented results for a 4-component reprocessing model computed with *STOKES*. In comparison with the 3-component model presented in Marin et al. (2012b), where polar dust scattering was absent, it appeared that the NLR cloud globally decreases the amount of polarization at type-2 viewing angles and may enforce perpendicular polarization also at type-1 viewing angles. The spectral shape of the polarization changes due to the additional Mie scattering in the polar directions.

An important conclusion to draw from this initial investigation is that the production of parallel polarization at type-1 viewing angles may become more difficult when the NLR is taken into account. It remains to investigate in a forthcoming study, to which extend the scattering origin of parallel polarization in type-1 AGN can be maintained. Inclusion of clumpy reprocessing media is important in such an investigation. On the positive side, the NLR helps to explain the observed degree of continuum polarization in type-2 objects.

The NLR region is an important ingredient of the unified AGN scheme, and if the extended outflows in Seyfert-2 galaxies are indeed photo-ionization by the emission of an obscured primary source, then the NLR is expected to sustain the same half-opening angle as the obscuring circumnuclear matter (Bianchi et al. 2012). Constraints on the half-opening angle of the NLR could thus provide estimates of the relative ratio of Seyfert-1 to Seyfert-2 galaxies in the local universe. The geometrical shape of the NLR region may also help us to determine if the symmetry implied by the unified model is broken (see Raban et al. 2009; Goosmann & Matt 2011; Marin et al. 2012a, for a study on NGC 1068). Such an asymmetry may explain the high degree of parallel polarization detected in peculiar objects like Mrk 231 (Gallagher et al. 2005) and ultimately lead to a better understanding of the launching of outflows inside the funnel of the circumnuclear medium.

This research was supported by the French *GdR* PCHE and the research grant ANR-11-JS56-013-01.

References

Antonucci, R. 1993, ARA&A, 31, 473
Antonucci, R. R. J. 1982, Nature, 299, 605
Antonucci, R. R. J. 1983, Nature, 303, 158
Antonucci, R. R. J. 1984, ApJ, 281, 112
Bianchi, S., Maiolino, R., & Risaliti, G. 2012, Advances in Astronomy, 2012
Capetti, A., Axon, D. J., Macchetto, F. D., Marconi, A., & Winge, C. 1999, Mem. Soc. Astron. Italiana, 70, 41
Cracco, V., Ciroi, S., di Mille, F., et al. 2011, MNRAS, 418, 2630
Gallagher, S. C., Schmidt, G. D., Smith, P. S., et al. 2005, ApJ, 633, 71
Goosmann, R. W. & Gaskell, C. M. 2007, A&A, 465, 129
Goosmann, R. W. & Matt, G. 2011, MNRAS, 415, 3119
Hoenig, S. F., Kishimoto, M., Antonucci, R., et al. 2012, ArXiv e-prints
Kay, L. E. 1994, ApJ, 430, 196
Marin, F., Goosmann, R., & Dovčiak, M. 2012a, Journal of Physics Conference Series, 372, 012065
Marin, F. & Goosmann, R. W. 2011, in SF2A-2011: Proceedings of the Annual meeting of the French Society of Astronomy and Astrophysics, ed. G. Alecian, K. Belkacem, R. Samadi, & D. Valls-Gabaud, 597–600
Marin, F., Goosmann, R. W., Gaskell, C. M., Porquet, D., & Dovciak, M. 2012b, ArXiv e-prints (1209.2915)
Mathis, J. S., Rumpl, W., & Nordsieck, K. H. 1977, ApJ, 217, 425
Nenkova, M., Sirocky, M. M., Nikutta, R., Ivezić, Ž., & Elitzur, M. 2008, ApJ, 685, 160
Nenkova, M., Sirocky, M. M., Nikutta, R., Ivezić, Ž., & Elitzur, M. 2010, ApJ, 723, 1827
Raban, D., Jaffe, W., Röttgering, H., Meisenheimer, K., & Tristram, K. R. W. 2009, MNRAS, 394, 1325
Smith, J. E., Young, S., Robinson, A., et al. 2002, MNRAS, 335, 773
Wilson, A. S. & Ulvestad, J. S. 1983, ApJ, 275, 8

SF2A 2012
S. Boissier, P. de Laverny, N. Nardetto, R. Samadi, D. Valls-Gabaud and H. Wozniak (eds)

MEASUREMENTS OF FLUORESCENCE YIELD OF ELECTRONS IN AIR UNDER ATMOSPHERIC CONDITIONS: A KEY PARAMETER FOR ENERGY OF COSMIC RAYS

D. Monnier Ragaigne[1], P. Gorodetzky[2], C. Blacksley[1], F. Wicek[1], H. Monard[1] and S. Dagoret-Campagne[1]

Abstract. The measurement of the fluorescence yield and its dependence on atmospheric properties such as pressure, temperature or pollutants, are essential to obtain a reliable measurement of the primary energy of cosmic rays. A new type of absolute measurement of the nitrogen fluorescence yield in the air will be performed at LAL using 3 items which will yield an unprecedented precision in all conditions of pressure, temperature, and pollutants. A 5 MeV electron beam will be provided by the new electron accelerator PHIL at LAL(Laboratoire de l'Accélérateur Linéaire, Univ Paris-Sud, CNRS/IN2P3, Orsay). This source will induce florescence yield inside an integrating sphere. The sphere will be surrounded by a spherical envelope to create a temperature controlled chamber (a Dewar). With this setup it will be possible to vary the temperature from -60 C to +40 C and the pressure from 1 to 0.01 atm. An output device on this sphere will be equipped with a set of optical fibers driving the fluorescence light to a Jobin-Yvon spectrometer equipped with an LN_2 cooled CCD. The fluorescence spectrum in the 300-430 nm range will be accurately measured in steps of 0.1 nm resolution. A PMT equipped with a BG3 filter (the same as on JEM-EUSO) will be set on the sphere to measure the integrated yield. The expected precision of the yield should be better than 5%.

Keywords: Ultra high-energy cosmic rays, air fluorescence technique

1 Introduction

A precise measurement of the energy is essential for the study of ultra-high energy cosmic rays. Basically, two types of detectors are used for this purpose:

- Surface arrays which sample the shower tail: this method records the lateral development of the shower of secondary particles using an array of particle detectors.
- Fluorescence detectors which record the longitudinal development of the shower and observe the atmospheric fluorescence induced by charged particles in the shower.

The second method is currently the most precise one to estimate the energy of cosmic rays, and is used by the Fly's Eye experiment (Bird et al. 1994), HiRes (Song et al. 2000), Telescope Array (Tokuno et al. 2008), and the Pierre Auger Observatory (Auger 2010). The future JEM-EUSO telescope (Takahashi et al. 2009) will also detect extensive air showers from the International Space Station with this method.

Fluorescence detectors record the longitudinal profile of air showers induced by cosmic rays through the detection of the fluorescence light generated by secondary charged particles. Since the fluorescence intensity is proportional to the deposited energy, the integration in depth of the fluorescence profile allows a calorimetric determination of the primary energy. This measurement of primary cosmic ray energy is relatively model independent, as the fluorescence intensity is proportional to the electromagnetic energy released by the shower into the atmosphere. For the Pierre Auger Observatory, the uncertainty in the energy using the fluorescence

[1] Laboratoire de l'Accélérateur Linéaire, Univ Paris-Sud, CNRS/IN2P3, Orsay
[2] Laboratoire Astroparticule et Cosmologie, APC, Paris, France

method is around 22%, and the main source of systematic uncertainties comes from the limited accuracy in the measurement of the air-fluorescence yield. In the Pierre Auger Observatory (Auger 2010) the uncertainty in the fluorescence yield contributes 14% to the total systematic error of the energy calibration. This parameter is thus a key for determining the energy of ultra-high energy cosmic rays detected by a fluorescence telescope. We will measure the fluorescence yield using a 5 MeV electron beam and calibrated detectors in order to improve the accuracy of this value to a precision of 5%.

2 Fluorescence yield

Air-fluorescence photons are produced by the de-excitation of atmospheric nitrogen molecules excited by the shower electrons. Excited molecules can also decay by colliding with other molecules, using the process of collisional quenching. This effect increases with pressure, reducing fluorescence intensity.

Atmospheric effects, including pressure, temperature, and composition, must also be reproduced and studied in order to understand the real conditions present during the production of fluorescence photons within an extensive air shower. As the excitation cross sections show a fast decrease with energy, secondary electrons from ionization processes are the main source of fluorescence light. For this reason, it is necessary to simulate the production of fluorescence photons in order to evaluate the fiducial volume needed for interaction. The fluorescence spectrum consists of a set of molecular bands represented by a set of discrete wavelengths λ. The range of this spectrum is the near UV between 300 to 430 nm.

The fluorescence yield for a line, Y_λ, is defined as the number of photons emitted by the primary charged particle per meter of path. The deposited energy of an electron per unit of length is defined as:

$$\rho \frac{dE}{dX} \tag{2.1}$$

The number of photons produced with this energy depends on the fluorescence efficiency of the line, ϕ_λ:

$$Y_\lambda(\text{photons/e/cm}) = \phi_\lambda \frac{\rho}{h\nu} \frac{dE}{dX}. \tag{2.2}$$

This efficiency, ϕ_λ, depends on the lifetime of the level (de-excitation) and also on the effect of pressure, temperature, and composition (Takahashi et al. 2009). For example, the dependence of Y_λ on atmospheric conditions can be described by the so-called characteristic pressure $P^{'}$. $P^{'}$ contains a contribution af all possible quenchers (I.E., N_2,O_2,H_2O).

$$Y_\lambda(P,T) = \frac{Y_\lambda}{1 + \frac{P}{P^{'}(\lambda,T)}}. \tag{2.3}$$

$$\frac{1}{P^{'}} = \sum_i \frac{f_i}{P_i^{'}} \tag{2.4}$$

$$P^{'} = \frac{kT}{\tau} \frac{1}{\sigma_{N_i} v_{N_i}} \tag{2.5}$$

With f_i is the fraction of molecules of type i in the mixture, σ_{N_i} is the collisional cross section which depends on the particular band, and v_{N_i} is the relative velocity of the molecules; k is the Boltzman constant and τ the radiative lifetime of the corresponding level.

The total fluorescence yield Y_{tot} is thus the sum of all Y_λ:

$$Y_{tot} = \sum_\lambda Y_\lambda. \tag{2.6}$$

Knowing both the fluorescence yield and its dependence on atmospheric properties accurately is essential in order to obtain a reliable measurement of the energy of cosmic rays in experiments using the fluorescence method (Rosado et al. 2011; Arqueros et al. 2009; Rosado et al. 2010). Even if the previous studies reproduce these effects by simulation and using the absolute value in dry air at a given pressure and temperature, the direct measurement of these effects is also essential in order to understand the different values used by the experiments (Monasor et al. 2009). Studying the total spectrum of fluorescence emission is also fundamental for JEM-EUSO in order to optimize data analysis.

3 Principle of the experiment

3.1 Experimental set up

The aim of this experiment is to measure the fluorescence yield of each line with a 5% accuracy using an electron beam as a source of electrons (reproducing the electrons of an extensive air shower), an integrating sphere with control of pressure, temperature, and composition in order to measure atmospheric effects, and calibrated detectors.

The electron beam will interact with gas inside an integrating sphere. A fraction of the emitted fluorescence light will be detected and measured with both a Jobin-Yvon spectrometer equipped with an LN_2 cooled CCD, in order to study each spectral line separately, and also a photo-multiplier tube equipped with a BG3 filter (the same filter as the JEM-EUSO project).

The integrating sphere must be vacuum-tight and part of a dewar to allow studying the yield at low temperatures (down to −60 C).The basic property of the integrating sphere being that the probability to detect light is independent from where the light is produced inside the sphere The size of the sphere depends on pressure (due to the pressure dependence of the distance of ionization of secondary electrons and multiple scattering) from a few centimeters at 1 atm to a few decimeters at very low pressure (0.01 atm). The exact size of the sphere is determined using Geant4 simulations to reproduce multiple scattering and the mean free path of secondary electrons.

The source of electrons is an electron accelerator (PHIL) developed at the Laboratoire de l'Accélérateur Linéaire (LAL) and presented in the next section.

The calibration of the detectors is fundamental in order to obtain an accurate measurement of the fluorescence yield.

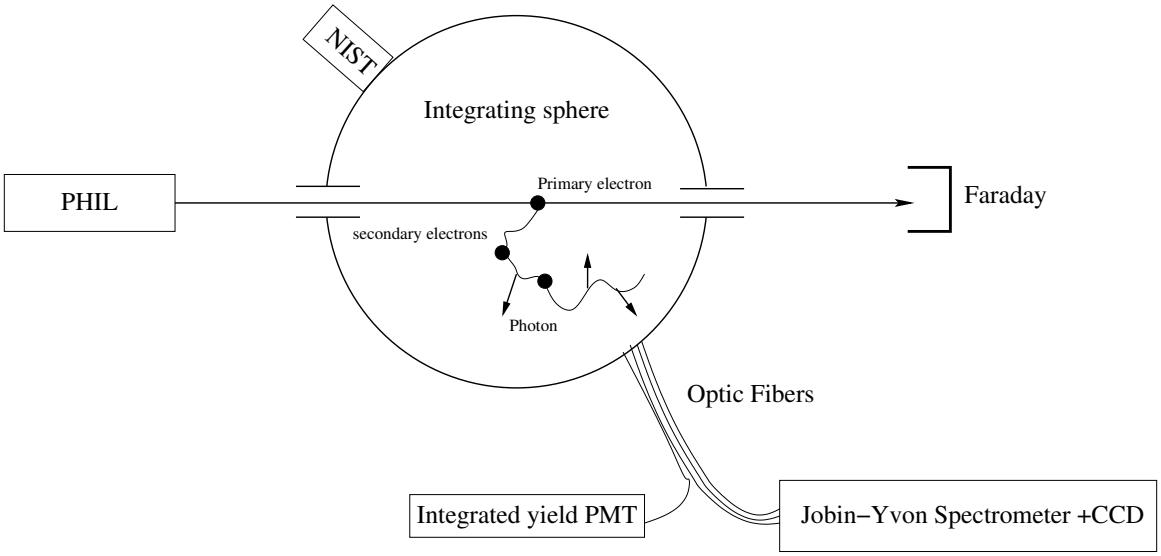

Fig. 1. Design of experiment

3.2 PHIL: the electron Beam

The "PHoto-Injector at LAL" (see Brossard et al. 2010, and `http://phil.lal.in2p3.fr/`) is an electron beam accelerator at LAL. This accelerator, which is primarily dedicated to the testing and characterization of electron photo-guns and high-frequency structures for future accelerator projects, can also be used to simulate the electrons emitted by an extensive air shower.

PHIL is currently a 6-meter-long accelerator with 2 diagnostic beam lines. The direct beam line will be used to inject electrons into an integrating sphere. An Integrating Current Transformer (ICT) and a faraday cage will provide the estimated beam charge, beam size, and beam position measurement with high accuracy. The main characteristics of PHIL, for our configuration, have been summed up in Table 1. For the measurement of the fluorescence yield, precise knowledge of the source (energy, position, charge...) is an important part of the

Table 1. Characteristics of PHIL

Characteristics	Values
Charge per bunch	between 50 pC to 300 pC
Energy	3-5 MeV
Energy spread	less than 10%
Bunch length	a few ps
Beam transverse dimension	0.5 mm

total accuracy. Using the PHIL accelerator, these parameters will be available with an accuracy of $\sim 2\%$. A separative window will connect the PHIL accelerator with the sphere.

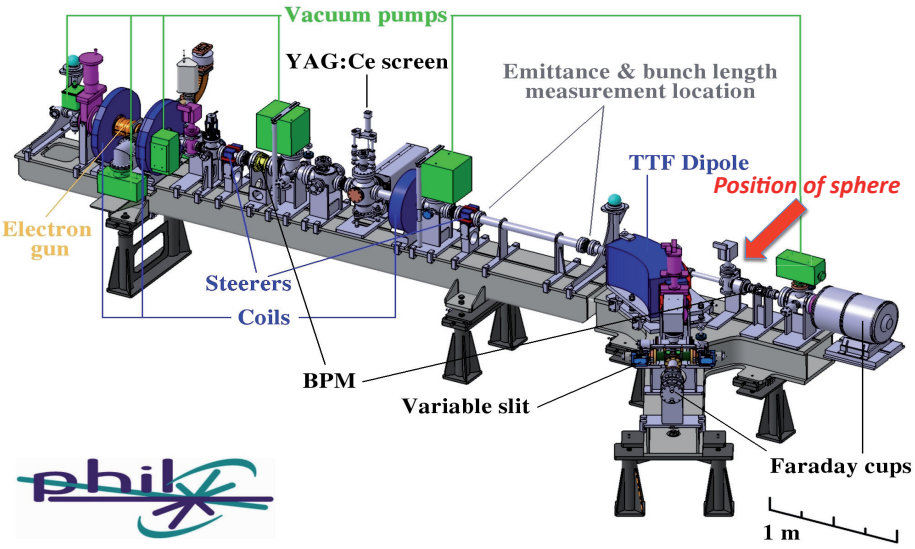

Fig. 2. The PHIL accelerator: Futur position of the sphere is indicated with the red arrow

3.3 Detectors

For the integrated measurement, fluorescence photons will be detected and counted by a photo-multiplier tube (PMT) with the same filter as in the JEM-EUSO project. The calibration of the detector is a key parameter in this kind of experiment. The overall PMT efficiency will be measured using a NIST photo-diode, accurate to 1.5%.

Spectral measurements are interesting because the effect of temperature, pressure, and composition are not the same for each spectral line. These effects are also interesting for the future JEM-EUSO project in order to study the signal to noise ratio, which changes with the wavelength.

The fluorescence lines will be measured using a Jobin-Yvon spectrometer equipped with a LN_2 cooled CCD. The CCD will be calibrated using the calibrated photo-multiplier tube at the second output of the spectrometer.

The patented method of calibration has been developed and used with success by G. Lefeuvre, P. Gorodetzky, and their collaborators, and is explained in the thesis of G. Lefeuvre (see Lefeuvre 2006; Lefeuvre et al. 2007).

The expected accuracy of the detectors (PMT and CCD camera) should be around 2 %.

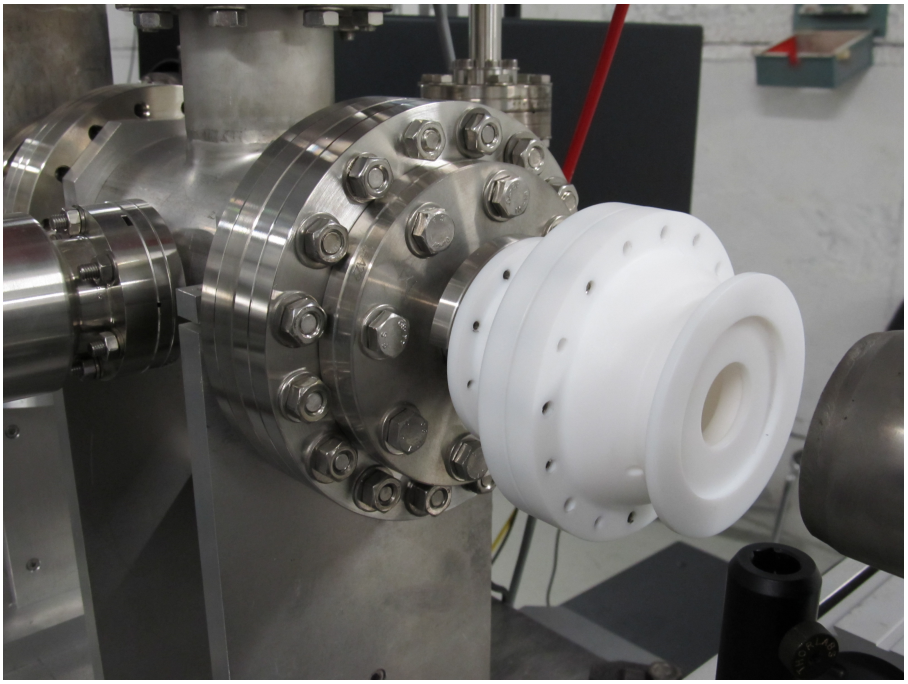

Fig. 3. First sphere in Teflon on the PHIL accelerator

4 Conclusions

The experiment will provide both the "integrated" measurement and "spectral" measurement of the fluorescence yield with high accuracy under a wide range of atmospheric conditions. The first step of the experiment will debug the measurement at 1 atm with a sphere of 6 cm in diameter. It will be performed during the next months (started in september 2012) and the study of atmospheric effects (temperature/pressure/composition) will be made during the year 2013.

A combined 2% accuracy for the detector and $\sim 2-3\%$ accuracy for the charge of the electron beam will allow measurement of the fluorescence yield with an accuracy of up to 5%.

This work has been financially supported by the GDR PCHE in France, APC laboratory, and LAL. We also thank the mechanics, PHIL, and vacuum team at LAL for the construction of the fluorescence bench.

References

Arqueros, F., Blanco, F., Rosado, J. 2009, New Journal of Physics, 11, 065011

Auger Collaboration 2010, Nucl. Instrum. Meth., A620, 227

Bird D.J. et al. 1994, ApJ, 424, 491

Brossard, J. et al. 2010, Proceedings of Beam Instrumentation Workshop, Santa Fe, New Mexico

Lefeuvre, G. 2006, PhD thesis, University Paris7- Denis Diderot (APC-26-06)

Lefeuvre, G. et al., 2007, Nucl. Instr. and Meth., A578, 78

Monasor, M., Vazquez, J.R., Arqueros, F. 2009, Proceedings of the 31 ICRC, Lodz 2009

Rosado, J., Blanco, F., Arqueros, F. 2010, Astropart. Phys, 34, 164

Rosado, J., Blanco, F., Arqueros, F. 2011, `http://arxiv.org/abs/1103.2022`

Song, C., Cao, Z., Dawson, B.R. 2000, Astroparticle Physics, 14, 7

Takahashi Y. and the JEM-EUSO Collaboration, 2009, New Journal of Physics, 2009, 11, 065009

Tokuno, H. et al. 2008, Journal of Physics Conference Series, 120, 062027

SF2A 2012
S. Boissier, P. de Laverny, N. Nardetto, R. Samadi, D. Valls-Gabaud and H. Wozniak (eds)

THE MAGNETIC COUPLING OF PLANETS AND SMALL BODIES WITH A PULSAR'S WIND

F. Mottez[1] and J. Heyvaerts[2]

Abstract. We investigate the electromagnetic interaction of a relativistic stellar wind with a planet or a smaller body in orbit around a pulsar. This may be relevant to objects such as PSR B1257+12 and PSR B1620-26 that are expected to hold a planetary system, or to pulsars with suspected asteroids or comets. Most models of pulsar winds predict that, albeit highly relativistic, they are slower than Alfvén waves. In that case, a pair of stationary Alfvén waves, called Alfvén wings (AW), is expected to form on the sides of the planet. The wings expand far into the pulsar's wind and they could be strong sources of radio emissions. The Alfvén wings would cause a significant drift over small bodies such as asteroids and comets.

Keywords: pulsars, exoplanets, astrophysical plasmas, MHD, Alfvén wings, non-Keplerian orbits

1 Introduction

Two pulsars with planets have been discovered, in 1992 and 1993 (Wolszczan & Frail 1992; Thorsett et al. 1993). In particular PSR B1257+12 hosts three planets at distances of the order of the astronomical unit. A pulsar is a neutron star with a fast spin (period $P \sim 0.001 - 5$ s) and surrounded by a magnetosphere that is a powerful source of radio and/or high energy emissions. (We use also the frequency $\Omega_* = 2\pi/P_*$). Precise timing of pulsars show that they spin down at a rate that is typically $\dot{P} \sim 10^{-15} - 10^{-19} P$. The dissipation of energy of PSR B1257+12 associated to the spin down is $\dot{E}_{rotation} = -M_I \Omega_* \dot{\Omega}_* = 4\pi^2 M_I \dot{P}/P^3 = 2. \times 10^{27}$ W, where M_I is their momentum of inertia. It can be compared to the planet's gravitational energy $E_G = GM_*M_p/2a = 4. \times 10^{32}$ J. If the flux dissipated by the spin down was captured through the planetary radius, the gravitational energy of the planet PSR 1257+12 "a" would be dissipated in only $8. \times 10^6$ years. Even with an inefficient coupling mechanism, can we expect heating, plasma acceleration and radio emissions from the planet, or a modification of its orbit ?

2 A planet in the wind

The planets (with an orbital period $P_{orb} >$ a few mn) are far beyond the light cylinder; they orbit in the pulsar's wind. This pulsar wind is an almost radial expansion of ultrarelativistic (Lorentz factor $\gamma \sim 10^2 - 10^7$.) and underdense plasma. Most pulsar wind models (Michel 1969; Contopoulos et al. 1999; Spitkovsky 2006; Kirk et al. 2009; Pétri 2012) converge on the following facts: This wind is highly magnetized ($B^2 >> \mu_0 \rho \gamma$), the magnetic field is quasi-azimutal ($B \sim B_\phi >> B_{poloidal}$). It is possibly sub-Alfvénic ($v_W \sim c$, $V_A \sim c$, until 100's of r_{LC}, (models) $v_W < V_A$). This last fact means that the planet is not preceded by a shock wave, but it is directly connected to the wind.

3 An electromagnetic wake behind the planet: Alfvén wings

Then, making simple hypothesis, it is possible to develop a theory of the interaction of the planet with the wind. The hypotheses are:

[1] LUTH, Observatoire de Paris, CNRS, Université Paris Diderot, 91190 Meudon
[2] Observatoire de Strasbourg, associé au LUTH

1. the plasma is locally uniform and incompressible (OK at 1st order (Wright & Schwartz 1990)). It can be non-relativistic (Neubauer 1980) or relativistic flow (Mottez & Heyvaerts 2011b; Heyvaerts et al. 2012).

2. Alfvén waves (MHD waves carrying mainly magnetic fluctuations) propagate almost only along the magnetic field

3. the planet is a conducting body (maybe because of a ionosphere)

Then, a potential drop is established by the plasma flow across the planet. The potential drop induces a current. This current is closed along the magnetic field lines, by two stationary Alfvén waves called Alfvén wings. This structure is a kind of electric circuit, sketched on see the left-hand side of Fig. 1. Its conductivity along the planet is those of the planet. Its conductivity Σ_A along the two ribbons of current that extend into space (the Alfvén wings) is, in the highly relativistic case, approximately equal to the vacuum conductivity

$$\Sigma_A \sim 1/\mu_0 c \sim 0.09 \text{ S}. \tag{3.1}$$

Then, it is possible (Neubauer 1980; Mottez & Heyvaerts 2011b) to estimate the total current circulating in the Alfvén wings

$$I_{AW} = 4(E_0 - E_i)R_P\Sigma_A, \tag{3.2}$$

where E_0 is the mean electric field associated to the unipolar inductor, E_i due to the planet's resistivity (that is low), R_P is the planetary radius, or more generally, the body's radius. For a $P = 10$ms PSR and an Earth-like planet at 0.2 AU, $I_{AW} \sim 10^9$ A. It is larger for a standard pulsar (of period $P = 1$s), $I_{AW} \sim 10^{11}$ A. For comparison, the pulsar's current i.e. the Goldreich-Julian current that powers the whole magnetosphere is $I_{GJ} = 2. \times 10^{11}$ A. For standard pulsars, the two currents are comparable !

4 Radio emissions ?

Of course, these strong and localized ribbons of electric current are probably unstable. Consequently, they may constitute powerful sources of radio emissions. A priori, there are two possible regions of emission (it is nothing more than a conjecture): (1) a radio source near the planet. Then, the source does not move in our frame of reference and the emissions might be similar to "usual" planetary radio emissions, generally associated to instabilities with $J_\parallel$, as it happens with the couple Jupiter-Io (Queinnec & Zarka 1998; Hess et al. 2008; Hess et al. 2009). It would be difficult to predict the angles of emission. (2) The radio source is along the Alfvén wing, and it is convected with the pulsar's wind. Then, the source is moving fast $V \sim c$ and the emission is beamed by the relativistic aberration (see the right-hand side of Fig. 1). In that case, the radiation would be well collimated, and it might be observable, under lucky circumstances (Mottez 2011).

5 Alfvén wings have a large influence on comets and asteroid's orbits

In the Alfvén wing electric circuit, the current density $\mathbf{j}$ flowing along the planet, crossed with the ambient magnetic field, is the cause of a $\mathbf{j} \times \mathbf{B}$ force density. The force has a component that is tangential to the orbit. It gives a non Keplerian contribution to the motion. This force and its effect on the orbit of a body in the pulsar wind can be estimated analytically (Mottez & Heyvaerts 2011a). Then, the evolution of the orbital elements can be computed numerically. For planets this force has a negligible contribution to the orbit. But it becomes very important when small bodies, like comets, asteroids and planetesimal are concerned. Figure 2 shows the time evolution of the semi-major axis of a 1 km sized rocky body in orbit around a standard pulsar (pulsar period $P = 1s$). The forces acts differently if the orbital spin is parallel or anti-parallel to the neutron star' spin. When they are parallel, the semi-major axis and the eccentricity tend to increase, while they are reduced for anti-parallel spins. In this last case, we see that a body can be precipitated onto the neutron star in less than 10,000 years.

This effect of the magnetic force on the objects orbiting a pulsar, especially planetesimals, may have important consequences in scenarios of planetary formation after the transformation of the star into a neutron star, from the debris of the supernova.

Name	U (V)	I (A)	$\dot{E}_{Jmax}$ (W)	$\Delta a/year$ (m)	$\Delta e/year$
PSR 1257+12 a	1.1×10^{12}	3.0×10^{9}	2.5×10^{21}	0.02	0
PSR 1257+12 b	$3{,}5\times10^{12}$	9.4×10^{9}	2.5×10^{22}	$1.\times10^{-3}$	3×10^{-16}
PSR 1257+12 c	$2{,}6\times10^{12}$	7.0×10^{9}	1.4×10^{22}	$1.\times10^{-3}$	2.4×10^{-16}
PSR 1620-26 a	$6{,}0\times10^{11}$	1.5×10^{9}	7×10^{20}	$3.\times10^{-6}$	0
PSR 10ms b 100 km	2.4×10^{9}	$6.\times10^{6}$	1.2×10^{16}	$8.\times10^{-3}$	$6.\times10^{-14}$
PSR 10ms b 1 km	2.4×10^{7}	$6.\times10^{4}$	1.2×10^{12}	0.8	$6.\times10^{-12}$
PSR 1 s b 100 km	2.4×10^{11}	6×10^{8}	1.2×10^{20}	8×10^{4}	6.4×10^{-8}
PSR 1 s b 1 km	2.4×10^{9}	$6.\times10^{6}$	1.2×10^{16}	$8.\times10^{5}$	$6.\times10^{-6}$

Table 1. Electric potential drop, total electric current associated to the Alfvén wing. Electrical energy $\dot{E}_{Jmax}$ dissipated in the Alfvén wing. Variation per (terrestrial) year of the semi-major axis. Variation of the eccentricity, per year, $\Delta e/year$.

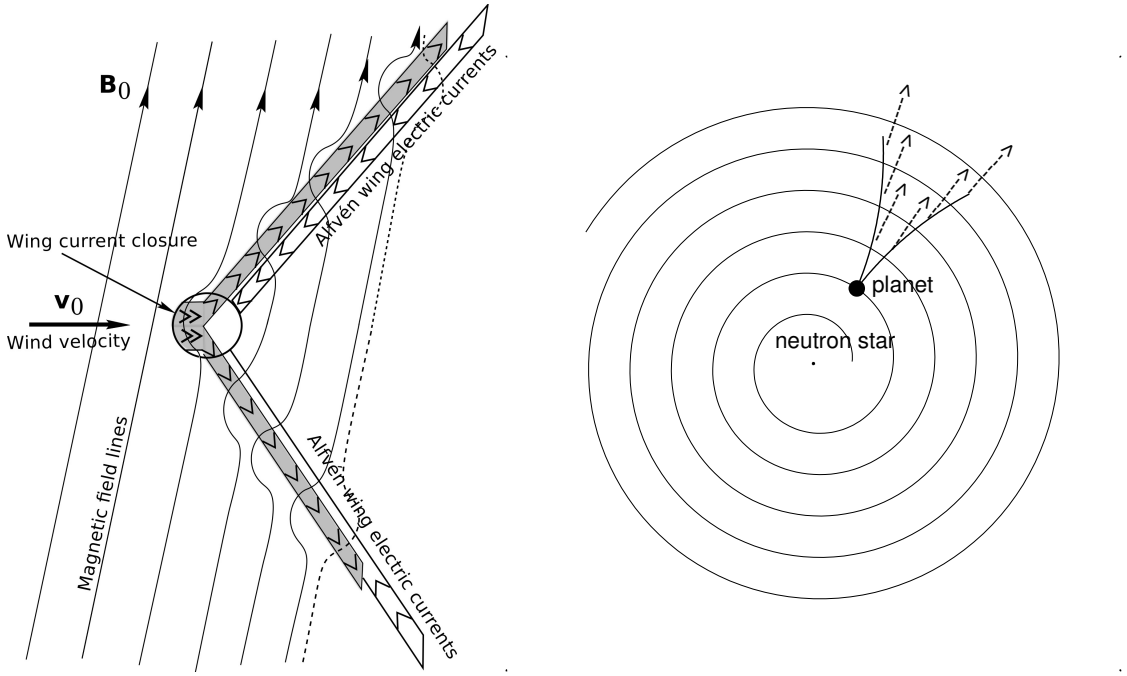

Fig. 1. Left: The engine of the Alfvén wing is a unipolar inductor. The unperturbed wind's magnetic field $\mathbf{B}_0$ and velocity $\mathbf{v}_0$ are almost, but not exactly, perpendicular. The electric field $\mathbf{E}_0$ created by the unipolar inductor is perpendicular to these two vectors; it induces an electric current (of density $\mathbf{j}$) along the body. This current then goes into the interplanetary medium, forming two structures, each of them made of an outwards and an inwards flow. The current density $\mathbf{j}$ flowing along the planet is the cause of a $\mathbf{j}\times\mathbf{B}$ force density. **Right:** general shape of the Alfvén wings on a larger scale. The spiral is the shape of a magnetic field line. The arrows show the directions of emissions of the radio waves if they are emitted by a source that is propagated by the wind.

6 Conclusions

A planet orbiting around a pulsar would be immersed in an ultrarelativistic underdense plasma flow.

It would behave as a unipolar inductor, with a significant potential drop along the planet. As for Io in Jupiter's magnetosphere, there would be two stationary Alfvén waves (Alfvén wings) attached to the planet.

The AW are supported by strong electric currents, comparable to those of a pulsar. It would be a cause of strong radio emissions, with sources all along the AW, highly colimated through relativistic aberration.

There would be a chance to detect these radio-emissions from Earth.
The emission would be pulses as for ordinary pulsars, but highly dependent on the planet-star-observer angle, maybe one very brief sequence once every orbit.

The Alfvén wing exerts a force unpon the orbiting body. This force has no influence of the motion of a

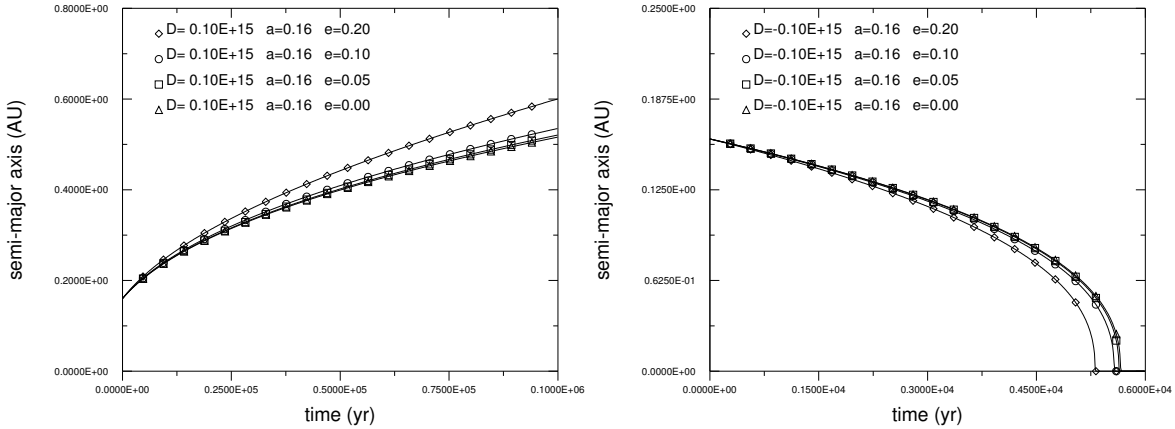

Fig. 2. Time-evolution of the semi-major axis of a 1km sized asteroid under the influence of the magnetic thrust. The initial distance a is 0.16 AU. The different curves are traced for various values of the orbit eccentricity e. **Left:** The orbital spin is *parallel* to the neutron star spin axis. In that case, the semi-major axis increases. The time axis covers 100,000 years. **Right:** The orbital spin is *anti-parallel* to the neutron star spin axis. The semi-major axis decreases. The time axis covers only 10,000 years.

planet. On the time scale of millions of years, it can however affect the orbit of bodies with a diameter of 100 kilometres around standard pulsars with a period $P \sim 1$ s and a magnetic field $B \sim 10^8$ T. Kilometer-sized bodies experience drastic orbital changes on a time scale of 10^4 years.

References

Contopoulos, I., Kazanas, D., & Fendt, C. 1999, ApJ, 511, 351

Hess, S., Mottez, F., & Zarka, P. 2009, Geophys. Res. Letters, 36, 14101

Hess, S., Mottez, F., Zarka, P., & Chust, T. 2008, J. Geophys. Res. (Space Physics), 113, 3260

Heyvaerts, J., Lehner, T., & Mottez, F. 2012, A&A 542, A128

Kirk, J. G., Lyubarsky, Y., & Petri, J. 2009, Astrophysics and Space Science Library, ed. W. Becker, Vol. 357, 421

Michel, F. C. 1969, ApJ, 158, 727

Mottez, F. 2011, in Proceedings of the 7th International Workshop on Planetary, Solar and Heliospheric Radio Emissions held at Graz, Austria, ed. H. O. Rucker, W. S. Kurth, P. Louarn, & G. Fischer, 315

Mottez, F. & Heyvaerts, J. 2011a, A&A, 532, A22

Mottez, F. & Heyvaerts, J. 2011b, A&A, 532, A21

Neubauer, F. M. 1980, J. Geophys. Res. (Space Physics), 85, 1171

Pétri, J. 2012, MNRAS, 424, 605

Queinnec, J. & Zarka, P. 1998, J. Geophys. Res. (Space Physics), 103, 26649

Spitkovsky, A. 2006, ApJ Letters, 648, L51

Thorsett, S. E., Arzoumanian, Z., & Taylor, J. H. 1993, ApJ Letters, 412, L33

Wolszczan, A. & Frail, D. A. 1992, Nature, 355, 145

Wright, A. N. & Schwartz, S. J. 1990, J. Geophys. Res. (Space Physics), 95, 4027

SF2A 2012
S. Boissier, P. de Laverny, N. Nardetto, R. Samadi, D. Valls-Gabaud and H. Wozniak (eds)

GRAVITATIONAL WAVE AND HIGH ENERGY NEUTRINO COINCIDENCES : RESULTS OF THE FIRST ANTARES - VIRGO/LIGO COINCIDENT SEARCH

T. Pradier[1] and the ANTARES Collaboration, the LIGO Scientific Collaboration and the Virgo Collaboration

Abstract. Sources of gravitational waves (GW) and emitters of high energy neutrinos (HEN) both involve compact objects and matter moving at relativistic speeds. GW emission requires a departure from spherical symmetry, which is the case if clumps of matter are accreted around black holes or neutron stars, and ejected in relativistic jets, where neutrinos are believed to be produced. Both messengers interact weakly with the surrounding matter, hence point directly to the heart of the engines that power these emissions. Coincidences between GW and HEN detectors would then give a unique insight on the physics of the most powerful objects in the Universe.

This contribution describes the results of the first joint GW+HEN search using concomitant data taken with the Antares, Virgo and LIGO detectors in 2007, when Antares was operating with 5 of its 12 lines, and Virgo/LIGO joint runs VSR1/S5 were underway. This search allowed to put the first constraints on the density of possible GW+HEN astrophysical sources.

Keywords: Neutrinos, Gravitational waves, multi-messenger astronomy

1 Introduction

A new generation of detectors offer unprecedented opportunities to observe the universe through all kind of cosmic radiations. In particular, both high-energy ($\gg$GeV) neutrinos (HEN) and gravitational waves (GW), which have not yet been directly observed from astrophysical sources, are considered as promising tools for the development of a multi-messenger astronomy (see e.g. Becker 2008; Márka 2011; Pradier 2010, for recent reviews). Both HEN and GW can escape from the core of the sources and travel over large distances through magnetic fields and matter without being altered. They are therefore expected to provide important information about the processes taking place in the core of the production sites and they could even reveal the existence of sources opaque to hadrons and photons, that would have remained undetected so far. The detection of coincident signals in both these channels would then be a landmark event and sign the first observational evidence that GW and HEN originate from a common source. The most plausible astrophysical emitters of GW+HEN are presented in Section 2.

The concomitant operation of GW and HEN detectors is summarized in the time chart of Fig. 1. Section 3 briefly describes the detection principles and the performances achieved by the Antares neutrino telescope (Aguilar et al. 2011) as well as by the GW interferometers Virgo (Acernese et al. 2008) and LIGO (Sigg et al. 2008), that are currently part of this joint search program. As both types of detectors have completely independant sources of backgrounds, the correlation between HEN and GW significances can also be exploited to enhance the sensitivity of the joint channel, even in absence of detection. The combined false alarm rate is indeed severely reduced by the requirement of space-time consistency between both channels. In Section 4, the strategies being developed for joint GW+HEN searches between Antares and the network of GW interferometers using the currently available datasets are presented. The results of the first GWHEN search will be published soon (Adrián-Martinez et al. 2012).

[1] Institut Pluridisciplinaire Hubert Curien, Department of Subatomic Research, Strasbourg, France
pradier@in2p3.fr

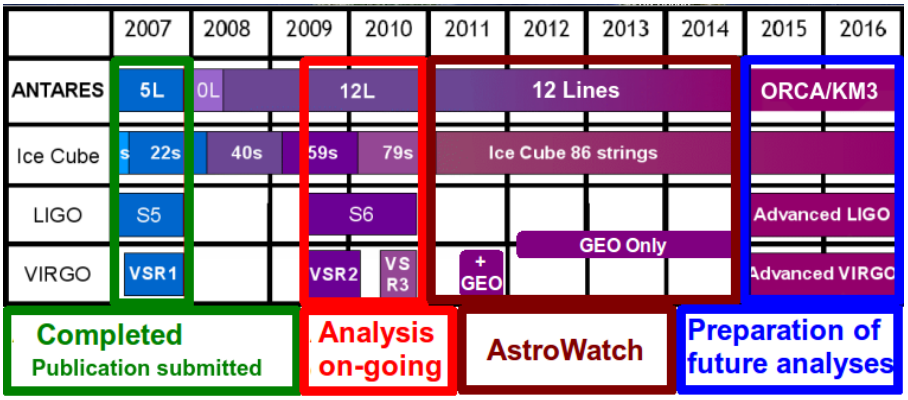

Fig. 1. Time chart of the data-taking periods for the ANTARES, VIRGO and LIGO experiments, indicating the respective upgrades of the detectors (as described in the text). The deployment of the KM3NeT neutrino telescope is expected to last three to four years, during which the detector will be taking data with an increasing number of PMTs before reaching its final configuration (Hernandez-Rey 2009).

2 Astrophysical emitters of gravitational waves and high-energy neutrinos

Potential sources of GWs and HENs are likely to be very energetic and to exhibit bursting activity. For more details, refer to Ando et al. (2012). **Soft Gamma Repeaters (SGRs)** are highly magnetized galactic X-ray pulsars with a soft γ-ray bursting activity. In the popular magnetar model (Thompson & Duncan 1995), the outbursts are caused by star-quakes associated to large-scale rearrangements of the magnetic field. The deformation of the star during the outburst could lead to the emission of GW within range of current interferometric GW detectors (Abadie et al. 2011). Sudden changes in the large magnetic fields would also accelerate protons or nuclei interacting with thermal radiation and generating a flux of HENs (Ioka et al. 2005).

But the most promising class of known extragalactic bursting sources are surely Gamma-Ray Bursts (GRBs), most frequent and better modelled. In the prompt and afterglow phases, HEN ($10^5 - 10^{10}$ GeV) are expected to be produced by accelerated protons in relativistic shocks and several models predict detectable fluxes in km^3-scale detectors (Waxman & Bahcall 1997; Rachen & Meszaros 1998; Alvarez-Muniz 2000), although no evidence for GRB neutrinos has been observed yet by IceCube in its 40- (Abbasi et al. 2011) or 59-strings configuration. While gamma-ray and HEN emission from GRBs are related to the mechanisms driving the relativistic outflow, GW emissions are closely connected to the central engine and hence to the GRB progenitor. **Short-hard GRBs** are thought to originate from coalescing binaries involving black holes and/or neutron stars; such mergers could emit GW detectable from relatively large distances, with significant associated HEN fluxes (Kochanek & Piran 1993; Nakar 2007). **Long-soft GRBs** are most probably induced by "collapsars", i.e. collapses of a massive star into a black hole, with the formation of an accretion disk and a jet that emerges from the stellar envelope (Woosler & Bloom 2008). **Low-luminosity GRBs**, with γ-ray luminosities a few orders of magnitude smaller, are believed to originate from a particularly energetic type Ibc core-collapse supernovae. They could produce stronger GW signals together with significant high- and low-energy neutrino emission; moreover they are more frequent than typical long GRBs and often discovered at shorter distances (Razzaque et al. 2004). Finally, **choked GRBs** are thought to be associated with supernovae driven by mildly relativistic, baryon-rich and optically thick jets, so that no γ-rays escape (Meszaros & Waxman 2001). Such "hidden sources" could be among the most promising emitters of GW and HEN, as current estimates predict a relatively high occurrence rate in the volume probed by current GW and HEN detectors (Ando & Beacom 2005).

3 Detectors and concomittant data taking

The Antares detector (Aguilar et al. 2011) is the first undersea neutrino telescope; its deployment at a depth of 2475m in the Mediterranean Sea near Toulon was completed in May 2008. It consists in a three-dimensional array of 884 photomultiplier tubes (PMTs) distributed on 12 lines anchored to the sea bed and connected to the shore through an electro-optical cable. Before reaching this final (12L) setup, Antares has been operating in various configurations with increasing number of lines, from one to five (5L) and ten (10L).

ANTARES detects the Cherenkov radiation emitted by charged leptons (mainly muons, but also electrons and taus) induced by cosmic neutrino interactions with matter inside or near the instrumented volume. The knowledge of the timing and amplitude of the light pulses recorded by the PMTs allows to reconstruct the trajectory of the muon and to infer the arrival direction of the incident neutrino. The current reconstruction algorithms achieve an angular resolution (defined as the median angle between the neutrino and the reconstructed muon) of about 0.4° for neutrinos above 10 TeV (Adrián-Martinez et al. 2011). The design of ANTARES is optimized for the detection of up-going muons produced by neutrinos which have traversed the Earth and interacted near the detector; its field of view is $\sim 2\pi$ sr for neutrino energies 100 GeV $\lesssim E_\nu \lesssim$ 100 TeV. Above this energy, the sky coverage is reduced because of neutrino absorption in the Earth; but it can be partially recovered by looking for horizontal and downward-going neutrinos, which can be more easily identified at these high energies where the background of atmospheric muons and neutrinos is fainter. ANTARES, especially suited for the search of astrophysical point sources, and transients in particular (Ageron et al. 2012), is intended as the first step towards a km^3-sized neutrino telescope in the Mediterranean Sea (Hernandez-Rey 2009).

The GW detectors VIRGO (Acernese et al. 2008), with one site in Italy, and LIGO (see e.g. (Sigg et al. 2008)), with two sites in the United States, are Michelson-type laser interferometers. They consist of two light storage arms enclosed in vacuum tubes oriented at 90° from each other. Suspended, highly reflective mirrors play the role of test masses. Current detectors are sensitive to relative displacements (hence GW amplitude) of the order of 10^{-20} to 10^{-22} Hz$^{-1/2}$. Their detection horizon is about 15 Mpc for standard binary sources.

The first concomitant data-taking phase with the whole VIRGO/LIGO network VSR1/S5 was carried on in 2007, while ANTARES was operating in 5L configuration (see Fig. 1). A second data-taking phase was conducted between mid-2009 and end 2010 with upgraded detectors, S6/VSR2 and VSR3, in coincidence with the operation of ANTARES 12L. Another major upgrade for both classes of detectors is scheduled for the upcoming decade: the Advanced VIRGO/Advanced LIGO and KM3NeT projects should gain a factor of 10 in sensitivities with respect to the presently operating instruments. The VIRGO/LIGO network monitors a good fraction of the sky in common with ANTARES: the instantaneous overlap of visibility maps is about 4 sr ($\sim$ 30% of the sky) (Pradier 2009).

4 First joint GW+HEN search using ANTARES data in 2007

GW interferometers and HEN telescopes share the challenge to look for faint and rare signals on top of abundant noise or background events. Preliminary studies on the feasibility of such searches (Aso et al. 2008; Pradier 2009) indicated that, even if the constituent observatories provide several triggers a day, the false alarm rate for the combined detector network can be kept at a very low level ($\sim$1/(600 yr)).

4.1 Coincidence Time Window

An important ingredient of these searches is the definition of an appropriate coincidence time window between HEN and GW signals hypothetically arriving from the same astrophysical source. A case study that considered the duration of different emission processes in long GRBs, based on BATSE, Swift and Fermi observations, allowed to derive a conservative upper bound $t_{GW} - t_{HEN} \in [-500s, +500s]$ on this time window (Baret et al. 2011). For short GRBs, this time-delay could be as small as a few seconds. For other sources, this delay is poorly constrained.

4.2 Analysis Strategy

The strategy chosen for the 2007 search consists in an event-per-event search for a GW signal correlating in space and time with a given HEN event considered as an external trigger. Such a search is rather straightforward to implement as it allows to make use of existing analysis pipelines developed e.g. for GRB searches. It has been applied to the concomitant set of data taken between January 27 and September 30, 2007 with ANTARES 5L-VSR1/S5. Such a triggered GW search has been proven to be more efficient than a classical "all-sky" analysis, because of the knowledge of the direction and time of arrival of the signal.

The ANTARES 5L data were filtered according to quality requirements similar to those selecting the well-reconstructed events that are used for the standalone searches for HEN point sources (see Adrián-Martinez et al. 2012, for more details). The list of candidate HEN includes their arrival time, direction on the sky, and an event-by-event estimation of the angular accuracy, which serves to define the angular search window for the GW search. For the purpose of this joint search, the angular accuracy is defined as the 90% quantile (and

not the median) of the error distribution on the reconstructed neutrino direction, obtained from Monte Carlo studies. The on-source time window is taken to be $[-500s, +500s]$ around the neutrino arrival time.

The list of HEN triggers is then transmitted to the X-pipeline (Sutton et al. 2010), an algorithm which performs coherent searches for unmodelled bursts of GWs on the combined stream of data coming from all active interferometers (ITFs). The background estimation and the optimization of the selection strategy are performed using time-shifted data from the off-source region in order to avoid contamination by a potential GW signal. Once the search parameters are tuned, the analysis is applied to the on-source data set. If a coincident event is found, its significance is obtained by comparing with the distribution of accidental events obtained with Monte-Carlo simulations using time-shifted data streams from the off-source region ; this is particularly efficient to look for strong signals but one can also look for an accumulation of weakest signals, by performing a dedicated statistical test, as will be shown later.

4.3 HEN candidates and error box for the GW search

The HEN candidates have been selected using the BBFit reconstruction (Adrián-Martinez et al. 2012). A total of 414 events, among which 198 reconstructed with 2 lines, with 2 azimuthal possible solutions, and 18 more energetic events reconstructed with more than 2 lines, were selected. Finally, when taking into account the fact that 2 or more ITFs are needed in order to reconstruct a possible GW arrival direction on the sky, 144 2-line events and 14 3-line events were analyzed for a possible GW counterpart, see Figure 2.

The angular accuracy with which the HEN arrival direction is reconstruted depends on the energy of the event and its direction. The space-angle error distribution between the true neutrino direction and the reconstructed muon direction has been parametrized using a log-normal law in intervals of declination and energy. The parameters of the function has been used in the GW analysis to estimate the consistency of a reconstructed signal with the HEN arrival direction. This is the 90% quantile of this distribution which is used as a angular window for the GW search, see Figure 2.

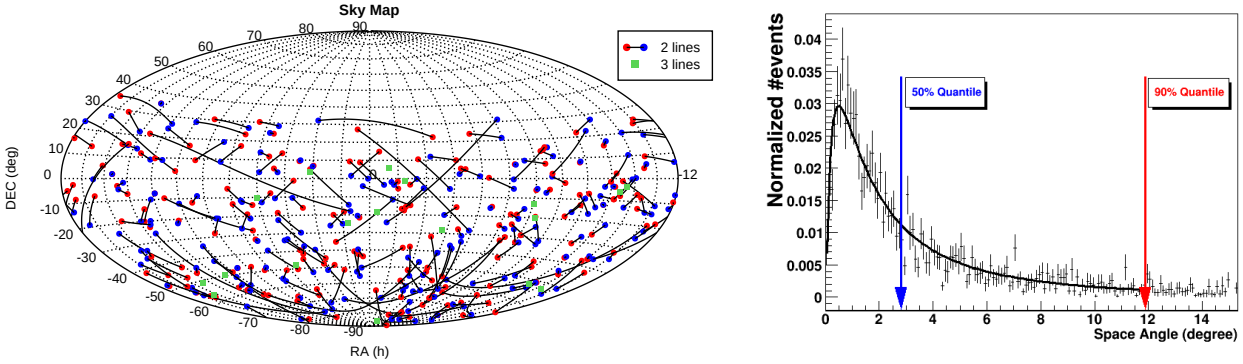

Fig. 2. Left: Skymap in equatorial coordinates of the 2-line and 3-line HEN events, selected in 2007 ANTARES data for the search. **Right:** Space angle error between the true neutrino direction and the reconstructed muon direction, together with the log-normal parametrization.

4.4 The GW search and its results

A low-frequency search, with a cut-off frequency at 500 Hz, was performed for all the HEN events. An additional high-frequency search up to 2kHz, more time-consuming, was performed for the 3 line events, more energetic and more likely to be of astrophysical origin.

No GW candidate was observed. This allowed to extract GW exclusion distances for typical signal scenarios. For binary merger signals, expected in the case of short GRBs, the null observation means that no merger of this type has occured within $\sim$ 10 Mpc. The exclusion distances obtained are similar for collapse-like signals, which are to be expected in the case of long GRBs for instance.

A binomial test has been performed to look for an accumulation of weak GW signals, as can be seen in Figure 3 (for the low-frequency search only). Its results are negative for both the low and high frequency searches - the post-trial significance of the largest deviation from the null hypothesis is 66%.

5 Astrophysical interpretation of the search

The non-observation of a GW+HEN coincidence during the $\sim$ 100 days of concomittant data taking allows to set that the actual number of coincidences verified $N_{\rm GWHEN} = \rho_{\rm GWHEN} V_{\rm GWHEN} T_{\rm obs} \leq 2.3$ at the 90% confidence level. Here $\rho_{\rm GWHEN}$ is the density of objects aimed at with the present analysis, typically the collapse or coalescence of compacts stars, GW emitters, followed by a jet, in which HEN are produced, in the local universe. This is a novel way to test the non-constrained gravitational origin of astrophysical jets formation.

$V_{\rm GWHEN}$ is the effective volume of universe probed by the search, which depends on the horizon of the involved experiments for typical signals. The GW horizon has been estimated to be $\sim$ 10 Mpc for mergers, and $\sim$ 20 Mpc for collapses. The HEN horizons are weaker for the ANTARES 5 line detector, of the order of 5 Mpc for mergers (computed using typical short GRB models), and 10 Mpc for long GRBs. The variation of the detection efficiencies of both experiments with distance have to be taken into account to have a realistic estimate of the effective volume.

Converting the null observation into a density yields a limit ranging from 10^{-2} Mpc^3.yr^{-1} for short GRB-like signals down to 10^{-3} Mpc^3.yr^{-1} for long GRB-like emissions. The comparisons with existing estimates of occurence rates for short/long GRBs or other objects of interest is made in Figure 3.

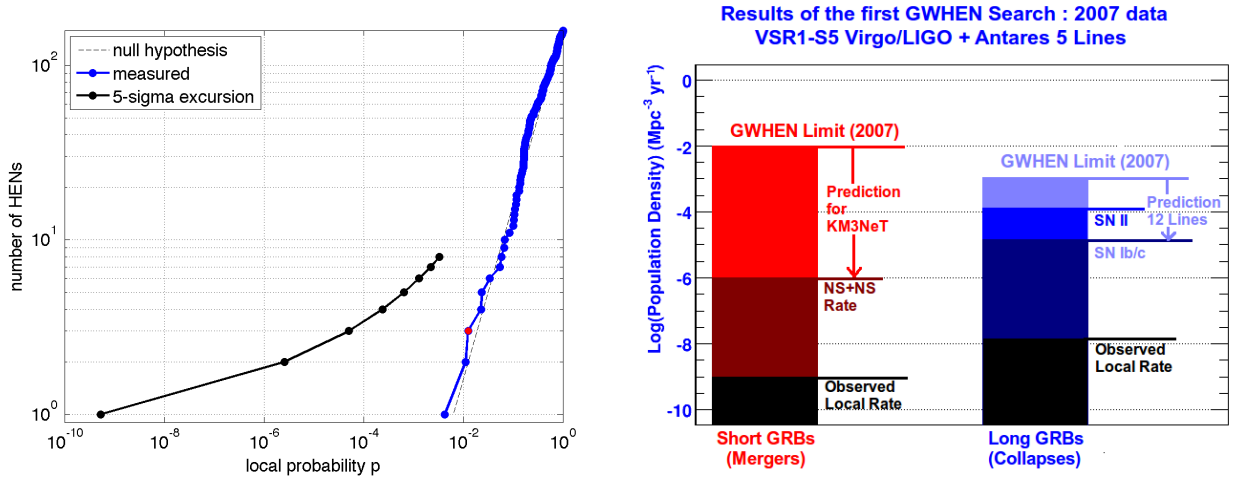

Fig. 3. Left: Binomial test which shows the probability to get $N_{\rm HEN}$ GW signals with a p-value higher than p. The black dots shows the number of GW+HEN associations needed to reach a 5σ significance. **Right:** GWHEN 2007 astrophysical limits are compared with local short/long GRB rates, merger rates (for short GRB-like sources), and SN II and SN Ib/c rates (for long GRB-like models). Also shown are the potential reach of future analyses.

6 Future analyses and conclusions

The analysis of the data taken with the full 12 lines of the ANTARES detector in 2009-2010, concomittant with the VIRGO VSR2 and LIGO S6 joint run, with GW upgraded detectors, has now started. A new HEN reconstruction algorithm has been used in order to reduce the HEN angular error. Moreover, a new GW software has been used which allows to perform joint simulations in order to optmize the joint analysis. The false-coincidence rate of the GW+HEN search depends on the individual false-alarm rates $f_{\rm HEN}$, $f_{\rm GW}$: for instance, if $f_{\rm HEN}$ is high, because of loose selection cuts, $f_{\rm GW}$ has to be reduced to conserve the same significance in case of a detection. Of course, this optimization strongly depends on the, e.g., HEN spectrum index, and the GW assumed signals. This optimization is currently underway to find the optimal HEN selection cuts. This search could be able to constrain for the first time of fraction of star collapses followed by the ejection of a hadronic jet (see Figure 3).

This first pioneering GW+HEN search, developed in Adrián-Martinez et al. (2012), opens the way towards a new multi-messenger astronomy. Beyond the benefit of a potential high-confidence discovery, future analyses, particularly the one involving a km^3 HEN telescope (Hernandez-Rey 2009) and advanced interferometers (Harry et al. 2010), could be able to constrain the density of joint sources down to astrophysically-meaningful levels -

hence contrain for the first time the fraction of binary mergers followed by the emission of a relativistic jet, as shown in Figure 3.

References

Abadie, J. et al. 2011, ApJLett., 734, L35
Abbasi, R. et al. 2011, Phys. Rev. Lett., 106, 141101
Acernese, F. et al. 2008, Class. Quant. Grav., 25, 184001
Adrián-Martinez, S. et al. 2011, ApJLett., 743, 14
Adrián-Martinez, S. et al. 2012, submitted for publication, arxiv:1205.3018
Ageron, M. et al. 2012, Astropart. Phys., 35, 530
Aguilar, J. A. et al. 2011, Nucl. Instrum. Meth. A, 656, 11
Alvarez-Muniz, J., H. F. a. H. D. W. 2000, Phys. Rev. D, 62, 093015
Ando, S. & Beacom, J. 2005, Phys. Rev. Lett., 95, 061103
Ando, S. et al. 2012, arxiv:1203.5192
Aso, Y. et al. 2008, Class. Quant. Grav., 25, 114039
Baret, B. et al. 2011, Astropart. Phys., 35, 1
Becker, J. K. 2008, Phys. Rept., 458, 173
Harry, G. M. et al. 2010, Class. Quant. Grav., 27, 084006
Hernandez-Rey, J. J. 2009, J. Phys. Conf. Ser., 171, 012047
Ioka, K. et al. 2005, ApJ, 633, 1013
Kochanek, S. & Piran, T. 1993, ApJ, 417, L17
Márka, S. 2011, Class. Quant. Grav., 28, 114013
Meszaros, P. & Waxman, E. 2001, Phys. Rev. Lett., 87, 17
Nakar, E. 2007, Phys. Rept., 442, 166
Pradier, T. 2009, Nucl. Instrum. Meth. A, 602, 268
Pradier, T. 2010, Class. Quant. Grav., 27, 194004
Rachen, J. P. & Meszaros, P. 1998, Phys. Rev. D, 58, 123005
Razzaque, S. et al. 2004, Phys. Rev. Lett., 93, 181101
Sigg, D. et al. 2008, Class. Quant. Grav., 25, 114041
Sutton, P. J. et al. 2010, New J. Phys., 12, 053034
Thompson, C. & Duncan, R. 1995, MNRAS, 275, 255
Waxman, E. & Bahcall, J. N. 1997, Phys. Rev. Lett., 78, 2292
Woosler, S. E. & Bloom, J. S. 2008, Ann. Rev. Astron. Astroph., 44, 507

The authors gratefully acknowledge the support of the United States National Science Foundation for the construction and operation of the LIGO Laboratory, the Science and Technology Facilities Council of the United Kingdom, the Max-Planck-Society, and the State of Niedersachsen/Germany for support of the construction and operation of the GEO600 detector, and the Italian Istituto Nazionale di Fisica Nucleare and the French Centre National de la Recherche Scientique for the construction and operation of the Virgo detector. The authors also gratefully acknowledge the support of the research by these agencies and by the Australian Research Council, the International Science Linkages program of the Commonwealth of Australia, the Council of Scientic and Industrial Research of India, the Istituto Nazionale di Fisica Nucleare of Italy, the Spanish Ministerio de Educacion y Ciencia, the Conselleria d'Economia Hisenda i Innovacion of the Govern de les Illes Baleares, the Foundation for Fundamental Research on Matter supported by the Netherlands Organisation for Scientic Research, the Polish Ministry of Science and Higher Education, the FOCUS Programme of Foundation for Polish Science, the Royal Society, the Scottish Funding Council, the Scottish Universities Physics Alliance, The National Aeronautics and Space Administration, the Carnegie Trust, the Leverhulme Trust, the David and Lucile Packard Foundation, the Research Corporation, and the Alfred P. Sloan Foundation. The authors also acknowledge the financial support of the funding agencies for the construction and operation of the ANTARES neutrino telescope: Centre National de la Recherche Scientique (CNRS), Commissariat à l'Énergie atomique et aux énergies alternatives (CEA), Agence National de la Recherche (ANR), Commission Européenne (FEDER fund and Marie Curie Program), Région Alsace (contrat CPER), Région Provence-Alpes-Côte d'Azur, Département du Var and Ville de La Seyne-sur-Mer, France; Bundesministerium fur Bildung und Forschung (BMBF), Germany; Istituto Nazionale di Fisica Nucleare (INFN), Italy; Stichting voor Fundamenteel Onderzoek der Materie (FOM), Nederlandse organisatie voor Wetenschappelijk Onderzoek (NWO), the Netherlands; Council of the President of the Russian Federation for young scientists and leading scientic schools supporting grants, Russia; National Authority for Scientic Research (ANCS), Romania; Ministerio de Ciencia e Innovacion (MICINN), Prometeo of Generalitat Valenciana (GVA) and Multi-Dark, Spain. They also acknowledge the technical support of Ifremer, AIM and Foselev Marine for the sea operation and the CC-IN2P3 for the computing facilities.

This work has received support from the **Groupement de Recherche Phénomènes Cosmiques de Haute Energie**.

SF2A 2012
S. Boissier, P. de Laverny, N. Nardetto, R. Samadi, D. Valls-Gabaud and H. Wozniak (eds)

ATMOSPHERE COMPOSITION OF QUIESCENT ACCRETING NEUTRON STARS IN GLOBULAR CLUSTERS

M. Servillat[1,2]

Abstract. Through the study of the quiescent X-ray emission of neutron stars in low-mass X-ray binaries it is possible to constrain the equation of state of dense matter. However, the chemical composition of the neutron star atmosphere is still uncertain. Using deep *Chandra* observations, we report the detailed spectral analysis of a neutron star in the globular cluster M28. For the first time for this kind of object, different atmosphere models composed of hydrogen, helium or carbon are used. The carbon model can be ruled out, and the derived mass and radius are clearly distinct depending on the composition of the atmosphere, leading to different constraints on the equation of state. We compare those results with the other similar neutron stars studied with a hydrogen atmosphere model only and show that a helium model could be relevant in many cases. Measurements of neutron star masses/radii by spectral fitting should consider the possibility of heavier element atmospheres, which produce larger masses/radii for the same data, unless the composition of the accretor is known independently.

Keywords: equation of state, stars: neutron, globular clusters: individual (M28 or NGC 6626), X-rays: binaries, X-rays: individual (CXOGlb J182432.8-245208)

1 Introduction

Neutron stars (NS) are composed of the densest form of matter known to exist in our Universe, providing us with a unique laboratory to study cold matter at supra-nuclear density. In particular, it is still not well understood whether exotic condensates occur in the NS core. The chemical composition of the outer envelope is also uncertain, as well as the symmetry energy, the behavior of superfluidity among neutrons and protons, and the conductivity of the NS crust. Measuring the masses or radii of these objects can lead to useful constraints on the dense matter equation of state (EOS), and give insights of the composition of NSs (see Lattimer 2010 for a recent review).

The mass and radius of isolated NS or ones in transient low-mass X-ray binaries (LMXBs) can be inferred from spectral modeling if their distances are accurately determined. In the case of accreting NSs located in globular clusters (GCs), relatively accurate distances are known. It has been shown that the surface of a weakly magnetic ($B < 10^{10}$ G) NS should be chemically very pure and dominated by the lightest element present as the heavier elements settle out of the atmosphere within seconds to minutes (Alcock & Illarionov 1980; Brown et al. 2002). If there is accretion after the NS formation, the atmosphere could be composed of hydrogen –H– or helium –He– as heavier elements are expected to be destroyed via nuclear spallation reactions (Bildsten et al. 1992; Chang & Bildsten 2004). A fraction of the incident He also suffers spallation reactions and may reform through fusion reactions (Bildsten et al. 1993). The ratio of H to He is thus not well determined. If no accretion takes place or if all lighter elements are burned, heavy elements are expected (Chang et al. 2010, and references therein).

Different NS atmosphere models have been developed, but most recent work for low magnetic fields has focused on a pure H model, such as the ones developed by Zavlin et al. (1996), Gänsicke et al. (2002), or Heinke et al. (2006). The latter model, NSATMOS, was further developed to represent atmospheres of pure He, carbon, nitrogen, oxygen or iron (Ho & Heinke 2009). In particular, such models were used for the low magnetic field NS located at the center of the Cassiopeia A supernova remnant, which was shown to harbor a carbon atmosphere (Ho & Heinke 2009).

[1] Lab. AIM (CEA/DSM/IRFU/SAp, CNRS, Université Paris Diderot), CEA Saclay, Bat. 709, 91191 Gif-sur-Yvette, France
[2] Harvard-Smithsonian Center for Astrophysics, 60 Garden Street, Cambridge, MA 02138, USA

2 Chandra observation of the quiescent accreting neutron star in M28

The GC M28 (NGC 6626) is located at a distance of $D = 5.5 \pm 0.3$ kpc (from Harris 1996, 2010, using measurements in Testa et al. 2001) at RA $= 18^h24^m32.81^s$ and Dec $= -24°52'11.2''$ (J2000). The reddening toward M28 is $E(B-V) = 0.42 \pm 0.02$ (Testa et al. 2001), implying a H column density of $N_{\rm H} = (2.33 \pm 0.12) \times 10^{21}$ cm^2 (using Predehl & Schmitt 1995 for conversion).

Becker et al. (2003) have previously reported on a set of ∼40 ks *Chandra* X-ray Observatory ACIS-S observations of M28 (ObsIds 2683, 2684, 2685). They suggested that the luminous, soft *Chandra* source numbered 26 in their work (IAU-approved source name CXOGlb J182432.8-245208) is a transiently accreting NS in a LMXB in quiescence (qLMXB). We keep the name source 26 throughout the text. Two additional long observations were acquired on 2008 August 7 (ObsId 9132) and 2008 August 10 (ObsId 9133) for 144 and 55 ks, respectively. Using all the available data, the qLMXB candidate is detected with a total of 10332 counts (∼0.043 cts s^{-1}) in the 0.3–6 keV energy band. The complete analysis of this dataset is presented in Servillat et al. (2012).

The source showed no significant variability in all Chandra observations. We thus fitted simultaneously the five spectra extracted from the five different epochs with Xspec 12.7.0e (Arnaud 1996), using the pure H atmosphere model NSATMOS (Heinke et al. 2006) and a photoelectric absorption $N_{\rm H}$ along the line of sight (TBABS, with abundances from Wilms et al. 2000). We fixed the distance to 5.5 kpc and the normalization to 1 (i.e. we assume that all the NS surface is emitting). We used the pile-up model component available in Xspec (Davis 2001) with a frame time set to 3.1 s and a free α parameter (related to the probability of events being retained as a good grade after filtering). The best fit model (χ^2_ν/dof = 0.87/141) is obtained for $\alpha = 0.41 \pm 0.15$, $N_{\rm H} = (2.5 \pm 0.3) \times 10^{21}$ cm^2, a temperature $kT_{\rm eff} = 125 \pm 40$ eV, a mass $M = 1.4^{+0.4}_{-0.9}$ $M_\odot$ and a radius $R = 9 \pm 3$ km. Errors are at 90% significance and we considered only masses higher than 0.5 $M_\odot$ and radii higher than 6 km. The 0.3–6 keV absorbed flux of the source (after removing the pile-up effect) is then $(1.8 \pm 0.2) \times 10^{-13}$ erg s^{-1} cm^{-2}, and the unabsorbed luminosity $\sim 1.6 \times 10^{33}$ erg s^{-1} (at 5.5 kpc). We then ran the command *steppar* and obtained confidence contours for the mass and radius of the NS, which are more instructive than the best fit parameter values and errors (see Figure 1, left).

We performed the same fitting procedure with an atmosphere model composed of pure He (using opacity tables computed by the Opacity Project[i]; see Ho & Heinke 2009 for details), and including the pile-up model. A similar good fit was obtained (χ^2_ν/dof = 0.88/142) with $N_{\rm H} = (2.65 \pm 0.25) \times 10^{21}$ cm^2, a temperature $kT_{\rm eff} = 170^{+50}_{-90}$ eV, a mass $M = 2.0^{+0.5}_{-1.5}$ $M_\odot$ and a radius $R = 14^{+3}_{-8}$ km. The confidence contours obtained with the *steppar* command are reported in Figure 1 (right). We note that the regions delimited by the contours are not consistent at the 80% confidence level with the contours obtained with the H model.

Finally, we performed a similar fit with a carbon atmosphere model (Ho & Heinke 2009). We obtain an acceptable fit (χ^2_ν/dof = 0.88/142) but the parameter values are excluded by causality (Rhoades & Ruffini 1974): $M > 2.6$ $M_\odot$ for $R = 10 \pm 2$ km.

3 Discussion

For both a H and a He model, we found good fits with an absorption consistent with the expected absorption from the GC reddening, suggesting that the source is located in the core of M28 with no or very low intrinsic absorption. The mass and radius are as expected for a typical NS (e.g. Lattimer 2010), and the temperature is in the expected range for qLMXBs.

The only striking difference is that H and He atmosphere models give distinct contour regions of masses/radii at the 80% confidence level (Figure 1). On the one hand, the H model gives a mass and radius consistent with the canonical value of 1.4 $M_\odot$ and 10 km, and allows for the presence of exotic matter inside NSs (hyperons, quarks). On the other hand, the He model provides solutions with higher masses/radii, consistent with the stiffest EOS for NS interiors, most of them composed of neutrons and protons.

The composition of the NS atmosphere depends on the accreting material, physical processes occurring during the accretion, and conditions on the NS surface. A non-evolved star will produce mostly H, which will quickly stratify to provide a pure H atmosphere. White dwarf donors (in so-called ultra-compact LMXBs) will provide mostly He, C/O, or O/Ne/Mg depending on the white dwarf. Ultra-compact LMXBs are observed to be much more common in GCs than in the rest of the Galaxy (Deutsch et al. 2000). Of 16 bright LMXBs in 13 clusters, we have 11 orbital period measurements, of which 5 indicate ultra-compact systems (e.g. Zurek et al.

[i] http://cdsweb.u-strasbg.fr/topbase/TheOP.html

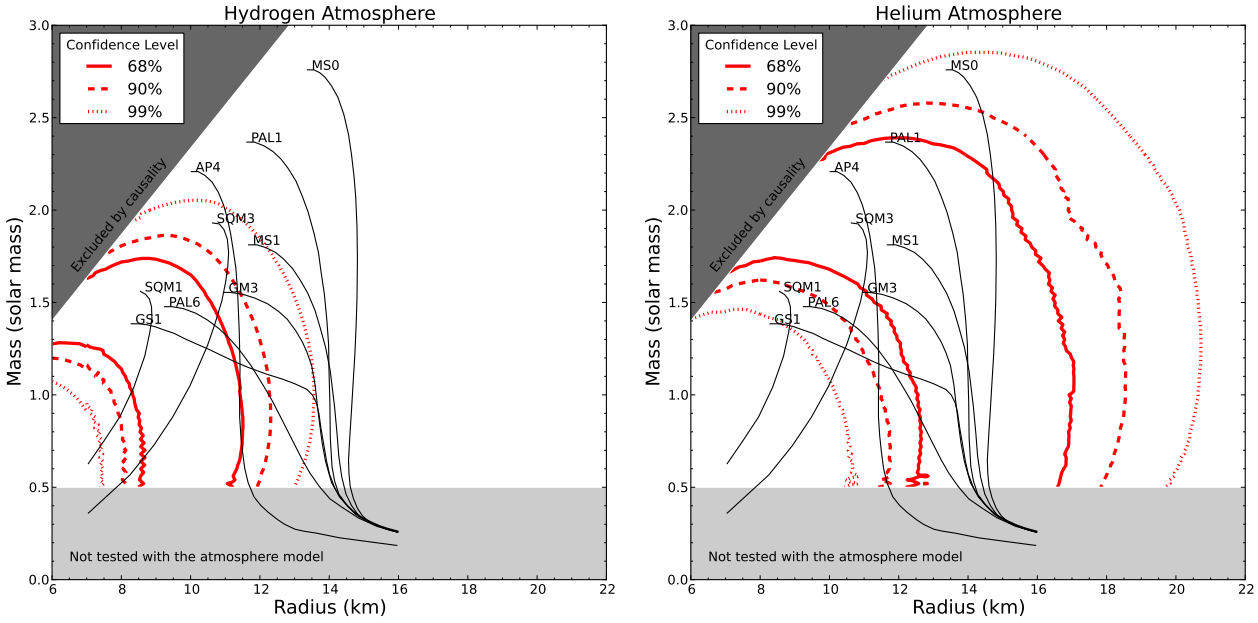

Fig. 1. Confidence levels for the mass and radius of the M28 NS *Chandra* source 26, using a H (**left**) or He (**right**) atmosphere model. A representative selection of EOS are reported (labelled as in Lattimer & Prakash 2001). The parameters were not allowed to vary in the area "Not tested with the atmosphere model". We report in dark gray the area excluded by causality (Rhoades & Ruffini 1974).

2009; Altamirano et al. 2010). In the rest of the Galaxy, only 9 ultra-compact systems are known among the ∼80 bright LMXBs with period measurements (Ritter & Kolb 2003, 2010). Dynamical formation of ultra-compact LMXBs in GC cores explains this difference (Verbunt 1987; Ivanova et al. 2005).

It is unclear whether spallation always produces H during accretion (Bildsten et al. 1992, 1993; Chang & Bildsten 2004). Theoretical work is needed to clarify the conditions for spallation. Also, obtaining a high-quality X-ray spectrum of an neutron star ultra-compact LMXB in quiescence at known distance would help clarify this question.

4 Comparison with other GC qLMXBs

Table 1. Results from spectral fits with NSATMOS for qLMXBs in GCs. Objects are ordered with decreasing radius. We give the absorption, the temperature, mass and radius of the NS, and error on R_∞. Brackets indicate that the value was frozen during the fit. References are [a] Heinke et al. (2006), [b] Lugger et al. (2007), [c] Webb & Barret (2007), [d] Guillot et al. (2011a), [e] Servillat et al. (2012), [f] Guillot et al. (2009b), [g] Guillot et al. (2011b), [h] Servillat et al. (2008b), [i] Servillat et al. (2008a).

source name	Distance kpc	Obs.	$N_{\rm H}$ 10^{21} cm^{-2}	$T_{\rm eff}$ eV	$M_{\rm NS}$ $M_\odot$	$R_{\rm NS}$ km	R_∞ error km
47 Tuc X7[a]	4.85 ± 0.18	Chandra	4.2 ± 1.8	100 to 160	[1.4]	$14.5^{+1.6}_{-1.4}$	±2.5
M30 A1[b]	9.0 ± 0.5	Chandra	$2.9^{+1.7}_{-1.2}$	94^{+17}_{-12}	[1.4]	$13.4^{+4.3}_{-3.6}$	±3
ω Cen X3[c]	5.3	XMM	$1.2^{+0.4}_{-0.2}$	82^{+28}_{-9}	$1.66^{+0.84}_{-1.16}$	$11.6^{+7.0}_{-5.0}$	±2
M13 X7[c]	7.7	XMM	$0.12^{+0.04}_{-0.03}$	86^{+1}_{-8}	$1.30^{+0.06}_{-0.12}$	$9.8^{+0.1}_{-0.3}$	±2
NGC 6397 U24[d]	2.5 ± 0.06	Chandra	[1.4]	76^{+2}_{-3}	$1.13^{+0.47}_{0.32}$	$9.7^{+0.9}_{-0.8}$	±1
M28 #26[e]	5.5 ± 0.3	Chandra	2.5 ± 0.3	125 ± 40	$1.4^{+0.4}_{-0.9}$	9 ± 3	±2.5
NGC 6304 #4[f]	5.97 ± 0.08	XMM+Ch	[2.66]	122^{+31}_{-45}	[1.4]	$8.1^{+4.2}_{-2.4}$	
NGC 6553 #3[g]	6.0	XMM+Ch	[3.5]	134^{+21}_{-34}	[1.4]	$6.4^{+2.1}_{-0.8}$	
NGC 2808 C2[c,h,i]	9.6	XMM	$1.6^{+1.4}_{-0.5}$	92^{+1}_{-23}	$0.9^{+1.6}_{-0.4}$	$6.1^{+11.5}_{-1.1}$	±6

We list in Table 1 all the NS studied with the NSATMOS NS atmosphere model (Heinke et al. 2006) found in the literature. Those are the best studied cases, but there are further candidates with reported values using other models and lower quality data (see Heinke et al. 2003, Table 2, and Guillot et al. (2009a), Table 4). For NGC 6304, the model used was NSA (Zavlin et al. 1996), but we re-analysed the data with NSATMOS and checked that the results were consistent. We found $M_{\rm NS} < 1.4\ M_{\odot}$ and $R_{\rm NS} < 9.0$ km (90% error).

Due to the strong surface gravitational field, the observed radius is different from the physical radius, and linked to the NS mass: $R_{\infty} = R_{\rm NS} \times (1 - 2GM_{\rm NS}/c^2 R_{\rm NS})^{-1/2}$. As the shape of the contours in Figure 1 show the degeneracy between the NS mass and radius, it is instructive to give the error on R_{∞}. This can be seen as the error along a line of constant $M_{\rm NS}/R_{\rm NS}$ ratio, and it is almost constant over the range of NS masses and radii. The error on R_{∞} is around ± 2 using the best available data. This opens some discussions on the favored EOS, but cannot provide strong constraints on the equation of state. Combining all those results can give slightly better constraints (Steiner et al. 2010). We note that in some cases the absorption or the NS mass was frozen in the fit, which probably led to underestimated errors. Moreover, the distance error is generally not included in the error budget.

Among the qLMXBs in GCs that were used to derive constraints on the mass and radius of their NS using a H atmosphere models, some were reported to have a low mass or radius. Following our study of the qLMXB in M28, it is possible that some of those sources harbor a NS with a He atmosphere, rather than a H atmosphere. This would favor higher radii and masses for NS, and thus stiffer EOS, in agreement with the precise measurement of relatively high masses for some NS (e.g. $\sim 2\ M_{\odot}$, Demorest et al. 2010). We will thus try fitting other quiescent LMXBs with He (and carbon) atmospheres in future work.

Identifying the composition of the atmosphere of known quiescent LMXBs is clearly of key importance, and we suggest three means of doing so. i) Spectroscopy, or (less time-consuming) narrow-filter photometry of optical counterparts can identify Hα emission from LMXBs in quiescence or outburst and thus the presence of H; the LMXB in ω Cen (Haggard et al. 2004) and X4 and X5 in 47 Tuc (van den Berg et al., in prep) therefore possess H atmospheres. ii) Orbital periods differentiate between ultra-compact and longer period systems; we note that long periods are known for X5 and W37 in 47 Tuc (Heinke et al. 2005), suggesting a main-sequence companion and accretion of H. iii) Finally, thermonuclear bursts can distinguish between H-rich and H-poor environments, particularly at low ($< 0.01\ \dot{M}_{\rm Edd}$) accretion rates where H should burn unstably (e.g. Fujimoto et al. 1981; Galloway et al. 2008).

This last point is of particular interest for the M28 qLMXB, since a peculiar X-ray burst was observed from this GC (Gotthelf & Kulkarni 1997). This burst was unusually low-luminosity, suggesting burning on only one patch of the star. The short timescale of this burst (τ=7.5 s) requires He burning without the presence of H, and thus (given the quiescent state) pure He accretion and a pure He atmosphere. Unfortunately we cannot be certain that this burst originated from the known qLMXB, as other qLMXBs may be hidden among the fainter sources in this cluster.

MS acknowledges supports from NASA/Chandra grant GO0-11063X and the Centre National d'Etudes Spatiales (CNES).

References

Alcock, C. & Illarionov, A. 1980, ApJ, 235, 534
Altamirano, D., Patruno, A., Heinke, C. O., et al. 2010, ApJ, 712, L58
Arnaud, K. A. 1996, ADASS V, ASP Conference Series, 101, 17
Becker, W., Swartz, D. A., Pavlov, G. G., et al. 2003, ApJ, 594, 798
Bildsten, L., Salpeter, E. E., & Wasserman, I. 1992, ApJ, 384, 143
Bildsten, L., Salpeter, E. E., & Wasserman, I. 1993, ApJ, 408, 615
Brown, E. F., Bildsten, L., & Chang, P. 2002, ApJ, 574, 920
Chang, P. & Bildsten, L. 2004, ApJ, 605, 830
Chang, P., Bildsten, L., & Arras, P. 2010, ApJ, 723, 719
Davis, J. E. 2001, ApJ, 562, 575
Demorest, P. B., Pennucci, T., Ransom, S. M., Roberts, M. S. E., & Hessels, J. W. T. 2010, Nature, 467, 1081
Deutsch, E. W., Margon, B., & Anderson, S. F. 2000, ApJ, 530, L21
Fujimoto, M. Y., Hanawa, T., & Miyaji, S. 1981, ApJ, 247, 267, a&AA ID. AAA029.066.544
Galloway, D. K., Muno, M. P., Hartman, J. M., Psaltis, D., & Chakrabarty, D. 2008, ApJS, 179, 360

Gänsicke, B. T., Braje, T. M., & Romani, R. W. 2002, A&A, 386, 1001
Gotthelf, E. V. & Kulkarni, S. R. 1997, ApJ, 490, L161
Guillot, S., Rutledge, R. E., Bildsten, L., et al. 2009a, MNRAS, 392, 665
Guillot, S., Rutledge, R. E., & Brown, E. F. 2011a, ApJ, 732, 88
Guillot, S., Rutledge, R. E., Brown, E. F., Pavlov, G. G., & Zavlin, V. E. 2009b, ApJ, 699, 1418
Guillot, S., Rutledge, R. E., Brown, E. F., Pavlov, G. G., & Zavlin, V. E. 2011b, ApJ, 738, 129
Haggard, D., Cool, A. M., Anderson, J., et al. 2004, ApJ, 613, 512
Harris, W. E. 1996, AJ, 112, 1487
Harris, W. E. 2010, arXiv, 1012, 3224, 6 pages, 4 figures
Heinke, C. O., Grindlay, J. E., & Edmonds, P. D. 2005, ApJ, 622, 556
Heinke, C. O., Grindlay, J. E., Lugger, P. M., et al. 2003, ApJ, 598, 501
Heinke, C. O., Rybicki, G. B., Narayan, R., & Grindlay, J. E. 2006, ApJ, 644, 1090
Ho, W. C. G. & Heinke, C. O. 2009, Nature, 462, 71
Ivanova, N., Rasio, F. A., Lombardi, J. C., Dooley, K. L., & Proulx, Z. F. 2005, ApJ, 621, L109
Lattimer, J. M. 2010, New A, 54, 101, elsevier B.V.
Lattimer, J. M. & Prakash, M. 2001, ApJ, 550, 426
Lugger, P. M., Cohn, H. N., Heinke, C. O., Grindlay, J. E., & Edmonds, P. D. 2007, ApJ, 657, 286
Predehl, P. & Schmitt, J. H. M. M. 1995, A&A, 293, 889
Rhoades, C. E. & Ruffini, R. 1974, Phys. Rev. Lett., 32, 324
Ritter, H. & Kolb, U. 2003, A&A, 404, 301
Ritter, H. & Kolb, U. 2010, VizieR On-line Data Catalog, 1, 02018
Servillat, M., Heinke, C. O., Ho, W. C. G., et al. 2012, MNRAS, 2965
Servillat M., Dieball A., Webb N. A., et al. 2008a, A&A, 490, 641
Servillat M., Webb N. A., & Barret D., 2008b, A&A, 480, 397
Steiner, A. W., Lattimer, J. M., & Brown, E. F. 2010, ApJ, 722, 33
Testa, V., Corsi, C. E., Andreuzzi, G., et al. 2001, AJ, 121, 916
Verbunt, F. 1987, ApJ, 312, L23
Webb, N. A. & Barret, D. 2007, ApJ, 671, 727
Wilms, J., Allen, A., & McCray, R. 2000, ApJ, 542, 914
Zavlin, V. E., Pavlov, G. G., & Shibanov, Y. A. 1996, A&A, 315, 141
Zurek, D. R., Knigge, C., Maccarone, T. J., Dieball, A., & Long, K. S. 2009, ApJ, 699, 1113

SF2A 2012
S. Boissier, P. de Laverny, N. Nardetto, R. Samadi, D. Valls-Gabaud and H. Wozniak (eds)

LATEST RESULTS OF THE CODALEMA EXPERIMENT: ANTHROPIC NOISE SOURCES AND POLARIZATION ANALYSIS

D. Torres Machado[1] and the CODALEMA collaboration[1,2]

Abstract. Dedicated to the measurement of the radio transients coming from the extensive air showers (EAS), the CODALEMA experiment was started in 2001 at the Nançay Observatory, in France. Benefiting of an easy deployment and a low cost compared with Cherenkov detectors or fluorescence telescopes, this alternative method appears to be an interesting tool for the understanding of the physics of high energy cosmic rays observed through EAS. A new configuration of the CODALEMA experiment was implemented in 2011 based on a standalone detection, which will be essential for the next generation of giant detector array. One of the major challenges of this promising detection mode is the control (identification and rejection) of the fluctuating and transient noise events in an inhabited area and the knowledge of the shower radio-detection capabilities such as the effective efficiency and the data purity. Some results concerning the electric field polarization are also presented and seems to be crucial to the understanding of the secondary emission mechanisms by EAS such as the charge excess.

Keywords: ISM: cosmic rays, ultra high energy cosmic ray, radio detection

1 Introduction

Since its implementation in 60's (Jelley et al. 1965), the cosmic rays detection through radio transients has made some significant progress from a theoretical and experimental point of view . Thanks to some technological advances, more particulary in electronics, this detection mode was relauched in 2002 by experiments such as CODALEMA (Ardouin et al. 2005) in France, and LOPES (Falcke et al. 2005) in Germany. The purpose of this detection method is to characterize the EAS radio signals in order to deduce the primary cosmic ray properties (energy, nature and direction). The first recorded data with CODALEMA experiment has revealed a north-south asymmetry in the arrival directions of the radio detected cosmic rays. Indeed, the charged particles of the shower are deflected by the Lorentz force and the intensity of this effect depends on the angle between the shower direction and the geomagnetic field (Ardouin et al. 2009). A systematic shift between the shower core using separately data coming from scintillator and antenna arrays has been also observed (Marin 2011). This effect is associated with a charge-excess contribution in the shower radio emission.

Despite a better understanding of the mechanisms of radio emission by EAS, key elements still have to be assessed such as its ability to run on a large surface and in an inhomogeneous environment as well as its capacity to provide valuable observables sensitive to the main properties of the primary cosmic ray.

2 The experimental setup

Recently, CODALEMA has been upgraded with the installation of CODALEMA 3, composed of 34 so-called butterfly antennas (Fig. 1 right) and surronding the existing short-dipole antenna array. This initial array consists of 24 dipole antennas triggered by an ensemble of 13 particle detectors. In addition to confirm the shower detection through scintillators, the energy of the primary cosmic ray can be estimated by the latter. The autonomous detection stations of CODALEMA 3 feature some news technological developments. Compared to the previous version, butterfly antenna has been designed to be more sensitive at low frequencies, which will

[1] SUBATECH, Université de Nantes/École des Mines de Nantes/IN2P3-CNRS, Nantes, France
[2] LESIA, USN de Nançay, Observatoire de Paris-Meudon/INSU-CNRS, Meudon, France

permit the detection of EAS at large distance from its core (Charrier 2012). A particular attention has been put in the reduction of its gain in the AM and FM bands in order to avoid saturating signals. Antenna signals in dual polarization (EW and NS) feed a trigger board where analog triggering decision is made on a simple voltage threshold level in a 45-55 MHz filtered band. The selected events are dated by a GPS with an uncertainty of about 5 ns and signals are digitized by an ADC (1 GS s^{-1} over 2560 points for 2.56 μs record). A PC and a control boards are then responsible for collecting, saving data and communication with the outer world. On the site of Nançay, communication with the autonomous stations is opered through optical fiber and powered by a dedicated electrical network. However, these stations are well able to be supplied with solar panels and to use a wireless link for communication. The block diagram of a station is presented Fig. 1 left, showing the main functions of the station and links between separate boards.

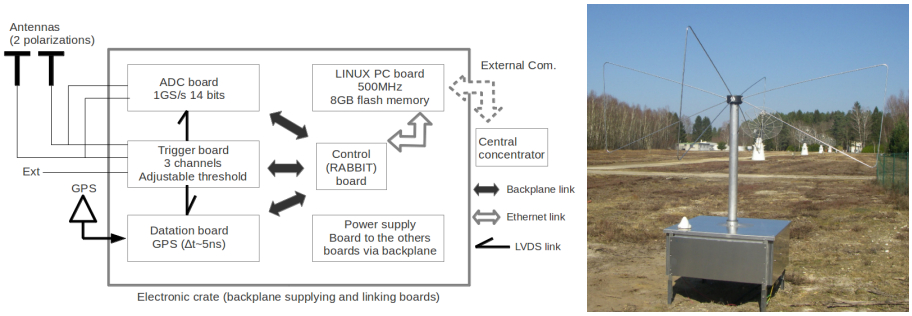

Fig. 1. Left: Schematic description of the station elements. **Right:** A butterfly antenna on the field at the Nançay Observatory.

Using the galactic background as a calibrating signal is a very convenient way to measure the antenna sensitivity and to validate the antenna modelization with respect to calculations. Indeed, with butterfly antenna, we observe a variation of about 2.8 dB of the galactic background as function of the UTC time for the 55 MHz frequency, as expected by Eznec simulations (Charrier 2012).

3 The anthropic noise sources

3.1 First data set

Although the experiment is located at the Nançay Observatory in a radio-protected environment, antennas are not intrinsically shielded against radio interferences. Indeed, one of the main requirements for a radio self-triggered system is to design it for a high attenuation of man-made RFI (Radio Frequency Interferences). Data analysis were performed between March and July 2011 in order to assess the radio environment at the Nançay Observatory and consequently, the noise source features. During this period the event rate varies between 10^4 and 10^6 per day, whereas with a surface of about 0.5 km^2, one cosmic ray event within our acceptance is expected per day. Most RFI events are observed by one antenna or very few antennas and are linked to nearby (inside the array) and weak sources. Certain sources emit radio transients with a periodicity greater then 28 Hz, which implies a dead time of about 100% during their presence (Fig. 2 left). Therefore, it becomes essential for an optimal operation of the experiment to identify and control the radio noise sources. Furthermore, the localization and knowledge of the nature of the source can give information on the radio detection sensitivity as well as on the direction reconstruction accuracy.

3.2 Reconstruction of the radio signal front

Concerning nearby noise sources, in first approximation, the radio wave front can be assumed to be spherical and emmited by point-like sources on the ground. Reconstruction method makes use only of the measured arrival times of the radio signal at the individual antennas, and its accuracy will depend strongly on the time resolution of the detector. The position of the source will be associated to the coordinates for which the deviation evaluated with a χ^2, between the radio wave and the sphere is minimum (Fig. 2 right). Due to uncertainties regarding the reconstruction, a large number of events is required in order to have a pertinent mean value. Thus, some man-made noise sources have been located in the vicinity of the Nançay Observatory and electric transformer stations are the most likely candidates.

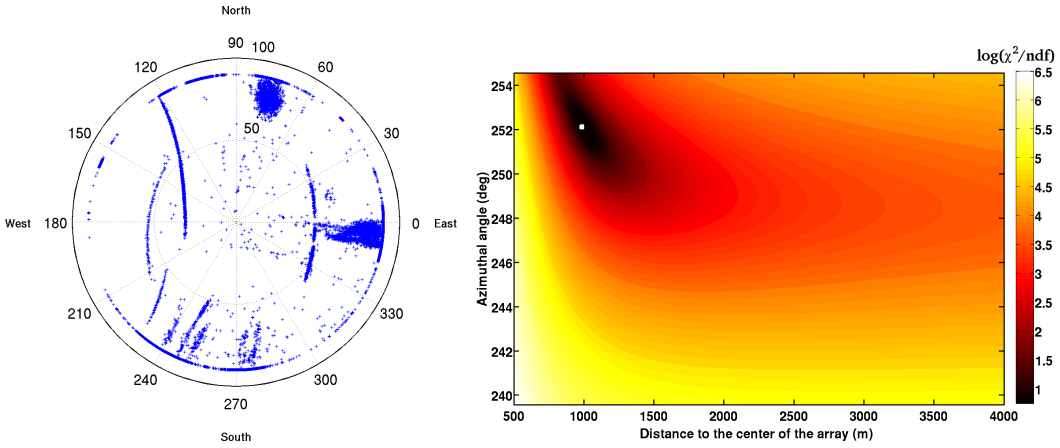

Fig. 2. Left: Arrival direction of the reconstructed events for one day of data taking. We can observe the trajectory of some planes and a large number of events near the horizon, that correspond to noise sources. **Right:** χ^2 evolution as function of the source position on the ground. This source is located at 252 °(SW) and at 1050 m from the center of the array (white dot).

Other online methods are been tested currently on the field as the elimination of periodic events and selection by wave form analysis. A fast reconstruction of the arrival direction before its recording is also conceivable in T3 level trigger in order to eliminate events coming from the horizon.

4 EAS detection and polarization

Several models predict that the electric field created by EAS is polarized and proportional to $\vec{v}\times\vec{B}$, in particular the transverse current model (Huege et al. 2012). Here, $\vec{v}$ corresponds to the arrival direction of the shower and $\vec{B}$, to the geomagnetic field at Nançay. Having access to both horizontal polarizations of the electric field with the standalone array, it becomes possible to investigate the weight of the geomagnetic component and consequently, others emission mechanisms such as the charge excess, whose polarization vectors are oriented radially toward the shower axis (Fig. 3 left). This implies that, for a mix of charge excess and geomagnetic contributions, the orientation of the detected electric field will depend on the relative position of the antenna with respect to the shower core.

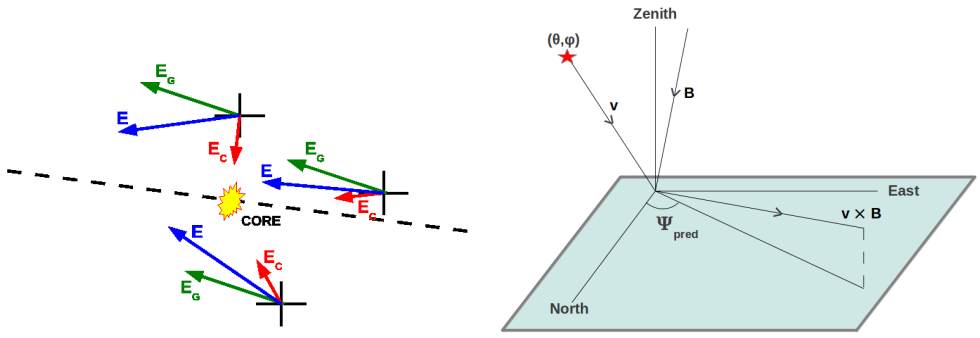

Fig. 3. Left: Illustration of the dependance on the relative position of the antenna with respect to the shower axis (dashed line) of the total intensity of the electric field (blue) due to the charge excess (red) and the geomagnetic (green) contributions. **Right:** Definition of the predicted polarization angle.

We can define the angle of linear polarization as the angle between the geographic North and the projection on the ground of $\vec{v}\times\vec{B}$ (Fig. 3 right). In the case of a pure geomagnetic radiation, this angle is supposed to be equal to:

$$\Psi_{\text{measured}} = \arctan\left(\frac{E_{\text{EW}}}{E_{\text{NS}}}\right) \tag{4.1}$$

where E_{EW} and E_{NS} are the max of the transient electric field measured in each polarization.

In figure 4 right the polarization angles as derived from the measurements are compared to the predicted polarization from the dipole array reconstruction. This data set contains the first coincidences between the dipole array (CODALEMA 2) and the self-triggering array collected between September of 2011 and May of 2012, without thunderstorms monitoring. Events dispersed in this plot highlight undoubtedly the presence of secondary emission mechanisms.

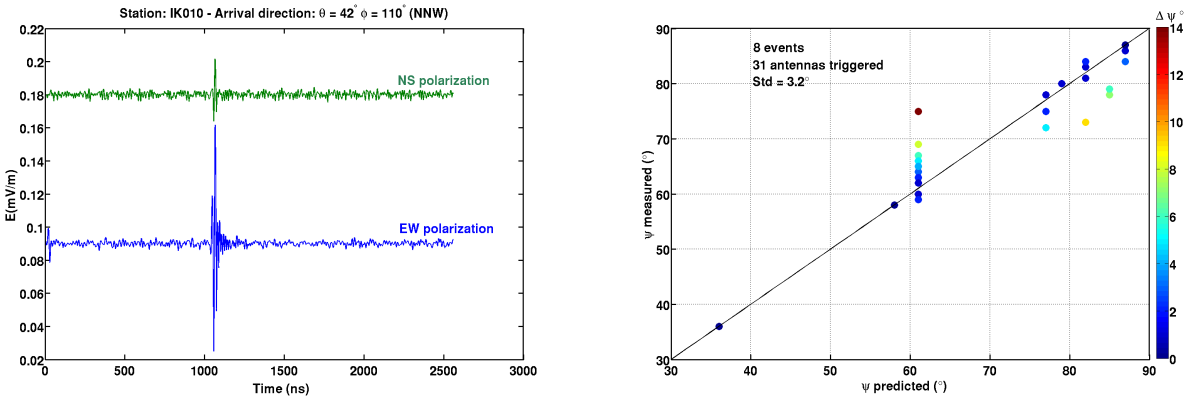

Fig. 4. Left: Wave shape for both East-West and North-South horizontal polarizations of the electric field filtered in the 30-80MHz band. **Right:** Polarization angle ψ_{pred} calculated according to $\vec{v} \times \vec{B}$ as function of ψ_{meas} deduced from the antenna signals. The angular difference $\psi_{\text{meas}} - \psi_{\text{pred}}$ are represented by colors.

Despite a relative good agreement shown in Fig. 4, some effects should be taken into account such as the azimuthal angle and the frequency range. Studies should be also carried out on the antenna response relative to the arrival direction of the signal. Besides confirming the geomagnetic effect as the main mechanism, this identification criterion can also be interesting to remove background sources.

5 Conclusion

The CODALEMA experiment has made great progresses over the recent years in the understanding on the electric field emission coming from EAS. First results of CODALEMA 3 have shown an antenna sensitivity to the galactic background but also to man-made radio emitting inside and in the vicinity of the Nançay Observatory. Reconstruction methods has been applied successfully and main radio background sources has been identified. Rejection methods based on emission periodicity and pulse shape analysis have been tested on data and have demonstrated to be efficient, while preserving EAS candidates.

From a physics point of view, a polarization signature of the geomagnetic emission mechanism is clearly present in this data set. Discrepancies between measured and predicted values of the polarization angle can suggest the presence of others emission mechanisms. Although the statistics on this data set are low, the polarization studies show promising results.

References

Ardouin, D. et al. 2005, Nucl. Instrum. Meth. A, 555, 148
Ardouin, D. et al. 2009, Astropart. Phys., 31, 192
Belletoile, A. for the CODALEMA collaboration 2011 Proc. Int. Conf. on Cosmic Ray (Beijing)
Charrier, D. 2012, Nucl. Instrum. Meth. A, 662, 142
Falcke, H. et al. 2005, Nature, 435, 313
Huege, T. et al. 2012, Nucl. Instrum. Meth. A, 662, 179-186
Jelley, J. et al. 1965, Nature, 205, 327
Marin, V. for the CODALEMA collaboration 2011 Proc. Int. Conf. on Cosmic Ray (Beijing).

SF2A 2012
S. Boissier, P. de Laverny, N. Nardetto, R. Samadi, D. Valls-Gabaud and H. Wozniak (eds)

TOWARD A MODEL FOR HFQPOS IN MICROQUASARS

P. Varniere[1], M. Tagger[2], F. H. Vincent[1] and H. Meheut[3]

Abstract. There have been a long string of efforts to understand the source of the variability observed in microquasars but no model has yet gained wide acceptance, especially concerning the elusive High-Frequency Quasi-Periodic Oscillation (HFQPO). We first list the constraints arising from observations and how that translates for an HFQPO model. Then we present how a model based on having the Rossby Wave Instability (RWI) active in the disk could answer those constraints.

Keywords: Microquasars

1 What does a HFQPO model need to explain

Even if High-Frequency Quasi-Periodic Oscillations are much weaker than their Low-Frequency counterparts we now have data from several outbursts from eight different sources. Indeed, sources like XTE J1550-564, have exhibited HFQPOs with enough regularity to obtain a stringent list of constraints for any theoretical model wishing to provide an explanation for them (Remillard & McClintock 2006).

The first observational fact that one needs to explain is the **modulation of the flux** associated with the frequency. Indeed, even if HFQPO has a rms amplitude much lower than in the case of the LFQPO, the flux still modulates at a level of a few percent and it has been shown to be stronger at higher energies (see Remillard & McClintock 2006, for examples).

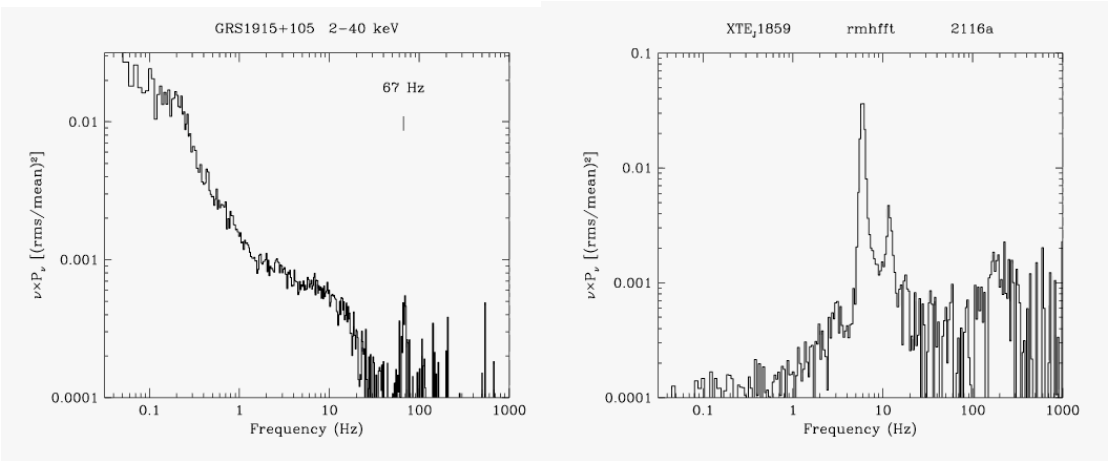

Fig. 1. Left: Power density spectrum (PDS) of GRS 1915+105 showing the 67 Hz. **Right:** PDS of XTE J1859+226 with LFQPO and HFQPO.

Since the observation of the 67 Hz HFQPO of GRS 1915+105 we know that HFQPOs can occur in the absence of LFQPOs. It is therefore required that the HFQPO model be independent of the LFQPO model.

[1] APC, Université Paris 7
[2] LPC2E, Orléans
[3] Physikalisches Institut, Universitat Bern

However, most HFQPO detections do occur in the presence of a LFQPO, as observed for example during the outbursts of XTE J1550-564 or XTE J1859+226. When they co-exist we have type A and B LFQPOs, not the standard type C.

All of this demonstrates that, even if **HFQPO and LFQPO models need to be independent, they also need to be coherent with each other as the two QPOs co-exist in the disk**. This is a more stringent requirement than it may at first seem, as one need not only find a model for the HFQPO's characteristics, but also a model that can coexist in a disk with an LFQPO.

Another exacting requirement coming from observation is the fact that the frequencies of HFQPOs, albeit more stable than in the case of the LFQPO, show a small but significant variation. In the case of XTE J1550-564 the Figure 2 represents the observed occurrences of the HFQPOs in 10 Hz bins during the outburst of 1998-99 and 2001.

Any model aiming to explain the HFQPOs must be able to reproduce the observed dispersion in the frequency.

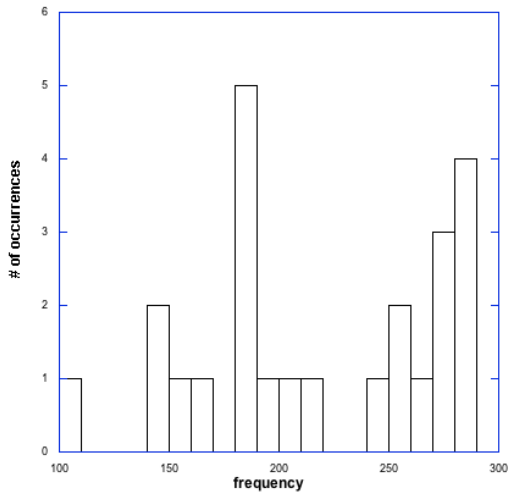

Fig. 2. Observed occurrences of the HFQPOs in 10 Hz bins during the outburst of 1998-99 and 2001.

Another characteristic of HFQPOs is that they can be observed either alone **or** in 'pairs' (with closely related frequencies, most of the time near a 2:3 ratio). **This points toward a mechanism that can select several linked frequencies depending on the disk conditions.**

Any model wishing to explain HFQPOs must be able to explain this small but stringent list of requirements. As we get more observations with future detectors we will be able to add to this list and further constrain the models.

2 The Rossby Wave Instability as a model for HFQPOs

The Rossby Wave Instability is an hydrodynamical instability that occurs in the presence of an extremum of the vortensity (defined by $\Sigma\Omega/(2\kappa^2) \cdot p/\sigma^\gamma$ where κ is the disk epicyclic frequency, Ω is the rotation frequency and σ is the surface density). Because of its characteristics, we proposed the RWI as a possible explanation for HFQPOs (Tagger & Varniere 2006).

In the case of a disk in which the inner edge approaches its last stable orbit an extremum of the vortensity becomes possible therefore leading to the RWI as shown in the hydrodynamic simulation shown on Fig.2. These graphs represent a slab ($z = 0$) of the density in a 3D disk in the Paczynsky & Wiita (1980) gravitational potential, which means a spin $a = 0$. We later used modified Newtonian potential (Artemova et al. 1996) to model the full range of spin and confirmed the results.

Because the inner edge of the disk must be close to its last stable orbit but not 'exactly' at it, there is a small radial range where the instability can develop (Tagger & Varniere 2006) leading to a change in observed frequency. As we do not know precisely the density profile in the disk, especially close to its last stable orbit, it is hard to put a hard boundary on the frequency changes but it could reach 30% without a dramatic change to the profiles.

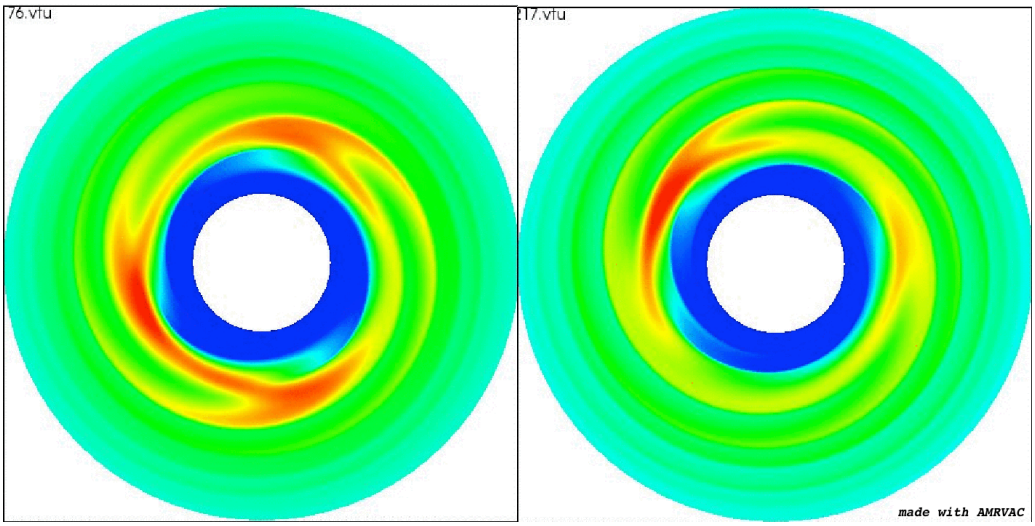

Fig. 3. Density slab of the disk from an hydrodynamic simulation of the RWI at two different times, using the code AMRVAC

Another interesting point is that the RWI does not require the disk to be in the condition for a LFQPO model to occur (Tagger & Varniere 2006). Nevertheless, the RWI was also demonstrated to be stronger in the presence of a vertical magnetic field[4] and we have recently shown the ability of the RWI and the AEI (a candidate to explain the LFQPO) to co-exist in a magnetized accretion disk (Varniere et al. 2001, 2012). Therefore, it could give rise to either HFQPOs alone or HFQPOs and LFQPOs depending on the disk condition, as is observed.

From numerical simulation, we also found that, depending on the disk conditions, the dominant mode can be $m = 3, m = 2$, (see Fig.2) more rarely $m = 1$, or a mix of these (Tagger & Varniere 2006) which fit well with the observed characteristics of HFQPOs.

We now perform 3D simulations of the RWI and confirm the previous 2D and analytical results and also produce the associated image(see Fig.4)/light curve using the code Gyoto (Vincent et al. 2011).

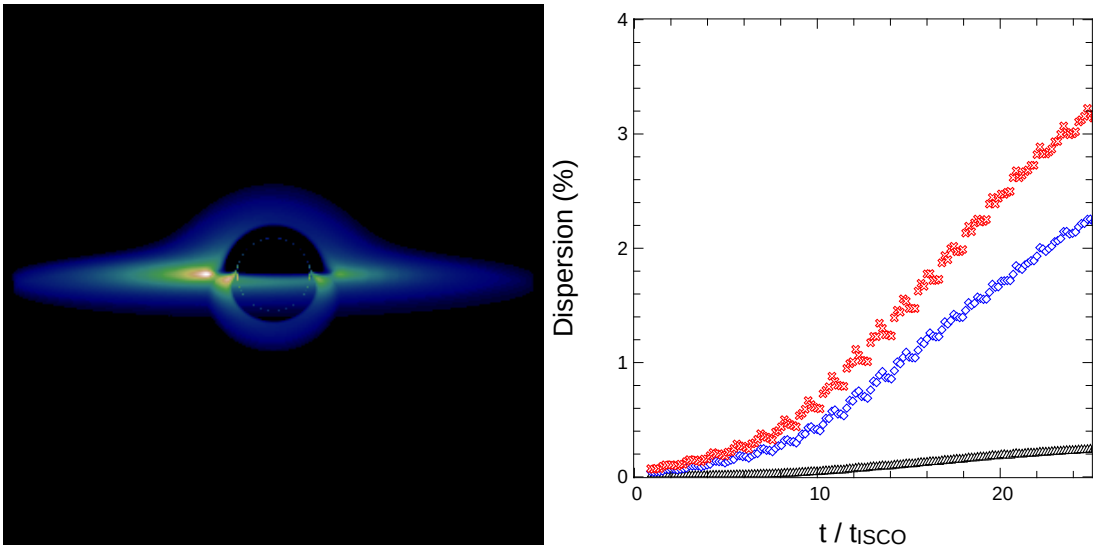

Fig. 4. Left: Ray tracing of a 3D simulations of the RWI at 85° inclination. Right: time evolution of the rms of the flux modulation at 85° , 45° and 5° inclination.

When the RWI is active in the disk the light curve is modulated up to a few % (Vincent et al. in prep.) and this modulation is energy dependent. The precise impact of the spin, especially the case of high spin, is still

under study, but the RWI is present and modulate the flux.

3 Conclusions

The RWI is a promising model for HFQPOs as it gives rise to several observed features such as the possibility to have small variations in the frequencies as well as mode selection depending on the conditions in the disk. Moreover, this instability can co-exist with the Accretion-Ejection Instability (Varniere et al. 2001, 2012) proposed as a model for the ubiquitous LFQPO. Lastly, we have recently shown that this instability can effectively modulate the X-ray flux within the observed limit (Vincent et al. in prep.). In the future, we will explore the impact of the spin of the black hole, the link with ejection and the overall evolution of the system.

This work has been financially supported by the GdR PCHE in France and the "campus spatial Paris Diderot".

References

Artemova, I. V., Bjoernsson, G., & Novikov, I. D., 1996, ApJ, 461, 565
Paczynsky, B. & Wiita, P. J. 1980, A&A, 88, 23
Remillard, R. A. & McClintock, J. E., 2006, Ann. Rev. Astron. Astrophys. 44, 49
Tagger, M. & Varniere, P., 2006, ApJ, 652, 1457
Varniere, P., Tagger, M. & Rodriguez, J., 2011, A&A, 525, 87
Varniere, P., Tagger, M. & Rodriguez, J., accepted A&A
Vincent, F. H., Paumard, T., Gourgoulhon, E., & Perrin, G. 2011, Classical and Quantum Gravity, 28, 225011
Vincent, F. H., Meheut, H., Varniere, P., Paumard, T. in preparation

SF2A 2012
S. Boissier, P. de Laverny, N. Nardetto, R. Samadi, D. Valls-Gabaud and H. Wozniak (eds)

THE ELECTROMAGNETIC CALORIMETER OF THE AMS-02 EXPERIMENT

M. Vecchi[1], L. Basara[2], G. Bigongiari[3], F. Cervelli[4], G. Chen[5], G. M. Chen[5], H. S. Chen[5], G. Coignet[2], S. Di Falco[4], S. Elles[2], A. Fiasson[2], D. Fougeron[2], G. Gallucci[4], C. Goy[2], M. Incagli[4], R. Kossakowski[2], V. Lepareur[2], Z.H. Li[5], M. Maire[2], M. Paniccia[2], F. Pilo[4], S. Rosier-Lees[2], X.W. Tang[5], C. Vannini[4], J.P. Vialle[2] and H.L. Zhuang[5]

Abstract. The electromagnetic calorimeter (ECAL) of the AMS-02 experiment is a 3-dimensional sampling calorimeter, made of lead and scintillating fibers. The detector allows for a high granularity, with 18 samplings in the longitudinal direction, and 72 sampling in the lateral direction. The ECAL primary goal is to measure the energy of cosmic rays up to few TeV, however, thanks to the fine grained structure, it can also provide the separation of positrons from protons, in the GeV to TeV region. A direct measurement of high energy photons with accurate energy and direction determination can also be provided.

Keywords: cosmic rays, calorimeter, high energy photons

1 Introduction

The Alpha Magnetic Spectrometer (AMS-02) (see Aguilar et al. (2002)) is a large acceptance particle physics detector, operating onboard the International Space Station (ISS) since May 19th 2011. Since the launch, the detector has collected more than 20 billion events. The main goals of AMS-02 are the search for antimatter and dark matter, and the precise measurements of cosmic rays composition and flux. Moreover, AMS-02 could provide information on gamma rays in the GeV to TeV range.

The apparatus is composed of several subdetectors, arranged as in figure 1.

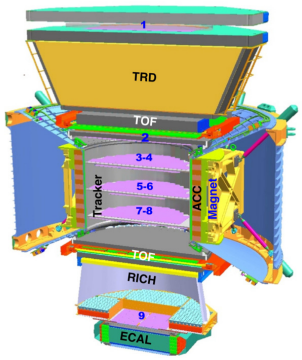

Fig. 1. Sketch of the AMS-02 detector.

[1] Academia Sinica, 128 Academia Road, Section 2, Nankang, Taipei 115, Taiwan (R.O.C.), and National Central University, No.300, Jhongda Rd., Jhongli City, Taoyuan County 32001, Taiwan (R.O.C.)

[2] LAPP, Université de Savoie, CNRS/IN2P3, Annecy-le-Vieux, France

[3] Universita' degli Studi di Siena, 53100 Siena, Italy

[4] Istituto Nazionale di Fisica Nucleare, Sezione di Pisa, 56100 Pisa, Italy

[5] Institute of High Energy Physics, CAS, Beijing, 100049, China

- a Transition Radiation Detector (TRD), equipped with 20 layers, each one using polypropylene/polyethylene as radiator and Xe/Co2 filled proportional wire straw tubes. This detector is used to complement the ECAL in particles identification, up to few hundred GeVs.
- a Time of Flight (TOF), made of 4 layers of plastic scintillators, providing timing information and the trigger for the experiment.
- a Magnetic Spectrometer, made of double sided silicon strips, arranged on 9 layers, to measure the sign of the electric charge and the rigidity (momentum/charge) of cosmic rays. The measured quantity is the deflection, i.e. the inverse of the rigidity, for particles in a 0.15 T magnetic field, provided by a permanent magnet.
- an Anti-Coincidence scintillator Counter (ACC) system surrounds the tracker planes installed within the magnet volume. The ACC system provides the veto signal to the trigger, in order to reject multi-particle events, generated in the interaction of cosmic rays entering the detector through the sides.
- a Ring Imaging Cherenkov Detector (RICH), to estimate cosmic rays velocity and charge with high accuracy.
- an electromagnetic calorimeter (ECAL), to measure particles energy, for the electron/hadron separation and for the photon detection.

2 The ECAL detector

The ECAL (see Cadoux et al. (2002)) is a lead-scintillating fibers sampling calorimeter, in which particles crossing the active volume produce light collected by photomultipliers (PMTs). The structure has been designed to have a high granularity (one radiation lenght in the longitudinal direction, half a Molière radius in the lateral direction) and to maximize the ratio between radiation and interaction lenght. The resulting composite structure has a lead-fiber-glue volume composition of 1:0.57:0.15 cm^3, as well as an average density of 6.8 g/cm^3. The active part of the detector has a total weight of approximately 638 kg and a total active size of $68.5 \times 68.5 \times 16.7$ cm^3 (figure 2). The total depth of the calorimeter is 17 radiation lenghts (0.6 nuclear interaction lengths). Hamamatsu R-7600-00-M4 multianode photomultipliers are the core sensors of the ECAL, while the coupling to fibers is realized by means of plexiglass light guides, that maximize light collection and reduce cross-talk. Optical contact is enhanced by silicone joints, placed on light guides. Each PMT accommodates four 8.9×8.9 mm^2 anodes. Anodes define ECAL granularity: the detector allows for 18 longitudinal and 72 lateral samplings, for a total of $18 \times 72 = 1296$ readout units, usually referred to as *cells*. A 3-D imaging of the shower development has been achieved by alternating 5 *superlayers* (SL), i.e. 10 layers, with fibers along X axis and 4 SL, i.e. 8 layers with fibers along Y axis. In order to obtain the necessary energy resolution on Minimum

Fig. 2. The Electromagnetic Calorimeter honeycomb structure, before the final integration. PMTs are installed on the squared holes.

Ionizing Particles (used for detector performance monitoring and equalization) as well as to measure energies up to 1 TeV, the digitization is performed at two different gains: High Gain for low energy measurements, and Low Gain for highest ones, with a conversion factor HG/LG of about 33. Besides the 8 signals from anodes, each PMT last dynode signal is also readout and its information used to build up ECAL standalone trigger.

2.1 Trigger

The AMS-02 calorimeter has a key role in photon identification. When a high energy-deposit is recorded in the innermost layers of the calorimeter, a fast signal is generated and processed by the trigger board, which can enable the event acquisition, within 240 ns.

In order to discriminate between photons and charged particles, entering the calorimeter from outside its field of view, an angular cut is performed as an additional trigger request. The incident particle direction is evaluated by taking, for each view, the average position of the fired PMTs and a cut at 20 degrees is applied to select particles inside AMS-02 geometrical acceptance.

The efficiency for photons is about 20% at 1 GeV and reaches about 99% at 10 GeV, for an average polar orbit rate of 115 Hz (approximately 10% of total AMS-02 rate).

3 Detector performance

The full AMS-02 detector has been tested in 2010 using the primary 400 GeV proton beam of the CERN Super Proton Synchrotron (SPS): protons, electrons and positrons beams of energies between 8 and 400 GeV have been used to evaluate the performance of the detector.

Before the energy can be reconstructed, several processes have to be taken into account: the first step is to equalize all channels, i.e. to obtain the same response to the same energy deposit.

After this step is completed, the deposited energy must be corrected for leakage, in order to recover the fraction of the shower energy not deposited in the calorimeter. After these corrections, deviation from linearity is smaller than 1% in the energy range between 8 and 180 GeV, as can be seen in the left plot of figure 3, while the the energy resolution, is below 2 % at energies higher than 50 GeV, as can be seen in figure 3-right.

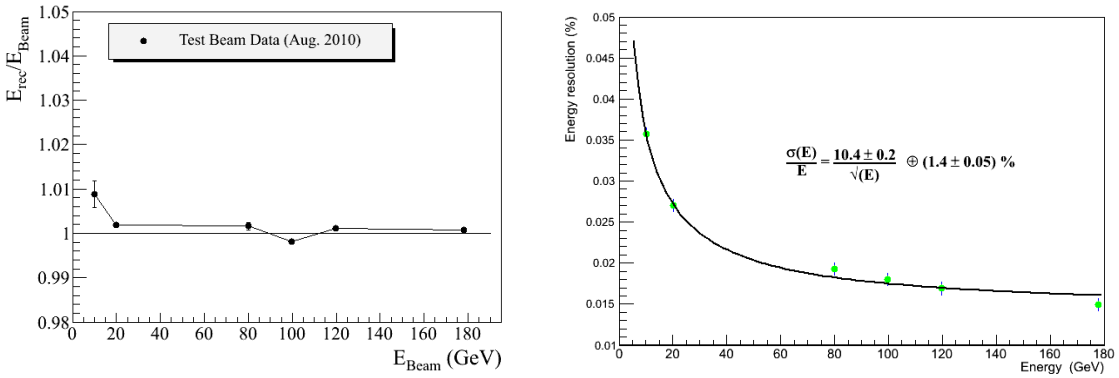

Fig. 3. Left: Linearity as a function of the energy beam. **Right:** Energy resolution as a function of the energy beam.

Angular resolution is also an important parameter, in particular for gamma ray physics. Under the assumption that a shower initiated by an electron is compatible to a shower initiated by a photon in the ECAL, the angular resolution has been computed using electrons Test Beam data. Figure 4 shows angular resolution as a function of the beam energy: this result is compatible to the one obtained with flight data.

3.1 Detector calibration in space

The detector has been operating onboard the ISS since May 2011: a Low Earth Orbit is followed, at about 400 km of altitude from the Earth surface. The thermal environment in space is severe: Sun light as well as the position of the solar panels onboards the ISS can affect the thermal configuration of the instrument, causing performance variations or potential sources of permanent damage. Given the extreme conditions that can be experienced in space, the performance of the detector are continuously monitored. It has been possible to observe that the gain of the PMTs is slightly affected by temperature variations: the ratio between High and Low Gain decreases by $3\times\ 10^{-5}$ per degree, while the pedestals can increase by half a percent per degree. The identification of MIPs is used to equalize the response of PMTs, the MIP value decreases by about 0.2 percent per degree. All those effects are accounted for in the offline analysis.

4 Particles identification

One of the main scientific targets of the AMS-02 detector is to identify the antimatter component out of the most abundant cosmic-ray components. Positrons, for example, must be identified out of a background of

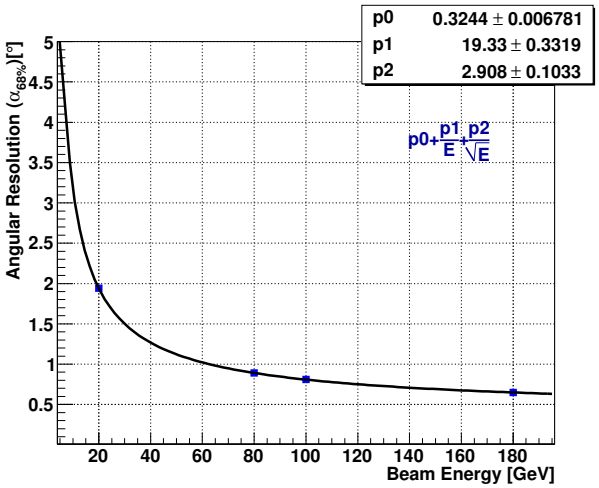

Fig. 4. ECAL angular resolution, evaluated as the angular interval containing 68% of reconstructed angles, a function of energy, for Test Beam data. For electrons, the angle between the tracker track and the shower axis direction is measured.

protons, that is $10^{3\div4}$ times more abundant than the positrons component. Main sources of background in the antimatter samples comes from charge confusion (i.e. electrons reconstructed as positrons) and from the wrong electron-hadron separation (i.e. protons identified as positrons).

In order to identify antimatter particles, all the AMS-02 subdetectors are involved: the Time-Of-Flight system is used to provide the trigger as well as to select down-going particles, the TRD is used to distinguish between protons and leptons, while the magnetic spectrometer is used to identify charge-one particles together with their sign and their rigidity.

Electromagnetic and hadronic showers differ in their spatial development and energy distribution in a way that can be distinguished by the calorimeter. The fraction of energy deposited in each ECAL layer allows for an effective separation between hadronic and electromagnetic showers: for hadrons of a given energy, the

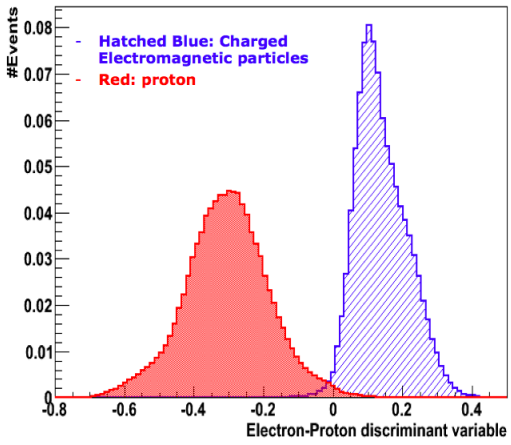

Fig. 5. Boosted Decision Tree distribution for electrons and positrons (blue distribution), as well as for protons (red distribution) for all energies.

distribution of the fraction of energy deposited is essentially flat in each ecal layer, with a sharp peak at low energies for non-interacting hadrons. For electrons and positrons, the fraction of energy deposited is different from layer to layer, and it increases until the shower maximum is reached.

Several approaches have been developed within the AMS-02 collaboration, in order to achieve the necessary separation between electrons and protons: Boosted Decision Tree, Neural Network, Likelihood methods and cut based methods. The distribution of the Boosted Decision Tree for electrons (and positrons) and hadrons is shown is figure 5.

Those methods, only based on ECAL-related variables, provide a rejection power on protons between 10^2 and 10^3, with a signal efficiency of 90%. Taking into account the match between energy and momentum (as measured by the tracker), the rejection power raises up to about 10^4. If the TRD is also taken into account, the rejection can further improve of about one order of magnitude, while keeping the same signal efficiency. The rejection of those methods have been validated using Test Beam data: at energies higher than 180 GeV, where Test Beam data are only available for protons, Monte Carlo has been used to study their performance.

5 Conclusions

The AMS-02 electromagnetic calorimeter design has been described, as well as its performance. The main goal of the detector is to measure the energy of particles up to the TeV: the detector allows for energy linearity better than 1%, and an energy resolution better than 2% at energies higher than 50 GeV.

Due to its granularity, ECAL allows for hadron-electron separation: a rejection power of the order of 10^4 is needed to distinguish positrons of the background of protons. This goal is achieved using informations concerning the shower lateral and longitudinal development in the ECAL, as well as the match between energy and momentum (as measured by the magnetic spectrometer). The use of the TRD can further improve the rejection power, up to few hundreds GeV.

References

Aguilar, M., et al. 2002, Phys. Rept., 366, 331

Cadoux, F., Cervelli, F. et al. 2002, Nucl. Phys. Proc. Suppl., 113, 159

SF2A 2012
S. Boissier, P. de Laverny, N. Nardetto, R. Samadi, D. Valls-Gabaud and H. Wozniak (eds)

CONSTRAINING THE NATURE OF THE GALACTIC CENTER BLACK HOLE SGR A* WITH PRESENT AND FUTURE OBSERVATIONS

F. H. Vincent[1], E. Gourgoulhon[2], O. Straub[3], M. Abramowicz[4], J. Novak[2], T. Paumard[5] and G. Perrin[5]

Abstract. The Galactic center is an ideal laboratory to study strong-field general relativistic phenomena, as the supermassive black hole Sgr A* has the biggest angular Schwarzschild radius among all black holes. This article presents three different ways of using the immediate surroundings of Sgr A* as a probe in order to either constrain its spin, or even test the very nature of this compact object.

Keywords: Galaxy:center, Black hole physics, ray-tracing, numerical relativity

1 Introduction

The Galactic center is by far the closest galactic nucleus. It can thus be studied with great accuracy and give insights on the physics of galactic nuclei in general (Genzel et al. 2010). Nearly four decades of observing campaigns have now made it extremely likely that the center of our Galaxy harbours a supermassive black hole, Sgr A* (Ghez et al. 2008; Gillessen et al. 2009). With its mass of $4.3 \times 10^6\,M_\odot$ at a distance of 8.3 kpc from Earth, Sgr A* has the biggest projected angular Schwarzschild radius among all black holes: $10\,\mu$as. This translates to an angular radius of the black hole shadow (i.e., to an apparent size of the event horizon) of around $24\,\mu$as and an apparent angular radius of the ISCO of around $29\,\mu$as for a spin of $0.5\,M$ (M being the black hole mass)[i] . Its surroundings are thus an ideal laboratory to study physics in extremely strong gravitational fields. Investigating strong-field general relativity (i.e. the effect of gravitation in the vicinity of compact objects) is one of the avenues for future tests of gravitation (Will 2009). Sgr A* certainly is among the best targets to try performing such tests.

The aim of this paper is to discuss three different ways of constraining the nature of the compact object Sgr A*, either with current or near-future observations:

- Fitting the spectrum emitted by the accretion structure surrounding Sgr A* (section 2),
- Constraining the black hole silhouette with future VLBI data (section 2),
- Simulating observations in the vicinity of alternative compact objects (section 3).

A fourth way must be cited here: the near-future GRAVITY instrument (Eisenhauer et al. 2008, 2011) that will allow constraining Sgr A*'s parameters by studying the dynamics of the Galactic center flares of radiation (see e.g. Vincent et al. 2011b, and references therein). This fourth way will not be investigated here.

[1] Laboratoire AstroParticule et Cosmologie, CNRS, Université Paris Diderot, 10 rue Alice Domon et Léonie Duquet, 75205 Paris Cedex 13, France
[2] LUTH, Observatoire de Paris, CNRS, Universitńe Paris Diderot, 5 place Jules Janssen, 92190 Meudon, France
[3] Nicolaus Copernicus Astronomical Center, Bartycka 18, 00-716 Warsaw, Poland
[4] Department of Physics, Göteborg University, SE-412-96 Göteborg, Sweden
[5] LESIA, Observatoire de Paris, CNRS, Universitńe Paris Diderot, 5 place Jules Janssen, 92190 Meudon, France

[i] Let us insist on the vocabulary used here. The *projected* Schwarzschild radius is the angular size of the Schwarzschild radius that would be measured by a distant observer in a flat spacetime. The *apparent* Schwarzschild radius is the actual angular size measured by a distant observer in the physical, curved spacetime. Due to general relativistic bending effects on the photons null geodesics, the apparent size is bigger than the projected size. For instance, in the Schwarzschild metric, the *projected* radius of Sgr A* event horizon is 10 μas, whereas the *apparent* radius of Sgr A* event horizon (i.e., the radius of the shadow) is $3\sqrt{3}/2 \times 10 \approx 26\,\mu$as. It is the *apparent* size of an object, of course, that must be compared to the angular resolution of an instrument.

2 An ion torus surrounding Sgr A*

The accretion structure that surrounds Sgr A* has been shown to be part of the advection dominated accretion flows (ADAFs) as demonstrated by Narayan et al. (1995). In this paper, this accretion structure is modeled by an ion torus (Rees et al. 1982), derived from the Polish doughnuts class (Abramowicz et al. 1978), the emitted radiation following the ADAF requirements given in Narayan & Yi (1995). This ion torus model is completely analytical and depends only on a few parameters with clear physical meaning: the black hole spin, the inclination parameter, the angular momentum value (assumed constant), the central energy and temperature, the ion to electron central temperature ratio and the magnetic to gas pressure ratio. The aim of this model is not to give a realistic description of the actual accretion structure surrounding Sgr A*, that could only be described in details with GRMHD simulations. Instead, the ion torus model only aims at catching the main observable characteristics of the Galactic center accretion structure (see Qian et al. 2009, for comparison of Polish doughnuts predictions and GRMHD simulations).

A detailed description of the physics of the ion torus model can be found in Straub et al. (2012). Here, we only investigate the prospects of constraining the black hole parameters assuming its accretion structure can be correctly described by an ion torus. To do so, the emitted spectrum and the image of the torus are computed by means of the open source ray-tracing algorithm GYOTO[ii] (Vincent et al. 2011a).

Fig. 1 shows the torus emitted spectrum and image for different values of the black hole spin, the other parameters being kept fixed at standard values, typical of the Galactic center accretion flow (see Straub et al. 2012, for details).

It appears that the ion torus is able of reproducing the order of magnitude of the very faint emission at the Galactic center (except at radio wavelengths, however see the discussion in Straub et al. 2012). The emitted spectrum is very similar at different spins for radio and infrared wavelengths. However, the X-ray part of the spectrum is highly dependent on the spin value. This is due to the fact that at higher spin, the torus shrinks and gets closer to the black hole: the flux is then shifted to higher energies. This dependency of the spectrum on the spin value makes it possible that Sgr A* spin could be constrained by means of X-ray spectroscopic data. Future work will thus be devoted to fit the ion torus prediction to X-ray data: this is the first way of constraining Sgr A* spin.

The right panel of Fig. 1 shows two superimposed images of the ion torus at two different values of spin. This clearly demonstrates the fact already mentioned above that the torus shrinks at higher spin. What is mostly interesting in this Figure is that the diameter of the black hole silhouette (the thin circle of illuminated pixels at the center of the torus images) depends on the spin value: there is a difference of 3 μas in angular size for the silhouette of black holes with spin 0.5 and 0.9. This is very interesting as the angular size of the silhouette is nothing but the projection of the black hole's event horizon on the observer's sky. This size is thus independent on the other parameters describing the ion torus. If the angular size of the black hole silhouette can be constrained by observations, this would lead to a robust constraint on Sgr A* spin. Such a constraint at the μas scale should be within reach of the future VLBI Event Horizon Telescope (see e.g. Broderick et al. 2011): this is the second way of constraining Sgr A* spin.

3 Ray-tracing in the vicinity of non-Kerr compact objects

One of the specificities of the GYOTO code is its ability to perform ray-tracing in non-analytic metrics, different from the Kerr case. Here, we give the first examples of images computed by GYOTO in such numerically computed metrics.

When used with an analytical Kerr metric, GYOTO integrates the standard 4-dimensional equations of geodesics. When used with a numerically computed metric, GYOTO uses the 3+1 quantities describing the spacetime geometry, the 3-metric, lapse, shift and extrinsic curvature. The 4-dimensional geodesic equation can then be recast to a 3+1 equivalent that is integrated by GYOTO. For details, the reader is referred to Vincent et al. (2012).

Fig. 2 shows four successive images of a collapsing spherically symmetric neutron star, assumed to be optically thick and emitting as a blackbody with temperature 10^6 K. The evolving metrics of the collapsing star are computed by means of the `CoCoNuT` code (Dimmelmeier et al. 2005), and the ray-tracing is performed by GYOTO. This Figure shows the first example of images computed in numerical spacetimes, in a realistic

[ii] Available at `http://gyoto.obspm.fr`.

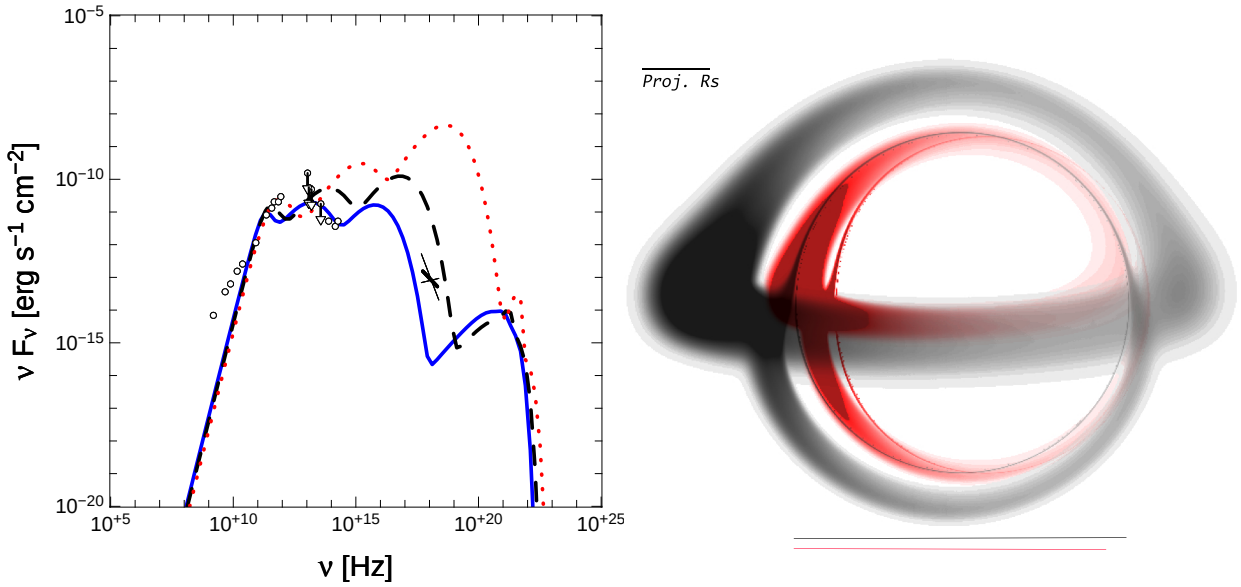

Fig. 1. Effect of the black hole spin parameter on the observables. **Left:** Emitted spectrum of the ion torus. The spin parameter is $a = 0$ (solid blue), $0.5M$ (dashed black) or $0.9M$ (dotted red). References for the observed data points in black can be found in Straub et al. (2012). **Right:** Superimposed images of the ion torus for a spin parameter $a = 0.5M$ (black) and $0.9M$ (red). The angular size of the projected Schwarzschild radius ($10\,\mu$as) is given by the upper left solid line. The solid lines at the bottom of the figure show the angular diameters of the black hole silhouettes in both cases. The two angular diameters differ by an amount of approximately $3\,\mu$as. Adapted from Straub et al. (2012).

(although simplified) astrophysical context. The growing of the event horizon is very clear on the different panels. It appears first at the center of the image as photons reaching the center of the observer's screen are emitted by closer parts of the star: they reach the observer sooner. It could seem strange that the shrinking of the neutron star is so tiny between the left panel (very beginning of the collapse) and the right panel (when nearly the whole star has disappeared behind the event horizon). However, this is due to the strong bending of null geodesics in the vicinity of the collapsing star that makes the apparent angular size of the image much bigger than the simple projection of the star (as if in flat spacetime). The same effect makes the angular size of a black hole shadow (as those depicted in the right panel of Fig. 1) appear bigger than the projected size of the event horizon.

Fig. 2 is an illustration of what kind of computation GYOTO can do in numerical spacetimes. It is not (yet) relevant for astrophysical purposes. A natural development of such works would be to compute light curves and spectra of astrophysical phenomena in the vicinity of Sgr A*, assuming this object is no longer a black hole of general relativity, but an alternative compact object. The numerical relativity group at Observatoire de Paris/LUTH is currently developing numerical metrics of such an alternative object: a boson star. It is a fascinating perspective to be able in the near future to develop simulations of observations of a probe phenomenon (such as a radiation flare) assuming the central object is either a Kerr black hole or a rotating boson star. Such simulations will allow to determine whether there is any observable differences between the two scenarii, and what kind of instrument could put to the light such a difference: this is the third way of constraining Sgr A*'s nature.

4 Conclusions

Near-future instruments should allow to give reach to the immediate vicinity of black holes, that is to say, to the direct probing of strong-field general relativistic phenomena.

This paper presents three different ways of constraining the nature of the Galactic center black hole Sgr A*, by means of current or near-future instruments. Assuming that Sgr A* is surrounded by an ion torus, it shows that spectroscopic measurements in the X-rays could allow constraining the black hole spin. The same goal may be achieved by determining the angular size of Sgr A* shadow by using the VLBI Event Horizon Telescope. Finally, the very nature of the central compact object may be probed by performing simulations of observations

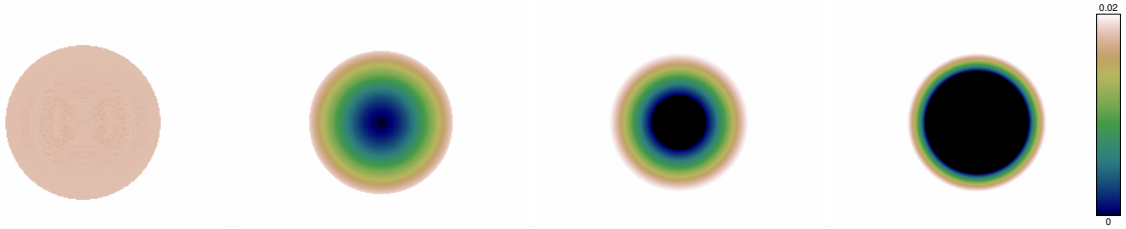

Fig. 2. Images (i.e. map of specific intensity) of a non-rotating collapsing neutron star, with an optically thick surface emitting black body radiation at 10^6 K. The color bar is common to the four panels and is given in SI units, $\mathrm{J\,s^{-1}\,m^{-2}\,ster^{-1}\,Hz^{-1}}$. The frequency of the photons in the observer's frame is chosen to be 10^{17} Hz, close to the maximum of the Planck function at 10^6 K.

using alternative compact objects metrics.

References

Abramowicz, M., Jaroszynski, M., & Sikora, M. 1978, A&A, 63, 221

Broderick, A. E., Loeb, A., & Reid, M. J. 2011, ApJ, 735, 57

Dimmelmeier, H., Novak, J., Font, J. A., Ibáñez, J. M., & Müller, E. 2005, Phys. Rev. D, 71, 064023

Eisenhauer, F., Perrin, G., Brandner, W., et al. 2011, The Messenger, 143, 16

Eisenhauer, F., Perrin, G., Brandner, W., et al. 2008, in Society of Photo-Optical Instrumentation Engineers (SPIE) Conference Series, Vol. 7013

Genzel, R., Eisenhauer, F., & Gillessen, S. 2010, Reviews of Modern Physics, 82, 3121

Ghez, A. M., Salim, S., Weinberg, N. N., et al. 2008, ApJ, 689, 1044

Gillessen, S., Eisenhauer, F., Trippe, S., et al. 2009, ApJ, 692, 1075

Narayan, R. & Yi, I. 1995, ApJ, 452, 710

Narayan, R., Yi, I., & Mahadevan, R. 1995, Nature, 374, 623

Qian, L., Abramowicz, M. A., Fragile, P. C., et al. 2009, A&A, 498, 471

Rees, M. J., Begelman, M. C., Blandford, R. D., & Phinney, E. S. 1982, Nature, 295, 17

Straub, O., Vincent, F. H., Abramowicz, M. A., Gourgoulhon, E., & Paumard, T. 2012, A&A, 543, A83

Vincent, F. H., Gourgoulhon, E., & Novak, J. 2012, ArXiv e-prints gr-qc/1208.3927

Vincent, F. H., Paumard, T., Gourgoulhon, E., & Perrin, G. 2011a, Classical and Quantum Gravity, 28, 225011

Vincent, F. H., Paumard, T., Perrin, G., et al. 2011b, in SF2A-2011: Proceedings of the Annual meeting of the French Society of Astronomy and Astrophysics, ed. G. Alecian, K. Belkacem, R. Samadi, & D. Valls-Gabaud, 689–693

Will, C. M. 2009, Space Sci. Rev., 148, 3

SF2A 2012
S. Boissier, P. de Laverny, N. Nardetto, R. Samadi, D. Valls-Gabaud and H. Wozniak (eds)

THE ACCRETION DISC, JETS AND ENVIRONMENT OF THE INTERMEDIATE MASS BLACK HOLE CANDIDATE ESO 243-49 HLX-1

N.A. Webb[1,2], D. Barret[1,2], V. Braito[3], S. Corbel[4], D. Cseh[4], S. A. Farrell[5], R.P. Fender[6], N. Gehrels[7], O. Godet[1,2], I. Heywood[8], T. Kawaguchi[10], J.-P. Lasota[10,11], E. Lenc[12], D. Lin[1,2], B. Plazolles[1,2] and M. Servillat[4]

Abstract. The Ultra Luminous X-ray (ULX) source HLX-1 in the galaxy ESO 243-49 has an observed maximum unabsorbed X-ray luminosity of 1.3×10^{42} erg/s (0.2-10.0 keV). From the conservative assumption that this value exceeds the Eddington limit by at most a factor of 10, the minimum mass is then 500 $M_{\odot}$. The X-ray luminosity varies by a factor of 40 with an apparent recurrence timescale of approximately one year. This X-ray variability is associated with spectral state transitions similar to those seen in black hole X-ray binaries. Here we discuss our recent modelling of all the X-ray data for HLX-1 and show that it supports the idea that this ULX is powered by sub- and near Eddington accretion onto an intermediate mass black hole. We also present evidence for transient radio emission which is consistent with a discrete jet ejection event as well as comment on the nature of the environment around HLX-1 in light of recent Hubble Space Telescope photometry.

Keywords: Accretion, accretion discs, Black hole physics, Galaxies: individual: ESO 243-49, Methods: data analysis, X-rays: individual: HLX-1

1 Introduction

Two varieties of black holes (BHs) have been observed to date: stellar mass ($\sim$3-20 $M_{\odot}$) BHs and supermassive ($\sim 10^{5-10}$ $M_{\odot}$) BHs present in the cores of most large galaxies. It is believed that stellar mass BHs are formed from the collapse of massive stars (e.g. Fryer 2003), but it is not yet clear how supermassive ones are formed. One model proposes that they are formed from the mergers of smaller mass ($\sim 10^{2-5}$ $M_{\odot}$) BHs, the so-called intermediate mass black holes (IMBHs, e.g. Madau & Rees 2001). Another model proposes super-Eddington accretion onto smaller mass BHs, to form supermassive black holes, which would again imply the existence of IMBH (Kawaguchi et al. 2004). But if either of these scenarios are correct, why have IMBH not been observed? How IMBHs form and where they reside is also a subject of intense debate (Miller & Colbert 2004). They may be formed through accretion and reside in the centres of old dense stellar clusters (globular clusters) or directly in young star forming regions (Miller & Colbert 2004). IMBHs constitute the missing BH link. They are also of interest to a wide variety of fundamental physics and astrophysical topics. It is thought that they may play a

[1] Université de Toulouse; UPS-OMP; IRAP, Toulouse, France
[2] CNRS; IRAP; 9 avenue du Colonel Roche, BP 44346, F-31028 Toulouse Cedex 4, France
[3] Department of Physics and Astronomy, University of Leicester, University Road, Leicester LE1 7RH, UK
[4] Laboratoire Astrophysique des Interactions Multi-echelles (UMR 7158), CEA/DSM-CNRS-Université Paris Diderot, CEA Saclay, F-91191 Gif sur Yvette, France
[5] Sydney Institute for Astronomy, School of Physics, The University of Sydney, NSW 2006, Australia
[6] School of Physics and Astronomy, University of Southampton, Highfield, Southampton, SO17 1BJ, UK
[7] Astroparticle Physics Laboratory, NASA/Goddard Space Flight Center, Greenbelt, MD 20771, USA
[8] University of Oxford, Department of Physics, Keble Road, Oxford OX1 3RH, UK
[9] Center for Computational Sciences, University of Tsukuba, 1-1-1 Tennodai, Tsukuba, Ibaraki 305-8577, Japan
[10] Institut d'Astrophysique de Paris, UMR 7095 CNRS, UPMC Université Paris 06, 98bis Boulevard Arago, 75014 Paris, France
[11] Astronomical Observatory, Jagiellonian University, ul. Orla 171, 30-244 Krakow, Poland
[12] Australia Telescope National Facility, CSIRO Astronomy and Space Science, PO Box 76, Epping NSW 1710, Australia

role in the stability of globular clusters (e.g. Hut et al. 1992), that they could be strong sources of gravitational waves if they are in elliptical binary systems with other compact objects (Miller & Colbert 2004), that dark matter may be comparatively easy to detect around them (e.g. Fornasa & Bertone 2008), that gas accretion onto IMBHs should have contributed significantly to the UV background (Kawaguchi 2003) and that IMBHs may have participated in the cosmological ionisation (Madau et al. 2004).

Ultra-luminous X-ray sources (ULXs) are non-nuclear extragalactic objects with bolometric luminosities $>10^{39}$ erg s^{-1} (e.g. Roberts 2007). Luminosities up to $\sim10^{41}$ erg s^{-1} can be plausibly explained through beaming effects (King 2008; Freeland et al. 2006) and/or hyper-accretion onto stellar mass BHs (King 2008; Kawaguchi 2003; Begelman 2002). A rare class of ULX – the hyper-luminous X-ray sources – have X-ray luminosities $>10^{41}$ erg s^{-1} and require increasingly complicated and unlikely scenarios to explain them without invoking the presence of an IMBH. We discovered a hyper luminous X-ray source (Farrell et al. 2009), dubbed HLX-1, consistent with being in the edge-on early-type galaxy ESO 243-49 at 95 Mpc, thanks to our FORS2 spectroscopy of the faint optical counterpart to HLX-1 (Wiersema et al. 2010; Soria et al. 2010). Using the maximum unabsorbed X-ray luminosity of $\sim10^{42}$ erg s^{-1} (0.2-10.0 keV, Farrell et al. 2009) and the conservative assumption that it exceeds the Eddington limit by at most a factor of 10 (Begelman 2002), a lower mass limit of 500 M$_\odot$ was derived for the BH (Farrell et al. 2009).

Our regular monitoring of HLX-1 with *Swift* (Gehrels et al. 2004; Burrows et al. 2005) has revealed significant flux changes , see Fig. 1, in conjunction with simultaneous spectral changes in the same way as Galactic BH X-ray binaries (Godet et al. 2009), thus strengthening the case for an accreting BH in HLX-1. From the four well sampled outbursts along with two prior to these, it has become evident that HLX-1's X-ray variability follows a fairly distinct pattern over approximately 1 year (Lasota et al. 2011).

2 X-ray data: Modelling the disc emission

Over the last four years we have carried out a monitoring campaign of HLX-1 with the *Swift* X-ray Telescope. During this time HLX-1 has shown four fast rise and exponential decay (FRED) type X-ray outbursts, with increases in the count rate of a factor 40. We have also obtained two *XMM-Newton* and two *Chandra* dedicated pointings that were triggered at the lowest and highest luminosities. From simple spectral fitting, the unabsorbed luminosities range from 1.9×10^{40} to 1.3×10^{42} erg s^{-1}. Using these data we confirm the proposed spectral state transitions from HLX-1. At high luminosities, the X-ray spectrum shows a thermal state dominated by a disc component with temperatures $\leq$0.26 keV, and at low luminosities the spectrum is dominated by a hard power law with $1.4 \leq \Gamma \leq 2.1$, consistent with a hard state. The source was also observed in a state consistent with the steep power law state, with Γ=3.3$\pm$0.2. In the thermal state, the luminosity of the disc component appears to scale with the fourth power of the inner disc temperature which supports the presence of an optically thick, geometrically thin accretion disc. The low fractional variability (rms of 9$\pm$9%) in this state also suggests the presence of a dominant disc. The spectral changes and long-term variability can not be explained by variations of the beaming and are not consistent with the source being in a super-Eddington accretion state as is proposed for most ULX sources with lower luminosities. HLX-1 is therefore an unusual ULX as it is similar to Galactic black hole binaries, which have, for the most part, non-beamed and sub-Eddington emission. However, HLX-1 differs from them as it has a luminosity three orders of magnitude higher. Comparing HLX-1 to the Galactic black hole binaries, from Eddington scaling we determine a lower limit on the mass of the black hole of >9000 M$_\odot$. The relatively low disc temperature in the thermal state also suggests the presence of an IMBH of few 10^3 M$_\odot$ (Servillat et al. 2011).

We then fitted more complex models to similar multi-epoch data collected with *Swift*, *XMM-Newton* and *Chandra*. We used a disc model (Kawaguchi 2003) for a wide range of sub- and super-Eddington accretion rates assuming a non-spinning black hole and a face-on disc (i = 0°). Thanks to the wide range of the accretion rates of this model, one does not need to assume a priori whether the source is in sub- or super-Eddington phases, unlike with other disc models. Using this model implies that the black hole in HLX-1 is in the intermediate mass range ($\sim2\times10^4$ M$_\odot$) and the accretion flow is in the sub-Eddington regime. The disc radiation efficiency is $\eta = 0.11 \pm 0.03$. We also confirm that the source does follow the $L_X \propto T^4$ relation for this mass estimate. At the outburst peaks, the source radiates near the Eddington limit. The accretion rate near the Eddington limit then stays constant around 4×10^{-4} M$_\odot$ yr $^{-1}$ for several days and then decreases exponentially, with a brutal decrease at the end of the outburst that may indicate that the accretion regime changes to an Advection Dominated Accretion Flow (ADAF). *Plateaus* in the accretion rate could be evidence that enhanced mass transfer rate is the driving outburst mechanism in HLX-1 (Godet et al. 2012). We also obtained good fits to disc-dominated

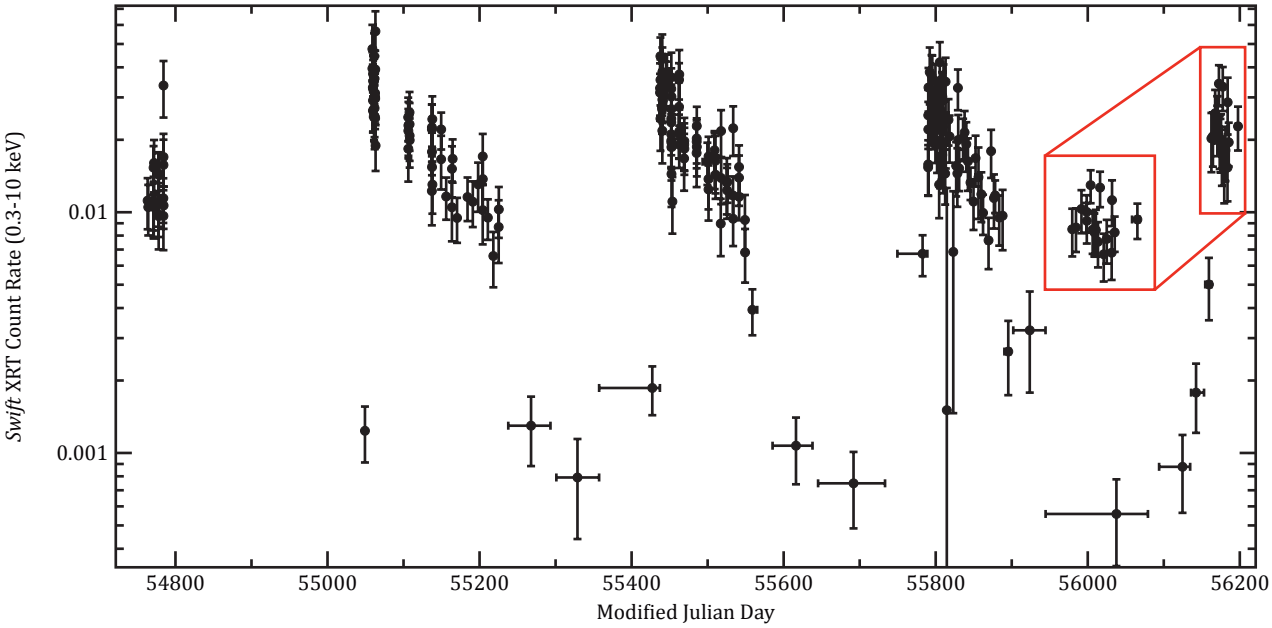

Fig. 1. Longterm Swift lightcurve. Four X-ray state transitions from the low/hard state (count rate $\lesssim$ 0.002, 0.3-10.0 keV) to the high/soft state (0.01 $\lesssim$ count rate $\lesssim$ 0.05, 0.3-10.0 keV) can be seen.

observations of the source with BHSPEC, a fully relativistic black hole accretion disc spectral model (Davis et al. 2011). Due to degeneracies in the model arising from the lack of independent constraints on inclination and black hole spin, there is a factor of 100 uncertainty in the best-fit black hole mass M. Nevertheless, spectral fitting of *XMM-Newton* observations provides robust lower and upper limits with 3000 $M_\odot \lesssim M \lesssim 3 \times 10^5$ $M_\odot$, at 90% confidence, again placing HLX-1 firmly in the intermediate-mass regime. The upper bound on M is sensitive to the maximum allowed inclination i, and is reduced to $M \lesssim 1 \times 10^5$ $M_\odot$ if the inclination is taken to be below 75°.

3 Radio emission: Detecting the jets

We observed HLX-1 with the Australia Telescope Compact Array (ATCA) in the 750 m configuration on 13 Sep. 2010, when regular X-ray monitoring of HLX-1 with the *Swift* satellite showed that HLX-1 had just undergone a transition from the low/hard X-ray state to the high/soft X-ray state. The transition occurs for HLX-1 when the count rate increases by more than a factor 10 in just a few days (Fig 1) (Godet et al. 2012; Servillat et al. 2011). Galactic BH binaries are known to emit radio flares around the transition from the low/hard to the high/soft state, (e.g. Fender et al. 2009; Corbel et al. 2004). These are associated with ejection events, where, for example, the jet is expelled which can lead to radio flaring when the higher velocity ejecta may collide with the lower-velocity material produced by the steady jet. As well as detecting radio emission from the galaxy nucleus, we detected a radio point source at Right Ascension (RA) = $01^h10^m28.28^s$ and declination (dec.) = -46°04'22.3", coincident with the *Chandra* X-ray position of HLX-1 (Webb et al. 2010). Combining the 5 GHz and 9 GHz data gives a detection of 50 μJy/beam, a 1 σ noise level of 11 μJy, thus a 4.5 σ detection at the position of HLX-1, at a time when such emission can be expected (Fig 2, left, Table 1 & Webb et al. 2012).

The radio flares in Galactic BH binaries are typically a factor 10-100 (and even more) brighter than the non-flaring radio emission (Körding et al. 2005) and generally last one to several days, e.g. XTE J1859+226 (Brocksopp et al. 2002). Once the high/soft state has been achieved, the core jet is suppressed (e.g. Fender et al. 2009). To determine whether the radio emission that we detected was transient and thus associated with a radio flare, we made another observation with the ATCA in the 6 km configuration on 3 Dec. 2010, when HLX-1 was declining from the high/soft state and when no flaring is expected. This observation again showed emission from the nucleus of the galaxy, consistent with that of the previous radio observation, but revealed no source at the position of HLX-1. The 3 σ non-detection for the combined 5 GHz and 9 GHz data is 36 μJy/beam (Fig 2, right & Table 1). These observations suggest that the source is variable.

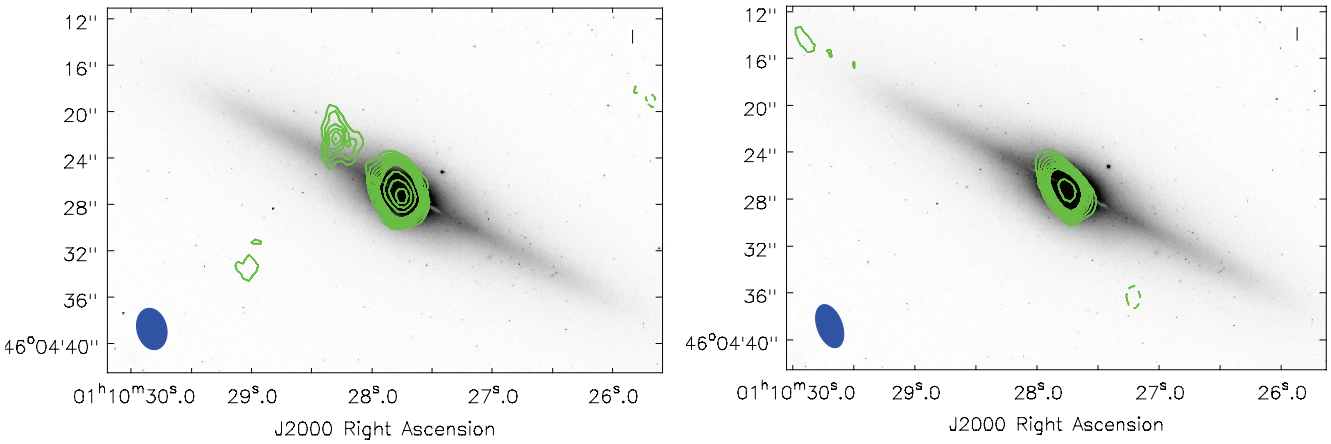

Fig. 2. Left: Left: 5 and 9 GHz combined radio observations (contours: -3, 3, 4, 5, 6, 7, 8, 9, 10, 15, 20, 25 times the 1 σ rms noise level (5.6 μJy/beam)) using radio data taken on the 13th September 2010, 31st August 2011, 3rd and 4th September 2011 with the ATCA and superimposed on an I-band Hubble Space telescope image of ESO 243-49 (inverted colour map). The beam size is shown in the bottom left hand corner. The galaxy, ESO 243-49, is clearly detected in radio. An 8 σ point source falls at RA = $01^h10^m28.28^s$ and declination = -46°04'22.3" (1 σ error on the position of RA=0.43" and dec.=0.67"), well within the 0.3" Chandra error circle of HLX-1. **Right:** 5 and 9 GHz combined radio observations (contours: -3, 3, 4, 5, 6, 7, 8, 9, 10, 15, 20, 25 times the 1 σ rms noise level (7.0 μJy/beam)) made from the 3rd December 2010, 25th August 2011 and 1st September 2011 ATCA observations and superimposed on the same I-band Hubble Space telescope image of ESO 243-49. The galaxy ESO 243-49 is again clearly detected, but no source is found within the Chandra error circle. Again the beam size is shown in the bottom left hand corner.

To confirm the variability, we re-observed HLX-1 when it had just undergone another transition from the low/hard X-ray state to the high/soft X-ray state in August 2011 (Fig 1). All five of the 2011 observations (Table 1) were made in a similar configuration to the December 2010 observation. We observed three non-contiguous detections ($\geq 4\ \sigma$) and two non-contiguous non-detections of the source (Table 1). This indicates that two flares were detected during this period.

To determine if the source was indeed variable, we fitted each observation using a point source, using the point spread function. We used the position of HLX-1 when the source was not detected. This allowed us to estimate the flux and the associated errors (Table 1) even for a non-detection. We tested whether the data could be fitted with a constant, namely the mean of the data. We compared these data to the mean flux value using a chi-squared test. We found a reduced chi-square (χ^2_ν) value of 2.5 (5 degrees of freedom) which is much greater than unity, demonstrating that a constant is a poor fit to the data and supporting the variable nature. Further, combining all of the detections (5 and 9 GHz), the source is observed at 45 μJy/beam, with a 1 σ noise level of 5.5 μJy, which shows a confident detection at the 8 σ level. Combining, in a similar fashion, the data in which no radio emission was detected, we obtained a 3 σ upper limit in the combined 5+9 GHz data of 21 μJy/beam (Fig 2). The variability rules out emission from a nebula. The observed variable radio emission is then again consistent with a transient jet ejection event (Webb et al. 2012).

It has been shown that observations of super massive BHs and stellar mass BHs support the scale invariance of jets (Merloni et al. 2003; Körding et al. 2006). This was done by comparing X-ray and radio measurements, tracers of mass accretion rate and kinetic output respectively, with the BH mass to form a "fundamental plane of black hole activity". Under the hypothesis that HLX-1 is indeed an intermediate mass black hole, we can test the proposed relation. We take what is generally considered to be the maximum mass of intermediate mass black holes, $\sim 1\times10^5$ $M_\odot$ (Miller & Colbert 2004) and the X-ray luminosity, 5.43×10^{41} erg s^{-1} (0.5-10.0 keV), determined from *Swift* X-ray telescope observations made at the same time as our radio detection. Continuum (non flaring) radio emission could then be estimated with the aforementioned relationship (Körding et al. 2006), which is based on a sample that includes BHs in all different X-ray states. This relation implies a continuum radio emission at the $\sim 20\mu$Jy level. This is slightly lower than the 3 σ non-flaring upper limit, suggesting that the mass of the BH is likely to be less than $\sim 1\times10^5$ $M_\odot$ (Webb et al. 2012).

Radio flares are seen to occur in Galactic black hole binaries when the X-ray luminosity is 10−100 per cent of the Eddington luminosity (Fender et al. 2004). HLX-1 has already shown similar behaviour to the Galactic black

Table 1. The 7 radio observations organised by date and showing the *Swift* X-ray unabsorbed flux (0.5−10.0 keV) × 10^{-13} erg cm^{-2} s^{-1} (and the 90% confidence errors) along with the combined 5 and 9 GHz peak brightness radio flux (with the associated 1 σ noise level) or the 3 σ upper limit for the non-detections. The final column gives the radio flux from fitting a point source (using the point spread function) (and the associated 1 σ noise level).

Observation date	X-ray flux	5+9 GHz peak flux (μJy/beam)	5+9 GHz flux density (μJy)
13 Sep. 2010	$4.57(\pm^{0.68}_{0.50})$	50 (11)	42 (10)
3 Dec. 2010	$2.40(\pm^{0.60}_{0.50})$	<36	11 (20)
25 Aug. 2011	4.57(±0.30)	<30	14.5 (7)
31 Aug. 2011	4.57(±0.30)	51 (10)	63 (18)
1 Sep. 2011	4.57(±0.30)	<31	25 (10.5)
3 Sep. 2011	4.57(±0.30)	45 (10.5)	43 (10)
4 Sep. 2011	4.57(±0.30)	30 (7.5)	27 (7.5)

hole binaries. Therefore assuming that the radio flares that we observed also occur when the X-ray luminosity is 10−100 per cent of the Eddington luminosity indicates a black hole mass between ∼9.2 ×10^3 M$_\odot$ and ∼9.2 ×10^4 M$_\odot$, commensurate with the mass estimate above and those of (Davis et al. 2011; Servillat et al. 2011; Godet et al. 2012) and confirming the intermediate mass black hole status (Webb et al. 2012).

4 Multiwavelength data: Identifying the host population

Fitting the spectral energy distribution from the near infra-red (Hubble Space Telescope) to X-ray (*Swift* X-ray Telescope) wavelengths, we showed that the broadband spectrum is not consistent with simple and irradiated disc models, but is well described by a model comprised of an irradiated accretion disc plus a ∼10^6 M$_\odot$ stellar population. The age of the population cannot be uniquely constrained, with both young (∼13 Myr) and old (∼13 Gyr) stellar populations allowed. However, the old solution requires excessive disc reprocessing and an extremely small disc, so we favor the young solution (∼13 Myr). In addition, the presence of dust lanes and the lack of any nuclear activity from X-ray observations of the host galaxy suggest that a gas-rich minor merger may have taken place less than ∼200 Myr ago. A merger event between a dwarf galaxy and ESO 243-49 could explain the presence of the IMBH (remnant of the stripped dwarf galaxy) and the young stellar population (whose formation was triggered by the merger) (Farrell et al. 2012). Soria et al. (2012) also made ground based VLT U, B, V, R and I band observations of HLX-1 when the X-ray luminosity had dropped to half the peak luminosity. They found that the optical magnitudes had also dropped by ∼1 magnitude. They modelled the Comptonized, irradiated X-ray spectrum of the disc, and found that the optical luminosity and colours in the 2010 November data were consistent with emission from the irradiated disc but state that they strongly rule out the presence of a young superstar cluster, which would be too bright. However, HLX-1 is contaminated by the diffuse galaxy emission in these ground based images and Soria et al. (2012) do not fit the X-ray and optical data simultaneously, as in (Farrell et al. 2012), which could cause the differing results. New *HST* and *XMM-Newton* data is expected to resolve this issue (Farrell et al. in prep.).

References

Begelman, M. C. 2002, ApJ, 568, L97
Brocksopp, C., Fender, R. P., McCollough, M., et al. 2002, MNRAS, 331, 765
Burrows, D. N., Hill, J. E., Nousek, J. A., et al. 2005, Space Sci. Rev., 120, 165
Corbel, S., Fender, R. P., Tomsick, J. A., Tzioumis, A. K., & Tingay, S. 2004, ApJ, 617, 1272
Davis, S. W., Narayan, R., Zhu, Y., et al. 2011, ApJ, 734, 111
Farrell, S. A., Servillat, M., Pforr, J., et al. 2012, ApJ, 747, L13
Farrell, S. A., Webb, N. A., Barret, D., Godet, O., & Rodrigues, J. M. 2009, Nature, 460, 73
Fender, R. P., Belloni, T. M., & Gallo, E. 2004, MNRAS, 355, 1105
Fender, R. P., Homan, J., & Belloni, T. M. 2009, MNRAS, 396, 1370
Fornasa, M. & Bertone, G. 2008, International Journal of Modern Physics D, 17, 1125
Freeland, M., Kuncic, Z., Soria, R., & Bicknell, G. V. 2006, MNRAS, 372, 630

Fryer, C. L. 2003, Classical and Quantum Gravity, 20, 73
Gehrels, N., Chincarini, G., Giommi, P., et al. 2004, Astrophys. J., 611, 1005
Godet, O., Barret, D., Webb, N. A., Farrell, S. A., & Gehrels, N. 2009, ApJ, 705, L109
Godet, O., Plazolles, B., Kawaguchi, T., et al. 2012, ApJ, 752, 34
Hut, P., McMillan, S., Goodman, J., et al. 1992, PASP, 104, 981
Kawaguchi, T. 2003, ApJ, 593, 69
Kawaguchi, T., Aoki, K., Ohta, K., & Collin, S. 2004, A&A, 420, L23
King, A. R. 2008, MNRAS, 385, L113
Körding, E., Colbert, E., & Falcke, H. 2005, Astron. Astrophys., 436, 427
Körding, E., Falcke, H., & Corbel, S. 2006, Astron. Astrophys., 456, 439
Lasota, J.-P., Alexander, T., Dubus, G., et al. 2011, ApJ, 735, 89
Madau, P. & Rees, M. J. 2001, ApJ, 551, L27
Madau, P., Rees, M. J., Volonteri, M., Haardt, F., & Oh, S. P. 2004, ApJ, 604, 484
Merloni, A., Heinz, S., & di Matteo, T. 2003, Mon. Not. R. Astron. Soc., 345, 1057
Miller, M. C. & Colbert, E. J. M. 2004, International Journal of Modern Physics D, 13, 1
Roberts, T. P. 2007, Ap&SS, 311, 203
Servillat, M., Farrell, S. A., Lin, D., et al. 2011, ApJ, 743, 6
Soria, R., Hakala, P. J., Hau, G. K. T., Gladstone, J. C., & Kong, A. K. H. 2012, MNRAS, 420, 3599
Soria, R., Hau, G. K. T., Graham, A. W., et al. 2010, Mon. Not. R. Astron. Soc., 405, 870
Webb, N., Cseh, D., Lenc, E., et al. 2012, Science, 337, 554
Webb, N. A., Barret, D., Godet, O., et al. 2010, ApJ, 712, L107
Wiersema, K., Farrell, S. A., Webb, N. A., et al. 2010, ApJ, 721, L102

SF2A 2012
S. Boissier, P. de Laverny, N. Nardetto, R. Samadi, D. Valls-Gabaud and H. Wozniak (eds)

AXION-LIKE PARTICLES AND γ-RAY SOURCE SPECTRA

D. Wouters[1] and P. Brun[1]

Abstract. Oscillations from high energy photons into Axion Like Particles (ALPs) in an external magnetic field are expected to leave an imprint on the spectra of astrophysical γ-ray sources. We show that the usual observables, that are a drop in the energy spectra and a boost of fluxes at very-high energies in case of propagation through the intergalactic medium, are only valid when averaging observations over a multitude of sources. A new signature of ALPs in the case of observations of single sources is outlined, that could be used as an efficient method to tag photon-ALP oscillations.

1 Introduction

Axion-like particles (ALPs) are a class of hypothetical light pseudoscalar particles that only to Standard Model components through a two-photon vertex. This coupling allows for photon-ALP oscillations in an external magnetic field. Such process has recently gained interest in astrophysics as being a possible explanation for various phenomena; these phenomena includes the anomalous cooling of white dwarves (Isern et al. 2008), the scatter in the luminosity relations of sources (Burrage et al. 2009) or possibly the dimming of type Ia supernovae (Csáki et al. 2002). In very-high energy (VHE, E > 100 GeV) astrophysics, ALPs were introduced as an exotic explanation to the problem of the lack of opacity of the universe to TeV γ-ray, opacity due to the absorption of γ-rays on the the extragalactic background light (EBL) through pair creation (De Angelis et al. 2007; Simet et al. 2008; Horns & Meyer 2012). Back in 2006 when the Cherenkov telescope array H.E.S.S. observations of two blazars implied a low level of EBL compared to semi-empirical models (Aharonian et al. 2006), it has been proposed that γ-ALPs oscillations in the Inter-Galactic Magnetic Field (IGMF) could reduce the observed opacity as photons travel shielded to EBL when they are in the ALP state. The same effect has been proposed to explain the VHE emission from dense regions in blazars (Tavecchio et al. 2012). A second signature of γ-ALPs oscillations in γ-ray spectra is a dimming of the fluxes above the energy threshold at which the mixing starts to be efficient, the composition of the beam being on average 2/3 of photons and 1/3 of ALPs (Mirizzi et al. 2007; Hooper & Serpico 2007; Hochmuth & Sigl 2007).

In astrophysical environments relevant to this study, be it a galaxy cluster or the intergalactic medium, magnetic fields are turbulent so that the exact structure of the magnetic field crossed by the beam is not predictable. This results in a consequential randomness of the observable effects. For instance, Mirizzi & Montanino (2009) have shown that there exist realizations of the IGMF leading to a decrease of the γ-ray flux through γ-ALPs oscillations and EBL absorption, stronger than what is predicted from the EBL absorption only. The two expected signatures of ALPs in γ-ray source spectra, a more transparent universe and a drop in energy spectra at the threshold of coupling are in fact based on an average structure of the turbulent magnetic field. Such observables are thus useless to look for ALPs through the observation of a single source leaving only the possibility of a population study to average the effects over a collection of sources. A signature outlined in Wouters & Brun (2012) that applies to observations of only one source is studied here.

2 γ-ALPs mixing for a single-source spectrum

Magnetic fields involved in a possible coupling between ALPs and photons from astrophysical TeV sources are usually turbulent. To model the evolution of the γ-ALPs system when propagating through a turbulent magnetic field, the simplest way is to divide the path between domains of constant size typical of the coherence length

[1] CEA, Irfu, Centre de Saclay, F-91191, Gif-sur-Yvette, France

of the magnetic field. In each domain, the strength of the magnetic field is considered as constant and only the orientation is randomly varying. In this picture, one realization of the magnetic field is a set of randomly chosen orientation of the magnetic field for each domain, corresponding to the structure of the magnetic field crossed by a photon beam from a source randomly picked on the sky. This is a crude description of the turbulent magnetic field but it proves useful to understand the simple basics of the behavior of the coupling. The validity of such a description when considering other turbulence models is latter addressed in section 3 and in particular that it is conservative compared to more accurate descriptions.

The structure of the turbulence model is such that in each domain, the magnetic field is coherent. γ-ALPs mixing in a coherent magnetic field has long been studied. It turns out that only the magnetic field component transverse to the propagation is involved in the coupling (Raffelt & Stodolsky 1988). Moreover, only one polarization state of the photon parallel to the field couples, such that the problem depends in fact on two geometrical angles, encoding the orientation of the magnetic field. The mixing is efficient above en energy threshold given as function of the mass of the ALPs, m_a, the coupling strength, g, and the projection of the magnetic field on the polarization plane of the photon B_T:

$$E_{\rm thr} = \frac{m_a^2}{2gB_T} \, .$$

The conversion probability of the photon crossing the coherent magnetic domain of size s has the following dependence: For $E \ll E_{\rm thr}$ no conversion occurs, for $E \sim E_{\rm thr}$, spectral oscillations happen and for $E \gg E_{\rm thr}$, the conversion is no longer energy dependent and takes the value $\sin^2 \delta/2$ where $\delta = gB_T s/2$. Therefore, the condition required for a significant conversion is $\delta \gtrsim 1$, similar to the Hillas criterion for the acceleration of ultra-high energy cosmic rays (Hooper & Serpico 2007), suggesting that the two processes could take place in the same astrophysical environments. As an example, the photon survival probability as a function of the energy for an allowed large IGMF value of 1 nG, an ALP mass of 2 neV and a coupling $g = 8 \times 10^{-11}\,{\rm GeV}^{-1}$ at the limit of current experimental constraints (Arik et al. 2011) is shown for different values of δ (increasing s) on fig. 1. For the parameters chosen, $E_{\rm thr}$ is fixed at 1 TeV.

For each domain of the turbulent magnetic field, a transfer function of the system giving the conversion probability can be constructed. The total transfer function corresponding to one random realization of the magnetic field is given by the product of all individual transfer functions. For each single domain transfer functions, the spectral oscillations around $E_{\rm thr}$ such as those displayed on fig. 1 have a different structure, depending on the orientation of the magnetic field (giving different values for B_T). The global survival probability is therefore the result of interferences of all these oscillation patterns, yielding a very complex energy dependence around $E_{\rm thr}$. An example is shown on fig. 2, for a source at redshift 0.1 whose photons travel trough the IGMF assuming a coherence length $s_0 = 1$ Mpc, and for the same set of ALP parameters. The figure is displayed using the EBL model from Kneiske & Dole (2010). One can see that the prediction of a model with ALPs is the presence of a significant level of noise over one decade or so around $E_{\rm thr}$. At VHE, a smooth behavior of the spectrum is retrieved, as the interferences weaken. Although the exact shape of the spectrum is not predictable, as it depends on one single random realization of the magnetic field, the noise level can be predicted as shown in the next section.

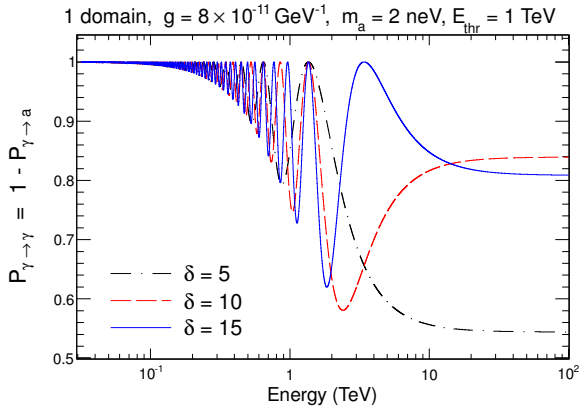

Fig. 1. Survival probability of an unpolarized photon as function of the energy for three values of δ

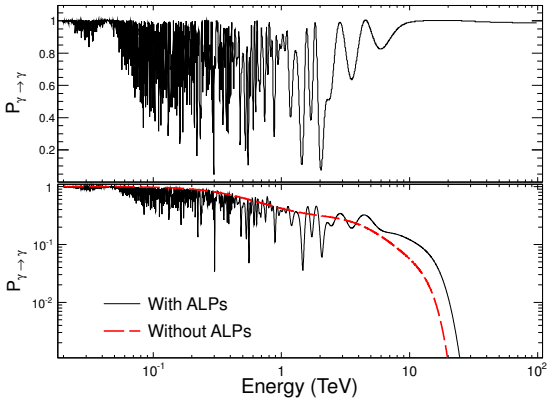

Fig. 2. Survival probability as function of the energy for a source at z = 0.1 using $B = 1$ nG, $s_0 = 1$ Mpc, $g = 8 \times 10^{-11}\,\mathrm{GeV}^{-1}$ and $m_\mathrm{a} = 2$ neV without absorption (upper panel) and with EBL absorption (lower panel)

3 Observational effects

The spectrum obtained in sec. 2. from the simulation of the propagation through the IGMF is the theoretical continuous spectrum that will be observed. In practice, astrophysical sources spectra at TeV energies are observed with a given energy resolution, that is approximately 15% for the latest generation of atmospheric Cherenkov telescopes, HESS, MAGIC or VERITAS. This finite energy resolution tends to smooth the alternation of peaks and drops that form the noisy behavior around E_thr, so that it could remain unobservable.

To study the experimental relevance of the proposed signature, a simulation is performed considering 50 h of observations of a source at redshift 0.1 emitting at the Crab level. To match current generation of instruments, an effective area of $10^5\,\mathrm{m}^2$ is assumed in addition to the 15% energy resolution. The source spectrum is the product of the intrinsic spectrum, here for example following a log-parabola shape, and a survival probability pattern generated for a random realization of the IGMF convolved with EBL absorption. This spectrum is then binned in bins of size corresponding to the energy resolution to obtain the observed binned spectrum. For each bin, the number of detected photons is redistributed with a Poisson distribution, to account for statistical errors. An example of such simulation is shown on the left panel of fig. 3, together with a fit of the binned spectrum with a log-parabola shape moduled by EBL absorption. The relative residuals of that fit are displayed on the right panel of fig. 3. As compared to the case without ALPs for which the residuals evenly spread around 0, the noisy behavior of the underlying unbinned spectrum in the ALPs model clearly impacts the binned measured spectrum, the relative fit residuals displaying anomalous strong and chaotic deviations from 0.

To further quantify this noise, the variance of these relative fit residuals is computed. An average of this variance over 5000 simulations of different realizations of the IGMF is shown on tab. 1 for different scenarios. From this table, the variance, which is a prediction of given ALP parameters, instrumental response functions and chosen source, scales with the coupling strength g. For the coupling strengths tested, the effect turns out to be significant compared to the conventional expectation. Observations of a Crab-level source for 50 h has been chosen as an illustration, but for the same redshift and energy range, a hint of effect would still be visible but with less significance by observing only 5 h.

The turbulence as it has been described so far is the simplest model one could think of. A more realistic description is to use a Kolmogorov-like turbulence, that accounts for the power distribution of a large range

Table 1. Values of the RMS of the fit residuals to mock data with different assumptions for g and m (in units of GeV^{-1} and neV resp.), for constant size magnetic field domains and Kolmogorov turbulent magnetic field.

Model	Variance of the fit residuals Constant size domains	Variance of the fit residuals Kolmogorov turbulence
No ALP	0.04 ± 0.01	*idem*
$g = 10^{-11}$, $m = 0.7$	0.11 ± 0.04	0.18 ± 0.05
$g = 8 \times 10^{-11}$, $m = 2$	0.20 ± 0.05	0.42 ± 0.14

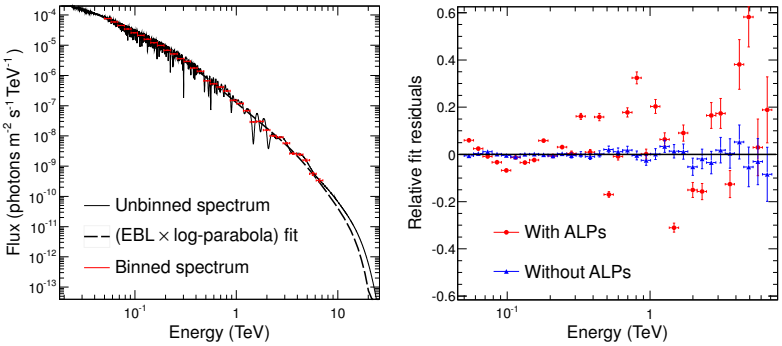

Fig. 3. Simulation of the observation of one γ-ray source at z=0.1, with the effect of γ-ALP mixing (left), and distribution of the residuals of fits to a conventional model and a model with ALPs (right).

of modes $k = 2\pi/s$ where the power in each mode scales as $k^{-5/3}$. In this framework, magnetic fields that are coherent on small scales should have contributions that become rapidly negligible due to two effects: first, because of the Kolmogorov power-law, the magnetic field involved is weaker. Second, for small coupling, the averaged conversion probability is proportional to B^2L/s so that even for a magnetic field uniform over all scales, the mixing is less and less efficient at small scales. Finally, given the two mentioned effects, the conversion probability for a scale $s/10$ is only 2.5‰ of the probability at scale s ($P \propto s^{-8/3}$), so that one can safely consider that only the largest scales contribute. The results of the variance of the fit residuals assuming a Kolmogorov-like turbulence over scales between 0.1 and 100 Mpc and a rms intensity of B of 1 nG at 100 Mpc are also reported on table 1. The variance of the fit residuals is still significantly larger in the ALP model.

4 Conclusion

In this study, the effects of γ-ALP oscillations on γ-ray source spectra have been discussed, making the difference between average observables, valid for a large collection of sources, and single source observables. For the first time, a signature of ALPs for observations of a single has been outlined with an explicit example given in the case of mixing in the IGMF. It has been checked that this signature is experimentally detectable given current generation of instruments. Such effect could be used to constrain ALP models in the range of very small masses ($m_a \sim 10^{-10} - 10^{-7}$ eV).

References

Aharonian, F., Akhperjanian, A. G., Bazer-Bachi, A. R., et al. 2006, Nature, 440, 1018
Arik, M., Aune, S., Barth, K., et al. 2011, Physical Review Letters, 107, 261302
Burrage, C., Davis, A.-C., & Shaw, D. J. 2009, Physical Review Letters, 102, 201101
Csáki, C., Kaloper, N., & Terning, J. 2002, Physical Review Letters, 88, 161302
De Angelis, A., Roncadelli, M., & Mansutti, O. 2007, Phys. Rev. D, 76, 121301
Hochmuth, K. A. & Sigl, G. 2007, Phys. Rev. D, 76, 123011
Hooper, D. & Serpico, P. D. 2007, Physical Review Letters, 99, 231102
Horns, D. & Meyer, M. 2012, JCAP, 1202, 033
Isern, J., García-Berro, E., Torres, S., & Catalán, S. 2008, ApJ, 682, L109
Kneiske, T. M. & Dole, H. 2010, A&A, 515, A19
Mirizzi, A. & Montanino, D. 2009, JCAP, 0912, 004
Mirizzi, A., Raffelt, G. G., & Serpico, P. D. 2007, Phys. Rev. D, 76, 023001
Raffelt, G. & Stodolsky, L. 1988, Phys. Rev. D, 37, 1237
Simet, M., Hooper, D., & Serpico, P. D. 2008, Phys. Rev. D, 77, 063001
Tavecchio, F., Roncadelli, M., Galanti, G., & Bonnoli, G. 2012, ArXiv e-prints: 1202.6529
Wouters, D. & Brun, P. 2012, Phys. Rev. D, 86, 043005

Sessions 15 & 18

Outreach activities and teaching

SF2A 2012
S. Boissier, P. de Laverny, N. Nardetto, R. Samadi, D. Valls-Gabaud and H. Wozniak (eds)

C2PU: AN ORIGINAL MIX OF RESEARCH AND PEDAGOGY AT OBSERVATOIRE DE LA CÔTE D'AZUR

P. Bendjoya[1], L. Abe[1], J.-P. Rivet[1], O. Suárez[1] , D. Vernet[2] and D. Mékarnia[1]

Abstract. C2PU stands for "Centre Pédagogique Planète et Univers" and consists in an experimental and observational facility located at 50 km from Nice (France), at the Calern Plateau. It is dedicated to the pedagogy in Earth and Universe sciences by and through research projects.

Keywords: Methods: observational, Techniques: photometric, Techniques: polarimetric, Techniques: interferometric

1 Introduction

C2PU offers an infrastructure devoted to the immersion of students in the experimental environment in astrophysics and geophysics (`http://c2pu.oca.eu/`). C2PU stands in French for "*Centre Pédagogique Planète et Univers*", that is: "Center for Pedagogy in Planet and Universe sciences". It is a project both for pedagogic and research purposes. Concerning the astrophysical part, it relies on the renewal of two 1-meter diameter telescopes. These two telescopes are located in southern France, 50 km away from the city of Nice, on the so-called "Calern Plateau". The coordinates are $6^o\,55'\,22''$ East in longitude, $43^o\,45'\,14''$ North in latitude and 1260 m in elevation. The average number of clear nights per year is around 200 and the sky background level ranges from 20.7 to 21 magnitudes per square arc-seconds. One of the telescopes is planed to be operated by remote access in order to offer undergraduate classes the possibility to participate to sky observations after several sessions of teacher training in the framework of the EduCosmos project, the astronomical counterpart of the French educational outreach project "*Sismo à l'Ecole*" (`http://educosmos.oca.eu/`). This remote access capability will also be offered to national and international universities in partnership with C2PU.

The center offers a capacity of 28 sleeping arrangements, a restaurant, a visio-conference facility and a computer room with high speed internet connection which allows a complete immersion of the students during their stay at the observatory. Groups can be driven to the center with a van owned by the Observatoire de la Côte d'Azur (OCA).

The Calern Plateau and its surrounding display several geophysical and geological structures of interest,. They can be used both for experimental and practical lectures. Several unique geological sites are easily reachable from the Observatory. Both astrophysical and geophysical practical trainings can be combined within a common infrastructure.

The project is supported by the *Observatoire de la Côte d'Azur*, the University of Nice Sophia-Antipolis (UNS), the *Collège de France* (CdF), the *Conseil Général des Alpes Maritimes* and the *Conseil Régional Provence Alpes Côte d'Azur*.

2 Astrophysics

2.1 Instruments

The two telescopes that C2PU will offer, were earlier coupled as part of an interferometric instrument called SOIRDETE (for "*Synthèse d'Ouverture en Infra Rouge avec DEux Télescopes*"), described in Rabbia et al.

[1] Laboratoire Lagrange UMR 7293, Université de Nice Sophia-Antipolis, Observatoire de la Côte d'Azur, CNRS
[2] Laboratoire d'Interférométrie Stellaire et Exoplanétaire, Collège de France

(1990). These two instruments are planed to be renewed in two phases. The first one which began in September 2010 involves the shaping and polishing of a 1-meter primary mirror for the West-telescope (W-Tel), out of a Zerodur blank provided by OCA. This phase ended late 2011. During this polishing operation by D. Vernet from CdF, the refurbishing of the mechanical structure of the telescope is undertaken. In parallel, the C2PU team has designed and implemented the hardware and software for the remote control of W-Tel through Internet. The W-Tel is presently in beta-testing phase, and is not yet remote-operable. Its Cassegrain $F/12.5$ focus is in a temporary configuration for characterization tests. The second phase will begin in 2013 and will concern the second 1-meter telescope, the East-telescope (E-Tel).

The W-Tel is planed to have two different focus configurations : an $F/3.24$ primary focus for wide field imaging, and a Cassegrain $F/12.5$ focus. Switching from one configuration to the other will only consist in plugging or unplugging an opto-mechanical module. The whole mechanics have been designed and manufactured by the department of mechanics at OCA. The telescope will be driven by a control computer, accessible through an internet interface, to allow for remote observations.

The $F/3.24$ focus will be equipped with a 4096×4096 SBIG STX-16803 CCD camera with a set of filters. This will lead to a pixel scale of $0.6''$/pix and a $40' \times 40'$ field of view. The 20^{th} magnitude is expected to be reachable at $5\,\sigma$ with a 1 minute exposure. This configuration will be dedicated to wide field imagery and transit photometric surveys.

The $F/12.5$ focus will receive a SBIG ST8XME CCD camera. This will provide for a $3.8' \times 2.5'$ field of view, with a pixel scale of $0.15''$/pix. Magnitude 17 is expected to be reachable at $5\,\sigma$ with a 1 minute exposure. This configuration will be used for polarimetry and photometry.

The E-Tel will have an $F/12.5$ focus, quite similarly to W-Tel, plus an $F/35$ "coudé" focus and should be available early 2014. The $F/12.5$ focus of E-Tel will be either a Cassegrain or Gregory combination. It should be dedicated to spectroscopy. Concerning the "coudé" focus, the focal image will be delivered on a very stable optical bench, at a fixed point, regardless of the position of the astronomical target. On this optical bench, all kind of focal instrumentation will be welcomed, such as a deformable mirror and a wave front sensor for a low-order adaptive optics system. With a SBIG ST8XME CCD camera, this configuration would lead to a $1.3' \times 1'$ field of view, with a pixel scale of $0.05'$/pix. Magnitude 15 should be reachable at $5\,\sigma$ with 1 minute exposure.

2.2 Research Projects

C2PU will offer a list of conventional observational practical lessons to undergraduate and graduate students in order to acquire the fundamental techniques for performing observations and processing data : imagery, photometry, spectroscopy, polarimetry. For this purpose, smaller telescopes (two 14 inches commercial telescopes), both equipped by SBIG ST402 CCD cameras, will be available. But the original purpose of C2PU is to make students participate to research observations in order to feed professional data bases and/or characterize transient events. With this philosophy, C2PU offers a list of research programs for which observations will be performed essentially by supervised master students, but in case of alerts during a non pedagogic period, dedicated staff will be available for an in situ observation and/or remote session assistance.

- **CAPS : Calern Asteroid Polarimetric Survey**. The W-Tel Cassegrain $F/12.5$ focus will be equipped by a CCD polarimeter build at Torino Observatory which will be dedicated to asteroid polarimetry. The CAPS project consists in a survey of asteroids, down to magnitude 18, to study the linear degree of polarization as a function of the phase angle (angle between asteroid-solar axis and asteroid-earth axis). From this analysis, both albedo and diameter of asteroids can be estimated, leading to the determination of crucial lacking physical parameters. CAPS is possible thanks to a collaboration with Torino Observatory, which builds the polarimeter and furnishes the dedicated CCD camera. Near Earth asteroids and space mission targets are under the scope of this survey but systematic studies of main belt and possibly Kuiper belt asteroids will benefit from he data bases of small body physical parameters that will be accessible via the Virtual Observatory.

- **GAIA-FUN : GAIA Follow-Up Network** (`https://www.imcce.fr/gaia-fun-sso/`) is a worldwide network of ground based telescopes that is coordinated by the *Institut de Mécanique Céleste et de Calcul des Ephémérides* (IMCCE) of the *Observatoire de Paris*, whose aim is to follow the alerts of the GAIA probe concerning transient events. GAIA is a space mission of the European Space Agency (ESA) that will be launched in 2013 with the main goal of obtaining micro arcsec precision astrometry of 1 billion stars

in our galaxy. GAIA will also provide a huge amount of "secondary results" in several fields of astronomy. Among them, transient events will be detected but will not be followed by the satellite itself : novae, exoplanetary transits, fast near earth asteroids, comets, collisions... Alerts will be sent to the IMCCE node that will relay the informations over the GAIA-FUN. C2PU belongs to this network and will be well adapted for asteroid recovery and astrometry computation, photometry light curves and spectroscopic characterizations (asteroids, exoplanets, novae and collisions). Depending on the thresholds chosen for the alerts the number of relayed information could reach 600 per day.

- **PISCO : Pupil Interferometry Speckle COronagraph** (`http://userpages.irap.omp.eu/~jprieur/Pisco_e.html`) is a speckle camera that has been designed and built at *Observatoire Midi-Pyrénées* (Prieur et al. 1998). After several years of operation on the 2-meter telescope "Bernard Lyot" at the *Observatoire du Pic du Midi*, PISCO has been transferred at the *Osservatorio Astronomico di Brera*, in Merate (Italy) (Scardia et al. 2004). It has yield eleven articles on astrometric measurement of visual binaries and orbit determinations. PISCO will be mounted on the E-Tel within the framework of an agreement between *Osservatorio Astronomico di Brera* and OCA. This project has been approved and encouraged by the IAU Commission 26 (Double Stars) and will be used not only in the pedagogic framework to introduce speckle interferometry but also for double star studies.

- **TEP2C : Transient Event Photometric Characterization at Calern**. Independently of photometric GAIA alerts, C2PU will be involved in the characterization of photometric events novae photometric follow-up, asteroid occultations, search for optical counterparts of gamma ray bursts, variable stars.

- **EXOTIME : EXOplanet search with the TIming MEthod** (`http://www.na.astro.it/~silvotti/exotime/`) is a long time photometric monitoring of pulsating stars for the detection of exoplanets. Following the example of V391 Peg b (Silvotti et al. 2007), the main goal of this project is to detect planets orbiting evolved pulsating stars such as sub-dwarf B (sdB) stars or white dwarfs (WDs) through the timing method, using the stellar pulsation as a clock. The EXOTIME collaboration is based on a network of ground-based one to four meters class telescopes.

- **QS2C : Quasar Spectroscopic Characterization at Calern**. By the means of a collaboration with University of Liège in Belgium, C2PU will participate to the spectral characterization of the quasars detected by gravitational lensing on the International Liquid Mirror Telescope (*ILMT*: `http://www.aeos.ulg.ac.be/LMT/instruments.php`). It is a 4 meter class telescope project, in which several institutions from different countries are actively involved (Belgium, Canada, Poland, India). The primary mirror of the telescope is a rotating container with highly-reflecting liquid in it (mercury). The surface of the spinning liquid takes the shape of a paraboloid. It will be installed at Devasthal (India) where it will monitor a strip of sky of 0.5 degree of declination down to a limiting magnitude of about 23 in the I band in a single integration. This survey will last for about five years (Poels et al. 2012).

- **Instrumental development**. The "coudé" focus of the E-Tel will deliver the sky light onto a very stable optical bench, regardless of the position of the astronomical target. This configuration is ideal to develop and test a wide range of focal instrumentation (adaptive optics, stellar coronagraphy, aperture interferometry). This telescope can also be seen as a R&D tool both for pedagogic and research purposes.

All these research projects are addressable with a 1 meter class telescope and will provide the students with the opportunity to be in touch with the astrophysics issues underlying the observations and also to participate to the data acquisition and processing. Results will be either immediately exploited or will feed data bases depending on the nature of the observation. The list of research projects is not exhaustive and will be adapted to the forthcoming scientific proposals.

2.3 Test and first lights

The first light of the W-Tel occurred on August the 10^{th}, 2012, with temporary, not optimized equipment (color SBIG ST-4000XCM and B&W SBIG ST-10XME cameras). Figures 1 and 2 show samples of the processed astronomical images obtained this night. The commercial field corrector was a Type 2 Parracor providing an F/3.31 ratio. This configuration was not optimal since a SBIG-STX camera (4096×4096 pixels) with a customly designed 3-lenses Wynne corrector will soon be fabricated and installed as mentioned before. The custom Wynne corrector, under construction at OCA, will provide for a 3 times larger field of view ($40' \times 40'$), with a better

and more uniform wide band coma correction. It is to be reminded that the color CCD used for the images in Figures 1 and 2 lowers the potential resolution due to its built-in Bayers matrix. Moreover, these images have been obtained without any auto-guiding system (to be implemented soon). These sample images (more images at `https://c2pu.oca.eu/`) show both that the Plateau de Calern site is optically and that the telescope promises high performances.

Figure 1 is an image of the well-known Herculis globular cluster M13 taken with the C2PU. The upper-right frame is a zoom on the central part of the main image, and the lower-right frame is the same field from the Hubble Space Telescope.

To assess the photometric quality of this new observation facility, we have followed the transit of exoplanet HAT-P-5b across its V=12 host star, on August 17th, 2012, with the same optical configuration (C2PU E-Tel ; primary focus at F/3.31; commercial type 2 Parracor field corrector, B&W camera SBIG ST-10XME). Each individual frame was obtained with 8 seconds exposure time, on defocused images (FWHM between 2" and 3"). The achieved photometric accuracy is 3 millimagnitude on un-binned data, which appears to be highly promising for the future photometric and polarimetric research projects.

Fig. 1. The globular cluster M13 from the C2PU W-Tel. Upper-right frame : a magnified crop of the center of the cluster. Lower-right frame : the same zone extracted from a HST image.

3 Geophysics

Specific characteristics of Plateau de Caussols make this site an ideal location for the study of some geophysical aspects:

- The Plateau de Caussols is one the biggest slopes of gravitational deformation of the Alps with three collapses
- these collapses affect the whole slope in front of Caussols and involve 160 million m^3 of rocky materials.
- Important perturbations in the morphology are present in the landscape : typical gravitational morpho-structures (steep slopes, inverted steep slopes, rift valleys,...)

The morpho-geological cartography can be coupled to deep geophysical surveys (electrical resistivity tomography) in order to point out correlations between morpho-structures and resistivity anomalies. The "Risk Team" of Laboratory GeoAzur at OCA uses on the Plateau a specific instrumentation that allows long term survey for

Fig. 2. The NGC7331 galaxy from the C2PU W-tel.

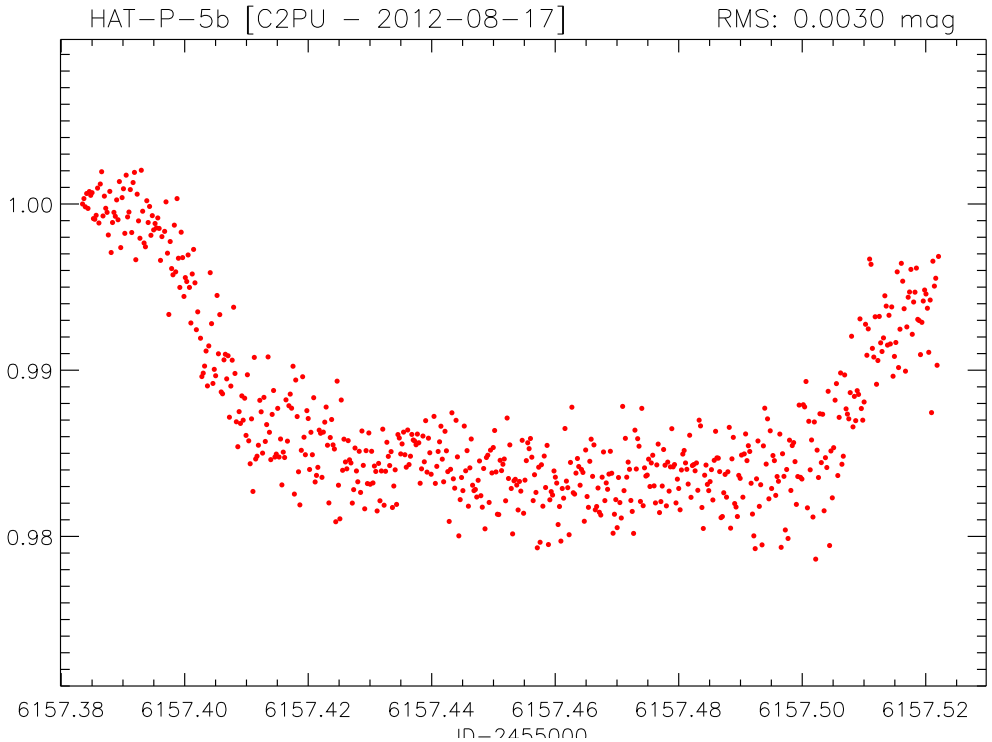

Fig. 3. The light curve of the transiting exoplanet HAT-P-5b, with C2PU W-Tel (August 17$^{\text{th}}$, 2012).

the observations of collapses and long term evolution of electric resistivity

In the framework of a collaboration OCA/IPGS (Institut de Physique du Globe de Strasbourg), a seismological short period instrumentation was installed by the Réseau National de Surveillance Sismique (RENASS)

in 1980 at the Plateau de Calern, as an element of the real-time seismological watching of the Nice region. This site was closed after loyal services in 2011.

In 1994, one of the most ancient broad band seismological stations of from the RLBP (Réseau Large Bande Permanent) was installed at the Plateau de Calern. This station is the premise of the large metropolitan seismological antenne RESIF (REseau SIsmologique Français). From the beginning of 2000, it has been integrated to the VEBSN (Virtual European Broad Band Seismological Network), coordinated by ORFEUS (Observatoires and Research Facilities for European Sismology), whose data is distributed in real time to the scientists for the quick interpretation of the major world-wide seisms and for several studies about terrestrial structures.

From June 2011, this station has been equipped by the CEA (Commissariat à l'Energie Atomique et aux énergies alternatives) with a satellite data transmission to contribute to the French tsunami detection system (`http://www.info-tsunami.fr/`).

A station belonging to the Réseau Accélérométrique Permanent français (RAP) has been associated in 1997 and is mainly devoted to the recording of large magnitude seisms.

Real-time data contribute, within the different French groups concerned, to the detection and quick characterization of the regional seismicity (`http://www.geoazur.net/sismoazur/`) and eventually worldwide.

After a manual verification of the signal, data contributes to the elaboration of the official seismic catalogue of the French territory, that is distributed by the Bureau Central de Sismologie Français (BCSF). These data also contribute to the studies of the seismicity, the seismic risks and also of the deep terrestrial structure.

Data recorded during the last week can be consulted on the site
`http://www.geoazur.net/sismoazur/helicorders.php`.

4 Conclusions

C2PU offers professional class telescopes and a site with many geological interests with an infrastructure that allows complete immersion of students in astrophysical and goephysical experimental works. It offers the possibility to train graduate and undergraduate students to astronomical observation techniques and make them participate to research programs. The remote access of C2PU will open this facilities to many other audiences that will have the opportunity to be introduced to actual research subjects covering a vast field of modern astronomy. Astrophysics and geophysics theoretical lectures, practical data analysis, signal processing, practical and experimental optics lectures will be in situ or remotely given thanks to this original tool proposed to the community.

Authors are grateful to the *Observatoire de la Côte d'Azur* (OCA), the University of Nice Sophia-Antipolis (UNS), the *Collège de France* (CdF), the *Conseil Général des Alpes Maritimes* and the *Conseil Régional Provence Alpes Côte d'Azur*, for their support to the C2PU project. C2PU team want also to thank Anne Deschamps from GéoAzur Laboratory for her fruitful inputs on the geophysics section.

References

Poels, J., Borra, E., Hickson, P., et al. 2012, in IAU Symposium, Vol. 285, IAU Symposium, ed. R. E. M. Griffin, R. J. Hanisch, & R. Seaman, 394–396

Prieur, J.-L., Koechlin, L., André, C., Gallou, G., & Lucuix, C. 1998, Experimental Astronomy, 8, 297

Rabbia, Y., Mekarnia, D., & Gay, J. 1990, in Society of Photo-Optical Instrumentation Engineers (SPIE) Conference Series, Vol. 1341, Society of Photo-Optical Instrumentation Engineers (SPIE) Conference Series, ed. I. J. Spiro, 172–182

Scardia, M., Prieur, J. L., Koechlin, L., et al. 2004, IAU Commission on Double Stars, 153, 2

Silvotti, R., Schuh, S., Janulis, R., et al. 2007, Nature, 449, 189

SF2A 2012
S. Boissier, P. de Laverny, N. Nardetto, R. Samadi, D. Valls-Gabaud and H. Wozniak (eds)

THE FUTURE OF ASTRONOMY PHDS IN FRANCE

S. Boissier[1]

Abstract. This contribution presents a poll undertaken at the beginning of 2012, and addressed to every doctor in astronomy who obtained his/her degree in France. Its goal is to motivate the French astronomical community to think and discuss about what should be the training of PhDs, and what should be its objective. Further discussions and reactions can be posted e.g. on http://docastro.blogspot.fr/. A worrying results from the poll is that the majority of the participants would not encourage a young student to start a thesis in astronomy. The main reasons for this fact may be the high pressure on astronomy positions and the little interest a doctorate has for other careers in France. I suggest we either have to modify our training or reduce the number of thesis starting each year in astronomy.

Keywords: Sociology of Astronomy

1 Introduction and a personal motivation

French permanent astronomers are encouraged to take students under their supervision (enhanced chances of promotions and grants in addition to the obvious human and scientific interest, as well as pressure from pairs: e.g. the astronomy CNRS section[i] encourages students supervision when evaluating career progresses). With various funding schemes coming into existence (ERC, ANR), the number of astronomy-related thesis has increased during the last 10 years or so. However, the number of permanent positions has stayed stable during the same period, leading to an increasing pressure (see Fig. 1). The pressure is even stronger as opportunities in other countries are becoming scarcer and foreigners are attracted by the French positions. As the number of post-doctoral positions in astronomy has also increased (especially via the ANR and ERC schemes), many young doctors stay longer (up to about 10 years, see Fig. 2) on a job market offering less and less opportunities. Clearly, we are training more and more people in astronomy, while many of them will not join the astronomy community in the end. What is the meaning of *formation* in this situation ?

Some astronomers reply that we are performing a "formation par la recherche" (training through research: a thesis would allow to gain useful experience for jobs elsewhere than in academia). However, if in some other countries, being a "doctor" has a meaning in society and is recognized by the private sector, it is felt in France as a handicap as businesses tend to prefer engineers or peopled trained in our "grandes écoles" since the best students are usually drained to them by the french elitist educational system. This is despite the fact that doctors are likely to have useful competences to bring to businesses (Durette et al., 2012). Another "problem" is that most students starting a PhD in astronomy hope to get a position in research (e.g. Seth et al., 2009). Said in another way, students do not share the "formation par la recherche" point of view. They should know their chances of success to end up in research before starting a thesis (and even a master) in astronomy.

Facing this situation, we cannot supervise students without wondering about the interest of long training in astronomy and the number of people that should be trained as astronomers. For this reason, I started with the help of many people (see acknowledgments) a poll to know what has become of french astronomy doctors and how they feel about their current and past experience.

[1] Aix Marseille Université, CNRS, LAM (Laboratoire d'Astrophysique de Marseille) UMR 7326, 13388, Marseille, France
[i] Committee appointed for 4 years in charge of both careers evaluation and hiring at national positions.

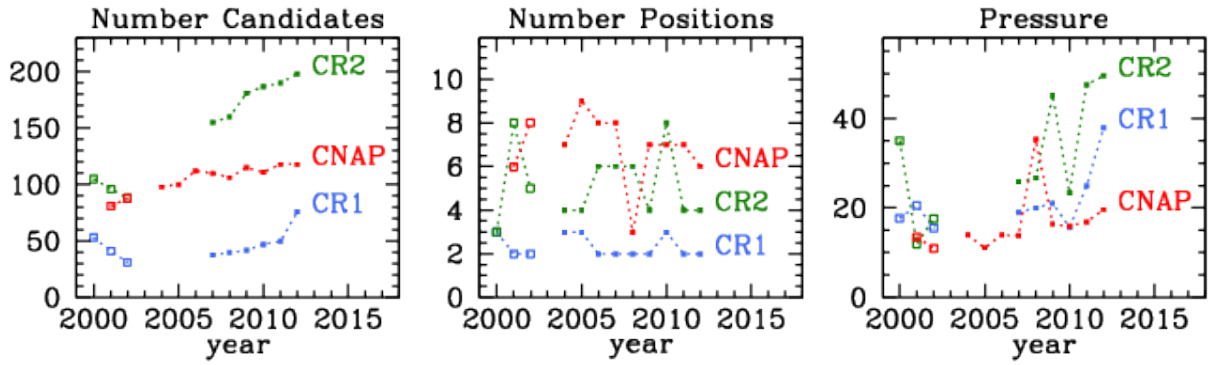

Fig. 1. Evolution of the number of candidates (left); of the number of opened positions at the national level by the CNRS as CR1 and CR2, and by the CNAP (middle); and of the pressure (right). Data compiled by Mederic Boquien (private communication) are shown as filled symbols and by Mamon (2003) as open symbols.

2 Other studies

Before describing this study, I should mention that other people have tackled similar questions in the past. All of these works are not as well known as they should, and I am happy to mention a few initiatives here.

The "Ecole doctorale d'ile de France" (concerning only astronomy, what makes their results especially pertinent to our community) maintains a site with statistics on the becoming of their students (`http://ufe.obspm.fr/rubrique293.html`). According to them, about 60 % of the doctors who got their degree around the year 2000 are in research (40% in France as researchers or engineers, 20% as researchers abroad). These numbers are elevated with respect to the situation in other "Ecoles doctorales[ii]", at least as described by some of the poll participants.

Turning to astronomy laboratories, 50 % of people passing their thesis in the "Institut d'Astrophysique de Paris" (IAP) found a permanent job as a researcher in France or abroad (Gary Mamon, private communication). The "Institut d'Astrophysique Spatiale" (IAS) also has a clear record of the future of their PhD (`https://www.ias.u-psud.fr/website/modules/content_the/index.php?id=9`) showing that about 40 % get a research or IR (engineer in research) permanent position in French public jobs for the period 2001-2005. Their results are *posted* on their web-page. I can only encourage other laboratories to follow this example as this sort of transparency is *asked* by young people, and necessary if we assume what we do.

The present study (and those quoted above) concern thesis defended in France. It is important to take into account the national specificity for such works. For instance, we should take into account the chance to have strong national corps in France (CNRS and CNAP). On the other hand, in e.g. the USA or UK, being a doctor has quite some valor outside academia, what is not as true in France. Other studies may certainly exist but I will quote only a few here. In the USA, Seth et al. (2009) shows that 170 thesis start per year for 60 to 90 permanent jobs in astronomy (35 to 55 percent of astronomy PhDs would get permanent positions) without much temporal evolution (contrary to the French recent increase of the PhDs/jobs ratio). These numbers are confirmed by Metcalfe (2007) who mentions that at best 50% of astronomy PhDs find a faculty position, while the other half is likely to end up in "research and support" positions. In comparison, about 50 thesis started each year in Paris during the last years. It is hard to have complete data, but from what could be found on internet through a quick search, 7 thesis started in Marseilles and 7 more in Toulouse in the last years on average. That's already about 75 thesis per year (certainly a lower limit since I did not count other important laboratories in Strasbourg, Bordeaux, Grenoble, ...) for a total number of jobs each year (including university, CEA, CNRS and CNAP positions) of about 25. The comparison of the French and American numbers seems to indicate better perspectives for young people in the USA. Nevertheless, Seth et al. (2009) make political recommendations, such as *"shifting priorities from early career temporary positions towards more long-term employment will create a more sustainable, equitable, and productive astronomy workforce"*. The French astronomical community should do as much as the American one and get a critical look at the training of astronomy PhDs in France, and

[ii] Administrative part of universities in charge of thesis

their becoming. A good analysis of the hiring situation in France almost 10 years ago was presented in Mamon (2003). To this, should be added the reports from the CNAP and CNRS sections that are made at the end of each mandate. However these concern mostly their own work and we are still missing clear statistics on the rate of success for PhDs in astronomy to get permanent positions. Independent assessment of the situation are too rare, and this paper is an attempt to discuss the situation and open the debate in the French community. Everyone is invited to react, for instance on the "docteurs en astrophysique" (`http://docastro.blogspot.fr/`) blog. Hopefully, this study could also be useful abroad for comparison with foreign policies and situations.

3 Poll description

The poll was opened at this address `http://sondagedocteurastro.wikidot.com` and 200 replies were collected between February and june 2012. It was sent to the SF2A newsletter (1400 addresses), astronomy masters, a French young researcher mailing list, and advertised in a "Doctor in Astronomy" group in Facebook. Many questions were asked to the participants (year of the thesis, subject, job...) especially concerning the utility of their studies in astronomy, and letting open the possibility to send comments. No field was compulsory. While it was opened to every doctors in astronomy who obtained their degree in France, the people who replied defended their thesis mainly between 2000 and 2010 (see Fig. 2). Older doctors may not be so interested in the destiny of their students, did not feel concerned, or are lazier. Many of the results are already available online (`http://sondagedocteurastro.wikidot.com/results`) and I will focus in the next section only on one important question.

4 To be (a doctor) or not to be ?

200 replies are too few to be complete or representative. Nevertheless, I tried to define three populations and analysed their respective replies :

- A) permanent in astronomy,
- B) post-docs,
- C) people who left astronomy.

While their relative numbers are not representative, each of this group is homogeneous enough to allow a comparison. Also, with an incomplete poll, "success rates" are meaningless, thus I will focus on the feelings of the participants (happiness concerning their situation, usefulness of their studies, advice to a student, see the distributions of the answers in Fig. 3) and their commentaries.

Most of the participants are happy about their current situation (we remind that this is not a complete survey). Most have no regrets about having done a thesis (even among those with no permanent positions, or those who left astronomy). This by itself is a nice message: a thesis is in general a good personal experience, whatever happens (except in a few exceptional cases). However, we should not be too happy, as only about 50 % of *permanent* staff would advise a young student to start an astronomy thesis. This number fall to 30 % among those who left astronomy for which on the contrary 50% would not advise a student to start a thesis. Moreover, the percentage of people suggesting to start a thesis decreases with the thesis defense year, even when the study is restricted to permanent staff : the situation is getting worse.

In my opinion, this negative message (that may push good students towards other careers) is directly linked to the increasing pressure on jobs (and thus the increase of the number of thesis defended each year). The comments collected during the study allow us to understand even more why the fraction not advising to start a thesis is so high. They stressed:

- the very bad preparation for a career outside academia. Some of my colleagues may say "we do science, students are here to learn to do science". While I respect this opinion, I do not believe the argument is valid if we teach hordes of students how to do science, while they will not do science in the future. If we want to perform "training through research" with large number of students, then the one among them ending up elsewhere must have gained a useful *formation* in the process. The alternative is of course to train less students.
- the bad connection between academia and the private sector (teachers in astronomy are unaware of the existence of local businesses that may be interested in our training).

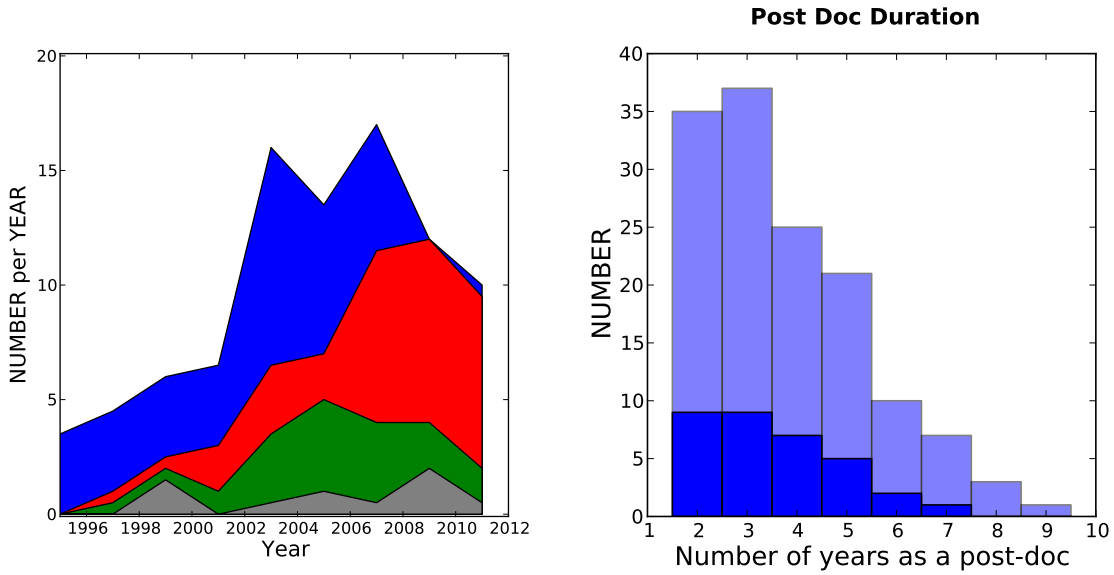

Fig. 2. Left: cumulative distribution of the defense year (smoothed over 2 years) of participants by categories (blue: category A-permanent, red: category B-post-docs, green: category C-out of astronomy, grey:unknown). Right: Number of years spent as a post-doc by the participants (the darker part correspond to women, the lighter part correspond to men).

- the fact that having an astronomy degree is not recognized in the private sector, and simply outside astronomy.
- the length of the the unstable life as a post-doc and its negative effects on personal life.
- the very large role of chance (see also the discussion in Mamon 2003), and especially the advantage for a student to have had a supervisor well-known in the community or participating to hiring committees. I remind that this is not a personal assertion but an opinion frequently stated in the replies to the poll (even from category A participants). If the young doctors have this impression, it might be that it is partly true (*"il n'y a pas de fumée sans feu"*) or that some of the hiring process lack transparency.

5 Some conclusions

As members of the French astronomy community, we should be careful about the situation of young PhDs to prepare a better future for our domain (and make it more attractive to *good* students). At the present, I do not think there is even a coherent vision at the national level of the ensemble of thesis defended in astronomy each year in France. A listing of all of those would be interesting and allow us to follow more easily the becoming of PhDs and their career (in astronomy or elsewhere). May be the SF2A should perform this service for the community.

Concerning the number of PhDs, we need to be logical and face the facts. If we want to increase the number of PhD students well beyond the number of opened jobs in astronomy each years (and this seems to be the mainstream trend according to what I hear from some of my colleagues; and the increasing funding possibilities -e.g. ERC, ANR-), then we have to clearly state that we are developing a "training through research" model. But *saying it* is not *doing it*. In order to adopt this model we *have to* make sure that a PhD in astronomy is a real *formation*, a positive professional experience so that persons spending 3 years of their life on an astronomical project have really earned something useful also outside the small world of research. If we do not make this effort, it means that we are not training people, but just employing cheap manpower (I believe most astronomers have too much honnor to do such a thing). How to do it is another question. We may need to establish stronger bridges with industries, to include in our lectures useful also for non academic careers, or to push institutions to open more easily their doors to PhDs. On the contrary, if we decide to be happy to train our students only to astronomy and that this is not a preparation for anything else (an acceptable proposition), then we have to

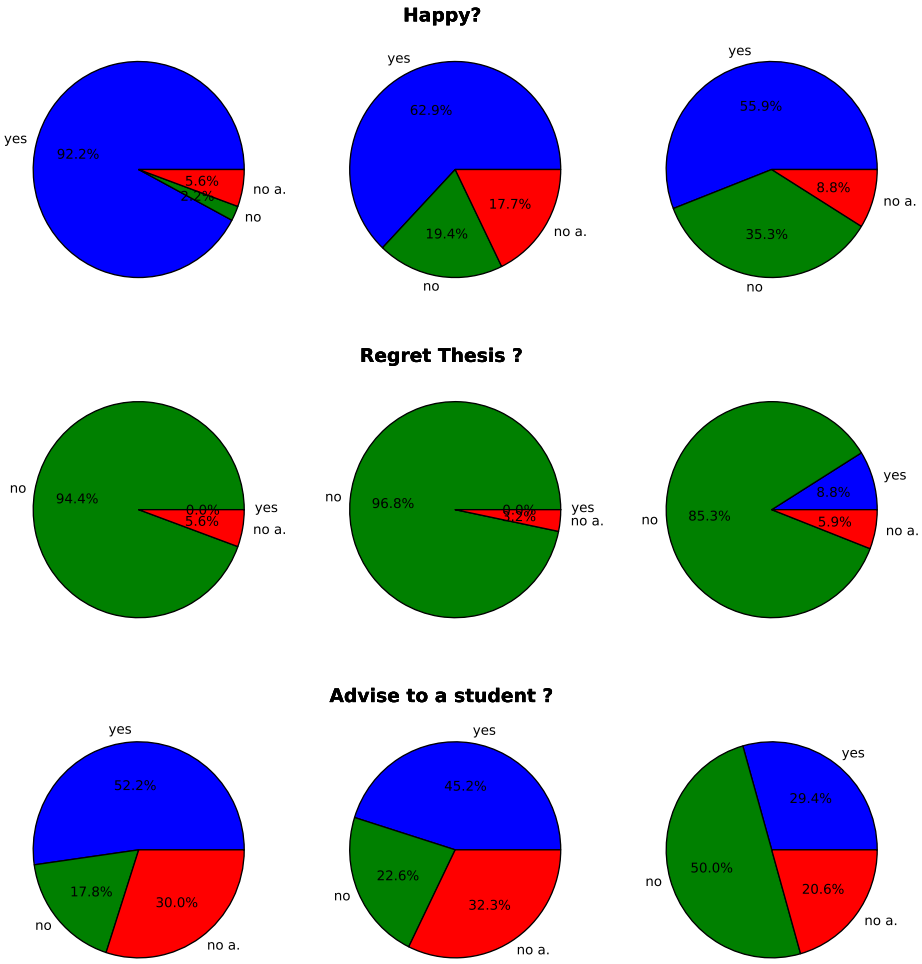

Fig. 3. The top row shows the happiness of the poll participants concerning their current situation, the middle row their reply to the question "do you have regrets about having done a thesis in astronomy ?", the bottom row their reply to the question "would you advice a student to start a thesis in astronomy ?". From left to right : permanent staff, post-docs, people who left astronomy. "no a." means "no answer".

start lowering down the number of thesis in astronomy starting each year. The best way to do so is for each of us not to increase artificially the number of persons trained in astronomy by using funding from e.g. ANR, ERC grants (that did not exist a few years ago). Whatever is our choice (the debate is open), it is our collective responsibility to make one and act in consequences.

I decided to write this proceeding by myself because it includes very personal motivations and conclusions. However, this study would not have existed without the suggestions of S. Vives whom I thank deeply for motivating a wider work that I originally thought of. I also thank many people who encouraged me and made suggestions, citing a few of them: M.H. Aumeunier, M. Boquien, L. Ciesla, O. Cucciati, S. Heinis. I thank the SF2A council who fully supported this idea. I thank finally all the persons who replied to the poll, and especially those who sent to me detailed comments, suggestions, mentions to other studies or even complementary data (especially G. Bonello, M. Boquien, G. Mamon, M. Vincendon).

References

Durette, B., Fournier, M., Lafon, M., 2012, Compétence et employabilité des docteurs, `http://www.competences-docteurs.fr/`

Mamon, G., 2003, The selection of tenured astronomers in France, arxiv:03033552

Metcalfe, T., 2007, The production rate and employment of PH.D. astronomers, arxiv:0712.2820

Seth, A., Agüeros, M., Covey, K., et al. 2009, astro2010: The Astronomy and Astrophysics Decadal Survey, 2010, 51P

SF2A 2012
S. Boissier, P. de Laverny, N. Nardetto, R. Samadi, D. Valls-Gabaud and H. Wozniak (eds)

CONNECTING CLASSROOMS TO THE MILKY WAY

P. Salomé[1,2], A. Radiguet[1,2], B. Albert[1], M. Batrung[1], M. Caillat[1], M. Gheudin[1], Y. Libert[1,2], R. Ferlet[3], A. Maestrini[1,2], A.-L. Melchior[1,2], J.-M. Munier[1] and A. Rudolph[1,2,4]

Abstract. 'Connecting Classrooms to the Milky Way' is a project of the EU-HOU Consortium (Hands-On-Universe, Europe), involving 11 European countries. It is supported by the lifelong Learning Programme of the European Community. The main goal of this project was to set up the first network of small radio-telescopes dedicated to education all around Europe and directly accessible from a simple Web interface. Any classroom connected to Internet via any Web-browser can now remotely control one of the radio-telescopes and observe the HI emission coming from our Galaxy. The interface also provides the users with simple tools to analyse the data: (i) derive the Milky-Way rotation curve and (ii) map the spiral arms HI distribution. A special emphasis has been made to enable the young generation to understand the challenges of these wavelengths, which are currently at the frontline of the new instruments with the development of the ALMA (Atacama Large Millimeter Array) and SKA (Square Kilometer Array) projects.

Keywords: Galaxy: kinematics and dynamics, Miscellaneous: Science Education

1 The EUHOU-MW project

This project is part of the COMENIUS European Commission Lifelong Learning Programmme (2010-2012). It is coordinated by Anne-Laure Melchior and Roger Ferlet (University Pierre et Marie Curie, UPMC), in the framework of the EU-HOU consortium whose objectives are to (i) raise the attractiveness of science education, (ii) participate to the development and modernisation of learning technics in EU schools and (iii) promote scientific methods/knowledge. The EU-HOU consortium has been structured through the 2004-2006 MINERVA project that involved 8 European countries. This first project was then followed by a COMENIUS Programme (2008-2010) involving 14 European partners. The actual project was built in the perspective of the future large radio-submillimeter facilities (ALMA [i] , SKA [ii]). It involves 11 countries and is focused on radio-astronomy. The consortium has delivered educational material (updated versions of the SalsaJ software, exhibition on Radio-Astronomy, pedagogical resources including kinesthetic activities), organised teachers training sessions, and built a radio-telescope network for teachers and schools. In this article, we emphases the activities developed by the coordinator's team at Univ. Pierre & Marie Curie, in France, supported by the European partners for the deployment of a network of radiotelescopes and its dissemination in European schools.

2 Radio-astronomy Network

We will focus here on one aim of *Connecting Classrooms to the Milky Way* that was to develop the first European network of radio-telescopes for education, enabling European schools to explore the Milky Way via the HI emission line with Internet (with a simple web browser). The scientific goals are (i) to derive the Milky-Way rotation curve and to discuss the need of dark matter and (ii) to map the Milky-Way spiral arms structure, enabling to discuss our place in the Universe. In order to do so, we provide the teachers with multilingual

[1] LERMA, UMR8112, Paris Observatory, F-75014 Paris, France
[2] UPMC 4 Place Jussieu, F-75252 Paris
[3] IAP, F-75014 Paris, France, CNRS
[4] Department of Physics and Astronomy, California State Polytechnic University, Pomona, CA, USA
[i] `http://www.almaobservatory.org/`
[ii] `http://www.skatelescope.org/`

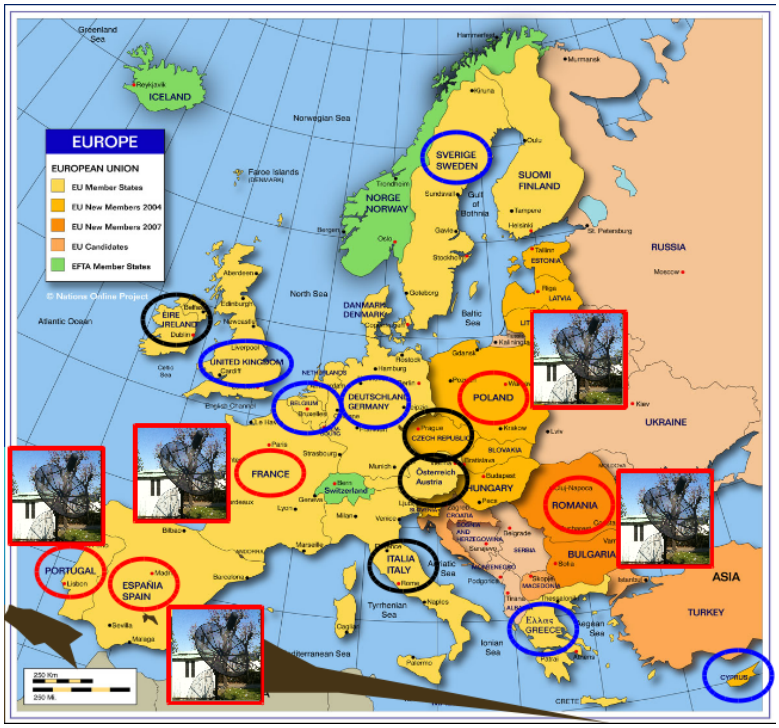

Fig. 1. Network of radio-telescope and countries involved in the present COMENIUS project (red and blue).

tools: a scheduling system to remotely access the five T3m radio-telescopes[iii], archives to retrieve and/or analyse previous observations, and a simulator of observation enabling to perform (off-line) the exercise with high quality data (LAB[iv] survey, Kalberla et al. (2005)). The Internet Control Web page of the EU-HOU-MW radiotelescope network is accessible from the project Web site `http://www.euhou.net/`.

Any teacher can go to this page and register. Once he has open an account (under the control of a local administrator), he can book a free time slot on any antenna of the network. The connection to the *Observer* page (the remote control interface) will be possible during this time slot only. Simple inputs are required: position on the sky, observing frequency, integration time. The interface provides the users with interactive maps in Az/El and Galactic Long/Lat coordinates. A Webcam shows the telescope moving in real time. Once the observations are done, the spectrum is displayed and the user can remove a baseline and/or redo an observation. This spectrum can then be directly retrieved from the *Archive*, where more analysis can be performed. The user can select some peaks in the HI spectra. These peak velocities, together with the Galactic coordinates of the pointed region, can be translated into a rotation velocity and a radius (by simple geometric arguments) and/or into a x/y position in kpc on the face-on Galaxy plot. Those two outputs are directly computed by the interface from the selected peaks and compared to professional data outputs and to some modelling of Galaxy potential wells and spiral arms (see Fig. 2 and 3).

3 The EU-HOU-MW Web Interface

In order to remotely control the antenna, we used the java control system delivered with the antenna and the receiver: `http://www.haystack.mit.edu/edu/undergrad/srt/oldsrt.html`. The EU-HOU interface was designed in javascript, php and python, like a wrapper which uses the original control system commands. The *Account manager*, the *Scheduler*, the analysis tools, the administration tools, the communication protocols have been written by A. Radiguet, the software engineer of the project (Orsay IUT). The telescope outputs are also connected to a SQL database to archive the data and post-process or download them. A central server hosts

[iii] Actually, six antennas are connected. UPMC acquired a slightly smaller antenna for the 2009 International Year of Astronomy, which has been used as a prototype to develop the present network. Both french antennas are on the Paris Observatory campus.

[iv] `http://www.astro.uni-bonn.de/en/download/data/lab-survey/`

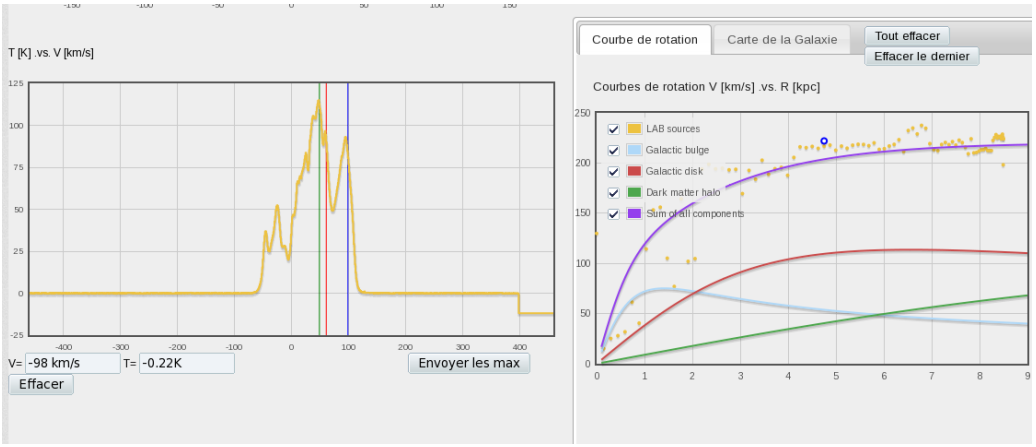

Fig. 2. Milky-Way rotation curve (**right panel**) derived from HI observations (**left panel**) with the EU-HOU-Simulator.

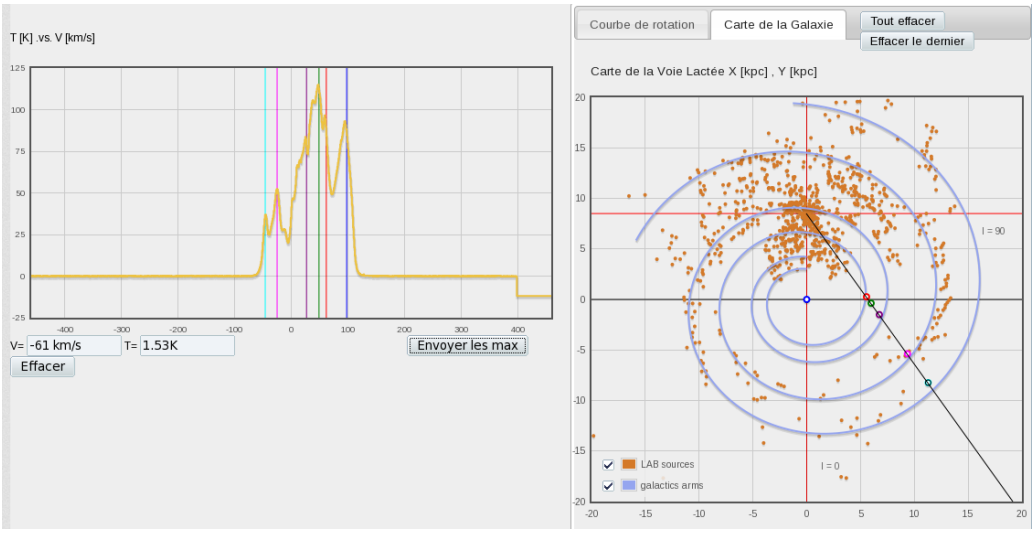

Fig. 3. Milky-Way spiral arms derived from HI observations with the EU-HOU-Simulator.

the *Archive*, the *Scheduler*, the *Account manager*, the homepage and the identification protocols to authorise the connection to each antenna. The *Observer* pages are hosted on local computers directly connected to the antenna in France (Paris), Poland (Cracovia), Portugal (Pampilhosa), Romania (Craiova) and Spain (Madrid).

4 Pedagogical support

Although a lot of efforts have been dedicated to the development of tools easy to use by secondary schools pupils, these tools lack the pedagogical and science explanation that could benefit to the learners. In parallel, Alexander Rudolph, an astronomer and astronomy education researcher, has worked on the pedagogical material which can be proposed to secondary school teachers along with the EU-HOU-MW Web interface. The challenge was two-fold: 1) because the observations of redshift and blueshift are made from the moving platform of the Solar System from within the rotating Galaxy, it is difficult to conceptualize the relative motion of the Sun and observed HI clouds for different quadrants of the Galaxy; and 2) the principles of a rotation curve computation and of the Galactic spiral structure determination are not easy to understand. To address these difficulties, a kinesthetic activity has been developed in order to explain the rotation of the Milky Way, the Galactic System of coordinates, as well as the blue and red-shifts of the velocities along different lines of sight. This activity has been video-taped by the *Centre de Production Multimedia* at UPMC, and is currently translated. After this attractive introduction, the teachers are led through the technical calculations of the rotation curve velocities, now with some intuitive understanding of the mathematics to support their understanding, and are

Fig. 4. Top panel: Homepage of the radio-telescope network remote control interfaces. **Bottom panel:** Account manager.

then introduced to the Web interface and are asked to reproduce the phenomena observed with the kinesthetic activity with the EU-HOU-MW simulator.

An exhibition presenting the radioastronomy and its challenge has also been prepared in the course of the project. It explains some important concepts to understand basics of radioastronomy, such as the wavelengths, cosmic radio-sources and the use of radio-wavelengths in the world surrounding us.

5 Future prospects

The use of this radio-telescopes network can also be extended to introduce University students to radio-astronomy. For this dedicated purpose, we do not use the remote control interface, but the original java software, which is more flexible. Observations like the antenna temperature calibration and pointing on the Sun are then possible. These calibrations can be analysed with a python library we purposely prepared.

Synergies exist with several research institutes, outside the EU-HOU-MW network which have acquired the same kind of small radio-telescope for outreach or education purposes: Bologna (Italy), Madrid (Spain), Hanoi (Vietnam), Green Bank (USA). In France, the Paris Observatory (Nançay) and the Observatoire Midi-Pyrénées (Toulouse) will also install these small radio-telescopes in 2012/2013. Any of these other telescopes can easily be integrated into the EU-HOU-MW antenna network.

The Web interface is now fully operationnal and the concept has been demonstrated. Much more material can be added to the webpages to illustrate the radio-astronomy principles (heterodyn receiver, interferometry, continuum/line observations) as well as the astronomy topics concerned (Galaxies structure and content: dust,

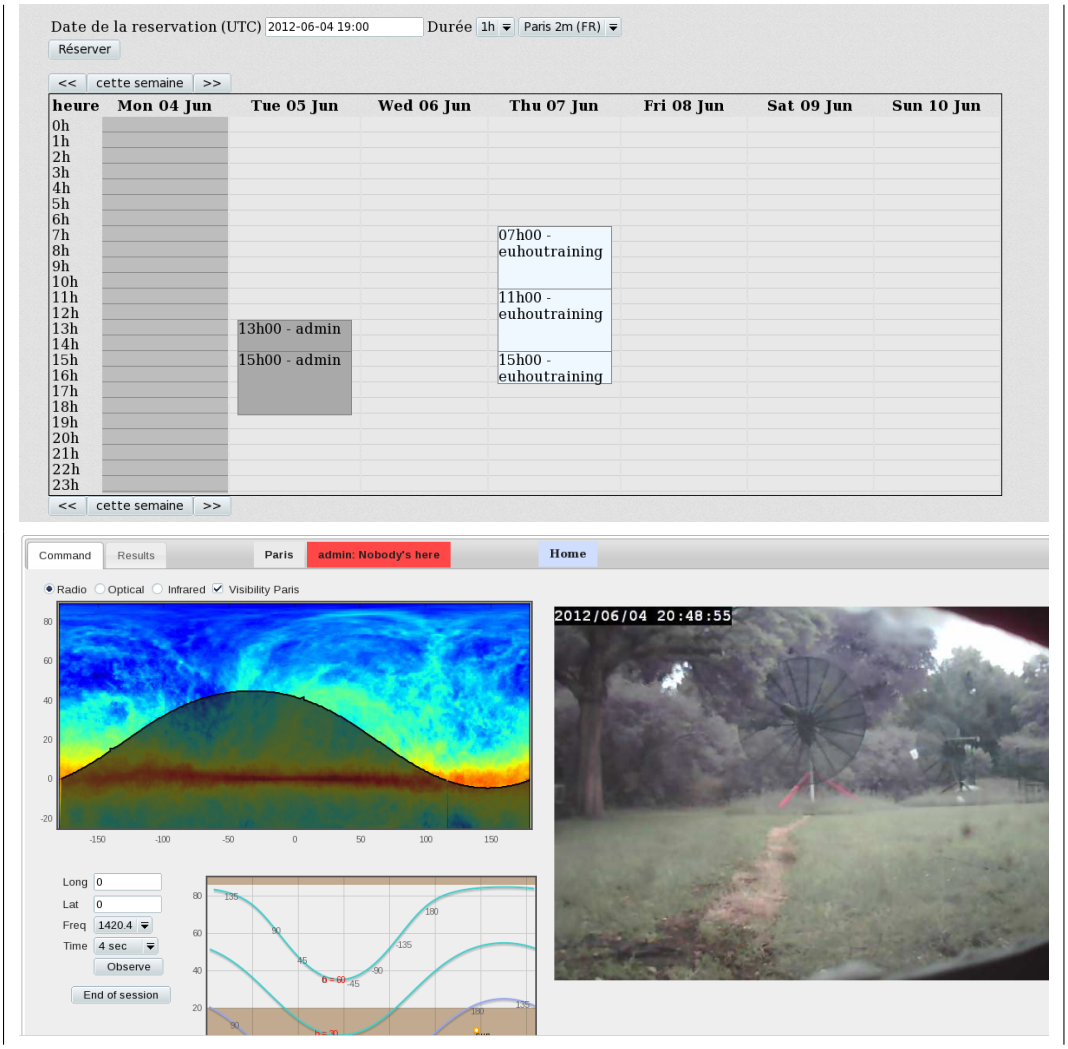

Fig. 5. Top panel: Telescopes booking interface. **Bottom panel:** Remote control interface.

gas, stars, dark matter...). This tool will thus evolve, enabling secondary school pupils to explore different subjects and to get a better idea of the golden age open by the new generation of instruments like ALMA and SKA. Besides showing students what real science can be, the project might inspire some of them for doing science and consider a scientific carrier.

We would like to thank all the partners of this project: France - UPMC ; Spain - Universidad Complutense de Madrid; Portugal - Nuclio Nùcleo Interactivo de Astronomia; Greece - National Observatory of Athens; Cyprus - Lykeio Agiou Ioanni; Poland - Jagiellonian University; Romania - University of Craiova ; Belgium - Royal Observatory of Belgium; United Kingdom - Cardiff University; Sweden - Stockholm House of Science; Germany - Förderverein Astropeiler Stockert e.v.
This project has been funded with support from the European Commission. This publication reflects the views only of the authors, and the Commission cannot be held responsible for any use which may be made of the information contained therein.

References

Kalberla, P.M.W. et al., 2005, A&A, 440, 775

SF2A 2012
S. Boissier, P. de Laverny, N. Nardetto, R. Samadi, D. Valls-Gabaud and H. Wozniak (eds)

TOOLS FOR TEACHING RADIO-ASTRONOMY

P. Salomé[1,2], A. Radiguet[1,2], B. Albert[1], M. Batrung[1], M. Caillat[1], M. Gheudin[1], Y. Libert[1,2], R. Ferlet[3], A. Maestrini[1,2], A.-L. Melchior[1,2], J.-M. Munier[1] and A. Rudolph[3,4]

Abstract. In 2011, the worldwide radiotelescope ALMA (Atacama Large Millimeter Array) has started preliminary operations. Radio-astronomy is thus entering a new golden age, a fantastic opportunity for widening formal and informal educational training and public involvement, for making a science impact on young people. The EU-HOU consortium has developed a small radiotelescope network (6 antenna) spread over Europe and directly accessible from the web via a remote control interface. These antenna are mostly dedicated to high school teachers in the context of the COMENIUS European commission Lifelong Learning Program: "Connecting classrooms to the Milky-Way". However, such small antenna can also be used to teach at University and introduce students to radio-astronomy principles.

Keywords: Galaxy: kinematics and dynamics, Miscellaneous: Science Education

1 What is EU-HOU ?

The present project is part of the COMENIUS European commission Lifelong Learning Program (2010-2012). It is coordinated by Anne-Laure Melchior and Roger Ferlet (University Pierre et Marie Curie, UPMC), in the framework of the EU-HOU consortium (Hands-On Universe - Europe) whose main goals are to (i) raise the attractiveness of science education, (ii) participate to the development and modernisation of learning technics in EU schools and (iii) promote scientific methods/knowledge. The EU-HOU consortium has been structured through the 2004-2006 MINERVA project that involved 8 European countries. This first project was then followed by a COMENIUS program (2008-2010) involving 14 European partners. The actual project was built in the perspective of the future large radio-Submm facilities: ALMA[i] (Atacama Large Millimeter Array), SKA[ii] (Square Kilometer Array). It involves 11 countries and is focused on radio-astronomy. The consortium has delivered education material (updated versions of the SALSA-J software, exhibition on Radio-Astronomy, exercices), organised teachers training sessions, and built a radiotelescope network for teachers and schools.

Fig. 1. Radio-telescopes installed in the Paris Observatory campus.

[1] LERMA, UMR8112, Paris Observatory, F-75014 Paris, France
[2] UPMC 4 Place Jussieu, F-75252 Paris
[3] IAP, F-75014 Paris, France, CNRS
[4] Department of Physics and Astronomy, California State Polytechnic University, Pomona, CA, USA
[i] http://www.almaobservatory.org/
[ii] http://www.skatelescope.org/

2 A radiotelescope for high school students

The main purpose of *Connecting Classrooms to the Milky Way* was to develop the first European network of radio-telescopes for education, enabling European schools to explore the Milky Way via the HI emission line through the Internet (with a simple web browser). The scientific drivers, for setting up such tools, are (i) to derive the Milky-Way rotation curve and to discuss the need of dark matter (ii) to map the Milky-Way spiral arms structure and to discuss our place in the Universe. In order to do so, we provide the teachers with a multilingual (i) scheduling system to access the telescope (ii) remote access to the 5 telescopes (iii) archive to retrieve and/or analyse previous observations (iv) simulator to perform the exercise offline, with higher quality data (from the LAB[iii] (Leiden-Argentina-Bonn Survey) survey (Kalberla et al., 2005).

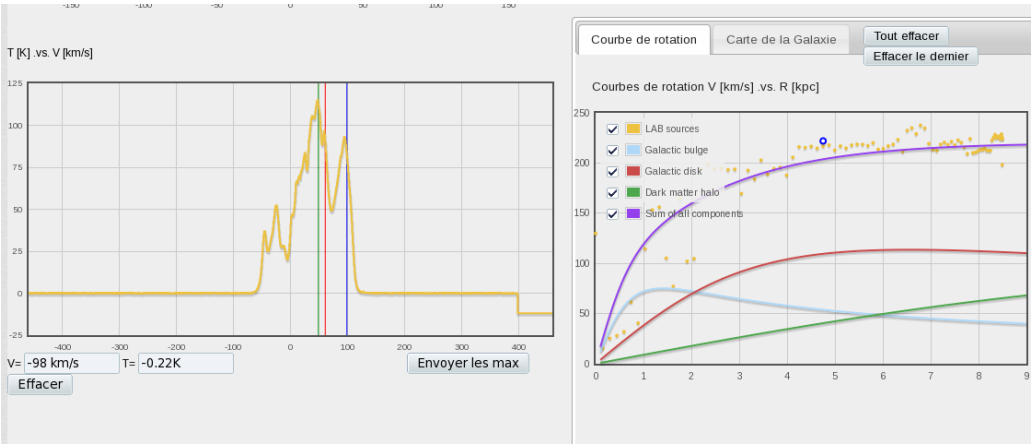

Fig. 2. Milky-Way rotation curve derived from HI observations with the EU-HOU-Simulator.

The website is accessible at `http://euhou.obspm.fr/`. Any teacher can go to this page and register. Once he has open an account (under the control of a local administrator), he can book a free time slot on any antenna of the network. The connection to the Observer page (the remote control interface) will be possible during this time slot only. Simple input are required: position on the sky, observing frequency, integration time. The interface provides the users with interactive maps in Az/El and Galactic Long/Lat coordinates. A web-cam shows the telescope moving in real time. Once the observation is done, the spectrum is displayed and the user can, if he wants, remove a baseline and/or redo an observation. This spectrum can then be directly retrieved from the Archive. There, further analysis can be done. The user can select some peaks in the HI spectra. These peak velocities, together with the galactic coordinates of the pointed region can be translated into a rotation velocity and a radius (by simple geometric arguments) and/or into a x/y position in kpc on the face-on Galaxy plot. Those two outputs are directly computed by the interface from the selected peaks and compared to professional data outputs and to models of galaxy potential wells and spiral arms (see Fig. 1).

3 A radiotelescope for the University

On the Paris Observatory campus, 2 radio-telescopes have been installed. With a diameter of 2.3m and 3m, they have a beam size of 7° and 5.4° respectively. The antenna are equipped with an heterodyn receiver, working at 1.4 GHz around the atomic hydrogen HI frequency. This instrumentation has been bought to CASSICORP `http://www.cassicorp.com/`, an American company, and was designed by the Haystack Observatory `http://www.haystack.mit.edu/edu/undergrad/srt/oldsrt.html`. On top of the main goal of the project, we used the antenna to teach students from the University. In the next subsections, we will describe the different projects we achieved in the last 2-years.

[iii] `http://www.astro.uni-bonn.de/en/download/data/lab-survey/`

Fig. 3. Homepage of the radio-telescope network remote control interfaces.

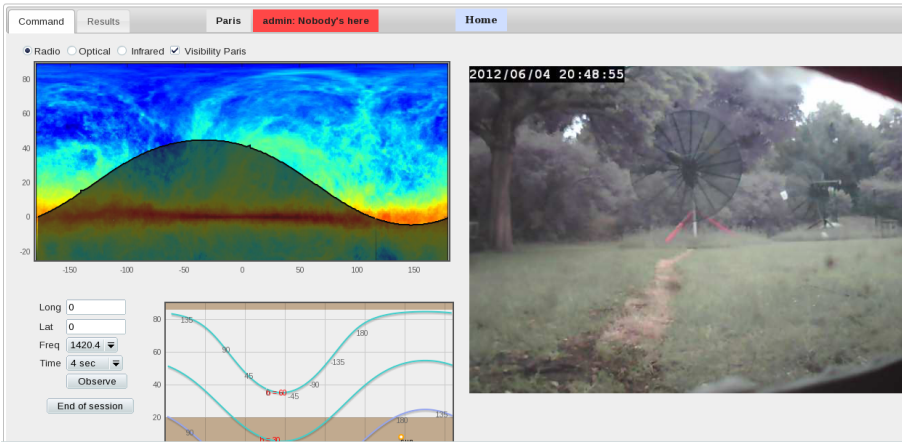

Fig. 4. Remote control interface.

3.1 Student work: One year

A. Radiguet, from the 'Licence Professionnelle - Programmation en environnement réparti' IUT d'Orsay - Paris XI worked during one year within the EU-HOU team (2-3 days/week). As a software engineer, he participated to the design and did all the implementation of the antenna remote control interface, the scheduling/booking system and the account manager. The EU-HOU interface was designed in javascript, php and python, like a wrapper that uses the original control system commands. We started from a list of requirements and produced the final software deliverable. Such a project of evolution/improvement of the radio-telescope was particularly well suited for long-term work with engineering students. In the future, we can think of new projects of this kind: design and build a new receiver/backend, create the associated software...

3.2 Student work: One/two months

It is also possible to use the antenna for teaching astrophysical technics and data analysis methods to students from University. Since 2010, several students have been involved and worked with the antenna at the Paris Observatory. From the UPMC Master 1: *Physique et Applications*, K. Noel spent 1.5 months at LERMA in 2010 (setup of the antenna and the control system, first calibrations and monitoring). From the UPMC Licence 3 *Physique Fondamentale*, C. de Roulhac/A. Bouvet spent one month with us in 2011 (improvement of the data analysis methods and HI mapping of the Milky-Way). Finally, P. Luzi/G. Quinsac spent respectively one and two months at LERMA in 2012 (Milky-Way rotation curve, gravitational potentials and matter distribution inside and outside the Solar ring).

3.3 Student work: Half a day (practical exercises)

A set of three practical exercises of 3 hours each have been prepared and proposed to L2 students in 2012. The first exercise consists in getting familiar with the antenna and its software plus doing an antenna temperature scale calibration and introducing some basics of radio-astronomy. The second one is based on the measurement of pointing offsets and the determination of the beam size. The third one focuses on the observation of HI emission in the Milky-Way: determination of the Milky-Way rotation curve and mapping its spiral arms. A set of python scripts is provided to perform the data reduction and analysis.

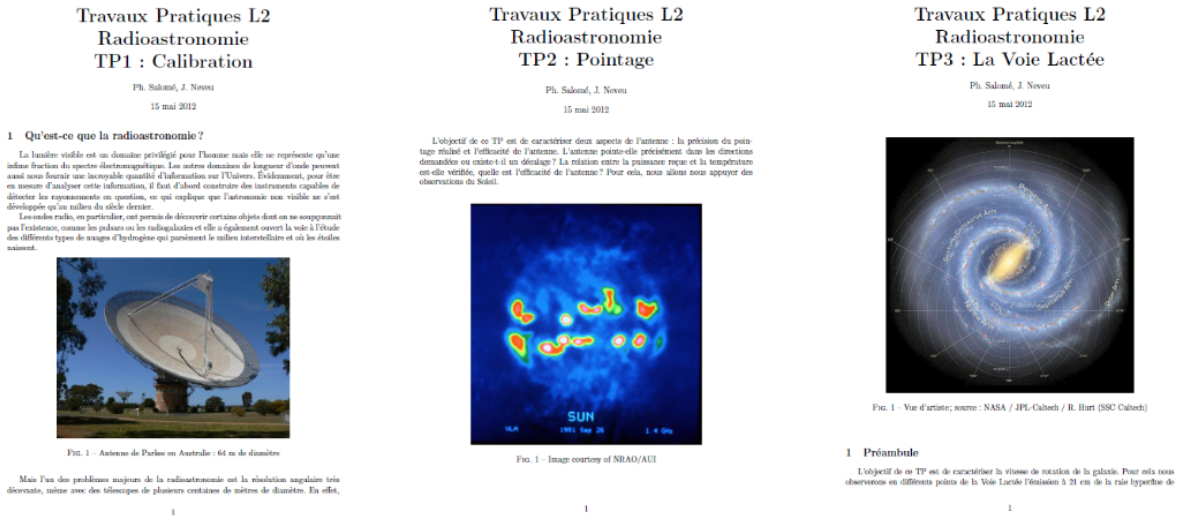

Fig. 5. Practical exercises UPMC L2, 2012

4 Next

The EU-HOU remote control interface will be used in the context of the Paris Observatory teachers tutoring in 2012/2013 *(UFE)*. In order to extend the use of these facilities, short training sessions could be organised to introduce these new tools to astronomer tutor. Observing the Milky-Way in HI could thus be integrated in the activities proposed to teachers as part of the existing *(UFE)* multimedia material.
After the pilot study of 2011/2012 with a small group of students, a practical exercise with the radiotelescope will be included in the LP210 UPMC Licence 2 for all students in 2012/2013. This is just a beginning and obviously, the radiotelescope could also be used by many other students (ie *Ecole Doctorale 127 Astronomie et Astrophysique d'Ile de France*)
The UPMC prepares a place dedicated to practical exercises in astronomy (for observations in the optical and in the radio wavelengths). This station will be installed on the roof of the Paris University building (*75005, Jussieu*). At least one of the two antenna, now hosted by the Paris Observatory, will move to the University campus by 2014/2015. Teaching activities will then be adapted to the new organisation.

We would like to thank all the partners of this project: France - UPMC; Spain - Universidad Complutense in Madrid; Portugal - Nuclio Ncleo Interactivo de Astronomia; Greece - National Observatory of Athens; Cyprus - Lykeio Agiou Ioanni; Poland - Jagiellonian University; Romania - University of Craiova ; Belgium - Royal Observatory of Belgium; United Kingdom - Cardiff University; Sweden - Stockholm House of Science; Germany - Frderverein Astropeiler Stockert e.v.
This project has been funded with support from the European Commission. This publication reflects the views only of the authors, and the Commission cannot be held responsible for any use which may be made of the information contained therein.

References

Kalberla, P.M.W. et al., 2005, A&A, 440, 775

SF2A 2012
S. Boissier, P. de Laverny, N. Nardetto, R. Samadi, D. Valls-Gabaud and H. Wozniak (eds)

TEACHING AND PUBLIC OUTREACH ACTIVITIES AT THE OBSERVATOIRE DE LYON

I. Vauglin[1] and L. Bommersbach[1]

Abstract. The Observatoire de Lyon receives young and large public since more than thirty years. We propose and are largely involved in numerous events destinated to scolar and large publics. We reach an annual average of 3500 pupils as well as 2500 to 6000 (the years with open house days) people with our actions. The public is largely satisfied with our events and the pupils get involved with enthousiasm when they work on "astronomy" projects.

Keywords: Outreach, teaching

1 Introduction

Besides beeing a very active research laboratory, the Observatoire de Lyon posseses a remarquable historical patrimony including interesting astronomical instruments. An equatorial coudé refractor dating from 1880, still in its original state, together with others ancient measuring instruments are classified as "Monuments Historiques".
To take avantage of these resources, a specific department named "Service de Diffusion des Connaissances "(SDC) has been created in 1998 with the charge of organizing various activities for school population and large publics (visits, astronomical evenings, open house days...). The SDC is led by an astronomer, has two scientific mediators(not in a permanent position!) and an assistant in charge of the logistics.
About 3 500 school children and 3 000 to 6 000 visitors are concerned every year by our actions.

2 Setting the scene

Even if the Lyon observatory had a long tradition of contacts with the publics, we put a new dynamics to these activities over the last years seizing several regional and international opportunities.
In 2007, we have set and managed a regional network financially supported by the Région Rhône-Alpes during four years (2007-2010) and federating all the astronomical activities intended for the publics in Rhône-Alpes.
During the International Polar Year (IPY, 2007-2008), we have led an ANR programm for communication and public activities dedicated to polar researches, proposed in collaboration with the Nice, Marseille and Liège observatories.
In 2009, the International Year of Astronomy IYA09, we have developped numerous local and regional actions and we participated to several national and international programms for IYA09.
Moreover, we participate every year to the Journées européennes du Patrimoine, to the week called Fête de la Science and we support classes taking part to regional and national competitions like ExpoSciences, CGénial contest, Rallye des Mathématiques or Olympiades de Physique.

[1] Observatoire de Lyon, UMR 5574, F-69230, Saint-Genis Laval, France, Université Lyon1, Université de Lyon, F-69622, Lyon, France

3 Actions towards pupils

Begining with the worrying established fact that, since several years, there is a disturbing falling off interest among the youngs for scientific studies, we are willing to attract younger generation to mathematics and sciences through the captivating astronomy. Our goal is to lead children to discover the scientific approach, that is: observations, analysis and interpretation. If they are doing this through an astronomical project, they are usually very interested and attracted.
We proposed different actions: The pupils can make a visit of the observatory, an astronomer can go in their classrooms, and we bring a scientific support to teachers leading astronomical projects with their students over the school year. Different actions are proposed also to teachers: in-service training course , workshops one afternoon per month, educational documents (Brémond et al., 2009), demonstration models.
We participate to the national ASTEP program (Accompagnement en Sciences et Technologie à l'Ecole Primaire), we are partner of the departemental programm for secondary schools with "Odyssée Spatiale" in La-Classe.com. For high school pupils, we have built experiments for physic classes: the experiment to measure the light velocity, the Foucault pendulum and the Cavendish balance.
Our actions concern about 3 500 pupils per year from primary to high schools. A dedicated web page presents all these actions on the web site of the Lyon Observatory:
`http://www.http://www-obs.univ-lyon1.fr/spip.php?rubrique126&lang=fr/`

The results of this work with schools are very encouraging: every year several classes with which we are worked award a prize or are winners in different contests and more generally the youngs are very involved in their project, really enthousiastic at the end of the year and proud of what they succeeded to do.

Fig. 1. Left: High school students visiting the lab. **Right:** Classical music concert in the park of the observatory.

4 Large public

Through these actions again, we aim at opening our visitors to the understanding of the scientifical process besides to valorize the advance scientific research made in the laboratory. The large number of people coming to our actions prouve the interest that the public demonstrate to this domain of science.
Our main event are the open house days, every other year, that the general public are waiting for: we have 2500 to 4500 visitors during this week-end. Another success is the Journée européenne du Patrimoine (one day) during which 1200 to 1600 personns are visiting the observatory. We organize also exhibitions with public libraries and museuum, multi-cultural events with theater, orchestra...
With the financial support of SF2A in 2012, we have organized in the park of the observatory two classical music concerts in collaboration with musicians from the Orchestre National de Lyon. They both have been great success.
And to answer to a real demand from the public, we organize one evening per month a visit of the observatory

with observations with the 1m telescope and the ancient Coudé refractor as well as public observations of all astronomical phenomenon such as lunar eclipses, Venus transits, planets' occultations and so on (Merlin et al., 2011).

5 New technology in science mediation

For over a year, the Observatoire de Lyon tries to innovate in scientific mediation. We opened a Twitter account (@obslyon) in May 2011. It has more than 400 followers, we can put forward scientific news from our laboratory but also from our partners and more generally on astronomy. The implementation of a tool like Twitter in a research institution requires to define precisely an editorial and a policy of communication and interaction.
The moments of exchanges are uninterrupted via Twitter. Every day we are asked through this media about questions related to our disciplines, we must answer the questions and breed the desire to visit the lab (at open days or observation evenings). Twitter opens new possibilities in the field of mediation and scientific communication, emphasizing horizontal interactions rather than top-down relations.
In addition, we acquired a touchpad late 2011, which allows: first, to have with us a portable and lightweight device at conferences outside the laboratory. Second, to use the numerous applications of sky charts. These applications allow touchpad, thanks to the 10-inch screen to show in real time what the public has above his head. Late, the last and probably the most innovative, is to offer substantially improved visits of Observatoire de Lyon. With this tool, we can illustrate our talks with pictures and videos of sky objects or instruments developed at the Observatory.
Scientific mediation in astronomy is at a turning point for us to make the right choices in the tools, by remaining close from scientific facts.

6 Conclusions

The developpement of our activities of public outreach have been establish in close collaboration with :
- the CNRS DR7 communication service for which the observatory is a reference laboratory and with which we are working on a project to catch the 15-25 years-old public,
- the Lyon1 University communication service which recognize our know-how in science diffusion to the public, specifically to reach the high school pupils. Although being a rather small laboratory in the university, we are doing 80% of the outreach of all the Lyon1 university.
- the Rectorat of Lyon which also recognize our expertise and awarded us a teacher position "professeur-relais" to help us in the relations with the teachers'world and to adapt as well as possible our actions to the needs of the teaching profession.

All these actions are very time-consuming but our results are really encouraging: the public is always very pleased with their visits and the teachers are astonished by the enthousiasm and involvement of the class in astronomical projects. And we are not able to answer to all the demands. So, our experiments prove that the young generation can be very much interested with maths and physics tackled with the attractive aspect of astronomy.
These actions towards pupils can be driven thanks to the contribution of several researchers and engineers of the lab and all the public events are made possible thanks to the large involvement of the complete staff of the Observatoire de Lyon. But we are worried not having any scientific mediator permanent position in the SDC, who is however compulsory to maintain these public outreach activities over the time.

References

Brémond, A., Vauglin, I., Wernli, E., Paturel, G., 2009, Galilée 1609 - 2009 Observations astronomiques, ISBN - 2-908288-09-5

Merlin, P., Adam, G., Brémond, A., Bommersbach, L., Sibille, F., Vauglin, I., 2011, 2012 21 décembre, un solstice maya, ISBN 978-2-35916-021-5

Session 19

SKA-LOFAR

SF2A 2012
S. Boissier, P. de Laverny, N. Nardetto, R. Samadi, D. Valls-Gabaud and H. Wozniak (eds)

SIMULATED HISTORIES OF REIONIZATION WITH MERGER TREE OF HII REGIONS

J. Chardin[1] and D. Aubert[1]

Abstract. We describe a new methodology to analyze the reionization process in numerical simulations: The evolution of the reionization is investigated by focusing on the merger histories of individual HII regions. From the merger tree of ionized patches, one can track the individual evolution of the regions such as e.g. their size, or investigate the properties of the percolation process by looking at the formation rate, the frequency of mergers and the number of individual HII regions involved in the mergers. By applying this technique to cosmological simulations with radiative transfer, we show how this methodology is a good candidate to quantify the impact of the star formation adopted on the history of the reionization. As an application we show how different models of sources result in different evolutions and geometry of the reionization even though they produce e.g. similar ionized fraction or optical depth.

Keywords: Reionization, HII regions , first stars, Methods: numerical

1 Introduction

The reionization of the Universe occurred between $z \sim 20$ and $z \sim 6$. During this period the first generation of ionizing stars created a multitude of HII regions. Therefore a challenge was to simulate the reionization process numerically (see Trac & Gnedin 2009 for a complete review of these models). In this context, multiple approach can be overtaken in order to investigate the reionization in numerical simulation. Usually the time sequence of the process is explored by focusing on global quantities such as the evolution of the averaged ionized fraction or the optical depth evolution (Iliev et al. 2006 and Aubert & Teyssier 2010 for example).

We propose here to present an alternative method that allows us to see the reionization through the evolution of the HII regions thanks to a merger tree. Such a merger tree enables us to follow the evolution of the individual HII regions properties and then leads to a 'local' perspective with multiple histories of reionization instead of one 'general' scenario with the quantities commonly used to analyze the simulations.

We apply here this methodology to three simulations of reionization. In each of them we vary the prescription to generate the ionizing sources. We thus aim to show in what the merger tree approach is a good estimator to quantify the differences induced by the ionizing source models in the related histories of reionization.

2 Methodology

2.1 friend-of-friend algorithm

Firstly we need to identify the individual HII regions in each snapshots of the simulation. We have assumed that a cell of the grid is ionized if its ionization fraction $x \geq 0.5$. We then explore the box and when we encounter a ionized cell we allocate to it an identification number corresponding to the ionized region being tested. Then, the *friend-of-friend* algorithm proceeds by allocating to the ionized nearest neighbors of this cell the identification number of the HII regions being explored. We are therefore able to separate all the ionized regions and to keep track of each of them with the identification number.

[1] Observatoire Astronomique de Strasbourg, Université de Strasbourg, CNRS UMR 7550, 11 rue de l'Université, F-67000 Strasbourg, France

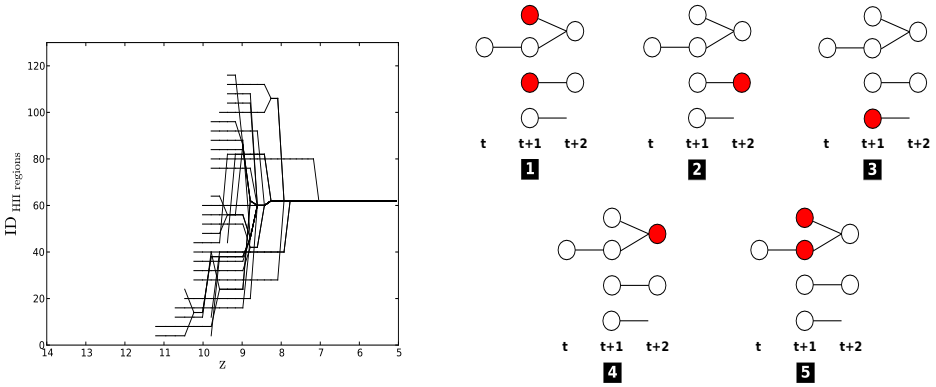

(a) (b)

Fig. 1. Left: An illustration of the merger tree of HII regions. Each black line represents an ID evolution with the redshift for a distinct HII region. For clarity, we represent here only the ID evolution for 30 regions. **Right:** representation of the typical properties investigated with the merger tree. In each diagram, red items symbolize the kind of properties that we follow. 1: the number of new HII regions between two snapshots, 2: the number of growing ionized regions, 3: the number of HII regions which recombine, 4: the number of HII regions resulting from mergers and, 5: the number of parents involved for an HII region resulting from mergers.

Table 1. Summary of the simulations properties.

Model name	Box size	Source type	Emissivity
Boosted Star	200 Mpc/h	Stellar particles	Converged number of photons at each instant (Decreasing emissivity with time)
Star	200 Mpc/h	Stellar particles	Converged number of photons at $z \sim 6$ (Constant emissivity with time)
Halo	200 Mpc/h	DM halo	Proportional to halo masses

2.2 Merger tree

Secondly we can build the merger tree itself in order to follow with time the evolution of the properties of the HII regions. We simply proceed by following the evolution of the identification numbers of the HII regions allocated during the identification step. In practice, we extract where are located the cells of an HII region at time t and look at the identification number that they received at time $t+1$. We then link the two identification number between the two snapshots. We repeat this process for all the HII regions and between all the snapshots of the simulation.

Left panel (a) of Fig. 1 shows a representation of the merger tree for 30 regions. The right panel (b) shows the typical properties that can be investigated with the merger tree.

2.3 simulations

We propose in this work to apply the merger tree methodology on three simulations of cosmic reionization to compare the impact of three different ionizing source models on the observed reionization history. We performed two simulation with stellar particles generated with the RAMSES code (Teyssier 2002). These two models are based on the same sources maps and only differ in regard to the adopted emissivity law with time for the sources. We also performed a third model where the dark matter halos extracted from the density fields are assumed as ionizing sources with an emissivity proportional to the halo masses. In all cases the radiative transfer is done with the ATON code (Aubert & Teyssier 2008). The simulations properties of each model are reported in Table 1.

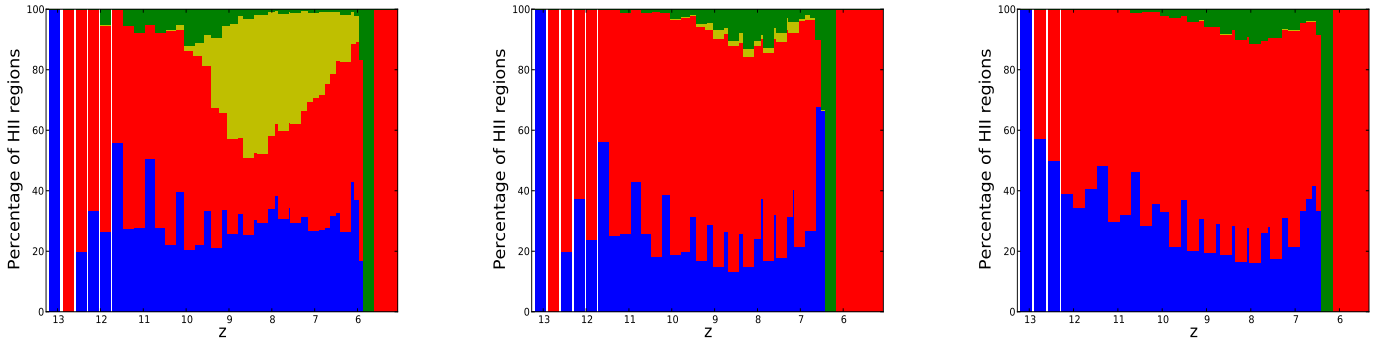

Fig. 2. Evolution of the proportion of each kind of HII regions as a function of redshift for the three models of ionizing sources. The colors stands the new HII regions (blue), the expanding regions (red), the regions that will recombine (yellow) and, the regions resulting from mergers (green). The black vertical line shows the peak of the absolute number of HII regions: z_{peak}.

3 Results

3.1 Number of HII regions

Fig. 2 shows the evolution of the relative proportion of each kind of HII regions as a function of redshift. The Star and Halo models present a significant proportion of regions resulting from merger around a redshift of $z \sim 8$. On the other hand, this period where a significant population of regions resulting from mergers is detected happens earlier in the Boosted Star model $9 \leq z \leq 12$. Early large regions, that are created in early reionization due to the greater correction in the photons emissivity at high redshift, merge quickly in this model and would lead to a main region that then drive the reionization process. Conversely the HII regions in the Star and Halo models are smaller in early reionization and the individual growth process of HII region can be tracked during a longer period before the *overlap period*.

On the other hand the Star model presents few recombination episodes from $z \sim 10$ while the Halo model presents no recombining regions detected. Alternately the Boosted Star model shows a significant fraction of regions that recombine from $z \sim 10$. In this last model these regions are the result of the dislocation of the early large HII regions that can not be sustained because the renewal rate of sources inside these regions, combined to their decreasing emissivities, is not powerful enough. In the Star model the emissivity of sources is constant during the whole simulation. Thus, we find less recombining regions than in the Boosted Star model because recombinations only occur inside pre-existing regions where the renewal rate of sources is not sufficient. Finally the Halo model shows no recombinations because the sources are more numerous than in both other models and have no finite lifetime. Thus the regions have always smaller sizes and are always sustained compared to both other models.

3.2 Sizes of HII regions

Fig. 3 shows the evolution of the radius distribution for the different kinds of HII regions with redshift according to the related color code. The black solid line presents the evolution of the average radius for the detected regions and the black dashed line presents the evolution of the single last region detected when the reionization is achieved. With the help of the merger tree we follow back in time this region and, each time, we calculate the radius of its main progenitor.

First, wee find that every kind of regions occupy a dedicated range of radius in the distribution in every model. The new regions occupy the bottom of the distribution while the regions resulting from mergers are in the top and the expanding ones in the middle of the distribution. We can note that the range of radii covered by a distinct type of region eventually overlap with the distribution of the other kinds of regions. This reflects the fact that the time sampling of the simulation allows us to detect regions with same radii but belonging to different kinds of regions.

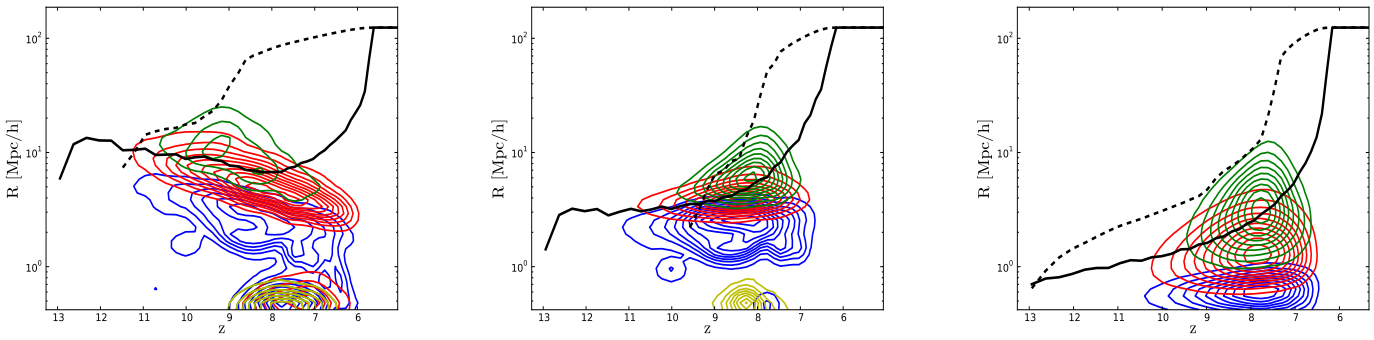

Fig. 3. Evolution of the radius distribution of each kind of HII regions as a function of redshift for the three models of ionizing source formation. The colors stands the new HII regions (blue), the expanding regions (red), the regions that will recombine (yellow) and, the regions resulting from mergers (green).

Second, we find in every models, that the evolution of the radius distribution traces the underlying law of evolution of the source emissivities. Thus in the Star model we see an average constant radius for the HII region, at least during the pre-overlap period, that traces the constant boost emissivity of ionizing sources. The Boosted Star model shows a decreasing gradient for the radii of HII regions that typically reflects the decreasing emissivity of ionizing sources as reionization progresses. Finally the Halo model presents the largest ranges of radii covered by each type of regions which is representative of the underlying range of halo masses that dictates the emissivity law of ionizing sources in this case.

As expected before, we see from $z \sim 9$ that the recombining regions are the smallest regions in the distribution in the Boosted Star and the Star model. This comfort us to say that these regions are small regions resulting from the dislocation of early large regions because they are detected as small patches around large HII regions in fragmentation.

Finally we find the emergence of a single main region in size in every models followed with the black dashed line. This region appears at first in the Boosted Star model at $z \sim 9$ and would be typically the result of the rapid mergers of early large HII regions. The moment of emergence of this region is delayed in the Star model at $z \sim 8$ and at $z \sim 7.5$ in the Halo model because the region are smaller and their individual growing step can be tracked much longer than in the Boosted Star model.

3.3 Merger of HII regions

Fig. 4 shows the evolution of the distribution of the number of parents for HII regions resulting from mergers. Again, we represent the evolution of the average number of parents (solid green line) and the evolution of the number of parents of the main region in size (green dashed line).

First, we find, in every models, that the process of mergers between the HII regions occurs in a binary-tertiary manner as seen with the peak at 2-3 in the distributions during the whole simulated period. This tells us that the time sampling of the simulations allows us to detect the individual mergers.

Second, in all models, we find the emergence of a region that concentrates the mergers with a greater number of parents in the distributions. This region corresponds each time to the main region in size detected before. Indeed, the evolution of the number of parents of this main region in size matches the evolution of the number of parents of this region that concentrates the mergers in the distributions.

This region appears, as already seen before, at first in the Boosted Star model at $z \sim 9$, then in the Star model at $z \sim 8$ and finally in the Halo model at $z \sim 7.5$. The Star model shows few regions, except the main regions, that can reach a number of parents greater than 10 while the distribution in the Halo model is much smoother with a significant proportion of regions that can reach this number. In other words, the Halo model can track much longer the individual merger histories of multiple regions at the expense of a single region that impose its domination by phagocytising the others. The Boosted model finally shows only the main region that can reach a number of parents greater than 10. This is thus definitely in this model where the reionization is

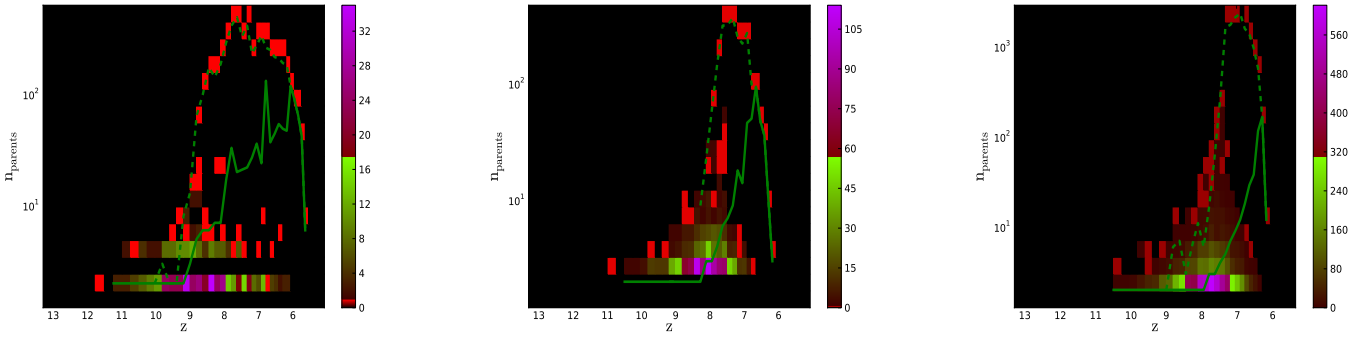

Fig. 4. Distribution of the number of parents for the HII regions resulting from merger as a function of redshift for the three kinds of ionizing sources. We show the average number of parents (solid green line) and the evolution of the number of parents of the main region in size (green dashed line).

driven by a single region that concentrates the most the mergers. This is finally the model the least able to track the individual merger episodes during a longer period of time and thus the least able to follow the "local" reionization.

4 Conclusions

We have developed a new technique to analyze simulations of cosmic reionization. By constructing a merger tree of HII regions and applying this measuring probe to three simulations, we have shown how we can quantify the impact of the variation of the ionizing source models on the related histories of reionization (see Chardin et al. 2012 for a more quantitative and detailed work on this topic). We have demonstrated that a semi-analytic prescription for the ionizing sources based on dark matter halos is the most able to track the 'local' histories of reionization. We have also shown that we can match a similar history with the Star model that use stellar particles as ionizing sources with a constant emissivity during the whole experiment. On the other hand the Boosted Star model, that uses the same source maps as the Star model but with a different emissivity evolution for the sources, presents a reionization history that sensibly differ from both other models. This model presents an early large ionized region that manages the reionization merger history at the expense of the tracking of 'local' evolutions. We finally plan in the future to apply repetitively this technique to study the impact of the inputs in simulations of reionization.

We want to thank B.Semelin, P Ocvirk, R. Teyssier and H. Wozniak for comments and discussion. This work is supported by the LIDAU ANR.

References

Aubert, D. & Teyssier, R. 2008, MNRAS, 387, 295
Aubert, D. & Teyssier, R. 2010, ApJ, 724, 244
Chardin, J., Aubert, D., & Ocvirk, P. 2012, ArXiv e-prints (1210.1445)
Iliev, I. T., Mellema, G., Pen, U., et al. 2006, MNRAS, 369, 1625
Teyssier, R. 2002, A&A, 385, 337
Trac, H. & Gnedin, N. Y. 2009, ArXiv e-prints (astro-ph/0906.4348)

SF2A 2012
S. Boissier, P. de Laverny, N. Nardetto, R. Samadi, D. Valls-Gabaud and H. Wozniak (eds)

FIRST LOFAR RESULTS ON GALAXY CLUSTERS

C. Ferrari[1], I. van Bemmel[2], A. Bonafede[3,4], L. Bîrzan[5], M. Brüggen[3,4], G. Brunetti[6], R. Cassano[6], J. Conway[7], F. De Gasperin[3], G. Heald[2], N. Jackson[8], G. Macario[1], J. McKean[2], A. R. Offringa[9], E. Orrù[2,10], R. Pizzo[2], D. A. Rafferty[5], H. J. A. Röttgering[5], A. Shulevski[11], C. Tasse[12], S. van der Tol[5], R. J. van Weeren[5,2,13], M. Wise[2,14], J. E. van Zwieten[2] and the LOFAR collaboration

Abstract. Deep radio observations of galaxy clusters have revealed the existence of diffuse radio sources related to the presence of relativistic electrons and weak magnetic fields in the intracluster volume. The role played by this non-thermal intracluster component on the thermodynamical evolution of galaxy clusters is debated, with important implications for cosmological and astrophysical studies of the largest gravitationally bound structures of the Universe.

The low surface brightness and steep spectra of diffuse cluster radio sources make them more easily detectable at low-frequencies. LOFAR is the first instrument able to detect diffuse radio emission in hundreds of massive galaxy clusters up to their formation epoch ($z \sim 1$). We present the first observations of clusters imaged by LOFAR and the huge perspectives opened by this instrument for non-thermal cluster studies.

Keywords: galaxies: clusters: general, telescopes, radio continuum: general

1 Introduction

Galaxy clusters are both powerful cosmological tools and unique astrophysical laboratories to study the evolution and interaction processes of baryons along the history of the universe (see e.g. Voit 2005, and references therein). Number counts of clusters as a function of mass and redshift can give important constraints on cosmological parameters (e.g. Borgani & Guzzo 2001; Vikhlinin et al. 2009). We firstly need to be able to identify clusters – through the multi-wavelength emission related to their different components or through the gravitational lensing effect – and to measure their redshift. And of course we need to be able to estimate their mass from observable quantities (e.g. X-ray luminosity; optical richness; velocity dispersion of cluster members; temperature and density profiles of the thermal intracluster medium; ...). For this, a detailed characterization of the complex gravitational and non-gravitational physical processes acting on galaxy clusters is essential (e.g. Böhringer & Werner 2010).

[1] Laboratoire Lagrange, UMR 7293, Université de Nice Sophia-Antipolis, CNRS, Observatoire de la Côte d'Azur, 06300 Nice, France
[2] ASTRON, Postbus 2, 7990 AA Dwingeloo, The Netherlands
[3] Hamburger Sternwarte, Universität Hamburg, Gojenbergsweg 112 21029 Hamburg, Germany
[4] Jacobs University Bremen, Campus Ring 1, 28759, Bremen, Germany
[5] Leiden Observatory, Leiden University, PO Box 9513, 2300 RA, Leiden, The Netherlands
[6] INAF/Istituto di Radioastronomia, via Gobetti 101, 40129 Bologna, Italy
[7] Onsala Space Observatory, Dept. of Earth and Space Sciences, Chalmers University of Technology, 43992 Onsala, Sweden
[8] Jodrell Bank Center for Astrophysics, School of Physics and Astronomy, The University of Manchester, Manchester M13 9PL, UK
[9] RSAA, The ANU Mt Stromlo Observatory, Australia
[10] Department of Astrophysics/IMAPP, Radboud University Nijmegen, PO Box 9010, 6500 GL Nijmegen, The Netherlands
[11] Kapteyn Astronomical Institute, PO Box 800, 9700 AV Groningen, The Netherlands
[12] GEPI, Observatoire de Paris-Meudon, 5 place Jules Janssen, 92190, Meudon, France
[13] Harvard-Smithsonian Center for Astrophysics, 60 Garden Street, Cambridge, MA 02138, USA
[14] Astronomical Institute "Anton Pannekoek", University of Amsterdam, Postbus 94249, 1090 GE Amsterdam, The Netherlands

In the last years, much interest has been paid to the influence of the non-thermal component of the intracluster medium on the thermo-dynamical evolution, heating transport processes and mass determination of galaxy clusters (e.g. Parrish et al. 2009; Laganá et al. 2010). The existence of relativistic electrons and magnetic fields in the volume in between cluster galaxies has been pointed out by radio observations of diffuse synchrotron sources (see e.g. Feretti et al. 2012, for a recent review). Mpc-scale cluster radio sources are generally divided in "halos" and "relics" depending on their position in the cluster, morphology, polarization properties (Ferrari et al. 2008). The left panel of Fig. 1 shows the radio contours overlaid on the X-ray map of one of the most studied nearby galaxy clusters, Abell 2256 (A 2256 in the following). This system hosts both a bright and elongated radio relic in its North-West external region and a central, very low-surface brightness radio halo. The morphology of this latter source is very similar to the X-ray emission of the cluster, which is related to the thermal intracluster component.

A detailed understanding of the origin of the intracluster non-thermal component is still missing (e.g. Dolag et al. 2008; Brunetti & Lazarian 2011). Theoretical models need to be compared to statistical samples of clusters emitting at radio wavelengths, while only a few tens of radio relics and halos are known up to now (Feretti et al. 2012; Nuza et al. 2012). Diffuse intracluster radio sources are generally characterized by steep synchrotron spectra ($\alpha \geq -1$, $S_\nu \propto \nu^\alpha$). This, together with their low-surface brightness and the possible spectral steepening at high radio frequencies due to electron aging, make them difficult to be imaged in the GHz regime and more easily detectable at the long wavelengths observed by LOFAR. This instrument is therefore expected to be the first to allow the detection of diffuse radio emission in hundreds of massive galaxy clusters up to z $\sim$ 1 (Cassano et al. 2010).

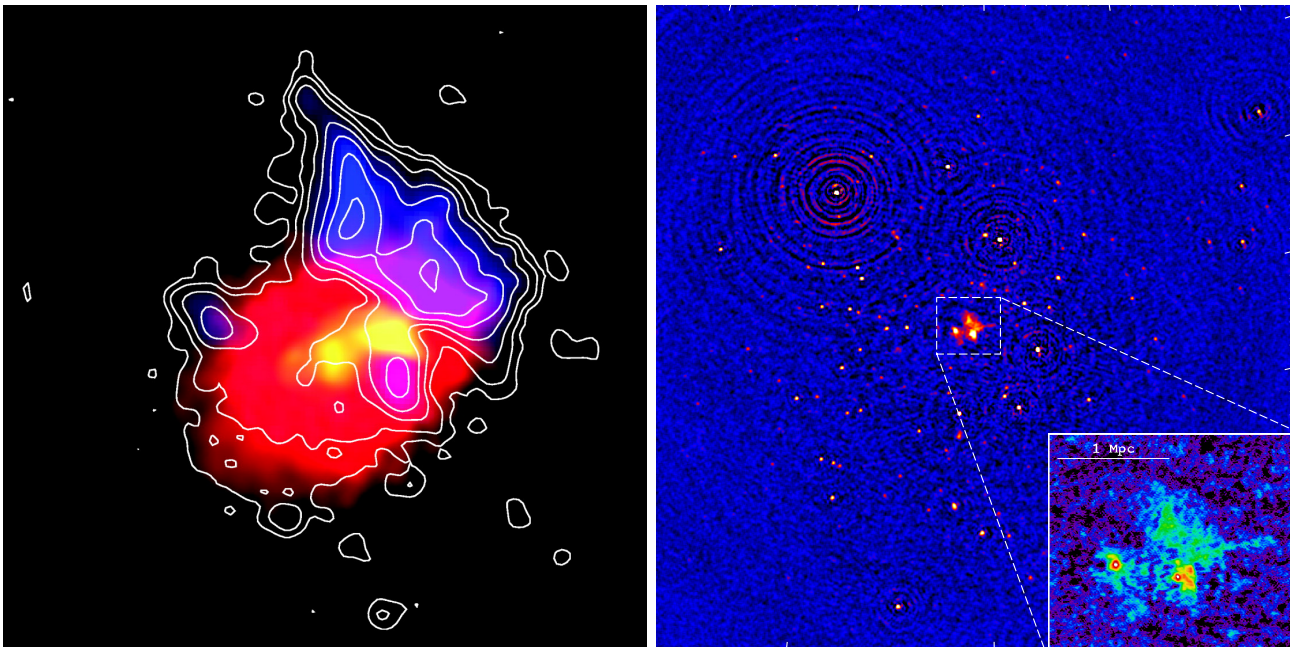

Fig. 1. Radio observations of A 2256 at ≈1400 MHz (white contours in the left panel; VLA observations) and at ≈ 60 MHz (color maps on the right; LOFAR observations). On the left, radio contours are overlaid on the Chandra X-ray image of A 2256. The right image shows the low-resolution ($80'' \times 80''$) large-scale LOFAR map of the cluster, with a zoom in its central field shown at higher resolution ($22'' \times 26''$) in the inset. Figures are extracted from Clarke & Ensslin (2006) and van Weeren et al. (2012).

2 First LOFAR observations of galaxy clusters

Thanks to its large field of view (FoV), frequency coverage and high sensitivity, LOFAR is an excellent survey instrument that opens enormous perspectives for the study of radio plasma in the ICM (Röttgering et al. 2011).

Issues related to direction dependent effects (such as beam variations in both time and frequency, or ionospheric distortions of the wavefront propagation on scales smaller than the LOFAR FoV; see e.g. Tasse et al.

2012) are particularly critical in the calibration and imaging phases of LOFAR data. For this, a detailed and complex data reduction chain is being tested and implemented during the LOFAR commissioning phase (Heald et al. 2011). Very briefly, after the initial phase of data flagging and compression, the brightest radio sources in the sky (the so-called "A-team"), that during observations move in and out the side-lobes of the station beams, need to be subtracted. New calibration and imaging algorithms, taking into account direction dependent effects as well as the non-coplanarity of the array, are under development (Tasse et al. 2012).

LOFAR project started his commissioning activities about three years ago. A lot of progress has been made thanks to commissioning events called "Busy Weeks", where expert commissioners get together and work on specific topics. Besides the "Busy Weeks", since September 2010 we kept the commissioning work very active with the "Busy Days", taking place every other week at ASTRON, with EVO sessions organized for commissioners located all around the world.

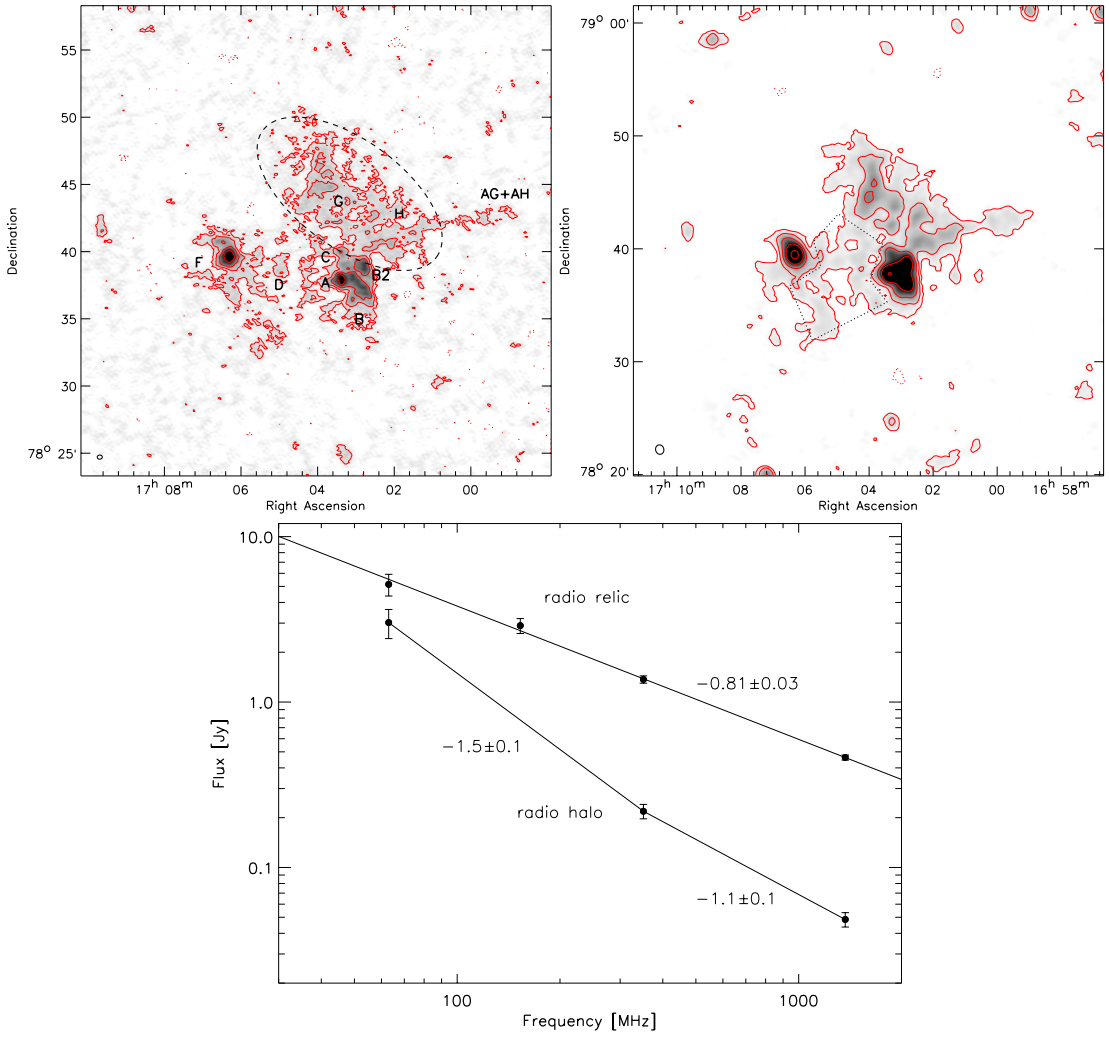

Fig. 2. Top: high- and low-resolution ($22'' \times 26''$, **left**, and $52'' \times 62''$, **right**) LOFAR maps of the galaxy cluster A 2256 at ≈ 60 MHz. The radio relic is indicated by a dashed ellipse on the left, while the area used to measure the radio halo spectral index is shown by the dotted polygon on the right. **Bottom**: radio spectra for the relic and the halo in A 2256. Figures extracted from van Weeren et al. (2012).

One of the very first galaxy clusters observed by LOFAR has been A 2256 (van Weeren et al. 2012). X-ray and optical observations provide strong evidence that A 2256 is undergoing a merger event between a main cluster, a major sub-structure and, possibly, a third infalling group. As introduced in the previous section and shown in Fig. 1, it is a nearby ($z = 0.0581$) system that contains a giant radio halo, a relic and a large number of tailed radio galaxies. The relic has a large integrated flux compared to other sources of the same class, of about

0.5 Jy at 1.4 GHz. A spectral analysis by (Brentjens 2008) shows that the radio halo component dominates the integrated cluster spectrum at very low frequencies. The large angular extent of the diffuse emission and its large integrated flux make A 2256 a prime target for low-frequency observations which typically suffer from low spatial resolution and sensitivity, compared to observations at high frequencies.

The LOFAR 63 MHz image reveals some of the well known tailed radio sources, the main relic, and part of the radio halo (Fig. 2), which is more easily detectable on the lower resolution map. The integrated fluxes of the radio halo and relic are difficult to be measured because they are partly blended with some of the complex head-tail radio sources in the cluster. To estimate their flux contribution, both the high and low resolution images have therefore been used (see van Weeren et al. 2012, for more details).

In the case of radio relics, the origin of cosmic ray electrons is generally explained in the framework of the diffusive shock acceleration (DSA) theory. The spectral index of A 2256 radio relic, integrated over the full extent of the source, is however too flat ($\alpha = 0.81 \pm 0.03$) to be explained by classical DSA. Different hypotheses have been proposed, such as the fact that we are observing a relic related to a young shock, in which energy injection and losses are not yet balanced, or that we are observing electron re-acceleration in a possibly inhomogeneous shock downstream region, or finally that our flux measurements are severely affected by projection effects (van Weeren et al. 2012).

Also the radio halo spectral shape is puzzling, since it presents a somehow unexpected low-frequency steepening (see Fig. 2). This could be related to: a) the superposition of two (or more) spectral components (see also Kale & Dwarakanath 2010), b) observation of turbulent re-acceleration – giving rise to the steep spectrum – plus hadronic component – related to the flat part of the spectrum, or c) inhomogeneous turbulent re-acceleration, whose efficiency changes with space and/or time in the emitting volume (van Weeren et al. 2012).

Several other clusters have been observed during the LOFAR commissioning phase. Preliminary results have been presented at the meeting "LOFAR's view of galaxy clusters" held last spring in Nice and can be found at the conference web page (see `https://gandc.oca.eu/spip.php?article398`). The emission from halos, relics and head-tail radio galaxies observed at higher frequencies is generally fully recovered in all the observed clusters, with in addition evidence of more extended low-frequency radio emission (de Gasperin et al. submitted, Pizzo et al. in prep., Macario et al. in prep., Bonafede et al. in prep., Orrù et al. in prep.). We can conclude that LOFAR commissioning observations of galaxy clusters have started to show the great potential of this instrument for the study of the non-thermal component in large-scale structures.

Chiara Ferrari and Giulia Macario acknowledge financial support by the *"Agence Nationale de la Recherche"* through grant ANR-09-JCJC-0001-01.

References

Böhringer, H. & Werner, N. 2010, A&A Rev., 18, 127
Borgani, S. & Guzzo, L. 2001, Nature, 409, 39
Brentjens, M. A. 2008, A&A, 489, 69
Brunetti, G. & Lazarian, A. 2011, MNRAS, 410, 127
Cassano, R., Brunetti, G., Röttgering, H. J. A., & Brüggen, M. 2010, A&A, 509, A68
Clarke, T. E. & Ensslin, T. A. 2006, AJ, 131, 2900
Dolag, K., Bykov, A. M., & Diaferio, A. 2008, Space Sci. Rev., 134, 311
Feretti, L., Giovannini, G., Govoni, F., & Murgia, M. 2012, A&A Rev., 20, 54
Ferrari, C., Govoni, F., Schindler, S., Bykov, A. M., & Rephaeli, Y. 2008, Space Sci. Rev., 134, 93
Heald, G., Bell, M. R., Horneffer, A., et al. 2011, Journal of Astrophysics and Astronomy, 32, 589
Kale, R. & Dwarakanath, K. S. 2010, ApJ, 718, 939
Laganá, T. F., de Souza, R. S., & Keller, G. R. 2010, A&A, 510, A76
Nuza, S. E., Hoeft, M., van Weeren, R. J., Gottlöber, S., & Yepes, G. 2012, MNRAS, 420, 2006
Parrish, I. J., Quataert, E., & Sharma, P. 2009, ApJ, 703, 96
Röttgering, H., Afonso, J., Barthel, P., et al. 2011, Journal of Astrophysics and Astronomy, 32, 557
Tasse, C., van Diepen, G., van der Tol, S., et al. 2012, Comptes Rendus Physique, 13, 28
van Weeren, R. J., Röttgering, H. J. A., Rafferty, D. A., et al. 2012, A&A, 543, A43
Vikhlinin, A., Kravtsov, A. V., Burenin, R. A., et al. 2009, ApJ, 692, 1060
Voit, G. M. 2005, Reviews of Modern Physics, 77, 207

SF2A 2012
S. Boissier, P. de Laverny, N. Nardetto, R. Samadi, D. Valls-Gabaud and H. Wozniak (eds)

JUPITER SYNCHROTRON IMAGING WITH LOFAR

J. N. Girard[1], P. Zarka[1], C. Tasse[2], S. Hess[3] and the LOFAR Collaboration

Abstract. Since its detection in the mid-fifties, the synchrotron radiation, emitted by the Jupiter radiation belts at decimeter wavelengths ("DIM"), has been extensively observed over a wide spectrum (from >300 MHz to 22 GHz) by various instruments (VLA, ATCA, WSRT). They provided accurate flux measurements and resolved images of the emission that reveal spatial, temporal and spectral variabilities. However, no instrument was able to image the radiations belts below 100 MHz (at meter and decametre wavelength). The LOw Frequency ARray (LOFAR) (van Haarlem et al. 2012), which is a phased-array interferometer operating in the [30-80] & [110-250] MHz bandwidth, observed for the first time the Jupiter synchrotron emission. The antenna distribution provided baselines from 70 m up to ∼20 km that resolved the emission at low frequencies (127-172 MHz) during its commissioning phase. In November 2011, a single 10-hour track enabled to cover an entire planetary rotation in a bandwidth of 24 MHz. We present here the specific methods and steps implemented to reduce and to image the planetary data at low frequencies. At this stage of the commissioning, the smoothness of the synchrotron spectrum enabled the direct comparison between the expected flux density and the measurements from VLA data obtained in 1994 and 1998 (Kloosterman et al. 2008). We measured a total flux density of $3.5 - 4 \pm [0.1 - 0.3]$ Jy, slightly lower to what was obtained from VLA observations and models ($\sim 5 - 6$ Jy). Future joint observations that cover the whole spectrum of the emission will enable the tracking of its temporal short- and long-term variability. The study of this variability brings information about the source, loss and transport processes taking place in the inner Jovian magnetosphere, improving in the same time the existing radiative code and magnetospheric models.

Keywords: Jupiter, synchrotron emission, LOFAR, low frequency radioastronomy.

1 Radio emissions at Jupiter

1.1 Various sources of radio emissions

The giant magnetized planet Jupiter is known to be a strong source of radio emissions from few kHz to few hundreds of GHz (Dessler 2002a; Zarka 2004). These radio emissions have three main components. The most powerful comes from the sporadic bursts of (non-thermal) emissions ($> 10^7$ Jy[i]) below 40 MHz in the decametre (DAM) range (Burke & L. 1955; Zarka 2004). Accelerated electrons (of energy $E \sim$ keV) emit radio waves at the local cyclotron frequency presumably by the non-linear wave-particle interactions known as the "Maser Cyclotron Instability" mechanism (Treumann 2006; Wu & Lee 1979).
The second radio emission dominates in the dm-cm range (DIM) and is associated to relativistic motion of high-energy electrons (from E≈100 keV to MeV Mayer et al. (1958)). They emit at the local synchrotron frequency in the vicinity of Jupiter radiation belts (forming Van Allen belts analog to Earth belts).
The third radio component is the thermal emission from the planet atmosphere which dominates above 5 GHz. These components are depicted on Fig. 1 (left) from (Zarka 2004).

[1] LESIA, Observatoire de Paris, CNRS, UPMC, Université Paris-Diderot, 5 place Jules Janssen, 92195 Meudon, France
[2] GEPI, Observatoire de Paris, CNRS, 92195 Meudon, France
[3] LATMOS/IPSL, OVSQ, Guyancourt, France
[i] 1 Jy= 10^{-26} W.m^{-2}.Hz^{-1}

1.2 Synchrotron emission & previous observations

The relativistic electrons radiate synchrotron radio waves as they travel along a helix with a "pitch angle" α in the inner magnetic field $\vec{B}$ of the planet. This results in a collimated forward emission with a beaming angle $\theta_b \propto \frac{2}{\Gamma}$ with Γ the Lorentz factor of the electrons. From Dessler (2002b), it has the following characteristics:

- This synchrotron radiation shows a high level of linear polarization (of order 20%) and a low level of circular polarization (≈1%). The polarization direction is nearly orthogonal to that of $\vec{B}$.
- Along with source and loss processes occurring between the electrons and the ionosphere, the satellites and the dust, the sources of emission are closely confined to the planet in the plane of the magnetic equator (Roberts 1976) perpendicular to the planet magnetic moment. They form a donut-like belt around the planet that extends from 1.6 to 3 R_j (with R_j the Jupiter radius).
- The emission is optically thin and therefore the radio emission seen by a remote observer accumulates on both sides of the planet in the magnetic equator and forms two radiation peaks at low Jovian latitudes. Another component exists at higher magnetic latitudes ($\approx \pm 35^o$) in both hemisphere and originates from electrons populations having a different value of the pitch angle. The separation between low and high magnetic latitudes sources is due to the interaction of electrons with Jovian satellites(de Pater et al. 1997) .
- The synchrotron spectrum is relatively flat (see Fig. 1) over a wide range of frequencies and peaks at a maximum frequency $\nu_{max} \propto E^2 B$ with ν_{max} in MHz, B in Gauss and E the energy of electrons in MeV (Dessler 2002b). The resulting spectrum is the superimposition of all spectra received from different electron populations (at different energy E) located at different distances from the planet (i.e with different B).
- This emission is continuous and relatively stable at very short term (few min) as compared to the sporadic DAM emissions at lower frequencies. The received power, projected on the sky, is the accumulation of the emission along the observer line of sight. The planetary rotation will therefore induce the variation of the location of the "piercing" points and that of the optical path through the optically thin radiation belts. As a consequence, the extended emission projected on the sky varies notably at timescales of ~ 30 (corresponding to a planetary longitude variation of $\sim 18^o$, referred to as the Central Meridian Longitude (CML) in the system III (1965) coordinate system (Dessler 2002a)). In addition to this apparent variability, intrinsic temporal variations were observed at times scales from few days Santos-Costa et al. (2009) to years (de Pater & Klein 1989). The origins of these variations are multiple and were attributed to diffusion processes occurring inside the belts (de Pater & Goertz 1994; Tsuchiya et al. 2011), variation of the solar wind properties (de Pater & Goertz 1994), interaction with galilean satellites or caused by impact events (Brecht et al. 2001; Santos-Costa et al. 2011).

The radio emissions mapping of Jupiter radiation belts improved by using large interferometers such as the WSRT, the ATCA and the VLA. As a proxy for the distribution of electrons, it led to the development of advanced models (see de Pater (1981); de Pater & Sault (1998); Santos-Costa et al. (2001)). By confirming the observed emission, these models enabled the identification of the source and mode of transport of the electron populations in Jupiter radiation belts. Not much is known about the low ($\lesssim$200 MHz) and high ($\gtrsim$ 10 GHz) frequency components of the synchrotron radiation, nor about their variation with time. The knowledge of these properties is of great importance to refine these models (de Pater 2004) and to formulate an accurate description of inner magnetic field of Jupiter.

2 The LOFAR Observation

With LOFAR[ii] (van Haarlem et al. 2012), we were able to make the first resolved observations at frequencies below 200 MHz. Jupiter was observed continuously during ten hours from 2011/11/10:18h24 UT to 2011/11/11:4h24 UT with LOFAR in interferometer mode configured with 49 antennas. Each antenna (or "station") is an array or a sub-array composed of High Band Antennas (HBA) which signals undergo digitization and processing that result in a virtual pointing (beamforming) toward the direction of interest. Two

[ii] www.lofar.org

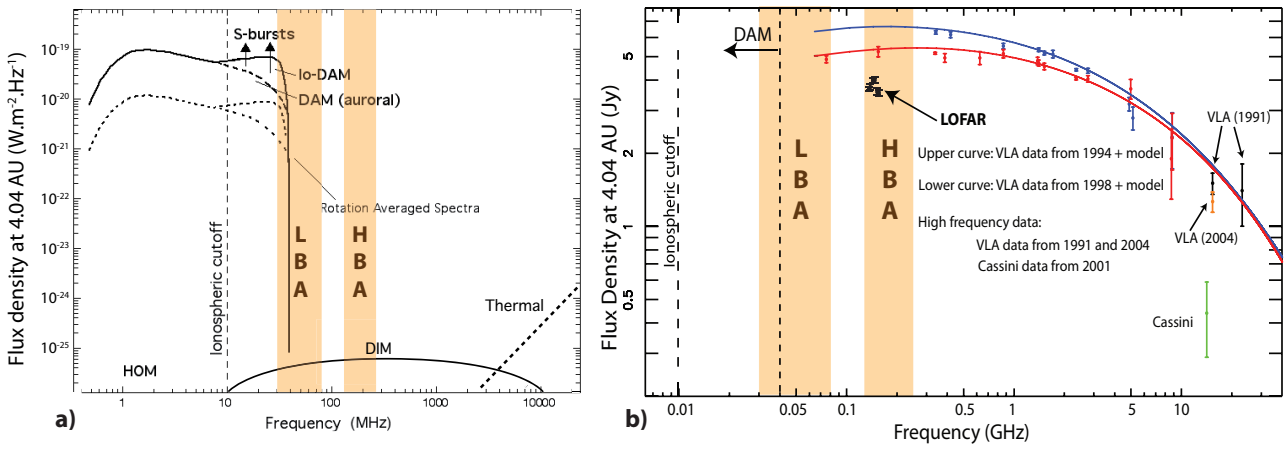

Fig. 1. The two bandwidths of the LOFAR is represented with the shaded area. The "low band antenna" (LBA) bandwidth is ≈30 to 80 MHz and the "High Band Antenna" (HBA) bandwidth is ≈120 to 240 MHz is (from `lofar.org`). **Left:** Spectrum of the existing radio emissions at Jupiter (DAM, DIM and thermal) adapted from Zarka (2004). **Right:** Measurements of the DIM emission with Cassini (2001) and the VLA measurements at three periods (1991, 1994, 1998) superimposed with models (Kloosterman et al. 2008) from 74 MHz up to 13 GHz. To account for the varying distance between Jupiter and the observer, flux densities are scaled to the standard 4.04 AU distance. LOFAR points with errors bars are the total flux density measurement on unresolved LOFAR images from 127 to 149 MHz. These error bars are computed from the RMS noise in source-free patches of the images.

numerical beams (of $\sim$ 24 MHz) were synthesized and pointed toward two directions: one was pointed toward the Jupiter mean position at the time of observation and the other toward a phase calibrator (4C15.05) situated 4^o away from Jupiter. For a total bandwidth of 47.26 MHz, 24 MHz was attributed to each beam and distributed in 121 sub-bands (SB) over [127-172] MHz. We used a high temporal and spectral resolution (dt=0.3ms x df=763Hz) to enable RFI excision before the data processing. The data are measurement sets of the visibilities between each antenna.

2.1 Data processing

Data bins polluted by RFI (representing $\approx 5-10\%$ of the data) and misbehaving stations were flagged. The data were then rebinned to dt=9.01s and df=195kHz. The first 1.5h and the last hour of the 10hrs observation were heavily polluted data. This behavior is partly due to the low elevation of the source ($\mathrm{dec}_{start} \approx 27^o$ & $\mathrm{dec}_{end} \approx 10^o$) and the local ionospheric conditions (at dusk).

The data were calibrated using the phase calibrator and the standard calibration tools provided by the LOFAR system. Since there is no specific planetary imaging mode implemented in LOFAR and no planetary tracking capability, we used the standard imaging mode (that can track source of constant RA/DEC). Indeed, in contrast to "fixed" sources that rotate with the sky (at 15^o/hr), Jupiter had an additional motion of ≈2-3' (across the beam) during a 10h observation.

Moreover, the 10^o tilt between its magnetic and rotation axes make the main radiation peaks to "wobble" of the projected image plane, as these are aligned with the magnetic equator. The magnitude of these two effects varies with the source-to-observer configuration and induces a smearing of the emission structure in resolved radio maps after long-integration. This smearing effect makes the scientific interpretation next to impossible. It is possible to know the accurate position of the planet (with ephemeris provided by JPL Horizons[iii] & IMCCE[iv]) and the geometrical configuration of the observer w.r.t. the spin & magnetic axes of the planet (Earth jovicentric latitude $D_E = 3.29^o$ in november 2011). We derived the direction and angle of projected magnetic equator containing the two radiation peaks with respect to the sky reference frame. These two major effects can be corrected by the application of rotation matrices and phase corrections coefficients directly on the visibility data at each time steps. However, the nearby sources that have constant RA/DEC coordinates will undergo an artificial smearing

[iii] `http://ssd.jpl.nasa.gov/`
[iv] `http://www.imcce.fr/fr/ephemerides/`

with these corrections. Therefore it was necessary to subtract a maximum number of background sources from the target field visibilities before applying the corrections. This stage requires a preliminary wide-field imaging (using AWimager from (Tasse et al. 2012) dealing with direction-dependent effects) around the target, the source detection, visibility simulations of these sources and their subtraction (known as "peeling"). We used a parallel source peeling algorithm on unresolved wide-field images which removed ~ 50 sources from the visibilities. The set of tools developed for these commissioning data may become the standard way to automatically process LOFAR planetary visibility data.

2.2 Preliminary results

2.2.1 Total flux measurements

We used the Cotton-Schwab (Schwab 1984) CLEAN algorithm (in a CASA environment) to image the Jupiter DIM emission. A first set of images was produced to measure the total flux in the direction of Jupiter. These images were integrated over 7hrs from 19:00 UT to 2:00 UT. On Fig. 1 (right), we added the LOFAR flux measurements (scaled to the standard 4.04 AU distance from Jupiter) to previous measurements from the VLA (adapted from Kloosterman et al. (2008)). The errors bars were computed using the RMS noise of the corresponding images in empty patches of the sky. No systematic error was evaluated here.
We measured flux densities of [3.5-4]$\pm$[$0.1-0.3$] Jy which are lower to what was obtained from tabulated values derived from models and observations (Kloosterman et al. 2008) ($\approx$5-6 Jy at these frequencies).
The variation of the spectrum shape between the two VLA datasets between 1994 and 1998 is $\sim$1-1.5 Jy and is addressed in de Pater & Dunn (2003). The LOFAR data were obtained more than 10 years after these VLA values and the flux difference observed can result from the combination of both geometrical (target-to-observer parameters, different optical paths) and the intrinsic variations of the emission at the source. Long-term (decades) variations of the DIM flux density was reported by Klein et al. (1989). Flux measurements at 13 cm taken from 1964 to 1987 were compiled and revealed flux variations of 3 Jy to 5.5 Jy ($\approx 40\%$) over the years.

2.2.2 Resolved radio maps

We have produced 12 images, each computed from 10 consecutive SB and integrated over 7hrs. We present on Fig. 2, the surface brightness obtained from the accumulation of the 12 LOFAR images over 7hr (averaged over 70% of the planet rotation). The final spatial resolutions obtained with this dataset was 17.8"-15.5" (the white ellipse represents the average CLEAN beam). We compare the obtained map to that obtained by de Pater & Dunn (2003) with VLA data at 15 GHz. We can identify the two main radiation peaks at each side of Jupiter (represented with a black circle) matching the radiation peaks from the VLA dataset. The 1-2^o misalignment is due to the different observer-to-target configurations of the two periods of observation ($D_E = 0.45^o$ in 1991 and $D_E = 3.29^o$ in 2011). The distance of the peaks from the planet center is ~ 1.3 R$_j$ on the two datasets. No clear sign of long-term variability can be derived at this resolution between 1991 and 2011.

3 Ongoing work and perspectives

We measured for the first time, the flux density of the Jupiter DIM emission with LOFAR in the [127-149] MHz. We also produced resolved maps of the emission from [127-172] MHz by using the standard interferometer mode of LOFAR. We developed and validated a toolkit that handles the planetary imaging data with LOFAR. Advanced methods, available in the LOFAR toolkit,were used such as direction-dependent calibration, wide-field imaging at low frequencies and source peeling. With supplementary operation on the (u,v) data, we corrected for the planetary motion on the sky and the radio source wobbling.
We obtained flux levels of the same order of magnitude of that obtained with previous VLA observations with a sensitivity of $\pm$0.2 Jy. The comprehensive scientific exploitation as well as other observations with LOFAR and the VLA will be carried in the next few months. An observation proposal was submitted to answer the first Public Call for observations with LOFAR. These future observations include observations with in HBA band and in LBA band (at frequency/time where there is no dominating DAM emissions). We plan to observe several calibrators during the future observations with LOFAR (during Cycle 0). Two beams will be used, one pointing at the planet and the other pointing at a phase calibrator close to Jupiter to monitor the local conditions of the targeted area in the sky. A primary flux calibrator will also be used to bootstrap the value of flux density on a known source. In addition, a polarized calibrator will be observed from time to time during the observation to

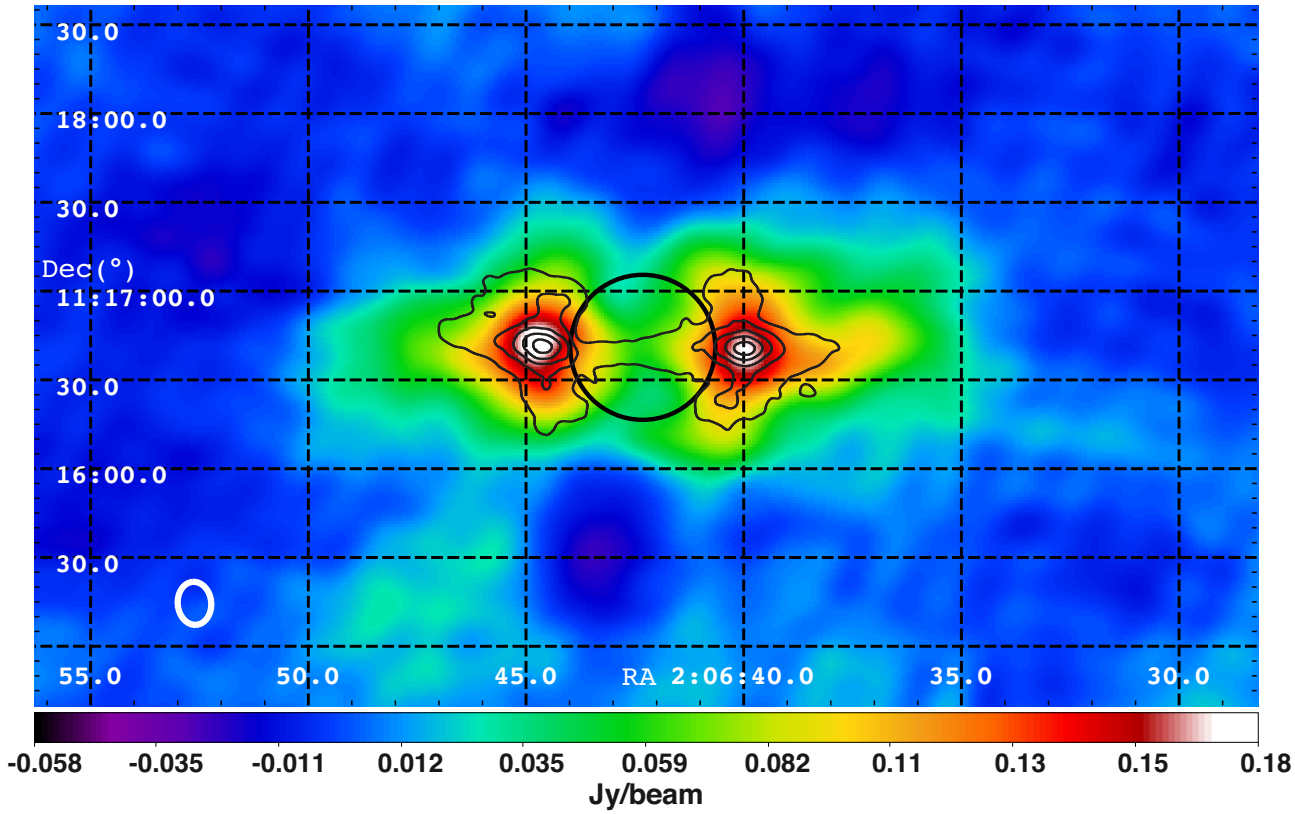

Fig. 2. The rotation-averaged image of the Jupiter radiation belts emission over 127-172 MHz is represented with the color map in celestial coordinates. The image RMS noise is 4 mJy/beam. The contours are the linearly polarized flux levels at 15 GHz from VLA data taken during March 1991 (de Pater & Dunn 2003). The black circle locates the Jupiter disk on the sky. The VLA map was scaled up to match the LOFAR data to take into account the change of Jupiter apparent size between the two dates (Jupiter was at a distance of 4.55 AU in March 1991 and 3.99 AU in november 2011). The contour interval is 3 mJy/beam and starts at 2 mJy/beam.

monitor the change of polarization due to the ionospheric & instrumental effects. The polarization information of these emissions are decisive, especially that of the circular component of the radiation. If measured, it will provide much information on the non-dipolar character of Jupiter magnetic field (de Pater 1981). Estimates indicate that the 5-10 mJy level of the circular component may just be in the scope of LOFAR detectability (1-10 mJy). This observation was carried during the LOFAR commissioning phase. Therefore the data quality was not guaranteed, but the essential reduction tools were fully functional and enabled the advanced implementation of reduction scripts to treat planetary data. An additional set of observations covering more than two Jupiter rotations will enable:

1. the search for yearly temporal variations (2011-2013) in the LOFAR data.

2. the investigation of the polarization of the emission by combining the information from different datasets from various instrument.

3. the measurement of the total spectral content over a very wide range of frequencies from 60 MHz up to $\sim$ 14 GHz.

LOFAR, the Low Frequency Array designed and constructed by ASTRON, has facilities in several countries, that are owned by various parties (each with their own funding sources), and that are collectively operated by the International LOFAR Telescope (ILT) foundation under a joint scientific policy. The authors thank Roberto Pizzo (ASTRON, Dwigeloo) for his assistance with the raw data and Jean-Mathias Grießmeier (LPC2E, Orléans) for the observation setup. We thank the members of the LOFAR Planetary & Exoplanetary Working Group (PeWG) from the LOFAR Key Science Project: Planets & Exoplanets.

References

Brecht, S. H., de Pater, I., Larson, D. J., & Pesses, M. E. 2001, Icarus, 151, 25

Burke, B. F. & L., F. K. 1955, J. Geophys. Res., 60(2), 213

de Pater, I. 1981, J. Geophys. Res., 86, 3397

de Pater, I. 2004, Planetary and Space Science, 52, 1449

de Pater, I. & Dunn, D. E. 2003, Icarus, 163, 449

de Pater, I. & Goertz, I. 1994, J. Geophys. Res., 99, 2271

de Pater, I. & Klein, M. J. 1989, NASA Special Publication, 494, 139

de Pater, I. & Sault, R. J. 1998, J. Geophys. Res., 103, 19973

de Pater, I., Schulz, M., & Brecht, S. H. 1997, J. Geophys. Res., 102, 22043

Dessler, A. 2002a, Physics of the Jovian Magnetosphere, Vol. 3 of Cambridge Planetary Science Series (Cambridge University Press), 498–504

Dessler, A. 2002b, Physics of the Jovian Magnetosphere, Vol. 3 of Cambridge Planetary Science Series (Cambridge University Press), 231–250

Klein, M. J., Thompson, T. J., & Bolton, S. 1989, NASA Special Publication, 494, 151

Kloosterman, J. L., Butler, B., & de Pater, I. 2008, Icarus, 193, 644

Mayer, C. H., McCullough, T. P., & Sloanaker, R. M. 1958, ApJ, 127, 11

Roberts, J. A. 1976, Proceedings of the Astronomical Society of Australia, 3, 53

Santos-Costa, D., Bolton, S. J., & Sault, R. J. 2009, A&A, 508, 1001

Santos-Costa, D., Bolton, S. J., Sault, R. J., Thorne, R. M., & Levin, S. M. 2011, Journal of Geophysical Research (Space Physics), 116, 12236

Santos-Costa, D., Sault, R., Bourdarie, S., et al. 2001, Advances in Space Research, 28, 915

Schwab, F. R. 1984, AJ, 89, 1076

Tasse, C., van der Tol, B., Bhatnagar, S., van Diepen, G., & van Zwieten, J. 2012, in prep

Treumann, R. 2006, Astronomy and Astrophysics Review, 13, 229

Tsuchiya, F., Misawa, H., Imai, K., & Morioka, A. 2011, Journal of Geophysical Research (Space Physics), 116, 9202

van Haarlem, M. P., Wise, M. W., Gunst, A., et al. 2012, A&A, submitted

Wu, C. S. & Lee, L. C. 1979, ApJ, 230, 621

Zarka, P. 2004, Planet. Space Sci., 52, 1455

Zarka, P. 2004, Advances in Space Research, 33, 2045

SF2A 2012
S. Boissier, P. de Laverny, N. Nardetto, R. Samadi, D. Valls-Gabaud and H. Wozniak (eds)

LSS/NENUFAR: THE LOFAR SUPER STATION PROJECT IN NANÇAY

P. Zarka[1], J. N. Girard[1], M. Tagger[2], L. Denis[3] and the LSS team[4]

Abstract. We summarize the outcome of the scientific and technical study conducted in the past 3 years for the definition and prototyping of a LOFAR Super Station (LSS) in Nançay. We first present the LSS concept, then the steps addressed by the design study and the conclusions reached. We give an overview of the science case for the LSS, with special emphasis on the interest of a dedicated backend for standalone use. We compare the expected LSS characteristics to those of large low-frequency radio instruments, existing or in project. The main advantage of the LSS in standalone mode will be its very high instantaneous sensitivity, enabling or significantly improving a broad range of scientific studies. It will be a SKA precursor for the French community, both scientific and technical.

Keywords: Radioastronomy, Low-Frequency, Array, LOFAR, Nançay, LOFAR Super Station, Antenna, Preamplifier, Receiver, Phasing, Exoplanets, Pulsars, ISM, Cosmology, Transients

1 Introduction

LOFAR is a new European multi-scale low-frequency (LF) radio interferometer in the range 30−250 MHz, with baselines from ∼50 m to ∼1000 km (van Haarlem et al. 2012). Its large effective area and extent will allow its users to address a variety of astrophysical topics, including cosmology (the Epoch of Reionization − EoR − of the young Universe), deep sky surveys, star formation, AGN, galaxy clusters, the distribution of cosmic magnetic fields, transient emissions at all timescales (from cosmic-ray-induced to pulsars, flare stars and other eruptive or variable souces), planetary (and hopefully exoplanetary) plasma physics, as well as Solar and space physics. The constitutive elements of LOFAR are phased arrays or "stations", distributed in The Netherlands and surrounding European countries. One of these stations – FR606 – is installed in the Nançay radio observatory (France). Each station consists of two arrays of antennas and a "backend" that preprocesses antenna signals (filtering, digitization, spectral channelization and beamforming). Preprocessed digital data are then sent at ∼ 3 Gbits/sec to the central computer (in Groningen, NL) that performs the correlations per interferometric baseline and/or final pencil beamforming. The Low-Band Antenna (LBA) array covers the range 30−80 MHz and consists of 96 elementary crossed dipoles in international stations such as FR606 (48 in Dutch stations). The High-Band Antenna (HBA) array covers the range 110−250 MHz and consist of 96 "tiles" of 16 analog-phased crossed dipoles (2×24 in Dutch stations). The radio FM band in between, saturated by man-made emissions, is carefully avoided. At any given time, the backend can be connected to either the LBA or the HBA (not both simultaneously). A third input to the backend exists, that was initially planned for an LBL (Low-Band Low, 10−50 MHz) array that never existed due to limited funding. The phasing of HBA tiles and the initial signal filtering before digitization are the only analog steps in LOFAR, which is essentially a digital radiotelescope.

[1] LESIA, Observatoire de Paris, CNRS, UPMC, Université Paris Diderot, 92190 Meudon, France

[2] LPC2E, CNRS, Université d'Orléans, 45071 Orléans, France

[3] USN, Station de Radioastronomie, Observatoire de Paris, CNRS, 18330 Nançay, France

[4] N. Aghanim, L. Alsac, M. Arnaud, S. Barth, F. Boone, S. Bosse, D. Capayrou, C. Capdessus, B. Cecconi, D. Charrier, A. Coffre, I. Cognard, F. Combes, S. Corbel, N. Cornilleau-Wehrlin, P. Cottet, H. Dole, C. Dumez-Viou, I. Falkovych, C. Ferrari, F. Floquet, S. Garnier, G. Georges, B. Gond, N. Grespier, J.-M. Griessmeier, S. Joly, A. Konovalenko, L. Lamy, M. Lehnert, M. Pommier, H. Rucker, P. Sandré, B. Semelin, C. Taffoureau, C. Tasse, E. Thétas, G. Theureau, P. Tokarsky, W. Van Driel, J.-B. Vimon, R. Weber

2 The LOFAR Super Station concept

The bandpass filtering of the LBL input to the backend is 10−90 MHz (thus including the LBA range). The basic idea underlying the LOFAR Super Station (LSS) concept is to add a 3^{rd} antenna array to a LOFAR station (FR606 in our case), that will be fully compatible with LOFAR operations in the LBA band (i.e. that can be correlated with LBA arrays of other LOFAR stations, instead of the FR606 LBA array) and at the same time provide a considerably increased instantaneous sensitivity and frequency coverage. In order to meet these constraints, the LSS will consist of 96 groups of dual-polarization antennas (or LF "tiles") with a large gain from 10-15 MHz to 85-87 MHz (i.e. a ratio f_{max}/f_{min} double of that of the LBA range). Each of these LF tiles should be analog phased (as the HBA tiles) in order to provide only 2 inputs (1 per polarization) to the LOFAR antenna backend digitizers. The number of antennas within each tile should be of the order of 16 (again as in HBA tiles) in order to provide at least an order of magnitude increase of the instantaneous sensitivity. As we explain below, the "ideal" number we have reached is 19 crossed dipoles per LF tile. The 96 tiles should be arranged in a relatively dense layout (within a few hundred meters diameter), providing a smooth overall beam with a low side lobe level and compatible with the available land in an observatory such as the Nançay station, and at the same time minimize the overlap between antennas' effective areas in order to maximize the LSS sensitivity.

An instrument of a few hundred meters diameter will provide an angular resolution of the order of 1° in the 10−88 MHz range, so that the LSS by itself is not a powerful imaging instrument. But its collecting area, and thus its sensitivity, will bring several significant improvements to LOFAR:

- The long LOFAR baselines including the LSS will be $\sim \sqrt{19}$ times more sensitive than long baselines between two LBA arrays; as the available radio power corresponding to fine angular details is generally weak, this increased sensitivity will give access to an increased number of calibrators (typically ×10) in the vicinity of the studied target; this will improve LOFAR's capabilities for high resolution imaging in the LBA range.

- By adding 96×19=1824 antennas to the present ∼2700 LOFAR LBA antennas, the LSS will almost double LOFAR's sensitivity in the LBA imaging mode.

- When most of the "core" (closely-packed) LOFAR stations will be used for time-demanding projects such as observing the EoR, the LSS will provide an alternative core and, by correlation with the "remote" LBA arrays, will preserve good imaging capability in parallel with the above projects; provided that the central correlator can handle two streams of data from two LOFAR sub-arrays (namely the core, and the LSS+remote stations) the LSS will improve LOFAR-LBA imaging capabilities for a significant fraction of the time.

- Correlation of signals from the LF tiles within the LSS will provide sensitive baselines 2 to 3 times shorter than a LOFAR station diameter − the shortest baseline presently available −, permitting to image large-scale structures, larger than an instantaneous station beam ($\sim 10°$ at 30 MHz); short baselines are presently available by correlation of LBA antennas within a station, but with much lower sensitivity.

- The LSS will also be a very large standalone instrument: it will have an effective area (and thus sensitivity) ∼19 times larger than the LBA array of an international station, i.e. ∼70% to 85% of all LOFAR-LBA arrays, but this area will be instantaneously and fully available during use, especially in coherent tied-array (or phased-array) beam mode (TAB); by contrast, the coherent phasing of LOFAR-LBA array signals is limited to the 24 core stations that share the same reference clock (and have the same ionosphere above them); thus, the instantaneous sensitivity of the LSS in coherent TAB mode will be ≥1.6 times better than the LOFAR-LBA one (Figure 1).

- Finally, in standalone mode, the LSS will extend the observation bandwidth to significantly lower frequencies than the LBA range.

3 LSS design and prototyping

We performed feasibility and optimization studies of all elements of the LSS design:

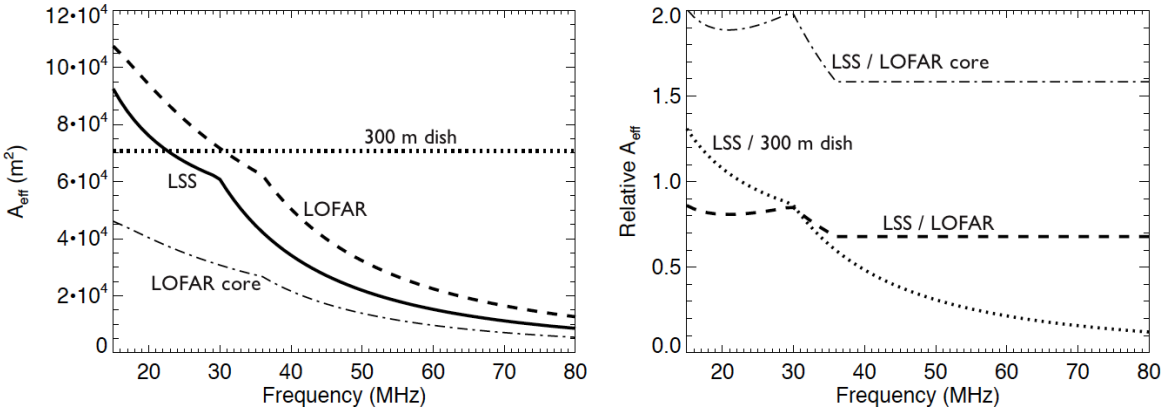

Fig. 1. LSS effective area compared to that of LOFAR, LOFAR's core, and an Arecibo-like antenna (∼300 m in diameter).

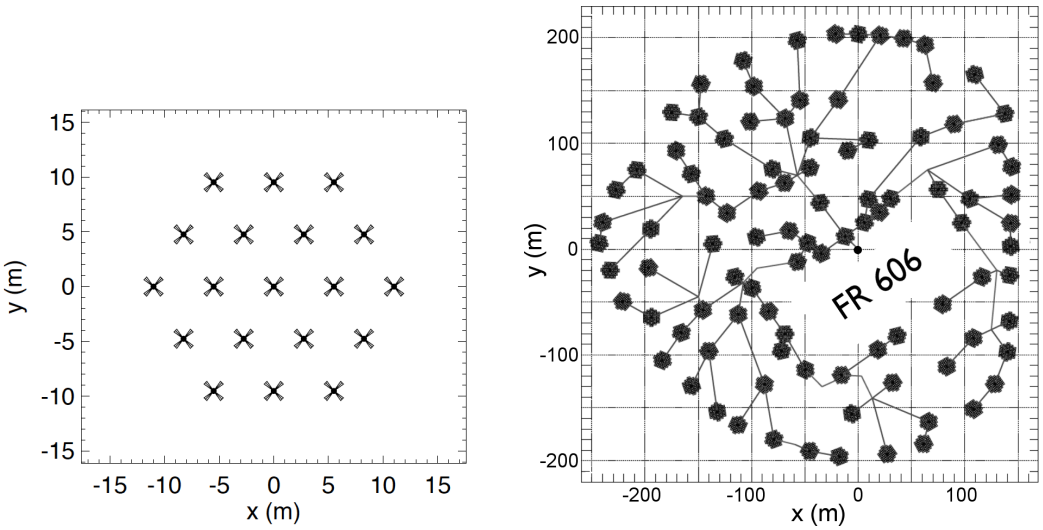

Fig. 2. Left: LF tile layout. Elementary crossed dipoles will always be at 45° from the meridian whatever the rotation of the tile. Inter-antenna distance is 5.5 m. **Right:** LSS antenna distribution optimized for a gaussian coverage of the (u,v) plane, taking into account local positioning constraints (forbidden zones). LF tiles are represented with their random rotations. The layout of the connections between LF tiles and the LOFAR backend (black dot at 0,0) follows from the optimization of the trench-cable problem applied to the LSS. The total length of trenches will be ∼4 km and that of RF cables connecting the tiles to the backend ∼21 km per polarization.

- First, we optimized the diagram of the antenna radiator via electromagnetic simulations with the NEC code and tests on the sky; optimized parameters include a broad and smooth beam (nearly isotropic, albeit with extinction below 20° elevation) and maximum efficiency (related to electrical and ground losses), over a large frequency bandwidth; this implies an antenna radiation resistance and (low) reactance as constant as possible over the band of interest and versus time; cost effectiveness and compatibility with LOFAR strongly favoured linearly polarized crossed dipoles; we found that the optimal compromise is a "thick" inverted-V dipole similar to the LWA Fork, with a metallic ground screen (Girard et al. 2011, 2012).

- Three designs have been studied and realized for the antenna preamplifier, which is a key element for the antenna gain and its susceptibility to radio-frequency interference (RFI): (1) the "GURT2" design from the Kharkov Institute of Radio Astronomy,(2) the Subatech/Nançay design, and (3) the Nançay microelectronics laboratory design. (1) is based on discrete components, whereas (2) & (3) are based on ASIC circuits. All have good characteristics, with a noise ∼10 dB below the sky noise level. The final choice will result from tests on the sky (see below).

- Then, the antenna distribution within each LF tile was optimized for a low side lobe level and a large field of view symmetrical around the zenith; Girard & Zarka (2012) found that a distribution with a central antenna surrounded by two circular rings of antennas meets these requirements, especially if the rings have different (or no) symmetry axes, i.e. if the global distribution cannot be superposed to itself by a rotation $< 2\pi$. In parallel, we have calculated that analog phasing of each LF tile using 7-bit delay lines (cable lengths) allows to perform achromatic phasing over the whole LSS band (10-87 MHz) with gain variations $\leq$10% across the beam, and provide one input per polarization to the backend. In order to be cost-effective, delay lines must be mutualized for groups of antennas, e.g. by arranging antennas with a regular spacing in two orthogonal directions. Taking into account this constraint we modified the above optimized antenna distributions to obtain an LF tile of 19 antennas (a central one surrounded by an hexagon of 6 antennas and a second one of 12 antennas, or equivalently regular lines of 3 / 4 / 5 / 4 / 3 antennas with each line shifted by 1/2 inter-antenna spacing relative to its neighbours − Figure 2 Left). The absolute value of inter-antenna spacing was set to 5.5 m in order to maximize the effective area without overlap at LF, while keeping the LSS extent compatible with its hosting at the Nançay station (see below). The instantaneous LF tile beam will have an angular size of $10°-50°$ over the LSS spectral range ($\sim 25°$ at 30 MHz).

- The optimal distribution of the 96 LF tiles was computed using the Boone (2001) algorithm, taking into account a "site mask" of the Nançay station including its limits and forbidden areas (the station FR606 itself and other antennas of the site). It provides a smooth, gaussian distribution of visibilities in the (u,v) plane, and thus a near-gaussian LSS beam pattern. The layout of trenches and cables connecting the LF tiles to the FR606 backend was optimized using a reasonable cost ratio per unit length of trench/cable in input to a specific optimization algorithm (Vasko et al. 2002). The obtained LF tiles distribution and layout is displayed in Figure 2 Right). It implies an LSS beam size of $0.5°-3°$ ($\sim 1.5°$ at 30 MHz). In order to reduce the side lobe level resulting from the regular antennas arrangement in the LF tiles, each tile will be rotated by a random amount with respect to each other, but all crossed dipoles within all tiles will be oriented along the same directions, at 45° from the meridian (Figure 2).

- The LSS pointing will be controlled by a dedicated LCU (Local Command Unit) connected to 96 electronic modules, one in each LF tile, specifying the phasing scheme to be applied at any given time (different for each LF tile due to their random rotations); these modules are designed to be completely "radio-quiet" outside pointing time; pointing will occur at intervals from 20 to 60 sec, ensuring low gain variation in the main beam direction. The LSS LCU will be connected to the LOFAR LCU of station FR606. When the LSS will be used jointly with other LOFAR LBA arrays (so-called "International" mode), pointing orders will come from the LOFAR operations center via the LOFAR LCU and be translated into LF tiles phasing commands by the LSS LCU; data recorded by the LOFAR backend will be sent to the LOFAR central correlator. In "Standalone" mode, pointing orders will come from a local command computer, and the data will be recorded locally (see below).

- Finally, a site study was conducted by ONF (Office National des Forêts) which granted the authorization to clear 10 hectares of land for constructing the LSS.

The antenna radiator and preamplifier designs are being tested on the sky. Figure 3 is an observation of Jupiter with a single LSS antenna (equipped with GURT preamplifier), allowing us to test the antenna characteristics in its LF part ($\sim$ 10 to 35 MHz). Jupiter's decameter radiation is detected at a fraction of dB above the galactic background (i.e. at a few % of the level of the galactic background integrated over the broad antenna diagram) down to $13-14$ MHz, showing the correct behaviour of the antenna at LF. Comparison with a simultaneous observation by the Nançay Decameter Array allowed us to compute the directional gain of the LSS antenna over the observed range. This gain is $\sim$5 dB over the range $20-30$ MHz, consistent with our NEC simulations, and the effective area of the LSS dipole appears to vary in $\sim \lambda^2/3$.

In order to fully test the LF tiles, including the antennas + preamplifiers and the phasing and command systems, 3 prototype LF tiles have been built in Nançay in 2012. The first one is displayed on Figure 4. Each prototype tile is equipped with a different set of antenna preamplifiers. Extensive tests on the sky are being performed, including point source and extended source measurements, gain / effective area / sensitivity measurements, immunity to RFI, polarization response, and comparison of the performances of the 3 preamplifiers. For these tests, a dedicated receiver has been built in Nançay that can acquire in parallel the 3 tiles $\times$ 2 polar-

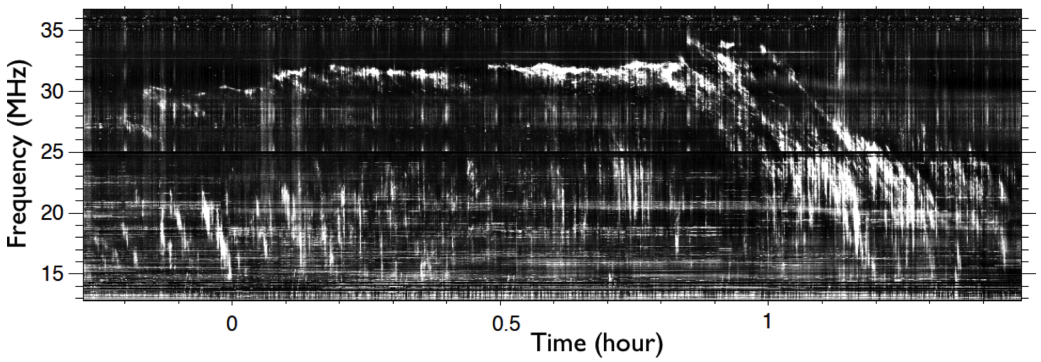

Fig. 3. Dynamic spectrum of Jupiter's decameter emission observed by a single LSS antenna with GURT preamplifier, on 9 oct. 2011. Jupiter bursts, inclined in the displayed time-frequency plane, have an intensity of a few % of the galactic background (the latter has been subtracted in the displayed dynamic spectrum). They are clearly detected down to 13−14 MHz.

Fig. 4. The first LF tile prototype of the LSS built in Nançay in 2012, consisting of 19 crossed dipoles.

izations, digitize these 6 inputs at 196 Msamples/sec, and compute their full correlation matrix over 2048 point spectra (∼47 kHz spectral resolution) with high time resolution.

4 Science objectives of the LSS

The LSS will bring new capabilities not available to LOFAR, as briefly described in the "concept" section above. These capabilities will enable new observations not possible with LOFAR, or improve on LOFAR observations in several domains. We summarize below the LSS science case sorted by broad scientific domains.

- **Exoplanets and binary/eruptive stars**: the larger instantaneous sensitivity of the LSS in standalone coherent TAB mode, and its access to lower frequencies, will bring new possibilities of detection and study of weak radio emission from stars, exoplanets (Zarka 2011), star-planet interactions, and comparative (exo-)magnetospheric physics. This is especially true *if the LSS can be used in standalone with a large duty-cycle*. Also, independent simultaneous detection of weak sources in parallel with the LSS and LOFAR will permit to confirm detections with a better immunity to local RFI or ionospheric perturbations. Correlation of the LSS with LOFAR LBA will increase the total sensitivity for imaging the environment of these sources.
- **Pulsars and Rotating RAdio Transients (RRATs)**: various figures of merit combining instantaneous sensitivity and field of view show that the LSS in standalone mode will be a more powerful transients detector than LOFAR, especially at LF (where the LSS effective area is largest − *again, a large duty-cycle will be crucial*). It will allow to address the physics of the environment of compact objects, the nature of RRATs, giant pulses, to search planets around pulsars (Mottez & Heyvaerts 2011), and study the structure of the ISM via propagation effects (Zakharenko et al. 2012).
- **Structure of the Galactic interstellar medium (ISM)**: when used jointly with LOFAR, the LSS short baselines will give access to extended radio sources (envelopes, nebulae ...), whereas the more

sensitive long baselines will enable small-scale magnetic fields imaging via rotation measure measurements (without depolarization due to spatial integration), and to study radio recombination lines (Asgekar et al. 2012). Standalone LSS measurements of the temporal broadening of transient radio pulses will put constraints on the largest scale of the ISM turbulence.

- **Cosmology and galaxy formation**: LSS in standalone mode will allow us to search the spectral signature of pre-EoR dark ages, as predicted in the LBA/LSS range by e.g. Visbal et al. (2012). *This will require a careful calibration of the bandpass and ionosphere that can be performed via instantaneous auto- and cross-correlations of the LSS tiles.* Sensitive long baselines from the LSS used in correlation with LOFAR will permit to address large structures formation (AGN at $z < 1$, clumps up to $z \sim 2$, star formation in nearby galaxies, magnetic fields).

- **The "impulsional" Universe**: as for pulsars and RRATs, the LSS in standalone mode will be a powerful transients detector, *provided that an adapted backend is available with a high duty-cycle.* In coherent or incoherent TAB mode and/or with extended Transient Buffer Boards (i.e. antennas waveform data buffers − cf. (van Haarlem et al. 2012) and `http://www.astron.nl/radio-observatory/astronomers/users/technical-information/transient-buffer-boards/transient-buffer-b`), it will permit the blind exhaustive exploration of the impulsive Universe, ideal in LF radio due to absence of photon noise. Addressed topics will include time and frequency scales of (dispersed) pulses, the nature of emitters (Gamma Ray bursts, cosmic rays, neutrinos impacting the Moon), and a broad range of potential serendipitous discoveries.

- **Transient Luminous Events (TLE) in the Earth and planetary atmospheres**: in the same modes as above, the LSS will enable the radio exploration of counterparts of sprites and other TLEs, addressing their origin, distribution and dynamics over center France, time and frequency scales, and physical mechanisms.

LSS objectives will of course address Solar system physics (ionospheric scintillations and opacity, Jupiter radio emissions, Solar bursts, space physics: interplanetary scintillation and possibly active − Radar − studies), but these studies do not crucially depend on LSS capabilities. However, the LSS may bring in a larger duty-cycle than the one available with LOFAR, permitting monitoring studies.

5 Dedicated receiver and Standalone use

The importance of a high duty-cycle of LSS standalone mode and of a dedicated receiver have been stressed in italics in the previous section. The standard LSS concept consists of the 96 additional LF tiles and their phasing and command system, that are connected to the LOFAR backend of FR606. The contract of any European station owner with the International LOFAR Telescope board includes the right to use that station in standalone mode for $\geq$10% of the time. As the standard LOFAR station backend only allows to record low frequency-time resolutions observations (typically in 200 kHz $\times$ 1 sec bins), the full scientific exploitation of standalone LSS observations requires either LOFAR's "Single Station" mode (cf. `http://www.lofar.org/operations/doku.php?id=singlestation:start`) or a dedicated post-backend (Serylak et al. 2012). The former consists of a sub-array formed by a single station, which high resolution data are sent to the central correlator for processing as TAB data. The latter is for example the ARTEMIS (Advanced Radio Transient Event Monitor and Identification System) post-backend dedicated to transients detection and study, that ingests high resolution station data and locally computes high-resolution time-frequency planes including parametric dedispersion (Armour et al. 2011).

If one wants to compute locally more than time-frequency planes with LSS standalone data (e.g. auto- and cross-correlations of tile signals), then a dedicated receiver is necessary. Such a dedicated receiver has been studied in the frame of the LSS design study. It will consist of either a post-LOFAR-backend (ARTEMIS-like), or a fully independent backend. The LOFAR backend digitizes the LBA or LSS tile signals, channelizes it in 200 kHz bands (called "subbands"), and computes beamforming within each subband. The beamformed signal of 244 subbands is sent to the LOFAR central correlator. The latter further channelizes (down to 0.76 kHz resolution) the signals of all subbands from all stations, and computes auto-/cross-correlations and/or incoherent or coherent (adequately time-shifted) summation in order to produced polarized images and/or TAB data (cf. `http://www.astron.nl/radio-observatory/astronomers/technical-information/lofar-signal-path/lofar-signal-path/`).

Table 1. Characteristics of *the LSS* compared to those of large LF radio instruments (capable of observing below 100 MHz), existing or in project. *(a) at 20 MHz. (b) at 30 MHz. (c) at 150 MHz.*

Name	Antennas	Eff. area	Freq. range	Ang. Res.	N beams	Polar.
NDA	144 circ. dipoles	4000 m^2 $^{(a)}$	10-110 MHz	11° $^{(a)}$	1 beam	4 Stokes
UTR-2	2040 dipoles	143000 m^2	8-32 MHz	0.5°	5 beams	1 lin. polar.
VLA	27 dish.× 25 m	∼2000 m^2	73-74.5 MHz	0.5'	1 beam	4 Stokes
LWA	256 X dipoles	8000 m^2 $^{(a)}$	10-88 MHz	9° $^{(a)}$	4 b.×20 MHz	4 Stokes
MWA	2048 X dipoles	∼2000 m^2 $^{(c)}$	80-300 MHz	3' $^{(c)}$	1 b.×30 MHz	4 Stokes
LOFAR-LBA	2688 X dipoles	72000 m^2 $^{(b)}$	30-80 MHz	2" $^{(b)}$	8+b.×4 MHz	4 Stokes
LSS standalone	*1824 X dipoles*	*62000 m^2* $^{(b)}$	*15-80 MHz*	*1.5°* $^{(b)}$	*4 b.×65 MHz*	*4 Stokes*
LSS+LOFAR	*4512 X dipoles*	*134000 m^2* $^{(b)}$	*30-80 MHz*	*2"* $^{(b)}$	*8+b. ×4 MHz*	*4 Stokes*
SKA	>3000 dish.+AA	1000000 m^2	0.07-10 GHz	<0.1"	many beams	4 Stokes

A post-LOFAR-backend dedicated receiver would ingest locally the station products (as does ARTEMIS) and channelize, auto-/cross-correlate, and integrate them. A fully independent backend would perform the tasks of both the LOFAR backend and the central correlator, but in an optimized integrated way. A large computing power is required, but a preliminary design study suggests that this is within the scope of new generation FPGAs. Additional "intelligent" processing like RFI mitigation or parametric dedispersion could be included. Transient Buffer Board data will also be processed in all cases.

A dedicated receiver is important not only because it allows local, flexible processing, but primarily because it will greatly increase the duty-cycle of the LSS standalone use beyond the "guaranteed" 10% fraction of the time, albeit with some pointing constraints. With a post-LOFAR-backend receiver, usable in parallel to all LSS observations (standalone or in correlation with LOFAR LBA), the standalone analysis of LSS data will be possible 100% of the time during which the LSS tiles are connected to the FR606 backend, but the target will necessarily be within the 0.5°−3° LSS beam fixed by the current LOFAR observation program. Conversely, with a fully independent backend that would process LSS data in parallel with the standard station backend, standalone mode becomes possible 100% of the time, whatever array (LBA, HBA or LSS) is connected to the LOFAR backend. The only pointing constraint of this standalone LSS mode is that the target must be located within the 10°−50° analog LF tile beam.

6 Conclusion

The LSS characteristics are compared to those of other existing international instruments in Table 1. In the european context, several instrumental projects are developed by LOFAR participants, such as ARTEMIS (from Oxford Univ. − see above) or AARTFAAC (from Univ. Amsterdam − it aims at cross-correlating the 288 LBA and HBA signals from the 6 central LOFAR stations to perform permanent all-sky monitoring (Prasad 2012)). LSS is a LOFAR extension and a standalone instrument with emphasis on very high instantaneous sensitivity. We foresee it as an "Arecibo in Nançay". It is also a SKA precursor for the French community, both scientific (see above objectives) and technical (for SKA-low).

The team involved in the LSS design and prototyping gathers about 25 researchers and 15 engineers and technicians from 8 french laboratories (Nançay (USN), LESIA, GEPI, & LERMA of the Observatoire de Paris, LPC2E & Prisme in Orléans, Subatech in Nantes, and IRAP in Toulouse), and a strong technical and scientific support from the Kharkov Institute of Radio Astronomy (Ukraine) and from the Graz Space Research Institute (Austria). Potential users of the LSS also belong to LUTh, CEA (SAp, DASE & AIM), OCA, IAS, IAP, Univ. Lyon, ENS/LRA, E. Polytechnique, APC, and IN2P3. Foreign support has been expressed from ASTRON (the main LOFAR institute), Radbout Univ. Nijmegen, Oxford Univ., and several national LOFAR consortia (UK, Germany, Sweden, Ireland, and Latvia).

The LSS design study and prototyping was performed in the frame of an ANR contract ending in Feb. 2013. The last (ongoing) phase consists of extensive tests and characterization on the sky. The project was fully costed and represents in total 4-5 times the cost of a standard LOFAR station (incl. the dedicated independent standalone backend). Funding for construction is being looked for. The calendar of the construction phase will extend over 30 months. It will involve major participation of industrial subcontractors (many of them being situated in "Région Centre"), and at the same time be a major project of the Nançay radio observatory. In

construction and exploitation phases, the project code name will change from LSS to NenuFAR[i] (New extension in Nançay upgrading LOFAR). The outcome of the LSS design study will be made freely available to all European participants in LOFAR and more generally to all interested parties. If several LSS are built in Europe, they will collectively represent a further step in LF radioastronomy, beyond LOFAR.

The authors acknowledge the support of the Observatoire de Paris, the CNRS/INSU, and the ANR (French "Agence nationale de la recherche") via the program NT09-635931 "Study and Prototyping of a Super Station for LOFAR in Nançay".

References

Armour, W., Karastergiou, A., Giles, M. et al. 2011, in proc. ADASS XXI, eds. P.Ballester and D.Egret (ASP Conf. Series)

Asgekar, A., Oonk, J. B. R., Yatawatta, S. et al. 2012, A&A, submitted

Boone, F. 2001, A&A, 377, 368

Girard, J. N., & Zarka, P. 2012, A&A, submitted

Girard, J. N., Zarka, P., Tagger, M. et al. 2011, in Planetary Radio Emissions VII, eds. H. O. Rucker et al. (Vienna: Austrian Acad. Sci. Press), p. 495

Girard, J. N., Zarka, P., Tagger, M. et al. 2012, C.R. Phys., 13, 33

Mottez, F., & Heyvaerts, J. 2012, A&A, 532, A22

Prasad, P. & Wijnholds, S. J. 2012, in proc. New Windows on Transients across the Universe (Royal Society, London, April 2012)

Serylak, M., Karastergiou, A., Williams, C. et al. 2012, in proc. Electromagnetic Radiation from Pulsars and Magnetars conference, Zielona Gora, 2012)

van Haarlem, M. P., Wise, M. W., Gunst, A. et al. 2012, A&A, submitted

Vasko, F. J., Barbieri, R. S., Rieksts, B. Q., Reitmeyer, K. L., & Stott Jr., K. L. 2002, Computers & Operations Res., 29, 441

Visbal, E., Barkana, R., Fialkov, A., Tseliakhovich, D., & Hirata C. M. 2012, Nature, 487(7405), 70

Zakharenko, V. V., Vasylievz, I. Y., Konovalenko, A. A. et al. 2012, MNRAS, submitted

Zarka, P. 2011, in Planetary Radio Emissions VII, eds. H. O. Rucker et al. (Vienna: Austrian Acad. Sci. Press), p. 287

[i]Le projet dans les temps.

Session 20

Astronomy in the Antarctica: First results and perspectives

SF2A 2012
S. Boissier, P. de Laverny, N. Nardetto, R. Samadi, D. Valls-Gabaud and H. Wozniak (eds)

DOME C SITE TESTING: LONG TERM STATISTICS OF INTEGRATED OPTICAL TURBULENCE PARAMETERS AT GROUND LEVEL

E. Aristidi[1] and Astroconcordia team[1]

Abstract. We present long term site testing statistics obtained at Dome C, Antarctica with various experiments deployed within the Astroconcordia programme since 2003. We give values of integrated turbulence parameters in the visible at ground level and above the surface layer, vertical profiles of the structure constant C_n^2 and a statistics of the thickness of the turbulent surface layer.

Keywords: site testing, atmospheric effects

1 Introduction

The AstroConcordia program has been up to now, dedicated to the qualification of the site of Dome C, Antarctica, for astronomical purposes. After almost 10 years of operation since the first results (Aristidi et al. 2003) including 8 winterovers, we could measure long terms characteristics of the turbulent atmosphere and extract important parameters of the so-called "boundary layer" that we now understand quite well (global and temporal statistics). With the huge volume of data collected throughout the years, Dome C is probably among the most extensively characterized sites in the world, at least from the optical turbulence point of view. In this contribution we present the results of 8 years of turbulence monitoring. We give statistics of the seeing, the isoplanatic angle, the coherence time and the outer scale during the polar winter, at ground level as well as above the turbulent surface layer. We also give statistics of the thickness of the surface layer as estimated by various instruments.

2 The instruments

The instruments that were deployed on the site aim at characterizing the statistical properties of the optical turbulence. They can be split into two families: the "profilers" and the "integrators". The latter is composed of telescope-based instruments which observe a bright star in the visible wavelengths and perform continuous measurements of the seeing, the isoplanatic angle and the outer scale. These instruments named DIMM, Thetameter and GSM are described in previous papers (Aristidi et al. 2005, 2009, Ziad et al. 2008). Several DIMM were placed at different elevations to measure the seeing inside the turbulent surface layer discovered during the first winterover in 2005 (Agabi et al. 2006).

The other family includes all instruments capable of measuring vertical profiles of the refractive index structure constant $C_n^2(h)$ as a function of the altitude h. The balloon-borne microthermal sensors used in 2005 (Trinquet et al. 2008) and the sonic anemometers on the 45 m high mast (Travouillon et al. 2008) belong to this group and perform in-situ measurements (in the whole atmosphere for the balloons, inside the surface layer for the sonics). The Single Star Scidar (Vernin et al. 2009) and the Lunar Limb Profiler use optical techniques to access the turbulence profile though the observation of a bright star (scidar) or the lunar/solar limp (LLP). The latter was installed at Dome C in 2011 and the first winter data are under processing at the moment of writing this paper. Note that integrated parameters (including the coherence time of turbulence) can also be derived from some of these profilers (Balloons, SSS, LLP).

The period of operation of each instrument is summarized in Table 1.

[1] Laboratoire Lagrange, Parc Valrose, F 06108 Nice Cedex 2

3 Results

3.1 Statistics of integrated parameters

A complete statistics of integrated parameters in winter (period April to September) obtained with all the instruments is presented in table 2. Values are given for an altitude of 8 m above the snow. The seeing is actually poor because of the presence of a very turbulent surface layer (SL), but it was discovered (Aristidi et al. 2009) that the upper edge of this SL is very sharp. The seeing distribution splits into two regimes corresponding to the DIMM being inside or outside the SL, giving histograms composed of two bumps (Fig. 1). The area under these bumps depends on the altitude h above the ground: at $h = 20$ m, the DIMM spent 45% of the time above the SL. Statistics of the integrated parameters above the SL could be derived from profiler data (Balloons and SSS) as well as combined analysis of measurements from the 3 DIMM (Aristidi et al. 2009). They are given in Table 3.

As noticed by Bonner et al. (2010) for the case of Dome A which present similar properties, this situation is very peculiar. We are now convinced that site characterization in Antarctica can be performed by (i) measuring the properties of the SL (in particular its thickness) and (ii) measuring the free atmosphere turbulence parameters.

3.2 Thickness of the surface layer

The presence of a very turbulent surface layer in the first tens of meters above the ice of the plateau was discovered with the first balloon launches in March 2005 (Agabi et al. 2006). Several experiments were deployed to monitor this SL by in-situ measurements. The first one is a set of microthermal sensors (same sensors used on the balloons) placed in 2005 and 2006 on the 32 m high US Tower (800 m from the Concordia buildings). But the accumulation of ice on the sensors spoiled the results (and eventually broke the sensors). This approch was abandoned to the benefit of fast sonic anemometers able to estimate the structure constant of the temperature C_n^2 (Travouillon et al. 2008).

6 anemometers were deployed on the tower (which was prolongated up to 46 m in 2008) at regular altitudes from 8 m to 45 m. These instruments are periodically heated to prevent frost deposit. The period of the cycle was adjusted empiricaly by the winterers on site to optimize the quantity of usable data. The data are still under processing, but we start to obtain reliable measures as illustrated by the vertical profile of C_n^2 in Fig. 2. It is interesting to note that the histograms of all sonic data exhibit a two bumps structure, exactly like the DIMM. Fig. 3 shows the histograms of $\mathrm{Log}(C_n^2)$ in winter (April to September) for the anemometers at elevations 31 m and 39 m. On the same figure we displayed the histogram of balloon measurements taken in 2005 at the same altitude, which also show the same structure. The abcissa of the center of these bumps is the same in both cases. The leftern bump correspond to situations where the sonic is outside the surface layer and then to the histogram of $\mathrm{Log}(C_n^2)$ in the free atmosphere. From all sonic data, we can have an estimation of the median thickness of the SL at a value $h_{SL} = 35$ m. Once again, this is a preliminar number but is in agreement with the thickness published by (Trinquet et al. 2008). Table 4 summarizes published values of the surface layer thickness at Dome C.

		2003-2004	2005	2006	2007	2008	2009	2010	2011	2012
Integrators	DIMM									
	DIMM_ground									
	DIMM_roof		*2 months*							
	GSM									
	Thetameter									
Profilers	Balloons									
	SSS									
	Microthermals									
	Sonic				*(3)*	*(6)*	*(6)*	*(5)*	*(3)*	*(2)*
	PBL									

Table 1. Operating periods for each instrument (colored boxes). For Sonic we give also the number of available anemometers.

Table 2. Integrated parameters in winter (April to September) at an altitude of 8 m from various instruments. Meso-NH is a computer-based model developped by the Arcetri Observatory (Italy). A comparison with values at other sites is provided (the outer scale value for Mauka Kea is from (Schöck et al. 2002)).

	Seeing [arcsec]	Isoplan. angle [arcsec]	Coh. time [ms]	Outer scale [m]
DIMM/GSM	1.7 [1.0 – 2.4]	4.1 [2.7 – 5.9]		7.5 [5 – 11]
SSS (Giordano et al. 2012)	1.0	6.9	3.4	
Balloons (Trinquet et al. 2008)	1.4	2.7	5.7	
Meso-NH model (Lascaux et al. 2011)	1.7			
South Pole (Marks et al. 1999)	1.8	3.2	1.6	
Mauna Kea (Racine & Ellerbroek 1995)	0.6	1.9	2.7	17
Paranal (Sarazin 2012)	0.8	2.6	3.3	22

Table 3. Free astmosphere integrated parameters in winter (April to September) above the surface layer. AASTINO was an experiment deployed in 2004 by the University of New South Wales, Australia.

	Seeing [arcsec]	Isoplan. angle [arcsec]	Coh. time [ms]
DIMM/GSM (Aristidi et al. 2009)	0.4	4.1	
SSS (Giordano et al. 2012)	0.3	6.9	10.2
Balloons (Trinquet et al. 2008)	0.4	2.7	6.8
AASTINO (Lawrence et al. 2004)	0.3	5.7	7.9
Meso-NH model (Lascaux et al. 2011)	0.3		

Fig. 1. Left: Seeing histogram at an elevation of $h = 8m$ for the period April to September. **Right:** Idem for $h = 20m$ from available data in 2005 and 2012. Red (solid) and blue (dashed) lines are Gaussian fit of the two bumps. They give the fraction of time spent by the DIMM inside (blue line) or outside (red line) the SL. At $h = 20m$ the DIMM is in the free atmosphere 45% of the time (12% at $h = 8m$).

4 Conclusions

We have presented statistics of the optical turbulence at Dome C in winter, using all data collected by our instruments since 2004. We confirm the general scheme of a thin but strong turbulent layer above the surface, which cause the ground seeing to be very poor, as well as the coherence time. Above this surface layer whose thickness is measured between 27m and 35m, the conditions are exceptionnal, the seeing can attain values of 0.4 arcsec half of the time. We also discovered that the distribution of the values of C_n^2 and the seeing display a bimodal structure. This indicates, as pointed by (Aristidi et al. 2009), that the upper edge of the surface layer is very sharp and that a telescope at a given altitude would be either inside or outside this surface layer with very little intermediate cases.

The authors gratefully acknowledge the polar agencies IPEV and PNRA, the US NSF and the french agencies INSU and ANR for logistical support and funding. We are in debt to the Dome C local staff and winter-overs of 2005 to 2012 for their assistance.

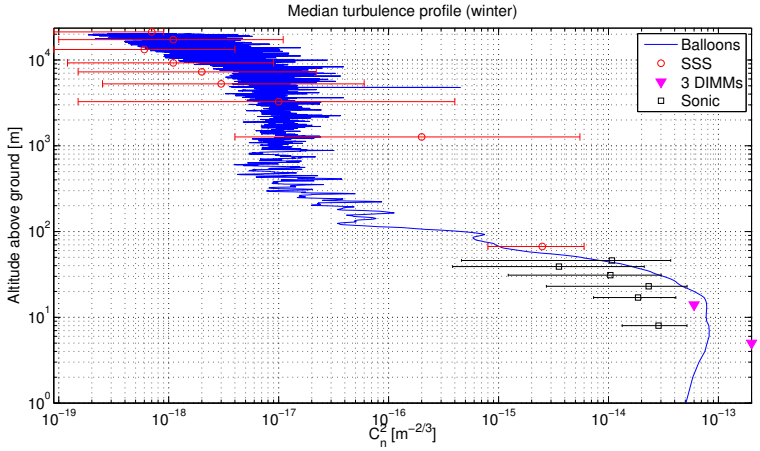

Fig. 2. Median vertical profile of the structure constant C_n^2 as a function of the altitude above the ground, measured by various instruments.

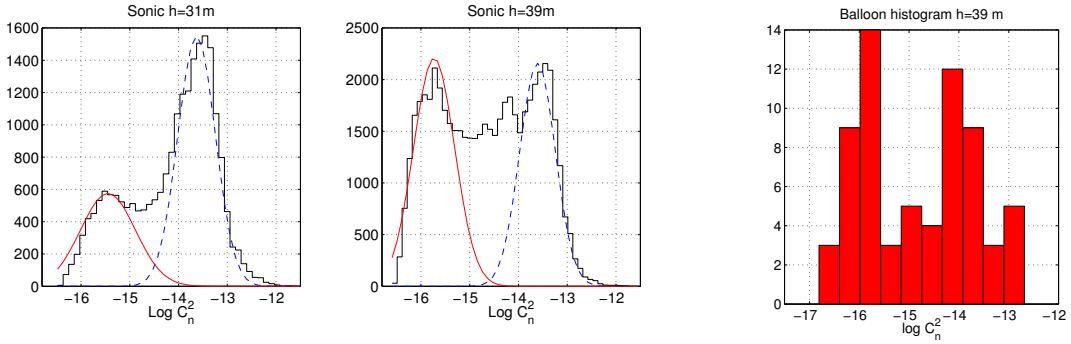

Fig. 3. Left: Histogram of Log(C_n^2) in winter (April to September, 2008 to 2011) measured by the sonic anemometer at an elevation of 31 m. The structure constant C_n^2 is in $m^{-2/3}$. The data being still under processing, these results are preliminar. **Middle:** Same for the sonic at 39 m. **Right:** Histogram of Log(C_n^2) measured by the balloon-borne experiment in 2005 at the elevation $h = 39$ m ($\simeq 80$ values. available).

References

Agabi, A., Aristidi, E., Azouit, M., et al. 2006, PASP, 118, 344
Aristidi, E., Agabi, A., Fossat, E., et al. 2005, A&A, 444, 651
Aristidi, E., Agabi, A., Vernin, J., et al. 2003, A&A, 406, L19
Aristidi, E., Fossat, E., Agabi, A., et al. 2009, A&A, 499, 955
Bonner, C., Ashley, M., Cui, X., et al. 2010, PASP, 122, 1122
Giordano, C., Vernin, J., Chadid, M., et al. 2012, PASP, 124, 494
Lascaux, F., Masciadri, E., & Hagelin, S. 2011, MNRAS, 411, 693
Lawrence, J., Ashley, M., Tokovinin, A., & Travouillon, T. 2004, Nature, 431, 278

	h_{SL} $[m]$
Sonic	35
Balloons (Trinquet et al. 2008)	33 [23 – 42]
DIMMs (Aristidi et al. 2009)	27 [16 – 54]
Meso-NH model (Lascaux et al. 2011)	44 [20 – 69]

Table 4. Median thickness of the turbulent surface layer, estimated from various instrument as well as the Meso-NH code. Values in brackets are the 1st and 3rd quartile.

Marks, R., Vernin, J., Azouit, M., Manigault, J.-F., & Clevelin, C. 1999, A&A, 134, 161

Racine, R. & Ellerbroek, B.-L. 1995, in Proc. SPIE Vol. 2534, Adaptive Optical Systems and Applications, ed. R.-K. Tyson & R.-Q. Fugate (SPIE), 248–257

Sarazin, M. 2012, `http://www.eso.org/gen-fac/pubs/astclim/paranal/`

Schöck, M., Ziad, A., Chun, M., et al. 2002, Internal report

Travouillon, T., Aristidi, E., Fossat, E., et al. 2008, in Proc. of the SPIE, vol. 7012, Ground-based and Airborne Telescopes II, ed. L. Stepp & R. Gilmozzi (SPIE), 70124B–70124B–5

Trinquet, H., Agabi, A., Vernin, J., et al. 2008, PASP, 120, 203

Vernin, J., Chadid, M. Aristidi, E., Agabi, A., Trinquet, H., & van der Swaelmen, M. 2009, A&A, 500, 1271

Ziad, A., Aristidi, E., Agabi, A., et al. 2008, A&A, 491, 917

SF2A 2012
S. Boissier, P. de Laverny, N. Nardetto, R. Samadi, D. Valls-Gabaud and H. Wozniak (eds)

ANTARCTIC OPTICAL/IR ASTRONOMY, BRIGHT FUTURE OR DEAD-END

N. Epchtein[1]

Abstract. A few thoughts about optical/IR Antarctic astronomy 3 years after the conclusions of the European network ARENA.

Keywords: Antarctica, Infrared Surveys, Astronomical prospects

1 Antarctic astronomy, the context

A decade ago, many optical/IR astronomers were keen on the awesome potential of the Concordia station at Dome C to carry out breaking observations at almost every wavelengths and envisioned the study of an international facility over there.

Although millimetre-wave observations had been carried out for several decades from the US station Amundsen–Scott at the South–Pole, mostly to investigate the properties of the cosmological background, very little was done in the optical/IR range, except the Australian–US SPIREX attempt (Burton *et al.*, 2000). Promising prospects were expected with the opening of the French Italian station Concordia at Dome C, the first exciting measurements of the optical turbulence properties above this site (Lawrence *et al.*, 2004, Aristidi *et al.*, 2009) and IRAIT, the Italian project of 80-cm infrared telescope. Prospects were also made to study the design of larger instruments including 2-m multipurpose telescopes such as the Australian PILOT or even more sophisticated optical/IR interferometers and radiotelescopes.

By 2005, the enthusiasm of astronomers leads in Europe to the creation of a coordinated action of the Research Infrastructure (FP6) of the European Commission to evaluate the potential of Concordia in various observational techniques and spectral domains. The European network, ARENA, started activity in 2006 under my coordination. Although I had not been previously involved personally in Antarctic activity, my interest stemmed from the unique possibility of extending deep infrared wide–band surveys beyond the limit of 2.3 μm that cannot be adequatly overcome from the ground because of the high thermal brackground emission of the sky above usual ground sites.

Three years after the release of the decadal *vision* of ARENA (Epchtein 2010), I thought useful to take stock of the situation and revisit these prospects in a somewhat deteriorated context essentially dominated by the repercussions of the economical *crisis*, the uncertainties about funding large future projects such as the E-ELT in Europe, somewhat tempered by the rise up of the Chinese potential and enthusiasm with the creation of a new Antarctic station at Dome A (Kunlun) (see *e.g.*, *Phys. Today, Jan 2011*) a result of the International Polar Year (2007-8).

These facts lead me to propose this small workshop in the framework of the Sf2A annual meeting 2012, and in advance of the Symp. 288 to be held subsequently in Beijing (Burton *et al.*, 2013).

2 Prospects *vs.* reality

The ARENA network lasted for 4 years (2006-2009) with an overall budget of 1.3 Meuros. It dealt with 4 main topics: i) aggregate results and support new obervations of the atmospheric properties, mostly from Dome C, ii) evaluate the most suitable science cases that could take full benefit from Antarctic conditions, iii) draft instrumental concepts and support instruments already in their implementation phase, iv) estimate the logistics requirements to build and operate these instruments. It involved about 20 laboratories in 7 European countries

[1] CNRS, UNS, OCA, Parc Valrose, Nice, France (epchtein@unice.fr)

(De, Fr, It, UK, Pt, Sp, Be) and Australia. Reports on the work achieved during the 4 years were essentially gathered in the proceedings of the 3 ARENA conferences (Epchtein & Candidi 2007, Zinnecker *et al.*, 2008, Spinoglio & Epchtein 2010), and the decadal vision. They resulted from an excellent collaboration between laboratories and the Polar Agencies. Accent was put on middle-size projects rather than on small size instruments that do not require international collaborations for their implementation and exploitation. This was mainly aimed to make a step forward from "team" instruments, to some facility managed in an international context. Unfortunately, the conclusions occured during the worst period of the "world crisis".

2.1 The ARENA conclusions

Six working groups were set up to propose a set of recommendations in their respective areas. Each of them supported a few science cases and one or several instrumental concepts able to undertake them. Their conclusions are summarized in six reviews dealing with, i) the study of a 2 m class wide field optical/IR telescope, ii) a prototype of optical/IR interferometer (called Aladdin), iii) a submillimetre-wave antenna (AST), iv) 3 small telescopes, namely, IRAT, Ice-T and SIAMOIS, v) BRAIN a project to measure the polarization of the CMB, and vi) a solar coronograph. These reviews were prepared by Burton *et al.*, Coudé du Foresto & Surdej, Minier *et al.*, Rauer & Deeg, De Bernardis *et al.*, Damé & Andretta, respectively; all published in the Proceedings of the last ARENA conference (Spinoglio & Epchtein 2010)

2.2 What remains of these conclusions

Several highly interesting and well advanced projects were simply abandoned even in the "small" category for lack of further funding and resources or for unability to set up a robust international collaboration, SIAMOIS, Ice-T and the large submillimetre-wave antenna, AST. Of course, unrealistic project such as KEOPS (kilometric interferometric array) or even ALADDIN were simply disregarded or put aside. What finally remained active in 2012 are, the IRAIT telescope, which will eventually get its first IR light in 2013 after a succession of disappointments and funding shortages, the ASTEP transit telescope currently producing fine data on planetary transits of extrasolar planets (Rivet *et al.*, 2013) and the CMB BRAIN project. Among the larger projects that made progress in the meantime is a 2-m class telescope following the PILOT phase-A study made by the Australians (Lawrence *et al.*2009abc), which, in my opinion, should be entirely dedicated to a new generation infrared survey (see section 3) and for which a European Consortium was set up to submit a proposal of Design Study in 2010 under the name *Polar Large Telescope (PLT)* (Epchtein *et al.*, 2010, 2011).

2.3 Antarctic Astronomy vision revisited

There is little doubt that the vision elaborated by the ARENA consortium for this decade will not be achieved, at least in the foreseen timeline. There are several reasons for that, number one is the crisis that stroke the entire world and particularly Europe. Besides, there is still persisting doubts about the feasibility of building and operating large instruments in polar environment, a loss of enthusiasm of most actors (*e.g.*, IRAIT project), the disappointments about the thickness and time behaviour of the turbulent layer above Dome C requiring the erection of extremely stiff towers of several tens of meters, the underestimation of development timeline, finally the lack of an extremely convincing (so called, "killer") science case that would justify the cost of a large facility. Is big Antarctic Astronomy in a dead-end? My answer, at the present time is yes at Dome C and for the optical/IR range, owing to the stressed economical environment and as long as there is no official strong international organization able to manage an overall astronomy programme in Antarctica. To overcome these difficulties, one must continue to improve and better specify the scope of the projects following the progress of other large instruments, to single out more accurately the specificity of the antarctic conditions and their advantages, proceed with comparative atmospheric monitoring on the various existing sites and, possibly, on still undocumented ones, implement and operate relatively low demanding resources demonstrators, for instance, Ground Layer Adaptie Optics devices, and towers to monitor the atmospheric parameters in the 20-30m height range above ice.

3 Toward a new generation of infrared large scale surveys, possible role of an Antarctic telescope

The next generation of large astronomical instruments either set up on the ground (30-40 m class telescopes such as the E-ELT the TMT etc..) or space borne (JWST) will require a new generation of large scale optical/IR

surveys, providing lists and basic properties of sources fainter by several orders of magnitudes than those archived in currently available databases (*e.g.*, 2MASS or even VISTA). In the optical range, the LSST, will probably provide the necessary bank of data, but little has been investigated to provide similar data in the near-infrared range, so far, in order to extend VISTA surveys to fainter magnitudes, longer wavelengths (K_d, L_s) and to the northern sky, possibly from an Arctic site (Greenland) providing atmospheric conditions german to those prevailing in Antarctica.

The present projects for a new generation IR survey are essentially SASIR a US-Mexican initiative to survey the sky from San Pedro Martir (Mexico) (Bloom *et al.*, 2009) and the NISSA project using the PLT in Antarctica (Epchtein *et al.*, 2011, 2013), which could make use of a 2 to 4 m off-axis mirror configuration (Moretto *et al.*, 2013), the KDUST telescope currently envisioned by the Chinese teams at Dome A, and the Australian project proposed by Mould (2011). Attempts are currently made to merge all these projects because they have very similar objectives.

4 Conclusions

Mainly for economical *"crisis"* reasons, but also for lack of a sufficiently striking science case, the development of optical/IR Antarctic Astronomy is now in standby (all recent attempts that I made to raise funding from EC and ANR failed and none was supported by our agencies). The worldwide interest raised 7 years ago has somewhat weakened and the much expected *"Europeanization"* of Concordia has essentially failed to the great disappointment of our potential partners. Althoug time is probably not ripe for big investments there, it does not mean that one must give up definitively, but clearly a great opportunity has been missed, mostly because of the versatility of our Research Agencies and their unability to set up a robust long term vision in this topic. Concordia costs quite a lot of money to the French and Italian tax payers and cutting a promising exploratory branch for which French and Italian teams are exquisitely well trained, expert and deeply involved is not an error, it is a fault. We are now facing a situation in which China, Australia and the USA will probably be able to set up a consortium that will manage an international project at Dome A, but without a renewed strong impetus, Europeans will certainly stay on the roadside.

References

Abe L. *et al.*, 2013, Proc. Symp. IAU, 288, Beijing (in press)

Aristidi E., Fossat E. Agabi, A. *et al.*, 2009, A&A, 499, 955

Bloom J., *et al.*, 2009, arXiv:0905.1965v2

Burton M. *et al.*, 2000, ApJ 542, 359

Burton M., Cui X., Tothill N. (eds.), 2013, Proc. Symp IAU 288 on *Astrophysics from Antarctica* (in press)

Epchtein N. (coordinator) and the ARENA consortium, 2010, *A Vision for European Astronomy and Astrophysics at the Antarctic station Concordia, DomeC* , the ARENA roadmap, Novaterra (download at: `http://arena.oca.eu`)

Epchtein, N., Candidi M. (eds.), 2007, Procs. first ARENA Conference on *"Large Astronomical Infrastructure at Concordia, prospects and constraints for Antarctic Optical/IR Astronomy*, Roscoff, 2006, EDP EAS Ser. Vol. 25 (ARENA1)

Epchtein N. (coordinator) and the PLT Consortium, *A proposal for the Design Study of a Large Polar Telescope*, submitted to the EC RI call # 10 of the 7^{th} Framework Program in November 2010.

Epchtein N., *et al.*, Proc. Conf. Sf2A 2011 p. 10

Epchtein N., *et al.*, *NISSA A New Infrared Synoptic Survey from Antarctica* (in preparation)

Lawrence J.S., Ashley M.C.B., Tokovinin A., Travouillon T., 2004, Nature, 431, 278

Lawrence *et al.*, 2009abc, PASA, **26**, 379, 397, 415

Moretto G. *et al.*, 2013 Proc. SPIE Vol. 8444, 84445E, Amsterdam 2012 (in press)

Mould J., 2011, PASA, 28, 266

Rivet J.-P. *et al.*, 2013, Proc. Symp. IAU, 288, Beijing (in press)

Spinoglio L., Epchtein N. (eds.), 2010, Procs. third ARENA Conference on *"An Astronomical Observatory at Concordia (Dome C, Antarctica)"*, Frascati 2009, EDP EAS Publication series, Vol. 40 (ARENA3)

Zinnecker H., Epchtein, N., Rauer R. (eds.), 2008, Procs. second ARENA Conference on *"The Astronomical Science Cases at Dome C"*, Potsdam, 2008, EDP EAS Ser. , Vol. 33 (ARENA2)

SF2A 2012
S. Boissier, P. de Laverny, N. Nardetto, R. Samadi, D. Valls-Gabaud and H. Wozniak (eds)

AN OFF-AXIS TELESCOPE CONCEPT FOR ANTARCTIC ASTRONOMY

G. Moretto[1], I. Vauglin[2], M. Langlois[2] and N. Epchtein[3]

Abstract. The site of the CONCORDIA station at Dome C on the Antarctic Plateau offers exceptional atmospheric and environmental conditions for astronomical observations over a wide range of wavelengths and is uniquely favorable to infrared astronomy. To make the best use of these exceptional environment, especially the very low sky brightness throughout the near- and mid-infrared, we must develop a telescope offering the highest possible dynamic range for photometry, a high angular resolution and a wide-field. In these conditions, a modest-sized 2m off-axis telescope achieves comparable sensitivity to that of a larger ground-based 8-10m class telescope or a same sized space-borne ones.

Keywords: off-axis telescope, infrared astronomy, Antarctic astronomy

1 Introduction

The properties of the atmosphere above the Antarctic Plateau are known to be unique on the Earth surface. Atmospheric turbulence is concentrated in a thin layer of a few tens of meters, the sky transparency, particularly in the infrared, is considerably increased and the thermal infrared sky background radiation is lower by a factor of 10 to 20 in the 2-3 μm windows (Philips et al. 1999). The combination of these advantages makes a 2m class telescope comparable to an 8m one in a conventional site in terms of sensitivity.
The Antarctic Plateau is thus likely to become in the coming decades a new major platform for advanced astronomical observations. A medium/large aperture telescope on the Antarctic Plateau have the potential to undertake tasks previously thought to be possible only in space, for example, the imaging and crude spectroscopy of Earth-like extra-solar planets (Angel, Lawrence and Storey, 2004). In the short/medium term, it is expected that infrared imaging and spectro-imaging surveys, from Antarctica could play an critical role in the context of the future large ground based and space projects such as E-ELT, JWST, LSST, EUCLID, GAIA.
Three astrophysical key-domains for an optical/IR facility had been identified in the ARENA vision (2010), namely (1) the search and characterization of Type Ia supernovae and the investigation of the distant Universe, (2) the stellar populations and evolution in the local group of galaxies, (3) the identification and characterization of extra-solar planets.
We present here a new preliminary concept of telescope able to achieve the three above mentioned key-domains. Such concept offers a wide range of cutting edge technological investigations that would definitely overcome the scope of Antarctic astronomy.

2 Why an off-axis telescope in Antarctica?

An off-axis telescope is the only way to capitalize the exceptional atmospheric and environmental antarctic conditions for astronomical observations in the near- and mid-infrared. An off-axis telescope provides an inherently low scattered light design because there are no obstruction in the beam. All mirrors can be robustly supported and articulated because of the easy access allowed by this design. All warm components, sources of the telescope self-thermal emission, will be out of optical beam minimizing its emissivity. Such a design reduces the sources

[1] Institute of Nuclear Physics of Lyon, IN2P3-CNRS, Université de Lyon, F-69622, Lyon, France
[2] Centre de Recherche Astrophysique de Lyon, UMR 5574, F-69230, Saint-Genis Laval, France, Université Lyon1, Université de Lyon, F-69622, Lyon, France
[3] Laboratoire Lagrange, UMR 7293, Université de Nice Sophia Antipolis, F-06000, Nice, France

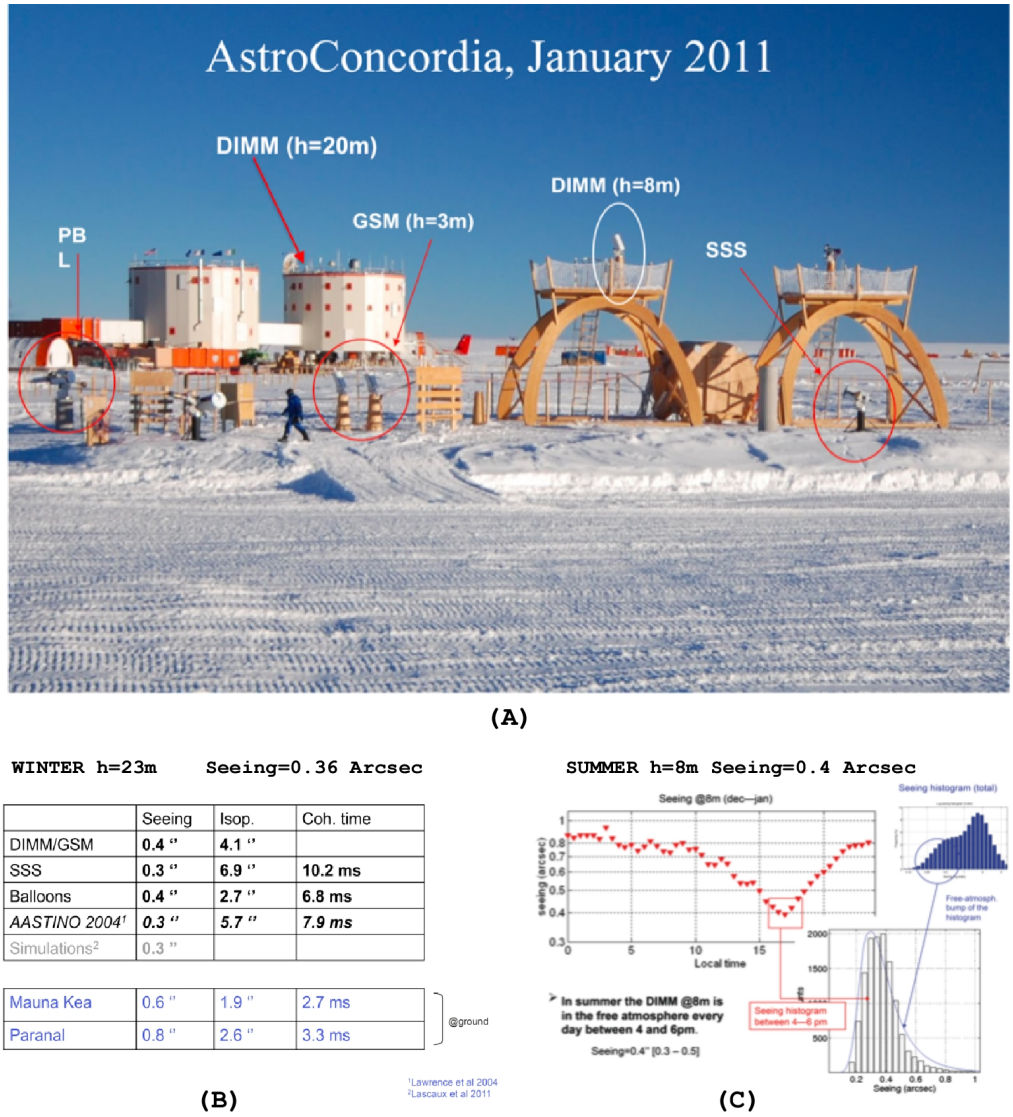

	Seeing	Isop.	Coh. time
DIMM/GSM	**0.4 ''**	**4.1 ''**	
SSS	**0.3 ''**	**6.9 ''**	**10.2 ms**
Balloons	**0.4 ''**	**2.7 ''**	**6.8 ms**
AASTINO 2004[1]	***0.3 ''***	***5.7 ''***	***7.9 ms***
Simulations[2]	0.3 ''		
Mauna Kea	0.6 ''	1.9 ''	2.7 ms
Paranal	0.8 ''	2.6 ''	3.3 ms

Fig. 1. The French/Italian Concordia base at Dome C - showing in the backline the staff headquarters (two cylindrical structures) and in the frontline the seeing measurements instruments. The data for winter and summer seeing measurements are presented respectively by (D) and (C), from Aristidi et al. (2009)

of light scattering and self thermal emissivity.
This is a tremendous advantage for studies of planets near bright stars and faint nebulosity surrounding young stars, where planets may be forming. Moreover, it has no azimuthal PSF structure, no missing or interpolated wavefront errors. That is natural advantages for interferometry and adaptive optics performance!
Thus to have the highest possible dynamic range for photometry and angular resolution from the optical to thermal infrared, an off-axis design optimized for low scattered light and low emissivity is needed. Besides, a 3-mirror design optimized to get a wide field of view is called to achieve wide-field imaging.

3 Optical design

A precise description of this off-axis 2.5m telescope for Antarctica is given in Moretto et al. (2012).
Optically speaking an off-axis telescope is not an asymmetric system, it is a decentered system preserving its bi-lateral symmetry. This means that the system preserves many of the optical performances, tolerances and sensitivities characteristics of the parent concentric system - a deal for system opto-mechanical alignment. A three-mirror decentered Paul-Baker (Paul, 1935; Baker, 1969) system is our guideline concept reference, where

some variation on the shape of the three mirrors is allowed to achieve good image quality across a wide field of view. One of the main constraints during such optimizations is the necessity to have compact designs, making it possible to be installed on top of a ≥20m high tower to overcome the boundary layer that extends between 2m to 23m (Gredel 2010).

A preliminary study gives the design presented in Fig.1. A baseline design for Dome C relies on a 2.5 meter unobstructed aperture M1 which should produce a F/8 system optimized over an 1deg x 1deg field of view. We generate a Paul-Baker configuration by adding auxiliary convex secondary mirror (M2) and a concave tertiary (M3).

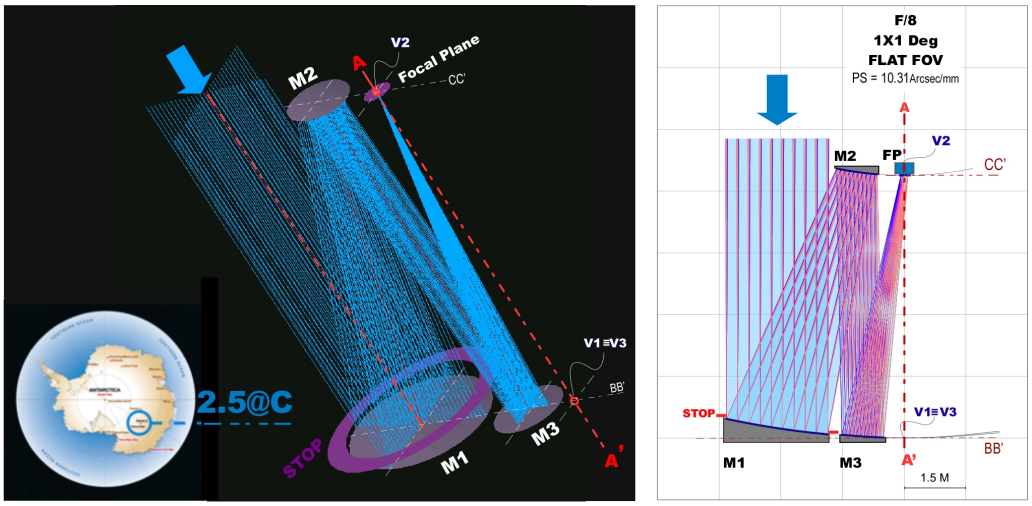

Fig. 2. The design of an off-axis telescope for Dome C. A 2.5 meter unobstructed aperture M1 yielding in a F/8 system optimized over a 1x1 deg FOV. *AA* is the parent mirrors M1, M2 and M3 optical axis. M1 and M3 verteces V1 and V3 are coincident as well as for M2 (V2) and FP. Note that the primary mirror M1, the secondary M2 and the tertiary M3 are not tilted mirrors but are a decentered piece of concentric system, preserving its bi-lateral symmetry.

The plate scale is 10.31 arcsec/mm. The decision on plate scale is a compromise between an optimal sampling for high resolution and a compact design. An effective focal length (EFL) of 20m produces a support structure long of $V1V2 = V1FP < 7m$, short enough for our proposes.

We consider a typical detector pixel size of 15 μm, which for an $EFL = 20m$ results in a sampling of $FWHM = 2.35$ pixels. This is the Nyquist criterion, the standard deviation. Some discussion has been flown confirming that a sampling of $FWHM = 3.5$ pixels or more is the optimal for high resolution.

The optical performance at the edges of 1x1 Deg2 FOV is show in Fig. 2. The PSF spots at corner-edges (F5, F6, F8, F9) of 1x1 Deg2 FOV are diffraction limited at 1000nm wavelength and elsewhere they are diffraction limited at 550nm or even better. Note that the blur in this system is only weakly dependent on the off-axis angle and the telescope will be entirely seeing limited.

4 Conclusions

In terms of feasibility there are several myths about off-axis telescopes. Many areas of modern astrophysics are not flux-limited but are rather dynamic-range limited. Simply collecting more photons will not solve the problem: for these topics, *we don't need bigger telescopes,* **we need better telescopes set up at exceptional sites**. We need off-axis telescopes! Moretto et al (2012) reviewed the technology of off-axis telescope and show their present feasibilyty.

This new telescope concept allows exceptional dynamic range for photometry and high angular resolution + wide field imaging and capitalizes the exceptional atmospheric and environmental Antarctic conditions for astronomical observations over the optical and thermal infrared wavelengths is what we proposed.

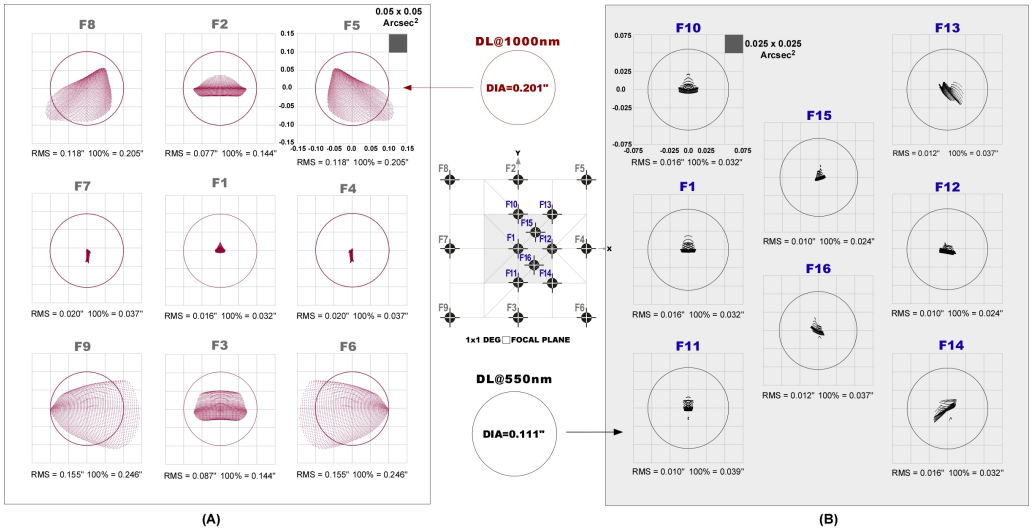

Fig. 3. The geometric optical performance over a flat FOV. (A) The PSF computed on the edge and center of a 1x1 deg2 FOV. The PSF computed across a 0.5 x 0.5 deg2 FOV is shown in (B). DL stands for diffraction limit diameter at 1000nm and 550nm wavelength. Note in (A) the spots F8&F5, F7&F4 and F9&F6 confirm the optical bi-lateral symmetry of a decentered system

References

Angel, R., Lawrence, J., Storey J. 2004, Proc. SPIE 5382 (Part 1), 76-84

ARENA consortium 2009, A vision for European Astronomy and Astrophysics at the Antarctic station Concordia, Dome C in the next decade 2010-2020, ed., N. Epchtein, (Publisher Nova Terra)

Aristidi, E., Fossat, E., Agabi, K., et al. 2009, A&A, 499, 955

Baker, J.G. 1969, IEEE Transactions of Aerospace and Electronic System, AES-5, 26

Gredel, R., Proc. 3rd ARENA Conf., eds. L. Spinoglio & N. Epchtein 2012, EDP EAS Ser. Vol. 40, 11

Moretto G., Epchtein N., Langlois M., Vauglin I. 2012, Proc. of SPIE Vol. 8444, 84445E

Moretto, G., Kuhn, J.R. and Goode P. 2012, Proc. of SPIE Vol. 8444, 8444OY

Paul, M. 1935, Rev. Opt. 14, 169

Phillips, A., Burton, M.G., Ashley, M.C., et al. 1999, ApJ, 527, 1009

Session 22

Patrimoine des OSU

SF2A 2012
S. Boissier, P. de Laverny, N. Nardetto, R. Samadi, D. Valls-Gabaud and H. Wozniak (eds)

LES COLLECTIONS D'ASTRONOMIE ET D'ASTROPHYSIQUE : PROBLÈMES ET PERSPECTIVES

J. de La Noë[1] and C. Ducourant[1]

Résumé. Les collections patrimoniales astronomiques françaises sont considérables et très variées. Dans les différents OSU, des initiatives importantes de sauvegarde, conservation et exploitation ont été réalisées et sont en cours. Mais il y a méconnaissance importante entre les différents OSU. Il est important de développer la concertation des responsables des collections patrimoniales d'astronomie pour une meilleure connaissance mutuelle des mesures prises dans chaque établissement pour ce qui concerne de nombreux problèmes de tous ordres. Cela prend son sens dans la valorisation des collections d'astronomie auprès du public et son exploitation en concertation avec les historiens des sciences. Au stade actuel de l'existant dans les OSU et dans un contexte national difficile, la création d'un réseau pérenne de responsables de collections permettra une politique cohérente de soutien, de conservation et de valorisation des collections d'astronomie en France.

Keywords: History and philosophy of astronomy

1 Introduction

Depuis les années 1990, sous les auspices de la concertation du Ministère de la Recherche via l'INSU et du Ministère de la Culture et de la Communication, Françoise Le Guet Tully, Jean Davoigneau et de nombreux collègues, ont réalisé un important travail de sensibilisation de la communauté scientifique sur l'inventaire, l'histoire, la protection et la valorisation du patrimoine astronomique en France en collaboration avec les DRAC régionales.

Plus récemment Emmanuel Pécontal et Evelyne Damm ont effectué une tournée des observatoires afin d'établir un état des lieux de la situation du patrimoine astronomique. Ils ont rédigé un rapport[i] qui est présenté ci-après. François Vernotte a développé un travail de sensibilisation de la direction de l'INSU et des directeurs d'OSU sur cette mission avec l'idée de la formation d'un réseau des responsables lors d'une réunion qui s'est tenue le 30 janvier 2012 au siège du CNRS. Les participants souhaitaient qu'un tel réseau soit soutenu financièrement par la direction de l'INSU qui n'a malheureusement pu satisfaire ce souhait. Il s'en est suivi une très forte déception du non-engagement de l'INSU.

Cependant il est apparu qu'en dépit de l'absence d'un soutien national, les responsables de patrimoine astronomique étaient en mesure de s'organiser pour se coordonner et travailler ensemble par eux-mêmes. En conséquence, sans remettre un tel projet à plusieurs semaines ou mois, il a été convenu d'organiser une session « Patrimoine astronomique des OSU » à l'occasion de l'assemblée générale annuelle de la SF2A. Nous sommes reconnaissants aux organisateurs et aux membres du conseil d'administration d'avoir accepté ce projet tardif qui fait l'objet de la session 21.

2 Quelques éléments importants

Il nous paraît important de rappeler quelques éléments généraux sur les collections. Tout d'abord, les collections patrimoniales astronomiques sont constituées de propriétés, de bâtiments, d'instruments associés à certains bâtiments, de petits instruments, de clichés astronomiques et divers, de fonds d'ouvrages anciens et d'archives

[1] Laboratoire d'Astrophysique de Bordeaux, Observatoire Aquitain des Sciences de l'Univers, 33270 Floirac, France

[i] Évelyne Damm et Emmanuel Pécontal, Rapport sur l'état du patrimoine astronomique dans les observatoires français de la fin du XIXe siècle, 2012, cette publication.

anciennes et récentes car ouvertes aux astronomes partant à la retraite, et d'archives orales. La majorité des collections d'astronomie appartiennent aux universités auxquelles sont rattachés les observatoires (sauf l'Observatoire de Paris qui a le statut d'une université), et donc à ce titre elles sont la propriété des observatoires des sciences de l'univers. Actuellement, il y a un très gros effort de sensibilisation des responsables d'université sur l'ensemble de leurs riches collections universitaires à plusieurs niveaux, localement dans les universités, nationalement à la Conférence des présidents d'université par la présentation d'un manifeste pour le patrimoine universitaire en préparation lors de la récente réunion sur les collections universitaires de Strasbourg, et internationalement en Europe et dans le monde. Dans les observatoires, il existe de nombreuses initiatives pour la sauvegarde, la conservation adéquate, la protection et l'exploitation mais grande méconnaissance mutuelle des mesures prises et travaux effectués. Il s'agit donc d'engager dès maintenant un processus d'information mutuelle, de concertation, d'entraide et de collaboration pour, à terme, disposer d'une collection globale d'astronomie cohérente.

Selon les établissements, de nombreuses questions se posent qui ont parfois trouvé réponse dans certains d'entre eux. Nous pouvons en dresser une liste non exhaustive :

- Des problèmes juridiques à clarifier : quel(s) est/sont le/les propriétaire(s) des collections ou de parties de collections d'astronomie
- Des problèmes d'inscription par les Conservations régionales des Monuments historiques, puis de classement au niveau national : quel établissement est inscrit ou protégé ? quel observatoire ne l'est pas ? que faut-il préconiser ? quelles procédures faut-il engager ? et par quelle instance ? On considère très important de pouvoir bénéficier des avis et conseil d'un représentant de la DRAC ou du Ministère de la Culture.
- Des besoins pour la sauvegarde et la conservation des coupoles et des grands instruments que ce soit pour l'entretien les systèmes mécaniques et des circuits électriques.
- Des difficultés de tri et de sauvegarde des petits instruments : faut-il tout garder ? quels éléments conserver même si la valeur esthétique est absente ? Comment assurer la protection contre le vol pour les instruments qui ont de la valeur.
- Faut-il conserver tous les clichés astronomiques sur plaques de verre ? dans quels lieux ? dans chaque établissement ? ou les rassembler dans un même établissement ? Dans tous les cas il faut assurer une conservation à température et hygrométrie constantes ?
- Faut—il également conserver les collections d'héliogravures des « cartes du ciel » imprimées ?
- Les fonds d'ouvrages anciens de nos bibliothèques nécessitent des soins spécifiques de conservation, d'inventaire, de manipulation et surtout de référencement dans le catalogue collectif SuDoc. Peut-être faut-il proposer une concertation des responsables de bibliothèques des OSU ?
- Se pose aussi la question des archives anciennes et modernes qui doivent rester ouvertes pour accueillir les archives des personnels partant à la retraite : une fois établi leur inventaire, où les conserver dans les OSU ou les déposer aux Archives départementales ?
- Comment valoriser les collections d'astronomie auprès du public ? visites, journées portes ouvertes, parcours d'interprétation, centre d'animation astronomique ? Quels personnels : les astronomes et personnels de la recherche ? Des médiateurs professionnels ?
- Enfin, lancer des concertations avec les historiens des sciences pour identifier les travaux de mastère et de thèse à envisager, mais aussi envisager des travaux d'histoire des sciences ou d'épistémologie, éventuellement inter-établissements avec des chercheurs de laboratoires comme le Centre François Viète de Nantes, l'Atelier-Sciences-Histoire-Cité de l'UPMC, Laboratoire SPHERE de l'Université Paris-Diderot, et bien d'autres ...

3 Conclusion

Nous venons d'établir une liste non limitative de questions très concrètes à discuter entre tous les responsables de patrimoine des OSU pour trouver des solutions cohérentes même si elles ne sont pas adoptées de façon identique dans tous les OSU. Pour mettre en place une concertation, une meilleure connaissance réciproque des responsables est absolument indispensable ainsi qu'une meilleure connaissance de ce qui se fait ailleurs. Il est urgent de développer l'entraide et la concertation entre les établissements. C'est pourquoi nous plaidons pour la mise en place d'un réseau des responsables de patrimoine des OSU et autres observatoires français, qui serait coordonné par un animateur pour une durée limitée de deux ou trois ans. Enfin nous suggérons de prévoir une réunion annuelle à l'occasion des assemblées générales de la SF2A. Nous espérons très fortement que cette session pourra aboutir à un tel projet.

4 Post-scriptum

Après discussion à la fin de la session, il est donc décidé de fonder un réseau de responsables et de spécialistes du patrimoine, avec un animateur pour une durée limitée de deux à trois ans. Ce réseau prévoira au moins une réunion annuelle à l'occasion des assemblées générales annuelles de la SF2A. Emmanuel Pécontal, astronome adjoint au Centre de Recherche Astrophysique de Lyon a accepté d'être le premier animateur de ce réseau. Nous l'en remercions et souhaitons bonne route au réseau.

SF2A 2012
S. Boissier, P. de Laverny, N. Nardetto, R. Samadi, D. Valls-Gabaud and H. Wozniak (eds)

LE PATRIMOINE DES OSU : PROBLÉMATIQUES D'UNE « COLLECTION » UNIQUE ÉCLATÉE GÉOGRAPHIQUEMENT

F. Le Guet Tully[1] and J. Davoigneau[2]

Résumé. Après avoir rappelé les efforts consentis il y a une quinzaine d'années par les ministères de la Culture et de la Recherche en faveur de la connaissance du patrimoine astronomique des observatoires, on décrit rapidement l'opération d'inventaire lancée par les auteurs, ainsi que quelques-unes de ses retombées. On montre ensuite comment de ce travail a émergé la notion de « collection » unique éclatée géographiquement, puis on évoque certaines des problématiques que soulève le devenir de cet ensemble patrimonial d'importance mondiale.

Keywords: observatoires, patrimoine astronomique, inventaire, instruments, archives, collection, conservation-sauvegarde, valorisation, UNESCO

1 Le patrimoine des OSU : de la réflexion à l'action

Au début des années 1990 se tint à Paris à l'initiative de Carlos Jaschek[i], astronome à Strasbourg, une série de réunions informelles organisées en vue de créer un groupe de recherche (GDR) « Histoire de l'astronomie et ethno-astronomie » et de réfléchir à des questions sur le thème « Astronomie et société ». Dans ce cadre surgirent des discussions sur les thèmes histoire de l'astronomie au sens large, bibliométrie, sociologie et philosophie de l'astronomie et connaissance du patrimoine. Ce dernier thème fut soulevé par FLGT qui, s'intéressant au patrimoine de l'observatoire de Nice depuis quelques années déjà[ii], s'était rendu compte que pratiquement tous les observatoires étaient confrontés aux mêmes problèmes, qu'il s'agisse des instruments anciens ou obsolètes, des archives, ou des ouvrages anciens.

Grâce à la perspicacité de Guy Simon, directeur de la section astronomie de l'INSU/CNRS, et de Jean-Dominique Wahiche, représentant de la Mission Musées[iii], une réflexion sur le thème spécifique du patrimoine astronomique en général et des instruments en particulier s'ensuivit rapidement. Simon et Wahiche étaient à la fois conscients des dangers encourus par ce patrimoine souvent prestigieux qui disparaissait ou était démantelé au gré des départs à la retraite ou de l'arrivée de nouveaux instruments, et persuadés que l'absence d'un musée d'astronomie en France était dommageable non seulement pour l'image de l'astronomie, mais aussi pour le public.

De ces réflexions générales est née la certitude qu'avant de valoriser quelque patrimoine que ce soit, il faut d'abord savoir de quoi il est constitué. La première action consista à réaliser une pré-enquête – commandée par l'INSU – sur le patrimoine astronomique. Menée dans treize établissements et réalisée durant l'été 1992 par Jaschek et FLGT, cette étude a été tirée à 50 exemplaires – bien vite épuisés.

---

[1] LISE Collège de France et OCA

[2] Mission Inventaire général du patrimoine culturel, Direction générale des patrimoines, Ministère de la Culture et de la Communication

[i] Jaschek (1926-1999), intéressé notamment par l'archivage des observations astronomiques, était alors responsable d'un séminaire en ethno et en archéo-astronomie.

[ii] Les premières réflexions formalisées sur le patrimoine astronomique institutionnel remontent au travail que James Bradburne et FLGT ont présenté à l'occasion du colloque Muséologie des sciences et des techniques organisé en 1991 au Palais de la Découverte (`http://science-societe.fr/remus-la-museologie-des-sciences-et-des-techniques-actes-du-colloque-des-12-et-13-decembre-1991-paris-ocim-1993/`) dans le cadre d'un programme interministériel de recherche en muséologie (REMUS) lancé en 1989.

[iii] En charge notamment des collections universitaires au sein du ministère chargé de la recherche.

Les conclusions de cette enquête – le patrimoine des observatoires est riche, varié, souvent en danger et largement méconnu – a conduit la Mission Musées à créer fin 1993 un « groupe de réflexion sur le patrimoine astronomique » (GPA) chargé de « faire des propositions pour sa conservation et sa mise en valeur »[iv].

Deux constats sont rapidement apparus. Si les bibliothèques des établissements publics sont régies par une loi, s'il en va de même pour leurs archives[v], il n'existe rien de tel pour les instruments qui une fois obsolètes tombent dans un vide juridique alarmant. Pour les instruments fixes, le danger est leur abandon[vi] faute d'intérêt ou de crédits ou les deux. Quant aux instruments déplaçables, ils risquent soit de disparaître – quitte à réapparaître dans des ventes aux enchères. . .–, soit d'être « bennés » pour libérer de l'espace, le tout au grand dam de l'histoire des sciences et des techniques, de l'histoire individuelle des établissements. . .et du public. D'où le second constat. Avant d'envisager des actions de valorisation de ce patrimoine, il faut le connaître. Et pour le connaître, il faut en premier lieu le nommer, puis l'étudier. Ce qui conduisit à proposer une opération nationale d'inventaire du patrimoine astronomique, avec l'espoir sous-jacent que connaître les richesses des OSU constituerait un premier rempart contre les menaces avérées de leur disparition[vii].

En 1994, sur la recommandation de Bruno Jacomy, directeur-adjoint du Musée des Arts et Métiers, le GPA rencontre Claudine Cartier, responsable du Bureau de la méthodologie de l'Inventaire au ministère de la Culture[viii] qui, alors qu'elle venait de procéder à des développements en direction de patrimoines industriels et techniques, s'est montrée très intéressée par l'adaptation de la méthodologie au patrimoine scientifique. La collaboration qui s'ensuivit aboutit en 1995 à la signature d'un premier protocole interministériel Culture/Recherche stipulant que l'opération d'inventaire du patrimoine des observatoires, financée par le ministère de la recherche, bénéficierait de la méthodologie du ministère de la Culture et, en Région, de la collaboration des photographes des DRAC[ix]. Placée sous la responsabilité conjointe de JD (volet méthodologique) et de FLGT (volet scientifique), l'opération bénéficia au total de trois protocoles.

2 De l'inventaire d'objets. . . à la notion de « collection » unique éclatée géographiquement

Les préalables à la mise en œuvre de l'opération d'inventaire consistèrent à

- mettre au point une méthodologie éprouvée : adaptation de la méthodologie de l'Inventaire, création d'un vocabulaire pour les instruments scientifiques, développement d'un thésaurus, définition de critères pour l'insertion ou non des objets dans l'étude, phase de test sur un corpus d'objets ;
- identifier sur chaque site les correspondants qui allaient nous accueillir et ouvrir placards, remises, caves et greniers ;
- identifier des personnes ressources au plan national : Thérèse Charmasson pour les archives scientifiques, Paolo Brenni et Anthony Turner pour les instruments scientifiques ;
- identifier des communautés internationales de spécialistes : Conseil International des Archives (CIA/ICA, siège aux Archives nationales à Paris), International Council of Museums (ICOM, siège à la Maison de l'UNESCO à Paris).

Une fois sur le terrain, nous avons rapidement pris conscience que l'instrument fixe ne pouvait s'étudier sans son abri, que les décors d'architecture étaient porteurs d'information sur l'institution à laquelle appartenait l'instrument, que la disposition des bâtiments était cruciale dans la conception du site, que les mires faisaient partie intégrante d'un cercle méridien. . .D'où une réflexion sur les composantes du patrimoine à étudier qui aboutit à la liste suivante : site et disposition des bâtiments sur le site, bâtiments et édicules, grands instruments en place, grands instruments démontés et/ou détruits, petits instruments, objets, décors d'architecture. Par ailleurs, sur

[iv] Initialement composé de neuf personnes nommées par le ministère et placé sous la responsabilité de FLGT, le groupe s'est rapidement élargi. Il était composé d'historiens des sciences, d'historiens des techniques, de conservateurs du patrimoine (spécialistes des instruments, spécialistes des archives ainsi qu'une spécialiste des bibliothèques) et d'astronomes personnellement intéressés par divers aspects du patrimoine de leurs établissements respectifs (dont Jérôme de La Noë et James Caplan, présents à cette session).

[v] Reprises depuis 2004 respectivement dans les Livres III et II du Code du patrimoine (`http://www.legifrance.gouv.fr/affichCode.do?cidTexte=LEGITEXT000006074236`).

[vi] Tel est le cas du grand équatorial coudé de l'Observatoire de Paris.

[vii] Un objet inventorié existe et, s'il existe, non seulement le risque qu'il disparaisse diminue mais la chance qu'il suscite des recherches historiques de qualité augmente. D'où la possibilité d'une valorisation fondée sur un matériau historique solide et validé, par conséquent respectueuse du public.

[viii] Le ministère de la Culture poursuit deux politiques patrimoniales : l'Inventaire général, entreprise documentaire de connaissance et de recherche créée par André Malraux en 1964, et la protection Monuments historiques, mission de sauvegarde et de conservation créée par François Guizot en 1831.

[ix] Direction Régionale des Affaires Culturelles.

place nous explorions systématiquement les fonds iconographiques, archives et ouvrages documentant bâtiments, instruments, décors, etc.[i]

Les principaux sites astronomiques étudiés dans le cadre des protocoles interministériels furent Besançon, Bordeaux, Hendaye, Lyon, Meudon, Paris, OHP, Marseille, Montpellier, Nice et Strasbourg[ii].

Au fil de notre découverte des observatoires historiques et de leurs instruments nous avons rapidement pris conscience de grandes similitudes entre eux, ce qui nous a rapidement amenés à concevoir l'ensemble des objets étudiés comme une « collection » unique éclatée géographiquement, intuition confortée par nos travaux sur l'histoire institutionnelle comparée des observatoires – tous fondés ou refondés en l'espace d'un demi-siècle[iii] et, à l'exception de celui du Pic du Midi, tous peu ou prou inspirés de celui que Struve avait créé pour le tsar en 1839 à Pulkovo[iv]. Conçus et réalisés durant la même période et donc dans un contexte politico-scientifique identique, ces observatoires institutionnels ont ensuite évolué en fonction des spécificités qui leur étaient assignées au plan national – chronométrie, astronomie physique, Carte du ciel, etc. Si naturellement leur patrimoine instrumental XXe siècle reflète ces spécificités, il n'en reste pas moins que l'on retrouve partout les mêmes types d'instruments, les mêmes séries d'horloge, les mêmes accessoires, dus pour l'essentiel aux mêmes constructeurs[v].

Ainsi ne serait-ce que dans la famille des grands instruments avons-nous identifié dix grands cercles méridiens, trois « très grandes » lunettes équatoriales, trois lunettes de 38 cm, cinq lunettes coudées de Loewy, quatre lunettes de la Carte du ciel, six télescopes de Foucault, trois chercheurs de comètes, trois sidérostats, deux altazimuts, deux astrographes... et leurs instrumentations accessoires.

3 Conclusion

En impulsant une considérable collecte d'information et d'images sur le patrimoine astronomique, l'opération d'inventaire a bien sûr contribué à la création de connaissances sur les objets pris isolément, enrichissant ainsi le socle de connaissances validées nécessaire à toute opération de valorisation de qualité les concernant. En ce qui nous concerne, cette opération nous a également conduits à effectuer des travaux de recherche sur l'histoire comparée des instruments – ce qui nous a permis de proposer des thématiques transverses en vue d'études préliminaires pour l'inscription de sites astronomiques sur la Liste du Patrimoine mondial de l'UNESCO[vi] – et sur l'histoire institutionnelle des observatoires français ou d'inspiration française.

Par contre elle n'a en aucun cas « sauvé » matériellement ce patrimoine, cette prérogative relevant de son (ou ses) propriétaires. Les seuls pas en avant dans cette direction qui puissent lui être attribués sont les protections au titre des Monuments historiques qu'à la suite de l'inventaire certains établissements ont souhaité obtenir pour leurs bâtiments[vii] et/ou pour leurs instruments[viii]. Comment aller au-delà de ces protections, sachant d'une part que la conservation-sauvegarde du patrimoine et sa valorisation auprès du public sont affaires de professionnels hautement qualifiés et d'autre part que les établissement à qui la responsabilité de ce patrimoine incombe n'ont souvent ni le temps, ni les compétences, ni les moyens de s'en occuper ? Sachant également que le patrimoine reçu en héritage par les astronomes a par définition vocation à être transmis aux générations suivantes et qu'il

[i] Ce qui dans nombre de cas a permis aux OSU de découvrir dans leurs murs des richesses insoupçonnées en termes d'archives, d'iconographie et d'ouvrages.

[ii] Les autres sites étudiés sont la Cime de l'Aspre, le Mont-Chiran, Saint-Véran. Des opérations de repérage seul ont été effectuées à Toulouse, au Pic du Midi, au plateau de Calern et au plateau de Bure. L'étude d'instruments parisiens appartenant au Bureau des longitudes, à la Cité des Sciences et de l'Industrie et au musée des Arts et Métiers avait permis au préalable de tester la méthodologie. Enfin, une collaboration avec l'observatoire d'Alger (CRAAG) a été menée à l'occasion notamment d'une mission diagnostique bâtiments, instruments, archives.

[iii] Pour mémoire, dates de création des observatoires patrimoniaux : 1842 Toulouse (Jolimont) ; 1862 Marseille (Longchamp) ; 1872 Strasbourg ; 1878 Besançon, Bordeaux, Lyon ; 1879 Hendaye, Meudon, Montpellier ; 1881 Nice, Alger ; 1892 Pic-du-Midi. Une partie importante du patrimoine de l'observatoire de Paris remonte à la même période.

[iv] La conception de l'OHP, pensée dans les années 1920, relève de la même inspiration.

[v] Seul l'observatoire de Strasbourg se distingue partiellement des autres avec les éléments de son patrimoine de conception et de construction allemandes.

[vi] Dans le cadre de l'Initiative UAI/UNESCO « Astronomy and World Heritage » qui vise à définir des critères pour les sites astronomiques susceptibles de demander leur inscription sur la Liste du Patrimoine mondial en raison de leur « valeur universelle exceptionnelle ».

[vii] Besançon, inscrit MH 2005 et classé MH 2012 ; Lyon, inscrit MH 2007et classé MH 2008 ; Bordeaux, inscrit MH 2010 ; OHP - avis favorable de la CRPS en 2008. Observatoires protégés auparavant : Paris, classé MH 1926 et inscrit MH 2009 (+ site) ; Meudon, classé MH 1956/1972 (+ site) ; Hendaye, classé MH 1984 (+ site) ; Toulouse, inscrit MH 1987 ; Nice, inscrit MH 1992 et classé MH 1994 (+ site).

[viii] Juvisy, classé MH 1997 ; Marseille, classé MH 2003 ; Nançay , inscrit MH 2003 ; Hendaye, classé MH 2004 ; Montpellier, classé MH 2006 ; Besançon, classé MH avis favorable 2007 ; Lyon, classé MH 2012 ; Bordeaux, en cours d'instruction.

ne devrait donc ni être ni laissé à l'abandon, ni soustrait au public...

Il se trouve que – spécificité française – la gestion continûment centralisée des observatoires institutionnels mis en service sur le territoire depuis 150 ans a pour conséquence la présence aujourd'hui sur les sites historiques d'un patrimoine XIXe et XXe siècles d'une richesse et d'une cohérence intellectuelle exceptionnelles qui – les travaux de l'inventaire l'ont montré – peut être considéré comme un ensemble unique.

D'après nos estimations – probable conséquence de cette spécificité française –, sur les 90 observatoires astronomiques qui ont plus de 100 ans, onze se trouvent en France métropolitaine et trois ont de très fortes similitudes avec ces derniers (Alger, La Plata et Rio de Janeiro).

La communauté astronomique française ne doit-elle pas se mobiliser tout entière pour que ce patrimoine exceptionnel occupe la place qui lui revient au plan international ? En trouvant le chemin de la nécessaire collaboration avec les professionnels du patrimoine et avec les organismes nationaux, européens et internationaux au sein desquels des collègues réfléchissent aux problématiques que le patrimoine universitaire soulève. Dans l'intérêt bien compris du public – individus, collectivités – et dans son propre intérêt...

SF2A 2012
S. Boissier, P. de Laverny, N. Nardetto, R. Samadi, D. Valls-Gabaud and H. Wozniak (eds)

RAPPORT SUR L'ÉTAT DU PATRIMOINE ASTRONOMIQUE DANS LES OBSERVATOIRES FRANÇAIS DE LA FIN DU XIXÈ SIÈCLE

E. Damm[1] and E. Pécontal[2]

Résumé. Suite au colloque sur la sauvegarde du patrimoine astronomique organisé par le MAEE et la SAF, sous l'égide de l'UNESCO, qui a conduit à l'adoption de la Déclaration de Paris, les directeurs d'observatoires institutionnels qui étaient absents du colloque ont ressenti le besoin de discuter de ces conclusions prises en leur nom. L'initiative d'organiser une réunion des directeurs des Observatoires des Sciences de l'Univers (OSU) à ce sujet le 30 janvier 2012 a été prise par François Vernotte, directeur de l'Observatoire de Besançon. Le présent compte-rendu de visite résulte d'une initiative spontanée d'Emmanuel Pécontal, astronome responsable du Patrimoine à l'observatoire de Lyon, et d'Evelyne Damm, membre de la Commission Nationale de classement des Monuments Historiques (CNMH) et élue à la communauté d'agglomération des Portes de l'Essonne où est sis l'observatoire de Camille Flammarion.

Keywords: patrimoine astronomique, observatoires

1 Introduction

Le choix des observatoires visités s'est fait au regard de l'unité de leur époque de construction. L'étude que nous présentons ici se borne, excepté pour l'Observatoire de Paris, aux établissements fondés à la fin du XIXè siècle lors du mouvement de décentralisation qui suivit la défaite de 1871. Avant cette date, en effet, l'immense majorité des travaux astronomiques français était faite à l'Observatoire de Paris. Les nombreux observatoires privés ou dépendant d'académies locales ou d'établissement d'enseignement sous l'Ancien Régime, avaient pour la plupart périclité après la Révolution. Dans les années 1860, Urbain Le Verrier, directeur de l'Observatoire de Paris, avait pris le contrôle de l'ancien Observatoire de Marseille qui existait depuis le début du XVIIIè siècle, et l'avait déplacé sur le plateau de Longchamp pour en faire une annexe de l'Observatoire de Paris. À la même époque, l'Observatoire de Toulouse fonctionnait encore mais était fortement dégradé. Bien que plusieurs autres villes aient souhaité la création d'un observatoire sur leur territoire, ce n'est qu'après la guerre de 1870-71 que la fondation de nouveaux établissements commença.

Toulouse fut réorganisé en 1872. À Besançon, Lyon et Bordeaux, des observatoires d'État furent ensuite fondés par décret en 1878 et effectivement installés entre 1880 et 1887. En 1875, un décret créait un observatoire d'astronomie physique dont la direction fut confiée à Jules Janssen qui luttait avec opiniâtreté depuis des années pour voir un tel projet se concrétiser. Cet établissement fut installé à Meudon où Janssen travailla à partir de 1876.

L'histoire de l'Observatoire du Pic du Midi, est différente de celle des autres observatoires institutionnels. Fondé d'abord sur une initiative privée du général en retraite Charles Nansouty et de l'ingénieur Célestin-Xavier Vaussenat de 1878 à 1882, ces derniers durent en faire don à l'État, ne pouvant pas faire face à la gestion d'un tel établissement.

Enfin, en ce qui concerne Strasbourg, c'est encore dans les années 1870-1880, pendant la période allemande, que l'Observatoire actuel fut créé. Les astronomes allemands s'installèrent d'abord dans le petit observatoire existant, mais ils érigèrent rapidement un observatoire beaucoup plus important dans un nouveau quartier. Cet observatoire fut inauguré en 1881.

[1] Maire adjointe de la Commune d'Athis-Mons, France
[2] Centre de recherches astrophysiques de Lyon, 9 avenue Charles André, 69230 Saint-Genis-Laval, France

Cette unité de temps témoigne du grand intérêt porté à l'astronomie en cette fin de XIXème siècle. Cet intérêt dépassait d'ailleurs largement les frontières, puisqu'on a vu dans le monde entier la création de nouveaux observatoires à la même époque.

Parallèlement aux créations institutionnelles, on vit aussi naître des observatoires privés. Le premier fut l'œuvre d'Antoine d'Abbadie, explorateur et savant éclectique qui avait déjà installé un petit observatoire en 1857 à Hendaye qu'il remplaça en 1876 par un bâtiment monumental.

À la même époque, le banquier Raphaël Bischoffsheim, mécène de l'astronomie de cette fin de siècle, décida « *d'élever à la science française un monument durable digne d'elle* ». Ce fut la création de l'Observatoire de Nice sur le Mont Gros, construit par Charles Garnier dont les bâtiments et les instruments furent réalisés entre 1880 et 1892. Le but de Bischoffsheim était de donner cet observatoire au Bureau des Longitudes, mais ce dernier n'ayant pas la personnalité juridique adéquate, c'est à l'Université de Paris qu'il le légua.

Un autre observatoire important d'initiative privée de cette époque fut celui de Camille Flammarion. Ce dernier, après des débuts dans l'astronomie professionnelle à l'Observatoire de Paris, a eu surtout un impact essentiel dans la diffusion de l'astronomie auprès du grand public. Flammarion a mené diverses activités à caractère expérimental au sein de son observatoire, installé dans un bâtiment légué par un de ses admirateurs en 1882, et dont il finança les aménagements et les instruments grâce aux bénéfices tirés de l'édition de son Astronomie Populaire. L'établissement subsiste après des legs successifs, et possède un fonds d'archives et des instruments remarquables.

Enfin, nous évoquons aussi le cas de l'observatoire de Lucien Rudaux à Donville dans la Manche, fondé en 1884. Bien que cet observatoire n'existe plus en tant que tel, son bâtiment ayant été transformé en habitation, nous avons contacté un historien local qui nous a renseigné sur le sort de ses archives et de son patrimoine instrumental.

Ce compte-rendu n'a pas d'autre objectif que de constituer un état des lieux faisant ressortir les constantes et les différences, les bonnes pratiques et les difficultés de ces observatoires, dans la mise en valeur de leur patrimoine historique.

Il est apparu au cours de nos visites que les observatoires astronomiques étaient des entités cohérentes qui méritaient un prise en compte globale, comme s'il s'agissait d'un écosystème. Dès lors que nous élargissions le champ de nos questionnements, non seulement à la sauvegarde du patrimoine matériel, mais aussi à la problématique de la transmission inter-générationnelle d'un patrimoine immatériel, nous nous sommes sciemment écartés de l'approche méthodologique définie par le Service de l'Inventaire dans son guide Principes, méthodes et conduites de l'Inventaire pour pouvoir appréhender les observatoires astronomiques historiques comme des entités « en mouvement ». Considérant qu'une des dimensions de l'écologie politique pourrait être l'étude de l'écosystème d'organismes institutionnels, nous nous sommes attachés à observer des microcosmes évoluant différemment dans le temps, interagissant avec d'autres entités « gravitantes » ou « englobantes » dans un macrocosme politico-institutionnel beaucoup plus large.

2 Microcosme des observatoires : le support de culture d'une « discipline orchidée »

Au sein des Universités, l'astronomie est une science particulière. Un des vice-présidents de l'université de Strasbourg en charge des finances l'a qualifiée de « discipline orchidée » : c'est une discipline délicate dont il faut prendre soin. Il nous est apparu que cette discipline observationnelle prise dans le contexte des observatoires astronomiques historiques se présentait comme un tout organisé autour des exigences liées à la performance des instruments.

2.1 La finalité de l'observation scientifique facteur de cohérence du patrimoine naturel et matériel

L'observation du ciel a été à la source de plusieurs disciplines de recherche scientifique, de la mesure de la Terre elle-même (géodésie), à la mécanique céleste (astrométrie) en passant par l'étude de l'atmosphère (météorologie et aéronomie) et la détermination du temps (chronométrie). Dans tous ces champs, la précision requise dans les observations demande un soin particulier dans la réalisation des instruments mais aussi dans celle des bâtiments les hébergeant et dans le choix des sites où ils sont installés.

2.1.1 Rationalité des lieux choisis

Les scientifiques qui ont présidé au choix des sites des observatoires appartenaient généralement aux instances centrales françaises qu'étaient l'Observatoire de Paris, le Bureau des Longitudes et l'Académie des sciences. Leur

démarche était empreinte d'une rationalité toute scientifique et la topographie même des lieux correspondait à des nécessités fonctionnelles.

Histoire des emplacements. L'emplacement d'un observatoire est toujours un compromis entre son accessibilité et sa mise à l'écart des nuisances pouvant perturber les observations. Ces deux exigences sont évidemment contradictoires car l'accessibilité est liée à la proximité de concentrations humaines, comme les brumes de pollution ou les vibrations du sol engendrées par la circulation, qui sont une des sources de nuisances.

L'Observatoire de Paris, qui est le plus ancien construit en France, était à l'époque de sa fondation (1667) situé très à l'écart du cœur de la cité, ce qui le mettait à l'abri des perturbations humaines, tout en assurant son accessibilité aux chercheurs de l'Académie des sciences, dont il était une extension. À la fin du XIXème siècle, cette situation n'était plus du tout satisfaisante, la ville s'étant considérablement étendue.

Dans les années 1860, une vive polémique a opposé le directeur de l'Observatoire, Urbain Le Verrier, à un de ses astronomes, Antoine-Joseph Yvon Villarceau, ce dernier plaidant en faveur du déplacement pur et simple de l'Observatoire à l'écart de la ville. Mais des questions de prestige s'opposèrent à cette solution radicale et il fut décidé de n'établir qu'une succursale de l'Observatoire à Marseille sur le plateau de Longchamp, à l'époque suffisamment éloigné du centre de la ville.

Lorsqu'il fut décidé, dans les années 1870, d'établir des observatoires astronomiques en province, le choix des sites d'implantation a reposé sur une série de critères récurrents. Il fallait que la ville de proximité soit un centre intellectuel important, possédant une faculté des sciences, et que le site lui-même en soit éloigné de quelques kilomètres. De plus, on a choisi dans la mesure du possible, des points de relative altitude, surplombant la ville et mettant les instruments au-dessus des brumes industrielles.

À l'époque de la fondation des observatoires de province, il n'était plus question de construire des édifices monumentaux mais bien au contraire d'isoler plusieurs petits bâtiments bien séparés ayant chacun sa spécificité. Il fallait donc pour cela un grand parc pour accueillir l'établissement. C'est une des caractéristiques de ces observatoires qui sont restés des îlots verts malgré la progression des villes et des sites universitaires.

Le choix du site de l'Observatoire de Strasbourg, bien que répondant à des critères assez similaires, a été un peu différent. La ville venait d'être conquise par les Allemands, et l'installation d'un important centre universitaire ainsi que d'un grand observatoire était une question de prestige visant à valoriser la nouvelle conquête. Si le choix fut fait d'un site éloigné du centre urbain, la raison était plus politique que scientifique : il fallait créer une extension de la ville destinée à accueillir les nouveaux immigrants allemands, et c'est là qu'on décida d'implanter le complexe universitaire et l'observatoire. À la différence de ce qui était fait en France, on avait érigé un établissement à l'écart du centre, tout en accélérant volontairement l'urbanisme aux alentours. L'idée de placer l'observatoire hors des fortifications de la ville, et donc dans un site mieux protégé des nuisances, fut écartée pour des raisons stratégiques. C'est peut-être la raison de la qualité médiocre des mesures astrométriques réalisées par la suite dans cet établissement. Ainsi, lorsque les scientifiques allemands présentèrent une série de mesures tendant à prouver l'existence d'une variation de la latitude, ils écartèrent les données obtenues à Strasbourg à cause de leur manque de fiabilité.

Contrairement à tous les autres observatoires, celui de Nice a été implanté après une campagne de recherche de site et, la qualité du site primant sur toute autre chose, à proximité d'une ville ne possédant pas d'université. C'est en fait le premier observatoire permanent de montagne en Europe. Il n'est pas innocent que l'observatoire idéal voulu par Bischoffsheim et Garnier ait été implanté dans un territoire devenu français depuis peu, en réponse en quelque sorte au plus bel observatoire allemand construit à Strasbourg.

L'apparition des nuisances. Malgré l'intention initiale de se placer à l'écart des villes, l'urbanisation galopante du début du XXème siècle, accompagnée par le développement des moyens de transport, a très vite rattrapé les observatoires, affectant gravement leur potentiel scientifique. Une conséquence parmi d'autres fut l'abandon des mesures géophysiques du magnétisme terrestre à l'Observatoire de Lyon et à l'Observatoire de Nice à cause des champs magnétiques induits par l'arrivée du tramway à proximité. Afin d'inciter les collectivités territoriales à réduire leurs émissions lumineuses, l'idée de créer une réserve de ciel étoilé, calquée sur celle du Mont Mégantic au Québec, a conduit à l'élaboration d'une charte pour la préservation de l'environnement nocturne autour du Pic du Midi. Cette démarche nouvelle s'inscrit dans le cadre de la protection du patrimoine naturel que la communauté des astronomes devrait tout particulièrement promouvoir. S'inscrivant dans une logique d'économie d'énergie et de développement durable, l'initiative du Pic du Midi a été reprise dans le cadre du Grenelle de l'environnement.

Dans cet esprit, l'éclairage nocturne de la rocade Est de Bordeaux a pris en compte la présence de l'ob-

servatoire à Floirac en utilisant une lumière au sodium pouvant être filtrée facilement par les instruments, des projecteurs dirigés vers le sol, et une réduction de l'intensité lumineuse après 23 heures.

Dès lors que l'on considère que le patrimoine naturel des observatoires astronomiques va du sous-sol du site au ciel qui le surplombe, l'approche de protection devient beaucoup plus globale et doit être négociée avec les villes voisines.

Bien que l'observation soit devenue marginale dans les observatoires historiques à part celui du Pic du Midi, les astronomes pourraient avoir un rôle à jouer dans la sensibilisation des élus à cette problématique de la pollution lumineuse. En effet, si l'accès au ciel nocturne est extrêmement dégradé dans ces sites, il est important d'entamer la décroissance et la rationalisation de l'éclairage nocturne pour rendre progressivement l'accès au ciel étoilé à la population. Les sites hébergeant un observatoire pourraient jouer un rôle pilote dans cette prise de conscience.

La préservation administrative des sites. Peu d'observatoires historiques ont fait l'objet d'une protection de leur site en tant qu'espace naturel sensible. Pour l'instant, seul le domaine de 35 hectares de l'Observatoire de Nice a été étudié de manière scientifique par une association, le CEEP. L'inventaire de ce patrimoine naturel exceptionnel (faune, flore, milieux naturels) et typiquement méditerranéen a justifié que ce site soit inscrit comme Zone Naturelle d'Intérêt Faunistique et Floristique. La gestion scientifique de ce patrimoine naturel et la mise en valeur auprès des publics ont été confiées au CEEP au terme d'une convention.

À Lyon, dans le cadre de l'étude scientifique de huit jardins anciens de la Région Rhône-Alpes, la DRAC vient d'engager une étude du parc de l'Observatoire qui va être bientôt menée par une spécialiste de l'École Nationale Supérieure de Paysages. Les archives concernant le tracé du parc sont éparses voire égarées. Un gros travail pour les rassembler devra être effectué à cette occasion.

A Besançon, des documents d'archives ont permis de retrouver le tracé des parties végétalisées datant de 1903, qui avait été demandé par le directeur de l'Observatoire afin que le site soit moins exposé aux intempéries. Outre la motivation d'ordre esthétique qui a justifié ces aménagements, le directeur a cherché à faire du parc un outil au service de la météorologie : c'est ainsi que l'engazonnement sélectif devait permettre des mesures spécifiques comme celle de la température de l'air au-dessus du sol engazonné et non engazonné etc[i].

À Bordeaux on dispose d'un plan des parcelles naturelles ou plantées avant la fondation de l'observatoire mais G. Rayet le fondateur de l'observatoire a procédé à la plantation d'un certain nombre d'arbres d'espèces remarquables dont certains subsistent encore.

Sur le site du Pic du Midi, des études de botanique sur l'adaptation des espèces végétales au climat rigoureux de la montagne ont été retrouvées sans pour l'instant avoir été mises en valeur. Le Conservatoire Botanique Pyrénéen qui a son siège à Bagnères de Bigorre assure la continuité sur ces recherches et a récupéré les fonds d'archives, et une étude, *Histoire des jardins du Pic du Midi – Proposition muséographique*, a été menée sous sa direction (Rapport Youna Morizur 2004).

Sur le site de 35 hectares de l'Observatoire de Haute Provence, qui fait partie de l'Observatoire Astronomique Marseille-Provence (OAMP), des plates-formes expérimentales de grande ampleur, relatives au suivi des changements climatiques sur les forêts et la biodiversité, ont été mis en place avec l'appui du personnel sur place.

Il faut noter que la complémentarité des disciplines scientifiques au tournant du XIXè siècle était plus évidente qu'aujourd'hui, et les astronomes que furent Antoine d'Abbadie, Camille Flammarion et Lucien Rudaux, qui tous trois édifièrent leur propre observatoire, se livrèrent à des expérimentations scientifiques très diverses. Ainsi Camille Flammarion dans le parc de son observatoire de Juvisy, a construit des serres de couleurs différentes pour étudier l'impact des effets chromatiques sur la croissance des végétaux.

L'immense parc autour du château d'Abbadia qui est propriété du Conservatoire du Littoral, est aujourd'hui un site naturel protégé de 65 hectares. Géré par la Ville d'Hendaye avec l'aide financière du département des Pyrénées Atlantiques, il est ouvert au public qui peut bénéficier de nombreuses animations naturalistes et culturelles grâce au CPIE Littoral basque (Centre Permanent d'Initiatives pour l'Environnement porté par l'association « *Abbadiako Adixkideak – Les Amis d'Abbadia* ». On peut regretter que cette association ne porte pas également intérêt aux aspects astronomiques du site ni aux travaux scientifiques d'Antoine d'Abbadie.

[i] Voir « *L'Observatoire de Besançon* » Collection « *Parcours du Patrimoine* »

2.1.2 L'architecture adaptée à l'outil

La spécialisation architecturale des bâtiments par type d'activité. Par opposition à l'Observatoire de Paris, dont le bâtiment principal date de 1667, tous les observatoires construits au XIXè siècle partagent un même concept architectural hérité de l'Observatoire de Pulkovo (1839) qui était à cette époque la référence en terme d'astronomie de précision (Voir par exemple L'Observatoire de Besançon. Parcours du Patrimoine, p.11). Les différents instruments sont installés dans des bâtiments séparés, et reposent sur des piliers profondément ancrés dans la roche souterraine, indépendants des fondations des abris. De plus, les édifices dédiés à l'observation étaient indépendants des immeubles d'habitation.

À Strasbourg, les architectes ont été sensibles au confort des astronomes, et cette séparation des lieux d'observation et d'habitation est compensée par des couloirs abrités desservant chaque partie. Ces couloirs, récemment restaurés, se croisent sous une petite rotonde.

Dans le cas de Nice, cette séparation des bâtiments a même été mise en scène par l'architecte Charles Garnier qui a distribué tous les abris d'instruments le long de la ligne de crête du Mont Gros tout en respectant les impératifs d'orientation liés à leur utilisation scientifique. La bibliothèque, les habitations et les bâtiments de service sont quant à eux en contrebas de la crête de manière à ne pas gêner les observations par des ≪ réfractions anormales ≫. L'architecture des bâtiments vernaculaires est très différente de celle de la bibliothèque et des abris d'instruments.

Sur tous les sites, la maison du directeur faisait l'objet d'un effort architectural particulier, en raison de l'importance du personnage. Malheureusement, certaines de ces demeures sont aujourd'hui abandonnées (Besançon, Bagnères de Bigorre, Bordeaux) voire squattées et détériorées. Leur prise en compte et leur restauration sont pourtant essentielles à la présentation de la spécificité architecturale des observatoires.

Spécificité architecturale des abris d'instruments. Chaque type d'instrument nécessitant des aménagements particuliers, la construction des bâtiments les abritant a été d'emblée différente. Les instruments méridiens, destinés à la mesure de la position des astres et ne pointant que dans un plan donné, pouvaient être couverts par des abris dont le toit était droit avec un système de trappes ouvrantes. Au contraire, les instruments équatoriaux devaient être abrités sous des coupoles tournantes pour pouvoir pointer le ciel dans toutes les directions. Dans tous les cas, un soin particulier était apporté au choix des matériaux d'isolation, permettant de protéger les instruments de variations thermiques importantes pendant la journée.

Il faut aussi considérer les piliers de mire des instruments méridiens comme indissociables des bâtiments car bien que construits en dehors de l'édifice lui-même ils étaient indispensables aux observations.

En France, l'équatorial coudé conçu par Maurice Loewy, astronome d'origine viennoise, a été très en vogue au moment même de la construction des observatoires de la fin du XIXème siècle. On en a construit 7 : deux exemplaires, le prototype et le plus grand ont été installés à Paris, quatre ont été implantés en province (Alger, Besançon, Lyon, Nice), le septième est à Vienne en Autriche.

Ceux de Paris ont malheureusement été tous les deux démontés, les pièces étant éparpillées de telle façon qu'elle rend difficile, voire impossible, la restauration. Celui de Besançon a aussi été démonté, mais toutes ses pièces ont été conservées sur site, et son bâtiment héberge aujourd'hui une société d'astronomes amateurs. Celui de Nice a subi des modernisations ayant permis de prolonger son utilisation scientifique. Celui d'Alger ne fonctionne pas mais pourrait être restauré. À Vienne, l'instrument a pratiquement disparu, mais le bâtiment subsiste. Seul celui de Lyon existe encore dans son état d'origine.

Les bâtiments abritant ces équatoriaux coudés ont une conception très particulière : le poste d'observation est dans une salle fixe et l'abri est un wagon coulissant sur des rails. Là encore, un grand soin avait été porté sur le choix des matériaux d'isolation, l'intérieur du wagon étant capitonné de varech.

Certains édifices ont été conçus avec des dispositifs très originaux de soutien des instruments, comme le système de rails encerclant la grande coupole de Strasbourg, sur lesquels roulait la chaise du chercheur de comètes lors des observations.

Dissociations des instruments et de leurs abris. Au cours du temps, la plupart de ces instruments ont perdu de leur intérêt scientifique et ont été abandonnés ou ont fait l'objet d'adaptation. Parfois même, certains ont été démontés, afin d'utiliser certaines de leur pièces pour des montages instrumentaux. De ce fait les bâtiments d'observation ont été détournés de leur vocation initiale.

La forme rectangulaire des grandes salles abritant les lunettes méridiennes rend leur réutilisation plus simple que celle des coupoles rondes. De plus leurs toits ouvrants posant des problèmes d'étanchéité ont souvent été définitivement fermés. Paradoxalement, à Nice le toit ouvrant a été restauré mais la salle est vide, l'instrument

ayant été supprimé dans les années 1960. Il reste de ce fait peu d'exemples de méridiennes installées permettant l'observation.

Pourtant, l'utilisation auprès du public de ces instruments, qui a jusqu'ici été négligée au profit des observations équatoriales, aurait un grand intérêt car elle permettrait de rendre tangibles les techniques de mesure du temps et de l'astrométrie.

Il ne reste en place dans des salles adéquates que le grand cercle méridien de Bordeaux qui a été modernisé et sert encore à des observations scientifiques, ceux de Besançon et Paris qui sont dans leur état d'origine, mais dont l'absence de restauration de la toiture interdit l'utilisation, et celle de Toulouse en parfait état dont le toit ouvrant a été restauré par la ville en 2004, mais dont l'absence d'oculaires interdit l'usage.

À Besançon qui possède un des spécimens les plus intacts, la conservation est menacée par le très mauvais état de la toiture qui fuit, et laisse même entrer des oiseaux dont les déjections abiment l'instrument.

À Lyon et Strasbourg, les salles méridiennes ont été respectivement transformées en laboratoire d'optique et en bibliothèque.

Celle de Nice a été transformée en salle de conférence, d'exposition, etc

D'une manière générale, les toitures mobiles quelle que soit leur forme, sont les parties les plus fragiles et les plus délicates à restaurer car les mécanismes sont sujet à l'usure, et parfois les solutions techniques adoptées à l'origine sont tellement exceptionnelles que leur entretien ou leur restauration devient hors de prix, ou ne répond plus aux exigences modernes.

C'est le cas de la coupole du grand équatorial de Nice. À l'époque l'ambition de Raphaël Bischoffsheim ayant été de doter l'Observatoire de la plus grande lunette au monde, on touchait les limites de la technologie existante des coupoles roulantes. Quelques années auparavant, Gustave Eiffel avait proposé une coupole pour l'observatoire de Paris dont le principe était de la faire pivoter sur un coussin d'eau. C'est le système que Bischoffsheim choisit pour son grand dôme. Lors de la restauration de la coupole dans les années 1960, le système Eiffel n'avait plus d'intérêt pratique, et on utilisa des moteurs puissants qui n'existaient pas au XIXè.

Problème des restaurations partielles ou séparées. Compte tenu des difficultés de financement, la plupart des restaurations se font sans cohérence d'ensemble au coup par coup, conduisant à des restaurations partielles ou séparées. De plus la logique de guichets séparés des financements publics crée des contraintes particulières qui ajoutent à la perte de sens des ensembles abris/instruments.

Les restaurations entreprises pour des bâtiments destinés recevoir du public (ERP) impliquent des contraintes d'accessibilité et de sécurité.

C'est ainsi qu'à Nice, la superbe scénographie de découverte de la grande coupole que Garnier a soulignée par un élégant muret classé MH a été endommagée par la pose d'une rambarde de sécurité métallique peu esthétique.

De manière générale, la problématique de l'accessibilité des sites aux personnes handicapées est abordée lors des restaurations de bâtiments ou d'instruments. À Lyon, l'étude en cours de la restauration du bâtiment abritant l'équatorial coudé a inclus un projet d'ascenseur qui a été écarté par l'architecte des bâtiments historiques tant il défigurait l'édifice.

Par contre la salle vide de la méridienne de Nice a été rendue accessible par un ascenseur alors que quelques mètres plus loin, la grande coupole, clou de la visite du site, reste inaccessible aux handicapés en attendant une phase ultérieure des travaux.

À Toulouse, la subvention de la restauration de la coupole Vitry et de la lunette de 38cm a été conditionnée à l'installation d'une plate-forme élévatrice permettant l'accès des handicapés à l'oculaire.

Intérêt d'un classement concomitant des instruments et de leurs abris. Au regard de la règlementation de protection des monuments historiques, il n'est pas possible de classer ensemble les objets mobiliers et immobiliers. Les demandes de classement se font séparément et on observe une grande disparité des niveaux de classement sur les différents observatoires. Cette disparité s'explique par diverses réticences des propriétaires des terrains, des bâtiments et des instruments du fait de l'inaliénabilité des monuments historiques.

On peut penser qu'un classement peut hâter les restaurations, dans la mesure où l'État, lorsqu'il n'est pas lui-même propriétaire, participe pour moitié au financement des travaux.

Mais il faudrait éviter des situations où l'instrument est classé avant son abri. À Besançon le grand cercle méridien est classé Monument Historique, mais son abri attend l'accord de l'Université pour obtenir le même degré de protection. Or ce classement serait d'autant plus nécessaire que la toiture n'est plus étanche, menaçant l'intégrité de l'installation.

À l'Observatoire Camille Flammarion de Juvisy, la grande lunette astronomique a été classée Monument Historique bien avant le bâtiment qui ne présentait aucune spécificité architecturale. Mais dans la mesure où le classement du bâtiment est intervenu au moment où la lunette était sur le point d'être restaurée, les financements publics sont allés à la restauration de la coupole, permettant ainsi la remise en service de l'ensemble d'observation. Il s'agit là d'une coïncidence heureuse qu'il faudrait généraliser en permettant le classement concomitant des instruments et de leurs abris.

Dans un article de 2005 consacré aux cercles méridiens, Françoise Leguet-Tully et Jean Davoigneau posaient déjà la question de la pertinence de la distinction entre instruments et abris :

> *≪ L'étude des cercles méridiens dans le cadre de l'Inventaire fait apparaître d'emblée une difficulté dans leur désignation : ces instruments relèvent-ils du meuble ou de l'immeuble ? Leur mobilité réduite à un seul degré de liberté - mouvement dans le plan méridien autour d'un axe horizontal orienté est-ouest, la nécessaire stabilité de leur monture, les travaux de maçonnerie indispensables à leur installation fixe et permanente constituent sans hésitation des arguments en faveur de leur qualification d'immeuble par "destination" : objets indissociables du lieu qu'ils occupent. ≫*

Il apparait que le même diagnostic pourrait s'appliquer à tous les ensembles bâtiments/instruments des observatoires. En effet, les instruments équatoriaux sont eux-aussi installés sur des piliers indépendants, et leurs abris construits ≪ sur mesure ≫ autour d'eux.

Les collections d'objets concourant à l'observation astronomique. Au delà de cette cohérence à préserver entre bâtiment et instrument, il y a tout un ensemble d'objets liés à l'utilisation de chaque instrument qui mériterait une attention particulière.

Certains de ces objets sont incorporés au bâtiment : ainsi tous les accessoires montés sur rail, comme les mécanismes de retournement ou les bains de mercure des lunettes méridiennes, ou les escabeaux circulant autour des grands équatoriaux. De même, à Bordeaux, dans un bâtiment contigu à la coupole de l'équatorial photographique, était installé le laboratoire de développement des clichés, dont la superbe paillasse en chêne est encore présente.

D'autres objets, bien que n'ayant pas été intégrés dans la conception des bâtiments, sont indissociables des instruments et devraient être conservés sur le site afin qu'ils puissent être présentés dans leur contexte dans un but pédagogique.

Le but des lunettes méridiennes était de mesurer la hauteur et le temps de passage des étoiles sur certains repères dans l'oculaire au cours de leur rotation apparente. Les horloges et/ou les chronographes permettant ces mesures par la méthode de l'œil et de l'oreille ou la méthode électrique sont intéressantes à présenter auprès de l'instrument. De même, le matériel destiné à l'élevage des araignées et à la préparation de leur fils, utilisés dans les oculaires comme repères, est à conserver in situ. Il semble d'ailleurs n'en rester qu'un exemplaire à Strasbourg.

Enfin, pour certains instruments, des parties essentielles au fonctionnement ont été progressivement remplacées par des dispositifs plus modernes. Ainsi, dans les lunettes équatoriales, la compensation de la rotation terrestre était assurée par des mécanismes très élaborés (système d'horlogerie, régulateurs de Foucault ou de Villarceau), intégrés à l'instrument. Ils ont souvent été remplacés par des moteurs électriques modernes. Il est très important de conserver les rares exemplaires encore en situation, et ceux qui ont été démontés méritent eux aussi attention.

La perte de sens des instruments présentés hors de leur contexte. Il existe peu de cas de conservation de collections complètes associant bâtiment, instrument, et objets annexes. Dans certains cas on trouve exposées des parties de ces ensembles dont la présentation hors contexte est dénuée de sens.

Dans le cas de Strasbourg, plusieurs objets sont exposés dans un petit musée lié au planétarium au sein de l'observatoire. Ainsi, le chercheur de comète précédemment mentionné est exposé dissocié de son système de guidage autour de la coupole. Cette présentation, déjà peu satisfaisante, risque même d'être aggravée par le déménagement du musée prévu concomitamment avec celui du planétarium, pour aller dans un site rassemblant les collections scientifiques de l'Université.

À Besançon, un compromis a été trouvé s'agissant de la conservation des horloges à pression constante. En effet, il y avait quatre horloges dans les sous-sols de l'observatoire, deux y ont été conservées sur place, mais ne fonctionnent pas, les deux autres sont exposées au Musée du Temps de la ville et fonctionnent. Dans la mesure où ces horloges servaient à la distribution du temps à l'observatoire et à la ville, il pourrait être intéressant de remettre en service les horloges en sous-sol afin de rétablir le fonctionnement d'origine pour présenter concrètement au public le système de distribution.

À Lyon, la lunette méridienne n'étant plus utilisée depuis les années 1930, elle a été démontée pour permettre la transformation de la salle en laboratoire d'optique dans les années 1980. La lunette a été alors confiée à la Cité des Sciences qui l'a rarement exposée, mais toujours à des fins d'ornementation sans aucune explication sur son utilité. Pire encore, ses cercles gradués, pièces essentielles à la mesure, ont été sablés car jugés trop oxydés, faisant ainsi disparaître les graduations. La lunette a été rendue à Lyon pour être exposée dans le nouveau « musée des confluences ».

La question se pose de l'intérêt de la restauration de cette méridienne, hors du site de l'observatoire et de son abri. Il faut noter qu'au moment des dégradations mentionnées ci-dessus, l'instrument n'était pas classé. Aujourd'hui son classement n'aurait de sens que si la restauration était concomitante à sa réinstallation dans sa salle d'origine et en état de fonctionnement.

Dans la plupart des sites l'inquiétude relative au classement des instruments est qu'il y ait une obligation de conservation en l'état, empêchant toute modification qui permettrait leur maintien en fonctionnement.

Or il y aurait lieu de privilégier, lors de la présentation sur site des instruments, l'accès à l'observation, afin non seulement de susciter l'émerveillement du néophyte, ce que peuvent apporter les clubs d'astronomes amateurs avec leurs télescopes compacts, mais aussi de faire comprendre toute la variété des instruments de mesure qui étaient nécessaires à la connaissance astronomique au XIXè siècle.

Présentation muséale de certains objets. Par opposition aux grands instruments liés à leur collection d'objets annexes et à leur bâtiment, il y a toute une série d'instruments portatifs : petits cercles méridiens, sextants, chronomètres (dans presque tous les observatoires), cercles répétiteurs de Borda (un exemplaire splendide à Marseille), baromètres anéroïdes, thermomètres, électromètres, magnétomètres, sismographes etc. Ces instruments étaient souvent utilisés ensemble au cours d'expéditions d'observation de phénomènes exceptionnels. Tous les observatoires visités, à l'exception de Nice, consacrent un espace à l'exposition de certaines de ces pièces. Celles-ci pourraient faire l'objet d'exposition en tant que collection sous réserve d'une explication de leur usage concomitant.

Parfois, certains de ces petits objets sont exposés dans des musées, comme par exemple certains instruments astronomiques de l'observatoire de Toulouse (astrolabe, héliomètres, chronomètre) qui sont exposés au musée municipal Paul Dupuy (musée historique de Toulouse), assurant ainsi leur protection et leur valorisation.

Il y a aussi des pièces uniques, instruments conçus par leur astronome inventeur pour répondre à un besoin particulier. C'est le cas du théodolite à réflexion d'Antoine d'Abbadie exposé au château d'Abbadia, malheureusement sans mise en valeur de son utilité originale. Pire encore, la machine à équation personnelle de l'observatoire de Lyon, pièce fondamentale qui servait à mesurer les temps de réaction des astronomes observateurs, gît en pièces détachées au fond d'un placard.

Enfin, il y a des objets anciens particulièrement rares, dont le classement et la protection en tant que patrimoine historique s'impose. En l'absence d'inventaire et de classification, certains objets sont exposés à des risques de vol ou simplement de dégagement intempestif dans les bennes à ordure. Les observatoires n'étant pas équipés pour exposer des trésors nationaux, les objets de grande valeur sont conservés dans des lieux plus ou moins inaccessibles allant du coffre fort au bureau du directeur (livres très anciens, globe de Coronelli).

Tous ces objets exceptionnels trouveraient une place plus sécurisée dans un musée de l'Astronomie qui n'existe pas encore.

Une réflexion pourrait être menée au niveau européen pour un projet plus ambitieux présentant l'histoire très spécifique de l'astronomie sur le continent, notamment dans son rapport à la technique et l'instrument. Une mise en réseau des observatoires historiques de chaque état membre, avec pour objectif de constituer des collections communes illustrant les progrès scientifiques et la circulation des idées par delà les conflits, pourrait insuffler une dynamique collective permettant d'aboutir à la conception du premier musée européen.

Le cas particulier des livres anciens. Les collections de livres anciens parfois ni triés ni inventoriés sont souvent conservées sur des étagères dans les bibliothèques ou dans des armoires métalliques fermées à clé. Tous les livres anciens n'ont pas la même valeur, mais même lorsqu'on veut se débarrasser de certains d'entre eux, il vaudrait mieux se renseigner d'abord sur les prix du marché des antiquités plutôt que d'opter systématiquement pour l'élimination.

À Bordeaux, un important travail de tri scientifique des collections de livres anciens a été entrepris pendant trois ans à raison d'une matinée par semaine par deux astronomes retraités, Jérôme De la Noë et Michel Rapaport. Méthodiquement, pour chaque série d'annales ou autres publications anciennes, il a été procédé, en collaboration avec la bibliothécaire Marie-Paule Pomiès. à une analyse comparative de ce qui restait dans les

autres bibliothèques scientifiques de Bordeaux pour s'assurer qu'il restait au moins une collection complète sur site au niveau régional.

Pour les publications d'observatoires, cette analyse comparative a été effectuée, dans la mesure du possible, avec les bibliothèques des autres observatoires astronomiques et des doublons ont été envoyés pour compléter des collections. Enfin, un référencement dans le catalogue SuDoc (Système Universitaire de Documentation) a été mené par madame Pomies assistée par un agent temporaire. Il s'agit là certainement d'une démarche exemplaire qu'il faudrait pouvoir adopter dans les autres observatoires.

Enfin, dans le cadre d'un projet d'étude du livre scientifique ancien, la bibliothèque de l'observatoire a contribué au projet URANIE, une base de données de livres d'astronomie anciens de la région qui sont numérisés.

Dans la plupart des observatoires historiques, de beaux rayonnages meublent les bibliothèques originelles et il est important que soient maintenues sur place les collections des ouvrages des autres observatoires, attestant de la modalité de la circulation des idées au XIXème siècle, et de l'importance accordée aux travaux des autres entités, y compris des publications de vulgarisation telle que *L'Astronomie* de Flammarion ou la *Revue Scientifique* d'Émile Algave.

Difficulté de mise en valeur d'objets démontés et disparates. Au delà des objets qui ont été d'une façon ou d'une autre mis en valeur, il existe dans tous les observatoires visités, des objets plus ou moins complets, généralement inventoriés mais pouvant provenir d'instruments non identifiés, amassés en désordre dans les rares pièces encore disponibles car aveugles. Dans certains cas ces pièces sont même en attente d'aménagement et le sort de ces objets disparates est préoccupant. Parmi ces objets hétéroclites il est souvent difficile de faire la part entre ceux qui ont une réelle valeur patrimoniale et le tout venant des rebuts.

Le patrimoine scientifique a si longtemps été négligé, que ceux qui ont pris la charge de s'en occuper à titre bénévole n'osent plus faire de tri. Ainsi, on trouve notamment sur plusieurs sites des stocks de vieux matériels informatiques (consoles, imprimantes...) qui pourraient faire l'objet d'un inventaire comparé entre les observatoires du réseau afin de ne conserver que les machines les plus représentatives de l'évolution technique et d'en faire don à un éventuel musée de l'informatique.

Avec l'apparition de l'électronique, une nouvelle problématique patrimoniale apparaît : autant il était possible de remettre en état un appareil mécanique, même difficilement, autant il sera impossible de retrouver le fonctionnement d'une machine électronique sans avoir les documents afférents sous forme papier car les logiciels de conception ne sont consultables que sur des machines elles-même obsolètes.

L'usage de certains instruments démontés a été parfois tellement perdu de vue qu'on ne prend plus les précautions nécessaires de manipulation. Outre la fragilité des objets, il peut même y avoir un danger pour les personnes qui manipulent des contenants de substances dangereuses. C'est le cas des tubes de détecteurs de particules qui étaient utilisés au Pic du Midi, et sont stockés dans le bric-à-brac de Bagnères de Bigorre.

Peu de personnel dans les observatoires s'intéresse à ces objets épars et démontés. Bien souvent seuls quelques astronomes et techniciens retraités viennent bénévolement faire du tri, de l'inventaire avec un sentiment de culpabilité par rapport à tout ce qui a déjà été jeté et qui manque désormais de façon irréversible. Il y a même parfois un souci de sécurité par rapport à l'intervention de certaines personnes très âgées sur de grands instruments.

Lorsqu'il s'agit de personnel en activité qui s'intéresse au patrimoine, le travail est considéré comme un violon d'Ingres ne faisant pas partie de leur tâche de service. En l'absence de reconnaissance de l'intérêt pour le patrimoine historique, il est souvent difficile à un astronome d'obtenir l'aide d'un technicien pour réparer un instrument ancien, la priorité étant toujours donnée aux activités scientifiques.

Les associations d'amateurs remédient partiellement à cette carence en s'investissant sur la collecte et la restauration d'objets astronomiques anciens.

À Strasbourg, l'AMUSS (Association de culture et de MUSéographie Scientifique), regroupant des historiens et des scientifiques universitaires, a pris en charge cette tâche dans un cadre plus large que l'astronomie seule. La ville lui a attribué des locaux pour stocker les instruments en l'attente de constitution de collections. Mais la municipalité vendant progressivement ses bâtiments, l'association se trouve monopolisée par des tâches de déménagement et de recherche de nouveaux lieux de stockage, sans plus espérer trouver les financements pour créer un musée du type du musée des sciences de Manheim, qui était l'objectif initial de l'association. Cette dernière organise encore des expositions et des animations scientifiques à partir de ses collections, mais a conscience de son épuisement en l'absence d'une volonté politique locale qui permettrait un véritable essor. Un des lieux de stockage restant est une petite salle à l'Observatoire de Strasbourg où des collections disparates d'instruments scientifiques remarquables, tous inventoriés, allant de la presse à imprimerie à un phonographe

d'Edison en passant par divers petits objets liés à l'astronomie, sont entassés.

À Toulouse, la SAP (Société d'Astronomie Populaire) est responsable de l'entretien et de la présentation au public des quatre grands instruments anciens du site de Jolimont. La moyenne d'âge des membres de cette association, comme des autres associations affiliées à la Société Astronomique de France, est assez élevée. Les bénévoles font un énorme travail de recherche dans les archives préalable à la restauration des instruments, participent à la rédaction des cahiers des charges pour les entreprises lorsque certains travaux sont externalisés. Ils regrettent toutefois le manque de relève des générations plus jeunes.

La préservation du patrimoine astronomique repose essentiellement sur la bonne volonté de quelques bénévoles, passionnés mais souvent vieillissants, sans qu'il puisse être espéré une transmission inter-générationnelle des connaissances. Or la spécificité de la transmission d'un savoir aussi spécialisé que l'astronomie implique non seulement la protection d'un patrimoine matériel, mais aussi immatériel. Il serait nécessaire d'assurer la transmission du savoir faire technique permettant la reconstruction, l'entretien et l'utilisation des instruments anciens, indissociables des progrès scientifiques et de l'histoire des sciences.

2.2 Complémentarité des patrimoines matériel et immatériel comme source de vie des observatoires

Les points communs mobiliers et immobiliers des observatoires du XIXè siècle avaient pour corollaire une communauté d'activités scientifiques. Chaque instrument était dédié à un type d'observation particulier, et chaque site avait connaissance des observations menées dans les autres observatoires aux niveaux national et international.

L'implication de l'astronome pouvait aller de la conception à l'entretien de son instrument et au développement de méthodes de travail permettant d'atteindre la précision la plus parfaite possible des observations.

Lorsqu'il sera question de présenter les instruments historiques au public, il sera aussi important de montrer les objets dans leur contexte que d'en faire comprendre la finalité d'utilisation.

2.2.1 Préserver les sites historiques en redonnant vie aux instruments

Pour redonner vie aux instruments il est nécessaire, à l'occasion des recherches d'archives, de s'intéresser à la documentation technique.

L'apport des archives techniques à l'histoire des idées scientifiques. L'histoire a retenu essentiellement le nom des directeurs fondateurs d'observatoires, occultant la plupart du temps le rôle joué par les autres astronomes. En fait le personnel des observatoires de province était très réduit : autour de cinq astronomes. Chacun se trouvait donc responsable d'un instrument ou d'un projet particulier. Bien des recherches en matière d'histoire des sciences se sont attachées aux biographies des astronomes célèbres (Arago, Le Verrier, Janssen...). Or le progrès scientifique n'est pas que le fait de quelques grands hommes, mais découle de tout un contexte de méthodes, de techniques, de savoirs et de savoir-faire dont l'évolution a été portée par un ensemble de contributeurs dont les noms ont été oubliés et dont l'apport a parfois été essentiel. Les recherches dans les archives des observatoires et des diverses institutions scientifiques (académie des sciences, universités...) et les publications scientifiques de l'époque permettraient de retracer le cheminement des idées.

Les différents besoins d'accès aux archives. Il y a divers types de profils parmi les personnes susceptibles de s'intéresser aux archives des observatoires. Certains historiens ont une approche sociologique de l'astronomie tant pour situer un personnage dans l'histoire des idées que pour traiter de l'activité scientifique des observatoires. Ils ont besoin des témoignages que l'on retrouve entre autre dans les courriers ou les journaux de bord des astronomes. La documentation purement scientifique leur reste souvent inaccessible de par sa spécificité.

Souvent, dans les observatoires, un astronome s'est investi de sa propre initiative dans la recherche historique concernant son établissement. Les préoccupations sont assez disparates. Le plus souvent, elles partent d'une préoccupation de conservation du patrimoine qui, il y a une vingtaine d'année, a été encouragée par le ministère de la recherche, qui incitait les observatoires à s'investir dans ce domaine. En effet, les instruments du patrimoine astronomique ont été recensés et étudiés par l'Inventaire dans le cadre d'un protocole signé entre le ministère de la Recherche et le ministère de la Culture.

Un travail considérable a été mené par Françoise Le Guet Tully et Jean Davoigneau selon une méthode scientifiquement validée (Principes, méthode et conduite de l'Inventaire général. Paris : Monum, Editions du patrimoine, 2001, p. 15.). Dans un article consacré à l'inventaire du patrimoine astronomique (In Situ n°6) ils indiquent le sens dans lequel les responsables du patrimoine astronomique doivent mener leurs travaux :

« La valorisation de ce patrimoine par les observatoires nécessite de le connaitre,d'étudier son histoire et de le resituer dans son contexte, à la fois pour le comprendre et pour comprendre l'évolution des techniques qui ont accompagné sa conception. »

Pour ce faire, un important travail de recherche a été entrepris sur chaque site, à partir des archives disponibles. Néanmoins, en l'absence de formation suffisante en histoire des sciences pendant leur cursus universitaire, les astronomes doivent se former sur le tas à la méthodologie de l'histoire des sciences et de la conservation du patrimoine pour pouvoir publier le fruit de leurs travaux de recherche dans ce domaine, et obtenir une reconnaissance de cet investissement. Notons que dans certains cas, des astronomes amateurs sont aussi amenés, dans le cadre de conventions, à assurer l'entretien et la présentation au public des instruments historiques. Leurs préoccupations sont centrées sur la restauration des instruments et la connaissance des méthodes d'utilisation. Ils ont eux aussi besoin d'un accès aux archives techniques.

Certains personnels retraités des observatoires conservent une connaissance vivante du fonctionnement d'instruments anciens qu'ils ont utilisés au début de leur carrière. Ils restent indispensables aux directeurs lorsque des réparations s'imposent, mais compte tenu de leur âge et des difficultés d'accès aux instruments, ce recours est considéré comme de plus en plus périlleux. Malheureusement la transmission de ce savoir-faire technique est difficile à demander car tous ces retraités n'ont pas forcément la fibre pédagogique et en l'absence de documentation, c'est la connaissance même qui est menacée.

Difficulté d'accès aux archives des observatoires privés. Dans le cas des fonds d'archives exceptionnels des astronomes qui avaient créé leur propre observatoire (Antoine d'Abbadie, Camille Flammarion, Lucien Rudaux) les archives n'ont pas toutes la même accessibilité.

Le fonds légué par d'Abbadie à l'Académie des sciences a fait l'objet d'un inventaire méthodique par le conservateur des archives de l'Académie des sciences, qui a révélé bien des disparitions. Les correspondances et la plupart des livres ont été conservés dans la superbe bibliothèque du château d'Abbadia. Toutefois le site est assez isolé et peu de chercheurs souhaitent étudier les documents sur place. Néanmoins une partie des archives de d'Abbadie a été consultée et va être numérisée pour les besoins d'une étude particulière de la littérature basque. Il serait intéressant que l'Académie des Sciences, Arts et Belles Lettres de Bordeaux constitue un comité d'Abbadie afin de créer une dynamique de recherche sur cet éminent personnage de la région.

Le fonds Rudaux a été légué à la bibliothèque de la ville de Donville en Normandie, et les archives ont été déposées aux archives départementales, qui ont organisé l'année dernière une exposition et un colloque sur le personnage tout à fait exceptionnel de Lucien Rudaux, à la fois astronome et précurseur du « space art ».

Le fonds Flammarion a été légué à la Société Astronomique de France (SAF) mais l'inventaire fait à l'époque du classement Monument Historique de ces archives a été très succinct. Une partie des archives a été microfilmée au moment où elle a été versée aux archives départementales, mais l'inventaire n'est pas adapté aux besoins des chercheurs en histoire des sciences. En outre, les livres et archives restés sur le site sont entassés avec un classement fantaisiste, dans deux réduits attenants à l'observatoire, et leur accessibilité est limitée par la faible disponibilité des bénévoles de la SAF responsables de ces archives, qui habitent pour la plupart à plusieurs centaines de kilomètres de l'Observatoire.

Dans la mesure où les archives des observatoires privés concourent à la connaissance de l'astronomie et ont une très grande importance, notamment pour évaluer l'impact de la vulgarisation dans la circulation des idées scientifiques à la fin du XIXème siècle, il apparait indispensable qu'un inventaire exhaustif soit réalisé de manière professionnelle afin de permettre leur accessibilité aux chercheurs.

La dispersion des archives au détriment de la recherche historique. De manière générale, les archives des observatoires ont été déplacées par souci de gagner de la place ou pour éviter leur destruction. Toutefois, avant déplacement il n'y a pas eu d'inventaire et il est très difficile dans certains sites de savoir où chercher les documents souhaités. Lorsque les archives ont fait l'objet de dépôts aux archives départementales, dépôts qui sont définitifs, leur inventaire a été fait par le personnel du ministère de la culture qui n'est pas initié à la spécificité de l'astronomie.

À Marseille, les archives anciennes (jusqu'en 1950 environ) ont été inventoriées par les archives départementales, et sont revenues à l'observatoire dans la maison des astronomes dans les années 1990. Elles ont été numérisées par le centre de conservation du livre d'Arles et y sont encore provisoirement conservées. Elles doivent être récupérées et redéposées au Plateau de Longchamp.

Dans le cas de Toulouse lors du déménagement de l'Observatoire de Jolimont, les documents ont été confiés aux archives municipales qui n'ont effectué aucun tri, mais ce dépôt est temporaire. À terme, ces archives

devraient revenir sur le site avec l'ensemble du patrimoine instrumental historique. Pour l'instant elles ne sont accessibles que sur autorisation préalable de l'astronome responsable du patrimoine qui est le seul à connaître leur contenu. Si elles devaient revenir à Jolimont dans le futur espace muséal, ce qui serait souhaitable, un inventaire devrait être réalisé de manière à les rendre plus facilement accessibles aux chercheurs.

À Bordeaux, les archives de l'Observatoire ont été entièrement inventoriées et classées par Laetitia Maison-Soulard dans le cadre de sa thèse en collaboration avec les Archives départementales de la Gironde. Elles sont laissées en dépôt organisé à l'observatoire, dans le but d'un maintien documenté proche des instruments. Cela permet les versements d'archives au fur et à mesure des départs à la retraite des scientifiques. Elles ont aussi fait l'objet de versements au fur et à mesure du tri du fonds ancien de la bibliothèque et de la découverte d'archives dispersées.

Toutefois, en l'absence d'une méthode de conservation des archives des observatoires, celles-ci se trouvent dispersées au gré des dépôts effectués à différentes périodes aux archives municipales, départementales ou nationales. Malheureusement, beaucoup ont été détruites sans tri préalable, ou détériorées à cause de conditions de stockage inappropriées. Ainsi, les carnets d'Émile Marchand, un des premiers directeurs de l'observatoire du Pic du Midi, ont été retrouvés pourris dans un sous-sol humide. Seuls deux ont pu être sauvés, qui ont été une mine de renseignements pour la rédaction du livre d'Emmanuel Davoust sur l'histoire du Pic.

Pour les archives qui subsistent sur site, il serait nécessaire lorsque cela n'a pas déjà été fait comme à Nice, de développer une méthodologie élaborée en collaboration avec les services d'archives, permettant de prendre en compte la spécificité de la recherche en matière d'histoire des sciences et des techniques. Pour faciliter les recherches, il faudrait pouvoir mettre dans une base de données commune l'ensemble des descriptions de documents d'archives existant dans les différents sites. Pour l'instant, il ne semble y avoir que des initiatives dispersées non coordonnées.

Ainsi à Lyon, tous les documents concernant l'observatoire trouvés dans les différents centres d'archives ont été numérisés et sont en cours de classement par référence et description dans une base de donnée locale propre à l'observatoire.

À l'Observatoire de Paris, la base de données Alidade contient un grand nombre de documents tantôt numérisés, tantôt seulement décrits, et est accessible en ligne. Toutefois, par manque de moyens, une nouvelle version de cette base beaucoup plus complète et performante attend depuis un an et demi d'être finalisée pour remplacer la première.

En ce qui concerne les instruments il y a de très grosses lacunes dans les archives techniques. La conception était faite en collaboration entre l'astronome et le constructeur, et il arrive qu'on retrouve les correspondances entre eux à ce sujet. Mais on ne retrouve par contre généralement pas les plans de construction des instruments qui seraient pourtant précieux pour leur restauration. Dans certains cas, on a oublié même le fonctionnement de certaines parties d'instruments comme le système d'éclairage de l'altazimut de l'Observatoire de Strasbourg. Dans les réserves des observatoires maints instruments ou pièces d'instruments sont conservés sans qu'on sache, par faute de documents, quelle était leur utilité.

Regrouper les bonnes volontés pour rendre vie au patrimoine instrumental. Quand bien même un effort serait fait en faveur de l'accessibilité des archives, pour faciliter la tâche des rares personnes compétentes en matière de patrimoine astronomique, il semble qu'il serait opportun de constituer sur chaque site des petits groupes de personnes venant d'horizons différents, et susceptibles de s'épauler dans leurs efforts. Pour ce faire, l'impulsion devrait partir des observatoires avec la constitution, lorsqu'elle n'existe pas, d'un pôle patrimoine dont l'animation serait confiée à un astronome investi dans des tâches de recherche en matière d'histoire des sciences.

À Strasbourg, la Région a demandé au directeur de l'Observatoire de fédérer les clubs et associations d'astronomes amateurs, afin de n'avoir qu'un seul interlocuteur pour le montage des projets d'animation. Il faudrait pouvoir s'appuyer sur ce rôle fédérateur pour pouvoir drainer les bonnes volontés vers la restauration du patrimoine historique, la transmission des savoirs et des savoir-faire.

À Marseille l'association Andromède, créée en 1976, gère les actions de diffusion de la culture scientifique (planétarium fixe et itinérant). Elle met en valeur quelques grands instruments historiques, comme le télescope de 80 cm de Foucault ou le grand équatorial, conservés sur le site. Son action est essentiellement tournée vers le milieu scolaire et le grand public. Cette association très active, qui reçoit plusieurs milliers de scolaires par an, est liée par une convention avec l'Université.

À Toulouse où l'observatoire historique n'est plus un centre d'activité scientifique, la Société d'Astronomie Populaire, installée sur le site de Jolimont, participe à la réalisation des cahiers des charges pour la restauration

des instruments anciens dont elle a la responsabilité aux termes d'un contrat signé avec l'OMP.

Sur le campus, des instruments inventoriés mais démontés sont amassés dans les recoins d'un garage en attente d'être restaurés, mais il est difficile d'obtenir l'aide des services techniques pour réaliser les interventions qui seraient nécessaires dans la mesure où le patrimoine n'est pas considéré comme une priorité. Il n'y a aucune passerelle entre les deux sites pour la restauration du patrimoine instrumental.

Le projet de la municipalité de créer un quartier scientifique dans le centre de Toulouse qui accueillera les associations qui sont actuellement à Jolimont, permettra de libérer le site historique sur lequel pourra être regroupé l'ensemble des archives et des instruments, recréant ainsi une cohérence. Toutefois, en l'absence d'activité scientifique, il sera difficile de redonner vie au site à moins d'en faire un musée.

Plutôt que de transformer les observatoires en musées, il semble préférable de s'appuyer sur la force d'attraction de sites encore en activité pour tenter de redonner vie aux instruments et de s'en servir comme moyen pédagogique de transmission des connaissances.

Promouvoir l'importance de l'observation dans la démarche scientifique. L'intérêt scientifique de l'observation du ciel n'est pas directement tangible pour le public. La seule vue d'un instrument ancien n'apporte pas grand-chose à la connaissance qu'on peut avoir de son utilité. C'est pourquoi il est très important de préserver les observatoires astronomiques comme des témoignages d'une démarche scientifique d'observation plutôt que comme des musées.

Pour éveiller la curiosité du jeune public, une première étape peut être la découverte des astres par un instrument ancien, complétée par l'observation avec des instruments modernes illustrant ainsi l'évolution des techniques.

Mais il est indispensable d'expliquer aussi l'adéquation de l'instrument à un projet scientifique. Les instruments anciens se prêtent particulièrement bien à l'explication des enjeux de l'observation, car les principes physiques étudiés à la fin du XIXème siècle sont suffisamment simples pour être présentés de manière pédagogique. Par exemple on fera très bien comprendre la mesure du temps ou des positions des étoiles par une observation dans une lunette méridienne, telle qu'elle se faisait autrefois.

C 'est pourquoi il est nécessaire de conserver autour des instruments tous les objets annexes qui permettaient les mesures. Il serait intéressant de pouvoir présenter la méthode de l'œil et de l'oreille ainsi que l'utilité des fils d'araignée à cette occasion. Il pourrait même être envisagé de faire tester à chacun son équation personnelle dans la mesure du temps de passage des étoiles, pour faire comprendre l'extrême exigence de précision requise par la manipulation de ces instruments.

2.2.2 Faire valoir la complémentarité des activités sur les sites historiques

Si l'on s'oriente vers une conservation cohérente d'un ensemble constitué des patrimoines naturel, instrumental, mobilier et immobilier des observatoires, on ne peut laisser de côté la complémentarité des activités qui animaient le site.

Complémentarité des activités dans les observatoires. Lors de la création des observatoires, les différents domaines de compétence pouvaient être à la portée des mêmes personnels. Ainsi, si chaque astronome avait la responsabilité d'un instrument, il pouvait aussi bien faire des relevés météorologiques, mener des observations hors de son champ de spécialité, entretenir les instruments et les systèmes mécaniques des bâtiments.

Une grande partie du travail d'astronome était la réduction des données et les calculs afférents. Dans certains observatoires, spécialement ceux impliqués dans le projet de la carte du ciel, un personnel spécifique, souvent féminin, était employé dans un service des calculs. Dans d'autres cas, le directeur faisait appel ponctuellement à la collaboration de personnes extérieures suffisamment instruites, tels des instituteurs, pour alléger le travail des astronomes.

Les seules tâches vraiment distinctes et considérées comme subalternes étaient celles de gardiennage et de jardinage. Petit à petit, les astronomes ont conçu des dispositifs permettant de perfectionner leurs mesures, ou des instruments secondaires montés sur les lunettes et télescopes (photomètres, spectromètres...) et le travail technique est devenu de plus en plus lourd. Sont apparus alors de nouveaux métiers au sein des observatoires tels que photographes, mécaniciens, opticiens, électriciens puis électroniciens... Cette diversité existe encore dans les observatoires qui ont gardé une forte activité instrumentale comme à Lyon par exemple, bien que la tendance croissante à l'externalisation de beaucoup de réalisations menace cette diversité de métiers.

Complémentarité des métiers. La complémentarité des métiers et des activités était plus forte encore sur un site comme celui du Pic du Midi et de sa station de plaine de Bagnères de Bigorre compte tenu des conditions de vie quasi autarcique.

Sur le site du Pic, il reste peu de témoignage des conditions de vie extrêmes des astronomes. Par contre, dans les placards du site de l'OMP à Tarbes, et dans les remises décrépites de Bagnères, on trouve encore quelques objets porteurs de cette mémoire particulière : Pains de sucre, skis de fonds, portraits en bas relief de terre cuite des premiers directeurs modelés par un des météorologistes, convertisseur d'énergie solaire basé sur le principe du radiomètre de Crookes, lit en bois du général Nansouty (fondateur du premier observatoire météorologique du Pic). Il serait souhaitable que ces objets puissent être regroupés et éventuellement présentés dans un petit musée qui pourrait prendre place à Bagnères dans la maison abandonnée du directeur.

En outre, il reste à Bagnères de Bigorre le témoignage de la complémentarité des métiers dans un bâtiment des années 1960, où cinq ateliers (forge, mécanique, optique, menuiserie, électricité) sont en enfilade. Ce bâtiment, bien qu'abandonné, a gardé quelques équipements, en premier lieu la forge, de telle façon qu'il serait intéressant d'en faire un écomusée[ii] compte tenu de l'implication de la municipalité dans la sauvegarde du site du Pic du Midi et de la vie scientifique de la localité.

La photographie, un métier intimement lié à l'astronomie. À l'époque de la fondation des observatoires astronomiques du XIXè siècle, la photographie était encore une technique récente et peu répandue. C'est précisément à cette époque qu'elle a fait son entrée dans les moyens d'investigation de l'astronomie. En 1887, un vaste projet international de photographie du ciel entier, initié par des astronomes français, entraina la construction d'un instrument particulier : l'astrographe.

En France, des astrographes furent installés à Paris, Toulouse, Bordeaux et Alger. Le cas de Besançon est particulier : le directeur, René Baillaud, décida dans les années 1930 d'installer un astrographe de la carte du ciel, grâce au leg du fondateur de l'Observatoire, Louis-Jules Gruey. Mais des difficultés administratives différèrent le projet qui ne put voir le jour avant la guerre. Lorsque l'instrument fut finalement installé en 1952, le projet de la carte du ciel était moribond et déjà obsolète au regard des grands relevés effectués avec des télescopes modernes.

L'abandon de la Carte du Ciel s'étant fait progressivement, il n'y a pas eu de démarche concertée sur les témoignages que l'on devait garder de cette expérience. Sur les deux sites visités, Bordeaux et Toulouse, il reste de très intéressants témoignages de la participation à ce projet : l'astrographe lui-même, mais aussi beaucoup de matériel auxiliaire comme les machines à mesurer les clichés, des châssis photographiques, à Toulouse un ensemble de plaques photographiques et à Bordeaux une collection inventoriée de clichés conservés en ambiance climatisée. Ces objets pourraient être rassemblés et mis en situation, notamment à Toulouse sur le site de Jolimont, dans une perspective muséale présentant ce projet de coopération internationale scientifique.

Il faut noter aussi l'existence sur certains sites comme à Besançon de plaques photographiques vierges. Ces plaques en vieillissant vont devenir inutilisables, si ce n'est déjà le cas. La question est ouverte de leur devenir. Faut-il les utiliser dans des projets pédagogiques ? Faut-il les conserver pour en analyser les émulsions lorsque plus personne n'en aura la connaissance ?

La carte du ciel n'a pas été la seule activité astronomique faisant appel à la photographie. Une immense quantité de plaques photographiques a été produite dans les différents observatoires, dont très peu nous sont parvenues. À Meudon, par exemple, des milliers de plaques ont été détruites sans aucun effort de recensement ni de tri.

De plus les astronomes ont fait énormément de clichés de leurs installations, et même de leur vie quotidienne, qui sont autant de témoignages précieux pour les recherches historiques. À Lyon par exemple, ont été trouvés des clichés d'astronomes entourant un des frères Lumière, dans des scènes sportives, destinés à tester les émulsions rapides qu'ils venaient de mettre au point. Malheureusement, il reste très peu de photographies sur le site, et des recherches sont en cours auprès des descendants des premiers astronomes pour retrouver une partie de ces témoignages iconographiques.

Il reste partout un travail à faire pour inventorier ces stocks de photographies. À Toulouse, une démarche systématique de numérisation des clichés est en cours, menée par le photographe de l'établissement, qui a trouvé ainsi une reconversion après l'abandon brutal de la photographie en astronomie au profit des techniques électroniques.

[ii] La notion d'écomusée a été établie par le Conseil international des musées en 1971, elle vise avant tout à valoriser le patrimoine matériel (outils, habitat, ...) et immatériel (savoir-faire, métier, ...) d'un territoire et d'une population.

3 La « nasse » de l'environnement institutionnel

Les observatoires astronomiques sont depuis leur origine en interaction avec diverses entités « englobantes », villes et universités, et la recherche d'autonomie s'avère difficile devant l'accroissement du poids de celles-ci. Toutefois si l'on parvient à préserver la spécificité des sites historiques, il est possible que leur force d'attraction attirant les entités « gravitantes » permette de constituer des groupes attachés à la préservation du patrimoine. La mise en réseau de ces groupes permettrait de surmonter les divers cloisonnements administratifs.

3.1 L'attachement à l'autonomie au cœur de la jungle politico-administrative

La forte croissance des villes et des universités a eu tendance à étouffer le rayonnement scientifique des observatoires astronomiques historiques. Pour éviter la dilution au sein des universités, des structures réunissant les sciences observationnelles ont été créées. Pour que soit reconnue la spécificité des sites astronomiques historiques, il ne suffit pas de participer à cette course au gigantisme institutionnel, mais il faut rechercher à faire des alliances permettant de les mettre en valeur sans les transformer en musée.

3.1.1 La perte de visibilité de l'astronomie

L'astronomie participant au rayonnement scientifique des villes. Sous l'Ancien Régime plusieurs observatoires existaient à Paris comme dans les principales villes de province. Ces établissements avaient un lien avec les institutions savantes locales : Académie des Sciences Arts et Belles Lettres, faculté des sciences ou lycées. Après la Révolution, les observatoires de province, victimes de la centralisation jacobine ont périclité.

Sous le Second Empire, au paroxysme de cette centralisation, les grandes villes ont commencé à réclamer la création de nouveaux observatoires en province. Les objectifs pouvaient être purement utilitaires, comme les prévisions météorologiques ou la distribution de l'heure à la ville, mais dans certains cas, les archives prouvent que les édiles avaient le souci du rayonnement scientifique de leur cité.

À Besançon, c'est un impératif économique qui fut la principale raison de l'édification de l'Observatoire : il s'agissait de concurrencer l'industrie horlogère suisse qui bénéficiait de l'expertise de l'Observatoire de Neuchâtel pour la certification des montres et des chronomètres. L'orientation du nouvel observatoire fut d'emblée la chronométrie.

À Lyon, les archives ont montré que le fondateur de l'Observatoire, Charles André, a dû, pour obtenir une subvention de 25000 Francs de la Ville, « prendre l'engagement formel d'installer avant la fin de l'été [1883] un service de garantie des chronomètres qui dispensera nos horlogers d'aller chercher leurs certificats à Genève ou Neufchatel ». Ce service ne fut pas créé, et c'est finalement la météorologie qui assura à l'observatoire le soutien des collectivités locales.

Même si les établissements finalement installés dans les années 1870 furent des observatoires d'État, les villes comme les départements ont significativement contribué à leur édification – à l'exception de Nice où il y eut peu d'interaction entre la ville, non universitaire, et l'observatoire.

Dans les premières années, les liens avec les collectivités locales se sont maintenues du fait de l'autonomie dont jouissaient les observatoires vis à vis des facultés.

Les observatoires au sein de l'Université, du fauteuil au strapontin. Les interactions entre les observatoires et les universités ont été assez analogues dans tous les sites, si on excepte Paris et Nice, qui ont toujours été des établissements indépendants.

Bien qu'ailleurs les observatoires aient été associés à l'activité des facultés des sciences notamment par le biais des charges d'enseignement des astronomes, ils bénéficiaient d'une large autonomie de gestion. Leur rattachement aux nouvelles universités qui virent le jour à la toute fin du XIXè siècle par la fusion des facultés préserva la reconnaissance de leur indépendance et de leur spécificité, leur directeur étant membre de droit du conseil de l'Université.

Dans les années 1960, ce qui avait justifié la fusion des facultés fut balayé par une nouvelle séparation des disciplines et un éclatement des universités en plusieurs établissements. Les observatoires furent alors rattachés à l'université scientifique, gardant le statut de composante à part entière au même titre que les Unités d'Étude et de Recherche (UER). Cette évolution a continué dans le même sens au cours des années et les directeurs d'observatoires ont fini par perdre leur présence de droit aux conseils des universités.

Dès lors, les observatoires astronomiques n'étant plus associés aux instances universitaires décisionnelles, ont perdu en visibilité pour l'université, et la reconnaissance de leur spécificité a laissé place à un traitement banalisé.

L'évolution des techniques d'observation astronomique ne justifiant plus l'utilisation des anciens instruments, la justification de l'existence même de ces établissements excentrés s'est amoindrie.

Cette évolution a été préjudiciable à la conservation du patrimoine astronomique historique, dans la mesure où les préoccupations patrimoniales de l'Université se sont bornées à une gestion administrative des locaux.

Alors que les observatoires jusqu'à la moitié du XXè siècle avaient très peu de personnel, l'astronomie a profité de la vague de recrutement des années 1960 dans les universités liée à la massification de l'enseignement supérieur. Pour permettre au personnel en forte croissance de travailler sur les sites, de nouveaux bâtiments ont été construits dans les observatoires. Ces bâtiments ont été construits sans aucun souci de préservation d'une cohérence architecturale sur les sites historiques.

Lorsque les besoins en surfaces nouvelles de travail ont encore augmenté, les bâtiments destinés aux instruments anciens ont été reconvertis en bureaux, en bibliothèques, en salles de réunion ou en salles techniques. De la même façon, de la place a été gagnée aux dépens des archives dont beaucoup furent détruites.

Instabilité liée aux flux et reflux de la décentralisation. En plus de l'accroissement des personnels des observatoires existants, de nouveaux laboratoires d'astrophysique ont été créés dès 1965 (Laboratoire d'astronomie spatiale à Marseille), et au cours des années qui ont suivi.

À Toulouse, une équipe parisienne d'astrophysiciens a été décentralisée dans les années 1980. À Lyon, un groupe d'astrophysique a été créé dans les années 1990 au sein de l'École Normale Supérieure (ENS), nouvellement décentralisée.

La coexistence de plusieurs entités traitant de questions d'astronomie et d'astrophysique a créé des tensions entre elles. La tentation des tutelles de regrouper au sein d'un même établissement ces groupes d'activités voisines a été très forte. Et compte tenu de la perte d'attractivité des observatoires historiques, le choix été fait à Toulouse et Marseille de les abandonner au profit de nouveaux établissements situés sur des campus universitaires.

Notons qu'à Marseille la réorganisation du site de Longchamp après le départ des astronomes, a été préjudiciable à la mise en valeur d'une partie du patrimoine. La maison des astronomes, qui permettait d'exposer une partie des collections, a été affectée à l'Institut Méditerranéen d'Études Avancées (IMéRA) et elles ont dû être déplacées dans d'autres locaux sans site d'exposition.

À Lyon, le rapprochement des équipes de l'observatoire du groupe d'astrophysique de l'ENS a été envisagé en 2000, mais l'abandon du site historique a été évité du fait de sa spécificité instrumentaliste rendant nécessaires de vastes plates-formes techniques ne pouvant pas être créées sur le nouveau site. Récemment, la volonté des tutelles de rapprocher les astronomes des physiciens dans le cadre du plan campus a réactivé le projet d'abandon du site historique.

À Bordeaux, la question du transfert se pose aujourd'hui, mais les locaux proposés sur le campus sont plus exigus que ceux du site historique de Floirac, où les personnels sont déjà à l'étroit.

3.1.2 Les alliances nécessaires pour retrouver une place au soleil

La tendance centralisatrice des politiques patrimoniales des universités. La tendance à fusionner les établissements dépasse largement le niveau des observatoires. Dans un retour de balancier on assiste depuis quelques années à un mouvement vers la fusion des universités d'une même ville (parfois même d'une région) en des établissements uniques de très grande taille. Cette orientation semble avoir pour origine le constat du mauvais rang des universités françaises dans le classement de Shanghai. Des structures temporaires, les Pôles de Recherche et d'Enseignement Supérieur (PRES), regroupant les universités avec l'objectif de les fusionner, ont été créées dans la plupart des villes, sauf à Strasbourg où la fusion s'est faite sans étape préalable.

Plusieurs PRES ont consacré une partie de leur budget au patrimoine historique. Ainsi le PRES de Toulouse possède un Service de diffusion de la culture scientifique et technique, composé d'une titulaire et deux contractuelles qui consacrent une partie importante de leur activité à la sauvegarde et la valorisation du patrimoine scientifique matériel et immatériel, et disposent pour cela d'un budget significatif. À Paris le PRES a un projet « patrimoine » qui devrait être doté de 5 à 6 M€, et dont la gouvernance n'est pas encore définie.

À l'Université de Strasbourg, l'intérêt pour le patrimoine est partagé entre le vice-président chargé du patrimoine qui est surtout préoccupé par les aspects logistiques, et le vice-président en charge de la mission culture scientifique et technique qui s'attache au travers de la structure du Jardin des Sciences à la diffusion de la culture scientifique et à la gestion du patrimoine historique.

Il semble que dans plusieurs universités scientifiques, la prise de conscience de la nécessité de sauvegarder le patrimoine entraine un inventaire des derniers vestiges épars et dans le meilleur des cas un regroupement des

collections sur un même site.

À Lyon le projet d'IDEX « *propose la création de structures destinées respectivement à l'inter-fécondation des savoirs (Cité des Savoirs), à la médiation, et à la valorisation du patrimoine scientifique (Musée des Collections de la Recherche Universitaire)* ».

Le problème de ce type de valorisation par regroupement d'objets qui seront uniquement proposés à la vue est qu'il crée une distance entre l'activité scientifique et l'outil de recherche. La crainte de plusieurs disciplines est que le classement et l'exposition dans un musée rende définitivement inutilisable ces objets, alors que seul le maintien dans un contexte de recherche peut faire comprendre au public la méthode scientifique d'utilisation de ces outils de travail.

De plus, dans la mesure où l'astronomie est au carrefour de toutes les sciences physiques et mathématiques, il serait plus logique que des instruments pédagogiques anciens de physique soient présentés au sein des observatoires que d'exposer des instruments d'observation au milieu de la collection d'instruments de physique du musée de l'Université.

Le regroupement des collections universitaires dans des musées est un premier signe d'intérêt des universités pour le patrimoine historique, mais il risque de ne créer que des passerelles illusoires entre les différentes disciplines scientifiques à l'instar des fusions d'universités si elles ne restent que des coquilles administratives.

En ce qui concerne l'astronomie la chance d'avoir des sites historiques cohérents et encore en activité doit permettre d'éviter le départ des instruments anciens dans des collections universitaires afin que la diffusion des connaissances puisse témoigner de réels savoirs et savoir-faire.

La course actuelle au gigantisme pour retrouver une spécificité. En réponse aux fusions des Universités et à la Loi Relative aux Universités (LRU), donnant à celles-ci une bien plus grande autonomie et un rôle de pilotage de la recherche, l'Institut National des Sciences de l'Univers (INSU) a lancé une politique de regroupement des disciplines d'observation, pour disposer au sein des universités de grands laboratoires placés sous son égide, lui permettant ainsi de conserver son influence en matière de recherche.

De grands Observatoires des Sciences de l'Univers (OSU) ont été créés administrativement en regroupant des laboratoires le plus souvent situés sur des sites différents avec l'intention de réaliser des économies d'échelle par une mise en commun des moyens, et avec l'espoir que ces rapprochements puissent permettre des synergies scientifiques entre les sciences allant de l'astronomie à l'environnement en passant par la paléontologie.

Ces OSU sont à géométrie variable mais nulle part il n'y a de cohérence complète entre les regroupements administratifs et les lieux de travail. Dans certains cas, les personnels sont regroupés sur le même site mais ne se connaissent pas. Quand ils sont sur des sites séparés les projets communs sont encore plus difficiles à concevoir.

Pourtant, il pourrait être intéressant de consolider le regroupement des sciences de l'observation par le biais de recherches historiques communes afin de faire ressortir les points communs des sciences observationnelles du XIXè siècle. Ainsi que vu précédemment, le tracé des parcs des observatoires historiques mériterait que des recherches d'archives soient approfondies à l'occasion d'un projet partenarial entre l'Observatoire astronomique et les laboratoires de botanique. À Strasbourg, la proximité du jardin botanique qui jouxte l'Observatoire se prêterait particulièrement à ce type d'étude.

Mais il y aurait aussi intérêt pour le patrimoine des Observatoires astronomiques de créer des passerelles entre les sciences humaines et les sciences physiques. Un partenariat avec des centres de recherche en histoire des sciences (Centre Alexandre Koyré à Paris ou François Viète à Nantes) permettrait d'accueillir leurs doctorants de manière privilégiée sur les sites des observatoires historiques.

Défendre une conception particulière de la diffusion des connaissances. Dans la mesure où les Universités adoptent une stratégie muséale en matière de patrimoine historique, les observatoires astronomiques ont tout intérêt à défendre leur rôle en matière de diffusion des connaissances en insistant sur les spécificités des sciences observationnelles en présentant les instruments historiques en fonctionnement.

À Strasbourg, le Jardin des Sciences fait de la diffusion de la culture scientifique, par le truchement de médiateurs, et il s'est aussi lancé dans la formation permanente, en s'insérant dans le plan académique de formation.

Or la diffusion des connaissances est aussi une des compétences des astronomes qui sont relativement peu sollicités, et les présentations faites par les professionnels sont souvent très appréciées.

L'étape de la détermination des modalités de gouvernance des PRES est importante pour bien préparer la fusion en terme d'équilibre des pouvoirs.

Pour éviter les conflits de compétences en matière de diffusion des connaissances et de conservation du patri-

moine, il serait souhaitable que les présidences d'Université se dotent de conseils qui réuniraient les représentants des différentes disciplines et qui pourraient donner des orientations stratégiques et prioriser de manière objective les projets.

Le soutien de la ville à des observatoires historiques vivants. Les observatoires ont toujours été construits assez loin des centres des grandes villes, mais l'extension urbaine les a très vite rattrapés. Toutefois, leur intégration dans le tissu urbain moderne s'est faite différemment selon les cas.

À Toulouse ou Marseille, la ville a progressivement encerclé l'observatoire qui est devenu un îlot enclavé au sein même de la grande cité. Au contraire à Bordeaux et Lyon, les établissements ont été installés sur les territoires des petites communes de Floirac et de Saint-Genis-Laval qui, malgré l'extension des agglomérations, restent administrativement distinctes de leurs métropoles respectives.

Paradoxalement, ce sont les petites communes qui hébergent les sites historiques qui aujourd'hui perçoivent le mieux l'intérêt d'y maintenir une activité scientifique pour éviter leur abandon. Le paradoxe n'est qu'apparent : pour une ville de dix à vingt mille habitants, comme c'est le cas de Saint-Genis ou Floirac, l'Observatoire représente un pôle intellectuel important dans la vie culturelle de la cité. L'avantage d'avoir des professionnels sur le site est que la diffusion des connaissances est assurée par des personnes compétentes qui ne pourraient pas être mises à disposition d'un observatoire devenu musée.

À Saint-Genis, la municipalité est toujours partie prenante des manifestations organisées par le service de diffusion des connaissances de l'Observatoire, comme la science en fête ou les portes ouvertes. En ville, certains éléments du mobilier urbain ont été choisis pour attirer l'attention sur la présence de l'observatoire sur le territoire de la commune.

À Besançon, la ville s'est étendue jusqu'à l'Observatoire, du fait de la construction du campus universitaire tout autour. Une cohérence a été trouvée entre la ville et l'Observatoire avec la création par la commune du Musée du Temps qui fait le pendant de l'activité chronométrique de l'Observatoire. Pour la diffusion des connaissances, la ville organise des visites conduites par des médiateurs scientifiques recrutés par l'Office de Tourisme, qui viennent compléter les visites des professionnels, afin de ne pas trop peser sur l'activité des astronomes.

À Nice, malgré la pression immobilière, l'Observatoire a maintenu son activité astronomique tout en se dotant d'une structure d'accueil du public. Toutefois la richesse patrimoniale exceptionnelle du site qui a justifié plusieurs type de protection (classement des monuments, instruments, parc) mériterait une mise en valeur beaucoup plus marquée.

Dans le cadre d'un partenariat avec la ville de Nice, un chemin touristique à caractère historique et architectural pourrait être développé autour des constructions de Charles Garnier sur la Riviera. Françoise Leguet-Tully a fait valoir dans plusieurs articles dont un paru dans l'ouvrage collectif *Les Riviera de Charles Garnier et Gustave Eiffel. Le rêve de la raison* (Marseille : Editions Imbernon, 2004) tout l'intérêt qu'il y aurait de s'intéresser aux autres réalisations de Charles Garnier à Monaco (salle de concert du Casino) et Bordighera (Villa de Bischoffscheim).

On pourrait mettre en exergue l'apport d'élites éclairées aux sciences à la fin du XIXè siècle en faisant le lien entre l'Observatoire astronomique fondé par Raphaël Bischoffsheim et le Musée Océanographique du prince Albert Ier de Monaco.

Par contre, dans des métropoles comme Marseille ou Toulouse, l'intérêt de l'Observatoire est moins tangible aux yeux des élus qui ont à gérer de multiples institutions culturelles. En général, ces grandes villes délèguent à des associations sur place les activités d'animation ou de diffusion des connaissances. Elles leur demandent aussi parfois d'organiser des manifestations artistiques qui n'ont qu'un vague rapport avec l'astronomie et qui rencontrent peu de succès. Les sites étant déconnectés des activités scientifiques, leur pouvoir d'attraction pour le public en est réduit d'autant.

Pour Marseille, la qualification de la municipalité comme « *Capitale Européenne de la Culture 2013* » représenterait une opportunité pour transformer une partie du site de Longchamp en un musée de l'astronomie qui n'existe pas encore en France. Toutefois, au vu de l'expansion que prend l'IMéRA, dont les sujets de recherche sont complètement étrangers à l'astronomie, et qui occupe aujourd'hui une grande partie du site, on peut se demander si l'installation d'un musée est encore possible. Cet institut a en effet pour but d'accueillir une quinzaine de chercheurs résidents ayant leurs locaux d'habitation et de travail sur place. L'ancienne maison des astronomes lui est déjà entièrement dédiée, et « *l'aménagement du bâtiment universitaire débutera fin 2011 et permettra d'aménager une dizaine de logements, des espaces dédiés aux projets de l'IMéRA, ainsi que des*

aires de service et de détente ≫[iii].

En ce qui concerne le Pic du Midi, c'est une mobilisation collective très importante allant des professionnels jusqu'aux collectivités territoriales qui a permis d'éviter le démantèlement de l'Observatoire. Toutefois, si le syndicat mixte qui gère désormais le site a réussi à y développer des activités touristiques, la station de plaine de Bagnères de Bigorre qui était étroitement lié à l'Observatoire est quasiment abandonnée : elle reste utilisée comme garage et lieu de stockage, et certaines parties sont utilisées par la mairie de Bagnères. Un projet existe de convention de transfert d'usage à la Mairie qui souhaiterait l'orienter vers les arts plastiques.

Enfin, dans le cas particulier des observatoires privés de Camille Flammarion à Juvisy et d'Antoine d'Abbadie à Hendaye, les villes qui sont chargées de l'exploitation touristique au terme d'un bail emphytéotique peinent à assurer la dynamique nécessaire pour rendre ces sites astronomiques attractifs.

L'investissement des villes ne saurait pallier l'abandon des sites par les professionnels et l'idée de confier aux bénévoles d'associations la lourde responsabilité de l'entretien du patrimoine, de l'animation des sites désertés et de la diffusion des connaissances est irréaliste, d'autant que ces associations souffrent d'un faible renouvellement de leurs membres, et peinent à assurer toutes ces missions.

Les sites historiques qui ont maintenu leur activité de recherche scientifique se sont ouverts au public pour assurer la diffusion des connaissances, et le partenariat avec les villes et les associations permet d'organiser un accueil motivant pour le public sollicitant ponctuellement les astronomes professionnels, sans pour autant perturber leurs activités.

3.2 Le mille-feuilles interne des observatoires

Il existe de nombreux cloisonnements administratifs au sein des observatoires historiques qui empêchent un traitement cohérent et global de la problématique patrimoniale. Mais la force d'attraction que représente les sites pourrait permettre de surmonter ces cloisonnements par la mise en réseau des compétences internes et externes.

3.2.1 Cloisonnement administratif au sein des observatoires

Les cloisonnements administratifs concernent à la fois le régime juridique afférent au patrimoine naturel, mobilier et immobilier, et les statuts des personnels travaillant dans les observatoires.

Cloisonnements administratifs liés à la diversité des régimes de propriété du patrimoine. Selon les observatoires, et au gré de leur évolution historique respective, la propriété des terrains, des bâtiments a été dissociée et éclatée entre les niveaux nationaux, régionaux et locaux. Alors que la sauvegarde du patrimoine astronomique nécessiterait une cohérence dans la mise en œuvre des restaurations, la diversité des régimes de propriété entraine des blocages préjudiciables aux actions entreprises, d'autant que les démarches de classement Monuments historiques requièrent l'accord du propriétaire. Cet accord peut être refusé ou retardé dans la mesure où le propriétaire d'un monument historique est responsable de son entretien. Même si ces travaux bénéficient d'une aide substantielle de l'État, le renchérissement des coûts liés à la nécessité d'une étude préalable d'un Architecte des Bâtiments de France, fait hésiter. De plus, toute restauration de patrimoine mobilier ou immobilier effectuée avec des financements publics impose de rendre accessible au public ce qui a été restauré.

Par ailleurs, compte tenu de l'instabilité liée aux dévolutions du patrimoine entre l'État et les collectivités locales, celles-ci peuvent être préjudiciables à l'engagement de restaurations dans la mesure ou les conditions de cofinancement par l'État en sont modifiées. En effet, certaines dévolutions peuvent se faire de la ville à l'État, et lorsque le propriétaire devient le ministère de la Recherche, l'aide du ministère de la Culture ne peut plus être accordée, l'État ne pouvant se subventionner lui-même.

La juxtaposition administrative des statuts des personnels. Au sein des observatoires coexistent des personnels qui même s'ils partagent une activité commune ont des statuts différents :

- Les chercheurs peuvent appartenir à plusieurs corps : enseignants chercheurs des Universités et des Écoles Normales Supérieures, chercheurs CNRS, membres du corps des Astronomes et des Physiciens
- Les ingénieurs et les techniciens dépendent de l'Université, du CNRS ou dans certains cas d'une École Normale Supérieure

[iii] Citation tirée du site web de l'IMéRA `http://www.imera.fr/index.php/fr/devenir-resident/hebergement.html`

- Des personnels sous contrats à durée déterminée sont financés par diverses institutions nationales et internationales, voire les collectivités locales.
- Des étudiants de divers niveaux fréquentent sur de plus ou moins longue durée les observatoires.
- Les professionnels des bibliothèques dépendent de l'Université ou du CNRS.
  À l'Observatoire de Paris, le patrimoine et la documentation sont confiés à des conservateurs qui sont des personnels scientifiques des bibliothèques et non des bibliothécaires.

Les statuts des chercheurs de chaque corps sont régis par des décrets différents qui leur attribuent une répartition variable de leurs tâches de service.

Entrecroisement des tâches. Par définition, la recherche est la tâche majeure de tous les chercheurs qu'ils soient membres du CNRS, astronomes, enseignants chercheurs, étudiants post-doctoraux et doctorants. Un astronome, quel que soit son statut, effectue ses recherches dans un champ d'étude qui évolue au cours du temps, et qui peut être radicalement différent du domaine pour lequel il a été initialement recruté. Ainsi, son implication dans un travail d'histoire des sciences est tout à fait envisageable dans la mesure où il publie ses travaux. Dès lors que le chercheur atteint une notoriété dans son domaine d'investigation, son observatoire de rattachement ne peut que bénéficier de cet investissement et a tout intérêt à l'encourager.

Les tâches d'enseignement supérieur sont partagées entre enseignants chercheurs, astronomes, et certains doctorants. Les chercheurs CNRS ne sont pas tenus d'enseigner mais peuvent le faire à leur gré.

En ce qui concerne la diffusion des connaissances auprès du grand public, les astronomes et les enseignants chercheurs ont l'obligation statutaire d'y participer.

Enfin, le décret portant statut des astronomes mentionne une activité particulière à ce corps : celle d'observation et de conservation des données. Compte tenu de la nécessité d'accumulation des données sur le long terme, cette activité, appelée tâche de service, le libère partiellement de la pression de l'enseignement et de la publication.

Les personnels techniques ont moins de diversité que les astronomes dans la définition de leurs tâches et moins de liberté dans l'orientation qu'ils souhaitent leur donner. Leurs activités sont déterminées par la direction de l'établissement auquel ils sont rattachés, et il faut une volonté affichée de cette dernière pour qu'ils puissent participer aux travaux relatifs au patrimoine historique, comme la restauration ou des réparations ponctuelles d'instruments.

Le rôle des bibliothécaires des observatoires a dû s'adapter aux nouvelles techniques et pratiques informationnelles. Ils apportent une aide documentaire différente aux astronomes qui effectuent l'essentiel de leurs recherches bibliographiques sous forme numérique.

Gérer le fonds documentaire dont celui des livres anciens est une des missions qui leur incombent. L'aide professionnelle qu'ils peuvent apporter aux astronomes en matière de recherches patrimoniales est considérable. Parfois, elle est réduite par une transformation des postes à temps plein en poste à mi-temps.

3.2.2 Dynamique attendue d'une mise en réseau des compétences

Si les tutelles considèrent que la sauvegarde du patrimoine astronomique est une priorité, et compte tenu de l'importance des cloisonnements, il faudrait qu'elles donnent une impulsion en terme de reconnaissance d'activités et de moyens financiers pour lancer une réelle dynamique.

Valoriser l'intérêt pour le patrimoine historique pour créer une dynamique. Parmi tous les personnels cités dans la section précédente, on trouve peu de volonté pour s'investir dans les activités relatives à l'entretien ou à la connaissance du patrimoine historique. Le fait que la recherche scientifique soit par essence tournée vers l'avenir entraine une fréquente absence d'intérêt des scientifiques pour leur histoire et peut expliquer cette désaffection. Et le fait qu'aucune reconnaissance spécifique ne soit prévue statutairement aggrave encore la situation.

Seuls les plus passionnés s'engagent dans la recherche historique, souvent au détriment de leur carrière, ou bénévolement sur leur temps libre. Ces personnes s'investissent généralement aussi dans les activités de diffusion des connaissances, les observatoires historiques étant des lieux privilégiés de découverte et d'éducation populaire, indépendamment de l'éducation nationale. Mais dès lors que ces activités de diffusion des connaissances ne s'adressent pas à des classes constituées mais à des publics variés, elles ne sont pas considérées comme des tâches statutaires d'enseignement. De ce fait sont mises au même niveau la simple présentation de l'observatoire à un public de visiteurs qui relève de la communication, et la réalisation d'un véritable cours (comme ceux

donnés à l'Université Populaire Européenne de Strasbourg par exemple) qui implique un effort particulier de préparation.

Bien souvent, ces personnes passionnées par l'histoire continuent après leur départ à la retraite de participer à la mise en valeur du patrimoine historique de l'observatoire en déplorant l'absence de relève dans les jeunes générations. La conséquence de ce manque de relève est que la moyenne d'âge des personnes actives s'occupant du patrimoine astronomique est élevée, et n'est même pas compensée par l'arrivée de jeunes doctorants d'histoire des sciences, car les rares étudiants qui sont présentés par les formations doctorales sont souvent eux-aussi des retraités, ce qui a l'inconvénient de donner une image un peu surannée à ce domaine de recherche.

Parmi les bénévoles, outre les astronomes professionnels retraités, les amateurs des diverses associations pallient dans certains cas le manque de bonnes volontés pour s'occuper du patrimoine instrumental délaissé. Malheureusement, on rencontre le même problème de relève générationnelle dans le monde associatif que dans les observatoires.

Comme on vient de le voir, les activités liées à la conservation et la mise en valeur du patrimoine astronomique historique reposent sur quelques bonnes volontés éparses et non coordonnées, et il est impossible de maintenir l'effort cohérent et continu que justifierait l'ampleur de cette tâche.

Constituer des pôles patrimoine au sein des observatoires. Malgré la diversité statutaire des personnels, la complémentarité des compétences pourrait servir de levier pour créer une dynamique de groupe au sein des observatoires, sous réserve que la sauvegarde du patrimoine soit considérée comme un enjeu d'importance au niveau des tutelles. Si tel était le cas, il faudrait que l'investissement dans cette tâche soit prise en compte et valorisée dans l'évolution de carrière des personnels. Compte tenu de la diversité statutaire, c'est au niveau des tutelles que devrait être insérée une tâche spécifique au patrimoine historique dans les référentiels d'activité.

Dans la mesure où la sauvegarde du patrimoine astronomique implique de se préoccuper à la fois de la transmission des savoirs et des savoir-faire, il serait indispensable d'associer les recherches faites dans le domaine des idées, relevant de l'histoire des sciences, et celles faites pour restaurer les instruments.

Aussi, il pourrait être constitué au sein des observatoires des pôles/comités de patrimoines rassemblant plusieurs compétences professionnelles (astronomes, historiens des sciences, bibliothécaires, archivistes, techniciens) qui pourraient s'ouvrir à la participation des professionnels du patrimoine de la Direction Régionale des Affaires Culturelles (DRAC) et des bénévoles des associations intéressés par le patrimoine astronomique.

Il y a en effet souvent une association d'astronomes amateurs dont le siège social est à l'observatoire. Ainsi, la Société d'Astronomie Populaire (SAP) à Toulouse, la Société Astronomique de Lyon (SAL), l'Association Astronomique de Franche-Comté (AAFC) à Besançon et la Société Astronomique de France Groupe Alsace (SAFGA) à Strasbourg.

Bien que beaucoup de ces associations soient plus ou moins affiliées à la Société Astronomique de France (SAF) elles sont toutes très attachées à leur autonomie, et si une mise en réseau avec les observatoires institutionnels est concevable, elles s'opposeraient à un pilotage parisien de quelque nature qu'il soit.

Mettre en réseau des observatoires historiques au niveau national et européen. Dès lors que les tutelles auraient reconnu l'importance de la sauvegarde du patrimoine dans chacun des observatoires historiques, une mise en réseau des groupes de travail de chaque établissement permettrait le partage des connaissances et des bonnes pratiques. Pour assurer la vie du réseau, ce partage devrait donner lieu à des rencontres des personnels ayant les mêmes compétences. De plus, des passerelles devraient être mises en place entre des centres de recherches en histoire des sciences et les observatoires astronomiques historiques. C'est pourquoi un budget devrait être déterminé au niveau national pour permettre la mobilité des personnels et soutenir la production de travaux. Les orientations stratégiques devraient être définies au terme d'un protocole entre les ministères de la Culture et de l'Enseignement Supérieur et de la Recherche.

Il existe aussi dans d'autres pays européens des observatoires historiques qui ont plus ou moins les mêmes difficultés de conservation et d'entretien du patrimoine. Toutefois les projets de coopération entre observatoires qui existent pour l'instant sont centrés sur des enseignements d'astrophysique communs et non sur le partage des problèmes communs concernant la sauvegarde du patrimoine.

Mais la transmission des savoir-faire techniques est beaucoup plus importante en Allemagne qu'en France où la formation artisanale est souvent méprisée. Aussi pourrait-il être intéressant de développer des projets de coopération en matière de restauration des instruments historiques qui impliqueraient des partenaires nouveaux pour les observatoires comme les chambres des métiers et les entreprises. Ce type de projet soutenus par des composantes publiques et privées, dans au moins deux pays européens, pourrait être éligible à des financements

européens.

La mise en perspective historique des coopérations ayant pu exister dans le domaine de la fabrication des instruments pourrait de surcroit faire ressortir une spécificité identitaire de l'astronomie européenne dans son rapport aux instruments. Chaque découverte associée à un progrès instrumental pourrait être mise en valeur dans un musée européen de l'astronomie auquel les travaux de coopération en matière de sauvegarde du patrimoine historique apporteraient une contribution.

Pour la mise en œuvre d'une stratégie d'envergure européenne, se pose toutefois la question de l'absence d'intérêt des Régions en matière de gestion du patrimoine culturel. Pourtant celles-ci ont bénéficié, à l'occasion du transfert de compétence posé par la loi Liberté et responsabilité locale du 13 août 2004, d'un transfert des personnels du ministère de la Culture. Mais si la précieuse expertise de ces personnels est sollicitée au cas par cas par les observatoires, aucun portage politique régional n'est perceptible dans le domaine du patrimoine historique. Pourtant il serait indispensable que les Régions deviennent des promoteurs de valorisation et de coopération, notamment pour des projets qui pourraient bénéficier de financements européens.

4 Conclusions

Le travail d'observation critique présenté dans ce rapport sur la situation du patrimoine historique des observatoires astronomiques, a été entrepris de manière spontanée par un astronome et une élue locale, soucieux de comprendre pourquoi la sauvegarde du patrimoine astronomique avait justifié l'organisation par le Ministère des Affaires Étrangères et Européennes et la Société Astronomique de France d'un colloque à ce sujet en septembre 2011.

A l'issue de ce colloque, dans le cadre des discussions pour la rédaction de la Déclaration de Paris, une phrase a été suggérée qui n'a pas été retenue dans le texte final, mais qui pourrait néanmoins être la conclusion de ce rapport : *nous souhaitons que les astronomes réinvestissent leur culture et leur histoire en redonnant vie au patrimoine naturel, matériel et immatériel des sites astronomiques historiques*

Nous tenons à remercier les personnes qui nous ont accueillis sur les sites visités et/ou nous ont fait bénéficier de leur expertise :

- À Besançon : François Puel, Joëlle Schirer, François Vernotte.
- À Bordeaux : Jérôme De La Noë, Marie-Paule Pomies.
- À Hendaye : Céline Davadan.
- À Juvisy : Gérard Dufour, Francis Ogier.
- À Lyon : Émilie Wernli.
- À Marseille : James Caplan, Bruno Vila.
- À Nice : Christophe Benoist, Françoise Le Guet-Tully, Farrokh Vakili.
- À Paris : Laurence Bobis, Jean Davoigneau, Christine de Joux, Florence Greffe, Françoise Launay, Isabelle Rouge-Ducos, Jean-Yves Sarrazin.
- À Strasbourg : Pascal Dubois, Philippe Vonflie, Hervé Wozniak.
- À Tarbes et Bagnères de Bigorre : Francis Beigbeder.
- À Toulouse : Emmanuel Davoust, Michel Esteves, Jean-Noël Perolle, Roland Trotignon, Sébastien Vauclair.
- Aux archives départementales de l'Essonne : Laurence Mayeur.

SF2A 2012
S. Boissier, P. de Laverny, N. Nardetto, R. Samadi, D. Valls-Gabaud and H. Wozniak (eds)

L'OBSERVATOIRE ASTRONOMIQUE DE STRASBOURG

H. Wozniak[1]

Résumé. La problématique de la préservation et de la conservation du patrimoine a dépassé le cadre de la recherche en Histoire des Sciences pour devenir un enjeu de société. En utilisant l'exemple particulier de l'Observatoire astronomique de Strasbourg, on montre la nature des contraintes auxquelles est soumis l'observatoire, les antagonismes créés par des missions parfois incompatibles, les difficultés à mener des actions de sauvegardes et celles engendrées par la multiplicité des acteurs. Des pistes de réflexions sont proposées afin de réconcilier, voire rendre compatibles, les différentes missions et responsabilités des observatoires.

Keywords: patrimoine, observatoires

1 Introduction

Lorsqu'on parle de patrimoine, flanqué ou non de l'adjectif « historique », qu'il soit immobilier (bâtiments et instruments à demeure) ou mobilier (généralement les instruments portatifs et les livres), il convient de distinguer sa conservation, c'est à dire *l'action de le maintenir en bon état* (`http://www.cnrtl.fr/definition/academie9/conservation`), de sa préservation, qui consiste *à le protéger d'un mal et, en particulier, de l'altération, de la destruction* (`http://www.cnrtl.fr/definition/academie9/préservation`). Privilégier l'une ou l'autre de ces actions, voire les deux lorsqu'elles sont compatibles entre elles, n'est pas sans conséquence sur le patrimoine des observatoires, d'autant que lorsque l'activité scientifique y est vive, la tendance naturelle est d'adapter les locaux et les instruments aux besoins contemporains.

Conserver suppose implicitement que le patrimoine est encore en usage, tel que prévu lors de sa conception, ce qui est le cas à Strasbourg. La notion de « bon état », lorsque le patrimoine, en particulier instrumental, n'est pas utilisé selon sa finalité première, revêt une signification forcément différente selon l'interlocuteur. Par exemple, un instrument peut être considéré comme étant en bon état de par son aspect visuel, mais ne plus remplir correctement ses fonctions d'origine. Un instrument n'est pas seulement un bel objet, il renseigne également sur la technologie et l'ingéniérie d'une époque et donc doit remplir sa fonction.

Préserver le patrimoine, c'est faire un choix définitif pour chacun des objets ou bâtiments qui n'a plus d'usage pour les missions premières d'un observatoire, à savoir la recherche, l'enseignement et les services d'observation. L'irréversibilité du choix explique que toute décison est jugée à l'aune de l'Histoire par les générations suivantes. La préservation implique donc une prise de décision réfléchie et guidée par des critères objectifs.

Par conséquent, conserver et préserver ne sont pas des actions neutres au regard de la recherche en Histoire des Sciences. Mais depuis le milieu du XX^e siècle, un nouvel acteur a pris peu à peu sa place : le grand public, autrement dit le non-spécialiste, ni en Astronomie, ni en Histoire des Sciences, ni en Patrimoine. D'un objet d'étude, le patrimoine est devenu au fil du temps un objet de visite, de contemplation, de fierté (locale ou nationale), voire même un argument politique ou électoral. Ceci n'est pas sans effet sur la politique de conservation et de préservation.

Nous revenons donc brièvement sur l'histoire de l'Observatoire astronomique de Strasbourg, et sur quelques spécificités qui le distinguent dans le paysage astronomique français. Nous le prendrons en exemple pour illustrer la complexité du « microcosme patrimonial », avec un point particulier sur la préservation des bâtiments. Puis au travers de quelques questions et illustrations, nous nous interrogerons sur les contraintes patrimoniales qui pèsent de plus en plus sur les observatoires, avant de dégager quelques pistes de réflexions sur des actions visant à équilibrer les différentes missions des observatoires.

[1] Observatoire astronomique de Strasbourg, 11 rue de l'Université, F-67000 Strasbourg

2 L'Histoire, toujours, pour commencer

L'Observatoire astronomique de Strasbourg, appelé simplement *Observatoire de Strasbourg* avant le décret fondateur des Observatoires des Sciences de l'Univers (OSU), occupe son troisième site depuis sa toute première création. En effet, suite à la victoire de la Prusse en 1870, Wilhelm Ier décide de faire de Strasbourg une vitrine de l'Empire germanique. Une nouvelle Université va naître de cette volonté politique forte, dotée de bâtiments modernes, adaptés à la science triomphante de la fin du XIX^e siècle, abritant des laboratoires équipés des toutes dernières technologies (Heck 2005).

Mais de fait c'est bien plus qu'une Université qui sort de terre, c'est tout un nouveau quartier, la *Neustadt*, incluant des bâtiments officiels, comme le Palais Impérial qui deviendra l'actuel Palais du Rhin et de nombreux immeubles d'habitations afin de loger les allemands qui s'installent alors. L'ensemble représente un ensemble architectural globalement homogène car construit sur une échelle de temps relativement courte (1871-1914), même si certains architectes germaniques ont parfois disposé de la liberté d'explorer divers styles brisant l'harmonie de l'ensemble.

Une Université nouvelle en cette fin du XIX^e siècle ne peut se concevoir sans un observatoire moderne, inspiré des plus récents et plus performants observatoires au monde. Celui de Poulkovo servira d'exemple (Service de l'inventaire et du Patrimoine de la Région Alsace 2009). Inauguré le 22 septembre 1881, l'Observatoire est l'un des tout premiers ensembles de bâtiments sortis de terre. C'est en effet la Grande Coupole qui permettra l'alignement du reste du campus sur l'axe qui la relie au centre de la Place Impériale, actuelle Place de la République. Organisé autour de trois édifices reliés par une galerie couverte en forme de Y, l'ensemble ne verra pas de grandes modifications avant 1932, treize ans après son retour à la France. À cette date un quatrième immeuble est construit au 13 rue de l'Observatoire, dont le rez-de-chaussée verra les premières expériences de Lallemand sur ce qui deviendra, plus tard et à l'Observatoire de Paris, la caméra électronographique. Cet immeuble, rehaussé d'un étage en 1958, représente aujourd'hui à lui seul près de la moitié de la superficie totale occupée par les bureaux du personnel de l'Observatoire.

La dernière modification immobilière notable date de 1999. Le hall de la lunette méridienne Repsold est alors transformé en bibliothèque, la méridienne toujours présente tronant au milieu des ouvrages et revues professionnels. Le bâtiment qui l'abrite (dit bâtiment Est ou méridien) et l'immeuble de 1932 sont alors joints par une extension largement vitrée. Le même type d'architecture alliant aluminium et verre est retenu pour les quatres extensions, *les cubes*, qui aggrandissent le bâtiment de la Grande Coupole. Sans ces extensions, l'Observatoire ne disposerait d'aucun amphithéâtre et le bâtiment de la Grande Coupole d'aucun bureau (hormis la direction qui occupe ce qui fut la bibliothèque à l'origine, et l'administration).

Concernant le patrimoine instrumental, l'Observatoire a été équipé d'une lunette Merz-Repsold de 49 cm dès 1880. Plusieurs cercles méridiens viennent compléter le parc instrumental, qu'ils aient été fabriqués pour l'Observatoire allemand (cercle méridien de Repsold), ou qu'ils aient une origine plus ancienne (la lunette de Cauchoix daterait de 1828 mais a été par la suite modernisée sous l'ère allemande).

L'Observatoire dispose d'une collection très variée de pièces plus petites qui a fait l'objet d'un inventaire entre 2000 et 2004 (`http://www.hp-physique.org/OBSERVATOIRE`). Parmi les pièces majeures figurent un globe de Coronelli du XVII^e siècle, deux astrolabes dont le plus ancien remonte au XIII^e siècle (astrolabe marocain) et de nombreuses horloges de précision de Leroy et Ungerer. La provenance de ces instruments est parfois inconnue. L'inventaire allemande débuté en 1886 sert souvent de repère. À ce patrimoine s'ajoute la collection de l'AMUSS (Association pour les Musées des Sciences de Strasbourg, fondée en 1982). Cette association souhaitait créer un musée scientifique et technique à Strasbourg afin de mettre en valeur l'instrumentation scientifique des laboratoires. Au fil des ans, une grande partie de sa collection s'est retrouvée entreposée à l'Observatoire. On y trouve majoritairement des instruments de physique, dont certains ont servi lors de l'expédition de Paul Emile Victor. Beaucoup ont été sauvés des poubelles des laboratoires voisins.

3 Une singularité dans l'astronomie française

Par ses bâtiments de style néorenaissance, ses instruments de facture allemande et son emplacement au sein d'un campus universitaire, de nos jours en pleine agglomération de 280 000 habitants, l'Observatoire de Strasbourg représente une forme d'exception dans le paysage astronomique français. De nombreux autres observatoires sont le fruit d'une délocalisation partielle de l'Observatoire de Paris, et/ou situés sur des collines, tandis que tous les instruments dont ils sont équipés portent la trace d'une tradition d'opticiens et de mécaniciens bien différente de leurs homologues germaniques.

Figure 1. L'Observatoire astronomique de Strasbourg en 2009 vu depuis la tour de chimie. Les trois bâtiments principaux : à gauche, la Grande Coupole qui abrite une lunette de 49 cm, troisième de France par le diamètre ainsi le bâtiment Sud au toit à quatre pentes qui hébergeait originellement les appartements du directeur (désormais celui du DGS de l'Université) et d'une partie du personnel ; à droite, le bâtiment Est ou méridien ainsi que l'extention de 1932, 1958 et 1999. L'ensemble est situé dans des jardins qui lui sont propres mais qui jouxtent le Jardin Botanique (sur la gauche). Photo : Serge Le Gurun. Observatoire astronomique de Strasbourg.

De ce simple fait, l'Observatoire de Strasbourg mérite une attention toute particulière, d'autant plus que son activité scientifique est loin de s'étioler. Le Centre de Données astronomiques de Strasbourg (CDS), qui vient de fêter ses quarante ans, y a vu le jour sous le nom de Centre de Données Stellaires. Aux côtés des équipes « Galaxies » et « Hautes Énergies », le CDS participe à la visibilité internationale de l'Observatoire, et au-delà, à l'excellence de l'Université de Strasbourg dans son ensemble.

Autre singularité notable, le premier planétarium universitaire, hors Paris, y a vu le jour en 1982. Trente ans plus tard, il est toujours en activité au sein de l'Observatoire, occupant l'ancienne salle de la méridienne Cauchoix au bâtiment Est. Cette activité a été confiée à l'Université en 2008, qui la gère au travers d'une structure spécifiquement dédiée à la diffusion des connaissances, en charge également de la mise en œuvre de la politique muséale, le *Jardin des Sciences*. Au-delà des séances de planétarium, les visites de la Grande Coupole et de l'exposition permanente d'instruments anciens dans les sous-sols du bâtiment Est (la *crypte aux étoiles*) sont également organisées par le Jardin des Sciences. À l'horizon 2015-2016, un nouveau bâtiment spécialement dédié à la diffusion des connaissances et à la muséographie, financé dans le cadre du Plan Campus avec une forte participation des collectivités locales, verra le jour à une centaine de mètres de l'Observatoire. Il sera équipé d'un planétarium numérique et aura une plus grande capacité d'accueil.

4 Une conservation aux multiples acteurs

L'Observatoire de Strasbourg n'est donc qu'un exemple parmi d'autres d'un ensemble de bâtiments, totalisant 4600 m^2 de surface habitable, à forte valeur historique, dont l'usage est extrêmement varié : recherche, service d'observations (CDS et SSC-XMM), enseignement universitaire, formation des maîtres, cours du soir (Université Populaire Européenne, Université du Temps Libre), hébergement d'associations d'astronomes ama-

Figure 2. La lunette méridienne Repsold au centre de la bibliothèque vue depuis la mezzanine. Photo : Caroline Rose. INSU-CNRS. Observatoire astronomique de Strasbourg.

Figure 3. La Grande Lunette de 49 cm pendant une visite organisée par le Jardin des Sciences en 2008. A droite on aperçoit la chaise-escalier qui permet de suivre le mouvement de la lunette sur 360°. Photo : Caroline Rose. INSU-CNRS. Observatoire astronomique de Strasbourg.

Figure 4. L'entrepôt mis à disposition de l'AMUSS. Tous les instruments sont inventoriés et étiquetés. Photo : Caroline Rose. INSU-CNRS. Observatoire astronomique de Strasbourg.

Figure 5. Une partie de la crypte aux étoiles, aménagée en 1987 dans le sous-sol du bâtiment Est. On y voit, entre les piliers qui portaient le cercle méridien de Repsold, la lunette de Cauchoix (au centre) et le chercheur de comètes (à droite). Photo : Caroline Rose. INSU-CNRS. Observatoire astronomique de Strasbourg.

teurs, diffusion des connaissances, expositions d'instruments anciens, logement du Directeur Général des Services de l'Université, etc. Les infrastructures sont donc soumises à un ensemble de contraintes, relevant le plus souvent de réglementations simplement différentes dans le meilleur des cas, mais parfois incompatibles entre elles. Ainsi,

l'accueil du public imposerait la présence d'un ascenseur afin de ne pas avoir à gravir les 77 marches menant à la Grande Lunette, ce qui est techniquement impossible et architecturellement dommageable à l'intégrité du bâtiment.

Dans un monde idéal, la conservation de l'ensemble devrait être une opération administrativement simple car de la responsabilité exclusive de l'OSU. En apparence cela semble le cas, mais un certain nombre d'évolutions de nature trés différentes viennent brouiller chaque jour un peu plus le paysage. Tout d'abord, il est bon de rappeler que l'Observatoire de Strasbourg est une école interne de l'Université, comme toutes les structures de statut OSU. Il n'est pas propriétaire de ses bâtiments. La relation patrimoniale avec l'Université est, au jour d'aujourd'hui, celle d'un locataire. Le « clos et le couvert » relèvent donc exclusivement des services centraux de l'Université. Pour le reste, l'Observatoire disposant d'une équipe autonome capable d'intervenir rapidement en lieu et place de différents corps d'état, l'Université lui octroie une dotation annuelle d'infrastructure pour l'entretien et les interventions courantes. Ce n'est pas le cas d'autres composantes de l'Université pour lesquelles toutes les interventions sont centralisées par la Direction du Patrimoine Immobilier (DPI). Cette situation ne doit rien au statut administratif d'un OSU. La LRU a renforcé, dans ce domaine comme d'en d'autres, le pouvoir exécutif central de l'Université qui pourrait vouloir intervenir également en lieu et place du locataire. Dans un contexte de réduction globale des effectifs des agents de catégories C, une telle centralisation aurait pour conséquence immédiate une perte de réactivité qui nuirait à la haute disponibilité des services du CDS.

Si cette répartition consensuelle des tâches peut sembler logique dans le contexte local, elle n'est cependant pas simple en mettre en œuvre à cause de la diversité des publics et des acteurs. En effet d'autres élélements interviennent :

- L'entretien de la Grande Lunette doit être réalisée par ceux qui la connaissent le mieux. Or toute activité instrumentale ayant cessée à l'Observatoire depuis les années 80, ce sont des amateurs éclairés de la Société Astronomique de France Groupe Alsace qui graissent la monture, démontent et nettoient les optiques, le tout sous le contrôle de l'Observatoire en matière de sécurité.
- Lorsqu'un essieu de la Chaise de l'Observateur, dispositif qui permet l'observation à la Grande Lunette, menace de s'effondrer, c'est non seulement un élément du patrimoine qui se trouve en danger, mais aussi le public tant nocturne que diurne, lors des visites organisées par le Jardin des Sciences. En cas d'accident, la responsabilité de l'Observatoire serait engagée alors même qu'aucun personnel de l'Observatoire n'est concerné. La réparation comme l'entretien de cet outil sont officiellement du ressort de l'Observatoire « au même titre que n'importe quel instrument de recherche ». Usant de ce prétexte, l'Université a refusé sa prise en charge alors que le Jardin des Sciences en est le principal utilisateur.
- Lorsque la DPI décide d'étanchéiser une coupole ou la toiture des galeries extérieures, ou encore de remplacer les marches en pierre centenaires du perron de la Grande Coupole ou un balcon au bâtiment Sud, c'est sans aucune concertation préalable et sans que l'Observatoire en fasse la demande. La réception des chantiers se fait rarement en présence d'un personnel de l'Observatoire. Le résultat est parfois contestable (et contesté) : une coupole ne tournait plus (« ha bon, ca devait tourner ? »), un ornement en zinc à la jonction des galeries a été remplacé par un autre motif sans soucis de conservation. Quant aux marches du perron, l'opération était inutile mais il fallait liquider le marché en cours. En revanche, depuis une dizaine d'années l'Observatoire demande le remplacement des fenêtres du bâtiment 1932, sans succès.

Ces quelques exemples montrent que l'entretien ou la conservation d'un patrimoine technique aussi particulier que celui d'un observatoire n'est pas qu'une affaire de maçons, de couvreurs ou de plombiers. S'agissant d'un patrimoine immobilier, mais pas immobile, il ne faut jamais perdre de vue la fonction première du bâtiment ou de l'instrument. Or malgré la bonne volonté et la qualité des agents d'un service central ou d'une entreprise, le savoir-faire initial, la technicité astronomique, réside au sein de l'Observatoire. C'est vrai pour le patrimoine immobilier technique (typiquement les coupoles) mais c'est encore plus criant pour les instruments d'observation. Encore faut-il que l'Observatoire dispose lui aussi des moyens de pérénisation de son savoir-faire, ce qui est nullement garanti aujourd'hui. D'une part, à cause des difficultés à renouveler certains postes de catégorie C au sein d'une structure qui n'est pas centrale et d'autre part, par la volatilité des agents qui, en fonction des possibilités de promotion, vont de structure en structure, sans avoir eu le temps de compléter leur formation ou de transmettre leur savoir-faire longuement acquis. C'est ainsi qu'au fil du temps, une grande partie de la mémoire sur le fonctionnement des infrastructures et des instruments repose sur les retraités, catégorie de *non-personnel* puisqu'elle n'a aucune existence légale au sein de nos institutions. Ce point n'est pas mineur puisqu'en cas d'accident, ces personnes prennent le risque de n'être couvertes ni par leur assurance responsabilité civile, ni par celle de l'Université.

Enfin, les sources de financement pour l'entretien du patrimoine se font rares. Face au refus de l'Université

de financer la restauration de la Chaise d'Observation, c'est au mécénat que l'Observatoire de Strasbourg doit faire appel. En effet, la dotation d'infrastructure allouée par l'Université est largement insuffisante pour couvrir des frais de restauration. C'est également le cas lorqu'il s'agit de restaurer le Globe de Coronelli du XVII^{e} siècle ou de fabriquer une copie en plâtre de l'astrolabe du XIII^{e} siècle afin de les exposer au public. Dans ce cadre, la Fondation de l'Université a proposé son aide pour trouver les bonnes personnes ou entreprises capables de nous soutenir financièrement.

5 Préserver l'Observatoire ?

Cette relation entre services centraux et composante de l'Université, que nous venons de décrire dans le cadre simple de l'entretien des bâtiments et des instruments, éclaire le cadre légal et institutionnel dans lequel se situe toute discussion qui viserait à *transformer* des bâtiments. Par transformation, on entend ici tout autant la création de nouveaux immeubles, comme ce fut le cas en 1932, d'extensions, comme en 1999, de transformations lourdes, comme la création de la bibliothèque actuelle, voire la suppression pure et simple d'un immeuble, comme celle envisagée par la Cellule Plan Campus de l'Université de Strasbourg. On est ici en pleine thématique de la préservation et non plus seulement de la conservation.

Ainsi, si l'Astronomie fut à la source de la création de l'Observatoire, l'architecte Eggert travaillant selon les plans de l'astronome Winnecke, si tous les instruments furent voués à la recherche, si l'architecture de certains bâtiments fut pilotée par des besoins techniques précis, aujourd'hui l'astronomie n'est plus que la *locataire* des lieux. Autrement dit se pose depuis plus de vingt ans la question de son déménagement, accompagnée de l'argument récurrent : changer pour les locaux plus adaptés à la recherche contemporaine.

S'il est vrai que certains observatoires ont eu ou auraient tout à gagner en déménageant dans des locaux plus adaptés à des activités d'instrumentation, à se rapprocher des lieux d'enseignement supérieur ou à profiter de plateformes mutualisées, dans tous les cas l'épine dorsale de la réflexion a été ou doit être l'amélioration des conditions d'exécution de leurs missions principales que sont la recherche, l'enseignement et les services d'observations. L'Observatoire de Strasbourg a mené cette réflexion. L'étude publiée en mai 2010 a démontré qu'il était possible d'accomplir toutes nos missions sans avoir à envisager la création de nouvelles infrastructures jusqu'en 2025 environ, en adoptant un modèle de croissance raisonnable extrapolant l'évolution des personnels depuis 1992.

D'autre part, en partie grâce à l'action du planétarium depuis trente ans, l'ancrage de l'Observatoire dans la mémoire collective alsacienne (et non loin de là, en Allemagne) est extrêmement profond. Peu ou prou toutes les écoles primaires de l'Académie du Bas-Rhin ont visité l'Observatoire, sa crypte aux étoiles et vu fonctionner le planétarium. Nombreux sont les parents qui accompagnent leurs enfants en souvenir d'une expérience ancienne. Les Journées du Patrimoine attirent en moyenne 1000 personnes sur le week-end alors que seule la Grande Coupole est ouverte à la visite pendant 2×4 heures. La Nuit des Musées, la Nuit des Étoiles, le Jour de la Nuit, sont autant d'évènements qui drainent régulièrement leurs milliers de curieux. 5 000 personnes ont participé au week-end d'anniversaire des 30 ans du planétarium pour lesquelles les jardins de l'Observatoire étaient ouverts. Pour le grand public, Planétarium et Observatoire sont devenus synonymes.

Cette passion du grand public pour l'Astronomie n'est pas le seul fruit du planétarium. Elle se décline à l'échelle nationale, mais aussi dans les écoles au travers de la formation des maîtres, les conférences dans les clubs et associations d'astronomes amateurs, dans les lieux publics, dans les cours de l'Universités du Temps Libre ou les cours du soir de l'Université Populaire Européenne.

Elle montre également un autre visage qui ne cesse de prendre de l'ampleur : un intérêt de plus en plus affirmé pour le patrimoine historique, sans doute plus en direction des bâtiments et des grands instruments que des petits astrolabes ou autres horloges. Sans étude précise, il est cependant difficile d'affirmer l'origine de cet engouement pour le patrimoine immobilier, mais les Journées du Patrimoine ont sans doute leur part.

Depuis longtemps, Strasbourg met son patrimoine en valeur au travers d'un *Plan de Sauvegarde et de Mise en Valeur* (PSMV), zone également classée au Patrimoine Mondial de l'UNESCO. Ces zones, introduites par la loi Malraux de 1965, sont protégées par un dispositif réglementaire plus contraignant pour l'obtention des permis de construire, de démolir ou de transformer. La réglementation d'un PSMV est intermédiaire entre celle applicable par défaut (permis délivré par la commune après avis de la commission d'urbanisme) et la protection maximale accordée par le classement au titre des Monuments Historiques. Ainsi, pour toute demande de permis, l'Architecte des Bâtiments de France (ABF) rend un avis, qui ne peut faire l'objet d'aucun appel (sauf par le Maire et exclusivement pour les projets de la commune). Le périmètre d'intervention de l'ABF s'étend alors jusque dans les intérieurs, que les bâtiments soient publics ou privés. À ce titre, la réglementation du PSMV est

très proche de celle d'un classement « Monuments Historiques ».

Figure 6. L'actuel Plan de Sauvegarde et de Mise en Valeur (en vert) et son extention pour 2017 (en orange). L'Observatoire est à l'extrémité droite de la zone orange et se reconnait à la forme de Y des galeries liant les trois bâtiments principaux. Image : Communauté Urbaine de Strasbourg (`www.strasbourg.eu`).

Au-delà des maisons à colombages de la Petite France, c'est le quartier allemand, la Neustadt, qui est certainement la plus grande fierté de la ville. Aussi depuis quelques mois, les collectivités locales, en particulier la Communauté Urbaine de Strasbourg, aidée par le Service de l'Inventaire et du Patrimoine de la Région Alsace, ont entamé la révision, c'est-à-dire l'extension, du PSMV à la Neustadt. Depuis fin 2011, le campus de l'Université Impériale, et par conséquent l'Observatoire, est intégralement inscrit dans le futur PSMV.

Quel impact pour l'Observatoire ? Au premier abord on pourrait se satisfaire, à l'unisson de l'Université et du microcosme patrimonial, de disposer enfin des moyens juridiques de protection du patrimoine architectural, à supposer qu'il ait été martyrisé par des directeurs successifs peu scrupuleux. Mais est-ce vraiment le cas ? Certes, les bâtiments de l'Observatoire ont évolué, tant dans leur finalité que leur esthétique au gré des besoins, et ceci dès l'origine. La coupole métallique construite en 1874, avant l'achèvement des bâtiments, a bel et bien disparue. Les toits ouvrants des méridiennes Repsold et Cauchoix sont définitivement condamnés, le bois ayant même été remplacé par un bardage et des tuiles en fibro-ciment (contenant de l'amiante). Serait-il possible de nos jours, dans le cadre protégé du PSMV ou d'un classement au titre des Monuments Historiques, d'adjoindre les fameux cubes en verre aux quatre angles de la Grande Coupole ? Serait-il possible de construire un immeuble de trois étages en prolongement du Bâtiment Est ?

A entendre les différents acteurs contemporains du patrimoine universitaire, il est peu probable que l'Observatoire eut réussi autant de mutation patrimoniale sur un siècle. Pourtant peut-on aujourd'hui dire que l'Observatoire n'a pas été préservé ? Il ne reste rien des deux premiers observatoires des XVII et XVIII^{e} siècle. La Cellule Plan Campus, dirigée par un Architecte Urbaniste de France (AUF), réclame pourtant la démolition du bâtiment 1932-58 afin de revenir à un état proche de celui de 1881. Mais le même service s'accomode de la présence des cubes qui flanquent la Grande Coupole, cubes qui ont fait l'objet de sévères critiques par le passé. Critiques non fondées en ce qui concerne les autorisations car l'ABF de l'époque, avait donné son feu vert à condition que les structures soient, justement, métalliques et démontables. On peut s'interroger sur les motifs qui poussent à rendre l'Observatoire incommode à la recherche scientifique au nom de la préservation du site, tout en démolissant un bâtiment presque centenaire, symbole du retour de l'Alsace à la France.

Quand on se penche sur les aménagements intérieurs, les travaux de transformation seront eux aussi soumis

à l'approbation de l'ABF. Serait-il possible encore aujourd'hui d'aménager une pièce de 30 m^2 en sous-sol, avec plancher technique et climatisation en haute-disponibilité, afin d'y installer les armoires de serveurs et de stockage du CDS, accompagnées de deux groupes aéro-réfrigérants longeant sur 5 mètres le bâtiment ?

6 Quelques questions qui peuvent déranger

Ces questions ont souvent été posées par l'auteur aux différentes personnes qui composent le microcosme du patrimoine historique, ce qui explique qu'elles n'ont parfois de sens que dans le contexte alsacien. Les réponses sont loin de donner une vision claire de l'avenir d'un site inscrit dans un PSMV et peut-être à terme inscrit au Patrimoine Mondial de l'UNESCO ou classé Monument Historique. Au moment où l'on parle d'observatoires à l'UNESCO, questions comme réponses ont leur intérêt.

6.1 A qui appartient le patrimoine ?

Au-delà de la question purement juridique (à l'État à l'heure qu'il est), c'est la question morale qui se pose. En effet, l'état actuel du patrimoine, sa bonne préservation et conservation, résulte du travail de quelques astronomes et personnels techniques passionnés, dans les observatoires ou dans les associations de bénévoles, qui ont soigneusement entretenu les instruments, les bâtiments, les livres, les revues, les plaques photographiques, les petits outils pour tirer les fils d'araignées, etc. Peut-on aujourd'hui expliquer à ces mêmes astronomes et à la cohorte de passionnés que les derniers arrivés, dont certains n'ont jamais travaillé dans un observatoire, sont mieux qualifiés pour reconnaître la pièce rare, pour entrenir une lunette, pour empêcher la réforme d'un télescope devenu inutile ? La réponse n'est pas si simple car si l'astronome a su préserver, c'est généralement par application du principe « on ne jette rien » plutôt que par un raisonnement circonstancié. Le spécialiste est capable en revanche, d'estimer la valeur de l'objet. Ceci étant, à contrario, il est souvent plus facile de décréter qu'un instrument doit être préservé lorsqu'il date du XIX^e siècle que lorsqu'il n'a que vingt ou trente ans. Ainsi, personne n'a été en mesure d'estimer (qualitativement) la valeur du dernier spectrographe construit à l'Observatoire dans les années 70. La décision de le jeter ou de le préserver n'a donc pas pu être prise objectivement. Le principe du « on garde, on ne sait jamais » l'a alors emporté.

6.2 Peut-on détruire un observatoire ?

Autrement dit, au nom du patrimoine et au seul motif de revenir à un instant donné du passé, doit-on détruire ce que les générations précédentes ont élevé, en faisant table rase des missions d'un observatoire, voire en mettant en danger sa pérenité sur les lieux de sa création ? Pendant plusieurs millénaires, l'homme a détruit et ré-utilisé ce que les générations précédentes avaient construit pour faire plus grand, plus beau, plus moderne, pour répondre à de nouveaux besoin. Les cathédrales sont bâties sur les ruines d'églises ou de chapelles bien plus modestes. Lorsqu'on écoute certains acteurs, on pourrait se demander, avec malice, si aujourd'hui le choix ne serait pas davantage de préserver la chapelle et de construire la cathédrale en périphérie de la ville pour ne pas nuire au patrimoine ou à l'homogéneité esthétique du quartier. Ici, on retrouve très souvent l'argument cité plus haut qui consiste à dire que la recherche ne peut être moderne et à la pointe que si elle dispose de bâtiments flambant neufs et high-tech. Là encore, nous l'avons écrit plus haut, l'adaptation aux missions est le seul critère qui doive être retenu. L'Observatoire de Paris s'accomode très bien encore aujourd'hui de son bâtiment Perrault ; l'Observatoire Impérial avait grandement besoin de nouveaux bâtiments ; l'Observatoire astronomique de Strasbourg, 132 ans plus tard, n'en a pas besoin à condition qu'on ne vienne pas lui détruire la moitié de sa superficie de bureaux.

6.3 L'Observatoire est-il un musée ?

La question choque autant ceux qui œuvrent auprès du grand public que ceux qui y effectuent leurs recherches au quotidien. Si l'Observatoire n'était qu'un centre de recherches, la crypte aux étoiles n'existerait pas, la Grande Coupole ne serait pas ouverte au public pour les Journées du Patrimoine, on ne ferait pas visiter la Grande Lunette deux fois par jour en moyenne. Mais, toutes ces activités qui aujourd'hui sont bien ancrées dans le calendrier, suffisent-elles à justifier que l'Observatoire doive participer, de plus en plus souvent, à des opérations au caractère muséal fortement marqué, comme la Nuit des Musées ou à des visites du Patrimoine historique spécialement créées suite à l'extention du PSMV ? Dans le cadre d'une politique muséale ambitieuse dont l'Université de Strasbourg a souhaité se doter, il est évident que l'Observatoire représente un des points d'intérêt

important, en contradiction apparente, mais perceptible par le grand public, avec la communication importante qui est faite sur les résultats scientifiques des chercheurs et l'activité du CDS. Autrement dit, « comment peut-on faire de la science aussi bonne dans des locaux aussi anciens » est l'une des questions récurrentes entendue lors des Journées du Patrimoine.

6.4 Pourquoi conserver ? L'exemple de petits instruments

Hormis la Grande Lunette et la méridienne Repsold, tous les autres instruments ont été déplacés pour être remisés, exposés ou prétés. À ce titre, l'Observatoire de Strasbourg et l'AMUSS peuvent s'enorgueillir d'avoir su préserver et conserver pléthore d'instruments de toutes sortes, la plupart en état de fonctionnement. Mais hormis les quelques heureux élus visibles dans la crypte aux étoiles, ou exposés dans l'escalier qui mène à la Grande Lunette, ces instruments restent cachés du public. Et globalement, ces instruments restent intouchables. Les entrepôts, bien qu'à l'abri des inondations, ne permettent pas d'espérer les mêmes conditions de conservation et de sécurité que des musées nationaux. Dans ces conditions, on peut se demander quel est l'intérêt de la conservation. S'il s'agit d'exposer des instruments dans des vitrines, loin de leur port d'attache et en dehors de leur contexte d'origine, leur fonction est réduite à l'aspect décoratif, qu'ils soient ou non en bon état de fonctionnement, tout en augmentant le risque de vol ou de détérioration (voir le cas à l'Observatoire de Lyon). Aussi, des reproductions ou des copies font parfaitement l'affaire. S'il s'agit de les mettre dans les mains du public ou d'en faire un usage répété en démonstration, l'expérience montre bien que l'on prend de grands risques à les voir se détériorer par usure. La seule personne qui est finalement légitime à les manipuler est l'historien des sciences et des techniques. L'esprit « conservatoire », au sens proche des « Arts et Métiers », prend alors ici tout son sens, mais suppose que cette vocation des observatoires (qui n'est qu'une déclinaison de leur mission de recherche) soit protégée de la pression muséale.

7 Conclusions

En réponse à la question « comment peut-on faire de la science aussi bonne dans des locaux aussi anciens », on peut dire que c'est possible, la preuve ! Cependant, assurer le maintien de l'Observatoire astronomique de Strasbourg dans ses murs actuels, aussi longtemps qu'il ne soit pas absolument nécessaire de le déménager, nécessite toute la clairvoyance de la tutelle hébergeante et une certaine souplesse avec la réglementation du PSMV. Une application stricte des règles d'urbanisme, sous pression des voisinages, sans concertation, sans analyse de l'impact en termes de recherche, d'enseignement universitaire ou de fonctionnement des services d'observation, ne peut conduire qu'à des dysfonctionnements qui mettront à mal la qualité de la production scientifique. Or dans le cadre législatif actuel, la loi Malraux, une personne et une seule, l'Architecte des Bâtiments de France, dispose du pouvoir final de bloquer une transformation immobilière et quasiment sans recours possible. Dans ces conditions de d'éséquilibre des pouvoirs, rare en démocratie, mettre la priorité sur la mission scientifique et éducative de l'Observatoire lors d'une prise de décision qui relève du patrimoine historique peut devenir rapidement une gageure. Il faut donc s'en remettre à l'intelligence des acteurs, jusqu'au bout de la chaine.

Il faut également conserver l'implication des astronomes, ingénieurs et techniciens des observatoires, actifs et retraités, dans la conservation du patrimoine immobilier comme mobilier. Cela peut sembler évident sur certains sites, mais la volonté et les moyens politiques croissants des Universités, notamment ceux conférés par la LRU, peuvent de ci de là créer des situations conflictuelles. La conservation du patrimoine ne peut que pâtir d'un manque de confiance entre services centraux et observatoires.

La communication autour du patrimoine, qu'il soit immobilier ou mobilier, doit elle aussi être le fruit d'une collaboration raisonnée entre les spécialistes de la médiation et les astronomes. Seule une collaboration étroite menant à une communication équilibrée entre patrimoine et recherche contemporaine peut garantir une image fidèle de la nature d'un observatoire aux yeux du Grand Public. Une emphase excessive sur le patrimoine produira invévitablement une distorsion de cette image sur le long terme. Or la recherche, financée encore majoritairement sur des deniers publics, est redevable auprès des citoyens de ses avancées et progrès contemporains et pas seulement de la conservation et préservation des savoirs séculaires.

C'est également pour cette raison qu'il faut laisser les scientifiques au cœur des villes. Symboliquement cela illustre la place qu'une société fait à l'avenir, à la découverte, à la science. En reléguant les scientifiques en périphérie on les ghéttoisent, on les sort du « coeur » de la ville, de la cité, et du « coeur » de ses habitants.

Une coordination entre tous les acteurs est indispensable, et ceci à toutes les échelles. Ainsi, dans le cas de l'astronomie, il est indispensable de concilier la politique (locale) universitaire et une vision nationale qui peut être portée par le Ministère de la Culture et/ou le groupement des observatoires qui se met en place. Une

vision multi-échelle du patrimoine astronomique peut permettre également de se prémunir de changements trop radicaux des politiques universitaires, surtout dans un contexte tendu financièrement.

Enfin, des règles simples et claires définissant ce qui doit être ou non préservé est indispensable pour les décideurs. Couplées à une vision nationale du patrimoine, on pourrait ainsi éviter de tout préserver ou jeter inconsidéremment. Il n'est sans doute pas nécessaire de conserver N copies d'un ouvrage ou d'un instrument fabriqué de façon industrielle. Notons cependant que dans le cas de Strasbourg, la facture allemande de ses instruments nécessite une vision transnationale du patrimoine afin de déterminer avec précision ce qui en fait une spécificité par rapport aux autres observatoires allemands (e.g. Berlin) plutôt que français.

Au-delà, une fois la structure française de coordination sur les rails, il sera indispensable de l'intégrer dans une démarche européenne. La grande rivalité des observatoires européens s'est soldée par des influences croisées qu'il est bon de pouvoir identifier, comparer, et ceci non seulement dans l'intérêt du public ou de la sauvegarde mais aussi celui de la recherche en Histoire de l'Astronomie, et des Sciences et Techniques plus généralement.

Je souhaite remercier les personnes qui m'ont sensibilisé au patrimoine de l'Observatoire astronomique de Strasbourg : Agnès Acker (professeur d'université, en retraite), Olivier Bienaymé (astronome, ancien directeur), Pascal Dubois (astronome, en retraite), Bernard Traut (responsable administratif et logistique de l'Observatoire, en retraite), Philippe Vonflie (documentaliste et responsable du centre de documentation du CDS), Delphine Issenman et Sébastien Soubiran (Jardin des Sciences, patrimoine et politique muséale de l'Université de Strasbourg), Milène Wendling (Jardin des Sciences, responsable du planétarium).

Références

Heck, A. 2005, The Multinational History of Strasbourg Astronomical Observatory, 330

Service de l'inventaire et du Patrimoine de la Région Alsace, ed. 2009, L'Observatoire astronomique de Strasbourg (Editions Lieux-dits)

SF2A 2012
S. Boissier, P. de Laverny, N. Nardetto, R. Samadi, D. Valls-Gabaud and H. Wozniak (eds)

LE PATRIMOINE ASTRONOMIQUE PROVENÇAL

M. Rous[1], P. Figon[1] and S. Guyot[1]

Résumé. L'OSU OAMP/Institut Pythéas porte les missions de conservation, inventaire et valorisation du patrimoine. Suite à la fusion de l'Observatoire de Marseille et du Laboratoire d'Astronomie Spatiale en 2000 pour créer le Laboratoire d'Astrophysique de Marseille, le déménagement des équipes sur le site de Château-Gombert en 2008 a soulevé le problème du devenir des collections des deux sites d'origine. Nous ferons le bilan des actions passées en matière de conservation et de valorisation de ce riche patrimoine : versement à l'inventaire général du Ministère de la Culture, classement de 22 instruments au titre des Monuments Historiques, inventaire et numérisation des archives anciennes, montage d'expositions et réalisation du catalogue « *Telescopium, 400 ans de lunettes et de télescopes* ». Nous présenterons les actions en cours : mesures de conservation préventive, inventaire des archives et des instruments. Nous parlerons enfin des projets : création d'un espace d'exposition permanente, participation à des expositions temporaires.

Keywords: History of astronomy, Marseille, Provence, legacy, instrumentation, exhibitions

1 Un fonds patrimonial important accumulé au cours des siècles

L'historique est résumé ci dessous. Les fonds patrimoniaux accumulés lors de celui-ci sont localisés sur nos différents sites (voir Figs. 1 et 2).

- 1702 : premier observatoire créé par les jésuites, quartier des Accoules à Marseille
- 1862 : établissement de l'Observatoire de Marseille sur le plateau Longchamp
- 1937 : début de la construction de l'Observatoire de Haute Provence (OHP) au nord du Luberon
- 1965 : création du Laboratoire d'Astronomie Spatiale (LAS)
- 2000 : fusion administrative de l'Observatoire de Marseille et du LAS ; création du Laboratoire d'astrophysique de Marseille (LAM) et de l'Observatoire astronomique de Marseille-Provence (OAMP)
- 2008 : regroupement des équipes de recherche marseillaises sur un site unique à Château-Gombert
- 2011 : démolition des bâtiments du LAS
- 2012 : création de l'Institut Pythéas, nouvel OSU pluridisciplinaire : 5 Unités Mixtes de Recherche (LAM, MIO, CEREGE, IMBE et LPED) et une Unité Mixte de Service avec le site d'observation de l'OHP

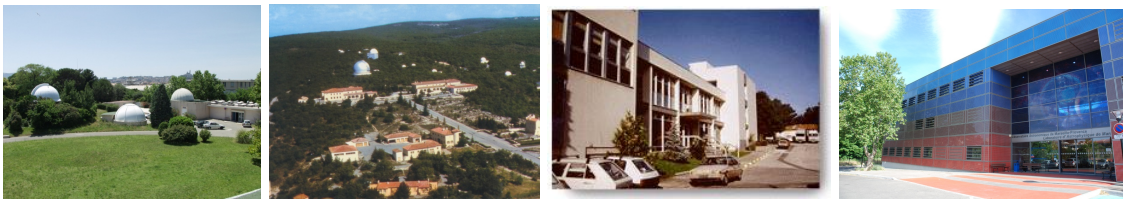

Figure 1. De gauche à droite : site longchamp (Marseille), vue aérienne de l'OHP (Saint-Michel l'observatoire), Bâtiments du LAS, Site Château-Gombert).

[1] OSU Institut Pythéas, 38 rue F. Joliot-Curie, 13388 Marseille Cedex 13, France

Les fonds patrimoniaux	Localisation
Archives, ouvrages et instruments anciens	Site Longchamp
Archives contemporaines (Observatoire de Marseille et LAS)	Site Longchamp
Instruments contemporains (<1950) (incluant le spatial)	Site Longchamp, OHP, Aix-Marseille Université Site Saint-Charles
Clichothèque	OHP
Patrimoine immobilier (bâtiments, coupoles)	Site Longchamp, OHP

Figure 2. Localisation des fonds patrimoniaux

2 Actions réalisées

2.1 Gestion des collections 1995-2012

- 1995-1999 : Tri, classement, inventaire et microfilmage des archives anciennes (XVIIIème siècle-1950) par les Archives départementales des Bouches-du-Rhône : 52 pages d'inventaire. Compte-tenu de l'importante source historique qu'il représente, ce fonds est destiné à être conservé avec la collection d'instruments anciens
- 1996 : Opération pilote de l'Inventaire général du patrimoine culturel à Marseille « *recenser, étudier et faire connaître le patrimoine français* ». Utilisation d'une grille de critères adaptée au patrimoine scientifique et astronomique 2001 : environ 60 notices versées sur la base du Ministère de la Culture « Palissy ». Prises de vues, caractéristiques techniques, historique de l'objet.
- 2003 : Classement de 22 instruments anciens au titre des Monuments Historiques.
  « *Les objets mobiliers, soit meubles proprement dits, soit immeubles par destination, dont la conservation présente, au point de vue de l'histoire, de l'art, de la science ou de la technique, un intérêt public peuvent être classés au titre des monuments historiques par décision de l'autorité administrative.* » art. L622-1 du code du patrimoine
  Les propriétaires d'objets classés MH sont tenus : *i*) d'assurer leur bonne conservation *ii*) d'effectuer un récolement au moins tous les 5 ans.
- 2009-2011 : Numérisation et mise en ligne des archives anciennes par le Centre de Conservation du Livre d'Arles (CCL). Partenariat dans le cadre du projet Internum, cofinancé par l'UE et la région PACA. Plus de 100 000 fichiers disponibles sur `www.e-corpus.org/oamp`.
- Février 2011 : Création et réunion d'un Comité de Réflexion sur le patrimoine astronomique du plateau Longchamp sur le site historique de l'Observatoire de Marseille. Rapport final établit en juillet 2011

2.2 2008-2012 : le '« chantier » des réserves sur le site Longchamp

- 2008 : Suite au départ des équipes, stockage du fonds contemporain (archives papier, photographies sur plaques de verre, instruments...) au sous-sol du bâtiment C.
- 2010-2011 : nécessité de vider le sous-sol du bâtiment C en vue de la restructuration des locaux pour les besoins de l'IMéRA (Institut Méditerranéen de Recherches Avancées).
  Tri, conditionnement de 50 cartons d'archives scientifiques, 20 cartons d'archives administratives et techniques prises de vues, mesures, afin de préparer les futurs espaces de conservation.
- 2012 : Déménagement des collections dans les réserves actuelles situées au rez-de-chaussée du bâtiment D.

Figure 3. Site internet et exemple de document scanné par le CCL.

2.3 Valorisation des collections

- Tricentenaire de l'Astronomie en Provence (2002) : Réalisation d'un CD-ROM : présentation des instruments à partir des clichés réalisés lors de la campagne de l'Inventaire général. Organisation d'un colloque sur l'histoire de l'astronomie à Marseille et en Provence
- Expositions temporaires 2009-2010 : *Telescopium, 400 ans de lunettes et de télescopes* (en collaboration avec le Museum d'Histoire Naturelle de Marseille)
- 2009 : Année mondiale de l'astronomie, organisation d'expositions par les BU de Saint-Charles (Université de Provence) et d'Avignon
- Septembre 2011 : « *Objets et Histoire des Sciences. 100 ans de la faculté des Sciences de Saint-Charles* »
- Juillet-octobre 2011 : « *La Mémoire vivante* », Saint Michel l'Observatoire.
  Prêts d'instruments et d'ouvrages anciens. Réalisation de vidéos de présentation des instruments exposés.
- 2012 : Réalisation du catalogue de l'exposition Telescopium

2.4 Patrimoine de l'OHP

Environ 160 instruments et objets inventoriés (télescopes, spectrographes, oculaires, machines à mesurer) par Sergio Ilovaisky (Directeur de Recherche) consultables en ligne : `http://www.obs-hp.fr/histoire/histoire.shtml` 263 clichés de l'OHP figurent dans la base « *Mémoire* » du Ministère de la Culture.

2.5 Patrimoine du LAS

2010 : inventaire réalisé par le CNES (Centre National d'Etudes Spatiales) sous l'égide du service patrimoine de l'OAMP .

3 Actions en cours

Mesures de conservation préventive et élaboration d'un document général d'inventaire regroupant les collections du patrimoine astronomique provençal.

4 Projets

2012–2014 est une phase de transition :

Lunette équatoriale à monture allemande lors de l'expédition à Guelma, 1905
Photo Observatoire de Marseille

Vue générale de l'instrument
Photo Marc Heller

Lunette équatoriale à monture allemande

Lieu de conservation : Marseille, Observatoire
Date : 1803
Auteur (s) : Bellet, fabricant
Matériaux : laiton, acier, verre
Dimensions : hauteur 82cm ; longueur 76cm ; largeur 30cm ; longueur de la lunette : 135cm

N° inventaire : CM25/MH1564

Cette lunette, à monture allemande, a un objectif fabriqué par Dollond, de 9 cm de diamètre et 140 cm de distance focale. Sa monture, datée de 1803, a été construite par Bellet (élève de Lenoir), et dispose d'un réglage permettant de l'utiliser à différentes latitudes. Grâce à cela, elle a pu être été utilisée par des astronomes de l'Observatoire de Marseille lors d'une expédition à Guelma, en Algérie, le 30 août 1905. Il s'agissait d'aller observer une éclipse totale de Soleil et l'expédition était dirigée par Edouard Stéphan, directeur de l'Observatoire de Marseille.

10

Figure 4. Extrait du catalogue de l'exposition *Telescopium*.

- Sécurisation des espaces de stockages actuellement occupés sur le site Longchamp
- Réflexion sur un projet d'envergure permettant la valorisation des collections en les conservant sur le site historique de l'Observatoire de Marseille

Volonté de continuer à faire vivre l'exposition *Telescopium* (itinérance)

SF2A 2012
S. Boissier, P. de Laverny, N. Nardetto, R. Samadi, D. Valls-Gabaud and H. Wozniak (eds)

PERROTIN ET LA MEILLEURE MESURE FRANÇAISE DE LA VITESSE DE LA LUMIÈRE

G. Bogaert[1] and W. Blanc[2]

Résumé. À la fin du $19^{ème}$ siècle, la détermination de la vitesse de la lumière a fait l'objet d'une controverse scientifique impliquant d'éminents scientifiques français et américains : Alfred Cornu et Hippolyte Fizeau, d'un côté, Simon Newcomb et Albert Michelson de l'autre. Cette controverse prendra fin de façon inattendue avec les deux mesures réalisées en 1898 et 1902 par Henri Perrotin, le directeur de l'Observatoire de Nice.

Keywords: Henri Perrotin, Alfred Cornu, Observatoire de Nice, vitesse de la lumière

1 La vitesse de la lumière pour déterminer la taille du système solaire

En 1874, Cornu, soutenu par Fizeau, réalise une nouvelle mesure la vitesse de la lumière à la demande de Le Verrier. Après avoir étudié attentivement les dispositifs de Fizeau (roue dentée) et de Foucault (miroir tournant), il construit un nouveau dispositif à roue dentée, plus sophistiqué que celui de Fizeau mais permettant des mesures plus précises. 1874 est aussi l'année du passage de Vénus devant le Soleil, et plus de cent expéditions d'astronomes des grandes nations se dispersent une fois de plus sur le globe, pour déterminer les dimensions du Monde. La mesure de Cornu permettra à Le Verrier de pester contre ces expéditions coûteuses devenues inutiles, les dimensions du Monde étant désormais mieux connues sans quitter Paris !

Sa mesure de la vitesse de la lumière, avec une précision meilleure que 1/1000, et l'article qui la détaille, un monument de 300 pages (Cornu 1876), lancent sa carrière qui sera exceptionnelle. Cornu, jeune professeur de physique à Polytechnique, présidera plus tard la Société Française de Physique, le Bureau des Longitudes, l'Académie des Sciences, et atteint un prestige rarement égalé. Mascart, lors de ses funérailles, dira : « M. Cornu avait conquis la plus haute situation scientifique, consacrée par les suffrages des Académies du monde entier. »

2 Le désaccord franco-américain

Après les travaux de Cornu, de nouvelles tentatives de mesures ont lieu, hors de France. Forbes et Young tentent une mesure en 1882, mais leurs résultats seront aisément disqualifiés. Entre 1877 et 1883, Albert Michelson, alors jeune instructeur à la US Navy, et Simon Newcomb, tous deux en utilisant la méthode du miroir tournant de Foucault, obtiennent un résultat 5 fois plus précis et strictement incompatible avec celui de Cornu. Newcomb rapporte une valeur de 299 810 $\pm$ 50 km s^{-1}, celle de Cornu étant de 300 400 $\pm$ 300 km s^{-1}, les valeurs d'incertitudes indiquant les valeurs extrêmes admissibles.

Pour Fizeau et Cornu, la méthode du miroir tournant pose plusieurs questions théoriques auxquelles personne ne sait répondre. C'est la raison pour laquelle Cornu a préféré la méthode de la roue dentée : est-on sûr que l'éther ne modifie pas la vitesse de la lumière quand le mouvement du faisceau balaye l'espace à une vitesse du même ordre de grandeur ? Par ailleurs, comment s'ajoute ou se retranche la vitesse du miroir tournant à celle de la lumière ? En 1900, lors du Congrès International de Physique, qu'il présidera, Cornu argumentera ainsi pour conclure que les erreurs affichées par les américains sont très sous-estimées.

[1] ARTEMIS, UNS-OCA-CNRS, 06304 Nice Cedex 3
[2] Université de Nice Sophia-Antipolis, Laboratoire de Physique de la Matière Condensée, CNRS UMR7336, Parc Valrose, 06108 Nice Cedex 2, France

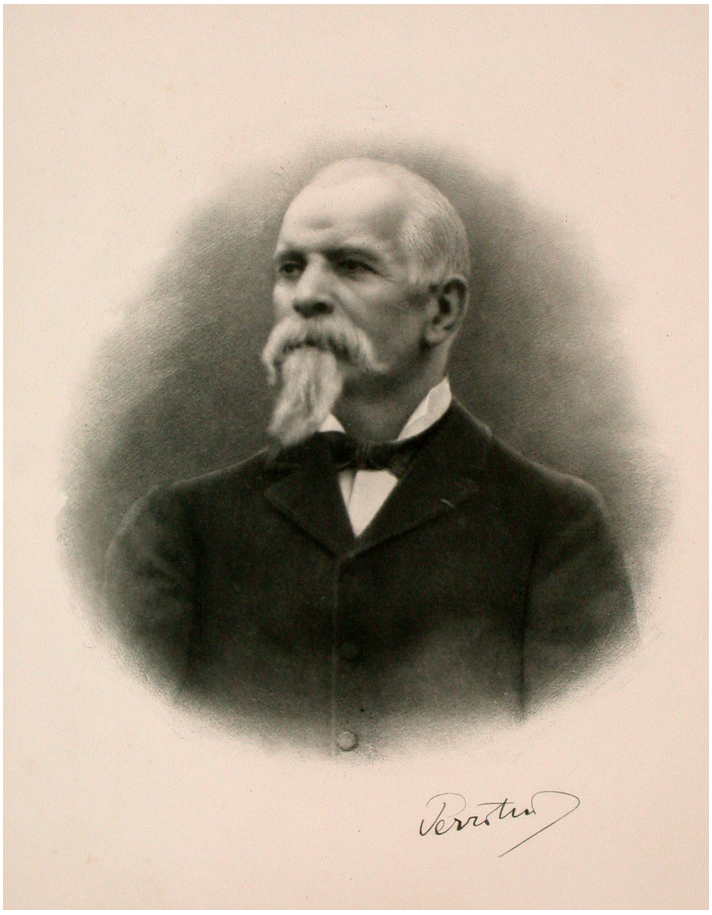

Figure 1. Portrait de Perrotin, archives de l'Observatoire de la Côte d'Azur. Cliché Marc Heller @ Observatoire de la Côte d'Azur.

3 Les mesures de Henri Perrotin

En 1881, Raphaël Bischoffsheim fonde l'observatoire de Nice et nomme à sa tête Henri Perrotin. Sous son impulsion, le tout jeune observatoire livre une impressionnante moisson de données sur les étoiles doubles, comètes, astéroïdes, nébuleuses. En 1897, Perrotin décide ensuite de profiter de la qualité exceptionnelle des instruments de l'Observatoire pour se lancer dans une aventure plus apte que toute autre à faire connaître et reconnaître l'Observatoire de Nice : la détermination de la vitesse de la lumière.

Entre 1898 et 1904, Henri Perrotin (Figure 1) procède aux mesures, avec Stéphane Javelle et Maurice Prim, deux jeunes astronomes de l'Observatoire de Nice (Bogaert & Blanc 2012). Ils utilisent le dispositif de roue dentée d'Alfred Cornu, que celui-ci fait rénover pour l'occasion. Cornu prête son matériel, explique son maniement, apporte quelques conseils, exécute deux mesures avant de repartir à Paris en laissant les niçois en effectuer des milliers. Elles sont effectuées en 1898 sur un parcours aller-retour entre l'Observatoire de Nice et La Gaude, distants de 12 km (Figure 2), au prix de nombreuses difficultés. Bien qu'utilisant le même matériel que Cornu, le résultat diffère de celui obtenu par ce dernier, et s'approche plutôt de celui des américains. Ils ne seront publiés (Perrotin 1900) que fin 1900 après une deuxième mesure de la distance par triangulation en présence de Cornu (en mai 1900), et même après le congrès de Physique (qui s'est tenu en août). Les mesures suivantes entre l'Observatoire de Nice et le Mont Vinaigre à 46 km ont lieu en 1902, mobilisant la grande lunette de l'Observatoire pendant un an (Perrotin 1902, 1908). Les mesures de distance sont dirigées en parallèle par Martial Simonin.

Les deux séries de mesures conduisent à des résultats voisins et une moyenne de 299 880 km s^{-1} ramenée au vide (la vitesse de la lumière a été fixée en 1983 à 299 792 458 m s^{-1}), avec une précision finale meilleure que 50 km s^{-1}, en désaccord avec le résultat de Cornu, mais en accord avec les mesures d'Albert Michelson et Simon Newcomb, de précision similaire.

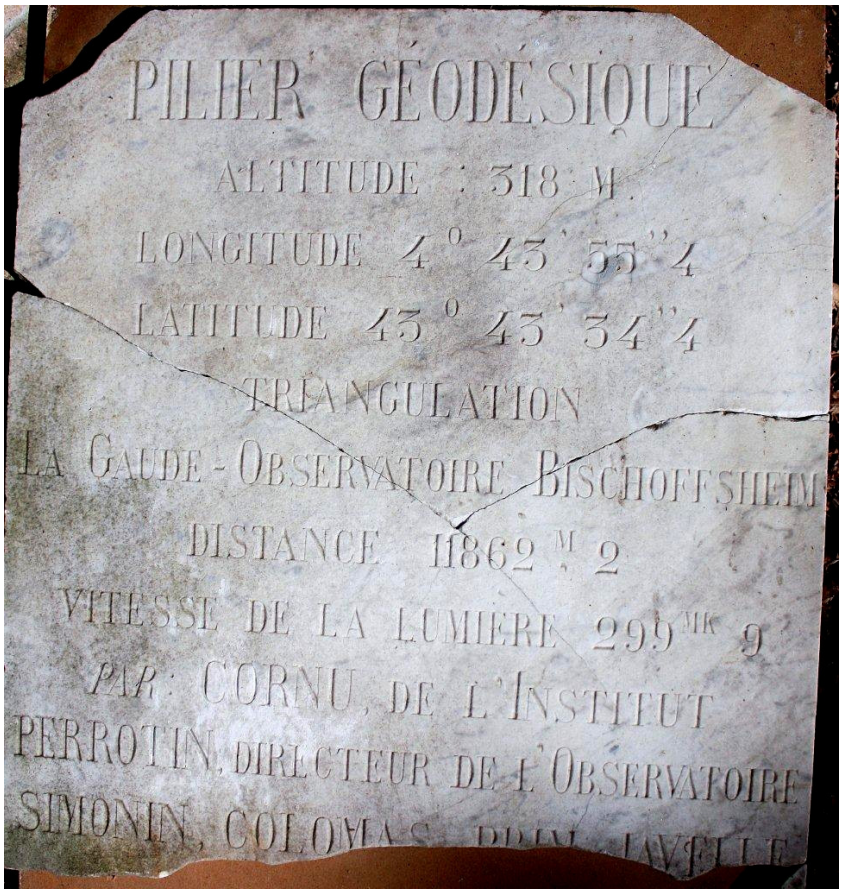

Figure 2. Plaque commémorative de la mesure de la vitesse de la lumière entre La Gaude et l'Observatoire de Nice. Crédits photos Élizabeth Choleva.

Afin d'augmenter de façon radicale la précision de sa mesure, Perrotin prépare la dernière phase de l'expérience : il envisage un trajet de 500 km aller-retour entre le Mont Mounier (Alpes-Maritimes) et le Monte Cinto en Corse. Son décès soudain, en février 1904, aura raison de cette expérience audacieuse et grandiose.

4 Épilogue

Les archives donnent l'occasion de se pencher sur l'histoire méconnue de l'Observatoire de Nice, le plus grand, le mieux équipé des observatoires de l'époque, et d'exhumer l'œuvre de Perrotin, son premier directeur. Son travail sur la vitesse de la lumière a fait référence dans la littérature mondiale durant des années, comme la meilleure mesure française de la vitesse de la lumière, et finalement la seule qui compte. Pourtant, H. Perrotin, malgré cette reconnaissance internationale, reste méconnu en France.

Elle montre aussi l'irruption de facteurs humains dans le fonctionnement policé de la science, lors d'un conflit d'intérêt spectaculaire. Celui-ci sera dramatique pour Cornu au plan personnel, et privera Perrotin de la reconnaissance et des honneurs, qu'il espérait, pour lui-même et pour l'Observatoire de Nice.

Références

Bogaert G. & Blanc W. 2012, L'Astronomie, 53, 33
Cornu A. 1876, Annales de l'Observatoire de Paris, Mémoires, Tome XIII
Perrotin H., 1900, CRAS, 131 (19), 96
Perrotin H. 1902, CRAS, 135, 881
Perrotin H., Prim M. 1908, Annales de l'Observatoire de Nice, 11

SF2A 2012
S. Boissier, P. de Laverny, N. Nardetto, R. Samadi, D. Valls-Gabaud and H. Wozniak (eds)

À QUOI DOIT SERVIR LE PATRIMOINE ASTRONOMIQUE FRANÇAIS ?

J. Caplan[1] and B. Vila[2]

Résumé. Les deux auteurs, l'un astronome l'autre botaniste (et chargé de mission « patrimoine » de l'université d'Aix-Marseille), présentent quelques idées sur la gestion des collections historiques d'astronomie, dans un contexte universitaire. Nous mettons en avant la spécificité de ces collections par rapport à celles des musées traditionnels et leur importance pour l'histoire des sciences notamment. Nous rappelons également la nécessité de suivre la déontologie « muséale » soutenue par l'association Universeum, réseau européen pour le patrimoine universitaire. Enfin nous rappelons le rôle essentiel que jouent les réserves et la nécessité de travailler en collaboration.

Keywords: patrimoine, déontologie, histoire des sciences

1 Introduction

Bien que l'un de nous a beaucoup et depuis longtemps travaillé avec les collections astronomiques marseillaises, nous ne rentrons pas dans les détails de celles-ci. Nous proposons – avec un peu de provocation ! – des suggestions générales pour les collections des observatoires français.

2 Le contexte universitaire

Nos observatoires français, autrefois autonomes, sont aujourd'hui intégrés dans, ou étroitement liés avec, des universités. Il est donc normal, et même utile, que les observatoires conservent leur patrimoine en coordination avec les autres unités de leurs universités. Nous pensons que – à l'instar d'universités réputées ailleurs en Europe – les musées et collections universitaires doivent, d'une part, bénéficier d'une séparation raisonnable des collections selon les disciplines, et d'autre part être chapeautés par un service universitaire approprié. La séparation des disciplines est nécessaire pour assurer une gestion professionnelle spécifique (on ne conserve pas les instruments d'astronomie de la même façon que les spécimens des herbiers). Et un service central est souhaitable pour fournir de l'aide, des conseils et une coordination *professionnelle*, et également – dans le contexte de pénurie actuel – un personnel au service de l'ensemble pour les besoins qui ne sont pas quotidiens.

La fréquentation d'Universeum (`http://Universeum.it/`) nous a appris que les musées et collections jouent un rôle important dans l'intégration (du personnel et des étudiants) dans une université. Cela se constate dans le cas des universités comme Oxford, Cambridge et Harvard, qui possèdent de nombreux musées, dans divers domaines des sciences exactes, des sciences humaines et sociales, des lettres et des arts. Bien que les musées soient ouverts au public et de ce fait communiquent une image culturelle positive de l'université, ils ne sont pas pour autant rattachés à son service de communication mais aux diverses disciplines, et ils sont gérés par des universitaires. En fait, les musées universitaires sont importants surtout pour leur impact « interne », envers la communauté universitaire, comme intégrateurs et porteurs d'identité commune.

[1] Aix Marseille Université, CNRS, Laboratoire d'Astrophysique de Marseille, UMR 7326, 13388, Marseille, France
[2] Aix Marseille Université, CNRS, Institut méditerranéen d'Écologie et de Biodiversité, UMR 6273, 3 place V. Hugo, 13331 Marseille cedex 3, France

3 À quoi doit servir le patrimoine astronomique français ?

Par comparaison aux musées qui n'exposent que des objets et documents conservés en dehors de leur contexte d'usage et dont le sens est par conséquent amoindri, les collections universitaires conservées dans leurs lieux d'usage permettent de considérer le site comme un ensemble qui comprend toutes les expressions des activités scientifiques qui y ont été conduites. Ceci confère aux collections universitaires une valeur exceptionnelle. Ainsi, nous pensons que, dans un contexte universitaire, ce patrimoine doit servir en premier lieu pour l'*histoire* de l'astronomie, surtout la recherche mais également pour l'enseignement et la diffusion de cette discipline.

Le patrimoine *ne doit pas* servir de simple « accessoire de théâtre » pour décorer des expositions sur l'astronomie (ou autre chose), sauf exception et seulement si l'objet ancien est vraiment pertinent, et si le risque pour l'objet est vraiment négligeable. Ce patrimoine est souvent très fragile. Une pièce perdue ne se remplace pas comme celle d'un instrument moderne. Et le vol est un danger réel. Ainsi les objets classés « MH » ne doivent pas être déplacés sans l'accord du conservateur des monuments historiques.

Le patrimoine n'est pas un simple outil de promotion des sciences ! Nous pensons que toute utilisation et déplacement frivole est à proscrire.

D'ailleurs, il est probablement contre-productif d'exposer des objets sans pertinence, surtout dans des conditions non idéales. Vous gagnerez peut-être bien en célébrité facile auprès du grand public, mais vous perdrez certainement en réputation auprès d'un public doué de plus de discernement, pour lequel les « relations publiques » seront mieux servies en réservant les objets historiques pour des bonnes expositions où les questions historiques sont traitées correctement.

En d'autres termes, il convient d'exposer ce patrimoine de manière rationnelle et réfléchie. Tout ceci sous-entend de suivre les principes élémentaires de la déontologie muséale.

4 La déontologie muséale

Ainsi, certaines règles peuvent paraître contraignantes ! Mais ces règles n'ont pas été inventées par nous-mêmes ! Nous les avons apprises après de longues fréquentations avec des conservateurs et notamment des spécialistes des instruments scientifiques. Elles correspondent grosso modo aux règles exposées dans les manuels de déontologie muséale que l'on trouve facilement sur le Web. En particulier, plusieurs bonnes publications émanent des organismes muséaux canadiens, ainsi que des organismes tels l'International Council of Museums (ICOM) et son comité « University Museums and Collections » (UMAC). Au niveau européen, l'association Universeum (`http://Universeum.it/`) met en contact des responsables de collections universitaires de nombreux pays. De plus, la revue française bimensuelle « Lettre de l'OCIM » (Office de Coopération et d'Information muséales) publie très souvent des rapports de collections universitaires.

Dans le même esprit, une recommandation du Conseil de l'Europe du 7/12/2005, vise « à définir les lignes directrices et les bonnes pratiques en matière de gouvernance et de gestion du patrimoine des universités européennes » (`http://universeum.it/docs/RecommendationRec(2005)13_FR.pdf`). Universeum, en particulier, s'appuie sur cette recommandation.

Ces questions de déontologie muséale nous amènent à nous poser des questions sur les entrées des objets dans les collections.

5 Le problème de « quoi garder »

C'est un problème très grave. Nous l'avons vu récemment à Marseille au moment des déménagements. Il ne faut pas oublier tous les objets qui *ne sont pas* les chefs d'œuvre dont nous a parlé Emmanuel Pécontal ! Le problème se présente d'une façon différente dans un musée « ordinaire », avec une collection acquise par achat, par don, etc. (comme pour la plupart des grands musées). Certes, un tel musée ne peut pas tout acquérir. Il est normal que, dans ce cas, un conservateur choisisse selon sa politique, la conjoncture, son goût...

Mais avec des collections comme les nôtres où les choses sont là simplement parce qu'elles ont servi dans un laboratoire universitaire ou un observatoire, la question est différente. La valeur d'une collection est souvent davantage liée à sa cohérence qu'à la valeur des objets individuels. Et si on considère que le patrimoine comprend non seulement les instruments mais également les archives, les livres et autres objets, et même l'immobilier et les terrains qui sont un ensemble historique, la question « quoi garder » devient vraiment difficile ! Surtout que dans la pratique le responsable d'une collection doit souvent décider sur-le-champ d'acquérir un objet (mais où le mettre ?) ou le laisser, sachant qu'il sera jeté dans une benne quelques heures plus tard.

Comme ce problème extrêmement difficile se pose dans toutes les universités, l'association européenne Universeum a créé le *groupe de travail* « Recent Heritage of Science », auquel nous deux faisons partie, pour étudier ces questions. Parmi les choses en discussion est la constitution d'un lieu appelé « purgatoire », où un objet *susceptible* d'intégrer une collection peut être entreposé, vu et étudié, dans de bonnes conditions (et non empilé par terre dans le noir), pendant assez longtemps pour que des spécialistes puissent consulter avant de décider de le faire entrer officiellement dans la collection – situation difficilement révocable – ou de le rejeter.

Il est important de se rappeler que le patrimoine d'un observatoire n'est pas uniquement constitué d'instruments, et que les questions concernant les autres composantes que sont les livres et les archives passent par un contrôle où l'ensemble est coordonné – ce qui fera intervenir d'autres spécialistes et/ou historiens.

6 La charrue avant les bœufs

Au moment où l'on se soucie de plus en plus du patrimoine astronomique, la pression de l'« exploiter » augmente. En l'absence de salles d'exposition, on préconise souvent de montrer les instruments par-ci, par-là, parfois dans un contexte loin de l'histoire de ces instruments et même de l'astronomie. Il faut, bien sûr, réaliser de vraies salles d'exposition. Mais il ne faut pas aller trop vite ! Une salle d'exposition qui n'est pas conforme aux règles de sécurité et de bonne conservation n'est pas acceptable. Et même si les salles sont conformes, a-t-on pensé aux réserves ? Elles sont *essentielles*. Il faut réaliser des réserves, de préférence « visitables », *avant* le reste ou éventuellement en même temps. Et il faut qu'elles soient conformes aux normes de sécurité et de conservation du matériel en question.

Il est acceptable d'avoir des réserves – surtout visitables – *sans* salles d'exposition, mais il est inacceptable de faire des salles d'exposition sans réserves. La conservation et la protection des objets est d'une importance absolue ; elle ne peut pas attendre des jours meilleurs tandis qu'une collection (il y a beaucoup d'exemples) peut très bien survivre en parfait état pendant des années sans être vue (ce n'est pas l'idéal, bien sûr !). Il y a une autre raison pour donner priorité aux réserves : c'est tout simplement que dans des collections comme les nôtres on ne souhaite pas exposer l'ensemble du matériel en même temps. Ainsi beaucoup de choses doivent être conservées pour leur intérêt historique, même si elles ne seront jamais exposées. Au Musée des Arts et Métiers, par exemple, il n'y a que quelques pour cent des objets exposés à Paris, les autres restant dans les réserves de Saint-Denis.

7 Les historiens des sciences – où sont-ils ?

Si votre université comporte des historiens des sciences parmi ses enseignants-chercheurs, vous pouvez très utilement les associer au travail sur le patrimoine astronomique. S'ils s'intéressent aux aspects matériels des sciences, notamment aux instruments mais également aux institutions (comme les observatoires) cela peut les intéresser au plus haut degré. Mais s'ils ne s'intéressent qu'aux aspects purement théoriques ou philosophique des sciences il faudra chercher ailleurs !

Il se trouve qu'au Centre François Viète de l'université de Nantes des historiens des sciences ont déjà beaucoup travaillé sur les observatoires et leurs instruments, et sont prêts à collaborer avec les observatoires sur ces questions (voir à ce sujet la communication de G. Boistel et S. Tirard dans ce volume, session S21, p. 769).

8 Conclusion

Nous espérons que cette communication intentionnellement provocatrice puisse encourager les acteurs du patrimoine des observatoires à nouer des liens avec d'autres disciplines universitaires, notamment l'histoire des sciences, et avec des professionnels du patrimoine et des musées, pour que ces collections de grande valeur historique ne soient pas gaspillées pour des utilisations frivoles.

SF2A 2012
S. Boissier, P. de Laverny, N. Nardetto, R. Samadi, D. Valls-Gabaud and H. Wozniak (eds)

LE GROUPE D'HISTOIRE DE L'ASTRONOMIE DU CENTRE FRANÇOIS VIÈTE DE L'UNIVERSITÉ DE NANTES, ET LE PATRIMOINE ASTRONOMIQUE

G. Boistel[1] and S. Tirard[1]

Résumé. Le Groupe d'Histoire de l'Astronomie (GHA) du Centre François Viète d'histoire et des techniques de l'Université de Nantes, travaille et publie régulièrement des travaux de recherche depuis l'année 2000 dans les domaines de l'histoire des observatoires astronomiques et des observatoires navals, civils ou militaires, et des questions liées à la sauvegarde du patrimoine. Ces recherches se font en collaboration avec des astronomes acteurs de la sauvegarde du patrimoine des observatoires (observatoires de Marseille, de Nice, de Bordeaux notamment). Au sein du Centre François Viète existe une expertise sur les questions patrimoniales qui doit permettre d'accompagner les astronomes dans la réflexion portant sur la sauvegarde des archives et des instruments des observatoires, ainsi que sur leur valorisation auprès de différents publics.

Keywords: History of science, history of astronomy, nautical astronomy, heritage

1 Introduction

Le Groupe d'histoire de l'astronomie (GHA) du Centre François Viète s'est constitué en 2000 autour du Professeur émérite Jacques Gapaillard, ancien professeur de mathématiques et d'histoire de l'astronomie à l'Université de Nantes. Certains d'entre nous ont fait leur thèse sous sa direction (Guy Boistel et Colette Le Lay).

Durant l'année 2000, Jacques Gapaillard et Olivier Sauzereau ont participé activement à la sauvegarde de l'ancien observatoire de la Marine de Nantes, en agissant auprès de la DRAC et du service culturel de la Ville. Olivier Sauzereau a contribué à restituer un pan entier d'une histoire qui avait été oubliée : celle des observatoires de la Marine en France au cours du XIXe siècle, Guy Boistel attaquant cette même histoire de manière indépendante sous l'angle de l'enseignement de l'astronomie nautique dispensée aux marins et de l'histoire des éphémérides astronomiques et nautiques depuis la moitié du XVIIIe siècle, en restituant notamment une histoire de la *Connaissance des temps*.

2 Histoire des observatoires et patrimoine astronomique

En Juin 2001, le GHA a organisé un premier colloque « Observatoires et patrimoine astronomiques français » qui a rassemblé des historiens, des astronomes et des acteurs de la sauvegarde du patrimoine astronomique des observatoires : James Caplan pour l'OSU de Marseille, Françoise le Guet-Tully pour l'observatoire de Nice et Frédéric Soulu pour l'Académie des sciences et l'observatoire d'Abbadia à Hendaye. Un ouvrage a été publié en 2005 par la Société Française d'Histoire des Sciences et des Techniques et l'ENS de Lyon sous la direction de Guy Boistel.

Ce travail a été en partie poursuivi dans l'ACI « *Savoirs et techniques de l'observatoire* » dirigée par David Aubin pendant six ans. Ces recherches n'ont malheureusement pas abouti à l'ouvrage programmé mais elles ont favorisé des rencontres, des 'echanges et un certain nombre de travaux doctoraux, comme ceux de Laetitia Maison sur l'observatoire de Bordeaux au XIXe siècle, de Jérôme Lamy sur l'ancien observatoire de Toulouse (XVIIIe-XIXe siècles), de Stéphane Le Gars sur les débuts de l'astronomie physique ou de l'astrophysique en France (1870–1900), d'Arnaud Saint-Martin sur l'astronomie française au début du XXe siècle (1900–1940),

[1] Centre François Viète, Université de Nantes.

ou encore des recherches de Guy Boistel sur l'observatoire de la Marine et du Bureau des longitudes au parc Montsouris, créé par Ernest Mouchez en 1875.

Le colloque de Bordeaux organisé en 2008 par Jérôme de la Noë et Caroline Soubiran, « *La (re)fondation des observatoires sous la IIIe République* » fut une rencontre s'inscrivant dans la lignée de ces travaux ; un certain nombre de recherches entreprises au GHA ou au sein de l'ACI de David Aubin, y ont trouvé leur plénitude et un certain aboutissement.

Récemment, le GHA a organisé des rencontres autour du patrimoine scientifique et astronomique, dans le cadre du séminaire hebdomadaire du Centre Viète. Ces échanges ont donné lieu à une publication récente, en 2011, dans les Cahiers François Viète : « *Patrimoine scientifique : le temps des doutes ?* » (Cahiers F. Viète, série II, n°3, 2010) où l'on y trouve des contributions de Jérôme Lamy, Frédéric Soulu, Sébastien Soubiran, Arnaud Saint-Martin et Olivier Sauzereau[i]. Guy Boistel travaille actuellement à un livre regroupant des exposés sur les relations entre les observatoires astronomiques et les sciences maritimes, suite au colloque organisé en novembre 2010 à Nantes par G. Boistel et O. Sauzereau « *Entre Ciel et Mer. Des observatoires pour l'astronomie et les sciences maritimes* ». Ce colloque est né de la constatation que certains observatoires navals européens au XIXe siècle ont contribué à certaines découvertes astronomiques (petites planètes, comètes) et se sont assez rapidement tournés vers l'océanographie ou la géophysique au début du XXe siècle (Bidston à Liverpool, Hambourg, pour les cas les plus marquants).

Enfin, Le GHA s'est associé à Madame Martina Schiavon, MCF en histoire des sciences aux Archives Poincaré de l'Université de Nancy-2, et au Bureau des longitudes, pour déposer un projet de numérisation et d'exploitation scientifique des procès-verbaux des séances du Bureau des longitudes sur la période 1795–1930 (projet CORPUS ou ANR en cours d'élaboration, et dépôt prévu en 2013-2014).

Enfin, Olivier Sauzereau achève actuellement une thèse très importante restituant l'histoire des observatoires chronométriques des ports militaires français au XIXe siècle, à partir d'une exploration inédite de fonds d'archives français (soutenance prévue à l'Automne 2012).

Le GHA est ainsi très impliqué dans la restitution de l'histoire récente des observatoires astronomiques et navals français, ainsi qu'aux questions relevant du patrimoine, d'autant plus que Jean-Louis Kerouanton, MCF en histoire des techniques au Centre Viète, vient d'être nommé vice-président de l'Université de Nantes pour les questions patrimoniales.

Il existe donc au sein du Centre Viète une réelle expertise sur ces questions, expertise renforcée par un réseau de connaissances et d'acteurs du patrimoine lui permettant d'accompagner les astronomes dans la réflexion sur les problèmes posés par la sauvegarde, le classement des archives ou des instruments astronomiques et leur valorisation auprès de différents publics.

3 Vers une action concertée entre historiens et astronomes

Le GHA souhaite participer et être associé à des actions locales ou nationales sur la sauvegarde du patrimoine astronomique français. Il reste de nombreux travaux historiques à mener pour mieux mettre en perspective certaines activités des observatoires de Lyon, de Besançon, ou de Strasbourg notamment, ou encore explorer les histoires récentes des observatoires de Nice ou de Marseille par exemple. Ces travaux nécessitent des actions claires concernant la sauvegarde et la valorisation des archives et de l'instrumentation de ces observatoires, ainsi que leur mise à disposition des chercheurs.

Seule une collaboration concertée entre les directions des observatoires et de l'INSU, des astronomes et des historiens des sciences impliqués dans ces recherches, permettra de réelles avancées sur ces questions.

[i]Ce numéro peut être demandé facilement en s'adressant à Stéphane Tirard, directeur du Centre F. Viète ou à défaut, à moi-même.

Author Index